IGARSS'97

1997 International Geoscience and Remote Sensing Symposium

03-08 August 1997

Singapore International Convention & Exhibition Centre • Singapore

Remote Sensing -- A Scientific Vision for Sustainable Development

DISTRIBUTION STATEMENT A
Approved for public release
Distribution Unlimited

19970801 014

Volume I

IEEE Catalog Number: 97CH36042
Library of Congress Number: 97-70575

DTIC QUALITY INSPECTED 1

1997 IEEE INTERNATIONAL GEOSCIENCE AND REMOTE SENSING SYMPOSIUM

Editor: Tammy I. Stein
Production: IEEE Publications

Copyright and Reprint Permissions: Abstracting is permitted with credit to the source. Libraries are permitted to photocopy beyond the limits of U.S. copyright law for private use of patrons those articles in this volume that carry a code at the bottom of the first page, provided the per-copy fee indicated in the code is paid through the Copyright Clearance Center, 222 Rosewood Drive, Danvers, MA 01923. For other copying, reprint, or republication permission, write to the IEEE Copyright Manager, IEEE Service Center, 445 Hoes Lane, Piscataway, NJ 08855-1331. All rights reserved. Copyright © 1997 by The Institute of Electrical and Electronics Engineers, Inc.

IEEE Catalog Number:	97CH36042 (softbound) 97CB36042 (casebound)
Library of Congress Number :	97-70575
ISBN Softbound:	0-7803-3836-7
ISBN Casebound:	0-7803-3837-5
ISBN Microfiche:	0-7803-3838-3
CD-ROM:	0-7803-3839-1
ISSN:	N/A

Additional copies of this publication are available from the following source:

IEEE Operations Center
P. O. Box 1331
445 Hoes Lane
Piscataway, NJ 08855-1331 USA

1-800-678-IEEE
1-908-981-1393
1-908-981-9667 (FAX)
833-233 (Telex)
email: customer.services@ieee.org

IGARSS'97

1997 International Geoscience and Remote Sensing Symposium

03-08 August 1997

Sponsors

IEEE Geoscience and Remote Sensing Society

Centre for Remote Imaging, Sensing and Processing
The National University of Singapore

National Aeronautics and Space Administration (NASA)

National Oceanic and Atmospheric Administration (NOAA)

Office of Naval Research (ONR)

International Union of Radio Science (URSI) ... Technical Sponsor

ORGANIZING COMMITTEE

Hock Lim
General Chairman

Tat Soon Yeo
Janet Nichol
Jian Kang Wu
Dayalan Kasilingam
Technical Co-Chairmen

Leong Keong Kwoh
Finance Chairman

Karen Wong
Publicity Chairman

Choong Weng Mak
Ngi Kun Chng
Exhibits Co-Chairmen

Jonnovan Hong
Chiat Keng Yew
Fen He
Local Arrangements Co-Chairmen

Tammy Stein
GRSS
Director of Conferences and Information Services

TECHNICAL COMMITTEE

Alpers, Werner
Aschbacher, Josef
Bechacq, Yves
Blanchard, Andrew J.
Boerner, Wolfgang-Martin
Cracknell, Arthur
Chan, Philip
Chappelle, Emmett W.
Chen, A.J.
Choi, Soon Dal
Chua, Poh Kian
Chuah, Hean Teik
Cumming, Ian
D'Aranjo, Wesley Gerard
Duchossois, G.
Durana, Jim
Forster, Bruce
Friedman, Ami Ben-Shalom
Fung, Adrian
Gasiewski, Albin J.
Gatlin, James A.
Goodenough, David
Guo, Huadong
Gupta, Avijit
Hallikainen, Martti T.
Hardesty, R. Michael
Ho, Anthony
Hong, Ye
Ishimaru, Akira
Jackson, Thomas J.
Kam, Suan-Pheng
Keydel, Wolfgang
Khazenie, Nahid
Khorram, Siamak
Kong, J.A.
Kuga, Yasuo
Lau, William K.M.
Le Toan, Thuy
Lee, Jong-Sen
Lewis, Anthony J.
Liew, Soo Chin
Lin, I-I
Lu, Yi Hui
Lui, Pao Chuen
Luther, Charles
Mariton, Michel
Massonet, Didier
Milne, Anthony K.
Moon, Wooil M.
Murai, Shunji
Nik Nasruddin Mahmood
Njoku, Eni
Ong, Jin Teong
Pampaloni, Paolo
Prati, C.
Quegan, Shaun
Quek, Gim Pew
Rais, Jacob
Reagan, John
Rees, W.G.
Salomonson, Vincent
Schumann, Robert
Shimoda, Haruhisa
Shu, Peter K.
Sieber, Alois
Singh, Kuldip
Su, Guaning
Takagi, Mikio
Tan, Bernard T.G.
Tilton, James C.
Tomiyasu, Kiyo
Tsang, Leung
Ulaby, Fawwaz
Wiesbeck, Werner
Winebernner, Dale
Zhang, Cheng Bo

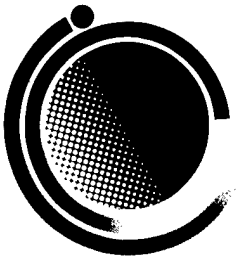

IGARSS'97

1997 International Geoscience and Remote Sensing Symposium

03-08 August 1997

Table of Contents

Interactive Area 1: Aerosols

Aerosol Profile Variations Retrieval Through Kernel Functions in the Oxygen Absorption Band at 762 nm 3
Gabella, M., A. Leone, and G. Perona

Atmospheric Correction of Landsat-TM Images Using Radiative Transfer Code with Image-Extracted Aerosol Optical Depth NA
Kwon, T.Y., K.S. Ryu, S.N. Oh, and H.G. Lee

Seasonality of Ozone Profile at Reunion Island: The Role of Biomass Burning and of Transport 6
Randriambelo, T., S. Baldy and M. Bessafi

Preliminary Aerosols Observations by Lidar Technique at Reunion Island (20.8° S, 55.5°E) NA
Riviere, E., and J. Leveau

Interpretation of Ground-Based Measurements of Atmospheric Aerosols 9
Sano, I., S. Mukai, M. Yasumoto, K. Masuda, M. Sasaki and H. Ishida

Lidar Investigation of Time and Spatial Distribution of the Atmospheric Aerosol in Mountain Valley NA
Savov, P., and I. Kolev

Interactive Area 2: Applications of Radar and SAR Techniques

HF Radar Detection and Tracking of Oil Spills in the Marine Environment NA
Anderson, S.J.

High Spatial Resolution Radar Altimetry for Global Earth Topography Mapping 15
Angino, G., F. Impagnatiello and C. Zelli

Radar-Radiometer Images of the Zone of Underwater Gas Jet Activity NA
Arakelian, A.K.

RA-2 Radar Altimeter: Instrument EM Model Performance Results 18
Zelli, C., F. Provvedi, F. Buscaglione and R. Croci

Ultrawideband Radar Tolerance to Antennas Phase Distortion NA
Cherniakov, M., and L. Donskoi

Combined Radar-Radiometer System for the Earth Surface Remote Sensing and Efficiency of Radar-Radiothermal Images in Environmental Monitoring NA
Hambaryan, A.K., and A.K. Arakelian

Non-Spherical Hydrometeor Signature in Melting Layer Obtained with Ku-Band Multi-Parameter Radar NA
Hanado, H., H. Hiroaki, and H. Kumagai

Relief Restitution by Radargrammetry Using RADARSAT Images: Example in French West Indies 21
Marinelli, L., O. Ferger, L. Laurore and V. Poujade

SARSCAT-A Ground-Based Scattermeter for Space-Borne SAR Applications 24
Wu, J., and B. Sun

"NA" indicates not available at time of printing.

Interactive Area 3: Applications of Remote Sensing

Artificial Recharge Studies Through Remote Sensing in Central Part of Tamil Nadu, India 29
Anbazhagan, S., S.M. Ramasamy and J.M. Edwin

Satellite Remote Sensing of Arctic Marine Mammals Sea-Ice Habitats NA
Belchansky, G.I., I.N. Mordvintsev, V.G. Petrosian, W.G. Garner and D.C. Douglas

Global Survey of Jet Contrails Using AVHRR Data: Spatial Distributions and Optical Property Retrievals 32
Kliche, D.V., J. Chou, J.M. Weiss, S.A. Christopher, R.M. Welch, T. Berendes and K.S. Kuo

Reception Condition of Optimization in the Case of Simulated by the Regression Models Earth Surface Parameters Esitmation by Passive Remote Sensing NA
Kravchenko, V.F., V.K. Volosyuk and V.R. Tilinskii

Recent Observing System Experiments on the Impact of ERS Scatterometer Wind Data on Numerical Weather Simulations of Cold Surges 35
Lim, T.K., R. Zhang, I.I. Lin, D. Kasilingam and V.H.S. Khoo

Coastline Detection with Polynomial Transforms and Markovian Segmentations 38
Moctezuma, M., B. Escalante, R. Mendez, J.R. Lopez, and F. Garcia

Applications of ERS SAR-Interferometry in Hydrologic Modelling NA
Riegler, G., K.P. Papathanassiou and W. Mauser

The Concept of Russian Fisheries Industry Service for Satellite Monitoring of Fishing Areas in Global Ocean 41
Romanov, A., A. Rodin and V. Mishkin

The Probability Description of Diurnal Solar Radiation Absorption in the Atmosphere Within Different Regions NA
Rublev, A.N., A.N. Trotsenko and N.E. Chubarova

The Estimate of Atmospheric Solar Radiation Absorption Over the Moscow Area Using Data the AVHRR/NOAA NA
Rublev, A.N., A.N. Trotsenko, N.E. Chubarova and P.Y. Romanov

Estimating Potential Mosquito Breeding Sites and Malaria Using Satellite Remote Sensing Techniques NA
Saarnak, C.F., T.T. Nielsen and S. Lindsay

Estimation of Precipitable Water from GMS-5 Split Window Channels NA
Suh, A.S., and S.H. Sohn

Land-Use Classification Using Temporal SAR-Images 44
Torma, M., and J.Koskinen

Using RADARSAT-1 for Fisheries Enforcement Operations 47
Wahl, T.

The Detection of the Great Wall Using SIR-C Data in North-Western China 50
Xinqiao, L, G. Huadong and S.Yun

Interactive Area 4: Atmospheric Sounding

Water Vapor Profile Retrieval Possibilities by Low Angle GPS Data NA
Gaikovich, K.P., and M.B. Tchernjaeva

Application of Kitt Peak Solar Flux Atlas for Studying Air Pollution in Tokyo Area 55
Jianguo, N., D. Tanaka, X. Yanquen, Y. Sakurada, H. Kuze and N. Takeuchi

Atmospheric Temperature Profile Retrieval Using Multivariate Nonlinear Regression 58
Miao, J., K. Zhao and G. Heygster

Retrieval of Total Water Vapor in Polar Regions Using SSM/T2 Channels 61
Miao, J., N. Schlueter and G. Heygster

TOVS and ATOVS Retrievals for Local Use NA
Rochard, G.

Interferometric Sounding of the Atmosphere for Meteorology NA
Wilson, S.H.S., N. Atkinson, P.J. Rayer, J. Smith and D.R. Pick

Simulation on Determination of Cirrus Cloud Optical and Microphysical Properties from Satellite IR Measurements: New Channel Approach NA
Xu, L., G. Zhang, and J. Ding

Interactive Area 5: Clouds and Precipitation

Radiance Thresholds and Texture Parameters for Antarctic Surface Classification 67
Baraldi, A., G. Meloni, and F. Parmiggiani

Dual-Frequency and Multiparameter Radar Techniques for Rain/Snow Measurements NA
Horie, H., R. Meneghini, H. Kumagai, and N. Takahashi

A Rainfall Estimation with the GMS-5 Infrared Split-Window and Water Vapour Measurements NA
Kurino, T.

Radar and Microwave Radiometer Sensing of Typhoon Ryan 70
Mitnik, M.L., L.M. Mitnik and M.K. Hsu

Cloud and Sea Ice Detection Using NOAA/AVHRR Data 73
Muramoto, K., H. Saito, K. Matsuura and T. Yamanouchi

Lidar Observation of Multiple Scattering in Fogs and Clouds in the Low Atmosphere NA
Tatarov, B., B. Kaprielov, V. Naboko, A. Blagov and I. Kolev

Interactive Area 6: Crops, Soils and Forestry

Technology of the AVHRR Data Processing and Their Application for the Solution of Agronmeteorological Problems NA
Arushanov, M.L., E.N. Alexeev, and I.N. Kanash

Improved Fourier Modelling of Soil Temperature Using the Fast Fourier Transform Algorithm 79
Axelsson, S.R.J.

Modeling Bidirectional Radiance Distribution Functions of Conifer Canopies Using 3-D Graphics 84
Burnett, C.N., G.J. Hay, K.O. Niemann and D.G. Goodenough

Forest Cartography of Spain Based on the Classification of NOAA-AVHRR Multitemporal Images 87
Gonzalez-Alonso, F., and J.L. Casanova Roque

Remote Sensing for Estimating Chlorophyll Amount in Rice Canopies 89
Hong, S., S. Rim, J. Lee, and J. Kim

"NA" indicates not available at time of printing.

Estimation of Leaf Area Index and Total Dry Matter of Rice Canopy by Using Spectral Reflectance Field 92
Lee, J.T., C.W. Lee, S.Y. Hong and M.E. Park

Spectral Unmixing and Mapping of Surface Features Related to Soil Erosion 95
Metternicht, G.I., and A. Fermont

Simulation of Forest BRDF with the Coupling of High and Medium Resolution Reflectance Models NA
Pinel, V., and J.P. Gastellu-Etchegorry

Forest Decline Dynamics Around the Severonickel Smelter in the Kola Peninsula, Arctic Russia: Remote Sensing and Mathematical Modelling NA
Rigina, O., O. Hagner and H. Olsson

Ku-Band SAR Data for Bare Soil Moisture Retrieval Over Agricultural Fields 98
Sano, E.E., M.S. Moran, A.R. Huete, and T. Miura

Airborne Remote Sensing to Support Precision Farming 101
Wehrhan, M.J.G., and T.M. Selige

Amazon Rainforest Visualisation/Classification by Orbiting Radar, Enabled by Supercomputers (ARVORES) 104
Siqueira, P., B. Chapman, S. Saatchi, and T. Freeman

Utilization of Coherence Information from JERS-1/SAR for Forest Type Discrimination 107
Takeuchi, S., and C. Yonezawa

Monitoring Changes in the Tropical Moist Forests of Continental Southeast Asia NA
Wagner, T.W., and K. Nualchawee

Interactive Area 7: Damage Assessment and Management

A Flexible Environment for Earthquake Rapid Damage Detection and Assessment 113
Casciati, F., P. Gamba, F. Giorgi, A. Marazzi and A. Mecocci

Remote Sensing of Global Fire Patterns, Aerosol Optical Thickness and Carbon Monoxide During April 1994 116
Christopher, S.A., M. Wang, D.V. Kliche, R.M. Welch, S. Nolf, and V.S. Connors

Use of SIR-C/X-SAR to Monitor Environmental Damages of the 1991 Gulf War in Kuwait 119
Dobson, M.C., A.Y. Kwarteng and F.T. Ulaby

Modelling of Human Dimension on Soil Erosion Processes for Remote Sensing Applications 122
Gaillard, C., F. Zagolski and F. Bonn

Moisture and Temperature Condition of Lahar-Affected Area Around Mt. Pinatubo 125
Inanaga, A., M. Watanabe, J.D. Rondal, M. Yoshida, T. Ohkura and A.G. Micosa

Evaluation of RADARSAT Image for Landslide Susceptibility Mapping: Application in Bolivia 128
Peloquin, S., Q. Hugh, J. Gwyn, D. Haboudane, R. Mendez and L.A. Rivard

The Use of ERS SAR Interferometry for Planning and Monitoring of Siberian Pipeline Tracks NA
Streck, C., and U. Wegmuller

Interactive Area 8: Detection of Buried Objects and Voids

Near Field SAR and Noisy Target Identifications 133
Afifi, M.S., and A.G. Al-Ghamdi

Reconstruction of a 3-Dimensional High-Contrast Penetrable Object in the Pulsed Time Domain by Using the Genetic Algorithm 136
Choi, H.K., S.K. Park and J.W. Ra

The Properties of GPR Antennas Near Lossy Media Calculated by FD-TD Method NA
Guangyou, F., and Z. Zhongzhi

Imaging Layered Subsurface Using a Multi-Frequency, Coil-Type Sensor NA
He, X., and C. Liu

Imaging the Shape of a Two-Dimensional Cylindrical Void Near a Plane Surface by Electromagnetic Wave Scattering NA
Liu, L., and L. Xiao

Generalized Detection Algorithm for Signals with Stochastic Parameters 139
Tuzlukov, V.P.

Applications of Ground Penetrating Radar Forward Calculus with Finite Offset for Point Scattering 142
Wang, H.

Derivative Seismic Processing Method for GPR Data 145
Yu, H., and X.Ying

Detection of the Man-Made Objects (PIPES) with Electromagnetic Induction NA
Zhu, K., T. Sakurai and F. Tohyama

Interactive Area 9: Detection and Monitoring of Ships and Ocean Pollution

Sea Surface Imaging at Millimeterwave Frequencies NA
Boehmsdorff, S., and H. Essen

Wind Data in Operational Oil Spill Detection Using ERS SAR NA
Espedal, H.A., and T. Hamre

Ship and Ship Wake Detection in the ERS SAR Imagery Using Computer-Based Algorithm 151
Lin, I.I., L.K. Kwoh, Y.C. Lin and V. Khoo

Oil Spills Detection Using ALMAZ-1 and ERS-1 SAR NA
Litovchenko, K.T., and A.Y. Ivanov

Adapting Operations of the Radarsat SAR to Enhance Ship Monitoring 154
Luscombe, A.P., and L. Lightstone

Incorporation of Prior Knowledge in Automatic Classification of Oil Spills in ERS SAR Images 157
Schistad Solberg, A.H., and E. Volden

Phytoplankton's Fluorescence-Possible Tool for Remote Detection of the Radioactive Pollution in the Ocean NA
Tsipenyuk, D. Yu.

Automatic Detection of Ship Tracks in Satellite Imagery 160
Weiss, J.M., R. Luo, and R.M. Welch

"NA" indicates not available at time of printing.

Interactive Area 10: Emission and Scattering

Rainfall Effect on Microwave Thermal Emission Characteristics of Sea Surface NA
Bulatov, M.G., V.G. Pungin and E.I. Skvortsov

Studies of BRDF in Conifer and Deciduous Boreal Forests Using the 4-Scale Model and Airborne POLDER and Ground-Based PARABOLA Measurements 165
Chen, J.M., S.G. Leblanc, J. Cihlar, P. Bicheron, M. Leroy, D. Deering and T. Eck

Six Years of Microwave Radiative Transfer Validation Using Airborne Radiometers: The Main Results NA
English, S.J., T.J. Hewison, and P.J. Rayer

Feasability to Measuring Directly Distribution of the Emissivitied of Territorial Surface on the Remote Sensing Platforms 168
Zhang, R., X. Sun and Z. Zhu

Third Order Microwave Radiative Transfer Equation Solution with SSM/I Data NA
Givri, J.R., and E.A. Decamps

A Comparison of Mixture Modeling Algorithms and Their Applicability to the MODIS Data 171
Kalluri, S.N.V., C. Huang, S. Mathieu-Marni, J.R.G. Townshend, K. Yang, R. Chellappa and A. Fleig

Retrieval of Bidirectional Reflectance Distribution Function (BRDF) at Continental Scales from AVHRR Data Using High Performance Computing 174
Kalluri, S.N.V., Z. Zhang, S. Liang, J. Jaja, and J.R.G. Townshend

Radiative Transfer Analytical Solutions for Remote Sensing Through the Atmosphere NA
Katkovsky, L.V.

RCS Computation of Dielectric-Coated Bodies Using the Conjugate Gradient Method and the Fast Fourier Transform NA
Neo, C.P., M.S. Leong, L.W. Li and T.S. Yeo

Study of the Polarization Behavior of Complex Natural and Man-Made Clutter at Middle and Grazing Angles 177
Onstott, R.G.

Sensitivity Analysis for a SAR Backscatter Model NA
Slatton, K.C., M.M. Crawford, J.C. Gibeaut and R.O. Gutierrez

Determination of the Earth's Emissivity for Use in Studies for Global Climate Change 180
Stephenson-Hawk, D., K. Stephens and A. Shah

A New Approach to the Problem of Wave Scattering in Random Media and Its Application to Evaluating the Effective Permittivity of a Random Medium 184
Tateiba, M.

Algorithms for Retrieving Land Surface Temperatures and Emissivities from Satellite Radiative Measurements NA
Zhao, G., and H.Q. Wang

Interactive Area 11: Geology and Geomorphology

Influence of Neotechtonic Movements on Exogenic Processes on the Territory of the Russian Plane NA
Bronguleyev, V.V.

Spectral and Geomorphometirc Discrimination of Environmental Units: Application to the Geomorphological Processes of Land Degradation 189
Haboudane, D., F. Bonn, S. Peloquin, A. Royer, and S. Sommer

Geo-Environmental Assessment of Landslide Hazards in the Sikkim Himalaya Utilising Remote Sensing Techniques for Sustainable Development in the Mountain Environment NA
Krishna, A.P.

Environmental Geoscientific Assessment for Sustainable Development Priorities in Sikkim Himalaya: An Integrated Remote Sensing Approach NA
Krishna, A.P., and Y.K. Rai

Balance and Restoration of Three Cross-Sections in Eastern Tethys-Himalayan Orogeny Belt in Southwest China NA
Qing, X.

Analysis of the Areal Valcanism Zones of Klyuchevskoy Volcano Using SIR-C Data NA
Shkarin, V.E., V.V. Zaitsev and A.P. Khrenov

The Design of a Methodology for Volcanic Hazard Mapping Using GIS and Remote Sensing Techniques in the Bulusan Volcano Area, Bicol District, Phillippines 192
Slob, S.

New Principles of Morphotectonic Mapping of Asia NA
Timofeev, D.A., and V.V. Bronguleyev

Interactive Area 12: GIS

Geographical Information System (GIS) Based on National Base Maps of Iran at 1:100,000 by Satellite Images NA
Bushehri, S.N., and N. Khorsandian

Integration of GIS and Remote Sensing Techniques for EIA in Chilika Lake Region (India) NA
Das, T.K., O. Dikshit, and K.S. Bhatta

Desertification and Land Degradation Using High Resolution Satellite Data in the Nile Delta, Egypt 197
El-Khattib, H.M., N.M. El-Mowelhi and A.A. El-Salam

Biodiversity Assessment Using GIS and RS Technology for Protected Area Management and Conservation in Xe Paine, Laos PDR NA
Kamal, G.M.

On Integrated Scheme for Vector/Raster-Based GIS's Utilization 200
Kim, K.S., M.S. Kim and K. Lee

The Application of Rational Formula Based on Remote Sensing and Geographical Information Systems NA
Leu, C.

Precision Rectification of Airborne SAR Image 204
Liao, M., and Z. Zhang

Contribution of Mathematical Morphology and Fuzzy Logic to the Detection of Spatial Change in an Urbanized Area: Towards a Greater Integration of Image and Geographical Information Systems 207
Maupin, P., P. Le Quere, R. Desjardins, M.C. Mouchot, B. St-Onge and B. Solaiman

Correlation Between Malaria Incidence and Changes in Vegetation Cover Using Satellite Remote Sensing and GIS Techniques NA
Nualchawee, K., P. Singhasivanon, K. Thimasarn, D. Darasri, K. Linthicum, S. Suvannadabba, P.L. Rajbhandari, and R. Sithiprasasna

Application of Remote Sensing for Assessing the Habitat Structure of the Whooping Cranes in Nebraska, USA NA
Richert, A., S. Narumalani, S. Richert and K. Church

"NA" indicates not available at time of printing.

An Application of GIS Information and Remotely Sensed Data for Extraction of Landslide 210
Shikada, M., Y. Suzuki, T. Kusaka, S. Goto and Y. Kawata

Accuracy Assessment of Elevation Data Obtained from Radarsat Stereo Images 213
Singh, K., O.K. Lim, L.K. Kwoh and H. Lim

Parallel Ladex Spatial Index Mechanism 216
Xiao, W., and Y. Feng

Spatial Information System Applications for Sustainable Development in Korea: Necessity, Possibility and Methodology NA
Xiu-wan, C., C. An, D. Shin, and S. Oh

GIS Modeling in Coastal Flooding Analysis: A Case Study in the Yellow River Delta, China 219
Yang, X.

Software Development Project for the National Geographic Information System (NGIS) Initiative NA
Yang, Y.K., J.H. Lee and C.H Ahn

Combination Between Remote Sensing and Ecosystem Observation Network in China 222
Zhang, Q., and R. Zhang

Interactive Area 13: Ground Penetrating Radar

Full-Wave 3D Modeling of Ground-Penetrating Radars by a Finite Element/Boundary Element-Hybrid Technique 227
Eibert, T.F., V. Hansen and N. Blindow

Subsurface Remote Sensing with Electromagnetic Pulsed Beam NA
Kolchigin, N.N., S.N. Pivnenko and V.M. Lomakin

GPR Attenuation Tomography for Sensing Subsurface Contaminants NA
Liu, L.

Mineral Sands Deposits Investigation in Australia Using Subsurface Interface Radar (SIR) NA
Marschall, D.L., and R.A. Marschall

Scattering from Periodically Located Objects Embedded Near the Randomly Rough Surface of a Moist Soil 230
Timchenko, A.I., and V.P. Tishkovets

The Applications of GPR to Civil Engineering in China 232
Ying, X., and H. Yu

Interactive Area 14: Image Processing

Separation of Character Strings and High Quality Vectorization for Digitized Korean Cadastral Map Images 237
Bang, K., and D. Hong

A Multi-Strategic Approach for Land Use Mapping of Urban Areas by Integrating Satellite and Ancillary Data 240
Caetano, M., J. Santos and A. Navarro

Development of a Feature-Based Approach to Automated Image Registration for Multitemporal and Multisensor Remotely Sensed Imagery 243
Dai, X., and S. Khorram

Imitation Modeling of Radar Images Using a Complexing Method NA
Gernet, N.D.

A Quality Assurance Algorithm for NASA Scatterometer Wind Ambiguity Removal 246
Gonzales, A.E., and D.G. Long

Mosaicking of ERS SAR Quicklook Imagery of South East Asia 249
Kwoh, L.K., X. Huang and M. Li

Change Detection from Remotely Sensed Multi-Temporal Images Using Morphological Operators 252
Le Quere, P., P. Maupin, R. Desjardins, M.C. Mouchot, B. St-Onge and B. Solaiman

Symbolic Data Analysis of Multitemporal Data: An Application to Seasonal Analysis NA
Prakash, H.N.S., P. Nagabhushan and K.C. Gowda

Multiscale Markov Random Fields for Large Image Data Sets Representation 255
Rehrauer, H., K. Seidel and M. Datcu

Gibbs Random Field Models for Image Content Characterization 258
Schroeder, M., K. Seidel and M. Datcu

Techniques for Large Zone Segmentation of Seismic Images 261
Simaan, M.A.

SAR Image Interpretation Based on Markov Mesh Random Fields Models NA
Smits, P.C., F. Giorgini, A. Martuccelli, M. Petrou and S.G. Dellepiane

Automatic Segmentation of Oceanic Linear Structures on AVHRR Thermal Infra-Red Images NA
Thonet, H., B. Lemmonier and R. Delmas

Segmentation of Multispectral Remote-Sensing Images Based on Markov Random Fields 264
Tsai, I.W., and D.C. Tseng

Interactive Area 15: Land Cover Applications

Land Cover Change: A Method for Assessing the Reliability of Land Cover Changes Measured from Remotely Sensed Data 269
Aspinall, R.J., and M.J. Hill

Remote Sensing of the Effects of Irrigation Activities on Vegetation Health in Ephemeral Wetlands of Semi-Arid Australia 272
Benger, S.N.

Mapping Pastures in Eastern Australia with NOAA-AVHRR and Landsat TM Data 275
Hill, M.J., and G.E. Donald

Evaluating Quaternary Climatic Change in West Africa Using the NOAA AVHRR 1KM Land Dataset 278
Nichol, J.

Landuse Planning for Sustainable Development of Southeastern Desert of Egypt: An Integrated Remote Sensing and GIS Approach NA
Rahman, S.I. Abdel

The Method of Early Drought Detection with AVHRR/NOAA Data 281
Spivak, L., A. Terehov, N. Muratova and O. Arkhipkin

Land Cover Classification of East Asia Using Fourier Spectra of Monthly NOAA AVHRR NDVI Data 284
Sugita, M., and Y. Yasuoka

Identifying Urban Features Using RADARSAT Images Taken at Multiple Incidence Angles 287
Weydahl, D.J.

"NA" indicates not available at time of printing.

Interactive Area 16: Optical Measurement of the Ocean

On the Peculiarities of SSM/I Brightness Temperature Variations in Kuroshio Region NA
Cherny, I.V., and V.P. Nakonechny

Simulation of Satellite Measurements of Radiance over Water for Operational Testing of MODIS Ocean Color Algorithms NA
Fleig, A.J., and K. Yang

Resolution Enhancement in SAR Images 293
Guglielmi, V., F. Castanie and P. Piau

Diffuse Reflectance of the Optically Deep Sea Under Combined Illumination of Its Surface 296
Haltrin, V.I.

Light Scattering Coefficient of Seawater for Arbitrary Concentrations of Hydrosols 299
Haltrin, V.I.

Multi-Wavelength Laser Scattering at the Air-Sea Interface 302
Lin, C.S.

The MUBEX Experiment - Validation of Satellite Data and Air-Sea Interaction Studies at Mutsu Bay, Japan NA
Llewellyn-Jones, D.T., I.M. Parkes, D.T., R. Yokoyama, S. Tamba, M. Takagi, C.T. Mutlow, T. Nightingale, C. Donlan and V. Bennett

Line Noise Extraction of Thermal Infrared Camera Image in Observing Sea Skin Temperature 305
Tamba, S., and R. Yokoyama

Spatial and Temporal Behaviors of Sea Skin Temperature Observed by Thermal Infrared Camera 308
Tamba, S., S. Oikawa, R. Yokoyama, I. Redley, I. Parkes and D. Llewellyn-Jones

MUBEX: Japan and U.K. Collaboration for Mutsu Bay Sea Surface Temperature Validation Experiment 311
Yokoyama, R., S. Tamba, T. Souma, D. Llewellyn-Jones and I. Parkes

Laser Spark Spectroscopy in Remote Sensing of Sea and Land Surfaces Element Analysis NA
Tsipenyuk, D.Yu, and M.A. Davydov

Interactive Area 17: Remote Sensing Data Processing Techniques

Simulation of Split-Window Algorithm Performance 317
Axelsson, S.R.J., and B. Lunden

Analysis of Single and Multi-Channel SAR Data Using Fuzzy Logic 322
Benz, U.

Processing and Validation of the ERS-1 Radar Altimeter Data at the Italian PAF 325
Celani, C., A. Bartoloni and F. Nirchio

A Visual Tool for Capturing the Knowledge of Expert Image Interpreters: A Picture is Worth More than a Thousand Words 328
Crowther, P., J. Hartnett, and R.N. Williams

Data-Driven Decomposition of Mixed Pixels for Crop Area Esitmation NA
Gebbinck, M.S.K., and T.E. Schouten

Radarsat Processing Using the Desk-Top Synthetic Aperture Radar Processor NA
Goulding, M., P.R. Lim, L. Wilke and P. Vachon

Congestion Data Acquisition Using High Resolution Satellite Imagery and Frequency Analysis Techniques 331
Kim, K.H., J.H. Lee and B.G. Lee

Geoinformation Monitoring System - Gims (The Concept, Structure, Examples of Application) NA
Krapivin, V.F., and A.M. Shutko

The ENVISAT-1 Advanced Synthetic Aperture Radar Generic Processor NA
Lim, P.R., D.R. Stevens, D. Rae, Y.L. Desnos, H. Laur and T. Gach

A Framework for SAR Image Classification: Comparison of Co-Occurrence Method and a Gabor Based Method 335
Manian, V., and R. Vasquez

A Network Distributed Processing System for TRMM Ground Validation NA
Merritt, J.H., N.T. Nguyen, D.B. Wolff and D. Han

Fuzzy Supervised Classification of JERS-1 SAR Data for Soil Salinity Studies 338
Metternicht, G.I.

Land Cover Change Detection Using Radiometrically-Corrected Multi-Sensor Data NA
Mispan, M.R., and P.M. Mather

Quality Assurance of Global Vegetation Index Compositing Algorithms Using AVHRR Data 341
van Leeuwen, W.J.D., T.W. Laing and A.R. Huete

Interactive Area 18: Remote Sensing of the Ocean

Investigations of Possibilities of Using SAR Data for Monitoring of Volga Estuary and Kalmykija Shore of Caspian Sea 347
Armand, N.A., A.S. Shmalenyuk, Y.F. Knizhnikov, V.I. Kravtsova and E.N. Baldina

Laboratory Investigations of Nonlinear Surface Wave Transformation in a Field of Two-Dimensionally Inhomogeneous Currents 350
Bakhanov, V.V., S.D. Bogatyrev, V.I. Kazakov and O.N. Kemarskaya

Global Optimization Algorithms for Field-Wise Scatterometer Wind Estimation 353
Brown, C.G., and D.G. Long

Retrieval of Air-Water Interaction by Thermal Radio Emission Dynamics at 60 GHZ NA
Gaikovich, K.P.

Ka-Band Ocean Wave-Radar and Wave Envelope-Radar Modulation Transfer Function Measurements and Modeling NA
Grodsky, S.A., V.N. Kudryavtsev and A.N. Bol'shakov

Gulf Stream Signatures and Surface Wave Observation Using ALMAZ-1 SAR NA
Grodsky, S.A., V.N. Kudryavtsev and A.Y. Ivanov

Ocean Wave Spectrum Reconstruction for ERS-1 Satellite Scatterometer Data 356
He, Y., and J. Zhao

The Fine Grained Sediment Load of the Mississippi River: A Land Building Commodity NA
Huh, O.K.

"NA" indicates not available at time of printing.

Studies of Ocean Surface Processes Which Influence Climate NA
Jenkins, A.D., H.A. Espedal, H. Drange and O.M. Johannessen

SICH-1 Real Aperture Radar Imagery of Ocean Temperature Fronts NA
Malinovsky, V.V., A.V. Rodin and V.N. Kudryavtsev

Validation of Models and Algorithms for Microwave Radiometric Investigations of Tropical Cyclones 359
Petrenko, B.Z., A.F. Nerushev, L.I. Milekhin and G.K. Zagorin

Bistatic Model of Ocean Scattering NA
Picardi, G., R. Seu and S. Sorge

Azimuthal Anisotropy of Sea Surface Polarized Microwave Emission NA
Pospelov, M.

Simultaneous Observation of Oceanic and Atmospheric Internal Waves by Air-Borne Dual Polarization Ku-Band Side Looking Radar NA
Pungin, V.G., and M.I. Mityagina

The Satellite Data "Resource" and NOAA/AVHRR for Black Sea Dynamics Investigation NA
Stanichy, S.V., and D.M. Solov'ev

The Surface Active Sea Films: Properties and Dynamics 362
Talipova, T.

Aerocosmic Method of Investigations of Short Time Hydrodynamic Processes and Phenomena at the Surface of Seas and Oceans NA
Tomilov, G.M., and V.P. Bobykina

Interactive Area 19: Remote Sensing Techniques and Instrumentation

L-Band 300-Watt Solid State Pulse Power Amplifiers for SAR 367
Deng, Y.

Development of a PC Based System for Real-Time, Local Reception of High Resolution Satellite Data for Environmental Monitoring 370
Downey, I.D., J.B. Williams, J.R. Stephenson, R. Stephenson and W. Looyen

A Real Aperture Radar for Low Resolution Mapping at Low Costs 374
Impagnatiello, F., G. Angino and G. Leggeri

Effects of Faraday Rotation on Microwave Remote Sensing from Space at L-Band 377
Le Vine, D.M., and M. Kao

Using JPEG Data Compression for Remote Moving Window Display 380
Leung, P.S., M. Adair and J.H. Lam

The Universal Multichannel Technique for Enhancing Images Obtained from Different Sensors 383
Petrenko, B.Z.

YSAR: A Compact, Low-Cost Synthetic Aperture Radar 386
Thompson, D.G., D.V. Arnold, D.G. Long, G.F. Miner, T.W. Karlinsey and A.E. Robertson

The China Airborne Radar Altimeter Control System 389
Xu, K., M. Li, N. Zhou, Y.L. Xue and Y.S.Liu

Miniature Ocean Radar Altimeter NA
Xu, K.

Computer Simulation of Spaceborne Multimodes Microwave Sensors 392
Zhang, Y., and J. Jiang

Interactive Area 20: Snow and Glaciers

Improved Elevation Change Measurements of the Greenland Ice Sheet from Satellite Radar Altimetry 397
Davis, C.H., and C. Perez

Multi-year Ice Concentration from RADARSAT 402
Fetterer, F., C. Bertoia and J.P. Ye

Analysis of a Microwave Airborne Campaign Over Snow and Ice NA
Hewison, T., and S. English

Vector Radiative Transfer for Scattering Signature from Multi-Layer Snow/Vegetation at SSM/I Channels 405
Jin, Y.Q.

Deriving Glaciers Variation Integrated Remote and GIS in Tibetan Plateau 408
Li, Z., and Q. Zeng

On the Accuracy of Snow Cover Segmentation in Optical Satellite Images 411
Luca, D., K. Seidel and M. Datcu

A Comparison of Antarictic Sea Ice Concentration Derived from SSM/I, SAR, and Ship Observations NA
Lytle, V.I., and M. Rapley

Sea Ice Concentration and Flow Size Distribution in the Antarctic Using Video Image Processing 414
Muramoto, K., T. Endoh, M. Kubo and K. Matsuura

Spectral RF Reflection from Water and Ice Layers NA
Noyman, Z. Zlotnick, and A. Ben-Shalom

Compatability of Sea Ice Edges Detected in ERS-SAR Images and SSM/I Data 417
Schmidt, R., and T. Hunewinkel

Snow-Cover Mapping Experiment by EMISAR C Band - Discrimination and Optimum Resolution NA
Solberg, R., A. Schistad Solberg, E. Volden, H. Koren and A. Teigland

Characterization of Snow Cover from Multispectral Satellite Remote Sensing and Modelling Runoff Over High Mountainous River Basins NA
Swamy, A.N., and P.A. Brivio

"NA" indicates not available at time of printing.

Interactive Area 21: Lidars

Statistical Approach for Lidar Sensing of Turbulence Parameters with a Vi to Atmosphere Pollution NA
Avramova, R.P.

Accurate Height Information from Airborne Laser-Altimetry 423
Lemmens, M.J.P.M.

Technique Doppler Lidar Measurement of the Atmospheric Wind Field NA
Li, S.X., B.M. Gentry, and C.L. Korb

A New Airborne Remote Sensing System Integrating Scanning Altimeter with Infrared Scanner 427
Liu, Z., and S. Li

Air Turbulence Measurements Using CCD Camera for Obtaining Laser Spot Fluctuations NA
Mitev, V.

Interactive Area 22: SAR Interferometry

Local, Global and Unconventional Phase Unwrapping Techniques 433
Collaro, A., G. Fornaro, G. Franceschetti, R. Lanari, E. Sansosti and M. Tesauro

Applicaiton of Wavelets to Improve IFSAR DEM Reconstruction NA
Curlander, J.C., G. Burkhart and C. Johnson

ERS Tandem INSAR Processing for Exploration of the Svalbard Archipelago NA
Eldhuset, K., Amlien, J., P.H. Andersen, S. Hauge, E. Isaksson, T. Wahl and D.J. Weydahl

Motion Compensation Effects in Wavelength-Resolution VHF SAR Interferomtry 436
Frolind, P.O., and L.M.H. Ulander

The Exact Solution of the Imaging Equations for Crosstrack Interferometers 439
Goblirsch, W.

SAR Interferometric Analysis of ERS Tandem Data over an Alpine Terrain NA
Kenyi, L.W., and H. Raggam

Baseline Estimation Using Ground Points for Interferomteric SAR 442
Kimura, H., and M. Todo

Development of an Interferometric SAR Data Processing System NA
Li, J.F., H. Liu and H.D. Guo

Phase Noise Filter for Interferometric SAR 445
Lim, I., T.S. Yeo, C.S. Ng, Y.H. Lu and C.B. Zhang

Calibration and Classification of SIR-C Polarimetric and Interferometric SAR Data in Areas with Slope Variations 448
Pasquali, P., F. Holecz, D. Small and T. Michel

On the Motion Compensation and Geocoding of Airborne Interferometric SAR Data 451
Sansosti, E., R. Scheiber, G. Fornaro, M. Tesauro, R. Lanari, and A. Moreira

A Method for Precise Reconstruction of INSAR Imaging Geometry NA
ShiPing, S.

Baseline Estimation in Interferometric SAR 454
Singh, K., N. Stussi, L.K. Kwoh, and H. Lim

Removal of Residual Errors from SAR-Derived Digital Elevation Models for Improved Topographic Mapping of Low-Relief Areas 457
Slatton, K.C., M.M. Crawford, J.C. Gibeaut and R. Gutierrez

Digital Elevation Models from SIR-C Interferometric and Shuttle Laser Altimetry (SAL) Data 460
Sun, G., and K.J. Ranson

Interactive Area 23: SAR Techniques

A High Precision Workstation - Based Chirp Scaling SAR Processor 465
Breit, H., B. Schattler and U. Steinbrecher

Investigations of Coastal Zones in the North West Pacific by Remote Sensing NA
Bobykina, V.P.

SAR Image Simulation of Moving Targets with LOCOSAR NA
Cazaban, F., M. Deschaux-Beaume, J.G. Planes and M. Busson

Automated Acquisition of Ground Control Using SAR Layover and Shadows 468
Gelautz, M., E. Mitteregger, and F. Leberl

An Accelerated Chirp Scaling Algorithm for Synthetic Aperture Imaging 471
Hawkins, D.W., and P.T. Gough

Analysis of Code Error Effect in Spaceborne SAR Imaging Processing 474
Jiang, Z., and J. Song

High Quality Spotlight SAR Processing Algorithm 477
Jin, M.Y.

Interpretation of Brightness Temperature Retrieved by Supersynthesis Radiometer 481
Komiyama, K., Y. Kato and K. Furuya

Non-Iterative Spotlight SAR Autofocusing Using a Modified Phase-Gradient Approach 484
Chan, H.L., and T.S. Yeo

Real Time Synthetic Aperture Radar Preprocessor Design Via Three-Dimensional Modular Filtering Architecture 487
Chan, H.L., and T.S. Yeo

High Resolution SAR Processing Using Stepped-Frequencies 490
Lord, R.T., and M.R. Inggs

RADARSAT Attitude Estimates Based on Doppler Centroid of SAR Imagery 493
Marandi, S.R.

A Research of Moving Targets Detection and Imaging by SAR 498
Pan, R., G. Li and X. Zhu

Tree Structured Filter Banks for Speckle Reduction of SAR Images 501
Sveinsson, J.R., and J.A. Benediktsson

Feasibility of Satellite On-Board SAR Processing NA
Thompson, A., H. Jiang, S. Spenler and A. Macikunas

"NA" indicates not available at time of printing.

Near Real-Time RADARSAT Data System for NOAA CoastWatch Applications 505
Tseng, W.Y., W.G. Pichel, A.K. Liu, P. Clemente-Colon, G.A. Leshkevich, S.V. Nghiem, R. Kwok and R.N. Stone

Interactive Area 24: Surface Temperatures

Land Surface Temperature Interpretation of Equatorial South America from AVHRR Data 511
Li, G., and P.J. Hardin

Tropical Model for Retrieving Surface Temperature from Satellite Data NA
Mansor, S.B.

Sea Surface Temperatures from NOAA Satellites in the Swordfish and Jack Mackerel Fisheries of Chile's Central Zone NA
Yanez, E., M.A. Barbieri, V. Catasti, C. Silva and K. Nieto

Interactive Area 25: Neural Network and Intelligent Systems

Pollution Analysis of Hyperdimensional Data Using Neural Networks NA
Benediktsson, J.A., K. Arnason and S. Jonsson

A Classification of Multispectral Landsat TM Data Using Principle Component Analysis of Artificial Neural Network 517
Chae, H.S., S.J. Kim and J.A. Ryu

Unsupervised Classification for Remotely Sensed Data Using Fuzzy Set Theory 521
Dinesh, M.S., K.C. Gowda and P. Nagabhushan

Development of a Intelligent Image Analysis System for the Detailed Analysis of the Land Surface Information 524
Kim, K.O., Y.L. Ha, I.S. Jung, J.Y. Lee, K.H. Choi and J.H. Lee

Study on the Characteristics of the Supervised Classification of Remotely Sensed Data Using Artificial Neural Networks 528
Paek, K.N., Y.S. Song, H.S. Chae and K.E. Kim

Interactive 26: Missions and Programs

The Advanced Remote Sensing Data from MOMS-2P on PRIRODA 533
Bodechtel, J., and Q. Lei

Multi-Frequency and Multi-Polarization SAR System Analysis with Simulation Software Developed at CSA 536
Huang, Y., G. Seguin, and N. Sultan

Oceanological Results from the ALMAZ-1 Mission: An Overview 539
Ivanov, A.Y., and K.T. Litovchenko

Some Options for RadarSAR-II NA
Parashar, S., E.J. Langham and S. Ahmed

A Summary of the Upper Atmosphere Research Satellite (UARS) 542
Schoeberl, M., A.R. Douglass and C.H. Jackman

BEAWARE: Budget Effective All Weather Accurate Radar for Earth Observation 545
Vincent, N., E. Souleres and N. Suinot

Design of MACSIM Cloud Radar for Earth Observation Radiation Mission 548
Vincent, N., N. Suinot and C.C. Lin

Interactive 27: Inverse Techniques

Ice Concentration Estimation Based on Local Inversion 553
Arai, K.

Retrieving of LAI and FAPAR with Airborne POLDER Data over Various Biomes 556
Bicheron, P., M. Leroy and O. Hautecoeur

The Uncertainty and Confidence in BRDF Model Inversion NA
Jindi, W., and L. Xiaowen

SAIL Model Experiment of the Inversion of Growth Indices from Rice Conopy Reflectance Using the Information on Variation and Regulation of Leaf Spectral Characteristics NA
Kushida, K.

Algorithms for Estimating Some Optically Active Substances and Apparent Optical Properties from Subsurface Irradiance Reflectance Measurements in Lakes NA
Reinart, A.

Geometry-Based Deconvolution of Geophysical Data 559
Simaan, M.A.

A Priori Information in Inverse Problems of Atmospheric Optics 562
Timofeyev, Y.M.

Three-Dimensional DC Resistivity Inversion at a Gasoline Contaminated Site NA
Xiao, L., and L. Liu

Retrieval of Electrical Properties of a Stratified Medium with Slightly Rough Surface Using an Inversion Method NA
Zhuck, N.P., D.O. Batrakov and K. Schuenemann

Interactive 28: Calibration

Characterization of Passive NMMW Backgrounds at 140 and 220 GHz NA
Ben-Shalom, A., Y. Oreg, and M. Engel

Some Issues on Calibration/Validation Algorithms of SSM/I Data 567
Jin, Y.Q.

Calibration and Validation of ADEOS/NSCAT in Japan NA
Masuko, H., and Japanese ADESO/NSCAT CAL/VAL Team

Calibration Experiments of the CRL/NASDA X/L-Band Airborne Synthetic Aperture Radar 570
Satake, M., T. Kobayashi, H. Masuko and M. Shimada

"NA" indicates not available at time of printing.

Interactive 29: Education and Information Systems

Development of Interactive, Graphical, Computer-Based Teaching Tools for Remote Sensing in Tcl/Tk NA
Barnsley, M., and P. Hobson

Ocean Expeditions: El Nino — An Interactive Education Tool Based on Remote Sensing Data NA
Gautier, C.

Meteorological Satellite Image Service via WWW 575
Lee, H.G.

Interactive 30: Wavelet Techniques in Remote Sensing

Wavelet Techniques Applied to Lidar Temperature Profiles in the Middle Atmosphere to Study Gravity Waves 581
Chane-Ming, F., F. Molinaro, and J. Leveau

Robust Terrain Classification Using Wavelet Packets NA
Keshava, N., and J.M.F. Moura

High Resolution Image Classification with Features from Wavelet Frames 584
Kim, K.O., I.S. Jung and Y.K. Yang

A Hierarchical Stereo Matching Algorithm Using Wavelet Representation Based on Edge and Area Information 588
Um, G.M., C.S. Ye and K.H. Lee

Interactive 31: Classification

The Impact of the Initial Land-Cover Classification on the Retrieval of Land Use Information from Remotely-Sensed Images Using Structural Pattern Recognition Techniques NA
Barr, S., and M. Barnsley

Snow Covered Area Classification Using Time Series ERS - 1 SAR NA
Li, Z., and J. Shi

From the Satellite to the Airborn Platforms Imagery: Behavioral Classification and Segmentation NA
Orban-Ferauge, F., J.P. Rasson and S. Baudart-Lissoir

Symbolic ISODATA Clustering Procedure Useful for Land Cover Classification: A Case Study Employing IRS-1B LISS II Data for Nagarahole Forest, Karnataka State, India) NA
Prakash, H.N. S., P. Nagabhushan and K.C. Gowda

Interactive 32: Coastal Environment

Retrieval of the Remote Radiance Reflection Coefficient of Coastal Waters from the Inherent Optical Properties 595
Haltrin, V.I.

Monitoring Coastal Water Systems: An Integrated Approach 598
Krishnan, P.

Near-Bottom Fluxes of Sediment Matter on a Shelf and Their Research by Remote Techniques 601
Likht, F.R., and L.M. Mitnik

The Analysis and Comparison of Satellite and " In Situ" Temperature Measurements for Coastal Zone Dynamic Processes Investigation NA
Stanichnaya, R.R., A.S. Kuznetsov, S.A. Shurov, D.M. Solov'ev and S.V. Stanichny

Interactive 33: General Applications

New Method of the Characterization of the Simiconductor Plate Homogeneity by its Thermal Image NA
Bolgov, C., and V. Morozhenko

Ozone Distributions in the Stratosphere-Troposphere System Using the Interdisciplinary Physics Modelling 607
Caldararu, F., S. Patrascu, M. Caldararu, A. Paraschiv and D. Nicolaescu

An Improved Description of the MTF of the Moderate Resolution Imaging Spectroradiometer and a Method for Enhancing Its Cross Track Resolution NA
Fleig, A.J., and K. Yang

Spectral Identification of Coral Biological Vigour 610
Holden, H., and E. LeDrew

Variance Fractal Dimension Analysis of Crustal Seismic Refraction Signals NA
Jiao, L.X., and W.M. Moon

A Study of the Micro-Scale Disturbances Associated with a Shear Layer in the Lower Atmosphere 613
Natarajan, M.P., and M. Isaac

New Architecture for Remote Sensing Image Archives 616
Seidel, K., R. Mastropietro and M. Datcu

The Evaluation of Bending Waves and Modified Path Profile NA
Uz, B., O. Yildrim and H.M. El-Khattib

Combined Resistive and Conductive Three-Part Plane: Oblique Incidence Plane Wave NA
Yildrim, O.

Constraint Propagation in the Multi-Granularity World NA
Zequn, G., and L.Deren

"NA" indicates not available at time of printing.

A01: Remote Sensing of Snow and Glaciers

A01.01 Improving the MODIS Global Snow-Mapping Algorithm 619
Klein, A.G., D.K. Hall and G.A. Riggs

A01.02 The HUT Brightness Temperature Model for Snow-Covered Terrain 622
Hallikainen, M., J. Pulliainen, L. Kurvonen and J. Grandell

A01.03 Snow Crystal Shape and Microwave Scattering 625
Foster, J.L., D.K. Hall, A.T.C. Chang, A. Rango, W. Wergin and E. Erbe

A01.04 Mapping Snow Cover with Repeat Pass Synthetic Aperture Radar 628
Shi, J., S. Hensley and J. Dozier

A01.05 Snow Monitoring Using EMISAR and ERS-1 Data Within the European Multi-Sensor Airborne Campaign EMAC-95 631
Guneriusson, T., H. Johnsen, R. Solberg and E. Volden

A01.06 Ground Penetration Radar and ERS SAR Data for Glacier Monitoring 634
Hamran, S.E., T. Guneriusson, J.O. Hagen and R. Odegard

A01.07 Comparison of Ranging Scatterometer and ERS-1 SAR Microwave Signatures Over Boreal Forest Zone During Winter Season 637
Koskinen, J., J. Pulliainen, M. Makynen and M. Hallikainen

A01.08 Multi-Source Snow Cover Monitoring in the Swiss Alps 640
Piesbergen, J., and H. Haefner

A02: Image Processing Techniques

A02.01 The Use of Mathematical Morphology for Accurate Detection and Identification of Microwave Images in the K-Space Domain 643
Gader, P., and A.J. Blanchard

A02.02 New Classification Techniques for Analysis of Remote Sensing Integrated Data 646
Console, E., and M.C. Mouchot

A02.03 From the Unsupervised Remote Sensing Data Behavioral Classification to the Image Segmentation NA
Rasson, J.P., F. Orban-Ferauge and S. Baudart-Lissoir

A02.04 Hughes Phenomenon in the Spatial Resolution Enhancement of Low Resolution Images and Derivation of Selection Rule for High Resolution Images 649
Nishii, R., S. Kusanobu and N. Nakaoka

A02.05 Forming Digital Elevation Models from Single Pass Spot Data: Results on a Generation from Optical Stereo Data 652
Massonnet, D., A. Giros, and B. Rouge

A02.06 A Mixed Fractal/Wavelet Based Approach for Characterization of Textured Remote Sensing Images 655
Marazzi, A., P. Gamba, A. Mecocci and E. Costamagna

A02.07 Significance-Weighted Classification by Triplet Tree 658
Yoshikawa, M., S. Fujimura, S. Tanaka and R. Nishii

A02.08 On-Line System for Monitoring and Forecasting Earth Surface Changes Using Sequences of Remotely-Sensed Imagery 661
Lee, S.

A03: Data Fusion I

A03.01 Effect of Scale on the Information Content in Remote Sensing Imagery 664
Niemann, K.O., D.G. Goodenough and G.J. Hay

A03.02 Multisensor Classification of Wetland Environments Using Airborne Multispectral and SAR Data 667
Ricard, M.R., A.L. Neuenschwander, M.M. Crawford and J.C. Gibeaut

A03.03 Automated Forest Inventory Update with SEIDAM 670
Goodenough, D., D. Charlebois, A.S. Bhogal, S. Matwin and N. Daley

A03.04 Modeling Soil Erosion Hazard by Using a Fuzzy Knowledge-Based Approach 674
Metternicht, G.I.

A03.05 Comparing Raster and Object Generalization 677
Daley, N., D.G. Goodenough, A.S. Bhogal, Q. Bradley, J. Grant and Z. Yin

A03.06 Expert Maps: An Alternative for Integrating Expert Knowledge in Satellite Imagery Classification 680
Campagnolo, M.L., and M. Caetano

A03.07 Data Fusion in a Context of Data Mining, Identification and Classification NA
Wu, D., and J. Linders

A03.08 Infusion of Altimeter Data to Same Spatial, Temporal Resolution Infrared Images to Improve the Accuracy of Classification of Images and DEM 683
Liu, Z., and S. Li

A03.09 Data Integration in Support of Research on the Gulf of Mexico NA
Mason, M., G.L. Rochon, M. Singletary, N. Blackmon, D. Bardell, C. Jernigan and M. Fernandez

A04: Innovations in Remote Sensing Educational Programs and Information

A04.01 NASA's Mission to Planet Earth Invests in the Future Through a Broad National Education Program 685
Khazenie, N., and S. Stockman

A04.02 What is Earth System Science? 688
Johnson, D.R., M. Ruzek, and M. Kalb

A04.03 A Web-Based Earth Systems Science Graduate Course for Middle School Teachers 692
Myers, R.J., E.L. Shay, H. Shay, H.B. Davis, and J.A. Botti

A04.04 Globe: An International Science and Education Collaboration to Obtain Accurate Data for Monitoring Earth Systems NA
Becker, M.L., R.G. Congalton, R.Budd, and A. Fried

"NA" indicates not available at time of printing.

A04.05 Teacher Enhancement Programs in the Atmospheric Sciences: The American Meteorological Society's Project Atmosphere and DataStreme NA
Moore, J.D.

A04.06 Global Classroom Education Network NA
Mesarovic, M., and N. Sreenath

A04.07 System Thinking and System Modeling in the Earth System Science Classroom 695
Mahootian, F.

A04.08 Practical Uses of Math and Science (PUMAS) 698
Kahn, R.

A04.09 An Earth System Science Education and Training Program for the Inter American Institute for Global Change Research (IAI) 699
Johnson, D.R., M. Ruzek, M. Kalb

A05: Rough Surface Scattering

A05.01 An Exact Technique for Calculating the Scattering from Roughness Surfaces NA
Kasilingam, D.

A05.02 Application of an Extended IEM to Multiple Surface Scattering and Backscatter Enhancement 702
Hsieh, C.Y., and A.K. Fung

A05.03 Numerical Study of Shadowing in Electomagnetic Scattering form Rough Dielectric Surfaces 705
West, J.C., and J.M. Sturm

A05.04 Precise Estimation of Surface Roughness Parameters for Field-Measured Ground Truth Data 708
Oh, Y.

A05.05 Some Features of Low-Grazing-Angle Backscatter from the Sea Surface in X- and Ka-Bands: Modeling and Observations NA
Skirta, E.A., L.A. Ostrovsky, M.B. Kanevsky, V.I. Titov, E.M. Zuikova, N.A. Sedunov and V.Y. Karaev

A05.06 Laboratory Study of Polarized Microwave Scattering from Steep Waves at Grazing Incidence 711
Rozenberg, A., D. Quigley, M. Ritter and W.K. Melville

A05.07 Inside the Sea-Spike: Low Grazing Angle Radar Imaging of Laboratory Waves Repeatedly Breaking in Wave Groups 714
Fuchs, J., S. Welch, T. Waseda, D. Regas and M.P. Tulin

A05.08 Monte Carlo Simulation of Backscattering from Natural Soil Surfaces 719
Casarano, D., F. Posa, F. Mattia, G. De Carolis, J.C. Souyris, T. Le Toan and G. Pasquariello

A05.09 Qualitative Analysis of the Effect of Roughness on Backscattered Signal Derived from SIR-C Data NA
Rao, Y.S., and K.S. Rao

A06: SAR Processing Algorithms

A06.01 A Processing Algorithm for the ENVISAT Alternating Polarization Mode Single Look Complex Product 722
Stevens, D.R., F. Wong, P. Lim and Y.L. Desnos

A06.02 Phase Preserving Processing of ScanSAR Data with Modified Range Doppler Algorithm 725
Wong, F., D.R. Stevens and J. Cumming

A06.03 Synthetic Aperture Radar Out of Slant Plane Motion Compensation 728
Stacy, N.J.S.

A06.04 A Comparison of Phase-Preserving Algorithms for Burst-Mode SAR Data Processing 731
Cumming, I., Y. Guo and Y. Wong

A06.05 Precision Two-dimensional Focusing of Spaceborne Synthetic Aperture Radar Data with Range-Varying Doppler Centroid 734
Heng, A.W.C., H. Lim, S.C. Liew and B.T.G. Tan

A06.06 SAR Image Interpretation Based on Markov Mesh Random Fields Models 737
Smits, P.C., F. Giorgini, A. Martuccelli, M. Petrou and S.G. Dellepiane

A06.07 The Spaceborne SAR Imaging Algorithms Research 740
Li, G., M. Zhu and X. Zhu

A06.08 Speckle Filter Based on Correlation Between Wavelet Transform Scales NA
Zhang, K., and M. Zhu

A07: Geology and Geomorphology

A07.01 Joint Analysis of Radar and VNIR/SWIR Images for Mapping Alluvial Fans NA
Gillespie, A.R.

A07.02 Multisensoral Approach for Studying the Geology and Tectonics of the Dead Sea Rift/Israel 743
Bodechtel, J., M. Frei, T. Wever, H. Kaufmann, Y. Xia and M. Beyth

A07.03 Mapping Evolutive Surface Deformations in Semi-Industrial and Urban Areas by Differential SAR Interferometry and Modelisation NA
Carnec, C., C. Delacourt, E. Burov, D. Legendre, H. Fabriol and C. King

A07.04 Estimation of SiO2 Content from TIR Spectra Measured on Weathered Surfaces of Igneous Rocks NA
Ninomiya, Y., and T. Matsunaga

A07.05 Volcanic Mapping with SIR-C/X-SAR Data for Western Kunlun of China 746
Wang, C., G. Huadong, and J. Liao

A07.06 Modeling Spatial Data Applied for Geomorphologic Mapping NA
Tuan, V.A., N.T. Cong, P.V. Cu, P.T. Hai, C.X. Huy, D.V. Khac, N.T. Thanh and L.A. Tuan

A07.07 Viewing China with the ERS-1 WSC Data 749
Wang, X., C. Wang, and G. Huadong

A07.08 Integrated Imaging of RADARSAT and Other SAR Data for Earthquake Tectonic Investigation of the Nahanni Earthquake Area in Northwest Territories, Canada NA
Moon, W.M., J. Ristau, V. Singhroy, Y. Yamaguchi, M. Lamontagn and R. Kuoda

A07.09 Effects of Terrain Types on the Selection of RADARSAT Beam Modes for Geological Mapping 752
Singhroy, V.

"NA" indicates not available at time of printing.

A08: Properties and Processing of SAR Speckle

A08.01 Comparison of the Statistical Properites of SAR Data, and Their Applications to SAR Classification NA
Sant'Anna, S.J., C.F. Yanasse, and S. Quegan

A08.02 Influence of Canopy Shape on SAR Speckle Distributions Over Woodland 755
Williams, M.L.

A08.03 Prior Scene Knowledge for the Bayesian Restoration of Mono- and Multi-Channel SAR Images 758
Nezry, E., A. Lopes, and F. Yakam-Simen

A08.04 Statistical Properties of Speckle and Full Polarimetric Filters in SAR 761
Sery, F., and A. Lopes

A08.05 Effects of Parameter Tuning and De-Speckle Filtering on the Accuracy of SAR Image Classification Based on Gray-Level Co-Occurrence Matrix Features 764
Bruzzone, L., S.B. Serpico, and G. Vernazza

A08.06 Bayesian Approach to SAR Image Reconstruction 767
Walessa, M., and M. Datcu

A08.07 Validation of Segmentation Techniques for SAR Images 770
Preston, M.I., and S. Quegan

A08.08 The Effect of Forest Understory on Synthetic Aperture Radar Backscatter 773
Silva, T., and J.B. Dias

A08.09 Block-Based Maximum Likelihood Classification for Hyperspectral Remote Sensing Data 778
Jia, X.

A09: Radar Observations of Forest

A09.01 SAR Image Analysis Methods for Forest Applications 781
Quegan, S., and J. Yu

A09.02 On the Coupling of Backscatter Models with Tree Growth Models - Part I: A Realistic Description of the Canopy Using the AMAP Tree Growth Model 784
Castel, T., A. Beaudoin, J.F. Barczi, Y. Caraglio, N. Floury, T. Le Toan and L. Castagnas

A09.03 On the Coupling of Backscatter Models with Tree Growth Models - Part II: RT Modelling of Forest Backscatter 787
Floury, N., T. Le Toan, J.A. Kong, T. Castel, A. Beaudoi and, J.F. Barcz

A09.04 Forest Applications of ERS, JERS, and SIR-C SAR Interferometry 790
Wegmuller, U., T. Strozzi and C. Werner

A09.05 Use of SAR Interferometry for Monitoring Clear Cutting of Forests 793
Smith, G., and J. Askne

A09.06 Analysis of CARABAS VHF SAR Data from BALTASAR-96 797
Ulander, L.M.H., P.O. Frolind, A. Gustavsson, H. Hellsten, T. Jonsson, B. Larsson and G. Stenstrom

A09.07 Modelling of VHF Radar Backscattering from Forests Based on Radiative Transfer 800
Israelsson, H., J. Askne and L. Ulander

A09.08 Radar Backscatter from Boreal Forest in Winter 803
Hallikainen, M., M. Makynen, J. Pulliainen and T. Vanska

A10: Coastal Environments

A10.01 Air/Sea/Land Interaction in the Coastal Zone Seen by Satellite RAR and SAR 806
Mitnik, L., V.B. Lobanov, M.K. Hsu, R.S. Tseng and K.S. Chen

A10.02 Remote Sensing Analysis of Submerged Coral Reefs: Applications for Integrated Coastal Management in Fiji 809
LeDrew, E., D. Knight and H. Holden

A10.03 Active and Passive Remote Sensing of Colored Dissolved Organic Matter (CDOM) in Marine Waters NA
Blough, N.V., A. Vodacek, F.E. Hoge and R.N. Swift

A10.04 Landcover Classification Using ERS SAR/INSAR Data Over Tropical Areas 813
Stussi, N., S. Liew, L.K. Kwoh, H. Lim, J. Nichol and K.C. Goh

A10.05 Potential Applications of Remote Sensing in the Coastal Environmental Management of Bangladesh NA
Khan, M.H., M. Emch and A. Islam

A10.06 Preliminary Study on Development and Management Information System of China Coastal Resources Environment 816
Jiang, X., and C. Yun

A10.07 Radarsat SAR Investigations of South Coasts of Korea for Coastal Zone Management: Preliminary Results NA
Won, J.S., J.K. Park and K.H. Chi

A10.08 Status of the Development of an In Situ Plankton Monitor 819
Campbell, W., J. Nault and R.A. Warner

B01: Marine Biochemistry

B01.01 Microbial Particles and Oceanic Optics: Where Do We Go Next? 821
Stramski, D.

B01.02 Light Absorption Measurements of Aquatic Particles: Status and Prospects 825
Tassan, S., B.G. Mitchell, D. Stramski and A. Bricaud

B01.03 Physico-Biological Oceanographic Remote Sensing of the East China Sea: Satellite and In Situ Observations NA
Ning, X., M. Fang, Z. Liu and J.C.Chen

B01.04 The Dependence of the Spectrum-Derived Chlorophyll a Concentration on the Profile of Chlorophyll a Concentration NA
Liu, C.T., M.H. Chang, C.L. Lee and Y.L.L. Chen

B02: Clouds and Precipitation I

B02.01 Retrieval of Liquid Water Distribution in Convective Clouds Using Microwave Computerized Tomography 830
Bobylev, L.P.

B02.02 Microwave Brightness Temperature Difference of Vertical and Tilted Tropical Convective Systems NA
Hong, Y., J. Haferman, and C.D. Kummerow

B02.03 Low Cost Digitalization of an X-Band, Non Coherent Weather Radar 833
Galati, G., G. Russo, G. Dargaud and G. Pavan

B02.04 Cloud Contamination in Cross Track and Conical Scanning Configurations NA
Divakarla, M.G., and L.M. McMillin

"NA" indicates not available at time of printing.

B03: Remote Sensing and Urban Planning

B03.01 Environmental Quality and Changes: A View from NDVI in Hong Kong 836
Fung, T.

B03.02 Urban Planning Using Data Fusion of Satellite and Aerial Photo Images 839
Cheng, P., and T. Toutin

B03.03 Information System for Monitoring the Urban Environment Based on Satellite Remote Sensing: Shanghai as an Example 842
Zhang, Y.

B03.04 Test of a Digital Camera Integrated with INS/GPS for Urban Environment Monitoring NA
Gong, P., G. Biging, K.P. Schwarz, M. Mostafa and Y. Sheng

B04: Educational Initiatives/Student Programs

B04.01 Investigation of the North-East Monsoon Characteristics in the Region of South East Asia Using ERS Wind Scatterometer Data 845
Guo, Y., J. Toh, Z. M. Zhang, I.I. Lin and V.H.S. Khoo

B04.02 Remote Sensing Educational Resources on the World Wide Web 848
Sivaprakash, S., J. Ng, N.L. Teo, V.H.S. Khoo and S.C. Liew

B04.03 National GIS Training Program: Korean Experiences 850
Lee, K., H.G. Lee and M.S. Kim

B04.04 Issues of WWW-Based Data Visualization in the Earth System Science Classroom 854
Mahootian, F.

B05: Remote Sensing of Sea Ice

B05.01 Temperature Corrected Bootstrap Algorithm 857
Comiso, J.C., and H.J. Zwally

B05.02 An Evaluation of Error Sources in the Retrieval of Antarctic Sea Ice Concetrations from Satellite Passive Microwave Data NA
Massom, R.A., J.C. Comiso, A.P. Worby, V. Lytle and I. Allison

B05.03 Bistatic Microwave Investigations of Media with Sea Ice-Like Properties NA
May, G.C., J.W. Bredow, A.K. Fung, S. Nadimi and J. Jin

B05.04 Wave Dispersion by Frazil-Pancake Ice from SAR Imagery 862
Wadhams, P., G. De Carolis, F. Parmiggiani, and M. Tadross

B06: SAR Interferometry: Phase Unwrapping

B06.01 Multiresolution Signal Representation for Phase Unwrapping and Interferometric SAR Processing 865
Bamler, R., and G.W. Davidson

B06.02 Phase Unwrapping by Fusion of Local and Global Methods 869
Reigber, A., and J. Moreira

B06.03 Comparison of Path-Following and Least-Squares Phase Unwrapping Algorithms 872
Pritt, M.D.

B06.04 Congruence in Least-Squares Phase Unwrapping 875
Pritt, M.D.

B06.05 How Global and Local Phase Unwrapping Techniques Are Connected 878
Fornaro, G., G. Franceschetti, R. Lanari, E. Sansosti and M. Tesauro

B07: Remote Sensing of Coral and Coastal Environments

B07.01 Modeling Water Surface Reflectance Signatures and In-Water Irradiance Profiles in Shallow Tropical Waters Influenced by Bottom Reflectance 881
Bostater, C.

B07.02 Analysis of the Diffuse Attenuation Coefficients for Radiance and the Implications for Retrieval of the Spectral Signature of Submerged Tropical Corals 885
LeDrew, E., and H. Holden

B07.03 Coastal Water Studies in Hong Kong -- Satellite Remote Sensing and Realtime Hydrology NA
Fang, M., D.R. Kester, Y. Li and X.R. Ning

B07.04 Environmental Monitoring of the Venice Lagoon Using MIVIS Data 888
Barducci, A., and I. Pippi

B08: Monitoring Urban Settlements

B08.01 Analysis of Radar Response from Urban Areas 891
Forster, B., C. Ticehurst and Y. Dong

B08.02 Inferring Urban Land Use from Very Fine Resolution Satellite Sensor Images Using Region-Based, Graphic-Theoretic Techniques NA
Barnsley, M., and S. Barr

B08.03 Road Network Extraction from Airborne Digital Camera Images: A Multi-Resolution Comparison 895
Gong, P., and J. Wang

B08.04 A Complex Spatial Analysis of Urban Areas Using Airborne Thermal Radiometry and GIS Techniques NA
Ben-Dor, E., H. Saaroni, A. Tshudnovski and A. Bitan

B08.05 Remote and In Situ Monitoring of Peri-Urban Wetlands NA
Fernandez, M., G.L. Rochon, J.K. Terry, J. Smith, C. Jernigan, D. Bardell and M. Mason

B09: Microwave Emission & Scattering from Rough Surfaces

B09.01 On the Surface Roughness Characterization for SAR Data Analysis 898
Mattia, F., J.C. Souyris, T. Le Toan, D. Casarano, F. Posa and M. Borgeaud

B09.02 Bare Soil Surface Observations and Modelling NA
Le Toan, T., P. Borderies, M. Borgeaud, I. Chenerie, F. Mattia, T. Mannenen and J.C. Souyris

"NA" indicates not available at time of printing.

B09.03 Electromagnetic Scattering Interaction Between a Dielectric Cylinder and a Slightly Rough Surface 901
Chiu, T., and K. Sarabandi

B09.04 Experimental Validation of Surface Scattering and Emission Models 904
Coppo, P., S. Lolli, G. Macelloni, G. Nesti, P. Pampaloni, R. Ruisi and D. Tarchi

B10: Image Processing and Feature Extraction

B10.01 Discontinuity Adaptive MRF Model for Remote Sensing Image Analysis 907
Smits, P.C., and S.G. Dellepiane

B10.02 Application of Adaptive Filters for Multisensoral Image Fusion 910
Steinnocher, K.

B10.03 Classification of Hyperdimensional Data Using Data Fusion Approaches 913
Benediktsson, J.A., and J.R. Sveinsson

B10.04 Integrated Mineral Exploration Using Multiple Exploration Data and JERS-1 SAR Data (East Java, Indonesia) NA
Jiang, W.W., S.K. Choi, Y. Yamaguchi, C.S. So, L. Feng and W.M. Moon

B11: NOAA Data Processing

B11.01 ATOVS & AVHRR Processing Package NA
Rochard, G.

B11.02 Comparison of Land Cover Indices of AVHRR Data 916
Sakurai-Amano, T., J. Iisaka, and M. Takagi

B11.03 Global Land Surface Temperature Products from AVHRR NA
Arino, O., Y. Kerr, J.P. Lagouarde, F. Nezry and C. Ottle

B11.04 Satellite-Derived Atmosphere Aerosol Optical Thickness and Size Distribution NA
Lynch, M.

C01: Electrical Geophysics Related to Complex Media

C01.01 Monte Carlo Simulations of Scattering of Electromagmetic Waves from Dense Distributions of Nonspherical Particles 919
Tsang, L., K.H. Ding and S.E. Shih

C01.02 A finite Difference Time Domain Simulation of Electromagnetic Wave Propagation and Scattering in a Partially Conducting Layered Earth 922
Calhoun, J.

C01.03 Complex Permittivity Measurements of Two Conifers 925
Franchois, A., R. Lang and Y. Pineiro

C01.04 3D Electromagnetic Modeling Using Staggered Finite Differences 929
Newman, G.A., and D.L. Alumbaugh

C01.05 3D Electromagnetic Inversion Using Conjugate Gradients 933
Newman, G.A., and D.L. Alumbaugh

C01.06 A Stable Algorithm for Simualtion of Two-and-Half Dimensional Problems in Electromagnetic Well Logging NA
Tian, X., C. Liu and L.C. Shen

C01.07 Inversion of 6FF40 Induction Tool Measurement Using the Distorted Born Iterative Method 938
Chen, S., W.C. Chew and W.D. Kennedy

C01.08 A New Numerical Method for Large-Scale Complex Media: The PSTD Algorithm 942
Liu, Q.H.

C01.09 3D PML-FDTD Simulation of Ground Penetrating Radar on Dispersive Earth Media 945
Teixeira, F.L., W.C. Chew, M. Straka, M.L. Oristaglio and T. Wang

C02: Educational Technologies/Student Programs

C02.01 The NASA Academy: A Four Year Experiment in Education NA
Soffen, G.

C02.02 Applications of Satellite Imagery, Visualizations, and Remote Sensing in Environmental/Science Education: An Earth Systems Science Approach NA
Moore, J.D.

C02.03 The International Space University: Its Mission and Programs 948
Bali, S.

C02.04 Project SUN (Students Understanding Nature) 951
Yanow, G., and A. Herzog

C02.05 The CSU-Chill Fully Polarimetric S-Band Weather Radar Facility: Providing Research Experience to Undergraduates 954
Bringi, V.N., and V. Chandrasekar

C02.06 Using the World Wide Web for Distributed Learning: Two Examples 957
Skiles, J.W., K.D. Kennedy, W.B. Rundberg, and D.L. Peterson

C02.07 " Winds of Change:" The NSCAT CD-ROM 960
Yanow, G.

C02.08 Landuse Study of the Sentosa Island Using SPOT Images 963
Zhao, L., F.Y. Tan, W. Quek, P. Chen and S.C. Liew

C03: Image Analysis and Information Fusion Technologies

C03.01 Evaluation of Elevation Derived form Interferometric SAR Data with DEM 966
Iwamoto, M., T. Fujisaka, C. Satoh, K. Kawabata and Y. Hara

C03.02 Applicability of Category Decomposition for the Fusion of Multi-Resolution Data 969
Takeuchi, S., and A. Inanaga

C03.03 Estimation of Topographic Effects in NVI Data Obtained form Satellite Images 972
Kusaka, T., and M. Sakane

"NA" indicates not available at time of printing.

C03.04 A Method for Object-Oriented Feature Extraction Hyperspectral Data - Generation of New Channels by Fusion of Data 975
Fujimura, S., and S. Kiyasu

C03.05 Bayesian Feature Selection for Classifying Multi-Temporal SAR and TM Data 978
Yamagata, Y., and H. Oguma

C03.06 Rainfield Detection Comparison in Small Regions with Particular Microclimatic Characteristics Using Meteosat and SSM/I Navigated Images 981
Piazza, E., P.F. Pellegrini and M. Tommasini

C03.07 Terrain Classification of SAR Images by Combined Distributional and Contextual Classifier NA
Muller, H.J., and P. Vieira

C03.08 Automatic Interaction Detector (Aid) Applied on Classified Images NA
Ho, L.L., and J.A. Quintanilha

C04: Emerging Technologies and Techniques

C04.01 Meeting Future Landsat Requirements with Emerging Technologies NA
Irons, J.R., D.L. Williams and S.G. Unger

C04.02 Geosynchronous Technology Infusion Studies 984
Hilliard, L., D. Jenstrom, D. Chesters and P. Racette

C04.03 Technologies for Future Remote Sensing Systems 987
Dionisio, C., M. Oricchio and F. Mura

C04.04 An Outlook for European Spaceborne Synthetic Aperture Radar 990
Heer, C., S. Mahdi, G. Angino, and A. Torre

C04.05 Future Operational Spaceborne Synthetic Aperture Radar System Considerations 993
Velten, E., and C. Heer

C04.06 The Radar Sail: An Innovative Satellite Concept for Reduced Cost and High Performance Radar Mission NA
Aguttes, J.P., J. Sombrin and E.Conde

C04.07 Next-Generation Coherent Radar Depth Sounder for Measurement of Greenland Ice Sheet Thickness 996
Legarsky, J., T. Chuah and S.P. Gogineni

C04.08 A New Airborne Remote Sensing Platform for Acquiring Spatial and Radiation Information 999
Liu, Z., and S. Li

C05: Remote Sensing of Ocean Surface Parameters

C05.01 Combined High-Resolution Active and Passive Imaging of Ocean Surface Winds from Aircraft 1001
Gasiewski, A.J., J.R. Piepmeier, R.E. McIntosh, C.T. Swift, J.R. Carswell, W.J. Donnelly, E. Knapp, E.R. Westwater, V.I. Irisov, L.S. Fedor and D.C. Vandemark

C05.02 High-Resolution Multiband Passive Polarimetric Observations of the Ocean Surface 1006
Piepmeier, J.R., and A.J. Gasiewski

C05.03 Multi-Frequency Polarimetric Ocean Wind Direction Retrievals 1009
Chang, P., P.W. Gaiser, K. St.Germain and L. Li

C05.04 Satellite Remote Sensing of Air-Sea Energy Fluxes NA
Schluessel, P.

C05.05 Sea Surface Temperature Estimation Using Active/Passive Microwave Remote Sensing NA
Wang, N.Y., and J.F. Vesecky

C05.06 Development of a Sea Surface Temperature Algorithm for the ADEOS II/AMSR 1012
Galloway, J., M. Goodberlet and C. Swift

C05.07 A Neural Network Approach to the Determination of Ocean Latent Heat Flux from Multisensor Satellite Data NA
Gautier, C., P. Peterson and C. Jones

C05.08 Estimation of Ocean Wave Height from Grazing Incidence Microwave Backscatter 1015
Buckley, J.R., and J. Aler

C06: High Resolution 3D SAR

C06.01 Ramses Interferometer: A Step to High Resolution NA
Pairault, B., D. Sicard and J.M. Boutry

C06.02 A Comparison of Two Airborne Interferometric SAR Systems NA
Huelskamp, R.M., D.L. Bickel and D.A. Yocky

C06.03 The JPL Dual Frequency/Dual Baseline Interferometer for Geophysical Topographic Mapping Research NA
Hensley, S., P. Rosen, E. Rodriquez, E. Chapin, A Freeman and Y. Kim

C06.04 Calibration of a High Resolution Airborne 3-D SAR 1018
Dall, J., J. Grinder-Pederson and S.N. Madsen

C06.05 The Mount Etna Case Study: A Multisensoric View 1022
Horn, R., K.P. Papathanassiou, A. Reigber, R. Scheiber, P. Hausknecht, P. Strobl, R. Boehl, M. Scheele, R. Reulke, W. Baerwald, G. Puglisi and M. Coltelli

C06.06 Results of the German DO-SAR in C- and X-Band Interferometric NA
Fritsch, B.

C06.07 An Airborne Radar for High Precision Digital Elevation Model Generation NA
Moreira, J.R.

C06.08 First Results in 3D SAR Imaging Using a Three Antenna Sensor NA
Schmitt, K., and W. Wiesbeck

C07: Neural Networks

C07.01 Feature Extraction for Neural Network Classifiers Using Wavelet and Tree Structured Filter Banks 1026
Sveinsson, J.R., J.A. Benediktsson and O. Hilmarsson

C07.02 Two-Layer Perceptrons for Urban Landuse Classification: Evaluation of Conjugate Gradient Based Learnin NA
Staufer, P., and M.M. Fischer

C07.03 Neural Network-Based Cloud Classification Using Textrual Features NA
Tian, B., M.A. Shaikh, M.R. Azimi-Sadjadi, T.H. Vonder Haar and D. Reinke

"NA" indicates not available at time of printing.

C07.04 Evaluation of the Performance of the Self Organized Feature Map Neural Network Using Various Texture Descriptions for Cloud Detection NA
Stephanidis, C.N., T. Parrinello, A.P. Cracknell and R.A. Vaughan

C07.05 Development of New Automated Land Cover Change Detection System for Remotely Sensed Imagery Based on Artificial Neural Networks 1029
Dai, X., and S. Khorram

C07.06 Characterisation of Agricultural Land Using Signal Processing and Cognitive Learning Techniques 1032
Herries, G.M., and T. Selige

C07.07 The Implementation of a Fuzzy Self Organised Feature Map Neural Network for Digital Image Classification NA
Stephanidis, C.N., and A.P. Cracknell

C07.08 The Prediction of the Upwelling Phenomenon at the Northwest African Atlantic Coast — A Connectionist Approach 1035
Kriebel, S.K.T.

C08: SAR Speckle Filtering and Classification

C08.01 Polarimetric SAR Speckle Filtering and Its Impact on Classification 1038
Lee, J.S., M.R. Grunes and G. De Grandi

C08.02 The Principles of Polarimetric Filtering 1041
Quegan, S., and J. Schou

C08.03 Optimal Bayesian Texture Estimators for Speckle Filtering of Detected and Polarimetric Data 1044
Lopes, A., J. Bruniquel, F. Sery and E. Nezry

C08.04 Radar Reflectivity Estimation Using Multiple SAR Scenes of the Same Target: Techniques and Applications 1047
De Grandi, G.F., M. Leysen, J.S. Lee and D. Schuler

C08.05 Control Systems Principles Applied to Speckle Filtering and Geophysical Information Extraction in Multi-Channel SAR Images 1051
Nezry, E., F. Zagolski, I. Supit and F. Yakam-Simen

C08.06 Multiresolution Adaptive Speckle Filtering: A Comparison of Algorithms 1054
Aiazzi, B., L. Alparone, S. Baronti and G. Borri

C08.07 The Application of Wavelet Transform for Speckle Suppression in Radar Imagery 1057
Dong, Y., B. Forster, A. Milne and C. Ticehurst

C09: RADARSAT

C09.01 RADARSAT Applications Development at CCRS NA
Brown, R.J., B. Brisco and M.A. D'Iorio

C09.02 Use of RADARSAT ScanSAR Products for Regional Mapping in Southeast Asia 1060
Nazarenko, D.M., G. Mitchell and G.C. Staples

C09.03 Assessment of RADARSAT Data for Tropical Forest Observations NA
Le Toan, T., F. Ribbes, J. Bruniquel, N. Stussi, S.C. Liew, H. Lim, U.R. Wasrin

C09.04 Using the RADARSAT SAR Versatility to Enhance Fine Resolution Imaging Capabilities 1063
Luscombe, A.P., D.A. Furseth, S. Srivastava and W.C. Jefferies

C09.05 Interferometric RADARSAT Data for Topographic Mapping of the Three Gorge Area and Yellow River Delta NA
Huadong, G., S. Yun, L. Jingjuan, W. Changling, L. Hao and L. Junfei

C09.06 Delineating and Mapping Rainfed Dry Direct-Seeded Rice in the Mekong River Delta, Vietnam, Using RADARSAT SAR Imagery NA
Kam, S.P., T.P. Tuong, L. Balababa, V.Q. Minh and R. Brown

C09.07 RADARSAT Image Quality and Calibration Results 1066
Srivastava, S.K., R.K. Hawkins, T.I. Lukowski, B. Banik and M. Adamvic

C09.08 A Preliminary Study of Phenological Growth Stages of Wetland Rice Using ERS1/2 SAR Data 1069
Bakar, S.B.A., A.T. Shaari, H.T. Chuah and H.T. Ewe

C10: Monitoring Crops and Forests

C10.01 Application of Radar Remote Sensing in Mapping and Monitoring Tropical Forest Types in Amazon Basin NA
Saatchi, S., B. Nelson, A. Freeman and B. Chapman

C10.02 Effects of Within-Season Dielectric Variations on Terrain Classification Using SIR-C/X-SAR 1072
Bergen, K., M.C. Dobson, L. Pierce and F. Ulaby

C10.03 Scale Integration of Bi-Directional Reflectance Effects in Remotely Sensed Vegetated Surfaces 1075
Burgess, D.W., J.R. Dymond, D. Pariman and J. Shepherd

C10.04 Airborne SAR in an End-To-End System for Sustainable Forest Management 1078
Greidanus, H., D.H. Hoekman, R.J.A. Grim and W.J. Looyen

C10.05 Comparing Accuracy of Satellite and Airborne Remote Sensing Data in the Retrieval of Forest Stand Attributes 1081
Hyyppa, J., M. Inkinen, H. Hyypa, M. Engdahl and M. Hallikainen

C10.06 Tasseled Cap Transformation and Spectral Angle Mapper Classification of Fujo 1 OPS Data for Winter Cover Monitoring NA
Kim, C.

C10.07 Application of Multitemporal ERS Synthetic Aperture Radar in Delineating Rice Cropping Systems in the Mekong River Delta 1084
Liew, S.C., S.P. Kam, T.P. Tuong, P. Chen, V.Q. Minh, L. Balababa and H. Lim

C10.08 Combined ERS SAR and Optical Satellite Data for the Estimation of Forest Structual Attributes 1087
Kattenborn, G., and E. Nezry

"NA" indicates not available at time of printing.

D01: Soil Moisture I

D01.01 Soil Moisture Estimation Under Sparse Vegetation Using Microwave Radiometry at C-Band 1090
Chanzy, A., Y. Kerr, J.P. Wigneron, and J.C. Calvet

D01.02 Microwave Remote Sensing of Soil Moisture for Estimation of Soil Properties 1093
Mattikalli, N.M., E.T. Engman, and T.J. Jackson

D01.03 Retrieval of Soil Moisture Using a Dynamic Learning Neural Network Trained with a 1-Dimensional Hydrology/Radiobrightness Model 1096
Liou, Y.A., Y.C. Tzeng and A.W. England

D01.04 Passive Microwave Observation of Soil Water Infiltration 1099
Jackson, T.J., T.J. Schmugge, W.J. Rawls, P.E. O'Neill and M.B. Parlange

D01.05 Land Surface Hydrological Processes Using Satellite Data 1102
Lakshmi, V., and J. Susskind

D01.06 Soil Moisture Profile Determination Using Remote Sensing Techniques 1105
Timchenko, A.I., and Y.V. Gorishnya

D01.07 Dielectric Model of Bound Water in Wet Soils for Microwave Remote Sensing 1108
Tikhonov, V.V.

D02: Remote Sensing of Precipitation

D02.01 Rain/No-Rain Discrimination for TRMM Precipitation Radar 1111
Kumagai, H., T. Kozu and T. Igushi

D02.02 Assessment of Multiparameter Radar Rain Rate Algorithms Using an Optimal Area Approach 1114
Bolen, S., V.N. Bringi and V. Chandrasekar

D02.03 Non-Uniform Beam Filling Correction for Spaceborne Rain Radar Measurement: A Simulation Study by Using Shipborne Radar Data Over Tropical Pacific 1117
Kozu, T., and T. Iguchi

D02.04 Space-Borne Remote Sensing of Cloud Liquid Water Content by Combined Radarmeter 1120
Liu, J., L. Zhang and D. Lu

D02.05 Applications of Self-Consistency Principle to Multiparameter Radar Measurements in Rainfall NA
Scarchilli, G., and E. Gorgucci

D02.06 Attenuation Compensation Technique for an X-Band Polarimetric Weather Radar 1123
Galati, G., G. Pavan and G. Scarchilli

D02.07 Dual Polarisation and Multifrequency Measurements of Rain Date and Drop Size Distribution by Ground-Based Radar and Radiometers 1126
Hornbostel, A., A. Schroth, B.G. Kutuza and A. Evtuchenko

D02.08 Indian Doppler Weather Radar System - An Overview 1129
Viswanathan, G., Members of Project Team, R.C. Bhatia, V.P. Kamble and S.R. Rao

H08: Aerosols

H08.01 The Aerosol Optical Thickness Retrieval from GOME Spectra 1908
Bartoloni, A., M. Mochi, C. Serafini, M. Cervino, R. Guzzi and F. Torricella

H08.02 Aerosol Optical Thickness Over Ocean Areas and Its Relationship With Cloud Droplet Size 1911
Han, Q., J. Chou, and R.M. Welch

H08.03 Effects of Atmospheric Aerosol Models on the Single Scattering Point Spread Function in Optical Remote Sensing 1914
Liew, S.C.

H08.04 Aerosol Retrieval Using Synthetic POLDER Multi-Angular Data 1917
Kuo, K.S., R.C. Weger and R.M. Welch

H08.05 Aerosol Optical Thickness and Scattering Phase Function Retrieval from Solar Radiances Recorded over Water: A Revised Approach 1920
Paronis, D.K., and J.N. Hatzopoulos

H08.06 The Long Distance Transport of Sand Dust and Aerosols from Northern China to Hong Kong NA
Fang, M., M. Zheng, K.S. Chim and S.C. Kot

H08.07 Comparing Optical Models of Atmospheric Aerosol with Results of Multi-Wavelength Laser Sounding NA
Chaikovsky, A.P., A.P. Ivanov, F.P. Osipenko, and V.N. Shcherbakov

H08.08 Satellite Remote Sensing of Fires, Smoke and Regional Radiative Energy Budgets 1923
Christopher, S.A., M. Wang, K. Barbieri, R.M. Welch and S.K. Yang

H09: Advance Sensors and Sensor Calibration II

H09.01 Polarimetric Effects in Repeat-Pass SAR Interferometry 1926
Papathanassiou, K.P., and S.R. Cloude

H09.02 Height Model Generation, Automatic Geocoding and Mosaicing Using of Airborne AES-1 InSAR Data 1929
Holecz, F., J. Moreira, P. Pasquali, S. Voigt, E. Meier and D. Nuesch

H09.03 Calibration of Airborne AES INSAR Data NA
Holecz, F., J. Moreira and P. Pasqauli

H09.04 InSAR Takes over the Former Roll of Photogrammetry NA
Moreira, J., and F. Holecz

H09.05 Coherence Optimisation in Polarimetric SAR Interferometry 1932
Cloude, S.R., and K.P. Papthanassiou

H09.06 The X-Band SAR Demonstrator Development 1935
Zahn, R., H. Braumann and M. Schlott

H09.07 A Novel Model of the Platform Attitude Drift for SAR 1938
Song, H., M. Zhu and Y. Bai

H09.08 SIR-C Polarimetric Calibration by Using Polarization Selective Dihedrals and a Polarimetric Active Radar Calibrator 1941
Fujita, M., T. Masuda, Y. Fujino and M. Satake

"NA" indicates not available at time of printing.

D05: Remote Sensing of Mesoscale Features

D05.01 Coastal Wind Field Retrievals from ERS SAR Images 1153
Korsbakken, E., J. A. Johannessen and O.M. Johannessen

D05.02 Climatology of Wind and Waves from Satellite Altimeters 1156
Hwang, P.A., W.J. Teague and G.A. Jacobs

D05.03 Towards Extracting Fine-Scale Winds from Synthetic Aperture Radar Images 1159
Mourad, P.D.

D05.04 Study of Atmospheric Boundary Layer Rolls Near Spitsbergen by Using ERS SAR Images of the Sea Surface and a Numerical Model 1162
Alpers, W., G. Muller and B. Brummer

D05.05 COASTWATCH'95: Upper Ocean Features from ERS SAR Imagery 1165
Johannessen, O.M., E. Korsbakken, H.A. Espedal, V. Jensen, A.D. Jenkins and J.A. Johannessen

D05.06 Remote Sensing of Estuarian Ocean Fronts During the Chesapeake Bay Outflow Plume Experiment (COPE-1) NA
Trizna, D., M. Sletten, N. Allen, G. Marmarino and T. Donato

D05.07 ERS-1/2 SAR Detection of Natural Film on the Ocean Surface 1168
Espedal, H.A., O.M. Johannessen, J.A. Johannessen, E. Dano, D. Lyzenga and J. Knulst

D05.08 Tilting Effect on the Derivation of Wind Speed from Satellite Altimeters 1171
Hwang, P.A., W.J. Teague, G.A. Jacobs and D.W. Wang

D06: SAR Image Filters & Non-Bayesian Classification Techniques

D06.01 Automated Hierarchical Classification of SAR Images 1174
Smits, P.C., R. Vaccaro and S. Dellepiane

D06.02 Identifying Classes in SAR Sea Ice Imagery Using Correlated Texture 1177
Soh, L.K., and C. Tsatsoulis

D06.03 Use of SAR Image Texture in Terrain Classification 1180
Dobson, M.C., L. Pierce, J. Kellndorfer and F. Ulaby

D06.04 Efficiency of Bi-Polarization and Correlative Radar-Radiometer System for Detection and Identification of Observed Surfaces Anomalous Formations NA
Arakelian, A.K.

D06.05 Fuzzy Clustering of Textured SAR Images Based on a Fractal Dimension Feature 1184
Alparone, L., M. Barni, M. Betti and A. Garzelli

D06.06 A Knowledge Based Approach for Mapping of Road Networks Using GIS Database NA
Forghani, A.

D06.07 Multiresolution Analysis and Processing of Synthetic Aperture Radar Images Using Wavelets 1187
Fukuda, S., and H. Hirosawa

D06.08 Suitability of Selected Structural Properties and Relations for Inferring Land Use from an Initial Land Cover Classification of Remotely-Sensed Images NA
Barr, S., and M. Barnsley

D07: Neural Network Applications in Remote Sensing

D07.01 Trends on Information Processing for Remote Sensing 1190
Chen, C.H.

D07.02 Artificial Neural Network-Based Inversion Technique for Extracting Ocean Surface Wave Spectra from SAR Images 1193
Kasilingam, D., and J. Shi

D07.03 Neural Computing for Seismic Principal Components Analysis 1196
Huang, K.Y

D07.04 Filtering Effects on Polarimetric SAR Image Classification 1199
Chen, K.S., Y.C. Tzeng, C.T. Chen and J.S. Lee

D07.05 Training of Neural Networks for Classification of Imbalanced Remote-Sensing Data 1202
Serpico, S.B., L. Bruzzone

D07.06 Land Use Analysis of Remote Sensing Data by Kohonen Nets 1205
Nogami, Y., Y. Jyo, M. Yoshioka and S. Omatu

D07.07 Wind Reconstruction form ERS-1 Scatterometer Data Using Neural Network 1208
Tzeng, Y.C., and K.S.Chen

D07.08 The Application of Artificial Neural Networks and Standard Statistical Methods to SAR Image Classification 1211
Ghinelli, B.M.G., and J.C. Bennett

D08: Satellite and Airborne Missions

D08.01 First Airborne Tests with the New VHF SAR CARABAS II 1214
Gustavsson, A., B. Flood, P.O. Frolind, H. Hellsten, T. Jonsson, B. Larsson, G. Stenstrom and L.M.H. Ulander

D08.02 RADARSAT-1 Background Mission for a Global SAR Coverage 1217
Mahmood, A.

D08.03 The MODIS BRDF/Albedo Product: Prototyping Albedo Retrieval Using AVHRR and GOES 1220
Strahler, A., R. d'Entremont, W.W. Lucht, B. Hu, X. Li and C. Schaaf

D08.04 A Cost-Effective, Airborne Digital Video System for Producing Rectified, Geo-Referenced Digital Images 1224
Kemppinen, M., and T. Auer

D08.05 A Test Site Network for EOS-MODIS Global Land Cover Classification Based on Representativeness Criteria 1227
Muchoney, D., J. Hodges, A. Hyman and A. Strahler

D08.06 First In-Flight Results from POLDER/ADEOS over the Terrestrial Biosphere 1230
Leroy, M., and O. Hautecoeur

D08.07 Activities at the Institute of Industrial Science, University of Tokyo as a Distributed Data Center Via Network NA
Takagi, M.

D08.08 The Remote Sensing Programme of the German Aerospace Research Establishment (DLR) NA
Ottl, H.

"NA" indicates not available at time of printing.

D09: Surface Temperature: Observations and Applications

D09.01 Instrumentation for Land Surface Temperature Measurements NA
Kahle, A.B.

D09.02 Temperature and Emissivity Separation from Advanced Spaceborne Thermal Emission and Reflection Radiometer (ASTER) Images NA
Gillespie, A.

D09.03 Application of the TES Algorithm to TIMS Data Aquired in HAPEX-Sahel 1233
Schmugge, T., S. Hook and C. Coll

D09.04 Hyperspectral TIR Remote Sensing of Fans and Bedrock Near Yuma, Arizona, USA NA
Gillespie, A.

D09.05 Potential Interest of a Combined Use of MODIS and ASTER Data for the Determination of Surface Temperature and Emissivity NA
Becker, F., and Z.L. Li

D09.06 Lithologic Mapping in the Iron Hill, Colorado, USA Area Using Airborne Multispectral Thermal-Infrared Data and Simulated Advanced Spaceborne Thermal Emission and Reflection Radiometer (ASTER) Data NA
Rowan, L.C., and K. Watson

D09.07 An Overview of Volcanological Application of Infrared Remote Sensing NA
Realmuto, V.J.

D09.08 ASTER Observations for the Monitoring of Land Surface Fluxes 1236
Schmugge, T.

D09.09 Application of High Resolution Side-Looking MSS Data to Heat Island Potential in Urban Area 1239
Hoyano, A., and A. Iino

D10: Data Standards and Distributions

D10.01 Derivative Analysis of Hyperspectral Data for Detecting Spectral Features 1243
Tsai, F., and W. Philpot

D10.02 Reading SAR Data: A New General Reader and a Proposed New Standard 1246
Pierce, L.

D10.03 Operational Performance of Radarsat's Canadian Data Processing Facility NA
Jefferies, W.C., D.J. Wilson and R. Periard

D10.04 Standard Data Products form the MODIS Science Team 1249
Fishtahler, L.E.

D10.05 Intelligent Guide to Earth Observation - IGEOS NA
Zingler, M.

D10.06 Towards a Common Language in Satellite Data Management: A New Processing Level Nomenclature 1252
Gutman, G., and A. Ignatov

D10.07 Innovations in Response to Floods of Data 1255
Ziskin, D.C., and P. Chan

D10.08 A Catalog-Browse System with Quick-Look Images for SPOT, ERS and RADARSAT Data Archives 1257
Kwoh, L.K.

E01: Soil Moisture II

E01.01 Soil Moisture Estimation with RADARSAT NA
Brisco, B., T.J. Pultz, R.J. Brown and Q.H.J. Gwyn

E01.02 Estimating Hydrological Parameters with Multifrequency SAR Data 1260
Paloscia, S., G. Macelloni, P. Pampaloni and S. Sigismondi

E01.03 Profile Soil Moisture Estimation Using the Modified IEM 1263
Walker, J.P., P.A. Troch, M. Mancini, G.R. Willgoose and J.D. Kalma

E01.04 Examination of Soil Moisture Retrieval Using SIR-C Radar Data and a Distributed Hydrological Model 1266
Hsu, A.Y., P.E. O'Neill, E. F. Wood and M. Zion

E01.05 A Hybrid Algorithm for Soil Surface Backscattering and Its Use for Soil Moisture Retrival NA
Su., Z., P.A. Troch and R. Hoeben

E01.06 Estimation of Soil Moisture for Vegetated Surfaces Using Multi-Temporal L-Band SAR Measurements 1269
Shi, J., G. Sun, A. Hsu, J. Wang, P. O'Neill, J. Ranson and E.T. Engman

E01.07 On the Retrieval of Soil Moisture Retrieval from SAR Data Over Bare Soils 1272
Pasquariello, G., G. Satalino, F. Mattia, D. Casarano, F. Posa, J.C. Souyris, and T. Le Toan

E01.08 Soil Moisture Estimation Using SIR-C Data: A Case Study Over Bhavnagar Test Site, India NA
Rao, K.S., and Y.S. Rao

E02: Hydrological Cycle

E02.01 Global Pattern of Potential Evaporation Calculated from the Penman-Monteith Equation Using Satellite and Assimilated Data NA
Choudhury, B.J.

E02.02 Precipitation Efficiency, Free-Tropospheric Vapor, and Global Warming NA
Spencer, R.W., and W.D. Braswell

E02.03 Climatological Features of the East Asian Summer Monsoon Based on Satellite Estimates of Heat Budget and Hydrological Variables NA
Sohn, B.

E02.04 Passive Microwave Signatures of the Melting Layer in Stratiform Clouds 1275
Bauer, P., J.P.V. Poiares Baptista and M. de Iulis

E02.05 Atmospheric Latent Heating Distributions Retrieved from SSM/I Passive Microwave Measurements NA
Smith, E.A., and S. Yang

E02.06 Recent Advances in Observing the Distribution and Variability of Thunderstorms from Space NA
Goodman, S.J., H.J. Christian, K.T. Driscoll, R.J. Blakeslee, D.J. Bocippio, D.A. Mach, and D.E. Buechler

E02.07 The TRMM Mission NA
Kummerow, C., J. Simpson, and Y. Hong

E02.08 Linking Passive Microwave Observations to a Summertime LSP/Radiobrightness Model for Northern Prairie Grassland NA
Judge, J., and A.W. England

"NA" indicates not available at time of printing.

E03: Detection of Buried Objects and Voids II

E03.01 Range of Effectiveness of Electromagnetic Detection of Buried Cylindrical Conductors NA
Moses, R.W., J.M. Mack and L.G. Stolarczyk

E03.02 Ultrawideband Radar Detection of Buried Objects 1278
Daniels, D.J.

E03.03 Preliminary Field Results of an Ultra-Wideband (10-620 MHz) Stepped-Frequency Ground Penetrating Radar 1282
Stickley, G.F., D.A. Noon, M. Cherniakov and I.D. Longstaff

E03.04 Extraction of Discriminant Features from Impulse Radar Data for Classification of Buried Objects 1285
Brunzell, H.

E03.05 Radar Detection of Near-Surface Buried Metallic Reflectors in Wet Soil 1288
O'Neill, K.

E03.06 Radar Detection of a Void in Lossy Clay Ground NA
Murray, W., C. Williams and C. Lewis

E03.07 The Mapping of Buried Pipes and Cables in a Street Environment NA
Chignell, R.J., H. Dadis and H. West

E03.08 Short-Pulse Ground Penetrating Radar (SP-GPR) for Buried Objects Detecting: Signal Processing and 3-D Mapping NA
Fang, G., Zengyi, J. Guo, C. Wang, Zhanyi, Y. Yuan and X. Chen

E04: Sea Ice Remote Sensing and Applications to Global Change Detection

E04.01 A Comparison of Sea Ice Type, Sea Ice Temperature, and Snow Thickness Distributions in Arctic Seasonal Sea Ice Zones With the DMSP SSMI 1291
St.Germain, K., D.J. Cavalieri and T. Marcus

E04.02 Global Sea Ice Cover - Retreating in the North and Advancing in the South NA
Cavalieri, D.J., C.L. Parkinson, P. Gloersen, J.C. Comiso, and H.J. Zwally

E04.03 Results of Satellite and In-Situ Remote Sensing Measurement and Modeling Studies of Arctic Sea Ice Which Support the Monitoring of Changes in the Global Climate 1294
Onstott, R.G.

E04.04 SeaSAT Scatterometer Observations of Sea Ice 1297
Swift, C.T.

E04.05 Surface Temperatures from 1979 Through 1995 in the Antarctic Region Derived from Satellite Infrared Data 1300
Comiso, J.C., and L. Stock

E04.06 Modeling and Interpretation of Ultra-Wideband Microwave Scattering Measurements of Simulated Sea Ice 1305
Kanagaratnam, P., S.P. Gogineni and K. Jezek

E04.07 Modeling Interpretation of Active and Passive Measurements from Sea Ice 1308
Fung, A.K., and S. Tjuatja

E04.08 The Influence of the Atmosphere on the Remote Sensing of Sea Ice Using Passive Microwave Radiometers 1311
Oelke, C.

E04.09 Analysis of Sea Ice Thickness and Mass Estimation with a Spaceborne Laser Altimeter 1314
Luntama, J.P., S. Koponen and M. Hallikainen

E05: Hydrodynamic Modeling of Oceanic Interactions

E05.01 Wave-Breaking Effects in Radar Signatures from 2-Dimensional Modelling of the HI-RES-1 Rip Features 1317
Chubb, S.R., A.L. Cooper, R.A. Fusina and R.W. Jansen

E05.02 Intercomparison and Validation of Bathymetry Radar Imaging Models 1320
Greidanus, H., C. Calkoen, I. Hennings, R. Romeiser, J. Vogelzang and G.J. Wensink

E05.03 The Bathymetry Assessment System NA
Wensink, G.J., C.J. Calkoen and G.H.F.M. Hesselmans

E05.04 Stress Modulation Account in the Problem of the Wave Spectrum Transformation Caused by Nonuniform Currents 1323
Trohkimovski, Y.

E05.05 On the Polarization-Dependent Signatures of Atmospheric and Oceanic Features in Radar Images of the Ocean Surface 1326
Romeiser, R.

E05.06 Dynamics and Statistics of Intense Internal Waves Over a Continental Slope 1331
Talipova, T., E. Pelinovsky and P.E. Holloway

E05.07 Spectral Nonlinearities of the Gravity-Capillary Waves and Their Effect on Sea Surface Radar Signatures 1332
Pavlakis, P.J.

E05.08 Radar and Optical Measurements of Damping of Small-Scale Wind Waves in Artificial Slicks 1335
Ermakov, S.A., E.M. Zuikova, I.A. Sergievskaya, Yu.B. Shchegolkov, S.V. Kijashko, A.G. Luchinin, J.C. da Silva, N. Stapleton and J.C. Scott

E06: SAR Interferometry: DEM Generation and Assessment

E06.01 Producing Ground Deformation Maps Automatically: The DIAPASON Concept 1338
Massonnet, D.

E06.02 RADARSAT Repeat-Pass SAT Interferometry Results NA
Geudtner, D., and P.W. Vachon

E06.03 A Flexible System for the Generation of Interferometric SAR Products 1341
Eineder, M., and N. Adam

E06.04 Operational DEM Generation by Means of SAR Interferometry 1344
Herland, E.A., and A. Vuorela

E06.05 Calibrating Interferograms with High-Quality DEMs NA
Seymour, M., and I. Cumming

E06.06 ERS SAR Interferometry: An Operational Evaluation of the DTM Production 1347
Dupont, S., P. Nonin, L. Renouard, G. Pichon and M. Berthod

"NA" indicates not available at time of printing.

E06.07 Map Generation Utilizing IFSARE Imagery and Digital Elevation Models from the Intermap STAR-3i System 1350
Bullock, M.E., G. Lawrence, R.V. Dams and K. Tennant

E06.08 The AIRSAR/TOPSAR Integrated Multi-Frequency Polarimetric and Interferometric SAR Processor 1358
van Zyl, J.J., A. Chu, S. Hensley, Y. Lou, Y. Kim and S.N. Madsen

E07: Terrain Scattering Models and Their Applications

E07.01 Implementation of the Integral Equation Model for Rough Surfaces with Generic Isotropic Autocorrelation Functions 1361
Nesti, G., R. Estevan de Quesada, J.M. Lopez and A.J. Sieber

E07.02 A Reappraisal of the Validity of IEM Model 1365
Wu, T.D., K.S. Chen, A.K. Fung, Z. Su, P.A. Troch, R. Hoeben and M. Mancini

E07.03 Sensitivity of Radar Backscattering to Soil Surface Parameters: A Comparison Between Theoretical Analysis and Experimental Evidence 1368
Hoeben, R., P.A. Troch, Z. Su, M. Mancini and K.S.Chen

E07.04 Topography Sensing by Polarimetric SAR: Theoretical Basis and Application Using Orthogonal-Pass AIRSAR Data 1371
De Grandi, G.F., D.L. Schuler, T.L. Ainsworth and J.S. Lee

E07.05 Interpretation of Radar Measurments from Rough Soil Surface with a Permittivity Profile 1376
Fung, A.K., J. Boisvert and B. Brisco

E07.06 Polarimetric Radar Response of Forest Canopies: A Sensitivity Study Based on a Monte Carlo Coherent Model NA
Lin, Y.C., and K. Sarabandi

E07.07 A Successive Approximation Series for TE and TM Scattering from One-Dimensional Conducting Rough Surfaces 1379
Moyssidis, M.A., C.N. Vazouras, P.G. Cottis and J.D. Kanellopoulos

E08: Advance Sensors and Sensor Calibration I

E08.01 Influence of the Radiometer System Parameters and the Frequency Used in the Ground-Based Microwave Measurement of the Atmospheric Water Vapor NA
Hashimoto, S., N. Yamashita, and T. Mikami

E08.02 Radarsat Elevation Antenna Pattern Determination 1382
Lukowski, T.I., R.K. Hawkins, C. Cloutier, J. Wolfe, L.D. Teany, S.K. Srivastava, B. Banik, R. Jha and M. Adamovic

E08.03 The Effect of Atmospheric Correction on AVIRIS Data to Obtain Consistent Multiyear Foliage Chemistry Results 1385
Goetz, A.F.H., K.B. Heidebrecht and B. Kindel

E08.04 The Airborne X/L-Band SAR System of CRL/NASDA: System Description and Preliminary Results 1389
Kobayashi, T., M. Satake, H. Masuko, M. Shimada, H. Oaku and T. Umehard

E08.05 A Study on Radiometric Calibration of Next Generation Spaceborne SAR 1392
Hara, Y., C. Ohno, M. Iwamoto, N. Kondo, Y. Kamiya and Y. Nemoto

E08.06 Efficient Technique for Holographic Imaging Diagnostic to Antennas in Cylindrical Near-Field Scanning NA
Hussein, Z.A.

E08.07 ARIES - A Simulator for the Next Generation of Spaceborne IR Meteorological Sounders 1395
Wilson, S.H.S., N.C. Atkinson, P.J. Rayer, J. Smith and D.R. Pick

E08.08 Calibration of AVHRR Data Generated by the On-Board TIROS-N Using Ocean and Cloud Views 1398
Cracknell, A.P., and I. Busu

E08.09 93 GHz Dual-Channel Airborne Imaging Radiometer (AIR-93) and its Data Examples NA
Kemppinen, M., T. Auer, I. Mononen and M. Hallikainen

E09: Polarimetric and Interferometric Remote Sensing

E09.01 Polarimetry in Remote Sensing: Basic and Applied Concepts 1401
Boerner, W.M., H. Mott and E. Luneburg

E09.02 The NASA/JPL Airborne Synthetic Aperture Radar's 1996 Pacrim Deployment 1404
Lou, Y., Y. Kim, J. van Zyl, L. Maldonado, T. Miller, E. O'Leary, G. Romero, W. Skotnicki and V. Taylor

E09.03 Littoral Remote Sensing Using Polarimtery SAR 1407
Lee, J.S., D.L. Schuler, T.L. Ainsworth and L.J. Du

E09.04 Classification Using Polarimetric and Interferometric SAR-Data 1411
Hellmann, M., S.R. Cloude and K.P. Papathanassiou

E09.05 Radar Polarimetry: A New Dimension in Geological Mapping and Exploration Within Australia's Arid and Semi-Arid Lands NA
Tapley, I.J.

E09.06 Texture and Speckle Statistics in Polarimetric SAR Synthesized Images 1414
De Grandi, G.F., J.S. Lee and D.L. Schuler

E09.07 Model Based Decomposition in Polarimetric Radar Remote Sensing of Coniferous Forests NA
Robin, E. and A. Guissard

E09.08 A Feature Motivated Sinclair Matrix Sphere-Diplane-Helix Decomposition and its Application to Polarimetric Remote Sensing in Agriculture, Forestry and Hydrology NA
Krogager, E., S.R. Madsen and W.M. Boerner

E10: Remote Sensing Research in Asia

E10.01 Remote Sensing Research in Malaysia 1418
Mahmood, N.N., K.F. Loh and S. Ahmad

E10.02 GIS for Natural Disaster Monitoring and Estimation in Mongolia NA
Ykhanbai, H., and M. Bayasgalan

E10.03 Multisource Data Integration for Cartography of Humid Zones and Flooding Risk Evaluation in the Red River Delta, Vietnam NA
Cu, P.V., L.A. Tuan, C.X. Huy, J. Simoneau-Coulombe, P. Lafrance, B. Brisco and N.C. Tuyet

"NA" indicates not available at time of printing.

E10.04 An Overview of Microwave Remote Sensing Research at the University of Malaya, Malaysia 1421
Chuah, H.T.

E10.05 The Use of Satellite Imagery for Monitoring Coastal Environment in Taiwan 1424
Chen, C.F., K.S. Chen, L.Y. Chang and A.J. Chen

E10.06 A Study of Dense Medium Effect in a Simple Backscattering Model 1427
Ewe, H.T., and H.T. Chuah

E10.07 Estimation of Rice Growth Stage Using RADARSAT Data 1430
Yun, S., C. Wang, X. Fan and H. Lim

E10.08 Forest Biodiversity Study in Thailand Using Remote Sensing Techniques NA
Wara-Aswapati, P., and L. Garcia

E10.09 PACRIM, Deployment of AIRSAR in the Australian-ASEAN Region 1433
Milne, A.K.

IGARSS'97 DIGEST VOLUME IV

F01: Global Monitoring and Remote Sensing for Climate Studies

F01.01 The Earth's Radiation Field: Comparison Between Models and Observations NA
Arking, A.

F01.02 Observation of the Interactions of Clouds and Radiation from EOS NA
Barkstrom, B.R.

F01.03 Observation of Global Ocean-Atmosphere Exchanges from Spaceborne Sensors 1435
Liu, W.T.

F01.04 Water Vapor and Cloud Feedback Mechanisms: Inferences from Satellite Observations and Numerical Modeling 1438
Lau, W.K.M.

F01.05 Wavelet Analysis of Satellite Images for Coastal Monitoring 1441
Liu, A.K., S.Y. Wu and W.Y. Tseng

F01.06 Cloud Macrostructure and Radiation 1444
Cahalan, R.F., A. Davis, A. Marshak, D. Silberstein and W. Wiscombe

F01.07 Global Monitoring and Retrivals of Atmospheric Aerosols and Clouds 1448
Tsay, S.C.

F01.08 Effects of Large Structure in Wet Snow Cover on SAR Measurements 1451
Shi, J., R. Kattlemann and J. Dozier

F02: Clouds and Precipitation II

F02.01 Microwave Rainfall Monitoring: A Tuscany Study Case 1454
Nativi, S., M. Padoin, P. Mazzetti, L. Baldini, and D. Giuli

F02.02 Simultaneous Radar and In-Situ Aircraft Based Observations of Convective Storms: Intercomparison Study 1458
Abou-El-Magd, A.M., V. Chandrasekar, V.N. Bringi, and J.W. Strapp

F02.03 Airborne W-Band Radar Measurements of the Doppler Spectrum of Light Precipitation 1460
Galloway, J., A. Pazmany, R. McIntosh, D. Leon, J. French, S. Haimov, R. Kelly and G. Vali

F02.04 Development of Model for Predicting the Rainfall Rate Around Singapore Using Radar Reflectivity Measurements NA
Ong, J.T., Y.Y. Shan, T.K. Lim, D. Kasilingam, I.I. Lin and V. Khoo

F02.05 Analysis of the Structure of a Tropical Squall Line, a Stratiform System and a Cyclone Using the NASA Millimeter-Wave Imaging Radiometer (MIR, 89-220 GHz), MODIS Airborne Simulator (MAS, 0.66-13.95 μm) and Advanced Microwave Moisture Sounder (AMMS, 90-183 GHz) in TOGA/COARE NA
Zhan, J., and J. Wang

F02.06 Tracking the Evolution of Rain Patterns by Mean of Modal Matching 1463
Dell'Acqua, F., P. Gamba and A. Marazzi

F02.07 The NASA DC-8 Airborne Cloud Radar: Design and Preliminary Results 1466
Sadowy, G.A., R.E. McIntosh, S.J. Dinardo, S.L. Durden, W.N. Edelstein, F. Li, A.b. Tanner, W.J. Wilson, T.L. Schneider and G.L. Stephens

F02.08 High Performance Digital Pulse Compression and Generation 1470
Mavrocordatos, C., M. Martin-Neira, N. Vincent and N. Suinot

F03: Detection of Buried Objects and Voids III

F03.01 Microwave Imaging Radar System for Detecting Buried Objects 1474
Chen, F.C., and W.C. Chew

F03.02 A High-Resolution Imaging of Objects Embedded in a Lossy Dispersive Medium 1477
Sato, T., K. Takemura, and P. Huimin

F03.03 The Influence of Ground Stratification Upon a Field of Magnetic Dipole 1480
Dmitriev, W.V.

F03.04 Selection of Optimum Correlation Functions for the Processing of GPR Data for Point Scatterers NA
Detlefsen, J., and D. Felbach

F03.05 Magnetic Dipole Localization with a Gradiometer: Obtaining Unique Solutions 1483
Wynn, W.M.

F03.06 Numerical Analysis of Radar Cross-Sections of a Conducting Cylinder in a Strong Turbulent Medium 1486
Tateiba, M., and T. Hanada

F03.07 Genetic Algorithm Applied to the Detection of a Buried Conducting Cylinder NA
Shi, S.Y, Y.B. Yan and D.B. Ge

F03.08 Imaging of a Penetrable Object Buried in a Lossy Half-Space for a Multipoint Bistatic Measurement Configuration Above the Interface 1489
Lyu, J.W., and J.W. Ra

"NA" indicates not available at time of printing.

F04: Data Processing

F04.01 Selection of an Optimum Patch for an Area-Based Stereo Matching Algorithm 1492
Kim, T., and S.D. Choi

F04.02 Visualization of Satellite Derived Time-Series Datasets Using Computer Graphics and Computer Animation 1495
Meisner, R.E., M. Bittner and S.W. Dech

F04.03 Passive Microwaves Protection NA
Rochard, G.

F04.04 Super Computing of 10-Years HRPT Data Set of AVHRR-Derived SSTs for Analysis 1499
Kawamura, H., F. Sakaida and J.I. Kudo

F04.05 Online Access to Weather Satellite Imagery through the World Wide Web 1502
Emery, W.J.

F04.06 ESA Fire Product: The Algorithm, the Products, the Results, the Operations, the Services, the Plans for the Future NA
Arino, O., and J.M. Melinotte

F04.07 Operational Generation of AVHRR-Based Level-3 Products at the German Remote Sensing Data Centre: Status and Perspectives 1505
Dech, S.W., R.E. Meisner and P. Tungalagsaikhan

F04.08 Incorporating Remotely-Sensed Land Surface Parameters in a Land Surface Parameterization 1509
Oleson, K.W., P.S. Thames and W.J. Emery

F04.09 A Fast Forward Model for the Satellite Data Assimilation with Numerical Weather Forecasting NA
Aoki, T.

F05: Remote Sensing of the Ocean by Radar Techniques

F05.01 A Study of the Effect of Swell in Scatterometer Wind Measurements Using SAR Wave Mode Data 1512
Kasilingam, D., I.I. Lin, V. Khoo and L. Hock

F05.02 SAR Imaging of the Ocean Surface: Nonlinearities Simulation and Estimation 1515
Garello, R., and J.M. Le Caillec

F05.03 Observation of Internal Waves in the Andaman Sea by ERS SAR 1518
Alpers, W., W.C. Heng and H. Lim

F05.04 Study of Gulf Stream Features with a Multi-Frequency Polarimetric SAR from the Space Shuttle 1521
Askari, F., S.R. Chubb, T. Donato, W. Alpers and S.A. Mango

F05.05 Effect of Azimuth Bandwidth Spreading on SAR Imaging and SAR Interferometry Over the Ocean 1524
Zhou, B., and D. Kasilingam

F05.06 A Quantitative Study of Tropical Rain Cells from ERS SAR Imagery 1527
Lin, I.I., D. Kasilingam, W. Alpers, T.K. Lim, H. Lim and V. Khoo

F05.07 Signature of the Gulf Stream in Wavebreaking Field Observations NA
Dulov, V., V. Kudryavtsev, S. Grodsky and O. Sherbak

F05.08 Experimental Investigation of Doppler Spectra of Microwave Signals Backscattered from Sea Slicks 1530
Kanevsky, M.B., S.A. Ermakov, E.M. Zuikova, V.Y. Karaev, V.Y. Goldblat, I.A. Sergievskaya, Y.B. Shchegol'kov, J.C. Scott and N. Stapleton

F06: SAR Interferometry: Systems and Applications

F06.01 Probing the Ultimate Capabilities of Radar Interferometry for Deformation with Low Gradient: A New Mission? 1533
Massonnet, D., and F. Adragna

F06.02 Reduction of the Phase-Unwrapping Drawbacks by the Three-Antenna Interferometric SAR System 1536
Corsini, G., M. Diani, F. Lombardini and G. Pinelli

F06.03 A Comparison of Interferometric Radar Ocean Surface Velocity Measurements to Subsurface Current Structure 1539
Moller, D., D.L. Porter, S. Frasier and R. McIntosh

F06.04 The Use of Man-Made Features for Long Time Scale INSAR 1542
Usai, S.

F06.05 The Effect of Scattering from Buildings on Interferometric SAR Measurements 1545
Bickel, D.L., W.H. Hensley and D. A. Yocky

F06.06 Quality Assessment of Coherence Between 35-Day and Tandem Modes in ERS-1/2 Interferometric Studies 1548
Stussi, N., S.C. Liew, K. Singh, L.K. Kwoh and H. Lim

F06.07 Quantitative Analysis of Atmospheric Effects on ERS Interferometric SAR Data NA
Kenyi, L.W., and H. Raggam

F06.08 Combination of Linear and Circular SAR for 3D Features 1551
Rudolf, H., D. Tarchi and A.J. Sieber

F06.09 Results of the Mt. Etna Interferometric E-SAR Campaign 1554
Coltelli, M., G. Fornaro, G. Franceschetti, R. Lanari, A. Moreira, G. Puglisi, E. Sansosti, R. Scheiber and M. Tesauro

F07: Tropical Forest Monitoring

F07.01 Detecting Change in Equatorial Regions of Brazil Using Medium Resolution Satellite Imagery 1557
Emmett, C.F., R.R. Jensen, P.J. Hardin and D.G. Long

F07.02 Deforestation Monitoring in Tropical Regions Using Multitemporal ERS/JERS SAR and INSAR Data 1560
Ribbes, F., T. Le Toan, J. Bruniquel, N. Floury, N. Stussi, S.C. Liew and U.R. Wasrin

F07.03 Reconstructed Imagery for Equatorial Monitoring: Combining AVHRR with Reconstructed NSCAT 1563
Hardin, P.J., D.G. Long and R.R. Jensen

F07.04 BRDF Behavior of a Tropical Forest Surveyed from Space 1566
Gastellu-Etchegorry, J.P., V. Demarez, V. Trichon, D. Ducrot and F. Zagolski

F07.05 Spectral and Textural Features of Amazon Rain Forests Obtained from Landsat-TM NA
Chen, S.C., and R. Herz

F07.06 Remote Sensing and GIS Tools to Support Vegetation Fire Management in Developing Countries 1569
Flasse, S.P., P. Ceccato, I.D. Downey, M.A. Raimadoya and P. Navarro

F07.07 Mapping Forest Fragments in Atlantic Coastal Moist Forest of Bahia, Brazil: A Case Study for Conservation and Biodiversity NA
Saatchi, S., K. Alger, S. Filoso, C. Alves, C.A. Mesquita and R. Rice

F07.08 Identifying and Monitoring Change in Wetland Environments Using SAR 1573
Milne, A.K.

"NA" indicates not available at time of printing.

F08: Interferometric and Differential Interferometric SAR

F08.01 A Study of the Rainforests of borneo by the JERS-1 Repeat-Pass InSAR — NA
Ouchi, K., S. Takeuchi, Y. Suga, C. Yonezawa, I.B. Ipor and S. Maedoi

F08.02 SAR Interferometry for the Study of Earth Crust Movement and Topography — NA
Rao, K.S., and Y.S. Rao

F08.03 Terrain Elevations from InSAR Incorporating Ground Control Data — 1576
Mirbagheri, M., J.C. Trinder and B.C. Forster

F08.04 Improved Digital Elevation Models Via Multi-Baseline Interferometric SAR — 1579
Homer, J., I.D. Longstaff and Z. She

F08.05 SAR Data Processing for Interferometry Using a Personal Computer — 1582
Omura, M., K. Koike, K. Doi and S. Aoki

F08.06 Development of JERS-1 SAR Interferometry Software Set — NA
Ono, M.

F08.07 Fault Model of 1995 Neftegorsk, Northern Sakhalin, Earthquake Based on Crustal Deformation Detected by JERS-1/SAR Interferometry — 1585
Nakagawa, H., M. Tobita, S. Fujiwara, S. Ozawa, K. Nitta, M. Murakami, M. Murakami, M. Shimada and P.A. Rosen

F08.08 Multi Baseline SAR Interferometry for Automatic DEM Reconstruction — NA
Ferretti, A., A. Monti Guarnieri, C. Prati and F. Rocca

F09: PS-PR Polarimetric Propagation and Scattering, Sounding and Radiometry

F09.01 Optimum Antenna Elevation for HF Surface Wave Radars — NA
Anderson, S.J., G.J. Frazer and G.M. Warne

F09.02 Synthetic Aperture Radar Image Reconstruction Algorithms Designed for Subsurface Imaging — 1588
Gough, P.T., and B.R. Hunt

F09.03 On the Proper Polarimetric Scattering Matrix Formulation of the Forward Propagation Versus Backscattering Radar Systems Description — 1591
Luneburg, E., S.R.Cloude and W.M. Boerner

F09.04 HF Skywave Radar Measurements of Wind and Sea Condition in the SE Asian Region — NA
Anderson, S.J.

F09.05 Scattering and Cascading Matrices of the Lossless Reciprocal Polarimetric Two-Port Microwave Versus Millimeter-Wave Optical Polarimetry — NA
Czyz, Z.H., and W.M. Boerner

F09.06 Determination of Propagation Parameters from Fully Polarimetric Radar Data — 1594
Santalla del Rio, V., and Y.M.M. Antar

F09.07 A Low Cost Polarimetric Radiometer for Real Time Stokes Parameter Measurements — 1597
Lahtinen, J., and M. Hallikainen

F09.08 Volume Scattering Properties of Glass Particles as a Function of Size and Absorption Coefficient — 1600
Betty, C.L., A.K. Fung and S. Tjuatja

F10: Surface Backscatter Modeling

F10.01 Modeling of Extremely Heterogeneous Radar Backscatter 1603
Muller, H.J.

F10.02 Electromagnetic Scattering and Fractal Analysis of Bare Soil Surfaces 1606
Rouvier, S., E. Bachelier, P. Borderies, I. Chenerie, J.C. Souyris, T. Le Toan and M. Borgeaud

F10.03 Investigation of Surface Scattering Mechanisms by Means of High Resolution SAR Imaging NA
Tarchi, D., G. Nesti and A.J. Sieber

F10.04 Semi-Rough Surface Scattering and Its Fading Effects for Active Microwave Sensors 1609
Wu, J., J. Jiang and L. Wang

F10.05 Empirical and Theoretical Backscattering Behavior as a Function of Roughness for Arid Land Surfaces 1612
Remond, A., and J.P. Deroin

F10.06 Simulation of Unpolarized Scattering in Synthetic Aperture Radar Images 1615
Tomiyasu, K.

F10.07 3-D Landscpae Modeling Using High Resolution Data NA
Lavoie, P., D. Ionescu and K.B. Fung

F10.08 Modelling and Experimental Study of Scattering from a Heterogeneous Random Medium Embedded with Seeds NA
Nedeltchev, N.M., J.C. Peuch and H. Baudrand

G01: Soil and Vegetation Biophyscial Properties I

G01.01 On the Retrieval of Rice Crop Parameters from ERS, JERS and RADARSAT Data NA
Le Toan, T., F. Ribbes, N. Floury, L. Wang, K.H. Ding and J.A. Kong

G01.02 Relating Vegetation Aerodynamic Roughness Length to Interferometric SAR Measurements NA
Saatchi, S., and P. Siqueira

G01.03 Assessement of ERS-1/2 Interferometric Data for Soil Moisture Estimation NA
Souyris, J.C., T. Le Toan, O. Casamian, F. Mattia, E. Bachelier, F. Borderies, I. Chenerie and M. Borgeaud

G01.04 A Vegetation Classification Scheme Validated by Model Simulations 1618
Ferrazzoli, P., L. Guerreiro and G. Schiavon

G01.05 The Role of Frequency and Polarization in Terrain Classification Using SAR Data 1621
Dobson, M.C., L.E. Pierce and F.T. Ulaby

G01.06 Mapping Vegetation Structure for Biodiversity Analysis Using Synthetic Aperture Radar 1624
Imhoff, M.L., A.K. Milne, T.D. Sisk, W.T. Lawrence and K. Brennan

G01.07 Relationship Between Surface Temperature Diurnal Range and Vegetation Cover as Derived from Meteorological Satellite NA
Gutman, G.

"NA" indicates not available at time of printing.

G01.08 Comparative Assessment of Multisensor Data for Suitability in Study of the Soil Salinity Using Remote Sensing and GIS in the Fordwah Irrigation Division, Pakistan 1627
Ahmed, I., and H.H. Andrianasolo

G01.09 Scientific Visualization of Drought-Related Famine Conditions in Sudan: An Approach to Temporal and Spatial Analysis of Remotely-Sensed Multi-Spectral Data NA
Rochon, G.L.

G02: TRMM Precipitation Radar: Its Algorithm and Validation

G02.01 Development Results of TRMM Precipitation Radar 1630
Oikawa, K., T. Kawanishi, H. Kuroiwa, M. Kojima and T. Kozu

G02.02 Rain Type Classification Algorithm for TRMM Precipitation Radar 1633
Awaka, J., T. Iguchi, H. Kumagai and K. Okamoto

G02.03 Rain Profiling Algorithm for the TRMM Precipitation Radar 1636
Iguchi, T., T. Kozu, R. Meneghini and K. Okamoto

G02.04 Effects of Non-Uniform Beam-Filling on TRMM PR Rainfall Measurements 1639
Durden, S.L., Z.S. Haddad, A. Kitiyakara and F.K. Li

G02.05 Bayesian Fusion of TRMM Passive and Active Measurements 1642
Haddad, Z.S., S.L. Durden and E. Im

G02.06 Simultaneous Observation of a Rain Event Using the MU Radar and an Airborne Doppler Radar for Simulating TRMM Ground Validation 1645
Sato, T., R. Peng, H. Hanado and H. Horie

G02.07 Radar Measurements form Papua New Guinea and Their Implications for TRMM PR Retrieval Algorithm 1648
Ladd, D.N., C.L. Wilson and M. Thurai

G02.08 The Dual Beam Airborne Technique as a Tool for Validation of the TRMM Rain Radar Retrieval 1651
Testud, J., and S. Oury

G03: Data Fusion II

G03.01 A Comprehensive Data Management and Fusion System for Multi-Band Imaging Systems and Associated Data 1654
Cooley, T., L. Standley and J. Erickson

G03.02 An MSOM Framework for Multi-Source Fusion and Spatio-Temporal Classification 1657
Wan, W., and D. Fraser

G03.03 Urban Land Use Mapping with Multi-Spectral and SAR Satellite Data Using Neural Networks 1660
Heikkonen, J., I. Kanellopoulos, A. Varfis, A. Steel and K. Fullerton

G03.04 Multisource and Multisensor Data in Land Cover Classification Tasks: The Advantage Offered by Neural Networks 1663
Chiuderi, A.

G03.05 Fusion of Optical and Microwave Remote Sensing Data for Vegetation Studies NA
Qi, J., M.S. Moran and E.E. Sano

G03.06 Combining Structural and Spectral Information for Discrimination Using Pulse Coupled Neural Networks in Multispectral and Hyperspectral Data 1666
Cooley, J.H., and T.W. Cooley

G03.07 Classification of Hyperdimensional Data Using Data Fusion Approaches 1669
Benediktsson, J.A., and J.R. Sveinsson

G03.08 A Self-Organizing Map Based on Framework for Data Fusion II NA
Wan, W., and D. Fraser

G03.09 Application of Fuzzy Logic for Integration of SIR-C and Geological Exploration Data for Base Metal Exploration in Hwang-Gang-Ri District, Korea NA
Jiang, W.W., C.S. So, S.K. Choi, L. Feng and W.M. Moon

G04: Sea Ice, Climate and Weather Applications in Polar Region

G04.01 The Origin and Evolution of Sea-Ice Anomalies in the Beaufort Sea NA
Tremblay, B., and L.A. Mysak

G04.02 Determination of the Dominant Spatial Modes of Terrestrial Snow Cover Over North America Using Passive Microwave Derived Data 1672
LeDrew, E., C. Derksen and B. Goodison

G04.03 Microwave Measurements of Sea Ice in the Kara and Laptev Sea 1675
Johnsen, K.P., A. Darovskikh, G.Heygster and A. Wiesmann

G04.04 Indentification of Clear-Sky Sea-Ice Albedo Feedbacks with Advanced Very High Resolution Radiometer Data NA
De Abreu, R., and E. LeDrew

G04.05 First Realtime Use of RADARSAT SAR Imagery for Ship Navigation in Antarctica 1678
Danduran, P., M.C. Mouchot, R. Garello, D. Fleury and I. Thepaut

G04.06 ICEWATCH - Real-Time Sea Ice Monitoring of the Northern Sea Route Using Satellite Radar Techniques 1681
Johannessen, O.M., S. Sandven, L.H. Pettersson, K. Kloster, T. Hamre, J. Solhaug, A.M. Volkov, V. Asmus, O.E. Milekhin, V.A.Krovotyntsev, V.D. Grischenko, V.G. Smirnov, L.P. Bobylev, V.V. Melentyev and V. Alexandrov

G04.07 Comparison of Cloud Parameters and Downwelling Radiative Fluxes over Sea Ice Computed from TOVS and AHHRR NA
Schweiger, A., J. Francis, J. Key and D. Lubin

G04.08 Sea Ice Concentration in Response to Weather Systems in the Weddell Sea: Comparison Between SSM/I Data and Model Simulations 1686
Fischer, H., and C. Oelke

G04.09 Design and Development of an Operational Sea Ice Mapping System for Meteorological Applications in the Antarctic 1689
Williams, R.N., P. Crowther and S. Pendlebury

"NA" indicates not available at time of printing.

G05: Sea Surface Modelling

G05.01 Beyond the Two-Scale Composite Backscatter Model for Modelling Radar Return from the Ocean Surface NA
Chubb, S.R., A.L. Cooper and G.M. Nedlin

G05.02 Microwave Scattering from a Slightly Rough Surface of a Medium Possessing a Finite Large Dielectric Constant, and Application to an Air-Water Scattering 1692
Nedlin, G.M., S.R. Chubb and A.L. Cooper

G05.03 On Combining Satellite Altimetry Data With Models in Improving the Simulation of Ocean Circulation NA
Fu, L.L.

G05.04 Ocean Wave-Radar Modulation Transfer Function: A Nonlinear System Modelling Approach NA
Bao, M., and A. Schmidt

G05.05 Validation of Wave Model Using ERS Altimeter and SAR Wave Mode Data 1695
Zhang, R., T.K. Lim, D. Kasilingam, I.I. Lin, and V. Khoo

G05.06 On the Cross Spectrum Between Individual-Look Synthetic Aperture Radar Images of Ocean Waves NA
Bao, M., and W. Alpers

G05.07 Studying the Monsoon Circulation in the Indian Ocean Using Altimeter Data 1698
Jensen, V.E., P. Samuel and O.M. Johannessen

G05.08 Ekman Heat Transport Estimated by Using Microwave Scatterometer Data NA
Kubota, M., A. Tamada and H. Yokota

G06: SAR Intereferometry: Simulation and Noise Reduction

G06.01 Efficient Simulation of SAR Interferometric Raw Signal Pairs 1701
Franceschetti, G., A. Iodice, M. Migliaccio and D. Riccio

G06.02 Simulator for Repeat-Pass Satellite InSAR Studies 1704
Xu, W., and I. Cumming

G06.03 High Doppler Centroid CSA Based SAR Raw Data Simulator NA
Carrasco, D., J. Closa and A. Broquetas

G06.04 Optimization of SAR Interferogram by Using Coherence Information 1707
Yonezawa, C., and S. Takeuchi

G06.05 Decorrelation by Interpolation Errors in InSAR Processing 1710
Bamler, R., and R. Hanssen

G06.06 An Interferometric SAR Processor Avoiding Phase Ambiguities 1713
Schmitt, K., and W. Wiesbeck

G06.07 Processing Low Noise Interferograms form ERS1 - SLC Radar Images NA
Michel, R., J.P. Avouac and J. Taboury

G06.08 Suppressing the Noise of Single-Look InSAR Interferogram with Wavelet Analysis NA
Tang, J., and Z.S. Wang

G06.09 A New Technique for Noise Filtering of SAR Interferogram Phase Images 1716
Lee, J.S., K.P. Papathanassiou, T.L. Ainsworth, M.R. Grunes and A. Reigber

G07: Ecosystem Studies with Microwave Remote Sensing

G07.01 Toward Consistent Global Physiognomic Vegetation Mapping Using ERS/JERS SAR Classification 1719
Kellndorfer, J.M., M.C. Dobson and F.T. Ulaby

G07.02 Agro-Ecosystem Monitoring in Canada with RADARSAT NA
Brown, R.J., B. Brisco, T. Huffman, T. Hirose and D. Major

G07.03 Effect of Environmental Temperatures on SAR Forest Biomass Estimates 1722
Ranson, K.J., and G. Sun

G07.04 Enhanced Flood Mapping Using ERS SAR Interferometirc Data: An Example in South France NA
Beaudoin, A., L. Marinelli, R. Michel, and J. Astier

G07.05 The Global Rain Forest Mapping - An Overview NA
Rosenqvist, A., M. Shimada, B. Chapman and G. De Grandi

G07.06 The ERS-1 Central Africa Mosaic: A New Role for Radar Remote Sensing in Global Studies of the Tropical Ecosystem 1725
Malingreau, J.P.G., G. De Grandi, M. Leysen, P. Mayaux and M. Simard

G07.07 Land Cover Type and Forest Biomass Assessment in the Colombian Amazon 1728
Hoekman, D.H., and M.J. Quinones

G07.08 Radar Monitoring for Sustainable Forest Management in Indonesia 1731
Hoekman, D.H.

G07.09 Tabular Summary of SIR-C/X-SAR Results: Synthetic Aperture Radar Frequency and Polarization Requirements for Applications in Ecology and Hydrology 1734
Schmullius, C.C., and D.L. Evans

G08: Remote Sensing of Clouds and Aerosols

G08.01 Airborne Millimeter-Wave Radiometric Observations of Cirrus Clouds 1737
Wang, J.R., and P. Racette

G08.02 Application of Space Lidar to the Remote Sensing of Clouds and Aerosols 1740
Winker, D.M.

G08.03 Ground-Based Validation of the EOS Multiangle Imaging SpectroRadiometer (MISR) Aerosol Retrieval Algorithms and Science Data Products 1743
Conel, J.E., W.C. Ledeboer, S.H. Pilorz, J.V. Martonchik, R. Kahn, W. Abdou, C. Bruegge, M.C. Helmlinger and B.J. Gaitley

G08.04 LITE Aerosol Retrievals 1749
Reagan, J.A., and H. Liu

G08.05 Lidar Measurements of Stratospheric Aerosol Over Hefei, China During 1990-1996 NA
Hu, H., and J. Zhou, and Y.W. Anhui

G08.06 A New Method for Detection of Absorbing Aerosols (Dust and Smoke) fromTOMS Data NA
Herman, J.R., C. Hsu, O. Torres, P.K. Bhartia and M. Schoeberl

G08.07 Non-Rayleigh Scattering Applied to Hydrometeor Size Estimation 1753
Sekelsky, S.M., R.E. McIntosh, W.L. Ecklund and K.S. Gage

"NA" indicates not available at time of printing.

G08.08 Modified Gamma Model for Singapore Rain Drop Size Distribution 1757
Ong, J.T., and Y.Y. Shan

G08.09 Relationship Between Cirrus Particle Size and Cloud Top Temperature 1760
Han, Q., J. Chou, and R.M. Welch

G09: Accuracy Assessment Issues in Remote Sensing

G09.01 A Review of Sampling Strategies for Determining the Accuracy of Change Maps NA
Biging, G.S., and R.C. Congalton

G09.02 Techniques for Managing Errors Associated with Geometric and Attribute Data Derived from Remote Sensing Sensors NA
Karimi, H.A., and M.A. Chapman

G09.03 Application of Adaptive Sampling in the Assessment of Accuracy of Landcover Maps Developed from Remotely-Sensed Data NA
Colby, D.R.

G09.04 Earth Observation in Understanding Terrestrial Dynamics NA
Clandillon, S., N. Tholey and K. Fellah

G09.05 Quantification of the Impact of Misregistration on the Accuracy of Remotely Sensed Change Detection 1763
Dai, X., and S. Khorram

G09.06 Assessing the Accuracy of High Spatial Resolution Image Data and Derived Products 1766
Stow, D., A. Hope, S. Phinn, A. Brewster and B. Bradshaw

G09.07 NOAA's Coastal Change Analysis Program (C-CAP): Field Verification NA
Dobson, J.E.

G09.08 Accuracy Assessement Issues for Global Data: Lessons form the Grass Global CD-Rom Project NA
Madry, S.

G09.09 An Introduction to Using Generalized Linear Models to Enhance Satellite-Based Change Detection 1769
Morisette, J.T., and S. Khorram

G10: IRS-1C Data Products and Applications

G10.01 A Total Solution Approach Using IRS-1C and IRS-P3 Data NA
Jayaraman, V., and M.G. Chandrasekhar

G10.02 Role of NIC in RS and GIS Applications A Case Study: Srirama Sagar Command Area NA
Rao, N.V.K.

G10.03 Image Classification and Performance Evaluation of IRS 1C LISS-III Data 1772
Muralikrishna, I.V.

G10.04 IRS-1C Applications for Land Use/Landcover Mapping, Change Detection and Planning 1775
Gautam, N.C.

G10.05 IRS-1C Applications for Forest Resources Assessment NA
Dutt, C.B.S.

G10.06 IRS IC's LISS-III Data Application Potential in Coastal Studies NA
Krishnamoorthy, R., I. Gnappazham and V. Selvam

G10.07 Contrast Enhancement of IRS - 1C LISS Sensors 1778
Ramesh Babu, I., and I.V. Murali Krishna

G10.08 IRS-1C Data Applications NA
Rao, P.S., G. Chandrasekhar and V.R. Hegde

G10.09 Operationalisation of New Tehcnology - A Case Study of IRS-1C Application NA
Rao, T.G., and G.S. Kumar

H01: Soil and Vegetation Biophysical Properties II

H01.01 Angular Signatures of NASA/NOAA Pathfinder AVHRR Land Data and Applications to Land Cover Identification 1781
Liang, S., and J.R.G. Townshend

H01.02 Spatial Assessment of Soil Properties for Agricultural Land Using Remotely Sensed Imagery, Relief Analysis and GIS 1784
Selige, T.M.

H01.03 A Modelling Study of BRDF Canopy and Radiation Regime for Boreal Forests 1787
Zagolski, F., P. Guillevic, J.P. Gastellu-Etchegorry, C. Gaillard, D. Deering and M. Leroy

H01.04 Ground Reflectance and Albedo Extracted from NOAA-AVHRR Time-Series in a Topographically Complex Terrain NA
Eibl, B., and W. Mauser

H01.05 Estimation of Surface Reflection Parameters Over Lands Using Linear Polarization Data by Airborne POLDER 1790
Takemata, K., and Y. Kawata

H01.06 Radiometric Estimates of Grain Yields Related to Crop Aboveground Net Production (ANP) in Paddy Rice 1793
Hong, S., J. Lee, S. Rim and J. Shin

H01.07 Passive Microwave Technology of Rice Crop Fields Monitoring at the Different Stages of Vegetation NA
Yazerian, G.G., A.M. Shutko and E.P. Vorobeichick

H01.08 A Simple Model for the Estimation of Biomass Density of Regenerating Tropical Forest Using JERS-1 SAR and Its Application to Amazon Region Image Mosaics 1796
Luckman, A., and J. Baker

H02: Fluorescent Measurements in Remote Sensing

H02.01 New Instrumentation for Plant/Crop Monitoring Uses Fluorescence Imaging and Image Processing to Detect Pre-Symptomatic Plant Stress NA
Lussier, R.R.

H02.02 Time Resolved Laser Induced Flourescence Spectroscopy of Chemicals and Phytoplankton in Waters NA
Vebel, U., J. Kubitz, J. Wienke and A. Anders

"NA" indicates not available at time of printing.

H02.03 Flourescence and Reflectance Spectral Response of Crop Residue for Assessing Erosion Control and Analysis of Previous Crop Condition NA
McMurtrey, J.E., M.S. Kim, E.W. Chappelle, L.A. Corp and C.S.T. Daughtry

H02.04 Laser Induced Imaging of Blue/Red and Blue/Far-Red Fluorescence Ratios, F440/F690 and F440/F740, as a Means of Early Stress Detection in Plants 1799
Lichtenthaler, H.K., N. Subhash, O. Wenzel and J.A. Miehe

H02.05 Non-Destructive Detection of Increased Tropospheric Ozone Carbon Dioxide Effects on Crops with Fluorescence Imaging System NA
Kim, M.S., C.L. Mulchi, C.S.T. Daughtry, E.W. Chappelle, J.E. McMurtrey and L.A. Corp

H02.06 Characterization of Soybean Flavonol Isolines with Flourescence Imaging NA
Kim, M.S., E. Lee, C.L. Mulchi, J.E. McMurtrey and E.W. Chappelle

H02.07 Applications of Flourescence Imaging and Spectal Measurements to the Remote Assessment of Plant Nitrate Supply NA
Corp, L.A., E.W. Chappelle, J.E. McMurtrey and M.S. Kim

H02.08 Bark and Leaf Flourescence as Potential Tool in Remote Sensing: A Reflection of Some Aspects of Problems in Comparative Analysis NA
Kharouk, V.I.

H03: HF Radar Remote Sensing

H03.01 Over-the-Horizon Radar: Ground-Based Ocean Remote Sensing on Basin-Wide Scales 1802
Georges, T.M., and J.A. Harlan

H03.02 A Study of SeaSonde Bearing and Signal Stability Using Transponder Measurements NA
Barrick, D.E., and J.D. Paduan

H03.03 A Comparison of Surface Current Fields Derived by Beam Forming and Direction Finding Techniques as Applied by the HF Radar WERA 1805
Gurgel, K.W., G. Antonischki and T. Schlick

H03.04 Initial Observations of Ocean Currents and Current Shears, Wind Direction Using Multifrequency HF Radar 1808
Teague, C.C., J.F. Vesecky, P.E. Hansen, N.G. Schnepf, J.M. Daida, R.G. Onstott, K. Fischer and D.M. Fernandez

H03.05 Observations of Near-Surface Currents at Varying Depths Using a New Multifrequency HF Radar 1811
Vesecky, J.F., C.C. Teague, R.Onstott, P. Hansen, N.Schnepf, D. Fernandez, J. Daida and K. Fischer

H03.06 Two-Dimensional Diurnal to Monthly Period Surface Currents in Monterey Bay from CODAR-Type HF Radar 1814
Paduan, J.D., M.S. Cook and D.M. Fernandez

H03.07 Coastal Near-Inertial Wave Bursts Detected by OSCR 1817
Shay, L.K.

H03.08 Measurement of Surface Current Fields with High Spatial Resolution by the HF Radar WERA 1820
Gurgel, K.W., and G. Antonischki

H04: Scattererometer Applications

H04.01 Snow Acculmulation on Greenland Estimated from ERS Scatterometer Data 1823
Wismann, V., D.P. Winebrenner, K. Boehnke and R.J. Arthern

H04.02 Thawing Processes During Siberian Spring Observed by ERS Scatterometer and SAR 1826
Boehnke, K., and V. Wismann

H04.03 Assessment of Scatterometer Data for Environmental Studies in Thar Desert 1829
Stephen, H., R.L.G. Schumann, K. Honda and K. Nualchawee

H04.04 Observations and Simulations of the ERS Wind Scatterometer Response over a Sahelian Region 1832
Frison, P.L., E. Mougin and P. Hiernaux

H04.05 Characterizing Earth's Surface Using Moderate Resolution 14 Ghz Scatterometer Imagery: Early Results from NSCAT Reconstruction 1835
Hardin, P.J., D.G. Long, R.R. Jensen

H04.06 Ice Classification in the Southern Ocean Using ERS-1 Scatterometer Data 1838
Early, D.S., and D.G. Long

H04.07 Automated Antarctic Ice Edge Detection Using NSCAT Data 1841
Remund, Q.P., and D.G. Long

H04.08 Enhanced Resolution Imging from Irregular Samples 1844
Early, D.S., and D.G. Long

H05: Radar Measurements of Ocean Winds

H05.01 Wind Field Models and Model Order Selection for Wind Estimation 1847
Brown, C.G., P.E. Johnson, S.L. Richards and D.G. Long

H05.02 A Neural Network-Based Model for Estimating the Wind Vector Using ERS Scatterometer Data 1850
Kasilingam, D., I.I. Lin, V. Khoo and L. Hock

H05.03 On a New Relationship Between Radar Cross Section and Wind Speed Using ERS-1 Scatterometer Data and ECMWF Analysis Data Over the Mediterranean Sea 1853
Migliaccio, M., P. Colandrea, A. Bartoloni and C. D'Amelio

H05.04 Backscatter Observed in C-Band and Ku-Band Scatterometer Data 1856
Johnson, P.E., and D.G. Long

H05.05 An Aggregate Spectral Model for ERS-1 Wind Retrievals 1859
Lettvin, E., and J. Vesecky

H05.06 An Inversion Technique for Estimating the Wind-Dependent Short Wave Spectral Density from the CMOD4 and Composite Surface Models 1862
Chen, J., and D. Kasilingam

H05.07 The Influence of Topography on Wind Over the Sea of Japan 1865
Wu, P., H. Kawamura, and F. Kimura

H05.08 A Synergistic Approach for Estimation of High Winds Within Tropical Cyclones NA
Sarker, A., B.M. Rao, C.M. Kishtawal and M. Mohan

"NA" indicates not available at time of printing.

H06: Application of SAR/INSAR in Forestry

H06.01 A Study of SAR Interferometry over Forests: Theory and Experiment 1868
Floury, N., T. Le Toan, J.C. Souyris and J. Bruniquel

H06.02 An Electromagnetic Scattering Model for Tree Trunks Over a Tilted Rough Ground Plane 1871
Esteban, H., J.M. Lopez, M. Baquero, J. Fortuny, G. Nesti, and A.J. Sieber

H06.03 Effect of Temporally Varying Parameters on L- and C-Band SAR Observations of Boreal Forests 1874
Pulliainen, J., L. Kurvonen and M. Hallikainen

H06.04 Numerical Studies of Forest Backscatter in the VHF-Band 1878
Ulander, L.M.H., T. Martin and H. Israelsson

H06.05 Estimating Soil Moisture in a Boreal Old Jack Pine Forest 1881
Moghaddam, M., S. Saatchi and R. Treuhaft

H06.06 Forest Vertical Structure from Multibaseline Interferometric Radar for Studying Growth and Productivity 1884
Treuhaft, R.N., M. Moghaddam, and B.J. Yoder

H06.07 Simulation of Interferometric SAR Response to Deciduous and Coniferous Forest Stands 1887
Sarabandi, K., and Y.C. Lin

H06.08 Processing and Analysis Techniques for Continental Scale Radar Maps of the Tropical Forest 1890
Simard, M., G. De Grandi, S. Sattchi, M. Leysen and K.P.B. Thomson

H07: Atmospheric Radiation

H07.01 Adjacent Effects Over Rugged Terrains NA
Li, X., and B. Hu

H07.02 Atmospheric Correction Over a Composite Land and Water Surface 1893
Takashima, T., and K. Masuda

H07.03 Algorithms for Atmospheric Correction for Ocean Color Data 1896
Mukai, S., I. Sano and K. Masuda

H07.04 Multi-Angle Remote Sensing of Aerosols Over Ocean NA
Kahn, R., J. Martonchik, D. Diner and R. West

H07.05 An Atmospheric Correction Algorithm for Space Remote Sensing Data an Its Validation 1899
Yamazaki, A., M. Imanaka, M. Shikada, T. Ohumura and Y. Kawata

H07.06 Estimation of Adjacent Effects in Polarization Measurements over the Coastal Zone 1902
Kusaka, T., N. Taniguchi and Y. Kawata

H07.07 Information Content of Outgoing Reflected and Scattering Solar Radiation in UV and Visible Spectral Ranges 1905
Timofeyev, Y.M., A.V. Vasilyev and V.V. Rozanov

H07.08 Correction of Atmospheric Effects on Earth's Image - Mathematical Model & Analysis NA
Wang, A.P., and S. Ueno

H08: Advance Sensors and Sensor Calibration II

H08.01 The Aerosol Optical Thickness Retrieval from GOME Spectra 1908
Bartoloni, A., M. Mochi, C. Serafini, M. Cervino, R. Guzzi and F. Torricella

H08.02 Aerosol Optical Thickness Over Ocean Areas and Its Relationship With Cloud Droplet Size 1911
Han, Q., J. Chou, and R.M. Welch

H08.03 Effects of Atmospheric Aerosol Models on the Single Scattering Point Spread Function in Optical Remote Sensing 1914
Liew, S.C.

H08.04 Aerosol Retrieval Using Synthetic POLDER Multi-Angular Data 1917
Kuo, K.S., R.C. Weger and R.M. Welch

H08.05 Aerosol Optical Thickness and Scattering Phase Function Retrieval from Solar Radiances Recorded over Water: A Revised Approach 1920
Paronis, D.K., and J.N. Hatzopoulos

H08.06 The Long Distance Transport of Sand Dust and Aerosols from Northern China to Hong Kong NA
Fang, M., M. Zheng, K.S. Chim and S.C. Kot

H08.07 Comparing Optical Models of Atmospheric Aerosol with Results of Multi-Wavelength Laser Sounding NA
Chaikovsky, A.P., A.P. Ivanov, F.P. Osipenko, and V.N. Shcherbakov

H08.08 Satellite Remote Sensing of Fires, Smoke and Regional Radiative Energy Budgets 1923
Christopher, S.A., M. Wang, K. Barbieri, R.M. Welch and S.K. Yang

H09: Aerosols

H09.01 Polarimetric Effects in Repeat-Pass SAR Interferometry 1926
Papathanassiou, K.P., and S.R. Cloude

H09.02 Height Model Generation, Automatic Geocoding and Mosaicing Using of Airborne AES-1 InSAR Data 1929
Holecz, F., J. Moreira, P. Pasquali, S. Voigt, E. Meier and D. Nuesch

H09.03 Calibration of Airborne AES INSAR Data NA
Holecz, F., J. Moreira and P. Pasqauli

H09.04 InSAR Takes over the Former Roll of Photogrammetry NA
Moreira, J., and F. Holecz

H09.05 Coherence Optimisation in Polarimetric SAR Interferometry 1932
Cloude, S.R., and K.P. Papthanassiou

H09.06 The X-Band SAR Demonstrator Development 1935
Zahn, R., H. Braumann and M. Schlott

H09.07 A Novel Model of the Platform Attitude Drift for SAR 1938
Song, H., M. Zhu and Y. Bai

H09.08 SIR-C Polarimetric Calibration by Using Polarization Selective Dihedrals and a Polarimetric Active Radar Calibrator 1941
Fujita, M., T. Masuda, Y. Fujino and M. Satake

"NA" indicates not available at time of printing.

H10: Weather Information Systems & Data Analysis Methods

H10.01 Knowledge Based Weather Image Processing Classification 1944
Siddiqui, K.J.

H10.02 Remote Sensing of Surface UV Radiation from Multi-Sensor Satellite Observations NA
Gautier, C., and M. Landsfeld

H10.03 Infectious Disease and Climate Change: Detecting Contributing Factors and Predicting Future Outbreaks 1947
Andrick, B., B. Clark, K. Nygaard, A. Logar, M. Penaloza and R. Welch

H10.04 Infectious Disease and Climate Change: A Fuzzy Database Management System Approach 1950
Penaloza, M.A., and R.M. Welch

H10.05 Environmental Monitoring in Italy Using the Optical Sensors of the Priroda Module 1953
Armand, N.A., V.V. Efremenko, L. Pantani and I. Pippi

H10.06 Climatology of Light Equivalents of Integral and Photosynthetically Active Radiation and of PAR Portion in Integral Solar Radiation Derived from Ground-Based Surface Measurements NA
Shilovtseva, O.A.

H10.07 Variability of Solar Radiation in Different Solar Spectrum and Natural Illuminance by Clear Sky on the Ground-Based Long-Term Measurements NA
Abakumova, G.M., E.V. Gorbarenko, E.I. Nezval, and O.A. Shilovtseva

H10.08 A Joint Chain Between Thermal Interia Model and Geometric Optical Model of BRDF 1956
Zhang, R.

I01: Soil and Vegetation Process Model

I01.01 Importance of Soil Depth in the Estimation of Net CO2 Exchange Over the FIFE Site NA
Divakarla, M.G., and J.M. Norman

I01.02 Retrieval of Land Surface Temperature and Water Vapor Content from AVHRR Thermal Imagery Using an Artificial Neural Network 1959
Liang, S.

I01.03 A Combined Temperature and Water Content Model for Bare Soil 1962
Kjellgren, J.

I01.04 The Use of Vegetation Indices in Forested Regions: Issues of Linearly and Saturation 1966
Huete, A.R., H. Liu and W.J.D. van Leeuwen

I01.05 A Sensitivity Analysis of a Coupled Leaf-Canopy-Growth Model NA
Hobson, P., and M. Barnsley

I01.06 Validation of a Summertime LSP/Radiobrightness Model for Bare Soils in Northern Prairie NA
Judge, J., J.R. Metcalfe and A.W. England

I01.07 Investigating Surface Heterogeneity in Semi-Arid Lands NA
Chehbouni, A., and J. Qi

I01.08 Scaling Issues Related to Estimating Land Surface Evapotranspiration Using Remote Sensing Data NA
Toll, D.L., and F.M. Vukovich

I02: Atmospheric Processing and Dynamics

I02.01 Examining the Influences of Water Vapor Profile on the SSM/I - Derived Column Water Vapor Over the Global Oceans — NA
Sohn, B.J.

I02.02 Simulataneous Measurements of Water Vapor Profiles from Airborne MIR and LASE — 1969
Wang, J.R., P. Racette, M.E. Triesky, E.V. Browell, S. Ismail and L.A. Chang

I02.03 Volume Imaging Radar Observations of Atmospheric Boundary Layer Turbulence with Large Eddy Simulations — 1972
Pollard, B.D., S.J. Frasier and R.E. McIntosh

I02.04 BIAS: A Straightforward Algorithm for the Retrieval of Tracegas Vertical Columns from Near Infra-Red Earthshine Measurements by the SCIAMACHY Remote Sensing Spectrometer — NA
Spurr, R.J.D.

I02.05 A Tomographic Infrared System for Monitoring Atmospheric Pollution in Urban Areas — 1975
Giuli, D., F. Cuccoli, L. Facheris, and S. Tanelli

I02.06 Data Analysis of Lidar Measurements of Atmospheric Boundary Layer Aerosols from a Black Hawk Helicopter — NA
Karl, Jr., R.R., W.K. Grace, JR. Busse, J.G. Sutton, N.A. Kurnit, A. Koskelo, O.G. Peterson and W.S. Huntgate

I02.07 A Study of Gravity Waves in the Atmospheric Boundary Layer Using Sodar and Microbarograph — NA
Reddy, K.K., and D.N. Rao

I02.08 Aerosol Atmospheric Pollution in Some Industrial Cities of Former Soviet Union — NA
Gorbarenko, E.V.

I03: Remote Sensing Research in China

I03.01 Remote Sensing in China: Techniques and Applications — 1978
Huadong, G.

I03.02 Several Airborne Imaging Spectrometers Developed in China — NA
Wang, J., and Y. Xue

I03.03 Data Fusion of China Advanced Microwave Remote Sensor — 1981
Zhang, X., and J. Jiang

I03.04 Research and Development on Synthetic Aperture Radar System in China — 1984
Zhu, M.H.

I03.05 A New Airborne Remote Sensing Platform for Generating Geocoding Image Without Ground Control Point — 1987
Li, S., Y. Xue and Z. Liu

I03.06 Short-Term and Imminent Earthquake Prediction and Satellite Remote Sensing Thermal Infrared Technology — NA
Zuji, Q., D. Changgong and L. Linzhi

I03.07 The Development of China's Meteorological Satellite and Satellite Meteorology — NA
Fang, Z., J. Xu and L. Guo

I03.08 GIS Development and Application in China — NA
Zhou, C.

"NA" indicates not available at time of printing.

I03.09 Mission Analysis of the China - Brazil Earth Resources Satellite (CBERS) NA
Yiyuan, C.

I04: Data Compressson Techniques and Visualization

I04.01 Reversible Compression of Multispectral Imagery Based on an Enhanced Inter-Band JPEG Prediction 1990
Aiazzi, B., P.S. Alba, L. Alparone and S. Baronti

I04.02 A DCT-Based Adaptive Compression Algorithm Customized for Radar Imagery 1993
Andreadis, A., G. Benelli, A. Garzelli and S. Susini

I04.03 SPOT Image Compression Using Block Truncation Coding Techniques 1996
Ma, K.K., L. Huang, S. Zhu and A.T.S. Ho

I04.04 Effects on Image Quality for MPEG Video Over Satellite Channel NA
Liren, Z.

I04.05 Lossless Compression of Satellite Images Using Nueral Network & Arithmetic Coding NA
Yann, S.I., Y.C. Kiat and H.Y. Yi

I04.06 Construction of Multi-Resolution Terrain Models Using Hierarchical Delaunay Triangulated Irregular Networks 1999
Huang, S.J., and D.C. Tseng

I04.07 Raw Data Compressing Technology Study in Spaceborne SAR NA
Ru-liang, Y., and W.Y. Bai ping

I05: Sea Surface Temperature and Its Validation

I05.01 Wind Speed Forcing of the Bulk-Skin Sea Surface Temperature Difference as a Function of Wind Speed and Heat Flux 2002
Emery, W.J., and C.J. Donlon

I05.02 Characteristics of the AVHRR-Derived Sea Surface Temperature in the Oceans Around Japan 2005
Kawamura, H., and Y. Kawai

I05.03 Global and Regional Pathfinder SST Fields: Characterization and Validation 2008
Casey, K., P. Cornillon, R. Evans and G. Podesta

I05.04 Spatial and Temporal Variability of Sea Surface Temperature in the Seas Around Korea Using Satellite Data (NOAA/AVHRR) NA
Park, K.A., and J.Y. Chung

I05.05 The Detection of the Diurnal Variation of SST by GOES NA
Wu, X.Q.

I05.06 Investigation of Large-Scale Oceanographic Phenomena Using Data from ATSR on ERS-1 and Other Satellite Sensors NA
Llewellyn-Jones, D.T., S.P. Lawrence, Y. Xue and C.T. Mutlow

I05.07 The Retrieval and Validation of Ocean Color Products NA
Lynch, M.

I06: SAR Techniques

I06.01 Passive SAR Reusing Digital Television Signals NA
Caroti, L., I. Pippi and C. Prati

I06.02 Measurement of Interferometer Instrument Line Shape 2011
Atkinson, N.C., and S.H.S. Wilson

I06.03 Progress on the SASAR System - First Results 2015
da Silveira, M., J. Horrell, M. Inggs and E. Abenant

I06.04 SASAR External Polarimetric Calibration Considerations 2018
de Silveira, M.

I06.05 Spotlight SAR Processing Using the Extended Chirp Scaling Algorithm 2021
Mittermayer, J., and A. Moreira

I06.06 Wavelet Based Approaches for Efficient Compression of Complex SAR Image Data 2024
Brandfaß, M., W. Coster, U. Benz and A. Moreira

I06.07 A SAR Auto-Focus Technique Based on Azimuth Scaling 2028
Moreira, A., J. Mittermayer and R. Scheiber

I06.08 Speckle Reduction in SAR Images - Techniques and Prospects 2031
Schwarz, G., M. Walessa and M. Datcu

I07: Crop Monitoring and Classification

I07.01 Early Identification and Surface Estimation of Agricultural Crops Using ERS SAR Images 2035
Nezry, E.

I07.02 Landcover Classification Over the Mekong River Delta Using ERS and RADARSAT SAR Images 2038
Liew, S.C., S.P. Kam, T.P. Tuong, P. Chen, V.Q. Minh and H. Lim

I07.03 Comparison Between Classified Result of Paddy Field and Statistic Data of the Production 2041
Tsuhasa, H., and S.A.P. Ceballos

I07.04 Winter Crops Classification Using Satellite Data 2044
Kryvobok, O.

I07.05 Shortperiodic Variability of Different Landscapes in MM-Wave Range 2047
Vasilyev, Y.F., B.D. Zamaraev, V.L. Kostina and A.N. Roenko

I07.06 Ground Surface Sensing Through Wheat Foliage NA
Noyman, Y., I. Shmulevich, and A. Ben-Shalom

I07.07 Monitoring Crop Growth on China Plains by Using SSM/I Data 2050
Jin, Y.Q.

"NA" indicates not available at time of printing.

I08: SAR Image Processing

I08.01 An Exploration of Features for SAR Classification 2053
Pierce, L.E.

I08.02 Segmentation of Radar Imagery Using Gaussian Markov Random Field Models and Wavelet Transform Techniques 2054
Dong, Y., B. Forster and A. Milne

I08.03 Efficient Calculation in the Map Domain of SAR Layover and Shadow Masks 2057
Pairman, D., and S. McNeill

I08.04 Different Approaches to Multiedge Detection in SAR Images 2060
Fjortoft, R., A. Lopes, P. Marthon and E. Cubero-Castan

I08.05 Terrain Classification Via Texture Modeling of SAR and SAR Coherency Images 2063
Meagher, J., J. Homer, R. Paget, and D. Longstaff

I08.06 Multifractal Analysis of the Digital Terrain Model for Terrain Classification in a Polarimetric SAR Image NA
Martinez, P., D. Schertzer and K. Pham

I08.07 Adaptive Texture-Preserving Filtering of Multitemporal ERS-1 SAR Images 2066
Aiazzi, B., L. Alparone, S. Baronti and R. Carla

I08.08 Internal Waves Detection and Characterization from ERS-1 SAR Images Using the 2-D Wavelet Transform 2069
Rodenas, J.A., D. Cabarrocas and R. Garello

I09: ADEOS

I09.01 Results of CAL/VAL and Preliminary Scientific Results of ADEOS 2072
Shimoda, H.

I09.02 OCTS (Ocean Color and Temperature Scanner) 2075
Kawamura, H., M. Shimada, H. Nakumura, H. Oaku, Y. Mitomi and A. Mukaida

I09.03 Calibration and Validation of AVNIR Data NA
Yasuoka, Y., M. Naka, and M. Shimada

I09.04 Atmospheric Trace Species Measurements by ILAS and RIS 2078
Sasano, Y., and N. Sugimoto

I09.05 Initial Result of IMG on Board ADEOS NA
Ogawa, T., H. Shimoda, H. Kobayashi, S. Kadokura, A. Shimoda, R. Imasu, and M. Hayashi

I09.06 Studies of Atmospheric and Oceanic Phenomena with the NASA Scatterometer 2082
Liu, W.T.

I09.07 TOMS-ADEOS Initial Results NA
Krueger, A.J.

I09.08 The Analysis of the Polder Data 2084
Kawata, Y., Y. Yamazaki K. Takemata and T. Kusaka

I10: Atmospheric Profile

I10.01 Cloud Classification and Retrieval from Spaceborne Microwave Radiometry Using a Simulated Cloud Database 2087
d'Auria, G., F.S. Marzano, N. Pierdicca, R. Pinna Nossai, P. Basili and P. Ciotti

I10.02 On the Measurement of Stratus Cloud Properties with a Cloud Radar and Microwave Radiometer 2090
Frisch, A.S., T. Uttal, C.W. Fairall and J.B. Snider

I10.03 Remote Sensing of Boundary-Layer Temperature Profiles by a Scanning 5mm Microwave Radiometer and RASS: A Comparison Experiment 2093
Westwater, E.R., Y. Han, V.G. Irisov, V. Leuski, E.N. Kadygrov and S.A. Viazankin

I10.04 A Neural Network Algorithm for the Retrieval of Atmospheric Profiles from Radiometric Data 2097
Del Frate, F., and G. Schiavon

I10.05 The Role of a priori Information in Designing Retrieval Algorithms for Microwave Radiometric Profiling of the Atmosphere 2100
Basili, P., P. Ciotti, G. d'Auria, F.S. Marzano, N. Pierdicca and S. Bonafoni

I10.06 Cirrus Characteristics and Remote Sensing Retrievals from Airborne Active/Passive Observations NA
Spinhirne, J.D

I10.07 Calibration/Validation of Wind Profile Measurement by V.H.F. Radar NA
Givri, J.R.

I10.08 Developmental Studies for Remote and In-Situ Detection of Halogenated Compounds by Laser-Induced Photogragmentation/Fragment Detection Spectrometry 2103
Sausa, R.C., and J.B. Simeonsson

Author's Index

Volume I *Follows page* 618
Volume II *Follows page* 1089
Volume III *Follows page* 1434
Volume IV *Follows page* 2106

"NA" indicates not available at time of printing.

IGARSS'97

1997 International Geoscience and Remote Sensing Symposium

03-08 August 1997

Singapore International Convention & Exhibition Centre

Technical Program

Interactive Area 1: Aerosols

Aerosol Profile Variations Retrieval Through Kernel Functions in the Oxygen Absorption Band at 762 nm

M. Gabella, A. Leone, G. Perona
Dipartimento di Elettronica, Politecnico di Torino,
Corso Duca degli Abruzzi 24, 10129 Torino, Italy,
Tel: +39-11-5644104, Fax: +39-11-5644015, E-mail:PERONA@POLITO.IT.

Abstract -- The *aerosol kernel functions*, relating (through a Fredholm integral equation) the variations in radiance measured by satellites to the variations of aerosol extinction profile, have been computed with a 20 cm^{-1} spectral resolution within the Oxygen A-band (LOWTRAN atmospheric database has been used). The kernel was originally evaluated at wavelengths in the near infrared region outside absorption bands. Notwithstanding the fact that a higher spectral resolution should be adopted to fully take advantage of the Oxygen band possibilities, even the 20 cm^{-1} resolution permits to get a better information content and an improved accuracy with respect to the wavelengths previously investigated: indeed the retrieval relative error is approximately reduced to a half.

INTRODUCTION

The problem of retrieving the aerosol profile by means of different observational parameters (wavelength and scattering angle) rather than by means of measurements made at different altitudes is ill posed in the sense of Hadamard [1]. Furthermore, even in the simple case of single scattering approximation, the retrieval of the atmospheric aerosol profiles by inverting nadir and quasi nadir-viewing satellites measurements cannot be performed in a straightforward manner owing to the non linear relationship between the observable parameter (i.e. the radiance) and the unknown (i.e. the aerosol profile). Gabella et al. [2] found out that, by restricting the investigation to monitor the variations on the total upward radiation due to a variation in the aerosol profile, it is possible to derive a linear relationship between the variation in the upward radiance at the top of the atmosphere δL and the variation in the aerosol extinction coefficient $\delta\alpha_A(z)$: precisely a Fredholm integral of the first kind relates the observable parameter δL to the indirect remote sensed quantity $\delta\alpha_A(z)$ by means of the sensitivity weighting function $W(\gamma,\lambda;z)$ as follows:

$$\delta L(\gamma,\lambda) = \int_0^\infty W(\gamma,\lambda;z)\, \delta\alpha_A(\lambda;z)\, dz, \qquad (1)$$

where the scattering angle, γ, and the wavelength, λ, dependence is explicitly evidenced. A full description of the sensitivity weighting function $W(\gamma,\lambda;z)$ and of all the terms appearing in it can be found in [2].
Equation (1) originates from the solution of the radiative transfer equation within the approximation of single scattering and the assumption of a non reflecting low boundary: the first approximation is reasonable for atmospheric optical depth much more less than 1, the second one is valid for clear waters at wavelengths greater than 694 nm. These assumptions cover well defined scenarios over open ocean waters in clear sky conditions (no clouds and meteorological range at least greater than 23 km). Of great importance is also that the sensitivity weighting function $W(\gamma,\lambda;z)$ has been derived with the basic assumptions that the deviation from the reference profile $\alpha_A(z)$ is not arbitrary and that the variations of the total upward radiance are a consequence of variations in the aerosol extinction profile only. From a mathematics point of view the latter condition can be expressed as

$$\frac{\delta\left(\omega_0^A P_A\right)}{\omega_0^A P_A} << 1, \qquad (2)$$

while, for what concerns the former one, the conditions that must be fulfilled are the followings:

$$\int_0^\infty \delta\alpha_A(\xi)\, d\xi << 1, \qquad \frac{\delta\tau_A}{\tau_A} << 1. \qquad (3)$$

If the previous conditions are not satisfied, the use of the above defined sensitivity weighting function $W(\gamma,\lambda;z)$ provides only a rough estimate of δL due to aerosol profile variations, as the accuracy of the linear approximation becomes low [3].

Equation (1) shows that the indirect remote sensed quantity (the variation in the aerosol extinction coefficient $\delta\alpha_A$ at different heights) still has a dependency on the wavelength, hence banishing the possibility of using different wavelengths in order to retrieve the variations with altitude. Furthermore, the aerosol extinction profile $\alpha_A(z)$ decreases by almost ten orders of magnitude from the boundary layer to the top of the atmosphere: therefore the characteristic values of the quantity $\delta\alpha_A(z)$ are also highly variable over the vertical. Consequently, it is more convenient from the numerical point of view to deal with the relative aerosol variations $f(z)=\delta\alpha_A(z)/\alpha_A(z)$ in the aerosol extinction coefficient, more representative for the layer as a whole and, at the same time, independent of wavelength. In such a case, equation (1) can be rewritten in the form:

$$g(\lambda,\gamma) = \int_0^\infty K(\lambda,\gamma;z)\, f(z)\, dz, \qquad (4)$$

where $g(\lambda,\gamma)$ represents the variations in the radiance at the top of the atmosphere and $K(\lambda,\gamma;z)= \alpha_A(\lambda,z)\, W(\lambda,\gamma;z)$ are the *aerosol kernel functions*.

0-7803-3836-7/97/$10.00 © 1997 IEEE

REFERENCE ATMOSPHERIC MODELS AND KERNEL NUMERICAL ASSESSMENT

For the numerical evaluation of the aerosol kernel functions, the atmospheric models and parameters stored in the LOWTRAN code [4] have been used. The total vertical transmittance within the *A* Oxygen absorption band, has been obtained directly from LOWTRAN simulations with a 20 cm^{-1} spectral resolution. The following wavenumbers and geometrical parameters of observation have been assumed to compute the kernel functions presented here:

- 13080, 13135, and 13165 cm^{-1} corresponding to 765, 761, and 760 nm.
- Scattering angle ranging from 130° to 170° with 20° steps.

It is to be noted that at these absorbing wavelengths the total optical thickness (23 km meteorological range) spans from 0.9 to 1.6; however, the low values of the total single scattering albedo (that is about 0.2÷0.25) make the single scattering approximation still reasonable.

The quadrature scheme used to numerically evaluate the kernel function and the Fredholm integral equation can be found in [3]. The quadrature formula reduces the integral equation to a linear approximation having the following matrix form:

$$\mathbf{g} = \mathbf{A}\mathbf{f}. \tag{5}$$

INVERSION AND INFORMATION CONTENT

The inversion procedure for (5) should include the analysis of unavoidable measurement errors and, consequently, the set of linear equations describing the problem at hand is better expressed by

$$\mathbf{g} + \mathbf{dg} = \mathbf{A}\mathbf{f}, \tag{6}$$

where **dg** represents the experimental uncertainties in **g**. For this type of problems the application of the linear constrained inversion methods turns out to be adequate. In particular, by applying it in the form developed by Twomey [5], we can write

$$\mathbf{f} = (\mathbf{A}^t\mathbf{A} + \zeta\,\mathbf{H})^{-1}\mathbf{A}^t\,(\mathbf{g} + \mathbf{dg}). \tag{7}$$

Matrix **H** permits to dampen the oscillations of the solution vector and for the cases presented here, best results have been obtained with **H** minimizing the second differences.

The validation of the method has been pursued through the following procedure:

I) LOWTRAN code is used to compute L and $L+\delta L$ relative to the initial reference profile $\alpha(i)$ and to the final one $\alpha+\delta\alpha$; in this way a LOWTRAN evaluated **g** vector is obtained. Aim of the procedure is to compare the retrieved relative variation in the presence of error with this "true" relative variation $\mathbf{f}=(\delta\alpha/\alpha)_T$.

II) Then matrix **A** relative to the initial reference profile is computed.

III) At this point, a **dg** vector is added to **g** and the full inversion scheme is implemented to retrieve an estimated relative aerosol variation $\mathbf{f}_E=(\delta\alpha/\alpha)_E$ to be compared with the true one $\mathbf{f}=(\delta\alpha/\alpha)_T$.

In the following numerical examples, each component of the simulated noise added vector **dg** is equal to the corresponding component of **g** multiplied by, alternatively, + or −0.01, i.e. the Relative Error [6] $\|\mathbf{dg}\|/\|\mathbf{g}\|$ is set to 1%. In an analogous way, the quantitative comparison between the estimated and the true profile is hereafter performed by estimating the "retrieval relative error" $\|\mathbf{f}_e-\mathbf{f}\|/\|\mathbf{f}\|$. It is to be noted that, within such a quantitative comparison, the retrieval error has been monitored both in presence (Ξ) and in absence (Ψ) of a simulated error vector, **dg**, added to the process; in other words the two quantities

$$\Xi = \left\| \left(\mathbf{A}^t\mathbf{A} + \zeta\,\mathbf{H}\right)^{-1}\mathbf{A}^t\left(\mathbf{g} + \mathbf{dg}\right) - \mathbf{f} \right\|,$$

$$\Psi = \left\| \left(\mathbf{A}^t\mathbf{A} + \zeta\,\mathbf{H}\right)^{-1}\mathbf{A}^t\mathbf{g} - \mathbf{f} \right\|,$$

have been computed and monitored as a function of ζ.

According to Twomey's analysis [7], the N equations contained in the matrix equation (7) are fully *independent* only if the inequality

$$\lambda_i >> \left(\frac{\|\mathbf{dg}\|}{\|\mathbf{f}\|}\right)^2 \tag{8}$$

is satisfied for all the eigenvalues λ_i of the covariance matrix $\mathbf{A}^t\mathbf{A}$. On the contrary, the dimension N of *independence* must be reduced by one for every eigenvalue which is too small to meet this requirement. If N' equals the number of eigenvalues of $\mathbf{A}^t\mathbf{A}$ satisfying (8), then it can be considered a measure of the information content of the observations and can be called the *number* of *independent information elements*. As it is clearly seen, N' depends both on the magnitude of the experimental errors and on the "distinctive features" of the covariance matrix $\mathbf{A}^t\mathbf{A}$. The Twomey's analysis has been used to assess the amount of information retrievable from the measurements made at different wavelengths and at different scattering angles; in addition to N' the condition number of the system matrix and the error amplification coefficient are evaluated to quantitatively characterize the quality of the inversion procedure: as it is well known, the condition number of the system matrix, cond(A), represents an upper limit for the error amplification coefficient, χ_{ill}, that is:

$$\chi_{ill} = \frac{\|\mathbf{df}\|/\|\mathbf{f}\|}{\|\mathbf{dg}\|/\|\mathbf{g}\|} = \frac{\|\mathbf{A}^{-1}\mathbf{dg}\|}{\|\mathbf{A}^{-1}\mathbf{g}\|}\frac{\|\mathbf{g}\|}{\|\mathbf{dg}\|} \le \mathrm{cond}(\mathbf{A}) = \|\mathbf{A}\|\,\|\mathbf{A}^{-1}\|.$$

RESULTS AND CONCLUSIONS

By way of example, the changes in the lower atmosphere resulting from variation of the meteorological range from 23 to 50 km, as described in the LOWTRAN data set, are

Table 1 Parameters characterizing the retrieval scheme performance as a function of the available measurements within the Oxygen A-band (wavelengths at 13080, 13135, 13165; 13100, 13145, 13155 cm^{-1})

Measurements	cond(A)	χ_{ill}	N'	ζ	$\Xi/\|\|f\|\|$	$\Psi/\|\|f\|\|$
3 Wavelengths, 2 Scattering angles	4.6×10^4	33.9	III	10^{-6}	7.9%	8.7%
6 Wavelengths, 2 Scattering angles	1.9×10^4	38.9	III	10^{-8}	6%	13.1%

Table 2 Parameters characterizing the retrieval scheme performance as a function of the available measurements outside molecular absorption bands (wavelengths at 0.694, 1.06, 1.54 μm)

Measurements	cond(A)	χ_{ill}	N'	ζ	$\Xi/\|\|f\|\|$	$\Psi/\|\|f\|\|$
3 Wavelengths, 2 Scattering angles	9.3×10^5	1.5×10^4	II	10^{-4}	17%	28%

presented here; only the first six nodes (0+5 km height with a 1 km vertical resolution) of the layered reference model are involved. In the left side of table 1, for each set of observational parameters (measurements made at different wavelengths and at different scattering angles), the condition number of the matrix **A**, the error amplification coefficient and the number of independent information elements, N', (Relative Error=1%) are reported. In the right side of the same table the last three columns show the results of the linear constrained inversion: namely, the fourth column indicates the value of the Lagrange multiplier ζ used, the fifth and sixth ones show the "retrieval relative error" respectively with and without a simulated error vector **dg** added to the process. The chosen value of ζ is the one for which Ξ reaches its minimum. Note that in the absence of error ζ can be set to zero since $\Xi\rightarrow\Psi\rightarrow0$. Of course this result is not reasonable, since, owing to the unavoidable presence of errors, a finite value for ζ (in turn function of the estimated Relative Error) has always to be adopted. Consequently the accuracy of the procedure has to be evaluated in two different cases, both characterized by not null value of ζ (with **dg** equal or different from zero). The first example refers to 3 wavelengths and 2 scattering angles (chosen at the largest "angular distance" among those analyzed, i.e. 130° and 170°); the second one to 6 different wavelengths (kernels at 13100, 13145, 13155 cm^{-1} have been added) and alternatively 130° and 170° scattering angles.

A comparison with the results (listed, for convenience, in table 2) obtained by Gabella et al. [2] in the near infrared region outside the molecular absorption bands (precisely at 0.694, 1.06, 1.54 μm) shows that the results obtained here present a lesser interdependence among the kernels, lower error amplification and an increase (from two to three) in the number of *independent information elements*, N'; hence the relative variations in the aerosol profile can be retrieved with a considerable higher accuracy connected with a lower value for the Lagrange multiplier ζ.

The simple mathematical scheme here developed seems to be a useful tool for satellite monitoring of tropospheric aerosol profile variations on a global scale in clear and cloudless atmosphere.

REFERENCES

[1] Hadamard J, "Lectures on Cauchy's problem in linear Partial differential equations", *Yale Univ. Press*, 1923.

[2] Gabella M., Guzzi R., Kisselev V., Perona G., "Retrieval of aerosol profile variations in the visible and near infrared: theory and application of the single scattering approach", *Applied Optics*, vol. 36, pp. 1328-1336, 1997.

[3] Gabella M., *GOME, Retrieval delle variazioni nel profilo dell'aerosol*, Ph. D. Dissertation, Torino, Politecnico di Torino, 1995.

[4] Kneizys F. X., E. P. Shettle, L. W. Abreu, J. H. Chetwind, G. P. Andreson, W. O. Gallery, J. E. A. Selby, S. A. Clough, *Users guide to LOWTRAN 7*. AFGL-TR-88-0177 Env. Res. paper N. 1010, Air Force Geoph. Lab., Hanscom AFB, Mass. 01731-5000, 1988.

[5] Twomey S., "On the numerical solution of Fredholm integral equations of the first kind by the inversion of the linear system produced by quadrature", *J. Assoc. Comput. Mach.*, vol. 10, pp. 97-101, 1963.

[6] Shaw G. E., "Inversion of optical scattering and spectral extinction measurements to recover aerosol size spectra", *Applied Optics*, **18**, pp. 988-993, 1979.

[7] Twomey S., "Information content in remote sensing", Applied Optics, vol. 13, pp. 942-945, 1974.

The seasonality of ozone profile at Reunion island : the role of biomass burning and of transport

Tantely RANDRIAMBELO, Serge BALDY and Miloud BESSAFI.
Laboratoire de Physique de l'Atmosphere, Universite de la Reunion
15 avenue Rene Cassin 97490 REUNION
Tel : 00 262 93 82 39/ Fax : 00 262 93 81 66/ email : randriam@univ-reunion.fr

Abstract -- Vertical ozone profiles obtained from ozone soundings at Reunion island (21S-55E) present a seasonal variability. High values of ozone concentration are observed in the troposphere above the inversion level that caps the marine boundary layer during September to December. Satellite observations using NOAA (National Oceanic and Atmospheric Administration) data indicate that this period corresponds to active biomass burning and the beginning of deep convection clouds in Southeastern Africa and Madagascar. Furthermore, analysis of backtrajectories obtained from Reunion island clearly evidence the role of long distance transports from biomass burning sources. Strong variation of ozone profiles are associated, through this transport, with fires, smoke plumes and deep convective structures present in the studied regions.

INTRODUCTION

Tropical vegetation burning is considered to be responsible for tropospheric ozone enhancement. It also constitutes a significant global source of active radicates and chemically reactive gases [1]. To assess the relationships between fires, transports and for tropospheric ozone enhancement research studies focusing on Amazonia or Southern Africa zones have been undertaken. Although fire contaminations of the free troposphere above Atlantic and Pacific Oceans have been recently documented, still few studies concern the Indian Ocean. Yet, the INdian Ocean EXperiment (INDOEX) is planned for 1999 to study interactions between gases, particles, clouds and radiative properties.

The ozone vertical distribution obtained from ozone soundings at Reunion island (21S-55E) presents a seasonal character [2]. High values of ozone concentration are observed in the troposphere during September to December above the inversion level that caps the marine boundary layer. This period corresponds to active biomass burning in Southeastern Africa and Madagascar [3]. Recent analyses show that biomass burning emissions play the major role in these strong enhancements of ozone during the dry season [1]. Therefore, it is of interest to quantitatively document the fire and deep convection period which corresponds to tropospheric ozone enhancement observed at Reunion island.
This paper studies the relationships between tropospheric ozone enhancement, fire peaks, smoke plumes and deep convection. Fires, smoke plumes and deep convection clouds detections use NOAA-AVHRR-LAC (National Oceanic and Atmospheric Administration-Advanced Very high Resolution Radiometer-Local Area Coverage) data and are focused on Southeastern Africa and Madagascar. In order to determine the transports, air mass trajectories are calculated by Meteo-France from a kinematic trajectory model and data furnished by courtesy of the European Center for Medium-Range Weather Forecasts (ECMWF).

DATA AND METHODOLOGY

Ozone

Vertical ozone profiles are obtained from radiosounding using ECC (Electrochemical Cell) ozonesondes since September 1992 at Reunion island with launching frequency every two weeks. Ozone profiles show a strong seasonal enhancement during the dry season. These enhancements are observed over the free troposphere as in the marine boundary layer [2]. Since wind and temperature inversions capping the marine boundary layer are limiting ozone incomes, we will focus on this paper on ozone variations in the free troposphere.
Tropospheric ozone mixing ratio variations could reach up to 100 pbbv from September to December. These strong variations coincide with fire periods in Africa and Madagascar. Case studies of these ozone enhancements observed around 500 mbar and 300 mbar are presented on figure 1b and figure 1c. Conversely, during summer tropospheric ozone content is relatively low (Fig. 1a).

Fires - smoke plumes and deep convection clouds

Fires, smoke plumes and deep convection clouds were derived from NOAA-AVHRR-LAC data using Orstom-Reunion antenna. Data include the 5N to 40S and 20E to 90E region (Southeastern Africa and Madagascar). The fire detection method is based on Franca's multispectral method [3] and [4]. Smoke plumes are detected from a false colour composite in the visible and the thermal range [3] and [5].
The different geographical contributions to total fire-counts are detailed in figure 2 for the 1993. We note that the total peak of fire intensity could be splitted in two peaks : one in September for the Southeastern Africa and the another one in October for Madagascar. These periods correspond to the end of the dry season for each country. During clear sky conditions allowing smoke measurements, fire peaks are associated with well developed smoke plumes (Fig. 3).

0-7803-3836-7/97/$10.00 © 1997 IEEE

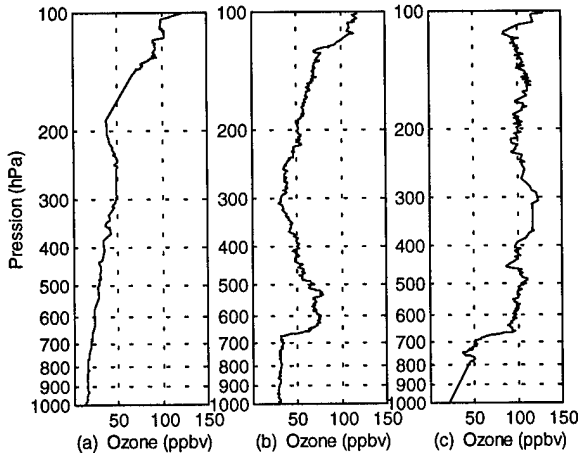

Fig. 1: Tropospheric ozone profiles obtained by radiosoundings at Reunion. (a) 23th of February 1993, (b) 24th of August 1993 and (c) the 12th of October 1993.

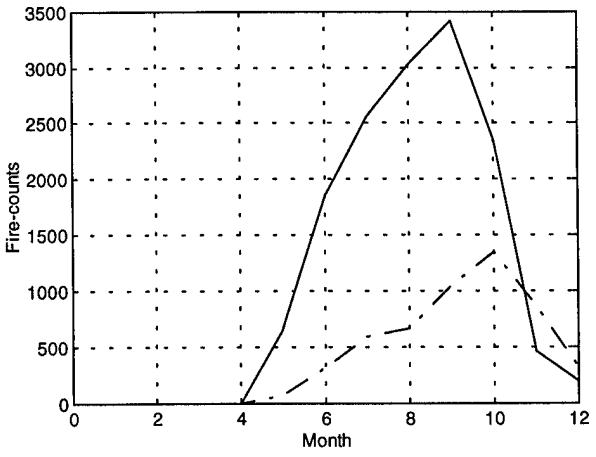

Fig. 2 : The different geographical contributions to one year (1995) time evolution of fire-counts for 1993 : Solid line for Africa and Dotted line for Madagascar.

NOAA-AVHRR images can also used to detect deep convection zones. Such zones are characterized by a high reflectance value of the channel 1(>70%) and a low brightness temperature value of the channel 4 (<70K). Deep convective clouds are extensive during the rainy season in tropics. Yet these clouds begin to develop in the end of the dry season [6].

CASE STUDIES

The selected days corresponds to strong enhancements of tropospheric ozone at Reunion island during 1993. The detection methods reveal that it coincides with the end of severe fire periods and the beginning of deep convective clouds in the studied regions.

Moreover, these deep convective clouds are observed near fire and smoke plumes areas. Hence, to better investigate the contribution of biomass burning emissions in ozone enhancements obtained at Reunion island we have to consider the transport from these areas where biomass burning by products could be injected in the free troposphere.

In order to describe the origin of air masses, backtrajectories are plotted for different altitudes. These altitudes correspond to peaks in tropospheric ozone profiles. Backtrajectories show that at these altitudes (600 mbar, 500 mbar and 300 mbar), all particles come from the west of Reunion island. Moreover, these air masses are crossing over Mozambique and Madagascar where biomass burning is intensive. In addition the trajectories from these regions are characterized by strong subsidences on the way to Reunion island following possible ascendances.

ANALYSIS AND DISCUSSIONS

These results suggest that some insight to the understanding of tropospheric ozone enhancement in remote regions could come from the comparison of fire, smoke, convection and ozone data. Although remote sensing is hindered by the presence of clouds or by image distortion, data could document the relationships between the seasonal variation of tropospheric ozone profiles, fire peaks, smoke plumes and deep convection clouds.

Ozone profiles show that before the ozone peak in the 24th of August 1993, tropospheric ozone content is relatively weak. After this peak and until the end of November the enhancement of tropospheric ozone is high as illustrated by 12th of October 1993 profile and can even reach the upper troposphere (Fig. 1).

It is note worthy that the ozone enhancement in the upper troposphere could be explained by the presence of deep convective clouds near fire and smoke plumes areas. Deep convective structures uplift air from the low troposphere to the higher levels. After clouds venting, biomass byproducts could be transported towards the East from their sources by upper-level westerlies winds and could reach Reunion island after a few days. In addition, it is noticeable that the studied regions consist of forestry zones where smoke plumes are well developed. Ground observations on the ground indicate that around these zones, thick smog is formed in the afternoon. This smog evidences widespread biomass burning emissions in these regions. Since, in the free troposphere the lifetime of ozone is around 90 days, convective uplift and horizontal transport in the free troposphere could induce large amount of tropospheric ozone over wind and temperature

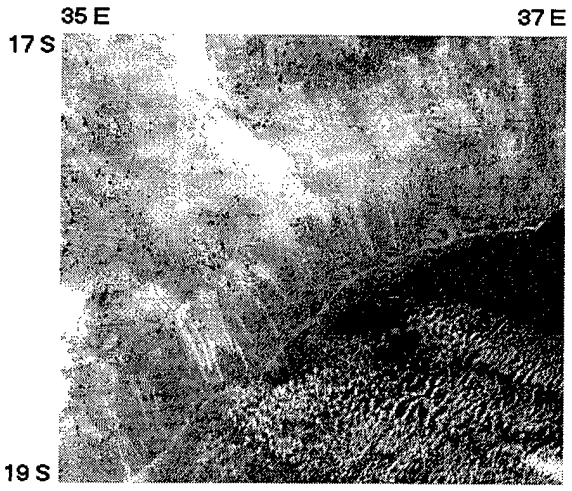

Fig. 3 : Grey level image showing fires and smoke plumes of biomass burning in the East coast of Mozambique. The image is based on the reflectance in channel 1 (0,63 μm) of NOAA-AVHRR-LAC 13h41TU September 18, 1993. Smoke plumes are showing as white and fire as black.

inversions in the Indian Ocean[7].

Backtrajectories traced from Reunion also suggest a vertical transport in deep convective cloud zones and document the long range transports. Particles emitted from fires could reach Reunion after 4 days from the Southeastern Africa and 2 days from Madagascar. The results evidence that high values of ozone are accordant with intense fires and smoke plumes and deep convection clouds episodes

In addition, the present results indicate that AVHRR sensor could be used to simultaneously monitor fires, smoke plumes and deep convection clouds.

Backtrajectories obtained from Reunion island further suggest that air masses could originate from intense fires, smoke plumes and deep convection areas in the Southeastern Africa and Madagascar.

This study provides an example of application of remote sensing to the understanding ozone profile enhancements at Reunion island. Period of strong variation of ozone profiles are concordant with fire, associated smoke plume and deep convection cloud periods in the studied regions. They demonstrate also that the observation of ozone mechanisms in an isolated tropical island are important.

Since ozone enhancements are occuring in the free troposphere of remote regions, it is also suggest that vertical ozone soundings in remote sites in the tropics like Reunion island could provide some insight to ozone contamination by biomass burning.

ACKNOWLEDGMENTS

The authors thank Orstom-Reunion station for providing NOAA-AVHRR data.

REFERENCES

[1] M. O. Andrea *et al*, Biomass burning in the global environment : "First results from the IGAC/BIBEX field campaign START/TRACE-A/SAFARI-92 ", in global Atmospheric-Biospheric Chemistry, edited by R. G. Prinn, pp. 83-101, Plenum Press, New York, 1994.

[2] S. Baldy, G. Ancellet,M. Bessafi, A. Badr and D. Lan Sun Luk, 1996, "Field observations of the vertical distribution of tropospheric ozone at the island of la Réunion". Journal of Geophysical Research. vol. 101, D19, pp. Octobre 30, 1996.

[3] T. Randriambelo, S. Baldy, M. Bessafi, M. Petit and M. Despinoy 1996 , "An improved detection and characterization of active fires and smoke plumes in Southeastern Africa and Madagascar", unpublished.

[4] J. R. A. Franca, 1994, "Télédétection satellitaire des feux de végétation en région intertropicale. Application à l'estimation des flux des composés en trace émis dans l'atmosphère". Thèse de doctorat de l'Université Paul Sabatier Toulouse.

[5] Y. S. Chung, and H. V. Le, 1984, "Detection of forest-fire smoke plumes by satellite imagery". Atmospheric Environnment, 18, 10, pp. 2143-2151.

[6] T. Randriambelo, S. Baldy, M. Bessafi 1997, "Deep convection cloud detection using NOAA satellite: Applications to convection transport of biomass burning emissions over Southeastern Africa and Madagascar", The 1997 EUMETSAT Meteorological Satellite Data User's Conference October 1997, unpublished.

[7] M. Garstang, P. D. Tyson, R. Swap, M. Edwards, P. Kalleberg and J. A. Lindsay, 1996, "Horizontal and vertical transport of air over Southern Africa". Journal of Geophysical Research, vol. 101, D19, pp 23, 721-23,736. October 30, 1996.

Interpretation of Ground-based Measurements of Atmospheric Aerosols

I. Sano, S. Mukai, M. Yasumoto, K. Masuda*, M. Sasaki* and H. Ishida†

Kinki University, 3-4-1 Kowakae, Higashi-Osaka, Osaka 577, Japan
Tel.+81-6-721-2332 / Fax.+81-6-730-1320 / sano@im.kindai.ac.jp

*Meteorological Research Institute, Tsukuba, 305 Ibaraki, Japan

†Maritime University of Kobe, Kobe, 658 Hyogo, Japan

Abstract – This work describes a procedure to estimate optical properties of atmospheric aerosols by using polarization data. Polarization degree and optical thickness of the atmospheric constituents have been simultaneously measured by a photopolarimeter, whose spectral bands are set up to correspond to the ADEOS/POLDER.

Our algorithms are based on light scattering simulations of the polarization field. It is found :

(1) the typical oceanic type aerosol is one candidate to investigate the photopolarimetry observed over the Seto Inland Sea,
(2) it is more natural to consider that the continental type aerosol exists together with the oceanic type,
(3) the magnitude of polarization degree is reduced due to multiple scattering diffusion.

INTRODUCTION

It is well-known atmospheric aerosols play an important role in the earth's environment. Unfortunately, aerosol model change greatly in temporal and regional scales. It has been shown in our previous work that polarization feature strongly depends on the aerosol model, and that aerosol retrieval can be accurately pursued by combining polarization with radiance [1].

POLDER (POLarization and Directionality of Earth Reflectance) aims to collect global-scale visible and near-infrared observations of polarized and directional solar radiance reflected by the Earth-atmosphere system [2]. ADEOS/POLDER data has not yet been released now. Therefore the measurements with a portable photopolarimeter on the ship in Seto Inland Sea are treated here. Our aerosol retrieval is based on single and/or multiple light scattering simulations of the polarization field.

SINGLE SCATTERING SIMULATIONS

The polarization degree and optical thickness of atmospheric constituents were observed over the Seto Inland Sea on March 18th in 1997. These measurements were undertaken by a portable photopolarimeter (named PSR1000), which has six observing bands at wavelengths of 0.443, 0.490, 0.565, 0.670, 0.765 and 0.865 μm. These wavelengths and their bandwidths are set up to correspond to the observing channels for the ADEOS/POLDER. The photopolarimeter makes an angle of 90° away from the solar direction in the principal plane which is determined by the sun, zenith and observation directions.

Two solid curves in Fig.1 represent the aerosol optical thickness by a sunphotometer and a photopolarimeter respectively. Although the values by photopolarimeter are less than those by sunphotometer, we found that both of them are less than the proposed standard optical thickness [3]. The dots in Fig.2 present the simultaneously observed polarization degree. Roughly speaking degree of polarization decreases with wavelength.

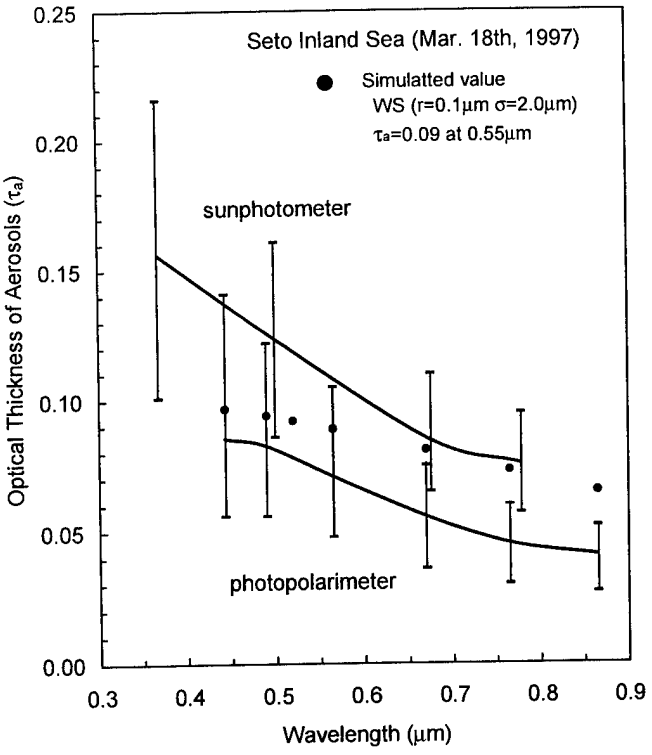

Fig.1 Aerosol optical thickness versus wavelength.

0-7803-3836-7/97/$10.00 © 1997 IEEE

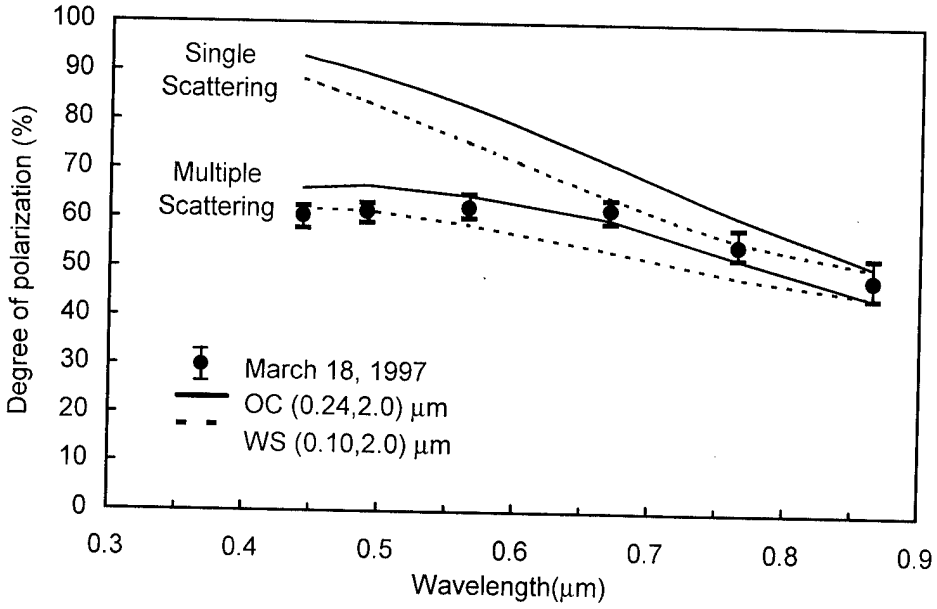

Fig.2 Degree of polarization. The dots, and the dashed and solid curves represent the observed, and calculated values for aerosol models of WS and OC, respectively.

These data are used for retrieval of optical parameters of aerosols such as size and refractive index based on scattering simulations. A single scattering phase matrix $\widetilde{\boldsymbol{P}}$ is expressed by Stokes parameters (I, Q, U, V) and composed of Rayleigh scattering by molecular gases ($\widetilde{\boldsymbol{P}}_{Ray}$) and Mie scattering by aerosols ($\widetilde{\boldsymbol{P}}_{Mie}$).

$$\widetilde{\boldsymbol{P}} = (1 - f_g) \cdot \widetilde{\boldsymbol{P}}_{Mie} + f_g \cdot \widetilde{\boldsymbol{P}}_{Ray} \ , \qquad (1)$$

where f_g represents the ratio of the molecular scattering cross-section to the total one. The values of the phase matrix elements strongly depend on the characteristics of aerosols because of the uniform distribution of molecular gases.

One of the most widely used size distributions, the single-mode log-normal representation with two parameters, the mode radius ($\overline{r}$) and the width of the log-normal curve (σ) is considered here. Thus it becomes our purpose to retrieve $(\overline{r}, \sigma)$ for the log-normal distribution. Based on single scattering simulations in the near-infrared wavelengths, it is found that a water soluble type (WS) aerosol with ($\overline{r} = 0.1\mu m$, $\sigma = 2.0\mu m$) can explain the polarization measurements. The dots in Fig.1 and the upper dashed curve in Fig.2 represents the calculated results. An oceanic type aerosol (OC) with ($\overline{r} = 0.24\mu m$, $\sigma = 2.0\mu m$) is also a good candidate to explain the measurements.

The observed polarization degrees in the visible wavelengths are smaller than those calculated from single scattering simulations.

MULTIPLE SCATTERING SIMULATIONS

Here multiple scattering calculations are concerned with an atmosphere-ocean model (see Fig.3). An inhomogeneous plane-parallel atmosphere is simulated by several homogeneous sublayers. The optical thickness of the Rayleigh scattering constituents and absorbent constituents such as ozone, water vapor and oxygen molecules is obtained by LOWTRAN 7 [3]. In our present calculations, an OC-type aerosol with ($\overline{r} = 0.24\mu m, \sigma = 2.0\mu m$) and WS-aerosol with ($\overline{r} = 0.1\mu m$, $\sigma = 2.0\mu m$) derived in the previous section are employed.

The equation of radiative transfer takes the following form

$$\begin{pmatrix} \mu & 0 \\ 0 & -\mu \end{pmatrix} \frac{d\boldsymbol{I}(\tau,\Omega)}{d\tau} = \boldsymbol{I}(\tau,\Omega) - \frac{1}{4\pi}\int_{-1}^{+1}\int_{0}^{2\pi} \widetilde{\boldsymbol{P}}(\tau;\Omega,\Omega')\boldsymbol{I}(\tau,\Omega')d\Omega', \quad (2)$$

where the optical depth, $\tau = 0$ and $\tau = \tau_1$, represents the top and bottom of atmosphere and Ω stands for (μ, ϕ), with μ the cosine of inclination angle to the upward normal and ϕ the azimuth angle. Radiation field is represented by the upward radiation $\boldsymbol{I}^+$ and the downward one $\boldsymbol{I}^-$, therefore solutions of transfer equation are required to satisfy the following boundary conditions :

$$\boldsymbol{I}^-(0,\Omega) = \pi \boldsymbol{F}\delta(\mu - \mu_0)\delta(\phi - \phi_0), \qquad (3)$$

$$\boldsymbol{I}^+(\tau_1,\Omega) = \frac{1}{\mu}\int_0^1\int_0^{2\pi} \widetilde{\boldsymbol{K}}(\Omega,\Omega')\boldsymbol{I}^-(\tau_1,\Omega')\mu' d\Omega', \quad (4)$$

where $\boldsymbol{F}$ represents incident solar flux and matrix $\widetilde{\boldsymbol{K}}$ represents the reflection pattern of the sea surface. The sea surface is simulated by multiple facets whose slopes vary according to the isotropic Gaussian distribution with respect to wind speed [4]. Wind speed is assumed to be $5m/sec$ as a typical value of clear day.

Several ocean models have been prepared. One of them is assumed to be homogeneous with an optical thickness of 20.0. The other is a completely diffused model, namely upward radiance out of the ocean is represented by the Lambert's law. Multiple scattering problem for the model of atmosphere-ocean is solved by the adding-doubling method.

In order to investigate our photopolarimetry, the values of downward intensity just above the sea surface $\boldsymbol{I}^{-}(\tau_1, \Omega)$ are desired. The numerical results are shown in Fig.2. It is found that multiple scattering light reduces degree of polarization especially in the visible wavelength. At present it is difficult to determine which is better to interpret the observed polarization data, OC- or WS- aerosols. It is natural to consider of mixture of several kinds of aerosols. Much more extensive measurements of atmosphere and ocean are desired to draw definite conclusions.

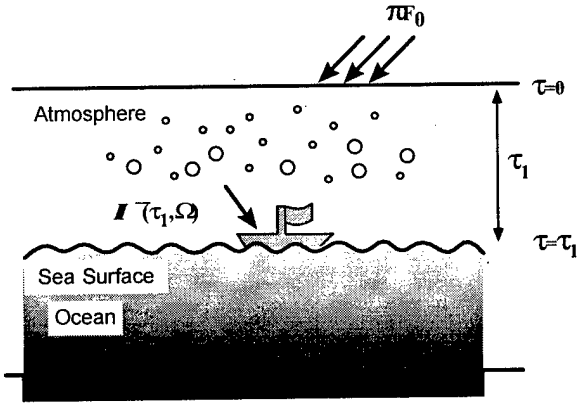

Fig.3 A simple illustration of atmosphere-ocean model.

SUMMARY

A procedure for aerosol retrieval by using photopolarimetric measurements based on single and/or multiple scattering calculations has been presented. It is possible to get another solutions with another combination of each model of aerosol, atmosphere, sea surface and ocean. At any rate, We obtained the following results from present simulations:

(1) the typical oceanic type aerosol is one candidate for aerosol model to investigate the photopolarimetry observed over the Seto Inland Sea,

(2) it is more natural to consider that the continental type aerosol exists together with the oceanic type,

(3) the magnitude of polarization degree is reduced due to multiple scattering diffusion especially in the visible region.

The aerosols have been assumed to be monotypic, but in general several kinds of aerosols could exist together in natural. Light scattering by the complex particles will be taken into account in a further work.

ACKNOWLEDGMENTS

The authors wish to express their thanks to Dr. Takashima of NASDA. This work was supported by NASDA (PSPC-18284), and also partially supported by scientific research funds from the Ministry of Education, Science and Culture of Japan (09780485).

REFERENCES

[1] S. Mukai, I. Sano and T. Takashima, "Investigation of Atmospheric Aerosols Based on Polarization Measurements and Scattering Simulations," *Opt. Rev.*, vol.3, pp.487–491, 1996.

[2] P. Y. Deschamps, F. -M. Bréon, M. Leroy, A. Podarie, A. Bricaud, J. C. Buriez and Sèze, "The POLDER mission: Instrument characteristics and scientific objectives," *IEEE Trans. Geosci. Remote Sensing*, vol.32, pp.598–615, 1994.

[3] F. X. Kneizys, E. P. Shettle, L. W. Abreu, J. H. Chetwynd, G. P. Anderson, W. O. Gallery, J. E. A. Selby, S. A. Clough, "Users Guide to Lowtran 7," Air Force Geophysics Laboratory, Hanscom AFB. MA, Rep. AFGL-TR-88-0177, 1988.

[4] C. Cox and W. Munk, "Measurements of the roughness of the sea surface from photographs of the sun's glitter," *J. Opt. Soc. Amer.*, vol.44, pp.838–850, 1954.

IGARSS'97

1997 International Geoscience and Remote Sensing Symposium

03-08 August 1997

Singapore International Convention & Exhibition Centre

Technical Program

Interactive Area 2: Applications of Radar and SAR Techniques

High Spatial Resolution Radar Altimetry for Global Earth Topography Mapping

G. Angino, F. Impagnatiello, C. Zelli
Alenia Aerospazio Space Division
Remote Sensing Engineering
Via Saccomuro 24, 00131 Rome ITALY
tel. +39-6-4151-1, fax +39-6-41512102
Email : angino@rm847.roma.alespazio.it
f.impagnatiello@roma.alespazio.it - c.zelli@roma.alespazio.it

Abstract -- This paper summarises the work performed by Alenia Aerospazio in the design of new radar altimeter systems suitable for high spatial resolution Earth topography observation. The instrument concept proposed herein is based on the application of synthetic aperture processing and interferometric techniques to a conventional Ku band pulse limited system. The major design features and expected performance are briefly presented.

INTRODUCTION

Radar altimeters designed up to now (Seasat, Geosat, ERS-1/2, Topex/Poseidon) have widely demonstrated the capability of performing measurements of the ocean topography from space. Nevertheless none of the mentioned systems provides an extensive capability to get topographic measurements over ice and land surfaces as requested by scientists. An improvement in this area will be possible with RA-2 [1], Advanced Radar Altimeter for ENVISAT-1 mission, currently under development in Alenia Aerospazio, thanks to its special on board tracker design. However novel concepts have to be developed to meet the severe horizontal resolution requirements (order of 100 - 300 meters vs. the several hundred meters provided by nadir-looking pulse limited systems) typical of ice/land topography missions [2].

Alenia Aerospazio, either by internally funded research activities or European Space Agency (ESA) feasibility study contracts, is currently studying the possibility of applying the synthetic aperture concept [3] [4] to radar altimetry for global Earth topography missions and is further moving towards the applicability of interferometry at very low off-nadir angles for the bidimensional retrieval of height measurements within the observed system swath [5] without recurring to phase unwrapping techniques, a really innovative measurement technique respect to conventional interferometry [6].

ALONG TRACK RESOLUTION ENHNACING BY SYNTHETIC APERTURE PROCESSING

The technique for synthetising a large antenna through radar motion is well established for side-looking systems. Such systems are able to produce high resolution images by exploiting the doppler shift caused by the relative motion between the radar and the imaged surface; the final effect can be viewed as a remarkable reduction of the antenna aperture in the direction of motion (along track). This basic principle certainly applies to radar altimeters [3] [4] [5] with some nice simplifications: a simple unfocused processing can in fact be considered. Furthermore tailoring the synthetic aperture processing time to the round trip time, a burst trasmission mode with synthetic apertures created on a single burst basis can then be envisaged leading to along track resolutions in the order of 250 m in Ku band, fully compatible with topography requirements.

The new developed system, however, must be designed to provide both conventional and high resolution altimetric measurements through synthetic aperture processing and interferometric processing following the basic considerations reported in the next section and in [5]. Full-deramping processing typical of any altimetric system should be retained in the basic scheme as shown in figure 1.

The transmitted signals are conventional long linear frequency modulated (FM) pulses that are coherently deramped and digitally converted, maintaining the in-phase and in-quadrature (I and Q) components. Looking at the primary Rx channel both conventional altimetric processing and synthetic aperture processing are applied to the data on a burst by burst basis. Conventional processing by a robust on board tracking algorithm (the Model Free Tracker of RA-2 [1], for istance) allows to set receiver tracking window position and receiver attenuation (AGC) for the deramping process.

The unfocused synthetic aperture processing is essentially based on an along track Fast Fourier Transform (FFT): data are extracted addressing the memory by its columns once they have been initially filled in by addressing the rows. Once the square module is taken , a "look" is produced for each burst and subsequent looks (after proper re-alignment) can be incoherently integrated to reduce the speckle. The final step is represented by the topography extraction from the multi-look image. In the along track direction the image is decomposed in doppler filters and each echo profile within a doppler filter can be processed through Centre of Gravity or Leading Edge Estimation algorithms to provide the height

0-7803-3836-7/97/$10.00 © 1997 IEEE

information as well as surface slope indication for an along track enhanced resolution altimetric product. The auxiliary Rx channel has actually the scope to provide measurement information for a fully enhanced resolution altimetric product using interferometric processing applied in cascade to the along track synthetic aperture processing as described in the following section. This also justifies the existence of a double antenna and receiving subsystem in the outlined instrument concept. Antenna beams should in this case be slightly tilted in the elevation plane identified by the satellite sub-nadir and across-track axes as here below explained.

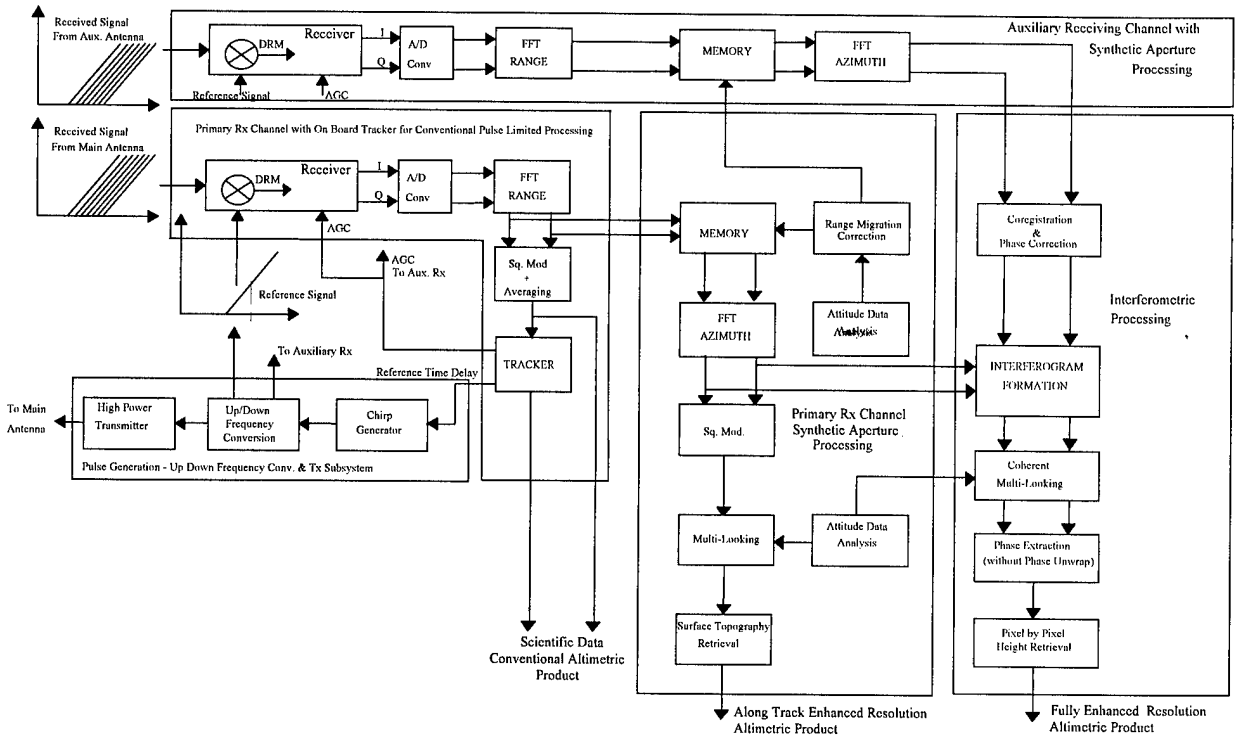

Figure 1 : Pulse Limited Altimetry with Synthetic Aperture/Interferometric Processing

INTERFEROMETRIC PROCESSING

SAR interferometry has shown to be one of the most promising techniques for deriving accurate and high resolution digital elevation models (DEM) of large areas. By using a couple of antennas separated by a distance B, it is in fact possible to derive the height of a target from the phase difference between the signals received by the two antennas. The relationship between the phase difference ($\Delta\Phi$) and the target's height (H) is very simple because only geometric system parameters are involved as shown by the (1), being R the slant-range, θ the off-nadir angle and B the baseline between the two antennas (see figure 2):

$$H = h - R\cos\theta$$

$$\Delta\Phi \approx \frac{2\pi}{\lambda}\left(B\sin\theta - \frac{B^2}{2R}\right) \qquad (1)$$

To obtain a phase difference image (interferogram) useful to retrieve the surface height through the (1), a synthetic aperture processing for each receiving channel for resolution enhancing in the along track, a data co-registration to compensate the different antennas point of view and a phase unwrapping to solve phase ambiguity shall be applied. This last operation, however, should be definitively avoided since completely automated and correct algorithms do not exist at present.

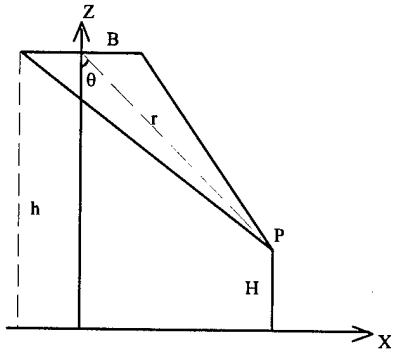

Figure 2 Interferometry Observation Geometry

The accuracy attainable on the height estimate depends on the knowledge of the parameters involved in the (1) and on various noise sources. A quick evaluation demonstrates that for the particular case of systems based on contemporaneous observation, height accuracy is mainly driven by the following term:

$$\frac{\partial H}{\partial \Delta\Phi} = \frac{(h-H)\cdot\lambda}{2\cdot\pi\cdot B}\cdot\frac{\sin\vartheta}{\cos^2\vartheta} \qquad (2)$$

Thus, at a first glance, the attainable accuracy in the determination of surface elevation through interferometric systems can be greatly increased either by decreasing the off-nadir angle θ or by increasing the antennas baseline once the system wavelength is fixed.

Being the main objective to avoid any phase unwrapping technique in the topography height retrieval processing, the baseline should then be constrained to the size of the antennas in use. More specifically, if conventional parabolic reflector of diameter D are employed in the system, the condition to avoid the phase unwrapping requires a baseline comparable to the diameter D. Improvement of the achievable system performance, according to the (2) can then be accomplished by strongly reducing the observation off-nadir angle which additionally allows to map the radar resolution into an across-track resolution. The goal for a system providing bidimensional surface topography within the swath is in this way met being:

- the along track resolution enhancing achieved through the along track synthetic aperture processing ;
- the across track resolution enhancing achieved through off-nadir observation geometry and the height within the swath retrieved on a pixel by pixel basis using the interferogram phase but without need of unwrapping techniques thanks to the short (near nadir interferometry). Care in the handling of potential range ambiguities shall however be dealt with, for istance recurring to decision criteria based on pixels energy analysis.

SYSTEM DESIGN AND PERFORMANCE

The key system features for the synthetic aperture/interferometric processing mode are summarised in table 1. Of course, the referenced radar pulse resolution applies only for the land / ice topography measurements, being instead required a much higher resolution (order of 0.5 m) to accomplish conventional nadir looking measurements over ocean. The expected theoretical resolution over ice/land using the full synthetic aperture / interferometric processing outlined herein is in the order of 1 m.

Operative Altitude	800 [Km]
Radar Frequency	13.6 [Ghz]
Antennas Diameter	1.2 [m]
Off-Nadir Observation Angle	1.75°
Tx Energy per Pulse	4 [mJ]
Radar Pulse Resolution	3 [m]
Synthetic Aperture Processing Time	5 [ms]
Along Track Synthetic Resolution	250 [m]
Across Track Ground Resolution	100 [m]
Height Retrieval Accuracy	1 [m]
Signal to Noise Ratio (σ_0=0 dB condition)	10 [dB] min.

Table 1 : Reference System Design Parameters

CONCLUSIONS

A new instrument concept based on the application of synthetic aperture / interferometric processing techniques to pulse limited altimetry has been presented in this paper. Near nadir Interferometry represents a new feature in the system design and appears to be suitable to accomplish bidimensional height within the swath once the resolution enhancing by synthetic aperture processing in the along track direction is preliminarly applied: 1 m height accuracy over 250 m (along track) x 100 m (across track) pixels without need of focused synthetic aperture processing and phase unwrapping. The method is fully compatible with conventional altimetric processing and leads to the design of a multipurpose instrument: various types of altimetric products can consequently be created (conventional ocean products, along track resolution enhanced products, fully enhanced resolution products) to satisfy science needs.

REFERENCES

[1] C. Zelli, F. Buscaglione, F. Provvedi, R. Croci: "RA-2 Radar Altimeter: Instrument EM Model Performance Results" *IGARSS 1997 Proceedings.*

[2] "The Nine Candidates Earth Explorer Missions" ESTEC 1996 ref. SP-1196.

[3] R. K. Raney, "A down-looking satellite SAR with on-board real time-rate processing: the delay/Doppler radar altimeter" *EUSAR'96 proceeding*, Königswinter, Germany 1996.

[4] Elachi, K. E. Im, F. Li and E. Rodriguez, "Global digital topography mapping with synthetic aperture scanning radar altimeter" *Int. J. Remote Sensing*, 1990, Vol. II, no. 4, pp. 585-601.

[5] C. Zelli, F. Impagnatiello, G. Alberti: "Developments in Satellite Radar Altimetry" EUROPTO 96 Taormina (ITALY) SPIE vol. 2958, pp.423-434.

[6] Rodriguez, E., Martin, J. M., "Theory and design of interferometric synthetic aperture radars" *IEE Proceedings*, Vol. 139, No. 2, April 1992, pp. 147-159.

RA-2 Radar Altimeter:Instrument EM Model Performance Results

C. Zelli, F. Provvedi, F. Buscaglione, R. Croci
Alenia Aerospazio - Space Division
Remote Sensing Engineering
Via Saccomuro 24, 00131 Rome ITALY
tel. +39-6-41512284, fax +39-6-41512102
Email : c.zelli@roma.alespazio.it

Abstract -- The European Space Agency (ESA) has awarded a contract to Daimler-Benz Aerospace, Dornier to fly on ENVISAT-1 mission the Radar Altimeter RA-2 developed by Alenia Aerospazio.
Aim of this paper is to provide an overview of the instrument performance derived from evaluation of the test results gathered during the instrument integration and characterization campaign carried out for the Engineering Model (EM).

INTRODUCTION

The main objective of the RA-2 instrument is to collect, on global scale, calibrated samples of the earliest part of the radar echoes from ocean, ice and land, as well as from their boundaries, without interruption. Ocean parameters estimation will then be performed via a dedicated on-ground processing algorithm. Radar altimeter measurements over oceans can be used to calculate mean sea level, ocean circulation (mesoscale and basin scale), wave height, wind speed and for bathymetry. Measurements over ice contribute to determination of ice extent, dynamic and mass balance. Over land, the radar altimeter can provide consistent elevation maps, level of lakes and rivers and support water-shed modelling.

RA-2 RADAR ALTIMETER

RA-2 is a nadir looking radar altimeter [1] operating at Ku (13.575 Ghz) and S (3.2 Ghz) band. The double frequency operation allows to automatically correct for ionospheric bias errors in the radar-surface distance measurement. The key system parameters of RA-2 are reported in table 1 with a functional block diagram available in figure 1.

The instrument is composed by the following sub-systems [2] : Antenna, Ku-band Front End Electronics (KFEE), S-band Front End Electronics (SFEE), Ku-band Transmitter (Ku HPA), S-band Transmitter (S HPA), Microwave Receiver (MR), Frequency Generation and Conversion Unit (FGCU), Chirp Generator (CG), Signal Processor Subassembly (SPSA), Low Voltage Power Supply (LVPS) and the Instrument Control Unit (ICU) which is in charge of interfacing with the satellite computer.

Orbit Range (H)	764 - 825 Km
Operative Frequency	13.575 Ghz (Ku) 3.2 Ghz (S)
Pulse Length (τ)	20 μsec
Ku Tx pulse Bandwidth (B_c)	320 - 80 - 20 Mhz - CW
S Tx pulse Bandwidth (B_c)	160 Mhz
Tx Peak Power (P_p)	60 W (Ku) 60 W (S)
Pulse Repetition Interval	557 μsec (Ku) 2228 μsec (S)
Antenna Gain (G_a)	41.5 dBi (Ku) 29.2 dBi (S)
Antenna Beamwidth (θ_B)	1.33 deg (Ku) 5.25 deg (S)
RF Losses (L_{RF})	3.7 dB (Ku) 4.0 dB (S)
Receiver Noise Bandwidth (B_n)	6.4 Mhz
Receiver Noise Figure (F)	4 dB (Ku) 4 dB (S)
FFT Processor	128 points
A/D conversion (no. bits)	8

Table 1: RA2 System Design Parameters

All the subsystems with the exception of the antenna are redounded to improve instrument reliability leading to a total payload mass of 110 Kg and to total power consumption of 122 W.

The antenna is a dual frequency central feed of 1.2 m diameter shared by the two channels. Each Front End connects the related transmitter and receiver input with the Antenna and isolates the receiver electronics during the transmission phase.

In the MR each received radar echo is mixed with a delayed replica of the transmitted chirps (deramping operation) and down converted to an Intermediate Frequency (IF) where signals can be more easily amplified and then split into their in-phase and quadrature components (I & Q) and filtered to 6.4 Mhz. An Automatic Gain Control (AGC) adjusts the whole value of the receiver amplification to

0-7803-3836-7/97/$10.00 © 1997 IEEE

maintain the I and Q components at a constant and suitable level for the sampling. The SPSA converts to digital samples the I & Q components of the signal and calculates the signal spectrum by an FFT on 128 points. After square modulus extraction, the samples are averaged over 100 Ku pulses (25 S pulses for the S channel), corresponding to a time span of 55.7 ms, to reduce the echo's statistical fluctuations and instrument data rate. The average samples from the Ku channel are then processed by the Model Free Tracker (MFT) algorithm to set the sampling window time position, the receiver gain and the radar resolution in order to allow altimeter autonomous operation in detecting, acquiring, locking-on and tracking ice/land/ocean echoes irrespective of surface topography variations along the orbit.

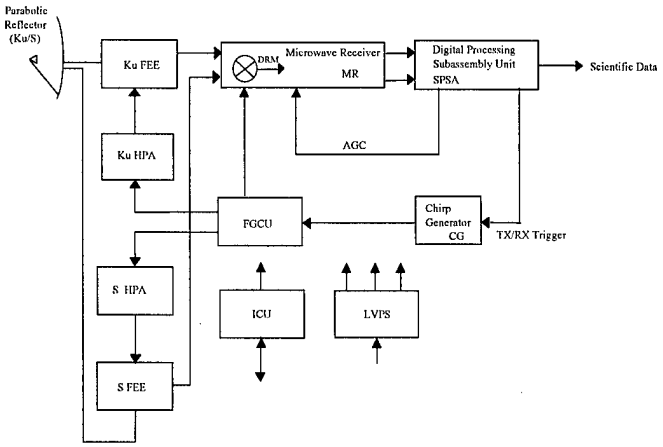

Figure 1: RA2 Functional Block Diagram

To this purpose the instrument can automatically operate in Ku band either with an unmodulated CW radar pulse to accomplish the acquisition phase or with any of three radar resolutions provided by 320 - 80 - 20 Mhz chirp signals during tracking. Radar echoes collected at S-band with a unique resolution corresponding to a pulse bandwidth of 160 MHz are actually not processed on-board but are used on-ground for the ionospheric bias correction of the radar-surface distance measured at Ku band once both Ku and S band data have been reprocessed. At this stage precise measurements of sea surface reflectivity σ_0 and roughness σ_s (or equivalently significant waveheight SWH) are also derived from the Ku data.

SYSTEM PERFORMANCE RESULTS

The instrument requirements demand for the verification of a series of quality parameters. In particular very stringent requirements have been established to guarantee the quality of the altimeter measurements over oceans. More generally, the instrument is required to be able to maintain the tracking and successfully perform acquisition over any type of surface such as those of mountains, deserts, wetlands, ice regions.

The early results obtained from the test campaign of the EM model are really promising.

Acquisition over ocean is always accomplished in less than 1 second: typical result is 0.33 seconds vs a requirement of 1 sec; transition from acquisition to tracking at highest resolution over ocean is achieved in approximately 1 second vs a requirement of 3 sec.

Figure 2 shows an acquisition test result for a sequence of steep height changes ranging from 10 to 20 Km spanning the whole orbit range. The upper plot shows the on board time delay measurement actually indicated as on board Rx distance once the pulse repetition frequency ambiguity rank is accounted for and conversion from time to metric units takes place. For convenience a mean reference height of 800 Km has been subtracted to the original data to aid plot comprehension. The lower plot represents the resolution switching sequence coded as follows: 3- CW acquisition pulse; 2 - 20 Mhz chirp pulse; 1 - 80 Mhz chirp pulse; 0 - 320 Mhz chirp pulse. The "Measurement Samples" unit used in the horizontal axis is a conventional unit representing the altimeter elementary time frame of 55.7 ms; it is worth to recall that the instrument is designed to provide measurements at 18 Hz rate. Lower rates can be derived on ground through an averaging process.

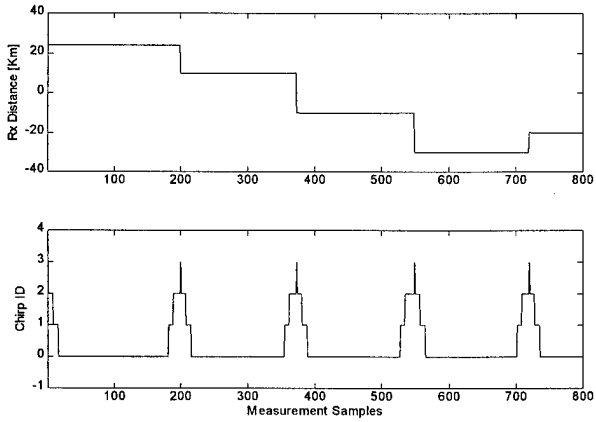

Figure 2: Acquisition Performance Test Result

Acquisition over land or ice has always been successfully accomplished and tracking performed using the most suitable resolution.

Figure 3 shows the reference surface height and sigma_0 profiles of a simulated sea ice scenario. The corresponding altimeter outputs in terms of Rx distance, on board AGC and resolution switching sequence are available in figure 4.

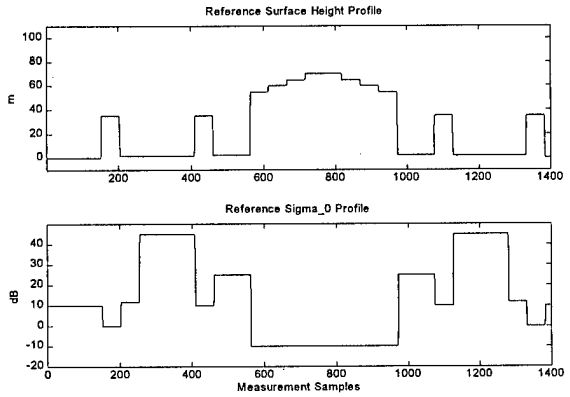

Figure 3: Simulated Land Scenario Profiles

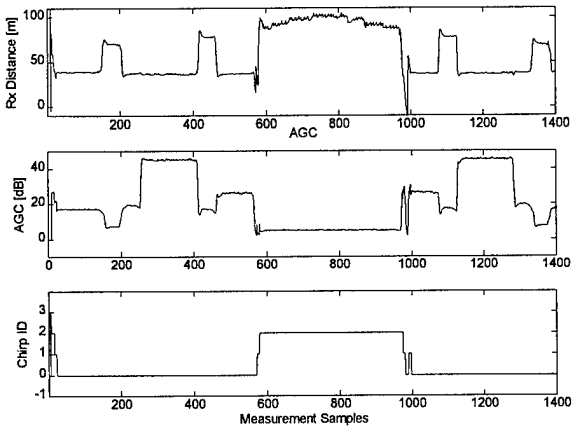

Figure 4: Altimeter Measurements over Land Scenario

The system point target response (PTR) has also been measured: a peak to side lobe ratio of 27.8 dB vs. a specification of 27 dB is met as shown in figure 5.

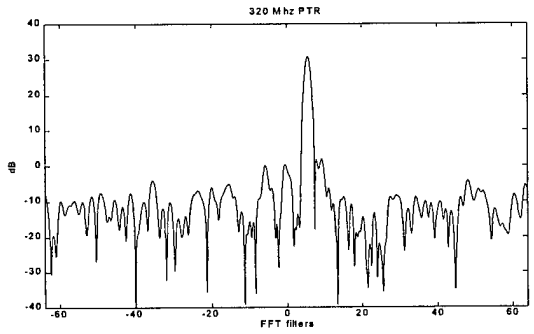

Figure 5: Instrument Point Target Response

Calibration corrections derived from the PTR measurements as well corrections extracted from the characterization campaign have been used in the re-processing of altimeter data over oceans (a dedicated Brown model [3] based re-processing algorithm has been developed by Alenia Aerospazio) reaching the following performance figures for an integration time of 1.114 seconds (equal to the time needed to collect the 2000 echoes) and 10 dB of Signal to Noise Ratio.

- time delay measurement accuracy on Ku band:
  - 1.7 cm for sigma_s=0.5 m (SWH= 2 m)
  - 2.4 cm for sigma_s=1 m (SWH= 4 m)
  - 2.8 cm for sigma_s=2 m (SWH= 8 m)
  - 3.9 cm for sigma_s=3 m (SWH= 12 m)
  - 4.3 cm for sigma_s=4 m (SWH= 16 m)

these figures are well within the system requirements of 4.5 cm for $\sigma_s \leq 2$ m and 5.5 cm for $\sigma_s > 2$ m .

- sigma_o accuracy: 0.8 dB slightly worse than the requirement of 0.5 dB but is mainly driven by the residual hardware calibration accuracy achieved in the EM testing.

- sigma_s accuracy:
  - 2.5 cm for sigma_s= 0.5 m (SWH= 2 m)
  - 2.5 % for sigma_s= 2 m (SWH= 8 m)

vs original system requirements of 5 % for $\sigma_s > 1.2$ m and 6 cm for $\sigma_s \leq 1.2$ m .

For the S band, only partial tests have been carried out on the EM. Nevertheless, a preliminary accuracy figure of roughly 10.5 cm has been measured over 2 m sigma_s scenario, fully in line with theoretical expectations being only 250 echoes available in this case over 1.114 second integration time.

CONCLUSIONS

The RA-2 instrument design has been aimed to achieving state of the art performances while minimizing development risk and cost. This objective has been met by exploiting as much as possible the experience coming from the previous ERS 1/2 Altimeter program and concentrating the efforts on new functions and improvements. Early results show that instrument EM model is performing well within the requirements. The Critical Design Review, to release the FM instrument model manufacturing, was successfully passed in November 1996 and final extensive performance tests will be carried on the flight model during summer 1997.

REFERENCES

[1] F. Provvedi, C. Zelli, A. Resti, S. Idler : "RA2 Radar Altimeter : Instrument Operation Concept and System Performance" 46th IAF October 2-6, 1995 Norway

[2] F. Buscaglione, R. Croci, F. Provvedi: "RA-2 Design and Technology" IGARSS 1995 Proceedings

[3] G.S. Brown: "The Average Impulse Response of a Rough Surface and its Applications" IEEE Trans. on Antennas and Propagation AP-25 Vol.1 January 1977.

Relief Restitution by Radargrammetry Using RADARSAT Images : Example in French West Indies

L.MARINELLI, O.FERGER, L.LAURORE, V.POUJADE

GEOIMAGE
Les Espaces de Sophia, 80 route des Lucioles, 06560 Valbonne, France
phone: 33 4 93 00 40 00, fax: 33 4 93 00 40 01, email: dev@geoimage.fr

Abstract -- Relief restitution by Radargrammetry is definitively operational using aircraft SAR images, nevertheless the use of satellite SAR images to obtain DEM by this method was not fully satisfactory up to now. This is due to the satellite features which were not dedicated to provide stereoscopic capabilities. With the launch of RADARSAT, Radargrammetry using satellite SAR images will be more efficient and operational. This satellite has real stereoscopic capabilities, as a wide range of incidence angles are available (range from 20° to 50°). It allows to create large scale DEM (nearly 100Km by 100Km), with a theoretical height accuracy better than 10 meters.
In order to process these stereoscopic data we added to the digital cartographic workshop developed by GEOIMAGE a Radargrammetric module. This module enables to automatically generate DEMs in a cartographic projection chosen by the user and create the associated ortho-images.

INTRODUCTION

Relief restitution by Radargrammetry is definitively operational using aircraft or shuttle SAR images [1] [2] [3], nevertheless the use of satellite SAR images to obtain DEM by this method was not fully satisfactory up to now. This is due to the satellite features which were not dedicated to provide stereoscopic capabilities.
For instance, , the constant low incidence angle (23°) of ERS1&2 generates important layover, and shows stereoscopic effects only in the overlapping area (40% of overlap surface for a latitude of 45°) of two images acquired on parallel orbits. The incidence angle difference is about 3° and then the theoretical height accuracy is not better than 30 meters [4].
With the launch of RADARSAT, Radargrammetry using satellite SAR images will be more efficient and operational. This satellite has real stereoscopic capabilities, as a wide range of incidence angles are available (range from 20° to 50°). It allows to create large scale DEM (nearly 100Km by 100Km), with a theoretical height accuracy better than 10 meters.
The GEOIMAGE Company is commercialising the GEOimage digital cartography software called. One module of this software package is dedicated to generate DEMs from optical stereoscopic pairs provided both by satellite images - SPOT, Landsat, .. - and airborne images. In order to take advantage of the RADARSAT satellite capabilities, we developed in GEOIMAGE a Radargrammetric module which allows to create automatically a DEM from two standard or fine beam mode RADARSAT images with different incidence angles. This software is divided in five major steps : calibration of the, radiometric improvements, matching of identical points of the two images in order to create a disparity map (we developed an original correlation algorithm based on hierarchical correspondence of the characteristical structures of both images). Finally, we convert the parallax difference in height and project the DEM in a cartographic reference.

THE GEOimage RADARGRAMMETRIC SOFTWARE

The GEOimage radargrammetric software is divided in five major steps. We describe below these successive stages.

Preparation of the data :
First, we select in the overlapping part of the images, the area in which we wish to generate the DEM. Then, in order to adjust the geometric model of each image, a ground control point is taken between the two images in the study working area previously selected area. This ground control point enables us to rectify a translation error which might be made in the computation of the geometric model and which can be due to the unreliability of the parameters included in the modelization.

Calibration :
This processing is carried out in order to limit the area of search for the homologous points. It consists in projecting both images in an epipolar reference. The search area is no longer the whole image but limited to a curve for each point in each image. Then, in order to still reduce the search time we rectify both images so as to make the epipolar curves straight and horizontal. At that point, the research is only monodimensional. Determining the epipolar curves requires the geometrical modelization of the viewing.

Radiometric improvements :
This phase aims at contrasting the images in order to improve the visual accuracy between the various structures contained

0-7803-3836-7/97/$10.00 © 1997 IEEE

in them. It includes among other processing like a global spreading of the dynamic followed by local enhancement of the contrasts and a radiometric equalisation of the images between each other.

The matching :
By means of this phase, we will be able to determine the matching between all the pixels in order to create a disparity map.
The algorithm which is developed is not based on a simple method of correlation of the grey levels which is too sensitive to the differences in radiometry and too heavy to operate ; but based on a principle of hierarchical correspondence of the characteristic structures of the image.
We proceed to a multi-scale matching. That is to say we extract the main structures of the image in a shaded resolution (by a sub-sampling of images) and match them. Afterwards we extract again the extraction the visible structures in a less shaded resolution but still taking into account the matching of the previous phase. The same process is reiterated the same process with less and less shaded images until we match the images in full scale and therefore the smallest objects which make them up.
The use of our correlator -which is based on a correlation of the image structures- with SAR images appears to be particularly well adapted. All the more the principle of multi-scale correlation enables us during the various sub-samplings to reduce the speckle noise and therefore to increase the accuracy of the matching. At each step it is possible to carry out manual corrections.

Altitude :
By using the geometrical model we can determine from the parallax difference the altitude at each point of the image.

Projection :
This last phase enables us not only to project the DEM in the cartographic reference, but also to create an ortho-image from either of the two images of the pair.

STUDY SITE

The Guadeloupe island in the French West Indies was selected as a test site. This island is located at 16° of latitude in the Caribbean sea. The climate is wet tropical, so it is advantageous to use SAR images. This island shows marked contrasts in term of relief as the altitude varies between 0 to nearly 1500 metres. In fact, the highest point is the *La Souffrière* volcano (1467 m) in the south of the island. The area is characterised by deep valleys with difference in height of 100 metres, and by large flat area to the east of the island.
Available data are a RADARSAT stereoscopic pair. These Path Image were supplied by RADARSAT Int. as part of a ADRO project (#274). The two images were acquired on ascending mode. The first image acquired on August 6th 199+6 (Orbit 3950) in standard mode, shows an important incidence angle of 47° (S6 mode). The second acquired on August 28th 1996 (Orbit 4250) also in standard mode, shows a lower incidence angle of 23° (S1 mode). RADARSAT data © Canadian Space Agency / Agence Spatiale Canadienne 1996.
We have then followed all our radargrammetric sequence as previously described. The results show a very coherent DEM all over the island. The west part of the DEM (Fig. 1) covering an area of 25*45 kilometres is the most interesting part of the island as it exhibits high relief. In fact the east part is mainly flat. The DEM was created in UTM zone 20 cartographic projection with a pixel spacing of 20 meters. The two ortho images were also created. Fig. 2 shows the ortho image of the west island side corresponding to the S6 image in the projection of the DEM. This ortho image was coloured according to its elevation and draped over the DEM. From this image we created a perspective view from the south of the Guadeloupe island (Fig.3).

CONCLUSION

In this article, we have presented the radargrammetry software developed by GEOIMAGE company. This software with an advanced Graphic User Interface allows to produce DEM's automatically from RADARSAT images in standard or fine mode. Using RADARSAT images allows to create large scale DEM (nearly 100km by 100km with standard images).
As an example we have shown the result obtained using a standard stereoscopic RADARSAT pair, composed by a S1 and a S6 image. A very coherent DEM was extracted and the two associated ortho images were also created.
RADARSAT images will give a new lease of life for the radargrammetry, all the more that interferometry for relief restitution with repeat pass seems to reach a limit due to atmospheric perturbations.

REFERENCES

[1] T.Toutin, "Airborne SAR stereo restitution in a mountainous area of Cost Rica : first results", in IEEE Transactions on Geoscience and Remote Sensing, vol. 33, no. 2, March 1995.
[2] F.W. Leberl, M. Millot, R.S. Wilson, M. Karspeck, B. Mercer, and S. Thornton, "Radargrammetric image processing with a softcopy stereo workstation", in Proc. 8th Thematic Conference Geologic Remote Sensing, Denver 1991.
[3] F.W. Leberl, "Radargrammetric image processing", Artech House, 1990.
[4] L.Marinelli and L.Laurore "Relief restitution by Radargrammetry", in Proceedings of the Second ERS Applications Workshop, London, UK, 6-8 December 1995 (ESA SP-383).

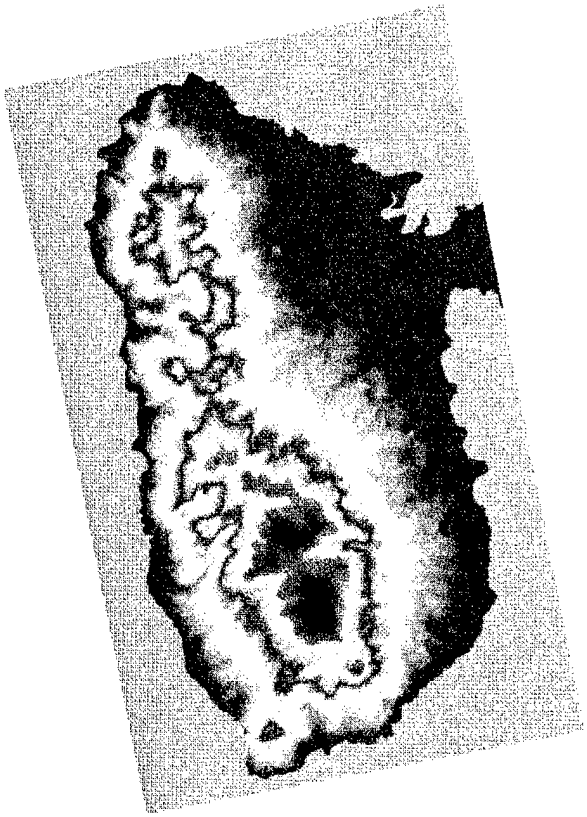

Fig. 1 : DEM in UTM zone 20

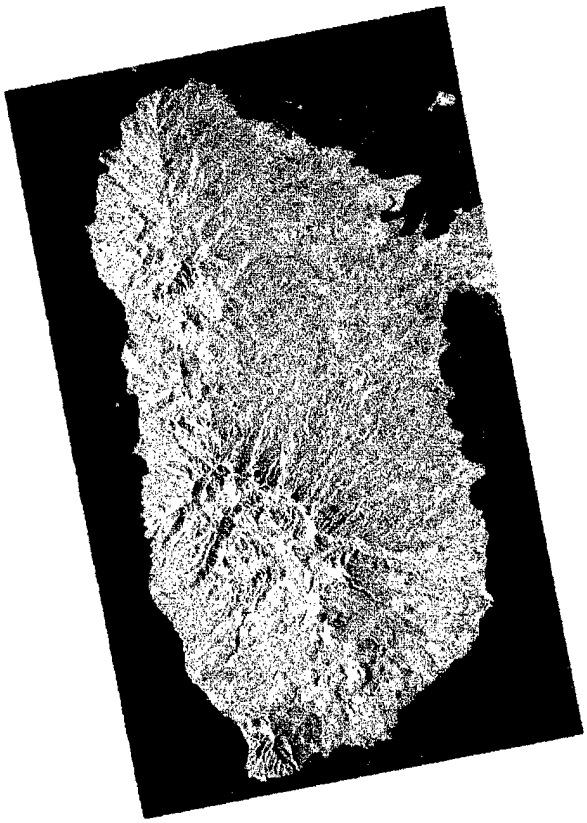

Fig. 2 : Ortho image S6 in UTM zone 20

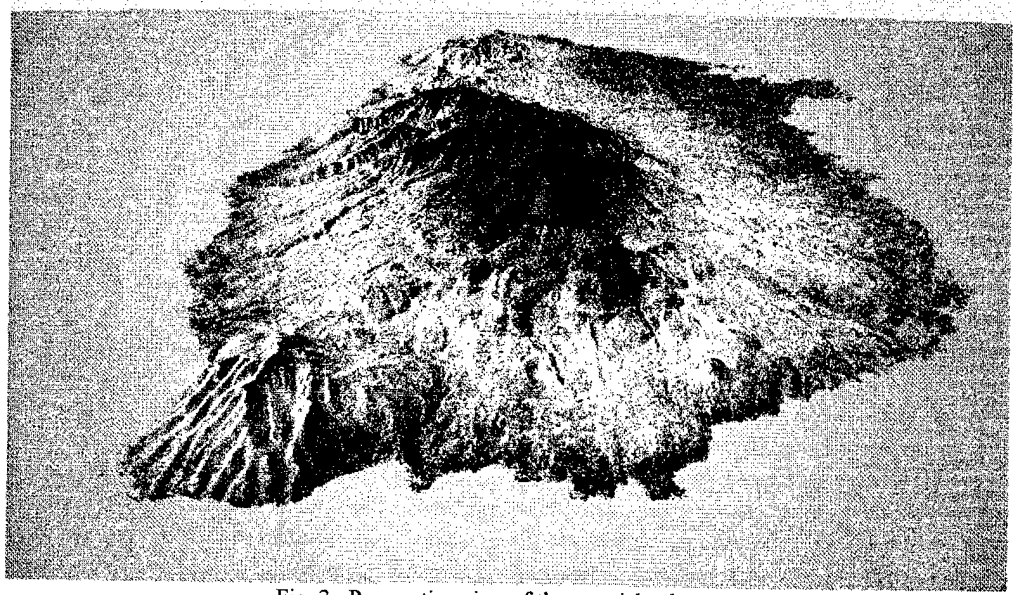

Fig. 3 : Perspective view of the west island part

SARSCAT - A Ground Based Scatterometer For Space-Borne SAR Applications

Bo Sun and Ji Wu
MIRIT, Center for Space Science and Applied Research
P.O.Box 8701, Beijing 100080, P.R. China
Tel.:+86 10 6255 9944-3417, Fax:+86 10 6257 6921, e-mail:wuji@sun20.cssar.ac.cn

Abstract - SAR imagine applications are usually carried out by tow ways: the physical/ mathematics models and the measured terrain material microwave signatures. In most of the cases, people like to use the mathematics models since the microwave signature database are not matching the practical case very well. In this paper, we will discuss the reason of the uncertainties provided by these database from the instrument point of view and propose a new ground-based scatterometer, SARSCAT, specially designed for SAR applications.

I. INTRODUCTION

Currently, there are several space-borne synthetic aperture radar operating such as ERS-1, ERS-2, JERS-1 and RADARSAT. They are now providing commercial radar images from the space. From these images, people can extract many unique information which visible and inferred frequency band sensors cannot or has difficulties to provide. However, applications of those radar images are still remain in a low level comparing with visible and inferred images. One of the main reason is that the ground measured terrain microwave signature or spectrum database are not complete. The incomplete is not referring the quantity but the quality of those data.

Historically, the purpose to measure the terrain microwave signature on the ground is to study the mechanism of microwave remote sensing. Therefore most of the measurements are made in the earlier years in 70's and 80's [1]-[3]. Since the purposes are different, with SAR applications, these signature data may not provide required accuracy and measurement conditions. In this paper, we will discuss the differences between the conventional terrain microwave signature measurements and the SAR application measurements and propose a new ground-based scatterometer system as shown in Fig.1, which will most closely represent the SAR measurement conditions.

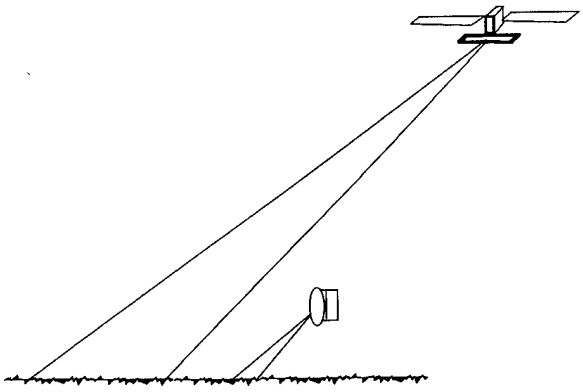

Fig. 1 Space and ground systems

II. GROUND-BASED BACKSCATTERING MEASUREMENTS AND BANDWIDTH CONSIDERATION

Radar measurement is based on the return signal from the object under illumination of the transmit antenna. For remote sensing application, the return signal is not from an single object, but an extended ground area. Therefore it is a continuous extended target. The backscattering signal at the receiving antenna is a coherent summation of the returns from many independent scattering points. It is obviously that a single measurement represent only a particular geometrical relation between the sensor and the ground scattering points. Once the sensor position changed, or the ground objects moved such as the ocean surface, the measurement result will be changed also. For this reason, the only way to get a meaningful measurement result is to

0-7803-3836-7/97/$10.00 © 1997 IEEE

move either the sensor position or the ground objects to make many independent measurements and calculate the average of them. This is actually what a scatterometer or SAR doing.

The number of independent samples used to calculate the average is important. The more samples are used, the more stable result will be got. In practice, the number of independent samples is always limited. Searching for more stable result with limited samples, many instruments use wide frequency band to compensate the measurement result fluctuations. Typically, a FM-CW system scatterometer may use 1GHz or more bandwidth at C band. However, the terrain react differently at different frequencies. To use wide frequency band will unable us to measure the terrain response at particular interested frequencies. In other words, the measurement results from to instruments with different frequency band are not usually comparable.

Most of existing terrain signature database were measured by FW-CW ground scatterometer system which has wide bandwidth. However the bandwidth of space-borne SAR is less than 100MHz. The measurement results must not the same even if the two instruments measuring the same terrain simultaneously. This is one of the reasons that we propose a new instruments for SAR applications.

III. GROUND PENETRATION AND POWER CONSIDERATIONS

Microwave remote sensing has the advantage to get information penetrate the terrain surface. The depth of the penetration in which the sensor can get the information depends not only on the frequency band, but also the incident power and the receiver sensitivities. Therefore, in order to get the same information as the space-borne SAR, the ground scatterometer for SAR applications must have the same penetration as the SAR does. To verify this, let us consider radar equation first

$$P_{RS} = \frac{P_{TS} G_S^2 \lambda^2 \sigma}{(4\pi)^3 R_S^4} \qquad (1)$$

where P_{RS} and P_{TS} is the space-borne SAR received and transmit power respectively, G_S is the SAR antenna gain and R_S is the distance between the satellite and the coverage center. σ is the ground backscattering coefficient.

For space-borne SAR, suppose P_{TS} is 5.3KW, the returned power at the receiver may vary from -104dBm to -56dBm representing the highest and the lowest σ from the terrain. From (1) we have

$$\sigma = \frac{P_{RS}}{P_{TS}} \frac{(4\pi)^3 R_S^4}{G_S^2 \lambda^2} \qquad (2)$$

Let G_S= 30dB; R_S = 1100km; λ = 0.0566m

$$\sigma = 9.07 \times 10^{23} \frac{P_{RS}}{P_{TS}} \qquad (3)$$

substitute the value for P_{RS} and P_{TS}, got

$$\sigma_h \approx 4.3 \times 10^{11} \qquad \sigma_l \approx 6.8 \times 10^{6}$$

For a 30dB gain antenna (3°×12°), 45° incident angle, the coverage area may be around 1.8×10^{10} m^2, therefor we have

$$\sigma_h^o \approx 23.9 \qquad \sigma_l^o \approx 3.8 \times 10^{-4}$$

For ground-based scatterometer, σ_h° and σ_l° should remain the same. Suppose a ground system has a 22dB (15°×15°), the coverage of the antenna at a 10 meter platform and incident angle 45° is about 15.3m^2. From (1) we have

$$P_T = \frac{(4\pi)^3 R^4 P_R}{G^2 \lambda^2 \sigma}$$
$$P_T \approx 1.7 \times 10^8 P_R \qquad (4)$$

If the receiver sensitivity is -85dBm, for σ_l° we have P_T = 0.54mW, or -2.6dBm. For the same transmit power and σ_h°, P_R = -37dBm, 48dB higher than the case with σ_l°.

This shows that, it is possible to represent the same penetration as the SAR did by a ground based system. On the other hand, if the output

power and the sensitivity of the ground system is too high, it may have more penetration than the SAR does. Consequently it will measure a different terrain spectrum and lead erroneous for SAR applications.

IV. CALIBRATION CONSIDERATIONS

Beside the above considerations on power and bandwidth, a ground-based scatterometer for space-borne SAR applications must has the same polarization as the SAR and it should use the pulse radar system and a single antenna for both transmit and receive.

With such a kind of scatterometer, one should has the possibility to obtain the same backscattering coefficient as the SAR if the scatterometer is calibrated carefully. However, as we have discussed before, if the environment conditions are different between the two measurements, one may still have problem to compare the results. Therefore the best way to calibrate the ground and space platform sensors is to make a simultaneous measurements. By this way, no matter which instrument has calibration inaccuracies, the ground scatterometer measurements will be fully calibrated according to the SAR and its sequential measurements after the simultaneous calibration will be very useful for any application measurements.

The so called simultaneous measurement is actually a quasi-simultaneous measurement. Because the two instruments using the same frequency, a purely simulations measurement will give the ground instruments a lot of interference from the SAR transmit signal. Therefore the best way to do it is to carry out the ground measurement a few minutes before or after the SAR overpass.

V. SYSTEM DESIGN FOR SARSCAT

As it is addressed in Section II, the backscattering measurement is based on the statistics of many independent samples. Furthermore, an single measurement must cover many single scattering points in the illuminated area in order to represent the terrain material. It is proposed that the ground based scatterometer system use a modest resolution antenna. Therefore a 22dB gain reflect antenna is proposed.

A diagram of SARSCAT is shown in Fig. 2. As it is discussed in Section II, SARSCAT must has the same bandwidth as the SAR. This is adjusted be the tow switches in the transmit channel and controled by the pulse generator. The transmit power is controld by CPU through the power amplifier. In the receiving channel, the return wave is amplified and detected directly from RF at 5.3GHz.

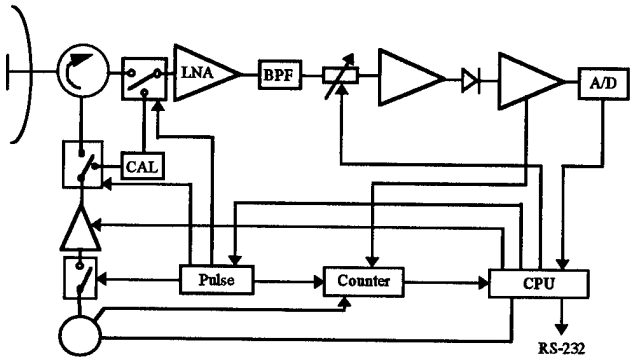

Fig. 2 Proposed SARSCAT design

V. CONCLUSIONS

Existing terrain microwave signature database are not suitable for SAR applications because of bandwidth, power and other considerations. A new ground-based system is then proposed to carry out the terrain microwave signature for space-borne SAR applications. It is shown that the ground-based system could repeat the SAR measurement from every technical aspects including power, bandwidth, calibration, etc. A design case for such a system is proposed.

REFERENCES

[1] F.T. Ulaby, "Radar Measurements of Soil Moisture content, " IEEE Trans. of AP, Vol. AP-22, 1974

[2] M.C. Dobson and F.T. Ulaby, "Microwave Backscatter Dependence on Surface Roughness, Soil Moisture, and Soil Texture: Part III-Soil Tension," IEEE Trans. on GE, Vol. GE-19, 1981

[3] F.T. Ulaby and M.C. Dobson, Handbook of Radar Scattering Statistics for Terrain, Artech House, 1989

IGARSS'97

1997 International Geoscience and Remote Sensing Symposium

03-08 August 1997

Singapore International Convention & Exhibition Centre

Technical Program

Interactive Area 3: Applications of Remote Sensing

Artificial Recharge Studies Through Remote Sensing in Central Part of Tamil Nadu, India

S.Anbazhagan
Humboldt Research fellow
Institute for Angewandte Geowissenschaften
der Justus Liebig University, Diezstr 15
35390 Giessen, Germany
Tel :0049 0641 99 36125, Fax 0049 0641 99 36109
e mail -Siddan. Anbazhagan@geo.uni-geissen.de

SM.Ramasamy
Director
Centre for Remote sensing, Bharathidasan University
Tiruchirappalli 620 023, India
Tel: 0091 0431 420667

and

J.Moses Edwin
Institute of Remote sensing
Madras 600 025, India

ABSRACT

A remote sensing based geological analysis was carried out in the hard rock terrains of Central Tamil Nadu, India. Rock-soil contact, pervious-impervious soil covered areas, structural trend lines and folded configurations and lineaments were interpreted from airborne and satellite data. Finally, the favourable domains were integrated with deep water level areas, the suitable sites for artificial recharge were identified.

INTRODUCTION

Artificially recharging the aquifer systems is essential where the water table conditions is rapidly falling down and considerable amount of water going as surface run-off. Such an area has identified in the central part of Tamil Nadu, India and artificial recharge studies were carried out . The area is bounded by northen latitudes 10°50′and 11°25′and eastern longitudes 78°10′ and 78°46′and approximately having an area of 1700 sq km. The region is comes under Musiri and Thuraiyur revenue taluks, Tiruchirappalli district, Tamil Nadu state. The nothern fringe of the area is covered by kolli hills and Pachamalai hills and southern limit is bounded by the Cauvery river. The major river Ayyar, which is flowing almost in the centre part of the region.

An analysis of water level fluctuation data in this region have shown that there is a steady decline of water table conditions. The annual average rainfall is 800 mm as against the state average of 980 mm. The ground water report has also indicates that the majority of the villages are already in over extraction of ground water condition and remarked as ′ dark areas ′ (3). At present condition, about 86% of recharged water is extracted. The authors have conducted an ellobrative work on selection of suitable sites for artificial recharge (9,10), site specific mechanisms (9) and surface water estimation (1). In the site selection processes they have analysed the gelogical, geomorphological and subsurface geological parameters through remotely sensed data, conventional ground based data and geophysical data. However, here, only the geological and structural parameters are discussed in detail.

The Study was sponsored by Tamil Nadu State Council for Science and Technology (TNSCS&T), India.

ARTIFICIAL RECHARGE STUDIES THROUGH REMOTE SENSING

Artificial recharge studies are being carried out through out the world by using various methods such as geological, geohydrological, gemorphological and geophysical methods (4,5,6,7). Artificial recharge studies have also been conducted by using the remote sensing techniques (8,9,10,11,12). In the present context, a remote sensing based integrated terrain analysis was carried out in the hard rock terrains of Tamil Nadu, India.. Using aerial photographs and satellite imagery, the geological and the geomorphological parameters were analysed for selection of suitable sites for artificial recharge. In the geological components, the thematic maps on lithology, rock-soil contact, pervious-impervious soil, structure and fold configurations and lineaments were generated.

Lithology and Rock-Soil contact

The lithological map was generated from the Geological Survey of India map (2). Geologically, the region is belonging to Archaean to Recent formations. Charnockites, Sillimanite-Kyanite-Corumdum mica schist,

0-7803-3836-7/97/$10.00 © 1997 IEEE

Magnetite Quartzites, Honblende biotite gneiss, Basic dykes, Granites and Alluvium are the some of the important rock types. The majority of the area is occupied by Gneiss and Charnockites. Hence, the lithological point of view, it is hard to recommend the particular area suitable for artificial recharge. In the next stage, in order to understand the regional view of soil covered area, the rock-soil contact map was prepared from the aerial photo interpretation on 1:25000 scale. The barren and vegetative covered rock exposures generally show light tone, medium to coarse texture, rounded and elongated shape, sharp contrast with soil, and high peaked hills associated with relief. Using these photo recognition elements, the rock forming plateau landforms, isolated hills, hummocky outcrops and tar complex were precisely interpreted from aerial photographs. The soil covered areas exhibit medium to darker tone (depending upon the moisture content), fine texture, moderate drainage pattern and sparse vegetative cover.

Pervious and Impervious soil

Since the majority of the study area is comprises of Hornblende biotite gneiss, the considerable area is under black cotton soil. Such black cotton soil, in some areas having high clay content and act as impervious layer. Those areas are not suitable for artificial recharge, since it prevents the surface infiltration. During the field work, such clay dominated domains were noticed and later fed into the computer as ground truth data in digital image proccessing. The clayey and impervious areas were separated out and designated as not suitable for artificial recharge. However, in the later stage, the impervious domains were integrated with the favourable subsurface geological conditions and further recommended for construction of recharge pitting.

Structures

The geological structures were interpreted from the black and white panchromatic aerial photographs and satellite imagery. The limbs of the folds, dipping beds, bedding planes, linear outcrops and the foliations exhibit linear and curvilinear structural trends in the aerial photographs and satellite imageries. Which are resembling cut onions owing to the erosion. The IRS 1A satellite imagery subjected to digital image processing and contrast stretched Pseudo Color Composite were generated by exposing the bands 2,3 and 4 under red, green and blue filters respectively. From such processed data, the major structural trend lines were picked out. The structural trend lines were also interpreted from the black and white aerial photographs on the basis of the linearities and the curvelinearities observed in the relief and the orientations of the outcrops, hills, drainage, soil tone variations, vegetation bandings etc. The third dimensional configuration of the structural trends were brought out on the basis of the shadows, break in slopes observed in the aerial photographs and thus each and every group of structural trends were mapped as anticlines and synclines. Later, such folded structures were finalysed with the help of strikes and dips measured in the field works. The area is having a series of anticlines and synclines wtih general trends of E-W and NE-SW orientations (Fig 1). Overall, three conspicuous synclinal structures were picked out and thus structures were recommended for artificial recharge.

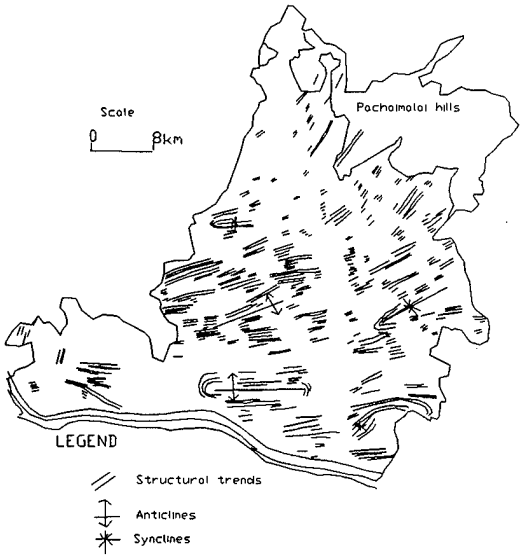

Fig 1 STRUCTURAL TRENDS

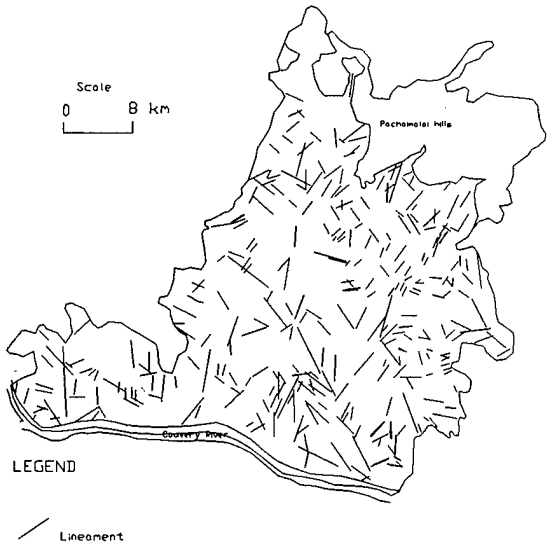

Fig 2 LINEAMENT

Lineaments

In the hard rock terrains, the lineaments are act as better conduits for ground water movement. Hence, detailed analyses were carried out to interpret and study the lineaments in the site selection processes. Initially, the major linear features were interpreted from IRS-1A LISS II FCC satellite imagery by obseving the linearity in the lithology, linear relict features, straightness in the drainages, soil tone linearities, vegetation linearities etc. The digitally processed outputs like filtered images were also used for interpreting the mega lineaments. In the next stage, the aerial photographs on 1:25000 scale were

interpreted for mapping the minor lineaments .The lineaments deduced from the satellite imagery and aerial photographs were integrated together and final lineament map was prepared (Fig 2). Thus the lineaments so derieved from the satellite image and the aerial photographs fall in four major azimuthal frequencies in N-S, NE-SW, NW-SE and E-W directions and amongst which the NE-SW and E-W sets are showing near parallism to the fold axis and other two are perpendicular to the fold axis. The lineament density diagram was prepared from the lineament map and it varied from 250 m to 1000 m per 0.25 sq km area.

INTEGRATED ANALYSIS

For artificially recharging the aquifer system, the system must have good infiltration with enough aquifer dimension. To do the same, the water level data were collected from Ground water, Public Works Departments for the period of 19 years (from 1972-1989). And there from the mean water level contours were drawn for the study area. From the water level contours, the areas falling more than mean (ie deeper water level) were buffered out and designated as suitable areas for artificial recharge. Finally, the areas of deeper water level were integrated with pervious soil, syclinal structures and regions of higher lineament density (ie > 500 m per 0.25 sq km area), so that such areas having good permeability with adequate aquifer dimension for rechargeable water.

CONCLUSION

The remotely sensed data given valuable informations on rock-soil cotact, pervious-impervious domains, folded structures and highly fractured areas. And thus facilitates the selection of suitable sites for artificial recharge. Futher, by integrating the remotely sensed data with the ground based hydrogeological parameters and socio economic data bases can give better information for implementing the artificial recharge projects.

ACKNOWLEDGMENT

The authors thank Groundwater department for providing water level data. The first author thanks to the Council of Scientific and Industrial Research for providing him Senior Research Fellowship during his research period.

REFERENCES

(1) S.Anbazhagan , ` Remote sensing based intergrated terrain analysis for artificial recharge in Ayyarbasin, Central Tamil Nadu, India, Ph.D thesis, Bharathidasan University, Tiruchirappalli December 1994, unpublished.

(2) Anon, Geological map of Tamil Nadu and Pondicherry, Geological Survey of India 1972.

(3) Anon, Ground water report for Ayyar basin, Ground water, Tiruchirappalli, unpublished.

(4) A.N.Bhowmick `The prospect of geophysical surveys for artificial recharge studies in granitic terrain- A futuristic approach'. Proc.on workshop on Artificial recharge of G. water in granitic terrain, Bangalore, 1992, pp. 46-64.

(5) P.O.Bourgeosis, `Notes on developing ground water ' Water and Pollution control, Vol .110, No.10, Oct. 1972, pp.24-28.

(6) R.Cochran, `Artificial recharge and its potential for Oklahomas Ogallala aquifer'. Oklahoma water resources board, Oklahoma, May 1981.

(7) K.R. Karanth, `Scope for adopting artificial recharge in Bhabar formations. Symposium on ground water. GSI misc pub. Calcutta, 1963. pp.206-214.

(8) A.S.Padmavathy et al `Modelling through GIS for surface water harvesting. Proceedings on National Symposium on Remote sensing for sustainable development, Remote sensing Application Centre, Lucknow. 1992, pp 193-198.

(9) SM.Ramasamy and S.Anbazhagan, `Remote sensing for Artificial recharge of ground water', Bulletin of National Natural Resources and Management System, Bangalore, 1994, Vol.18, pp.35-37.

(10) SM.Ramasamy and S.Anbazhagan,`Integrated terrain analysis in site selection for Artificial recharge in Ayyar basin, Tamil Nadu, India', Water resources journal, Bangkok 1997, unpublished.

(11) S.K.Sharma, `Remote sensing techniques to locate areas suitable for artificial recharge of ground water in granitic terrain', Proceedings on Workshop on Artificial recharge of ground water in granitic terrain, Bangalore, 1992, pp.14 - 44.

(12) P.Subramaniam, Hydrogeology and its variations in the granites and associated rock formations in India Proceedings on Workshop on Artificial recharge of ground water in granitic terrain, Bangalore 1992 pp 1-13.

Global Survey of Jet Contrails Using AVHRR Data: Spatial Distributions and Optical Property Retrievals

Donna V. Kliche[1], Joyce Chou[1], John M. Weiss[2], Sundar A. Christopher[1], Ronald M. Welch[1], Todd Berendes[1] and Kwo-Sen Kuo[1]
[1]Institute of Atmospheric Sciences
Phone: 605-394-2291/FAX: 605-394-6061/email: donna@ias.sdsmt.edu
[2]Department of Mathematics and Computer Science
South Dakota School of Mines and Technology
501 E. St. Joseph Street
Rapid City, SD 57701-3995

1. INTRODUCTION

Global survey of jet contrails is of major importance in the study of the atmospheric effects of aviation. Jet contrails are considered to be a subset of thin cirrus clouds. Due to their semitransparent nature, thin cirrus clouds are thought to be enhancers of the greenhouse effect [1]: they are almost transparent to the incoming solar energy reaching the surface, and also they reduce the planetary emissions to space due to their cold temperatures. However, jet contrails are considered responsible not so much to increase cloudiness, but to enhance the formation of natural cloudiness [2].

In the present study, one month of daytime global Advanced Very High Resolution Radiometer (AVHRR) data are used to 1) automatically detect contrails, 2) estimate the global frequency of occurrence of contrails, and 3) estimate the optical depth and particle size of jet contrails.

2. DATA

One month (April, 1993) of daily AVHRR LAC (Local Area Coverage) satellite data on board the NOAA-11 satellite is used in this investigation. The AVHRR instrument has a spatial resolution of 1.1 km at nadir, and 5 spectral channels (0.58-0.68 μm, 0.72-1.10 μm, 3.55-3.93 μm, 10.3-11.3 μm, 11.5-12.5 μm). The AVHRR channels 4 and 5 are used to create a difference channel, in which contrails usually appear as thin, nearly-straight bright lines, while most of the background features are suppressed.

3. METHODOLOGY

Based on the methodology developed by Weiss et al. [3], channel 4-5 difference of AVHRR data is used to automatically detect jet contrails. The first step in contrail detection is searching for elevated, linear patterns called "ridges", after which the ridges created by contrails, as well as cirrus streaks or natural image features, are greatly enhanced [4]. Then, a linear Hough Transform is applied to the ridges to locate contrail candidate signatures. The resulting line segments are approximately coincident with contrails, but since most of the time contrails are more than one pixel wide, an additional processing for segmentation is performed. Segmentation consists of searching across the identified contrails for the ridge profile (which is considered to resemble a Gausian curve) in the channel 4-5 difference image [3]. The output consists of an image with identified contrails.

Once the contrails are identified, channel 1 and channel 3 of the AVHRR LAC data are used to retrieve the jet contrail's optical properties. Ice clouds are characterized as randomly oriented hexagonal ice crystals [5]. The Discrete Ordinate model [6] is used to simulate Channel 1 and Channel 3 reflectances, and a look-up table is created to retrieve the contrail's optical properties. For the month of April 1993 we have selected several cases to perform this procedure.

4. RESULTS

Figure 1 shows an example of the detected contrails for April 8, 1993, between 30 and 75 N, as thick, black lines. The automatic contrail detection algorithm was applied to all images that were retrieved that day, and, as can be seen, the number of contrails detected globally is quite significant. A detailed analysis of each image for this day shows that the detection algorithm is robust in discriminating most of the contrails in these images, especially the "young" ones, which are usually straight, thin, bright lines. Some contrails are missed because they are either diffused over a large area so that the ridge detector is ineffective, or the background is so bright that contrails appear faint. Several methods were tried to achieve an increase in contrail detection, but in many cases it was at the expense of increasing false detections (cirrus streaks, street clouds, specific ground linear features). False detections are labeled as "F" in Fig. 1.

Acknowledgments. This research was conducted under NASA grant NAG 5-2712.

0-7803-3836-7/97/$10.00 © 1997 IEEE

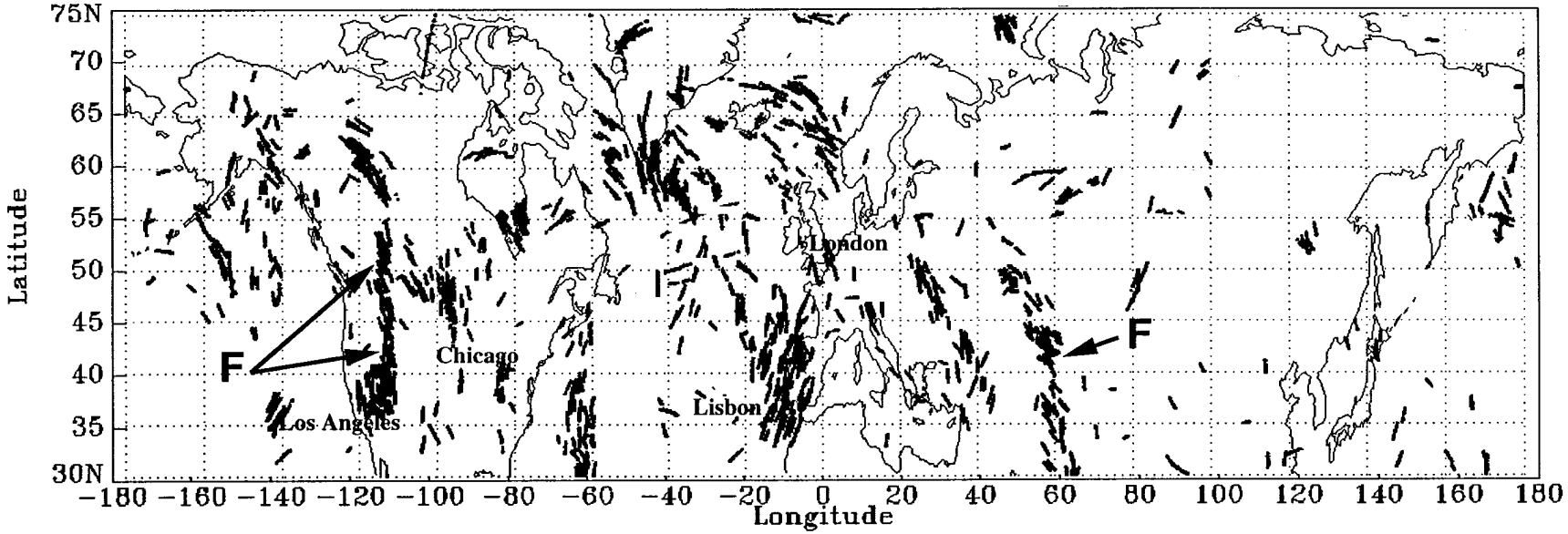

Figure 1: Automatic detection of contrails during April 8, 1993. The contrails are represented as black segments. False contrails are labeled with 'F'.

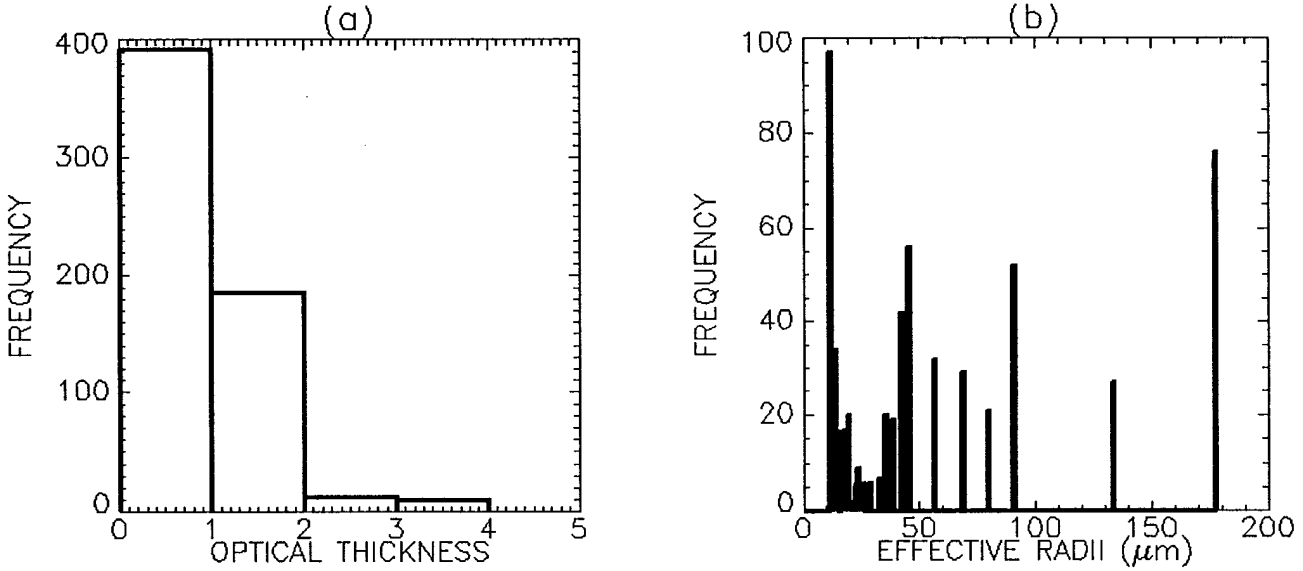

Figure 2: Jet contrails optical thickness (a) and corresponding effective radii (b) for the July 1, 1995 image.

This study represents a first attempt to retrieve contrail physical properties. At present, the contrail optical thickness and effective radii is determined for contrails over water only. Selected cases with contrails over land and water during April, 1993, will be presented at the conference. Figure 2 shows our preliminary results for optical thickness (Fig. 2a) and the effective radii (Fig. 2b) for an image acquired over the North Sea in July 1, 1995. For the identified contrails, the optical thickness is between 1 and 2, which is in agreement with the optical properties for thin cirrus clouds. The general trend for the effective radii shows a majority under 50 μm, and a decreasing number for a range between 50 and 100 μm. The values found over 100 μm are somehow suspicious, and more analysis is needed to identified the possible problems.

5. SUMMARY

With an increasing growth in commercial aviation, the study of the jet contrails becomes an important task in understanding their effects on regional climate. This study, in summary, addresses scientific issues such as detection of contrails in an automated fashion, estimation of the frequency of occurrence of contrails on a global basis, and an estimation of the jet contrail optical properties.

REFERENCES

[1] Stephens, G., and P. Webster, "Clouds and Climate: Sensitivity of simple systems," *J. Atmos. Sci.*, **38**, 235-247, 1981.

[2] Detwiler, A. G., "Comments on 'Jet contrails and cirrus clouds: A feasibility study employing high-resolution satellite imagery,'" *Bull Amer. Meteor. Soc.*, **67**, 1150-1151, 1986.

[3] Weiss, J., S.A. Christopher and R.M. Welch, "Automatic contrail detection and segmentation," paper conditionally accepted, *IEEE Transactions on Geoscience and Remote Sensing*, 1997.

[4] Engelstad, M., S.K. Sengupta, T. Lee and R. M. Welch, "Automated detection of jet contrails using the AVHRR split window," *Int. J. Remote Sensing*, **13**(8), 1391-1412, 1992.

[5] Liou, K.N., J.L. Lee, S.C. Ou, Q. Fu, and Y. Takano, "Ice Cloud Microphysics, Radiative Transfer and Large-Scale Cloud Processes," *Meteorol. Atmos. Phys.*, **46**, 41-50, 1991.

[6] Stamnes, and H. Dale, "Newlook at the discrete Ordinate method for radiative transfer calculations for anisotropically scattering atmospheres. Part 2: Intensity computations," *J. Atmos. Sci.*, **38**,2696-2706, 1981.

Recent Observing System Experiments on the Impact of ERS Scatterometer Wind Data on Numerical Weather Simulations of Cold Surge

Tian-Kuay Lim***, Ruixue Zhang**, I-I Lin*, Dayalan Kasilingam*, and Victor H.S. Khoo*

***Meteorological Service Singapore, P.O. Box 8, Changi Airport Post Office,
Singapore Changi Airport, Singapore 918141
Tel: (65)-5422863, Fax: (65)-5425026, E-mail: mssltk@pacific.net.sg

**DSO National Laboratories, 20 Science Park Drive, Singapore 118230
Tel: (65)-7727268, Fax(65)-7759011, E-mail:zruixue@dso.org.sg

*Centre for Remote Imaging, Sensing and Processing (CRISP), National University of Singapore, Singapore 119620
Tel: (65)-7723220, Fax(65)-7757717

Abstract -- This study examines the impact of scatterometer wind data from the ERS satellite on the performance of a Numerical Weather Prediction (NWP) model in simulating the planetary-scale characteristics of cold surge during the northern winter. A comprehensive set of Observing System Experiments (OSEs) were carried out using the Meteorological Service Singapore's (MSS) data assimilation and forecasting system. The period chosen for the OSEs was during a cold surge which occurred from 13 Nov 1995 to 23 Nov 1995. Two experiments, with ten day forecasts from 00 UTC, were carried out every day for this period: (1) control experiment, which uses both the conventional weather observations and the ERS scatterometer wind data, and (2) without ERS data experiment, which uses only the conventional weather observations. The comparison of the results from these experiments allows us to assess the impact of ERS scatterometer wind data on the data assimilation and forecasting system of MSS in simulating the characteristics of cold surge. Overall, the impacts on the performance of the NWP model in simulating the planetary-scale characteristics of cold surges are neutral, albeit an observed small positive impact on the lower and upper level forecast wind fields during the developing stage of the surge. We expect the impact of the scatterometer wind data in numerical forecasts to be more significant from the improvement in the wind scatterometer model, the assimilation method and the resolution of the NWP model.

INTRODUCTION

Over the last century, the vast improvements in the science of meteorology and the practice of weather forecasting are linked to very significant increases in our ability to observe the global atmosphere and in our computing capability. Currently, atmospheric observations include: direct (in situ) measurements of the primary atmospheric variables including wind velocity, pressure, temperature, and humidity; visual observations of clouds, visibility, and type of precipitation; and remotely sensed observations of temperature, moisture, clouds, and wind. This combination of observations provides an extensive data base for both initializing and verifying NWP models and for research to further our understanding of the atmosphere and its role in the Earth-Atmosphere-Ocean System. However, significant data deficiencies still remain and new observing systems are continually proposed to improve the accuracy of analysis and forecast products.

Significant data deficiencies continued to plague the East Asian region, particularly over the seas and oceans. Remote sensing data over data sparse areas has been recognised to be of significant potential [5]. In this study, the ERS scatterometer surface wind data is assimilated into the operational NWP model at MSS to study its impact on the performance of the NWP model in simulating one of the important regional phenomena: cold surges. During the northern winter, cold surges occur frequently over the South China Sea which bring cold air off the Asiatic Continent rapidly towards the tropics. The surface winds over the South China Sea also strengthen. With these dynamical characteristics, the selection of cold surge situations becomes rather interesting for our assessment study of the impact of ERS surface wind on the performance of NWP model.

OSERVING SYSTEM EXPERIMENTS

Impact studies of observations in NWP models are a means of assessing the value of observing systems in terms of the benefit they deliver to model forecasts, and guiding efforts to ensure cost-effective deployment of observations. There has been a great deal of work worldwide to assess the impact upon NWP of many different observation types [1], [3]. One technique for assessing the impact of observations is through Observing System Experiment (OSE):- after selecting a period for study, two model assimilation runs are performed, one "with" and one "without" use of the data type we wish to evaluate. Each assimilation run is normally followed by a forecast. The benefit of the data is then assessed by evaluating the greater accuracy (if any) of the "with" forecast compared to that of the

0-7803-3836-7/97/$10.00 © 1997 IEEE

"without" forecast. The evaluation either takes the form of statistical assessments of impact on a number of forecasts over a specified period and geographical region or by studying selected cases.

For our study, a comprehensive set of OSEs has been run using the MSS's data assimilation and forecasting system: a Global Analysis Model which uses multivariate optimal interpolation scheme, a Global Spectral Model, T63L16, nested with two limited area models with spatial resolution of 127km and 63.5km, as well as a wave model. These models were adapted from the Japan Meteorological Agency's models, the details are given in references [6] and [7]. For this study, we examine the impact of the ERS scatteromenter wind data on the performance of the Global Spectral Model in simulating the planetary-scale characteristics of cold surge.

The period chosen was during a cold surge that occurred from 13 Nov 1995 to 23 Nov 1995. Ten day forecasts were run from 00 UTC every day for this period. Quality assessment and ambiguity removal were applied to the ERS data, with a time window of ±6 hours from 00 UTC, before it is assimilated into the NWP model. The assimilation of the ERS data is treated in the same manner as buoy data. Two experiments were run daily: (1) control experiment with both the conventional weather observations and ERS data, and (2) without ERS scatterometer wind data only. Comparison of the performance of the NWP forecasts are then carried out for these experiments to assess the impact of ERS scatterometer wind data.

ANALYSIS

We shall examine the performance of the NWP model runs based on the planetary-scale characteristics of cold surge during its various development phases, namely: the initiation and the developing phases of the surge.

INITIATION PHASE

Intense baroclinic processes in the midlatitudes, possibly, triggered by deep upper-level troughs moving through the East Asia jetstream, initiate outbreaks of cold surges from the continent [8]. As these midlatitude processes are of planetary-scale, to examine the performance of the NWP runs we shall examine the performance of the forecasts of the 500 hPa geopotential field over the N. Hemisphere.

Fig. 1 shows the geopotential correlations at 500 hPa for the Northern Hemisphere in the extratropics. The scores are averaged over the 10 cases. Withdrawing the ERS data did not result in the deterioration of the forecasting performance in the Northern Hemisphere. As the assimilation of ERS data only affects the initial surface wind fields over the maritime area of the NWP model, the impact on the 500 hPa geopotential field over N. Hemisphere, which is mainly over land area, is expected to be negligible in the first few days of the forecast period. Data assimilation schemes, therefore, influence the extent of the observations' impact on model performance. In the medium range forecast period, however, there is an observed slight deterioration of the forecasting performance. However, this is insignificant as the slight deterioration occurred in the regime of low forecast skill.

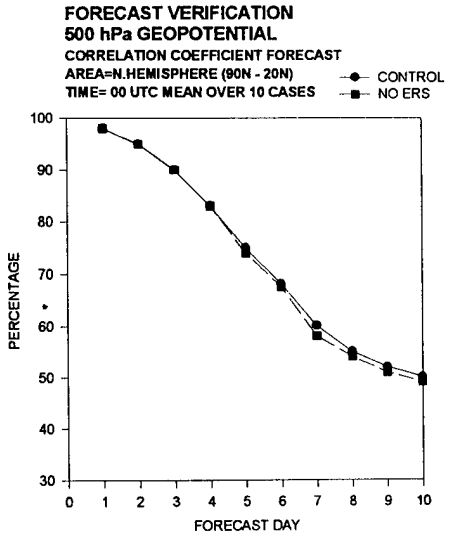

Fig 1: Mean 500 hPa geopotential forecast correlations in the Northern Hemisphere extratropics (20N to 90N).

DEVELOPING PHASE

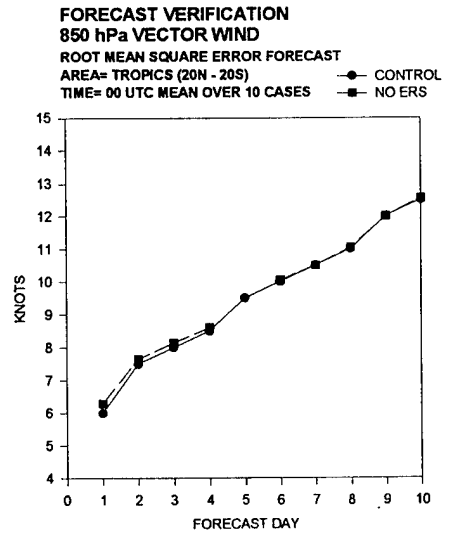

Fig 2: Mean 850 hPa wind forecast RMS errors in the tropical belt 20° N to 20° S.

A series of studies [3] shows that as soon as a surge is detected by a strengthening of surface northerly winds

over the South China Sea, the East Asia jetstream strengthens and the West Asia jetstreams weakens the Walker circulations over the Western Pacific and Indian Oceans also strengthen together with the upper-level divergence over the equatorial convection area.

The upper-level return flow of the East Asia local Hadley circulation also strengthens after about two days. To analyse the NWP model performance in simulating these characteristics of the cold surge, we shall examine the performance of the wind forecast at 850 hPa and 200 hPa levels over the equatorial region stretching from 20° N to 20° S.

Verifications were carried out in terms of Root-Mean-Square (RMS) errors of wind vectors at 850 hPa and 200 hPa, as shown in Fig. 2 and 3, respectively. In the beginning of the forecast period, some discrepancies are observed because of the fact that the operational analyses, which used all data, was used for verification. Nevertheless, in the medium range forecasts, the withdrawing of ERS data does not give rise to any deterioration of the forecasting performance over the tropics.

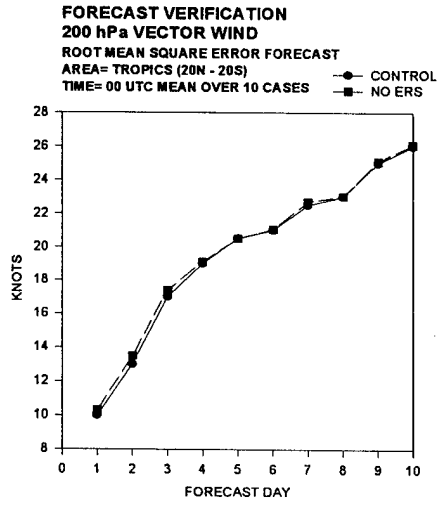

Fig 3: Mean 200 hPa wind forecast RMS errors in the tropical belt 20° N to 20° S.

CONCLUSION

Overall, from our study, the impacts of the scatterometer wind data on model performance in simulating the planetary-scale characteristics of cold surges are neutral for both the initiation and developing phases of cold surge, albeit an observed small positive impact on the forecast wind fields at the lower and upper levels of the atmosphere for the short range forecast during the developing phase of the surge. As the observed impact is small, it would require many cases to provide adequate evidence for justifying the impact. We should also remember that the experiments measure the combined effectiveness of observations and the data assimilation system. Hence their results must be interpreted with great care when seeking to draw conclusions about the impacts of each classes of observations. Our findings also indicated that the impact of the scatterometer data on numerical forecasts can be enhanced from the improvement in the wind scatterometer model, the assimilation methods and the resolution of the NWP models.

ACKNOWLEDGMENTS

The author would like to thank the Director, Meteorological Service Singapore, for his kind support and Ms Hu Yi-Hong for her assistance in the extraction of various data for this study.

REFERENCES

[1] Atlas, R., R.N. Hoffman, S.Bloom and P.M. Woiceshyn, "The Impact of Scatterometer Data on NWP", 11th Conf. On NWP, Norfolk, Virginia, USA, pp 99-101, Aug 19-23 1996.

[2] Balder, M.J. and R.J. Graham 1996, "Impact of Observations in NWP models: Techniques and Results of Recent Experiments", U.K. Met. Office Forecasting Research Division Scientific Paper No. 42.

[3] Chang, C.-P., and K.M. Lau, "Planetary-scale Motions of Winter Monsoons During Cold Surge and Break Periods", Proc. Int'l Conf. On Early Results of FGGE and Large-Scale Aspects of Its Monsoon Experiments, Tallahassee, U.S. National GARP Committee, pp 4-12, 1981

[4] Chang,S.W. and T.R. Holt, "Impact of Assimilating SSM/I Rainfall Rates on Numerical Prediction of Winter Cyclones", Mon. Wea. Rev., vol 122, pp 151-164, 1994.

[5] Katsaros, K.B., et al, "ERS-1 Studies at the department of Oceanography from Space, Ifermer/Brest", Proceedings of First ERS-1 Symposium, Space at the Service of Our Environment, Cannes, France, 4-6 November 1992. ESA SP-359, pp 61-66, March 1993.

[6] Outline of Operational Numerical Weather Prediction at Japan Meteorological Agency, Numerical Prediction Division, March 1993.

[7] Sugi, M., et al, "Description and Performance of the New JMA Operational Global Spectral Model (JMA-GSM88)", No. 27, June 1989.

[8] Webster, P.J., 1981, "Cold Surges of the Winter Monsoon; Dynamic Structures", Extended abstracts of International Conference of the Scientific Results of the Monsoon Experiment, Denpasar, Bali, Indonesia. 26-39 October 1981.

Coastline Detection with Polynomial Transforms and Markovian Segmentations*

Miguel Moctezuma[1], Boris Escalante[1], Ricardo Mendez[1], Juan R. Lopez[2] and Francisco Garcia[1]

Graduate Division, Faculty of Engineering[1]
National University of Mexico, DEPFI-UNAM
Apdo. Postal 70-256, 04510, Mexico, D.F., Mexico
Fax: (52 5) 616.10.73
Secretaria de la Defensa Nacional de Mexico[2]
Direccion General de Transmisiones
Administracion de Correos 48, Los Leones, Tacuba, Mexico, D.F., 53390

Abstract – In this paper, we present an original method for detecting coastlines on synthetic aperture radar (SAR) images. With this method, the processing of image data is performed in three steps: restoration, segmentation and coastline segment extraction. The problem of image restoration is solved via the polynomial transform. Based on the Markov random field theory, a model for image segmentation is applied. Optimization is achieved by a classical stochastic relaxation technique. The polynomial transform is an image description model which incorporates important properties of visual perception, such as the Gaussian-derivative model of early vision. Based on this, we present a technique for directional-sensitive image restoration. The restored image is obtained by means of an inverse polynomial transform which consists of interpolating the transformed coefficients with pattern functions that are products of a polynomial and a window function. We show in this paper how noise reduction task can be improved by detecting the position and orientation of relevant contours in images degraded by speckle. This method is applied in a coarse-to-fine resolution approach, in which, contour location is not degraded even at the stage of high resolution processing. The presented method performs in a semiautomatic fashion to effectively detect coastlines.

INTRODUCTION

The use of Synthetic Aperture Radar (SAR) images instead of visible and multispectral images is becoming more and more popular, because of their capacity of imaging even in the case of cloud-covered remote areas. In addition to the all-weather capacity, there are several well-known advantages of SAR data over other imaging systems [1]. Unfortunately, the poor quality of SAR images makes it very difficult to perform direct information extraction tasks. Even more, the incorporation of external reference data (in-situ measurements) is frequently needed to guaranty a good positioning of the results. In our particular case, both the multiplicative nature of speckle and the modulation of the sea surface by wind make it very difficult to perform the simple task of sea-land separation. Lee and Jurkevich [2] proposed a sequence of low resolution processing followed by an edge tracing algorithm. Land contours are detected from smoothed images. Consequently, contours are only rough estimations of coastlines. Based on dynamic programming, Wu and Maitre [3] proposed a different approach. The main disadvantage of this algorithm is that it is computationally intensive, even at low resolution representations. On a probabilistic approach, Zhang, Gool and Oosterlinck [4] focused to sea-land separation by means of Markon Random Fields (MRF) theory. Remaining in MRF, Descombes et al [5] designed a refined approach, based on a double segmentation. However, because of speckle, problems arise at the high resolution level and coast boundaries are not well represented. Even with markovian segmentations, speckle may introduce oversegmentations at the original pixel size. Clearly, a preprocessing stage must be included in order to take advantage of the high spatial resolution of SAR images. Numerous filters have been proposed [6], [7]. However, in most cases and even in the most elegant approaches, speckle filtering algorithms have a tendency to smooth speckle as well as information. For numerous applications, low-level processing of SAR images remain a partially unsolved problem. In this context, we propose a restoration algorithm that produces smoothed images. Its main advantage is that it retains subtle details.

*This work was partially supported by Conacyt, Mexico

0-7803-3836-7/97/$10.00 © 1997 IEEE

THE POLYNOMIAL TRANSFORM

Through local components, the polynomial transform allows to obtain an approximation to image data. Different sizes are employed in its multiresolution modality. Windowing is the first stage of processing. It takes place at several positions over the input image, comprising a sampling lattice S. The idea is to represent local information of every window by a family of polynomials. The window function takes into account orthogonal polynomials. The transformation from image data to polynomial coefficients is known as a forward polynomial transform. Original image can be recovered using the coefficients of the expansion and the proper synthesis filters. This process is called an inverse polynomial transform. The polynomial coefficients $L_{m,n-m}(p,q)$ are calculated by the convolution of the original image $L(x,y)$ with the analysis filters $D_{m,n-m}(x,y) = G_{m,n-m}(-x,-y)\,V^2(-x,-y)$. Outputs are selected computing $L_{m,n-m}(p,q)$ at the positions (p,q) in the sampling lattice S.

For reconstructing the original image from the polynomial coefficients the inverse polynomial transform is calculated by interpolation, that is

$$\hat{L}(x,y) = \sum_{n=0}^{N} \sum_{m=0}^{n} \sum_{(p,q)\varepsilon S} L_{m,n-m}(p,q)\, P_{m,n-m}(x-p, y-q), \tag{1}$$

where $P_{m,n-m}(x,y) = G_{m,n-m}(x,y)\,V(x,y)/W(x,y)$ is the interpolation function and

$$W(x,y) = \sum_{(p,q)\varepsilon S} V(x-p, y-q), \tag{2}$$

is the weighting function. In order to define a polynomial transform, some parameters have to be chosen. First, the characteristic of the window function. The gaussian window is the best option up now because of its property to adjust to Human Visual System. The orthogonal polynomials associated with the gaussian window are the Hermite polynomials. In this case, the analysis filters are a function of the Hermite transform. Another important parameter to be fixed is the size of the window (related to the spatial scale of the polynomial function).

IMAGE RESTORATION BY AN EDGE DIRECTIONAL SENSITIVE ALGORITHM

The basic idea is to develop an algorithm for restoring pixels at full resolution where edges are located while smoothing the regions with no edge information. We proceed, based on the one-dimensional projection of the polynomials and the edge direction estimation. Martens [8] demonstrated that the two-dimensional polynomial transform can be approximated by a one-dimensional polynomial transform in the case of one-dimensional patterns. Moreover, the first-order polynomial coefficients are near to an optimal edge detector [9]. The one-dimensional polynomial coefficient K of order k at angle θ is given by

$$K_{k,\theta} = \sum_{n=0}^{k} \sum_{m=0}^{n} L_{m,n-m}\; h_{k,\theta}(m, n-m), \tag{3}$$

where θ is the directions of the one-dimensional transform and $h_{k,\theta}$ is a specific angle function. Several orientations are predetermined for estimating edge directions. At every position where an edge is detected, a one-dimensional transform is assigned along the set of orientations. The zero order coefficients are kept in locations where no edge is detected (an homogeneous region) and higher order coefficients are set to zero. Next, it is necessary to find the optimal orientation of edges. This is done by maximizing the directional contrast C_θ defined by

$$C_\theta = \log\left[1 + \sum_{k=1}^{N} K_{k,\theta}^2\right] \tag{4}$$

along different angles θ. For a given edge, only the one-dimensional coefficients with the highest contrast are considered for further analysis. Objects having elements oriented at different directions at considered as noise and they are discarded. The restoration algorithm was tested on a SAR-ERS1 image. Experiments were realized with a pyramidal representation based on a gaussian function. From the original image (1024x1024 pixels), two low resolution images were computed (512x512 pixels and 256x256 pixels). Fig. 1(a) shows a subimage (100x100 pixels) of the third level (256x256 pixels) of the gaussian pyramid; Fig. 1(b)-(d) shows restorated images. In (b) the order of the polynomial expansion, s, is fixed to 4 and the energy threshold, d, is 0; in (c) s=4 and d=50; in (d) s=4 and d=65. The selected image for next stage of processing is the image (d).

MARKOVIAN SEGMENTATIONS AND COASTLINE DETECTION

Pyramidal representations are well adapted to Markov random field processing. After restoration of the low resolution image, we obtain a rough segmentation by means of a Potts model. Classical over-segmentation is avoided by assigning a cost function to each class. Coast functions are defined by data-driven terms derived from the gray level histogram. The resulting energy function is a modified version of the energy function of the classical Potts model. Optimization is achieved using simulated annealing. Coastline segments are extracted by means of the orthogonal gradient operator proposed by Descombes [5]. The result is a preliminary estimation of coastline.

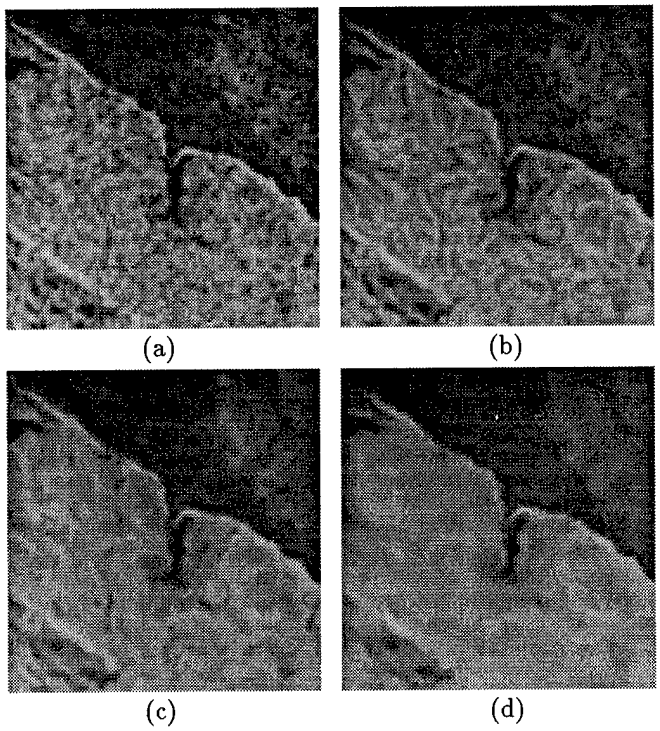

Figure 1: Restorated images. (a) Original subimage of 100x100 pixels derived from the third level (256x256 pixels) of a gaussian pyramid; (b)-(d) restorated images; (b): $s = 4$ and $d = 0$; (c): $s = 4$ and $d = 50$; (d): $s = 4$ and $d = 65$.This is the selected image for high resolution detection.

Next, coastline estimations are propagated to the highest resolution level and finer estimations are computed by means of a second MRF. It is reduced to a binary classifier. Computation takes place only at selected regions defined by the low resolution projection. Figure 2 shows the final result.

CONCLUSION

Based on polynomial transform and markovian segmentation, we proposed a methodology for detecting coastline. The combined techniques are devoted to take advantage of the high pixel resolution of SAR images. Because of the hierarchical approach, computing time is not a critical parameter. With some minor modifications, it can be also used to perform general low-level SAR image processing.

REFERENCES

[1] F. Leberl, "Radargrammetric image processing", Artech House, Inc., 1990.

[2] Lee and Jurkevich, "Coastline detection and tracing in SAR images", IEEE Trans. Geosci. Remote Sensing, 28, 1990, pp.662-668.

[3] Y. Wu and H. Maitre, "Registration of a SPOT image and a SAR image using multiresolution representation of a coastline", 1990, pp. 913-917 [Digests 10th ICPR, Atlantic City, N.J.].

[4] D. Zhang, L. Van Gool and A. Oosterlinck, "Coastline detection from SAR images", 1994, pp. 2134-2136 [Digests IEEE IGARSS94, Pasadena, Cal.].

[5] X. Descombes, M. Moctezuma, H. Maitre and J.P. Rudant, "Coastline detection by a Markovian segmentation on SAR images", Signal Processing, 55, 1996, pp. 123-132.

[6] V. S. Frost, J.A. Stiles, K. S. Shanmugan and J.C. Holtzman, "A Model for radar images and its applications to adaptive digital filtering of multiplicative noise", IEEE Trans. Pattern Analysis and Machine Intelligence, 4, 1982, pp. 157-166.

[7] A. Lopes, E. Nezry, R. Touzi and H. Laur, "Maximum a posteriori filtering and first order texture models in SAR images", May 1990, pp.2409-2412 [Digests IEEE IGARSS90, Washington, D.C.].

[8] J.B. Martens, "The Hermite Transform–Applications", IEEE Trans. Acoustics, Speech, and Signal Processing. ASSP-38, 1990, pp. 1607–1618.

[9] B. Escalante-Ramírez and J.-B. Martens, "Noise reduction in Computerized Tomography images by means of polynomial transforms", Journal of Visual Communication and Image Representation, 3, 1992, 272–285.

Figure 2: Result of the detection. Coastline overlay on one subimage of 400x400 pixels at original resolution.

The Concept of Russian Fisheries Industry Service for Satellite Monitoring of Fishing Area in Global Ocean

Alexei Romanov
Russian Federal Research Institute of Fisheries and Oceanography
17 Verkhnaja Krasnoselskaja St., Moscow, Russia, 107140
Tel: (095)2642096, Fax: (095) 2649187, E-mail: ROMAL@MX.IKI.RSSI.RU

Alexander Rodin
State Fishing Committee of Russian Federation, Moscow, Russia

Valentin Mishkin
Scientific and Technical Company "Complex Systems", Murmansk, Russia

Abstract - The strategy of the development and creation of the Russian fisheries industrial service for satellite monitoring of fisheries areas of the global ocean is described. The service intends to solve the problems concerned to oceanographic conditions monitoring, positioning of fishing fleet, marine ships safety, catch forecasting, etc.

INTRODUCTION

The necessity of creation of the service for monitoring an activity of a fishing fleet, as well as oceanographic conditions of marine environment as ecosystem for biological resources existence is stipulated today by several factors.

It is well known that the Council of European Economic Community in June 1993 has accepted the decision that till January 1 1996 the fishing vessels of community should be equipped by the system for continuous ship positioning based on either ground or space means of tracking, using satellite communication links for data transmission. This decision in 1995 was recognized compulsory for all North Atlantic Fishing Organization (NAFO) states, including Russia.

At the same time, a fishing fleet needs a significant efforts of the research institutes, which are regularly fulfilling an investigations of total biomass and fish stocks in various fishing areas with the help of research vessels. Today the costs of these cruises have become too expensive, that it has required to seek a new ways for increase of efficiency of scientific researches. Remote sensing methods of the monitoring of seas and oceans by means of the Earth Observation Satellites (EOS) and airplanes can permit in near future drastically decrease the expenses via the reduction of area of vessel surveillance and paying attention to the regions, where fishing could be potentially beneficial.

THE PRINCIPAL SUBJECT AND TASKS

The principal subject of this paper is the system analysis of scientific and practical tasks of fishing for monitoring of fish areas in EEZ and global ocean, ground infrastructure of data acquisition and technologies for complex processing of different types of data. This analysis has been intended to the creation inside the fishing industry a new subsystem of information support, which could integrate the latest achievements in such scientific areas as: remote sensing of the ocean, geoinformation systems (GIS), satellite telecommunication systems, global and local networks, distributed problem - oriented databases.

There are the tasks, which could be provided by satellite and airplane sensors inside the EEZ of Russia and in fishing areas of global ocean [1]:

1. Determination of a position of fishing vessels.
2. Continuous monitoring and determination of different oceanographic characteristics, such as: sea surface temperature (SST); speed and direction of sea wind; wave heights; water mass circulation.
3. Determination of primary bioproductivity characteristics in the ocean with the aim of water color.
4. Detection and determination of the positions of sea animals and seagrass plants.
5. Navigation support.
6. Monitoring of meteorological and sea ice conditions.
7. Data and message transmission to and from vessels via communication satellites.

Obviously, the set of tasks constantly expands, nevertheless all these problems could be divided in several independent classes:

- Operative monitoring problems (1, 4, 6).
- Problems of scientific research support (2, 3).
- Telecommunication problems (7).
- Marine transportation safety (5,6).

The similar classification of problems is necessary because of it assists to clarify the potential users of satellite information among fishermen.

The most advanced today are the problems of determination of fishing vessels position, navigation support and monitoring of meteorological and sea ice conditions. These problems have already passed from a scientific experiments to operative using. The end users for those information products could be the shipowners, as well as federal and regional governments, having control of industrial activity in fishing regions.

But, the maximum effect from satellite data using could be

0-7803-3836-7/97/$10.00 © 1997 IEEE

reached in case of short-term fishing forecasting and for reconnaissance of new areas of fishing. The main limitation to solve these problems, connected with a small set of parameters retrieved from space. Secondly, the results of survey are strongly depend on cloud coverage of a regions, because both visible and IR-sensors have these physical restrictions. At the same time the using of microwave techniques is at initial stage now. Moreover, anyone type of space data, can not decide considering problems by itself.

The only decision is an integration of satellite, airborne and in situ data, their mutual calibration and joint interpretation via GIS. Thus the requirements to technical and scientific equipment, hardware and software onboard the research vessel are grow up very high.

THE BRANCH REQUIREMENTS TO A SERVICE.

The main present activity of Russian fishing fleet is concentrated in EEZ on Northern and Far Eastern regions. To provide a space information on these regions it can be established a set of the satellite information receiving stations. As far as on these regions there are analytical centers of regional research fishing institutes already exist they could be also the centers for satellite data processing,.

Several receiving stations would be installed in Murmansk for a European region of Russia and in cities Vladivostok, Uzhno - Sakhalinsk and Petropavlovsk - Kamchatsky for the Far East region. The principle of a distributed center for Far East will be applied, as far as the accommodation, at least, three stations permits overlap all zones of interest.

An another way to decrease time of delivery of the space information to the end user is a creation of portable satellite receiving and processing stations directly on fishing vessels.

As for the fish areas in global ocean outside of Russian EEZ the remote sensing information could be ordered in foreign space centers via the Moscow's branch of service, situated at VNIRO, so called scientific coordination and methodological center. This center will integrate an activity of regional centers as well.

It is obvious, for the end users the more important requirements for growth of user's segment of the space information market are as follows: reduction of the size and cost of receiving stations. creation of more fast speed communication networks. creation of small expert systems, capable to process the information and to create an information product by end users themselves.

The third requirement we shall allocate especially, as it needs maximum automation of large volume of preparatory work with space data. Just in an expert system the whole accessible of experimental data about fishing area, received by various, and not only space means, is concentrated. Accordingly, the main element of a service the reliable functioning of similar expert systems should become.

All mentioned above permits to define the main requirements to the created service:

- Creation of an industrial infrastructure for the receiving, processing and delivering of the information products up to the end users.
- Creation of own telecommunication network to exchange data between regional centers in quasireal time scale.
- Creation of industrial distributed subject - oriented databases.
- Unification of the standards for data transfer between different levels of a branch information system.
- Training and education of the end users to the new approaches in operative using of space data products.

DATA RECEIVING AND PROCESSING.

Launches of the module "Priroda", connected to "Mir" orbital station, as well as specialized satellites for communication "Gonets", search and rescue "Kurs" were successfully carried out in 1996 in addition to "Resurs" and Ukrainian "Sich" [2,3].

Two newest foreign satellites, such as ADEOS (Japan) and IRS-P3 (India) [4] have characterized a new situation on providing the end users good quality specialized oceanographic space data.

The European center, equipped with HRPT receiving station, could receive space data from resource and meteorological satellites "Okean-O"and NOAA, from dual using satellite "EKO" and, in near future, from "Meteor - 3M" and SeaStar satellites, because all of them have a transmission downlink at 1,7 Ghz. The receiving of data from Indian IRS - P3 on northern latitudes is possible through Germany ground receiving station, and SAR data from ERS and Radarsat is possible via Tromse (Norway). More informative satellites, such as IRS, ERS, Radarsat and " Resurs - O" demand the installation of additional receiving stations, having another frequency ranges.

On Far East the similar opportunities are principally absent, since the data from SAR of ERS, Radarsat and data from MOS of IRS - P3 are transmitted only in a direct transmission mode, hence, the unique opportunity to receive them is an organization of own receiving ground stations there. As for satellites with 1,7 Ghz downlink, the situation is similar to European regional center.

The main requirements to processing of space data could be formulated as follows:

- Providing of processing of space image up to a level of a theme chart, clear understanding to user
- Development automated hardware/software and algorithms for receiving of space data on ship board.
- Management of ship information databases with an opportunity of data transfer to offshore archive.

The most important in this case is to develop an information technology of maximally simple level of using, when it could maintained and serviced by staff of an average and low level of qualification. For this reason today one of active developing approach is using of GIS. Controlled by reasonably simple commands GIS can be used for display and analysis spatial data by means of many different ways.

The GIS users have an opportunity of choice among different types of data, displayed on the map basis.

VERIFICATION OF SPACE DATA

For verification and validation of remote data it is necessary to assemble the synchronous data of sea truth hydrological, hydrochemical, hydrobiological, and ecological surveillance.

This work is especially important when the elements of information technologies are only developed and required essential volumes of experimental researches for confirmation of the efficiency of new developed technologies.

For improvement of regional algorithms of oceanographic data retriviation it is necessary to choose several polygons in fishing areas, given an applied using of developed technologies.

There could become the Barents or Norway seas on the North, and Sakhalin island's nearby area on Far East. This choice has been done because on specified regions there is a plenty of a'priori information on previous years. Moreover, there are the ground receiving stations, situated in Murmansk and Uzhno - Sakhalinsk already.

The main tasks, which would be solved during verification and validation procedures are as follows:

- Detection of oceanographic processes and phenomena on a marine surface from remote data in different ranges of electromagnetic spectrum.
- Synchronous survey of investigated polygon by research vessel and airplane means.
- Developing of regional algorithms of the retriviation of oceanographic parameters.
- Creation of models of remote sensing data using for short-term forecast of marine environment.

For realization of specified works in fishing industry service it is necessary to have appropriate means of experimental support: well equipped research vessel and airplane - laboratory [5,6].

THE MAIN STAGES OF SERVICE CREATION

The appropriate measures should be provided step by step with gradual escalating of service capacity. The main factor of development of a service should become training of the end users to effective use of new information technologies. For this reason, in a structure of a service educating and training base should be stipulated.

Taking into account all above-stated the following program on creation of a branch service for operative monitoring of fishing areas can be offered:

1997 - Beginning of operative industrial activity of the first stage of a European center of satellite monitoring.

1998 - 2000 - Establishing and creation of Far East distributed center of satellite monitoring.

1997 - 1998 - Creation of a Moscow's coordination and methodical center.

It is represented expedient the realization of particular demonstrative projects with obviously expressed results for a period not longer then one year. In accordance with transfer of developed technologies from the category experimental researches to operative, it could increase of volumes of services represented by service to the end users and gradual, even partial, commercialization of its use. On the first stage it should be only federal structure, ensuring both departmental, and national use.

CONCLUSIONS

1. The developed concept can be fixed in the basis of the branch system project on creation of a subsystem of satellite research and industrial monitoring.
2. Creation of a service of satellite monitoring is expediently to execute in several stages. First of all, it is necessary to ensure an industrial operative exploitation to solve the problems of fishing vessels positioning via satellites, as well as navigating and meteorological maintenance.
3. For the developing of a completed new information technologies, introduced in operative practice of service it can be recommended to fulfill some demonstration projects, which could be realized by joint efforts of organizations of various both environmental and fishing departments.

REFERENCES

[1] A.A.Romanov. "Modern Opportunities of Satellite Information Using for Industrial Problems of Short Term Forecasts and Fishing Fleet Management: State and Nearest Prospects" in New Information Technologies and Remote Methods for Industrial Monitoring of Fishing Areas of the Global Ocean, Moscow: VNIRO, 1996, pp.19-35, in Russian.

[2] Yu.G.Titshenko. Project "Priroda" for Remote Sensing of the Earth from Space, "Russian Space bulletin", v.2, N1, 1995, p.p. 3-5.

[3] "Gonets"- Low Orbit Satellite System of Personal Communication.Advertising materials of Scientific and Research Assisiation of Precision Instrument Making.

[4] G.Zimmermann. German Program for Ocean Remote Sensing. Proceedings of COSPAR Colloquium: Space RS of Subtropical Oceans (SRS SO), Taipei, September 13 - 16, 1995, p.p.1-10.

[5] A.I.Zhavoronkov, D.E.Levashov, V.V.Sapozhnikov. The Contemporary State and Prospects for Development of Research Fleet for Oceanic Fihing. Fisheries, N5, 1996, p.38 - 42, in Russian.

[6] V.I.Chernook, V.B.Zabavnikov. Marine Airborne Investigations for Fisheries. In "Remote Sensing Methods of Fishing Areas Monitoring in Global Ocean for Industrial Tasks of Information Support of Scientific Researches"./ Edited by A.Romanov, M.:, VNIRO, 1997, in press.

LAND-USE CLASSIFICATION USING TEMPORAL SAR-IMAGES

Markus Törmä[1], Jarkko Koskinen[2]
Helsinki University of Technology

[1]Institute of Photogrammetry and Remote Sensing, Otakaari 1, 02150 Espoo, Finland
Tel: +358-9-451 3896, Fax: +358-9-465 077, Email: Markus.Torma@hut.fi

[2]Laboratory of Space Technology, Otakaari 5 A, 02150 Espoo, Finland
Tel: +358-9-451 2170, Fax: +358-9-451 2898, Email: jarkko@avasun.hut.fi

Abstract -- 14 ERS-1 SAR images were classified using three different classification algorithms. Median filtering and principal component analysis were used in speckle reduction and feature extraction. Feature selection was performed using branch-and-bound algorithm. The best classification accuracy (55-60%) was achieved when principal component images computed from median filtered SAR images were used. In this case five best principal components gave as good results as all 14 images.

1. INTRODUCTION

Information about land-use is important for institutions which use and need spatial information and make planning about the use of earth. One significant parameter in forested areas is stem volume of trees, because it is directly related to forest biomass which is needed when studying the circulation of carbon in earth. Forests have also great economical value.

Optical aerial and satellite images have been used long time to produce this information. Unfortunately weather conditions limit the use of optical data. For example, here in Finland summertime is usually quite cloudy, there are usually only several days in summer when large area of Finland is cloud-free, and during wintertime there is dark also daytime. These facts have lead to investigate the use of microwave data to obtain spatial information.

The aim of this paper is to investigate the potential of ERS-1 SAR-images to obtain reliable land-use classification. Single day images do not provide enough information for reliable classification, so several images taken in different weather conditions and different times are used. Factors influencing classification accuracy are speckle reduction and selecting or extracting relevant features. Used methods for the speckle reduction are median filtering and principal component analysis and methods for the feature selection and extraction are branch-and-bound algorithm for feature selection and principal component analysis for feature extraction.

2. TEST AREA AND DATA

Test area is called Porvoo test area and it is situated in southern Finland. The area includes several land use classes like forests, swamps, agricultural fields, lakes and urban areas. The overall relief is quite low, elevation is well below 100m, but not flat because of small hills [1].

ERS-1 SAR images used in this study were taken during 30.6.1993 - 25.4.1994 within ESA AO-programme. First six images were take during snow-free conditions, fourth image was taken in quite rainy conditions, first two images in quite warm, images 10 and 11 in very cold. There was about 0.5 m dry snow during winter. SAR images have been topographically corrected [2] and averaged to 25 x 25 m^2 pixelsize. Size of each image is 1700 x 1700 pixels and they cover about 42.5 x 42.5 km^2 area. Digital land-use map made by National Forest Survey and stem volume map made by Finnish Forest Research Institute are used as reference data.

3. IMAGE PROCESSING

In order to investigate the effect of speckle and the number of required images to classification accuracy different datasets were computed:

A. Original 14 ERS-1 SAR images.
B. Median filtered SAR images.
C. Principal component images computed from original images.
D. Principal component images computed from median filtered images.

Median filter filters image so that the center pixel of the filter window has been replaced by the median of the pixel values in window [3]. In other words, this filter removes low- and high-valued pixels from image.

0-7803-3836-7/97/$10.00 © 1997 IEEE

Principal component analysis is a linear transformation which rotates coordinate axis according to variance of data. First principal component axis is placed according to the direction of the maximum variance of data determined by the largest eigenvalue of covariancematrix and its direction is determined by corresponding eigenvector. Second principal component axis is placed according to second largest variance of data and so that it is orthogonal to first axis and so on. The result of the transformation is new set of images, where in principle first images correspond to information needed in classification and latter images correspond to random components like speckle [3].

4. FEATURE SELECTION

The feature selection was performed using the branch-and-bound feature selection algorithm and the selection criteria was average interclass divergence. The branch-and-bound algorithm has been developed to obtain optimal set of images without exhaustive search. This is done by organizing search process efficiently. The divergence is measure of separability between two classes, computed using class means and covariances [4]. These were computed using areas from digital land-use map as training areas.

When original images are used, the most informative image is image number 6, then 1, 3, 9, 2, 11, 4, 5, 10, 14, 8, 7, 13 and 12. According to the feature selection, summer images are more important to land-use classification than winter images. The median filtering of the images changes the order of the images little bit (6, 1, 3, 9, 4, 2, 11, 5, 14, 10, 7, 8, 13 and 12), but same conclusion can be made also in this case. In principle, when principal component images are used, first principal components would contain more useful information for class separability. Now, the most informative image is the first principal component, then 3rd and 2nd (then order is 5, 7, 10, 9, 4, 6, 12, 11, 8, 13, 14). When principal components have been computed from the median filtered images, the 1st, 2nd and 3rd principal components are the most informative (then order is 9, 6, 10, 7, 4, 5, 8, 11, 12, 13, 14). So, the amount of the useful information for class separability does not necessarily follow the order of principal components. According to visual inspection of images, the best color combination of original and median filtered images is images 1, 4 and 7. The best color combination for principal component images is 1st, 2nd and 4th, in both cases.

In order to determine the increase of class separability when adding more images, class separability measure called Bhattacharyya-distance was also computed [3]. Separability is computed between each pair of classes and then mean value and minimum and maximum values are computed. When classes are separable, the value of Bhattacharyya-distance is 2.0 and if class separability is poor, distance is below 1.0. Fig. 1 shows Bhattacharyya-distances for each dataset as function of number of used images. Solid line correspond to original images (maximum distance is on top, mean distance is on middle and minimum distance is on below), dashed line correspond to median filtered images, dash-dot line correspond to principal component images computed from original images and dashed line correspond to principal component images computed from median filtered images. E.g. if six images are used, they are those most important images determined by the branch-and-bound algorithm. Fig. 1 shows, that median filtering increases class separability more than principal component analysis and the best solution is use principal component images computed from median filtered images.

5. CLASSIFICATION

In order to compare different classification methods, classifications were carried out using Kohonen self-organizing feature map (SOM), learning method quantization (LVQ) and Bayes rule for minimum error with maximum likelihood density function estimation method. Classes are water, forests with three subclasses according to stem volume (forest 1: stem volume under 100 m^3/ha, forest 2: stem volume 100 - 200 m^3/ha and forest 3: stem volume over 200 m^3/ha), agricultural field, swamp and urban area. Training and test areas were selected using digital land-use map and forest stem volume map. The size of the training and test areas for classes were about 2000 pixels. Classification were carried out using different feature dimensions, so that the effect of increasing number of images could be seen. Dimensions 3, 5, 7, 9 and 14 were used and they were same as in chapter 4.

SOM is self-organizing neural network which uses competitive learning to adapt itself to the density function of the input patterns. Network consists of processing elements arranged usually to two-dimensional sheet and each

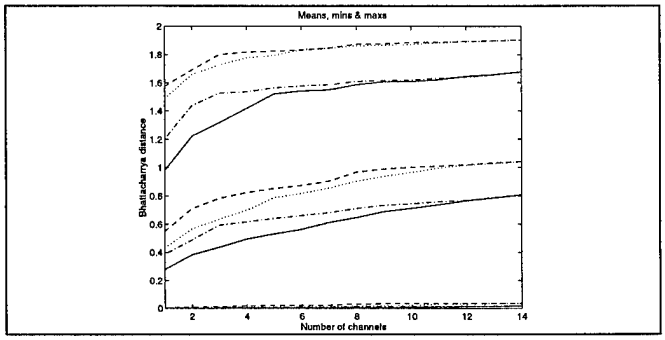

Figure 1: *Bhattacharyya-distances as function of number of images.*

processing element has weight vector. During learning the weight vectors converge to places where they approximate the density function of the input patterns. SOM has not intended to be pattern classifier (it is unsupervised method) but it can be used together with learning vector quantization methods [5].

Learning vector quantization methods try to find optimal places for the weight vectors representing different classes. Role of SOM is that it can be used to find approximate places for those weight vectors. Learning vector quantization method type 3 (LVQ3) has been used in this study [5].

When classifying image pixel, Bayes minimum rule for error computes a'posteriori probabilities for each class and assigns pixel to class with maximum probability. The density function of data is computed using maximum likelihood method. Data is supposed to be normally distributed and means and covariances are estimated from data. This classifier is also called maximum likelihood classifier (MLC) [4].

Fig. 2 represents classification accuracies when original images are used. Solid line correspond classification accuracies when SOM was used (upper line correspond to accuracy for training set and lower test set), dashed line LVQ3 and dash-dot line MLC. Fig. 3 represents classification accuracies when principal component images computed from median filtered images are used. Results indicate, that speckle reduction by filtering and computing principal components increase classification accuracy. LVQ3 gives best classification accuracies, SOM is surprisingly good (unsupervised method). When MLC is used, classification accuracy can even decrease when number of images increase (see fig. 2). Another advantage with principal component images computed from median filtered images is that five best images from 14 images give sufficient good results. This speed up classification and makes results more reliable.

6. CONCLUSIONS AND FUTURE DIRECTIONS

The best method used in this study to decrease speckle and feature dimension is principal component images computed from median filtered images. But also in this case classification accuracies are quite low, about 55-60%. In order to increase accuracy, there are several possibilities to investigate: use of another frequencies (JERS-images) and polarizations (RADARSAT-images), use more advanced filtering method or compute texture measures from images. Now it seems that best alternatives are to get more images (different frequencies and polarizations) and try some texture measures.

ACKNOWLEDGMENTS

This study is part of forest inventory activities made in Helsinki University of Technology, Laboratory of Space Technology. Author wish to thank Dr.Tech. Juha Hyyppä, Dr.Tech. Jouni Pulliainen for help and comments.

REFERENCES

[1] J.Pulliainen, P.Mikkelä, M.Hallikainen, J-P.Ikonen, "Seasonal Dynamics of C-Band Backscatter of Boreal Forests with Applications to Biomass and Soil Moisture Estimation," IEEE Trans. on Geoscience and Remote Sensing, Vol. 34, no. 3, May 1996, pp. 758-769.

[2] Y.Rauste, "Methods for Analyzing SAR images," Tech. Res. Ctr. Finland, Lab Instrument Technol., Espoo, Finland, Rep. 612, 1989.

[3] J.Richards, "Remote Sensing Digital Image Analysis," 2nd ed. Springer-Verlag, 1993.

[4] P.Devivjer, J.Kittler, "Pattern Recognition - A Statistical Approach," Prentice-Hall, 1982.

[5] T.Kohonen, "The Self-Organizing Map," Proc. of the IEEE, Vol. 78, no. 9, September 1990, pp. 1464-1480.

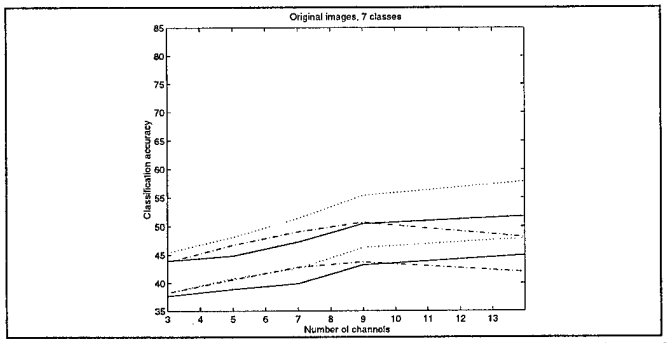

Figure 2: *Classification accuracies as function of number of images when original images were used.*

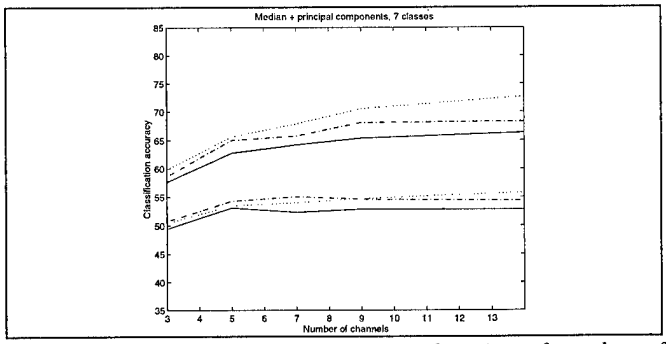

Figure 3: *Classification accuracies as function of number of images when principal component images computed from median filtered images were used.*

Using RADARSAT-1 for Fisheries Enforcement Operations

Terje Wahl
Forsvarets forskningsinstitutt - FFI (Norwegian Defence Research Establishment)
P O Box 25, N-2007, Kjeller, Norway
Phone: +47 63 80 70 00 Fax: +47 63 80 72 12
email: Terje.Wahl@ffi.no

Abstract -- RADARSAT's capabilities for detection of fishing vessels have been tested and demonstrated. A centre has been established for routine analysis of RADARSAT images in Norwegian waters. RADARSAT observations are used regularly for optimizing the use of other assets (aircraft, helicopters, ships) in fisheries enforcement operations.

INTRODUCTION

Norway has large economic ocean zones and fishery protection zones, in total more than 2 million km^2. Coastal radars, surveillance aircraft, and coast guard ships and helicopters have for many years been used regularly for monitoring the activities in these areas. Radar satellites can contribute to better surveillance, especially of the remote ocean areas. In 1991 Norway. established a national ERS-1 receiving and processing capability at Tromsø Satellite Station (TSS). The SAR instrument on ERS-1 was well suited for environmental monitoring in Norwegian waters, and a routine oil spill monitoring service was established at TSS in 1994 after two years of testing and demonstrations at the Norwegian Defence Research Establishment (FFI) [3]. Due to its steep incidence angle, ERS-1 was not well suited for detection of ocean-going fishing vessels [2], which typically are 50 m long. However, valuable experience was gained at FFI with ERS-1 for near real time detection of large ships, both manually and automatic [1] [4].

Predictions made prior to the launch of RADARSAT-1 indicated that certain RADARSAT modes were of high interest for ship detection [5] [6]. Especially, the ScanSAR Narrow Far mode (covering a 300 km wide swath with approx 50 m resolution) seemed like a promising compromise between wide area coverage, trawler detection capability, and cost per km^2.

During the fall of 1996 the capabilities of RADARSAT's ScanSAR Narrow Far mode have been verified and demonstrated for practical use in Norwegian waters. Fine resolution observations in the Oslofjord area for studies of identified ferries and very small (< 25 m length) fishing vessels have also been conducted. In parallell with the tests, a centre for routine analysis of RADARSAT images has been established, manned by defence personnell. Practical aspects related to fisheries enforcement in open ocean have been demonstrated in three geographical areas:

- The North-Eastern Barents Sea
- Bear Island (74.5°N, 19°E)
- Jan Mayen (71°N, 8°W)

BARENTS SEA

The first RADARSAT-1 image received at TSS for ship detection purposes was processed on 19 August 1996. This ScanSAR Narrow Far image, block averaged at TSS to 100m x 100m pixel size and sent to FFI, showed more than 40 foreign vessels which were fishing in international waters along the Norwegian Zone in the Barents Sea. This SAR image made headlines in Norwegian newspapers, and immediately showed the relevance of RADARSAT-1 for fisheries enforcement and coast guard operations. In-situ observations made the following day provided detailed information about 43 identified vessels. Table 1 shows the distribution of ship lengths. Wind speed was estimated to 6 m/s. Fig. 1 shows a part of the image after greyscale thresholding.

Table 1. Distribution of ship length for identified fishing vessels 19-20 Aug 1996. Average ship length was 56.5 m.

Ship length [m]	30-39	40-49	50-59	60-70
Number of ships	2	4	24	13

BEAR ISLAND

Groups of fishing vessels were regularly observed in the waters around Bear Island in Oct-Nov 1996. All passes showed clearly the location of major groups of fishing vessels. Of particular interest is the case of 11 Oct, where seven ships were seen just east of Bear Island in moderate winds. A weather front, easily seen in the RADARSAT image, was situated between Bear Island and North Cape, with winds of more than 15 m/s in the southern part of the Barents Sea. Based on the measured radar cross section of

the ships at Bear Island, two of the seven ships would have been lost by the SAR if they had been located in the strong wind area, while the other five would have been detected.

JAN MAYEN

Jan Mayen is a large remote island located at 71°N, 8°W, surrounded by a large fishery zone subject to Norwegian jurisdiction. On 11 Oct 1996 it was reported, based on analysis of RADARSAT ScanSAR Narrow Far imagery, that there probably were no ships in the large Jan Mayen zone. This absence of ships was confirmed later the same day by Norwegian P3 Orion aircraft. The use of radar satellites instead of aircraft for "clearing" large ocean areas is expected to give substantial cost savings in the future. Of course, there are limits to how small ships one can expect to detect from a radar satellite covering a large area. On the other hand one would not expect vessels much shorter than 50 m length to operate in the remote Jan Mayen area.

COMBINED USE

Several tests have been conducted with integrated use of RADARSAT images in routine fisheries enforcement operations during the winter of 1996/97:

- Planning next day's surveillance aircraft flight route
- Updating the surveillance aircraft while in flight
- Observing typical "transit zones" with satellite while surveillance aircraft cover the main fishing area
- Clearing the Jan Mayen zone without use of aircraft

RADAR CROSS SECTION OF FISHING VESSELS

Rough calibration of our RADARSAT-1 images has been done by use of corner reflectors, calm water or radar shadow. Radar cross sections of fishing vessels have then been estimated. On average, the radar cross sections at ScanSAR Narrow Far incidence angles (31°-46°) seem to be at least 3 dB higher than expected from Skolnik's [8] well-known rule-of-thumb ("RCS [m^2] = ship displacement [tons]"), supporting statements from Canada [7]. Table 2 shows the ship length values currently used by Norwegian operators when deciding what to expect from a RADARSAT image.

As wind speed is a critical factor for detection of fishing vessels, it is interesting to review meteorological statistics for ocean areas. Table 3 shows wind speed statistics for three different ocean areas, collected by Norwegian meteorologists over several decades.

Table 2. Excerpt from the Operator's Handbook, describing RADARSAT detection limits (ship length) in ScanSAR Narrow Far mode, as a function of wind speed, wind direction and incidence angle.

Wind velocity	Inner	Mid	Outer
4 m/s cross track	35 m	25 m	20 m
10 m/s cross track	60 m	45 m	35 m

Table 3. Percentage distribution of wind speed measurements reported over several decades from weather stations on Bear Island (Barents Sea), Utsira Island (North Sea), and the weather ship "Polarfront" (Norwegian Sea).

	0-7 m/s	8-13 m/s	> 14m/s
Bear Island	65 %	29%	6 %
"Polarfront"	46 %	38%	16%
Utsira	73 %	22 %	5 %

DISCUSSION

In general, the results from use of RADARSAT's ScanSAR Narrow Far are positive. It has been clearly demonstrated how RADARSAT can be used for tracking the movements of groups of fishing vessels in various parts of the Barents Sea, and for indicating the presence or absence of fishing vessels in the very remote Jan Mayen zone. However, the ScanSAR Narrow Far has limitations during winter storms.

2x2 block averaging at TSS before distribution of the image seems like a good compromise between throughput and detection requirements.

CONCLUSIONS

Tromsø Satellite Station started delivering RADARSAT images for ship detection tests in mid-August. Initial technical tests of RADARSAT for ship detection in Norwegian waters have shown positive results. A RADARSAT image analysis centre has been established in Norway, manned by defence operators trained by FFI. This centre is now regularly generating messages for use in fisheries enforcement operations. The image product mostly used is the ScanSAR Narrow Far, block averaged to 50m x 50m pixel size.

ACKNOWLEDGMENT

All RADARSAT SAR images used in this study have been bought commercially from Tromsø Satellite Station.
RADARSAT SAR data: (c) 1996 Canadian Space Agency.

REFERENCES

[1] K Eldhuset: An Automated Ship and Ship Wake Detection System for Spaceborne SAR Images in Coastal Regions. IEEE Trans on Geoscience and Remote Sensing, Vol 34, No 4, July 1996, pp 1010-1019.

[2] Å Skøelv, T Wahl: ERS detection of soft and hard targets at sea: What can be operationalized? Proceedings of the Second ERS Applications Workshop, London, 6-8 December 1995 (ESA SP-383, Noordwijk, NL, Feb 1996), pp 193-196.

[3] T Wahl et al: Radar satellites: A new tool for pollution monitoring. Coastal Management, Volume 24, No 1, Jan 1996, pp 61-71.

[4] T Wahl, Å Skøelv: NATO naval exercises as observed from civilian radar satellites. Submitted to Proceedings, AGARD SMP Symposium, Cannes, 3-6 June 1996.

[5] Å Skøelv, S T Dokken, T Wahl: Upcoming radar satellites and their potential for some maritime applications. In Parlow (ed): Progress in Environmental Remote Sensing Science Research and Applications. Balkema, Rotterdam, 1996.

[6] P W Vachon, R Olsen: RADARSAT SAR Mode Selection for Marine Applications. Backscatter, Vol 6, No 3, pp 3-4, 1996.

[7] P W Vachon, J W M Campbell, C Bjerkelund, F W Dobson, Rey M T: Ship detection by the RADARSAT SAR: Validation of detection model predictions. Canadian Journal of Remote Sensing, Vol 23 No 1, 1997.

[8] M I Skolnik: Introduction to Radar Systems. McGraw-Hill, New York, NY, USA, 1982.

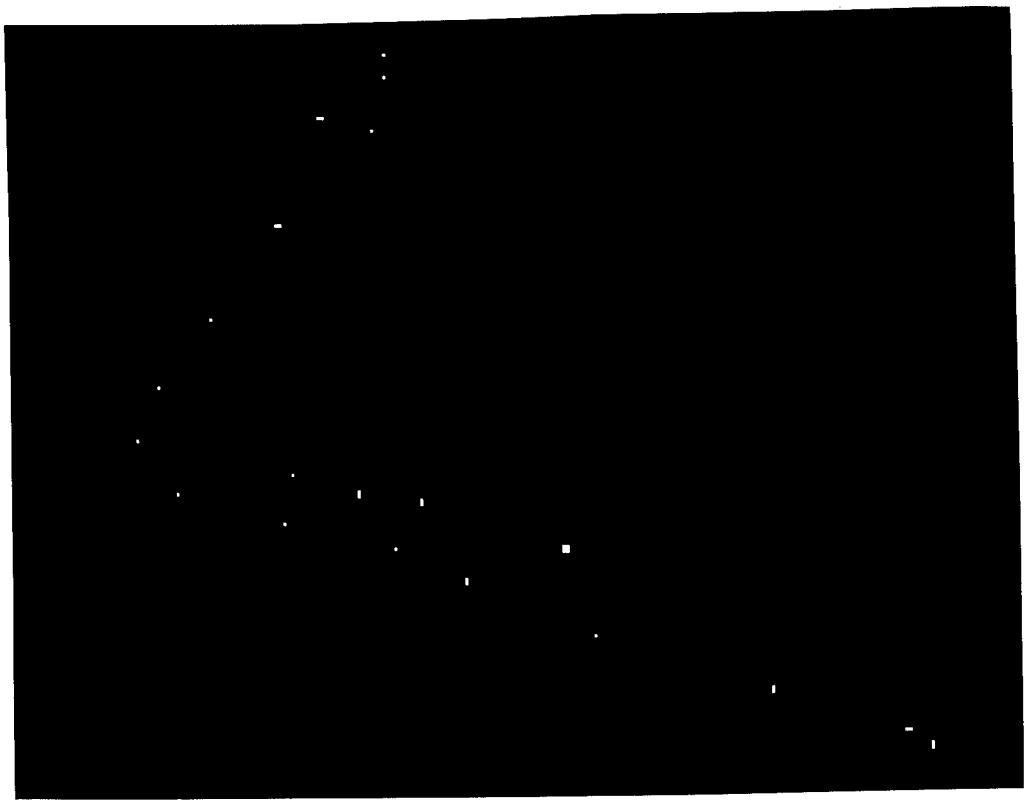

Figure 1. Thresholded RADARSAT-1 ScanSAR Narrow Far image from the Barents Sea 19 August 1996, showing numerous vessels fishing in international water along the border lines to Norwegian 200 nm economic ocean zone (bottom) and the Norwegian Svalbard zone (left). The scene is approx 24 km wide. SAR data: (c) CSA/TSS.

Detection of the Great Wall Using SIR-C Data in North-Western China

Lu Xinqiao Guo Huadong and Shao Yun
Institute of Remote Sensing Applications
Chinese Academy of Sciences
P. O. Box 9718, Beijing 100101, China
Tel:(86-10)64919740/Fax:(86-10)64915035
E-mail:luxin@public3.bta.net.cn

Abstract -- A segment of ancient Chinese Great Wall was imaged by Shuttle Imaging Radar-C. The Wall is situated in the desert region and even partly buried in a thin sand layer. SIR-C image reveals the whole segment of the wall. There are three walls imaged by SIR-C. Two were built in Ming Dynasty (1474 A.D. and 1531 A.D.) and one was built in Sui Dynasty (585 A.D.). Great Wall in Ningxia and Shanxi Province was made of loess soil taken from the local wind-blow sedimentary deposits. The Wall is seriously damaged by erosion. This paper presents the study on radar imaging mechanism of Great Wall, radar backscatter of the Wall in relation to the frequency and polarization. The study shows that the long wavelength, L-band radar image is better for detection the Wall, especially in sand covered area. Multi-frequency, Multi-polarization SAR image is an effective tool for detecting the special historic remains, such as the Silk road, the ancient graves etc.

GENERAL DESCRIPTION OF THE GREAT WALL IN NINGXIA AND SHANXI PROVINCE

The test site we have studied in is Ningxia and Shanxi province of north-western China. There are three lines of the Great Wall. One was built in Sui dynasty (585 A. D.), two were built in Ming dynasty (1474 A.D. and 1531 A.D.). The Great Wall was made of loess soil taken from the local wind-blow sedimentary deposits. The Wall is seriously damaged by erosion (fig.1). And also there were defense installations alone the Great Wall. Enemy broadcasting station which was for gathering intelligence about the enemy was built at a definite distance, about 100 meters. Beacon towers was for transmit messages about the invasion of enemy by firing.

Alone the Great Wall, there also have some forts. Fort is inside the Wall, built at a definite distance from each other. It was the military camp for station army and storing military supplies, governing a segment of the Great Wall and some enemy broadcasting stations. Xingwu Fort, Anding fort and Yanchi fort are detected by SIR-C image. Xingwu Fort is in the inside of the Great Wall where the first line and second line of Ming dynasty were separated. The area of the Xingwu Fort is 500 meter square. The wall of the fort was damaged by erosion, and the remains still stands on the ground about 8-10 meters high. The wall enclosed by brick in ancient time. But now the brick was destroyed. A lot of bricks still remains in the around of the wall.

The Wall was for defensing the enemy and protecting the country. In ancient times, some north nomadic tribe developed in north China and always intrude into north China. To protect north border, defense the nomadic tribe, the emperors of some dynasties had peoples built the Great Wall for eighteen times. There are a lot of lines of the Wall in north China, and also some forts, enemy broadcasting stations and beacon towers.

The Great Wall of Ming and Sui Dynasty

The Wall in Drift-sand Area

Fig.1 Characteristic Features of the Great Wall

0-7803-3836-7/97/$10.00 © 1997 IEEE

THE GREAT WALL IN SIR-C IMAGE

The data used in this paper is SIR-C data, acquired in April 10, 1994. It is L- and C-band, HH- and HV-polarization. The illumination of SIR-C is 24.706° and pixel size is 12.5m.

For the ability of detecting linear feature using SAR, the Wall shows clear in SIR-C image (fig. 2). Two walls of Ming dynasty and one wall of Sui dynasty are imaged by SIR-C image. In the north of the first wall is the wall of Sui dynasty. For the heavy damage of the wall, the wall shows discontinue in the image.

CHARACTERISTIC OF THE WALL IN MULTI-BAND, MULTI-POLARIZATION SAR DATA

The wall shows the difference in different band and polarization SAR data. Fig.3 shows the different characteristic of the wall in SIR-C image. The wall of Ming dynasty shows clear in L-HH image, but almost not show in C-HV. The Wall of Sui dynasty also shows clear in L-HH image. The long wavelength, L-band SAR image is better for the detection of the Wall. And HH is better than HV. Multi-frequency , Multi-polarization SAR image is more effective in archaeology research.

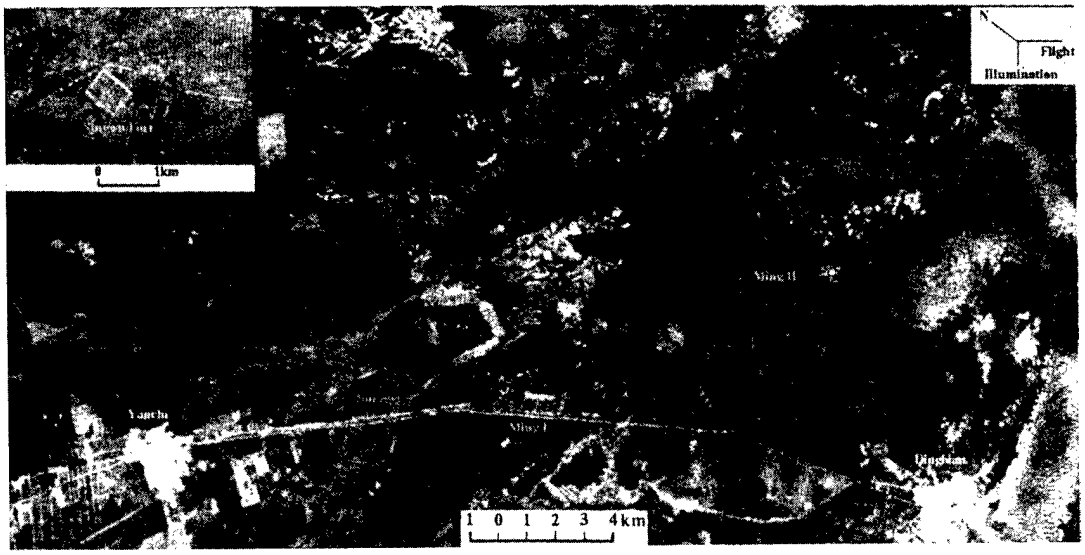

Fig.2 The Detection of the Great Wall Using SIR-C Data

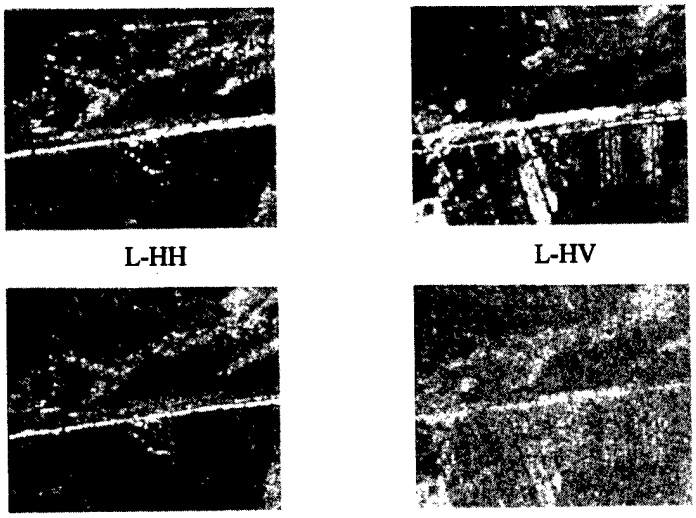

L-HH L-HV

C-HH C-HV

Fig.3 Different Characteristic of the Wall in Multi-frequency, Multi-polarization SIR-C Data

CONCLUSION

It has been shown that:

* For the effective detection of linear feature using SAR, the wall shows clear in SIR-C image. In this study. The wall, some enemy broadcasting stations and forts have been accurately mapped.
* In the very arid regions, the wall can be imaged even when covered by sand.
* The wall shows different in different freqency and polarization image.
* It also can indicate that the environment has been changed. From archaeology data, the sand were some area north of the wall in the time when it was built, but now some segments of the wall are covered by the sand.

It also illustrates that SAR image is an effective tool for the detection of sand-covered archaeological remains, such as the Silk road, etc.

ACKNOWLEDGMENT

In this paper, we wish to give our thanks to Li Junfei and Fan Xiangtao for their field works with us. And also we extend our thanks to JPL for providing data to this study

REFERENCES

[1] Derrold W. Holcomb, Shuttle Image Radar and Archaeological Survey in China's Taklamakan Desert, Journal of Field Archaeology, 1990.

[2] J. F. McCauley, G. G. Schaber, C. S. Breed, etc., Subsurface Valleys and Geoarchaeology of Eastern Sahara Revealed by Shuttle Radar, Science, vol. 218, pp. 1004-1020, 1982.

[3] Xu Cheng, The Great Wall in Ningxia Province, People's Press of Ningxia, 1988.

[4] Xu Cheng, The Remains of the Great Wall of Ming Dynasty in Ningxia Province, Social Science of Ningxia, vol. 4, 1983.

IGARSS'97

1997 International Geoscience and Remote Sensing Symposium

03-08 August 1997

Singapore International Convention & Exhibition Centre

Technical Program

Interactive Area 4: Atmospheric Sounding

Application of Kitt Peak Solar Flux Atlas for Studying Air Pollution in Tokyo Area

Niu Jianguo, Daisuke Tanaka, Xue Yanquen,
Yasushi Sakurada, Hiroaki Kuze, and Nobuo Takeuchi
Center for Environmental Remote Sensing, Chiba University,
1-33, Yayoi-cho, Inage-ku, Chiba 263, Japan
TEL: 81-43-290-3852; FAX: 81-43-290-3857; Email: niujian@rsirc.cr.chiba-u.ac.jp

Abstract – In this study, the air pollution in Tokyo area due to anthropogenic NO_2 has been observed. The method of optical absorption spectrometry based on Noxon method measures the whole spectral region of NO_2 absorption. Instead of using Langley method (long method) to retrieve extraterrestrial solar radiation, the solar radiation just above earth atmosphere is substituted by Kitt Peak Solar Flux Atlas. The large Fraunhofer features (20 – 40%) are eliminated by wavelength correction, resolution matching and ratioing of observed spectra to the reference. The NO_2 absorption structure is clearly observed. With this technique, the study of tropospheric air pollution in the urban area has been conducted with high-degree air pollution. The NO_2 vertical column density has turned out to change in accordance with the ground mixing ratio. The observation shows that high degree of air pollution appears in Kanto Plain area not only in the early winter but also in autumn .

INTRODUCTION

Human activities, the industrial and automobile effluent gases, contaminate the atmosphere near the ground. It has been pointed out that in Tokyo area in early winter, the concentration of NO_x often increases to a very high level under the stable air condition. With ground-based spectroscopic method the information of average air pollution and its thickness may be obtained. This is beneficial to the areas where network stations for observing ground level air pollution have not been established. Twilight method and direct sunlight method are the two techniques in ground-based spectroscopic observation. As it is well known, twilight zenith technique is quite useful since the sunlight scattered downward is detected after passing through the atmosphere nearly tangentially. However, since the enhancement of the absorption path takes place mostly in the stratosphere, this technique is suitable only for the trace gas monitoring in the upper atmosphere. For the purpose of studying air pollution in urban area, the ground-based spectroscopic method using direct sunlight is more suitable and therefore is used for this study.

Both the twilight method and the direct sunlight method need a "reference" spectrum with which the observed spectra are compared to retrieve the NO_2 absorption. A midday skylight and direct sunlight spectrum can be employed as a reference in which the slant column abundance is about 10 to 20 times less than the observations at large solar zenith angle. This will limit the observation just near the sunrise and sunset. The Langley method can also be utilized to derive the extraterrestrial solar radiation, which can serve as a reference spectrum. This method extrapolates the spectra taken at various solar zenith angles to zero air mass. It is required that the instrument be taken to a very clear place to avoid the influence of air pollution in the troposphere and that the weather condition must be stable when the observation is conducted. Unfortunately, these requirements are difficult to be met in most cases. In the network measurement of NO_2 and other trace gases, a standard reference spectrum is desired for the intercomparison of results taken from different instruments. Kitt Peak Solar Flux Atlas [1] can be used as such a reference under necessary precaution [2].

This paper shows how the Kitt Peak Solar Flux Atlas can be used as an extraterrestrial solar spectrum, explains the retrieving method used in this study, and describes the results of tropospheric observation in polluted urban area.

EFFECTIVENESS AND LIMITATION OF SUBSTITUTION OF KITT PEAK SOLAR FLUX FOR A REFERENCE

The Kitt Peak Flux Atlas, covering wavelength range of 296 to 1300 nm by eight charts, presents the solar flux measured with a Fourier transform spectrometer. The wavelength resolution from 296 to 576 nm is no large than 0.0002 nm. It was observed at Kitt Peak National Observatory located in the south of Arizona (32° N, 111.5 ° W), about 2000 m above the sea level. Although the original spectra have been corrected for pseudo-continuum, which corresponds to the slow change of the solar intensity and the instrumental response, the terrestrial perturbation still remains in the residual flux provided by this atlas.

Among the eight charts that cover the whole spectral range, Chart 7 is relevant to NO_2 absorption (430 – 450 nm). It has been taken from the observations in winter (November 23), 1980. The variance of the air mass factor is from 1.84 through a minimum value of 1.58, ending at

0-7803-3836-7/97/$10.00 © 1997 IEEE

1.63. Then an observation that would use chart 7 as a reference should be taken at a solar zenith angle larger than 88° to ensure a reasonable precision, if it be conducted in a clear area

At 32° N in November the abundance of NO_2 in the stratosphere is estimated [3, 4] to be 3.5×10^{15} cm^{-2}. For a free tropospheric background of NO_2, we assume that the vertical column density above 2 km is approximately 3×10^{15} cm^{-2} on the basic of 0.2 ppbv NO_2 mixing ratio reported by Kondo et al.[5]. Therefore we estimate the column density over the Kitt Peak in November to be 6.5×10^{15} cm^{-2}. Given the peak-to-peak variation of the NO_2 cross section of 3×10^{-19} cm^2 and the maximum air mass as 1.84, the relative absorption remaining in the Kitt Peak Solar Flux is 0.36%. Thus, when observations are conducted in a polluted area, and the NO_2 absorption is more than a few percent, the usage of Kitt Peak Flux Atlas as a reference spectrum is well justified.

OBSERVATION AND ANALYSIS

A grating spectrometer covering a range from about 300 to 800 nm was employed. It has an F number of 6.7, focal length of 500 mm, and linear dispersion of 1.6 nm/mm. Both the input and output slits were adjusted to give the resolution of 0.2 nm full width at half maximum. The number of observation points in the spectral region of 430-450 nm was 501, one step corresponding to 0.04 nm. A 12 cm heliostat was employed as a tracer to allow sunlight into the input slit. A light chopper was used to modulate the incident light at 1000 Hz. The signal was detected with a photomultiplier, and processed with a lock-in amplifier(PAR 5209).

The wavelength alignment of the observed spectra and Kitt Peak data is carried out as follows. First, in order to match the spectral resolution, the Kitt Peak spectrum is smoothed as

$$I_0(\lambda) = \int_{\lambda-\Delta\lambda}^{\lambda+\Delta\lambda} A(\lambda')(1 - \frac{|\lambda - \lambda'|}{\Delta\lambda})d\lambda', \quad (1)$$

where $\Delta\lambda$ is the spectral resolution of our spectrometer (0.2nm), $A(\lambda')$ is the "residual spectrum" of the Kitt Peak data.

Second, we slightly shift the hole of the observed spectrum over the smoothed Kitt Peak spectrum step by step. The data spacing of the observed spectrum is 0.04nm, while that of the smoothed Kitt Peak spectrum is 0.005 nm. This means that with the shift of eight, the whole spectrum will move 0.04 nm. By choosing a data point out of every eight points in such a manner we obtain reference spectrum, which has the same number of data points (hence the same data space) as the observed one.

The radiative transfer equation can be written as:

$$I(\lambda) = I_0(\lambda)T_A(\lambda)T_R(\lambda)exp[-\sigma(\lambda)Nm], \quad (2)$$

where $I(\lambda)$ is solar irradiance observed at the surface and $I_0(\lambda)$ is the extraterrestrial irradiance, for which we use the Kitt Peak spectrum given by eq.(1). The factors $T_A(\lambda)$ and $T_R(\lambda)$ are the transmittance determined by aerosol and Rayleigh scattering, respectively, $\sigma(\lambda)$ the absorption cross section of NO_2, m the air mass factor, and N the vertical column density of NO_2.

To calculate the ratio spectrum, both the reference and the observed spectra are normalized with respect to the values at a certain wavelength. Although the wavelength of this reference point (λ_0) can, in principle, be chosen arbitrarily, we put $\lambda_0 = 438.2$ nm. At λ_0 the absorption cross section of NO_2 takes a local minimum. The ratio spectrum $R(\lambda)$, then, is defined as

$$R(\lambda) = \frac{I(\lambda)/I(\lambda_0)}{I_0(\lambda)/I_0(\lambda_0)} \quad (3)$$

For quantitative retrieval of the NO_2 column density we make use of the NO_2 absorption band around 439 nm, more precisely the wavelength range of 438.2–442.2 nm which contains 100 data points. Although this spectral range is relatively narrow, the ratio spectrum is still affected by systematic effects such as Rayleigh scattering (the difference of 4 nm at 442 nm leads to the difference of Rayleigh scattering cross section of about 3.7%), Mie scattering and instrumental drifts. To remove these we compare two selected data points in the 439 nm absorption band, with equal values of the cross section. When these two data values are found to be different in the ratio spectrum, we renormalize it by using the slope of a straight line connecting these two points. From Eq.(2) and eq.(3) we obtain

$$\ln R(\lambda) = [\sigma(\lambda_0) - \sigma(\lambda)]mN. \quad (4)$$

The value of N is determined using the linear least-squares method. The resultant agreement between $\ln R(\lambda)$ and the right-hand side of Eq.(4) can be seen from Fig.1.

RESULTS

As pointed out that the concentration of NO_x and SPM (suspended particulate matter) in the urban area on Kanto Plain often increase to very high levels in early winter. The observation of this phenomenon was made at the campus of Chiba University, located at the edge of Kanto Plain, from October 1996 to January 1997, whenever the weather was suitable for the measurement. Fig.2 shows the observed values of average NO_2 vertical column density in the afternoon of a series of days. Fig.3 shows

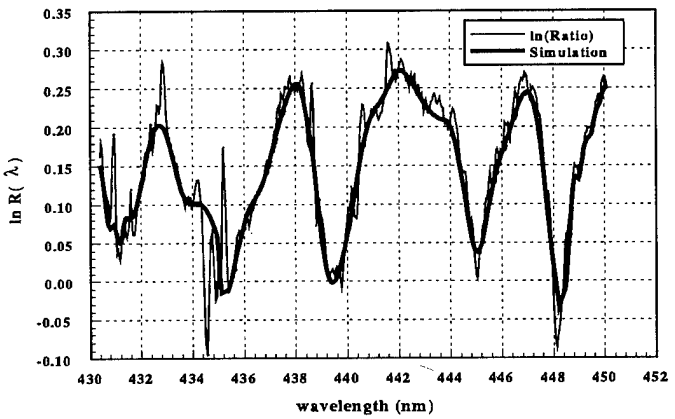

Figure 1: Ratio spectrum and simulated spectrum based on retrieved vertical column density(9.5×10^{16}) at airmass of 8.74 on Dec. 14 1995.

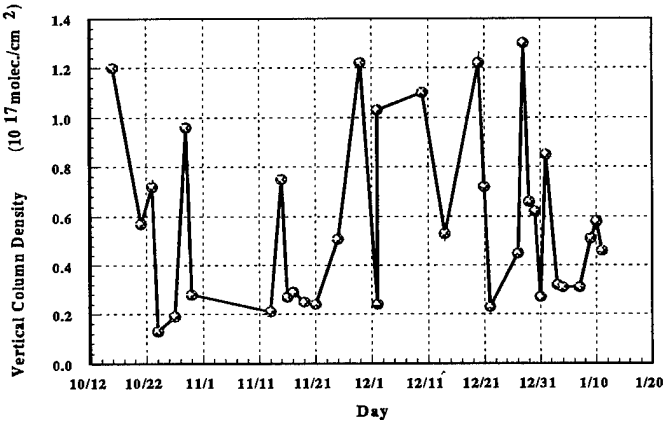

Figure 2: day-to-day variation of NO_2 vertical column density measured at Chiba university in different days around 15:00 from October, 1996 to January 1997.

the variation of ground level NO_2 mixing ratio observed at same time at Chiba university. From these two figures we can find that the variation trend of the vertical column density is basically similar to that of ground level mixing ratio. The lowest vertical column density (VCD) in this period is about 1.3×10^{16}, observed on October 24, while the highest level is about 10 to 20 times of the lowest one. Although the emission of NO_x around New Year's Day expected to be the lowest in the whole year, the lowest NO_2 VCD was not detected. That may be ascribed to the very shiny, stable weather which made the mixing layer very thick. High level NO_2 in the atmosphere was observed not only in the winter but also in the autumn.

The vertical column density was closely related to the weather condition. For example, in October 30 1996, a very thick fog spread in the morning and the weather was very stable. Around 10 a.m., vertical column density as large as 4×10^{17} molec./cm^2 was recorded. After 0 p.m. strong wind began to blow and the vertical column density abruptly decreased to about 2×10^{16} molec./cm^2.

Another example was the observation on December 28, 1996. When the measurement began, a very thick contaminated layer covered the observing site. The measured VCD (about 1.3×10^{17} molec./cm^2) was stable. However, a strong north wind began blowing after 3 o'clock, and the contaminated layer was gradually blown out from north to south. Thirty minutes later the atmosphere above the observing site became very clear, and our measured NO_2 VCD decreased to about 4×10^{16} molec./cm^2.

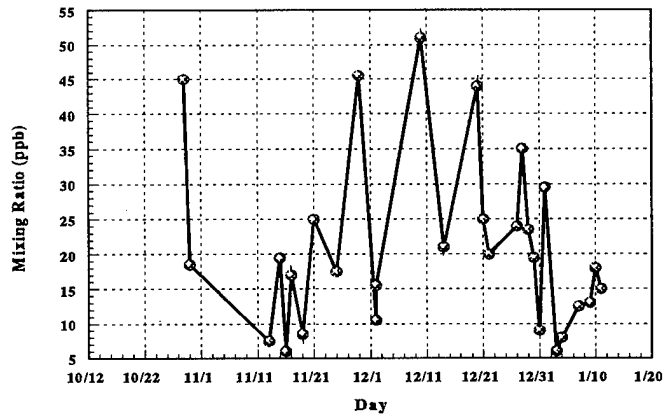

Figure 3: day-to-day variation of ground level NO_2 mixing ratio observed at the campus of Chiba university around 15:00

REFERENCES

[1] R. L. Kurucz,I.Furenlid, J.Brault, L.Testerman, "Solar Flux Atlas From 286 To 1300nm," Printed by the Office of the University Publisher, Harvard Uni., 1984.

[2] J.G.Niu, Y.Sakurada, H.Kuze, and N.Takeuchi, "Measurement of Atmospheric NO_2 Column Density with Kitt Peak Solar Flux Atlas as a Reference",Optical Review, 4. 1B. (1997)240-245.

[3] P.V. Johnston and R.L. Mckenzie, "NO_2 Observations at 45°s During the Decreasing Phase of Solar Cycle 21, From 1980 To 1987," J.Geophys.Res. 94 (1989) 3473.

[4] J.F. Noxon, E.C. Whipple, Jr., and R.S. Hyde, "Stratospheric NO_2 1. Observation Method and Behavior at Mid-Latitude," J. Geeophys. Res. 84 (1979) 5047.

[5] Y.Kondo, W.A.Matthews, A.Iwata, Y.Morita, and M.Takagi, "Aircraft Measurements of Oxides of Nitrogen along the Eastern Rim of the Asian Continent: Winter Observation," J.Atmos. Chem. 5 (1987) 37.

Atmospheric Temperature Profile Retrieval Using Multivariate Nonlinear Regression

Jungang Miao, Kun Zhao*, Georg Heygster
Institute of Environmental Physics, University of Bremen, 28334 Bremen, Germany
Tel.:+49-421-218-2584, Fax:+49-421-218-4555, E-mail:jungang@diana.physik.uni-bremen.de
* Institute of Computer Application and Simulation Technology, P.O.Box 142-213,100854 Beijing, P.R.China

Abstract – In this paper multivariate nonlinear regression was used to retrieve the atmospheric temperature profile from remotely measured microwace emissions of the atmosphere. In this method the nonlinear models for each layer of the atmosphere are at first established and the model for the whole profile is obtained by combining the layer models together. In model building we use the stepwise regression, which analyses the importance of all the predictor variables in the model and determines which of the predictor variables are allowed to enter the model under an entry and exit criterion, and finally calculates the coefficients of all the included predictor variables in the model using the least squares approach. Since the entry and exit criterion can be freely set, it is possible to find a compromise between the model accuracy and the model sensitivity to noise. Simulations were done for the region of the Weddell Sea in the southern ocean.

1 INTRODUCTION

Atmospheric temperature profiles can be retrieved from satellite radiometric measurements. The radiometers have several separated channels, and each channel measures a weighted thermal emission within a certain pressure (altitude) range. The temperature profile retrieval would ideally mean to obtain a continuous distribution of the atmospheric temperature versus altitude, but the retrieval using present radiometer measurements can be achieved only with a finite resolution, i.e. only N layer-mean temperatures of the atmosphere can be retrieved.

Because the layer number of the atmosphere is usually much larger than the channel number of the radiometer and the weighting functions of the radiometer are broad and overlap with each other, the retrieval problem is mathematically an under-determined and ill-posed problem. By *under-determined* we mean that the number of equations is less than the number of unknowns. For *ill-posed* inverse problems, the solution is not unique, and small errors in the input data induce great variations in the solution. Rodgers has summarized all the available retrieval methods [7] and discussed their error features in detail [8].

The temperature profile retrieval problem is intrinsically nonlinear due to the temperature dependence of the atmospheric transmission and the nonlinear frequency dependence of the Planck's function; it is only by simplifying assumptions that we can construct a linear problem. The method presented in this paper is statistical and makes use of the multivariate nonlinear regression based on a data set of radiosonde measurements. A similar procedure for the retrieval of humidity profiles has recently been proposed in [2].

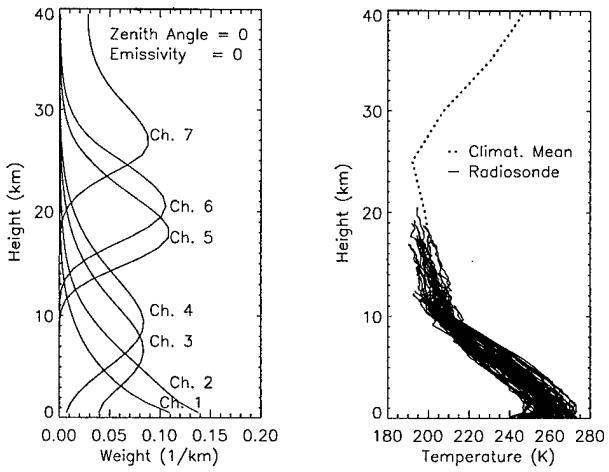

Figure 1: The weighting functions of SSM/T1 channels and the temperature profiles collected in the Weddell See in July 1992.

2 DATA SET

2.1 Radiosonde Data

The radiosonde profiles of temperature, pressure and humidity were collected by R/V Polarstern in the Weddell sea in July, 1992, and include 78 radiosonde ascends reaching 15–20 km (see Fig. 1).

The radiosonde measurements are with high vertical resolutions from a few meters to a few tens of meters. In the model calculation the profiles are smoothed to a resolution of 1 km and extrapolated to the climatological mean from their highest measurement points up to the altitude of 40 km.

2.2 Simulated Brightness Temperatures of SSM/T1

The Special Sensor Microwave/Temperature (SSM/T1) is on board the spacecraft of the Defense Meterological Satellite Program (DMSP). It operates in the molecular oxygen resonance band at 50–60 GHz and has 7 channels with its typical weighting functions shown in Fig. 1.

The simulated radiometer measurements corresponding to the radiosonde temperature profiles are calculated using a forward radiative transfer model, which is developed in the Institue of Environmental Physics of the University of Bremen. According to the radiative transfer theory, the measured brightness temperature of channel i is

$$T_i(\nu,\theta) = T_u(\nu,\theta) + T_e(\nu,\theta)e^{-\tau(\nu,\theta)} + (1-\varepsilon_s(\nu,\theta))T_d(\nu,\theta)e^{-\tau(\nu,\theta)}, \quad (1)$$

0-7803-3836-7/97/$10.00 © 1997 IEEE

where T_u and T_d are the up-welling and down-welling radiation from the atmosphere respectively, T_e is the radiation from the surface, and τ is the atmospheric opacity at frequency ν and zenith angle θ. T_u, T_d, and τ depend on the relative humidity distributions too [3], but here the climatological mean of the relative humidity profile was used instead of the actual relative humidity profiles due to the restriction of the forward radiative transfer model. By this simulation the surface emissivity ε_s is set to zero, therefore the simulated measurement includes only the contributions from the atmosphere,

$$T_i(\nu,\theta) = T_u(\nu,\theta) + T_d(\nu,\theta)e^{-\tau(\nu,\theta)}. \quad (2)$$

The data base then includes 78 temperature profiles with a resolution of 1 km from 0 to 40 km and 78 groups of brightness temperatures at the seven channels of SSM/T1.

3 RETRIEVAL USING MULTIVARIATE NONLINEAR REGRESSION (MNR)

3.1 Problem and Methodology

In order to retrieve the temperature profile we need to find the relationship between the incremental temperature profile vector, $\Delta\mathbf{t}$ $(= \mathbf{t} - \bar{\mathbf{t}})$, and the corresponding incremental brightness temperature vector, $\Delta\mathbf{T}$ $(= \mathbf{T} - \bar{\mathbf{T}})$, i.e.

$$\Delta\mathbf{t} = \mathbf{F}(\Delta\mathbf{T}). \quad (3)$$

Here, $\mathbf{t}$ ($\bar{\mathbf{t}}$) and $\mathbf{T}$ ($\bar{\mathbf{T}}$) are the (climatological mean) temperature profile vector and the corresponding (mean) brightness temperature vector respectively.

As mentioned above, estimating $\Delta\mathbf{t}$ using $\Delta\mathbf{T}$ is difficult due to the low number of radiometer channels and the significant overlapping between the channel weighting functions, which leads to a significant correlation between the channel measurements and finally loss of information. It is important to retrieve the profile with reasonable resolution, here from experience a resolution of 1 km is selected. The under-determined problem is transformed into a series of over-determined problems by assuming that each layer-mean temperature Δt_i, i.e. the ith element of the incremental temperature profile vector, is a function of the incremental brightness temperature vector, $\Delta\mathbf{T}$. That is

$$\begin{aligned} \Delta t_i &= f_i(\Delta\mathbf{T}) \\ &= \bar{f}_i(\Delta T_1, \Delta T_2, ..., \Delta T_M) + e_i, \end{aligned} \quad (4)$$

and $i = 1, ..., N$. N is the total layer number of atmosphere, and M $(= 7)$ is the number of SSM/T1 channels. e_i is the error introduced by the model $\bar{f}_i$ of layer i. The model of $\Delta\mathbf{t}$ can be obtained by combining all the layer models together.

3.2 Nonlinear Model

The relationship between Δt_i and the elements, ΔT_1, ΔT_2,...,ΔT_M of vector $\Delta\mathbf{T}$ is nonlinear. By analyzing the data set described in Sec. 2, it is found that a 2nd-order polynomial model is appropriate (see e.g. Fig. 2). The model of Δt_i is then constructed in the following full quadratic form:

$$\bar{f}_i = \beta_{i0} + \sum_{j=1}^{M} \beta_{ij}\Delta T_j + \sum_{j=1,k=j}^{M} \gamma_{ijk}\Delta T_j \Delta T_k. \quad (5)$$

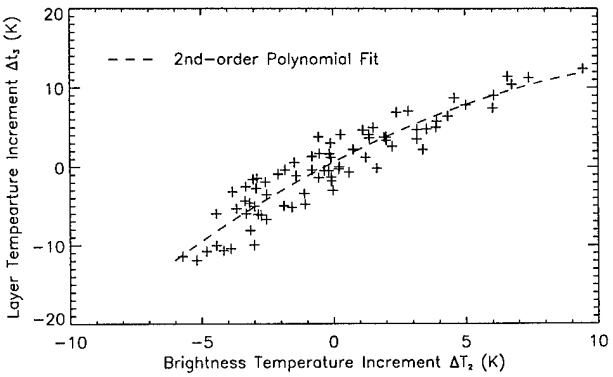

Figure 2: Scatter plot of Δt_3 vs. ΔT_2 and the second order polynomial fit.

3.3 Model Building Using Stepwise Regression

Equation (5) is the general form of the model which describes the relationship between the layer-mean temperature Δt_i and the predictor variables, ΔT_j and $\Delta T_j \Delta T_k$. Needless to say, all predictors do not possess the same importance level to the Δt_i, and strong multicollinearities exist among some of the predictor variables. It is believed that a subset of these predictors may be entirely adequate for the model. The stepwise regression is well suited for the selection of this subset of predictors [1, 6].

The stepwise regression procedure proceeds in a series of steps, each step consists of entering one predictor variable if

$$F_to_enter > F_to_enter_min \quad (6)$$

and deleting a variable if

$$F_to_exit < F_to_exit_max. \quad (7)$$

F represents F-ratio value. $F_to_enter_min$ and $F_to_exit_max$ correspond to importance levels $\alpha_to_enter_min$ and $\alpha_to_exit_max$ respectively and they can be preestablished, so the number of predictor variables which enter the final model equation can be controlled.

In the simulation we have used the stepwise regression package developed by the Beijing Institute of Computer Application and Simulation Technology, which uses a compact transformation method in the algorithm. This package calculates the coefficients β and γ in (5) together with the orders of importance of the included predictor variables.

4 CHARACTERISTICS OF THE MNR METHOD

The statistical method has the advantage that the relationship between the dependent variables and the independent variables can be analyzed and predictions can be made even if the intrinsic physical process is unknown. The MNR method makes the prediction more accurate with the introduction of the nonlinear terms and the modeling for every layer. Fig. 3 shows an example of a temperature profile retrieval using three different models produced under three different entry and exit importance levels. Satisfactory retrievals can be achieved for all 3 models. But it should be noticed that in the simulation the surface emission has been removed from all channels.

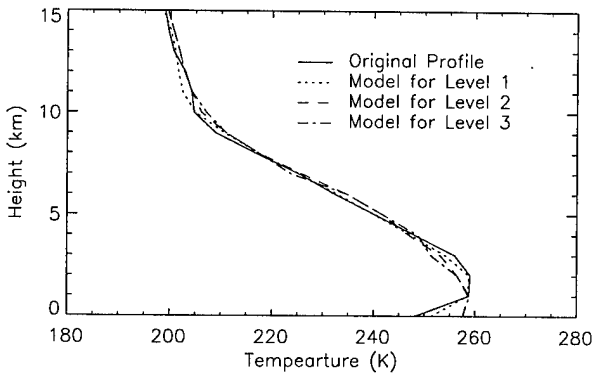

Figure 3: Comparison of the retrieved temperature profiles using 3 models produced under 3 different entry and exit levels of importance

Of course, the more nonlinear terms the model includes, the more accurate the retrieval will be, but at the same time, the more sensitive the model is to noise. By controlling the entry and exit importance level we can control the terms introduced into the model and as a result the model accuracy and sensitivity to noise. Fig. 4 shows the distributions of the model accuracy and the sensitivity-to-noise versus altitude; the sensitivity test was done by adding a zero-mean Gaussian noise with a standard deviation of 0.6 K to each ΔT_i.

It is clear that a compromise between the model accuracy and its sensitivity to noise can be done by controlling the entry and exit level of importance, and even a combination of layer models produced under different entry and exit criteria may give the best results, in considering the irregular distribution of the sensitivity-to-noise versus altitude.

5 CONCLUSIONS

We have demonstrated the feasibility of using MNR method in retrieving temperature profiles. The advantage of the method is the possibility to make compromises between the accuracy and the sensitivity-to-noise of the model and to analyze channel contributions using the importance order given by the stepwise regression procedure.

The *in situ* radiosonde data set plays an important role in the model building. It should be as complete as possible in order to describe all the possible variations of the temperature profile in the time period and region of interest. In this simulation the simulated brightness temperatures include only the contribution from the atmosphere, therefore a procedure to eliminate the influences of other factors, such as ground surface and clouds, must be done for the satellite SSM/T1 brightness temperatures before retrieving temperature profiles using the models obtained from this simulation.

ACKNOWLEDGMENTS

K.Z. thanks Prof. Kammeyer for his support to this work during K.Z.'s stay at the University of Bremen from Oct. 1995 to Mar. 1996.

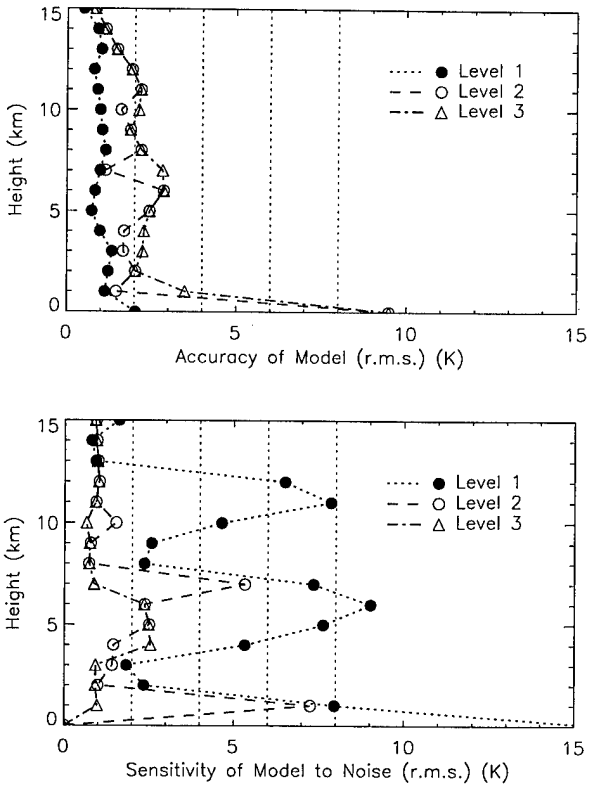

Figure 4: Accuracies (top) and sensitivities to noise (bottom) of 3 models produced under 3 different entry and exit levels of importance.

REFERENCES

[1] Affi, A.A., S.P. Azen: *Statistical Analysis, A Computer Oriented Approach*, Academic Press, Second Edition, London, 1979

[2] Braswell, W. D., R. W. Spencer: A Statistical Approach for Retrieval of Humidity Profiles from SSM/T2: Comparison to a Physical Retrieval Method; *Proceeding of Eighth Conference on Satellite Meteorology and Oceanography*, pp15–18, Atlanta, Georgia, Feb. 1996

[3] Brussaard, G., P.A. Watson: *Atmospheric Modeling and Millimeter Wave Propagation*, Chapman & Hall, 1995

[4] De Veaux, R.D., A.C. Gordon, J.C. Comiso, N.E. Bacherer: Modeling of Topographic Effects on Antarctic Sea Ice Using Multivariate Adaptive Regression Splines; *J. Geophys. Res.*, vol. 98, NO. C11, pp20,307-20,319, Nov. 15, 1993

[5] Miao, J., T. Markus, B. Burns: Retrieval of Temperature Profiles Over Sea Ice with Multi-sensor Analysis: Combination of the DMSP's SSM/I, OLS, and SSM/T1 Sensors ; *Proceeding of IGARSS'95*, pp1142-1144, Firence, Italy, July 1995

[6] Murphy, A.H, R.W. Katz (eds): *Probability, Statistics, and Decision Making in the Atmospheric Sciences*, Westview Press, 1985

[7] Rodgers, C.D.: Retrieval of Atmospheric Temperature and Composition from Remote Measurements of Thermal Radiation; *Rev. Geophys. Space Phys.*, vol. 14, NO. 4, pp609-624, Nov. 1976

[8] Rodgers, C.D.: Characterization and Error Analysis of Profiles Retrieved from Remote Sounding Measurements; *J. Geophys. Res.*, vol. 95, NO. D5, pp5587-5595, Apr. 20, 1990

Retrieval of Total Water Vapor in Polar Regions Using SSM/T2 Channels

Jungang Miao, Norbert Schlüter, Georg Heygster
Institute of Environmental Physics, University of Bremen, 28334 Bremen, Germany
Tel.:+49-421-218-2584, Fax:+49-421-218-4555, E-mail: jungang@diana.physik.uni-bremen.de

Abstract – A method to retrieve the total water vapor in the cloudless atmosphere using SSM/T2 channels is proposed based on a unique property of three contiguous channels situated on the flank of the water vapor absorption line at 183.31 GHz. One of its advantages is its independence to the surface emission, which is the main disturbing factor in retrieving atmospheric parameters from passive satellite measurements. Due to the high sensitivity of the SSM/T2 channels to water vapor, this method is suitable to the total water vapor retrieval for dry polar atmospheres. An algorithm is constructed for austral winter cases through model simulation using radiosonde profiles.

1 INTRODUCTION

The Total Water Vapor (TWV) over global ocean has been successfully retrieved using radiometric measurements at the weak water vapor absorption line near 22.235 GHz [4]. But the algorithm fails in polar regions due to the high and diverse surface emissions and the low water vapor burden of the atmosphere. The variations of surface parameters (the surface temperature, emissivities of different ice types, and the distribution of different ice types within the antenna footprint) are so large that a uniform and cold background, which is the prerequisite of the SSM/I algorithms using 22.235 GHz channel, is no longer present. Besides, for dry atmospheres (less than 10 kg/m^2) the SSM/I algorithm can only be used with large errors even over open oceans.

Since the water vapor absorption line at 183.31 GHz is much stronger than the line at 22.235 GHz, a channel near 183.31 GHz is much more sensitive to atmospheric water vapor than that near 22.235 GHz. The water vapor sounder SSM/T2 aboard the DMSP satellites has 5 channels with center frequencies at 91.655, 150.0, 183.31 ± 7, 183.31 ± 3, and 183.31 ± 1 GHz respectively, which are called here channels 1 to 5 consecutively. For the SSM/T2 channels the atmospheres in low and middle latitudes are sufficiently opaque, so that water vapor profile can be retrieved using the radiometric measurements. For dry atmospheres over ocean the total water vapor can be retrieved if the sea surface temperature is known [6].

Although the atmospheric emission contributes more to the SSM/T2 channels than to the SSM/I 22.235 GHz channel, the surface emission is still disturbing the retrieval of water vapor in polar regions, where the water vapor burden is low. It distributes from less than 0.5 kg/m^2 to a few kilogram per square meter near the edge of sea ice [5]. A retrieval method that takes account of the surface emission must suffer from the scarcity of *in situ* observations of surface emissivities of different ice types.

Through analyses of SSM/T2 data and calculations using a simplified radiative transfer model it is found that the ratios $\frac{T_3-T_4}{T_4-T_5}$ and $\frac{T_2-T_3}{T_3-T_4}$ are proportional to the TWV in the ranges of 0–2.0 kg/m^2 and 0–8.0 kg/m^2 respectively and that the ratios are almost independent of the surface emission [3]. Here T_i is the brightness temperature of the ith channel of SSM/T2. This unique feature of the ratios allows to construct an algorithm of TWV without considering the surface parameters. In this paper we examine this point through both mathematical derivation and model simulation using radiosonde profiles, with the goal of developing a retrieval algorithm of TWV in polar regions.

2 A RETRIEVAL METHOD WHICH IS INDEPENDENT OF GROUND SURFACE CONDITIONS

2.1 Radiative Transfer Equation in the Form of Guissard and Sobieski

Guissard and Sobieski [2] presented the radiative transfer equation in the form of the equation of an attenuating atmosphere at constant temperature, above a lossy dielectric rough surface, under the specular approximation, but including corrections for the atmospheric temperature profile,

$$T_b(\theta) = m_p T_s - (T_0 - T_c)(1-\varepsilon_s)e^{-2\tau_0 \sec\theta}. \quad (1)$$

Here, $T_b(\theta)$ is the brightness temperature measured by the radiometer at the zenith angle of θ. T_s, T_0, and T_c represent the ground surface temperature, the ground level air temperature and the cosmic background temperature respectively. ε_s is the surface emissivity and τ_0 is the total opacity of the atmosphere at nadir direction. m_p is of the order of unity and given by:

$$m_p = 1 + [(1-\varepsilon_s e^{-\tau_0 \sec\theta})\frac{T_0 - T_s}{T_s} - \frac{I_p}{T_s}], \quad (2)$$

with

$$I_p = I_1 + (1-\varepsilon_s)I_2 e^{-2\tau_0 \sec\theta}. \quad (3)$$

I_1 and $I_2 e^{-\tau_0 \sec\theta}$ are correction terms for the upwelling and downwelling emissions of the atmosphere respectively and have the following forms:

$$I_1 = -\int_0^\infty [1 - e^{-\tau(z,\infty)\sec\theta}]\frac{dT(z)}{dz}dz, \quad (4)$$

$$I_2 e^{-\tau_0 \sec\theta} = -\int_0^\infty e^{-\tau(0,z)}[1 - e^{-\tau(z,\infty)\sec\theta}]\frac{dT(z)}{dz}dz. \quad (5)$$

$\tau(z_1, z_2)$ is the atmospheric opacity between two levels of z_1 and z_2.

2.2 Radiative Transfer Equation for Simplified Case: One Layer Atmosphere with Constant Temperature

For the simple case, where the atmosphere would be at constant temperature T_0 and $T_0 \approx T_s$, the quantity m_p reduces to

0-7803-3836-7/97/$10.00 © 1997 IEEE

unity and (1) simplifies to

$$T_b(\theta) = T_s - (T_0 - T_c)(1 - \varepsilon_s)e^{-2\tau_0 \sec\theta}. \quad (6)$$

This is a good approximation if the atmosphere is nearly transparent.

2.3 3-Channel Method for Total Water Vapor, Independent of Surface Conditions

If 3 channels, with measured brightness temperatures of t_1, t_2 and t_3, locate on the flank of a water vapor absorption line adjacently and the ground surface presents the same emissivities to the 3 channels, then using (6), the Ratio of Brightness Temperature Differences (RBTD)

$$\frac{t_1 - t_2}{t_2 - t_3} = \frac{e^{-2\tau_{20}\sec\theta} - e^{-2\tau_{10}\sec\theta}}{e^{-2\tau_{30}\sec\theta} - e^{-2\tau_{30}\sec\theta}} \quad (7)$$

is independent of the ground surface emission. τ_{i0} is the total opacity of the atmosphere for channel i. This is the case of dry antarctic continental atmospheres for SSM/T2 channels.

But the atmosphere over sea ice can be so humid that compensations must be applied. If the biases b_{12} and b_{23} are precisely evaluated, even for atmospheres with low transmission the Ratio of Compensated Brightness Temperature Differences (RCBTD)

$$\frac{t_1 - t_2 - b_{12}}{t_2 - t_3 - b_{23}} \sim W \quad (8)$$

is also independent of ground surface emission and relates only to the atmospheric absorptions, which is proportional to the TWV. W represents TWV.

2.4 Bias b_{ij}

Using (1), b_{ij} is easy to obtain:

$$b_{ij} = I_{ip} - I_{jp} + \varepsilon_s(T_0 - T_s)(e^{-\tau_{i0}\sec\theta} - e^{-\tau_{j0}\sec\theta}) \quad (9)$$

Usually, T_0 is approximately equal to T_s and I_2 is small, then

$$b_{ij} \approx \int_0^\infty [e^{-\tau_i(z,\infty)\sec\theta} - e^{-\tau_j(z,\infty)\sec\theta}]\frac{dT(z)}{dz}dz, \quad (10)$$

which depends only to the atmospheric parameters.

2.5 General Behavior of $t_1 - t_2$ against $t_2 - t_3$

In order to better explain the retrieval method, we observe Fig. 1, in which the channels 2, 3 and 4 of SSM/T2, with center frequencies at 150.0, 183.31 ± 7 and 183.31 ± 3 GHz respectively, are used as the three adjacent channels mentioned in Sec. 2.3. In model calculation using MWMod (see Sec. 3.1) it is assumed that the surface emissivities at 150.0 and 183.31 GHz are equal, this should be reasonable for snow covered ice in polar regions. Analogous to the principal component transformation, the two variables of $t_1 - t_2$ and $t_2 - t_3$ constitute a two dimensional space, in which the influences of TWV, here represented by W, and surface emission (related to both surface emissivity and temperature) are easy to separate. After the biases are exactly compensated, TWV can be related to RCBTD, as a first order approximation, in a simple logarithmic form.

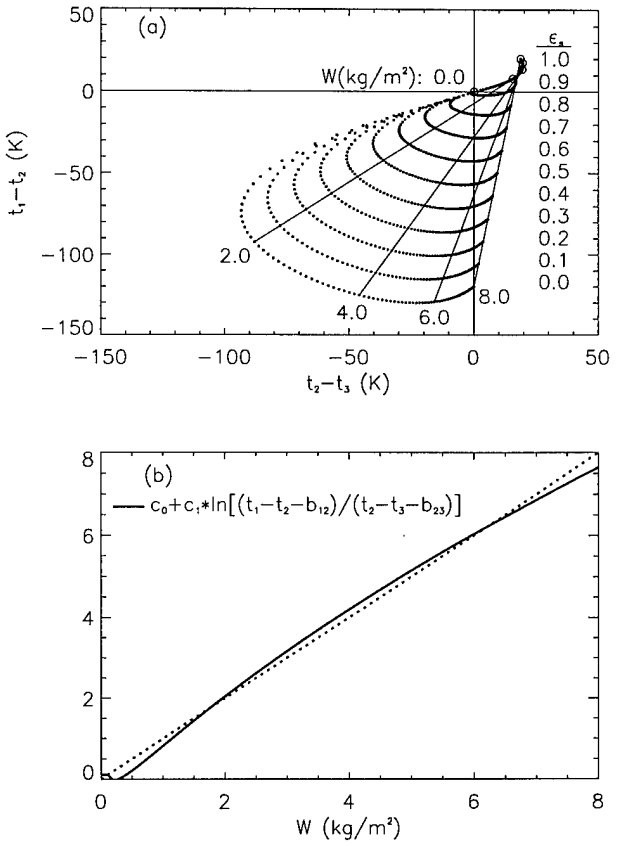

Figure 1: General behavior of $t_1 - t_2$ versus $t_2 - t_3$: (a) Point $(t_2 - t_3, t_1 - t_2)$ moves with W (dotted lines) and ε_s (solid lines) in nearly orthogonal directions, the circles represent the biases (b_{23}, b_{12}) for different W. (b) A simple logarithmic relation between TWV and RCBTD.

3 ALGORITHM CONSTRUCTION THROUGH MODEL SIMULATION USING RADIOSONDE PROFILES

3.1 The Radiative Transfer Model and Radiosonde Data

The radiative transfer model MWMod developed by Simmer calculates the microwave radiance in a planar-stratified, vertically inhomogeneous atmosphere [1]. The gaseous absorption of oxygen and water vapor is computed with Liebe's absorption model. The absorption and scattering of non-precipitating clouds is modeled by the Rayleigh-theory, precipitation is considered by the Lorenz-Mie-theory.

The radiosonde data set is a collection of 450 ascends from R/V Polarstern in 1992 in the Weddell sea and from the Antarctic station, Georg von Neumayer (70.37 S, 8.22 W), in the period of 1990–1994, all in June and July. Data analyses show that the surface air temperature ranges from 0 °C near ice edges to −45 °C over shelf ice and that 88 % of the profiles are with TWV less than 5.0 kg/m^2. For lack of observations of ice surface temperatures, the surface air temperatures were used as the ice surface temperatures in the model calculations.

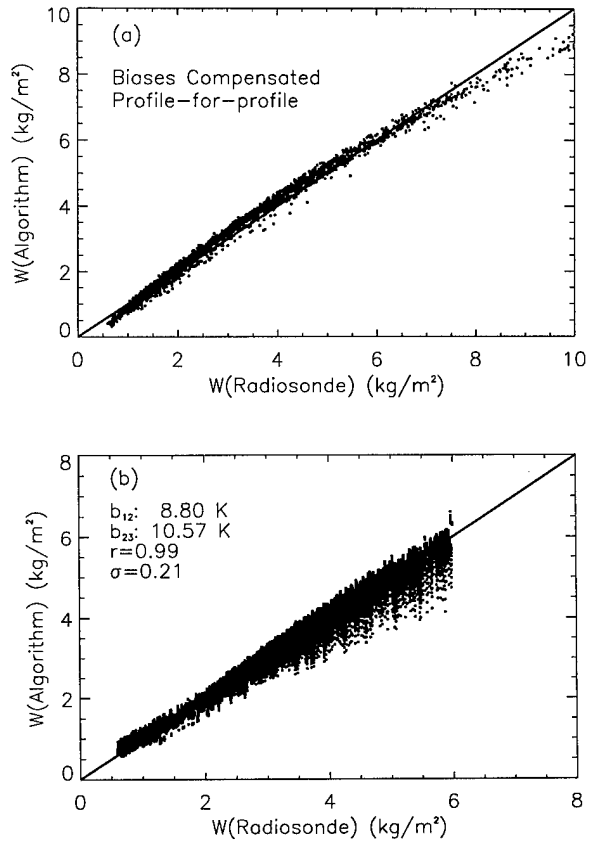

Figure 2: Algorithm using channels 2, 3, and 4 of SSM/T2: biases are compensated (a) profile-for-profile, (b) using average values for all profiles.

3.2 Construction of the RCBTD Algorithm

According to (7) and (8), the retrieval algorithm is constructed in the following form,

$$W \sec\theta = c_0 + c_1 \ln \frac{t_1 - t_2 - b_{12}}{t_2 - t_3 - b_{23}}. \qquad (11)$$

In polar region, channels 2, 3 and 4 of SSM/T2 are usually used. But, when the atmosphere is very dry, for example, on the Antarctic plateau, channels 3, 4, and 5 are selected, in order to improve the retrieval accuracy. In building the algorithm, simple linear regression was used. The regression data set consists of TWVs from radiosonde profile analyses and from SSM/T2 brightness temperatures which are calculated using MWMod for the radiosonde data set with surface emissivity from 0.56 to 0.88 and zenith angles from 1.7° to 47.26°.

In Table 1, the selected and regressed algorithm parameters are presented. The biases are selected as constant values considering that a profile-for-profile compensation of the biases is in practice impossible, although it would ensure a much higher retrieval accuracy as can be seen in Fig. 2. Nevertheless the algorithm achieved the r.m.s. accuracies of 0.09 and 0.21 kg/m^2 for $W \cdot \sec\theta$ in the ranges of 0.0–1.5 and 1.5–6.0 kg/m^2 respectively.

Table 1. Parameters of the RCBTD Algorithm

$W \sec\theta$(kg/m^2)	Channels	c_0	c_1	b_{12}	b_{23}
0.0–1.5	3, 4, 5	0.66	1.16	7.18	9.50
1.5–6.0	2, 3, 4	2.03	3.01	8.80	10.57

4 DISCUSSIONS

In this paper we have proposed a method to retrieve TWV using SSM/T2 channels and constructed the corresponding algorithm for austral winter in the Antarctic through model simulation using radiosonde profiles. This algorithm is insensitive to changes of the surface emission. But, when ε_s approaches 1, this method fails, because in this case the change of the contribution of the atmosphere to the measured brightness temperature would be perfectly compensated by that of the ground surface. By large ε_s, e.g. >0.9, large retrieval errors would appear, if the influences of surface emissions were not taken into account. Fortunately, most part of polar regions are covered with snow, the surface emissivities over 150 GHz should not exceed 0.9.

Another point is the better compensation of biases b_{12} and b_{23}. Although a profile-for-profile compensation is in practice impossible, an iteration procedure can improve retrieval accuracy by taking account of the relationship between biases and TWV and of the mean distribution of the water vapor over ice.

Validation and sensitivity test of the algorithm are being undertaken, through model simulations using independent radiosonde data set and through comparisons of the retrieved TWVs from satellite SSM/T2 data and those from coincident radiosonde measurements.

ACKNOWLEDGMENTS

The authors thank Prof. K. Künzi for his support to this work and A. Förster for his help in collecting the radiosonde data.

REFERENCES

[1] Fuhrhop, R., T. Grenfell, G. Heygster, K.-P. Johnsen, P. Schlüssel, M. Schrader, C. Simmer: A Combined Radiative Transfer Model for Sea Ice, Open Ocean, and Atmosphere; *Radio Science*, 1997, in press

[2] Guissard, A., P. Sobieski: A Simplified Radiative Transfer Equation for Application in Ocean Microwave Remote Sensing; *Radio Science*, Vol. 29, No. 4, pp881–894, July-August 1994

[3] Miao, J.: Retrieval of Atmospheric Parameters with SSM/T2 Data in Polar Regions; *Report to the Institute of Environmental Physics, University of Bremen*, Sep. 1996

[4] Schlüssel, P., W.J. Emery: Atmospheric Water Vapor over Oceans from SSM/I measurements; *Int. J. Remote Sensing*, pp753–766, 1990

[5] Schwerdtfeger, W: *Weather and Climate of the Antarctic*, Elsevier, 1984

[6] Wang, J.R., T.T. Wilheit: Retrieval of Total Precipitable Water Using Radiometric Measurements Near 92 and 183 GHz; *Journal of Applied Meteorology*, Vol.28, No.2, Feb. 1989

IGARSS'97

1997 International Geoscience and Remote Sensing Symposium

03-08 August 1997

Singapore International Convention & Exhibition Centre

Technical Program

Interactive Area 5: Clouds and Precipitation

Radiance thresholds and texture parameters for Antarctic surface classification

A. Baraldi, G. P. Meloni and F. Parmiggiani
IMGA-CNR, via Gobetti 101, 40129 Bologna (Italy)
ph.+39-51-639 8008 fax +39-51-639 8132 e-mail: baraldi@aliseo.imga.bo.cnr.it

Abstract – A sequence of AVHRR images is investigated in order to obtain information about sea ice distribution in the Ross Sea. A supervised classifier, based on decision rules in AVHRR NearIR (2) and thermal (3 and 4) channels, is tuned to the given data set to extract pixels belonging to classes: a) sea; b) multiyear ice (ice shelves and bergs); c) first season ice types (floes and pack); and d) clouds (thin/thick clouds, water clouds and ice clouds). Pixel-based classification is affected by underestimation of ice clouds due to interference of multiyear ice and pack. To reduce ice/cloud misclassification, an alternative classification approach exploiting textural information is attempted. Firstly, image segmentation is performed by means of a three-stage procedure consisting of: a) contour detection and segment extraction; b) region growing; and c) clustering of segment-based statistics by means of a neural network model. Secondly, three textural features (mean, recursivity and contrast) are extracted as within-segment statistics. Results show that these segment-based textural parameters cannot be clustered in the measurement space in line with their information classes, i.e., they cannot be effectively employed in the classification scheme to reduce the amount of interference between multiyear ice/first season ice types and ice clouds.

INTRODUCTION

The Advanced Very High Resolution Radiometer (AVHRR), installed on NOAA's satellites, plays an important role in monotoring large-scale polar sea ice coverage because: i) it provides nearly global coverage of Antarctica at least twice daily at a resolution of 1.1 km; and ii) its 5 spectral channels (1: red, 2: near infrared, 3: middle infrared, 4 and 5: thermal infrared) can be employed to classify clouds and ice.

Starting from the pixel-based Antarctic sea ice mapping scheme proposed in [1], which requires the continent information to be masked, our goal is to employ a set of 10 AVHRR images, acquired between November 1994 and February 1995 over the Ross Sea area, to extract the following surface classes: a) sea; b) multiyear ice (in this paper this class includes ice shelves and bergs); c) first season ice types constituting marginal ice zones (in this paper this class includes floes and pack); and d) clouds (thin/thick clouds, water clouds and ice clouds). In the first part of this paper, a pixel-based Antarctic ice/cloud classification scheme is proposed. Since the per-pixel mapping scheme may misclassify ice clouds due to interference with multiyear ice, the second part of this paper investigates whether textural parameters can be employed to improve inter-class separability.

PER-PIXEL CLASSIFIER

AVHRR image preprocessing, performed by means of the commercial software package TeraScan (SeaSpace Co., San Diego, CA), consisted of the following steps: i) extraction, of a window, 500×500 pixel size, over the area of Terra Nova Bay; ii) radiometric calibration; iii) geographical registration; and iv) land masking. An expert photointerpreter selected the training sets which were mapped in the multidimensional AVHRR measurement space to detect spectral thresholds. Figs. 1 and 2 show the multispectral thresholds retrieved from representative training patterns. AVHRR channels 2, 3 and 4 were selected, in line with [1]. Channel 2 is preferred to channel 1 because the former is less affected by atmospheric scattering; channel 4 is preferred to channel 5 because the latter is not employed onboard of all NOAA satellites. It is worth noting that in Fig. 1 the lower right decision area shows unsatisfactory separation between multiyear ice, first season ice types and cold clouds. Vice versa, Fig. 2 allows a neat separation between clouds, multiyear ice and pack. Fig. 3 shows channel 2 of one multispectral AVHRR image belonging to the test set (the meaning of the depicted rectangles will be described further in the text) and Fig. 4 shows a classification map obtained when the proposed pixel-based classification thresholds are applied to Fig. 3.

The proposed pixel-based Antarctic ice/cloud classification scheme exploiting AVHRR images provides good performances when its multispectral thresholds are set correctly, as shown in Fig. 4. Moreover, its low computation time makes its exploitation feasible in real-time applications [1]. However, since the decision thresholds have been finely tuned, the robustness of the classifier remains acceptable no longer than two months, because of sensor drifts (mainly involving channels 1 and 2, the drift being quantified in several percent each year [2]) and seasonal changes in Antarctic scenes. A second drawback of the proposed pixel-based classification scheme is that it may assign cloud pixels to multiyear ice or even to pack when cold clouds, that generally feature channel 4 radiances (temperatures) lower than those of both continental and sea ice (see Fig. 2), fail to satisfy this condition as shown in the upper right corner of Fig. 3. This anomalous situation typically develops during the colder months

0-7803-3836-7/97/$10.00 © 1997 IEEE

(March-November) when clouds are involved in the warm tropospheric inversion [1]. Additional problems are faced by the classifier in the detection of thin clouds. Finally, specular reflection of direct sun radiance of sea, snow and ice, high value of view angle, and low sun elevation may cause radiance variation causing misclassifications due to the insufficient robustness of non-adaptive multispectral thresholds.

TEXTURE PARAMETER ASSESSMENT

To improve system performance, exploitation of textural information computed from Gray Level Cooccurrence Matrices (GLCMs) was investigated in [3], where GLCMs are computed from fixed-size squared moving windows whose sides must be smaller than the smallest detail of interest. Recent developments in contour/texture detection algorithms employ banks of oriented Gabor filters [4]. Starting from non-connected contours, closed segments can be extracted and artifacts removed according to a robust procedure described in [5]. Overall, the segmentation procedure consists of the following steps: a) non-connected contour detection; b) closed segment extraction; c) artifacts removal by means of a region growing algorithm; and d) clustering of segment-based statistics by means of a neural network model. This process is user friendly, requiring a small set of user-defined parameters, and robust (the same processing model can be applied to monochromatic, multispectral, optical and SAR image segmentation). An example of the segmentation procedure applied to Fig. 3 is shown in Fig. 5. At this stage, the expert photointerpreter selected the rectangular windows shown in Fig. 1. Every segment belonging to Fig. 5 that underlies one of the rectangles shown in Fig. 1 is provided with an information label. Then, one Upper triangular GLCM (UGLCM) is computed from each spectral layer of every three-dimensional image segment [5]. Finally, three isotropic textural parameters, mean, recursivity and contrast [6], are extracted from each UGLCM (i.e., each segment is texturally represented by a three-dimensional mean, a three-dimensional contrast vector and a three-dimensional recursivity vector). It is important to stress that segment-based extraction of UGLCM textural parameters is functionally feasible because, with respect to segment size, texture parameters were almost insensitive (in line with [7], where texture parameters were almost insensitive with respect to window size). The textural separability of multiyear ice/firt season ice types with respect to clouds is shown in Figs. 6 to 8. Neither in these figures nor in the equivalent pictures obtained from the remaining spectral compenents these textural parameters ever feature enough sensitivity to separate ice/pack from clouds. Similar unsatisfactory results are obtained when either multi-spectral recursivity or contrast vectors are mapped in combination with the segment-based multi-spectral mean values.

CONCLUSIONS

A supervised pixel-based classification scheme providing ice/cloud labeling of AVHRR images over Antarctica is presented. This scheme is affected by underestimation of ice clouds due to both occasional and seasonal spectral signature overlaps occurring between multiyear ice/first season ice and ice clouds. To reduce ice/cloud misclassification, an alternative classification approach exploiting segment-based textural information is attempted. Segments are detected starting from a bank of oriented Gabor filters working in a joint space/spatial frequency domain. Three isotropic and uncorrelated textural features (second-order recursivity and first-order contrast and mean), are extracted as within-segment statistics. We conclude that these textural parameters cannot be clustered in the measurement space in line with their information classes, i.e., they cannot be effectively employed in the supervised classification scheme to increase information separability between multiyear ice/first season ice types and ice clouds.

REFERENCES

[1] G. Zibordi and M. L. Van Woert, "Antarctic sea ice mapping using the AVHRR," *Remore Sens. Environ.*, vol. 45, pp. 155-163, 1993.

[2] Teillet R.M., Slates P.N., Ding Y.,Santer R.P., Jackson R.D., Moran M.S., "Three methods for the absolute calibration of the NOAA AVHRR sensor in-flight." *Remote Sensing of Environment.*, 31 (1990), 105-120.

[3] I. Canossi, A. Baraldi, G. Zibordi ed F. Parmiggiani, "Integrazione di analisi spettrale e tessiturale nella classificazione di immagini AVHRR dell'Antartide," *Atti del V Convegno Nazionale AIT*, Milano, Maggio 1992, pp. 405-416.

[4] A. Baraldi and F. Parmiggiani, "Combined detection of intensity and chromatic contours in color images," *Optical Engineering*, vol. 35, no. 5, pp. 1413-1439, May 1996.

[5] A. Baraldi and F. Parmiggiani, "Segmentation of SAR images by means of Gabor filters working at different spatial resolution," *Proc. IGARSS '96*, Lincoln, NB, May 1996, vol. 1, pp. 709-713.

[6] A. Baraldi and F. Parmiggiani, "An investigation of textural characteristics associated with gray level cooccurence matrix statistical parameters," *IEEE Trans. Geosci. Remote Sensing*, vol. 33, no. 2, pp. 293-304, March 1995.

[7] M. E. Shokr, "Evaluation of second-order texture parameters for sea ice classification from radar images," *J. of Geophysical Research*, vol. 96, no. c6, pp. 10.625-10.640, June, 1991.

Fig. 1

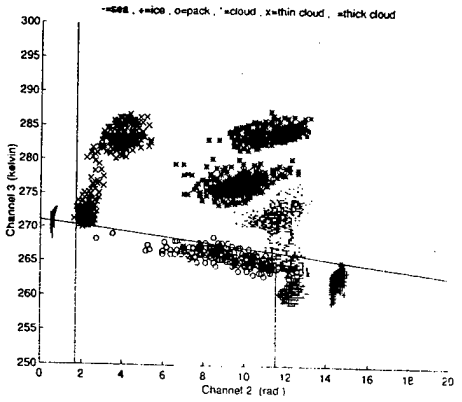

Fig. 2

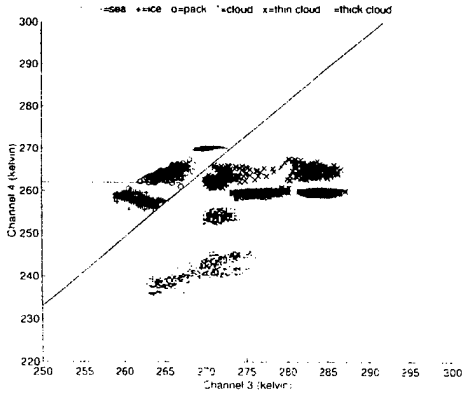

Fig. 3

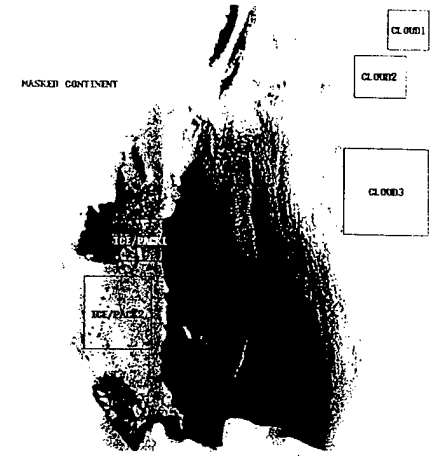

Fig. 4

Fig. 5

Fig. 6

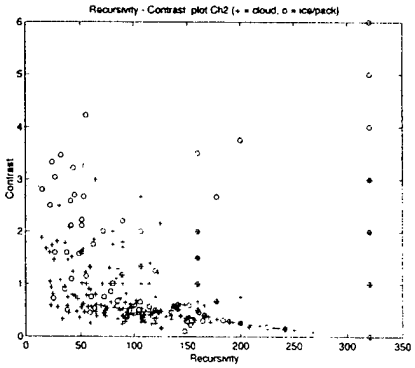

Fig. 7

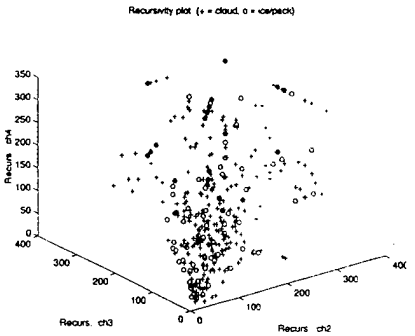

Fig. 8

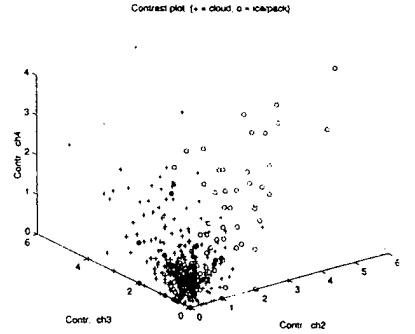

Radar and Microwave Radiometer Sensing of Typhoon Ryan

Maia L. Mitnik and Leonid M. Mitnik
Pacific Oceanological Institute, FEB RAS, Vladivostok 690041, Russia
Tel: 7 4232-312-854/Fax: 7-4232-312-573/E-mail: mitnik%dan32@poi.marine.su

Ming-Kuang Hsu
Department of Oceanography, National Taiwan Ocean University, 202 Keelung, Taiwan, R.O.C.
Tel: 886-2-462-2192, ext 6313/Fax: 886-2-462-3073/E-mail: hsumk@ind.ntou.edu.tw

ABSTRACT

Real aperture radar (RAR) and microwave images of typhoon Ryan (9514) obtained from Okean-8 and DMSP satellites are analyzed to reveal the fine details of surface wind and precipitation fields. Evolution of precipitation patterns is considered using the SSM/I data.

INTRODUCTION

The scarcity of conventional meteorological observations over the vast tropical oceans hinders improving the results of both analysis and numerical predictions of tropical cyclones (TC). Microwave radiometer and radar techniques are the best suited for TC sensing since the atmosphere even with heavy clouds is semitransparent medium for microwaves.

The passive microwave SSM/I observations allow us to determine spatial distribution of the total atmospheric water vapor content W, total cloud liquid water content Q, rainfall rate R and surface wind speed u. A field of view of the SSM/I channels changes from 15x13 km (at frequency $\nu = 85.5$ GHz) to 69x43 km ($\nu = 19.4$ GHz) [1], that is far beyond a typical area of individual rain cells. Pixel contamination by rain arising due to high absorption and scattering of microwaves by large water and ice particles is a cause of the reduced accuracy of geophysical parameter retrieval. At the same time, the dependence of spectrum of outgoing microwave radiation on rain parameters serves as a basis for estimating R.

Okean satellite side looking RAR operates at a $\nu \approx 9.6$ GHz with vertical polarization and has a 1-3 km spatial resolution within a swath width of 460 km. The incidence angle changes from 21 to 46° [2,3]. Such satellites have been orbiting with an inclination of 82.6° and an altitude of about 660 km since September, 1983. The Okean-8 was launched in August, 1995.

The brightness of radar image is proportional to the value of normalized radar cross-section (NRCS) which depends on sea surface roughness (wind characteristics and oceanic dynamics). The images are displayed qualitatively with low NRCS depicted by darker shades and higher NRCS in lighter shades of gray. Analysis of the RAR images have revealed the fine details of the surface wind fields in different weather systems including tropical cyclones [3,4].

Rain cells and bands can be detected by RAR too. Their radar signatures depend on 3D structure of rain zones, the location of these zones within a RAR swath and their orientation relative to illumination direction, damping of surface roughness by rain and backscattering by the splash products and on the brightness of background (surface wind), etc. [3,5,6]. As a result, the radar signatures of precipitation are variable and can have both positive and negative radar contrast against the background. At R > 20-30 mm/h and u < 7-10 m/s precipitation is seen as the bright patches (dots) and bands. They are accompanied by the dark lines (dots) and bands (radar shadows). The shadows result from attenuation of radar signals backscattering by sea surface [3,5,6]. With the increase of wind the shadows become more pronounced as opposed to the bright patches (dots) and bands.

This study analyzes the RAR and passive microwave images and SSM/I-derived parameters for TC Ryan. Wind speed was estimated with algorithm [7]. Estimates of rainfall rate R were calculated using a relationship between R and brightness temperature at 85 GHz at vertical polarization Tb(85V) [8]. The relationship was obtained by comparison of the SSM/I data with rainfall measurements on island stations of the tropical northwestern Pacific Ocean.

MICROWAVE OBSERVATIONS

Typhoon Ryan (9514) was formed in the South China Sea. Its truck was unusual and this feature increased the errors of operational prediction of the truck. Okean-8 RAR image (Fig.1) was taken during a weakening phase of Ryan when it moved fast northward. On 22 September, at 18:00 UTC a central pressure P_{min} was 950 mb, maximum wind speed u_{max} = 42 m/s and winds over 15 m/s were observed within 200 miles. In 6 h P_{min} increased on 10 mb, u_{max} decreased on 5 m/s and radius of winds over 15 m/s reduced to 160 miles.

The location of the Ryan center is determined with high precision on the image. A small central area of size about 8-10 km has a dark tone due to weak winds and the absence of precipitation. It was embedded in the light area with radius of about 25-30 km. The dark partial circle surrounded it is the western eyewall with heavy rains. South of the center, there was no dark band at the distance of 25-30 km, probably, due to lower rain rate. The areas farther north and south of the center have different brightness on the RAR image. The strongest winds and weak (if any) rains were observed south

0-7803-3836-7/97/$10.00 © 1997 IEEE

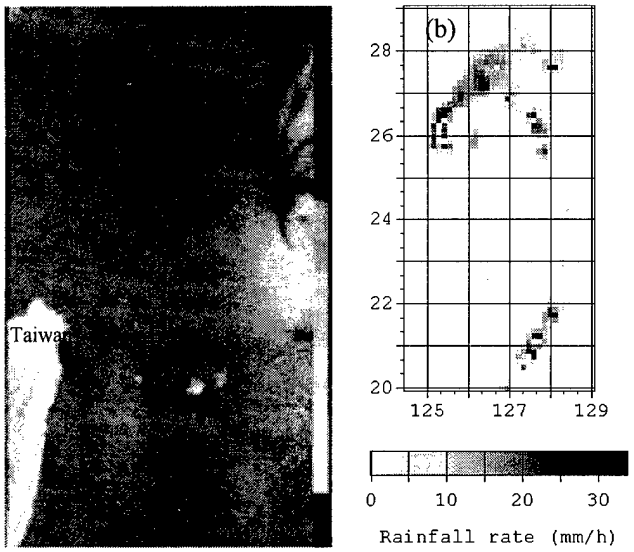

Fig. 1. RAR image of Ryan at 2130 UTC (a) and SSM/I-derived rainfall rate at 2230 UTC (b) on 22 September, 1995.

of the center. The more intensive precipitation, probably, in combination with weaker winds is the cause of the reduced brightness north of the center. In accordance with the weather map of the JMA for 23 September, at 0000 UTC eastern wind of 15 m/s was observed at 28.2°N, 126.3°E. Appearance of two curved dark bands beginning near the eyewall west of the center was most likely associated with the rain bands. The bands formed due to high attenuation of radar signals at their twofold propagation through precipitation are clearly visible against the brighter background. The lighter area between the bands is the area of the increased wind speed.

The SSM/I observations carried out 1 h later are also in agreement with the weather map for 23 September, at 0000 UTC and confirm the wind and precipitation patterns revealed at RAR image analysis. The areas of deeper convection manifest themselves as the areas of the reduced Tb(85V) and increased R (Fig.1b). Heavy rains were embedded in a long interrupted spiral band extending east and south to about 18°N from the inner-core region. The areas of the heaviest rains (> 20 mm/h) were in a semicircle extending southwest to northwest around the center. In precipitating areas estimate of u was impossible. SSM/I-derived wind speed was equal to 15 m/s at 170 km north of the center and 12.5 m/s at 180 km east and north of the center.

Ryan reached maximum intensity on 21-22 September when a central pressure of 940 mb and sustained maximum winds of 45 m/s were observed. The SSM/I Tb(85V) images revealed an intense eyewall with a radius of about 30 km on 21 September at 1355 UTC (Fig.2a) and about 20 km on 22 September at 0215 (Fig.2b).

The eye is characterized by the high Tb(85V) values. The low Tb(85V) values around the eye (dark ring) correspond to eyewall. The decrease of Tb(85V) to north and northeast of the center is associated with spiral rain bands and formation of an area of deep convection. The variations of the Tb(19H) are in counterphase to the Tb(85V) since attenuation by rain, cloud and water vapor is significantly below at 19 GHz. Thus, thick clouds and heavy rains in the eyewall are characterized by the enhanced values of Tb(19H), whereas the eye shows the lower Tb(19H) values. The Tb(37V) variations over the central region are mainly similar to Tb(19H), however, their magnitude is about 2.5 times below. The more pronounced western eyewall has the negative brightness contrast at 37 as opposite to 19 GHz. The Tb(22V) variations are the lowest compared to other frequencies due to the high values of the total atmospheric water vapor content in the area and higher absorption by water vapor at 22 GHz.

Relationships between the brightness temperatures change as a function of attenuation in the atmosphere. The cloudless area B (Fig.2a) exhibits pronounced correlation between Tb at different channels and also between polarization differences between the brightness temperatures at vertical and horizontal polarizations at each frequency. These dependencies are weakened and vanished for the cloudy area A, where attenuation of the atmosphere is significantly larger.

A comparison of two SSM/I-derived fields of rainfall rate for 21 September at 1355 UTC and for 22 September at 0215 UTC shows an intensification of precipitation in the large area north of the Ryan center and formation of the northward and southward spiral arms with heavy rains. On 21 September, at 1355 UTC the central area has no rain, in the eyewall R > 20 mm/h within the circular feature of width of about 30 km excepting the eastern part where R = 10-15 mm/h. Additionally to the eyewall, the areas of deeper convection were observed also north and northeast of the center. They were characterized by R > 10 m/h. In 12 h, the size of eye and rain rates in the eyewall decreased. The rains with R > 20 mm/h were noted in crescent area south of the center only. In

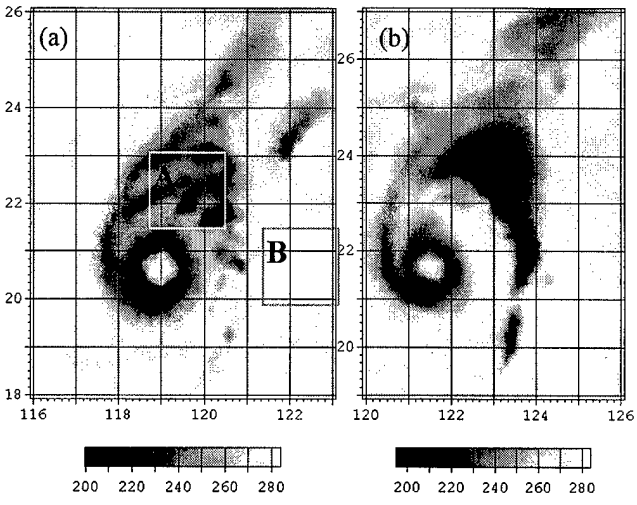

Fig.2. Field of Tb(85V) of typhoon Ryan for 21 September at 1355 UTC (a) and for 22 September at 0215 UTC (b).

other parts of the wall R = 10-15 mm/h. The area of developed convection northeast of the center increased, R also increased here till 15-20 mm/h. The highest rain rates were measured in several cores within southward rain band. The SSM/I-derived precipitation patterns were confirmed by the time-composite radar reflectivity maps obtained by the Kaohsiung and Hualien S-band weather radars on 21-22 September. The weather radar maps depicted the eyewall, the variations of rainfall rate within the area of heavy precipitation north of Ryan and spiral bands.

The southward band was then observed on three subsequent SSM/I passes: at 2230 UTC 22 September and at 0145 and 1255 UTC 23 September. After 0215 UTC 22 September the length of the spiral band at first increased to about 1400 km and then decreased to about 700 km but it remained quasi-stationary relative to the moving cyclone over a day and a half. The similar behavior was described for TC Hugo [11].

The fine structure of the temporal variations of the total amount of liquid water content in the atmosphere at the western periphery of Ryan was observed in Keelung with two microwave radiometers at wavelengths of 2.3 and 0.8 cm.

SUMMARY AND CONCLUSIONS

The results of active/passive microwave sensing from the Okean and DMSP satellites proved their effectiveness in typhoon Ryan study. Joint analysis was also carried out for TC Polly (9513), Angela (9520), Herb (9607). The analysis revealed the location, shape and size of the eye and the areas of deeper convection in the eyewall and spiral rainbands.

The rain cells and bands with R > 10-20 mm/h were characterized by the decreased values of Tb(85) due to scattering of microwave radiation by large ice/water particles in the upper parts of clouds. Radar signatures of heavy precipitation depended both on surface wind and rain parameters. Dark lines were indicators of the rain bands at strong winds. Light patches and bands accompanied by radar shadows were observed at lower wind speeds. An eye of TC was clearly visible on the RAR images as a small dark circular area surrounded by a lighter area. The location of the eye was also determined with high precision using 85 GHz SSM/I observations due to higher spatial resolution of the data and large difference in the Tb between the "hot" central area and the "cold" precipitating area surrounding it.

A comparison of the Okean RAR and microwave images with the SSM/I-derived fields of wind and precipitation demonstrated mutually supplementary character of medium resolution radar data within 460-km swath and low resolution radiometer data within 1400-km swath. A combination of the active/passive microwave measurements yields a more complete understanding of the observed TC.

Improvement of spatial resolution will increase accuracy of the technique. This goal can be reached by increasing antenna size and/or by measurements at higher frequencies. These possibilities will be realized on future satellites such as ADEOS-II.

ACKNOWLEDGMENTS

The authors thank the Far Eastern Regional Centers of Receiving and Processing Satellite Data for providing the Okean-8 radar image (Fig.1) and the Marshall Flight Space Center for providing the SSM/I data. This research was partly sponsored by the National Science Council through research grants NSC-84-2611-M019-009 and NSC-85-2611-M019-011 K2 and the NASDA through research grant A-0020.

REFERENCES

[1] J. Hollinger, R. Lo,. J. Poe, R. Savage, and J. Pierce, "Special Sensor Microwave/Imager User's Guide,"Naval Research Laboratory, Washington, DC, 120 pp., 1987.

[2] A.I. Kalmykov, V.B. Yefimov, S.S. Kavelin et al., "The radar system on the Cosmos-1500 satellite," Soviet J. Remote Sens., vol. 4, pp. 827-840, 1989 (Engl. transl.).

[3] L.M. Mitnik and S.V. Viktorov (editors), "Radar Sensing of the Earth's Surface from Space," Leningrad: Gidrometeoizdat, 1990, 200 pp. (in Russian).

[4] L. M. Mitnik, G.I. Desyatova, and M. L. Mitnik, "Fields of surface wind and cloudiness in tropical storm "Agnes" derived from satellite radiophysical data," Issledovanie Zemli iz Kosmosa (Soviet J. Remote Sensing), No. 6, pp. 20-28, 1990 (in Russian).

[5] A.P. Pichugin and Yu.G. Spiridonov, "Spatial structure of precipitation zones on radar images from space," Issledovanie Zemli iz Kosmosa, N 2, pp. 20-28, 1985 (in Russian).

[6] M.V. Bukharov, "Study of conditions of identification of hail precipitation on satellite side looking radar images," Issledovanie Zemli iz Kosmosa, N4, pp. 74-82, 1991 (in Russian).

[7] F. Wentz, "Measurement of oceanic wind vector using satellite microwave radiometers," IEEE Trans. Geosci. Remote Sens., vol. 30, pp. 960-972, 1992.

[8] R.F. Adler, G.J. Huffman, and P.R. Keehn, "Global tropical rain estimates from microwave-adjusted geosynchronous IR data," Remote Sensing Rev., vol. 11, pp. 125-152, 1994.

[9] D. Atlas, "Footprint of storms on the sea: A view from spaceborn synthetic aperture radar," J. Geophys. Res., vol. 99, pp. 7961-7969, 1994.

[10] M.S. Peng and S.W.Cheng, "Impacts of SSM/I retrieved rainfall rates on numerical prediction of a tropical cyclone," Mon.Wea.Rev., vol.104, pp.1181-1198, 1996.

[11] R. Alliss, S. Raman, and S.W. Chang "Special Sensor Microwave/Imager (SSM/I) observations of Hurricane Hugo (1989)," Mon. Wea. Rev., vol. 120, pp. 2723-2737, 1992.

Cloud and Ice Detection Using NOAA/AVHRR Data

Ken-ichiro MURAMOTO†, Hideo SAITO‡, Kohki MATSUURA†
and Takashi YAMANOUCHI‡

†Faculty of Engineering, Kanazawa University, 2-40-20, Kodatsuno, Kanazawa 920, Japan
E-mail : muramoto@t.kanazawa-u.ac.jp

‡National Institute of Polar Research, 1-9-10, Kaga, Itabashi, Tokyo 173, Japan

Abstract – In the polar region, it is difficult to discriminate between clouds and ground surface from satellite visible or infrared data, because of the high albedo and low surface temperature of snow and ice cover. In this paper, a method to classify cloud, sea ice and ground is proposed. This study is based upon analysis of the NOAA/AVHRR infrared images in Antarctica. The algorithm consists of two major approaches: extraction of image features and a classification algorithm. Minimum distance classifier was used to classify that region into one of three categories using five image features. To improve the classification accuracy, threshold boundaries for minimum distance classifier were changed. Both classified and misclassified areas were decreased with increasing the threshold levels.

INTRODUCTION

Antarctic sea ice is one of the important factors that affect the polar climate and the global atmospheric system [1]-[3]. Clouds in the Antarctic are also important because of their strong radiative influence on the energy balance of the snow and ice surface [4]. Since, however, in the polar region, cloud, snow and ice have almost the same albedo in the visible channel and the same brightness temperature in the infrared channel, it is difficult to distinguish among these regions using only the threshold of gray level of a satellite image [5], [6].

In this paper, techniques for classifying Antarctic satellite images into cloud, sea ice and ground using single channel data are proposed. The algorithm consists of two major approaches: extraction of image features and a classification algorithm. Minimum distance classifier was applied to classify the region into one of three categories using five image features. To improve the classification accuracy, threshold boundaries for minimum distance classifier were changed.

DATA

AVHRR data received from the NOAA satellite have been processed primarily and stored at Syowa Station, Antarctica, since 1987 [7]. We obtained the image data of the area near Syowa Station from the National Institute of Polar Research, Japan. The area is composed of 512 × 512 pixels with spatial resolution 2.2 km. At each pixel location, the image brightness was quantified into 256 gray levels for computer graphics display.

METHOD

Subregion

The satellite image area was divided into square areas. Features at each location of the subregion were extracted from a (32 × 32)-pixel block area in a sample image.

Image Features

Many natural surfaces possess structural similarities independent of scale. The fractal dimension is one measure of quantitative property of self-similar structure [8]. The gray level function in the region is defined by brightness temperature. The method relies on the assumption that regions of an image having a particular structure will usually produce a fractal gray level surface, with a particular value of the fractal dimension. For convenience, we used a three-dimensional cube to measure the fractal surface's dimension by covering the surface with a minimal number of cubes [9].

Texture is usually defined as some local property of an image, i.e. a measure of the relationship between the pixels in a neighborhood. There are many approaches to describe texture characteristics. The co-occurrence method is used in the present study [10].

Image Features of the Training Area

Representative areas of clouds, sea ice and ground were selected subjectively using infrared imagery (channel 4). More than one training area per class was used to include the range of variability. Average and standard deviation of brightness temperature, fractal dimension, and uniformity and correlation of texture features of subregion of image data were computed in each selected area.

The whole area of visible imagery (channel 1) was also classified manually to obtain supervised data for estimating the classification results.

0-7803-3836-7/97/$10.00 © 1997 IEEE

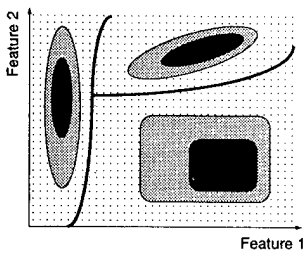

Fig. 1. Minimum distance classifier. Threshold boundaries are applied to limit the extent of each group.

Minimum Distance Classifier

Minimum distance classifier is a commonly used algorithm for image classification. Values of image features of each subregion are plotted on the multi-dimensional feature space. Mean value in each feature is determined. These values comprise the mean vector for each class. A pixel of unknown identity will be classified by computed the distance between of the unknown pixel and each of the class means. After computing the distances, the unknown pixels is assigned to the closest class. In this study, Mahalanobis distance was calculated for measurement of distance. Decision boundaries can be changed for ensuring the rate of a candidate class. Fig.1 shows threshold boundaries in two dimension for a distribution of the value of feature. Any pixel further away than the boundary distance is left unclassified. Thresholds prevent misclassification of pixels outside the boundary. Though classified areas are decreased with decreasing the distance from mean value to boundary, misclassified areas are also exclude.

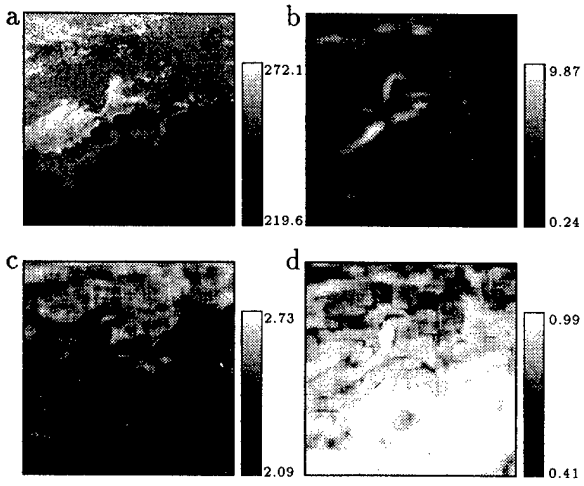

Fig. 2. Image features of NOAA satellite displayed by gray scale. (a) AVHRR image of channel 4. (b) Standard deviation of brightness temperature. (c) Fractal dimension. (d) Correlation of texture.

RESULTS AND DISCUSSION

First, five features for cloud, sea ice and ground in the satellite image were calculated using subjectively selected representative areas. These data were used to calculate decision boundary for minimum distance classifier. Fig.2 shows three examples of the image features of NOAA satellite displayed by gray scale. Fig.3 shows the histogram of standard deviation of brightness temperature, fractal dimension, and correlation of texture of the image. It can be seen that many parts of sea ice could be separated from others with average brightness temperature, and many parts of ground could be separated from others with texture. However, it was impossible to segment the image into three regions with only one feature. More than two features have to be used to separate all classes. Classified area and its estimation were examined by changing decision boundaries. In this study, a set of stages corresponding to 1, 2, 3, 4 and 5 used, corresponding to classified area of 100%, 90%, 80%, 70 and 60%, respectively. Fig.4 illustrates the effect of threshold of boundaries in the classification. In the stage 1, the upper right part was misclassified as a cloud class

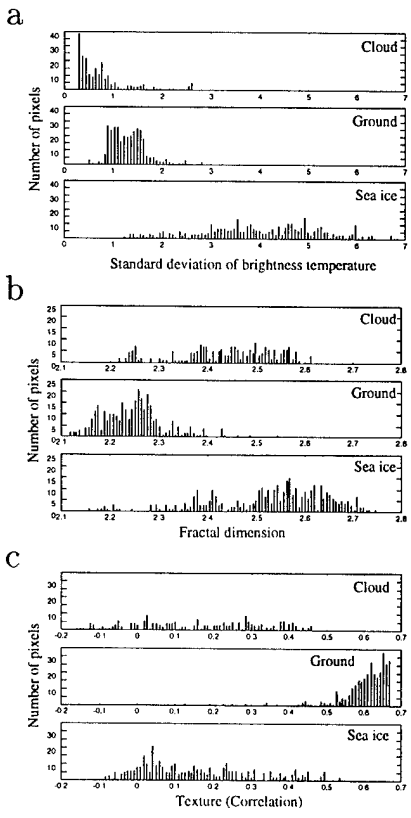

Fig. 3. Histograms of image features for 13 April 1989. (a) Standard deviation of brightness temperature. (b) Fractal dimension. (c) Correlation of texture.

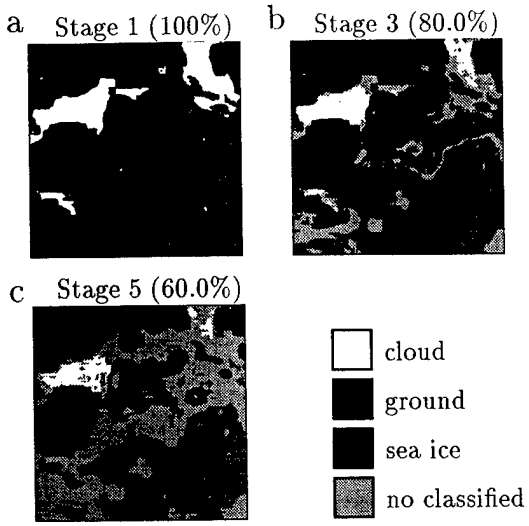

Fig. 4. Classified satellite image at three stages.

because of feature similarity between that part of the sea ice and the cloud training class. The application of thresholds (stages from 2 to 5) could exclude these misclassified pixels, and sometimes originally classified correctly pixels were similarly eliminated. The accuracy for each stage was estimated by dividing the number of correctly classified pixels by total number of classified pixels in that stage. Fig.5 shows the percentage of classified area and its estimation of stages from 1 to 5. Classified areas and error rates were decreased with increasing number of stages. When all pixels were classified, classified error was 37%. We can say that the number of stages will be decided according to the purpose.

CONCLUSION

A method to segment an Antarctic satellite image using a single infrared channel of AVHRR is proposed. Average and standard deviation of brightness temperature, fractal dimension and textural features of the image data, are used to classify into one of three regions. When all pixels were classified, the error was large. To ensure the accuracy of classification, the extent of each group was limited by changing decision boundaries. The accuracy for each stage was estimated. Error rate was decreased with decreasing classified area. In general, the error rates will be decided according to the purpose.

ACKNOWLEDGMENTS

This work was supported partly by the Japanese Ministry of Education, Science, Sports and Culture Grants-in-Aid for Scientific Research (08650482).

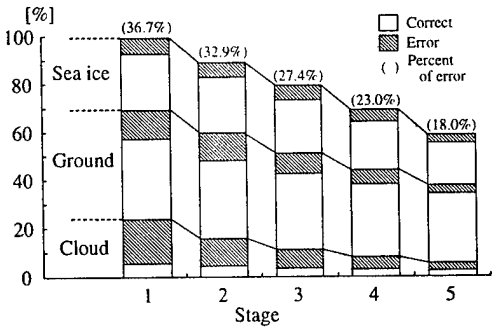

Fig. 5. Percentage of classified area and its estimation stages from 1 to 5.

REFERENCES

[1] A.L.Gordon and H.W.Taylor, "Seasonal change of Antarctic sea ice cover," *Science*, vol. 187, pp.346-347, 1975.

[2] G.Maykut and N. Untersteiner, "Some results from a time-dependent thermodynamic model of sea ice," *J. Geophys. Res.*, vol. 76, pp.1550-1575, 1971.

[3] A.Robock, "Ice and snow feedbacks and the latitudinal and seasonal distribution of climate sensitivity," *J. Atmos. Sci.*, vol.40, pp.986-997, 1983.

[4] B.Saltzman and R.E.Moritz, " A time-dependent climate feedback system involving sea-ice extent, ocean temperature, and CO2," *Tellus*, vol.32, pp.93-118, 1980.

[5] J.A.Coakley and F.P.Bretherton, "Cloud cover from high-resolution scanner data: Detecting and allowing for partially filled fields of view," *J. Geophys. Res.*, 87, C7. pp.4917-4932, 1982.

[6] M.Seze Desbois and G.Szejwach, "Automatic classification of clouds on METEOSAT imagery: Application to high-level clouds," *J. Appl. Meteor.*, vol.21, pp.401-412, 1982.

[7] T.Yamanouchi, H.Kanzawa, H.Ariyoshi and M.Ejiri, "Report on the first MOS-1 data received at Syowa Station, Antarctica," Proc. NIPR Symp. Polar," *Meteorol. Glaciol.*, 4, pp.22-30, 1991.

[8] A.Pentland, "A. Fractal-based description of natural scenes," *IEEE Trans. Pattern Anal. Machine Intell.*, vol.6, pp.666-674, 1984.

[9] K.Muramoto and T.Yamanouchi, "Classification of polar satellite data using image features and decision tree classifier," *Proc. NIPR Symp. Polar, Meteorol. Glaciol.*, vol.10, pp.127-137, 1991.

[10] R.M.Haralick, K.Shanmugam and I.Dinstein, "Textural features for image classification," *IEEE Trans. Syst. Man. Cybern.*, vol.3, pp.610-621, 1973.

IGARSS'97

1997 International Geoscience and Remote Sensing Symposium

03-08 August 1997

Singapore International Convention & Exhibition Centre

Technical Program

Interactive Area 6: Crops, Soils and Forestry

IMPROVED FOURIER MODELLING OF SOIL TEMPERATURE USING THE FAST FOURIER TRANSFORM ALGORITHM

Sune R.J. Axelsson
National Defence Research Establishment and Saab Dynamics AB
P.O. Box 1165, S-581 11 LINKÖPING
Fax:+46-13-186215, Email: sunax@weald.air.saab.se

Abstract --In the general case, the temperature field and the heat flow of soils are controlled by two coupled first-order differential equations with the boundary condition defined by the heat flow through the surface boundary due to the net radiation and the sensible and latent heat flows between the surface and the atmosphere. Periodic diurnal temperature variations have earlier been studied using Fourier modelling techniques. In this paper, it is shown how this method can be extended to non-periodic diurnal temperature variations due to changing weather conditions. The calculations can be speeded up significantly using FFT-processing. Furthermore, the algorithms are generalized to multiple soil-layers.

1. INTRODUCTION

For quantitative estimations of the temperature variations of a surface, mathematical models are required, which predict the surface temperature when the weather and surface parameters are well-defined. In the general case, the temperature field and the heat flow are controlled by two coupled first-order differential equations.

The boundary condition is defined by the heat flow through the surface boundary due to net radiation and the sensible and latent heat exchange between the surface and the atmosphere.

The most general modelling is based upon the numerical finite difference method, which can include the soil moisture transport as well. A simplified analytical solution of the heat diffusion equations for a homogeneous half-plane was developed by Jaeger [1] and Watson [2] in terms of a Fourier model and using simplified assumptions concerning the boundary conditions. Later on significant improvements were presented by Axelsson [4]. A basic assumption of these studies was that the diurnal weather variations can be considered strictly periodic.

In this paper, it is shown how the Fourier method can be extended to non-periodic day/night temperature variations by increasing the time of periodicity to several days or weeks.

It is also shown how these calculations can be speeded up very significantly by using the FFT-algorithm. Furthermore, the algorithms are generalized to multiple soil-layers.

2. BASIC RELATIONSHIPS

Let us assume a half-plane homogeneous in the y- and z-directions. The temperature field U(x,T) and the vertically directed heat flow q(x,t) are then controlled by the coupled differential equations

$$q(x,t) = -\lambda\, \delta U(x,t)/\delta x \qquad (2.1a)$$

$$\delta q(x,t)/\delta x = -\, C\, dU(x,t)/dt \qquad (2.1b)$$

where t is time, x is depth, λ is the thermal conductivity and C is the heat capacity per unit volume.

The boundary condition is defined by the heat exchange at the soil surface

$$Q_g = I(1-A) - \varepsilon\sigma(T^4 - T_{sky}^4) - H - LE \qquad (2.2)$$

where Q_g is the vertical heat flux, I is the short-wave irradiance on a horizontal surface, T is the surface temperature, A is the albedo of the ground surface, ε is the long-wave emissivity, σ is the Stefan-Boltzman constant, T_{sky} is the long-wave sky-temperature, H is the sensible heat flux, and LE is the latent heat flux.

The evaporation and sensible heat fluxes are highly complex processes [5]-[6]. Significant simplifications are necessary to reduce the number of parameters involved. A simplified one-parameter model of the evaporation from a moisty surface is to define $LE=M(LE_p)$, where $0<M<1$ and LE_p is the potential latent heat flux from a wet surface at the same temperature.

The sensible heat flux can be appoximated by

$$H = k_0(T - T_a) \qquad (2.3)$$

where T_a is the air temperature at a reference height. The factor k_0 is highly dependent upon the local wind-speed but also surface roughness and the stability conditions of the lower atmosphere have effects [5]-[6].

The application of Fourier modelling is based upon linearized boundary conditions:

$$Q_g = FT + Q_s(t) \qquad (2.4)$$

0-7803-3836-7/97/$10.00 © 1997 IEEE

In (2.4), F is a constant and $Q_s(t)$ is determined by the source functions I(t), $T_a(t)$ and $T_{sky}(t)$ which are considered independent of the surface temperature T.

The latent heat flux and the long-wave thermal radiation are both non-linear functions of T and a linear approximation about an arbitrary temperature T_m is introduced [4]

$$LE = LE_0 + k_1(T-T_m) \quad (2.5a)$$

$$\varepsilon\sigma T^4 = \varepsilon\sigma T_m^4 + 4\varepsilon\sigma T_m^3(T-T_m). \quad (2.5b)$$

where $LE_0=LE(T_m)$ and $k_1=L\delta E(T_m)/\delta T$.

Insertion of (2.5) into (2.2) yields after simplifications

$$Q_g = Q_{g0} - S(T - T_m) \quad (2.6)$$

where $S = 4\varepsilon\sigma T_m^3 + k_0 + k_1$ and $Q_{g0} = I(1-A) + \varepsilon\sigma(T_{sky}^4-T_m^4) - k_0(T_m-T_a) - LE_0$.

3. FOURIER MODEL

When the source functions are all periodic, they can be developed into Fourier series. If complex notation is applied

$$I = \sum I_k \exp[jk\omega t] \quad (3.1a)$$

$$T_a = \sum T_{ak} \exp[jk\omega t] \quad (3.1b)$$

$$T_{sky}^4 = \sum B_k \exp[jk\omega t] \quad (3.1c)$$

Consequently, the surface heat flux and temperature become also periodic with

$$T = \sum T_k \exp[jk\omega t] \quad (3.2a)$$

$$Q_g = \sum Q_k \exp[jk\omega t] \quad (3.2b)$$

The frequency components of Q_g and T are linked together by the thermal impedance Z_{gk} of the ground at frequency $k\omega$. By definition

$$T_k = Q_k Z_{gk} \quad (3.3)$$

Insertion of (3.1)-(3.3) into (2.6) will express the Fourier components of the surface temperature T(t) as follows

$$T_0 = [I_0(1-A) + \varepsilon\sigma(B_0 - T_m^4) + k_0(T_{a0}-T_m) + + ST_m - LE_0] [S + 1/Z_{g0}]^{-1} \quad (3.4a)$$

For k>0:

$$T_k = [I_k(1-A) + \varepsilon\sigma B_k + k_0 T_{ak}] [S + 1/Z_{gk}]^{-1} \quad (3.4b)$$

Insertion of (3.4) into (3.2a) defines the Fourier solution of the surface temperature. In the following, the impedance Z_{gk} of homogeneous and stratified ground solids will be estimated.

4. HOMOGENEOUS SEMI-INFINITE SOLID

The partial differential equations of (2.1) define relationships between the vertical heat flux and the temperature field in the ground. A related pair of equations also describes the propagation of electrical signals on a transmission line [7]. A similar approach will be applied below at the estimation of the thermal impedance Z_{gk}.

If $U(x,t)=U(x)\exp(j\omega t)$ and $q(x,t)=q(x)\exp(j\omega t)$ is assumed, we find from (2.1)

$$dU/dx = -(1/\lambda)q \quad (4.1a)$$

$$dq/dx = -j\omega CU \quad (4.1b)$$

which can be rewritten as

$$d^2U/dx^2 = \gamma^2 U \quad (4.2a)$$

$$d^2q/dx^2 = \gamma^2 q \quad (4.2b)$$

with

$$\gamma^2 = j\omega C/\lambda. \quad (4.2c)$$

A general solution of (4.2) is

$$U = U_1\exp(\gamma x) + U_2\exp(-\gamma x) \quad (4.3a)$$

$$q = Q_1\exp(\gamma x) + Q_2\exp(-\gamma x) \quad (4.3b)$$

where U_1, U_2, Q_1 and Q_2 are determined from the boundary conditions.

Insertion of (4.3b) into (4.1b) shows that

$$U = -Q_1 Z_0 \exp(\gamma x) + Q_2 Z_0 \exp(-\gamma x) \quad (4.4a)$$

where

$$Z_0 = \gamma/j\omega C = 1/(j\omega C\lambda)^{1/2} = 1/[P(j\omega)^{1/2}] \quad (4.4b)$$

and P is the thermal inertia defined by

$$P = (C\lambda)^{1/2} \quad (4.4c)$$

Similarly, we find after insertion of (4.3a) into (4.1a)

$$q = -(U_1/Z_0)\exp(\gamma x) + (U_2/Z_0)\exp(-\gamma x) \quad (4.5)$$

For an infinite half-space $U_1=Q_1=0$; if not, U and q would grow exponentially when x becomes large. In that case, Z_0 represents the impedance of a homogeneous half-space and the impedance Z_{gk} of (3.3) is determined by

$$Z_{gk} = 1/[P(jk\omega)^{1/2}] = Z_{g1} / k^{1/2} = Z_0 / k^{1/2} \qquad (4.6)$$

Hence $1/Z_{g0} = 0$ in (3.4a). We also find that

$$S + 1/Z_{gk} = S + P(jk\omega)^{1/2} = S + P(k\omega/2)^{1/2}(1+j) \qquad (4.7)$$

5. STRATIFIED SOLIDS

In [8], Watson derived an analytical solution of the surface temperature of a homogeneous solid covered by a surface layer of another material. In the sequel, this problem will be analyzed and generalized to multi-layers.

Let us start by investigating how the input impedance is changed between the two boundaries of a homogeneous layer defined by γ, Z_0 and $x_1-d<x<x_1$.

From (4.3), (4.5) and the boundary condition at $x=x_1$, we find

$$T_1 = U_1\exp(\gamma x_1) + U_2\exp(-\gamma x_1) \qquad (5.1a)$$

$$q_1 = -(U_1/Z_0)\exp(\gamma x_1) + (U_2/Z_0)\exp(-\gamma x_1) \qquad (5.1b)$$

Similarly, the temperature and the heat flux at $x=x_1-d$ are

$$T_2 = U_1\exp[\gamma(x_1-d)] + U_2\exp[-\gamma(x_1-d)] \qquad (5.2a)$$

$$q_2 = -(U_1/Z_0)\exp[\gamma(x_1-d)] + (U_2/Z_0)\exp[-\gamma(x_1-d)] \qquad (5.2b)$$

Elimination of U_1 and U_2 from (5.1)-(5.2) yields

$$T_2 = T_1\cosh(\gamma d) + q_1 Z_0\sinh(\gamma d) \qquad (5.3a)$$

$$q_2 = q_1\cosh(\gamma d) + (T_1/Z_0)\sinh(\gamma d) \qquad (5.3b)$$

The relationship (5.3) means that the input impedance Z_2 at $x=x_2=x_1-d$ can be expressed in terms of the input impedance $Z_1=T_1/q_1$ at $x=x_1$ and the interjacent characteristic impedance Z_0 as follows

$$Z_2 = T_2 / q_2 = \frac{Z_1\cosh(\gamma d) + Z_0\sinh(\gamma d)}{\cosh(\gamma d) + (Z_1/Z_0)\sinh(\gamma d)} \qquad (5.4)$$

A. One-layer case

Let us now consider a semi-infinite solid with thermal conductivity λ_1 and heat capacity C_1 covered by a layer of thickness d and conductivity λ_2 and heat capacity C_2.

The input impedance Z_{gk}, which from (3.4) and (3.2a) defines the surface temperature, is then derived from (5.4)

$$Z_{gk} = \frac{Z_{01}\cosh(\gamma_{2k}d) + Z_{02}\sinh(\gamma_{2k}d)}{\cosh(\gamma_{2k}d) + (Z_{01}/Z_{02})\sinh(\gamma_{2k}d)} \qquad (5.5)$$

where $Z_{01}=(j\omega\lambda_1C_1)^{-1/2}$, $Z_{02}=(j\omega\lambda_2C_2)^{-1/2}$ and $\gamma_2=(j\omega C_2/\lambda_2)^{1/2}$.

B. Multi-layers

The more general case of N layers covering a semi-infinite solid can be treated in a similar way.

First, thickness, thermal conductivity and heat capacity of the layers are defined (d_k, λ_k and C_k). The homogeneous half-space is characterized by λ_0 and C_0.

The input impedance of the lower half-space is for frequency ω: $Z_{i0}=Z_{00}=(j\omega P_0)^{-1/2}$, where $P_0=(\lambda_0C_0)^{1/2}$. Similarly, the input impedance at the upper boundary of layer n is

$$Z_{in} = \frac{Z_{i(n-1)}\cosh(\gamma_n d_n) + Z_{0n}\sinh(\gamma_n d_n)}{\cosh(\gamma_n d_n) + (Z_{i(n-1)}/Z_{0n})\sinh(\gamma_n d_n)} \qquad (5.6)$$

where $Z_{0n}=(j\omega\lambda_nC_n)^{-1/2}$ and $\gamma_n=(j\omega C_n/\lambda_n)^{1/2}$.

The input impedance of the ground Z_{g1} is estimated by computing successively the input impedance of the upper boundary of layer 1, 2, .., N using (5.6). The procedure is repeated for $k\omega$ giving Z_{gk}. Finally, the surface temperature of the top layer is computed from (3.4) and (3.2).

6. APPLICATION OF THE FFT-ALGORITHM

If we apply discrete time sampling of the processes involved $\{f_m\}$, we can apply the discrete Fourier transform with m, k=0 to M-1

$$F_k = (1/M)\sum_{m=0}^{M-1} f_m \exp(-j2\pi km/M) \qquad (6.1a)$$

with the inverse relationship (k=0 to M-1)

$$f_m = \sum_{k=0}^{M-1} F_k \exp(j2\pi km/M) \qquad (6.1b)$$

If, in particular, the Fast Fourier Transform algorithm (FFT) is applied at the computation, a much higher speed is achieved than if the discrete Fourier transform is applied [9].

When f_m are real numbers, $F_{M-k}=F^*_k$. If $M=2M_1$ is introduced, we can develop (6.1b) as follows

$$f_m = F_0 + \sum_{k=1}^{M1-1} F_k \exp(j2\pi km/M) + \sum_{k=1}^{M1-1} F^*_k \exp(-j2\pi km/M) \quad (6.2)$$

where $F_{M1} = 0$ follows from (6.1a).

Eq. (6.2) can also be rewritten as

$$f_m = F_0 + 2\,\mathrm{Re}\{\sum_{k=0}^{M1-1} F_k \exp(j2\pi km/M)\} \quad (6.3)$$

Obviously, we can from (6.1b) and (6.3) also derive a third expression to be used below. Let us introduce $U_0=0$ and $U_k=F_k$ for k=1 to M1-1 and $U_k=0$ for k=M1 to M-1. We can then apply the inverse FFT-transform

$$f_m = F_0 + 2\,\mathrm{Re}\{\sum_{k=0}^{M-1} U_k \exp(j2\pi km/M)\} =$$
$$= F_0 + 2\mathrm{Re}\{\mathrm{ICFFT}(\mathbf{U})\} \quad (6.4)$$

The estimation procedure of the surface temperature is now as follows. From the time samples of I, T_a and T_{sky}^4, the Fourier components are estimated using the complex FFT-transform (6.1a). Then the function U_k is formed by

$$U_k = H_k[I_k(1-A) + \varepsilon\sigma B_k + k_0 T_{ak}] \quad (6.5)$$

for k=1 to M1-1. For k=0 and k=M1 to M-1, $U_k=0$.

H_k is obtained from (4.7)

$$H_k = 1/[S + 1/Z_{gk}] \quad (6.6)$$

and the time samples of the surface temperature written in vector form are then estimated from

$$T = T_m + [I_0(1-A) + \varepsilon\sigma(B_0 - T_m^4) - LE_0 +$$
$$+ k_0(T_{a0}-T_m)]/S + 2\mathrm{Re}\{U\} \quad (6.7)$$

7. SIMULATIONS

Figure 1 shows the predicted diurnal surface temperatures of a horizontal rock surface covered by soil layers of varying thickness. T_{sky}=260 K, A=0.2, ε=0.9, latitude: 58°, solar declination: 20°, k_0=10 W/Km^2, clear sky and T_a=10-25° C.

In Figure 2, the surface temperature variations of a rock surface are predicted during a 10 day period of sunny weather with one single day of cloudy sky in the middle (30% of short-wave radiation compared with clear sky).

8. CONCLUSIONS

An extended Fourier model has been presented for predictions of the surface temperature variations of bare surfaces. This model includes stratified soil or rock materials and handles varying non-periodic weather conditions as well.

By applications of the FFT-algorithm, the processing is significantly speeded up. This makes it possible to predict diurnal surface temperature variations during months or more with standard PC-computers.

REFERENCES

[1] J.C. Jaeger: Conduction of heat in a solid with periodic boundary conditions with an application to the surface temperature of moon, Proc. Cambridge Phil. Soc., pp. 355-359, 1953.

[2] K. Watson: Geological applications of thermal infrared images, Proc. IEEE, vol. 63(1), pp. 128-137, 1975.

[3] A. Rosema: TELL-US, a combined surface temperature, soil-moisture and evaporation mapping approach, Proc. 12th Int. Symp. Remote Sensing and Environm., pp. 2267-2276, 1978.

[4] S.R.J. Axelsson: On the accuracy of thermal inertia mapping by infrared imagery, Proc. 14th Int. Symp. Remote Sensing and Environm., pp. 359-378, 1980.

[5] J.A. Businger, J.C. Wyngaard, Y. Zzumi and E.F. Bradley: Flux-profile relationships in the atmospheric surface layer, Journal of Atmospheric Science (28), pp. 181-189, 1971.

[6] G.J.R. Soer: Estimation of regional evaporation and soil moisture conditions using remotely sensed crop surface temperatures, Rem. Sens. 9: 27-44, 1980.

[7] F.E. Therman: *Radio Engineering*, chapter 4, McGraw-Hill, 1947.

[8] K. Watson: Periodic heating of a layer over a semi-infinite solid, Journal of Geophysical Research, vol.78(2), pp. 5904-5910, 1973.

[9] A.V. Oppenheim and R.W. Schafer: *Digital Signal Processing*. Prentice-Hall, NJ, 1975.

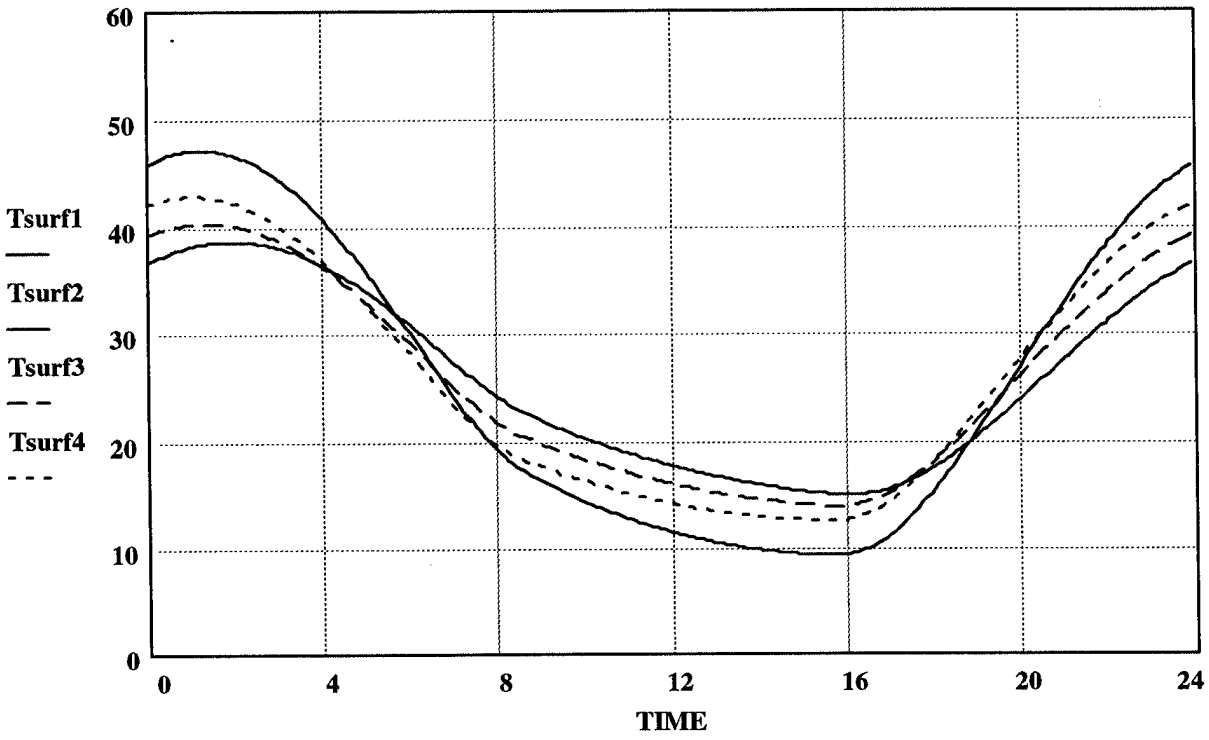

Figure 1: Predicted surface temperature of a horizontal rock surface (P=2750) covered by a soil layer (P=1000) of variable thickness: d=0 mm (——), d=20 mm (. . .), d=50 mm (- - -), and d=1000 mm (——).

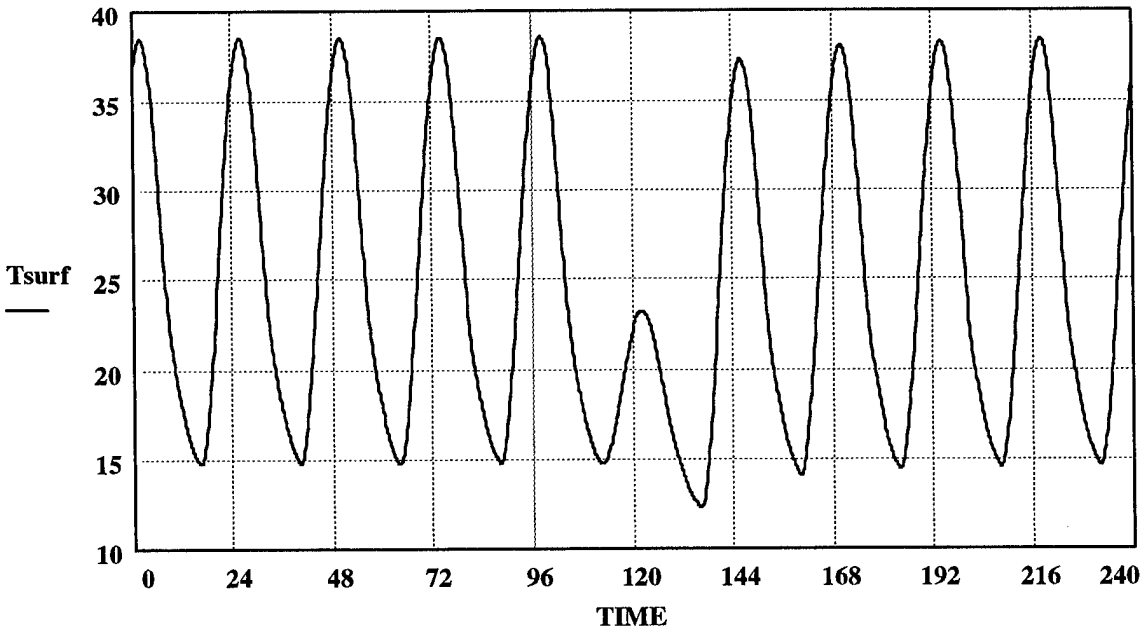

Figure 2: Predicted diurnal variations of the surface temperature of a rock surface (P=2750) during a 10 day period of sunshine with one day of heavy clouds in the middle.

MODELING BIDIRECTIONAL RADIANCE DISTRIBUTION FUNCTIONS OF CONIFER CANOPIES USING 3-D GRAPHICS

C. N. Burnett, G. J. Hay, K. O. Niemann
Department of Geography, University of Victoria,
PO. Box 3050, Victoria, BC. Canada V8W 3P5
cburnett@office.geog.uvic.ca

D. G. Goodenough
Pacific Forestry Centre, Canadian Forest Service, Natural Resources Canada
506 West Burnside Road, Victoria, BC. Canada V8Z 1M5

Abstract -- Bidirectional radiance functions (BRF) are estimated for two age-different conifer canopies using field mensuration data, a geometric-optical canopy reflectance (CR) model, ray-tracing software and imaging spectrometer data. The anisotropy or I-BRF (bidirectional change with reference to change in illumination direction, view direction constant) of two age-different stands are compared. Comments on the versatility of this BRF estimation methodology are offered.

INTRODUCTION

By analyzing the bidirectional radiance functions (BRF) of conifer canopies using a geometric-optical model and 3-D computer graphics, this research seeks to answer the following question: how significant is the I-BRF differences for conifer canopies of two different ages. I-BRF refers to the analysis of BRF with reference to change in illumination direction while view direction is held constant.

The research is based on the thesis that stand-level reflectance [or radiance] for canopies exhibiting distinct geometric features, such as conifers, is strongly related to shadow fraction, sunlit canopy fraction, sunlit background fraction, and their reflectances [1]. Canopy structure changes significantly with age, therefore differently aged stands should exhibit differences in anisotropy. Syrén [2] documented this through field experiments using helicopter-based radiometer measurements of immature and mature Scotch pine and Norway spruce.

The geometric-optical model used is a modified Li and Strahler (1985) [3] model wherein canopy objects (trees represented by a cone and two cylinders) cast shadows onto each other and onto the horizontal plane. The resulting scene is broken down into four canopy fractions: sunlit crown (C), sunlit background (G), shadowed crown (T) and shadowed background (Z). Scene brightness (Rs) for a single illumination direction is calculated as a linear combination of the canopy fractions and their respective radiances (Rc, Rg, Rt, Rz) as shown in equation 1.

$$Rs = C \cdot Rc + G \cdot Rg + T \cdot Rt + Z \cdot Rz \qquad (1)$$

Canopy fractions are estimated using 3-D graphics (canopy fractions C, G, T, Z) and digital remotely sensed data (radiances Rc, Rg, Rt, Rz) as presented in the Methods.

METHODS

Study Area

Tree mensuration data collected by Hay and Niemann [3] was used as a template for the 3-D graphics modeling. The examined forest stands are situated north of Sooke Lake, 30 km northwest of Victoria, Canada (48° 34'N, 123° 42'E) within the Greater Victoria Water District Supply Area. The dominant seral tree species is Coastal Douglas-fir (Pseudotsuga menziesii) mixed with smaller quantities of Coastal Western Hemlock (Tsuga heterophylla). Salal (Gualtheria shallon), Dogwood (Cornus nuttallii), ferns and mosses make up the sub-canopy growth. The immature stand (figure 1), planted in 1965 and spaced in 1975, was composed predominantly of Douglas-fir with some Western Hemlock. Trees height ranged from 11m to 25m. The mature stand contained trees ranging in age from 140 to 250 years and in height from 20m to 70m.

Quantifying End-Member Areal Abundance: C, G, T & Z

The areal abundance for each of the four canopy fractions was calculated using 3-D graphics ray-tracing software. Ray-tracing allows for highly accurate modeling of radiation/canopy interactions including mutual shadowing Figure 1 shows an oblique view of the two computer-generated canopies.

The three images in figure 2 demonstrate the POV-Ray product for three illumination directions. In each image the azimuth angle is 120°, while illumination zenith angle changes (0°, 25°, 60°) result in obvious changes in shadow regime within the canopy. Note that the inset in the middle image where the image has been 'classified' into the four model components. Canopy fraction areal abundance (C, G, T & Z) was quantified by an examination of the classified image's histogram.

Determining End-Member Spectra: Rc, Rg, Rt & Rz

Remote sensing imagery was acquired as part of the 1993

0-7803-3836-7/97/$10.00 © 1997 IEEE

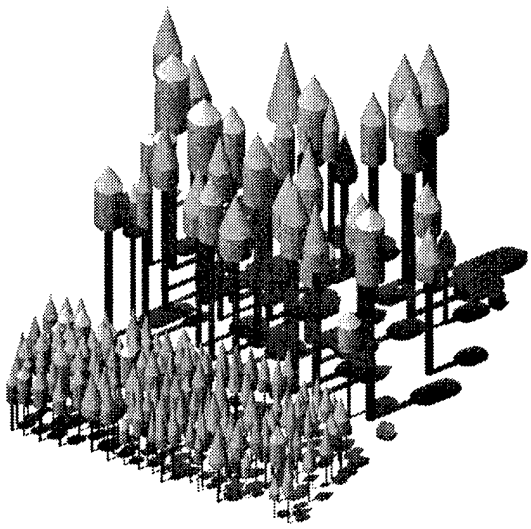

Figure 1. The fire-cracker forest rendered using POV-Ray

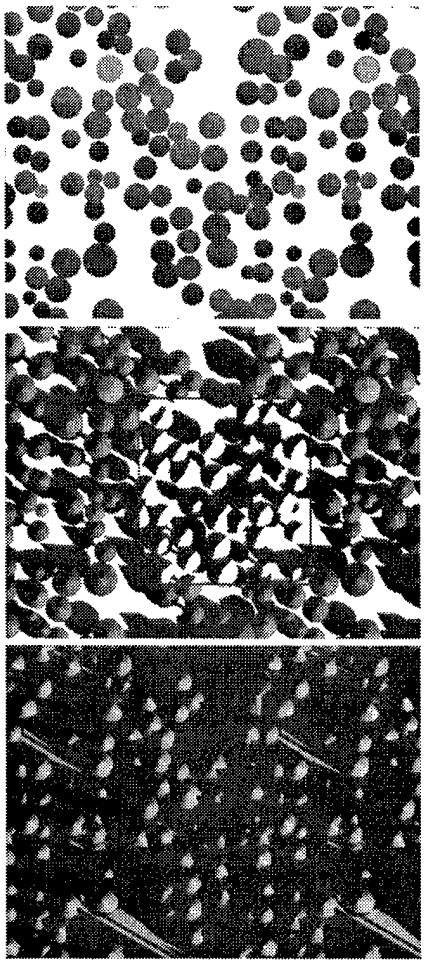

Figure 2. POV-Ray modeling output: azimuth angle = 120°, zenith angle = 0°, 30°, 60°. Note the 'classified' portion inset into the second image showing canopy fractions.

System of Experts for Intelligent DAta Management (SEIDAM) campaign [4]. The study site was imaged by the Multispectral Electro-optical Imaging Spectrometer MEIS II sensor [5] at 17:12:15 GMT (11:12:15 local) on August 1, 1993 (figure 3). Two of the eight MEIS II sensor's channels were used in this study.

Two transects were examined (a&b) to determine radiance (R) values. Transect a runs through the immature stand and the transect b runs through the mature stand. Figure 3 is a graph of the latter. Table 1 shows the radiance values extracted from the transect for each canopy fraction.

Scene Radiance Calculation & I-BRF Graphing

Scene radiance was calculated (for each illumination direction) as the linear combination of the individual component radiances weighted by their areal fractions using equation 1. 156 illumination directions were analyzed to produce a I-BRF graph for one canopy: twelve solar zenith angles (0, 5, 10, 15, 20, 25, 30, 35, 40, 45, 50, 55, 60) for thirteen solar azimuth angles (0° to 180° in 15° increments).

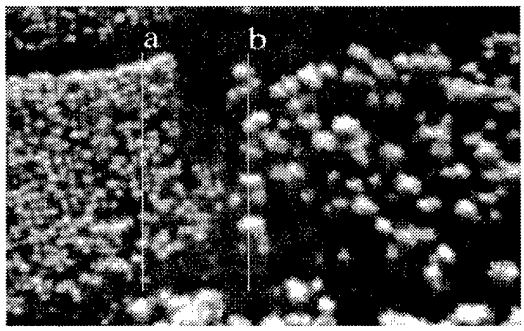

Figure 3. 1m GIFOV MEIS II image of the study site.

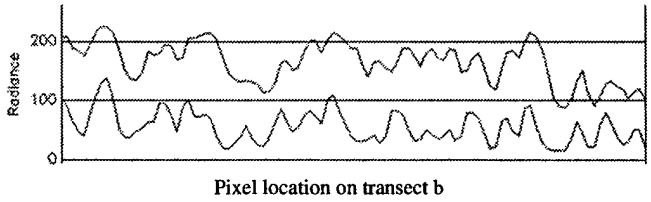

Figure 4. Radiance values for transect b, mature canopy, 875 nm (upper) and 641 nm. Note the crowns and wells apparent in this 1m dataset. Crowns averaged 3.003m in radius.

Table 1. MEIS channels and canopy fraction radiances

Band	Wave-length (nm)	Rc (sunlit canopy)	Rt (shad canopy)	Rg (sunlit back-ground)	Rz (shad back-ground)
CH2	641	153	15	181	0
CH4	875	199	81	208	19

RESULTS

Figure 5 shows a comparison of the BRFs for mature and immature canopies, for 641 nm and 875 nm. Each marker represents the average of 13 azimuth angles for each zenith angle. Second order polynomial curves are fit to each series. Though small, some ansiotropic differences can be seen when comparing the shape of the BRF curves for mature and immature canopies. The differences look similar, at first examination, to the slope differences seen in [2].

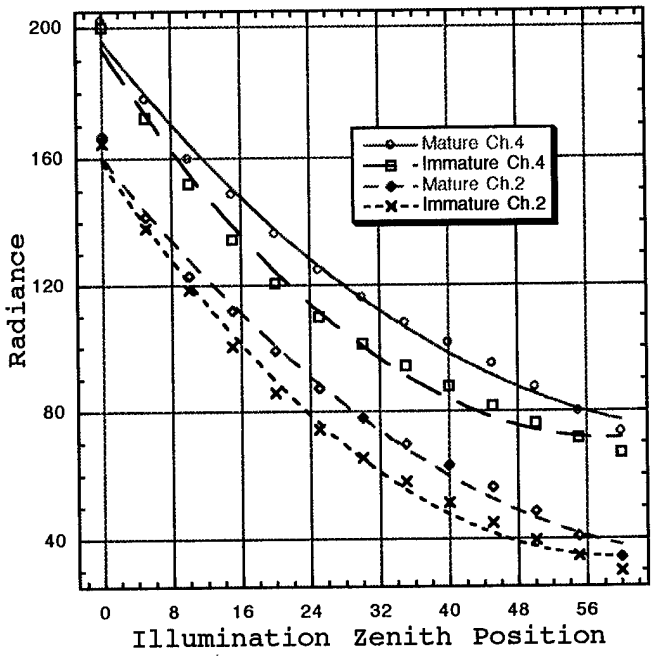

Figure 5. Scene radiance change with illumination position for mature and immature canopies at two wavelengths. The differences in slope and curve shape indicate some difference between mature and immature Douglas fir I-BRF (i.e. compare circle versus square for the 875 nm wavelength).

DISCUSSION

The goal of the research effort described herein was to develop a flexible methodology utilizing 3-D graphics with which to analyze conifer canopy anisotropy. This methodology takes advantage of developments in 3-D modeling software, which allow very accurate modeling of the radiation regime within a complex surface. Additionally, high spatial resolution imaging spectrometers are used to provide better estimation of canopy fraction radiance values.

The I-BRF plots produced in this study can now be compared to results from other modeling and field BRF campaigns. We are presently pursuing a number of ideas which will improve on this methodology, including increased automation of the BRF graph generation, production of V-BRF plots and use of more complex graphical representations of the trees. In addition, we hope to examine the effects of slope on BRF in the future.

REFERENCES

[1] Hall, F.G., Shimabukuro, Y.E. and K.F. Huemmrich, "Remote sensing of forest biophysical structure using mixture decomposition and geometric reflectance models," Ecological Applications, vol. 5, pp. 993-1013, 1995.

[2] Syrén, P., "Reflectance anisotropy for nadir observations of coniferous forest canopies," Remote Sensing of Environment, Vol. 49, pp. 72-80, 1994.

[3] X. Li and A. H. Strahler, " Geometric-Optical Modeling of a Conifer Forest Canopy," IEEE Transactions on Geoscience and Remote Sensing, Vol. 23, pp. 705-721, 1985.

[4] Hay, G.J. and K. O. Niemann, "Visualizing 3-D texture: a three-dimensional structural approach to model forest texture," Canadian Journal of Remote Sensing, Ottawa, Vol. 20, pp.90-101., 1994.

[5] D. G. Goodenough, M. Goldberg, G. Plunkett and J. Zelek, "An expert system for remote sensing," IEEE Transactions on Geoscience and Remote Sensing, Vol. 25, pp. 349-359, 1987.

Notes:

1. Software used in this research:

The 'fire-cracker forest' was rendered using POV-Ray 3.0 ray-tracing software (free at http://www.povray.org). Once set-up, each image took approximately 15 minutes to render on a PowerMac 7600/132. Images for one I-BRF (156 renderings) thus took 39 hours to generate. MEIS data analysis and POV-Ray output (PICTs) classification and histogram analysis were done utilizing RSI's IDL and ENVI. Scene radiance was calculated in Microsoft Excel and the final I-BRF graphs were produced using Surfer (Golden Software) and Kaleidagraph (Abelbeck Software).

2. The author gratefully acknowledge the support of the Greater Victoria Water District.

3. This research was supported in part by the Spatial Sciences Laboratory, Department of Geography, University of Victoria, and by the Canadian Forest Service, Natural Resources Canada and NSERC.

FOREST CARTOGRAPHY OF SPAIN BASED ON THE CLASSIFICATION OF NOAA-AVHRR MULTITEMPORAL IMAGES

Dr. Federico González-Alonso
Laboratorio de Teledetección
Instituto Nacional de Investigaciones Agrarias (INIA)
Apartado de Correos 8.111
28080 Madrid España
Tef: 34-1-3476828 Fax: 34-1-3572293 e-mail: alonso@inia.es

Dr. José Luis Casanova Roque
Laboratorio de Teledetección
Departamento de Física Aplicada
Facultad de Físicas. Universidad de Valladolid
Valladolid España
Tef: 34-83-423130 Fax: 34-83-423130

Abstract -- Fast and common forest cartography in the whole Spanish territory, based on the images provided by the AVHRR sensor, belonging to the NOAA satellites, can be of a great help to identify the areas where the most important changes of the forest covers have taken place. A non-supervised multitemporal classification based on six weekly composites images of the Normalized Vegetation Index - NDVI- has been done. Its results are promising. The purpose is to obtain a fast and inexpensive cartography of the whole country, which allows bring it up-to-date easily.

INTRODUCTION

Several authors have tried the cartography of the forest covers in a large scale, based on the data provided by the AVHRR sensor, installed in the NOAA satellites. Their results were very satisfactory. [1], [2], [3], [4], [5]

According to 1989 official statistics, the total forest territory of Spain occupies an area of 22,7 millions of hectares in which wooded and non-wooded ground are included.

However, one has to keep in mind the vulnerable conditions of the Spanish woods. Due to the strength of wild fires (during the last 25 years more than 5 millions of hectares of forest grounds have been destroyed) and the abandon of rural areas which increased bushes and woods, it is very hard to obtain a realistic and up-to-date data of the forest occupied area.

The goal of this work consists on obtaining in an approximate but frequent way cartography of the forest grounds based on the data contained on the images of the AVHRR sensor, belonging to the NOAA satellites. The antenna installed in the Laboratory of Remote Sensing at the University of Valladolid receives these data.

PROCEDURE

The procedure is based on the following steps:

1. Radiometric and atmospheric correction of AVHRR channels 1 and 2.
2. Geometric correction of the images.
3. Determination of the Normalized Vegetation Index (NDVI) based on the channels 1 and 2.
4. Calculation of the NDVI Maximum Value Composite for each weekly period.
5. Formation of a multitemporal 1994 year's file based on the following NDVI weekly composites:
   Forth week of March, forth week of April, forth week of May, forth week of June, third week of July, forth week of August.
6. Non-supervised classification in 12 types of the former multitemporal file, according to the ISODATA procedure.
7. Interpretation of the types obtained in the former step

0-7803-3836-7/97/$10.00 © 1997 IEEE

identifying their forest type, according to the evolution performed by the NDVI in a period of time and geographic area.

RESULTS

The results have allowed evaluate the Spanish forest area in 1994. The figure obtained was 24,6 millions of hectares which means an increase compared to the official figures of 1989.

The accurateness of this classification has been calculated as a 62.26%, taking as a reference the land use classification in Spain, in the CORINE project of the European Union.

The results obtained through the proposed procedure are promising. Moreover, they would allow achieve yearly forest cartography of Spain in a simple and economic way. There, it would be easy to detect the changes caused in the forest covers due to wild forest fires or other reasons such as the increase of woods and bushes in agricultural areas, and reforestation.

CONCLUSION

Cartography in a large scale of the Spanish forest areas which is based on the multitemporal classification of maximum weekly compounds of the Normalised Vegetation Index NDVI provided by the NOAA-AVHRR images, seems to be a feasible method. However, it is necessary to perform more methodological experiments that allow the gathering of more precise data.

ACKNOWLEDGMENTS

This work has been performed within the SC96-096 research project, sponsored by the National Institute of Research and Agrarian and Alimentary Technology (INIA), belonging to the Research and Development Program of the Ministry of Agriculture, Fishing and Food.

BIBLIOGRAPHY

[1] K.B. Teuber, "Use of AVHRR imagery for large-scale forest inventories". Forest Ecology and Management, vol33/34. pp. 621-131, 1990.

[2] Z. Zhu and D.L. Evans, "Mapping midsouth forest distributions". Journal of Forestry, pp. 27-30, December 1992.

[3] Z. Zhu and D.L. Evans, "US forest types and predicted percent forest cover from AVHRR data". Photogrammetric Engineering & Remote Sensing, vol. 60, n° 5. Pp. 525-531, May, 1994.

[4] W. J. Ripple, "Determining coniferous forest cover and fragmentation with NOAA-9 Advanced Very High Resolution Radiometer data". Photogrammetric Engineering & Remote Sensing, vol. 60, n°5, pp. 533-540, May, 1994.

[5] D.P. Roy, P. Kennedy, and S. Folving, "Combination of the Normalised Difference Vegetation Index and surface temperature for regional scale European Forest cover mapping using AVHRR data". International Journal of Remote Sensing, vol. 18 n°5, pp. 1189-1195, March 1997.

Remote Sensing for Estimating Chlorophyll Amount in Rice Canopies

Sukyoung Hong*, Sangkyu Rim*, Jeongtaek Lee*, and Jeeteh Kim**
Remote sensing Lab., Soil Management Div., *National Institute of Agricultural Science and Technology,
249 Seodungong, Kwonsungu, Suwon 441-707, Korea, Tel:+82-331-290-0246, Fax:+82-331-290-0222
Email:syhong@sun20.asti.re.kr

**College of Agriculture, Dankook University, Chunan 330-714, Korea

ABSTRACT

We examined the feasibility of radiometrical remote sensing for leaf chlorophyll amount of rice canopies under field condition and applications of this concept to crop condition related to leaf nitrogen content. We measured spectral reflectance, leaf chlorophyll amount, and leaf nitrogen content of rice canopies at each development state. LANDSAT TM equivalent band set was created by averaging measured spectral reflectance values to the real TM band range. Chlorophyll amount was highly significant in the visible ranged TM equivalent band and in the biband ratios of NIR(TM4) and VIS(TM3, TM2, TM1) region. In addition, leaf chlorophyll amount was closely related to leaf nitrogen content and was applied therefore to estimate the leaf nitrogen content in rice canopies.

Table 1. Correlations between leaf chlorophyll amount, leaf nitrogen content, TM equivalent bands, and VI's in rice canopies.

Parameter	Chl.	Nitrogen	Chl.	Nitrogen
	(Before heading)		*(After heading)*	
Chl.	1	0.97**	1	0.94**
Nitrogen	0.97**	1	0.57**	1
TM1	-0.68**	-0.68**	-0.13	0.01
TM2	-0.70**	-0.70**	-0.68**	-0.69**
TM3	-0.69**	-0.66**	-0.70**	-0.85**
TM4	0.43	0.47*	0.34	0.39*
TM5	0.28	-0.06	-0.23	-0.11
TM7	0.09	-0.23	-0.40*	-0.30
VI1	0.83**	0.86**	0.23	0.41*
VI2	0.91**	0.91**	0.87**	0.72**
VI3	0.78**	0.83**	0.68**	0.87**
VI4	0.90**	0.91**	0.24	0.20

VI1=TM4/TM3, VI2=TM4/TM2
VI3=TM4/TM1, VI4=log(TM4/TM3)

* Denotes significance at the 5 percent level
** Denotes significance at the 1 percent level

INTRODUCTION

Reflectance in the visible region of the electromagnetic spectrum is mainly influenced by cholorophyll pigments[1]. Therefore, reflectance spectra in this region can be used to estimate chlorophyll amount and nitrogen content[2]. Nitrogen is a dominant factor affecting plant chlorophyll content which is, in general, related to yield. Remote sensing of chlorophyll content offers the possibility of rapidly estimating crop N content and therefore crop productivity[3].

Our objectives in this study is to estimate chlorophyll amount (a+b) on a leaf-area basis of rice canopies using TM equivalent band and their ratio which can be also applied to diagnose leaf nitrogen status of rice canopies.

MATERIALS AND METHODS

We measured spectral reflectance of paddy rice canopies (Ilpumbyeo) using spectroradiometer(GER Inc. SFOV : 0.35 - 2.50 μm) *in situ* weekly or biweekly from transplanting to ripening stage. Leaf chlorophyll amount and leaf nitrogen content per unit ground area were also measured with 80 % acetone solution and micro-Kjeldahl method, respectively. Spectral reflectance values were calculated as the ratio of canopy radiance to the radiance of a reflectance standard

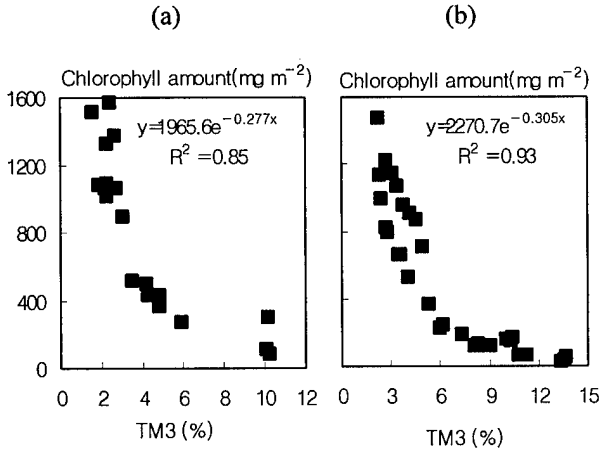

Figure 1. Regression model for estimating chlorophyll amount of paddy rice with TM3 equivalent band before(a) and after(b) heading stage.

0-7803-3836-7/97/$10.00 © 1997 IEEE

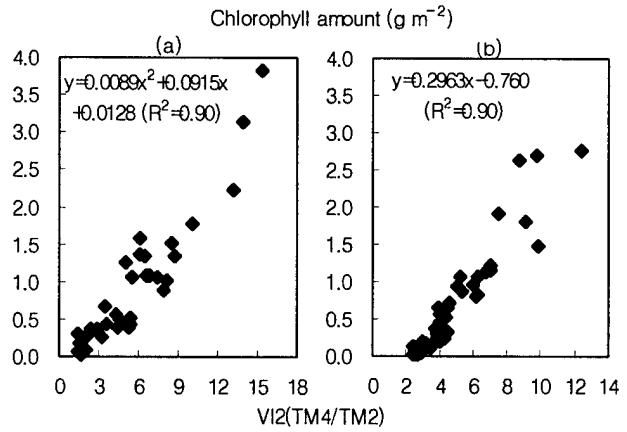

Figure 2. Regression model for estimating chlorophyll amount of paddy rice with VI2(TM4/TM2) before(a) and after(b) heading stage

which was a barium sulfate plate.

SAS procedures were used to determine the relations between the TM equivalent bands, leaf chlorophyll amount, and leaf nitrogen content, and to draw out the way for estimating chlorophyll amount of rice canopies using TM equivalent band set. LANDSAT TM equivalent band set was created by averaging measured spectral reflectance values to the real TM band range.

RESULTS AND DISCUSSION

Amount of chlorophyll a and b in the leaf is closely related with leaf nitrogen content during growing period as shown in Table 1, and it is related with other agronomic parameters, LAI, total dry matter, and plant height as well, especially before heading stage. This fact also infer the possibility of spectral estimation for nitrogen content. After heading, nutrients in the leaves moved to the grain just developed, leaf chlorophyll amount thus may show relatively low correlation coefficient with leaf nitrogen content.

Both leaf chlorophyll amount and nitrogen content were inversely related to the visible ranged TM equivalent bands, that is why light absorbtance by leaves in the visible region of the spectrum depends primarily on the concentration of the chlorophylls. Chlorophyll amount of leaf was estimated with TM3 equivalent band before and after heading stage. The relation was best described by an asymtotic model(Fig.1).

We examined some biband ratios of NIR(TM4) and VIS(TM3, TM2, TM1) for estimating leaf chlorophyll amount per unit area. In the spectral signature analysis by remote sensing, the combination of red and near-infrared bands is widely used for estimating the biomass and the productivity of vegetation. The cellular structure of leaf mesophyll scatters and reflects strongly near-infrared energy. In the visible part of the spectrum(0.4-0.7 ㎛) leaf reflectance is low because of absorptioon by chlorophyll. This concept could be applied to estimating leaf chlorophyll amount in this paper since that is closely related with other agronomic parameters such as LAI, total dry matter. Multispectral ratio of TM4/TM2 which was the best estimated chlorophyll amount of leaf before and after heading stage(Fig.2).

Estimated chlorophyll amount with TM4/TM2 was a little lower than the measured one(slope=0.91) during rice growing period(Fig.3)

Chlorophyll is a nitrogen compound, leaf chlorophyll amount is thus mainly determined by N availability. Scattergram of nitrogen content (g m^{-2}) versus chlorophyll amouont (g m^{-2}) is illustrated in Fig. 4. The coefficient od determination for before and after heading stage were 0.94 and 0.89, respectively, and the both plots lay on or around a single straight line.

The estimation of crop condition by remote sensing based on multi-channel band is difficult and research is still in the early stage. Chlorophyll aount monitoring is relatively simple in terms of crop condition than any other agronomic parameters because chlorophyll amount of leaf infer the leaf nitrogen content.

Estimated nitrogen content with chlorophyll amount observed was compared with the measured one(Fig.5). The ditermination coefficient of this linear model was 0.92 and the slope was 0.92 also. This model showed that leaf chlorophyll amount might be used to diagnose leaf nitrogen content in terms of crop condition in rice canopies.

CONCLUSIONS

Chlorophyll in plant has an important role as an indicator of photosynthesis, nutrient dificiency, pest infection, and so on.

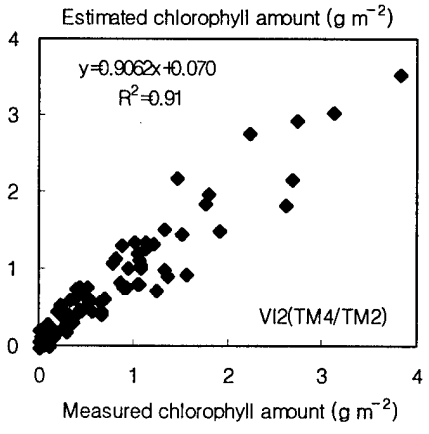

Figure 3. Relationship between measured and estimated chlorophyll amount with VI2(TM4/TM2) during rice growing period.

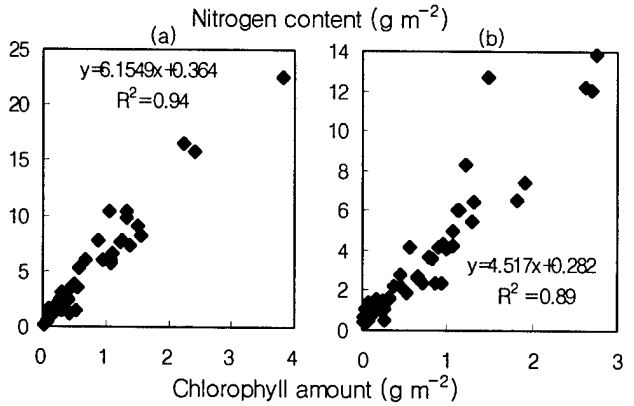

Figure 4. Relationship between leaf chlorophyll amount and leaf nitrogen content of rice canopies before(a) and after(b) heading.

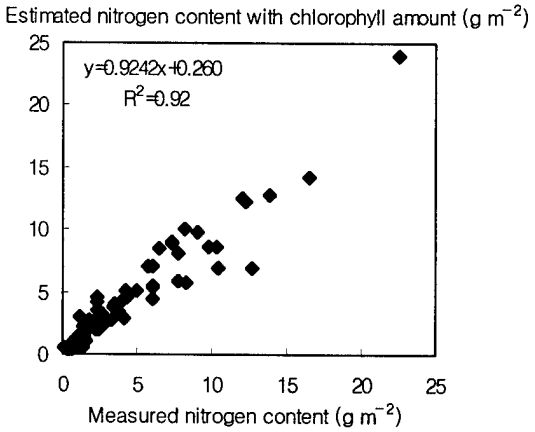

Figure 5. Relationship between measured and estimated nitrogen content with chlorophyll amount during rice growing period.

In consequence, advanced utilization procedures of remotely sensed field spectral data should be developed for growth diagnosis or stress detection in the next step.

In this study, we could follow a change in chlorophyll amount concerned with nitrogen content using reflectance measurements in rice canopies.

REFERENCES

[1] J. R. Thomas and H. W. Gausman, "Leaf reflectance versus leaf chlorophyll and carotenoid concentrations for eight crops," Agronomy J., 69, pp 799-802, 1977

[2] J. R. Thomas and G. F. Oerther, "Estimating nitrogen content of sweet pepper leaves by reflectance measurements," Agronomy J., 64, pp 11-13, 1972

[3] I..Filella, L. Serrano, J. Serra, and J. Peñuelas, "Evaluating wheat nitrogen status with canopy reflectance indices and discriminant analysis," Crop Sci., 35, pp 1400-1405, 1995

* NIAST 97-1-2-41

Estimation of Leaf Area Index and Total Dry Matter of Rice Canopy by Using Spectral Reflectance

Jeong Taek Lee* , Chun Woo Lee**,Suk young Hong* and Moo Eon Park*
*National Institute of Agricultural Science and Tecnology,Suwon ,441-707,Korea
**Hungnong Seed Co. Cheonan ,333-802.Korea

ABSTRACT

To estimate leaf area index(LAI) and total dry matter(TDM) of rice canopy by non-destructive method, the spectral reflectance from the canopy was measured weekly by the spectroradiometer during the growing season. The reflectivity of visible band remained less than 0.1 throughout the growing season, but that of near infrared band varied from 0.1 to 0.5, showing the positive correlation with LAI, Vegetation index by narrow band(10nm),R910/R460 showed strong correlation with LAI and TDM.

INTRODUCTION

Leaf area index(LAI) and total dry matter(TDM) of plant canopy are widely used indices of vegetative canopy structure that are difficult to measure directly [3],[4]. Non destructive measurement of leaf area index and total dry matter of rice crop was attempted by analyzing spectral property measured with a spectroradiometer in a paddy field in Suwon, Korea.
From this analysis, we have determined the most effective spectrum band and suitable vegetation index for estimating LAI and TDM.

MATERIALS and METHODS

Three rice varieties, Ilpum, Daechung(medium late maturing varieties) and Jinbu(early maturing variety) were cultivated in Suwon Meteorological Office paddy field (37·16 'N, 126 59 ' E,39m m.s.l.). The seeds were sown on 30 April and they were transplanted to the paddy field on 20 May in 1993. Planting density of the rice plant was 30cm x 15cm per hill (22.2 plants m^{-2}). Fertilizer application rates were 150-90-110 $kg \cdot ha^{-1}$(N-P_2O_5-K_2O). Spectral reflectance was measured by spectroradiometer (Licor 1800) around 11 o'clock on clear days, during which solar elevation changes were relatively stable. Spectral wavelength to be scanned ranged from 330nm to 1100nm at every 10nm interval.

Plant samples were taken from each plot after spectral measurements to determine LAI and TDM in every 10 days during the growing season. Estimations of LAI and TDM production were conducted by correlation analysis with spectral reflectance ratio and measured values. We selected the best fitting waveband ratio among calculated reflectance ratio and known several vegetation index.

RESULTS AND DISCUSSION

The changes of the spectral reflectance pattern in rice canopy before heading stage are shown in Fig 1. Spectral reflectance of early growth stage showed a peak at green light spectrum within visible band and relatively high value at 910nm and 1070nm within infrared band. Spectral reflectance

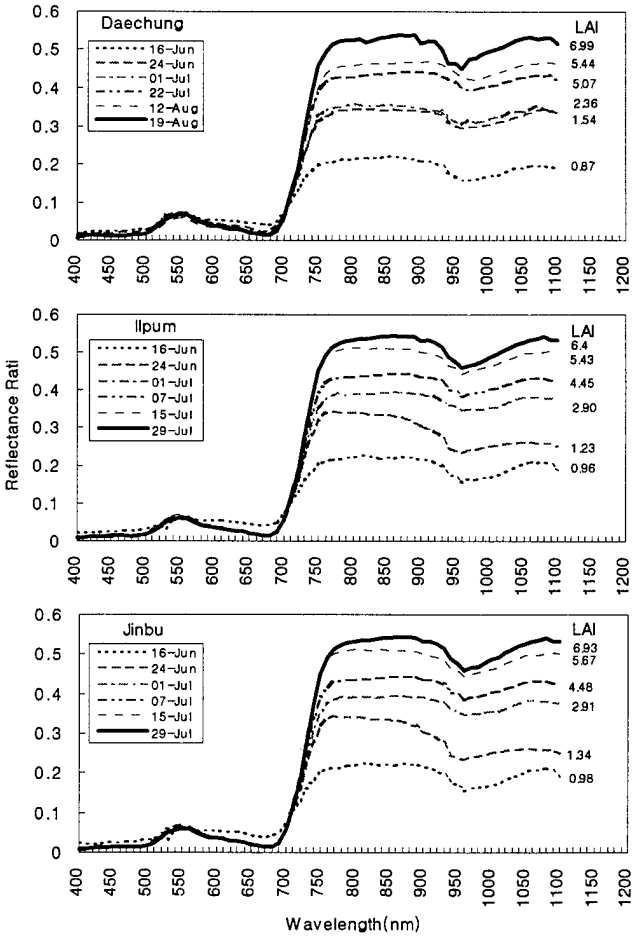

Fig. 1 Reflectivity profiles as affected LAI changes of three rice varieties

0-7803-3836-7/97/$10.00 © 1997 IEEE

Table 1. Correlation coefficients of LAI with vegetation indices.

Vegetation	Transplanting to heading			Heading to maturing		
Index	Daechung	Ilpum	Jinbu	Daechung	Ilpum	Jinbu
NIR/Blue	0.935**	0.977**	0.978**	0.525	0.680*	0.995*
NIR/Green	0.914**	0.911**	0.916**	0.752**	0..806*	0.960**
NIR/Red	0.908**	0.936**	0.920**	0.939**	0.910**	0.988**
R850/650	0.912**	0.942**	0.920**	0.957**	0.923**	0.982**
R800/550	0.902**	0.900**	0.891**	0.939**	0.857**	0.793*
R910/460	0.960**	0.979**	0.962**	0.740**	0.738**	0.987**
R950-550	0.899**	0.932**	0.974**	0.463	0.050	0.887**
R1050-550	0.898**	0.931**	0.979**	0.492	0.177	0.864*
ND7	0.768**	0.757**	0.788*	0.734*	0.950**	0.921**
NVI	0.760**	0.758**	0.750*	0.974**	0.963**	0.898**
MSS7/MSS4	0.917**	0.918**	0.920**	0.692*	0.791**	0.997**
MSS7/MSS5	0.909**	0.933**	0.921**	0.912**	0.897**	0.992**
TM4/TM1	0.941**	0.965**	0.931**	0.827**	0.800**	0.997**
TM4/TM3	0.977**	0.892**	0.915**	0.968**	0.920**	0.988**

*, ** : Significant at 5%, 1% level respectively.
ND7 : (MSS7-MSS5)/(MSS7+MSS5), NVI :(TM4-TM3)/(TM4+TM3)

Table 2. Correlation coefficients of total dry matter with vegetation indices.

Vegetation	Transplanting to heading			Heading to maturing		
Index	Daechung	Ilpum	Jinbu	Daechung	Ilpum	Jinbu
NIR/Blue	0.887**	0.914**	0.957**	0.582	0.780**	0.890**
NIR/Green	0.897**	0.843**	0.945**	0.791**	0.879**	0.958**
NIR/Red	0.882**	0.870**	0.933**	0.927**	0.978**	0.927**
R850/650	0.884**	0.875**	0.931**	0.907**	0.991**	0.931**
R800/550	0.898**	0.837**	0.933**	0.917**	0.922**	0.924**
R910/460	0.924**	0.926**	0.971**	0.750**	0.838**	0.919**
R950-550	0.835**	0.848**	0.920**	0.417	0.120	0.785*
R1050-550	0.843**	0.864**	0.917**	0.426	0.151	0.864*
ND7	0.693*	0.658*	0.736	0.944**	0.957**	0.966**
NVI	0.682*	0.658*	0.697	0.956**	0.974**	0.967**
MSS7/MSS4	0.899**	0.853**	0.948**	0.742**	0.865**	0.904**
MSS7/MSS5	0.884**	0.868**	0.937**	0.914**	0.967**	0.919**
TM4/TM1	0.909**	0.900**	0.943**	0.818**	0.897**	0.889**
TM4/TM3	0.886**	0.819**	0.928**	0.925**	0.991**	0.921**

*,** : Significang at 5%, 1% level respectively
ND7 : (MSS7-MSS5)/(MSS7+MSS5), NVI : (TM4-TM3)/(TM4+TM3)

in visible band changed from high to low with increasing LAI, however, spectral reflectance of infrared band was increased with increasing LAI [1],[5]. The reflectivity of visible band remained less than 0.1, but near infrared wave band ranged from 0.1 to 0.5 throughout growing season.

The relationships between reflectance of rice canopy and LAI are show in Table 1. Correlation coefficient between LAI and ratio of infrared band over blue, green, red band ranged from 0.91 to 0.98, and narrow band reflectance ratio which is R910/R460 ranged from 0.96 to 0.98 at three varieties from transplanting to heading date.

But several vegetation indices (ND7,NVI,MSS7/MSS5, and MSS7/MSS4) showed relatively low correlation coefficient. After heading stage, correlation coefficient between LAI and spectral reflectance ratio showed lower value than before heading stage. But wide band ratio such as ND7,NVI and TM4/TM3 showed high value.

Relationships between vegetation index (R910/R460)and measured LAI by destructive method in the rice canopies are shown in Fig. 2. They show strong linear relationship and their correlation coefficients are higher than 0.922.

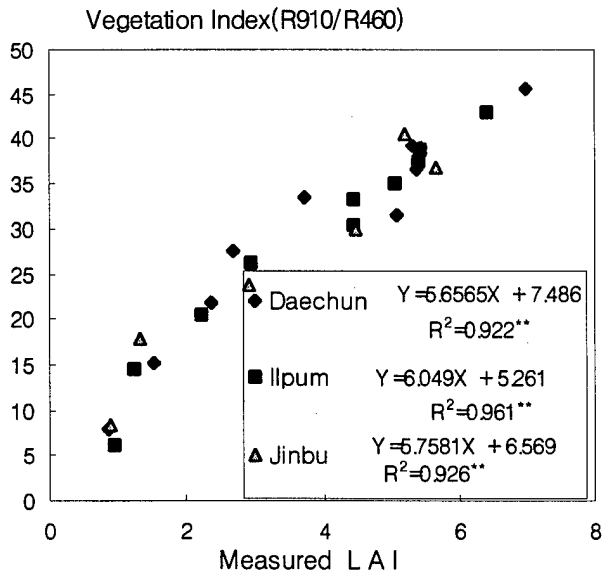

Fig.2 Relationships between vegetation index(R910/R460) and LAI in rice canopies.

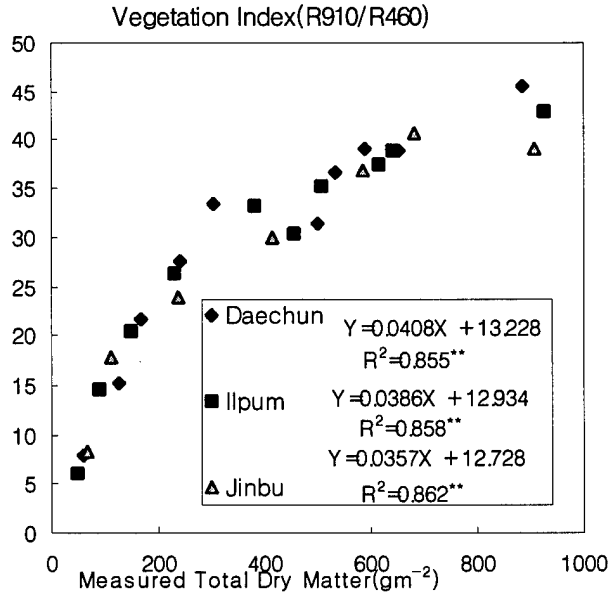

Fig.3 Relationships between vegetation index(R910/R460) and total dry matter in rice canopies.

The fully grown rice canopies with high LAI represent high vegetation index. Vegetation index increased about 5.7 by 1 increment of LAI and the rate was highest in Ilpum.

The relationships between reflectance and TDM are shown in Table 2. Correlation coefficient between TDM and ratio of infrared band over blue, green, red band ranged from 0.87 to 0.95. Narrow band reflectance ratio (which is R910/R460) ranged from 0.92 to 0.97 for three varieties during the period from transplanting to heading. These values are smaller than correlation coefficient with LAI but after heading several vegetation index (ND7, NVI, MSS7/MSS5, and (MSS7/MSS4) showed relatively higher correlation coefficient than before heading [2],[6].

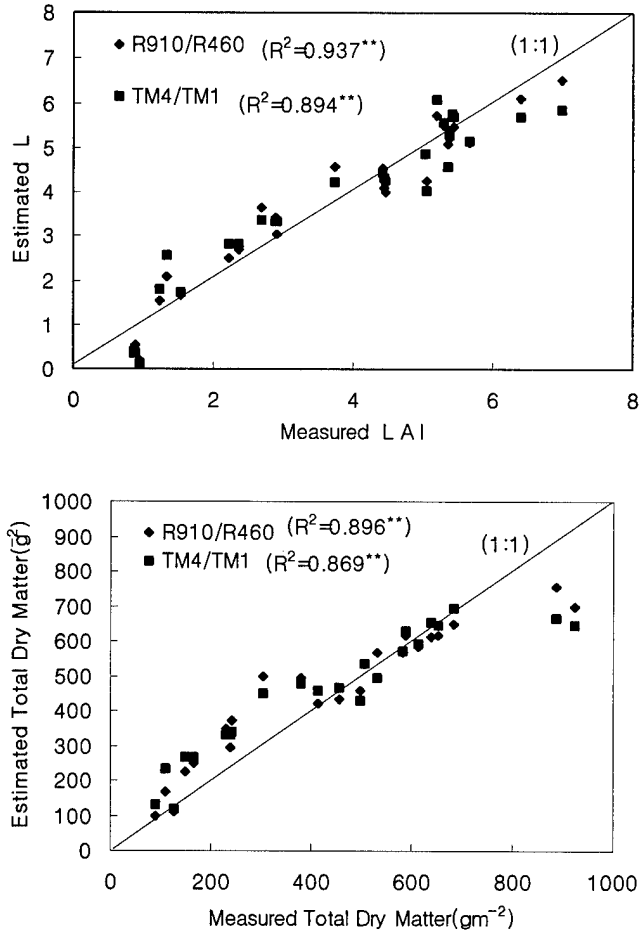

Fig. 4 Relationships between measured and estimated values of LAI and total dry matter in the rice canopies

Relationships between vegetation index (R910/R460)and measured total dry matter in the rice canopies are shown in Fig. 3. They show strong linear relationship and their correlation coefficients are more than 0.855 but these values are lower than the relationship with LAI and vegetation index (R910/R460). The rate of increase in vegetation index was about 0.04 with the 1 gm^{-2} of dry matter production. The rate was differ among varieties, higher in Daechung but lower in Jinbu.

The relationships between the measured and estimated values of the LAI and total dry matter are shown in Fig. 4. The measured and the estimated were distributed with one to one line. The correlation coefficient for the LAI were 0.937 with vegetation index(R910/R460), 0.894 with TM4/TM1. The correlation coefficient for TDM were 0.896 with vegetation index(R910/R460), and 0.8869 with TM4/TM1 respectively. These results suggest that the LAI and TDM can be estimated quantitatively by remote and non-destructive measurement using a optical property analysis.

References

[1] Inoue Y., K. Iwasaki. 1991. Spectral estimation of radiation absorptance and leaf area index in corn canopy architecture and growth stage. Japan. Jour. Crop Sci. 60(4):578-580.

[2] Shibayama, M. and K. Munakata. 1986. A spectroradiometer for Field (III). A comparison of some vegetation indices for predicting luxuriant paddy rice biomass. Japan Jour. Crop Sci. 55:47-52 Welles J. M.,

[3] Wellws J. M. 1990 Some indirect method of estimating canopy structure. .Remote Sensing Reviews Vol. 5. 31-43

[4] Welles J.M., J.m. Normanm. 1991 Instrument for indirect measurement of canopy architecture. Agronomy Journal Vol. 83. 818-825.

[5] Yamamoto H., H. Honjo, and Y. Wakiyama. 1990. Evaluation of leaf area index and biomass of soybean canopies using spectral reflectivity. J. Agr. Met.46(1):19-22.

[6] Yang, Young-Kyu. 1985. Correlation of rice grain yield to radiometric estmates of canopy biomass as a function of growth stage. J. of Korean Society of Remote Sensing. Vol.1 163-187

*NIAST 97-1-2-43

Spectral Unmixing and Mapping of Surface Features Related to Soil Erosion

G. I. Metternicht† and A Fermont‡
Curtin University of Technology, School of Surveying and Land Information,
GPO Box U 1987, Perth 6001, Western Australia
TE: + 618 9266 3935 - Fax: +618 9266 2703 - Email:Metternicht@cage.curtin.edu.au
‡Soil Science, Wageningen Agricultural University, The Netherlands.

Abstract -- Spectral mixture modelling was performed for identification and mapping of land degradation features related to soil erosion processes. End-members were characterised by using average pure pixel reflectance. The research has demonstrated that regional patterns of soil surface erosion features can be reliably mapped using linear spectral mixture analysis. Extrapolation of this approach to other regions where soil degradation features are correlated with spectrally distinguishable surface characteristics is feasible, provided an optimisation of the unmixing model as a function of local or regional surface component types is completed.

INTRODUCTION

Techniques for mapping soil surface conditions, such as soil erosion, are commonly based on the presence or absence of spectral absorption features related to a particular indicator of degradation, such as eroded topsoils, rock fragments or vegetation. Simple identification and mapping of degradation features can be performed by automated or supervised digital information extraction, based on spectral and/or structural pattern recognition techniques. However, the reflectance recorded within an image pixel may be a mixture of several surface components, or different surface features may exhibit the same or similar spectral responses causing inconsistencies in their detection.

To resolve these problems linear unmixing, artificial neural networks and fuzzy membership functions are used to identify and estimate ground cover proportions within a pixel [1]. Thus, this paper present the results of applying spectral mixture modelling for identification and mapping of land degradation features related to soil erosion processes in a semiarid environment located in the Sacaba valley, Bolivia.

METHOD

Modelling assumptions

Linear mixture modelling assumes that the signal received at the satellite sensor depends on the proportion of individual surface components such as soil, water and vegetation present in a particular pixel and on the properties of the mixing process. Thus, spectral mixing may be modelled as a linear combination of pure components (end-members) such that:
where Ri is the reflectance of the mixed pixel spectra in band

$$Ri = \sum_{j}^{n} Fj * REij + \varepsilon i; \sum Fj = 1$$

i; $Reij$ is the reflectance of the surface component j in band i; Fj denotes the proportion of the pixel area covered by the j ground cover type; and εi is the residual error in band i [1,2,3]).

The procedure followed to discriminate and map ground cover proportions at a sub-pixel level using a linear mixture model is illustrated in figure 1. The spectral unmixing results in an abundance image for each selected end-member (surface component), providing the relative proportion of a surface feature at every pixel. Additionally, an error image and an image summing the surface component abundances at each pixel are calculated. The individual proportion maps can be used as input in a geographic information system for further spatial modelling of erosional processes and as parameters of exploratory models for hazard prediction [4]. The error image indicates how well the spectral variability is explained by the selected end-members, and is therefore used to evaluate the mapping accuracy of surface component proportions. The root mean square method is used to determine the error between the original mixed spectrum and the reconstructed one from the calculated abundances.

The linear mixture model applied in the Sacaba valley allowed to use up to five surface components to characterise the selected area, since six bands (1,2,3,4,5 and 7) of the Landsat TM sensor were used as inputs. As the linear mixture model is applied by a least square fitting of the end-members to all pixels in the image, the software requires end-members to be $(n-1)$ the number of inputs to solve the equations.

Data set

The ground data set consisted of 89 geo-referenced composite topsoils samples, contemporaneous to the acquisition of a seven-band Landsat TM image. Soil surface features such as crust colour, texture, thickness, colour and density of surface rock fragments and vegetation type and cover percentages were determined. Water erosion features were observed and recorded in relation to erosion type (gully, rills, overland flow) and degree (slight, moderate and severe).

The Spectral Image Processing system SIPS [5] was used to model the proportions of different cover types within one pixel. The program assumes that spectral mixing can be modelled as a linear combinations of image components or end-members.

Identification of end-members

Six surface components were identified on Landsat TM false colour composites (3,2,1 and 4,3,2). Aerial photographs at scale 1:25,000 and field data were used to locate 'pure'

0-7803-3836-7/97/$10.00 © 1997 IEEE

pixels representing the end-members of interest. Selected end-members were:

- *class 1*: natural vegetation, colonizing moderately and extremely eroded areas as well as ephemeral brooks. They were assumed to indicate moderate and severe erosion degrees.
- *class 2*: miscellaneous land: beds of ephemeral brooks and erosion pavements typical in badlands, resulting from the removal of finer materials from gravel lenses of depositional sequences. Presence of these surface features in areas other than brooks were related to badlands (eg. extreme erosion).
- *class 3* whitish topsoil surfaces: theses overall highly reflecting surfaces were related to sparsely vegetated areas with truncated topsoils, where topsoils features such as depositional crusts, coarse loamy textures and very light colours dominate. Erosion is moderate and severe.
- *class 4* yellowish brown soils: areas with none to very sparse vegetation cover, relatively low organic matter contents, loamy textures and low percentage of surface rock fragments. These soils were related to non-eroded areas.
- *class 5*: yellowish soils: bare or sparsely vegetated topsoil surfaces, having fine silty to fine loamy textures and variable percentages of organic matter. They corresponded to slightly eroded areas.
- *class 6*: extremely eroded areas, with evidence of removal of the surface horizons and complex topography due to the presence of gullies, rills and surface erosion pavements. Their spectral signature is a mixture of the reflectance's produced by erosion pavements, natural vegetation and eroded soils.

Location of the end-members

The application of the linear mixture model required to identify 'pure' pixels corresponding to the selected end-members. Among the various methods commonly used to determine end-members from the satellite image, three were selected: (a) identification of one 'pure' pixel representing a particular surface component from false colour composites; (b) average of 'pure' pixels to characterise a particular end-member; and (c) a method based on principal components[6]. The latter assumes that pure end-members lie at the extremes of the distribution of pixel signatures in the principal component feature space, the number of extremes equalling the number of spectrally distinct surface components. Plotting a scattergram of the principal components reveals the extremes. Thus, the principal components were calculated and plotted for the area of interest. Spectrally distinct end-members were determined and used to locate the corresponding pixels on the image, allowing the extraction of end-member signatures from the original spectral bands. For techniques (a) and (b) pixels representing the surface components were selected from false colour composites. The subsequent step consisted in computing the proportion maps.

Spectral unmixing and proportion maps

Constrained unmixing was used, thus forcing the proportion estimates for each end-member to be greater or equal to zero and the sum of the abundances less or equal to one. Four spectral unmixing approaches were tested, differing in the way the 'pure' pixels for each end-member were selected and in the type of surface component considered. Although six end-members were determined, only five at a time could be used. In the first test, one 'pure' pixel per end-member was selected, considering natural vegetation, miscellaneous land, whitish topsoils, yellowish brown soils and gully areas as end-members. The same surface components were adopted in the second approach, but the spectral signature of the end-members was determined by averaging pixel values related to a particular end-member. The third approach was also based on averaging pixel values, but gully areas were replaced by yellowish soils. Finally, in the fourth approach, the purest pixels of each surface component were selected using principal component analysis and considering natural vegetation, whitish topsoils, yellowish soils, yellowish brown soils and gully areas as the end-members (table 1).

The output of the unmixing analysis consisted in a proportion map for each of the considered surface components, one image representing the sum of all the abundances and a root-mean-square (RMS) image.

RESULTS AND DISCUSSION

Histograms of the four error images were built up to compare the standard deviation, mean and median. These parameters were used, in addition to the analysis of numerical instability, to select the best set of end-members, and the best 'pure' pixel selection procedure. The analysis of numerical instability refers to the percentage of image pixels whose abundances violate the imposed constraints and generally indicate that the end-members used do not closely match some region of the image [5]. This drawback can be eliminated either by reducing the area of interest, so that only surfaces represented by the selected end-members will be considered, or modifying the end-members themselves (table 1).

According to table 1 the use of the average pure pixel reflectances to build up the spectral signature of classes 1, 2, 3, 4 and 6 (method B) provided the best characterisation of the surface components. Method C produced the highest percentage of image pixels violating the imposed constraints, expressed by a high numerical instability, while the lowest values corresponded to method B, also showing the lowest mean and standard deviation errors. Therefore, method B was assumed to best characterise the surface components of the selected area. The median of the abundance images shows that, in 95% of the cases, the individual pixel compositions were explained by the selected surface components.

Model validation

The RMS image, representing the error between the original and the best-fitted spectrum computed from the resulting proportions of end-members, was used as input in a geographic information system to verify the spatial distribution of the errors. The image was re-classified into error ranges: 0, 1, 10 and >30%. Table 2 presents the area, in hectares, and the percentage of the error ranges resulting from the unmixing.

Table 1: Analysis of the RMS error image, numerical instability and abundance image for the considered approaches

METHOD	BRIEF DESCRIPTION	N.I.(1)	ERROR IMAGE		ABUNDANCE IMAGE		
			Mean	St. dv.	Mean	St.dv.	Median
A	One 'pure' pixel per end-member. Classes: 1,2,3,4,6	0.74	1.86	2.16	59.9	48.0	99.8
B	Average 'pure' pixels per end-member. Classes:1,2,3,4,6	0.43	1.46	1.91	59.5	47.7	95.1
C	Average 'pure' pixels per end-member. Classes:1,2,3,5,6	1.06	1.28	1.79	58.5	47.0	91.2
D	End-members selected from extreme values of scattergram done with PC1 and PC2(*). Classes: 1,2,3,4,5	0.52	5.98	5.96	60.9	99.8	48.5

(*) PC: principal component bands; (1) N.I.: numerical instability, expressed as percentage of the image pixels.

CONCLUSIONS

This research has shown that regional patterns of soil surface erosion features can be reliable mapped by using linear spectral mixture analysis. The proportion maps derived from spectral mixture modelling of remotely sensed data can be utilised as input parameters in region-oriented exploratory models of soil erosion.

Errors equal or lower than 10% were evenly distributed on the area, expressing therefore a proper characterisation of the selected surface components. The inclusion of a sixth end member could have improved the results. But because of the data set utilised and software constraints the latter surface component could not be incorporated in the analysis.

Extrapolation of this approach to other regions where soil degradation features are correlated with spectrally distinguishable surface characteristics is feasible, provided an optimisation of the unmixing model as a function of local or regional surface component types is completed.

REFERENCES

[1] D. Smith et al. 'Vegetation in deserts. I. A regional measure of abundance from multispectral images'. *Remote Sens. of Environ.* 31:1-26, 1990a.

[2] J. Adams et al. 'Spectral mixture modelling: a new analysis of rock and soil types at the Viking Lander I Site, *J.Geophys. Res* 91:8098-8112, 1986.

[3] J. Hill. 'Land degradation and soil erosion hazard mapping in Mediterranean environments with operational earth observation satellites'.*Symposium Operationalization of Rem. Sensing*, April 1993, Enschede, The Netherlands, pp. 41-51.

[4] G. Metternicht 'Detecting and monitoring land degradation features and processes en the Cochabamba valleys, Bolivia. A synergistic approach'. PhD dissertation, Gent Univ., Belgium. ITC publication No.36.

[5] CSES-CIRES. 'SIPS user's manual, v.1.2, Univ. of Colorado, Boulder, 88 pages.

[6] M. Smith et al. 'Quantitative determination of mineral types and abundances from reflectance spectra using principal component analysis. Jnal of Geophysical Research, vol.90, Supplement, pp. C797-C804, 1985.

Table 2: Error levels resulting from unmixing

ERROR RANGE (%)	AREA (HECTARES)	AREA (%)
0 - 1	2068	36
1.1 - 10	3582	63
10.1 - 30	28	1
> 30	0	--

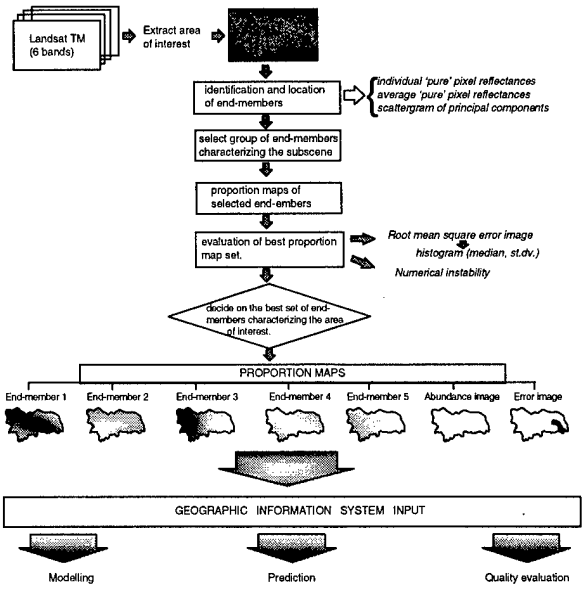

Figure 1: The mixture model

Ku-BAND SAR DATA FOR BARE SOIL MOISTURE RETRIEVAL OVER AGRICULTURAL FIELDS

E.E. Sano[1], M.S. Moran[2], A.R. Huete[1], T. Miura[1]

1 **University of Arizona, 429 Shantz Bldg. # 38, Tucson, AZ, 85721 USA**
(t) +1.520.621.1791 (f) +1.520.621.1647 email: sano@ccit.arizona.edu
2 **USDA-ARS, 200 E. Allen Road, Tucson, AZ, 85719, USA**

Abstract -- This study focused on the analyses of multiangle, Ku-band (14.85 GHz), synthetic aperture radar (SAR) data for bare soil moisture retrieval over agricultural fields. The radar data were acquired at three incidence angles (35°, 55°, and 75°), VV polarization, and 2-m nominal spatial resolution. The fields presented either a small-scale or an intermediate-scale periodic soil roughness components, associated with level-basin and furrow irrigation systems, respectively. Both of these periodic structures were randomly perturbed by the presence of soil clods. Radar backscatter and soil surface moisture data were obtained from 39 "borders" (within-field level basins). The results showed that the bare soil moisture retrieval over agricultural fields with periodic roughness components from Ku-band SAR data is dependent upon the incidence angle and the soil roughness condition. For fields with level-basin irrigation system, a good linear relationship between radar backscattering coefficients and volumetric soil moisture contents was found, especially at 35° incidence angle ($r^2 = 0.90$; for 55° and 75° incidence angles, $r^2 =$ 0.74 and 0.41, respectively). However, for fields with the furrow irrigation system, the radar backscattering data were nearly insensitive to soil moisture due to the stronger influence of soil roughness.

INTRODUCTION

Estimation of soil moisture in agricultural areas is important to improve yield forecasting, irrigation scheduling, and other farm management activities [1]. Remote sensing can provide indirect soil moisture estimates over large areas with frequent repeat coverage. The microwave region (from 1 mm to 1 m wavelength) has been the most favorable spectral region for surface soil moisture studies [2].

For a bare soil surface, the radar backscattering process is controlled by the dielectric property of the soil, which is related to the soil moisture content, and the soil random surface roughness [3], [4]. Depending upon the combination of frequency and incidence angle, the range of the radar backscattering coefficient $\sigma°$, due to variations in surface roughness, can vary up to 22 decibels (dB) [3]. The presence of periodic row or furrow structures in some agricultural sites can also exert considerable angular effects in the radar scattering process [5] - [7]. Thus, to obtain improved bare soil moisture estimates, the effects of soil roughness for a given sensor configuration need to be addressed by using either experimental data or theoretical/semiempirical models.

The objective of this study was to investigate the sensitivity of the Ku-band SAR data, acquired at three incidence angles (35°, 55°, and 75°), to the bare soil moisture content over agricultural fields with different periodic roughness structures. These sensor configurations were chosen because of their availability on existing aircraft sensor platforms.

EXPERIMENTAL DESIGN

The study site was at the University of Arizona's Maricopa Agricultural Center (MAC), a 770 hectare research and demonstration farm located south of Phoenix (33.08° N Latitude, 111.98° W Longitude), Arizona. The rectangular-shaped fields are oriented in either North-South (N-S) or East-West (E-W) directions. Each field was subdivided into 16 smaller areas defined as 'borders'. All fields selected contained the following structures produced by different tillage practices: a) a small-scale, periodic pattern associated with planting row structures with level-basin irrigation systems (approximate row spacing and amplitude = 23.6 and 1.7 cm, respectively); or b) an intermediate-scale, periodic pattern with furrow irrigation systems (measured furrow spacing and amplitude = 95 and 22 cm, respectively). Both of these periodic structures were randomly perturbed by the presence of soil clods (diameter: < 1.5 cm for fields with planting row structures and > 15 cm for furrowed fields).

A set of airborne, 16-bit magnitude SAR images acquired on January 30, 1996 by the Sandia National Laboratories (SNL) in Albuquerque, New Mexico, were analyzed in this report. The sensor operated at 14.85 GHz (Ku-band) frequency, three incidence angles (35°, 55°, and 75°), VV polarization, and 2 meter nominal spatial resolution. The radar look-direction was N72°E. Radar backscattering coefficients ($\sigma°$) were extracted using the following equation:

$$\sigma° \ (dB) = 10 \log[(DN \cdot K_1)^2] \qquad (1)$$

where DN is the average digital number for each border (average of at least 2000 pixels), and K_1 is the sensor calibration constant (0.001426 dB).

A field survey was conducted on the day before the aircraft overpass to record border-by-border qualitative estimates of the soil moisture and soil roughness conditions. Based on this survey, the following fields were selected for ground truth measurements:

0-7803-3836-7/97/$10.00 © 1997 IEEE

a) fields with planting row structures: field 18, borders 1, 15, and 16; field 23, borders 6, 7, 8, and 9; field 26, borders 1, 5, 9, and 13; and field 34, all 16 borders; b) furrowed fields: field13, borders 1, 2, 3 and 4; field 21, borders 1, 2, 5 and 6; field 27, borders 3 and 5; and field 31, borders 1 and 2. These fields were characterized by bare soil or near-bare soil (less than 5 % of wheat cover) conditions. The borders were selected taking into consideration the soil moisture variability within the field.

Soil samples for gravimetric soil moisture measurements within the top 2 cm were collected in all of the above fields during the Ku-band overpass. Because of the high homogeneity of the soil moisture condition within each border in the fields with planting row structures, one sample per border was collected at the center of its border. For the fields with furrow structures, three samples located at the bottom, middle and top of the furrows were collected and averaged for one reading. Volumetric soil moisture contents (*Mv*) were derived using an average bulk density of 1.4 g/cm^3 for the farm (D.F. Post, personal communication, 1996).

RESULTS

Figure 1 presents the linear relationship between radar backscattering coefficient $\sigma°$ and % volumetric soil moisture content *Mv* for fields with a planting row structure. The backscattering coefficients from all borders with the same soil moisture contents within the same field were averaged. The test of significance for the correlation coefficients indicated that the correlations were significant at 0.01 critical value. The best linear fit was found for the 35° incidence angle (slope = 23.71, $r^2 = 0.91$, for a confidence level of 95%), whereas the 75° incidence angle configuration was nearly insensitive to the soil moisture (slope = 6.85, $r^2 = 0.42$). Despite an overall positive trend, the Ku-band at a 55° incidence angle was nearly insensitive to soil moisture smaller than 25%. The sensitivity of $\sigma°$ to the planting row direction was weak: for similar soil moistures, the $\sigma°$ values from fields with N-S planting rows (Fields 23 and 34) were also approximately similar to those from fields with E-W planting rows (Fields 18 and 26).

Figure 2 shows the scatterplot between $\sigma°$ and *Mv* from the furrowed fields. The $\sigma°$ was insensitive to soil moisture for all sensor configurations, most likely because of the dominant influence of the soil roughness in the backscattering process.

CONCLUDING REMARKS

Results of this investigation presented two opposite results. SAR data from MAC was sensitive to soil moisture for fields with planting row structures, particularly for the Ku-band with a 35° incidence angle. The direction of the small-scale, periodic roughness components did not influence the scattering process, regardless of frequency and sensor incidence angle. For the Ku-band with a 55° incidence angle, the radar data were nearly insensitive to soil moisture levels below 25%. However, for furrowed fields, the SAR data from all configurations analyzed in this study were insensitive to soil moisture content. The relatively large, randomly distributed soil clods in the furrowed fields most likely played a major role in the radar backscattering process.

Therefore, the estimation of soil moisture from furrowed fields with large soil clods using SAR data operating at a single polarization and a single frequency seems to be difficult, unless some technique to reduce the effects of soil roughness is applied. For instance, [8] obtained an improved soil moisture estimation from a rocky soil in a semiarid region by subtracting wet season $\sigma°$ from a dry season $\sigma°$. The assumption was that the SAR data from a dry season was dependent only on the soil roughness. This technique, upon validation, can be an easy way to reduce the soil roughness effects and should be also tested in agricultural fields.

ACKNOWLEDGMENTS

The authors wish to thank Tom Mitchell for his help in processing the SAR images. Jiaguo Qi and Ed Barnes provided assistance in soil roughness and moisture content field measurements. Partial support for this research was provided by the National Science Foundation (INT-9314872). We are also grateful to personnel at the Maricopa Agricultural Center (MAC), for their assistance and cooperation.

REFERENCES

[1] S.B. Idson, R.D. Jackson, and R.J. Reginato, " Detection of soil moisture by remote surveillance," Amer.Sci. vol.63, pp. 549-557, 1975.

[2] E.T. Engman, and N. Chauhan, "Status of microwave soil moisture measurements with remote sensing," Remote Sens. Environ. vol. 51, pp. 189-198, 1995.

[3] F.T. Ulaby, P.P. Batlivala, and M.C. Dobson, "Microwave backscatter dependence on surface roughness, soil moisture and soil texture: Part I - bare soil," IEEE Trans. Geosci. Electron. vol.16, n. 4, pp. 286-295, 1978.

[4] R. Bernard, P.H. Martin, J.L. Thony, M.Vauclin, and D. Vidal-Madjar, "C-band radar for determining surface soil moisture," Remote Sens. Environ. vol.12, pp. 189-200, 1982.

[5] P.P. Batlivala, and F.T. Ulaby, "Radar look direction and row crops," Photogramm. Eng. Remote Sens. vol. 42, n. 2, pp. 233-238, 1976.

[6] F.T. Ulaby, and J.E. Bare, "Look direction modulation function of the radar backscattering coefficient of agricultural fields," Photogramm. Engin. Remote Sens. vol. 45, n. 11, pp. 1495-1506, 1979.

[7] A. Beaudoin, T. LeToan, and Q.H.J. Gwyn, "SAR observations and modeling of the C-band backscatter variability due to multiscale geometry and soil moisture," IEEE Trans. Geosci. Remote Sens. vol. 28, n. 5, pp. 886-895, 1990.

[8] E.E. Sano, A.R. Huete, D. Troufleau, M.S. Moran, and A. Vidal, "Sensitivity analysis of ERS-1 synthetic aperture radar data to the surface moisture content of rocky soils in a semiarid rangeland," unpublished.

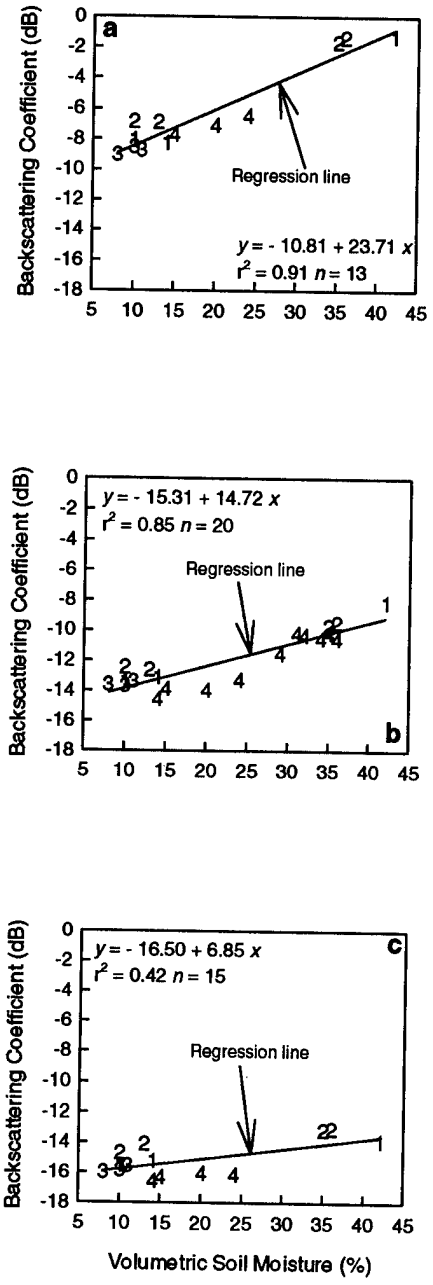

Fig. 1. Relation between SAR data and % volumetric soil moisture content for fields with planting row structure. (a) the Ku-band with a 35° incidence angle; (b) the Ku-band with a 55° incidence angle; (c) the Ku-band with a 75° incidence angle (n = number of samples; 1 = Field 18; 2 = Field 23; 3 = Field 26; 4 = Field 34).

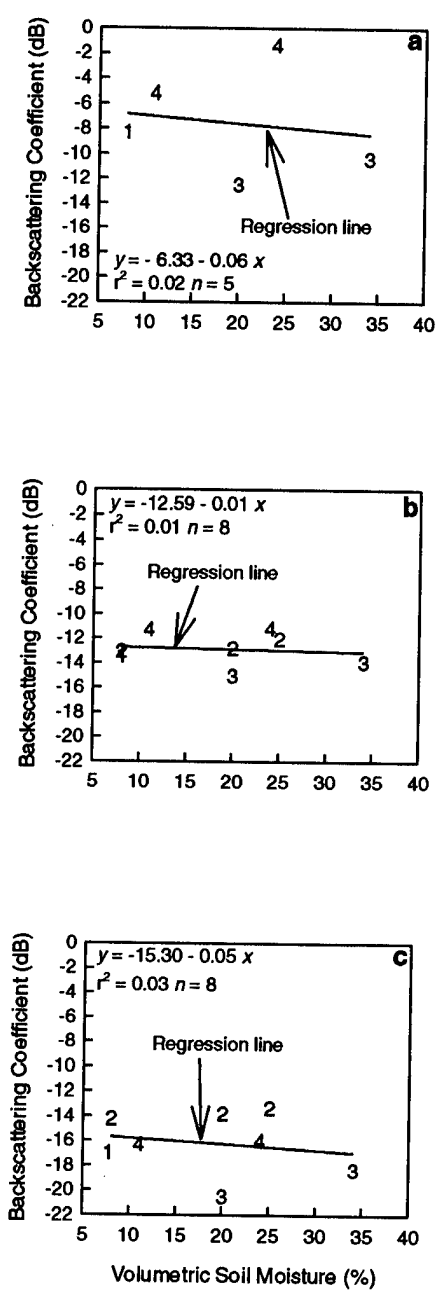

Fig. 2. Relation between SAR data and % volumetric soil moisture content for furrowed fields. (a) the Ku-band with a 35° incidence angle; (b) the Ku-band with a 55° incidence angle; (c) the Ku-band with a 75° incidence angle (n = number of samples; 1 = Field 13; 2 = Field 21; 3 = Field 27; 4 = Field 31).

Airborne Remote Sensing to Support Precision Farming

Marc J.G. Wehrhan, Thomas M. Selige
GSF-National Research Centre for Environment and Health
PO Box 1129. Ingolstädter Landstr. 1, Neuherberg, D-85758 Oberschleißheim, Germany.
Telephone: +49-(0)89-3187-2255, Facsimile: +49-(0)89-3187-3369, E-mail: selige@gsf.de

ABSTRACT

Spatial variability of crops within fields depend on soil variability. This spatial distribution of plant growth conditions, detected by airborne remote sensing, can provide modellers, regional planers and at least farmers with valuable information.
Ground truth data of crop parameters were collected and related to spectral information in red, middle - and thermal infrared wavebands derived from airborne scanner data. Simple regression analysis has been used to obtain classification functions. The classified spectral images are finally compared with soil properties. Results of three years under study indicate a high applicability of airborne remote sensing technique in order to detect spatial variability of plant growth conditions on field level.

INTRODUCTION

Spatial information about potential productivity of arable land in intensively cultivated landscapes is indispensable according to sustainable land use and development. In order to avoid ecological risks for soils and groundwater, but also to develop management recommendations, soil dependent site properties and their influence on biomass production have to be considered. This requires high spatial resoluted data which can not be obtained by time consuming and expensive conventional field methods. The combination of airborne remote sensing as a flexible and operational technique and only few ground truth plots is a practicable alternative.
In principle, remote sensing methods can be used in agriculture assuming that morphological and material proportions of plants change in a typical way during a vegetation period which is strongly related to reflexion, absorption and emission of electromagnetic waves. These relationships offers the opportunity to quantify differentiations of biomass production over space and time.
Although vegetation covered soils are „invisible" to remote sensing instrumentation, it is well known, that plant growth is controlled by underlying soil properties [1]. Rootability, plant available water and therefore nutrient supply are dependent on particle distribution and density of the particular soil layers. In consequence the spatial variability of these integrating effects on biomass production will cause a corresponding pattern of canopy variables which can be detected and classified by remote sensing. It will be shown in this paper, that the spatial pattern of site units will remain more or less the same in different years, although changes in climatic conditions may cause a certain shift in the quantity and range of biomass and yield.

SITE DESCRIPTION

Investigations are beeing carried out at the FAM (Forschungsverbund Agrarökosysteme München) experimental station „Klostergut Scheyern" in Bavaria, South Germany. The farm is situated in a hilly landscape with a very dynamic terrain and represents a huge area of intensively cultivated land. Field size does not exeed 7 ha which is typical for the whole region. Two different management systems, ecological and integrated, have been established since 1993.
The high spatial variability of soils can be explained by complex tertiary deposit conditions. Later, during the pleistocene, solifluction and erosion led to a concentration of fine quaternary sediments in hollows, while coarse tertiary sediments were layed open at slopes and tops.

METHODOLOGY

Airborne scanner data were aquired with a DAEDALUS AADS 1268 scanner on a DO 228 platform. The instrument offers 11 channels with an overall range from 0.42 µm (visible blue) to 13.0 µm (themal infrared) [2]. The overflights, presented in this study, were performed on the 4th of july 1994 and on the 11th of july 1995 around midday under clear sky conditions.
The multispectral images of the experimental farm were taken in three tracks from a height of 450 m, resulting in a geometric resolution of 1.3 m. After rectification and radiometric correction the tracks were merged and referenced to a geographical coordinate system (Gauss Krüger).
The study was focused on winter wheat, which is very ambitous on site properties and therefore show significant spatial patterns according to spatial variabilty of growth conditions. Overflight dates were chosen assuming a maximum spatial differentiation of winter wheat biomass due to significant morphological changes and beginning water loss.
Ground truth data were collected simultanously at representative locations including fresh and dry biomass, Leaf Area Index (LAI), stage of development (EC) and crop height.
The measured crop parameters were related to spectral information in single channels by using simple regression analysis. The resulting functions were used to classify canopy parameters for the different overflights. The classified images are converted into a grid format, which offers the opportunity to integrate the spatial data sets in a Geographical Information System (GIS).

RESULTS

Relations between crop parameters and spectral information

Correlation analysis was performed for charactaristical crop parameters of the test sites for both overflights. Results indicate, that nearly all channels are suitable to obtain classification functions. However, quality of classification is dependent on the fit of the resulting functions. Best correlations were found between crop parameters and spectral

0-7803-3836-7/97/$10.00 © 1997 IEEE

values derived from red (channel 5; 0.63 - 0.69 µm), middle-infrared (channel 9; 1.55 - 1.75 µm) and thermal infrared (channel 11; 8.5 - 13.0 µm) wavebands.

Tab.1: Correlations between crop parameters and spectral values in selected channels

DAEDALUS channels 04.07.1994	Biomass of winter wheat fresh weight [t/ha]	dry weight [t/ha]	LAI	Grain yield [t/ha]
9	-0.94	-0.89	-0.87	-0.83
11	-0.86	-0.78	-0.81	-0.81
11.07.1995				
5	-0.92	-0.92	-0.89	-0.86
11	-0.97	-0.92	-0.93	-0.83

Simple regression analysis was used to obtain classification functions. Defined classes for the overflight performed on the 4th of July 1994 is shown in Fig. 1.

Relations between crop parameters and soil properties

An often used soil property to characterize the yield potential of agricultural sites is the available water capacity of root zone (AWC_{rz}). It can be calculated by combining particle distribution and average effective rootability of the paticular soil layers and thus is a measure for plant available water. The amount of AWC_{rz} depends on the parent material of soil development. Two major groups of soil formations could be seperated according to their influence on biomass production and yield.

1. Soil formations from quaternary sediments.
   cummulic Anthrosol and eutric Cambisol of aeolian deposit
2. Soil formations from tertiary sediments.
   stagnic Gleysol and dystric Cambisol from sandy-gravel material

Characteristic soil properties and corresponding crop parameters of these major soil groups show significant differences (Tab.2).

Tab.2: Averrage values of characteristic soil properties and corresponding crop parameters in the major soil groups for 1994 and 1995.

soil properties	soil formations from quaternary sediments		soil formations from tertiary sediments	
	1994 n=8	1995 n=6	1994 n=14	1995 n=14
clay [%]	26.5	23.45	15.2	18.11
silt [%]	38.3	47.38	27.0	33.21
sand [%]	35.2	25.83	57.8	43.03
skelet [%]	3.9	2.89	22.6	11.67
AWC_{rz} [mm]	153	167	113	134
crop parameter	1994 n=8	1995 n=6	1994 n=14	1995 n=14
fresh biomass [t/ha]	32.6	32.7	20.4	26.6
dry biomass [t/ha]	10.5	13.4	7.9	11.5
LAI	4.2	3.6	3.1	2.94
grain yield [t/ha]		67		54

Translation of soil properties to spectral information

Correlations between AWC_{rz} and crop parameters where found to be significant (R =0.87 with n = 22 in 1994 and R = 0.86 with n = 20 in 1995 for fresh biomass). This relationship appears to be constant for both years (Fig. 2). In order to classify soil properties, the relations between crop paramerters and spectral information and between crop parameters and soil properties have to be combined. The generell expressions for a linear model are:

Eq. 1 spectral value channel x = a*fresh biomass + b

and

Eq. 2 fresh biomass = c* AWC_{rz} +d

Substituing fresh biomass in Eq. 1 through Eq. 2 a new classification function will be obtained:

Eq. 3 spectral value channel x = a*(c * AWC_{rz} + d) + b

Crop management and nitrogen (N)-balance

Taking ecological risks for soils and groundwater into account, nitrogen fertilization has to be adjusted to site specific properties. In order to investigate nitrogen utilization on winter wheat fields with variable site properties, a field study was performed in summer 1994 and 1995 before harvest. One of the fields under study in 1994 was chosen to demonstrate the effects of soil heterogenity on nitrogen utilization of plants. The field was fertilized equal with 185 kg/ha nitrogen. N-balances were calculated and compared with soil properties. The values presented in Tab. 3 are calculated for the three test sites selected in this field to collect ground truth data for remote sensing classification. They were found to be representative for the three major soil formations in this field. The Regosol is charactarized by the lowest absorption of only 93.4 kg/ha nitrogen, which is equivalent to a loss of 50% of the total application. The spatial extension of this soil formation is again related to tertiary sediments and low AWC_{rz} values. Although the stagnic Gleysol and the eutric Cambisol are both developed of quaternary sediments, N-uptake is related to differences in AWC_{rz}. Values for nitrogen loss were found to be 91.1 kg/ha (49% loss) for the stagno Gleysol and 54.8 kg/ha (29% loss) for the eutric Cambisol with higher AWC_{rz}.

Tab.3: Site properties, dry mass production and calculated nitrogen balances for the three selected test sites in 1994.

soil formation	AWC_{rz} [mm]	dry biomass [t/ha]	N-uptake [kg/ha]	N-balance [kg/ha]	grain yield [t/ha]
Regosol	111	6.8	93.4	+91.6	4.92
stagno Gleysol	130	7.4	93.3	+91.1	5.34
eutric Cambisol	156	10.6	130.2	+54.8	8.29

The effects of soil dependent site properties on biomass production and nitrogene utilization leads to corresponding differences in grain yield. Fig. 3 shows the relation between fresh biomass two weeks before harvest and grain yield (R = 0.9).

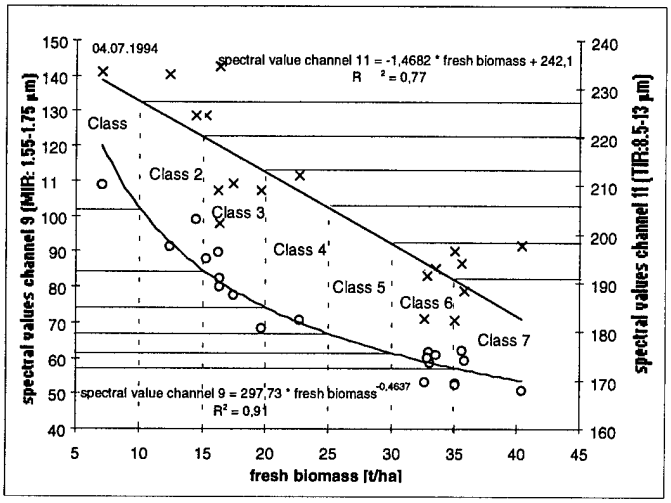

Fig.1: Classification functions and defined classes of fresh biomass of winter wheat for DAEDALUS channels 9 and 11. Date: 04.07.1994

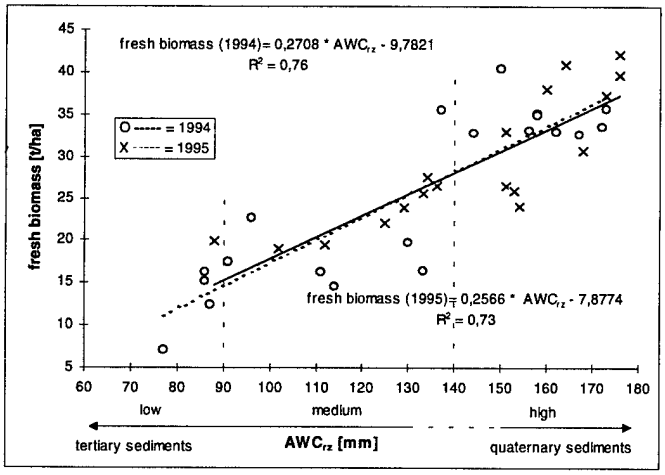

Fig. 2: Relation between fresh biomass and AWC_{rz} at overflight dates.

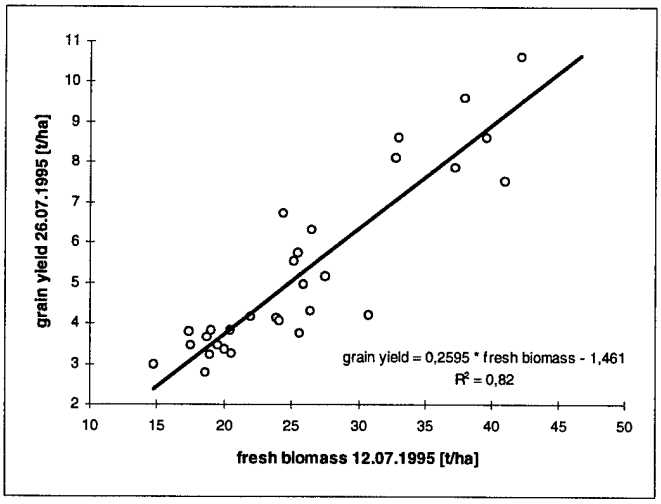

Fig.3: Relation between fresh biomass and grain yield of all test sites in 1995.

CONCLUSIONS

The presented examples, extracted from two overflight dates in summer 1994 and 1995, confirm the principal applicability of airborne remote sensing in order to detect spatial variability of site properties. Even in landscapes with high soil heterogenity and dynamic terrain, soil properties can be classified by translating the relations "biomass - spectral information" and "biomass - soil property" to a relation"soil property - spectral information". Results indicate, that the quantity of biomass production appears to be a sensible indicator for underlying soil properties and at least for the efficiency of fertilizers.

The spatial pattern of site properties on field level, which was found to be more or less constant over the years in study, enables the development of precision farming strategies. In the way crop stand quality and crop yield can be controlled, the efficiency of management costs increase while ecological risks for the natural ressources decrease.

These informations have to be available to practical management. While the technical equipment, including GPS, is already available [3], the development of an Agro-ecological Information System (AIS) [4] is in progress. The combination of both, accurate position of fertilizer distributor and corresponding site properties enables optimal site specific crop management

ACKNOWLEDGMENTS

The scientific activities of the research network „Forschungsverbund Agrarökosysteme München" (FAM) are financially supported by the Federal Ministry of Research and Technology (BmBF 0339370). Rent and operating expenses of the experimental farm in Scheyern are paid by the Bavarian State Ministry for Education and Culture, Science and Art.

Airborne scanner data were aquired by the German Space and Aircraft Establishment (DLR).

REFERENCES

[1] Th. Selige and Th. Vorderbrügge," Roots and Yield as Indicators of Soil Structure", Root Ecology and ist Practical Applications, L. Kutschera, E. Hübl, E. Lichtenegger, H. Persson, M. Sobotik (eds.), Verein für Wurzelforschung, Klagenfurt, 1992, pp. 121-124 [3. ISRR Symp. Wien, 1991].

[2] V. Amann," Multispektraler Linescanner `DAEDALUS AA DS 1268 (ATM)'", Leitfaden für den Datennutzer Oberpfaffenhofen, interne Mitteilung, 1986.

[3] John K. Schueller and Min-Wen Wang,"Spatially-variable fertilizer and pesticide application with GPS and DGPS", in Computers and electronics in agriculture, vol.11, H. Auernhammer, Ed. Amsterdam: Elsevier Science B.V., 1994, pp. 69-83.

[4] R. Lang, A. Müller and R. Lenz," Agroecological Information System (AIS) within the Research Network on Agroecosystems Munich (FAM)", Ecological Engeneering, 4, 1995, pp. 173-180.

Amazon Rainforest Visualization/Classification by Orbiting Radar, Enabled by Supercomputers (ARVORES)

Paul Siqueira, Bruce Chapman,
Sasan Saatchi and Tony Freeman

Jet Propulsion Laboratory, 4800 Oak Grove Drive, Pasadena, CA 91109
Tel: (818) 393-9285, Fax: (818) 393 5285
Mail Stop 300-243, e-mail:siqueira@jpl.nasa.gov

ABSTRACT

The ARVORES project is a specific science task (part of a larger supercomputing effort) whose purpose is to develop SAR resources based on JERS-1 multi-season coverage of the Amazon rainforest using available state of the art computing technology. Because of the basin-wide coverage of this data set, in addition to providing the immediate science goals of landcover classification, it will also serve as a foundation which present and future data sets may be overlain and compared to. In addition, it is the goal of this project to use the science requirements related to the study of the Amazon region to guide the development of a flexible, large-scale computing environment for addressing SAR specific tasks.

INTRODUCTION

The objective of the ARVORES project is to fold together two resources for the development and analysis of radar data over the Amazon region. The first of these is a basin-wide, dual season set of JERS-1 (L-band HH) imagery collected during the months of September/October 1995 (low flood) and May/June 1996 (high flood) under the JAMMS project [Rosenqvist, 1996; Freeman et al., 1996]. The entire data set consists of 3000 1-Mbyte low-resolution (100 m) images and 3000 64-Mbyte high-resolution (12.5 m) images. Initial, single-scene, analysis of the Rio Solimões near Manaus has indicated that the single band, single polarization data taken over two seasons provides enough information to discriminate between six classes, equivalent to a SIR-C analysis [Hess et al., 1995]. These preliminary results highlight the utility of this dual season resource, however the volume of data makes it difficult to fully explore its usefulness. For this reason, our approach is to develop our SAR tools in a computing environment that does not restrict the level of science analysis being performed, rather the science analysis will be used to draw upon the available resources to define which of these can be best used in achieving our scientific goals (Fig. 1). This is the opposite of the more common situation where our ability to process and analyze radar data is limited by the available computing resources. The results of this project will provide two benefits: i) they will provide valuable information related to the study of rainforest ecology and ii) will provide insight about which computational resources are the most important to efficiently process and analyze radar data to achieve science related ends.

COMPUTING RESOURCES

The computing resources at our disposal are considerable. They consist of a 256 node Cray T3E, a 2m x 2m (2400x3200 pixel) SGI visualization power wall, 500 Gbytes of hard disk storage, 5 Tbytes of tape backup, and a high performance communications network (500 Mbytes/sec). The sheer size and volume of these resources is sufficient to envision the accomplishment of even the most data/processing hungry tasks associated with SAR analysis.

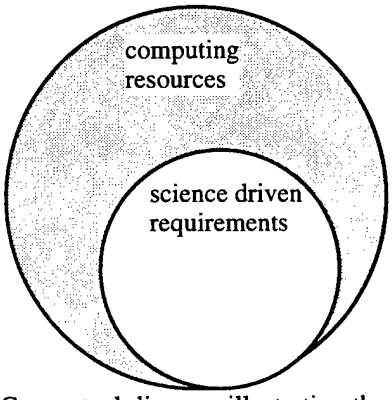

Figure 1: Conceptual diagram illustrating the superset of computing resources that the science driven requirements will be allowed to explore. The fact that the computer resources will be a superset of those required by the science demands will help determine which of those resources are most valuable in achieving our goals.

INTERMEDIATE STEPS

In the process of creating a resource of the two-season JERS-1 Amazon data, a number of tools have been created to facilitate future science analysis. These are i) implementation of a high performance SAR processor on the computing network, ii) implementation of an automated method for correcting the scale, rotation and geo-location of individual processed scenes and iii) provide a method of smoothly mosaicking multiple scenes together to provide a seamless radar image product. The second of these steps, geocoding, has proved to be the most useful and value added. Using a suite of routines

0-7803-3836-7/97/$10.00 © 1997 IEEE

developed at JPL [Shaffer and Hensley, 1996], common areas between adjacent scenes/orbits are used to simultaneously solve for scale, rotation and offsets of a single-season's worth of radar imagery. By determining these transformation matrices simultaneously, an optimization algorithm may be employed to minimize the correction applied to each scene. This process can be contrasted against the more common "wall papering" method of fixing a scene in place (as if to a wall) before adding further scenes. The wallpaper method has the undesired effect of propagating errors as the distance to the initially placed scene increases.

SCIENCE GOALS AND PRODUCTS

The driving force behind this project is to achieve high value added science products and to explore the JAMMS data set in new ways. For our mid- to long-term goals, we are in the process of developing our science goals to cover three critical areas i) land-cover classification, ii) quantitative analysis of river lengths and flooding extents and iii) forward modeling of the radar signal with specific targets of interest. Of these three goals, the first two have already provided useful results.

Landcover Classification

The availability of an addition season of radar data increases the dimension of the data analysis that can be performed on the JERS-1 data in much the same way as another polarization might. Collection of L-band HH imagery during the peak of the low and high flood seasons maximizes our ability to map inundation regions and to investigate other time-varying phenomena. Using a maximum likelihood supervised classification, we were able to discriminate between six classes (Fig. 2). These results are very comparable to those achieved using LHH, LHV and CHH polarizations of the SIR-C instrument [Hess et al., 1995]. The addition of a second season had the effect of improving the classification accuracy from 65% for any single season to 92% for the combined data set. A "confusion" matrix describing the classifier's accuracy for any particular class of landcover is given in Table 1.

Metrics of River Length and Flooded Regions

Once a method has been developed for mosaicking the satellite imagery and discriminating between landcover types, the next step is to quantify the data into a meaningful set of numbers. A simple summation of the flooded forest region will provide an estimate of the extent of the forest that goes through annual landcover change or a thinning algorithm can be used to mark the path of the river and determine its length (Fig. 3). Critical to both of these applications is to have an accurate geocoding for each processed scene so as to remove the effects of scene overlap and warping due to projection.

Figure 2: Classified region of the Amazon including both the Rio Negro (south) and the Rio Solimões. This image is the result of a maximum likelihood classification using the dual season, L-HH JERS-1 data. Class results are i) open water (black), ii) sandbar (dark gray), iii) flooded forest (white) iv) unflooded forest (med. gray), v) flooded shrubs (not shown) and vi) unflooded fields (light gray).

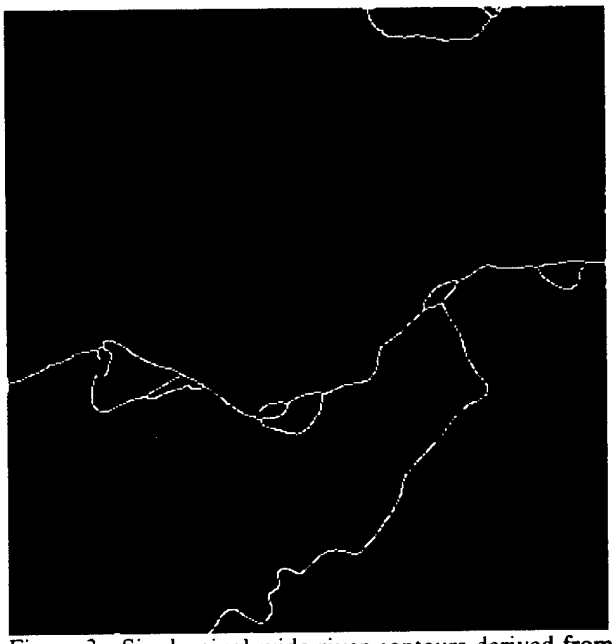

Figure 3: Single-pixel wide river contours derived from a classified image (not shown) using a thinning algorithm to determine the mean path of the river. This particular mosaicked image can be used for historical analysis of the changing nature of the river, to measure the river length and to monitor landcover change.

CONCLUSION

This paper reviews the work being performed to integrate large-scale computing resources with radar science applied to the Amazon rainforest. The front to end approach for developing this resource has been instrumental in integrating a number of important processing tools as well as providing valuable science data products. The most important application of this integrated system however will be to the entire Amazon region, an important component in the study of global environmental change (Fig. 4). By working on a region wide scale we will able to develop tools for studying the ecology of the area as well as to provide a historical record of landcover change.

REFERENCES

[1] Freeman, A., Chapman, B., and Alves, M., The JERS-1 Amazon Multi-Season Mapping Study (JAMMS), Proc. of 1996 Intnl. Geosci. Rem. Sens., pp830-833, Lincoln, Nebraska 1996.

[2] Hess, L., Melack, J., Filoso, S., and Wang, Y., Delineation of Inundated Area and Vegetation Along the Amazon Floodplain with SIR-C Synthetic Aperture Radar, IEEE Trans. Geosci. Rem. Sens., Vol. 33, No 4, pp 896-904.

[3] Rosenqvist, Åke, The 'global rainforest mapping project by JERS-1 SAR, Proc. of XVIII ISPRS Cong. in Vienna, Austria 1996

[4] Shaffer, S. and Hensley, S, personal communication regarding the "Multimosaic" algorithm suite, 1996.

ACKNOWLEDGMENTS

The authors wish to thank NASDA's Earth Observation Research Center for establishing the Global Rainforest Mapping Project, and the ASF SAR facility for processing the data. The research described in this paper was carried out by the Jet Propulsion Laboratory, California Institute of Technology, under a contract with the National Aeronautics and Space Administration.

Class	Water	Forest	Flooded Forest	Flooded Shrubs	Fields	Sandbar
Water	0.99	0.00	0.00	0.00	0.01	0.00
Forest	0.00	0.93	0.07	0.00	0.00	0.00
Flooded Forest	0.00	0.04	0.96	0.00	0.00	0.00
Flooded Shrubs	0.00	0.18	0.16	0.66	0.00	0.00
Fields	0.02	0.03	0.04	0.00	0.86	0.05
Sandbar	0.03	0.00	0.00	0.00	0.19	0.78

Table 1: Confusion matrix describing the accuracy of the supervised maximum likelihood classifier applied to the dual-season JERS-1 data.

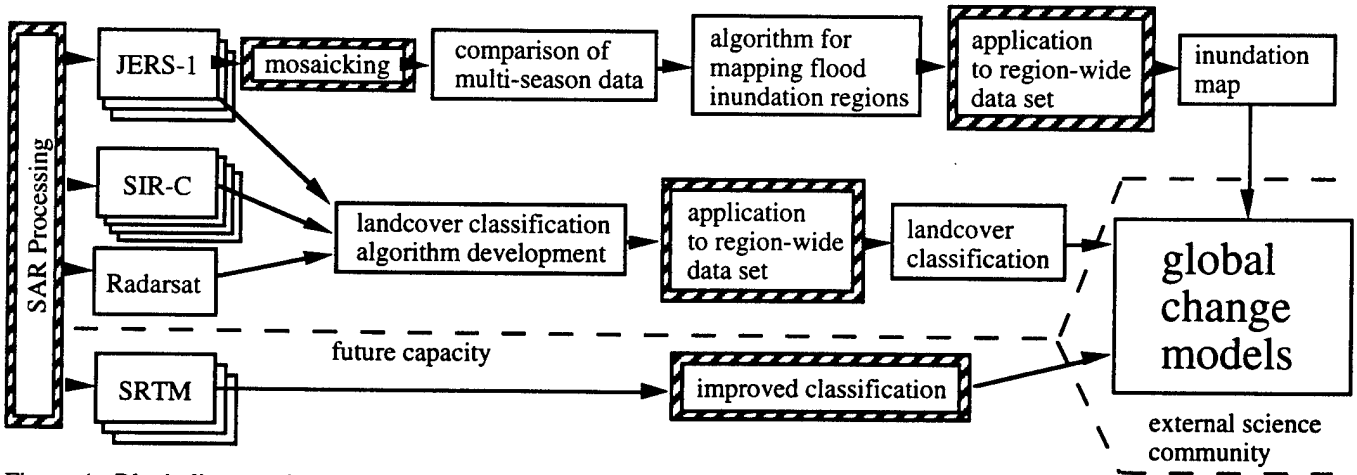

Figure 4: Block diagram describing the resources employed (current and projected) for the project. Highlighted areas indicate those steps that will derive benefit from the supercomputing resources. Our ultimate goal is to provide quantitative measures which can be used to augment models for global environmental change.

Utilization of Coherence Information from JERS-1/SAR for Forest Type Discrimination

Shoji Takeuchi and Chinatsu Yonezawa
Remote Sensing Technology Center of Japan
Roppongi First Bldg.8F, 1-9-9, Roppongi, Minato-ku, Tokyo 106, Japan
Tel:+813-5561-8778, Fax:+813-5561-9542, E-mail:takeuchi@restec.or.jp

Abstract -- The authors studied the applicability of coherence information which is obtained from interferometric SAR data pair for the discrimination of forest types. Two test sites, around Mt.Fuji in Japan and Phuket Island in Thailand, were tested with two interferometric JERS-1/SAR data pairs for each site. The coherence was computed by complex correlation coefficient in a small corresponding patch between single-look SAR complex data pair. The temporal changes of SAR intensity and coherence were investigated among various forest types and the results indicated that the coherence information is much superior than the intensity to discriminate different forest types. Especially in Phuket test site, Mangrove forest was easily discriminated from other tropical forest due to its relatively higher coherence, while that forest type is hardly discriminated by using SAR intensity.

1. INTRODUCTION

The multi-temporal SAR data regularly observed for a single area are generally useful information for differentiating the various land cover types in that area. However, for forested areas, the L-band SAR intensity images obtained from JERS-1/SAR offer relatively poor information about the differences of forest types, although they easily discriminate forest from other vegetation such as grass or field.

Phase information is also available from SAR data if a temporal SAR data pair satisfies the condition for interferometric SAR. This information is expected to reveal the differences of land cover types in a different way from the intensity of SAR data. The authors studied the possibility of using the coherence information which is obtained from the phase information in an interferometric SAR data pair for discriminating the differences of forest types.

2. TEST SITE AND TEST DATA

Two test sites, around Mt.Fuji in Japan and Phuket Island in Thailand, were tested with two interferometric JERS-1/SAR data pairs for each site. Table 1 shows the list of the data used for the two test sites and the baseline length for each pair. The baseline length is represented as the perpendicular component to the slant range. From the baseline length in Table 1, all the pairs basically satisfy the interferometric condition. However, actual interferogram was much better for Mt.Fuji than for Phuket Island.

Table 1 Data pairs and their baseline length

Test site	Data pair & Observation date	Date interval	Baseline (perp.)
Mt.Fuji	1)7/7/93-20/8/93	44 days	510 m
	2)7/9/95-21/10/95	44 days	298 m
Phuket	1)5/11/92-19/12/92	44 days	1012 m
	2)19/12/92-17/3/93	88 days	482 m

3. COMPUTATION OF COHERENCE

The two raw data in a single data pair were compressed in the range and azimuth direction using ERGOvista SAR processor respectively and the pair of single-look complex (SLC) data was obtained after the compression. For preserving the consistency of the phase between the two SLC data, the doppler centroid frequency for the azimuth compression was adjusted to be the same value between the two raw data. The spacing in the range and azimuth direction was 8.8 m and 4.5 m respectively.

The coherence was computed by complex correlation coefficient in a small corresponding patch between the two SLC SAR data after co-registration of them. The complex correlation coefficient was computed as follows;

$$\rho = \frac{\left| E\left(c_1 c_2^{*}\right) \right|}{\left[E\left(c_1 c_1^{*}\right) E\left(c_2 c_2^{*}\right) \right]^{1/2}} \qquad (3.1)$$

where C_1 and C_2 are complex values for the first and the second data, C_i^{*} means the complex conjugate of C_i and E( ) means the expectation.

In the computation of coherence by (3.1), the coherence value is much affected by the patch size. If the size is too small, the coherence value results in somewhat random patterns. If the size is large, the coherence value decreases according to the phase variation by the flat-surface fringe and the topographic fringe. In this experiment, the patch size was selected to be three in range direction and nine in azimuth direction, which was about 40 meters square on the ground and was the same size as the pixel size for extracting interferogram.

4. RESULT

4.1 Result at Mt.Fuji

Plate 1 shows the example of the coherence image at Mt.Fuji area together with the intensity image. In the intensity image shown at the upper part, the forest areas around Mt.Fuji are almost displayed in an almost homogenous intensity. Actually these areas are covered by different types of forest. In contrast, in the coherence image at the lower part, different coherence patterns in the forest areas are seen.

0-7803-3836-7/97/$10.00 © 1997 IEEE

Fig.1 shows the scattering diagram of coherence obtained from two data pairs for the typical samples of several kinds of forest types. The square symbols are Cedar or Cypress, the circles Pine, the crosses Larch and the triangles are Broad-leaf trees respectively. From Fig.1 the coniferous evergreen forest like Cedar and Cypress results in relatively higher coherence compared with the deciduous trees like Larch and Broad-leaf trees. As the coniferous evergreen trees are considered to be biologically stable even between different seasons, the result of Fig.1 suggests that the coherence is related to the biological stability of the forest.

There is an exceptional sample of Cedar/Cypress that results in lower coherence and this sample is located at a relatively steep slope. From some conventional studies it is known that the coherence is also affected by topography and it generally decreases at the steep slope areas. Therefore the topographic effect also should be considered for the interpretation of coherence patterns at the forest areas.

4.2 Result at Phuket Island

Plate 2 shows the examples of intensity and coherence images at Phuket Island. This island is mainly covered by the tropical forest and Rubber plantation distributes widely at the inner flat areas . In addition Mangrove forest distributes at the east side coast of this island.

In the intensity image at the left part, the back scatter intensity is almost homogeneous in these all forest areas and Mangrove forest is hardly discriminated from other forest types by the intensity image. On the contrary in the coherence image, the Mangrove forest is clearly discriminated by its higher coherence than other forest types.

Fig.2 shows the scattering diagram of coherence same as Fig.1 for three kinds of forest types, Mangrove, Rubber and other tropical forest. From Fig.2 it is clearly shown that the coherence in Mangrove forest is relatively higher than those for other forest types. The reason why Mangrove results in high coherence is also considered to be related to its biological stability because Mangrove is almost always standing in a water area.

5. CONCLUSION

Above experimental results suggest that the coherence information is much superior than the intensity to discriminate different kinds of forest types and thus suggest the possibility of the use of JERS-1/SAR data for forest type discrimination as one the applications of interferometric SAR technology. As the coherence is also sensitive to topographic features, the further investigation on the quantitative relation between the coherence and the topographic features should be conducted to utilize the coherence information practically for forest type classification .

REFERENCES

1) S. Takeuchi and C. Yonezawa, " Relation between Coherency and Landcover in Interferometric SAR" (Japanese), Proceedings of the 21th Japanese Conference on Remote Sensing. Nov.,1996.
2) C. Yonezawa and S. Takeuchi, " Relation between the Smoothness of SAR Interferogram and Topographic Features" (Japanese), Proceedings of the 22th Japanese Conference on Remote Sensing. May,1997.

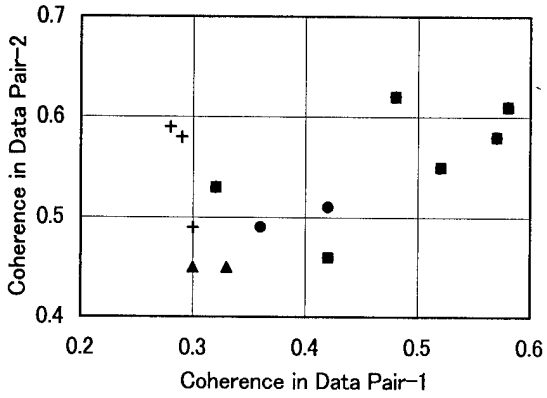

Fig.1 Scattering diagram of coherence from two data pairs at Mt.Fuji. The square symbols are Cedar or Cypress, the circles are Pine, the crosses are Larch and the triangles are Broad-leaf trees respectively.

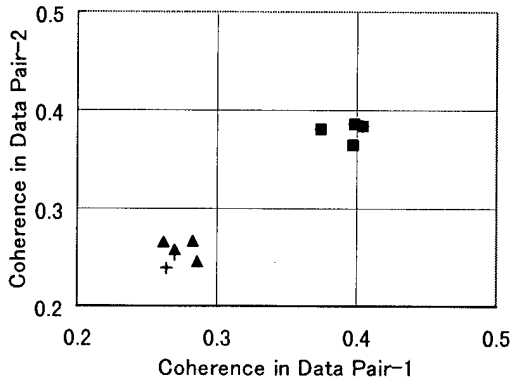

Fig.2 Scattering diagram of coherence from two data pairs at Phuket Island. The square symbols are Mangrove, the crosses are Rubber and the triangles are other tropical forest respectively.

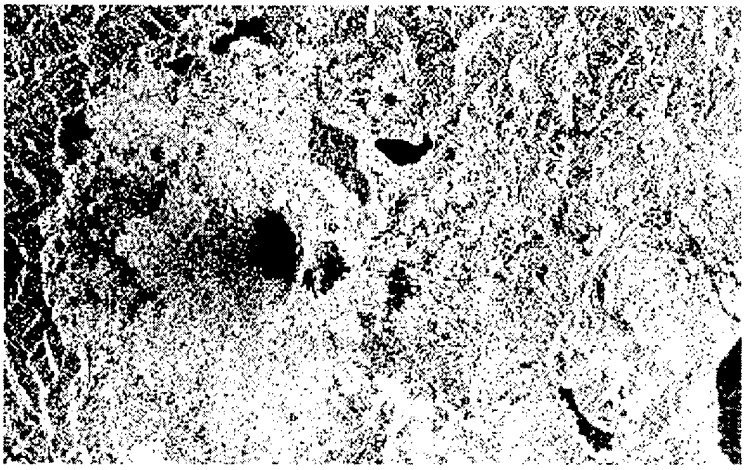

Intensity image of JERS-1/SAR data (7/7,1993)

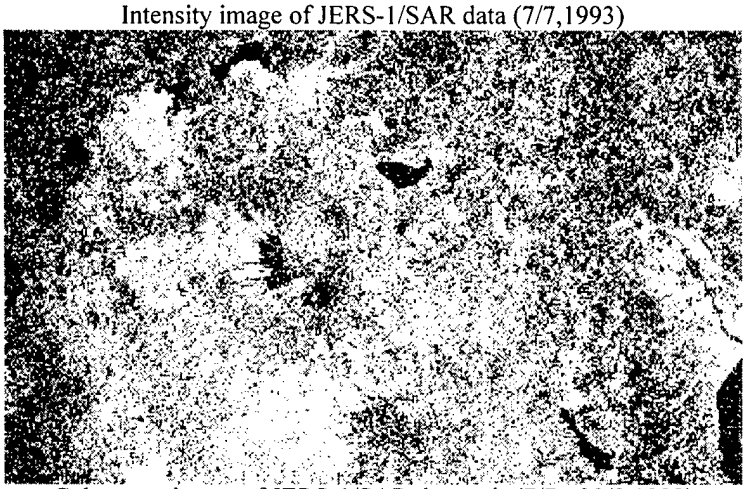

Coherence image of JERS-1/SAR data pair (7/7 - 20/8,1993)

Plate 1 Examples of intensity and coherence images of JERS-1/SAR data at the test site of Mt.Fuji.

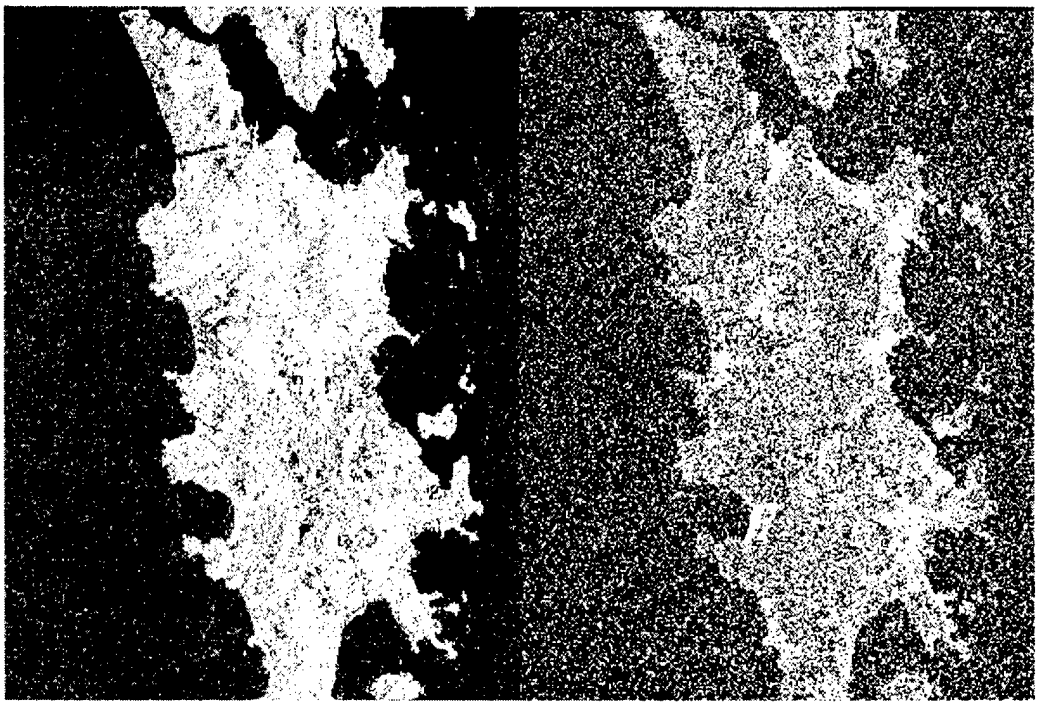

Intensity image (19/12,1992) Coherence image (5/11 - 19/12, 1992)

Plate 2 Examples of intensity and coherence images at the test site of Phuket Island

JERS-1/SAR : MITI/NASDA retains ownership of data.

IGARSS'97

1997 International Geoscience and Remote Sensing Symposium

03-08 August 1997

Singapore International Convention & Exhibition Centre

Technical Program

Interactive Area 7: Damage Assessment and Management

A Flexible Environment for Earthquake Rapid Damage Detection and Assessment

F. Casciati[o], P. Gamba[*], F. Giorgi[o], A. Marazzi[*], A. Mecocci[†]
[o]Dipartimento di Meccanica Strutturale, Università di Pavia, Via Ferrata, 1, I-27100 Pavia
[*]Dipartimento di Elettronica, Università di Pavia, Via Ferrata, 1, I-27100 Pavia
Tel: +39-382-505923 Fax: +39-382-422583 E-mail:{gamba,maraz}@comel1.unipv.it
[†]Facoltà di Ingegneria, Università di Siena, Via Roma, 77, I-55300, Siena

Abstract – This paper outlines a system architecture able to reduce the effects of a devastating seismic event by providing a rapid and reliable damage detection and estimation of the extent and location of the suffered area. This result has been accomplished by the integration of data access and standardization techniques, image processing tools, GIS technology, analytical modeling and communication tools. A two-phase operating model has been conceived. In the pre-event era, images and data about building and infrastructures are collected and analyzed exploiting GIS capabilities. Immediately after the occurrence of the earthquake, the system must be ready to receive near-real time satellite imagery of the affected area to be compared with the pre-event imagery data set. A correspondence between the integrated databases, within the GIS environment, and the real-time imagery is also established. The post-event imagery is then compared with the pre-event one, by means of different digital processing techniques to exploit the different resolution of satellite images.

1. INTRODUCTION

Recent natural disasters have stressed the importance of a rapid and reliable damage assessment and loss estimation in order to face both short and long term emergency response. It has been demonstrated that the entity of earthquake damage is only partly due to the strength of the natural event: it also depends on the delay and inadequacy of the rescue and reconstruction intervention. A reliable post disaster damage assessment should allow to guarantee rapid emergency response, sensibly reduce the effects by providing an immediate estimate of the extent and location of the suffered area and making this knowledge available to the responsible agencies, and suitably drive the reconstruction work.

It should be pointed out that, in case of suddenly occurring natural disasters, the identification of damage by means of analytical models alone is often unreliable since soil conditions, geological complexities and different environmental aspects may result in damage patterns difficult to predict. On the other hand, recent developments in Telematics and ODBC (Open DataBase Connectivity) techniques allow access to appropriate databases and data sources (including satellite imagery at varying resolution and time of coverage). Their integration with loss estimation and vulnerability models would make possible to investigate more effective approaches to the task of developing a reliable system for damage assessment.

2. THE RADATT PROJECT

The RADATT project discussed the feasibility for a system architecture satisfying the following requirements. For a seismic event occurred, can comparison of pre- and post-event imagery be used to detect the damage extent within a few hours from the shake? Can this comparison be conveniently supported by the appropriate interaction with an available building inventory? How is it more convenient to link, within a GIS environment, such a database with the spatial geo-referenced information of interest?

Three main aspects were considered: user requirements, system architecture and an application to the town of Egion in Greece, which suffered a devastating earthquake on June 15, 1995. The first task absorbed most of the activity and gave rise to a comparative study of the building inventory schemes and of the seismic vulnerability assessment experience in the countries involved in the project, i.e. Greece, Italy and Portugal.

The system architecture was conceived with reference to database management, geographical information system, airborne and satellite imagery acquisition and processing and final image comparison. The research project focused on a star networ with central as well as local nodes. In particular it was underlined the need for several central nodes: there, a specialized personnel is totally dedicated to the processing and updating the spatial and tabular data supplied by the local nodes. At the local nodes, the technical personnel is devoted to seismic risk mitigation, managing the municipality infrastructure system and the civil local protection. The data are collected from different sources and offered to the central nodes for appropriate links with the GIS software (fig. 1). Note that the goal is the detection, from the comparison of images taken before and after a seismic event, of any change corresponding to tangible and intangible losses. These changes can affect building, infrastructures and the territory in its extension (landslides).

0-7803-3836-7/97/$10.00 © 1997 IEEE

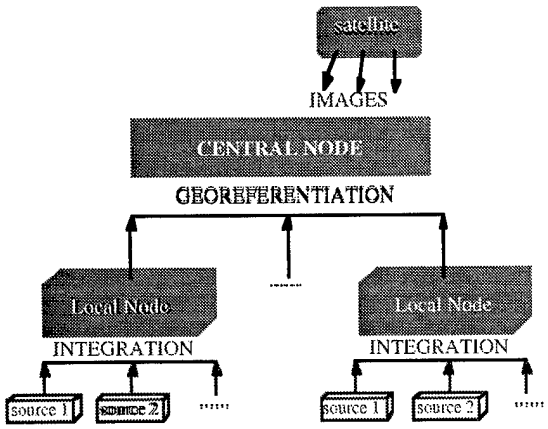

Figure 1: The RADATT proposed system architecture.

3. RADATT & REMOTE SENSING IMAGE PROCESSING

The conceived procedure for damage detection by image comparison was tested within a case study on the Greek town of Egion, which suffered a devastating earthquake on June 15, 1996. A complete database of the Egion area was collected and stored in a GIS environment. Unfortunately, no satellite pre-event image of the required resolution was available. An aerial photo was selected as pre-event image. A 10-meter ground resolution of the selected SPOT satellite image a week after the seismic event, prevented the analyst from a comparison on single buildings: this suggested a comparison on blocks through standard change detection techniques. The comparison required some manipulations on the airborne photo to make its resolution compatible with the one of the satellite image (see fig. 2).

The experience allowed to highlight some problems. In particular, it was found that the simple approaches to image comparison are generally not sufficiently robust to cope with data corrupted by noise, registered with different light and day conditions, with a different view angle or position of the sensor. Even if the same approaches could be changed in order to be more robust with respect to these problems, the feeling was that it is necessary to explore new and more suitable image processing methodologies, aimed to overcome the noise and, possibly, exploit all the characteristics of the images.

The most serious image problem arisen was due to the resolutions now available from the satellites. In fact, it was immediately clear from the efforts to obtain an high-resolution image of the city of Egion that the 2 meter resolution required to analyze building damages is very difficult to be achieved. To make the task more complex, often data from different sensors and/or sources are available, with different resolutions and different point of

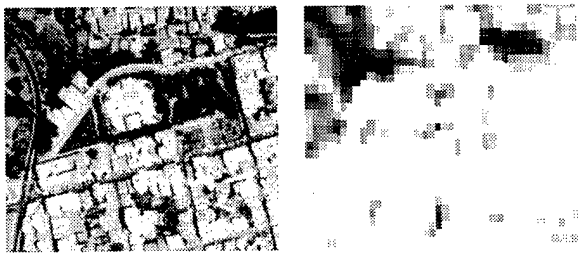

Figure 2: An aerial photo (*left*) and a SPOT image (*right*) of the town of Egion, Greece, respectively before and after the earthquake of June 15, 1995.

observation. Therefore, we must face the task to merge information from different sources, and to exploit as far as possible what is possible to extract from low (or, better, *lower than we would like*) resolution images. Moreover, the difficulties that were faced during the extraction of the differences and while adapting the images to be analyzed and used for comparison brought to the consideration that, for a rapid damage assessment, one needs a tool capable of performing change detection capabilities in a reduced time interval, optimizing the trade off between accuracy of analysis and the need to provide a prompt loss estimation. So, no complex and cpu-time consuming algorithm, extremely sophisticated approaches, or machine-dedicated programs can be allowed.

Therefore, some algorithms have been identified, on the basis of this experience, among which the post-event image analysis by means of perceptual organization concepts to infer structures of interest on images where a low profile analysis (e.g. edge detection) results in incomplete object detection, and SAR data analysis.

As for perceptual organization, we note that the complexity of the our environment is produced by a limited archive of elementary shapes and their combination in a huge number of different manners. A good representation of the grouped features allows to represent the internal structure of the environment and to create a model on how our perceptual apparatus is able to produce primitives deduced from the grey levels of an image [2].

Practically, we segment the original image in order to reduce the information: data at this level could be, for instance, constant curvature segments. At a successive level we extract continuous lines, ribbons, strands, and closed figure obtained by grouping the previously retrieved element by means of a voting method and graph operations [3]. The elements' associations are represented by means of Gestalt proximity, similarity, continuity and nearness graphs. The higher level is composed by polygons, ellipses, circles, and parallel ribbons, obtained by using some Bayesian network extensions called Perceptual Inference Networks (PINs). The basic knowledge, coded by means of the PINs, helps to overcome the data to pre-

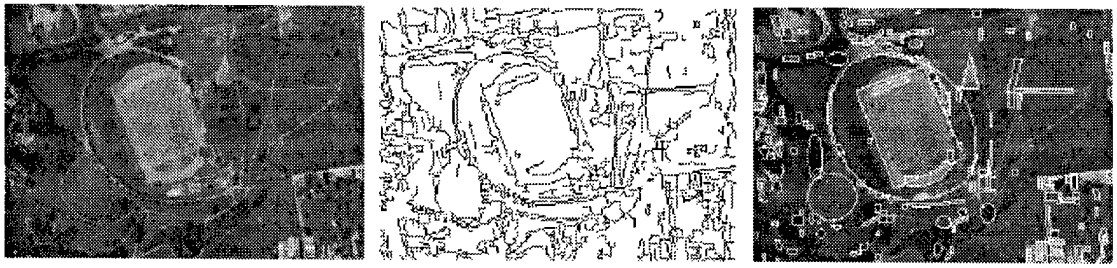

Figure 3: A simple example of PIN usage for image analysis: a remote sensing image (*left*) is simply treated by means of an edge extractor (*center*) and hypotheses about closed contours are shown (*right*).

dict more complex objects and integrate multiple sources of information. For instance, for a rectangle we consider the properties: *a)* it is a close polygon, *b)* it is composed by a couple of parallel lines, *c)* it has four right angles. If these properties are retrieved in the previous step, the PINs allow to make an hypothesis on the actual existence of a rectangle.

Three modules were implemented: a *preattentive* module, devoted to the recognition of the regularities and/or symmetries of the elements; an *attentive* module, able to retrieve some hypothesis about the existence of objects in the analyzed scene, based on the knowledge extracted by the previous module; one (or more) special purpose module(s). An example of the results obtainable by this method on a remote sensing image is shown in fig. 3, where one can observe on the right the hypothesis extracted from the scene on the left by means of some perceptual grouping rules applied to the edges presented at the center of the figure. The results are pretty good, in particular with respect with the very poor information contained in the edge figure.

As for SAR data analysis, we obeserved that radar data is now available from satellite sources, but with a too low resolution to be useful for structure damage analysis. However, the resolution increases when the radar is operated on board of an airplane, down to 0.3 meters [5] with super-resolution analysis techniques. The advantage of radar data is that they are available in any weather condition, and that they allow to have a quick and substantially weather-independent image of the situation. Many algorithms have been developed for the target recognition task ([6], for instance), but, as far as the authors know, no application at infrastructure analysis and damage detection has been implemented: thus, also this research field is open for future perspectives.

Moreover, all the image analysis approaches presented in the preceding paragraphs are devoted to obtain quickly information about damages, and therefore to the short-term assessment of the earthquake event. For a more detailed analysis of the changes in the earth surface, and other successive crustal deformations, able to cause further damages, it is necessary to compute somehow the small deviations of the earth surface with respect to its previous position. This is possible by means of a SAR technique, called SAR interferometry, that compares the phase information of the same part of the earth surface seen by two different satellite radar sources contemporarily, like with a pair of radars on board of the same satelliet, or by the same source, but in two successive moments. The SAR data now available do not allow to obtain precise horizontal resolution (in the order of the hundreds of meters); however, the vertical precision can be as high as 30 mm.

REFERENCES

[1] F. Casciati and F. Giorgi, "GIS for earthquake damage assessment," Proc. of the *First International Conference on Computing & Information Technology for Architecture, Engineering & Construction*, Singapore, 16 - 17 May, 1996.

[2] S. Sarkar and K.L. Boyer, *Computing Perceptual Organization in Computer Vision* Singapore: World Scientific, 1994.

[3] S. Sarkar and K. L. Boyer, "A Computational Structure for Preattentive Perceptual Organization: Graphical Enumeration and Voting Methods", *IEEE Transactions on Systems, Man and Cybernetics*, Vol. 24, no. 2, pp. 246 - 267, Feb. 1994.

[4] R. Birk, W. Camus, E. Valenti, W. McCandless, jr., "synthetic aperture radar imaging systems," *IEEE AES System Magazine*, pp. 16-23, Nov. 1995.

[5] M.Soumekh, "Super-resolution array processing in SAR," *IEEE Signal Processing Magazine*, pp. 14-18, Nov. 1996.

[6] A.W Rihaczek, S.J Hershkowitz, "Man-made target backscattering behaviour: applicability of conventional radar resolution theory," IEEE Trans. on Aerospace and Electronics Systems, Vol. 32, No. 2, pp. 809-824, Apr. 1996.

Remote Sensing Of Global Fire Patterns, Aerosol Optical Thickness, and Carbon Monoxide During April 1994

Sundar A. Christopher[1], Min Wang[1], Donna V. Kliche[1], Ronald M. Welch[1], Scott Nolf[2], and Vickie S. Connors[2]

[1]Institute of Atmospheric Sciences,
South Dakota School of Mines and Technology
Rapid City, SD 57701 USA

[2]Atmospheric Sciences Division
National Aeronautics and Space Administration
Langley Research Center
Hampton VA 23681 USA

Fires play a crucial role in several ecosystems. They are routinely used to burn forests in order to accommodate the needs of the expanding population, clear land for agricultural purposes, eliminate weeds and pests, regenerate nutrients in grazing and crop lands and produce energy for cooking and heating purposes[1]. Most of the fires on earth are related to biomass burning in the tropics, although they are not confined to these latitudes. The boreal and tundra regions also experience fires on a yearly basis. While biomass burning takes place whenever there is plant material that is dry, most fire activities are concentrated between June-October in the Southern hemisphere and between December-April in the Northern hemisphere[2]. Fires alter the state of the vegetation, release large amounts of trace gases, affect the hydrological balance through decrease in evapotranspiration and increased runoff, play a crucial role on tropospheric chemistry due to the gases and particles they release and affect the radiation balance both on regional and global scales. The current study examines global fire patterns, aerosol optical thickness (AOT) and carbon monoxide concentrations during April 9-19, 1994.

Recently, global Advanced Very High Resolution Radiometer (AVHRR) data at nadir ground spatial resolution of 1 km are made available through the NASA/NOAA Pathfinder project[3]. These data from April 9-19, 1994 are used to map fires over the earth. Daytime data with equatorial crossing time of 1340 Local Solar time (LST) from NOAA-11 during the ascending orbit is used in this investigation. The main reason for choosing this time period is to compare the fire patterns observed by the astronauts aboard space shuttle SRL-1 During this time, global mid-tropospheric measurements of carbon monoxide were also made from the MAPS instrument onboard the same space shuttle. The elevated levels of CO in the troposphere are often attributed to biomass burning. This provides a unique opportunity to obtain fire distributions from independent methods and to compare fire activities with carbon monoxide concentrations measured by MAPS. The AVHRR-derived AOT over oceans are also presented[4]. The AVHRR measures radiation in five spectra channels (0.58-0.68 μm, 0.725-1.1 μm, 3.55-3.93 μm, 10.3-11.3 μm, and 11.5-12.5μm). The mid-infrared channel (channel 3) at 3.7 μm is especially suited to detect fires due to the increased radiant energy from fires as opposed to the background.

The pre-processed AVHRR data are first used to eliminate clouds. Then deserts, open water and other water bodies such as lakes and rivers are further screened using available global data bases. Sunglint areas are removed using satellite-sun viewing geometry and for each clear-sky pixel, a series of tests are performed using the near-infrared (channel 2), mid-infrared (channel 3), and infrared channels (channel 4). Fires are characterized by high mid-infrared (channel 1) temperatures (T3>319K) and large mid-IR to infrared temperature (channel 4) differences (T3-T4>15K). T3 and T4 denote the channel 3 and channel 4 temperatures.

Figure 1 shows the zonal distribution of fires for April 9-19, 1994. One hundred thirty-nine global strips of AVHRR images were used to create this figure. More than 500 fires were detected in the belt between 10-20N which correspond to fire activities in Africa, Mexico, and the Indo-Burma region. These fire activities correspond to biomass burning due to agricultural practices. A comparison with the Olson ecosystem data base shows the majority of fires are in the savanna, grass shrub, and farm settlement categories. When compared to the Northern hemisphere, the Southern hemi sphere has fewer number of fires because April is the dry season in the Northern hemisphere. Typically, biomass burning fires are observed in the Southern hemisphere between June-October, and between December-April in the

Acknowledgments: This research was conducted under NASA Grants NAGW-3740, NAGW-5195, and NAS1-19077. We thank Drs. Robert Curran and Dr. Ghassem Asrar for their continued support.

0-7803-3836-7/97/$10.00 © 1997 IEEE

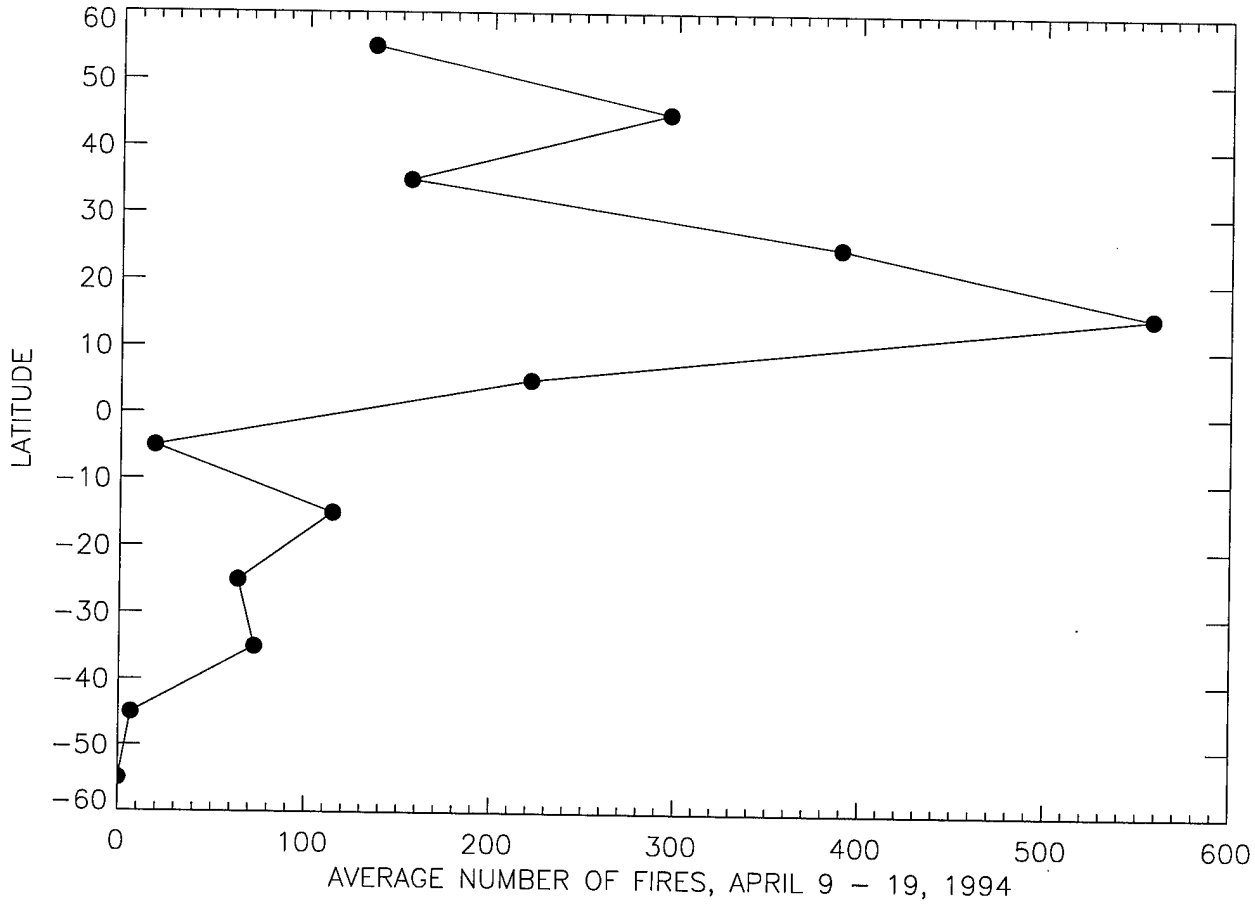

Fig. 1: Zonal distribution of fires for April, 1994.

Northern hemisphere. Fire activities in the Southern hemisphere are in northwest Australia, southeastern Africa, and small regions in South America. Fire counts in the latitudinal belt between 40-50N are associated with boreal fires.

Figure 2 shows the latitudinal distribution of MAPS-observed mid-tropospheric CO along with AVHRR-derived aerosol optical thickness product generated by NOAA/NESDIS. Note that the aerosol optical thickness values are retrieved only over water surfaces because the aerosols reflect more of the incoming radiation than the underlying background. Also, note that figure 2 is only for the Northern hemisphere because the AOT values are not retrieved in the Southern hemisphere due to solar geometry constraints. Latitudinally-averaged peak aerosol optical thickness values between 0.08-0.09 are found between 0-20N due to the aerosol transport from the biomass burning sources in West Africa into the Eastern Atlantic Ocean and the transport of aerosols from Asia into the Pacific Ocean. However, note that the MAPS-measured CO concentrations, when averaged over the latitudes, show a steady increase from the equator to 60N. Average MAPS values in the equatorial belt between 0-20N are around 100 ppbv due to the biomass burning activities in West Africa.

Figure 3 shows the longitudinal distribution of MAPS-measured CO and AOT derived from the AVHRR. The MAPS measurements show CO values greater than 90 ppbv for the entire globe, which shows the increase of CO due to biomass burning activities in the Northern hemisphere. High values of CO are between 170-180E in the Pacific Ocean due to the transport of CO from Asia. Other high-CO concentrations are found throughout Asia.

In summary, our analysis shows that fires from biomass burning appear to be the dominant factor for increased tropospheric CO concentrations as measured by the MAPS. The vertical transport of CO by convective activities, along

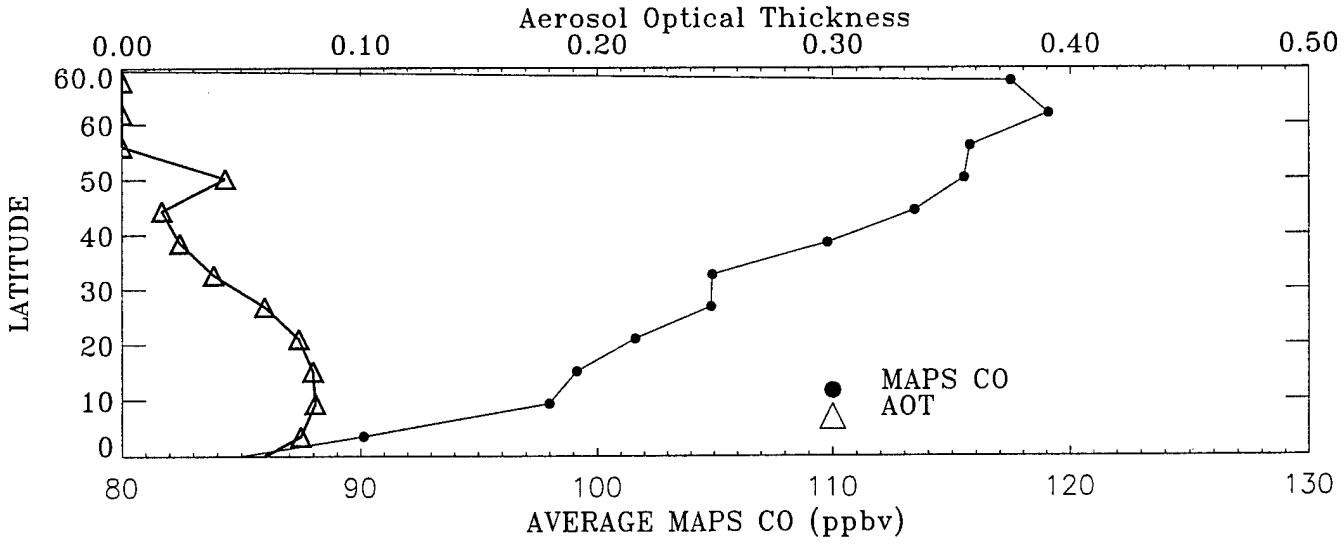

Fig. 2: Zonal distribution of aerosol optical thickness and MAPS measured mid-tropospheric carbon monoxide.

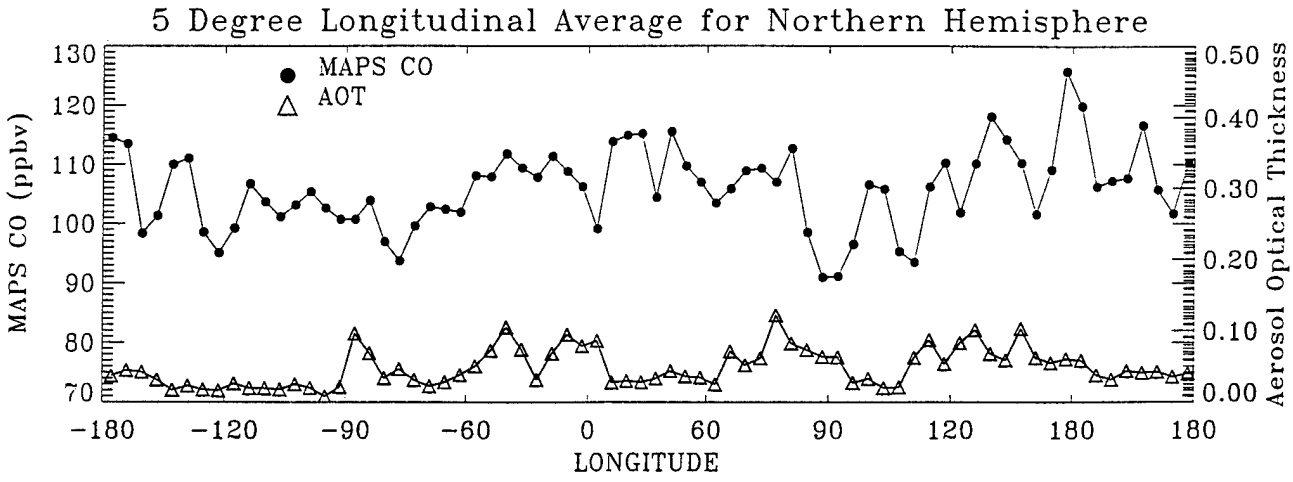

Fig. 3: Longitudinal distribution of aerosol optical thickness and MAPS-measured carbon monoxide.

with horizontal transport due to the prevailing winds, are responsible for the observed spatial distribution of CO.

References.

[1] Andreae, M.O., Biomass burning: Its history, use, and its distribution and its impact on environmental quality and global climate, *In Global Biomass Burning,* J.S. Levine, ed., 1-21, 1991.

[2] Andreae, M.O., Global distributuion of fires seen from space. EOS Trans., AGU, 74(13), 129-130, 1993.

[3] Eidenshink, J.C., and J.L. Faundeen, The 1km AVHRR global land data set: First stages of implementation. *Int. J. Rem. Sens.*, **15**, 3443-3462, 1994.

[4] Rao, C.R.N., L.L. Stowe and E.P. McClain, Remote sensing of aerosol over the oceans using AVHRR data,theory, practice, and applications. *Int. J. Remote Sensing,* **10**, 743-749, 1989.

Use of SIR-C/X-SAR to Monitor Environmental Damages of the 1991 Gulf War in Kuwait

M. Craig Dobson, Andy Y. Kwarteng *, Fawwaz T. Ulaby
The University of Michigan, Radiation Laboratory
Ann Arbor, MI 48109-2122 USA
Tel.: +1-313-647-1799, Fax: +1-313-647-2106, email: dobson@eecs.umich.edu
*Kuwait Institute for Scientific Research
PO Box 24885, 13109 Safat KUWAIT

Abstract -- During the war that engulfed Kuwait in 1991, over 50% of Kuwait's desert surface was disturbed by large-scale troop movements and clean-up operations. Iraqi forces detonated explosives laid at all 810 active oil wells, setting 656 wells ablaze while 74 others gushed oil uncontrollably from the well heads. The free-flowing oil accumulated into a network of oil rivers and approximately 300 oil lakes covering an area of more than 49 sq. km. Approximately 21 million barrels of oil was recovered but 1 million barrels of unrecoverable oil was left in the oil fields. Since then some of the oil had either evaporated, flowed beneath sand cover or been covered by aeolian deposits and is no longer visible at the surface. Since 1991, Kuwait has been imaged a number of times by orbital SAR systems including ERS-1, JERS-1 and SIR-C/X-SAR since 1991. SIR-C/X-SAR imaged the southeastern portion of Kuwait during both SRL-1 (April 13, 1994) and SRL-2 (October 4, 1994) in a non-polarimetric mode (hh- and hv-polarizations at L- and C-bands). Both scenes cover southeast Kuwait including parts of Kuwait City, Greater Burgan, Wafra and Umm Gudair oil fields. False color composites of the SIR-C/X-SAR data reveal a number features related to the environmental devastation wrought by the Gulf War. Of particular note are the buried oil lakes which are readily detected and mapped using the spectral gradient of hh-polarized backscatter (L_{hh}/C_{hh}). Knowledge of the location and extent of these bodies are of great importance to resource recovery and environmental remediation efforts.

INTRODUCTION

Kuwait is a low-relief desert country with a maximum relief of approximately 125 m. The land surface slopes gradually northeastwards with an average gradient of approximately 2 m/km. Kuwait's desert can be divided by into four main provinces, namely, (1) Al-Dibdibba gravely plain, (2) southern desert flat, (3) coastal flat, and (4) coastal hills [1]. The surface is overlain by several recent sediment deposits that include, eolian, residual, playa, desert plain, slope, and coastal deposits. Eolian deposits account for 50% of the surface deposits [2]. Observed surface outcrops consist of clastic deposits which are locally called the Kuwaiti Group and range in age from Miocene to recent. Kuwait's vegetation consists of undershrubs, perennial herbs and spring ephemerals. The vegetation types are controlled by four major ecosystems, i.e., sand dunes, desert plain, desert plateau, and salt marsh and saline depressions [3]. The major plant communities are: (a) Cyperus conglomeratus, (b) Rhanterium epapposum, and (c) Hammada salicornica. In most areas, shifting sand dunes are incapable of sustaining plant life.

The majority of remote sensing projects in Kuwait are either undertaken by or performed in collaboration with the Kuwait Institute for Scientific Research (KISR). Landsat Multispectral Scanner (MSS) data were used to classify the surface deposits of Kuwait in 1982 [4]. Twelve classes of surficial deposits were identified on a sedimentographic map of the scale 1:200,000. In 1994, the Gulf War-related surface changes were delineated on a change map (scale 1:250,000) produced from Landsat TM imagery (see Fig. 1) as a part of a project on "Damage Assessment of the Desert and Coastal Environment of Kuwait by Remote Sensing" [5]. Six classes consisting of thick tarcrete, thin tarcrete, minor changes, mobilized sand, little to no change, and water, were delineated. Landsat TM and NOAA/AVHRR data were used to monitor the temporal and spatial changes associated with the Kuwait oil fires and smoke plumes [6].

RADAR RESULTS

SIR-C data was acquired over southeastern Kuwait during both SRL-1 and 2 at angles of incidence of 48° and 55°, respectively. X-SAR data is available for SRL-1 only. Both scenes cover a portion of Kuwait City, Wafra and part or all of a number of oil fields including: Wafra, Burgan, Ahmadi and Magwa. An example of the SRL-1 SIR-C scene is shown in Fig. 2. Coastal features and the littoral environment are clearly shown. Man-made features such as buildings and oil storage facilities typically produce strong returns in all channels and result in white areas. Above-ground pipelines also appear as white or yellow linear features. Oil wells are clearly visible as are the dark square oil gathering centers. Roads and other smooth surfaces appear very dark. The shapes and extent of the oil lakes in

0-7803-3836-7/97/$10.00 © 1997 IEEE

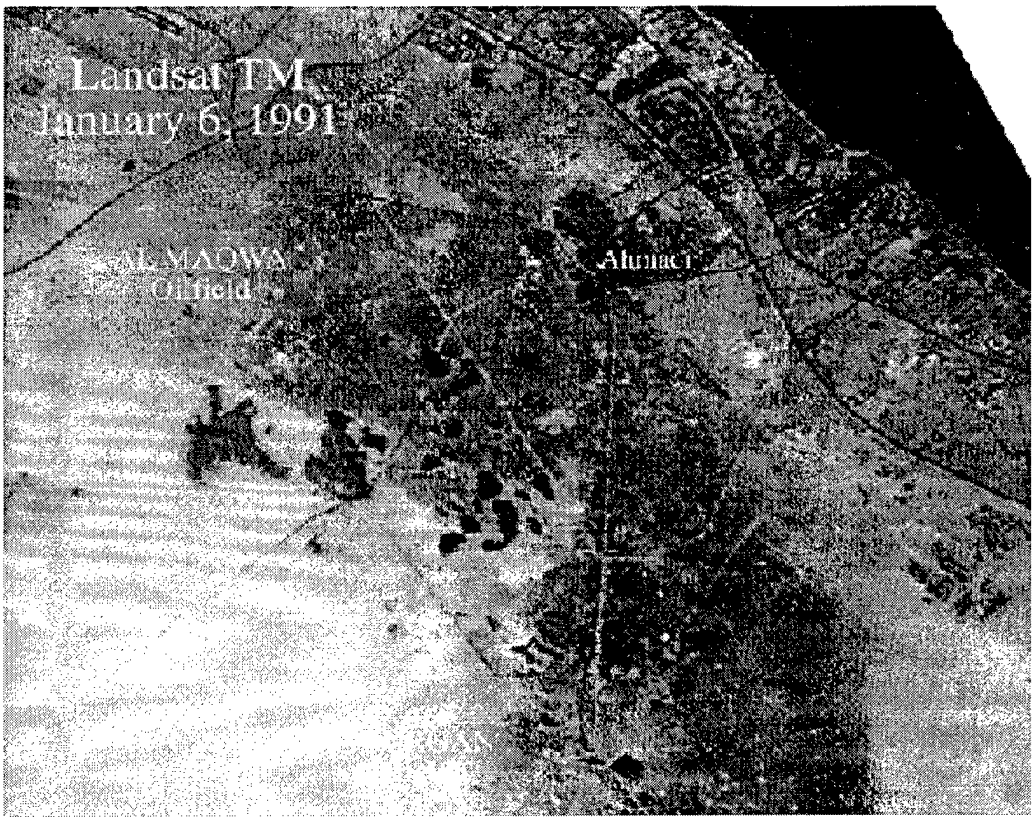

Figure 1. Landsat TM image of Kuwait obtained on January 6, 1991.

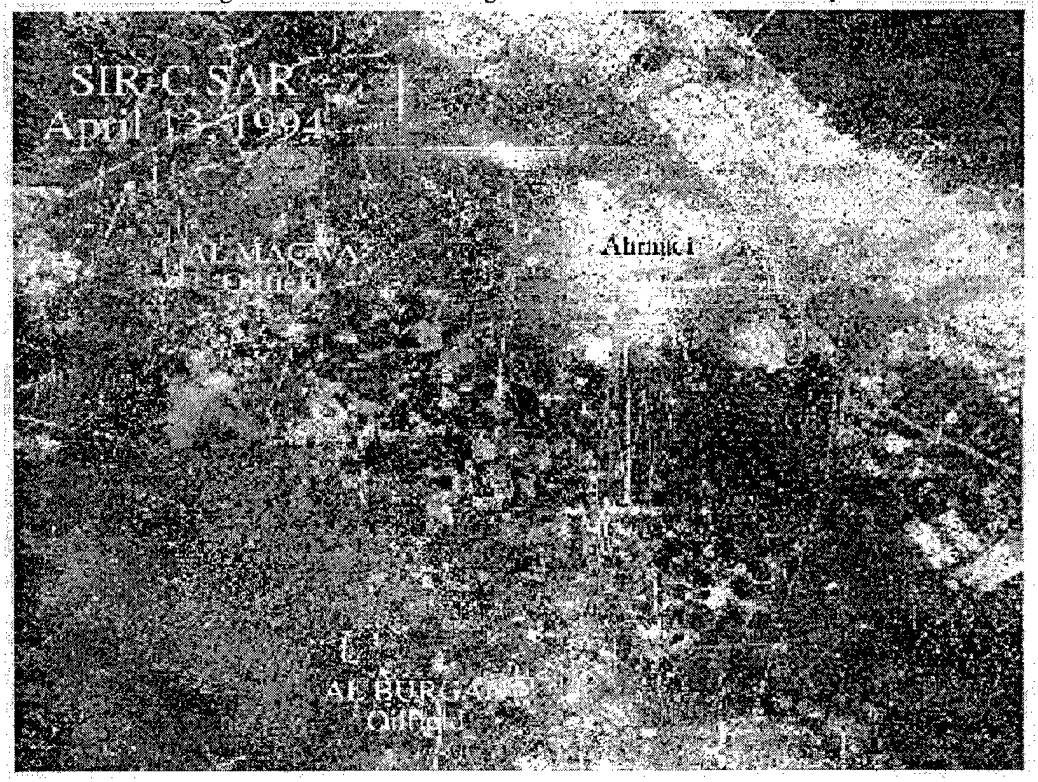

Figure 2. SIR-C false color composite of Kuwait acquired on April 13, 1994.
Red = L-hh, green = C-hh, blue = C-hv

the Burgan oil field are easily discerned. The general green and blue tones in the oil fields south of Kuwait city are attributed to relative differences in surface roughness and vegetation distribution. Of particular note are the red areas scattered throughout the oil fields. The 'red' color is the consequence of a strong L-band radar return (particularly for hh polarization) and weak radar return at C-band (at all polarizations).

The area containing the oil fields just to the south of Ahmadi is enlarged in Fig. 3 and clearly shows these areas of anomalous return. These are most likely the result of a pool of liquid (presumably oil or water) beneath a veneer of sand cover. In the vicinity of the Burgan oil field, such areas are most likely a veneer of aeolian sand covering some of the oil lakes. If these are 'buried' oil lakes, then the SAR data can easily be used to map their location and extent.

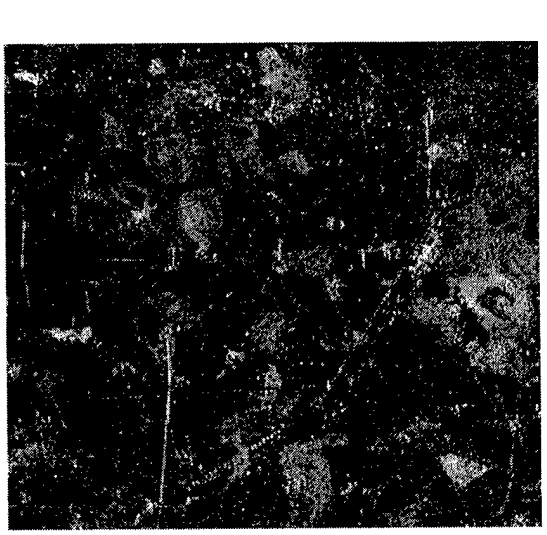

Figure 3. Enlargement of the SIR-C data showing the anomalous regions of high L-band return in red. Same color scheme as Fig. 2.

Although SIR-C/X-SAR data is not available for all of the Kuwait oil fields damaged during the war, a time sequence of both ERS and JERS SAR data has been acquired. It is expected that composites of JERS-1 (L-band) ERS-1 (C-band) SAR data should also show similar results for areas not covered by SIR-C. We expect to be analyzing these sources of data and collecting additional field observations over the next year.

REFERENCES

[1] F.I. Khalaf, I.M. Gharib, M.Z. Al-Hashash, "Types and characteristics of the recent surface deposits of Kuwait: Arabian Gulf," J. Arid Envir., vol. 7, pp. 9-33, 1984.

[2] F.I. Khalaf, "Desertification and aeolian processes in the Kuwait Desert," J. Arid Envir., vol. 16, pp. 125-145, 1989.

[3] Halwagy, R., and M. Halwagy, "Ecological studies on the desert of Kuwait, Part II. The vegetation," J. of Univ. of Kuwait (Science), vol. 1, pp. 87-95, 1974.

[4] A. Asem, F. Khalaf, S. Attasi, F. Palou, "Classification of surface sediments in Kuwait using Landsat data," Proc. of the First Thematic Conf. on Rem. Sens. of Arid and Semi-Arid Lands, Cairo, Egypt, January 1982, pp. 1057-104.

[5] D. Al-Ajmi, F. Misak, F.I. Khalaf, M. Al-Sudairawi, A.M. Al-Dousari, "Damage assessment of the desert and coastal environment of Kuwait by remote sensing," Kuwait Inst. for Sci. Res., Rep. No. KISR 4405, 1994.

[6] A.Y. Kwarteng and T. A. Bader, "Using satellite data to monitor the 1991 Kuwait oil fires," Arabian J. of Sci. and Eng., vol. 18, pp. 95-115, 1993.

MODELLING OF HUMAN DIMENSION ON SOIL EROSION PROCESSES FOR REMOTE SENSING APPLICATIONS

C. Gaillard [1], F. Zagolski [2], F. Bonn [1]

(1) CARTEL (Centre d'Applications et de Recherches en Télédétection),
Université de Sherbrooke, Sherbrooke - Canada J1K-2R1.
c/o 191 Gillespie, Sherbrooke - Canada J1H-4X2.
Phone / Fax : (+1) 819-569-4818 / (+1) 819-821-7944
E-mail: Charlotte.Gaillard@callisto.si.usherb.ca
Web-Link: http://www.callisto.si.usherb.ca/~cartel/

(2) PRIVATEERS (Private Experts in Remote Sensing),
De Weaver Drive 42, Philipsburg,
St Maarten - Netherlands Antilles.

Abstract: Spatial modelling of hydrological and erosion processes at watershed scale is subject to an increasing development simultaneously with the expanded use of remote sensing and Geographical Information System (GIS). Nevertheless, the raster structure of available spatial erosion models does not take into account some human landscape dimensions. Linear and directional features are commonly neglected in water and sediment transport modelling. This paper presents an attempt for integrating influences of spatial pattern discontinuities and directivity effects due to tillage and row of plants on the distribution of flows in agricultural watersheds. Introduction of these improvements in the ANSWERS (Areal Nonpoint Source Watershed Environment Response Simulation) model are in process.

INTRODUCTION

Studies which aim at characterising soil erosion processes are useful for understanding terrestrial ecosystemic functions. Moreover, these can be oriented to allow the planification of control measures against agricultural problems such as seedbed and topsoil losses. Among factors responsible for soil erosion in agricultural environments, human activity has an important impact. Especially, this influence can be expressed through modifications of land cover and soil surface properties. For example, tillage may have consequence to change the directions of water and sediment flows. Furthermore, the spatial occupation of terrestrial surfaces defining shapes of landscapes (*e.g.*, size and orientation of plots, presence of roads and hedgerows) also influences the erosion processes [1]. Because of the fine scale and linear forms of this type of information, these human dimensions are not yet really considered in the hydrological erosion models presently available, and if they are, they are incorporated as factors dependent on other parameters (*e.g.*, surface modifications caused by ploughing are included in soil roughness) or referred to an unique coefficient (*e.g.*, cultural practices) [2].

In order to allow a better assessment of the human impact on soil erosion processes, we present here some improvements on the distribution of water and sedimentation flows in a hydrological and erosion model, namely ANSWERS (Areal Nonpoint Source Watershed Environment Response Simulation) [3], by taking structural discontinuities of the landscape and aspect of tillage and plant rows into account.

WATERSHED EROSION SIMULATION

Among existing soil erosion models two categories can be distinguished: models relie on empirical considerations and others, more deterministical, called physically based distributed models. The latters which simulate surface hydrological processes and soil erosion during and immediately following a rainfall event need a raster grid (*i.e.*, cells matrix representation of landscape) for stocking input and output information. Computation of erosion and vertical water movements are integrated within each grid element, then runoff and sediment transfers are processing from one element to adjacent cells until the outlet element of watershed. ANSWERS belongs to this generation of models, such as more recently LISEM (Limburg Soil Erosion Model) [4].

These distributed models require several types of input. First, information concerning rainfall event and topographical data (*i.e.* Digital Elevation Model) from which are derived the slope and aspect for each grid element. These parameters are directly used in the computation of runoff directions and sediment movements. Then bio-pedological information, such as percent of vegetation cover or soil surface state, are also needed especially for detachement processes description.

0-7803-3836-7/97/$10.00 © 1997 IEEE

Thus, calculation of soil particles mobilization and transport by water flows lead to quantitative spatial repartition assessment of erosion and deposition.

Distributed models need lot of computer memory, which depends on total number of cells within the grid and decreases with spatial resolution degradation. At the same time, the elementary cell grid size or the spatial scale at which processes are simulated influences precision of model results. Choice of spatial resolution to run a model in the case of non uniform watersheds (*i.e.*, fragmented or heterogeneous landscapes) can be relevant for the forecasting of the hydrological response and eroded sediment transport and deposition due to a rainfall event in agricultural catchments. One basic assumption of distributed models is that each raster-grid square element is uniform. Our objective is to improve these erosion models by taking into account influences of linear and orientated features in preserving a standard spatial resolution appropriate to watershed study scale and remote sensing data. We choose to report those improvements in the ANSWERS model structure which is displayed in Figure 1.

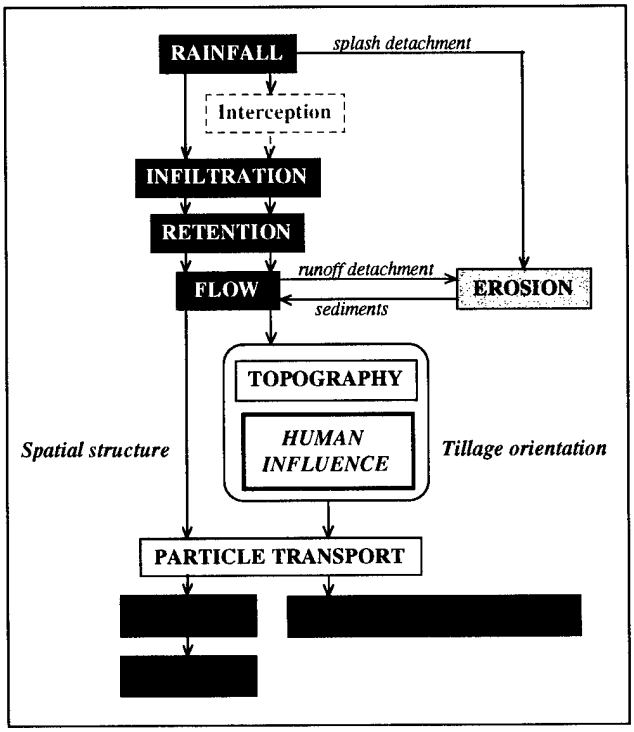

Figure 1: Flow chart of a distributed erosion model: representation of human influence on hydrological and erosion processes.

This diagram presents a simplified description of the principal component processes of the model and the two major modifications to be implemented: - the presence of landscape limits within a catchment and - the row ploughing aspect in cultivated parcels. We attach importance to these human parameters inasmuch as they can generate flow modifications, especially in terms of intensity and directions.

IMPROVEMENTS OF MODELLING SURFACE FLOW IN THE ANSWERS MODEL

Flow characterization of each element in the grid is computed by an explicit temporal backward difference solution of the following continuity equation:

$$Q_{in} - Q = \frac{dS}{dt} \qquad (1)$$

where, I is the inflow rate to an element from rainfall and adjacent elements, Q the outflow rate from this element, S the volume of water stored in this element and 't' the time.

Each element of the grid acts as an overland flow plane characterized by a slope and aspect of steepest descent. Overland outflow from a cell flows into neighbouring elements according to the direction of steepest slope as depicted by the solid line in Figure 2.

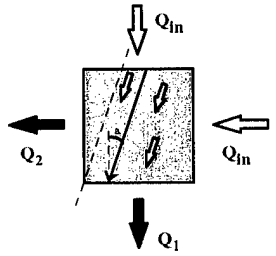

Figure 2: Flows characterization within a cell of a watershed grid.

The fractions of outflows from a cell going into the adjacent row (Q_2) and column (Q_1) elements is related to cell inflow (Q_{in}) weighted by the proportion of surface delimited by the dotted line as indicated in Figure 2, defined by the direction of steepest slope. Q_2 is expressed as:

$$Q_2 = 0.5 \,.\, tg\,(a) \,.\, Q_{in} \qquad \text{for } a \leq 45° \qquad (2)$$

$$Q_2 = 1 - 0.5 \,.\, tg\,(90 - a) \,.\, Q_{in} \qquad \text{otherwise}$$

and Q_1 is equal to $(1 - Q_2)$.

Landscape limits will be modelised as obstacles to the runoff, and these features will be integrated in model by relationships describing discontinuities of flow propagation. Figure 3-a shows the spatial distribution of flow in presence of a discontinuity (*e.g.*, tree hedgerow) within a cell. According to the type of limits, flow intensity will be attenuated and sedimentation increased, some discontinuities such as the roads can as well turn flow off course.

In presence of row tillage within cell, a new flow direction conditioning runoff and sediments movements along sides, is computed as function of row tillage aspect, cell slope and aspect values (Fig. 3-b). Of course, this directional flow must be comprised between the aspect cell and the row tillage aspect. The angle value of slope cell influences the computation of flow directions. In fact, beyond a critical cell slope value, runoff is no more dependent on tillage aspect and follows the steepest slope direction. In the same way, for a cell defined by a very low slope and oriented tillage presence, flows are conducted according to the slope along the ploughing direction. In this range of slope limit values, outflow redistribution in adjacent cells is calculated with equation (2) using a modified angle value.

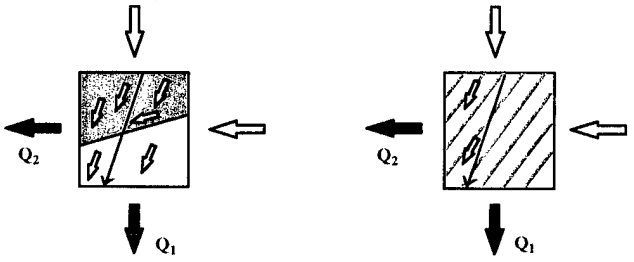

Figure 3: Flows modifications within cell (a) with spatial discontinuity and (b) presence of tillage rows.

USE OF REMOTE SENSING AND PERSPECTIVES

Jointly to the development of terrestrial models which aims to describe ecosystemic processes such as erosion, numerous methodologies have been developed using remote sensing data for risk erosion mapping [5] and as well as input to these quantitative simulation models [6] [7]. Remote sensing provide different informations which are essential to access erosion features and factors. For example, Leaf Area Index and percentage of vegetal cover can be indirectly derived from optical images even with the help of vegetation indices, semi-empirical relationships between these structural vegetation parameters to surface reflectance or by the use of physical reflectance models like SAIL (Scattering Arbitrary Inclined Leaves) [8] or DART (Discrete Anisotropic Radiative Transfer) [9] models.

The model will be linked with Geographical Information System and adaptated to receive as input remotely sensed data. Simulations will be tested to describe the influence of human factors on the soil erosion and especially to measure the effects of landscape pattern on energy and matters distribution at watershed scale [10]. These simulations will be conducted for the case of an agricultural watershed in Pays de Caux (France). Spatial discontinuities, linear and directional features in the landscape will be retrieved from optical satellite data with filtering and morphological image processing. These factors and surface parameters (*e.g.*, cover rate, roughness, *etc.*) will be extracted from SPOT and SIR-C data. However due to the late of delivery satellite data, we cannot present results of this study.

CONCLUDING REMARKS

Once these improvements introduced in distributed erosion ANSWERS model, this should allow a better understanding of terrestrials ecosystems and agricultural landscapes changes, by permitting to measure the influence of landscape patterns on the physical and environmental processes. Moreover they may contribute to watershed management and sustainable development.

REFERENCES

[1] M.G. Turner, 1989, "Landscape ecology: the effect of pattern on process", *Annual Review Ecology Systems, vol. 20, pp. 171-197.*

[2] W.H. Wischmeier and D.D. Smith, 1978, "Predicting rainfall erosion losses: A guide to conservation planning", *Agriculture Handbook, U.S. Depart. Agric., no. 537, 58p.*

[3] D.B. Beasley, L.F. Huggins, and E.J. Monke, 1980, "ANSWERS: A Model for Watershed Planning", *Trans. Amer. Soc. Agric. Eng., vol. 23, pp. 938-944.*

[4] A.P.J. De-Roo, 1996, "LISEM: a single-event physically based hydrological and soil erosion model for drainage basins. I: Theory, input and output", *Hydrological Processes, vol. 10, pp. 1107-1117.*

[5] E.T. Engman, 1995, "The use of remote sensing data in watershed research", *Journal of Soil and Water Conservation, vol. 50, no. 5, pp. 438-440.*

[6] S.M. De Jong, 1993, "Applications of Reflective Remote Sensing for Land Degradation Studies in a Mediterranean Environment", *Thèse de Doctorat. Netherlands Geographical Studies, 180 p.*

[7] K.D. Sharma and Surendra Singh, 1995, "Satellite remote sensing for soil erosion modelling using the ANSWERS model", *Hydrological Sciences J., vol. 40, pp 259-272.*

[8] W. Verhoef, 1984, "Light scattering by leaf layers with application to canopy reflectance modeling: the SAIL model", *Rem. Sens. Environ., vol. 16, pp. 125-141.*

[9] J.P. Gastellu-Etchegorry, V. Demarez, V. Pinel, and F. Zagolski, 1996, "Modeling radiative transfer in heterogeneous 3-D vegetation canopies", *Rem. Sens. Environ., vol. 58, pp. 131-156.*

[10] P.G. Risser, 1990, "Landscape pattern and its effects on energy and nutrient distribution", *In I.S. Zonnevert and R.T.T Forman (Dir.), Changing Landscapes: an ecological perspective. New York: Springer-Verlag, pp. 45-56.*

Moisture and Temperature Condition of Lahar-Affected Area around Mt. Pinatubo

Asako Inanaga [1], Makiko Watanabe [2], Jose D. Rondal [3],
Masao Yoshida [4], Toshiaki Ohkura [3], Alejandro G. Micosa [3]

[1] Remote Sensing Technology Center of Japan (RESTEC) and Tokyo Institute of Technology
RESTEC, Roppongi First Building, 1-9-9, Roppongi, Minato-ku, Tokyo, 106, Japan
Tel: +81-3-5561-8776 Fax: +81-3-5561-9542 e-mail: inanaga@restec.or.jp
[2] Department of Built Environment, Interdisciplinary Graduate School of Science and Engineering,
Tokyo Institute of Technology
4259, Nagatsuta, Midori-ku, Yokohama-shi, Kanagawa, 227, Japan
Tel: +81-45-924-5532 Fax: +81-45-924-5519 e-mail: makiko@n.cc.titech.ac.jp
[3] Bureau of Soils and Water Management, Agriculture Department, Philippines
Elliptical Road corner, Visayas Avenue, Diliman, Quezon City, 1100, Metro Manila, Philippines
Tel: +63-2-920-4364 Fax: +63-2-923-0454
[4] Tropical Environment Chemistry, Ibaraki University
3-21-1, Chuo, Ami-cho, Inashiki-gun, Ibaraki, 300-03, Japan Tel: +81-298-88-8687 Fax: +81-298-88-8525

Abstract -- Moisture and temperature condition of lahar deposit was investigated combining field survey and satellite image analysis. Characteristics of the deposit, such as moisture, temperature, particle size, and spectral reflectance were obtained by field survey. Referring to these field survey results, areal analysis on the relationship between moisture and temperature, temporal change of their distribution, and their condition for recovery was carried out using LANDSAT/TM images.

1. INTRODUCTION

Mt. Pinatubo in the Philippines made enormous eruption in June of 1991 and ejected huge amount of debris and ash. The ejected materials deposited around the mountain and flow down to plains forming lahars every rainy season. It is important to understand the nature and dynamics of lahar in order to pursue recovery and development in this area. This study investigates moisture and temperature condition of lahar deposit and considers their temporal change. Satellite imagery and field-measured data are combined for the analysis in order to understand largely-distributed lahar deposits in detail.

2. STUDY AREA AND DATA COLLECTION

2.1 Study Area

The study area is along Bamban River running out of Mt. Pinatubo in the northeast direction (approximately 15° 10' - 15° 25' N, 120° 30' - 120° 45' E). This area has been attacked by lahar every year. However, the lahar deposition area have been shifting to the upper-stream and vegetation is recovering at the lower edge.

2.2 Satellite Data Pre-processing

Five LANDSAT/TM images (path: 116, row: 49-50) taken on following dates are processed.

January 20, 1990 January 26, 1992
February 13, 1993 February 19, 1995
March 25, 1996 (all in dry season)

All images are rectified using GCPs. The target area is extracted from each rectified image. The image of 1990 is used to see the study area before the eruption. The other four images are used for the analysis (Fig. 1).

2.3 Field Survey

Field survey was made in December of 1996 at seven points along Bamban River and surface samples were collected at each point. The land surface of these points ranges from bare lahar deposit to mixture of the deposit and grass growing on it. Measurement items and instruments used are as follows.

- Water content by weight (Soil moisture meter SH-200, Atago Co., Ltd.).
- Surface temperature (Radiation thermometer ER-2008, Matsushita Communication Industrial Co., Ltd.).
- Surface spectral reflectance (Spectral radiometer MSR-7000, wavelength: 280 - 2500 nm, recorded by 10 nm, Opto Research Corporation).

3. ANALYSIS AND DISCUSSION

3.1 Characteristics of Lahar Deposit at Field Survey Points

Measurement Results

The collected lahar deposit samples were oven dried (120 °C, 1 hour) and screened into three particle size groups (< 0.2 mm, 0.2 - 2 mm, and ≧ 2 mm). The spectral reflectance measured on the field was averaged for the nominal wavelength range of TM reflection bands. The wavelength of band 7 was excluded from this analysis, since the measurement result was not stable. Table 1 shows the

0-7803-3836-7/97/$10.00 © 1997 IEEE

characteristics of lahar deposit obtained by the field survey.

Distribution of particle size constitution along the river shows the trend that the ratio of fine particles increases in the lower-stream. Water content by weight plotted along the river shows also clear trend to increase in the lower-stream. These two facts indicate the relationship between particle size constitution and water content. The comparison of these two items proved that the higher the ratio of fine particles (< 0.2 mm) becomes, the more water content is observed. This relationship suggests that water content by weight can be an index of particle size constitution for the lahar deposit.

Surface temperature tends to decrease in the lower-stream. It well agrees to the increase of water content in the lower-stream. Water content is assumed to be the main factor to differentiate surface temperature, as the clear relationship between surface temperature and water content by weight is observed for the four data collected in close location (Table 2). However, it is difficult to discuss the relationship between surface temperature and water content over seven survey points, because precise correction of measurement time is not available in this case. In terms of measurement time difference, TM is expected to provide more accurate information, since it senses large area in a few seconds.

Preparation for Areal Analysis

As a preparation for areal analysis using TM images, the relationship between spectral reflectance measured on the field and other items were examined. The averaged spectral reflectance and water content by weight have negative correlation in all the examined wavelength, which proves the usefulness of TM reflection bands to investigate moisture condition. Correlation coefficient is almost the same for visible and near infrared wavelength. The highest correlation coefficient (r) is for band 4 wavelength (r = -0.90), and the lowest is for band 5 wavelength (r = -0.67).

Spectral reflectance has negative correlation with the ratio of the fine particles (< 0.2 mm), and positive correlation with the ratio of coarser particles for all the examined wavelength. As same as the case for water content by weight, the highest correlation coefficient is found between reflectance of band 4 wavelength and the ratio of the fine particles (r = 0.67). Correlation between spectral reflectance and surface temperature is all positive. In this case, band 1 wavelength has the strongest relationship (r = 0.74). However, the correlation coefficients are almost the same for visible and near infrared, and rather low for band 5 wavelength for both of the particle size constitution and surface temperature.

It is assumed that spectral reflectance represents water content which is strongly related to particle size constitution. Furthermore, water content have much effect on surface temperature, which result in correlation between spectral reflectance and surface temperature. Therefore, it is expected that both reflection bands and thermal band (band 6) provide water content and particle size information, in addition to simple surface temperature information by the thermal band.

3.2 Areal Analysis

Relationship between Moisture and Surface Temperature

In order to find the relationship between moisture and surface temperature of lahar deposit, correlation coefficients between DN (digital number) of TM band 6 and the reflection bands (bands 1, 2, 3, 4, 5, and 7) were calculated. Band 6 DN represents surface temperature and DN of other bands represents surface spectral reflectance. For this analysis, pixels corresponding to lahar deposit were extracted from target area images using mask images generated based on the interpretation of color composite image and NVI calculated by following formula.

NVI = ((B4-B3)/(B4+B3))*100+100

Bx: DN of band x

The correlation is positive for all the reflection bands, which means surface temperature is high in dry area and low in wet area, since spectral reflectance well corresponds to moisture as seen in the previous analysis. Band 7 has the highest correlation coefficients ranging from 0.534 to 0.587.

Temporal Change of Moisture and Temperature Distribution

Moisture distribution over lahar deposit were interpreted on TM images. Though all the reflection bands' DN have relation to moisture, the color composite of band 4, 7, 5 for red, green, and blue creates the highest contrast between wet and dry area. High moisture area is shifting from the lower-stream to the upper-stream year by year. This indicates that the fine particles (< 0.2 mm) depositing area is expanding to the upper-stream. Water in the channel disappears on its way to the lower-stream and the point where water disappears is shifting to the upper-stream every year.

Surface temperature distribution is interpreted on band 6 pseudo color image. It generally corresponds to the moisture distribution, that is, temperature is high in low moisture area and low in high moisture area. However, some differences between two patterns are found. For instance, there is an area with high temperature and moderate moisture.

Moisture and Temperature Conditions for Recovery

Recovery forecast is important for regional planning. In order to find conditions for recovering from lahar flooding, moisture and temperature condition was compared among the areas on the different stage of recovery.

In practice, a test area was located at the lower-stream of the lahar-flooding seen on the 1992 image. The pixels corresponding to lahar deposit, which were extracted in the first areal analysis, were regarded as not-recovered area and the other pixels were regarded as recovered area. The recovered areas may contain both the area with vegetation coming in lahar deposit and the area with successive

vegetation where lahar deposit has been reduced. Not-recovered areas in each image are categorized in accordance with recovery stage. For the image of 1992, four categories are established:

areas defined as

1) recovered in 1993, 1995, and 1996,
2) not-recovered in 1993, recovered in 1995 and 1996,
3) not-recovered in 1993 and 1995, recovered in 1996,
4) not-recovered in 1993,1995, and 1996.

The other years' not-recovered areas are categorized in the same way. The DN of each TM band for each category in the same year was computed and compared.

Computation result show the tendency that the area which turns to recovered area in the next year have lower DN for all TM bands except for band 4. Higher DN of band 4 seems to reflect vegetation existence. In fact, some lahar-deposited areas have sparse grass which is hardly seen on TM images. This show the ability of TM image to indicate the areas covered with the primary vegetation, as the sparse grasses such as talahib (*Saccharum spontaneum*) are observed as the first vegetation coming in lahar deposit. Lower DN of other bands may reflect both of vegetation existence and rich moisture.

4. CONCLUSION

The field survey results showed that spectral reflectance of lahar deposit reflects moisture and particle size constitution. Surface temperature also presents moisture. Based on these findings, the areal investigation using TM images was carried out. Moisture and surface temperature are related to each other. Significant temporal change in the study area is the shift of high moisture area (i.e., fine lahar material depositing area) from the lower-stream to the upper-stream. The area recovering from lahar flooding can be detected by TM DN, because it shows difference in vegetation and moisture in accordance with recovering stages.

Combination of field survey and satellite image analysis facilitated understanding of lahar deposits condition. In further study, the effect of the lahar deposit on the adjacent regions should be considered based on the findings described above.

This study is partly supported by Nissan Science Foundation.

Table 2 Relationship between water content by weight and surface temperature.

Point ID*	3A	3B	3C	3D
Water content by weight (%)	1.2	3.4	1.9	2.4
Surface temperature (°C)	55.2	44.0	49.3	46.3

* All four points are closely located around survey point 3. Measured at almost same time.

Table 1 Characteristics of lahar deposit at field survey points.

Point ID*		3	4	1	5	2	7	6
Particle size constitution (%)	≧ 2 mm	21	41	1	31	13	0	13
	0.2 - 2 mm	63	58	47	18	44	3	40
	< 0.2 mm	16	1	52	51	43	97	47
Water content by weight (%)		3.2	3.8	2.8	9.3	17.3	30.3	21.3
Surface temperature (°C)		47.3	53.8	49.2	40.6	33.6	30.8	37.0
Spectral reflectance (%)	450 - 520 nm (TM band 1)	30.2	28.6	26.9	25.7	21.8	10.7	6.2
	520 - 600 nm (TM band 2)	31.4	30.5	28.9	28.1	24.9	11.9	8.6
	630 - 690 nm (TM band 3)	31.3	30.9	30.0	28.9	26.7	12.9	9.4
	760 - 900 nm (TM band 4)	33.5	31.6	31.4	30.3	28.7	14.9	14.4
	1550 - 1750 nm (TM band 5)	39.4	35.7	43.6	41.5	22.4	31.4	16.6

* From the upper-stream (left column) to the lower-stream (right columun).

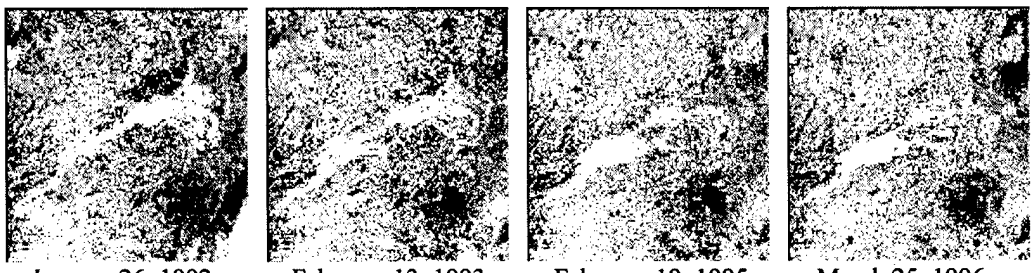

January 26, 1992 February 13, 1993 February 19, 1995 March 25, 1996

Fig. 1 LANDSAT/TM images of the target area.

Evaluation of RADARSAT Image for Landslide Susceptibility Mapping : Application in Bolivia

Stéphane Péloquin[1], Q. Hugh. J. Gwyn[1], Driss Haboudane,[1]
Roberto Mendez[2] and Lambert Rivard[3]
[1] Université de Sherbrooke
2500, boul. de l'Université, Sherbrooke (Québec), Canada, J1K 2R1
(819) 821-8000 (2187) - speloqui@courrier.usherb.ca
[2] Proyecto de Manejo Integral de Cuencas (PROMIC), Bolivia
[3]Études de Télédétection L.A. Rivard, (Québec), Canada

Abstract -- The problems relating to landslides and intensive gullying are of primary concern in Bolivia, especially around the city of Cochabamba where thirty nine watersheds, pointing toward the city, are generating an impressive quantity of sediments, destroying fertile lands, and putting in jeopardy many farmers who make there living in these areas. One way of changing this situation, is to evaluate the susceptibility of landslides and applying measures for restricting or correcting the highly susceptible zones. Most of the existing methodologies used to perform this evaluation are done from aerial photography to collect the necessary data, before applying proper models. This study shows that the use of RADARSAT image (Fine mode), has the potential to replace or complement aerial photography for the identification of many parameters essential in the mapping of different susceptibility classes.

INTRODUCTION

Like other dynamic geological phenomenon (volcanoes, earthquakes, etc.), landslide susceptibility (LS) mapping constitutes a real challenge for earth scientist. In this study, « susceptibility » refers to the probability of occurrence of a potentially damaging landslide without considering the time parameter, which is normally considered for «Hazard» mapping [1].

Ideally, LS maps show classes representing homogeneous geomorphological and geological conditions that are related to a certain level of fragility to landslides. Basically, three different methodologies are recognized in the literature [1] [2] [3] to deliver satisfactory approximations of LS level for a certain area; 1) direct evaluation from aerial photography; 2) indirect evaluation obtained by cross analysis of multiple parameters, and; 3) geotechnical measurements permitting to slope stability models (soil mechanics), and hence to obtain a deterministic LS mapping. The choice of one of these methodologies will depend primarily on the scale of the area to be evaluated, the precision anticipated, and the budget available [1][4].

This study is part of an overall research program evaluating the potential of remote sensing data as a primary source for applying existing models of LS mapping. Specifically, this phase concentrates on the evaluation of RADARSAT image for its potential to establish six geological, geomorphological and landuse conditions.

STUDY AREA

The evaluation was done in the vicinity of Cochabamba, located in the middle of Bolivia and considered is the third major city (Fig. 1). Cochabamba lies on a lacustrine plain at an altitude of 2 500 m, and is surrounded by 39 watersheds that reach an average altitude of 4 200 m . These watersheds are part of the eastern Andean Cordilliera. Specifically, our work concentrates on a 20km^2 pilot watershed named *Taquiña* which has a N-S axis. The watershed has been intensively studied since 1991 by PROMIC, a bilateral (Bolivia-Switzerland) organism which has the mandate of managing all the watersheds surrounding the city. To date, the PROMIC multidisciplinary team has accumulated, from field survey and aerial photography, all the necessary data for landuse, vegetation, soil, geology and geomorphology mapping.

Geological and Geomorphological Settings

Taquiña is characterized by two Ordovician lithologies ; 1) sandstone, exposed between altitude 3 800 and 4 200 m, and dipping at 55° toward the south ; 2) shale, showing mostly along small rivers principally on the eastern slope, between 2 800 and 3 500 m and also dipping in the same general slope direction. Lineament orientations are very clear in the sandstone area and present a principal orientation of NW-SE and a secondary direction, perpendicular to the first one. The thick layer of lodgment and supraglacial till between the altitude 2 500 - 3 500 m combined with the presence of four lateral and one terminal moraine, reveal the presence of an extensive glacial event in this area [5][6].

0-7803-3836-7/97/$10.00 © 1997 IEEE

Figure 1 Study area

Many small (100-500 m^2) active and dormant landslides were identified mainly on the western slope of *Taquiña*, where the thickness of glacial sediment is thicker [5]. It is also possible to appreciate the dynamic geomorphological state by the presence of intensive gullying that represent an enormous loss of fertile lands and constitute a significant problem for the security of the local population.

Landuse

The work done by [5] and [6], demonstrate that four main zones characterized *Taquiña* : 1) pasture, representing 60 % of the area, and mainly concentrate at high altitudes (>3000 m); 2) intensive agriculture cultivation (9%), and localized in the mid-altitude, principally on the western slope ; 3) eucalyptus forest, occupying 11 %, and found mainly in the down cutting valleys and in the lower altitudes, finally ; 4) bare bedrock covering most of the head of the *Taquiña* and representing 20 % of the area.

DATA

RADARSAT Image

The fine mode image was taken in May 1996, with an incidence angle of 41°, in ascending orbit. The data were resampled to a 10 m pixel spacing from the original Path Image Plus processing, offered by RADARSAT International Inc. This image format transforms the 8.4 m beam resolution to a 3.125 m pixel spacing. The full image was cropped to a 700 X 700 pixels image, centered on the watershed, and converted to a 8 bits pixel depth from the original 16 bits. A median filter was applied to remove speckle effects. Contrast enhancements were also perform to give better visual results.

Due to the topographical characteristics of the area, photogrammetric geographical correction was required to permit a reasonable fit (< 2 rms) between the different data sets [7].

Thematic Maps

All the available thematic maps were prepared at a scale of 1 : 20 000, from the interpretation of aerial photographs. The maps were created by digitizing the polygons traced on the photos in a at the same scale. The vector maps were then incorporated as new layers over the radar image in image processing software (EASI/PACE).

METHODOLOGY

Evaluated Parameters

The application of existing models for LS mapping, necessitate a prior evaluation of particular parameters. From the work by [2] [4], and the physiographic conditions of our study area, the following parameters have been identified to account for the most important in LS analysis: 1) presence of active or ancient landslides zones; 2) slope steepness; 3) overburden thickness; 4) structural and lithological geology ; 5) drainage network/density and gullying, and ; 6) vegetation density. The radar image was evaluated regarding the possibility of identifying correctly these conditions from a visual analysis. *Identification* means that it is possible to identify objects of variable form, spectral and textural characteristics, in a certain context within the background.

Evaluation Procedure

The first phase of the methodology is a detailed examination of a high quality (600 dpi) print out of the radar image to evaluate parameter 1), 2), 4) and 5) listed above. The second phase concentrates on the qualitative estimation of overburden thickness (till) and vegetation density. To achieve this second phase, contrasting land uses and land covers were isolated on slopes facing toward (brighter tones) and away from (darker tones) the radar. Both spectral (backscattering) and textural variations were used to estimate the level of differentiability. The slope orientation was obtained from a DEM classification. This step is very important because it allows us to evaluate similar land uses and land cover types in images that are considered highly contrasted.

RESULTS AND DISCUSSION

General

Once the selected enhancement parameters were correctly applied, the radar image revealed a surprising

quantity and quality of details given by the high spatial resolution. The nominal incidence of the image (41°) has the effect of representing the watershed with its fine topographic variations, and hence permitting the identification of many important features, even without stereo-viewing.

Drainage and Gullying zones

Due to dielectric differences between water, moist soil, riparian vegetation and erosion-induced topographic variations, the drainage network and gullying zones were easily identified in great detail. Even details regarding the erosion associated with these rivers were very clear. We could also identify new features that were not present during the aerial campaign of 1991.

Structural Geology and Lithology Recognition

Both sets of lineaments were identified clearly even though some of them were nearly parallel to the look direction. The orientation and dip could also be estimated with success from the sandstone lithology at the top of *Taquiña*. In the lower part of the watershed, the shale area was not identified with precision, although a few outcrops were correctly located along small rivers of the eastern slope and differentiated on the basis of there high backscattering values (light tones), probably induced by corner reflector effects.

Active/Dormant and Ancient Landslides

The five active/ancient landslides identified on the aerial photography were all identified with the radar image. Both, the surface roughness created by the movement and the semi-arc shape at the head of the fractured zone, gave enough differentiability within the background for easy delineation. In more vegetated areas, this was easier because of the vegetation density represented by the lighter tones in the bulging zones of individual landslides. These results represent a major result since these conditions are normally highly weighted in the LS analysis, and there presence alone suggests conditions prone to instability [1].

Vegetation Density and Overburden thickness

It was observed that more densely vegetated areas were characterized by darker tones and finer texture variations. From this distinction, three main units were correctly identified: 1) no vegetation; 2) medium coverage (agriculture and pasture), and; 3) dense vegetation coverage (forests). However, some areas covered with intensive cultivation were interpreted as forest and *vice-verca*. In contrast to the vegetation cover, it was possible to distinguish two classes of overburden thickness : 1) < 1 m and; 2) > 1 m. Obviously, the first unit represent the bare rock, where till cover is absent or thin. The second unit represents the rest of the area, where till depth varies between 1 and 20 m [5] and vegetation covered.

CONCLUSION

The results obtained during this evaluation show that RADARSAT images, in Fine Mode, constitute a valuable tool for establishing many important parameters for LS mapping. The low cost acquisition of these data, combined with there ability to be integrated with ancillary data in a GIS, has to be considered seriously when planning a general survey for establishing a LS analysis.

ACKNOWLEDGMENT

The authors like to acknowledge International Development Research Centre, Natural Science and Engineering Council - Canada (Grant A4250) and the Canadian Space Agency (ADRO Project 127) for their financial support.

REFERENCES

[1] D.J Varnes and Commission on Landslides and other Mass-Movements - IAEG, " Landslide hazard zonation : a review of principles and practice, " The Unesco Press, 1984, 63 pp..

[2] M.J. Crozier, " Landslides : causes, consequences and environment, " Croom Helm, Eds. London, England, 1986, 245 pp..

[3] A. Hansen, " Landslide hazard analysis," in Slope instability, D. Brunsen and D.B. Prior, Eds, Wiley & Sons, New-York, pp. 523-602.

[4] A. Carrara, " Multivariate models for landslide hazard evaluation," Mathematical Geology, vol. 15, no. 3, 1983, pp. 403-427.

[5] B.L. Claure, " Informe geomorphologico de la Cuenca Taquiña," PROMIC, 1993, 17 pp..

[6] R. Salinas, "Capacidad de uso mayor de la tierra y su relacion con el uso actual en la Cuenca Taquiña," PROMIC, 1995, 19 pp..

[7] T. Toutin, "La correction géométrique rigoureuse: un mal nécessaire pour la santé de vos résultats," Canadian Journal of Remote Sensing, vol. 22, no. 2, 1990, pp.184-189.

IGARSS'97

1997 International Geoscience and Remote Sensing Symposium

03-08 August 1997

Singapore International Convention & Exhibition Centre

Technical Program

Interactive Area 8: Detection of Buried Objects and Voids

Near Field SAR Noisy Target Identification

M.S. Afifi and A.G. Al-Ghamdi
King Saud University
P.O.Box 800 Riyadh 11421 Saudi Arabia
Tel. 966 1 4676733/Fax 966 1 4676757/e-mail F45E046@KSU.EDU.SA

Abstract -- Basic analysis are applied to near field identification of targets, with near field separated transmitters and receivers. Identification in noisy environments uses multifrequency imaging, with new unique addition and multiplication of images at different frequencies. This proved to be very flexible till signal to noise ratios of Zero dB.

INTRODUCTION

Synthetic Aperture Radar (SAR) Imaging can be performed using one antenna for transmission and reception, or it can use two separate antennas, each for one of the functions. The use of two antennas is more desirable for CW applications, as it would be hard to have enough isolation between both functions if one antenna is used. In previous work [1] the basic analysis are presented without consideration of the separation between the transmitter and the receiver. It was proved that resolution in the near field reaches low values, smaller than quarter of the wavelength. The analysis, especially in the near field applications, need to take the transmit-receive configuration into consideration. Fig.1, shows the basic configuration in this concern, where its influence on the results would be important when the distance between the transmitter and the receiver is a large fraction from the distant to the target.

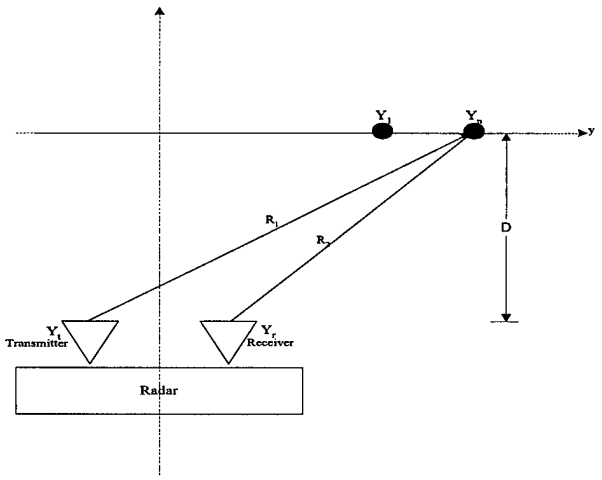

Fig.1 Configuration of linear array for two point objects.

Considering a stationary target region composed of a set of points with brightness A_n, where n represents the order of these points. The sampled SAR field E_m, along the synthetic length, when the distance between the transmitter and a target point is R1 and the distance to the receiver is R2. E_m is given in (1), with m indicating the target location along the synthetic length, and D is the lateral distance.

$$E_m = \sum_n A_n \frac{e^{-j\beta\left(\sqrt{D^2+(Y_n-Y_t)^2}+\sqrt{D^2+(Y_n-Y_r)^2}\right)}}{R_1 R_2} \quad (1)$$

In this situation the back transformed image I_n, at distance D, can be processed as given by (2)

$$I_n = \sum_m E_m \frac{e^{j\beta\left(\sqrt{D^2+(Y_n-Y_t-Y_m)^2}+\sqrt{D^2+(Y_n-Y_r-Y_m)^2}\right)}}{\sqrt{D^2+(Y_n-Y_r-Y_m)^2}} \quad (2)$$

In absence of interference and noise the image of a two point source as processed from (2) is shown in Fig.2. It can be seen that the side-lobes due to the finite aperture dimension is unavoidable in the reproduction, in this case, at the levels below -12 dB.

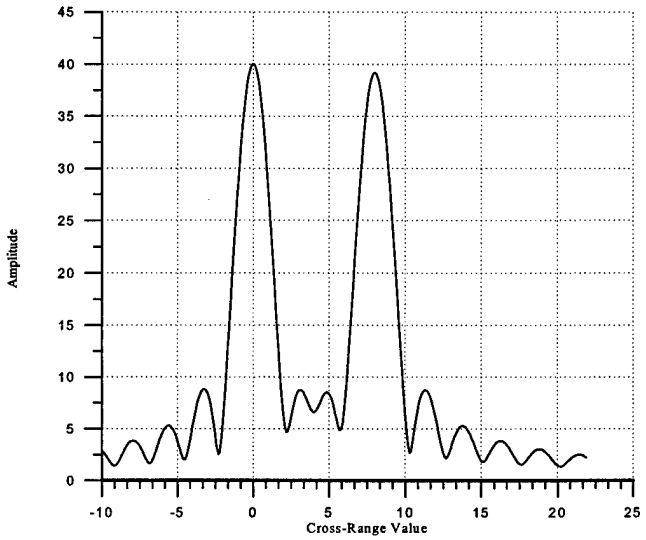

Fig.2 Two point identification at f=10GHz, with synthetic length L_s=41 cm, and distance D=60 cm.

0-7803-3836-7/97/$10.00 © 1997 IEEE

INTERFERENCE EFFECTS

In order to simulate the practical measurements, the interference should be considered. A new random amplitude and phase parameter ar_m is added to the received electric field E_m. Equation (1) would change to reflect this parameter in (3).

$$E_m = \sum_n (A_n \frac{e^{-j\beta(\sqrt{D^2+(Y_n-Y_t)^2}+\sqrt{D^2+(Y_n-Y_r)^2})}}{R_1 R_2}) + ar_m \quad (3)$$

These random values change continuously, reflecting the true interference effects. Specially in the near range, multiple interference arises, either from multiple mutual reflections, enhanced by the proximity of the object details, or due to direct leakage between the transmitter and the receiver circuits, and/or other interactions causing noisy field levels. Such effects can cause rapid image noise variations, which can be explained mistakenly as fast details, enhanced by the sharp resolution in the near range.

Simulation is made at X-Band (8-10GHz) for two adjacent objects, separated at a distance of 8 cms (at y=0 and y=8). Fig.3, shows the distorted image caused by the random parameter $ar_m=1.5A_n$ at 10GHz. All of the other simulations at other frequencies in this frequency range are similar in its random distortion.

ELIMINATION OF INTERFERENCE

In order to eliminate or reduce these interference effects, few processing techniques were proposed, making use of multifrequency imaging. In particular, we site [2 , 3 & 4]. It isolates the noise from the data E_m, before the production of the image [3]. We propose in this paper elimination of the noise from the image itself represented by I_n, which appears much more effective, than previously proposed eliminations of the noise from the data.

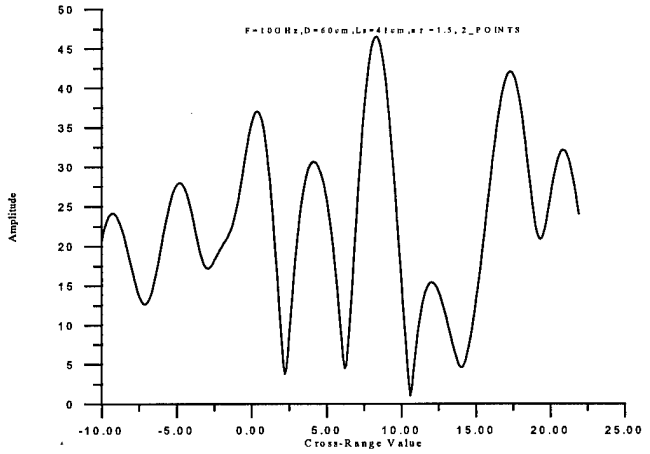

Fig.3 Distorted image caused by random parameter at10GHz.

Summation of Images

Based on the idea of removing uncorrelated portions of the images, it is discovered that the portions of the images formed from interference between the image data and the original data change its location in the image randomly at different frequencies. Whereas, the original image objects, always appear at the same location. When addition is applied, the original objects gray levels always increase. The interference part of the image, tend to be eliminated. This is demonstrated by simulation, using (3), at multiple frequencies. The total amplitude summation I_{ms} from the amplitudes at different frequencies I_{mn}, can be written as (4).

$$|I_{ms}| = |I_{m1}| + |I_{m2}| + \ldots + |I_{mn}| \quad (4)$$

The configuration of two adjacent objects, with distance (D= 60cm), synthetic length (L_s=41 cm), random parameter (ar_m=1.5 A_n), and at frequencies in the range of (8-10 GHz), with separation frequency of (0.5GHz) are processed in this way and shown in Fig.4. It is evident the effectiveness of this method.

Multiplication of Images

Another effective way is when using multiplication of multi-spectrum images. Fractional multiplicity effects, for side radiation yield tremendous decrease for the side-lobes. This approach is simulated using (5) for the same previous images, yielding Fig.5.

$$|I_{mm}| = |I_{m1}| * |I_{m2}| * \ldots * |I_{mn}| \quad (5)$$

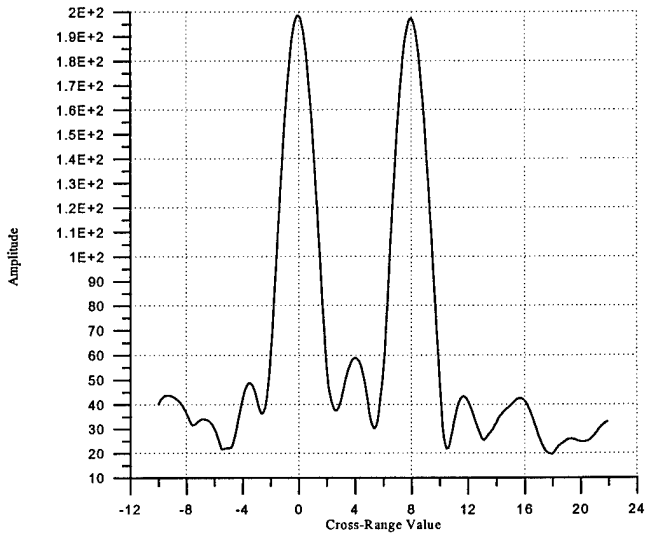

Fig.4 Summation technique at (8-10 GHz), step 0.5 GHz, L_s=41cm, D=60cm, and ar=1.5.

It can be seen that the two targets appear very distinguishable with no side-lobes, at all, indicating the idealism of this approach.

PRACTICAL VERIFICATION

A small anechoic chamber is used with a two port network analyzer and two wide band horns (representing the transmitter and the receiver), to verify these results. A (2 pin) target with foam supports are placed slightly far above a wooden stand. The two targets are separated by 8cm. The distance between the targets and the horns are 60cm, and the synthetic length is 41cm. Fig.6 shows the outcome of the processed images of the two pins, at 7.2, 7.38, 7.44, 7.56, 7.76 & 7.82 GHz.

The great similarity between Fig.6 and Fig.5 illustrates the practical validity of this technique. It also indicates that wide variety of frequency combinations yield always great improvements in identification.

CONCLUSION

In [3] the noise elimination from the image data at multiplicity of X-band frequencies (using multiple signal classification (MUSIC) Algorithm) could yield similar results as those between Fig.(2) and Fig.(5) at signal to noise ratio of 30 dB. In this paper the performance is better achieved, till signal to noise ratios approaching (0dB), using the processing on the images themselves. Note that the use of the eigenvectors of the correlation matrix (of the MUSIC approach), of the image processed data, has been tested and found to yield very similar results as those using this techniques but at much lower signal to noise ratio.

Note also that the use of complex level additions and multiplications yield slightly better results than those presented in this paper.

REFERENCES

[1] Al-Ghamdi, A.G, and M.S Afifi, "Near Range Resolution and Object Detection In High Interference Environments," 6th International Conference on Ground Penetrating Radar, Sendai, Japan, 30-Sept.-3 Oct., pp. 399-403, 1996.

[2] Tomiyasu K., "Tutorial Review of Synthetic-Aperture Radar (SAR) with Applications to Imaging of the Ocean Surface," Proc. IEEE, vol.66, pp. 563-583, May 1978.

[3] Odendal, J., W., Barnard, E., and Pistorius, "Two-Dimensional Superresolution Radar Imaging Using the MUSIC Algorithm", IEEE Trans. Antennas Propagation, Vol. AP-42, No. 10, pp. 1386-1391, October, 1994.

[4] Yasutaka, Ogawa, and Eric, K., "Estimating the Time-Delay and Frequency Decay Parameter of Scattering Components Using a Modified MUSIC Algorithm", IEEE Trans. on Antennas and Pro., Vol.42, NO.10, October, 1994.

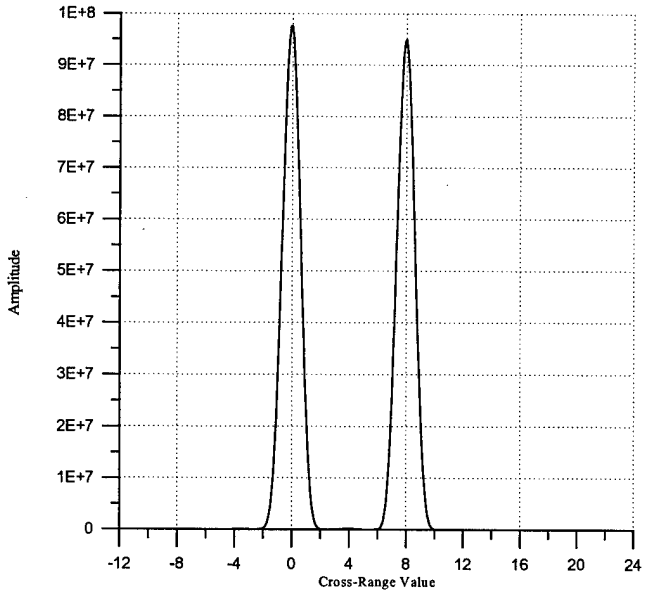

Fig.5 Multiplication technique (8-10GHz), step (0.5GHz), Ls=41cm, D=60cm, and ar=1.5.

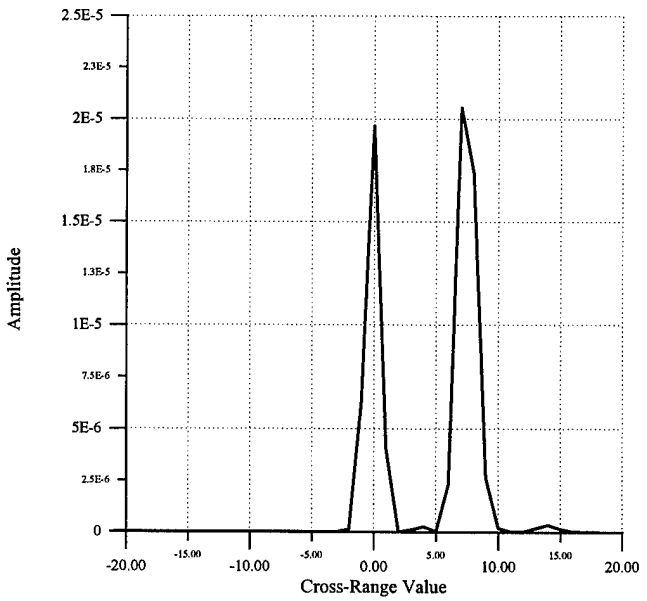

Fig.6. Image multiplications from measurements at frequencies of 7.2, 7.38, 7.44, 7.56, 7.76 & 7.82 GHz.

RECONSTRUCTION OF A HIGH-CONTRAST PENETRABLE OBJECT IN PULSED TIME DOMAIN BY USING THE GENETIC ALGORITHM

Hong-Ki Choi* , Seong-Kil Park , and Jung-Woong RA
Department of Electrical Engineering, KAIST
373-1, Kusong-dong, Yusong-gu, Taejon, 305-701, Korea

Abstract -- A three dimensional dielectric object having high relative dielectric constant of 7.0 and large size of wavelength cube is reconstructed from the scattered fields in the space-time domain when plane waves of gaussian pulse shine the object. This reconstruction is obtained from the iterative inversion method that minimizes the cost function by using the Levenberg-Marquardt algorithm and the genetic algorithm to find its global minimum, where the cost function is defined as the squared magnitude of the difference between the measured fields and the calculated fields from the assumed profile of the object. The scattered fields are calculated by the method of FDTD and measured fields used for reconstruction are assumed to have the measurement error.

1. INTRODUCTION

Three dimensional penetrable object is difficult to reconstruct since the integral equation describing the scattered field and the distribution of the medium parameters is non-linear in the sense of inversion and the limitation of the computing capability in handling the inversion of large matrix. One may linearize the integral equation to obtain the polarization and conduction currents by discretizing the penetrable object into small cells in which these currents may be taken as a constant outside of the integral and replace the integral into the summation over the total number of discretized cells and the integral of the Green function over each discretized cell[1].

In coping with the limitation of the computer capability, one may use the finite difference time domain(FDTD) method to calculated the forward scattered fields rather than using the method of moment. [2]. In the low contrast and the small penetrable objects, Born inversion,[3] Born iterative inversion,[4] and the iterative inversion[5] are used, where the iterative inversion uses the Newton type steepest descent optimization algorithms in order to find iteratively the minima of the cost function defined as the squared magnitude of the difference between the measured fields and the calculated fields from the assumed profile of the object.

For high contrast and large objects , however, the iterative inversion method with the hybrid algorithm combining the Newton type Levenberg-Marquardt algorithm(LMA) and the stochastic type simulated annealing algorithm(SAA) is shown to give the reconstruction successfully [6,7]. This is due to the property of the SAA to find the global minimum of the cost function, while LMA alone finds the local minima nearest to the starting profile of the iteration.

It is the objective of this paper to show that successful reconstruction of fairly large and high contrast three dimensional penetrable object is possible by using the FDTD method in the calculation of scattered fields and the genetic algorithm for the SAA in the hybrid algorithm of the iterative optimization of the cost function. The size of the dielectric object upto $1\lambda \times 1\lambda \times 1\lambda$ with its permittivity of $7.0\varepsilon_o$ located in the free space is reconstructed from the scattered fields at 36 points uniformly distributed in the spherical surface of its radius equals to 10λ and for incidences of two plane waves of the gaussian envelope in time , where ε_o is the permittivity of the free space and λ is the free space wavelength corresponding to the half power upper frequency of the gaussian pulse. The scattered fields in the pulsed time domain are sampled by 15 times with its interval corresponding to the width of the gaussian incident pulses. Ten percent random gaussian noise is included in the numerical simulation for the possible error in the measured fields.

2. FORMULATION AND NUMERICAL CALCULATIONS FOR THE RECONSTRUCTION

When a plane wave of gaussian pulse $\boldsymbol{E}^i$ is incident upon a three-dimensional dielectric object, the total electric field scattered from the object may be written as

$$\boldsymbol{E}(\boldsymbol{r},t) = \boldsymbol{E}^i(\boldsymbol{r},t) + \frac{1}{c^2} G(\boldsymbol{r},t) * [(\varepsilon_r(\boldsymbol{r}) - 1)\frac{\partial^2}{\partial t^2} \boldsymbol{E}(\boldsymbol{r},t)]$$

where * means the convolution, $(\boldsymbol{r}, t)$ is the space and time coordinate, G is the dyadic green's function in

0-7803-3836-7/97/$10.00 © 1997 IEEE

free space. c is the light velocity in free space, and $\varepsilon(\boldsymbol{r})$ is the distribution of relative permittivities of the object. The incident field $\boldsymbol{E}^i$ propagating in the direction $\boldsymbol{k}$ is given by the gaussian pulse of its pulse width $2W_o$

$$\boldsymbol{E}^i = \boldsymbol{z}_o e^{-(t-t_o-\frac{\boldsymbol{k}\cdot\boldsymbol{r}}{c})^2/W_o^2}$$

here $\boldsymbol{z}_o$, indicating polarization of the wave, is a unit vector along z-axis.

In the FDTD numerical method, scattered fields are calculated directly from the central difference approximations for the space and time derivatives of the Maxwell equation by discretizing the object into small Yee-cells. To save the computation time, the perfectly matched layer [8] is adopted as the absorbing boundary condition. The vector field at $(-0.75\lambda, 0, 0)$ scattered from the homogeneous dielectric cube of $1\lambda \times 1\lambda \times 1\lambda$ for the incidence of the plane wave of gaussian pulse propagating along the x-axis may be calculated by FDTD as in fig. 2 for the scattering configuration as in fig.(1). These near fields numerically calculated by FDTD in the cubic surface enclosing the scatterer may be transformed into the vector far fields via the near to far field transformation[9]. These far fields numerically calculated and transformed may be considered as the measured fields in the inversion.

For the iterative inversion, one may define the cost function f as the summation of the squared magnitudes of the difference fields as

$$f = \sum_{i=1}^{I}\sum_{j=1}^{J}\sum_{k=1}^{K}\sum_{p=1}^{2} |E_p^M(t_i, r_j, s_k, p\,; \varepsilon_n) - E_p^C(t_i, r_j, s_k, p\,; \varepsilon_n^q)|^2$$

where E_p^M and E_p^C are the measured fields and calculated electric fields from the assumed set of profiles $\{\varepsilon_n^q\}$ at the q-th iteration with p designating the two polarization dependences, t_i and r_j represent the incident plane waves (or the transmitters) and the sampled measurement points, respectively, and s_k represents the time sampling. I, J, and K represent the total number of incident waves, field points, and the time samples, respectively

One may obtain the original distribution of $\{\varepsilon_n\}$ by finding the global minimum of the cost function when the assumed set of distribution $\{\varepsilon_n^q\}$ at the q-th iteration is equal to the original distribution $\{\varepsilon_n\}$. Sufficiently large number of the data points larger than the total number of discretized cells are needed to have one global minimum[5]. Genetic algorithm is a stochastic optimization algorithm based on the survival of fitness[10] and finds the global minimum more efficiently if it is used with the LMA. The population and the chromosomes representing the possible distribution of $\{\varepsilon_n\}$ and the dielectric constants of a cell, respectively, are randomly generated in the GA and are evolved by repeated application of the selection, the cross-over, and the mutation to select the better survival according to the values of the cost functional. While LMA finds the nearest minimum of the cost function , GA searched some distribution in $\{\varepsilon_n\}$ giving the smaller functional and LMA finds the nearest minimum starting from the distribution found by GA. This process of the hybrid algorithm is repeated until the global minimum of the cost function is found, which gives the original distribution of $\{\varepsilon_n\}$

The object is divided into $4\times4\times4=64$ unknown cells by discretizing the object of $1\lambda\times1\lambda\times1\lambda$ cube into $0.25\lambda\times0.25\lambda\times0.25\lambda$ cubic cells. The forward scattered fields are numerically calculated by using FDTD method, where the object is discretized into $32\times32\times32=32,768$ cells of $\frac{1}{32}\lambda\times\frac{1}{32}\lambda\times\frac{1}{32}\lambda$ size small cubic cell. A homogeneous dielectric cube of its relative dielectric constant 7.0 is reconstructed , as in fig.3 (only 2nd layer cross-section profile is shown) , by using the iterative inversion method utilizing the hybrid algorithm combining LMA and GA. This reconstruction is obtained from the scattered fields at 36 different far field points in the sphere for 2 incidences of the gaussian pulsed plane waves, where the time varying scattered field at each field point is sampled upto 15 points by the pulse width, $2W_o$. This makes the total number of data $36\times2\times15=1080$, from which dielectric constants of 64 unknown cells are obtained.

As a possible measurement error, 10 percent gaussian noise is added in the scattered fields used for inversion in fig. 3. In dealing with the error, an additional regularization term is usually added to the cost function in eq.(3) to compromise with the ill-posedness of the inversion[4]. In this reconstruction, however, the usual ill-posedness due to the presence of noise in the scattered fields are regularized by filtering out the sampled data of small amplitudes or equivalently the spherical modes of higher order [11] without using the additional regularization terms. The reconstructed result obtained from 1,080 data and 32 population and after 12

generation in GA in fig.3 shows that the mean square error of the reconstruction of 64 cells becomes 4.9%

REFERENCES

[1] K.-S. Lee, and J.-W. Ra, 'Angular spectral inversion for reconstruction of complex permittivity profiles,' *Microwave and Optical Tech. Letter,* 1992, pp.359-361

[2] M. Moghaddam and W. C. Chew, 'Study of some practical issues in inversion with the Born iterative using time-domain data,' *IEEE Trans.,* 1993, AP-41 pp. 177-184

[3] M. Slaney, A. C. Kak, and L. E. Larsen, 'Limitation of imaging with first-order diffraction tomography,' *IEEE Trans.,* 1984, MTT-32 pp. 860-873

[4] Y. M. Wang and W. C. Chew, 'An iterative solution of the two-dimensional electromagnetic inverse scattering problem', *Int. J. Imag. Syst. and Technol.*, Vol.1, pp.100-108, 1989

[5] C.-S. Park, S.-K. Park, and J.-W. Ra 'Microwave imaging in angular spectral domain based on the improved Newton's procedure,' *Microwave and Optical Tech. Letter,* Jan. 1994, pp.28-31

[6] L.Garnero, A. Franchois, C. Pichot, and N. Joachimowicz,'Microwave imaging : complex permittivity reconstruction by simulated annealing,' *IEEE Trans.* 1991, MTT-39, pp.1801-1807

[7] C.-S. Park, S.-K. Park, and J.-W. Ra, 'Moment method and iterative reconstruction of two-dimensional complex permittivity by using effective modes with multiple sources in the presence of noise,' *Radio Science* , vol. 31, 1996, pp. 1877-1886

[8] J. P. Berenger, 'A prefectly matched layer for the absorption of the electromagnetic waves,' J. Comp. Phys., vol.114, No.1, pp.185-200,1994

[9] R.J. Luebbers, et al, "A finite-difference time-domain near zone to far zone transform", *IEEE Trans.* 1991, AP-39 pp.429-433

[10] Z. Michalewicz, 'Genetic Algorithms + Data Structure = Evolution Programs', 2nd ed. Springer Verlag, 1992

[11] C. T. Tai, 'Dyadic Green Functions in Electromagnetic theory', 2nd ed., IEEE PRESS 1994

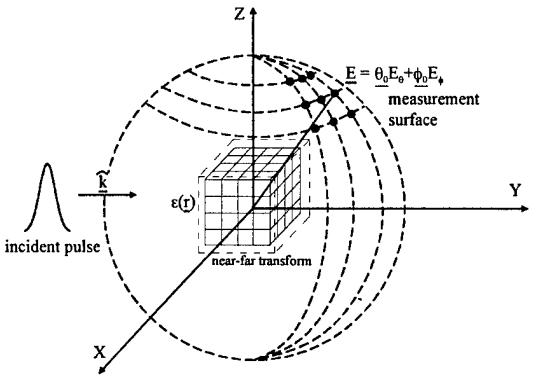

Fig.1 A cubic dielectric object and scattered far field in the spherical surface for the inversion

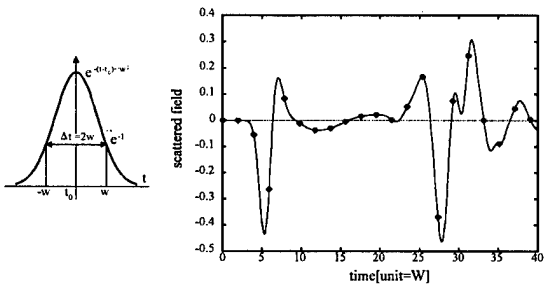

Fig.2 (a) Incident gaussian pulse (b) field calculated by FDTD at $(-0.75\lambda, 0, 0)$ and the sampling by the time interval $2W_o$

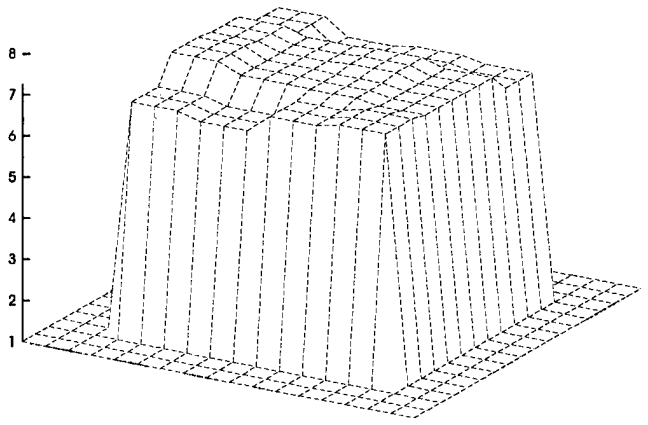

Fig.3 Reconstructed profile of a 3D cubic object with homogeneous relative dielectric constant of $\varepsilon_r = 7.0$ (only 2nd layer cross-section profile is shown), when 10 % Gaussian random noise is added in the measured field, RMS reconstruction error of 64 cells : 4.9 %

Generalized Detection Algorithm for Signals with Stochastic Parameters

Vyacheslav P. Tuzlukov

Belarusian Academy of Sciences, Institute of Engineering Cybernetics
Surganova 6, Minsk, 220012, Belarus
Tel.: 375 172 685161; Fax: 375 172 318403
E-mail: tuzluk@newman.basnet.minsk.by

Abstract -- Employment of the generalized algorithm creates a possibility to increase the noise immunity for complex detection systems of buried objects and voids more than twice in comparison with using of the optimal detection algorithms of signals with a priori known and unknown amplitude-phase structure.

1. INTRODUCTION

Suppose that a signal is a stationary stochastic process from process to process as well as additive noise, which is independent of a signal. Consider the detection problem of a signal with stochastic amplitude and random initial phase in additive noise. Noise adheres to the normal distribution law with the zero mean and finite variance. Signal can be written $a(t,\varphi_0,A) = A\times$ $\times S(t)\cos[\omega_0 t + \Psi_a(t) - \varphi_0]$ or $a(t,\varphi_0,A) = a'(t,A)\times$ $\times\cos\varphi_0 + a''(t,A)\sin\varphi_0$ where $a'(t,A) = AS(t)\times$ $\times\cos[\omega_0 t+\Psi_a(t)]$, $a''(t,A) = AS(t)\sin[\omega_0 t+\Psi_a(t)]$; ω_0 is a carrier frequency of the signal $a(t,\varphi_0,A)$; $S(t)$ is a known modulation law of the signal amplitude; $\Psi_a(t)$ is a known modulation law of the signal phase; φ_0 is a random initial signal phase, which is distributed uniformly on interval $[-\pi,\pi]$ and is not time variant on time interval $[0,T]$; A is an amplitude factor, which is a random value.

2. OPTIMAL DETECTOR

Block diagram of the optimal detector is represented in Fig.1. Effective bandwidth of the preliminary filter (PF) is equal to the bandwidth of signal frequency spectrum. Noise is a process with a constant spectral power density $N_0/2$, which is not varied in the signal frequency bandwidth. Process $X(t)$ at the PF output has a form $X(t) = a_1(t,\varphi_0,A)+\xi(t)$ where $a_1(t,\varphi_0,A)$ is a signal at the PF output. Process $\xi(t)$ is noise at the PF output $\xi(t) = \xi_1(t)\cos[\omega_n t + v(t)]$ where ω_n is a medium frequency of noise; $\xi_1(t)$ is a stochastic amplitude of noise; $v(t)$ is a random phase of noise. Signal model is (Fig.1) $a^*_{1,2}(t+\tau) = S^*(t+\tau)^{\cos}_{\sin}[\omega_0(t+$ $+\tau)+\Psi_a(t+\tau)]$. Under conditions $\tau = 0$ and $S(t) = S^*(t)$ process at the summator output is $Z^2_{op}(t) =$ $= \frac{1}{4}\int\limits_0^T S^2(t)dt\int\limits_0^T A^2S^2(t)dt+\frac{1}{2}\int\limits_0^T S^2(t)dt\int\limits_0^T AS^*(t)\xi_1(t)\times$ $\times\cos[\Psi_a(t)-v(t)-\varphi_0]dt+\frac{1}{4}\left\{\int\limits_0^T S^*(t)\xi_1(t)dt\right\}^2$.

3. GENERALIZED DETECTOR

According to the generalized signal detection algorithm [1] it is necessary to produce a reference sample for the generation of jointly sufficient statistics of the mean and variance of the likelihood function ratio. It is known a priori that "no" signal in a reference sample. For this purpose the additional filter (AF) is formed in a parallel way to the PF. Amplitude-frequency response of the AF is analogous on all parameters to the PF amplitude-frequency response but it is detuned on resonance frequency relative to the PF. A detuning value must be more than an effective bandwidth of signal frequency spectrum so much that processes at the PF and AF outputs will be uncorrelated. If detuning value is more than $3-4\Delta F_a$ processes at the PF and AF outputs are not correlated practically [2], where ΔF_a is an effective bandwidth of signal frequency spectrum. For the generation of sufficient statistics of the variance it is necessary to create an autocorrelation channel. These actions allow to carry out a compensation between the correlation channel noise component and autocorrelation channel random component in statistic sense. Process $\eta(t) = \xi_2(t)\cos[\omega_n' t + v'(t)]$ is formed at the AF output whether "yes" or "no" signal in the input stochastic process $W(t)$ by virtue of choosing of the AF response and has a stochastic envelope $\xi_2(t)$ and random phase $v'(t)$, ω_n' is a medium frequency of noise $\eta(t)$. Processes $\xi(t)$ and $\eta(t)$ are uncorrelated since the PF and AF have nonoverlapping amplitude-frequency responses.

Block diagram of the generalized detector is represented in Fig.2. Generalized detector contains the channel for a generation of sufficient statistics of the

0-7803-3836-7/97/$10.00 © 1997 IEEE

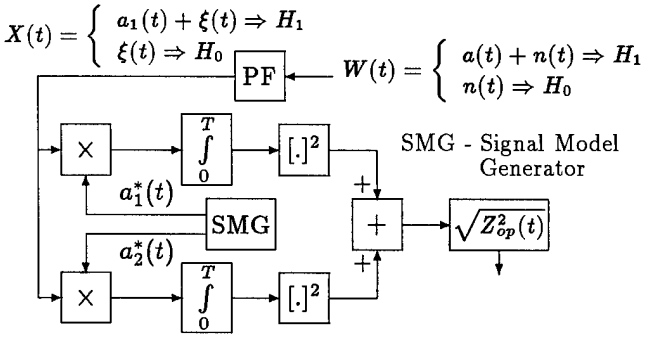

Fig.1. Optimal detector.

likelihood function variance: the PF and AF, delay blocks 1, 2 and 5; multipliers 3, 4 and 7; summator 1; integrator 3; amplifier " > ". Compensating channel consists of summators 3 and 4 and allows to compensate the correlation channel noise component and autocorrelation channel random component in statistical sense. Taking into consideration that signal model is matched with signal at the PF output $S(t) = S^*(t)$ and reasoning that $\tau = 0$ process at output of the summator 4 at "yes" signal in the process $W(t)$ is $Z_g^2(t) = \frac{1}{4}E_a \int_0^T A^2(t)S^2(t)dt - \frac{1}{4}\left\{\int_0^T [\xi_1^2(t) - \xi_2^2(t)]dt\right\}^2$.

Generalized detector increases signal-to-noise ratio in comparison with the optimal detector. Pursuance of research allows definite the following conclusions. There is a correlation function between the correlation channel noise component and autocorrelation channel random component. If the amplitude factor of signal is not a function of time on time interval $[0, T]$ then a compensation result is carried out by averaging on a set of processes. If the amplitude factor of signal is a function of time on the time interval $[0, T]$ then a generation of jointly sufficient statistics of the mean and variance of the likelihood function is possible within the boundaries of the time interval $[0, T]$ without averaging on a set of processes. Experimental detection characteristics are represented in Fig.3.

4. STABILIZATION OF DETECTION CHARACTERISTICS

In order for detection characteristics of the generalized signal detection algorithm to bring closely to potentially achieved it is necessary that signal should be long-term and broad-bandwidth at time. For this purpose the condition $T\beta \gg 1$ should be fulfilled where $T\beta$ is a signal base. The fulfilment of this condition is made possible if the generalized detector guarantees a constant signal-to-noise at its output at the same one

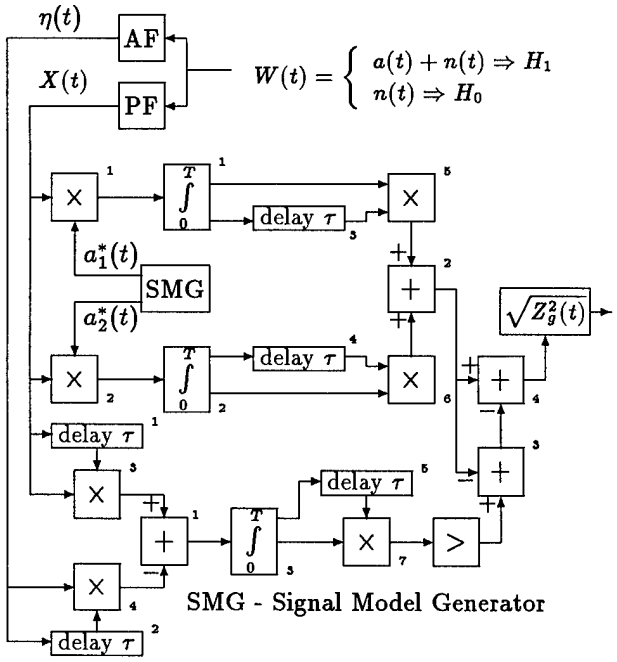

Fig.2. Generalized detector.

at the detector input independent of signal stochastic parameters. If we will apply severe constraints to signals $T\beta \gg 1$ then stabilization of detection characteristics for the generalized detector may be carried out by measurements of signal stochastic parameters, such, for example, as phase and amplitude in particular.

The generalized detector for deterministic signals is considered as a base. Consider the hypothesis H_1. Signal model is $a^*(t) = A^*S^*(t)\cos[\omega_0(t-\tau) + \Psi_a^*(t)]$ as amplitude and phase modulation laws of signal are known. Because of this, one would fulfil the condition $S^*(t) = S(t)$ and $\Psi_a^*(t) = \Psi_a(t)$. We can be assured that it is necessary to synthesize a receiver solving the detection problem of signals with stochastic amplitude and random initial phase and having the amplitude and phase tracking systems. Block diagram of the such generalized detector with tracking systems is represented in Fig.4. Under the conditions $\omega_0\tau = \varphi_0$ and $A = A^*$ the process at the detector output is $Z_g^{out}(t) = \frac{1}{2}A^2 \int_0^T S^2(t)dt + \frac{1}{2}\int_0^T [\xi_2^2(t) - \xi_1^2(t)]dt$. By this means, the end result coincides with results for deterministic signal with a precision of the coefficient A^2 [3].

Obtained results indicate that we will have a good chance of using the generalized detector for deterministic signals under solving the detection problems for

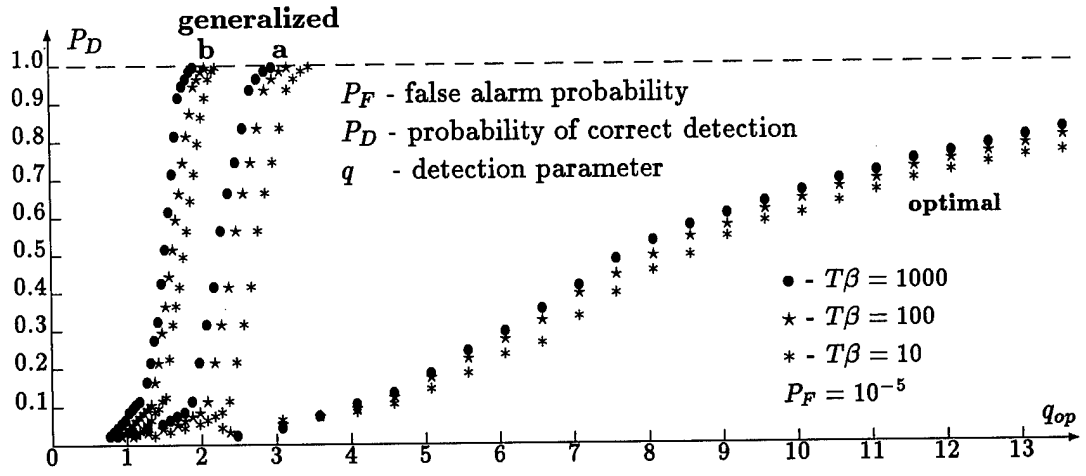

Fig.3. Detection characteristics (a - without tracking system, b - with tracking system).

signals with stochastic parameters. Proceed as follows: to create the amplitude and phase tracking systems which control corresponding parameters of signal model generated by the SMG. In principle the creation of the tracking systems is made possible using signal feature to the effect that product of echo duration and effective spectrum bandwidth must be vastly more 1 or signal base $T\beta \gg 1$. Amplitude and phase tracking systems may be variously types. One of variants of the tracking systems with the generalized detector is represented in Fig.4. Experimental detection characteristics of the generalized detector with the tracking systems are represented in Fig.3. Radar systems using the generalized detector with tracking systems have a detection range of buried objects and voids which is more than 1.7 in comparison with analogous systems using optimal detectors at the same P_D.

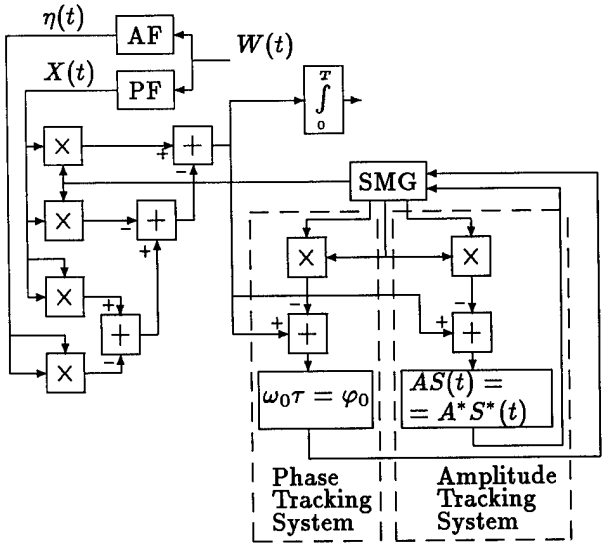

Fig.4.Generalized detector with tracking systems.

5. CONCLUSIONS

Employment of the generalized signal detection algorithm creates a possibility of noise immunity increasing in comparison with using of optimal detectors. Detection characteristics of the optimal and generalized detectors have been improved with increase in the signal base $T\beta$. Under the same conditions at inputs of the optimal and generalized detectors the detection characteristics of the latter offer the much more slope as a function of detection parameter. Displacement of detection characteristics for the generalized detector with increase in signal base $T\beta$ has the lesser dispersion than for the optimal one. Detection characteristics show that the generalized detector is less sensitive to variation of signal base $T\beta$. Boundary domain where the optimal detector is better than the generalized one is contained in nonoperative range ($P_D < 0.1$). Generalized detector with tracking systems allows: a)to stabilize detection characteristics of signals with stochastic parameters and to bring closely theirs to potentially achieved; b)to be away with practice realization of detectors with quadrature channels at the signal detection with stochastic parameters.

REFERENCES

[1] V. Tuzlukov, Signal Detection in Noise: A New Approach, IEC, Minsk, 1997.

[2] V. Tuzlukov, "Interference Compensation in Signal Detection for a Signal of Arbitrary Amplitude and Initial Phase," Telecom. and Radio Eng. 1989, vol.44, No 10, pp.131-132.

[3] V. Tuzlukov, "Signal-to-Noise Improvement by Employment of Generalized Signal Detection Algorithm," Proc. SPIE's Symp., 1995, vol.2496, pp.811-822.

Applications of Ground Penetrating Radar Forward Calculus with Finite Offset for Point Scattering

Huilian Wang
Dept. of Applied Geophysics
China University of Geosciences
29 Chengfu Road, Beijing ,100083, China
Tel.: 86-10-62327461-386

ABSTRACT--This paper introduced some results of the Ground Penetrating Radar(GPR) calculus for point scattering. The pattern confirmed by modeling test in a water pool and some practical results verified pretty well on the engineering spot also presented in this work.

INTRODUCTION

It is a general fact that so long as inhomogeneity exists within the Hertz-wave there is always wave scattering. Diffuse scattering or diffused reflection stems out of the finite interface or the small part of object that constitutes interfere or anomaly in field work. GPR worker should learn its main pattern so that he may interpret GPR data correctly. The calculus of scattering for a geometry point under the condition of GPR measurement may provide such a regular pattern. This paper introduced the results of the calculus operated under the following conditions: placing the single point within a half homogeneous space with the reflectance of 1 at a certain depth and value of wave velocity; keeping two antennas with finite constant separation and moving them in a straight line along the ground.

MAIN FEATURE

The calculus result showed that the arrival wave formed hyperbolic events(Fig.1). Its amplitude influenced by the absorptance of the surrounded medium would be weakened along with the increase of distance from the antenna with unalterable events. Three factors would effect the event form. They are the physical parameters of the medium, the buried depth and the antenna separation.

As other physical wave method, the wave velocity in medium can represent the physical parameters. The less the value of velocity is, the sharper the event will be. Also, the similar feature goes with the depth of the buried point. It will make the anomaly more obvious as the antenna separation becomes shorter.

Theoretically, a small spheroid may be treated as a point and it will also be right while the bigger spheroid is buried deeper. Owing to the receiver of GPR does not notably respond the field come from the lateral part of the body, the small 3D targets with long range such as cylinder or narrow plate may also be approximately regarded as

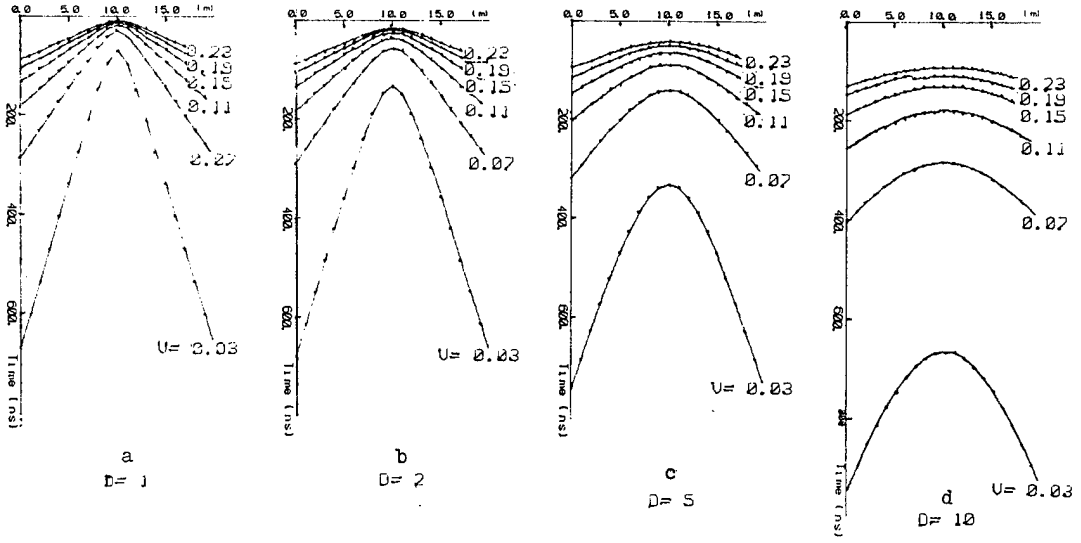

Fig.1 Theoretical events of GPR for a buried point

D- depth of point; V- velocity of medium

0-7803-3836-7/97/$10.00 © 1997 IEEE

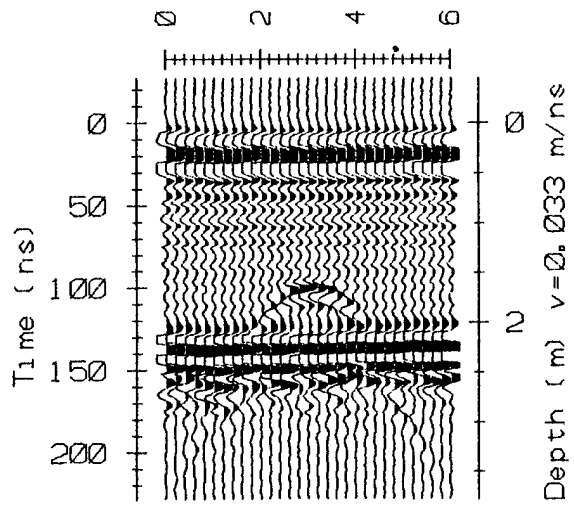

Fig.2a GPR map of modeling test - volley ball

a point. Thus, the hyperbolic events may stand for the main anomaly of the spheroid, cylinder and plate, and represent the cave with equiaxis or equiform object, the buried pipe, and the local or partial geological interface underground. And further, the event feature of a point may be related with the diffraction property of the tip or joint of the target.

SIMULATION WORK

A systematic simulation test has been made in a swimming pool with the depth of 2m[1]. The velocity value of the pool water was 0.033m/ns. The centre frequency was 100MHz, and the antenna separation was 0.3m. The pattern mentioned above was confirmed by the test work. The feature of these patterns all focused on a hyperbolic event but a stronger reflecting for the metal one, weaker form for the nonmetal, longer leaf at both sides of the cylinder, shorter at the spheroid side, gentler center for the plate with diffraction form at both ends and multi-reflections on its map. Fig.2 shows the GPR map of a volley ball with diameter of 0.11m and buried depth of 0.85m(Fig.2a) and two separated plates regarded as a small horizontal normal fault with throw of 0.27m(Fig.2b).

FIELD EXAMPLES

Fig.3 presents three field examples. One is the buried power cable location in Guangchou(Fig.3a). At the depth of 0.75m from the GPR map one can identify two anomalies that related two buried bunches of the cable. The other is a GPR map of the karst cave detection in Nangjing(Fig.3b). From the map, we can find many hyperbolic anomalies. The third example is a hidden danger inspection of the concrete foundation of a floodgate. There are some broken plates along the section.

CONCLUSION

The modeling test and the GPR practice on the engineering site[2] showed that the regularity of the calculus can supply the simple basis for discerning or

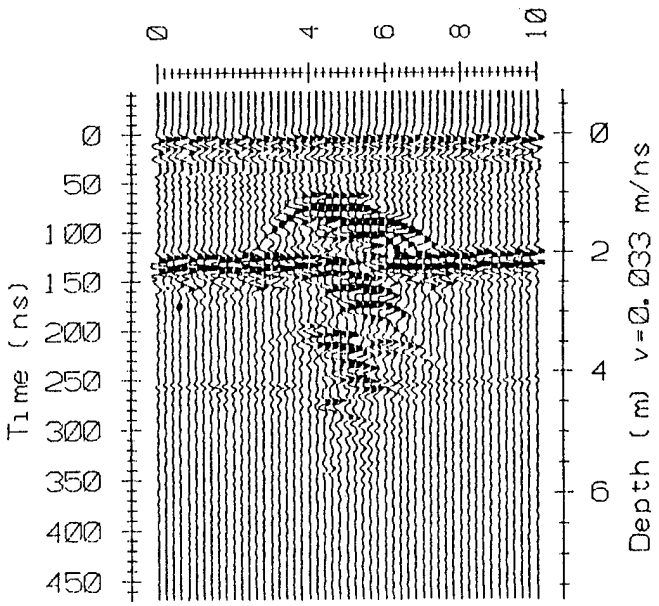

Fig.2b GPR map of modeling test - two plates

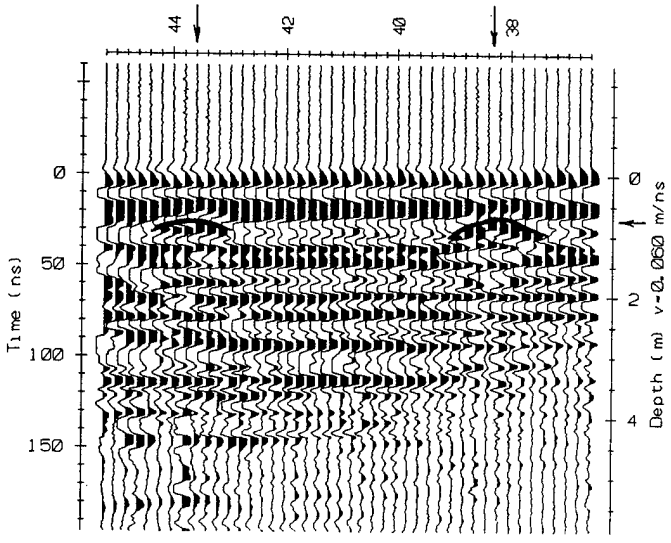

Fig.3a GPR section of buried cable

distinguishing the useful buried object anomaly from the GPR measurement section relating to the most of shallow pipes, cables caves, and small interfaces underground, and also the useless interference such as inhomogeneity within the surrounding medium.

ACKNOWLEDGMENT

The author would like to thank the GPR group of China University of Geosciences for the data support. The manuscript was expertly typed by Mr.Zhang Peng.

REFERENCES

[1] H.Wang, "Ground Penetrating Radar Studies in Physical Analogue", Earth Science--Journal of China University of Geosciences, Vol.18, No.3, pp.266-284, May 1993(in Chinese).

[2] H.Wang, and P.Zhang, " New Applications of GPR in Some China Key Engineering Projects", Proceedings of the 6th International Conference on Ground Penetrating Radar, pp.201-206, September 1996, Japan.

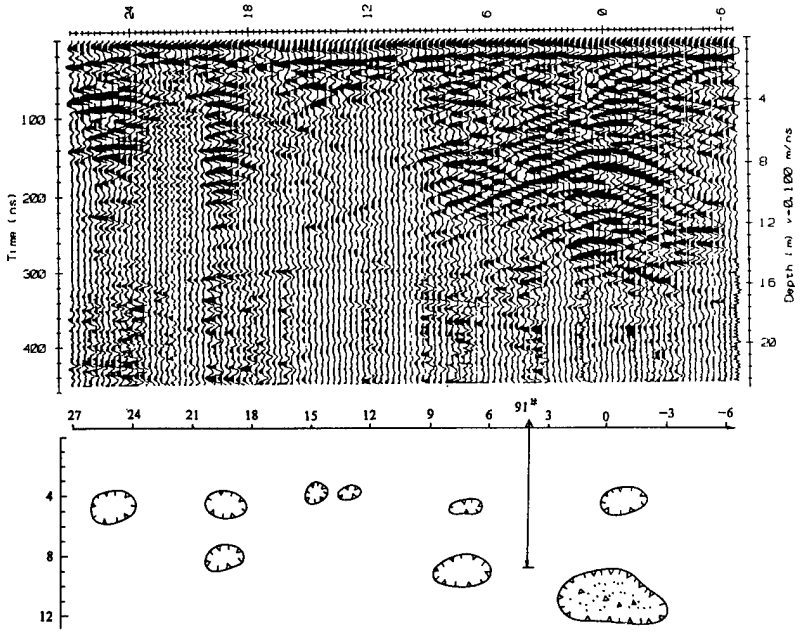

Fig.3b GPR map of karst cave probing

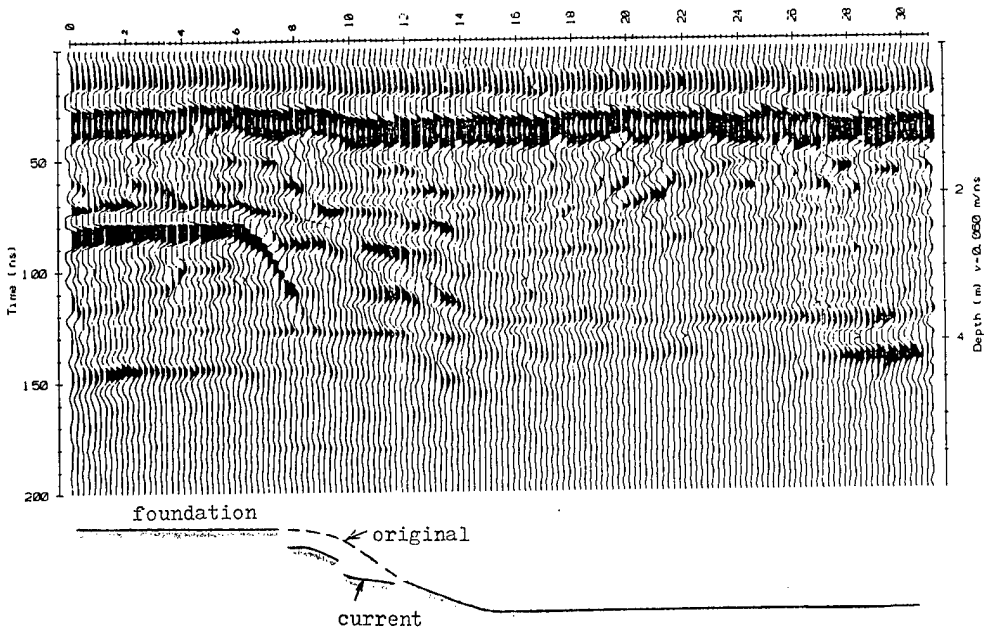

Fig.3c GPR inspection of floodgate

Derivative Seismic Processing Method for GPR Data

Yu Haizhong Ying Xiaojian
Shenzhen Dasheng Advanced Science & Technique Engineering Co.,Ltd.
A-12-10 of Zhongshen Garden Building , Caitian South Road, Shenzhen , 518026, P.R.China
Tel:+86755-3378301 Fax:+86755-3378300 E-Mail:dasheng@nenpub.szptt.net.cn

Abstract--Ground-penetrating radar(GPR) is a newly developed geophysics method. It belongs to one of the electromagnetic methods. In a broad sense, it is also a remote sensing technique, but the processing method for GPR data is quite different with the one for remote sensing data. The processing method is the key to develop a technique, so it is a urgent task to develop GPR processing method at current time. Basing on the close similarity between ground-penetrating radar and reflection seismic method, this paper will present the derivative seismic processing methods for GPR Data, including the CMP processing method, two dimension filtering, migrating and simulating techniques. The principle and concrete algorithm of these methods will be given in this paper. Demonstrated with some successful applications, this paper tells us the derivative seismic processing methods are very effective for GPR data. It also tells us GPR is a very convenient, rapid, precise way to get underground information.

INTRODUCTION

Ground-probing radar is a new technique developed recent years , and the ability of GPR to provide high-resolution information on near-surface earth properties and structure has been documented in a wide variety of applications [1]. The hardware of GPR develops very fast as well as the development of microelectronics technique, but the development of software is relative slow . More research about GPR software is needed . Analysis of the theory of electromagnetic and elastic body[2] reveals a number of similarities between radar and reflect seismic [3]. The dynamic behaviors of them are different (with regard to amplitude attenuation and dispersion), but the kinematic behaviors of them (such as pulse propagation times) are same . Just the kinematic similarities between radar and seismic wave propagation make it possible that many techniques have been extensively developed for processing of reflect seismic data can be directly or indirectly applied to radar data . Some techniques have been used to do so , such as reverse-time migration [3], predictive deconvolution [4], and a wide-aperture GPR data set were input directly into standard seismic processing sequence (filtering , static corrections , common-midpoint gathering , velocity analysis , normal- and dip-moveout corrections , stacking and depth migration)[1].

In this paper, we will introduce another derivative seismic processing methods to GPR, including CMP processing, two dimension filtering, migrating and simulating techniques.

THEORY AND METHODS

CMP Processing

In seismic prospecting, the original section recorded in field is common midpoint profile(CMP). It means all traces in this profile reflect the same point underground. Use the dynamic correction method, we can sum up all these traces to one stacked trace. In dynamic correction, velocity is a very important parameter. If the velocity value equal the real velocity of the media, the stacked energy will be large, if not, it will be low. Thus, in GPR prospecting, we can use this method to evaluate the velocity of electromagnetic wave in different subsurface media.

Two Dimension Filtering

Two dimension FK filtering is a process to remove unwanted frequency-wavenumber components from data by simple expedient of multiplying the FK amplitude spectrum by a suitable function . The simple diagram of FK filtering show in Figure 1 .

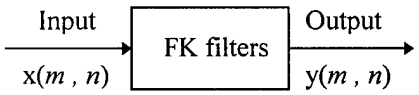

Figure1. FK filtering diagram

FK filtering is performed in FK domain . Firstly we should know about the FK amplitude spectrum of radar wave and disturbing wave . Then specify the pass zone and stop zone in FK domain . Various FK filters are designed for different objective. Such as low-pass filters , high-pass filters , zone-pass filters , dip-reject FK filters . But the design of FK filter is not very easy . There exist many difficulties , and the main problems are due to spatial aliasing , spectral overlap , windowing effects , the presence of multiples and the generally inadequate displays of FK spectra . It is harmful to radar data if the FK filter is poorly designed . Despite

0-7803-3836-7/97/$10.00 © 1997 IEEE

these difficulties , it is still possible to enhance data quality with the use of some relatively simple FK filters .

FK Migrating

A radar section is not a true representation of the geological structure along a survey line . The geometry involved in collecting make dipping reflectors appear less steeply dipping , and point reflector appears to a hyperbolic curve on the radar profile . The objective of migration is to correct dips of the geological bedding planes and to remove diffraction hyperbolas . FK migration is a method whereby the equation is solved in the frequency wavenumber domain . It was first introduced to seismic data processing by Stolt in 1978 . Then Chun and Jacwitz made a incisive analysis of the principle of FK migration in 1981 .

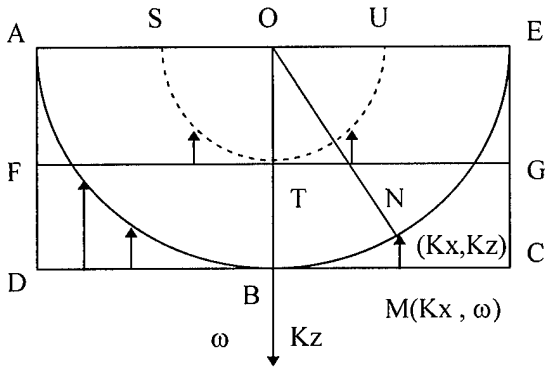

Figure 2. The Procedure of FK migrating

Figure 2 shows the complete frequency wavenumber domain mapping process . All the sample values on line FG are moved back to the semicircle STU . Similarly , all samples on line DE are moved back to semicircle ABC . It means point M in (Kx , ω) space moved to point N in (Kx , Kz) space . Thus , we can derive the equation that describes the frequency wavenumber domain mapping process as :

$$F'(Kx , Kz) = Kz \cdot F(Kx, (Kx^2+Kz^2)^{1/2}) / (Kx^2+Kz^2)^{1/2} \quad (1)$$

where F(Kx , Kz) is the 2D Fourier Transform of the unmigrated radar section . The factor $(Kx^2+Kz^2)^{1/2}$ is the expression for radius of a circle in (Kx , Kz) space . It also tell us that each sample must be weighted when it is moved and that the weighting depends on the radius vector and its projection on the vertical axis . For a point N in (Kx , Kz) space , It maybe has no sample value in the corresponding point M in (Kx , ω) space . Interpolation in the fourier-transform domain is needed for FK migration . There are two interpolation methods developed by Z.H.He and G.H.F.Gardner[5] . Linear interpolation is defined as :

$$C = w_1C_1 + w_2C_2 \quad (2)$$

Geometric interpolation is defined as :

$$\ln C = w_1 \ln C_1 + w_2 \ln C_2 \quad (3)$$

Where $w_1=1-x$, $w_2=x$, and x is the fractional distance from C_1 to C_2 , as shown in Figure 3 .

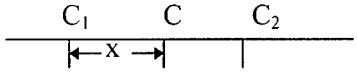

Figure 3 . Interpolation in Fourier-transform domain

FK Simulating

Just as we can perform migration with a mapping in the frequency wavenumber domain , then so can we perform the inverse procedure , we call it FK simulating. The details of FK simulating are similar to FK migration but essentially the mapping is in the opposite direction . Just as shown on Figure 2 , the mapping process is moving all the sample values in semicircle ABC to line DE . In other words , point N in (Kx , Kz) space should move back to point M in (Kx , ω) space . The equation that describes the FK simulating is :

$$F'(Kx , \omega) = (\omega^2-Kx^2)^{1/2} \cdot F(Kx, (\omega^2-Kx^2)^{1/2}) / \omega^2 \quad (4)$$

Figure 4 shows the procedure of FK modeling .

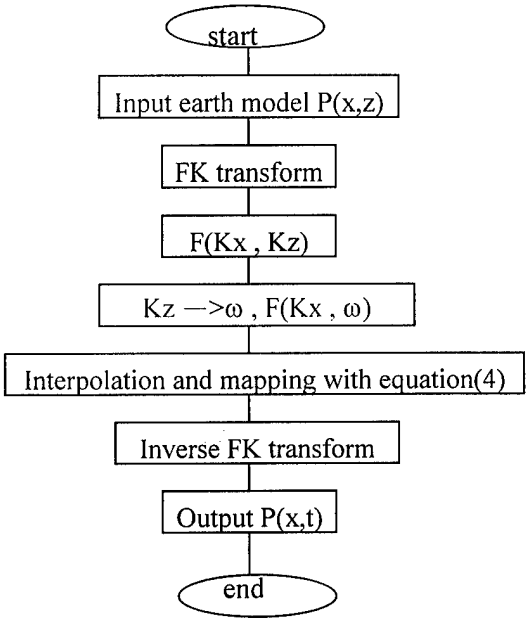

Figure 4. The diagram of FK modeling

APPLICATIONS

As an example, a radar section collected when

detecting buried pipes and cables in Shenzhen is displayed in figure 5. The field site locates at Shennan Road in Shenzhen.

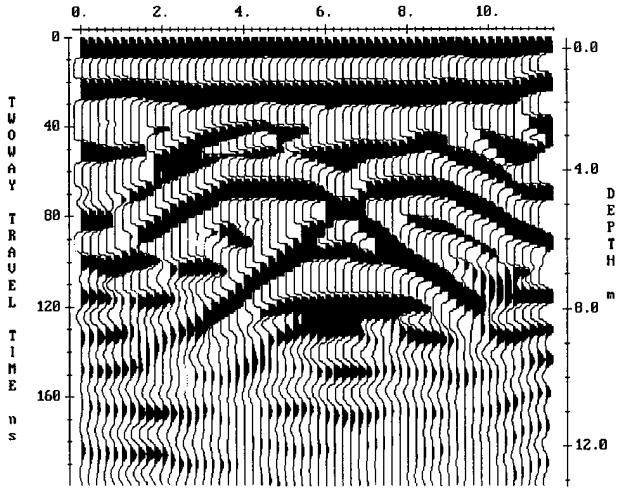

Figure 5. The radar section collected when detecting buried pipes and cables.

The section was collected in the direction perpendicular to the axis of the road. The pulse EKKO IV radar system was used. The center frequencies of antennae are 200 MHz, and the data were acquired at 0.2m intervals along the prospecting line. The distance between two antennae were 0.6m. In this section, we can see two diffraction waves. We can not sure whether they were formed by pipes or other reflectors, for example syncline formations. Therefore, the FK migration technique described above are implemented for determining the radar anomalies. Figure 6 shows the result.

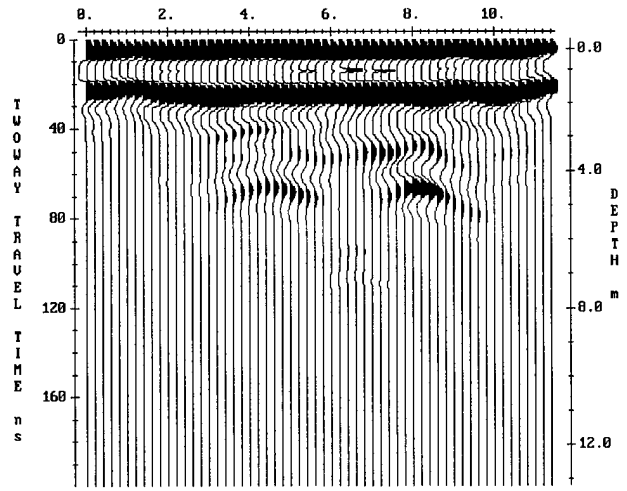

Figure 6 .The migrated radar section with the FK migration technique.

In the migrated radar section, the diffraction waves were moved back to its' original position, and two short arc events appear. This means two pipes are buried under ground, but not a syncline formation.

CONCLUSIONS

This paper introduced some derivative seismic processing techniques that widely applied in seismic data processing to GPR data processing. It indicates that some successful theory and methods in seismic data processing not only can be directly or indirectly applied in GPR data processing, but also can acquire perfect effects.

ACKNOWLEDGMENTS

The research leading to this paper was supported by Shenzhen Dasheng Advanced Science & Technique Engineering Co.,Ltd. and China University of Geosciences.

REFERENCES

[1]Elizabeth Fisher, George A.McMechan, A.Peter Annan,1992a. Acquisition and processing of wide-aperture ground-penetrating radar data. Geophysics, Vol.17, No.3(March 1992), pp.495-504.

[2]Szaraniec, E.,1976. Fundamental functions for horizontally stratified earth. Geophys. Prosp., Vol.24, pp.528-548.

[3]Elizabeth Fisher, George A.McMechan, A.Peter Annan, and Steve W.Cosway, 1992b. Examples of reverse-time migration of single-channel ground-penetrating radar profiles. Geophysics, Vol.57., No.4(April 1992), pp.577-586.

[4]P.T., LaFleche, J.P., Todoeschuck, O.G., Jensen, and A.S., Judge, 1991. Analysis of ground-probing radar data: predictive deconvolution. Can. Geotech. J., Vol.28, pp.134-139.

[5]Z.H., He and G.H.F., Gardner, 1985. Interpolation in the Fourier-Transform Domain with Applications to FK Migration. Advances in Geophysics Data Processing, Vol.2, pp.119-142.

IGARSS'97

1997 International Geoscience and Remote Sensing Symposium

03-08 August 1997

Singapore International Convention & Exhibition Centre

Technical Program

Interactive Area 9: Detection and Monitoring of Ships and Ocean Pollution

SHIP AND SHIP WAKE DETECTION IN THE ERS SAR IMAGERY USING COMPUTER-BASED ALGORITHM

I-I Lin, Leong Keong Kwoh, Yuan-Chung Lin, and Victor Khoo
Centre for Remote Imaging, Sensing and Processing (CRISP),
Faculty of Science, National University of Singapore,
Lower Kent Ridge Road, Singapore 119260,
Tel: 65-7727908 Fax: 65-7757717 Email: crslinii@nus.sg

ABSTRACT

A computer-based algorithm for ship and ship wake detection in the SAR imagery is being developed to monitor ship traffic near Singapore waters. This paper presents current progress made on the algorithm. In particular, issues on the elimination of false targets are addressed. The Morphological filter, half Radon (Hough) transform, and other wake criterion tests are applied to strengthen the detecting capability.

1. INTRODUCTION

Monitoring of ship traffic and routing is of operational importance in Singapore, as it is one of the busiest ports in the world. Since ship monitoring is a routine exercise, a computer-based algorithm is being developed in CRISP (Centre for Remote Imaging, Sensing and Processing), National University of Singapore. The theoretical consideration and the basic structure of the initial algorithm are described in Lin and Khoo (1997). This paper presents modifications made on the initial algorithm.

2. DETECTION ALGORITHM

The structure of the current algorithm is illustrated in figure 1. Different procedures are discussed accordingly in subsequent sections.

3. PRE-DETECTION PROCEDURE

As the aimed detection is for operational purpose, the algorithm is designed to take the ERS SAR PRI images as input. A standard PRI image consists of 8000 pixel by 8200 pixel and the pixel size is 12.5 m. A PRI scene is thus equivalent to 100 km by 102.5 km in physical dimension. In the pre-detection procedure, each PRI scene is geographical registered and the land regions are masked out. To efficiently process a PRI image, it is desirable to divide the original PRI into several small working windows to work on because each PRI file size takes around 130 mb. In this work, the size of the working window is chosen to be 500 pixel square. In order to avoid ship and wake targets being partially cut off at the working window boundary, each working window is overlapped with the neighbour window by 30 pixel in both range and azimuth direction. For each working window, the pixel intensity is calibrated to the Normalised Radar Cross Section (NRCS) so that subsequent procedures can be standarised and applicable to different types of SAR images, e.g., ERS-1, ERS-2, and RADARSAT.

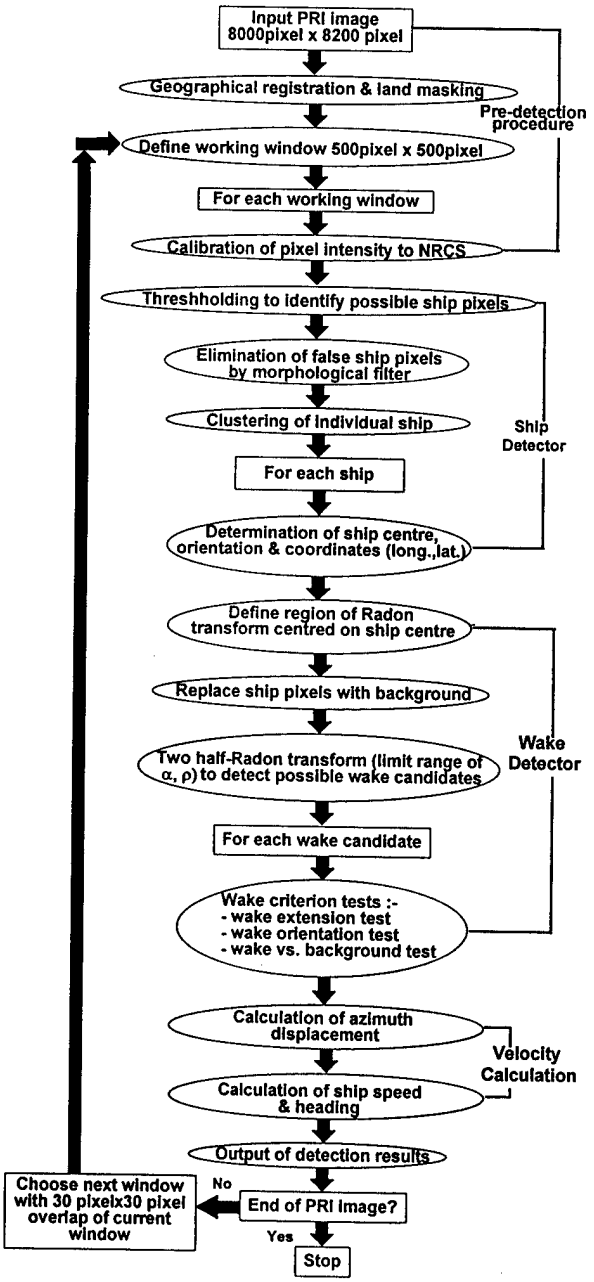

Figure 1: Flowchart of the current algorithm.

0-7803-3836-7/97/$10.00 © 1997 IEEE

4. SHIP DETECTOR

The Ship detector (figure 1) first uses a threshold to identify possible ship pixels since ships are of much higher NRCS than the background. Figure 2.a illustrate the situation. As can be observed in figure 2.a, thresholding does not exclude some false ship pixels since these pixels may also be of high NRCS.

The Morphological filter (Baxes, 1994) is applied to eliminate these false ship pixels. The Morphological filter is a logical filter which pertains to the structure and shape of objects. It has two basic operations, erosion and dilation. The erosion operation is incorporated in the algorithm. The filter is a 3 by 3 moving window. Each image pixel is examined by placing in the filter centre. The filter than examines the 8 neighbouring pixels. If more than 3 neighbouring pixels are possible ship pixels, the centre pixel is considered as a true ship pixel. This operation effectively remove singular false ship pixels due to speckle or other oceanic phenomena. The result is illustrated in figure 2.b. After the erosion operation, ship pixels are clustered into individual ships using neighbour clustering criterion. For each ship, the ship orientation is determined by an improved least square regression where errors are minimised in both axes.

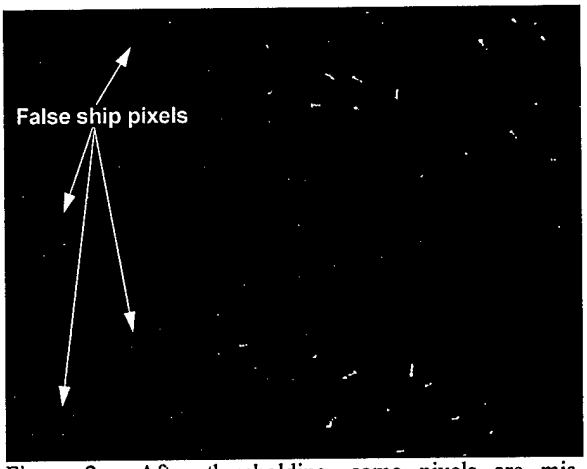

Figure 2.a: After thresholding, some pixels are mis-identified as ship pixels.

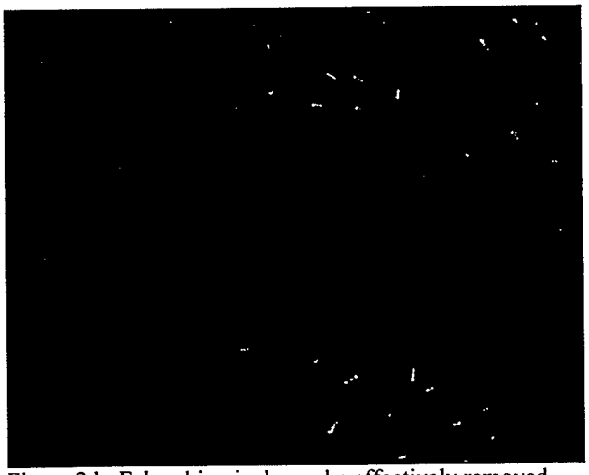

Figure 2.b: False ship pixels can be effectively removed by the Morphological erosion.

5. WAKE DETECTOR

The wake detector comprises two main portions, first the Radon (Hough) transform (Copeland et al, 1995; Lin and Khoo, 1997) and second the wake criterion tests. For each ship, a Radon region (typically 120 pixel square) centred at the ship centre is defined for wake detection. Ship pixels are replaced by the mean background NRCS so as to avoid ships being mis-identified as wakes. Any straight line in the x-y image plane can be defined as $\rho = x\cos\alpha + y\sin\alpha$. The Radon transform can (Copeland et al, 1995) thus be defined as

$$g(\alpha,\rho) = R\{f\} =$$

$$\iint_D f(x,y)\delta(\rho - x\cos\alpha - y\sin\alpha)dydx$$

Where D: the Radon region being examined, f(x,y): image DN at position (x, y), δ: Dirac delta function, ρ: length of the normal from o to the straight line, α: angle between normal and x-axis.

Details regarding the Radon transform is given in Lin and Khoo (1997). In the research, we propose to apply two half Radon transforms instead of one full transform. The Radon region is divided into two sub regions, the left and the right. The left sub region covers the left half of the original Radon region while the right sub region covers the other half. Radon transform is then applied to each half of the region. This half transform ensures that possible wake candidates are detected only at the two ends of the ship since wakes should locate at either end of the ship only. After the two half transforms, two sets (one for each side) of possible wake candidates (corresponding with peak and trough values of the transform) are located.

As wakes have much weaker signatures than ships, very often the detected wake candidates are false alarms from the background oceanic features. A set of wake criterion tests are imposed to reject the false wakes. For each possible wake candidate, three tests, the wake extension test, the wake orientation test, and the wake versus background test are imposed.

The wake extension test compares wake candidates from the two half transforms. Since wakes are characterised by ρ (normal length from the origin to the wake) and α (angle between the wake normal and the x-axis) (Lin and Khoo, 1997), if two wakes from both sides are of the same ρ and α, these two wakes are considered as one extended wake. As mentioned, since wake should not exceed its ship, the extended wakes are rejected.

The wake orientation test compares the wake orientation (ϕ_wake, where ϕ_wake=α-90°) with the ship orientation (ϕ_ship) (Lin and Khoo, 1997) . If $0 \le |\phi$ _wake-ϕ_ship$| <$ 5°, the wake is identified as a turbulent wake. If $5° \le |\phi$ _wake-ϕ_ship$| \le 10°$, the wake is identified as a narrow V wake. If $18° \le |\phi$ _wake-ϕ_ship$| \le 22°$, the wake is identified as a Kelvin wake (Wahl et al, 1993; Eldhuset, 1996). If ϕ_wake falls outside the above effective

domains, the wake is considered to be a false alarm and is rejected.

Finally, the wake versus background test is applied. The NRCS of the detected wake is compared with the mean background NRCS to determine whether the wake is bright or dark against the background. By combining the above mention tests, different wake types can be determined. For example, A turbulent wake can be determined from the wake orientation test while wake versus background test identifies whether this is a bright turbulent or dark turbulent wake. Figures 3-5 illustrate some results of detecting different wake types. Under extreme sea states, however, the detection algorithm may still perform unfavourably. An example is shown in figure 6 where the background sea was extremely rough and the high variability in the background often hinders the detection.

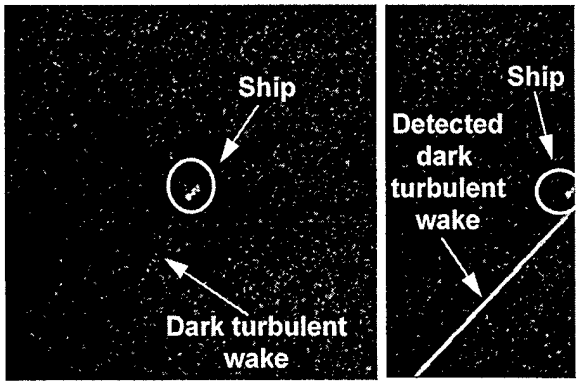

Figure 3: The detection of a dark turbulent wake. Left: the original Radon region; right: the wake is detected in the left Radon region.

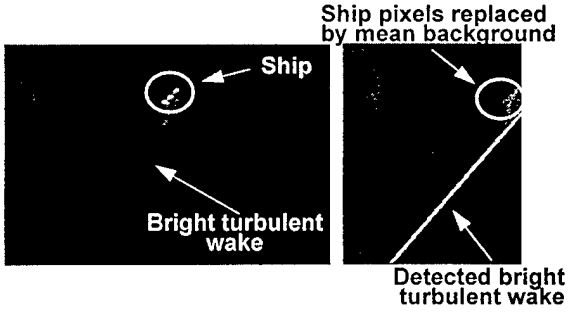

Figure 4: The detection of a bright turbulent wake. Left: the original Radon region; right: the wake is detected in the left Radon region.

6. CONCLUSION AND FUTURE WORK

A modified version of the CRISP ship detection algorithm is described. Issues regarding false target detection are addressed. It is found that accurate wake detection is much more difficult than the ship detection as wake signatures are often weak. Several wake criterion tests are necessary to reject various types of false wakes. Under rough sea states, the detection algorithm may not perform successfully. Future work is required to enhance the detection ability under rough conditions.

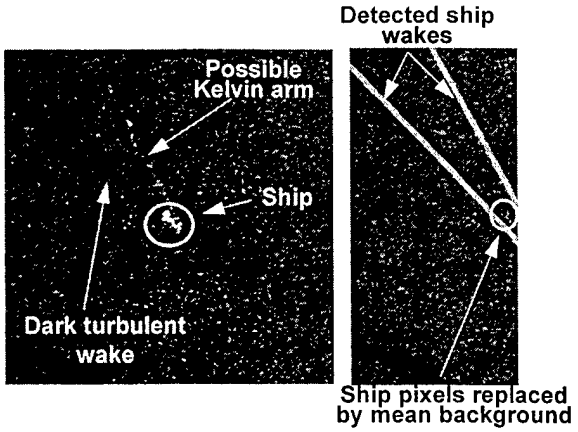

Figure 5: The detection of a dark turbulent wake and a bright Kelvin arm. Left: the original Radon region; right: the wakes are detected in the left Radon region.

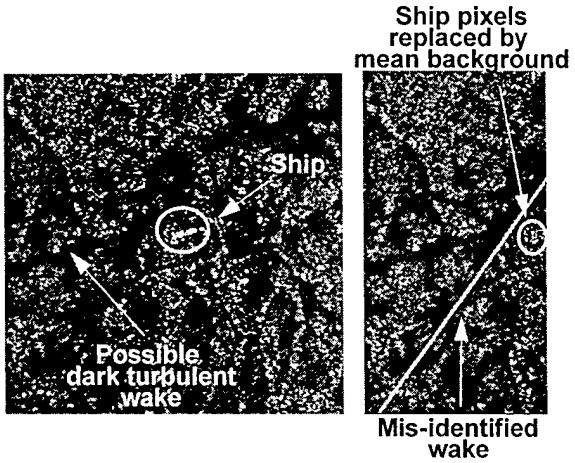

Figure 6: The detection algorithm may fail under very rough sea state.

7. REFERENCES

Baxes, G. A., "Digital image processing: principles and applications", Wiley, 1994.

Copeland A. C., Ravichandran G., and Trivedi M.M., 1995, " Localized Radon transform-based detection of ship wakes in SAR images", IEEE Transactions on Geoscience and Remote Sensing, vol.33, no. 1, January 1995, pp. 35-45.

Eldhuset K., 1996, "An automatic ship and ship wake detection system for spaceborne SAR images in coastal regions", IEEE Transactions on Geoscience and Remote Sensing, vol. 34, no.4, July 1996, pp. 1010-1019.

Lin, I-I, and Khoo, Victor, "Computer-based algorithm for ship detection from ERS SAR Imagery", Proceedings of the 3rd ERS Symposium, 18-21 March 1997, Florence, Italy.

Wahl T., Eldhuset K., and Skoelv A., 1993, "Ship traffic monitoring using the ERS-1 SAR", Proceedings of the First ERS-1 Symposium-Space at the Service of our Environment, Cannes, France, 4-6 November 1992, ESA SP-359 (March 1993), pp. 823-828.

Adapting Operations of the Radarsat SAR to Enhance Ship Monitoring

Anthony P. Luscombe
Spar Aerospace Limited
21025 Trans-Canada Highway, Ste-Anne-de-Bellevue, Quebec, H9X 3R2, Canada.
Tel. (514) 457-2150 (x3641) Fax. (514) 425-3041 E-mail aluscomb@spar.ca

Leo Lightstone
Atlantis Scientific, Systems Group Inc.
1827 Woodward Drive, Ottawa, Ontario, K2C 0P9, Canada.
Tel. (613) 727-1087 Fax .(613) 7272-5853 E-mail leonard@atlsci.atlsci.com

INTRODUCTION

The Radarsat Synthetic Aperture Radar (SAR) instrument [1,2] was designed to be very versatile in its capabilities, and the standard operations of the Radarsat SAR use only a subset of the potential imaging modes. The standard mode best suited to ship monitoring provides coverage of a swath of over 500km, but large scale ship surveillance at mid-latitudes is limited in this mode by two factors: the interval between repeat coverage and the steep incidence angle. Ideally, the system would allow any critical area to be imaged once each day, and at higher incidence angles, where ship-to-clutter ratio is better.

This paper considers alternative modes of operation for the Radarsat SAR which provide enhanced ship monitoring. These modes operate with wider beams and use significantly lower pulse repetition frequencies (PRF) and longer receive windows than the standard SAR modes. The proposed form of ship surveillance mode can be demonstrated with the system currently in orbit using the existing command data and downlink format, but with modified processing. It can provide coverage of a total swath of around 1000km at incidence angles of 40 degrees and above.

Some modest modifications which might be incorporated into a future SAR system are also suggested to enhance these capabilities further.

REQUIREMENTS FOR SHIP DETECTION

The principal requirements which were set for the purposes of this study were the following:

- o probability of detection > 0.9
- o probability of false alarm, P_{fa} (per cell) < 10^{-10}
- o target = naval vessel of length 50m
- o background sea state 4
- o target location error < 4km
- o geographical area, Atlantic above 45° N
- o local region revisit period minimised (goal < 12 hours)

With these requirements, some basic conclusions can be drawn about the ship surveillance mode.

- o The swath width is critical in achieving good revisit, and a minimum width of about 1000km must be aimed for.
- o The signal-to-clutter ratio is insufficient for steep angle viewing, and incidence angles of 35° or more are needed.
- o A system operating with a fixed wide angle beam (a 'staring' system) will give poorer performance than one which operates with multiple narrower beams in pulse bursts (a 'scanning' system).

RADARSAT VERSATILITY

The Radarsat SAR instrument was designed to provide several selectable parameters and programmable functions, with a payload command structure which allows full operational use of these features. This versatility is used routinely to support the wide range of standard imaging modes, from Fine Resolution to ScanSAR, but can also be used to provide a wide variety of other modes. The following paragraphs outline the main versatile features which can be used in defining a mode which is optimum for ship surveillance purposes. The range of choice for most of these features is generally much wider than is used for normal imaging, and the limits and the limiting factors are indicated.

Beam Direction and Width

The elevation beam is formed by a set of phase coefficients applied to the 32 element array with fixed amplitude weighting across the 1.5m antenna width. The coefficients for 20 beam patterns are stored on-board the satellite, but any of the beam tables can be replaced with a new set of beam coefficients uplinked from the ground. The physical antenna plane is tilted at an angle of about 30° from horizontal to the right of the satellite. For elevation angles more than about 15° from the normal to this antenna plane, significant grating lobes will be formed. Otherwise, beams with any required width and direction can be formed with suitable choices of coefficient.

ScanSAR Beam Combinations

The coverage of up to four separate beams can be combined through beam-switching in the ScanSAR mode [3]. Any beam that can be formed with the antenna can be used in this mode, provided that the coefficients are stored in one of the ScanSAR beam table locations.

Bandwidth

Three standard chirp pulses with different bandwidths (12, 17 and 30 MHz) are stored in digital registers, and a fourth register

0-7803-3836-7/97/$10.00 © 1997 IEEE

is available for any additional pulse uplinked from the ground. The radar receiver contains three filters and three A/D rates corresponding to the three pulse bandwidths.

Pulse Repetition Frequency (PRF)

The PRF is set by ground command for each image. The normal range for SAR imaging is from 1200 to 1400 Hz, but a much wider range is available. For ship surveillance purposes, a lower PRF is beneficial because it allows the returns from a wider region to be received in the interpulse gap. The lower limit on the PRF is about 263 Hz, determined by the wordlength used for this parameter in the payload commands.

Receive Window Duration and Timing

In normal SAR imaging operations, the receive window duration is either limited by the data rate or by the interpulse gap, depending on which A/D rate is being used. Both of these constraints are relaxed if the PRF is reduced. The wordlength used for this parameter provides an absolute limit on the window length, with a maximum value of about 1.9 ms.

RADARSAT SHIP SURVEILLANCE MODE

For the purposes of ship surveillance, the main limitations of the standard Radarsat imaging modes are the long revisit periods which result from the limited swath width, and the poor signal-to-clutter due to the relatively steep viewing angle. The ship surveillance mode that has been proposed for Radarsat is designed to overcome both of these limitations.

Mode of Operation

The proposed ship surveillance mode uses ScanSAR beam switching between four swaths, with bursts of pulses successively with each beam. Each of these swaths is illuminated by a wide elevation beam and imaged using a low PRF and long receive window. As far as possible, timing parameters are selected so as to restrict ambiguities from the nadir region and from areas illuminated by grating lobes of the beam. The minimum incidence angle is about 40° and the total coverage over 1000km wide. Sets of phase coefficients have been defined to provide the required beams. The key operating parameters are given in Table 1 and the beam positions and PRF selections are illustrated in Fig. 1. In this diagram, the bands represent regions whose returns intersect with pulse transmissions, and the single lines indicate the positions of nadir ambiguities.

Processing

Optimum detection performance is obtained from the radar signals if as much coherent processing of the target returns as possible is performed. The standard pulse compression operation is therefore applied to all signals, and coherent Doppler processing is performed across each burst of pulses. This latter operation is similar to the synthetic aperture (or azimuth processing) stage in normal SAR operation, providing increased signal-to-noise and signal-to-clutter for small targets. The low

Figure 1: RADARSAT-1 Ship Surveillance Beams

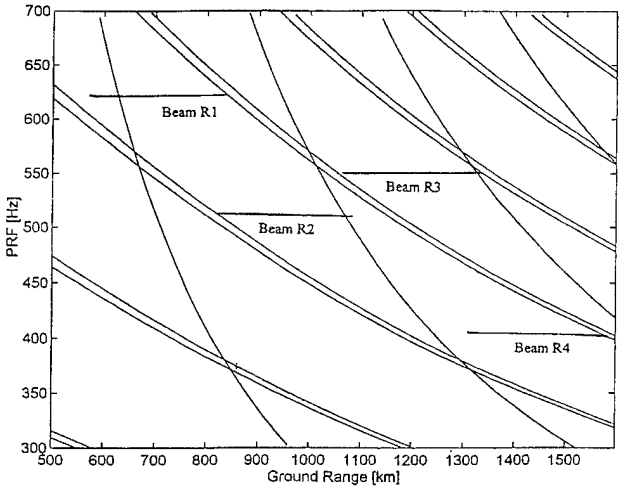

PRF means that the Doppler spectrum is undersampled (for SAR imaging purposes), and so each target also produces a series of lower level ambiguities uniformly-spaced in front of and behind the target. These ambiguities do not prevent detection, and provide a means for distinguishing targets from speckle in the clutter background.

Performance

Table 1 includes performance parameters assessed for the proposed mode. Each beam covers a width of over 250km, with an overlap between adjacent beams, to give total coverage of over 1000km. This wide swath allows mean response time of no more than 0.6 days for any point in the specified area.

	Beam R1	Beam R2	Beam R3	Beam R4
Elevation angles	34.6°-44.2°	43.8°-50.5°	50.1°-54.8°	54.4°-57.7°
Incidence angles	39.8°-51.7°	51.2°-60.3°	59.7°-66.8°	66.2°-72.1°
Swath width	262km	266km	274km	286km
Receive window	1.30ms	1.51ms	1.67ms	1.82ms
PRF	620Hz	510Hz	550Hz	410Hz
Pulses per burst	26	26	26	26
No. of bursts	2	2	3	3-4
Data rate	88.5Mbps	83.4Mbps	99.8Mbps	80.8Mbps
pulse SNR	1.3dB	-0.9dB	-1.3dB	-1.0dB
SNR after proc.	11.7dB	9.3dB	8.5dB	8.8dB
Swath SCR	4-11dB	11dB	11-13dB	12-14dB
Total SCR	4-11dB	10dB	3-5dB worst >8dB for 75%	0dB at edge >10dB for90%
Notes	nadir ambiguity	far edge nadir ambiguity	far edge nadir ambiguity	near edge grating lobe amb.
$P_d@P_{fa}=10^{-4}$	100%	88%	94%	97-100%

Table 1: Radarsat-1 Ship Surveillance Mode

The principal limitation on performance is in signal-to-noise (SNR). The single-pulse SNR is only about 0dB, but is increased by more than 10dB by the coherent Doppler processing. For the

highest beam, the grating lobe ambiguities also contribute a significant amount of clutter energy, raising the signal-to-clutter ratio (SCR) for the near part of the swath. ('Swath SCR' in the table covers only clutter contributions from the swath. 'Total SCR' includes all clutter.) This ratio is also significantly improved through the coherent processing. The probability of detection for a relaxed P_{fa} of 10^{-4} is given in the final row of the table. It should be noted that this high rate can be reduced in operation by eliminating apparent targets which do not have associated ambiguities.

MODIFICATIONS TO ENHANCE SHIP DETECTION

The existing Radarsat I SAR system can provide a ship surveillance mode with very good coverage and acceptable SNR and SCR performance, even though the instrument was not designed to perform this function. In a future SAR system, designed with this application in mind, some features might be included to enhance the ship surveillance capabilities. The features considered here are suggested for a design based on the current Radarsat SAR design, and are restricted to modifications which are modest in cost and complexity, and do not degrade normal SAR imaging. The performance that could be achieved if these modifications were incorporated into a modified Radarsat is summarised in Table 2 at the end of this section.

Longer Pulse Length

With the low PRFs used in the ship surveillance mode, Radarsat is operating with a mean power only about one third of its capacity. By providing the option for a longer pulse, the full available power could be used, improving the SNR by about 4.5dB.

Increased Antenna Tilt

For the high elevation beams, the mainlobe gain is reduced because of loss of energy into a grating lobe on the reverse side of the satellite. This grating lobe also introduces significant ambiguity clutter energy, and therefore degrades SCR. If the antenna plane were tilted at a higher angle to the side of the satellite, these high angle beams would be closer to the antenna boresight, and the grating lobe effects considerably reduced. With a tilt of 40°, instead of the current 30°, the effects are essentially removed for the proposed coverage angles. For steep angle imaging, the grating lobe is increased, but is in a direction away from the Earth and so does not contribute any ambiguity energy.

Increased Number of ScanSAR Beams

Radarsat ScanSAR operation is currently limited to a maximum of four beams. Provided that the SNR is sufficient over a wider angular range, an increase in this maximum number to five or six would allow target detection in a surveillance mode over an even wider area.

Enhanced Radarsat Ship Surveillance Mode

A system which included these three modifications, but retained the rest of the Radarsat system unchanged could support an enhanced ship surveillance mode covering a total of over 1400km and with improved SNR and SCR performance. The main operational and performance parameters are given in Table 2.

	Beam R1	Beam R2	Beam R3	Beam R4	Beam R5	Beam R6
Elevation	30.7°-44.2°	43.8°-50.5°	50.1°-54.6°	54.4°-57.7°	57.3°-59.4°	58.9°-60.2°
Incidence	35.1°-51.7°	51.2°-60.3°	59.7°-66.5°	66.2°-72.1°	71.3°-75.7°	74.5°-77.6°
Swath width	356km	266km	261km	286km	249km	213km
Rx. window	1.71ms	1.59ms	1.67ms	1.90ms	1.71ms	1.49ms
PRF	490Hz	520Hz	550Hz	400Hz	500Hz	540Hz
Pulses/ burst	15	15	15	15	15	15
No. of bursts	2	2	3	3	4	4
Data rate	92Mbps	91Mbps	100Mbps	82Mbps	94Mbps	87Mbps
pulse SNR	3-4dB	5-6dB	7-8dB	3-4dB	3-4dB	2-3dB
proc. SNR	11.0-12.0dB	12.6-14.5dB	14.5-15.5dB	10.3-11.3dB	10.3-11.3dB	9.2-10.2dB
Swath SCR	1-11dB	11dB	11-13dB	12-14dB	13-14dB	14-15dB
Total SCR	1-11dB	11dB	10-12dB	12-13dB	10-13dB	10-14dB
Notes	nadir ambiguity	nadir amb. near far edge	nadir amb. at far edge	.	nadir amb. near far edge	nadir amb. near far edge
$P_d@P_{fa}=10^{-10}$	50-80%	92-100%	100%	74-95%	95-100%	72-94%

Table 2: Enhanced Ship Surveillance Mode

CONCLUSIONS

The SAR system on-board the current Radarsat satellite is designed to be very versatile in its operations, and is capable of providing a much wider range of modes than are utilised for standard imaging. A mode providing wide coverage at relatively high incidence angle has been defined using wide elevation beams, low PRFs and long receive windows. The proposed processing of data from this mode includes coherent correlation of returns to produce a degraded image output in which targets will be visible. This mode, which is available using the current command structure, gives an average response time of less than 0.6 days for the Atlantic region off the coast of Canada with good detection performance.

With some modest modifications to the design, the ship surveillance capabilities of the system could be significantly enhanced. Total coverage could be increased to 1400km, giving average response time of 0.42 days or better, and detection probability of around 0.9 with false alarm rate of 10^{-10}.

References

[1] R.K.Raney, A.P. Luscombe, E.J. Langham and S. Ahmed, "RADARSAT", Proc. IEEE, vol. 79, pp. 839-849, June 1991.

[2] A.P. Luscombe, I. Ferguson, N. Shepherd, D.G. Zimcik, P. Naraine, "The RADARSAT SAR Development," Canadian Journal of Remote Sensing, vol. 19, pp. 298-310, Nov 1993.

[3] A.P. Luscombe, 'Taking a Broader View: Radarsat Adds ScanSAR to Its Operations', Proc. IGARSS '88, Edinburgh, 12-16 September 1988, 1027-32.

Incorporation of Prior Knowledge in Automatic Classification of Oil Spills in ERS SAR Images

Anne H. Schistad Solberg and Espen Volden
Norwegian Computing Center, P.O. Box 114 Blindern, N-0314 Oslo, NORWAY
Phone: +47 22 85 25 00 Fax: +47 22 69 76 60
e-mail: Anne.Solberg@nr.no Espen.Volden@nr.no

Abstract We present algorithms for automatic detection of oil spills in SAR images. The developed framework consists of first detecting dark spots in the image, then computing a set of features for each dark spot, before the spot is classified as either an oil slick or a "lookalike" (other oceanographic phenomena which resembles oil slicks). Knowledge about the external conditions like wind level and slick surroundings are modelled. The presented algorithms are tested on 84 SAR images. The improved algorithms achieve a much higher classification accuracy than a previous classification model which did not incorporate prior knowledge.

INTRODUCTION

Synthetic aperture radar (SAR) images from the ERS satellites have proved to be suitable tools for identification of oil spills in the ocean. Presently, Tromsø Satellite Station has a preoperational service for oil spill detection based on manual inspection of SAR images. A set of algorithms for automatic detection of oil spills was presented in [2]. A framework for automatic detection with the following steps was proposed: (i) detection of dark spots; (ii) feature extraction; and (iii) dark spot classification. The algorithms in [2] did to a limited extent incorporate prior knowledge about wind conditions and other external conditions. In this paper, improved algorithms utilizing prior knowledge about the conditions are presented. The improved algorithms result in large improvements in classification accuracy.

SAR IMAGING OF OIL SPILLS

Oil slicks appear as dark spots in SAR images because they have a dampening effect on the Bragg waves in the sea [3]. The SAR signature of an oil spill will depend on the external conditions. The contrast between the spill and its surroundings depends on a number of parameters like wind speed, wave height, and the amount and type of oil released. The shape of the spill will depend on whether the oil was released from a stationary object or from a moving ship, the amount of oil involved, and the wind and current history between the release and the image acquisition. The weather conditions also carry information about the likelihood of observing lookalikes, e.g., dark spots which are due to other oceanographic phenomena. With low wind conditions, many lookalikes can be observed. As the wind increases, the number of lookalikes will decrease. Lookalikes are rarely observed at high wind conditions.

Furthermore, the wind level will influence the values of the features. Oil slicks will with moderate and high wind have lower contrast to the surroundings than with low wind. This means that several databases representing class signatures for oil and lookalikes for different wind conditions are desired. Alternatively, a model describing the expected value of the features as a function of the wind speed could be used.

The human eye is superior when observing a slick in the context of the surrounding sea. If the surroundings are homogeneous, the prior probability of oil is higher than with heterogeneous surroundings. If a bright object (ship or oil platform) is seen close to a spot, the spot should be closely inspected. To facilitate this, we search for bright spots in the image prior to spot detection.

SPOT DETECTION

The algorithm for detection of dark spots is based on adaptive thresholding. This thresholding is based on an estimate of the typical backscatter level in a large window. The adaptive threshold is set to k dB below the estimated local mean backscatter level. Wind data (the wind level) is used to determine k. Currently, the wind level is set manually as one of four categories: low, low/medium, medium or high wind. The window is moved across the image in small steps to threshold all pixels in the scene.

In some cases for heterogeneous sea, the detected spot can include dark areas from the heterogeneous surrounding sea. After spot detection, each spot is clustered into two clusters. The idea is that if the spot includes parts of its surroundings, the true spot will consist of the darkest cluster. If the two clusters are sufficiently separated and the darkest cluster is sufficiently large compared to the brightest, the darkest cluster is used as the spot, otherwise the original spot is kept.

0-7803-3836-7/97/$10.00 © 1997 IEEE

SLICK FEATURE EXTRACTION

For each dark spot, a set of features is computed. The features constitute general, standard descriptors often applied for regions in general image analysis, and additional features particularly suited for oil slick detection. The features are:

- *Slick complexity*
- *Local area contrast ratio*
- *Border gradient*
- *Smoothness contrast locally*
- *Distance to a bright object*
- *Slick width*
- *Slick area*
- *First planar moment*
- *Power-to-mean (PMR) ratio of the slick*
- *Number of neighboring objects*
- *Number of objects in the scene*
- *Homogeneity of the surroundings*

SLICK CLASSIFICATION

Solberg et al.[2] used a hierarchical classification tree which automatically partitioned the data set into different subclasses. The present system uses a different classifier based on a multivariate probability distribution function in combination with a set of rules and loss functions taking into account the expected number of oil slicks and lookalikes given the wind level. This decision was made to ensure a more robust classification with respect to the values of the features and to be able to control how the features are used.

Some of the features carry information about a particular scene situation. If one of these special situations occurs, our prior expectation of the probability that a certain slick is oil might increase or decrease. When a trained operator classifies a slick manually, he/she will look at the surroundings of the slick and use all the available experience. Given two slicks with the same shape and contrast, he will use the surroundings to determine if they are oil or not.

To be able to control how these features are used in an automatic classification procedure, we will use them to model the prior knowledge about the scene, and not merely to compute their mean and variance in the class-conditional probability density. The features listed below are used to adjust the prior probability for single regions in some way. Based on these features, we have established a set of rules on how to adjust the prior probabilities. Each region is given a certain prior probability based on the rules outlined below.

- *Distance to bright object.* If a slick is close to a bright object, the prior probability of oil slick is increased.
- *Slick area.* In low/low-moderate wind, we can have very large dark spots corresponding to large areas with no wind and almost no backscattering from the sea. If the area is very large, the prior probability of lookalikes is increased. If the area is very small, the slick needs better contrast to be classified as oil, thus the prior probability of lookalikes is increased.
- *Number of regions in a scene.* If the number of detected spots in the scene is large, the scene is very complex and most of the slicks will be lookalikes. The prior probability of lookalikes is increased. If the number of regions is low, and the slick has homogeneous surroundings, the prior probability of oil is increased.
- *Number of neighboring regions.* If a slick has many neighboring regions, the prior probability of lookalikes is increased. If the slick has no neighboring regions and homogeneous surroundings, the prior probability of oil is increased.
- *Slick local contrast ratio.* Used in combination with other features, the slick contrast affects the prior probabilities. If the contrast is low for a slick with several neighboring regions in a scene with many regions, the prior probability of lookalikes is increased.
- *Slick width.* Used in combination with other features, the slick width affects the prior probabilities. In low-wind conditions, thick regions with large area and not very high contrast have increased probability of lookalikes.
- *Homogeneity of surroundings, PMR.* If PMR is large, the surroundings are heterogeneous. If, in addition, the number of regions in the scene and the number of neighboring regions is high, the prior probability of lookalike is increased. If PMR is low (homogeneous surrounding) and the scene is not very complex, the prior probability of oil is increased.

This kind of modification of the prior probabilities is not common in statistical classification. Rules like these are often used in knowledge-based classification methods, in which they are used to define boxes for a hard classification. We use them in combination with a statistical classifier. They allow the combination of several features, while a Gaussian classifier with a diagonal covariance matrix ignores the correlation between the features.

In addition to using subclasses for different wind levels, we also use subclasses for different shapes as given by the object's first planar moment [1]. We use the Gaussian probability density function to model the class-conditional probability densities. Only the features *complexity, mean local area contrast ratio, border gradient, smoothness contrast locally, homogeneity of surroundings, slick width* and *number of neighboring objects* are used to compute the

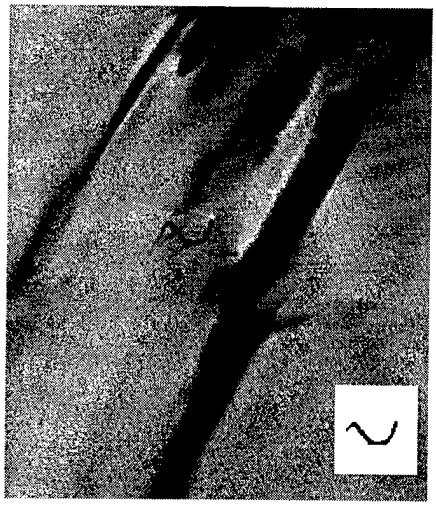

Figure 1: *Correctly classified oil slick from point source. The region classified as oil is shown in the small frame.*

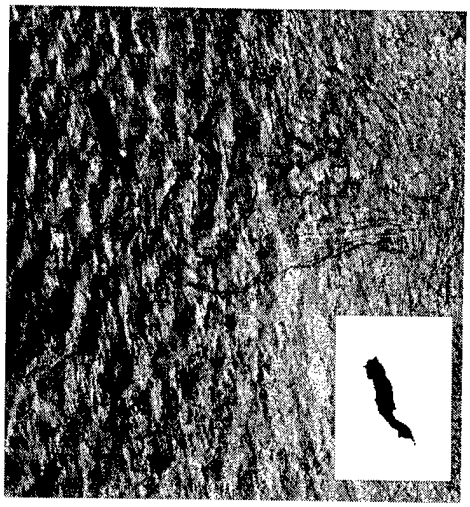

Figure 2: *Oil slick on heterogeneous background. The region classified as oil is shown in the small frame.*

probability density. Because the number of oil slicks is small, we use a diagonal covariance matrix. We also use a common covariance matrix for oil slicks and lookalikes because the number of lookalikes is several orders of magnitude larger than the number of oil slicks.

CLASSIFICATION PERFORMANCE

To evaluate the performance of the classifier, we use the leave-one-out method for classification error estimation. Our test data set consists of $S = 84$ SAR images. We have trained the classifier on $S - 1 = 83$ images, then classified the remaining image and computed the number number of correctly and incorrectly classified regions. This procedure is repeated $S - 1$ times until all S images have been classified.

Our data set of 84 images consisted of 71 oil outlets (sometimes the oil from one outlet was fragmented into several dark spots). 13 spots were manually marked as doubt, indicating that they might be either oil slicks or lookalikes. The data set contained 6980 lookalikes.

Out of a total of 71 oil slicks, 67 (94.4%) are correctly classified. 62 of the 6980 lookalikes were misclassified as oil (0.0088%). By inspecting these 62 spots, we found that for 34 of them classification as oil was quite reasonable, in the sense that an operator might want to have a closer look at them.

Figure 1 shows an example of an oil slick which was correctly classified as oil. This slick is originating from a point source, it has high contrast, regular shape and is fairly easy to discriminate from lookalikes when seen in context with its surroundings. Figure 2 shows an example of a correctly classified oil slick surrounded by heterogeneous sea.

CONCLUSIONS

The developed algorithm for automatic classification of oil slicks achieved a high classification accuracy. 94% of the oil slicks were correctly classified, while more than 99% of the lookalikes were correctly classified. These results are very good compared to a preliminary version of the algorithms [2], which did not attempt to incorporate prior knowledge about the scene. This paper clearly demonstrates that automatic discrimination between oil slicks and lookalikes is possible when knowledge about the weather conditions is incorporated in the classifier and each dark spot is classified in the context of its surroundings.

Acknowledgment This work was funded by Tromsø Satellite Station. We are grateful to Terje Wahl (NDRE), Heidi Espedal (NERSC), Harald Johnsen (NORUT-IT) and Tony Bauna (TSS) for sharing their knowledge about visually discriminating between oil slicks and lookalikes.

References

[1] M. K. Hu. Visual pattern recognition by moment invariants. *IEEE Transactions on Information Theory*, IT-8:179–187, 1962.

[2] A. Solberg and R. Solberg. A large-scale evaluation of features for automatic detection of oil spills in ERS SAR images. In *IEEE Symp. Geosc. Rem. Sens. (IGARSS)*, pages 1484–1486, Lincoln, Nebraska May 1996.

[3] T. Wahl, Å. Skøelv, J.P. Pedersen, L. Seljelv, J.H. Andersen, O.A. Follum, T. Anderssen, G.D. Strøm, T. Bern, H.H. Espedal, H. Hamnes, and R. Solberg. Radar satellites: A new tool for pollution monitoring in coastal waters. *Coastal Management*, 24:61–71, 1996.

Automatic Detection of Ship Tracks in Satellite Imagery

*John M. Weiss[1], Ruixuan Luo[1] and Ronald M. Welch[2]

[1]Department of Mathematics and Computer Science
[2]Institute of Atmospheric Sciences
501 East St. Joseph Street
South Dakota School of Mines and Technology
Rapid City, SD 57701-3995

*Corresponding Author: jweiss@silver.sdsmt.edu 605-394-2471

Abstract

Certain unusual cloud features visible over water in satellite images are caused by ship smokestack pollution. Ship tracks form long, thin, complex features in satellite images. These features do not typically follow straight lines or other low-order polynomial curves, making automated detection difficult. Nonetheless, the ability to automatically detect ship tracks is an important one, with military, navigation, environmental, and rescue applications.

A multi-step automated approach for detection of ship tracks in AVHRR images has been developed. First, an enhanced ship track image is produced from AVHRR channels 1, 3, and 4. Ship tracks stand out as bright linear features, or ridges, in this enhanced image. Then a new technique called *ridge detection by iterated erosion* is applied to this enhanced image. Finally, postprocessing based on connected components analysis is used to eliminate ridges that do not correspond to ship tracks.

Properties of ship tracks in AVHRR images

Some researchers [Morehead, 1988; Nielsen and Durkee, 1992] have investigated mechanisms responsible for the formation of ship tracks in satellite images. But because the structure of ship tracks can vary greatly, and the image backgrounds are complex, automatic ship track detection is a difficult, unsolved problem. In this paper, we present a promising new algorithm for automatic ship track detection in Advanced Very High Resolution Radiometer (AVHRR) images.

In AVHRR channel 1, ship track brightnesses are higher than that of the surrounding area. Ship tracks in channel 2 appear to be very similar to channel 1. Since channel 2 offers little additional ship track information, it is not used for ship track detection. Ship tracks are most readily observed in channel 3, where brightness values are lower than that of the surrounding area. Ship tracks appear very weakly, if at all, in channels 4 and 5. Channel 4 is used to help identify bright cloud masses that can obscure ship tracks in channel 3. Because channel 5 is so similar to channel 4, only channel 4 is used for this purpose.

Ship track appearance varies greatly in AVHRR imagery, making automated detection a challenging task. There is a wide variation in ship track contrast relative to the surrounding area. Ship tracks appear different in cloud-free areas compared to heavy cloud cover. The shapes and widths of ship tracks vary greatly, depending on whether the ship tracks were initiated by larger or smaller amounts of smokestack pollution, are younger (newly formed) or older (widely dispersed) ship tracks, dispersive forces (wind), etc. Even in the same ship track, the width, intensity and contrast may vary. For example, if there is a ship track under high cloud masses, the ship track will be segmented into several disconnected segments in AVHRR imagery.

The contrast of ship tracks against the surrounding neighborhood is quite low. The brightness differences between ship tracks and the background are in the range of 5 to 15 in channel 1 (out of 256 total intensity levels), and 10 to 25 in channel 3. Enhancing the contrast between ship tracks and the background is needed for automated ship track detection.

Automated ship track detection algorithm

Step 1: Preprocessing

The basic preprocessing step is subtracting channel 3 from channel 1. Since ship tracks are brighter than the surround in channel 1, but darker than the surround in channel 3, this creates a ship track-enhanced image. The methodology is:

1. Adjust the brightnesses of channels 1, 3 and 4 so that the average brightness values are equal.
2. Identify bright clouds in channel 4 using an intensity threshold. For each bright cloud pixel in channel 4, if the corresponding pixel in channel 3 has a significantly

Acknowledgments: This research was conducted under NASA grant NAG 5-2712.

lower intensity level, subtract a small constant from the pixel in channel 3 (from 5 to 20 intensity levels, depending on the ship track strength relative to the cloud brightness). This helps overcome the problem of bright clouds obscuring darker ship tracks in channel 3.

3. Subtract channel 3 from channel 1, creating an image of brightness and temperature differences. Since ship tracks are bright in channel 1 and dark in channel 3, ship tracks are enhanced relative to the background.

At this point, ship tracks show up as bright features on a dark background in the enhanced image. The range of intensity differences between ship tracks and the background is 50-100.

Step 2: Ridge detection

Ship tracks form thin features known as ridges in AVHRR images. A ridge is a connected structure that is long relative to its width, with a skeleton along which the pixel intensities change slowly [Haralick, 1983]. Ridge points are brighter than the surrounding background in at least two directions. The ridge width need not be constant, but should change slowly (if at all).

Ridge detection is therefore appropriate for detecting ship tracks in the AVHRR imagery. One serious problem with this approach is the varying width of ship tracks. Most ridge detectors are "tuned" to detect ridges of constant width. For example, the following 3x3 ridge templates are tuned for 1-pixel-wide ridges:

0 0 0	1 0 0	0 1 0	0 0 1
1 1 1	0 1 0	0 1 0	0 1 0
0 0 0	0 0 1	0 1 0	1 0 0

For each image pixel, these four templates are convolved with the image. If the maximum template response exceeds a ridge threshold, that pixel is marked as a ridge pixel. The ridge magnitude is given by the maximum response, and the ridge direction (within 45°) is indicated by the template giving the maximum response.

In order to deal with wider ridges, we have developed a technique which we call iterated erosion. Erosion is a morphological filtering operation [Gonzalez and Woods, 1993] that migrates the darker areas of the image into the brighter areas. It is usually implemented via a neighborhood minimum operation for gray-scale images.

Since erosion migrates the darker areas of the image into the brighter areas, it causes ridges to become progressively thinner. In iterated erosion, we perform ridge detection, followed by erosion, followed by ridge detection, followed by erosion, ... The first iteration identifies 1-pixel-wide ridges, the second iteration identifies 2-pixel-wide ridges, and so on. Typically just a few iterations are required to identify all the ship track pixels. Smoothing the image between iterations helps reduce the noise.

Step 3: Postprocessing

Iterated erosion clearly identifies linear features in an image, but tends to introduce undesirable elements as well, so some form of postprocessing is required. (Fischler and Wolf [1983] found this to be the case in their linear delineation technique, an alternative method for finding linear features.) Undesirable features include short isolated ridge elements, broken ridge segments, and ridge branches. In addition, some clouds will lead to highly clustered ridge structures.

To eliminate these undesirable side effects, we perform connectivity analysis [Weiss, 1996] to identify the connected components in the ridge image. This allows us to determine both the number of pixels belonging to a ridge, and to calculate the convex hull [Gonzalez and Woods, 1993] of a ridge.

After performing connectivity analysis and determining the convex hull of each ridge, we eliminate the following types of ridges:

- very short ridges (under 30 pixels in length).
- very low intensity ridges (average intensity under 100)
- very highly clustered ridges (short and compact rather than long and thin)

We then bridge small gaps between ridge segments by connecting ridge endpoints that are close together in the image (within 20 pixels of one another). This allows us to reconnect broken ship tracks that have been disconnected by bright clouds in the image.

Results

Figure 1 shows the results of automated ship track detection, performed on a 512x512 AVHRR subimage. We have achieved comparable results detecting ship tracks in a number of other AVHRR scenes.

Conclusions

The results shown in this paper indicate that it may be possible to automatically detect ship tracks in AVHRR imagery. We have presented an approach that uses channels 1, 3, and 4 to create an enhanced image in which ship tracks form ridges, together with a novel ridge detection scheme called iterated erosion.

Different ship tracks have different structures and may occur on different cloud backgrounds. There is a clear tradeoff between enhanced detection of weak ship tracks, and greater amounts of noise (which can result in more false identifications). Techniques which improve results for some images may not work well for others. In particular, the selection of certain thresholds is critical for successful detection of ship tracks. A global survey of ship track images is needed to determine the best thresholds.

Some ship tracks are segmented by high cloud masses. Our algorithm is able to connect small gaps (less than 20 pixels)

in ship tracks. Connecting larger gaps between ship track segments is a difficult future challenge.

References

Fischler, M. and Wolf, H. (1983): "Linear delineation", *Proc. IEEE Computer Vision and Pattern Recognition*, 351-356.

Gonzalez, R. and Woods, R. (1993): *Digital Image Processing*, Addison-Wesley Publishing Company.

Haralick, R. (1983): "Ridges and valleys on digital images", *Computer Vision, Graphics and Image Proc.*, 22, 28-38.

Morehead, S. (1988): "Ship track cloud analysis for the north pacific area", Master's Thesis.

Nielsen, K. and Durkee, P. (1992): "A robust algorithm for locating ship track cloud features using 3.7 micron satellite data", Sixth Conference on Satellite Meteorology and Oceanography, Atlanta, Georgia, Jan 5-10.

Weiss, J. (1996): "Connected Components Algorithms for Image Processing", *Journal of Computing in Small Colleges*, Vol. 12 (2).

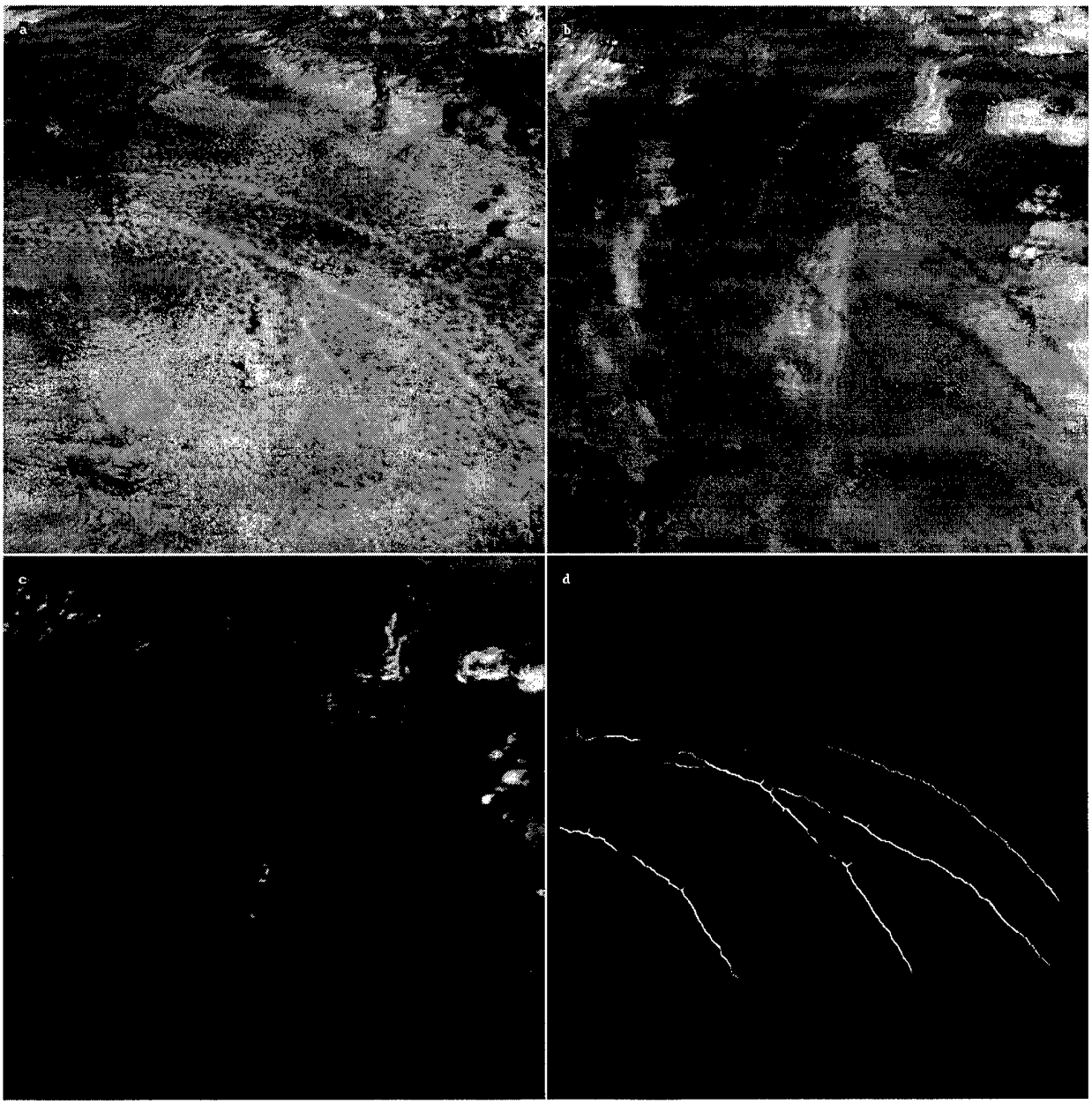

Figure 1: a) AVHRR channel 1; b) AVHRR channel 3; c) AVHRR channel 4; d) results of ship track detection.

IGARSS'97

1997 International Geoscience and Remote Sensing Symposium

03-08 August 1997

Singapore International Convention & Exhibition Centre

Technical Program

Interactive Area 10: Emission and Scattering

Studies of BRDF in conifer and deciduous boreal forests using the 4-Scale model and airborne POLDER and ground-based PARABOLA measurements

Jing M. Chen, Sylvain G. Leblanc and Josef Cihlar
Canada Centre for Remote Sensing
588 Booth St., 4th Fl., Ottawa, Ontario, K1A 0Y7 Canada
Tel: (613)947-1266 / Fax: (613)947-1406
email: jing.chen@ccrs.nrcan.gc.ca

Patrice Bicheron and Marc Leroy
CESBIO, 18 avenue Edouard Belin
31055 Toulouse Cedex, France

Donald Deering and Tom Eck
Code 923, Biospheric Sciences
NASA/GSFC, Greenbelt, M. D. 20771, USA

Abstract - An investigation of directional reflectance of boreal forests is conducted using airborne POLDER [1] and ground-based PARABOLA measurements [2] and the 4-Scale model [3]. The model simulates well the pronounced hotspots observed by POLDER and the slight bowl shape in the forward scattering direction observed by PARABOLA. The model is also used to demonstrate the importance of branch architecture in the directionality of NDVI calculated from the red and near infra-red reflectance.

INTRODUCTION

This paper presents an investigation of the angular behaviour of the reflected solar radiation from boreal forest stands using field measurements and a radiative transfer model. The model used is the 4-scale model developed by Chen and Leblanc [3]. The field measurements include airborne POLDER (POLarization and Directional Earth Radiation) and ground-based PARABOLA (Portable Apparatus for Rapid Acquisition of Bidirectional Observations of Land and Atmosphere) data acquired during the Boreal Ecosystem-Atmosphere Study (BOREAS) in summer 1994 in one deciduous and two conifer stands in Saskatchewan, Canada. Because of the difference in the measurement methodology, considerable differences in the bidirectional reflectance distribution function (BRDF) in red and near infrared bands are found between these two sets of measurements. The 4-Scale model is used to investigate the causes of the differences in relation to the effects of various scales of canopy architecture on the BRDF of these forest stands. Ground measurements of leaf area index, leaf optical properties and tree allometry for these sites are used as input parameters of the model.

4-SCALE MODEL

The 4-Scale radiative-transfer model [3-4] was developed with emphasis on the structural composition of forest canopies at different scales (Fig. 1). The 4-Scale is a geometric-optical model employing several new modelling methodologies: (1) The non-random spatial distribution of trees is simulated using the Neyman type A distribution [5] that creates patchiness of a forest stand. The model simulates tree crowns as discrete geometrical objects: cone and cylinder for conifers, and spheroid for deciduous species. The size of the crowns decreases when the trees are found in large clusters and the tree locations are also subject to repulsion effects to better represent the competition for light; (2) Inside the crowns, a branch architecture defined by a single inclination angle is included to improve the calculation of light penetration. A branch is in turn composed of foliage elements (individual leaves in deciduous and shoots in conifer canopies) with a given angle distribution pattern; (3) The hotspot is computed both on the ground and on the foliage based on gap size distributions between and inside the crowns, respectively; (4) The imaginary tree crown surface is treated as a complex medium rather than a smooth surface so that shadowed foliage can be observed on the sunlit side.

For optimum results, the model has multiple parameters that can be separated into three categories; (1) site parameters: domain size (which represents the pixel size), leaf area index (LAI), tree density, tree grouping factor in the sub-domain size, solar zenith angle (SZA), view zenith angle (VZA) and azimuthal angle difference; (2) tree architecture parameters: crown radius and height, apex angle and needle-to-shoot area ratio for conifers, foliage distribution angles (leaves or shoots orientation: α_L, branches inclination α_b, foliage thickness, branch leaf area index and thickness), clumping-index and typical size of the foliage elements; and (3) optical properties (reflectivities) of the foliage and the ground at desired wavelengths. When measurements are not available for some parameters, defaults or best estimates can be used. For canopies with an important understorey such as hazelnut shrubs in the BOREAS Old Aspen site, a double-canopy version of the 4-Scale model is used [4].

0-7803-3836-7/97/$10.00 © 1997 IEEE

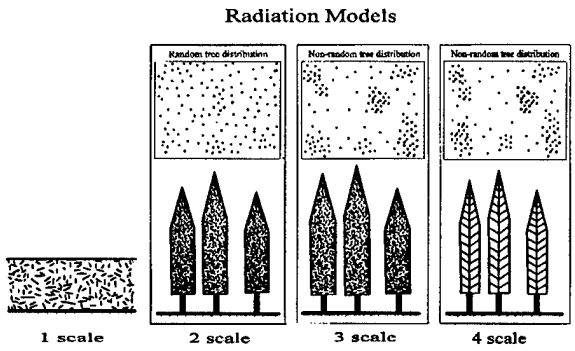

Fig. 1. Concepts of radiation models. The 4-Scale model considers non-random tree distribution and sub-canopy architecture.

RESULTS

The model results are compared with PARABOLA measurements in the BOREAS Old Black Spruce (OBS) site in Fig. 2. The model shows sharp spikes at the hotspot in comparison with the measurements. The gentle variation in the measurements may be a consequence of the low angular resolution (15°) which effectively produced window-averaged results. The effect of the averaging is to dampen and broaden the peak at the hotspot. Figure 2a and 2b shows the simulations and measurements in the red band for SZA of 40° and 55°. Figures 2c and 2d show comparisons between the model and measurements for the reflectance in the near-infrared (NIR) band for SZA of 40° and 60°. The model is able to simulate the measurements closely except for the largest view zenith angles on the backscattering side. The bowl shape of the measurements is simulated by the model in the near infra-red, but is underestimated in Fig. 2d on the forward scattering side, indicating the need to further improve the model.

Figures 3a and 3b show the comparison between the model and POLDER data in the red and NIR band respectively for the OBS site. Only the view zenith angle corresponding to the measurements were simulated. Overall, the model slightly overestimates the measurements, even when using leaf reflectivities in the lower end of measurements. Note that the case presented in Fig. 3a and 3b is about 10° from the principal solar plane, so the hotspot peak was not reached. The NIR modelling shows a very good agreement between the model and the measurements. The only noticeable difference can be seen on the backscattering side for view angles greater than the sun angle where the model shows lower reflectance values than POLDER. For the Old Aspen (OA) site, Fig. 3c and 3d also show good agreements between the model and the measurements. The model can simulate most angles except for large VZA values on the backscattering (Fig. 2d and Fig 3d). The maximum value of the BRDF measured by POLDER is not exactly at the hotspot, but at a larger view zenith angle. This phenomenon can not be simulated by the 4-scale model without accurate consideration of the multiple scattering effect. The small discrepancies between the model and the measurements on the forward scattering side of Fig. 3 may be due to the atmospheric correction algorithm used in the POLDER data processing.

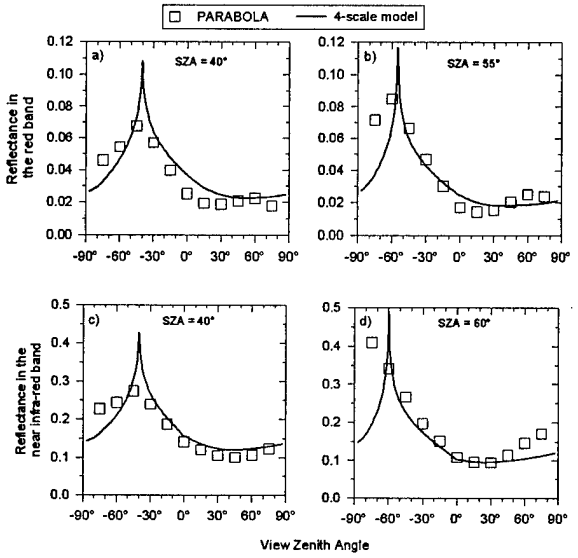

Fig. 2 Comparisons of PARABOLA reflectance measurements in the red and near infra-red bands in the principal plane of the Old Black Spruce BOREAS site.

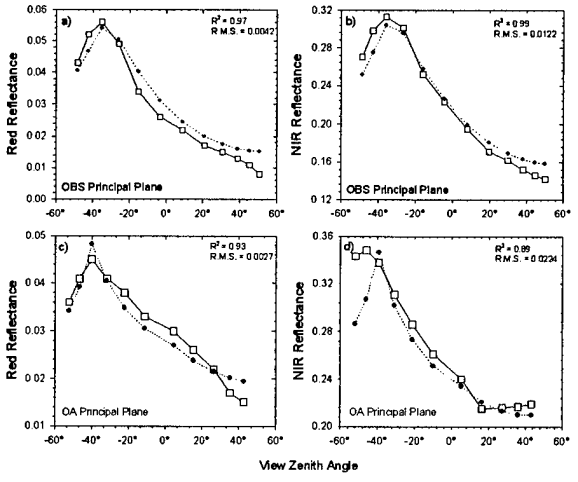

Fig. 3 Comparison between POLDER (□) and the 4-Scale model (•) for the Old Black Spruce BOREAS site (SZA=33.5°) in a) the red band and b) the near infra-red band, and for the Old Aspen site (SZA = 39.3 °) in a) the rd and b) the near infra-red band.

Figures 4a and 4b shows the directionality of NDVI [6] calculated from the red and near infra-red bands reflectance for the cases of near vertical (α_b and α_L at 75°, positive angles representing upward directions) and horizontal branches and shoots (α_b and α_L at 0°) for the OBS and Old Jack Pine (OJP) site, respectively, at SZA=45°. The branch architecture has a pronounced effect on the directional distribution of NDVI in OJP but the effect is much smaller in OBS. The difference in crown foliage density in these two stands is the main cause for the difference in the magnitude of the subcanopy architecture effect.

The foliage density in OJP crowns is low and therefore the change in the foliage organisation and orientation has large effect on the probabilities of light and viewline penetrations through the crowns. In OBS, where tree crowns are dense, the detailed foliage distribution within the crowns only have a secondary effect on NDVI. Near nadir, the NDVI is larger in the case of horizontal shoots and branches because the probability of seeing the background vertically is smaller through the horizontal foliage. At large view zenith angles on the forwardscattering side, the effect of the foliage orientation on NDVI increases. When the branches and shoots are horizontal, the probability of seeing sunlit foliage from the shaded side is larger than when the foliage is almost vertical. The vertical structure can be seen as a "wall" that prevents the viewer to see sunlit foliage through the crown. The NDVI increases because the viewer sees more shaded foliage which has larger NDVI because of the stronger multiple scattering effect on NIR than on red reflectivity. This subcanopy architectural effects should depend on the stand density which modifies the multiple scattering processes.

CONCLUSION

Both PARABOLA and POLDER measurements are of very high quality. These two instruments produced results in reasonable agreement, although considerable differences exist because of the different measurement methodology. The POLDER data have higher angular resolutions and larger spatial coverages than the PARABOLA data but suffer from some uncertainties in the atmospheric correction. The PARABOLA data have the advantage of being able to sample for given angle combinations (such as principle solar plane) and free from atmospheric interference but the measurements were made with a lower angular resolution (15°) and in smaller areas than the POLDER data. With detailed description of the architecture of the deciduous and conifer canopies, the 4-Scale model simulates closely the measurements from both instruments. Compared with PARABOLA, POLDER data generally show smaller reflectance in the red band and similar reflectance in the NIR band. In the 4-Scale simulation of POLDER data, red reflectivities are lowered to 11% and 4% for the foliage and ground, respectively, from 13% and 6% used in the simulation of PARABOLA data. These adjustments are due to the different wavelengths used: 660-680 nm for POLDER, which includes the minimum in the red reflectivity spectrum for conifer needles, and 650-670 nm for PARABOLA, which is located on one side of the minimum. In BRDF, the largest differences of scientific concern between these two types of measurements are found on the forwardscattering side where PARABOLA exhibits bowl shapes while POLDER doesn't. Further investigation is needed to understand the causes of the difference.

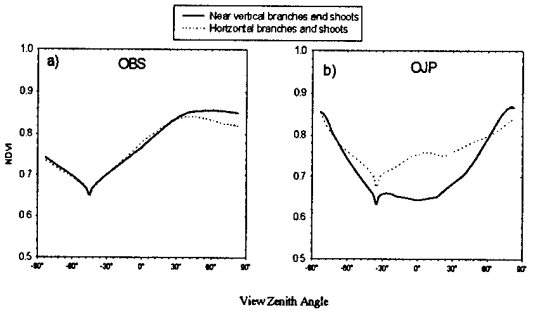

Fig. 4 Simulated principal plane NDVI with horizontal and near vertical shoots and branch structure for a) the Old Black Spruce (OBS) site and b) the Old Jack Pine (OJP) site. SZA = 45°.

REFERENCES

[1] Deschamps, P-Y et al.,1994. "The POLDER mission: instrumental characteristics and scientific objectives." *IEEE Trans. Geosc. Rem. Sens*, vol. 32, pp. 598-613.

[2] Deering D.W., S.P. Ahmad, and T.F. Eck 1995. "Temporal Attributes of the Bidirectional Reflectance for Three Boreal Forest Canopies." *Proc. IEEE Geosci. Remote Sensing Symposium*, pp. 1239-1241.

[3] Chen J.M. and S.G. Leblanc, 1997. "A Four-scale Bidirectional Reflectance Model Based on Canopy Architecture." *IEEE Transactions on Geoscience and Remote Sensing,* (in press).

[4] Leblanc S.G., P. Bicheron, J.M. Chen, M. Leroy and J. Cihlar, 1997. "Investigation of Directional Reflectance in Boreal Forest with an Improved 4-Scale Model and Airborne POLDER data." Submitted. to *IEEE Trans. Geosc. Rem. Sens.*

[5] Neyman, J., 1939. "On a New Class of 'Contagious' Distribution Applicable in Entomology and Bacteriology." *Annals of Mathematical Statistics*, vol. 10, pp. 35-57.

[6] Leblanc S.G., J.M. Chen and J. Cihlar, 1997. "Directionality of NDVI in Boreal Forests." Submitted to *Canadian journal of Rem. Sens.*

FEASIBILITY OF MEASURING DIRECTLY DISTRIBUTION OF THE EMISSIVITIED FOR TERRITORIAL SURFACE ON THE REMOTE SENSING PLATFORMS*

Zhang Renhua Sun Xiaomin Zhu Zhiling
Institute of Geography, Chinese Academy of Sciences
Beijing 100101, CHINA

Abstract-- This paper reviews the basic principle of measuring emissivity by using carbon dioxide laser in 10.6 μm for longer distance which is presented by author several years ago. When the technique is extended to determine two dimension distribution of the territorial surface emissivities on airborne or spaceborne platforms, key points should be completed (1) Power of the carbon dioxide laser must reach a level that can cause obvious change of signal in the thermal infrared detector for a distance between the detector and ground surface (2)Wavelength of the carbon dioxide laser should be coincided with thermal infrared scanner (3) Two images ought to be obtained which are before and after irradiating with the carbon dioxide laser, and its beam must keep a simultaneous scanning with a phase difference of one pixel. That means dual scanning fashion should be designed.

INTRODUCTION

The global warming is very significant research project which is certainly related to the information of land surface temperature (LST). Unfortunately , so far the remote sensing technology still can directly not measure the true LST with acceptable precision 1 °k which can be used to divers ground surface heat balance process and models. One of major obstructors in the inverting the true LST is the lack of exact emissivities data of the territorial surfaces .

Importance of the emissivity data of territorial surface in situ is evident. The emissivties are changed with soil moisture, roughness and other factors. So unacceptable error will cause if an approximate guess of the emissivity is used. The brightness temperature given by a thermal detector can differ substantially from the true surface temperature when the emissivity of the surface is slightly smaller than unity. Thermal radiance coming from a surface is a combination of emission from the surface and reflectance of downwelling irradiance from the surround. On a thermal infrared image, surface with different emissivities but the same radiance may have different true surface temperatures. For instance, if the mean surround (mostly, it is the sky) equivalent temperature is -30°C, the true temperature of the two surfaces is 15°C, and there is a difference of 0.015 in emissivity for the two surface , then their brightness (apparent) temperature may have a difference of about 1°C which can account for about 10 percent of the maximum temperature difference in the thermal infrared image.

Several methods have been presented for measuring emissivities at very small point which is just equal to circle area of the intersecting of the view angle for the detector.[1][2] In addition, those methods all adopted the change of radiance state in a hemisphere surface to obtain emissivity information. Obviously, this kind of methods can not meet the need of inversion of the true temperature in a large area. In order to realize the goal in measuring directly emissivity in the large scale, first of all, the hemisphere irradiance source should replaced with an active irradiance source which can scan a large area and transfer a long distance. In term of the need in application , author presented a method that adopted a carbon dioxide laser as a active irradiance source for measuring the emissivities in large area. And the measurements of emissivities have been succussed for 35 m distance. [3]. A proposed approach to determine the emissivity from airborne and spaceborne was conducted in 1989.[4]

At present there is increasing need to develop a way of inverting distribution of the land surface temperature. Therefore it seems to be necessary for approaching the feasibility of long distance measuring method by means of the carbon dioxide laser . This paper , first , reviews the principle of the method. Then, a feasible operating way in recent technology background was discussed. Expectation of this paper is to obtain more responses for the feasibility.

THE PRINCIPLE OF MEASURING

The most important key step of measuring emissivity is to change irradiance in very short time interview of two measurements. The step is crucial no matter hemisphere (πdownwelling incident angle)or active laser beam irradiance sources. In the method of measuring

*The project is supported by NSFC of China

0-7803-3836-7/97/$10.00 © 1997 IEEE

emissivity using carbon dioxide laser, the directional irradiance source may have three combinations: (1) irradiance sources of a surround (sky, clouds or ceiling and wall of a room) and a weak carbon dioxide laser (2) the surround and a strong carbon dioxide laser (3) the weak and strong carbon dioxide laser. The use of the three combinations is intended to verify whether the results of measurements of different outputs are the same , and whether there is a difference between the carbon dioxide laser and the commonly-used infrared irradiance sources.

When the surround irradiance source at air temperature and the weak CO_2 laser are combined , emissivity $\varepsilon_{10.6}$ can be expressed as:

$$\varepsilon_{10.6} = \frac{(V_{s1} - V_{s2}) + \tau_{aj}^2 V_{jm}}{\tau_{aj}^2 V_{jm}} \qquad (1)$$

When the surround irradiance and the strong CO_2 laser are combined the emissivity $\varepsilon_{10.6}$ is similar expression:

$$\varepsilon_{10.6} = \frac{(V_{s1} - V_{s3}) + \tau_{aj}^2 V_{jm}}{\tau_{aj}^2 V_{jm}} \qquad (2)$$

When the weak and strong CO_2 lasers are combined , the emissivity can be written as:

$$\varepsilon_{10.6} = \frac{(V_{s3} - V_{s2}) + \tau_{aj}^2 (V_{jb} + V_{jm})}{\tau_{aj}^2 (V_{jb} - V_{jm})} \qquad (3)$$

where V_{s1}, V_{s2} and V_{s3} respectively are the corresponding output voltages of the thermal infrared radiometer , V_{jm} and V_{jb} are the corresponding output voltages of the thermal infrared radiometer for the weak and strong CO_2 laser irradiance respectively, derived from the standard emissivity plate . $\varepsilon_{10.6}$ is the emissivity of the measured territorial surface at 10.6 μm ±δ . For simplicity, it is assumed that the distances from the CO_2 laser and the thermal infrared radiometer to the measured surface are equal, i.e. $\tau_{aj1} = \tau_{aj2} = \tau_{aj}$. The assumption is tenable as in the later airborne measurements, the thermal infrared scanner and the CO_2 laser are definitely on the same airborne platform. τ_{aj1} is transmissivity from the CO_2 laser to the measured surface at 10.6 μm ±δ , τ_{aj2} is transmissivity from the measured surface to the thermal infrared radiometer at 10.6 μm ±δ .

The CO_2 laser beam is a monochromatic light , but it still is limited within a very narrow bandwidth. Thus V_{jm} or V_{jb} can be expressed :

$$V_{jm} , V_{jb} \sim \int_{10.6-\delta}^{10.6+\delta} M_j \tau_{aj1} \tau_{aj2} d\lambda \qquad (4)$$

The wavelength of the radiance corresponding to V_{s1} is within the range of that of filter of thermal infrared radiometer, i.e. 8-12.5 μm , hence

$$V_{a1} \sim \int_8^{12.5} (\varepsilon_w M_L \tau_{ao} + (1 - \varepsilon_w) \varepsilon_E M_E \tau_{ao} (\tau_{ae}) d\lambda \qquad (5)$$

where M_L, M_E, M_j are radiances for the measured surface , surround and CO_2 laser respectively. ε_w is the average emissivity of the measured surface corresponding to the wavelength of radiance, ε_E is the average emissivity of the surrounds τ_{ao} and τ_{ae} are the average transmissivities for 8-12.5 μm from the measured surface to the thermal infrared radiometer and to the surrounds respectively.

When the emissivity at 10.6μm of the measured surface is known, it can be used as a reference surface . Through the inversion of (1)(2)(3) , the corresponding irradiance of the CO_2 laser can be calculated by:

$$V_{jm} = \frac{V_{s2} - V_{s1}}{\tau_{aj}^2 (1 - \varepsilon_{10.6})} \qquad (6)$$

$$V_{jb} = \frac{V_{s3} - V_{s1}}{\tau_{aj}^2 (1 - \varepsilon_{10.6})} \qquad (7)$$

$$V_{jb} - V_{jm} = \frac{V_{s3} - V_{s2}}{\tau_{aj}^2 (1 - \varepsilon_{10.6})} \qquad (8)$$

To reduce the errors caused by the changes in irradiance of he CO_2 laser, the laser is calibrated by inserting a reference surface in to the path of the beam. A granite sample is adopted as reference surface . The emissivity at 10.6μm of the natural surface of the granite is 0.848 which is determined in laboratory using the method in paper [1].

When the measurement is at a long distance,

such as an airborne platform, the absorption of the laser irradiance by the atmosphere cannot be neglected. Then transmissivity of the atmosphere will be deduced by the following equation

$$\tau_{aj} = [\frac{V_{s3} - V_{s2}}{(V_{jb} - V_{jm})(1 - \varepsilon_{10.6})}]^{0.5} \qquad (9)$$

According to the principle, so long as the wavelength for the CO_2 laser adjusted continuously , emissivities at different wavelengths can be obtained.

FEASIBILITY FOR REALIZING THE PLAN

In order to confirm the feasibility for realizing that the emissivities of territorial surfaces can be directly measured by using CO_2 laser on remote sensing platforms, three key points should be discussed. First, output power of the CO_2 laser ought to be strong enough, so that the measured surface will obtain a irradiance change which is needed in abstracting emissivity in term of (1) or (2) or (3). According to the calculation of an usual situation in which the surround is clear sky with average equivalent temperature -10°C and emissivity 0.9, the sky hemisphere irradiance is 244 wm^{-2} and its directional irradiance is 77 wm^{-2}. Generally when there is a increase of 10% for the irradiance , the emissivity can be abstracted . If the area of measured ground surface is 30 m^2 which is area of the pixel measured by airborne thermal scanner and the atmosphere transmissivity is 90%, the output power of CO_2 laser , at least , reaches 220 w. In term of resent technology condition , this kind of strong output power CO_2 laser may be realized. Now, there is a very strong output power CO_2 laser in China. Its power can exceed 10000 w . There are more than 30 different wavelength in 9-11μm which are almost continuous distribution with 0.02μm interval only. View of field of the laser can be made from 1-10 mini-radian which can coincide with view of field of the thermal scanner. This type of CO_2 laser is suitable to measure average emissivity in 9-11μm which includes most of information in atmosphere window of 8-12.5μm. Second, In order to measure emissivity distribution with wavelengths or any monochromatic emissivity in 9-11μm, there are two technique way to reach the goal: one is making different monochromatic CO_2 laser tubules and the other is by using a dividing light device on the CO_2 laser which has various very narrow wavebands in 9-11μm to obtain radiances of different monochromatic wavebands. However, if emissivity of each wavelength wants to make image i.e. to make two dimension space distribution, one emissivity image must carry out one

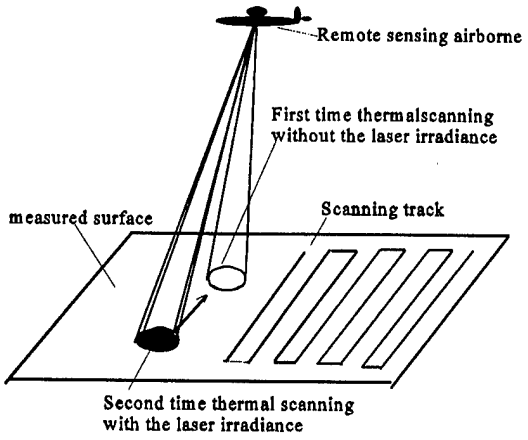

Fig.1 Sketch for measuring emissivity image

scanning measurement. Third, making emissivity image is a key step for this method. According to the principle of measuring ,two images ought to be obtained which are before and after irradiating with the carbon dioxide laser, and its beam must keep a simultaneous scanning with a phase difference of one pixel .That means dual scanning fashion should be designed. Following design may be as suggestion . (See Fig.1) Fig.1 shows how the dual thermal scanner carries out measurement of the emissivity images. First scanning without irradiance of the CO_2 laser and second scanning added irradiance shotted by the CO_2 laser can make two images . The view of field of the thermal scanner must overlap the irradiance of field of the CO_2 laser. Time interval of the two scanning at the same pixel ought to be very short, so that it can meet the need of the measuring principle.

REFERENCES

[1] R.H. Zhang and K.L. Tian, "Determination of emissivity of objects as normal temperature, KEXUE TONGBAO , vol.26:5,pp.447-452,1981.

[2] J.M.Chen and R.H. Zhang,"Studies on the mesurements of crop emissivity and sky temperature", Agricultural and Forest Meteorology, 49:23- 34, 1989.

[3] R.H. Zhang, " Emissivity measurements for long distance using CO2 laser," KUXUE TONGBAO , vol.23:1814-1818,1985.

[4] R.H. Zhang,"A proposed approach to determine the emissivities of territorial surface from airborne and spaceborne"INT. J. Remote Sensing vol.9:3 pp.591-595, 1989.

A Comparison of Mixture Modeling Algorithms and their Applicability to the MODIS Data

S. N. V. Kalluri[♦], C. Huang[♦], S. Mathieu-Marni[*], J. R. G. Townshend[♦*], K. Yang[✧], R. Chellappa[*], A. Fleig[♦]

[♦] Department of Geography, University of Maryland, College Park, MD - 20742, USA,
Email: sk71@umail.umd.edu, Fax: (301) 314 9299, Phone: (301) 405 6733

[*] University of Maryland Institute for Advanced Computer Studies (UMIACS)

[✧] Code 922, NASA-GSFC

ABSTRACT

The performance of three different mixture models is tested on two sets of synthetic data which were generated by spatially degrading a Landsat - TM image. The first data set was generated by using a simple weighted spatial averaging filter, whereas the second data set was generated by applying the point spread function (PSF) of the Moderate Resolution Imaging Spectroradiometer (MODIS). Two of the models (MIXWLS and UNMIX) solve the mixture decomposition problem by statistical least square methods, and require a priori information about the spectral signatures of the individual end-members. The third model (COCKTAIL) identifies the end-member spectral values from the image itself through factor analysis. All the three methods showed larger errors in their estimates of the proportion of end-member in each pixel in the MODIS data compared to those from the spatially averaged data due to PSF effects. However, the magnitude of errors was surprisingly similar from all the three models when the simulated MODIS data was used.

INTRODUCTION

Over heterogeneous areas, multispectral measurements from a coarse resolution satellite comprise a mixture of spectral values from different land cover classes present within each pixel. If we assume that the reflectance (r) of a mixed pixel in wavelength (i) is a linear sum of pure reflectances (a) from the individual components (j) of the mixture weighted by their fractional cover (x) in the mixture, then the reflectance of a mixture (k) can be written as:

$$r_{ik} = \sum_{j=1}^{n} a_{ij} x_{jk} \qquad (1)$$

where n is the number of independent components or end-members in the mixture. If the reflectance of the end-members (a_{ij}) is known, then (1) can be solved to determine the fraction of end-members within each pixel. The reflectances of the end-members are either determined from field measurements or from the image itself. Several models exist in literature to solve the linear model [eg. 1, 2, 3, 4). However, the effect of instrument point spread function in determining the fractional cover of end-members has apparently been ignored in previous mixture modeling studies. In this paper, we compare the performance of three different mixture modeling algorithms using a synthetic data set of the Moderate Resolution Imaging Spectroradiometer (MODIS) derived from a Landsat Thematic Mapper (TM) image.

DATA

To evaluate the performance of mixture models, very accurate ground information is needed which gives the percentage of individual end-members within each pixel in the image. However, there are usually significant uncertainties contained in both remotely sensed data and ground truth data which makes it difficult to assess the accuracy of these algorithms. A simplified test data set was thus created in this study to overcome these uncertainties.

The test data set was created as follows. A window of 320 pixels by 320 lines was selected from a Landsat TM image over Poolsville, Maryland (USA) and a land cover map corresponding to the image resolution was created from aerial photographs and field visits. The land cover map had three classes: forest, soil and water. Using the land cover map as a mask, the mean digital value of all the pixels within each cover type was calculated for the six reflectance channels of TM. A simplified image was then created from the land cover map by assigning the mean digital value of each land cover to all the pixels within that class. Through this process, the heterogeneity within each class was removed from the image. These mean reflectances from each of the classes were used as the pure end-member spectra in the mixture modeling algorithms.

The simplified TM image at 30 m resolution was spatially degraded using two different techniques: in the first method a simple spatial average filter was applied with a window size of 8 × 8 pixels in each TM band. In the second method, the image was blurred using the point spread function (PSF) of the MODIS sensor, and resampled by choosing every eighth pixel in the blurred image. Thus, both the spatially averaged image as well as the simulated MODIS image had the same ratio of spatial resolution (1:8) compared to the original TM image. From the land cover map, the

0-7803-3836-7/97/$10.00 © 1997 IEEE

percentage of each land cover class within the spatially degraded images was calculated. These percentages were used for validation of the results from the mixture models.

MIXTURE MODELING ALGORITHMS

We have tested the performance of three different mixture modeling algorithms on both the spatially averaged image as well as the simulated MODIS image. The percentage of forest, soil and water estimated by the mixture models in each pixel was compared with the true values which were derived from the land cover map as described in section 2 for validation.

Two of the models we tested [3, 5] work on the principle of least squares, wherein the sum of the squares of the errors in the estimated proportion of the end-members in each pixel is minimum. Both the methods have the following constraints:

$$x_j \geq 0 \text{ and } \sum x_j = 1,\ j = 1, 2, \ldots\ldots n \qquad (2)$$

The first method [3] is iterative, and solves (1) by Gauss elimination and forward and backward substitution algorithms [6]. The second algorithm [5] is non iterative and uses the single value decomposition method [7] to identify the proportion of each end-member in the mixture. Both these methods need a priori information about the end-member spectra. We will henceforth refer to the first algorithm as MIXWLS and the second algorithm as UNMIX.

Mathieu-Marni et al. [4] use Q-mode factor analysis and Varimax rotation on the raw TM scene and extract the principal factor images to reduce the dimensions of the working space. The two factors with the biggest variance are then projected onto a two dimensional space and the end-members are identified from the cloud of spectra. Mixing proportions of the end-members within each pixel are calculated by comparing its distance from the end-members in two dimensional space. This method has the same constraints as the first two methods discussed above, and this model is named as COCKTAIL.

RESULTS AND DISCUSSION

All the three mixture decomposition algorithms were applied on both the spatially averaged image as well as the MODIS simulated image. The percentage of end-members determined by each algorithm within a pixel was compared with the actual percentages determined from the land cover map for validation. Since all the pixels within a land cover class have the same spectral value in the simplified image, and because the end-member spectra are known, we expect all the mixture models to resolve the proportion of end-members within the spatially averaged pixels with a hundred percent accuracy. Figs. 1a-1c show the results from the three mixture models on the spatially averaged data. The standard errors in the estimated proportion of end-members from COCKTAIL (2.44) were larger compared to the standard errors from MIXWLS (0.63) and UNMIX (0.75).

When the mixture models were applied on the simulated MODIS image, they all had higher standard errors compared to those from the simplified image. The standard errors from MIXWLS, UNMIX and COCKTAIL were 4.53, 4.56, 4.83 respectively. Standard errors from the three models are comparable to each other, indicating that any of the three techniques could be used with equal confidence on the MODIS data. However, observation of results (Figs. 2a-2c) show that all the three models overestimated the proportion of an end-member when its actual value in any pixel is very low (close to zero), and underestimated its proportion when the actual value in any pixel is very high (close to hundred). When the reflectances of the end-members is not known, then it is advantageous to use COCKTAIL, since this method estimates the spectra of end-members from the image itself.

The errors from the simulated MODIS image are probably due to the non-linear mixing of spectra from end-members caused by the PSF of the instrument. If a deconvolution filter is designed to minimize the effects of point spread function on recorded radiances, then these errors could potentially be reduced.

CONCLUSIONS

Results from this research highlight the impact of the MODIS instrument's PSF on the estimated proportion of end-members in a mixed pixel when linear mixture decomposition algorithms are used. However, the magnitude of errors in the retrieved proportions of end-members in the simulated MODIS data from three of the algorithms that we have tested is similar. Results from MIXWLS and UNMIX algorithms were more accurate compared to those from COCKTAIL when tested on a simple spatially averaged image. But when the pure spectra of the end-members is not known a priori, using COCKTAIL is advantageous.

ACKNOWLEDGEMENTS

This research has been made possible by a grant from the National Science Foundation (BIR9318183)

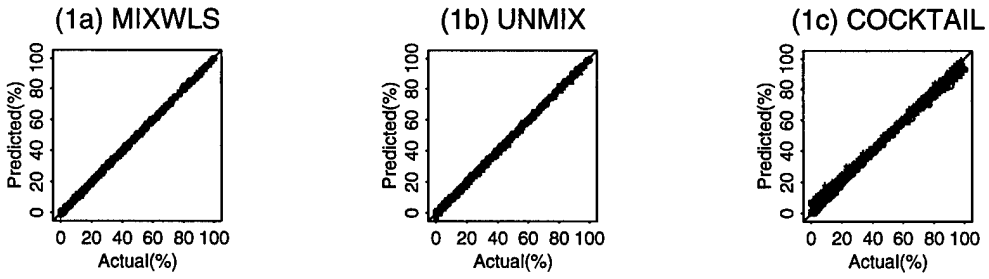

Fig. 1 A comparison of results from the three mixture models with the spatially averaged data set
o - soil, Δ - water, + - forest

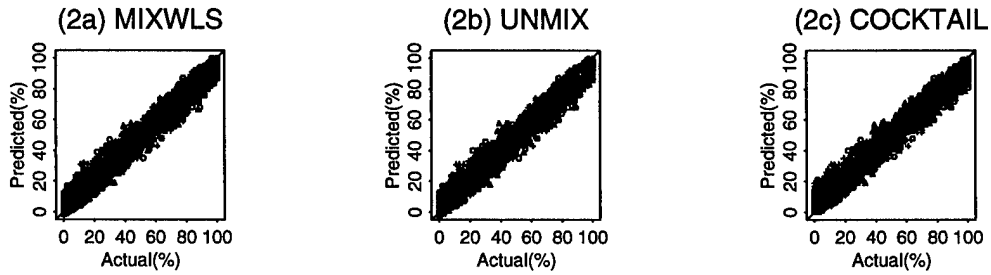

Fig. 2 A comparison of results from the three mixture models with the simulated MODIS data set
o - soil, Δ - water, + - forest

REFERENCES

[1] A. R. Heute, "Separation of soil-plant spectral mixtures by factor analysis". *Remote Sensing of Environment*, vol. 19, pp. 237-251, 1986.

[2] J. J. Settle, and N. A. Drake, "Linear mixing and the estimation of ground cover proportions". *International Journal of Remote Sensing*, vol.14, pp. 1159-1177, 1993.

[3] Y. E. Shimabukuro, and J. A. Smith, "Least-square mixing models to generate fraction images derived from remote sensing multispectral data". *IEEE Transactions on Geoscience and Remote Sensing*, vol. 29, pp.16-20, 1991.

[4] S. Mathieu-Marni, S. Moisan, and R. Vincent, "A knowledge-based system for the computation of land cover mixing and the classification of multi-spectral satellite imagery". *International Journal of Remote Sensing*, vol.17, pp. 1483-1492, 1996.

[5] P. Gong, J. R. Miller, J. Freemantle, and B. Chen, "Spectral decomposition of Landsat Thematic Mapper data for urban land-cover mapping". *Proceedings of the 14th Canadian Symposium on Remote Sensing*, pp. 458-461, (Calgary, Alberta, 6-9 May), 1991.

[6] S. D. Conte, and C. de Boor, *Elementary Numerical Analysis-An Algorithm Approach,* 3rd ed. New York: McGraw-Hill, 1980.

[7] J. W. Boardman, "Inversion of imaging spectrometry data using singular value decomposition". *IGARSS'89*, vol. 4., pp. 2069-2072, 1989

Retrieval of Bidirectional Reflectance Distribution Function (BRDF) at Continental Scales from AVHRR Data Using High Performance Computing

S. N. V. Kalluri†, Z. Zhang*, S. Liang†, J. Jaja*, J. R. G. Townshend†*,
Email: sk71@umail.umd.edu, Fax: (301) 314 9299, Phone: (301) 405 6733
† Department of Geography, University of Maryland, College Park, MD-20742, USA
* University of Maryland Institute for Advanced Computer Studies (UMIACS)

ABSTRACT

We have used high performance computing techniques to implement three different algorithms to model the Bidirectional Reflectance Distribution Function (BRDF) over land from AVHRR data. AVHRR data from the Pathfinder project has a spatial resolution of 8 km, and four years of data (1983-1986) was used in this study. Two of the models are statistical models, where the coefficients are derived from a set of directional reflectances for each solar zenith angle by curve fitting using a least square routine. The third model is semi-empirical, and the coefficients are derived by model inversion and numerical iteration. The semi-empirical model is computationally more expensive compared to the other two. One of the statistical models describes surface BRDF as a continuous temporal function using Fourier techniques. Analysis of the standard errors between observed and modeled reflectances from the temporal model show that the errors were larger in higher latitudes, probably due to interannual variations in surface conditions caused by changing snow cover in these areas. Results from the other two models are similar. The results from this study are expected to provide valuable inputs into BRDF retrieval algorithms proposed for future Earth Observation System (EOS) instruments.

INTRODUCTION

Land surface anisotropy causes variations in surface reflectances when measured under different illumination and view angles. For a wide field-of-view instrument such as the Advanced Very High Resolution Radiometer (AVHRR) whose satellite zenith angle varies from the nadir by as much as ±68.5°, the bidirectional reflectance distribution (BRD) effects can cause significant day to day variations in measured reflectances [1, 2, 3]. Characterizing surface BRD is essential to correct multi-date composite images for the effects caused due to variations in illumination and observation geometry, to help in the retrieval of surface structural attributes such as leaf area index of vegetation, and in climatological studies for the retrieval of surface broad band albedo [4].

Previous studies to characterize BRD function (BRDF) from AVHRR data have been done using samples of pixels selected from imagery at varying spatial resolutions [e.g. 3, 5, 6]. Application of BRDF models at continental and global scales is difficult because of the large volume of data that needs to be processed, and due to the computational complexity of these models. We have used high performance computing techniques to achieve this goal, and implemented three different models to retrieve the BRDF on a pixel basis for the entire land surface using data from the Pathfinder AVHRR Land (PAL) project [7]. This paper describes the processing scheme, computational performance, and results from these models.

DATA

The PAL data set has a spatial resolution of 8 km and is available at daily as well as 10 day temporal resolutions. Daily data are generated from the AVHRR Global Area Coverage (GAC) orbits, and then composited every 10 days following a maximum value Normalized Difference Vegetation Index (NDVI) criterion. Both the daily and composite data have twelve layers: consistently calibrated reflectances and brightness temperatures from the 5 bands of AVHRR, NDVI, scan and sun geometry for each pixel, earth location, cloud and quality flags, and the date of observation. The daily as well as composite data are available for the time period 1981-1994. For this study, we have used only the 10 day composite data from four years (1983-1986). The effects of clouds and atmosphere are minimized during compositing [1]. Each 12-layer composite image is about 230 Mbytes. For further information about this data set and its processing scheme, the user is referred to James and Kalluri [7].

ALGORITHMS

The first model we used is the modified Walthall model [8, 9], which is a statistical model with four coefficients. This model describes the surface BRDF as a second-order polynomial function of view and illumination zenith angles, and relative azimuth angle. The four model coefficients are derived from a set of directional reflectances for each solar zenith angle by curve fitting using a least square routine.

Rahman et al. [10] developed a semi-empirical model to retrieve BRDF from AVHRR data. This algorithm has been adopted for the generation of at-launch standard BRDF products from the Multi-angle Imaging Spectro Radiometer

0-7803-3836-7/97/$10.00 © 1997 IEEE

(MISR) and has been shown to work sufficiently well over different cover types [11]. There are three parameters in this model which are derived by model inversion and iteration. This is the second model that we used to retrieve the BRDF from AVHRR data.

The above models assume that the variations in surface reflectance are caused by changes in viewing and illumination geometry only. It is supposed that the target does not change significantly over the period of measurements. However, land cover types such as grass lands and deciduous forests exhibit seasonality, and a temporal BRDF model is thus required to account for phenological variations of the land surface. The temporal BRDF model of Liang et al. [12] uses Fourier techniques to account for variations in surface phenology, and we have also implemented it in this study. This model is an extension of the modified Walthall model and has eight coefficients: four for the modified Walthall model, and four for the temporal function. All the coefficients are derived by a least square method similar to the modified Walthall model.

ALGORITHM IMPLEMENTATION

As previously mentioned, the BRDF models of Walthall [8] and Rahman et al. [10] assume that the land surface is invariant during the time of observations. Thus, to ensure the availability of sufficient data to characterize the models while minimizing the effects of surface phenology on BRDF retrieval from these two algorithms, the PAL data from 1983 to 1986 was divided in to four quarters: January-March, April-June, July-September, October-December. The CLAVR [13] cloud flags in the PAL data set were used to identify clear land pixels, and only these pixels were used to derive the coefficients of the models. However, for the temporal model, the data are not divided into discrete time intervals, and all the cloud free data are used to derive the coefficients which are valid for all the twelve months [12]. The following global images were generated as outputs from each model: model coefficients, standard errors between model predicted and actual reflectances in channels 1 and 2 and NDVI, the correlation coefficients (R^2) from the least square regression equations that were used to derive the model coefficients, and the number of points used to derive the model coefficients.

The input data for the four year time period was 27 Gbytes consisting of 1296 images. All three algorithms were implemented on a 16 processor IBM SP2 computer. The algorithms were designed in the Single Program Multiple Data (SPMD) model, where each processor executes the same code on different parts of the image.

RESULTS AND DISCUSSION

Figs. 1 and 2 show the nadir reflectance values in channels 1 and 2 of AVHRR respectively from the modified Walthall model for the third quarter (July-September) during 1983-86. To our knowledge, this is the first time the coefficients of any BRDF model have been determined at a global scale. The spatial patterns of visible and near IR reflectances shown here are consistent with different land cover classes [e.g. 14]. Densely vegetated areas (e.g. central Africa, Brazil, Temperate and Boreal forests in Asia and Europe) and agricultural regions (e.g. central USA) show high reflectances in channel 2 and very low reflectances in channel 1. Deserts on the other hand show high reflectances in both the bands (e.g. Sahara, central Australia, Kalahari).

The standard errors in channel 1 and 2 reflectances from the modified Walthall model were similar to those from the iterative model of Rahman et al. [10] for the same time period. However, the iterative model is computationally more expensive (150 minutes) than the modified Walthall model (15 minutes).

Examination of standard errors in channel 1 and 2 reflectances from the temporal model indicate that the errors were larger in temperate regions of Asia, Europe and N. America, and also across the Sahel in Africa compared to other regions of the world. These errors could be due to large inter annual variations in surface conditions in these areas caused by changes in snow cover and rain fall in the higher latitudes and in the Sahel respectively. The computational time required to run the temporal model is 25 minutes.

CONCLUSIONS

We have demonstrated the feasibility of implementing both simple as well as complex algorithms to retrieve BRDF at global scales using high performance computing. Although the iterative model of Rahman et al. [10] was computationally more intense compared to the modified Walthall model, results from the two algorithms were similar. The input data for these two models had to be partitioned into discrete time intervals to minimize the effects of surface phenology on BRDF retrieval. However, the temporal model negates the partitioning of input data based on variations in surface phenology. Errors from the temporal BRDF model were higher in temperate latitudes, and across the Sahel region in Africa compared to other locations, and this could be caused due to strong interannual variations in surface conditions in these two areas. The results from this study are unique, and are expected to provide valuable inputs into BRDF retrieval algorithms proposed for future Earth

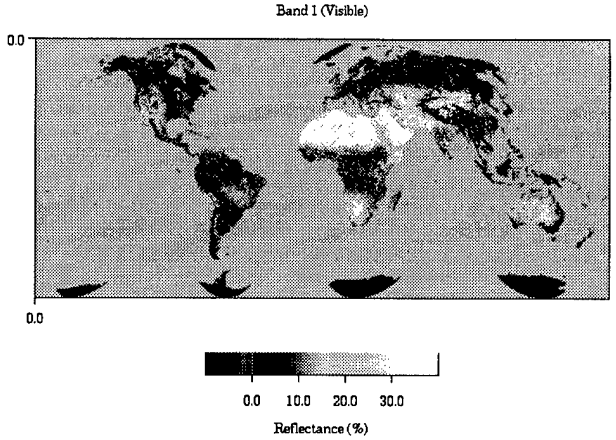

Fig. 1. Nadir visible reflectances in AVHRR band 1 for the time period July-September (1983-1986) derived from the modified Walthall model

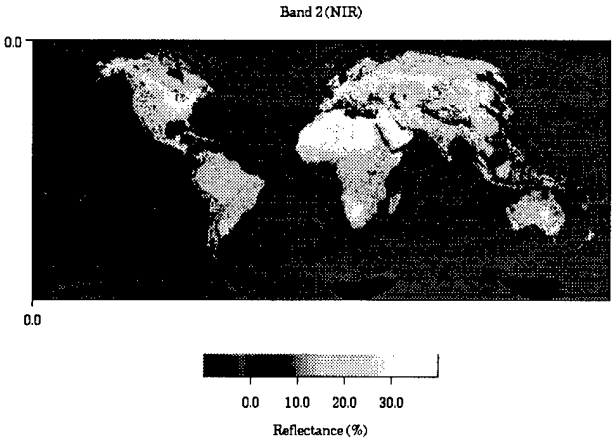

Fig. 2. Nadir NIR reflectances in AVHRR band 2 for the time period July-September (1983-1986) derived from the modified Walthall model

Observation System (EOS) instruments such as the Moderate Resolution Imaging Spectroradiometer (MODIS), and the Multiangle Imaging Spectroradiometer (MISR).

ACKNOWLEDGMENTS

This research has been made possible by a grant from the National Science Foundation (BIR9318183)

REFERENCES

[1] B. Holben, "Characteristics of maximum-value composite images from temporal AVHRR data". *International Journal of Remote Sensing*, vol. 7, pp. 1417-1434, 1986.

[2] G. G. Gutman, "Vegetation indices from AVHRR: an update and furutre prospects". *Remote Sensing of Environment*, vol.35, pp. 121-136, 1991.

[3] J. Cihlar, D. Manak, and N. Voisin, "AVHRR bidirectional reflectance effects and compositing". *Remote Sensing of Environment*, vol. 48, pp. 77-88, 1994.

[4] A. H. Strahler, et al. "*MODIS BRDF/Albedo Product: Algorithm Theoretical Basis Document (Version 3.2)*". URL: *http://eospso.gsfc.nasa.gov/atbd/modis/atbdmod09new.html*, 1997.

[5] J. L. Privette, W. J. Emery, and D. S. Schimel, "Inversion of a vegetation reflectance modelwith NOAA AVHRR data". *Remote Sensing of Environment*, vol. 58, pp. 187-200, 1996.

[6] B. H. Braswell et al. "Extracting ecological and biophysical information from AVHRR optical data: an integrated algorithm based on inverse modeling". *Journal of Geophysical Research*, vol. 101, pp. 23335-23348, 1996*of Geophysical Research*, vol. 101, pp. 23335-23348, 1996.

[7] M. E. James, and S. N. V. Kalluri, " The Pathfinder AVHRR land data set: an improved coarse resolution data set for terrestrial monitoring". *International Journal of Remote Sensing*, vol. 15, pp. 3347-3363, 1994.

[8] C. J. Walthall, J. M. Norman, J. W. Welles, G. Campbell, and B. L. Blad, "Simple equation to approximate the bidirectional reflectance from vegetated canopies and bare soil surfaces". *Applied Optics*, vol. 24, pp. 383-387, 1985.

[9] T. Nilson, and A. Kuusk, "A reflectance model for the homogeneous plant canopy and its inversion". *Remote Sensing of Environment*, vol. 27, pp. 157-167, 1989.

[10] H. Rahman, M. M. Verstraete, and B. Pinty, "Coupled surface-atmosphere reflectance model (CSAR), 1. Model description and inversion against synthetic data". *Journal of Geophysical Research*, vol. 98, pp.20779-20789, 1991.

[11] D. J. Diner, R. Davies, T. Varnai, C. Borel, and S. A. W. Gerstl, "*MISR Level 2 Top-of-Atmosphere Albedo Algorithm Theoretical Basis*". URL: *http://eospso.gsfc.nasa.gov/atbd/misr/atbdmisr08new.html*, 1996.

[12] S. Liang, and J. R. G. Townshend, "Angular signatures of NOAA/NASA Pathfinder AVHRR land data and applications to land cover identification". *Proceedings of IGARSS*, 1997.

[13] L. L. Stowe, et al. "Global distribution of cloud cover derived from NOAA/AVHRR operational satellite data". *Advances in Space Research*, vol. 3, pp. 51-54, 1991.

[14] R. S. Defries, and J. R. G. Townshend, "NDVI-derived land cover classifications at a global scale". *International Journal of Remote Sensing*, vol. 17, pp. 3567-3586, 1994.

STUDY OF THE POLARIZATION BEHAVIOR OF COMPLEX NATURAL AND MAN-MADE CLUTTER AT MIDDLE AND GRAZING ANGLES

Robert G. Onstott
Earth Sciences Group
Environmental Research Institute of Michigan
P.O. Box 134001, Ann Arbor, MI 48113-4001
Phone: (313)994-1200 FAX:(313)994-5824 Email: Onstott@erim.org

Abstract - A special mapping mission using an aircraft synthetic aperture radar (SAR) was conducted at an airport near a large metropolitan area to characterize the clutter found in association with the airport, and the surrounding area. These data were obtained specifically to support the building of a simulator for future generation radars which will operate from commercial aircraft to detect meteorological features, such as the microburst, during takeoff and landings. These data allow us to study and document the polarization and angular response behavior for a radar parameter region and clutter environment rarely studied. These behaviors are then linked to land use patterns, a topic of increasing importance for rapidly developing communities and countries with large land area.

INTRODUCTION

Knowledge of the scattering properties of complex clutter environments is important for a wide variety reasons which include: the design of radar sensing systems which observe the earth, the segmentation and identification of clutter categories, the conversion of clutter signatures to land use pattern information, and the inversion to physical property information. In the case of radars used on aircraft, the application may include the need to detect windshear and microbursts during take off and landing at an airport [1]. This investigation was conducted to refine the characteristics of clutter at (a) moderate-to-small grazing angles, and (b) to document the polarization behavior of various manmade and natural clutter regimes.

Description of the Synthetic Aperture Radar

The radar known as the ERIM/NADC P-3 SAR was used to acquire polarimetric radar data at 9.375 GHz (X-band) with a ground resolution on the order of 3 m for a grazing angle range from 2° to 45°. Polarimetric calibration was implemented so that interchannel gain and phase may be compared. Calibration was accomplished using SAR methods developed at ERIM [2]. In this case, an extensive array of calibration references targets were placed on the tarmac of an airport runway. The array included: (a) precision trihedrals, (b) dihedrals at three rotation angles, and active radar calibrators. These reference targets were used to determine the overall SAR system transfer function from the receiver to the output image product.

To study and document the angular response behavior, multiple passes by the aircraft were made of selected ground study sites. Four polarization channels were recorded simultaneously. In Fig. 1, the polarization response at HH-polarization is shown. The various study sites are annotated.

Genesis of Radar Backscatter From Clutter

Radar backscatter from natural and man-made clutter is produced due to a direct reflection from a target, from multiple scatterings from within a target, or from multiple paths such as from a ground-target interaction. The type of scattering often has a direct association with its absolute

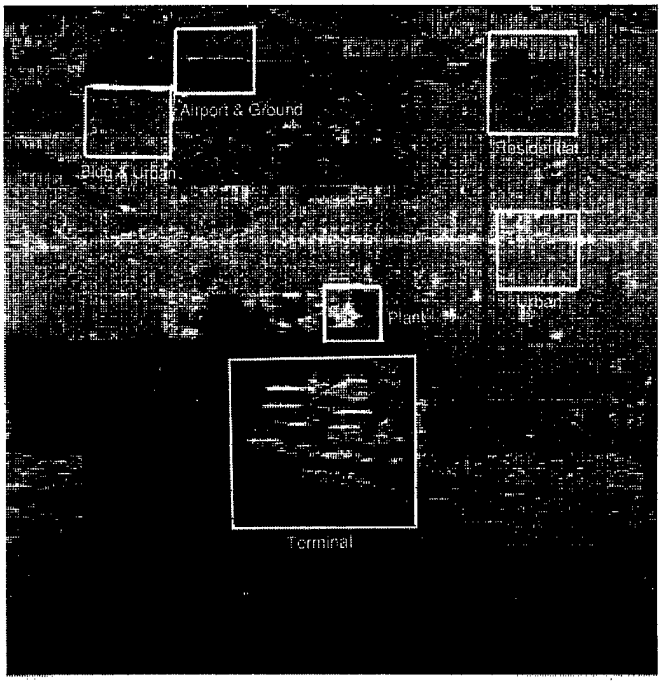

Figure 1. Denver Stapleton International Airport at HH polarization. Locations of special study areas are indicated.

0-7803-3836-7/97/$10.00 © 1997 IEEE

backscatter intensity. Ground-target scatterings are often orders-of-magnitude greater than all other scattering mechanisms. This is the scattering regime which produces the dominant scattering returns for targets observed at small grazing angles in an airport environment.

Denver Stapleton International Airport Environment

Data were collected of the Denver Stapleton International Airport, areas about the airport, and portions of the city of Denver, Colorado. This airport was chosen because it is representative of airports which serve large urbans areas. Clutter categories identified in this study area include: grass-covered terrain, tree-covered terrain, residential, urban, center city, industrial, warehouse complexes, very large buildings, very large parking lots, airport terminals, planes on the tarmac, and trucks on the tarmac. These measurements were made during mid-November when leaves were off the deciduous trees, and when there was only trace amounts of snow on the ground. Denver is located near the Rocky Mountains, flights were made parallel to the front range. Twenty-seven passes were acquired to provide data for the clutter analysis. The polarimetric radar data passes were used to form images frames of 10 km x 10km.

Data obtained from synthetic aperture radar was used because the resolution is fine enough that the correlation between the microwave response of specific image components and target types is easily performed. Oftentimes an image is similar to that obtained in oblique photography, therefore, is easily interpreted.

APPROACH

A very useful method of clutter characterization is based on using the measured samples of the received clutter power to calculate the first four moments. This results in a shape parameters, skewness, and kurtosis of the sample populations. Probability density functions were determined at the various polarizations. The retrieved clutter statistical parameters were tested as coming from clutter populations which are described according to three convenient and realistic models for clutter: Gamma, Inverse Gaussian, and Log-normal distribution types [3]. The observed sample distributions were compared to modeled distributions using a nonparametric statistical test. The nonparametric Kolmogrov goodness-of-fit test was used. Results indicate that, in almost every case, all three of the mathematical distributions matched the observed SAR image intensity distributions. Overall, the best fit was achieved using the Gamma distribution.

In addition, various polarimetric parameters were calculated to describe the polarization behavior. These include: (a) the ratio between copolarizations, the depolarization between co- and cross-polarizations, the correlation between the copolarizations, and the phase difference between the copolarizations.

DISCUSSION

Fully coherent calibrated data allows for the synthesis of any arbitrary transmit and receive polarization. This allows us to synthesize arbitrary polarizations which may be used to obtain the greatest ground clutter suppression, while producing the greatest enhancement of meteorological features. Polarization synthesis is used here to illustrate the polarization behavior of four clutter types: urban (see Fig.2) residential (see Fig. 3), plant facilities (see Fig. 4) , and the airport terminal area (see Fig. 5). Orthogonal polarizations are shown for both linear and circular polarizations.

Urban Areas

In this case, the urban clutter is segregated into a gridded system. Urban areas are found to have less extensive tree canopies, therefore buildings and streets contribute strongly to its spatial properties. Linear cross-polarizations show a behavior which is distinctively different from that of the other polarizations shown.

Residential Areas

Residential areas in cities are often characterized by the presence of mature trees. Even though the collection of manmade materials in such an area is high, the trees effectively mask the houses and other manmade objects. Curvilinear traffic ways and diffuse scattering behavior of tree canopies are characteristic of many residential area across the country.

Plants and Industrial Park Areas

Plants and industrial parks are characterized by complex building construction, large cleared areas, and cluttered parking lots. What is most notable about large plants is the ensemble of organized point scatterers which are polarization insensitive.

Airport Terminal Area

The terminal of an airport presents a critical problem to approaching aircraft in that it is a primary source of intense scatter within the immediate airport clutter area. Responses are similar at all of the polarization cases. The greatest number of scatterers are visible in the VV image when compared to all others. The terminal area response is similar to that observed for the centre city part of Denver.

Incidence Angle Response

A golf course with a few scattered trees surrounded by an urban area is used to illustrate incidence angle behavior. Angles range from 68° to 84°. The golf course is largely undulating terrain covered in grass. Its backscatter response decreases rapidly with increasing angle in this angle range. Very little backscatter is observed by 82°. The angle response for the urban area decreases more slowly. Point, and strong distributed scatterers oriented toward the radar are evident at all incidence angles, however.

SUMMARY

The polarization and angular response for various clutter categories are illustrated. The character of these clutter categories is often quite different and distinct. These differences give a clear indication of land use type.

REFERENCES

[1] Delnore, V.E., R.G. Onstott, E.M. Bracalente, Synthetic aperture radar (SAR) backscatter data at shallow depression angle for windshear detection radar research," Proceeding on the Progress in Electromagnetic Research Symposium, 25-26 July, Cambridge, Massachusetts.

[2] Larson, R.W. and A.L. Mafett, "Calibration model for SAR systems," Electromagnetics, vol. 4, no 2-3, 1984, pg 277 to 296.

[3] Miller, J.M., "Characterization of clutter and its use in maintaining CFAR operation," Electromagnetics, vol. 4, pg 185-203, 1984.

ACKNOWLEDGMENTS

This collection of the SAR image data and initial clutter analysis work was supported by NASA Langley Research Center under Contract NAS1-18465. The technical monitor of this program was E.M Bracalente.

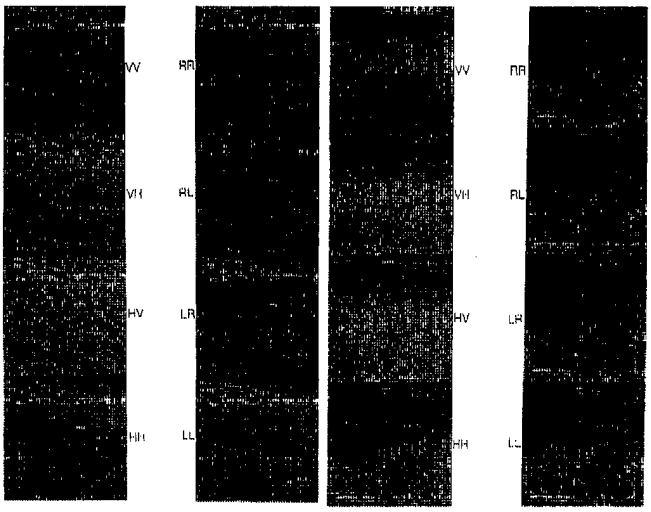

Figure 5. Urban area.

Figure 2. Residential area.

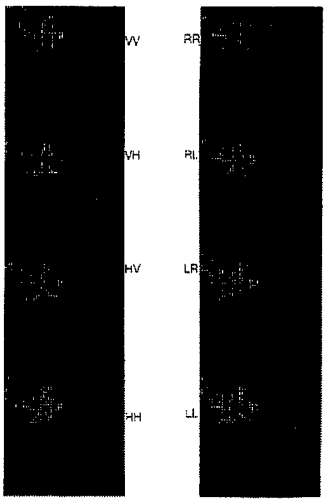

Figure 3. Plant.

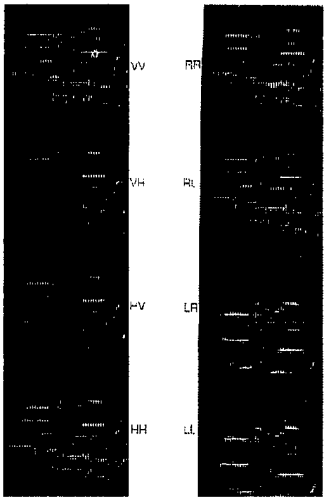

Figure 4. Airport terminal.

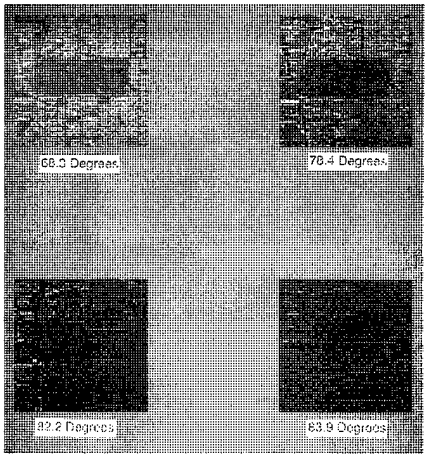

Figure 6. Golf course in urban area.

DETERMINATION OF THE EARTH'S EMISSIVITY FOR USE IN STUDIES OF GLOBAL CLIMATE CHANGE

Denise Stephenson-Hawk, Kelsha Stevens, and Ashok Shah
Clark Atlanta University
Department of Physics
Research Center for Science and Technology
Atlanta, Georgia 30314
(404) 880-6904 / (404) 880-8499 dhawk@denise.cau.edu

Abstract -- A four-dimensional data assimilation program is being developed which uses measurements of the emissivity of vegetation canopies to define the earth's surface temperature from remotely sensed measurements of radiance. Currently, there exists a paucity of data defining vegetative emissivity. The need for vegetative emissivity measurements in determining the global surface temperature from satellite radiances is established. The sensitivity of the radiance inversions to these data, however, is yet to be determined. The approach used to define the sensitivity of the inversion algorithms is presented. Provided also is the testbed developed to explore this sensitivity. A method to determine global surface temperatures given satellite radiance's and ground cover mosaics obtained from Landsat and Advanced High Resolution Radiometer (AVHRR) measurements using this sensitivity analysis is being investigated as part of this on-going study. A testbed and computer simulation to explore this sensitivity have been developed and tested. The satellite-infrared temperatures will be compared with canopy temperatures (in situ measurements) measured at ambient conditions away from direct sunlight exposure. Given this comparison, the accuracy of global maps of surface temperature obtained from satellite measurements of radiance can be defined when coupled with measurements of soil moisture and the known morphology of the vegetation.[1]

INTRODUCTION

Predictions of global and regional climate change are based upon general circulation model (GCM) estimates of temperature variability due to increased concentrations of greenhouse gases. These prognostic models require, as input, the specification of initial and boundary conditions which include global surface temperature. Global maps of surface temperature are not only needed to define the plausibility of global warming but also to enhance our understanding of the physics, structure, and dynamics of a variety of components of the Earth's interactive biogeochemical environment. The accuracy of our predictions of weather and global climate change is, therefore, dependent upon the spatial and temporal accuracy of global maps of surface temperature.

Traditional methods of measuring the surface temperature of the earth at discrete locations is cost prohibitive and impractical on a global basis, particularly, over ocean areas which comprise approximately 70% of the earth's surface. Also, measurements obtained using these methods are irregularly sampled in both the space and time domains and made using a variety of instruments, no two of which may produce identical measurements. To use these measurements in numerical modeling studies defining global climate change requires them to be interpolated onto an evenly spaced grid. This interpolation will, unavoidably, result in errors in the defined temperature field. Therefore, to obtain a more accurate and comprehensive description of the earth's surface temperature, the satellite platform is the measurement collection vehicle of choice. The use of satellite data is not only cost effective but also provides quasi-continuous, evenly spaced global surveillance of the earth's surface. If multiple satellites are used, as is proposed for the National Aeronautics and Space Administration's (NASA) Earth Observing System (EOS), then near synoptic coverage of the earth's surface variables can be obtained.

BACKGROUND

Satellite measurements of infrared radiation emitted by the earth's surface and atmosphere

[1] This work was funded by the U.S. Department of Energy contract number 136358-A-GA.

0-7803-3836-7/97/$10.00 © 1997 IEEE

can be used to infer the temperature of the earth's surface. Measurements of the emitted thermal radiation within the 8-12 micron window represent the "effective" temperatures of the radiating surfaces below a nadir-viewing satellite. These radiating surfaces are the tops of clouds in overcast areas and the Earth's surface in cloud free areas. The signal received by the satellite is further complicated by noise in the measurements and thermal radiation emitted by atmospheric gases and aerosols. The fraction of the signal attributable to radiation by atmospheric gases and reflection and absorption by aerosols must be subtracted from the satellite's retrieved signal to define the radiation emitted by the earth's surface.

The earth's surface temperature, therefore, can be defined in cloud free areas if knowledge of the space and time dependence of emissivity at the surface of the earth and the fraction of the satellite's received signal that is due to emission by atmospheric gases and aerosols is available. Methods of estimating surface temperature from satellite measurements have been described by [1]. It should be noted that previous work performed by [2] shows that the relative difference in the earth's middle atmospheric temperature at two spatial locations is better approximated from satellite measurements than is the absolute temperature at either location using these remote measurements. The appropriateness of this result as applied to the earth's surface temperature will further be explored in this study.

To define surface temperature from satellite radiances requires values of emissivity for the ground cover. Upon review of the literature, only a scant amount of data is available defining these emissivities. Therefore, enhancements to a four-dimensional data assimilation program, currently under development, is proposed to determine the sensitivity of radiance inversion algorithms to variations in vegetative and soil emissivities. Once this sensitivity is established, a procedure will be proposed and tested that will use the existing vegetative and soil emissivity data coupled with remotely sensed data, for example, AVHRR data, to enhance an existing regional and to-be-defined global mosaic map of vegetative and soil emissivity. This mosaic map, once complete, will be used to define a map of global surface temperature from satellite radiances. The accuracy of this map, as compared with in situ measurements of surface temperature will establish the need for a laboratory and field program to obtain additional measurements of the emissivity of vegetation canopies and soil moisture for use in defining the earth's surface temperature over land from remotely sensed measurements of radiance.

Temperature can be inferred from satellite radiances by making a series of approximations regarding the thermal radiation emitted by the earth's surface. If we assume that the satellite's footprint on the earth's surface acts as a perfect blackbody and there is no intervening atmosphere, then the radiance reaching the instrument can be defined by the Planck function, $W(\lambda, T_S)$, the spectral radiant remittance (or spectral excitance) of a blackbody with physical temperature T_S is defined as

$$W(\lambda, T_S) = \frac{2\pi hc^2}{\lambda^5\left(e^{\frac{hc}{\lambda k T_S}} - 1\right)}$$

Where

$h = 6.63 \times 10^{-34} J_S$, the Planck's constant

$c = 3 \times 10^8$ m/s, the speed of light

$k = 1.38 \times 10^{-23}$ J/K, the Boltzmann's constant,

λ = wavelength in meters.

Materials on the earth's surface, are not, however, perfect blackbodies but do emit some fractional part of the blackbody radiation. This fractional emitted radiance is given by the function

$$L(\lambda, Ts) = \varepsilon(\lambda) B(\lambda, T_S) = \varepsilon(\lambda) \frac{2hc^2}{\lambda^5\left(e^{\frac{hc}{k\lambda T_S}} - 1\right)}$$

where the Planck function has been multiplied by the spectral emissivity, $\varepsilon(\lambda)$. The emissivity varies not only as a function of wavelength but also depends upon the characteristics of the emitting material. Therefore, emissivities are needed to accurately infer relative spatial and temporal temperature differences on the earth's surface from satellite radiances.

Emissivity

The definition of surface temperature from satellite data is complicated by the need to quantify the emissivity of the surface cover. Emissivity is a function of the color, characteristics and wavelength of the emitting

body. The dependence of emissivity on these variables implies that it varies in the space, time, and spectral domains.

Generally, it is assumed that the emissivity of water is equal to one. Using this assumption, estimates of sea surface temperatures in cloud free environments routinely are inferred from satellite measurements. This assumption of an emissivity equal to unity is inaccurate for vegetative and geological surfaces, therefore, research must be conducted to determine the appropriate values.

To infer the surface temperature from measurements of emitted radiation received at satellite altitude, emissivity must be defined as a function of temperature and wavelength for the "footprint" viewed by the satellite. This footprint corresponds to an "area" on the earth's surface. This area has a diffuse boundary and may be comprised of a combination of several vegetation types, geological features or water types. If measurements can discern the vegetation type and geological feature, then the question of what is the "effective emissivity" of the satellite's footprint can be addressed. It is this effective emissivity, defined as a function of temperature and wavelength for the satellite's footprint, that is needed to infer surface temperatures from satellite measurements. This "effective emissivity" must be studied for a variety of plant and geological communities. Therefore, the work, as outlined, determines the surface scene viewed from the satellite platform and begins to define the effective emissivity for that scene using the existing database of vegetative and geological emissivity measurements.

The determination of the effective emissivity of the satellite's footprint is based on experimental laboratory measurements of plant and geological emissivities. These laboratory emissivities are coupled with theory defining the radiative transfer from plant communities and scene identification from Landsat satellites and AVHRR data to define the effective emissivity of an area on earth.

Because of the myriad of plants, soil types, rock formations, etc. covering the earth's surface, it is a formidable task to explicitly determine the emissivity for all scenes. A thorough search of the published literature has been performed to obtain available experimental data defining the emissivity of (1) plant species, (2) geologic formations and (3) water surfaces. A data base of these measurements has been assembled [3]. It is apparent from this search that very little is known regarding the precise functional dependence of vegetation canopy emissivities with respect to wavelength of radiation, temperature and moisture content.

The accuracy of the inferred surface temperatures is being determined via comparisons with in situ measurements over areas that are dominated by vegetation. It has been quantified, however, that the fraction of the ground in vegetative areas that has exposed soil can have a significant effect on the "effective emissivity" of the area within the satellite's footprint. Once the accuracy of the emissivities for the integrated vegetative and geological surface features is determined, the need for additional measurements of vegetative emissivity will be established. Preliminary results highlight the need for these data, therefore, a prototype laboratory set-up will be designed as part of the proposed research.

Available satellite measurements have been used to (1) define the surface cover (Landsat and AVHRR data) and (2) approximate the surface area from which radiation is emitted. This information is coupled with (1) data discerning the geology of the region, (2) existing laboratory and field measurements defining the emissivity of plants and their morphology for a region, and (3) theory detailing the emitted radiation from plant canopies, to define the emissivity needed to infer surface temperatures from satellite measurements of radiance.

TECHNICAL APPROACH

The first phase of this study has been completed. During this phase the following results were determined: (1) the approximate area of the earth's surface viewed by a single satellite measurement (NOTE: This information is required to determine the area from which the thermal radiation received by the satellite's instrument is being emitted and subsequently, the area of a typical vegetation canopy.), (2) the resolution of plant cover discernible from remote measurements of the earth's surface (e.g. [4]), (3) the types of methods available to measure emissivity of plant species, (4) an assessment of the relative merits of the existing methods of measuring emissivity and their limitations relative to providing the information needed to define the "effective emissivity" of a plant community, and (5) a database containing a

Assume that the random displacement from the uniformly ordered position is prescribed by the same statistics: $\sigma_j^2 = \sigma^2$ and

$$Q_j(\boldsymbol{\kappa}) = Q(\boldsymbol{\kappa}) \quad \text{for any } j \tag{3}$$

In addition, we introduce the following parameter

$$P(\boldsymbol{\kappa a}) \equiv \sum_{j=1}^{N} \exp\left[-i\boldsymbol{\kappa}\cdot\boldsymbol{a}_j\right] \tag{4}$$

If $\boldsymbol{r}_j$ and $\boldsymbol{r}_k$, $j \neq k$, are assumed to be statistically independent of each other: that is, all the particles may be move independently from $\boldsymbol{a}_j$ to $\boldsymbol{r}_j - \boldsymbol{a}_j$ within σ less than the average distance between particles $|\boldsymbol{a}| = a$, then N particles are completely described by the material parameters $\varepsilon(\boldsymbol{\kappa})$ and $\mu(\boldsymbol{\kappa})$ and the distribution parameters $Q(\boldsymbol{\kappa})$ and $P(\boldsymbol{\kappa a})$. Here $Q(\boldsymbol{\kappa})$ is the parameter of random displacement; hence, $Q(\boldsymbol{\kappa}) = 0$ means non-displacement and large $Q(\boldsymbol{\kappa})$ means large random displacement and $P(\boldsymbol{\kappa a})$ is the parameter of uniformity; and as $N \to \infty$, which means $N_x \to \infty$, $N_y \to \infty$ and $N_z \to \infty$, we have

$$P(\boldsymbol{\kappa a}) = (2\pi)^3 \sum_{l_x=-\infty}^{\infty} \sum_{l_y=-\infty}^{\infty} \sum_{l_z=-\infty}^{\infty} \delta(\kappa_x a_x - 2\pi l_x) \cdot\delta(\kappa_y a_y - 2\pi l_y)\delta(\kappa_z a_z - 2\pi l_z) \tag{5}$$

where $\delta(x)$ is the Dirac delta function.

The first and second moments of EM waves in a composite medium contained by the above N particles are approximately expressed as solutions of integral equations using a systematic method, and are valid for the transition region from periodic to random distribution of particles[1]. That is, when using $U = [\boldsymbol{E}, \boldsymbol{H}]_t$ where t denotes the vector transpose, then $\langle U\rangle$ and $\langle UU_t^*\rangle$, where the asterisk denotes the complex conjugate, satisfy each integral equation which includes well-known equations for two special cases that the distribution of particles for $N \to \infty$ is periodic and very sparse random; the sparse randomness means that Foldy-Twersky's approximation is valid.

The first moment yields the condition for random distribution of many particles to be random for a coherent field[2]. In order to evaluate the random condition, we introduce the parameter Δ defined as $|\langle U_p\rangle/\langle U\rangle|$ where p denotes the periodic distribution. When Δ becomes small, the distribution is regarded as such a random one that the periodicity of distribution is negligible for $\langle U\rangle$. Assuming that particles are dielectric spheres and the scalar wave approximation is valid, we can obtain Δ as a function of the wavenumber in free space k, a, ε, and the radius of the sphere b. Figs. 2 and 3 show that the distribution of particles becomes random or not according as the frequency is low or not.

Under the random condition, using the first moment, we analyze numerically the real part of effective dielectric constant of a random medium containing many dielectric spheres and show defects in the conventional methods: Foldy-Twersky's approximation(the effective field approximation: EFA), the quasi-crystalline (QCA) approximation and the QCA with coherent potential (QCA-CP) through the numerical analysis[3]. Moreover, we analyze numerically the imaginary part of effective dielectric constant of the random medium mentioned above and compare minutely the result with those of the conventional methods[4]. A part of the comparison is shown in Figs. 4, 5 and 6.

CONCLUSION

This paper shows a new approach to the scattering problem in a medium containing many particles and the advantages by calculating the condition of random distribution for a coherent field and the effective dielectric constant of a random medium. This approach is expected to be applied to the fields of remote sensing technology and material science.

REFERENCES

[1] M. Tateiba, "Electromagnetic wave scattering in media whose particles are randomly displaced from a uniformly ordered spatial distribution (invited)," IEICE Trans. Electron., vol. E78-C, no. 10, pp. 1357–1365, 1996.

[2] M. Tateiba and Y. Nanbu, "Condition for random distribution of many dielectric spheres to be random for a coherent field, " Radio Sci., vol. 28, no. 6, pp. 1203–1210, 1993.

[3] M. Tateiba, Y. Nanbu and T. Oe, "Numerical analysis of the effective dielectric constant of the medium where dielectric spheres are randomly distributed," IEICE Trans. Electron., vol. E76-C, no. 10, pp. 1461–1467, 1993.

[4] Y. Nanbu and M. Tateiba, "A comparative study of the effective dielectric constant of a medium containing randomly distributed dielectric spheres embedded in a homogeneous background medium, " Waves in Random Media, vol. 6, no. 4, pp. 347–360, 1996.

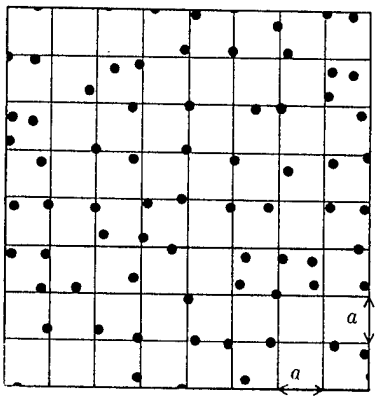

Figure 2. The distribution of spheres for $\sigma/a = 0.2$, which distribution is not random for the coherent field of $kb = 20\pi$ and random for the coherent field of $kb \leq 0.4\pi$ under the conditions $\Delta \leq 10^{-2}$ and $1 + \varepsilon = 3$.

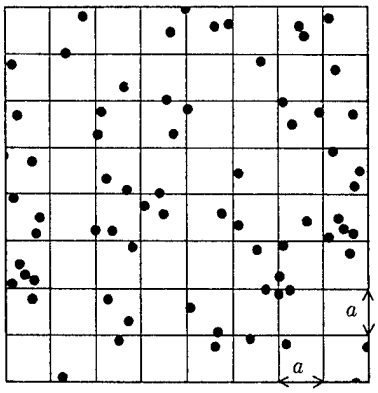

Figure 3. The distribution of spheres for $\sigma/a = 0.8$, which distribution is random for the coherent field of $kb = 20\pi$ under the conditions $\Delta \leq 10^{-2}$ and $1 + \varepsilon = 3$.

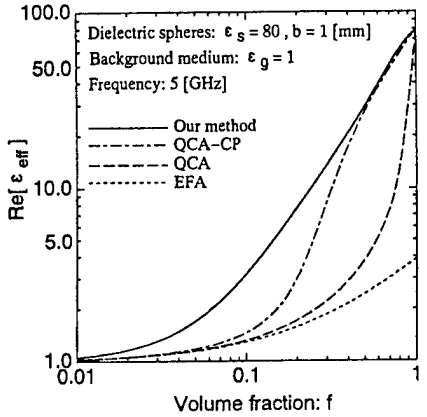

Figure 4. The real part of the effective dielectric constant ($\mathrm{Re}[\epsilon_{\mathrm{eff}}]$) as a function of the volume fraction of spheres whose dielectric constant $\epsilon_S\epsilon_0$ is $80\epsilon_0$.

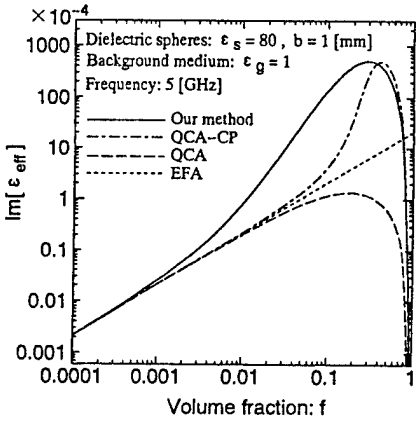

Figure 5. The imaginary part of the effective dielectric constant ($\mathrm{Im}[\epsilon_{\mathrm{eff}}]$) as a function of the volume fraction of spheres whose dielectric constant $\epsilon_S\epsilon_0$ is $80\epsilon_0$.

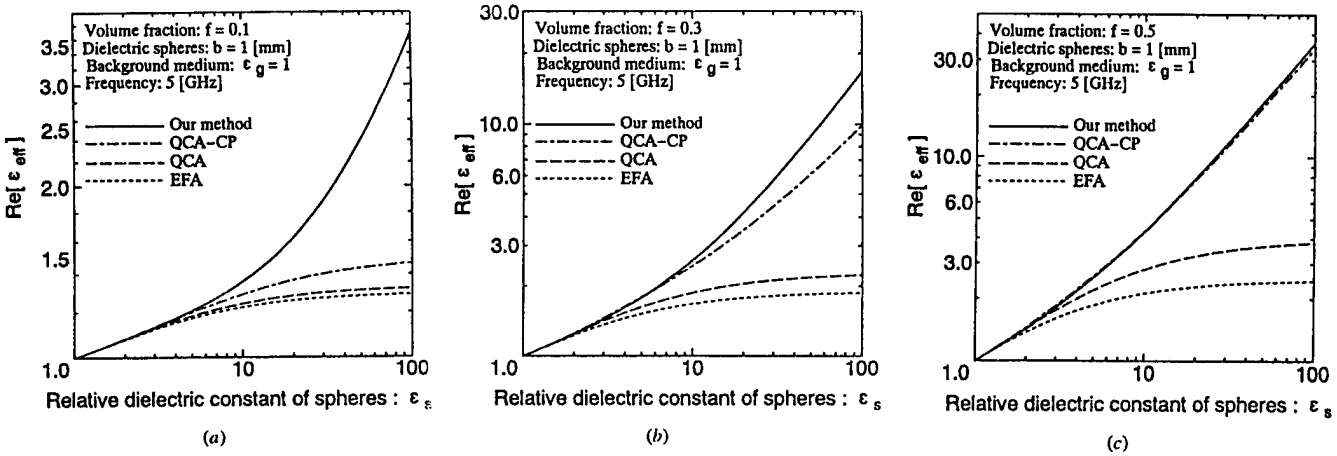

Figure 6. The real part of the effective dielectric constant ($\mathrm{Re}[\epsilon_{\mathrm{eff}}]$) as a function of the dielectric constant of spheres whose volume fraction f is (a) 0.1, (b) 0.3 and (c) 0.5.

IGARSS'97

1997 International Geoscience and Remote Sensing Symposium

03-08 August 1997

Singapore International Convention & Exhibition Centre

Technical Program

Interactive Area 11: Geology & Geomorphology

Spectral and Geomorphometric Discrimination of Environmental Units: Application to the Geomorpological Processes of Land Degradation

D. Haboudane[1], F. Bonn[1], S. Péloquin[1], A. Royer[1] and S. Sommer[2]
[1] CARTEL, Université de Sherbrooke, Sherbrooke (Québec), J1K 2R1
Tel: (819) 821 7180, Fax: (819) 821 7944, E-mail: driss.haboudane@callisto.si.usherb.ca
[2] JRC Ispra, Institute for Remote Sensing Applications, 21020 Ispra (VA), Italy

Abstract -- The Guadalentin basin, located in SE of Spain, has a semiarid climate and presents the characteristics of mediterranean landscape vulnerable to land degradation processes. This basin is one of the existing MEDALUS (MEditerranean Desertfication And Land USe) sites which has been chosen for continued intensive monitoring of land degradation and desertification in the mediterranean region. This paper presents an approach to identification of its landscape units, based on the combined use of remotely sensed data and digital elevation model (DEM) variables.

With the purpose of defining a set of indicators (spectral and topographic) for geomorphic processes and land degradation, the methodology adopted consists of radiometric corrections of topographically induced effects on satellite images and the extraction of the topographic derivatives in an attempt to classify the landscape units towards their susceptibility to land degradation. Thus, the Thematic Mapper (TM) images were used to discriminate different lithological units while the DEM was used to characterize landforms related to these lithological units. The combination of these imformations allows us to delineate boundaries of geomorphological and landscape units depending on their sensitivity to desertification processes.

INTRODUCTION

Water erosion is a major source of soil degradation in semi-arid countries. Combined with the destruction of vegetation cover, it contributes to the increase of land degradation and desertification risks. The definition and identification of areas sensitive to these phenomena requires the use of the major descriptive parameters of climate, land and vegetation. Prior research activities developed methodologies based on analysing correlations between agents of climate, physiography, lithology, vegetation and land use. While few of these parameters can be measured directly, previous studies have shown that remote sensing gains increasing importance in providing useful surrogate information. However, the extraction of geomorphically and environmentally significant information from this data source remains poorly developed because of the extreme complexity of the relationship between the spectral response and the ecological (environmental) parameters, namely geomorphic characteristics and physiographic conditions [1]. The aim of this research is the use of a remote sensing approach to evaluate the physiographic and lithologic controls on water erosion, and to classify the terrain into landscape units according to their susceptibility to land degradation and desertification processes.

GEOGRAPHICAL AND GEOLOGICAL SETTING

The Guadalentin basin, our study area, is centered about 20 km to the NW of Lorca, in Murcia and Almeria provinces, SE of Spain. It presents a semiarid climate with precipitation ranging between 260 and 400 mm and a mean temperature of about 17°C [2]-[3], and has altitudes ranging between 260 and 2036 m. These climatic conditions exert a strong infuence upon the vegetation cover, which is low and of various types, and control land-use types which are divided into semi-natural dispersed forests, scrubland, abandoned agricultural land and agricultutral land whith various types of culture like cereals and fruits. Geologically, the basin is located in the eastern sector of the Cordilleras Beticas, which is a part of the western segment of the European Alpine belt [4]. From the structural point of view, it is divided into two structural domains, the external and internal zones, differenciated by their paleogeographic and tectono-metamorphic evolution. Above these units, there is a filling material of the post-nappe basins developped after the upper Miocene.

The external zone consist of sedimentary units dominated by carbonates and marls. It comprises many lithological units including gypsum, clay, marls, limestones, dolomites, calcarenites and so forth. These outcropping materials cover about 75% of the basin area. The internal zone, which covers the southern part of the study area, consists of schists comprising different lithological units dominated by terrigeneous and carbonate materials, namely: greywackes, quartzites, conglomerates, phyllites, limestones and dolomites. The Quaternary deposits are made of clays, sands, conglomerates and calcareous crusts of small extension [4].

MATERIAL AND METHODS

Two types of data were collected for this research: satellite optical imagery and a digital elevation model (DEM). Satellite data consist of Landsat Thematic Mapper images acquired July 01, 1989 and July 25, 1992, whith the following solar illumination conditions 63° elevation, 115° azimuth and 59° elevation, 118° azimuth, respectively. The DEM was generated by stereocorrelation of SPOT

0-7803-3836-7/97/$10.00 © 1997 IEEE

panchromatic stereopairs, with a resolution of 20 m. The processing of these data was supported by other information sources like geological maps and field visits.

The methodology adopted uses an approach that combines spectral measurements, provided by remote sensing images, and geomorphometric variables, derived from a DEM, in order to define a set of spectral and topographic indicators for geomorphic processes and land degradation. The different steps of our methodoloy are summarized below.

First, the DEM was resampled to a common 30-metre grid, and served to extract the geomorphometric vatiables like slope, aspect, incidence and curvatures.

Second, satellite imagery was geometrically rectified, registred to UTM co-ordinates, and radiometrically corrected.

Third, radiometric corrections of topographically induced effects on TM images were performed using the non-Lambertian assumption and the Minnaert relationship. Thus, the satellite radiance is given by relationship [5]-[6]:

$$L(\lambda,e) = Ln(\lambda) \cos^{k(\lambda)} i \cos^{k(\lambda)-1} e \qquad (1)$$

where L = radiance of the image,
λ = wavelength,
e = surface normal zenith angle or terrain slope,
i = incidence angle,
k = Minnaert constant,
Ln = radiance when i = e = 0.

The Minnaert constant is derived by linearizing (1) and the correction of the radiance over an inclined surface to the radiance over a projected surface is achieved by the the following relationship [6]-[7]:

$$Ln = L (\cos e \cos^k z) / (\cos^k i \cos^k e) \qquad (2)$$

where z represents the solar zenith angle.

Fourth, the corrected images were used in a supervised classification, which was applied to the entire study area. The spectral classes involved in the training procedure were defined according to the lithological nature and the sensibility to the erosion factors. These definitions relied heavily on our knowledge of the terrain, on the geological maps and on the results of previous studies achieved in other similar regions of SE Spain [2]-[4].

Fifth, an integrated approach to terrain classification based on spectral and geomorphometric characteristics is proposed. It describes landscape units according to their susceptibility to land degradation and desertification processes.

RESULTS AND DISCUSSION

Correction of relief effects

A comparison between original bands and the toppographically corrected bands shows a reduction of the relief effect. This is illustrated by a removal of shadows observed on the northern and western slopes in limestone and schist regions. So, the three-dimension impression is lost in the illumination-corrected image.

These visual effects are corroborated by the substantial improvement of classification accuracy in rugged terrain regions. In fact, the overall accuracy is about 61% with original bands and about 74% with a topographically corrected bands. These moderate levels of accuracy could be related to the some confusion of spectral responses of the lithological classes belonging to the same lithological unit (i.e, calcarenite, dolomite and limestone, in carbonates unit), the spectral heterogeneity caused by the sparseness of the vegetation cover and, perhaps, the remaining relief effects.

Spectral classification

Before performing image classification, various ratios and band-combinations were used to make a preliminary visual interpretation leading to discriminate different vegetation and lithological classes. The most useful combination are the Tasseled Cap features (brightness, greeness, wetness), the false colour composites of TM bands 3,5,7 and 7,4,3; and the combination of the ratios 1/4, 3/5, 1/7 and 3/1, 4/3, 5/7.

In all, 16 classes were chosen over training and test areas and the image was classified by means of a supervised classification that used the maximum likelihood method. The accuracy of the classifcation was examined by means of the confusion matrix between training and test areas, and by comparison with geological maps. The confusion matrix leads to an overall accuracy of 74% and a Kappa coefficient of 0.70, which indicate a consistent classification results. Moreover, a visual qualitative interpretation of this classification reveals a good agreement with the existing geological maps.

The spectral classes relative to outcropping materials were regrouped to define a set of lithological units according to their sensibility to water erosion. This regrouping is based on the experience developed in our centre [8] as well as on the results of works realized on similar sites in SE of Spain [2] and [4]. The Table 1, below, summarizes the characteristics of the lithological units in decreasing order of soil sensitivity to water erosion processes.

Table 1. Definition of the lithological units in decreasing order of water erosion sensitivity (adapted from [4])

Lithological unit	Lithological characteristics	Vegetation cover	Relief
Gypsiferous	Gypsiferous sediments: gypsum, clay and marls	Low and medium bruchwood	Modrate
Marly	Marls, marly limestones	Sparse cover: Stipa, arid land grass	Low
Clayey	Clay, silts, Quaternary deposits	Cultivated lands, orchards	Very low
Terrigeneous/Schistose	Greywackes, quartzites, phyllites, conglomerates	Almond and olive trees, oak, shrubs	Moderate
Carbonate	Limestones, dolomites, calcarenites	Arboreal vegetation, high bruchwood	High

Landscape units characterization

Landscape units are described as areas of a relatively unique combination of topography, lithology, soils, and vegetation [9]. The most important parameters that define the various elements contibuting to each landscape unit are morphology, vegetation, geology, and their interactions [10]. On the basis of these definitions, we selected three types of criteria for the identification of lanscapes units: spectral, geomorphometric and textural. The spectral criterion is derived from satellite imagery, and used as a discriminant factor of different lithological units (Table 1), vegetation cover types and land-use. The geomorphometric criteria are related to landforms and are based on the expression, through the morphology, of the tectonic style and the geomorphological nature and processes. They are extracted from a DEM, and the most informative among them are slope, aspect and curvatures. The textural aspect concerns the visual analysis of patterns and shapes either on a satellite imagery or a DEM; textural patterns of slope seemed very useful for making discrimination between exposed bedrock cliffs and outcrops closely associated with carbonates, "mammillated" relief related to schist materials, moderately rugged relief of marly limestones and marls with limestone locally interbedded, gentle slopes in pediment regions, and relatively flat agricultural plains.

All these attributes were used together in an Arc/Info geographic information system in order to delineate boundaries of geomorphological and lanscape units. The rules used relied on subdividing the landscape into land components having a relatively uniform slope and aspect, and a common lithology and vegetation cover types. As slope and curvatures have a major impact on erosional processes, we used them as indicators to evaluate the vulnerability of each unit to land degradation, especially in the case of marly, gypsiferous, and clayey units that exhibit a high degree of erodability.

CONCLUSIONS

Landscape-unit analysis showed that DEM variables combined whith spectral information are very useful for land degradation assessment. This approach allowed us to segment the landscape into different units according to their lithology and vegetation characteristics, as well as their vulnerability to desertification processes.

ACKNOWLEDGEMENTS

The authors acknowledge le Programme Canadien de Bourses de la Francophonie; NSERC, Canada (A6043); and FCAR, Québec (ER2071) for their financial support.

REFERENCES

[1] G.J. McDermid and S.E. Franklin, "Spectral, spatial, and geomorphometric variables for remote sensing of slope processes," Remote Sens. Environ., vol. 49, pp. 57-71, 1994.

[2] M.T. Younis and J. Melia, "Interpretation of Landsat TM images for mapping erosion susceptibility in the area of Murcia, SE Spain," Actes du Symposium international MARISY'92, Rabat, 8 - 9 Octobre 1992, pp. 353-356.

[3] C. Forest, "Comparaison des données spectro-radiométriques et de terrain pour l'évaluation de la dégradation des sols, dans le Sud-Est de l'Espagne," Mémoire de maîtrise, Université de Sherbrooke, Québec, Canada, 1996.

[4] J. Melia, J. Bastida, S. Gandia, M.A. Gilabert, M.T. Younis, and A.L. Buendia, "Final report, MEDALUS project, " January 1993.

[5] J.A. Smith, T.L. Lin, and K.J. Ranson, "The Lambertian assumption and Landsat Data," PE&RS, vol. 46, No. 9, pp. 1183-1189, 1980.

[6] J.D. Colby, "Topographic normalization in rugged terrain", PE&RS, vol. 57, No. 5, pp. 531-537, 1991.

[7] S. Ekstrand, "Landsat TM-based forest damage assessment: Correction for topographic effects," PE&RS, vol. 62, No. 2, pp. 151-161, 1996.

[8] F. Bonn, J. Mégier, and A. Ait Fora, "Remote sensing assested spatialization of soil erosion models within a GIS for land degradation quantification: expectations, errors and beyond...," Proceedings of the 16th EARSel Symposium, Malta, 20-23 May 1996, pp. 191-198.

[9] S.E. Franklin, "Terrain analysis from digital patterns in geomorphometry and Landsat MSS spectral response," PE&RS, vol. 53, No. 1, pp. 59-65, 1987.

[10] V.B. Akerson, and E.B. Fish, "An evaluation of landscape units," PE&RS, vol. 46, No. 3, pp. 347-358, 1980.

The Design of a Methodology for Volcanic Hazard Mapping using GIS and Remote Sensing Techniques in the Bulusan Volcano Area, Bicol District, Philippines

Siefko Slob
Royal Museum for Central Africa, Department of Geology
Leuvensesteenweg 13, B-3080 Tervuren, Belgium
tel: +32-2 7695420 / fax: +32-2 7695432 / email: sslob@africamuseum.be

Abstract -- UNESCO's GARS-Asia project focuses on the application of Remote Sensing techniques for volcanic hazard analysis and mapping in the Philippines. The Bulusan volcano region in the Bicol district is one of the pilot areas in which a volcanic hazard mapping program is undertaken. Landsat TM and space borne SAR data is being used for general geologic and geomorphologic mapping of the area. A Geographical Information System (GIS) is used to create a reference database, with which the final hazard analysis will be carried out.

BACKGROUND

This decade (1990-1999) has been designated by the general assembly of the United Nations as the "International Decade for Natural Disaster Reduction (IDNDR)". One of UNESCO's contribution to the IDNDR is the implementation of activities related to the study of natural hazards of geological origin. The "Geological Applications of Remote Sensing" (GARS) programme was launched by UNESCO and the International Union of Geological Sciences (IUGS) in 1984. The first two projects of the GARS programme were implemented in Africa and Latin America. In the IDNDR framework a new phase of GARS has started in Asia, called GARS-Asia. This phase, in co-operation with the Philippine Institute of Volcanology and Seismology (PHIVOLCS), is aiming at mapping volcanic and related hazards on different target sites in the Philippines

OBJECTIVE AND METHODOLOGIES

The main objective of the GARS-Asia project is the use of advanced remote sensing techniques for the observation, description and hazard mapping of some active volcanoes in order to constitute a reference database. Geographic Information Systems (GIS) will be applied, with the use of optical and radar sensor imagery and other available geoscientific data provided by PHIVOLCS (e.g. seismics, topography, geology, etc.).

INTRODUCTION

More than 22 active volcanoes are present in the Philippine Archipelago. Many catastrophic volcanic events took place, of which the 1991 eruption of Pinatubo volcano is the best example. This event, which is considered one of the largest eruptions of this century, brought death and disaster in a wide area due to ashfall and subsequent laharic floods. The Taal and Mayon volcano, located on the Luzon main island as well, are also considered very dangerous, with an impressive record of catastrophic activities. One of the least known volcanoes in Luzon is Mount Bulusan. Although no major eruptions have been recorded, the volcano is active, with frequent mild eruptions and notable seismic activities over the years.

The main task for the Royal Museum for Central Africa within the framework of the GARS-Asia project is volcanic hazard analysis and -mapping of the Bulusan volcano area. As very few data is available for this specific volcano, the use of space borne sensors is devoted to a general geologic, geomorphologic and hydrogeologic survey of the volcano area for geologic hazard assessment. This study will demonstrate the importance of the use of remote sensing and GIS in volcano survey and preliminary hazard assessment. The methodology, which will be developed for this assignment, could be applied by PHIVOLCS for future surveys on other poor-known volcanoes in the Philippines.

BULUSAN VOLCANO

The Bulusan volcano is located in the south central part of Sorsogon Province in the Bicol region [Fig. 1]. The volcano covers an area of approximately 400 km^2 and rises 1559 meters above sea level. Mount Bulusan is part of the Bicol volcanic belt, running parallel to the Philippine Trench. The earliest recorded eruption took place in 1852 and was followed by frequent periods of eruptive activity up to 1933, mostly characterised by ash eruptions and lava outpourings. The volcano had been quiet for the next 45 years and started to show again increased activity from 1978 onwards when the volcano suddenly ejected ash and steam 1500 meters high. More mild phreatic eruptions followed up to 1983 [1]. The last recorded activity was in 1988 when a large ash ejection took place [2].

The whole geology of the Bulusan volcanic complex can roughly be divided into two periods: the so-called Pre-Irosin caldera volcanics and Post-Irosin caldera volcanics. The division of the two periods is characterised by the Irosin Calderagenic event, a major eruption of rhyolitic pumice flows which occurred about 40000 years ago, and resulted in the formation of the 11 km wide Irosin caldera [3]. The Present Bulusan volcano, located in the centre of the Irosin Caldera, is mainly of andesitic composition and is part of the last stage of the Post caldera volcanic complex. The types of

0-7803-3836-7/97/$10.00 © 1997 IEEE

volcanic hazards that can be identified in the Bulusan volcano area are:

- Lava flows
- Pyroclastic flows
- Tephra fall
- (Syn-eruption) lahars

VOLCANIC HAZARD MITIGATION

It is clear that Mount Bulusan could pose a serious threat for people living in the vicinity of the volcano. To mitigate the effects of natural hazards, a complete strategy for disaster management is required [4] [5], which involves the following aspects:

- Disaster prevention (hazard, vulnerability and risk analysis applied to planning)
- Disaster preparedness (warning and monitoring of disasters)
- Disaster relief operations

The Philippine Institute of Volcanology and Seismology (PHIVOLCS) is already carrying out various activities for volcanic hazard mitigation in the Philippines. Several schematic hazard maps and disaster preparedness plans [6] for the Bulusan volcano area have already been made or are in preparation.

VOLCANIC HAZARD ANALYSIS

The first and most essential step in disaster prevention is the hazard analysis. It is very difficult though, if not impossible, to predict a catastrophic volcanic event. What is possible is to attempt to determine the potential magnitude of a future event by examining the character, and extent of historic volcanic activities in an area. This involves detailed study of the recent geology with emphasis on the succession and character of volcanic events. Together with the information on the present physical characteristics of the volcanic area, such as topography, drainage patterns and other geomorpho-logic features, an estimation can be made about the conceivable magnitude of future volcanic disasters and the possible affected areas. In this study emphasis is placed upon geomorphologic mapping of the Bulusan study area, i.e. recognition and outlining of ancient lava flows, lahar deposits and pyroclastic flows by study of their geomorpho-logic characteristics.

In order to make this analysis, extensive information has to be gathered. Not only a thorough understanding of the geology, but also detailed information on the present geomorphologic, hydrogeologic and geographical characteristics of the subjected area has to be available. In the case of the Bulusan volcano area, limited information is present. Additional information has to be obtained using satellite data and fieldwork.

REMOTE SENSING- AND GIS ANALYSIS

Because of the tropical climate of the area, thick cloud cover is mostly present throughout the year, it has been very difficult to obtain cloud-free optical satellite imagery. One Landsat TM image has however been acquired with almost no cloud coverage. Stereo-SPOT data was preferred, because of higher resolution and the possibility for creating a Digital Terrain Model (DTM) of the area. Cloud coverage prevented SPOT to obtain good-quality images, notwithstanding the fact that programming of more than one year of acquisition has been carried out.

Therefore an attempt was made to obtain SAR radar images of the area, where no problems with cloud coverage occurs. ERS-1 [7], JERS-1[8] and RADARSAT [9] data have been acquired for this purpose. Because of the nature of the SAR images, large distortions due to topographic differences occur. These images can be corrected for the topography with information from a DTM of the area. Creating a DTM is extremely labour-extensive and thus very costly. Time has been saved in this instance, where topographic contour maps were available which could be scanned and converted to digital contour lines in the GIS.

From the Landsat image, the corrected and geocoded SAR images and the geologic information that was present in the form of maps and reports a geomorphologic map had been made, which had to be verified in the field. The abundant vegetation in the area, rice paddies in the valleys, coconut and abaca plantations on the lower slopes and lush tropical forest in the higher areas and steep slopes, hampered both the remote sensing interpretation as well as the field verification significantly.

The existing information (in the form of maps, reports, etc.), the information obtained from the satellite images and the fieldwork data are being combined in a GIS (ArcInfo) database. Once a complete reference database has been created the final hazard analysis will be carried out in the GIS and the result will be presented in hazard maps, depicting the danger areas.

CONCLUSION

The most important outcome of this exercise should be a practicle methodology which can be applied to poor-known volcanic areas in order to create an accurate reference GIS database. When a GIS database has been established it will be possible to objectively and accurately create volcanic hazard maps.

REFERENCES

[1] Volcanoes of the Philippines. PHIVOLCS publication,

1995.
[2] Bautista, L. P. "The 1988 Bulusan volcano activity". PHIVOLCS Observer, Vol. 4. No. 1. 1988, ISSN 01-16-07-45
[3] Delfin, G.F. 1991. "Petrogenesis of Mt. Bulusan volcanic complex, Bicol Arc, The Philippines". PhD-thesis Department of Geology, University of South Florida.
[4] OAS. 1990. "Disaster, planning and development: Managing natural hazards to reduce loss". Department of Regional Development and Environment. Organisation of American States. Washington, USA. 80 pp.
[5] UNDRO. 1991. "Mitigating natural disasters. Phenomena, effects and options". United Nations Disaster Relief Co-ordinator, United Nations, New York. 164 pp.
[6] Tayag, J. and Daag, A. 1988. "Disaster preparedness in Bulusan volcano danger zones". PHIVOLCS unpublished report.
[7] From: ESA, Appelle d'Offre France (AOF) #106
[8] From: NASDA, Research Agreement # 372. MITI/NASDA retains ownership of the data. NASDA supports author in acquiring the satellite data.
[9] From: RSI, Application, Development and Research Opportunity (ADRO) # 667

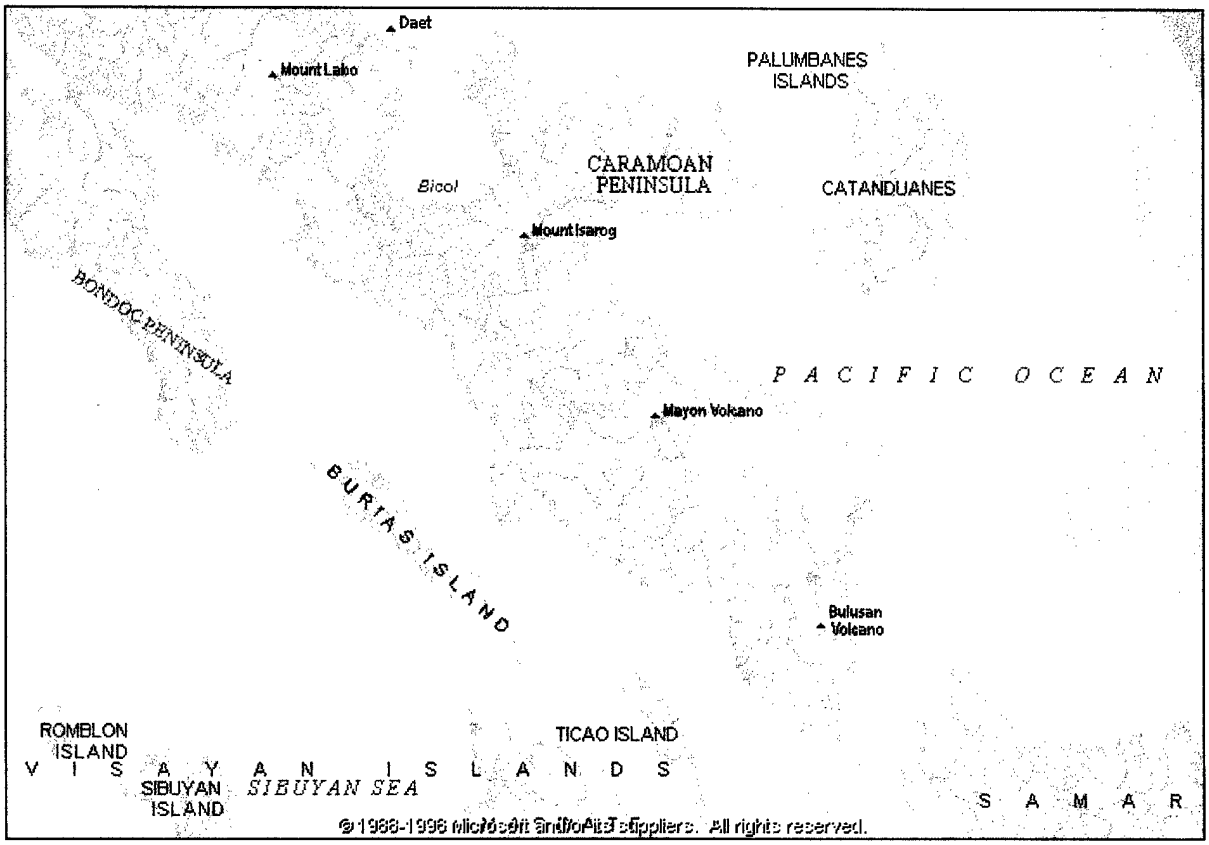

Figure 1. Bicol Region, Philippines

IGARSS'97

1997 International Geoscience and Remote Sensing Symposium

03-08 August 1997

Singapore International Convention & Exhibition Centre

Technical Program

Interactive Area 12: GIS

Desertification and land degradation using high resolution satellite data in the Nile Delta, Egypt

Hashem M., El-Khattib[1], Professor (Chief Researcher)
Nabil M., El-Mowelhi[1] and Director of SWERI
Ali Abd El-Salam[2] Professor Soil Science
1. Remote Sensing and Soil Information System, Soil, Water and Env. Res. Ins. (SWERI),
2. Soil and Chemical Department, Faculty of Agriculture, Moshtohor, Zagazig University.
Mailing address: 2 El-Nokali st., El-Nadi El-Riadi st., El-Haram area code, 12111, Giza, Egypt.
Tel : 202-5687421, 202-5720608 Fax: 202-5720608

Abstract -- Recently, recognition of the severity of the desertification problems in Egypt began to grow. Remote sensing data of different spectral, spatial and temporal resolutions and other ancillary data were used, including LANDSAT and SPOT images, topographic maps, soil survey studies conducted in 1963. Cases of land degradation and desertification in Egypt, especially soil salinity and urban desertification, are increasingly visible. The current investigation aims at studying desertification and soil degradation of agricultural lands in the north eastern part of the Nile Delta, adjacent to lake Manzala, Egypt. Modern techniques and most-up to date of satellite data using Multitemporal image processing analysis and the data were combined in CARIS GIS software for land degradation processes and calculations. Pedological, physiographic features and soil profiles were carefully studied with guidance of SPOT image for 1992 and LANDSAT TM for 1995. Soil samples were analyzed, maps of salinity and urban areas were carried out. The obtained results was compared with data collected on the same area in 1963 by the soil survey research department of the Soil, Water and Environment Research Institute (SWERI). Salinity and sodicity of soil was increased during the 1963-1992 period. Most of substantial changes in land degradation phenomenon in both soil salinization and urbanization are expected in the north eastern part of the Nile Delta in Egypt. Multitemporal images were processed for 12 settlements (villages and towns) for the period of 1952, 1963 and 1992, there were considerable 1952 urban expansion of using 40 years. The magnitude of increase in 1992 compared with 1952 was 1.1 to as high as 46 folds. Soil degradation and urban encroachment onto cultivated land are loss of productive lands as well as low values of NDVI are expected.

INTRODUCTION

Egypt has the lowest area of agricultural land per person of any country in Africa. Thus degradation or a decrease of the area of this vital resource could have devastating negative consequences. Under arid and semi-arid conditions especially in the areas of poor natural drainage, there is a potential hazard of salt accumulation and desertification. There is the hazard of saline-water intrusion from sea and salty lakes especially at the Northern part of the Nile Delta. Soil desertification and deterioration is closely related to many environmental factors such as, climate, geological, geochemical and hydrological conditions. The bad quality or misuse of irrigation water would also lead to soil salinity and/or soil sodicity. Also, there is urban desertification every where in Egypt, and particularly within the Delta, agricultural lands are being lost to urban expansion. UNEP considers desertification as a major environmental problem. According to UNEP, 35% of the world's land surface is currently at risk and more than 20 million hectares are reduced annually to near or complete uselessness. According to [1] 13% of desertified lands are mainly due to changes in the natural environments. The other 87% are mainly due to human mismanagement of resources, including overgrazing, over cultivation, deforestation, and inefficient or destructive irrigation practices. In Africa's 18% of arid land are severely desertified, 11% are moderately desertified, and 80% of the agricultural arid land of the world have moderate or severe desertification [2].

The objective of the current investigation is to studying desertification and soil degradation of agricultural lands in the north-eastern part of the Nile Delta, around lake Manzala, Egypt. Remote sensing techniques of satellite data using image processing analysis and Geographic Information System GIS were employed in this study.

MATERIALS AND METHODS

This work was conducted to study soil degradation and urban desertification in the areas

0-7803-3836-7/97/$10.00 © 1997 IEEE

adjacent to Manzala lake. Soil survey for the are of study had been done in 1963 and a map was made for such [3]. A SPOT image scene covering the same area having 112 K, 287 J acquired on 10/8/1992, and a LANDSAT TM image data Path 176, Row 38 was acquired on 2/8/1995 were used. Information were transformed from the topographic maps having scale of 1:100,000 acquired on 1952. EASI/PACE PCI image processing software under Sun Sparc-2 Workstation. The remote sensing output of PCI was converted to display and process on Computer Aided Resource Information System CARIS GIS software to elucidate degradation (either from salinization or urbanization). Thus an assessment about soil degradation and urban desertification would be possible.

Field investigation, were carried out to identify, classify and map soils under investigation. Soil profiles were dug to 150 cm or the ground water in a number of places in order to support the assessment. According to the variation in the morphological features of the soil profile, soil samples were collected at ten locations in 2 major areas, nine in El-Manzala area where saline lands salt crust make spots with little plant cover and one in Al-Hosinaia area represented a land of rather medium salinity with plant cover (clover).

The following analyses were carried out on the soil samples, particle size distribution [4]. Electrical conductivity EC, different soluble ions in the saturation extract and pH values in the soil paste, irrigation water, ground water, other natural waters and Exchangeable cations [5].

Data were assessed through multitemporal processed and analysis in terms of; soil degradation mainly regarding salinity by comparing the obtained data 1995 with old data taken from the same areas in 1963 and urban desertification during the period between 1952 and 1992.

RESULTS AND DISCUSSION

One of the greatest threats to agricultural production in Egypt is the desertification of agricultural land. Several processes contribute to the removal of landform agricultural production. They include; the salinization of soils, changes in land use such as urbanization, the covering of fertile soils by wind-blown sand, and loss of agricultural land to urban expansion and for building purposes. In the current study, data of soils analysis of profiles taken during 1995 were compared with similar data on soils taken in the same region during 1963. (Soils of the 1995 study were in locations rather similar to those of the 1963, in order for comparison to be of relevance). Such a comparison may reflect the extent of degradation or changes. Besides satellite data and aerial remote sensing during 1952 to 1995 were used in order to give indications of urbanization growth.

By comparing the total soluble salts (EC) of soils in profiles taken by the 1963, and those of the profiles take in the current study. It seems that in many cases, increases in the total soluble salts (EC) values occurred between 1963 and 1995, particularly for the uppermost layers as well as the deep layers of the soil profiles. Under arid and semiarid conditions as well as under conditions of poor natural drainage, there exists a real hazard of salt accumulation in soils. Most of the studied soil profiles of these locations have shallow and extremely saline ground water. Soil sodicity data which is mainly associated with the excess of exchangeable and soluble sodium, it expressed as soluble sodium percent (SSP), or sodium adsorption ration (SAR), or exchangeable sodium percent (ESP) were high for soil profiles in 1995 than in 1963. This may have been due to a shallow and high saline ground water as well as an increase in soil salinity illustrate such a sodicity degradation during 1963-1995 period. Concerning the soil pH values of the studied areas the data reveal obvious increase during the same period.

Since the construction of High Dam, considerable changes have occurred to arable soil in Egypt. Some of these changes affected by irrigation systems, water hydrostatic pressure against sea water intrusion, crop rotation, drainage systems, and soil management practices. The changes must have contributed to the salinization and alkalization of the soil. The inverse in soil salinity, soil sodicity and pH values during there 33 years reflects land degradation.

In the current study urbanization growth concerns expansion of old urban settlements which had already been established in the midst of agricultural lands. Therefore, it does include the creation of new settlements in the investigated areas. Nor does it include the settlements established in previously unproductive lands such as those in the desert lands or in coast lands, or in

areas previously identified as fields of reduced productivity or degraded lands. In this case, urbanization growth discussed in this investigation concerns lands that were taken out of production during the course of the time period studied (1952-1992). To assess urban expansion of some settlements in this study, multitemporal features for the change detection analysis were processed using CARIS GIS software. Urban areas for 12 settlements (villages and towns those are Al-Mataria, Al-Manzala, Al-Aziza, Al-Bosrat, Al-Gamalia, Meet Maraga Salsel, Meet Salsel, Al-Gawaber, Domiata, Faraskor, Raas El-Bar and Al-Hosinia) were calculated for 1952, 1963 and 1992 and compared to estimate urban areas topographic maps 1952; also a most up-to-date LANDSAT TM data was acquired on 1995 illustrating land use for the investigated areas. Comparative assessment of urban expansion area during 40 years were considerable. In 1952 the urban areas of selected human settlements (towns, villages, ... etc.) varied between 8 acre in Meet Maraga Salsel to 449 acre in Damiata areas. In 1992 increased, ranging from 47 acre in Al-Gawaber to as high as 2642 in Damiata. The magnitude of increase in 1992 compared with 1952 was 1.1 to as high as 46 folds. The nature of urban expansion, its direction and its extents were discussed.

From the remote sensing point of view, a land changes from a productive agricultural landform into desertification phenomena (degraded soil and urban land), there are changes in its Normalized Difference Vegetation Index (NDVI) values. While the land is cultivated, there initial high NDVI values. Once the land is not under agriculture subsequent NDVI values are low. A common source of confusion is the similarity between urban areas and uncultivated fields. Both have low NDVI values. This is true whether actual buildings are constructed on the site or the land rendered fallow or became saline soils with no plant canopy cover it or land merely taken out of production. A determinant NDVI value is measured for the SPOT and LANDSAT TM data. Healthy productive fields have high determinant NDVI values; urban and non productive fields have low determinant NDVI values. Thus, soil degradation and urban encroachment onto cultivated land are defined by both loss of productive lands and the severity of loss in NDVI determinant value.

CONCLUSIONS

Results show that in a span of 40 years there was a marked degradation of soils of North east of the Delta. This is most certainly a general trend which occurred in nearly all of agricultural lands of Egypt. The deterioration is reflected in an increased soil salinity and a formation of shallow ground-water table. Besides, there also, was a desertification of an urban nature. Even in such regions of the North Delta, where, population densities are not very high, a considerable portion of lands was lost to urban expansion. The urban area of settlement (villages and towns) in the study area increased several folds ranging from 1.1 to as high as 46 times during this period. There may be cases of expansion of great magnitudes, elsewhere in other Egyptian regions, particularly those of high population densities, such as Giza, Monofiya and Kaliobeya Governorates. Therefore, it is essential that an efficient and practical policy is needed to rectify and stop deterioration of arable lands and loss of important and relevant goals examples of which are as follows: a) Encouragement of land reclamation, particularly in new lands in the desert areas. b) urban expansion in the desert lands, c) encouragement of migration to the areas of new lands, and d) encouragement of establishing more new cities.

REFERENCES

[1] FAO, "Keeping the land alive: Soil erosion, its causes and cures" FAO Soils Bull. No 50, Rome, 1983 PP 3-25.

[2] H.E. Dregne, "Arid land development and the combat against desertification: An integrated approach." USSR Commission for UNEP, Moscow: Centre for International projects GKNT, 1986.

[3] SWRI, "Reports on soil survey of some areas in Dakahliya Governorate, Nile Delta "in Arabic), Depart of Soil Survey, Soil & Water Research Institute (SWRI), 1963, Ministry of Agric., Cairo, Egypt.

[4] C.S.Piper, "Soil and Plant analysis" Int. Sci Publishers, Inc. New York, 1950, USA.

[5] M.L. Jackson, "Soil Chemical Analysis" Prentic Hall of India, Private Ltd., Newdelhi Publ. Dept of Soils, Univ. of Wisc., 1963, USA.

On Integrated Scheme for Vector/Raster-based GIS's Utilization

Kwang-Soo Kim, Min-Soo Kim and Kiwon Lee

GIS Research Lab./Systems Engineering Research Inst.

P.O. Box 1, Yusung-gu, Taejon, 305-333, KOREA

Phone : +82-42-869-1465

FAX : +82-42-869-1479

E-mail : {enoch, minsoo, kilee}@seri.re.kr

Abstract: Recently, integrated Vector/Raster-based Geographic Information systems (GIS) is regarded as one of important issues for wide applications of GIS such as environmental studies, geoscientific approach, natural disaster prediction, urban utilities, or AM/FM (Automatic Mapping/Facilities Management). For this purpose, major vendors have provided concerned-modules in GIS S/W packages with us; however, it is somewhat difficult and high-cost task if not provided integrated system, even though its result normally present very significant ones toward a given GIS task. In this paper, we present one of GIS's results for this kind of approach, as the experimental study at Seoul, composed of vector data sets and remotely sensed image. Meanwhile, we developed Vector/Raster-based GIS using C and X Window/Motif on UNIX. Data structure, spatial operators, and accessibility to external-DBMS within these systems is basically similar to commercial GIS S/W packages, but main goal for this development is to provide cost-effective integrated system. Current main GIS's functions in this system is vector layer editing/error handling function, spatial query in access of DBMS, in/out zooming of vector layer on raster image, interested area exaggeration function, generation of vector topology, vector in/out buffering, vector/raster overlay or superposition and so forth. In this paper, key ideas of implementing process for this integrated system are presented, and then the following simultaneous utilization of vector/raster GIS under this system are also demonstrated. Finally, some technical suggestions for this kind of GIS development will be presented for further research through several actual cases.

INTRODUCTION

Generally, GIS can be defined as a computer-based integrated information systems that provide core modules for capturing, modeling, manipulating, retrieving, analysis and presentation of geographically referenced data[1]. GIS is divided into two categories according to data structure for representing topological information in space.

One is vector-based GIS system and the other is raster-based GIS system. These two approaches are distinguished by data modeling scheme of geographic information. They have peculiar their own features; furthermore, they have been inclined to develop in their own unique field. The raster-based GIS divides the objects of real world into uniform cells and represent the location and attribute of these cells. The vector-based GIS represents the objects of real world as three basic kinds - points, lines, and areas - in order to represent spatial information as accurately as possible. This type of GIS stores and manages data to be combined these three elements[2]. However, since the real world of geographical variation is infinitely complex and often uncertain, either vector or raster is insufficient for describing geographic reality. Approaches for combining the strength of vector structure and raster structure have processed in this study. Concerned with this kinds of approaches, Peuquet previously suggested a Vaster structure to be combined the chain code of raster structure and vector structure. But this vaster structure

0-7803-3836-7/97/$10.00 © 1997 IEEE

has been not realized but stayed in conceptual level[2]. In this paper, we proposed an integrated model for vector/raster-based GIS. This integration was accomplished, not at data structure level but at application level for using the strength of vector structure and raster structure.

INTEGRATION MODEL OF VECTOR/RASTER

The Feature of Raster Model

The use of a raster data structure in GIS can be summarized as the following reasons: First, the data structure is easy to understand. Second, the storage and manipulation of raster data in a computer is straightforward. Third, computer display devices - from color video displays to high resolution film recorders - almost exclusively use raster display technology[3]. Fourth, raster structure is closely related to remotely sensed imagery which is used to pixel processing. Fifth, this structure is easy to overlay several map sheets, each representing a different thematic coverage of the same geographic area. Sixth, raster data can directly be utilized to spatial operation focused on terrain analysis. However, raster data when stored in a raw state with no compression can be extremely inefficient in terms of usage of computer storage[1]; therefore, raster structure does not appropriate representation multi-dimensional space. In some extents, raster data have lower spatial accuracy than vector data, and they does not appropriate topological analysis, as general viewpoints of GIS utilization.

The Feature of Vector Model

Generally, vector-based systems should use less storage capacity than a raster based system of high resolution enough to emulate vector entities. Vectors are an appropriate representation for the higher-dimensional space and a wide range of spatial data[1]. The accuracy of vector data is higher than raster data. A vector data structure is convenient to represent the objects in real world. One of vector-based GIS's cores is to build topology which means spatial relationship between entities, and network analysis is one of popular GIS application by using topological operation. However, a vector data structure is more complex than raster data structure and this structure is complex to overlay several map sheets[4].

Integration Model

There is a integration model of vector/raster data structure. It is vaster structure which was proposed by Peuquet. But this vaster structure has been not realized but stayed in conceptual level. Since, a vector and a raster are different approach, it is far more useful method than to combine at data structure to combine the strength of vector and raster according to the characteristic of GIS's application. To this integration model, the data conversion between vector and raster will be hot issue. About the data conversion problem, Vector-to-raster conversion is perhaps easier than the raster-to-vector conversion [5].

In this paper, we proposed an integration model to consider the convenience of data conversion. This model employed vector data structure for capturing and storing geographic data and raster data structure for representing the process result in screen. In the data processing procedure, we simultaneously used vector data and raster data according to the convenience of data processing. There are two methods to display the processing result using raster data in screen. The first is panning window method. This method uses a panning window of uniform size to represent raster data. This window could be toggled. An example of this approach represented in Fig. 1. Because the window could be moved in the working region, we moved the window at the wanted location for comparing vector data to raster data and could certify the accuracy of vector data and processing result. The second is that vector data are overlaying on raster data. An case using this method demonstrated in Fig. 2.

DATA PROCESSING MODULE

Connecting raster data and vector data

In this integration, we used the name of raster data to connect vector data and raster image. Since one raster image can be connected to more than two vector data, we attached the number of raster image after the name in order to classify the raster image when the raster image was opened.

Vector layer editing/error handling module

Some errors could be made in the creating vector according to the accuracy of digitizer. In this study, the error

was found automatically and the error was displayed in screen. Then the panning window was moved the location. Being compared vector data and raster data, the error, which were overshoot, undershoot, and opened polygon, was automatically corrected.

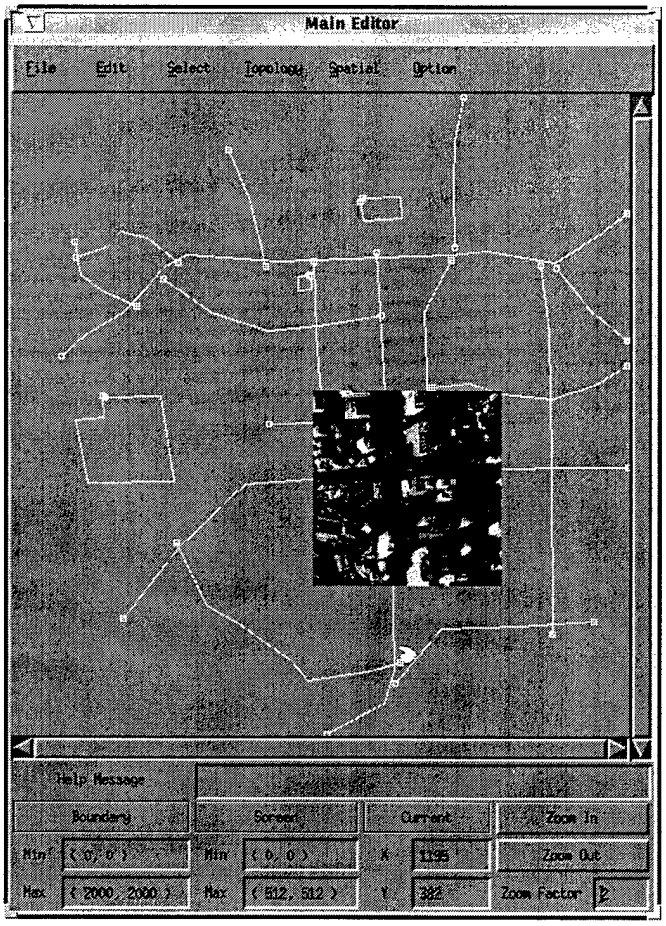

Fig 1. Representing raster using Panning Window

Spatial operators

Raster data can be used to effectively process some analytical queries such as overlays, proximity, and Boolean queries[4]. A few calculations are required to determine relative positions between layers, as long as initial georeferencing is done.

Vector/Raster overlay

In vector system, complex geometrical algorithms are needed in polygon overlay to avoid generation spurious polygons[4]. These requirements slow the response times of vector based systems. Therefore, various overlay are far more convenience in vector system than in raster system. After each polygon which has vector form is converted raster form, the overlay operations are processed. Then the result of overlaying is converted vector form. The vector formed polygon is converted easily to raster form using Point-in-Polygon algorithm. The major disadvantage of this approach is the loss of detail due to coding problems for assigning single values to pixels and the amount of area misclassified due to the rounding of area into a whole cell unit[6].

Fig 2. Vector overlaying on raster

Generation of in/out buffer

In GIS, the buffering is very useful function. The buffer is created around points, lines, and areas. The result by buffering operation becomes new areal information. In raster system, the buffering is performed easily to extend/reduce the spatial object. While in vector system, the buffering is required complex calculation. Therefore, the buffering is more convenience in raster system than in vector system. After a vector data is converted to raster data and creates buffer zone, the buffer zone is converted to vector data

through vectorization along the boundary of the buffer zone. The result of buffering is divided into two area, in buffer and out buffer.

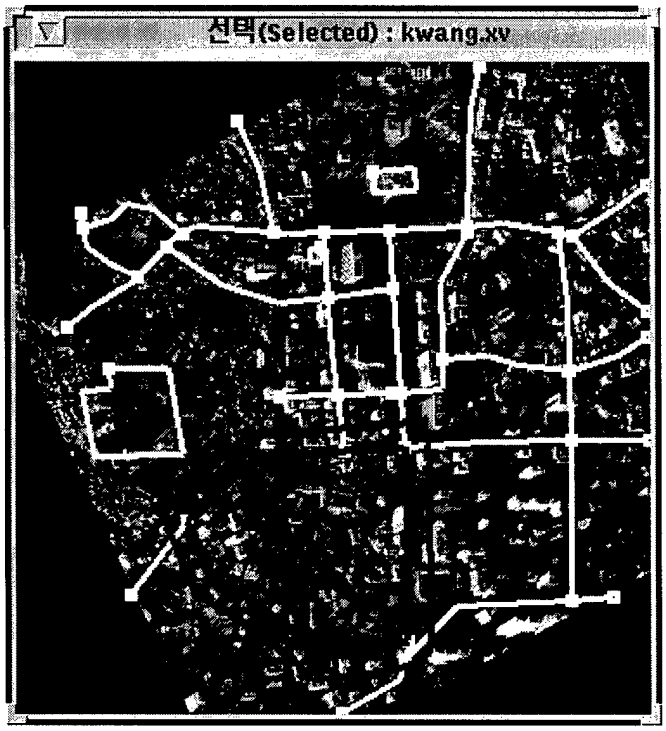

Fig 3. Polygon buffering

Generation of vector topology

This involves calculating and encoding relationships between the points, lines and areas, so vector topology is very complex. But vector topology is more convenience than raster topology.

CONCLUSION

In this paper, we proposed an integration model for vector/raster-based GIS's utilization. In this model, the integration was accomplished not at data structure level but at application level for using the strength of vector structure and raster structure. There were three basic characteristics: First, a vector data structure was used for capturing and storing a geographic data. Second, a raster data structure was used for representing the processing result in screen. Third, in order to reduce the difficulty and computation time, vector and raster were used in the processing procedure.

REFERENCES

[1] M.F. Worboys, "GIS : A Computing Perspective ", Taylor&Francis, 1995.

[2] K.B. Yoo, "A handbook for GIS supervisor course", Systems Engineering Research Institute, 1996, pp.14-21.

[3] A.H. Robinson , J.L. Morrison, P.C. Muehrcke, A.J. Kimerling, and S.C. Guptill, "Elements of Cartography", John Wiley & Sons INC, 1995.

[4] C. Parson, "Tutorial of GIS", NCGIA, 1995.

[5] R. Laurini and D. Thompson, "Fundamentals of Spatial Information Systems", Academic Press, 1992.

[6] R. G. Cromley, "Digital Cartography", Prentice-Hall, 1992.

Precision Rectification of Airborne SAR Image

Liao Mingsheng Zhang Zuxun
Wuhan Technical University of Surveying and Mapping, Wuhan 430070, China
Tel:+86-27-7881292 Fax:+86-27-7884185 Email: liao@wtusm.edu.cn
Poul Frederiksen Jergen Dall
Technical University of Denmark, 2800 Lyngby, Denmark
Tel:+45- 4525 3846 Fax:+45- 4593 1634 Email:jd@emi.dtu.dk

Abstract

A simple and direct procedure for the rectification of a certain class of airborne SAR data is presented. The relief displacements of SAR data are effectively removed by means of a digital elevation model and the image is transformed to the ground coordinate system. SAR data from the Danish EMISAR[7] is used. The EMISAR produces data with a geometrical resolution of 2.0 meters. The corrected image is tested against photogrammetric control measurements and an accuracy better than 0.5 pixel corresponding to 0.75 meters is obtained. The results indicate promising possibilities for the application of SAR data in the difficult process of map revision and updating.

Introduction

Synthetic Aperture Radar (SAR) has become one of the most attractive sensors in remote sensing since it can work almost independently of the atmospheric conditions and the time of the day. The geometric rectification of SAR data, which includes reduction of the relief effect and geo-coding of the image data, is a key issue in many applications of SAR data, where it is necessary to integrate the SAR data with other data sources. However, the rectification procedure of SAR images is different from that of conventional optical sensors because of the different imaging principles [1][3][4].

The methods for rectifying the radar images have been investigated by various researchers. Some two-dimensional image transformations have been tested in the case of large scenes [1][2]. These transformations are, however, not capable of reducing the distortion induced by the relief displacement.

Toutin et al. have presented an integrated method for rectification using a Digital Elevation Model (DEM) [4]. The investigators used a photogrammetric approach with the bundle adjustment technique based on the collinearity equations. The result obtained was about 10 meters measured as the root mean square (RMS) of the coordinate residuals in the ground control point (GCP).

Another procedure was presented by Olmsted where the SAR data was transformed into the cartographic coordinate system and then corrected for the relief distortion [2]. A general DEM-based rectification algorithm is described by several authors[5][6].

This paper presents the performance of a simple but accurate method applicable to SAR data processed with zero Doppler annotation. The procedure relies on the identification of GCPs. The purpose of this study is to investigate how accurate data from a high resolution SAR can be transformed into a reference coordinate system producing an ortho-image. The radar data was acquired by the Danish Center for Remote Sensing (DCRS) at the Department of Electromagnetic Systems, Technical University of Denmark where EMISAR was developed.

The paper focuses on the removal of the relief displacement. One of the characteristics of the presented procedure is to separate this from the transformation to the reference coordinate system. This separation and the fact that the Earth rotation can be neglected in the EMISAR case imply that the relief distortion is confined to the range direction and can be corrected line by line. The geometric correction model is based on the basic viewing geometry in order to avoid complex equations. The average residual error obtained is less than 0.5 pixel corresponding to 0.75 meters in the reference coordinate system.

Methodology

In conventional photogrammetry, geometric errors caused by variations in topographic relief are known to be radial and away from the principal point. This phenomenon is caused by the perspective projection of aerial photography. SAR works on a ranging and Doppler filtering principle that will produce geometric distortion when imaging anything but a simple smooth surface.

Assuming that the line-of-sight direction is perpendicular to the platform velocity relative to the scene, a target which is elevated by local relief to a height h above the reference level will be displaced in ground range by the Δx, as illustrated in Figure 1.

In this case the along track position is not affected by the target elevation, i.e. the relief distortion is exclusively in the range direction. This also applies to data acquired with a squinted geometry if the Earth rotation can be neglected.In accordance with the absolute location algorithm [6] ,the pixel location is confined to the intersect of a sphere and a cone. This intersect is a circle in the plane normal to the flight track and the location of the pixel on the circle is determined by its elevation.

The rectification technique presented in this paper is confined to SAR images processed with zero Doppler annotation. The layover and shadowing issues are not addressed in this paper as the test data used is neither subject to layover, nor to shadowing .The image can be corrected for local relief given by a DEM. The key point is to remove the displacement Δx due to the ranging geometry, i.e. restore the pixel value of point A from point A′. A backward transformation provides the positions, A′. In the distorded

0-7803-3836-7/97/$10.00 © 1997 IEEE

input image corresponding to a regular grid of point A, in the rectified output image. Since the A points do not in general coincide with the pixel positions, interpolation is needed to compute the desired pixel values. In Fig. 1, the displacement can be computed by the equations:

$$(H-H(x))^2 = H2 + (x + \Delta x)^2 \quad (1)$$

In case of flat terrain, it holds that $H>>h$ and $x>> \Delta x$, so equation (1) can be reduced to

$$\Delta x = -Hh(x) / x \quad (2)$$

Here it has implicitly been assumed that the input image is in pseudo ground range projection, i.e. it has been projected from slant range to ground range assuming a flat, horizontal earth at elevation $h(x) = 0$. If the input image is still in the slant range projection the pseudo ground range position, x+Δx,is simply expressed in terms of the slant range position, R. It should be emphazised that R is the distance of closest approach, i.e. it is measured in a plane normal to the SAR velocity vector. This also applies to squint mode SAR data processed with zero Doppler annotation.

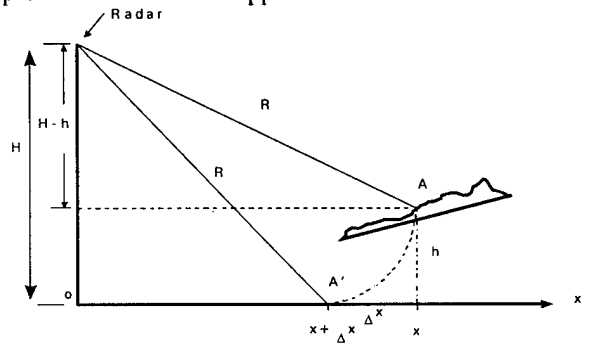

Figure 1 Basic viewing geometry and relief displacement

Strategy and Procedures

The rectification strategy is based on the assumption that a precise elevation model and a digital map of high quality showing relevant cartographic features are available. This could be the case when the radar imagery is supposed to be used for map revision.

The reference coordinate system based on the flight track can be defined as in Figure 2. The UTM system is selected as the cartographic system. The digital map, DEM and the final result of the rectification will be described in this system. The horizontal transformations can be implemented by polynomial equations.

In Figure 2, x is the ground range variable, which is the target position after removal of the relief displacement and y is the along track variable. In equation (1) or (2), the flight altitude, H, above a reference plane is obtained from the navigation

system of the SAR platform and it is assumed a constant. Thus x is the only variable meaning that the displacement is independent of the along track variable y. Therefore the relief distortion can be corrected if the elevation h(x) and x are known. The relief displacement will be corrected in the flight track coordinate system. This will maintain the details of the image as much as possible and keep the resampling of the pixel values to the range direction, i.e. process the image line by line.

All processing steps avoid complex equations and calculations and most of them can be performed in existing commercial GIS. If equation (1) is used, which describe the imaging geometric model exactly, the displacement can be calculated precisely and results obtained as in the practical experiment addressed in the next sections.

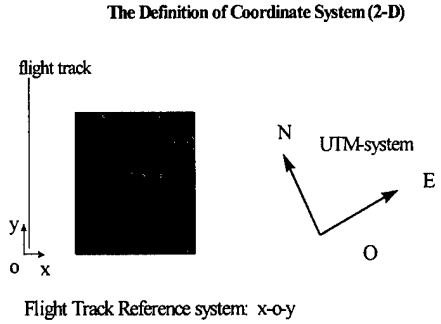

Figure 2 Flight track reference and ground coordinate system

Radar Data and The Test Site

The EMISAR system is a C&L band polarimetric SAR. The rectification algorihm has been tested with L-band polarimetric SAR data acquired† in Denmark on November 23, 1995. In the one-look, the pixel spacing is 1.5m x 1.5m (in pseudo ground projection). The flight altitude is 12222.1 m above the SAR reference plane which in turn is defined to be 75 m above the mean sea level. Unfortunately, the GPS did not operate with the P-code on the flight in question, and hence the accuracy was only in the order of 100 m. The slant range to the first pixel of each range line is 14396.4 m. For display purposes the intensities of the HV, HH, and VV channels are coded in red, green and blue, respectively. An undulating farmland close to the city of Vejle was selected as the test site for the rectification experiment. The elevations range from 48.2 m to 84.4 m. A detailed digital technical map and a DEM were available for this area. The corresponding digital image is 1300 X 1600 pixels.The topographic data covering the test site comprises digital technical maps and DEM measured photogrammetrically from aerial photos of 1:5.000 scale. Thus, the accuracy of the technical maps and the elevation data is superior to the geometrical resolution of the radar data. The digital map was used to identify and read the UTM coordinates of the GCPs and to check the accuracy of the final rectification. The DEM was measured with a grid spacing varying from 10 to 20 meters. A 1m x 1m grid was interpolated and then transformed into the flight track system based on the GCPs. Figure 4 is the map of the test site.

† The data acquisition and processing has been supported by the Danish National Research Foundation, who has established DCRS.

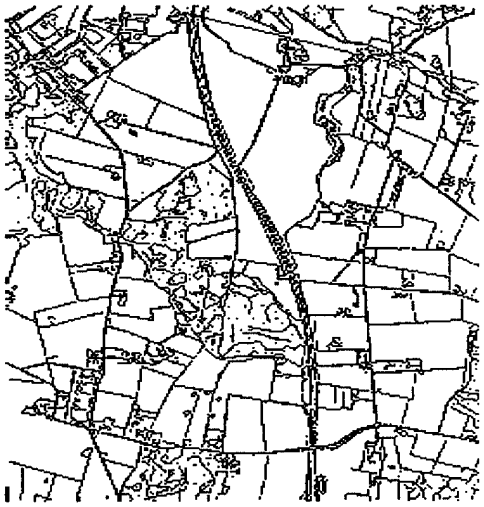

Figure 3 The technical map of the test site

Result

40 GCPs were manually identified in interpolated windows of the image using the ERDAS image processing platform. The points were chosen as well-defined features (also with respect to the elevation) such as the center of road inter-sections, fence corners etc.. The corresponding UTM coor-dinates were read from the digital technical map. The elevation data was calculated from the elevation model and attached to the points. Only 3 points were rejected because of residuals exceeding 2 pixels. The 2nd order polynomial was derived from the remaining 37 GCPs. The average root mean square error (RMS) of the residuals is 0.42 pix. (X direction: 0.26 pix. and Y direction 0.33 pix.).In order to check the reliability of the transformation, the 37 points were divided into GCPs (26 points) and Check points (CPs, 11 points) in 5 different combinations. The RMS of the 5 combinations are less than 0.55 pix.. The DEM data was transformed into the flight track system by the 2'nd order polynomial. The displacement for each pixel was computed by equation (2) and a corrected image was produced by resampling. The displacements found in the test site are between 34.4m and 63.1m. The image corrected was transformed into the UTM coordinate system by the inverse of the transformation used before. The quality of the SAR image rectification is illus-trated in Figure 4 where the main roads from the digital map are superimposed on the rectified image.

Conclusion

A portion of a SAR image has been rectified utilizing an existing and detailed photogrammetric map and a digital elevation model. An accuracy of less than 0.5 pixel has been achieved based on the elimination of the relief displacements. The procedures presented are simple and most of them can be implemented on existing commercial software systems for remote sensing or GIS.

Using high resolution SAR imagery the perspectives are found in the revision of existing digital maps in particular when further experiences on the identification of terrain objects and the interpretation of polarimetric SAR data has been achieved.

Figure. 4 Rectified image and superimposed roads from digital map.

Acknowledgment

Thanks are due to the firm Kampsax Geoplan and Vejle municipality for providing digital map data and DEM.

The Danish Research Academy has contributed with a scholarship for Mr. Liao Mingsheng.

References

[1] Curlander,J.C., R.N. McDonough, Synthetic Aperture Radar, System and Signal Processing, John Wiley & Sons, New York, 1991.

[2] Olmsted, C., Alaska SAR Facility Scientific SAR User's Guide

[3] Shahzanan,R. S., Y.A. Hussin, 1995. A Comparison between Optical and Microwave satellite data,IGARSS'95, pp1532-1534

[4] Toutin,Th., Y. Carbonneau, L. St-Laurent. 1992. An Integrated Method to Rectify Airbornee Radar Imagery Using DEM, PE&RS ,Vol.58, No4, 1992, pp.417-422

[5] Kwok R., J.C. Curlander, and S.S. Pang, 1987. Rectification of Terrain Induced Distortions in Radar Imagery, PE&Rs, Vol. 53, No. 5, pp 507-513

[6] CurlanderJ.C., R. Kwok and S.S. Pang, 1987. A Post-Processing System for Automated Retification and Registration of Spaceborne SAR Imagery, International Journal on Remote Sensing, Vol. 8, pp. 621-638

[7] Lintz Christensen, E., J. Dall, N. Skou, K. Woelders, J. Granholm, and S.N. Madsen, EMISAR: C- and L-Band Polarimetric and Interferometric SAR, IGARSS'96, pp. 1629-1632.

Contribution of Mathematical Morphology and Fuzzy Logic to the Detection of Spatial Change in an Urbanized Area : Towards a Greater Integration of Image and Geographical Information Systems

Key words : mathematical morphology, fuzzy logic, urban dynamics, change, geographical information systems

Patrick Maupin[1], Pascal Le Quéré[1], Robert Desjardins[2], Marie-Catherine Mouchot[1], Benoît St-Onge[2] and Basel Solaiman[1]

[1] Ecole Nationale Supérieure des Télécommunications de Bretagne, Département Image et Traitement de l'Information
[2] Université du Québec à Montréal (UQAM), Département de Géographie

Technopole de Brest-Iroise, B. P. 832, 29285 Brest Cedex, France
Telephone: +33 (0)2.98.00.13.58 Facsimile: +33 (0)2.98.00.10.98 E-mail: maupin@gti.enst-bretagne.fr

Abstract — This paper presents a new approach to spatial change detection. It emphasizes the use of topology for the comprehension of grey scale images, through mathematical morphology and fuzzy logic. In conclusion, issues to the problem of change detection and integration of images into GIS are proposed.

INTRODUCTION

For many years studies in the field of urban remote sensing were limited in their unfolding by problems due to the coarse spatial resolution of the captors [1]. In fact, if some features are visible to the naked eye, they are however very difficult to discriminate using conventionnal methods of statistical classification. Radiometric confusion is often important to the point that it is impossible to differentiate a plough-land from an urban implant. Local operators that take into account shape, size, arrangement and spatial structure [2] of observed entities, as well as a more flexible methodology as regard to radiometry would be of great use for a semi-automatic monitoring of urban and suburban areas. Effective solutions would yield to a more generalized use of remote sensing images into geographical information systems.

METHOD

In the change detection litterature, it is common to find frequency-oriented methodologies. The authors of such papers believe, in many cases, that it is possible to segregate efficiently the change information with thresholds determined over statistical parameters based on a gaussian assumption. These methodologies can be successful when large images with few changes are studied, and when obvious changes like vegetation to urban, forest to bare soil are surveyed. The sole radiometric criterion is however uneffective in the case of more subtle changes. Moreover, this frequential reasoning leaves aside the problems of topological relationship between possible particles of change (i.e. if a pixel of change is isolated then its possibility of beeing noise is higher than if it is connected (or near) to other pixels of change).

One must look for an answer to this paradigm in the nature of the criteria used to apprehend the remotely sensed reality. Like the photointerpreters do, this method will use the objects' topology as the fundamental criterion for recognition [2] [3]. The hypothesis is that grey scale mathematical morphology, as formulated by Serra and Matheron in the '70, can help us to model topological aspects [3] of entities in the images in the prospect of spatial change detection. Through this modelling new algorithms are proposed for the segmentation and comprehension of digital images used in remote sensing.

A case study on the spatial dynamic of the city of Trois-Rivières (Québec) is analysed using Landsat spectral bands TM3 (0.63-0.69 μm), TM4 (0.76-0.90 μm) and TM5 (1.55-1.75 μm) acquired on August 20th 1984 and August 29th 1993, at 10:00 local time in both cases. The grey scale image on wich mathematical morphology operators are applied was obtained through the fusion of fuzzy classifications [4] made on substacted spectral bands pairs. Figure 3 shows a color composite of TM3 1984 and TM3 1993 displaying *positive* changes in red and *negative* changes in turquoise. -These denominations of change will be discussed in a later part of this article- . An alternate sequential filtering of the scene is used to select pieces of urban and suburban space significantly altered between the two dates.

Pre-processing step

It is necessary to complete a band to band substraction in order to isolate the change information. By this treatment, it is assumed that all the existing radiometric change information is contained in the resulting differences. However the problem remains of discriminating between true change and noise. The noise has two principal causes : a bias due to unfit geometrical correction and differences in the acquisition conditions of the scenes. The general goal of the analyst is to segregate particles of change from the habitual noise found in difference images.

Classification step

0-7803-3836-7/97/$10.00 © 1997 IEEE

Usually in the change detection literature, change is detected through the tresholding of the image histogram as shown in figure 1a. The morphological methodology used is rather considering the difference image as a landscape in which the *valleys* and the *hills* are possible materializations of spatial change (fig. 1b).

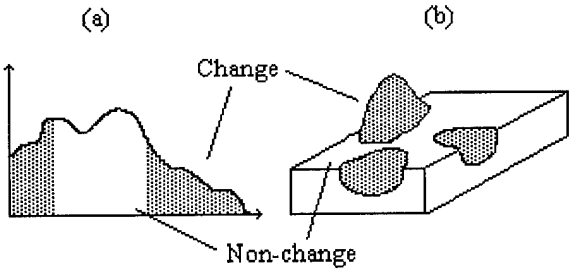

Figure 1 Two antagonist ideas of change detection

Once all channels are substracted it is possible to create a unique channel by aggregating the results of the fuzzy classifications of difference images using a t-norm operator (fig. 5).

The inverse triangular fuzzy memberbership function [4] of change we have used is defined as :

$$\mu(\delta) = \begin{cases} 1 & -1 \le \delta < \varpi \\ (\delta - mean)/(\varpi - mean) & \varpi \le \delta \le mean \\ (\delta - mean)/(\gamma - mean) & mean \le \delta < \gamma \\ 1 & \gamma \le \delta \le 1 \end{cases}$$

where $\mu(\delta)$ is a pixel degree of change membership for a grey value, ϖ and γ bounding the empirically determined core of the *positive* and *negative* change classes. The reader should keep in mind that this form of membership function was used only because it suited the present exemple, and that it should not serve as a model for all cases.

The arbitrary decision of detecting *positive* and *negative* spatial change over the entire scene is questionnable. In a fruitful way one could decide to detect only one class of objects behaviour through a more sophisticated modelization or to work directly on the raw difference image in order to detect all classes of change. It is also clear that the mergence of fuzzy classifications uncovers large and compact change islets, but also brings an important *speckle* to the result (fig. 4).

Morphological filtering step

The detection and selection of change particles using grey scale mathematical morphology focused on particles relevant to a 1: 125 000 scale, because of the regional nature of the project.

An isotropic hexagon is used as structuring element (fig. 2), because it is better adapted to the shape of the type of particles to study. The filter proposed by the theory is an alternate sequential filter built on increasing size of morphological openings and closings, the later derived from alternate dilations and erosions [5]. This filter enables us to remove, after each iteration, *peaks* and *valleys* of growing amplitude.

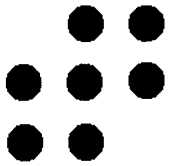

Figure 2 The isotropic hexagon used as a structuring element for contextual change detection (size one)

The final step of the algorithm is to merge, using an appropriate operator (i.e. mean, t-conorm or t-norm), the particles obtained through the entire process (fig. 5) and , presenting only *positive* changes . The choice of the operator will depend on the level of confidence to be given to the change detection.

RESULTS

Known regions of change have been quite successfully detected by our mixed fuzzy logic/mathematical morphology approach. Although the results are good, especially for an urban environment, they are not exceptional (table 1).

obs/truth	0	1	Total	K
0	1453	376	1829	0.553
1	24	547	571	0.964
Total	1477	923	2400	
K	0.964	0.553		0.704

Table 1 Results of change detection where K denotes the *Kappa index*, 0 denotes *non-change* pixels and 1 denotes *change* pixels. The sample image size is 1km * 1.5 km, and the α-cut ranges from 0.75 to 1 in membership of change.

One can notice that the basic operators of mathematical morphology are partly corrupting the results of change detection by introducing bias on the shape of the objects and also by shifting the edges in the displacement direction of the structuring element. Another perverse effect of the morphological filter is the disparition of change materialization due to the inadequate shape of the structuring element.

Figure 3 Color composite 1984/1993

Figure 4 Fuzzy «positive» changes

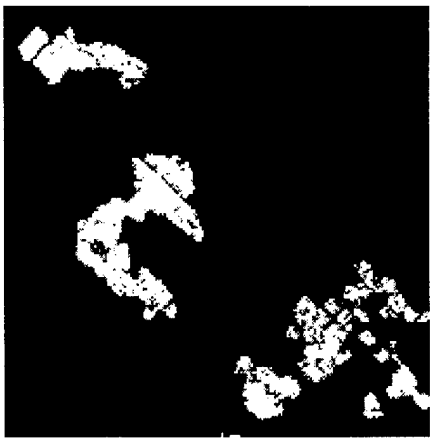

Figure 5 Result of ASF merging fuzzy «positive» changes

By example on figure 5 all linear or thin changes have disapeared. Nevertheless the proposed method gives a solid basis for a wide range of studies. In addition, geodetic transformations will be used for correcting these topological artefect in a forthcoming paper.

DISCUSSION

The greatest difficulty that we still encounter during the study of spatial change is the validation of results, because the quantity and quality of information mastered is usually maximal for the closest date (or present) and minimal for the farthest date. It is also common [6] [10], as shown here, to suppose that the values ranging to the right of the mode are *positive* changes and the values ranging to the left are *negative* changes, which is an untimely shortcut. It would be more appropriate to say that the very deap *valleys* on the difference image may be due to a "mineral ⇒ vegetal or very humid" type of change and that the very high *hills* may be due to a "vegetal or very humid ⇒ mineral" type of change. Therefore is rising the problem of intermediate values : what is the correct scheme ? Multi-criteria analysis on the particles extracted at the different levels (size of structuring element) of analysis is currently investigated with encouraging results.

It would be usefull to introduce in the change detection algorithm AI concepts such as the blackboard architecture and integrate knowledge on the geographical area through the use of a GIS database. Coarse knowledge such as a regional land uses maps, could improve to a great extent the results by permitting a differenciation on the application of the rules.

ACKNOWLEGMENT

The authors wish to acknowledge the financial and material support provided by the Université du Québec à Montréal, the Ecole Nationale Supérieure des Télécommunications de Bretagne, the Ministère des Affaires Etrangères de France, the Ministère des Affaires Internationales et de l'Immigration du Québec, the Communauté Urbaine de Brest (France) and finally, but not least, the city of Trois-Rivières.

REFERENCES

[1] Peter F. Fisher and S. Pathirana. 1990. «The Evaluation of Fuzzy Membership of Land Cover Classes in the Suburban Zone». Remote Sens. Environ., no 34, p. 121-132.

[2] Hugues Gagnon. 1974. *La photo aérienne : son interprétation dans les études de l'environnement et de l'aménagement du territoire*. Montréal: HRW, 278 p.

[3] Yacine Merghoub. 1985. *Reconnaissance et analyse de formes sur des images de télédétection : Modélisation par la morphologie mathématique*. p. 11-15. Doctoral thesis no 3140, Université Paul Sabatier de Toulouse.

[4] P. Gong. 1993. «Change detection using principal component analysis and fuzzy set theory». *Canadian Journal of Remote Sensing*, Vol. 19, no 1 (january), p. 23-29.

[5] Michel Schmitt and Juliette Mattioli. 1994. *Morphologie mathématique*, Paris (France): Masson.

[6] A. Dagorne, A. Dauphiné, G. Escleyne, L. Gueron, L. Baudoin and M. Lenco. 1990. «L'utilisation de la télédétection aérospatiale en mode multi-satellites, multi-capteurs et multi-dates pour l'étude de la reprise de la végétation après incendie», Photo-Interprétation, no 1990-5, p. 45-51.

An Application of GIS Information and Remotely Sensed Data for Extraction of Landslide

Masaaki SHIKADA,Yoshihiko SUZUKI , Takashi KUSAKA , Shintaro GOTO and Yoshiyuki KAWATA

Kanazawa Institute of Technology
Nonoichi-machi Ishikawa 921,JAPAN
Tel:+81-762-94-6712 Fax:+81-762-94-6713
E-mail shikada@manage.kanazawa-it.ac.jp

Abstract — We have already been conducted the analysis of the landslide areas with remote sensing data and thematic map data respectively. Estimation of landslide areas , however, has been considered very difficult because the principal factor of landslide complexly relates to some phenomena. The objective of this study is to find areas where landslide may occur in the near future by using satellite remote sensing data and thematic-map data related to landslide areas with GIS (Geographic Information System) techniques. In this report our research focused on the actual vegetation in landslide areas. The relationship between vegetation and landslide areas were extracted with the thematic maps including actual vegetation map.

INTRODUCTION

We considered that the remote sensing data combine thematic map data with Geographical Information System (GIS) may greatly facilitate for assessment and estimation of regional landslide hazards.

We used several data to extract the characteristics of landslide areas. There are Landsat TM data on the daytime, thermal data in the night time, NVI values from TM data, geological type and elevation map. In this research the actual vegetation map was introduced to combine the characteristics of landslides.

The reason why we used Landsat TM data in the daytime and thermal data in the nighttime is that the underground-water is one of the great factor on the occurrence of landslide. Then we considered that the thermal band data has information of ground surface temperature which related to underground-water.

We next calculated NVI (Normalized Vegetation Index) values from TM data in landslide areas and non-landslide areas for pilot district. The following thematic maps were prepared for GIS analysis. Used maps are geological type map , landslide distribution map ,elevation map for calculation of inclination angle and direction , and actual vegetation map.

The following subjects were performed by using GIS. Record of landslides was classified under geology and inclination angle of topography. We knew relationship between landslide and geological types. Relation between inclination angles and landslide areas give us topographical characteristics. Satellite data were overlaid with thematic maps. The actual vegetation map overlaid with the landslide distribution maps , geological maps and other thematic maps. This is the topic of the paper.

INVESTIGATION AREAS

In the Noto peninsula in Hokuriku district of Japan where we have investigated, most of landslide hazards occur near the stream in the valley. The area of the study site is about 600 km^2 and altitude is lower than 600m. This area is well-known as landslide areas in the Japan. Fig.1 shows the north district of Noto peninsula where we mainly conducted researches. The

0-7803-3836-7/97/$10.00 © 1997 IEEE

rectangular areas in the figure correspond to 1/25000 scale map about 10km wide to 10km long.

VEGETATION MAP

Fig.2 shows the actual vegetation map of Ishikawa Prefecture (a piece of map). Different color (gray scale) shows different kinds of vegetation. For example, a Japanese red pine, Japanese black pine, zelkova , a Japanese beech, a Japanese oak, and so on. Vegetations are classified into 36 categories. A Japanese ceder , Japanese cypress, Japanese red pine and zelkova were widely distributed in north district of Noto peninsula.

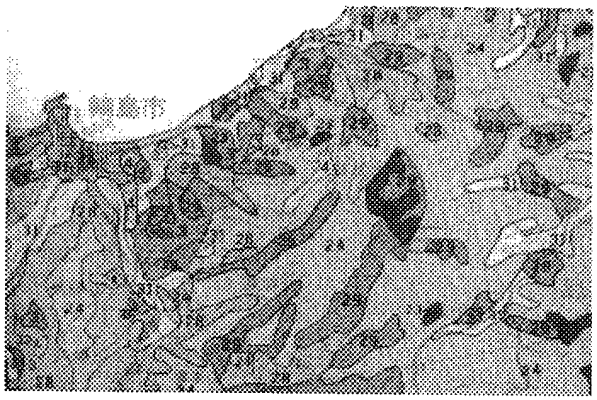

Fig.2 The actual vegetetion map of Ishikawa Prefecture

METHOD AND TECHNIQUES

FLOW OF ANALYSIS

Fig.3 shows the outline of analysis. Major parts are three data and GIS. Used data are vegetation map, landslide distribution map ,and thematic maps (Inclination Angle, Geology ,Shape Factor ,Landsat data and value of NVI). GIS connected the landslide areas and thematic map data. For example, GIS gives us virtual rivers and watershed from elevation data. We used GIS software of ARC/INFO ,however, algorithm does not open to users. Our object is not evaluate the algorithm for GIS software. How use the GIS software to extract characteristics of landslide areas with thematic maps.

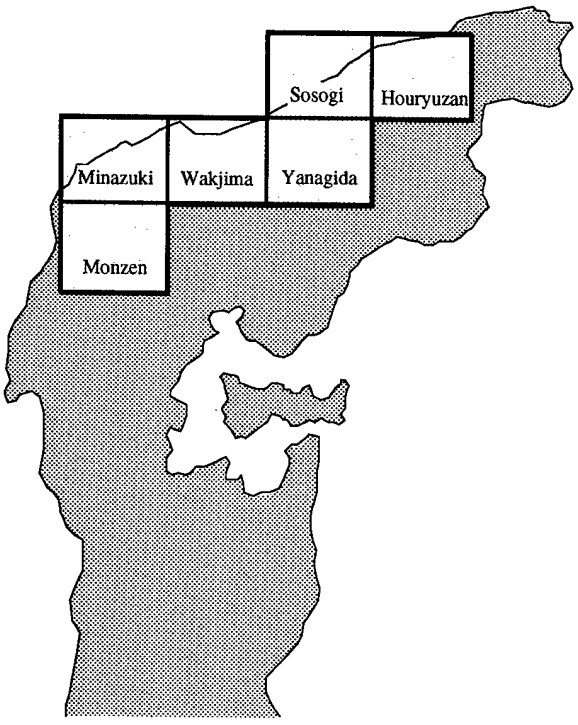

Fig.1 The north district of Noto peninsula

VEGETATION, TREE AND LANDSLIDES

Fig.4 shows the relationship between geological types and level of landslide for actual vegetation (ceder). Occurred zone means the landslide occurred in the past. Dangerous zone means the landslide may occur in the near future. The picture shows that occurrence of landslide relates the vegetation and geological types. The relation is not only ceder but also it appears other vegetation. Fig.4 shows that ceder grows mainly

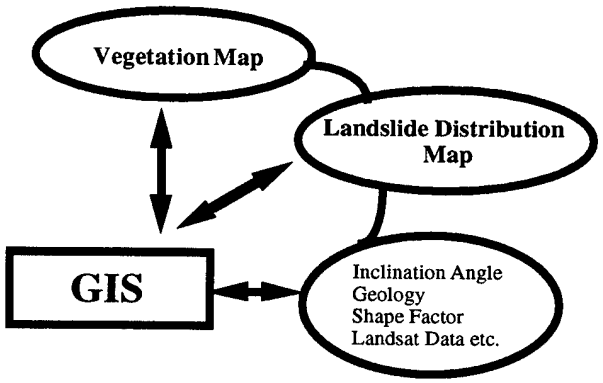

Fig.3 The outline of analysis

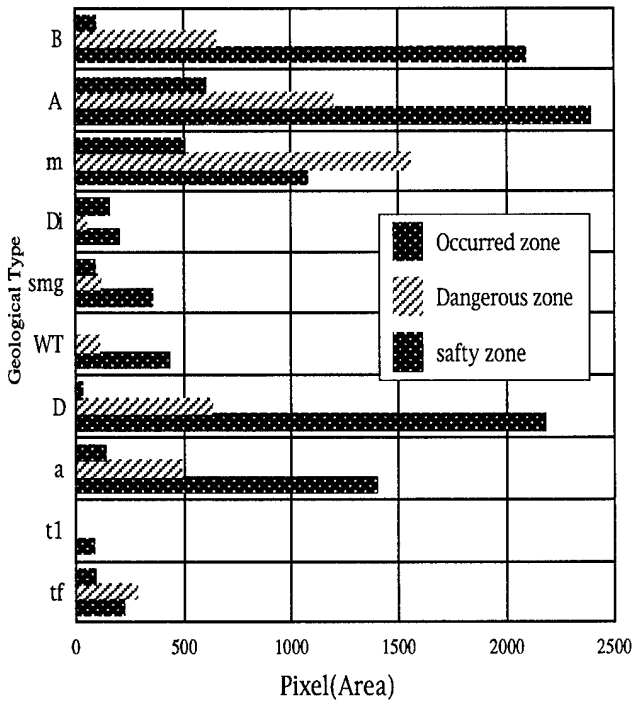

Fig.4 The relationship between geolgical types and landslide level for vegetation(ceder)

in geological type 'A' and 'm'. A and m means Andesite and Mudstone respectively. The actual vegetation of 36 categories were compared with geological types and level of landslides. We will show you the results on the interactive position by using poster.

CONCLUSIONS

We have been conducted the procedure mentioned above in the pilot area located north district of Noto Peninsula in the central of Japan. These pilot areas are correspond to 6 sheets of 1/25000 scale map. In the pilot area we got the interested results: (1)We can divide pilot areas into watershed areas by using GIS. (2)The rivers made automatically with GIS, which is correspond to the true rivers. (3) GIS is able to extract small rivers which does not exist on the map. (4)As the proportion of landslide area increase band6 CCT data decreases. (5)When the proportion of landslide area over 70 % the shape factor F increases sharply. (6)We also digitized the actual vegetation map to overlay with thematic maps. We find that landslide has relation with vegetation and trees.

As a results we will be able to get more sure results to estimate landslide areas. Combination of remote sensing data and GIS techniques may succeed landslide zone and estimation. These conclusions indicate that combining thematic maps and satellite data using GIS is successful estimating and zoning landslide areas.

ACKNOWLEDGMENTS

The authors wish to thank a student , Mr.Yoshiaki Suzuki contributed significantly to the computation and investigation for this analysis. We also wish to acknowledge the students of Kanazawa Institute of Technology for their assistance in analyzing the data.

REFERENCES

[1] M.Shikada,T.Kusaka and K.Miyakita, 1992. Extraction of Landslide areas Using MSS Data and Thematic Map Database System, International Archives of Photogrammetry and Remote Sensing, Vol.16. Part B4 Com.4,pp.386- 391.

[2] T.Kusaka,M.Shikada and Y.Kawata, 1992. Extraction of Landslide Areas Using Spatial Features of Topographic Basins,Proc.of IGARSS'92.

[3] T.Kusaka and M.Shikada, 1993. Inference of Land-slide Areas Using Spatial Features and Surface Temperature of Water-sheds, SPIE Int.Sympo. on Optical Eng. and Photonics Aerospace and Remote Sensing, pp241-246.

[4] T.Kusaka et.,al. 1993. Extraction of Topographic Features in Landslide Areas from ERS-1 SAR Data, Int. Geoscience and Remote Sensing Sympo.,(IGARSS'93),Vol.IV,pp.1222-1224.

[5] M.Shikada ,T.Kusaka,Y.Kawata and K.Miyakita, 1993. Extraction of Characteristic Properties in Landslide Areas Using Thematic Map Data and Surface Temperature,Int. Geoscience and Remote Sensing Sympo. , (IGARSS 93), Vol.II, pp. 103-105.

[6]M.Shikada ,K.Imagayashi,T.Kusaka and K.Miyakita,1994. Extraction of Landslide Ar-eas Using Inclination Angles and NVI Data,SPIE Int. Sympo. Recent Advanced in Remote Sensing and Hyperspectral Remote Sensing,Vol.2318,pp. 109-120.

[7] M.Shikada ,N.Muramatsu,T.Kusaka and S.Goto, 1995.Extraction of Landslide Areas Using Satellite Remote Sensing and GIS Technology, Geoscience and Remote SensingSympo.,(IGARSS 95),Vol.IV, pp.377-379.

[8] M.Shikada and T.Kusaka, 1996.Remote Sensing and Geotechnical Engineering, JSSMFE Ser. No. 456, Vol.44, No1.13-16.

[9]M.Shikada,N.Muramatu,T.Kusaka and S.Goto, 1996. Application of GIS and Remote Sensing to Extraction of Landslide Areas,International Archives of Photo-grammetry and Remote Sensing, Vol.17. Part B4, Com IV ,pp.786- 791.

Accuracy Assessment of Elevation Data Obtained From Radarsat Stereo Images

Kuldip Singh, Oo Kaw Lim, Leong Keong Kwoh and Hock Lim
Center for Remote Imaging Sensing and Processing
National University of Singapore, Singapore 119260
Tel : (65) 771 5070 Fax: (65) 775 7717 Email : crssingh@nus.sg

1. INTRODUCTION

Radar stereo maping or radargrammetery using high resolution spaceborne SAR data has been shown to be a potentially effective tool in obtaining terrain elevation maps. The all weather capabilities of SAR systems are especially useful in tropical areas where perennial cloud cover poses restrictions to the more conventional optical methods. In the mapping context, SAR systems have an added advantage of being ranging devices. Here the geometric relationship of a terrain point with respect to the SAR is intrinsically encoded in the image by its position on the image. Indeed, the pixel coordinates specifies the distance r of the satellite from the imaged point p and the azimuth position of the satellite at that instant (t). Mathematically this relationship is characterized by the equation

$$r = [(r_s - r_p).(r_s - r_p)]^{1/2} \qquad (1)$$

where r_s and r_p are sensor and target position vectors respectively at the time of imaging. This constitutes the first of the two equations that form the basis of the standard radargrammetric analysis [1]; the second being the doppler equation:

$$f_{dc} = \frac{2}{\lambda r}(v_s - v_p).(r_s - r_p) \qquad (2)$$

where f_{dc} is the Doppler centroid frequency, λ is the radar wavelength and v_s , v_t are the satellite and the target velocities respectively. The target velocity is related to the target position through

$$v_p = \omega_e \times r_p \qquad (3)$$

where ω_e is the earth's angular velocity vector. In a stereo configuration one solves the above equations for the coordinates r_p, of an arbitrary target point p from knowlege of the satellites' positions and velocities at the time of the two acquisitions. In the derivation values of r for a target point are obtained by colocating the corresponding pixels from the two images.

In this paper we present some preliminary assessment on the quality of elevation data generated from a stereo-pair of Radarsat images. Here we first compare the range values of control points, whose ground coordinates are accurately known, with the calcuated values based on (1).These residues give a measure of the inherent inaccuracies in the satellite's position vector which are obtained from the orbit ephermeris information provided with the SAR data. We show that the the values obtained warrants some adjustments in the satellite's orbit. To this end, we model the two-body Keplerian orbit with a cubic polynomial. The parameters characterising the orbit are initially estimated from the ephermeris information. Using suitable ground control points these parameters are further refined using a least-squares adjustment technique. The coordinates of arbitrary points are then evaluated using the standard radargrammetric equations and compared with values obtained from a DEM of the test site.

2. DATA AND TEST SITE

The recent launch of the Radarsat satellite with an inflight steerable beam provides a unique opportunity for stereo analysis. For this study two Radarsat images with S2 and S7 beam modes were acquired over a test site in Hong Kong. These beams have incidence-angle limits of 23.7-31.0 deg and 44.3 - 49.2 deg respectively. The data was processed at the Single Look Complex (SLC) level which presents its data in the slant range projection. At this level, the data retains its optimum resolution with nominal pixel dimension of 8.11m in range x 5.28m in azimuth for S2 and 11.59m in range x 5.13 m in azimuth for S7.

The orbital data comes in the form of 15 state vectors that provides both the positions and velocities at 8 minute time intervals. These coordinates are defined wth respect to an inertial reference frame with the earth center as its origin. Here the x-axis is taken in the direction of the vernal equinox, the z-axis in the direction of earth's rotational axis and the y-axis chosen othogonally such that the system is right-handed.
The data set also specifies the Greenwich angle which expresses the angle of longitude of the spacecraft at the equator crossing. (This angle is important in fixing the transformation parameters between the geocentric coordinates of target points and their inertial frame counterparts.)

As an initial check of the orbital data we compute the orbits of the satellite using two methods. In the first, we use an interpolation technique employing the state vectors provided to compute the position and velocity vectors at designated times. These being chosen to correspond to the azimuth

0-7803-3836-7/97/$10.00 © 1997 IEEE

locations of some ground control points (GCPs) on the image. In the second method we employ the state vector that is closest to the segment of image acquisition to generate the corresponding two-body Keplerian elements. This then defines the orbit of the satellite.

In both cases, we evaluate eqn (1) for the available GCP's. Here the range values which are given with a relatively high level of precision can be obtained from the location of the pixel within the image. The residues, which are taken as the difference between the given range values and those computed from (1) , *i.e.*

$$e = r - [(\boldsymbol{r}_s - \boldsymbol{r}_p).(\boldsymbol{r}_s - \boldsymbol{r}_p)]^{1/2} \qquad (4)$$

then gives an indication of the inaccuracies of the various parameters used in the orbital model. It should be noted that the Greenwich angle which is required in transforming the GCPs' geocentric coordinates to the inertial frame can also contribute considerably to the residues. Table I below gives the rms values of the residues computed for 18 GCPs using the two methods.

Beam Mode	Method I (m)	Method II (m)
S2	5.09×10^3	7.37×10^3
S7	7.28×10^3	1.06×10^4

Table I : RMS values of the residuals

ADJUSTMENT OF PARAMETERS

The figures obtained evidently shows the need for orbital adjustments. In this section, we briefly summarize the approach adopted here in refining the parameters. Here we begin by modelling the Keplerian orbit with a six-paramter time series with the coefficients being functions of the components of some reference state vector. Explicitly, given an initial state vector ($\boldsymbol{r}_o$, $\boldsymbol{v}_o$) at time t_o, for t close to t_o one can approximate the Keplerian orbit [2] by

$$\boldsymbol{r} = f\boldsymbol{r}_o + g\boldsymbol{v}_o \qquad (5)$$

$$\boldsymbol{v} = f'\boldsymbol{r}_o + g'\boldsymbol{v}_o \qquad (6)$$

with

$$f = 1 - \tfrac{1}{2}\mu u(t-t_o)^2 + \tfrac{1}{2}\mu us(t-t_o)^3 \qquad (7)$$

$$g = (t-t_o) - \tfrac{1}{6}\mu u(t-t_o)^3 \qquad (8)$$

$$u = \frac{1}{r_o^3}, s = \frac{\boldsymbol{v}_o.\boldsymbol{r}_o}{r_o^2}, \mu = GM \qquad (9)$$

where G is the Gravitational constant and M the mass of earth. (The primes in (4) denote differentiation with respect to t.) For the small segment of the orbit over which image acquisiton takes place, the above third-order polynomial gives a very good approximation to the orbit. Here the parameters that require adjustments are the six components of the initial state vectors ($\boldsymbol{r}_o$,$\boldsymbol{v}_o$).

In the adjustment process, the standard practice is to minimize the sum of squares of the residuals. Now the model we need to consider is essentially non-linear. The usual prescription , in this situation is to simply linearize the equations and to solve them using the linear least-squares technique. While such Gauss-Newton type algorithms may work well when estimates are close to the actual values or when the data is not multicollinear, they are known to be not very robust in general. Indeed, for the case at hand our attempt to apply this technique failed miserably. Further analysis revealed that the problem of mulicollinearity was present.

For such situations, it is well known that these problems [3] are best handled from the non-linear optimization approach. To this end, we adopt the method of steepest descent which is an example of such an appproach. Here one proceeds to minimize the quadratic form $S^2(\theta)$ composed of the sum of the squares of the residuals by parametrically shifting the parameters in a manner which maximally reduces $S^2(\theta)$. It can be shown [4] that for a general non-linear model

$$y_i = f(\boldsymbol{x}_i, \theta) + e_i \qquad (10)$$

the shift in parameters θ that achieves this is given by

$$\delta\theta_j = 2\kappa \sum_i e_i . \frac{\partial f(\boldsymbol{x}_j, \theta)}{\partial \theta_i} \qquad (11)$$

where κ is positive constant that has to be chosen such that

$$S^2(\theta + \delta\theta) < S^2(\theta) . \qquad (12)$$

For the problem at hand, the function f is given by

$$f = \left(\sum_m (x^s_m - x^p_m)(x^s_m - x^p_m) \right)^{1/2} \qquad (13)$$

where x^s_m and x^p_m are the components of the sensor and target respectively. In an inertial system the coordinates of a target point with geocentric coordinates $\tilde{\boldsymbol{x}}_p$ are given by

$$\boldsymbol{x}_p = \boldsymbol{R}_3(-\theta).\tilde{\boldsymbol{x}}_p \qquad (14)$$

Here $\boldsymbol{R}_3(-\theta)$ denotes the the rotational matrix about the z - axis with angular displacement of θ between the x-axes of the two coordinate systems. The angle θ at any time t is further obtained from the Greenwich angle θ_o and the time of the equator crossing τ through

$$\theta = \theta_o + \omega_e(t - \tau) \qquad (15)$$

where ω_e is the angular velocity of earth. In our adjustment procedure we also include θ_o as one of the adjustment parameters.

The algorithm is iterarative. We first estimate the parameters, which in this case are the components of the initial state vector and the Greenwich angle, from the ephermeris data. The parameters are then refined in accordance with (11). To obtain the increments we first differentiate (13) with respect to the various parameters. The choice of the parameter κ has to chosen carefully and it varies as the iterations proceed. The iterations are continued until $S^2(\theta)$ Table II below shows

the rms values of the residuals obtained for the two passes after the adjustment procedure.

Beam Mode	RMS values (m)
S2	25.82
S7	62.12

Table II : RMS values of residuals of adjusted orbits.

Comparison of tables I &II, shows the vector of errors has reduced significantly. Figs.(1) and (2) shows the absolute difference in the positions between orbits computed from the ephermeris (method 1) and the adjusted orbits.

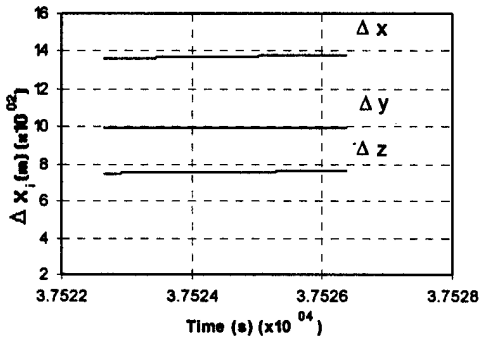

Fig. 1 : Difference in components between the adjusted orbits and the interpolated ones for the S2 mode.

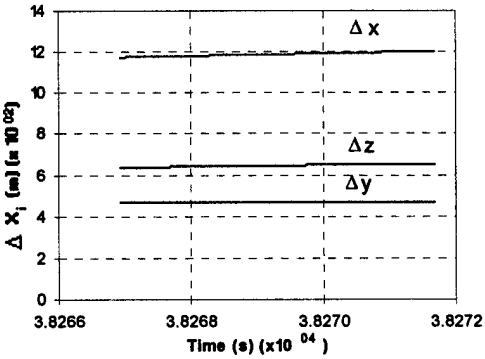

Fig. 2 : Difference in components between the adjusted orbits and the interpolated ones for the S7 mode.

RADARGRAMMETRIC ANALYSIS FOR THE STEREO PAIR

With the adjusted orbits equations (1) and (2) for each of the two orbits can be first linearized to yield four equations in three unknowns. This overdertermined system can then be solved in the standard linear least-squares algorithm [1,4]. Here, unlike the orbit adjustment case, the system does not suffer from multicollinearity problems. In fact one obtains convegence very rapidly. Table below shows the residuals obtained for 19 GCPs whose positions are very accurately known. It should be remarked that the rms errors obtained do not include errors due to misregistration.

GCP No	Δx (m)	Δy (m)	Δz(m)
1	28.24	38.25	60.66
2	44.11	7.74	38.11
3	86.17	28.64	61.82
4	50.54	11.73	4.51
5	110.02	22.45	12.79
6	107.36	8.62	2.20
7	15.09	10.69	11.72
8	42.20	20.19	25.15
9	54.59	22.43	5.13
10	50.35	24.66	19.52
11	34.25	16.85	18.97
12	29.22	6.32	4.35
13	79.81	23.36	85.08
14	45.73	22.05	34.93
15	1.51	3.58	21.96
16	17.05	12.29	11.96
17	120.59	27.42	4.23
18	59.62	21.53	5.85
19	58.43	31.09	17.23
RMS	**63.33m**	**21.02m**	**32.55m**

Table III : Difference in the component values between the computed and the actual values for 19 GCPs.

SUMMARY

To summarize briefly, we have found that the orbital data provided with the SAR data to be inadequate for radargrammetric analysis. This is primarily due to the large intervals (8 min) over which the state vectors are given. In this regard we show that the residuals between the observed distances r (between the satellite's position and some GCP) and the calculated ones to be very large. To improve these we have applied a non-linear optimization technique to refine the orbits. Using these refined orbits, we have obtained estimates of rms errors in the coordinates of points derived through the standard radargrammetric analysis.

REFERENCES

[1] F.W. Leberl, Radargrammetric Image Processing, Artech House,1990.

[2] A.E. Roy, Orbital Motion, 3rd ed., Adam Higler, 1988.

[3] G.A.F. Seber, C.J. Wild, Nonlinear Regrression, John Wiley &Sons Inc, 1989.

[4] A. Sen M. Srivastava, Regression Analysis, Springer Verlag,1990.

Parallel Ladex Spatial Index Mechanism

Xiao Weiqi Feng Yucai
Department of Computer Science and Engineering
Huazhong University of science and Technology
Wuhan, Hubei, 430074, People's Republic of China
Tel: +86-27-7544400 Fax:+86-27-7545438
Email: dbinst@hust.edu.cn

Abstract -- In this paper, we consider the problem of exploiting parallelism to improve the performance of Ladex spatial index. Our goal is to design a parallel Ladex spatial index mechanism for spatial database systems, so that to maximize the throughput of spatial queries. This can be achieved by (a)maximizing parallelism for large region queries, (b)by engaging as few processors and disks as possible on small region queries and point queries, and (c) by balancing the load among different processors in a shared-disk parallel hardware architecture.
Keywords: Spatial Index, Spatial Database, Access Method

INTRODUCTION

Spatial database systems have been used in many applications. The main problem in these applications is the data access efficiency. To solve this problem, a feasible effective approach is to utilize spatial access method or index mechanism. So far, many kinds of spatial index have been presented[1,2]. However, with the application data scale explosively increasing, the access efficiency remains a big problem. An other good solution is to parallelize the spatial index structure. At present, a parallel R+ tree based on multiple disks has been presented[3]. A lot of parallel spatial operations have also been presented based on R+ tree[4,5]. In this paper, we exploit parallelism to Ladex spatial index[1].

PARALLELIZATION STRATEGIES

Our spatial database server is based on a shared-disk multi-processor computer system.. On this kind of hardware architecture, all of the processors(CPUs for short) share a group of hard disks. Each CPU has its private main memory. All of the CPUs can communicate with each other through a high speed network. The data and messages are transferred or passed through the high speed network between each node. Fig. 1 shows the hardware architecture.

In order to improve access efficiency and achieve high throughput under concurrent queries, we present the following three strategies:

(1)Improve parallelism of large region query. Use more processors as possible to do large region spatial query, utilize the parallelism of the multiple disks to speed up I/O operation.

(2)Engage as few processors and disks as possible on small region query and point query. This is to avoid the small query taking up too many resources, including processors and disks.

(3)Balance the load among processors in a shared-disk parallel hardware architecture. This is due to the overall query execution time is determined by the slowest sub-query executed on one of the processors.

According to the above strategies, we parallelize the Ladex mechanism in the following two aspects:

(1)For disk I/O performance consideration, we partition a map space uniformly to all of the disks, and build a high speed correspondence between the map space and the disks. So, the I/O operation involved in a large region spatial query can be allocated to several disks to be concurrently executed.

(2)For overall performance of processors, we partition a map space uniformly to all of the processors, and build a high speed correspondence between the map space and the processors. So, the task of a large region spatial query can be distributed to several processors to be concurrently executed.

PARALLEL LADEX STRUCTURE

The main idea for Ladex is to partition a map into a lot of small blocks with equivalent size[1]. Suppose the partition of map space is $M \times N$. A small block could be represented as Block[i,j], $-1<i<M$, $-1<j<N$. The relationship between a bucket and a block is described as:

$$Block[i,j] \leftrightarrow Bucket[j \times M+i]$$

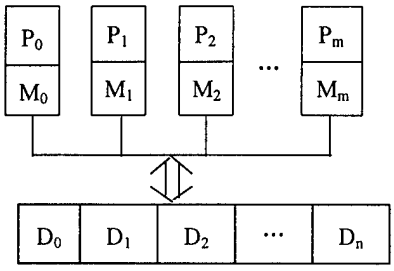

D — Processor M — Main memory D — Hard disk

Fig.1 The parallel hardware architecture

0-7803-3836-7/97/$10.00 © 1997 IEEE

Space to Disk Allocation

In order to improve I/O concurrence, we parallelize Ladex to meet the following three parallelism requirements.

(1)Non-intersection allocation. After being parallelized, different disk contains objects in different map space.

(2)Balanced allocation. We should uniformly allocate spatial objects to the disks according to the map space so that we can benefit from the parallelism of the disks.

(3) Reasonable space partition granularity. Use more disks as possible for large region, and avoid the small region taking up too many disks.

The Allocation Approach: Suppose the number of disks is D, they are labeled as $D_0,D_1,D_2,...,D_{D-1}$. Allocate the spatial objects which are correspondent to the small block Block[i,j] in Ladex structure to the disk (i+j) mod D.

It is obvious the above allocation approach can roughly meet the abovementioned parallel requirement(1) and (2). Suppose M×N can be divided by D without any remainder. It is also obvious that the area or space sizes assigned to the disks are equal. If the objects are randomly distributed in the map space, the storage loads of the disks are also equal. This allocation approach can meet the requirement(2) with the exception of extreme data skew of blocks.

As to partition granularity, Fig.2 shows a 8x8 Ladex structure with four disks. RQ1 and RQ2 are two region queries. Large query RQ1 intersects with the blocks Block[i,j], where 0<i<4, 4<j<8. Apparently, the relevant objects in these blocks are stored in all of the four disks. The small query RQ2 only intersects with Block[5,2] and Block[6,2]. So, in general only two disks will be activated. If we partition the map space more rough(for example 2×2), all of the objects related to RQ1 will be stored in only one disk. So, we can not make full use of the ability of parallel disk I/O. On the other hand, if we partition the space into 16×16 small blocks, the small query RQ2 will activate all of the four disks. Hence, the partition granularity should be made suitable for specific applications. Generally speaking, to determine the value of M and N, the following inequality is a good suggestion:

$$D\times 2\times 2 \leqslant M\times N \leqslant D\times 8\times 8$$

However, in real application, the objects in a map space can not be distributed uniformly, so data skew between in the disks is unavoidable. Two cases may arise: (1) A lot of small blocks have few objects, thus the storage utilization rate of the bucket pages is relatively low;(2) Some small blocks have got very high density of objects.

A good solution to the first case is to merge the low-storage-utilization-rate pages in each disk. To handle the second case, we can move some storage pages to other disks to make even number of pages between disks. Fig.3 shows the procedure.

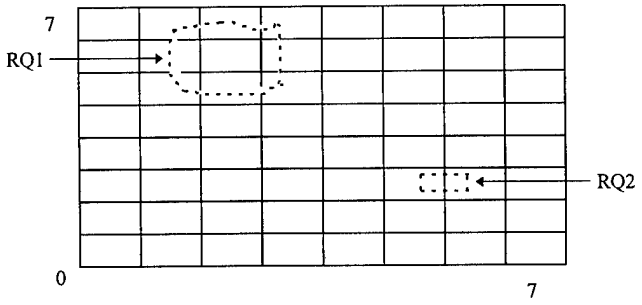

Fig.2 Space partition and region queries

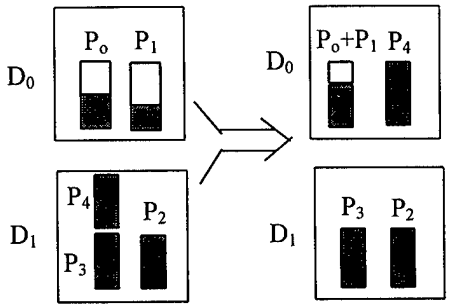

Fig.3 Page merging and balancing

(Here p_i is a page)

Space to Processor Allocation

We exploit multiple processors to execute a query or a set of queries cooperatively or concurrently. Suppose one of the processors undertakes the commission of query task partition, allocation and query control. This processor is called *manager*. The other processors are called processing units, which execute the query tasks. Actually, the responsibility of manager can be taken over by the processing unit.

The Allocation Approach: Suppose the number of processors is P, they are labeled as $P_0,P_1,P_2,...,P_{P-1}$. Allocate the query operation related to the small block Block[i,j] in Ladex structure to the processor (i+j) mod P.

The requirements of space to processor allocation is similar to that of space to disk allocation. Nevertheless, the former has the following three new features.

(1)The number of processors can be unequal to that of disks.

(2) The space to processor allocation is more flexible than that of space to disk allocation. In fact, it is easy to change the allocation approach to suit the application environment. For example, we can allocate query or subquery in Block[i,j] to processor (i/2 mod P), (j/2 mod P) or ((i+j)/3 mod P) without too much cost. However, while changing the space-to-disk allocation, a huge storage reorganization is needed.

(3)Dynamic load balancing among the processors. When the manager receives a query, it partition the query region according the space-to-processor allocation method, and

creates corresponding subquery tasks, distributes them to related processing units. In order to realize dynamic balance, we allocate subquery tasks to idle processors while the corresponding processors are busy. Fig.4 shows the ideas.

OPERATION ALGORITHMS

There are many kinds of the operations on parallel Ladex[1]. For the space limitation of this paper, we only introduce the main ideas for line insertion algorithm and region query algorithm.

Line Insertion Algorithm

(1)The manager receives the line to be inserted;

(2)According to the space-to-processor allocation, the manager partition the line into a group of point set;

(3)The manager passes each point set to corresponding processor(dynamic load balance is considered);

(4)The processing units receive the point set;

(5)Each of the relevant processing unit processes every point in its point set. After doing the space-to-disk transformation, the processing unit activates the related disk to do I/O operation and get the right page(The merge of storage pages and page redistribution are also considered);

(6)Register the point and the line-shape object in a data structure of index item;

(7)After every relevant processing unit has finished its insertion operation, the manager declare the end of the task.

Region Query Algorithm

(1)The manager receives the region query task to be executed;

(2)According to the space-to-processor allocation, the manager collects the relevant processing units;

(3)The manager passes the region condition to corresponding processing units(dynamic load balance is considered);

(4)The processing units receive the region condition;

(5)Each of the relevant processing unit processes the subquery in its related space. When an I/O operation occurs, the space-to-disk transformation are also considered in this step;

(6)After every relevant processing unit has got its result, the manager will union the results as a final result.

CONCLUSION

This paper has proposed the strategies and approaches to parallelize the Ladex index on a shared-disk parallel architecture. We parallelize the Ladex structure in two aspects: Space to Disk Allocation and Space to Processor Allocation. We have also discussed the relationship between the partition granularity and the performance. To improve the utilization rate of storage, we merge the sparse pages in each disk. To solve the data skewing problem in small blocks, we move some pages to other disks to balance the storage amount in each disk. We partition a query into subqueries and assigne them to corresponding processors to concurrently execute. In our experiments, the performance of the parallel Ladex mechanism is very good. Due to space limitation, we will not present the results here.

Seq.	Query No.	Partition (subqueries)			
0	Q_0	Q_{00}	Q_{01}	Q_{02}	
1	Q_1	Q_{10}	Q_{11}		

(a) Query partition and subquery allocation

Step	P_0	P_1	P_2	P_3
0	Q_{00}	Q_{01}	Q_{02}	ϕ
1	ϕ	Q_{01}	Q_{02}	ϕ
2	Q_{10}	Q_{01}	Q_{02}	Q_{11}
3	ϕ	ϕ	ϕ	ϕ

(b) Dynamic balancing

Fig.4 Query partition and load balancing

In our future work, we will extend the parallel Ladex mechanism to other kinds of parallel architecture, such as shared-nothing architecture. We plan to investigate on parallel spatial joins based on parallel Ladex. Furthermore, we want to extend the parallel Ladex mechanism to multi-dimension space.

REFERENCES

[1] Xiao Weiqi, Feng Yucai, "Ladex: A New Index Mechanism for Spatial Database System", International Archives of Photogrammetry and Remote Sensing. Vol. XXXI, Part B3. Vienna, 1996, pp. 930-935.

[2] A. Guttman, "R-tree: A dynamic index structure for spatial search", Proc. ACM SIGMOD, June, 1984, pp.47-57.

[3] Ibrahim Kamel and Christos Faloutsos, "Parallel R-tress", Proceedings of ACM SIGMOD,California, USA, June, 1992, pp.195-204.

[4] Hoel E., Samet H., "Performance and Data-Parallel Spatial Operations", Proc. 20th Int. Conf. On Very Large Databases, Santiago, Chile, 1994, pp.156-167.

[5] Thomas Brinkhoff, Hans-Peter Kriegel, Bernhard Seeger,"Parallel Processing of Spatial Joins Using R-trees", Proceedings of 12th IEEE International Conference of Data Engineering , 1996, pp. 258-265.

GIS Modeling in Coastal Flooding Analysis: A Case Study in the Yellow River Delta, China

Xiaojun Yang
Department of Geography
The University of Georgia
Athens, GA 30602, U.S.A.
Tel: (706)5422926 Fax: (706)5422388
Email: YANG@UGA.CC.UGA.EDU

ABSTRACT

The rising sea level caused mainly by global climate change has become an eminent global environmental problem. Around the coast of the Yellow River Delta, the relative sea-level is rising by 6-10 mm per year. By 2100, the accumulated sea-level rise will be 600-1000 mm. It would directly threaten the low-lying coastal area, home of the second largest oil field in China, the Shenli Oilfield. Some GIS modeling techniques have been used to calculate the area susceptible to coastal flooding due to sea level rise, by incorporating the database uncertainty and risk concept. The magnitude of sea level rise in 2100 has been simulated with respect to its flooding effect over the coastal lowland in the Yellow River Delta, China.

INTRODUCTION

The eustatic sea-level change has become an eminent global environmental problem. The effects of such slow changes may be severe. Around the coast of the Yellow River Delta, tectonic measurements indicate that the overall subsidence rate is approxiamtely 4 - 5 mm per year. According to the Inter-Governmenta Climate Committee, current eustatic sea-level is rising by 1 - 2 mm per year. In the future, this rate will increase up to 5 mm per year. Combining those two aspects, the future relative sea-level rise will be up to 10 mm per year (Ren, 1994). By 2100, the accumulated sea-level rise will be 1000 mm. The rising sea level caused by global climate change would directly threaten low-lying coastal lowland.

This work aims to use GIS techniques to calculate the area susceptible to coastal flooding due to sea level rise, by incorporating database uncertainty and risk concept. The magnitude of sea level rise in 2100 will be simulated with respect to its flooding effect over the coastal lowland in the Yellow River Delta, China.

STUDY AREA

The Yellow River Delta is situated in the north of Shandong Province, China (Fig. 1). Bounded within the latitudes of 36°16'00" - 38°13'00" and the longitudes of 118°5'00" - 119°23'00", the delta has an area of 5,800 km^2 in 1994. It is a relatively low lying, flat area. The height on the deltaic apex is 9m higher than the mean sea water level with a steepness of less than 0.1%. It was fromed by the present Yellow River which entered the Bohai Sea (again) in 1855. The delta area is one of the most important oil-producing areas in China. A large oil terminal and sea port, the Huangho Seaport, is presently under construction. The potential for future economic development is promising.

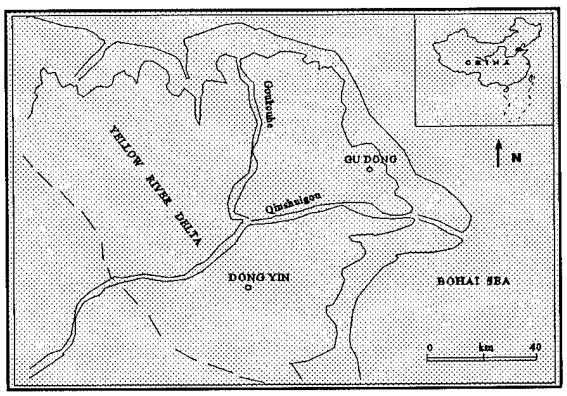

Figure 1 Location map of the study area.

DATA AND METHOD

The primary data for this study is a topographic map covering the Yellow River Delta. This study is mainly based on a classical approach, thresholding, by incorporating database uncertainty and risk. A work chart has been made to explain the procedure (Fig. 2).

A number of hypotheses have to be established in order to carry out the simulation:

- The contour map is without error;
- In 2100 the sea level rise will be exactly 1.8 m;
- Error is random (normal distribution);
- Ninety percent of all measurements fall within 1.645 standard deviations of the mean, i.e. 1.645 RMS = C/2. RMS = 0.30 C, where C is the contour interval;
- The accepted level of risk is 20%.

This study consists of three major steps:

- *Preparation of a digital elevation model (DEM)*. Digitizing the contour line using PC ARC/INFO program. Importing the digital contour line file into IDRISI program using DLG module

0-7803-3836-7/97/$10.00 © 1997 IEEE

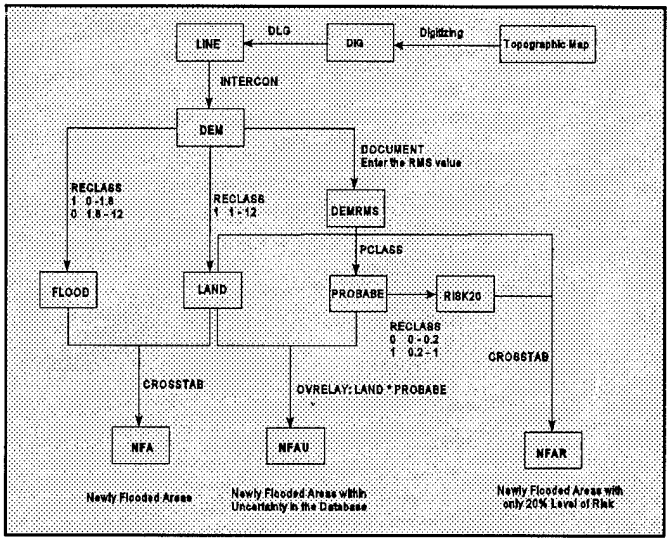

Figure 2 Procedure route of research study.

and rasterizing it using module LINERAS. Creating DEM under module INTERCON.

- *Data analysis* done using RECLASS, OVERLAY, PCLASS, CROSSTAB, DOCUMENT modules under IDRISI program.
- *Output and presentation.* Three important maps have been created: map of newly flooded areas, map of newly flooded areas within uncertainty in the database, map of newly flooded areas with only 20% level of risk.

RESULTS

Digital Elevation Model (DEM)

A digital elevation model (DEM) has been created using Module INTERCON under IDRISI program. In IDRISI, Module AREA allows to calculate area of each (integer) elevation unit. The result can be found in Table 1. This work permits an insight in the characterization of terrain conditions of the study area. As can be derived from Tab. 1, more than 50% of the subaerial part is lower than 2m.

Table 1 Some Topographic Statistics of the Yellow River Delta.

Elevation (m)	Area (km²)	Percentage (%)
0	728	6.27
1	4605	39.64
2	1228	10.57
3	943	8.12
4	900	7.75
5	670	5.77
6	783	6.74
7	599	5.16
8	1028	8.85
9	132	1.14
In total	11616	100

Map of Newly Flooded Areas

By proper reclassification of map DEM, two maps FLOOD, LAND have been created. 1.8 m was set as the thresholding value of sea level rise in 2100.

Please note that it is not possible to distinguish the present sea areas from the expected flooded areas. Map LAND is actually a boolean image of land areas before sea level rise. Using module CROSSTAB , a map NFA showing all combinations of the logical AND operation of maps FLOOD and LAND was created (Fig. 3). Unit 3 on map NFA is the newly flooded areas due to sea level rise in 2100. It has an area of 772 km², occupying 6.7% of the total *land* area in the delta (Tab. 2).

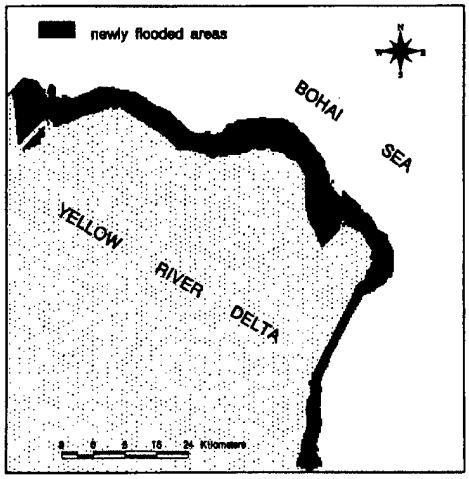

Figure 3 Map of newly flooded areas.

Table 2 Calculated newly flooded land areas.

Unit ID	Unit Name	Area (km²)	Percentage (%)
1	sea	4961	42.7
2	land	5882	50.6
3	newly flooded land	772	6.7

Map of Newly Flooded Areas within Uncertainty in the Database

Based on a number of hypotheses (see above), the RMS value was incorporated into modeling. Since the contour interval of DEM is 0.6 m, the RMS is therefore 0.18m (RMS = 0.3*C). Using module PCLASS, the probability that any pixel in the image exceed or is exceeded by a specified threshold value was assessed (PROBABE). By OVERLAY of LAND and PROBABE, a final map NFAU showing newly flooded areas within uncertainty in the database was created (Fig. 4). As can be seen from Fig. 4 and Tab. 3, the probability of uncertainty is increasing landwards.

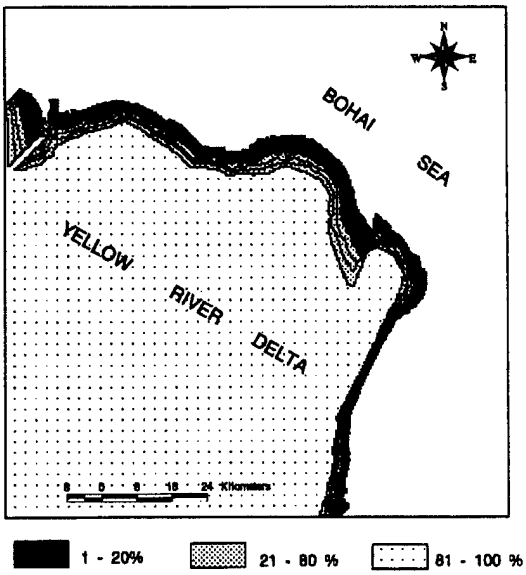

Figure 4 Map of newly flooded areas with only 20% level of risk.

Table 3 Calculating newly flooded areas within uncertainty in the database.

No.	Probability	Area (km²)	Percentage (%)
0	0	5392	46.42
1	0.067	98	0.84
2	0.133	58	0.5
3	1.2	53	0.46
4	0.267	46	0.4
5	0.333	38	0.33
6	0.4	35	0.3
7	0.467	38	0.33
8	0.533	48	0.41
9	0.6	48	0.41
10	0.667	46	0.4
11	0.733	58	0.5
12	0.8	30	0.26
13	0.867	128	1.1
14	0.933	397	3.42
15	1	5101	43.92

Map of Newly Flooded Areas with only 20% Level of Risk

Risk is the likelihood that the decision made will be wrong; it is a result of uncertainty, and it assessment requires a combination of uncertainty estimates from the various sources involved and procedures through which it can be determined. By accepting 20% levels of risk related to the probability of areas of being flooded, we can calculate the areas that will be inundated by a rise in sea level as a result of global warming (Fig.5 and Tab. 4).

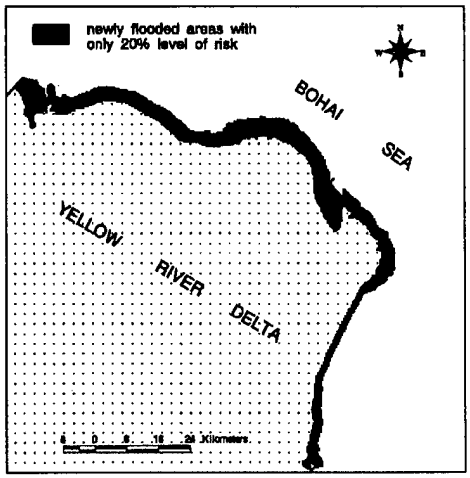

Figure 5 Map of newly flooded areas within uncertainty in the database.

Table 4 Calculating newly flooded areas with 20% level of risk.

Unit ID	Unit Name	Area (km²)	Percentage (%)
1	sea	4961	42.7
2	newly flooded areas with only 20% level of risk	474	4.1
3	land	6180	53.2

CONCLUSIONS

Based on a number of hypotheses, the newly flooded areas due to sea level rise in 2100 are 772 km², which is about 6.7 % of the total land area in the delta. However, by incorporating database uncertainty and 20 % level of risk, the areas that will be inundated by a rise in sea level are 474 km². The coastal lowland areas which will be flooded due to sea level rise are the most important oil-producing areas in the Yellow River Delta. Increasing sea level will result in large area loss of coastal lowland, thus definitely increasing the cost in oil-producing and posing other adverse effects on the environment. Immediate action on sea-level rise and its impacts should be addressed.

GIS modeling is found to be valuable in stimulating global sea level change and its flooding effect by incorporating database uncertainty and risk.

REFERENCES

[1] J. R. Eastman, "IDRISI Technical Reference", Clark University, 1-178pp, 1994.

[2] M. Ren,(edt.), "Sea Level Rise and Its Impacts on the Deltaic Lowland Area in China", Beijing, Science Press, pp353, 1994.

[3] X.Yang, "Monitoring Morphodynamic Aspects of the Present Huanghe River Delta, China, An Approach to the Integration of Satellite Remote Sensing and Geoinformatics Systems (GIS)", Enschede, TheNetherlands, pp192, 1995.

COMBINATION BETWEEN REMOTE SENSING AND ECOSYSTEM OBSERVATION NETWORK IN CHINA

Zhang Qijuan
Headquarters on remote sensing of Chinese Academy of Sciences
(Beijing , 100089, China)
Zhang Renhua
Institute of Geography, Chinese Academy of Sciences
(Beijing ,100101, China)

Abstract--This paper discussed about how to conduct quantitative remote sensing in China. First of all , there is increasing of quantitative application in ecological system. However obstructors for carrying out the quantitative remote sensing are limitation of remote sensing information and complicated atmosphere radiation transferring problem. At present, models with physical significance and statistic algorithm , time extension and space extension may improve the limitation of the remote sensing information. Simultaneous measurement will be able to help us to overcome some troubles in atmosphere radiation transferring .There are more than 80 ecological stations in China that has formed a effective ecological system network. Combination the remote sensing information and measurements in the ecosystem research network will promote development on quantitative application of remote sensing .

INTRODUCTION

Remote sensing technique and application in China have been developed for two decades. Remote sensing teams of China Academy Sciences is one of the most advanced institutions in China in developing various technology and applications . At present the most of remote sensing applications are developing towards to quantitative direction . For example , GCM in global change project needs to get more precisely quantitative boundary condition such as bidirectional reflectance, albedo , ground surface temperature, leaf area index , plant height and so on. Regional scale water balance and water cycle need to obtain usable soil moisture and evapotranspiration distribution information in large area . Estimation of crop yield should extent from visible and near infrared wavebands to thermal infrared waveband to procure crop water stress index which require identical precision crop surface temperature compare with air temperature .

However there are stronger challenge to reach these goals. In the beginning of remote sensing application, the most of the projects are limited on the land use , land cover investigation and so on. Changing of need with recent application such as the global warming , the climate change, regional water balance and water circle etc. , more and more quantitative remote sensing projects have been developed . For instance , quantitative inversion for vegetation structure and biomass using bidirectional reflectance distribution function (BRDF) , inversion of true land surface temperature , quantitative estimation of the ground surface fluxes and so on all belong to quantitative remote sensing application with considerable difficulties. In order to develop these quantitative application there are major obstacles.

(1) limitation of remote sensing information which only are reflectance and surface brightness temperature in the optical remote sensing; In order to transform the limited remote sensing information into application information , not only several supplemental parameters should be known but also extensions of the time and space must be down .

(2) Complex nature of the atmosphere radiation transferring , for which so far there is no perfect radiation transferring model. Practise points out such as 6s model still exists larger error. However, one do not use remote sensing information to develop quantitative application until the atmosphere problems are perfectly solved. Therefore an effective way of combination between ecological station network and remote sensing technology and simultaneous measurement method are presented .

In this paper, first of all, we will describe the role of the ecological stations and their network in the development for divers application models , for the time and space extensions . Then, we would like to discuss the methodology for carrying out the

0-7803-3836-7/97/$10.00 © 1997 IEEE

simultaneous measurement in detail. Finally we will summarize roles of those methods in several quantitative remote sensing results in the Water Center of Chinese Ecosystem Research Network

SIMULATED REMOTE SENSING

For developing quantitative remote sensing application it is important step to establish simulated remote sensing site, to conduct simulated remote sensing experiments and to develop remote sensing models. Through remote sensing model , one can transform remote sensing information into application information The most of remote sensing model needs both remote sensing data and supplemental data. Because, for general optical remote sensing , the remote sensing data just are reflectance and brightness temperature of the measured surface. To obtain application information supplemental data is necessary. A experimental site provide a convenient place for establishing remote sensing model which approach the quantitative relationship between the remote sensing data and supplemental data and create the physical function and statistic coefficient.[1][2][3][4].

The most of quantitative application needs a regional distribution , sometime, needs accumulated amount in a time interval (day or week). For this reason, the space extension of the supplemental data and the time extension of remote sensing data are very important steps. Fig.1 shows how do we carry out the space and time extension .

SIMULTANEOUS MEASUREMENT

In order to obtain the data of acceptable precise for the surface reflectivity and temperature in situ, a feasible method is to carry out simultaneous measurement with the satellites. According to our practice: so far, the atmosphere radiation transferring models or algorithms such as 5s, 6s models still have unacceptable error for quantitative applications. Even though , there is a perfect atmosphere radiation transferring model with acceptable precision , one still need to measure many atmosphere parameters in situ whose labour power and material resources cost are almost equal or more than the simultaneous measurement. Therefore we deemed the simultaneous measurement with satellites is reasonable.

We introduce the simultaneous measurement method and limitation.(see Fig.)1 At least, the

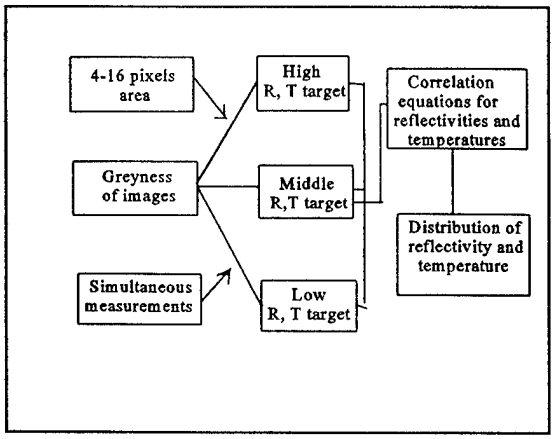

Fig1 Calibration using simultaneous measurement

surface targets with high, middle and low reflectivity and surface temperature, homogeneous and more than 4-16 pixels area should be established . Generally, we seek and choose sand land as high reflectivity and temperate target, homogeneous crop field or grass land as middle target, water body as low target.

The representative data of the reflectivity and the surface temperature in the targets must be obtained . To reach the goal, for surface temperature almost absolute simultaneous measurement is necessary. We used portable thermal infrared - radiometers with 15° field of view to measure surface temperature . When the satellite passed over the three targets , 50-100 readings of the thermal infrared radiometers should be measured by automatic data logging as short time interval as possible . Each measured tracks ought to be have two repeats . The measured order are 1,2 3,.....100 for first time , and 100, 99, 98.....1 for second time. Then the two repeats should be averaged .

For the reflectivity , approximate simultaneous measurements are needed only . We adopted CCD portable spectrum radiometer which can measure 200 readings automatically in 10 minutes to measure the reflectivities of the three targets . Bidirectional reflectance distribution function (BRDF) for each target should be observed . BRDF need not simultaneous measurements with satellites.

Using above mentioned simultaneous measurements to conduct the calibration of remote sensing images, we obtain acceptable precision for the reflectivity and surface temperature. As well know, the distribution images of the reflectivity and surface temperature are basic information for remote sensing application. The output signals of the remote sensing images such as TM, NOAA-AVHRR are just greyness levels in various wavebands. The greyness levels of the three targets with 4-16 pixels at corresponding position of the image can be transformed into reflectivities and surface temperature by the representative data of the three targets. Because the measurements of the three targets are almost from maximum to minimum greyness levels in the images. Correlation equations between the reflectivity (or surface temperature) and greyness levels can be established according to simultaneous measurements in situ. This kind of method is called "space extension". There is different meaning between the space extension and interpolated method which is used in some supplemental parameters such as the air temperature, wind speed.

For some application , total amount on whole day is needed . For this reason, a " time extension " should be used by the time profile data which is established at the ecologic or meteorological or horological stations . There are 80 ecological station in China, in which 30 stations can carry out simultaneous measurements. Those ecological stations are equipped by advanced computer system . There are 4 sub-centers in the Chinese Ecosystem Research Network (CERN) have advanced GIS,database and remote sensing image processing systems . Therefore , the ecological station network will give great support to the quantitative remote sensing

In the north China there is lack of water . So the projects concerning water circle and the water balance are very important in regional scale. The combination between the ecological station network and remote sensing technology will set into motion of the development of those projects.

Several results for applications in leaf area index, soil moister, evapotranspiration and so on have obtained using the space extension and the time extension.

Limitation for the simultaneous measurement still exists. Major limitation is the assumption that atmosphere parameters are the same approximately in the range of the image. The assumption may cause error when space distribution of atmosphere states is not homogeneous. However on a very clear day controlled by a identical air-mass, the assumption may not results in big error in the region .

CONCLUSION

At present , we deemed the simultaneous measurements and combination between the ecological station network and remote sensing are the feasible way for developing quantitative remote sensing applications. Meanwhile, more precise atmosphere radiation transferring model still ought to be developed . The simultaneous measurements also is a good validation and calibration for developing models of the atmosphere radiation transferring projects.

REFERENCES

[1] R. H. Zhang , X .M. Sun and Q.J. Zhang, "Simultaneous measurement --- A feasible way for the study of the quantitative remote sensing in various ecological system" , Research for Resources and Ecological Environment , Vol. 7:4 pp 8-16 1996.

[2] R.H. Zhang, "Remote sensing models and ground foundation", Science Press, 1996.

[3] P.N. Slater, S.F. Biggar, R.G. Holm," Reflectance and radiance-based method for the in-flight absolute calibration of multispectral sensors", Remote Sensing of Environment,Vol. 22 , pp. 11-37, 1987.

[4] G. Cuyot, X.F. Gu, " Radiometric correction for quantitative analysis of multispectral, multitemporal and multisystem satellite data, Remote Sensing of Environment, Vol 30:2 1992

IGARSS'97

1997 International Geoscience and Remote Sensing Symposium

03-08 August 1997

Singapore International Convention & Exhibition Centre

Technical Program

Interactive Area 13: Ground Penetrating Radar

Full-Wave 3D–Modeling of Ground-Penetrating Radars by a Finite Element/Boundary Element–Hybrid Technique

Thomas F. Eibert and Volkert Hansen
FB Elektrotechnik, Uni Wuppertal
Fuhlrottstr. 10, D-42119 Wuppertal — Germany
Tel.: +49 202 439 3666, FAX: +49 202 439 3045
email: eibert@wetet01.elektro.uni–wuppertal.de

Norbert Blindow
Institut für Geophysik, Uni Münster
Correnstr. 24, D-48149 Münster — Germany

Abstract

A full–wave 3D–hybrid field calculation technique is presented for the calculation of ground–penetrating radar systems. The approach combines the method of moments applied to a surface integral equation formulation (boundary element method (BEM)) being the favourite technique for the modeling of metallic antenna structures with the analytic Green's function description of plane layered media and with a finite element (FE) model of possibly buried objects. So, only the metallic parts of the antennas and the buried objects have to be discretized, whereas the air/soil–interface or interfaces between different soil layers are included into the formulation based on the Green's functions of the plane layered medium. The method was applied to the simulation and optimization of resistively loaded and shielded bow–tie antennas and to the simulation of practical radar configurations. Numerical results and measurements are presented.

1 INTRODUCTION

Electromagnetic modeling of ground-penetrating radars is mainly dependent on a proper description of the transmitting and receiving antennas, the object to be detected as well as the air/ground interface together with the correct ground parameters (lossy, dispersive). The modeling of the antennas can favourably be done by an integral equation technique together with the method of moments. Arbitrary objects buried in the ground can effectively be described by a local field calculation technique like finite differences or the finite element method, whereas the air/ground interface should be described based on the analytic Sommerfeld approach.
In [1] a two–dimensional analysis of a subsurface radar system based on the Transmission Line Modeling (TLM)–method was described and in [2] a fully 3D simulation based on the Finite Difference Time Domain (FDTD)–method was performed. In both methods the entire solution domain together with the antennas has to be discretized with the applied local technique. In this case an accurate modeling of the antennas is very difficult and severe problems with absorbing boundary conditions limiting the necessarily finite solution domains have to be overcome. An advantage of these time–domain methods is that the pulse behaviour can be dealt with in a straigth–forward manner.
In our method we start with a surface current density description of the antennas together with an integral representation of the fields. The field distribution in the unbounded layered structure consisting of air and different layers of soil is obtained with the help of the Green's function of the layered medium which is derived analytically based on the Sommerfeld approach. Buried objects in the soil layers are included into the model by equivalent Huygens' surface current densities on a surface completely enclosing the buried objects. Based on the boundary conditions the Huygens' surface current densities are coupled to a FE–model of the buried objects. The method is working in the frequency domain. Time domain responses are obtained with the help of a Fourier transform.
In section 2 the theoretical formulation of the hybrid method is summarized. In section 3 numerical results and measurements are presented.

2 FORMULATION

An illustration of the field theoretical model is given in Fig. 1. The unbounded solution domain consists of an arbitrary number of plane layers representing several soil layers and the air halfspace. The metallic antennas and possibly present other metallic objects are described by their surfaces A_c. The volume occupied by possibly inhomogeneous buried objects is designated by V_a, the remaining parts of the layered structure are called V_b. For the field representation in the layered structure we introduce equivalent Huygens' current densities on the Huygens' surfaces A_d and A_c. On A_c we only have an

0-7803-3836-7/97/$10.00 © 1997 IEEE

electric surface current density $\vec{J}_A$ which is equivalent to the physical electric current density in the metallization of the antennas. On A_d we have electric and magnetic surface current densities which are given by

$$\vec{J}_A = \vec{n} \times \vec{H}_b\,, \quad \vec{M}_A = -\vec{n} \times \vec{E}_b\,. \tag{1}$$

The index b indicates the fields in the volume V_b. $\vec{n}$ is the surface normal pointing into V_b.

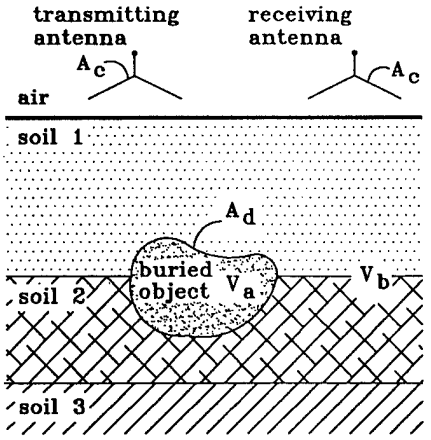

Fig. 1: Field theoretical model

The connection to the fields inside the volume V_a is given by the boundary conditions on A_d

$$\vec{n} \times \vec{E}_a = \vec{n} \times \vec{E}_b\,, \quad \vec{n} \times \vec{H}_a = \vec{n} \times \vec{H}_b\,. \tag{2}$$

The fields inside the volume V_b are calculated by the mixed potential integral representation

$$\begin{aligned} \vec{E}(\vec{r}) \;=\; & -j\omega \iint_A \overleftrightarrow{G}^A(\vec{r},\vec{r}\,') \cdot \vec{J}_A(\vec{r}\,')\, da' \\ & -\nabla \iint_A G^\Phi(\vec{r},\vec{r}\,')\rho_A(\vec{r}\,')\, da' \\ & + \iint_A \overleftrightarrow{G}^E_M(\vec{r},\vec{r}\,') \cdot \vec{M}_A(\vec{r}\,')\, da'\,. \end{aligned} \tag{3}$$

The electric surface charge density ρ_a is otained by the continuity equation

$$\rho_A(\vec{r}) = -\frac{1}{j\omega} \nabla_A \cdot \vec{J}_A(\vec{r})\,, \tag{4}$$

where $\nabla_A \cdot$ is the surface divergence operator. $\overleftrightarrow{G}^A$, G^Φ, and $\overleftrightarrow{G}^E_M$ are the Greens' functions of the solution domain. In this context it is very important that after introducing the equivalent Huygens' sources the fields inside V_a due to the integral representation (3) vanish. This means that V_a can be filled with arbitrary materials making it possible to use the Greens' functions of the undistorted layered structure which can be derived analytically in the spectral domain. By imposing the boundary conditions on the surface A_c and A_d we obtain an integral equation for the unknown surface current densities or the equivalent tangential components of the field strengths. The integral equation is discretized by edge element expansion functions on triangular meshes and transformed into a linear algebraic system of equations with the help of a Galerkin testing procedure. The fields inside V_a are described by the finite element method based on the variational formulation

$$\begin{aligned} F(\vec{E}_{ad},\vec{E}) \;=\; & \iiint_{V_a} \Big[\left(\nabla \times \vec{E}_{ad}\right) \cdot \overleftrightarrow{\mu}_r^{-1} \cdot \left(\nabla \times \vec{E}\right) \\ & \qquad -k_0^2\, \vec{E}_{ad} \cdot \overleftrightarrow{\varepsilon}_r \cdot \vec{E} \Big]\, dv \\ & + jk_0 Z_0 \oiint_{A_d} \vec{E}_{ad} \cdot \left(\vec{H} \times \vec{n}\right)\, da \end{aligned} \tag{5}$$

in terms of the electric field strength $\vec{E}$ and the electric field strength $\vec{E}_{ad}$ of the adjoint field problem. The functional is discretized by edge element expansion functions on tetrahedral meshes. A linear algebraic system of equations for the expansion coefficients is obtained by enforcing the stationarity condition with respect to $\vec{E}_{ad}$. Both linear algebraic systems of equations are coupled due to the boundary conditions on A_d and can be solved with the methods of linear algebra. A more detailed derivation of the formulation can be found in the references [4] and [5]. The excitation of the transmitting antenna is performed with the help of an impressed Δ–gap voltage soure that is omitted in (3). Also concentrated impedances can be considered within the model.

3 RESULTS

A major advantage of the presented method is the well–defined modeling of the input port of the transmitting antenna with the help of a Δ–gap voltage source. After the numerical calculations one obtains the feed current due to the voltage of the soure allowing a direct calculation of the input impedance of the antenna which is essential for the pulse behaviour of the antenna. As antennas we used shielded and resistively loaded bow–tie antennas (see Fig. 2). The antenna illustrated in Fig. 2 is similar to the antenna used in [2].

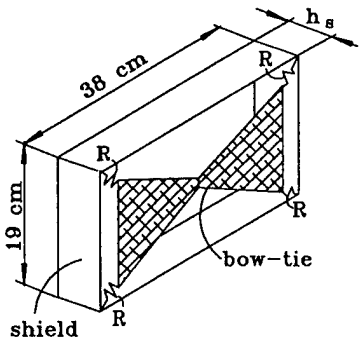

Fig. 2: Geometry of shielded bow–tie antenna

To investigate the broad–band and pulse behaviour of this antenna we performed calculations with one antenna 1 cm above a soil half–space with the relative permittivity $\varepsilon_r = 6 - j0.1$. The results for the input impedances of the antenna loaded with four 180 Ω–resistors can be seen in Fig. 3 for two different heights of the metallic shield. Based on these results we performed optimizations of the antenna form. The resulting input impedance is also illustrated in Fig. 3. The optimized antenna was loaded with four 150 Ω–resistors.

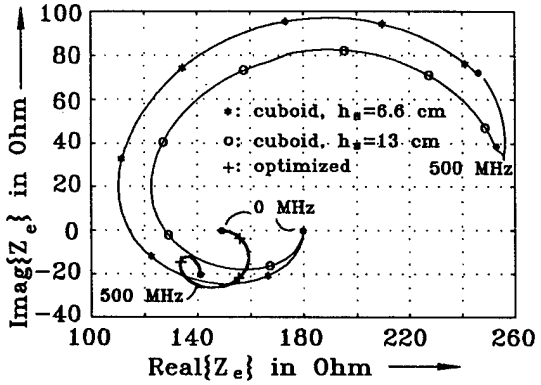

Fig. 3: Input impedances

Based on the optimized antenna form we performed calculations for several configurations with one and two antennas. In Fig. 4 the pulse response of the receiving antenna of a two–antenna configuration can be seen for a buried corner reflector in a soil half–space with $\varepsilon_r = 6 - j0.1$. The corner reflector had a height of 0.33 m and was placed in a depth of 1 m. The transmitting and receiving antennas were oriented parallel to each other with a distance between their feeding points of 0.8 m. The dashed line in Fig. 4 illustrates the used transmitter pulse which is the measured output signal of a commercial pulse generator.

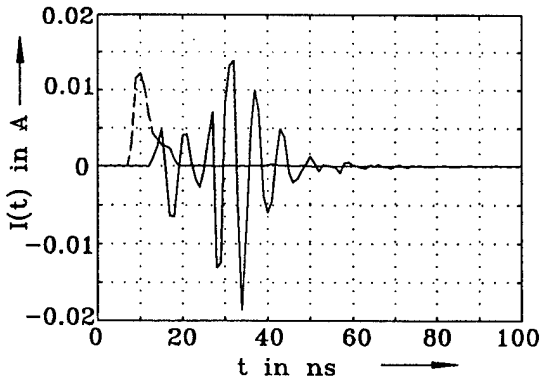

Fig. 4: Pulse response for a buried corner reflector

In Fig. 5 a measured pulse response for the optimized shielded bow–tie antenna is compared to an equivalent pulse response of a resistively loaded dipole (not shielded) of the company RAMAC. The measurements were performed on the island Spiekeroog with the GPR–system RAMAC/GPR. Again, the transmitting and receiving antennas were oriented parallel to each other with a distance of 1 m. To improve the ratio of the reflected signals and the direct signal between the two antennas the receiver signal was amplified with a linear time–dependent amplification. It can be seen that the reflected signal of the shielded bow–tie antenna is about 4 times larger than the reflected signal of the resistively loaded dipole. As compared to the calculated results in Fig. 4 in Fig. 5 the direct signals between the two antennas are considerably larger. This is due to the fact that the reflected signal of the corner reflector for the results in Fig. 4 is much larger than the measured reflected signals of the layered soil structure.

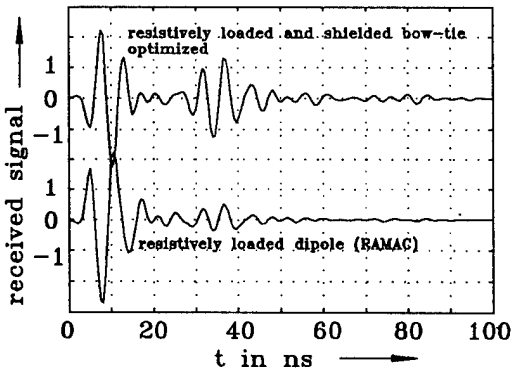

Fig. 5: Common midpoint measurement results for different antennas

References

[1] Liu, C., Shen, L. C., Numerical Simulation of Subsurface Radar for Detecting Buried Pipes, *IEEE Trans. Geosc. and Rem. Sens.*, Vol. 29, No. 5, Sep. 1991, pp. 795–798.

[2] Bourgeois, J. M., Smit, G. S., A Fully Three–Dimensional Simulation of a Ground–Penetrating Radar: FDTD Theory Compared with Experiment, *IEEE Trans. Geosc. and Rem. Sens.*, Vol. 34, No. 1, Jan. 1996, pp. 36–44.

[3] Shlager, K. L., Smith, G. S., Optimization of Bow–Tie Antennas for Pulse Radiation, *IEEE Trans. AP*, Vol. 42, No. 7, July 1994, pp. 975–982.

[4] Eibert, T. F., Hansen, V., 3D FEM/BEM–Hybrid Approach for Planar Layered Media, *Electromagnetics*, Vol. 16, No. 3, May–June 1996, pp. 253–272.

[5] Eibert, T. F., Hansen, V., 3D FEM/BEM–Hybrid Approach Based on a General Formulation of Huygens' Principle for Planar Layered Media, *IEEE Trans. MTT*, Aug. 1997.

Scattering from Periodically Located Objects Embedded near the Randomly Rough Surface of a Moist Soil

A.I.Timchenko, V.P.Tishkovets
Institute for Radiophysics and Electronics
National Academy of Sciences of Ukraine
Proscura 12, Kharkov, 310085, UKRAINE
Phone: 7-0572-448429/ Fax: 7-0572-441012/
E-mail:Timchenko@ire.kharkov.ua

Abstract -- A problem of scattering from some buried inclusions under a rough boundary has been considered. The angular backscattering for various relations between the wavelength and distance between inclusions, a depth from the boundary, various parameters of the rough boundary has been investigated. It is shown that the diffraction from the inclusions leads to the essential features of the backscattering intensity.

INTRODUCTION

There is a growing interest in using microwave remote sensing techniques to obtain information about buried objects. Usually the studies are oriented towards the detection of the separated target (see, for example, [1]). However, the situation where the illuminated area can contain some buried objects are often observed.

The main problem of this paper was to investigate the scattering problem, which arise when the electromagnetic wave is scattered from the some quantity of inclusions placed under the rough boundary.

At first, we develop the theory of rough surface scattering for the semi-transparent boundary based on the smoothing and diagram methods, which extends the range validity beyond the usual perturbation solution [2].

To describe the diffraction from the inclusions the dyadic Green's function in the case of a plane boundary was found, and a small inclusion volume compared to the wavelength was chosen.

The calculations were made for various inclusions number, various distances between them for the case of the backscattering. The optimal conditions for the detection of the buried objects are discussed.

THEORETICAL BACKGROUND AND RESULTS

Consider electromagnetic wave scattering, when the source is placed in the upper half-space bounded by the rough surface. There are some quantity of the inclusions N, embedded into the medium under the boundary.

To solve the scattering problem, first find the dyadic Creen's function for a plane boundary. The Green's function G_{1i} can be expressed as:

$$G_{1i} = G_{01} + k^2 \Delta\varepsilon \int_{-\infty}^{+\infty}\int\int d^3 r\, G_{11}\, G_{1i} - \\ - \sum_{n=1}^{N} \iiint_{v} d^3 r\, G_{11}\, G_{1i}, \qquad (1)$$

where k is the wave vector, G_{mi} ($m = \overline{0,1}$) are the Green's functions for the medium without the inclusions. The indexes 0,1 are related to the upper– and lower half-space, respectively; $\Delta\varepsilon = \varepsilon_1 - \varepsilon_2$ is the difference between the dielectric permitivities for the medium and inclusions and v is the volume of each inclusion. The Green's function G_{11} was determined for the medium with $\varepsilon = \varepsilon_0\, \vartheta(z) + \varepsilon_1\, \vartheta(-z)$ ($\varepsilon_0 = 1$, $\vartheta(.)$ is the Havyside function) with the source placed in the upper– and lower half-space, respectively.

Next, we assume that $k^3\, \Delta\varepsilon v \langle\langle 1$. Then the integral in (1) is evaluated with the method of the stationary phase. The first two terms in (1) are represent the Green's function G_{1x0} for the half-space with $\varepsilon = \varepsilon_0\, \vartheta(z) + \varepsilon_2\, \vartheta(-z)$, ($\varepsilon_0 = 1$). Taking into account this fact and calculating G_{1i} up the first-order G_{1x0} we obtain

$$G_{1i} = G_{1x0} - v_1 \sum_{n=1}^{N} G_{11}(\vec{r}\,, \vec{r}_n)\, G_{1x0}(\vec{r}_n, \vec{r}_0) \qquad (2)$$

where $v_1 = k^2\, \Delta\varepsilon v$, $\vec{r}_n$ means the coordinate of the "n" inclusion.

Similarly, for the Green's function in the upper half-space G_{1x0} we get:

$$G_{0i} = G_{0x0} - v_1 \sum_{n=1}^{N} G_1(\vec{r}_1\,, \vec{r}_n)\, G_{1x0}(\vec{r}_n, \vec{r}_0) \qquad (3)$$

where G_{0x0} is the Green's function for the medium with $\varepsilon = \varepsilon_0\, \vartheta(z) + \varepsilon_1\, \vartheta(-z)$.

Next, consider the electromagnetic scattering from the semi-transparent rough boundary. For this purpose expand

0-7803-3836-7/97/$10.00 © 1997 IEEE

the fields in the upper– and lower half-space about z=0. Substituting this expansion into the boundary conditions at the surface z = h(x,y) and taking into account the first-order term we obtain the boundary conditions at z=0. Then we make use of G_{1i} , G_{0i} and apply Green's theorem. Besides, express the Green's function as one part associated with the existence of the inclusions and the other part describing the scattering only from the rough surface.

The Dyson's equation can be obtained for the average Green's functions. Making use of the first-order smoothing we get the bilocal approximation. Finally, neglecting the terms $\sim v^2$ and applying the Fourier transform for all Green's function we find the $\partial G / \partial z$ as an algebraic expression.

In order to calculate the incoherent intensity we apply the Bethe-Salpeter equation. The first-order intensity is obtained by taking the first-term of its iteration. Besides, the terms, which are proportional to the volume of the separate inclusion, are only accounted.

Next, making use the Fourier transform representation we evaluate the intensity I in the far field. Finally, we obtain the scattering cross section σ, which is defined by Ishimaru [2] as $\sigma = 2\pi\rho\, I / x_c$, where x_c is the unit length of the rough surface, ρ is the distance between the surface and the source.

$$\sigma = \sigma_1 + \sigma_2. \tag{4}$$

Here σ_1 is the intensity scattered from the rough boundary, while σ_2 is determined by the interaction of the waves scattered from the inclusions and the rough surface.

$$\sigma_1 = \frac{k_{zi}^2 k_{zs}^2 T_{ai}^2 T_{as}^2 W(k_{\perp i} - k_{\perp s})}{\left|1-Q_i\right|^2 \left|1-Q_s\right|^2}, \tag{5}$$

$$\sigma_2 = 2\,\mathrm{Re}\{v_1 \frac{2k_{zi}^2 T_{ai}^2 \Sigma (T_{0i} T_{0s} + Q_e T_{ai} T_{as})}{\left|1-Q_i\right|^2 (1-Q_i)(1-Q_s)}\}, \tag{6}$$

where $\mathrm{Re}(.)$ means that the real part of the corresponding expressions was taken;

$Q_r = -k_{zr}\, T_{ar} \iint dk_\perp\, k_z\, T_a\, W(k_\perp - k_{\perp r})$,

$Q_e = k_{zi}\, k_{zs} \iint dk_\perp T_{oi}\, T_{os}\, W(k_\perp - k_{\perp r})\, \exp(i\,(k_{z1i} + k_{z1s})z_n)$,

$\Sigma = T_{as}\, \Sigma_1 + T_{ai}\, \Sigma_1^*$,

$\Sigma_1 = \sum_{n=1}^{N} \exp(-i(k_\perp - k_{\perp s})\, r_{\perp n})$,

$T_{ar} = 1 - R_{0r}$, $(r = \overline{i,s})$, R_{0r} is the reflection coefficient in the case of the flat surface z = 0, the indexes i, s are related to the incidence and scattered angles θ_r, respectively, $k_{zr} = \sqrt{k^2 - k_{\perp r}^2}$, $k_\perp$ is the wave vector projection at the plane XOY, $W(k)$ is Fourier transform from the spectral density of rough boundary:

As the illustration of the theoretical results the typical σ_1, σ_2 and σ (the curves 1,2,3 at Fig.1, respectively) are shown as functions of the incidence angle for the case of backscattering. Fig.1 presents the backscattering with the wavelength of 2m from the 20×20 buried inclusions along the x and y coordinates, respectively. The distances between inclusions are equal $0.5/k$, the volume of the each inclusion is $v = 0.1/k^3$, the depth from the boundary is $0.025/k$. The soil permittivity is 3.1 and the water content is equal 5%. The chosen roughnesses are small: the correlation lengths are $l_x = l_y = 0.1/k$, rms heights are on the order $0.1/k$. The typical diffraction pattern is due to the rescattering of the diffracting rays by the rough surface. The numerical analysis shows that the increase in the inclusions quantity leads to the stronger intensity fluctuation. Also, greater separation between backscatter returns from the inclusions and roughnesses may result if one employs greater incidence angle. Note that the expression (6) gives us a possibility to obtain σ for the inclusions, which can be unperiodically placed. To summarize, the typical feactures for the backscattering intensity occur when there are some quantity of the buried inclusions under the rough surface. These results show that a certain number of artificial objects can be detected (for example, mine fields) by remote sensing technique.

REFERENCES

[1] K.O'Neill, R.F.Lussky, Jr., and K.D.Paulsen,"Scattering from a metalic object embedded near the rough surfface of a lossy dielectric," IEEE Trans. Geosci. Rem. Sensing, vol. 34, pp. 367-377, March 1996.

[2] Akira Ishimaru, "The diagram and smoothing methods for rough surface scattering," The 1989 URSI International Symposium of Electromagnetic Theory, Stockholm, Sweden, 14-17 Aug. 1989 (Stockholm, Sweden; Royal. Inst. Technol., 1989, pp. 509-511).

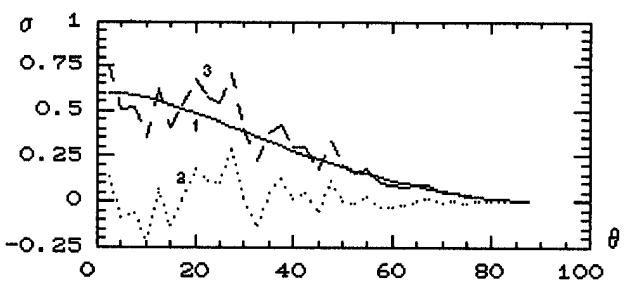

Fig.1

The Applications of GPR to Civil Engineering in China

Ying Xiaojian Yu Haizhong
Shenzhen Dasheng Advanced Science & Technique Engineering Co.,Ltd.
A12-10 of Zhongshen Garden Building, Caitian South Road, Shenzhen, 518026, P.R.China
Tel:+86755-3378301 Fax:+86755-3378300 E-Mail:dasheng@nenpub.szptt.net.cn
Wang Huiliang
China University of Geosciences(Beijing)

Abstract--Chinese civil engineering developed rapidly in the past decade. At the same time, some geotechnical problems are waiting to be solved urgently. Ground penetrating radar(GPR) can be used in broad range. It is a very effective way in solving some engineering geological problems and detecting buried objects under the ground. Since 1989, GPR gave play to its huge ability in proving, consulting, surveying and designing of over 200 key projects all over China. It includes stratigraphics division, outlining of filled stones in the muddy beach, geotechnical prospecting of old wall, karst detecting in the limestone terrain, caving detecting, landslide and slop surveying, the division of weathering zone, onion weathering zone, fracture zone and faulted zone in the granite area, detecting of buried objects (cable, metal & nonmetal pipe, channel, air raid shelter etc.) underground in the urban city, archaeology, tracing of orebody, coal measures strata division, testing of the dam and grouting site, quality checking of the surface and foundation of the highway.

In field, we always conduct GPR survey with two ways, they are reflect profile way and common depth profile way respectively. With regard to the different task and different dielectric feature of the objects, we choose different ways and different antenna to conduct the survey. Through years practical experiences of GPR survey, we have summed up a suit of techniques to solve various engineering geotechnical problems with GPR in China.

INTRODUCTION

GPR has played a more and more important role on civil engineering in China such as Engineering Geology and seeking of objects concealed underground since it was introduced in 1980s. It has strong adaptability and is portable suitable to the construction site under all kind of noisy surroundings in cities as well as its satisfactory penetrating depth and resolution in construction. So recent years in China mainland there are about 100 sets of GPR of various models and the number is increasing.

We imported GPR in 1989 and applied it to more than 200 projects in about 20 provinces and cities involved stratigraphics division, outlining of filled stones in the muddy beach, geotechnical prospecting of old wall, karst detecting in the limestone terrain, caving detecting, landslide and slop surveying, the division of weathering zone, onion weathering zone, fracture zone and faulted zone in the granite area, detecting of buried objects (cable, metal & nonmetal pipe, channel, air raid shelter etc.) underground in the urban city, archaeology, tracing of orebody, coal measures strata division, testing of the dam and grouting site, quality checking of the surface and foundation of the highway and obtained satisfactory result. We will introduce several practical examples for the application of GPR in this paper.

APPLICATION

1. Application of GPR in Three Gorges Project

Three Gorges Project in China attracts worldwide attention. Besides the detailed survey of the area of dam, GPR has given a good play in the 2 geological problems. One is dividing the weathered layer of the granite, the other is detecting the fracture in the granite.

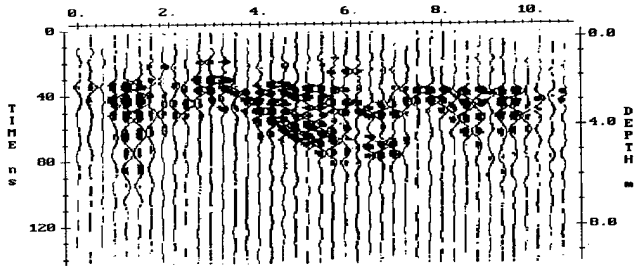

Figure 1. GPR Profile Collected in Three Gorges

Figure 1 is a profile collected by pulse EKKO 100 with 100 Mhz antenna and 1m trace interval. In this profile, the fracture are reflected clearly by the reflected radar wave.

2. Archaeological Application of GPR in Dunhuang

GPR's being applied to archaeology, tangible result has been archived because of the ancient tombs

0-7803-3836-7/97/$10.00 © 1997 IEEE

generally lie shallow underground and has distinguish difference in electricity from media surrounding .

Mogaoku in Dunhuang is a world-famous relics of ancient culture for its unrivaled frescoes. To protect it and make a further investigation of the adjacent caves, it is very important to exhume new frescoes and other relics.

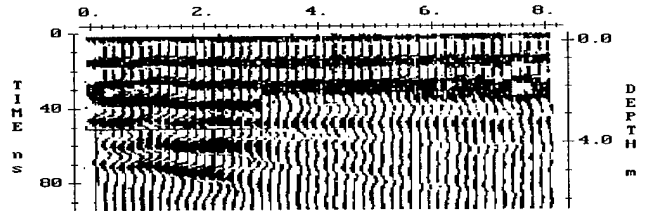

Figure 2. GPR Profile on Mogaoku in Dunhuang

Figure 2 shows an example of the penetration of GPR. Which was done from ground to subsurface on the collapsed section of the old cave with GPR pulse EKKO100, center frequency of 100MHz, antenna separation is 1 meter. We can see the hidden cave extends to right, the right interface is clear, the top and bottom interface is clear too. Beneath which , the width of the hidden cave is about 3 meters which was demonstrated by exhumation of the cave.

3. Application of GPR in Shenzhen Longkou Reservoir

Recent years in China, GPR was frequently applied to the survey of geological situation in many irrigation works. Especially in the limestone terrain which cause great harm to the construction of dam. It is very important to investigate the spread of karst before construction of the dam ant examine the quality of the grouting site after construction.

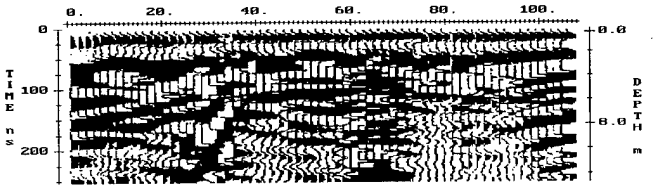

(a) Before Grouting

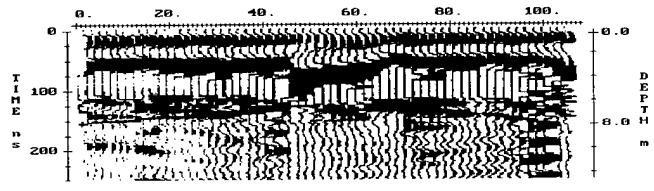

(b) After Grouting

Figure 3. GPR Profile in Shenzhen Longkou Reservoir

Figure 3 shows two profiles on the dam site of Shenzhen Longkou reservoir. They are collected by pulse EKKO IV with center frequency of 50 MHz and trace interval of 0.5 meter. Figure 3(a) shows the strong reflective wave, and the homophase waveform are staggered, which represent the distinct fault. Figure 3(b) also shows the distinct abnormality of fault, but the reflected energy is far lower which indicates that spaces within karst are filled up by grouting concrete.

4. Application of GPR in detecting of obstacles underground in cities

It is a very important task to find out obstacles underground in city construction. With the construction upsurge in China, pipe & cables and other obstacles under the ground of old cites are necessary to be investigate to prevent it from being damaged. The more developed the city is, the more work should be done underground.

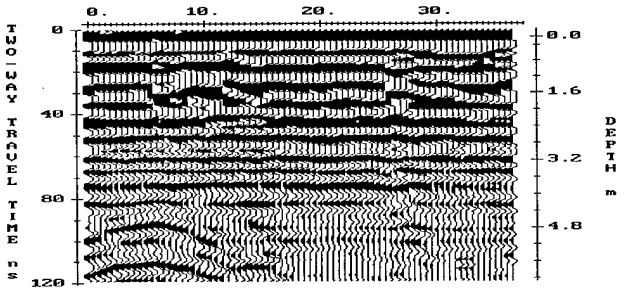

Figure 4. GPR Profile Detecting the Pipe

Figure 4 shows an example of application of GPR in Shenzhen, center frequency is 200MHz and antenna separation is 0.6 meter. A large water pipe was detected on the depth of about 4.6m.

5. GPR Application to The Project of Filling Sea

In some huge civil engineering of China, there are always some filling sea or lake project. In these project, it was necessary to outline the scope of filled soil or rock, the thickness of the silt beneath the filled soil or rock. Although the high conductivity of the sea water, provided that the filled soil or rock are not too deep, it still can be detected by GPR, because of the big difference between the filled soil or rock with silt or other sediment on the seabed.

Figure 5 is a profile collected on the filling sea site of the second phase project of Shenzhen Yantian Port. Pulse EKKO 100 was used, took 50Mhz antenna and 2m antenna separation. From this profile, we can clearly see the dividing line between the filled soil and the filled rock, and at position 80m-100m, we can see a

group of thin reflected wave, which represent the exist of the silt layer.

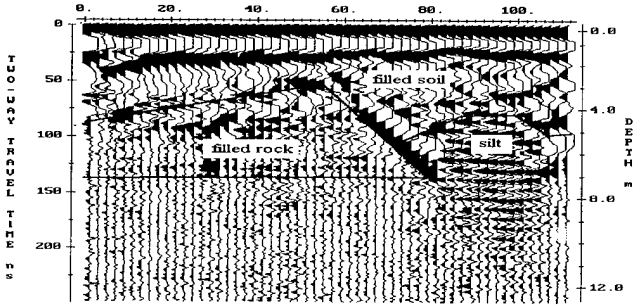

Figure 5. The Profile Collected on The Filling Sea Site

6. Application of GPR on landslide in Hongkong

Landslide is a kind of geological disaster. In Hongkong quite a number of houses are built on slope which leads to gravity landslide under special geological and geographical conditions on slope. Every year rainy season is the peak of geological disaster, so landslide is the main geological disaster to be solved.

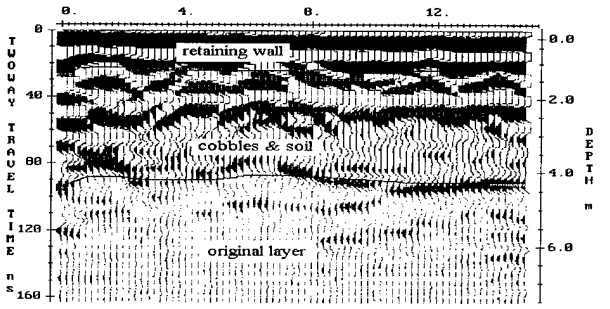

Figure 6. A Profile of Retaining Wall in HongKong

Figure 6 shows the radar profile collected on the retaining wall of high street clinic, in Hongkong. Pulse EKKO100 of Canada was used in field survey. From this profile, we can divide it to three layer from top to bottom. The first layer is retaining wall, about 1m thick; The second is cobbles & soil layer, buried on 1- 4.3m ; The bottom is the original layer, which tallies well with the drill hole. There is no clear slip surface on this profile, so we think the slope is stable.

7. Application of GPR in Karst Terrain

There is large limestone terrain in China, with an area of more than 1/3 of the total land area and Karst-developed zone is a main harmful factor to engineering construction. So it's necessary to make detailed investigation of the geological structure and distribution of Karst in these areas so as to provide enough references for engineering construction.

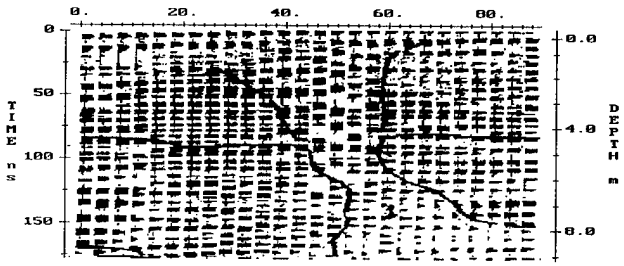

Figure 7. GPR Profile of Ground Breakdown

Figure 7 is a GPR profile of ground breakdown from a business street in Longgang district of Shenzhen, result in karst developing underground. Pulse EKKO IV penetrating radar from Canada was applied by reflection with the antenna frequency of 50MHz, antenna separation of 1 meter, trace interval of 0.5 meter. The graph shows that the overlying stratum above 10 meters is composed of fine clay with crushed-grained stone while the basement below 10 meters is of limestone and has distinct difference in electricity from the overlying stratum with high electrical resistivity and low conductivity. In the profile of the stratum above shows that the amplitude is higher, wavelength is longer and waveform wider while for limestone stratum below because of the existing of Karst cave, electromagnetic wave is absorbed by media of low resistivity and the amplitude of the waveform decreases evidently. The profile shows clearly that the karst cave in funnel style, linking up with overlying layer of Quaternary period which has evident disturbance. Breakdown occurred owing to the poor bearing capacity(houses were built on surface). High-pressure rotate grouting was done for the foundation settlement on the basis of the result of GPR surveying and the problem of breakdown was solved fairly well.

CONCLUSION

Practice indicates that supported with a little drilling work and other material on hand, GPR shows its more and more advantages in solving engineering geological problems in engineering construction, by which the underground strata (sole or layers) of the whole probing profile can be found out completely. Precisely because of this, with the improvement of GPR day by day and the more and more rich in practice and experience, GPR will be more and more extensively applied in engineering construction in China. Geophysical scientists are making a thorough study in this field such as GPR expert system, artificial intelligence which will be sure to spread the application of GPR in China. During the writing of this paper, we have received energetic assist and support from Mr. Zhang peng and Wang Jun.

IGARSS'97

1997 International Geoscience and Remote Sensing Symposium

03-08 August 1997

Singapore International Convention & Exhibition Centre

Technical Program

Interactive Area 14: Image Processing

Separation of Character Strings and High Quality Vectorization for Digitized Korean Cadastral Map Images

Keukjoon Bang, Daesik Hong
Comm. & Info. Lab., Dept. of Electronics Engineering, Yonsei Univ. Korea
Shinchon dong 134, Seodaemun gu Seoul Korea 120-749
Tel : +82-02-361-2865, Fax : +82-02-312-4887
bkj@sunlight.yonsei.ac.kr

Abstract - When making an automatic map interpreter for Geographic Information System(GIS) using printed maps, some difficulties lie in the interconnections between character strings and lines, and the distortions of vectorization at the line crossings and junctions.

In this paper, we focus on the fact that the problems are only found at the line crossings and junctions, which can be extracted using the conventional thinning algorithm. We propose a new method to overcome the two difficulties at the same time.

The proposed method is applied to Korean cadastral maps, and the experimental results show that the method is effective in separating the character strings from the lines and getting high quality vectorization for the digitized map images. At the same time we can reduce the processing time.

1. Introduction

Separation and recognition of character strings from map images the automated vectorization of digitized map images are become hot issues in recent years [1].

In conventional methods of vectorization using the pixel-wise thinning algorithms, the quality of vectorization is regarded as the same thing as digitizing accuracy, which is evaluated in terms of the error between the digitized image and the resultant vectorized line segments. But several distortions are caused at the line crossings and junctions. And separation of character strings is remained in problem in the case of the character strings are interconnected with other lines [2].

To overcome those problems, there have already been reports of these difficulties from several authors. For examples, Osamu Hori [3] proposed a method based on a generic object model to get a high quality vectorized building information from the urban maps. Markus Roosli [4] showed a high quality vectorization from the mixed raster images of straight lines and circular arcs by combining the local quality measures and global constraints. Marc Pierrot-Deseilligny separated character strings from cartographic context using a method of high level reconstruction [5]. And David Doermann attempted to combine the local and non-local thinning methods into a hybrid approach and got a good result of vectorization with character images [6].

However the reported approaches are focused on only one aspect of the difficulties. And it takes very long time to perform the reported approaches individually. The method proposed in this paper intended to solve the two problems at the same time to save the processing time, for the cases of the maps composed with straight lines and character strings such as Korean cadastral maps.

The proposed method first uses a conventional thinning algorithm. And then the crossings and junctions of the thinned image are removed with their neighbors, we define them as the uncertain areas. After then, the broken lines are connected each other to get high quality vectorization and the character strings are separated at the same time.

Chapter 2 gives explanation of the conventional approach of separation of character strings and vectorization from maps. In chapter 3, the proposed method is explained in detail. And some experimental results to show the effectiveness of the proposed method are given in chapter 4.

2. Conventional Approach [2]

A conventional approach to separate character strings and get high quality vectorization from digitized map images is shown in Fig. 1 [2].

But, as shown in Fig. 2, vectorization using the conventional method have several unacceptable results at the crossings and junctions, and the character strings are remained when the character strings are interconnected with other lines.

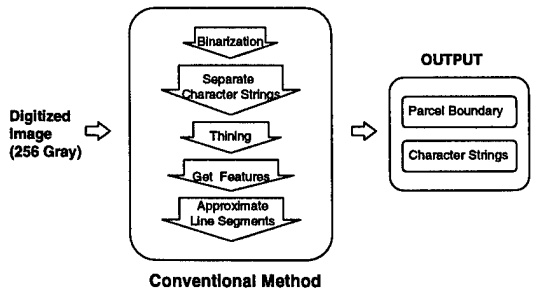

Fig. 1 Conventional approach to separate character strings and get high quality vectorization

This work was supported in part by the Korea science and Engineering Foundation of the contract 95-0100-11-01-3

0-7803-3836-7/97/$10.00 © 1997 IEEE

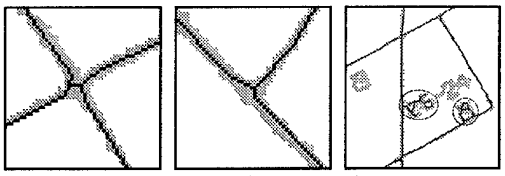

(a) (b) (c)

Fig. 2 Problems of conventional method
(a) distortion at line crossings
(b) distortion at line junctions
(c) samples of not separated character strings

3. Simultaneous Approach

The full description of the proposed method is shown in Fig. 3. And the proposed method uses some assumptions and some parameters for the simplification.

We first assume that the line width is uniform over the whole images. Since the Korean cadastral map uses uniform line width, the assumption is valid. The line thinning algorithm is an iterative process that strips out the edges of the objects. So, the line width is measured at the thinning process using the percentage of the pixels which can not be the candidate of deletion at the succeeding iterations. This method of getting the line width has advantages for it be used independent of resolution.

The proposed method classifies the results of vectorization into two classes, the certain thinned lines and the uncertain. The uncertain areas are the neighbors of the line crossings and junctions where the radius of the uncertain area is the line width and the center is the feature points as shown in Fig. 4. The uncertain areas are erased so that the distortions are canceled and also the interconnected character strings are separated. The erased areas are reconstructed in succeeding stages to get high quality vectorization, and the character strings are separated identically.

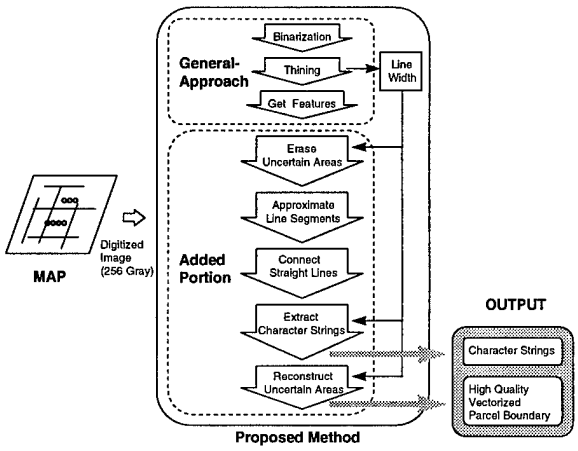

Fig. 3 Full Description of proposed method

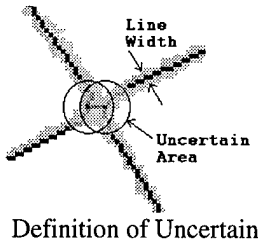

Fig. 4 Definition of Uncertain area

After the image is thinned and the uncertain areas are erased, the thinned image is converted to the approximated line segments. The approximated line segments are broken into several line segments because of the erased uncertain areas and the binarization noises. And the broken line segments are connected only if a straight line is created.

The connection coefficient is defined as.

$$Coef = aval_1 \times aval_2 \times aval_3 \times \frac{1}{\sqrt{Dist}} \qquad (1)$$

where,

$$aval_i = \begin{cases} 2.0 - \sin(Ang_i) & if\ Ang_i \le \pi/2 \\ \sin(Ang_i) & else \end{cases}$$

The connection coefficient is used to measure the connection probability of the selected two line segments. There are four factors used in (1) : the distance of the two line segments and the three types of angles are shown in Fig. 5. If the connection coefficient is over the predefined threshold, the two line segments are connected.

After connecting straight lines, the main parcel boundaries are assumed to be connected. Consequently, the remaining small segments can be assumed to the character strings. And it can be assumed that the separation is performed. But the small segment is somewhat ambiguous, and a threshold value to compare the length of the segment must be defined. Described by the multiples of line width, the threshold value is proportional to the size of the characters within the map.

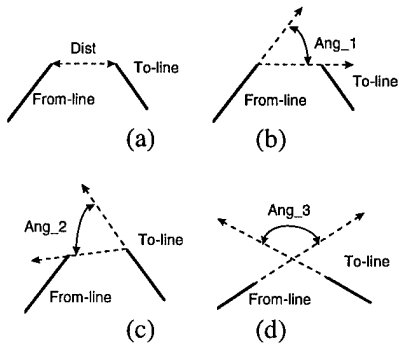

Fig. 5 Factors used in connection coefficient
(a) Dist : Gap between the two lines
(b) Ang_1 : Angle between extended from-line and to-line
(c) Ang_2 : Angle between extended to-line and from-line
(d) Ang_3 : Angle between the two extended lines

After connecting straight lines and separating character

strings from lines, only the parcel boundaries are left in vectorized format. However the erased uncertain areas are remained disconnected. The reconstruction method extends the end points of each segment until the extended line crosses the other vectorized lines or the other extended lines, in the constraint of the extended line neither escapes the original boundary nor is too long.

4. Experimental Results

Experiments were performed with Korean cadastral map which is digitized by 300-dpi resolution and 256-gray level. Pentium PC and OS of Windows-95 is used for simulation.

Parameters used in the experiments are as follows:

a. The uncertain area :
- the center of the uncertain area : each feature points
- the radius of a uncertain area : the value of the line width

b. The connection coefficient threshold : 0.5

c. The threshold value of separating the character strings :

$$\begin{cases} parcels; & if\ segment\ length > (line\ width \times 20) \\ characters; & else \end{cases} \quad (2)$$

d. The maximum length of the end point of the segment extended to reconstruct the erased uncertain area :

$$maximum\ extended\ line\ length < line\ width \times 5 \quad (3)$$

Fig. 6 shows the results that the proposed method overcomes the problems indicated in Fig. 2.

Fig. 7 shows the experimental results acquired by applying the proposed method to the Korean cadastral map. Fig. 7(a) is the original digitized map image. Fig. 7(b) shows the result of conventional method. Fig.7 (c) and (d) are the results of vectorization and the separated character strings using the proposed method, respectively. From these results, we can see that our new approach outperforms the conventional one.

Also, the time required to process the conventional method and the proposed method are measured, yielding 32 seconds and 12seconds, respectively. The difference can be accounted for the method of separating character strings : conventional method separates character strings from the binarized image, while the proposed method performs separation from the vectorized data after thinning.

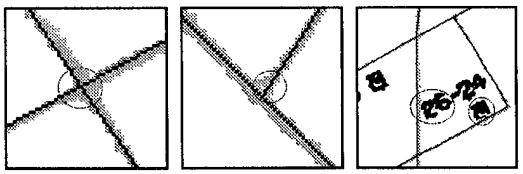

(a) (b) (c)

Fig. 6 Results of the proposed method
(a) Result at the crossing points
(b) Result at the junction points
(c) Result of the sample that are separated correctly

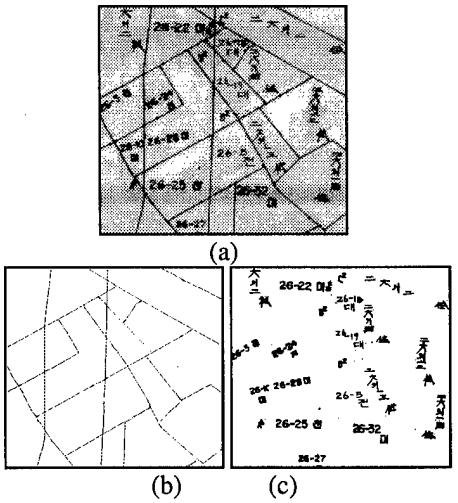

(a)

(b) (c)

Fig. 7 Experimental Results
(a) Original Map Image (Scan : 300dpi, 256-Gray)
(b), (c) Results using the proposed method

5. Conclusions

The proposed method intended to solve the problems of the separation of character strings and the vectorization distortions simultaneously, for the cases of the maps composed with straight lines and character strings such as Korean cadastral maps. And experiments are performed.

Experimental results show the effectiveness of the proposed method in high quality of vectorization. And also, simultaneous processing the separating character strings from map images and vectorization can reduce the processing time significantly.

6. References

[1] Rangachar Kasturi, Rodney Fernandez, Mukesh L, Amlani and Wu-chun Feng, "Map Data Processing in Geographic Information Systems", COMPUTER, vol. 22, no 12, pp.10-21, 1989.

[2] Haralick Shapiro, "Computer and Robot Vision", Vol. 1, Addison-Wesley Publishing Company, 1992.

[3] Osamu Hori and Akio Okasaki, "High Quality Vectorization Based on a Generic Object Model", Structured Document Image Analysis, Springer-Verlag Berlin Heidelberg, pp.325-339, 1992.

[4] Markus Roosli and Gladys Monagan, "A High Quality Vectorization Combining Local Quality Measures and Global Constraints", 3rd-ICDAR, pp.243-248, 1995.

[5] Marc Pierrot-Deseilligny, Herve Le Men and Georges Stamon, "Character string Recognition on Maps, a Method for High Level Reconstruction", 3rd-ICDAR, pp.249-252, 1995.

[6] David Doermann and Omid Kia, "Hybrid Thinning Through Reconstruction", 3rd-ICDAR, pp.632-635, 1995.

A Multi-strategic Approach for Land Use Mapping of Urban Areas by Integrating Satellite and Ancillary Data

M. Caetano, J. Santos and A. Navarro
Centro Nacional de Informação Geográfica (CNIG)
Rua Braamcamp, N. 82, 1 Dto, 1250 Lisboa, Portugal
Tel. 351-1-3860011, Fax: 351-1-3862877; e-mail: mario@helios.cnig.pt

A methodology for land use mapping of urban areas by using satellite imagery and ancillary data (road network and Census data) was developed. The integration of ancillary data was sequentially done to allow a cost/benefit analysis. In the analysis of the satellite imagery, special emphasis was put in the development of contextual operators for (1) discriminating pixels that have different land uses but have similar spectral characteristics, and (2) identifying land use classes that cannot be identified at a pixel level. A road network map was integrated with the satellite imagery for stratifying the study area into urban and rural areas. This stratification allowed the application of different algorithms to each stratum for an effective improvement of the land use mapping accuracy. In addition, Population and Habitation Census data were used for a refinement of land use classes discrimination. The methodology was tested with a SPOT image to generate a map with the CLUSTERS nomenclature for the *Área da Grande Lisboa*, Portugal. In the final map, 22 land use classes were identified with an overall accuracy of 88% (Kappa index). Most of these 22 classes were identified with user's and producer's accuracy larger than 85%.

INTRODUCTION

Urban planning requires updated and accurate land use maps. The low cost, periodic acquisition and coverage of large areas make satellite imagery an adequate tool for land use mapping of urban areas. For a long time that images acquired by satellites have been used for such a purpose, *e.g.* [1], [2], and [3]. However, there are problems that hamper the use of these type of data for generating land use maps with a satisfactory accuracy. In this study we directly address two of those problems and that are typical of urban areas: (1) unsuitability of the satellite data structure, *i.e.* pixel based, to the spatial structure of many land uses and (2) similar spectral characteristics of different land uses. To address the first problem we developed several algorithms to analyze spatial patterns within satellite data which allow the identification of land uses that cannot be identified at a pixel level. To help solving the second problem, we developed algorithms to integrate spectral data with two types of ancillary data, *i.e.* road network, and Population and Habitation Census data. Furthermore, a sequential integration of ancillary data allows the evaluation of the costs/benefits in using several types of data. The developed methodology is tested with SPOT imagery in the *Área da Grande Lisboa* (AGL), Portugal to create a map with the CLUSTERS (*Classification for Land Use Statistics: Eurostat Remote Sensing projects*) nomenclature [4].

STUDY AREA AND DATASET

The study area is the *Área da Grande Lisboa* (AGL) in Portugal, which includes 6 counties besides the Lisboa county. AGL has an area of 1046 Km^2 and is approximately 28,6 Km wide and 52,7 Km long. Man-made areas comprise a significant part of the study area but there are also significant forested and cultivated areas. A large part of the study area is characterized by small scale heterogeneous land use.

In this study we used SPOT multispectral and panchromatic images from June 27, 1991 (K23/J272 and K24/J272, respectively). As ancillary data, we used: (1) a road network digital file (1:25,000), purchased from the producer, i.e. *Instituto Geográfico do Exército* (IGeoE), and (2) the Population and Habitation Census data for 1991 at a Enumeration District (ED) level, which were provided by the producer, i.e. *Instituto Nacional de Estatística* (INE), in a Geographic Information System (GIS) format.

METHODOLOGY

The goal of this study was to generate a map for AGL with the CLUSTERS nomenclature, achieving level IV for the built up areas and level II for non-built up areas.

The panchromatic image was registered to the UTM projection of the road network digital map (1:25,000), using 69 ground control points (GCP) which were provided by the *Laboratório Nacional de Engenharia Civil* (LNEC). The multispectral bands were co-registered to the panchromatic image, using 30 GCPs. In each step we applied a polynomial of first order and a nearest neighbor resampling.

The study area was stratified per counties, before image classification, which allowed the definition of the correct set of CLUSTERS classes that effectively exist in each county. The methodology developed for land cover mapping entails three sequential phases. In each phase the results from the precedent phase are improved by integrating ancillary data

0-7803-3836-7/97/$10.00 © 1997 IEEE

using algorithms developed within the framework of this study.

In the first phase, a land use map (SATMAP) was generated just by analyzing the spectral and spatial patterns of the SPOT image by automatic procedures. We tried several classifications, using an iterative maximum likelihood classifier, with different combinations of bands, including band transformations such as texture and the Normalized Difference Vegetation Index (NDVI) [5]. The classification was performed with spectral classes instead of informational classes, in order to avoid classes with a large spectral diversity, which would increase the overlap of different land use spectral ellipses. The several spectral classes of the same informational class were merged after image classification. For post-classification improvement we used simple techniques based on the region growing theory, instead of applying the traditional majority filters. The application of these techniques helps solving for misclassifications of specific land uses that are spectrally similar and that are spatially contiguous. We also developed contextual algorithms to identify classes that cannot be identified at a pixel level, *e.g.* stadiums and associated sport fields (subset of the A502); beaches and dunes (E01.2); and airports and aerodromes (A32.3). The rationale behind the development of these algorithms was based on the rules that the humans use to identify some land uses by photo-interpretation.

In the second phase, a road network map was used to generate a road density map which was integrated with the panchromatic image, by using morphological operators, to stratify the study area into urban and rural areas. This urban/rural binary mask was then integrated with the spectral data for generating the map of this second phase, *i.e.* RUMAP. Methodologies for CLUSTERS classes discrimination, specific to each stratum, were developed and applied. Within the urban stratum, we developed contextual operators for trying to discriminate 5 residential classes based on the abundance (estimated with the NDVI) and spatial arrangement of vegetation. Misclassifications in each stratum, such as the built-up areas within the rural stratum, were reclassified based on techniques similar to region growing. Contextual operators were also developed for identifying urban parks and gardens.

In the third phase, Census data were integrated with the spectral data and with the RUMAP to generate the final map, *i.e.* CENMAP. The Census variables that were used include: number of residential buildings, population (resident and present), number of dwellings and the Census block area. Examples of the indices generated in this study are: number of dwellings per residential building index; building density index and population per dwelling index. We built automatic rules integrating spectral and Census data, for identifying classes that could not be identified in the previous phases, *e.g.* public services and local government (A12), river and maritime transport (A324). On the other hand, Census data were also used for improving the discrimination between some residential areas (A111, A112 and A113) and industrial or commercial activities (A2).

The assessment of the classification accuracy is performed with error matrices, one for each map. The overall quality of the land use maps was evaluated with the overall accuracy and the kappa indices, and the quality of the individual classes mapping was evaluated with the producer's and users accuracy. The reference data used in the classification accuracy assessment in this project is aerial photography (1:15,000) and data collected on the ground. We used a stratified random sampling to assure that enough samples were collected for each category and to minimize any periodicity in the data. We followed the rule of thumb that the number of samples per category should be larger than 75 [6].

RESULTS AND DISCUSSION

The RMS associated to both images registration were less than half of the pixel size, indicating that both images are registered at a pixel level not only to the map but also to each other.

The classification of the SPOT image to generate the SATMAP, was performed with the 4 original bands. Texture and NDVI did not prove to be efficient in the discrimination of the classes that we were interested on.

The SATMAP has a low overall accuracy (table 1), mainly because of the confusion between non-dense residential areas and agricultural lands and areas with herbaceous vegetation. This confusion is mainly a consequence of the similarity of spectral signatures of those land uses. Furthermore, many of those pixels have a mixed cover, due to the small plot size that exist in many parts of the study area. Classes that cannot be identified at a pixel level, were successfully identified (user's and producer's accuracy larger than 90%) with the contextual operators that were developed.

Table 1. Number of classes and overall accuracy, *i.e.* overall accuracy and kappa, for the three maps generated in this study, *i.e.* SATMAP, RUMAP and CENMAP.

Map	Total number of classes	Overall Accuracy	Kappa
SATMAP	18	80	78
RUMAP	19	86	85
CENMAP	22	89	88

The map generated in the second phase (RUMAP) has an overall accuracy 6% larger than the one of the SATMAP (table 1). This better accuracy is a consequence of the following: (1) many built-up classes that were classified as non-urban classes in the SATMAP are correctly classified in the RUMAP. This is a result of the stratification of the study area into urban/rural areas and the identification of the residential areas in the urban stratum; (2) residential areas discrimination was improved by contextual analysis; and (3) green areas within the urban areas are now correctly classified as part of a discontinuous residential class (A111 or A113) or as green urban areas (A503) and not as some non-built-up class as in the SATMAP.

The integration of the Census data generated a land use map (CENMAP) with an overall accuracy 3% larger than the one of the previous map, *i.e.* RUMAP (table 1). This is mainly due to a better residential areas discrimination (the producer's accuracy in the CENMAP for all the residential classes is higher than 95%), since it is based on the definition of the CLUSTERS classes. On the other hand, there was also some reduction of the confusion between residential classes and agricultural areas (problems that were not solved by the stratification of the study area). Confusions between the industrial areas and dense urban areas were also significantly reduced. Furthermore, in the CENMAP, 3 more classes could be identified, *e.g.* public services and local government (A12), collective residential areas (A115) and river and maritime transport (A324). The final map has an overall accuracy of 88%, which can be considered satisfactory. Many of the remaining problems are related to confusion among classes of non-built up areas. For example, confusion between agricultural lands and areas under grass. Many of these confusions could be minimized if a multitemporal image dataset were used, to take into account the change of plant phenology.

CONCLUSIONS

This study reveals the limitation of the satellite imagery, when it is the only information source, for generating a land use map with a nomenclature as detailed as the CLUSTERS. However, we show the importance of contextual analysis for a deeper exploration of the information that is retained in a the satellite image. Improvements on the accuracy were achieved by integrating low cost ancillary data such as the road network. The algorithm that was developed to build a urban/rural mask based on the road network and the panchromatic image proved to be an extremely helpful tool for discriminating land use classes with identical spectral characteristics. The integration of Population and Habitation Census data allowed a better discrimination of built up areas, namely residential areas and industrial areas. Nevertheless, the final map still has some misclassifications. To improve these results, the Image Processing Group of *Centro Nacional de Informação Geográfica* (CNIG) is currently working on techniques for a better exploration of the satellite data. The use of neural networks for spatial pattern analysis [7] is a promising technique for a better exploration of the contextuality of the satellite images. The use of techniques for unmixing the pixel, based on spectral mixture analysis, could also improve the results on the map generated only by satellite imagery. In CNIG, we have used this technique for other purposes and it performed extremely well [8]. In this project, spectral mixture analysis could be useful for solving for the confusion among built-up areas and non-built-up areas, and avoid the use of ancillary data.

AKNOWLEDGMENTS

This study was partially supported by EUROSTAT Contract RS/12/031/MF/SW (*Programme Teledetection et Statistics*).

REFERENCES

[1] J.P. Ormsby, "Evaluation of natural and man-made features using Landsat TM data", International Journal of Remote Sensing, vol. 13, pp. 303-318, 1992.

[2] C. Weber, and J. Hirsch, "Some Urban Measurements from SPOT Data: Urban Life Quality Indices", International Journal of Remote Sensing, vol. 13, pp. 3251-3261, 1992.

[3] D.C. He, L. Wang, T. Baulu, D. Morin, and A. Bannari, "Classification Spectral et Texturale des Données d'Images SPOT em Milieu Urbain", International Journal of Remote Sensing, vol. 15, pp. 2145-2152, 1994.

[4] CNIG, "Analysis of the Dynamic of the Lisboa Urban Agglomeration", Centro Nacional de Informação Geográfica, Lisboa, Portugal, p. 100, 1997.

[5] J.W. Rouse, R.H. Haas, J.A. Schell, and D.W. Deering, "Monitoring vegetation systems in the great plains with ERTS", Proceedings of the Third ERTS Symposium, pp. 309-317, 1973.

[6] R.G. Congalton, "A review of assessing the accuracy of classifications of remotely sensed data", Remote Sensing of Environment, vol. 37, pp. 35-46, 1991.

[7] S. Silva, and M. Caetano, "Using artificial recurrent neural nets to identify spectral and spatial patterns for satellite imagery classification of urban areas", Proceedings of Compares - Workshop on Methods for Preprocessing and Analysis of Remote Sensing Data, July 17 - 19, 1996, University of York (in press).

[8] M. Caetano, L. Mertes, L. Cadete, and J. Pereira, "Assessment of AVHRR data for characterizing burned areas and post-fire vegetation recovery", EARSEL Advances on Remote Sensing, vol. 4 (4-XI), pp. 124-134, 1996.

Development of a Feature-based Approach to Automated Image Registration for Multitemporal and Multisensor Remotely Sensed Imagery

Xiaolong Dai and Siamak Khorram
Computer Graphics Center, North Carolina State University
Campus Box 7106, Raleigh, North Carolina 27695 - 7106, USA
Tel: (919)515-3430 Fax: (919)515-3439 Email: xdai@unity.ncsu.edu, khorram@ncsu.edu

Abstract -- In this paper, a new feature-based approach to automated multitemporal and multisensor image registration is presented. The characteristics of this technique is that it combines moment invariant shape descriptors with modified chain code correlation to establish the correspondences between potential matched regions in two images. It also overcomes the difficulties in control point correspondence in image matching caused by the problem of feature inconsistency. In image segmentation, we use the improved Laplacian of Gaussian (LoG) zero-crossing edge detector. Feature matching is done in both feature space and image space based on moment invariant distance and improved chain code correlation. The centers of gravity are then extracted from matched regions and used as control points. The final transformation parameters are estimated based on the final matched control points. Experimental results using multitemporal Landsat TM imagery are presented.

Introduction

Image registration is the process of matching two images so that corresponding coordinate points in the two images correspond to the same locations being imaged. Automated image registration is one of the important procedure in remote sensing applications [1]: (1) Image registration is a critical process in multisensor data integration; (2) Multitemporal image analysis and change detection requires reliable and accurate image registration [2]; (3) Other problems such as finding cloud heights, satellite image composite generation, weather prediction, and wind direction measurements also involve the registration process; (4) Because of the anticipated large data volume and high data rates of the current and future high resolution sensors, the traditional approach of visual identification of tiepoints to register multitemporal data is not an acceptable solution. An automated multitemporal and multisensor registration system that requires little or no operator supervision is one of the critical procedures in automated remote sensing system [3]. There are mainly two classes of automated registrations: the area-based and feature-based methods [4]. This paper proposes a new feature-based registration technique for multitemporal and multisensor images using combined criteria of moment invariant distance and chain code correlation.

This work was partially supported by Cray Research, Inc. and North Carolina Supercomputing Center under the 1997 Cray Grant Program.

Feature Extraction

What we are after is a best technique that can produce a desirable number of useful boundaries to be used in control point finding process. Since the *LoG* operator produces closed edge contours, we use the *LoG* zero-crossing operator. However, the conventional *LoG* zero-crossing operator has two drawbacks: (1) thick edge; (2) discontinuity at weak edge points [5]. To overcome these drawbacks, we propose a method, called *Thin and Robust Zero-Crossing*, which produces thin edges and assures continuities at weak edge points as well. This technique can be performed in two stages: *selective zero-crossing point marking* and *edge refinement and sorting*. In the first stage, we mark every pixel which satisfies the following three conditions as edge point: (1) zero crossing point (sign change on the convolved image); (2) in the direction of the steepest gradient change; and (3) the closest pixel to the virtual zero plane of the *LoG* image among its eight neighbors. At the same time, edge strength (ES) is defined for every marked edge point for further processing, which is defined as the steepest gradient slope change along the eight directions in its 8-neighborhood based on the *LoG* values of itself and its eight neighbors.

In the *edge refinement and sorting* stage, we use two-threshold method [3] to search and clean the marked edge points to detect contours. This scheme applies the following two conditions to the detected zero crossing points: (1) the edge strength at each point along the edges is greater than T_1; (2) at least one point on the contour has an edge strength greater than T_2, where T_1 and T_2 are preset thresholds and $T_1<T_2$. T_1 preserves the whole contour around the region boundary without incurring discontinuity at weak edge points. This two-threshold scheme is implemented by the contour search and sorting program. The search operation continues until the whole edge strength array has been scanned. The detected closed contour points for each contour are then sorted and stored in order in any array for further processing. Sorted closed contours are then marked as region boundary.

Control Point Correspondence: Image Matching

After the closed contours are detected from two images, a correspondence mechanism between the regions must be established to match these two images. Region similarity is

0-7803-3836-7/97/$10.00 © 1997 IEEE

obtained by comparing the shapes of the segmented regions. Since the images may have translational, rotational, scaling differences, the shape measures should be invariant with respect to translation, rotation, and scaling. Some of the techniques that measure shape similarity in this fashion are Fourier descriptor, chain code correlation, shape signatures, invariant momentum and shape matrices [6].

Moment Representation of Regions: Moment Invariants

A very useful and practical set of shape descriptors is based on the theory of moments [7]. The moment invariants are moment-based descriptors of planar shapes, which are invariant under general translational, rotational, scaling, and reflection transformation [8]. Moments of higher order describe more slight variations in shape, but they are more sensitive to noise [9]. Based on our experience, the seven lower-order invariants are reliable enough for most practical tasks on remote sensed image matching.

Chain Code Representation of Regions

Another efficient representation of digital curves is the Freeman chain code. The original Freeman chain is improved by applying the following four operations to the original Freeman chain code: (1) *Shift Operation* by modulus operation; (2) *Smoothing Operation* by a five-point Gaussian filter; (3) *Normalization Operation* by subtracting its mean; and (4) *Resampling Operation* by resampling to the same length using spline interpolation.

Control Point Correspondence by Region Matching

Control point correspondence is performed in two steps. The first step includes region matching in the feature space based on combined criteria of minimum distance of seven moment invariants and maximum chain code correlation coefficients between a pair of regions. In this step, two similarity matrices between detected regions in two images are first computed. The first similarity matrix is the Euclidean distance matrix in 7-*D* moment invariant space. The second similarity matrix is the chain code correlation matrix. Based on these two similarity matrices, *Minimum Distance* classification is used to identify the most robust matches. The second step is performed in image space based on the image registration result of the first step. Given three most robust *GCP*'s from the result of the first step, the parameters of the first order bivariate polynomial can be simply calculated. Based on this transformation, we can map the other potential regions in the sensed image into the reference image. The distance between the center of gravity of the mapped region in the sensed image and the actual center of gravity in the reference image is computed. This distance is actually the root-mean-square error (*RMSE*) at this pair of corresponding points. A threshold can easily be set to avoid false matches. The final image transformation parameters are based on the final matched points resulted from the second step of the image match algorithm.

Experimental Results

In the experiment, two images of the coastal plain of North carolina are used. The reference image (image 1) was taken by Landsat 5 TM in November 1988. The sensed image (image 2, the image to be transformed) was taken in December 1994. A subscene of the size 512×512 pixels from the original images is used. Only mid-infrared band (band 5 in TM imagery) is used in registration experiments, as shown in Fig. 1 (a) and (c). In the image segmentation, the standard deviation of the *LoG* operator is 1.5 and the kernel size is 15×15 pixels. 22 regions in the reference image and 29 regions in the sensed image are detected by the contour search and sorting program, as shown in Fig. 1 (b) and (d), respectively.

From the detected regions in two images, we construct the moment invariant distance matrix and chain code correlation matrix. Three pairs of GCP's with minimum distance and highest correlation are detected and used to initially estimate the transformation parameters. The centers of gravity of 7 corresponding regions finally detected are used as control points.

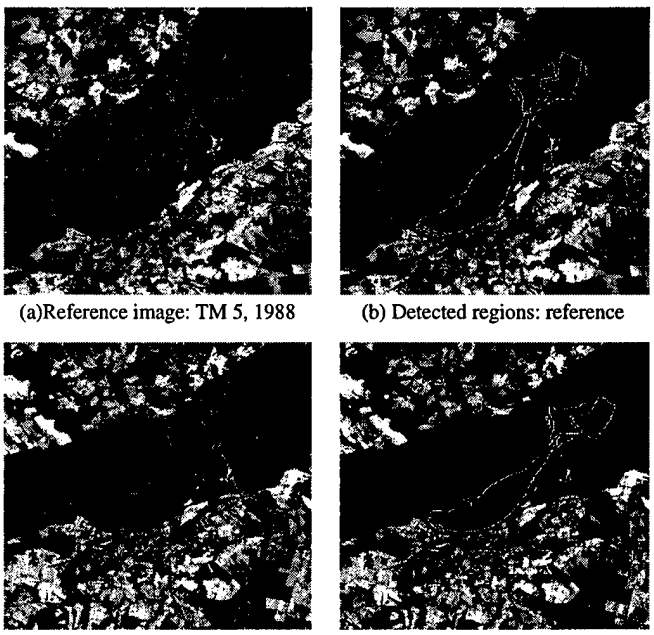

(a)Reference image: TM 5, 1988 (b) Detected regions: reference

(c) Sensed image: TM 5, 1994 (d) Detected regions: sensed

Fig. 1 Test windows and image segmentation results.

Knowing the mapping function, the sensed image is transformed and resampled using cubic convolution interpolation. The resampled image is shown in Fig. 2 (a). The resampled image is then mosaicked with the reference image, as shown in Fig. 2 (b). The registration accuracy is

estimated using at every control point. To do a fair comparison with the result of manual registration, we visually locate 7 control points using a magnifier on the standard false color composite image (TM bands 4, 3, 2). These 7 pairs of points are then used in image transformation parameter estimation. The manual registration result is then compared to that of the proposed automated algorithm. The result for comparison is shown in Table 1. From the result, we can notice that the proposed automated algorithm outperforms manual registration in terms of the registration accuracy at the control points by more than half a pixel.

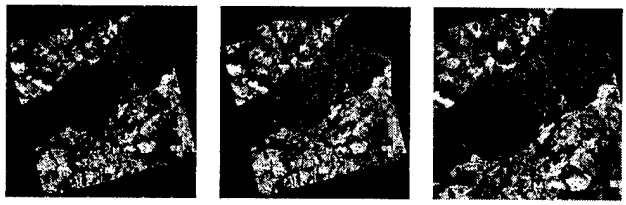

Fig. 2 (a) Registered image (b) Mosaicked image (c) Overlapped area

Table 1: Comparison: manual registration and the proposed algorithm

	Manual Registration	Proposed Algorithm
Total Error in *X*	0.6534	0.1883
Total Error in *Y*	0.5753	0.2640
RMSE	0.8706	0.3242

Conclusions

This paper has dealt with the automatic registration of multitemporal and multisensor images of the same scene. This requirement appears very often in the processing of multitemporal satellite images. In particular, automated digital change detection from multitemporal satellite images requires a reliable and automatic image registration. In this research, we explore the elements for an automated image registration procedure using Landsat TM imagery. Attention has been paid to the automatic region feature extraction and control point selection. The images are first segmented by the *Thin and Robust Zero-Crossing* edge extraction technique and the regions with closed boundaries are then extracted. Working on the matched regions, we develop a new method for the determination of corresponding regions using combined criteria of moment invariant distance and improved chain code correlation between the detected regions. Each region is represented by moment invariants that are affine-invariant features describing the shape of the region. Region matching is then implemented in feature space and sequentially in image space. After the correspondence between the regions has been established, centers of gravity of the corresponding regions are used as control points. The parameters of transformation are computed by the least square rule based on general affine transformation. The sensed image is then resampled by *Cubic Convolution* interpolation technique and mosaicked over the reference image.

The performance of the proposed algorithm has been demonstrated by registering two multitemporal Landsat TM images taken in different years. Registration accuracy of one-third of a pixel has been reached in the experiments. The proposed automated algorithm outperforms manual registration by over half a pixel in terms of *RMSE*. Based on our study, the technique developed in this research is promising in terms of its registration accuracy, computational efficiency, and robustness.

References

[1] Fonseca, L. M. G. and B. S. Manjunath, "Registration techniques for multisensor remotely sensed imagery," *Photogrammetric Engineering & Remote Sensing*, vol. 562, no. 9, pp. 1049-1056, September 1996.

[2] Dai, X., S. Khorram, and H. Cheshire, "Automated imageregistration for change detection from Thematic Mapper imagery", in Proceedings: IEEE/ IGARSS, Lincoln, Nebraska, vol. III, pp. 1609-1611, May 1996.

[3] Rignot, E. J. M., R. Kowk, J. C. Curlander, and S. S. Pang, "Automated multisensor registration: requirements and techniques," *Photogrammetric Engineering & Remote Sensing*, vol. 57, no. 8, pp. 1029-1038, August 1991.

[4] Li, H., B. S. Manjunath, and S. K. Mitra, "A contour based approach to multisensor image registration," *IEEE Trans. Image Proc.*, Vol. 4, No. 3, pp. 320-334, March 1995.

[5] Canny, J., "A computational approach to edge detection," *IEEE Trans. Pattern Analysis and Machine Intelligence*, vol. PAMI-8, no. 6, pp. 679-698, November 1986.

[6] Goshtasby, A., G. C. Stockman, and C. V.Page, "A region-based approach with subpixel accuracy," *IEEE Transactions on Geoscience and Remote Sensing*, vol. GE-24, No. 3, pp. 390-399, May 1986.

[7] Flusser, J. and T. Suk, "A moment-based approach to registration of images with affine geometric distortion," *IEEE Transactions on Geoscience and Remote Sensing*, vol. 32, No. 3, pp. 382 - 387, May 1994.

[8] Jain, A. K., *Fundamentals of Digital Image Processing*, Prentice Hall, Englewood Cliffs, 1989.

[9] Ventura, A. D., A. Rampini, and R. Schettini, "Image registration by recognition of corresponding structures," *IEEE Transactions on Geoscience and Remote Sensing*, vol. 28, no. 3, pp. 305-314, May 1990.

A Quality Assurance Algorithm for NASA Scatterometer Ambiguity Removal

Amy E. Gonzales and David G. Long
Brigham Young University, MERS Laboratory
459 CB, Provo, UT 84602
801-378-4884, FAX: 801-378-6586 gonzalae@sage.ee.byu.edu

Abstract— The recently launched NASA Scatterometer (NSCAT) estimates the wind speed and direction of near-surface ocean wind. This is done by directing microwaves toward the earth's surface and measuring the backscattered radiation. From this, several possible wind vectors are identified for each point over the swath. The correct wind must be distinguished from these in a step called ambiguity removal.

Unfortunately, ambiguity removal algorithms are subject to error. Because the true wind is not known, where these errors occur is difficult to determine, and there is little information in the measurements alone to detect the errors in this removal step. We have developed a method to assess the accuracy of the ambiguity removal algorithm by comparing the point-wise retrieved wind to winds inferred with a wind field model.

The performance of the algorithm achieves its goal to identify at least 95% of regions containing ambiguity removal errors. The algorithm provides a very simple tool to indicate regions of possible ambiguity removal errors in the point-wise retrieved winds for NSCAT data. This paper describes this algorithm and its performance for real NSCAT data.

INTRODUCTION

The NASA Scatterometer (NSCAT) is a microwave instrument capable of accurately measuring vector winds over the ocean during all weather conditions [1]. Scatterometers do not directly measure the wind; rather the speed and direction of the wind are inferred from the normalized radar cross section (σ^o) measurements of the ocean surface. The wind is related to σ^o via a geophysical model function. However, there are several possible wind vectors for any particular σ^o. Although the speeds are typically the same, the directions exhibit a 180 degree ambiguity. An ambiguity removal algorithm must be employed to determine the correct direction.

Point-wise wind retrieval is the traditional method for estimation of the winds over the ocean. It consists of two steps and uses only the σ^o measurements for a single wind vector. The first step is to find the multiple wind vectors for each cell of the scatterometer swath. The second step, ambiguity removal, selects one unique wind vector estimate for each of these cells, though this algorithm is prone to error. A quality assessment of these algorithms is essential to maintain the integrity of the data.

A second method to determine wind measurements is model based wind retrieval [2]. The wind field model provides a description of the near-surface wind field over the scatterometer measurement swath and is optimized for scatterometer wind retrieval. The swath is sectioned into rectangular regions and the wind is extracted over the entire region instead of by individual resolution elements. The model relates the components of the wind vector field over this region to a set of model parameters [2]. The models are either data-driven or physics-based and have been shown to provide more accurate wind measurements than point-wise wind retrieval [3].

The wind field models can also be used to improve the point-wise wind product by identifying ambiguity removal errors. One way to do this is to fit the estimated point-wise wind to a simple wind field model over a small area. Large errors in the fit suggest possible ambiguity removal errors while small errors suggest a realistic wind field. This is exploited in the ambiguity quality assurance algorithm which follows.

WIND FIELD MODELS

As discussed in [2, 3], a simple wind field model can be developed which is expressed as

$$\mathbf{W} = \mathbf{F}\mathbf{X}$$

where $\mathbf{X}$ is an L-element vector containing the model parameters and $\mathbf{F}$ is a constant model matrix where the rows of $\mathbf{F}$ form a basis set for possible wind fields. There are several different models for which this model matrix changes. Two particular twenty-two order models were examined for this algorithm: the Parameterized Boundary Conditions (PBC) model [2] and the Karhunen-Loeve (K-L) model [4].

To use the model as a quality assurance for the point-wise wind retrieval, the model is fit in a least-squares sense to the observed point-wise wind field. The error in the fit provides some information about how realistic the observed wind actually is.

A least squares estimate of the model parameter vector $\mathbf{X}$, $\underline{\mathbf{X}}$, can be obtained from the observed wind field $\mathbf{W}_0$ using the pseudo-inverse of $\mathbf{F}$, $\mathbf{F}^\dagger$, i.e., $\underline{\mathbf{X}}=\mathbf{F}^\dagger\mathbf{W}_0$. The reconstructed wind field $\mathbf{W}$, also known as the model-fit field, is $\mathbf{W} = \mathbf{F}\underline{\mathbf{X}}$ with the reconstruction error field $\mathbf{W}_E$ given by

$$\mathbf{W}_E=\mathbf{W}\text{-}\mathbf{W}_0=(\mathbf{F}\mathbf{F}^\dagger\text{-}\mathbf{I})\mathbf{W}_0.$$

0-7803-3836-7/97/$10.00 © 1997 IEEE

If the reconstruction error is small, the model-fit is good and the observed wind field is "realistic" for the specific model. Large reconstruction errors suggest that the observed wind field is not realistic due to either ambiguity selection errors or poor modeling. Thresholds for the reconstructed error field detect regions with possible ambiguity removal errors.

Figure 1 is an example of the observed JPL wind field and the model-fit field for a particular 12x12 region. Notice the smoothing. As can be seen from the all alias plot, the model-fit wind field corrects ambiguity removal errors in the observed wind field. Thus, the model-fit is a reasonable basis for determining realistic wind fields and locating regions with possible errors.

However, there are several considerations when implementing this simple algorithm. First, the error in the model-fit might be high in regions where the wind estimates are very noisy even if ambiguity removal is correct. Second, the wind field model inherently smoothes the wind field over the entire region, and cyclones and sharp fronts are not modeled well. The error in these regions will be very high due to the limitations of the model. Third, at low wind speeds, the wind is highly variable which is complicated by the low signal to noise ratio in these regions. As a result, the error in low wind speed regions is larger than in high wind speed regions–even for perfect ambiguity removal. Finally, the model must be fit to the wind field over a region. To produce an adequate fit, the input wind must be defined over the full region. Thus, for this simple algorithm, regions with significant amounts of land or missing measurements are not processed. Only those regions with fewer than eight cells of land or missing measurements are used. The missing measurements are replaced with the average of the cells surrounding it and then processed.

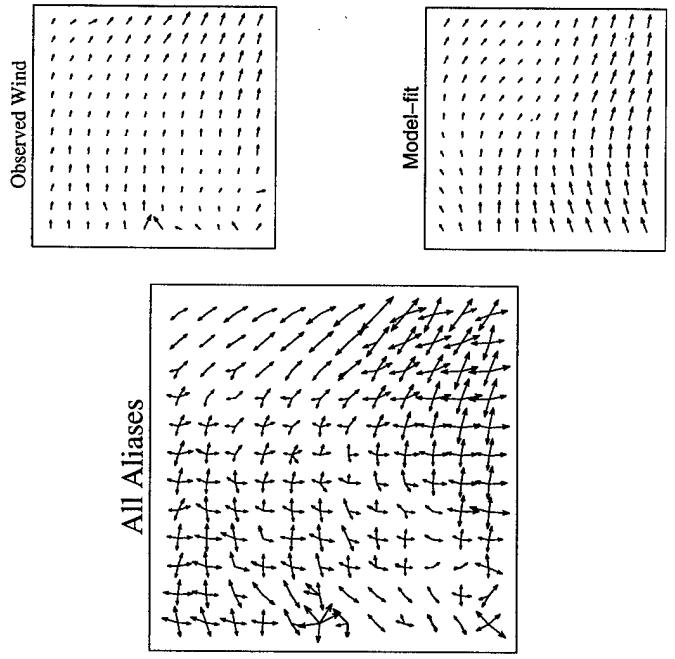

Figure 1: *The region on the upper left is the JPL product while the region on the upper right is the model-fit to this field. The lower figure plots all the alliases for this region.*

The model-fit error locates the boundaries of the regions that have possible ambiguity removal errors. The algorithm is very successful at identifying these regions, but so far does not correct the errors. It is designed only as a check of the consistency of the unique wind field.

ALGORITHM DESCRIPTION

A general procedural description of the algorithm follows:

1. Segment the swath into 12x12 overlapping regions (50% along track overlap).
2. For each valid region (regions with fewer than eight cells of land or missing measurements), compute the model-fit field $\mathbf{W}$, the reconstruction error field $\mathbf{W}_E$, the model parameter vector $\underline{\mathbf{X}}$, and the statistics of $\mathbf{W}_E$. These statistics include the rms error, the normalized rms error, the maximum component error, and the maximum angle error for each region.
3. For each region, determine if the statistics, including those for the model parameter vector $\underline{\mathbf{X}}$, are larger than the thresholds. If so, the region is identified as containing possible ambiguity selection errors.

IDENTIFYING THRESHOLDS

The reconstruction error field provides much information about the difference between the unique wind field and the reconstructed wind field. The value of the model parameter vector is also useful for identifying regions with ambiguity removal errors.

Model Parameter Statistics

To determine the thresholds for the model parameters, a histogram of the these parameters is examined for each model. Figure 2 shows the histograms of four of the parameters for the K-L model using 5488 regions of valid NSCAT data. As can be seen, while the X parameters are not Gaussian, they exhibit a Gaussian-like shape.

It has been found that large values for any of the parameters correspond to regions with possible errors. After some examination of the values for the parameters, the thresholds are subjectively set at twice the standard deviation for each of them. This provides an initial starting place for altering these numbers as needed to correctly identify error-prone regions.

Only a few of the model parameters are necessary for this algorithm. In the case of the K-L model, choosing

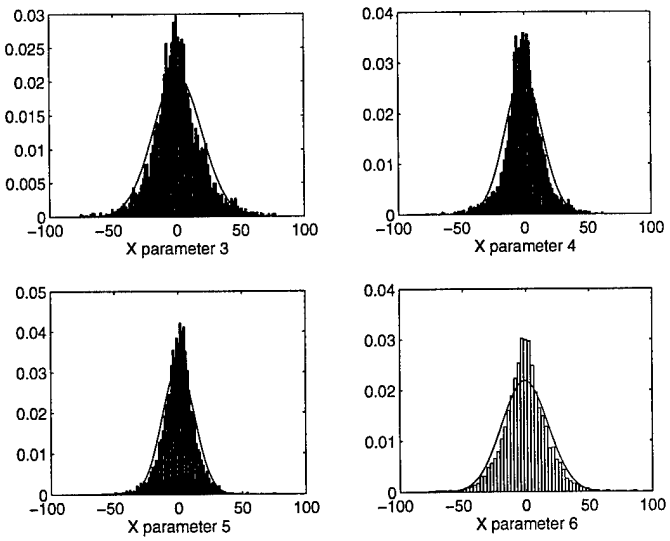

Figure 2: *The histograms for parameters three through six for the K-L model. Overlaid is a Gaussian distribution with the same mean and variance.*

them is an easy task. The columns of **F** are basis vectors in decreasing order, and only the first few parameters need be used. However, the PBC model is ordered quite differently, and the fewest number of model parameter thresholds are subjectively chosen that will accurately identify as many regions with ambiguity removal errors as possible.

Error Matrix Statistics

The other thresholds for locating ambiguity removal errors are determined from the reconstruction error field. These include the rms error, the normalized rms error, the maximum component error, and the maximum direction error for each region. The rms error is found by squaring the reconstruction error field, dividing by the number of terms, and taking the square root. The normalized rms error is found by squaring the reconstruction error field, dividing by the observed wind field, and taking the square root. The first two are useful for locating regions of obvious error. Both of these error measurements are calculated for the entire region and thus provide information about the region as a whole. The second two error measurements are useful for locating regions in which only a couple of the wind vectors are incorrect. These measurements are calculated by individual components. They locate regions with at least one individual wind vector error. The individual errors are easily identified by finding those that exceed the thresholds.

Selecting Thresholds

To select the threshold values for this algorithm, 527 regions (10 revs) of NSCAT data were inspected by hand, a small subset of the original 5488 regions. The regions were subjectively grouped into three categories: perfect, moderate (those with only a few isolated ambiguity removal error) and poor regions. The statistics of each of the regions were then calculated and compared to the initial two sigma thresholds. The thresholds are adjusted such that the maximum number of poor and moderate regions are identified with a minimum number of false alarms.

For this small set, the algorithm correctly identifies 100% of the poor regions and over 95% of the moderate regions with a false alarm rate of less than 5%. It should be understood that the thresholds can be altered to adjust the detection and false alarm probabilities. For example, if all regions with possible errors are to be detected, the number of false alarms will increase. The thresholds are determined for a specific trade-off between detection and false alarms.

CONCLUSIONS

The thresholds chosen above were tested on a withheld data set of 274 regions (5 revs) and achieved a similar level of performance. The algorithm correctly identified 100% of the poor regions and over 98% of the moderate regions with a false alarm rate of less than 5%.

The algorithm works very well in identifying regions with possible selection errors. Although the algorithm only detects ambiguity removal errors, ongoing research is being done to correct those regions with only a few individual vector errors. In this case, choosing the point-wise ambiguity closest to the model-based wind will correct the problem. How to correct the other regions with possible ambiguity selection errors is the focus of upcoming research.

REFERENCES

[1] F. Naderi, M.H. Freilich, and D.G. Long, "Spaceborne Radar Measurement of Wind Velocity Over the Ocean–An Overview of the NSCAT Scatterometer System," *Proceedings of the IEEE*, pp. 850-866, Vol. 79, No. 6, June 1991.

[2] D.G. Long and Jerry M. Mendel, "Model-Based Estimation of Wind Fields Over the Ocean from Wind Scatterometer Measurements, Part1: Development of the Wind Field Model," *IEEE Transactions of Geoscience and Remote Sensing*, pp. 349-360, Vol. 28, No. 3, May 1990.

[3] D.G. Long, "Wind Field Model-Based Estimation of SEASAT Scatterometer Winds," *Journal of Geophysical Research*, pp. 14,651-14688, Vol. 98, No. C8, 1993.

[4] Jacob Gunther and D.G. Long, "Models for the Near-Surface Oceanic Vorticity and Divergence," in *Proc. IGARSS '94*, (Pasadena, CA), pp. 951-953,1994.

Mosaiking of ERS SAR Quicklook Imagery of South East Asia

Leong Keong KWOH, Xiaojing HUANG, Min LI
Centre for Remote Imaging Sensing and Processing
National University of Singapore, Lower Kent Ridge Road
Singapore 119260
Tel : (65) 772 3220, Fax : (65) 775 7717
e-mail : crsklk@leonis.nus.edu.sg

Abstract – This paper presents a project in CRISP to mosaic a coverage of ERS SAR data over the landmass of South East Asia. It is estimated that about 1,500 ERS scenes will be required to cover the area spanning 40° east-west and 40° north-south. At a pixel size of 100m, the size of the final mosaic will be about 40,000 pixels by 40,000 lines, or a file size of about 1.6 Gbytes.

INTRODUCTION

The Centre for Remote Imaging, Sensing and Processing (CRISP), Singapore, operates a ground receiving station which has been actively acquiring ERS 1-2 data since March 1996. To date, there are more than 9000 scenes of ERS data, covering the whole landmass of South East Asia at least four times.

In CRISP, an ERS SAR quicklook processor has been developed and all the ERS data acquired by CRISP has been processed to quicklook images of 100-150m resolution. A lower resolution version of these quicklook images can be browse via internet with CRISP's WWW catalogue browse system (URL - http://www.crisp.nus.edu.sg).

With the quicklook images already processed, an initiative was taken to mosaic a complete coverage of the South East Asia's landmass. It is estimated that about 1,500 scenes may be required for this exercise. To cope with such large number of scenes, a set of software has been specially developed.

PROCESSING STEPS

The quicklook images generated at CRISP have a resolution of approximately 100-150m. They are presented in the slant range. Each image consists of 1013 lines of 1000 range pixels per line.

Starting with these quicklook images, the first step will be to join up the images into image strips. A slant range to ground range resampling is then performed for each of the image strip. The relationship for the slant range to ground range conversion is given in [1]. Range direction radiometric corrections are then applied to the image strip to account for the antenna elevation pattern and the range loss effect. Though published antenna elevation pattern were available (see [1]), the mosaic obtained with it showd some contrast differences at the joint between passes. To overcome this problem, we adopted a practical approach of computing the range direction correction (antenna pattern and range loss correction) from our data. This is done by averaging the range profiles of a number of image strips over the tropical forest of Borneo and then fitting the averaged profile with a fifth order polynomial. The same polynomial is then used to correct all the image strips.

The next step is to geo-reference the image strip. Though some geographic information already exists for the quicklook images, their accuracy of 1 - 2 km was insufficient for the mosaic. We have found that we can tolerate mismatches between adjacent strips of no more than 4 pixels, which is about 400m. The ERS PRI (precision) image, which have an accuracy of 100-200m seems to be an excellent choice to be used for controlling the geometry of the image strips About 3 PRI scenes well distributed along each image strip of about 10 to 12 scenes long was found to be sufficient to geo-reference the image strip. As the PRI images (for control) were generated from the same raw data as that for the quicklook images, the surface features in the image were identical. This make control point selection a relatively simple task. An image matching program for automatic selection of control points from the PRI images is currently under consideration.

After selection of the ground control points, the image strips are warped (or geocoded) to a background map/frame which have been geographically defined by latitudes and longitudes. For adjacent strips, there is an overlap area of about 25km. In this overlap area, a blending process is applied to provide for a smooth transition between image strips.

The warping of the image strip to the map/frame is performed by the usual polynomial functions. A second order polynomial is usually enough for the warping if the image strips do not span across the equator. For image strips

0-7803-3836-7/97/$10.00 © 1997 IEEE

that span across the equator, a third order polynomial becomes necessary since the ground trace of the satellite on each side of the equator curves in opposite direction.

BLENDING THE OVERLAP REGION

In the overlap region, the data will come from two different strips. For ocean area, the intensity of the data from these two strips will be very different due to differences in the backscatter between the near range and the far range. For land area, the intensity of data from the two strips are almost the same unless there are temporal changes to the land cover (e.g. agricultural fields). The blending procedure chosen for these overlap area is derived by computing the weighted mean of the image data from the two data source. The weights change linearly across the overlap region. It is obvious that the wider the blending region, the smoother will be the transition.

This procedure was able to give a very smooth transition in the flat area. Unfortunately, in the mountainous areas, some double images were visible. This double images arise because of differences in relief foreshortening between the near range (incidence angle of 19°) of one image strip and the far range (incidence angle of 29°) of the other. To avoid these double images, we will have to compromise the smoothness of the blending by narrowing the blending region. Luckily the mountainous areas are normally either bare soil or forest, which have very little temporal change. The transition in these areas will still be smooth even though the blending region is narrowed.

It is rather difficult to differentiate mountainous areas from flat lowlands from the data alone. Luckily, our objective is not in the differentiation of mountains and plains, but to just have a smooth transition between image strips yet at the same time avoiding the double image problems. The solution we finally arrived at is by varying the width of the blending region according to the differences in the mean of the pixel values between the two image strips over the same overlapping area. If the difference is large, the blending region is widen and if the difference is small, the blending region is narrowed

THE MOSAIKED IMAGE MAP

The limits of the South East Asia's landmass within CRISP ground station coverages stretches from about 90°E to 130°E and from 25°N to 15°S, an area of about 40° wide by 40° high. Choosing a pixel size of 100m, the final mosaic will be about 40,000 pixels by 40,000 lines, or a file size of about 1.6 Gbytes. In order to make the project more manageable, the approach taken was to divide the area up into geographically related regions for generation of sub-mosiacs. These sub-mosiacs have the same pixel sizes and have overlapping borders. The whole complete mosaic can later be created by mosaiking these smaller sub-mosaics.

The first sub-mosaic we have completed is one that covers the Indo-China, West Malaysia and Sumatra region. The second sub-mosaic covering of Java and Borneo is also near completion. A small portion of the mosaic over Malaysia and Sumatra is shown in figure 1. This portion of the sub-mosaic already consists of about 300 ERS scenes.

CONCLUSIONS

In this paper, we presented our work done in the mosaiking of ERS quicklook images over South East Asia's landmass. The mosaiked image, though at a relatively low (100-150m) resolution, is able to present a very interesting synoptic view of the whole area and also shows very well the geological structures of the area. It is hoped that such mosaic will be well received by the remote sensing community.

REFERENCES

[1] H. Laur, P.Bally, P. Meadows, J. Sanchez, B. Schaettler, E. Lopinto, "Derivation of the Backscattering Coefficient in ESA ERS SAR PRI Products", ESA Document No: ES-TN-RS-PM-HL09 Issue 2, Rev. 2, 28 June 1996.

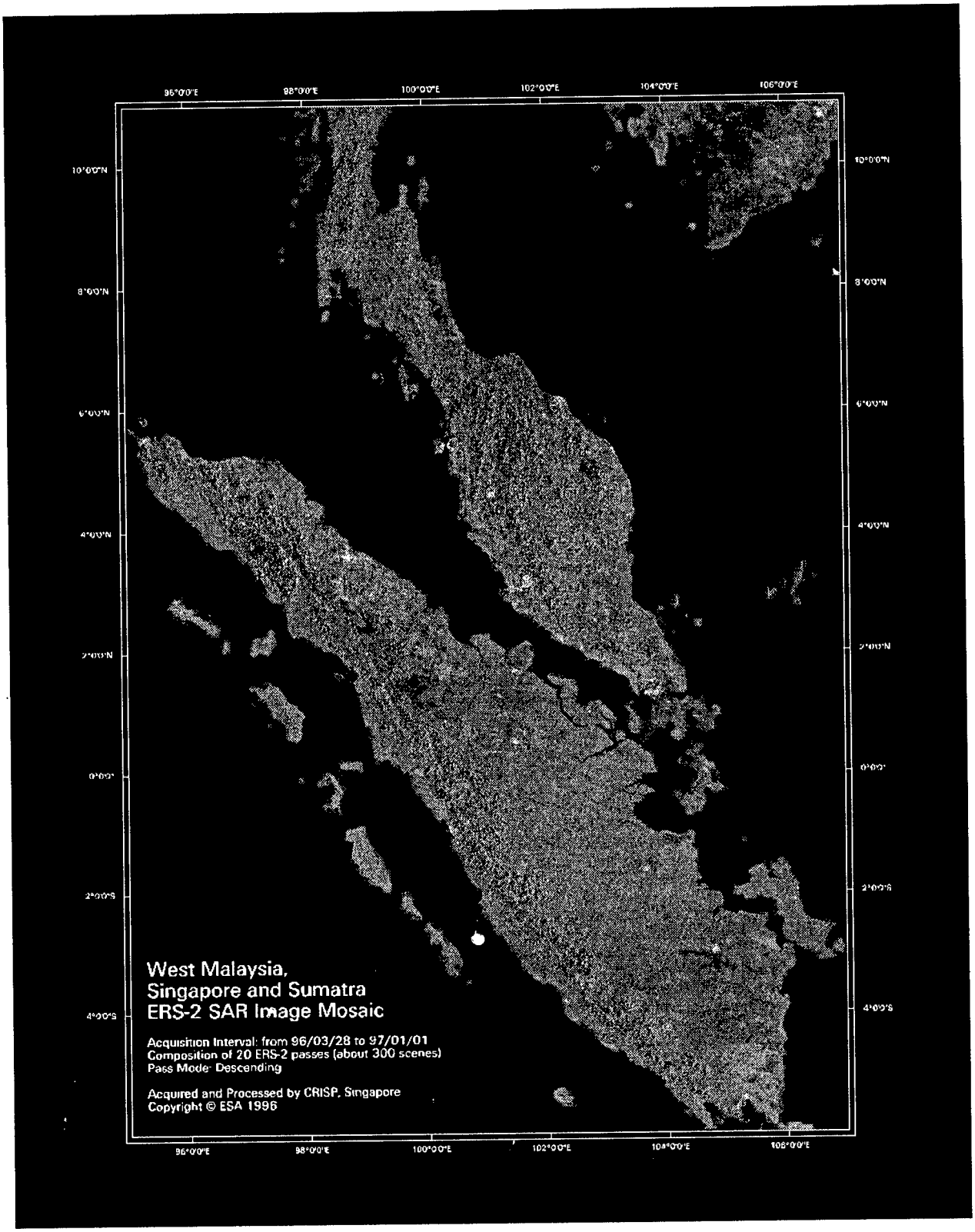

Fig. 1 - ERS SAR Image Mosaic

Change Detection from Remotely Sensed Multi-Temporal Images using Morphological Operators

Key words : mathematical morphology, fuzzy logic, urban dynamics, change, geographical information systems

Pascal Le Quéré[1], Patrick Maupin[1], Robert Desjardins[2], Marie-Catherine Mouchot[1], Benoît St-Onge[2] and Basel Solaiman[1]

[1] Ecole Nationale Supérieure des Télécommunications de Bretagne, Département Image et Traitement de l'Information
[2] Université du Québec à Montréal (UQAM), Département de Géographie

Technopole de Brest-Iroise, B. P. 832, 29285 Brest Cedex, France
Telephone: +33 (0)2.98.00.13.58 Facsimile: +33 (0)2.98.00.10.98 E-mail: maupin@gti.enst-bretagne.fr

Abstract — This paper presents a new approach to spatial change detection. The algorithms developped are based on the use of basic morphological filters and on more advanced concepts such as geodesic transformations. Such techniques are able to overcome the traditionnal problems associated with change detection from remotely sensed multi-temporal images. As a matter of fact it is already known that traditionnal methods using the concept of direction variation of the change vector are inadequate for a precise detection. These frequential techniques lay on very limitative statistical hypotheses : gaussian distribution, *a priori* determined ratio of change, very large images and relatively small ratio of change.

However in a prior study, it was determined that the basic operators of mathematical morphology were partly corrupting the results of change detection by introducing bias on the shape of the objects and also by shifting the edges in the displacement direction of the structuring element.

The geodesic transformations are correcting these topological difficulties in an elegant way. The usual threshold step is replaced by appropriate stucturing element interval of sizes. Thus, it becomes possible to treat the spatial change detection problem by using a single formalism. The first results show that the particles of change are detected even for very slight radiometric variations, with the advantage of taking into account the configuration of the neighbourhood.

INTRODUCTION

Change detection is a very important task in the progress of sustainable development and monitoring of the environment. There have been many methods developed for multi-temporal processing. Most of these detect temporal changes as directional variation of the spectral density vector assigned to each pixel [1]. However, only those with variation of their directional spectral density vector exceeding a threshold fixed on the base of restrictive hypotheses (type of distribution, prior change probability) are retained. This leads to an incomplete detection of change entities.

Usually, the image is filtered upsteam or downstream from the threshold for noise reduction. For this purpose, Maupin and al. [2] filters the image of temporal changes with an alternate sequential filter (combination of morphological openings and closings) in order to preserve the shapes of the detected entities. However, the position of the entities is not preserved and their outlines are altered. We can actually observe a shift in the direction of the moving kernel.

The algorithm described below solves those problems by using geodesic transformations which are more sophisticated morphological operators [3][4]. This research is conducted in the prospect of change masks to be used in a geographical information system [2].

METHOD

First, it is assumed that the two subsets of the images acquired at different times are, geometrically speaking, superimposed. The comparison is done through a difference image which is obtained by substracting one image from the other on a pixel-by-pixel basis. In the field of mathematical morphology, gray scale pictures are often regarded as topographic surfaces, the gray level of a pixel standing for its elevation. This analogy is used to better appreciate the effects of a given transformation on the image under study.

Such representation of difference images would show ideally a plane surface with some *hills* and *valleys*. These irregularities are the result of local variations of spectral properties of the objects between two dates. The *hills* detection algorithm is described in the two following steps.

The first step consists in generating as many images as there are objects classes in the difference image. The object reference model is a bi-dimensional hexagonal structuring element. By increasing the size of the reference object after each iteration we extract all *hills* from the image. It is carried out according to the following criteria :

A particle is extracted at the i^{th} iteration if its largest enrolled hexagon is smaller than the hexagonal structuring element used at this iteration.

0-7803-3836-7/97/$10.00 © 1997 IEEE

Generally, the area at the bottom of a peak is greater than the area at the top of it. Consequently, according to the criteria defined above, applying a growing reference object to the image yields to several cross-cut of hills. So the first image generated will be equal to the original image minus hills and top of hills that satisfies the criteria above with a size one hexagonal object model (structuring element). One can write :

Im(1)=difference image-obj<hex[1]

Im(i)=Im(i-1)-obj<hex[i]

with

hex[i]=size i structuring element

Im(i)=image generated at the i^{th} iteration

The algorithm stops when the topographic surface of the image is like a plateau with no positive irregularities.

The second step consists in simply isolating objects classes by a substraction of two consecutive images generated during the precedent step :

Class_obj(i)=Im(i-1)-Im(i)

Object extraction can simply be performed by using a morphological opening. However, this operator alters considerably the shape of the objects partially extracted. It is possible to rebuilt shapes of the objects by a geodesic dilation on the opening in the original image. In short, we implement a geodesic dilation on the erosion of the image by the structuring element since :

$$D_f^{\infty}(f \Theta B) = D_f^{\infty}(f_B)$$

where $f \Theta B$: denotes the erosion of the function f by the srtucturing element B.

f_B : denotes the opening of f by the structuring element B.

$D_f^{\infty}(g)$: denotes the dilation of the function g conditionally to the function f.

The above function is also named *algebraic opening*. Figure 1 shows the extraction of a monodimensional particle with a linear structuring element B. This particle is completely extracted at the third iteration with a size three segment (B_3).

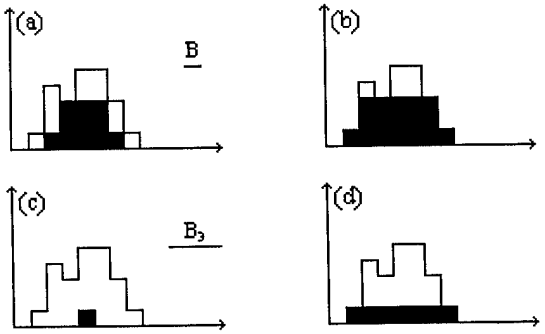

Figure 1 Sketch demonstrating a linear object extraction. (a) Original signal and its erosion (in black) by segment B. (b) Original signal and its algebraic opening (in black) by segment B. (c) Original signal and its erosion (in black) by segment B_3. (d) Original signal and its algebraic opening (in black) by segment B_3.

In the above example the algorithm detects two classes of objects : the first class by the substraction of the original signal by its algebraic opening (fig. 1b) and the second one through the substraction of the algebraic opening in fig. 1b by the algebraic opening in fig. 1d. The first class will not be retained, in the prospect change masks, because it shows clearly two distinct particles (the straw-hat shape) that can be expressed more simply by the second class particle.

Algebraic opening is well suited for this task but it is unfortenately very sensitive to noise, which is permanently present in image comparaison due to unfit geometrical correction and differences in the shooting conditions of the scenes. Accordingly, the algorithm will alternate algebraic openings (AOn) and closings (ACn) of growing sizes (n). By introducing the dual operation of the algebraic opening the authors are improving and generalizing the notion of alternate sequential filters (ASF) applied to change detection tackled in the previous part of this study [2]. The new procedure is described in fig. 2.

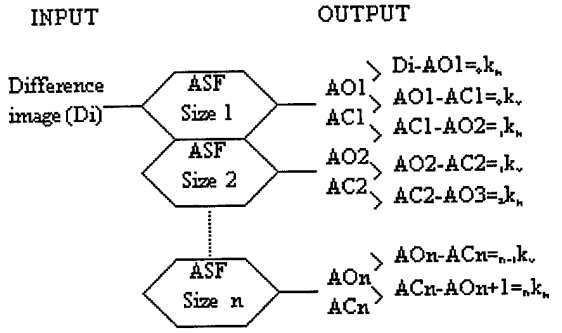

Figure 2 Improved change detection algorithm. *ASF size n* denotes *AOn* followed by *ACn* where *n* stands for the size of the filter. The change classes are denoted $_ik_{h,v}$ where *i* stands for iteration rank and *h* for *hill* and *v* for *valley* type of change. $_ok_v$ and $_ok_h$ can be computed but usually contain a lot of noise.

A case study on the spatial dynamic of the city of Trois-Rivières (Québec) is analysez using, for the sake of simplicity, Landsat TM3 images only acquired on August 20th 1984 and August 29th 1993, at 10:00 local time in both cases.

RESULTS

This section shows some results obtained with a 100*250 pixels (2.5 km*6.25 km) image including very disparate types of changes in a densely occupied urban/sub-urban area

[2]. The sample represents known changes of a mixed landuse area (residential, commercial, industrial, rural). It is clear that the initial *slice* or iteration ($_0k_v$, fig. 3 top) identifies a lot of noise of geometrical correction, but also some high intensity small particles of change that one would like to survey. The second iteration ($_1k_h$, fig. 3 middle) shows a multitude of fairly complex particles of change (linear particles, doughnut-like particles, etc.). The sixth iteration ($_5k_h$, fig. 3 bottom) is very interesting. Residential changes are almost perfectly detected (Kappa index of 0.95) and precisely indentified on the basis of their vegetation and bare soil contents.

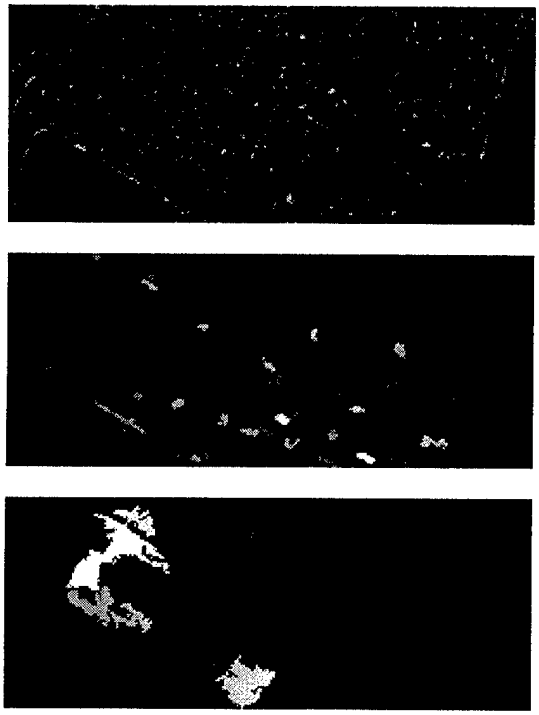

Figure 3 Three stages of processing with the change detection algorithm.

This new approach to change detection can be successfully applied to studies using images where the change proportion is very high (50% or more), contrarily to the presently used histogram-based methods.

DISCUSSION

Naturally, one can restrict the above results to a unique (few) class(es) of landuse change throught the production of a gray scale fuzzy classification as in [2] or by using appropriate fusion operators. On the other hand, the change analyst is still facing a harsh problem which resides in the polysemic nature of the so called *hills* and *valleys*. In some cases a *valley* (or a *hill*) will materialize only one type of change; or *a contrario* many surimposed landuses mutations. For example a dried pond might be represented by a ponctual high amplitude peak, thus leaving no ambiguity. But a new residential implant might show on the difference image through a fairly large and complex particle, each plateau calling for a class. Intuitively this situation leaves no choice but the study of the relations between the plateaus and a serious analysis of their geometrical and topological attributes.

This complementary work can be realised through a geographical information system making intensive use of multicriteria analysis concepts. Further publications will offer a view of these curently tested results.

ACKNOWLEDGMENT

The authors wish to acknowledge the financial and material support provided by the Université du Québec à Montréal, the Ecole Nationale Supérieure des Télécommunications de Bretagne, the Ministère des Affaires Etrangères de France, the Ministère des Affaires Internationales et de l'Immigration du Québec, the Communauté Urbaine de Brest (France) and finally, but not least, the city of Trois-Rivières.

REFERENCES

[1] A. Singh. 1989. «Digital change detection techniques using remotely-sensed data», International Journal of Remote Sensing, vol. 10, no 6, p.989-1003.

[2] P. Maupin et al. 1997. «Contribution of Mathematical Morphology and Fuzzy Logic to the Detection of Spatial Change in an Urbanized Area : Towards a Greater Integration of Image and Geographical Information Systems». (to be published in IGARSS'97 proceedings).

[3] M. Schmitt and J. Mattioli. 1994. *Morphologie mathématique*, Paris (France): Masson.

[4] L. Vincent. 1990. «Algorithmes morphologiques à base de files d'attente et de lacets : Extension aux graphes». Doctoral Thesis, Ecole des Mines de Paris.

Multiscale Markov Random Fields for Large Image Datasets Representation

Hubert Rehrauer, Klaus Seidel
Swiss Federal Institute of Technology ETH Zurich
Gloriastr. 35, CH-8092 Zuerich
Phone +41 1 632 5284, Fax +41 1 632 1251, Email: {rehrauer,seidel}@vision.ee.ethz. ch

Mihai Datcu
German Aerospace Research Establishment DLR
German Remote Sensing Center DFD
Oberpfaffenhofen, D-82234 Weßling
Phone + 49 8153 28 1388, Fax + 49 8153 28 1448, Email: datcu@dfd.dlr.de

Abstract – Future users of satellite images will be faced with a huge amount of data. The development of "Content-based image retrieval algorithms for Remote Sensing Image Archives" will allow them to efficiently use the upcoming databases of large images. Here, we present an image segmentation and feature extraction algorithm, that will enable users to search images by content. In our approach, images are modelled by multiscale Markov random fields (MSRF). This model is superior to spatial Markov random field models in that it is able to describe the long range as well as the short range behaviour of the image data. Image information extracted at multiple scales is incorporated naturally in the model. Additionally it is computationally less costly than the spatial random field models. The difference to similar work [1], [2] is that the multiscale process is not only used to find a reasonable segmentation of the image, but that the estimated parameters of the scale process serve also as image features. These image features together with the textural characteristics of the image are stored hierarchically in a pyramidal structure from large to small scales. Thereby even large datasets can be browsed fastly.

INTRODUCTION

Here, we present a model for the image interpretation at the signal level. The image is described as the result of a Markov process in scale [1]. The hierarchical structure of the model leads to hierarchically ordered features, so that images can be classified roughly according to the coarse scale features. The finer scale features lead then to a successive refinement of the classification.

If images are represented in databases by their features they can be searched by content. The special structure of our model makes fast search algorithms applicable.

Hence, this paper adresses one of the major difficulties of satellite image databases: the query of large images by content. It is the first step in the development of a database query and retrieval method that is designed around an image-feature extraction, image segmentation and recognition system [3]. The user of that database will be able to specify directly the information he wants –not the image "address"– in his request and the system will select a set of images that matches best the user's specifications.

MULTISCALE RANDOM FIELDS AND IMAGE SEGMENTATION

Pyramidal image model

The model is similar to the one presented in [1]. We make the assumption that the image is subdivided into regions that are covered homogeneously by a single texture. Then, a 2D array that gives the texture labels of each pixel can be associated to an image. We model the label array by a random field $X^{(L)}$, that is generated by a Markov process in scale as shown in Fig. 1. A single random variable $X^{(0)}$ at the top of the pyramid is the origin of the process and represents the coarsest scale field. The downward layers are created by stochastical transition processes. The assumption of Markovianity in scale is made:

$$\mathrm{P}[X^{(i)} \mid X^{(j)}, j \leq i] = \mathrm{P}[X^{(i)} \mid X^{(i-1)}]$$

0-7803-3836-7/97/$10.00 © 1997 IEEE

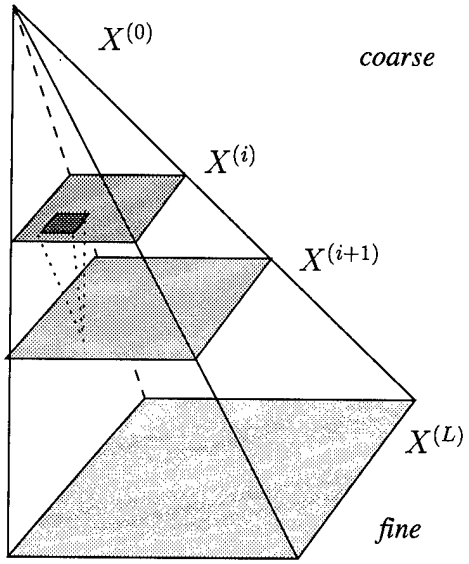

Figure 1: The random field pyramid. It is Markovian in scale. The neighbours of a variable at scale $i+1$ are located at the scale i (indicated by the dark shaded are). The values of the variables are interpreted as texture labels of the image.

The neighbours of a variable $X_s^{(i)}$ at the scale i are located in the next coarser layer $i-1$. This is different from the usual Markov random field, however it has been shown [4] that the pyramidal structure can be chosen in a way so that the resulting random fields are equivalent to spatial Markov random fields, i. e. Markov random fields are a subset of the fields that can be produced by the scale process.

When going down the pyramid one layer, the number of random variables in a layer quadruples. Finally the relation between the image and the label field $X^{(L)}$ is realized by an emission process. Through the transitions, the regions of different textures in the image are established. The final stochastic emission process fills the regions with a pattern and is governed by basic texture models like the ones presented in [5]. The statistical properties of the pyramid and the image depend on the parameters of the transition probability functions between levels. These parameters capture basic image properties such as size and distribution of textural regions in the image. There is a close relation between these parameters and the parameters extracted when MRF are applied to textured images, if an appropriate pyramid structure is used [4]. The transition parameters are used as features to characterize the image in addition to the texture parameters. The pyramidal parameters give information about the long range behaviour in the image that is not captured by the texture parameters.

Image segmentation

The segmentation of an image is the inversion of the image generating process described above. We have to find that pyramid configuration and those parameters of the pyramidal structure which have the highest probability to emit a given image. The estimation of the configuration and the parameters of the pyramid is done simultaneously using the expectation-maximization algorithm [6].

APPLICATIONS

Segmentation of an ERS-image

We applied the image segmentation algorithm to a despeckled radarimage of the ERS-1 satellite. Fig. 2 shows the original image. This image and a filtered and with a factor 4 subsampled version of it was used as input for the segmentation algorithm. As texture model Gaussian white noise was used. The bottom image of Fig. 2 shows the result of the segmentation. The algorithm detected clearly the three regions 'agriculture' at the bottom, 'water' in the middle and the 'mud flats' at the top as different. The fine scale segmentation gives even the detailed structure of the agricultural region at the bottom.

Segmentation of a Landsat TM scene

The second example shown in Fig. 3 is a part of a Landsat TM scene (channel 7 was used only). It covers different environmental areas: agriculture, forest, lake, city and mountains. The textural characteristics of the regions occur at different scales. The found segmentation gives clearly information about the large regions and the fine structure of the regions. Unfortunately, at the present status the algorithm can not distinguish between the forest and the deep mountain valleys. This is due to the simple texture model of Gaussian white noise. It is not a failure of the pyramidal segmentation model. More elaborated texture models like spatial Gibbs Markov random fields will resolve this ambiguity [5].

SUMMARY

The presented model for feature extraction and segmentation provides a mean to detect textural regions within satellite images and to classify the images. The algorithms will be extended to include better texture models. The presented methods are well adapted to the needs of future satellite database that will allow content-based queries.

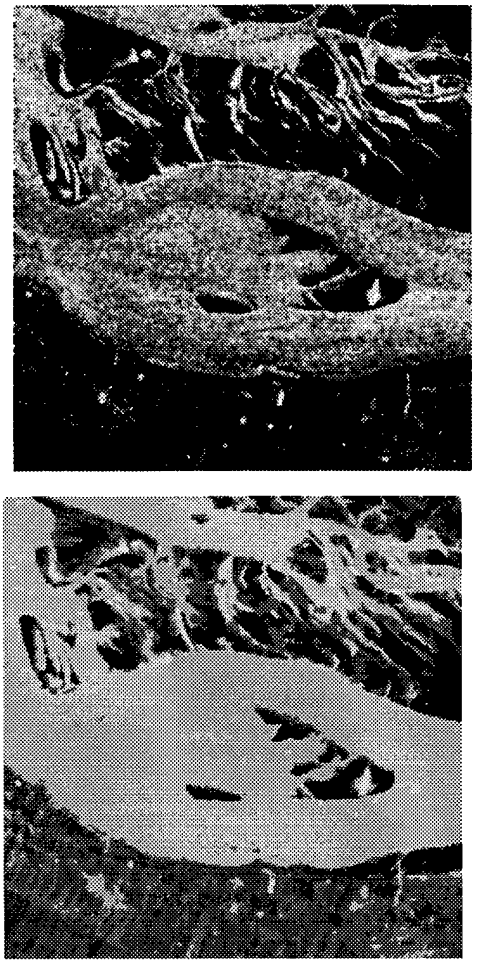

Figure 2: At the top an ERS satellite radar image is shown. The segmentation shown at the bottom was generated using the original image and scaled version (scale factor 1/4) as input for the segmentation algorithm.

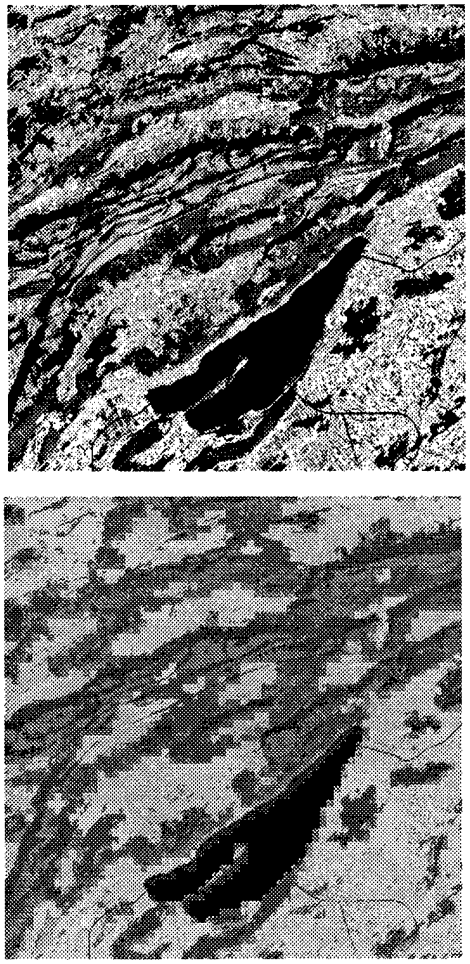

Figure 3: To find the segmentation at the bottom, the original image and scaled version (scale factor 1/16) was used.

REFERENCES

[1] Ch. A. Bouman and M. Shapiro. A multiscale random field model for Bayesian image segmentation. *IEEE Trans. on Image Processing*, 3(2):162–177, December 1994.

[2] A. Jain and J. Mao. Texture classification and segmentation using multiresolution simultaneous autoregressive models. *Pattern Recognition*, 25(2):173–188, 1992.

[3] K. Seidel, M. Datcu., and R. Mastropietro . New architecture for remote sensing image archives. 1997. In this proceedings.

[4] M. R. Luettgen, W. C. Karl, A. S. Willsky, and R. R. Tenney. Multiscale representations of Markov random fields. *IEEE Trans. on Signal Processing*, 41(12):3377–3396, December 1993.

[5] M. Schröder, K. Seidel, and M. Datcu. Gibbs markov random fields for image content characterization. 1997. In this Proceedings.

[6] T. Moon. The expectation-maximization algorithm. *IEEE Signal Processing Magazine*, pages 47–60, nov 1996.

Gibbs Random Field Models for Image Content Characterization

Michael Schröder[1], Klaus Seidel[1], and Mihai Datcu[2]

[1] **Swiss Federal Institute of Technology, ETH Zürich, Gloriastr. 35, CH-8092 Zürich**

Phone +41 1 632 5303, Fax +41 1 632 1251, Email: schro@vision.ee.ethz.ch

[2] **German Aerospace Research Establishment DLR, D-82234 Oberpfaffenhofen,**

Phone +49 8153 28 1388, Fax +49 8153 28 1448, Email: Mihai.Datcu@dlr.de

Abstract – Satellite images contain an enormous amount of spatial information. To capture that information we propose, in the framework of a stochastic modelling of the image, the use of Gibbs Markov random fields. We expand on a particular model suitable for the use with typical remote sensing images. We demonstrate the capabilities of that model with two examples. In particular, we perform directed queries for specific spatial information.

INTRODUCTION

The aquisition of huge amounts of remote sensing data immediately leads to the problem of archivation and subsequent retrieval of that data. The existing retrieval systems are oriented mainly to specification of the query by geographical position or name, sensor type, date of acquisition and, at a limited extent, to image content specified as pre-extracted attributes managed within the frame of conventional data-base management systems.

In our approach [1] we design the query and retrieval system around image-feature extraction, image segmentation and recognition systems allowing the user to automatically see the content of the archived images. At the heart of that approach lies the extraction of information from the data. Traditional methods [2] basically rely on the information of the single site characteristics in one or several spectral channels. To allow an appropriate description of the data also the spatial statistics have to be taken into account. However, in typical remote sensing images the use of the correlation function is very limited due to the large number of pixel values and the small regions of interest. As alternative several powerful stochastic models are available.

In this paper we propose Gibbs Markov random fields (GMRFs) to extract spatial information, whereas in a different approach stochastic processes in scale are applied [3]. The combination of both approaches will, together with traditional methods, provide a robust and time-efficient query process for spatial information, that is, for image content.

The article is organized as follows. In the next section we briefly give an overview of Gibbs random fields before we present a modified 'autobinomial model' [4]. This model we apply to two different examples of real satellite images before we conclude with a short summary.

GIBBS RANDOM FIELDS

We model the images as being configurations of a random field. With the assumption that local characteristics uniquely determine the statistics of the field we can model the resulting Markov field as Gibbs field with a certain neighborhood potential. For a single pixel site x this approach results in a conditioned probability distribution

$$p(x|\eta) = \frac{1}{Z}\, \mathrm{e}^{-H(x,\eta)}. \qquad (1)$$

With η we label the neighbourhood system which influences the statistics of the central pixel x via the energy function $H(x,\eta)$. The variable Z denotes the partition function of the distribution. In the following, we only use the second order neighbourhood shown in Fig. 1. In principle, however, we can choose an arbitrarily complicated neighbourhood system.

Gibbs distributions have a huge scope of applications, ranging from statistical physics [5] via lattice systems [6] up to image reconstruction [7] and segmentation [8]. In particular, detailed degradation models can be incorporated, such as the SAR speckle [9]. However, instead of expanding on the theory and applications of GMRFs we

r	v'	s'
u	x	u'
s	v	r'

$$\eta = a + b_{11}\frac{u+u'}{G} + b_{12}\frac{v+v'}{G} + b_{21}\frac{s+s'}{G} + b_{22}\frac{r+r'}{G}$$

Fig. 1: Neighbourhood of the pixel x used for the energy function $H(x,\eta)$. The quantity η represents the resulting influence of all neighbours in the binomial model.

0-7803-3836-7/97/$10.00 © 1997 IEEE

concentrate on one model and then demonstrate its capabilities for spatial image content extraction.

THE AUTOBINOMIAL MODEL

In the following, we discuss the 'autobinomial model' [4]. This model is well suited for both the characterization of real data and the generation of synthetic texture. In this model the energy function is defined as

$$H(x,\eta) = -\ln\binom{G}{x} - x\cdot\eta, \qquad (2)$$

where we denote the maximum grey value with G and the binomial coefficients with $\binom{n}{m}$. The influence of the neighbouring pixels is represented by the quantity

$$\eta = a + b_{11}\frac{u+u'}{G} + b_{12}\frac{v+v'}{G} + b_{21}\frac{s+s'}{G} + b_{22}\frac{r+r'}{G}. \qquad (3)$$

Hence, the parameter b_{11} weights the correlation between the pixel x and the horizontal neighbours u and u', whereas b_{12} weights the interaction with the vertical neighbours v und v'. A similiar interpretation is possible for b_{21} and b_{22}. Additionally, the pixel-neighbour interaction is rescaled by the maximum grey value G. Note that in typical remote sensing applications G can be quite large. The parameter a represents a self-interaction. All together the parameter vector

$$\boldsymbol{\theta} = (a,\ b_{11},\ b_{12},\ b_{21},\ b_{22})^T \qquad (4)$$

determines the statistical properties of the random variable $\{x\}$, that is, the appearance of an image which is a typical realization of such a random field.

We note that in terms of a mean field theory the parameter vector $\boldsymbol{\theta}$ determines quantities such as the mean and the variance of the pixel values in a straightforward manner. Therefore, this particular way of describing spatial information intrinsically includes the description of texture using just mean and variance. Additionally, we note that higher order energy funtions can be modelled by just adding the respective terms. However, such higher order terms are not necessary to represent textures with other angles of orientation than 0, 45 or 90 degrees as can be seen in Fig. 2 (right).

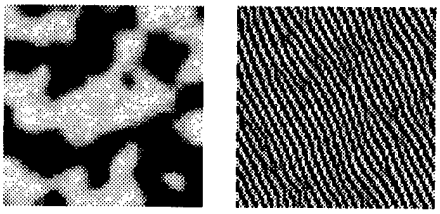

Fig. 2: Two example realizations of the binomial model. The visual perception is fundamentally different due to the different parameters $\boldsymbol{\theta} = (-2.5,\ 1.25,\ 1.25,\ 0, 0)$ (left) and $\boldsymbol{\theta} = (0,\ -1,\ 1,\ -1,\ 1)$ (right). In both cases the grey values range from 0 to $G = 255$.

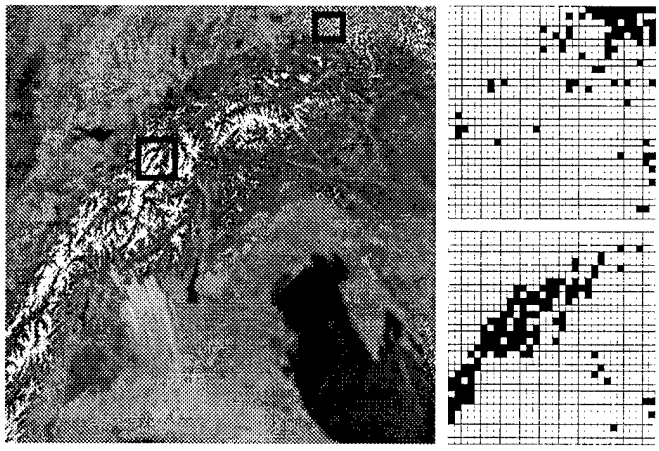

Fig. 3: Typical remote sensing images show a variety of different textures (left). After estimating the parameters of Eq. (4) in the indicated windows, we are able to search the image for similar regions using a Euclidean norm in the parameter space (upper right and lower right). As condition for similarity we have chosen $||\Delta\boldsymbol{\theta}||^2 \leq 2$.

RESURS-01 EXAMPLE

As first application to real satellite data we choose a RESURS-01 image shown in the left part of Fig. 3. This image was reduced to a much coarser scale (one pixel is approximately 1km×1km) compared to the original image.

To demonstrate the power of GMRFs we choose two typical windows ('snow' and 'clouds') with approximately equal mean and variance. After estimating the parameters in those windows using a maximum pseudo likelihood method we can use the resulting parameters as characterization in a five-dimensional feature space. We can then use these characterizations to search in the image for similar patches of textures. As measure for similarity we choose the simple Euclidean norm:

$$\begin{aligned} ||\Delta\boldsymbol{\theta}||^2 &= ||\boldsymbol{\theta}^{(1)} - \boldsymbol{\theta}^{(0)}||^2 \\ &\equiv (a^{(1)} - a^{(0)})^2 + \sum_{ij}(b_{ij}^{(1)} - b_{ij}^{(0)})^2, \end{aligned} \qquad (5)$$

with the superscripts (0) and (1) denoting the parameters of the test and the reference window, respectively.

We show the result of such a search for similar patches of 'snow' and 'clouds' in the right part of Fig. 3. Taking into account the additional influence of the different values of mean and variance enables us to directly search in the image or in a database for well-defined spatial features.

Fig. 4: Landsat TM image (left) showing different orientations of agricultural fields. At a coarser scale (factor 2) we can use the autobinomial model to separate fields of different orientations (middle and left). Here we show only those pixel values of the coarser scale which either fullfill the condition $b_{21} > -0.7$ (\-oriented texture, midlle) or alternativley $b_{22} > -0.7$ (/-oriented texture, right). For each pixel the parameter vector $\boldsymbol{\theta}$ has been estimated in a surrounding 8×8 window. In both cases the lake, fullfilling $a < -3.2$, is shown in a uniform grey for visualization.

LANDSAT TM EXAMPLE

We cannot only use the feature vector to calculate similarities between certain pieces of texture, we can also directly extract information from $\boldsymbol{\theta}$ according to a particular spatial criterion. However, at full resolution this information is not always represented by GMRFs in a clear way. Instead it may be more suitable to extract that information at a different scale.

This we demonstrate with a Landsat TM image shown in Fig. 4 (left). The clearly visible structures are agricultural fields with different orientations. To capture those orientations we estimate the parameters at a coarser scale of factor 2. The middle and right parts of Fig. 4 show a successful detection of / and \ oriented texture.

Note that the separation almost takes place on the pixel level and that this simple query can be easily extended by taking into account the values of more than one componet of $\boldsymbol{\theta}$. Also the inclusion of prior knowledge using Bayesian inference or a further segmentation [3] is possible.

SUMMARY AND CONCLUSION

In this paper we have presented Gibbs Markov random fields as a powerful tool for the extraction of spatial information of remote sensing image data.

The Gibbs energy function can be chosen as sophisticated as necessary. However, the estimation at different scales and the incorporation of multiscale random field models additionally promise the fast detection of long-range correlations and a robust and time-efficient query process even for large datasets.

REFERENCES

[1] K. Seidel, M. Datcu, and R. Mastropietro, 1997, New architecture for remote sensing image archives, in this Proceedings.

[2] E. Löffler, 1994, Geographie und Fernerkundung, B. G. Teubner, Stuttgart.

[3] H. Rehrauer, K. Seidel, and M. Datcu, 1997, Multiscale markov random fields for large image datasets representation, in this Proceedings.

[4] G. R. Cross and A. K. Jain, 1983, Markov random field texture models, IEEE Trans. PAMI, **5**, 25–39.

[5] L. D. Landau and E. M. Lifschitz, 1966, Lehrbuch der Theoretischen Physik, V. Statistische Physik, Akademie Verlag, Berlin.

[6] Julian Besag, 1974, Spatial interaction and the statistical analysis of lattice systems, Journal of the Royal Statistical Society, **36**, 192–236.

[7] S. Geman and D. Geman, 1984, Stochastic relaxation, Gibbs distributions, and the Bayesian restoration of images, IEEE Trans. PAMI, **6**, 721–741.

[8] S. Lakshmanan and H. Derin, 1989, Simultaneous parameter estimation and segmentation of Gibbs random fields using simulated annealing, IEEE Trans. PAMI, **11**, 799–813.

[9] M. Walessa and M. Datcu, 1997, Bayesian approach to SAR image reconstruction, in this Proceedings.

Techniques for Large Zone Segmentation of Seismic Images

Marwan A. Simaan
Department of Electrical Engineering, University of Pittsburgh
348 Benedum Hall, Pittsburgh, PA 15261
Tel: (412) 624-8002, Fax: (412) 624-8003, email: simaan@ee.pitt.edu

Abstract – Seismic techniques play an important role in the exploration for hydrocarbon deposits within the earth. In this paper, we describe three knowledge-based segmentation techniques and compare their performance on a real seismic image. The first technique is based on a run length statistics algorithm extended by a decision process which incorporates heuristic rules to influence the segmentation. The second and third techniques are based on texture energy measures algorithms augmented by two knowledge-based classification processes. The knowledge-based process of the second technique is controlled by a parallel region growing scheme and that of the third technique is controlled by an iterative quadtree spitting scheme. Our results show that the third technique, which is based on texture measures augmented with a knowledge-based quadtree splitting scheme, provides a better segmentation of the test image than the other two.

SEISMIC SECTION

One of the most popular and successful methods for imaging the earth's subsurface is the seismic exploration method [1,2]. Seismic data are typically displayed as a two-dimensional section (from now on we shall refer to it as an image) of stacked traces placed side-by-side. The vertical direction of such a display is time; which can be converted to depth once the signal velocities are known, and the horizontal direction is linear distance on the surface of the earth. The interpretation of a seismic image involves, among other things, the recognition of certain patterns such as faults, salt domes, strong reflectors etc ...; and the identification of large zones of common signal texture. Such zones are often associated with geologic events related to the deposition environments of the constituent sediments; and as such their identification is an important part of the overall interpretation task. Figure (1) shows a (very small) 512×512 piece of a seismic section with a horizontal distance sampling of 110 ft and vertical sampling of 8 msec. A manual segmentation which identifies four zones of common signal texture is superimposed on it. Zone 1 is characterized by short horizontal reflections with varying degrees of vertical spacing. Zones 2 and 3 both have long continuous reflectors with zone 2 having a smaller average vertical spacing between reflectors. Zone 4 is characterized by chaotic reflections and line noise with variable orientation.

Signal texture is a property define for small neighborhoods in an image. It may be viewed as a composition of elements in a set of gray-tonal primitives arranged in a certain repetitive spatial organization which may be random, may have a pair-wise dependence of one primitive on neighboring primitives, or may have a dependence on several primitives at a time [3]. Among the wide variety of features used for texture analysis, gray-level *run length* has been used in only a few applications [4]. A gray-level run is defined as a collinearly connected set of pixels all having the same gray tone. The length of the run is the number of pixels in the run. Run lengths can be extracted by making one dimensional scans across the image. Statistics calculated from these run lengths can capture the continuity as well as the density of reflectors and hence can be used for the purpose of segmentation. Our first knowledge-based approach uses *run length* to obtain an initial segmentation.

Another feature used for texture analysis is *texture energy measures* [5]. Our second and third knowledge-based approaches use texture energy measures to obtain an initial segmentation. The main idea of these measures revolves around convolving the image with small size masks (typically 5×5) to extract significant local texture events followed by appropriate size large masks (typically 20×20) to calculate statistical feature measures. A Certainty Factor vector *CF* is then assigned to each pixel unit. The *ith* entry in this vector denotes the degree of membership of this unit to the *ith* texture class. An initial segmentation is then obtained based on the *CF* array for the entire image.

KNOWLEDGE-BASED SEGMENTATION SYSTEMS

The main disadvantage of segmenting the image based only on run length statistics or texture energy measures is that these algorithms are purely numerical and do not take advantage of the structural and geologic properties of the seismic image. They do not take into consideration the fact that the various texture zones are influenced by the order of geologic events which characterize the entire region for which the image represents only a small piece. In this section we will describe three possible approaches for augmenting such algorithms with "knowledge-based" processing. This will be achieved by modeling heuristic constraints that a human interpreter would use in his segmentation. For example, an interpreter is aware that the zones to be segmented are contiguous areas. His classification of a particular area on the image is strongly influenced by the potential classification of neighboring areas. He might also use geologic information related to the depositional sequence of the various regions in the image. All this information is

0-7803-3836-7/97/$10.00 © 1997 IEEE

independent of whatever texture he sees in the image and may even influence what he thinks he sees. Heuristic information, like the above, may be implemented as rules which can alter the degree of membership of a particular texture unit to a certain texture class. As an example, rules such as the *Depth Prejudice Rule*, the *Sequence Rule*, the *Zone 4 Shape Rule* and the *Neighbors Rule* can be used [6-8]. In all three systems describe belwo these rules have been decomposed and translated into list form before being loaded into the knowledge databases.

A. Knowledge-Based Run Length Statistics: A block diagram of a system [6] in which the run length algorithm is augmented by a knowledge-based process is shown in Figure (2). This process does a depth first search guided by a hill climbing method. The initial state is a vector *CF* of certainty factors (or degrees of membership) of a particular texture unit to the various texture classes. This initial node is expanded by application of each of the four rules. The subsequent states are compared with a goal state which requires the unit to have one degree of membership above a minimum threshold and all others below a different lower threshold. If none of the states meets this goal, the search continues by expanding the node which is closest to it. Note that the rules that have not been applied to that point in the search are used to expand to the next depth. That is, along the search path from the initial state towards the goal state, there are no duplicate firing of the same rule. A segmentation of the test image of Figure (1) using this system is shown in Figure (3).

B. Knowledge-Based Region Growing: A block diagram of a system [7] in which the texture energy measures algorithm is augmented by a knowledge-based process is shown in Figure (4). In this system, the energy measures algorithm produces small clusters, called "islands" of texture units which are definitely classified. The controller assigns an "Intelligent Walker" (IW) to each island and controls the growth of these islands, in parallel, by applying the above four rules. The reasoning engine is a simple forward deduction process, equipped with a certainty factor model, which passes certainty factors in a probability based way. A segmentation of the test image of Figure (1) using this system is shown in Figure (5).

C. Knowledge-Based Quadtree Splitting: A block diagram of a system [8] in which the texture energy measures algorithm is augmented by an iterative quadtree splitting process is shown in Figure (6). In this system, the energy measures algorithm produces feature measure planes which are then smoothed by standard level reduction and median filtering. A quadtree data structure is then created through an iterative process in which there are two major steps. The first is a recursive splitting process of each node into four quadrants, and the second consists of knowledge-based leaf node classification by applying the above rules. The segmentation process starts with a root node (the entire image) and the iterations continue until all leaf nodes are classified. An interesting property of this approach is that the resultant segmentation is less dependent on the order in which the image is processes. A segmentation of the test image of Figure (1) using this system is shown in Figure (7).

Comparing Figures (3), (5) & (7) clearly leads to the conclusion that the second and third systems have produced a far better segmentation than the first. A closer examination of Figures (5) and (7) may lead to the conclusion that Figure (7) is a slightly better segmentation than Figure (5). Furthermore, the third system seems to possess more favorable properties. Among these, the multiresolution data structure and the iterative refinement scheme during the classification process make it possible to use both global and local information before a definite classification is reached.

REFERENCES

[1] Simaan M., and Aminzadeh, F., Eds. Advances in Geophysical Data Processing: AI and Expert Systems in Petroleum Exploration, JAI Press, Greenwich, CT, 1989.

[2] Mutter, J.C., "Seismic Images of Plate Boundaries," Scientific American, pp. 66-75, 1986.

[3] Haralick, R.M., "Statistical and Structural Approaches to Texture," *Proc. of IEEE*, Vol 67, pp. 786-804, May 1979.

[4] Gulloway, M.M., "Texture Analysis Using Gray Level Run Lengths," CGIP, Vol. 4, pp. 172-179, 1975.

[5] K.I. Laws, "Texture image segmentation," Ph.D. Dissertation, USC, 1980.

[6] P.L. Love and M. Simaan, "Segmentation of a seismic section using image processing and artificial intelligence techniques," *Pattern Recog.*, Vol. 18, pp. 409-419, 1985

[7] Z. Zhang and M. Simaan, "A rule-based interpretation system for segmentation of seismic images," *Pattern Recognition*, Vol. 20, pp. 45-53, 1987.

[8] Z. Zhang and M. Simaan, "A knowledge-based system for segmentation of seismic sections controlled by an iterative quadtree splitting scheme," *IEEE Trans. Geos. & Remote Sensing*, Vol. GE-26, pp. 518-524, 1988.

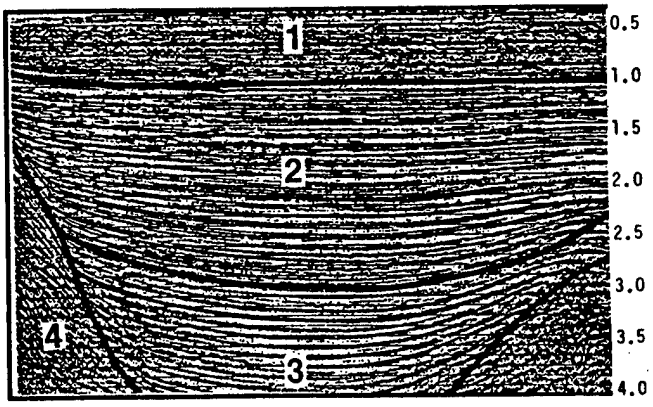

Figure 1: Test image; a small piece of seismic section. A manual segmentation into four zones of common signal texture is superimposed.

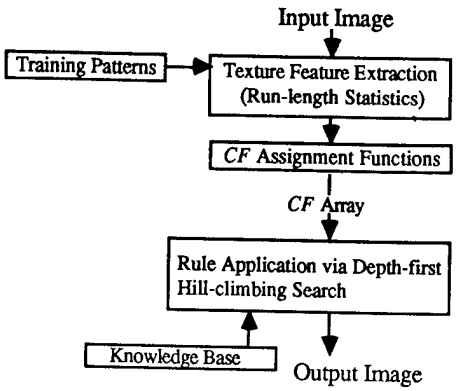

Figure 2: Block diagram of a knowledge-based run length statistics texture image segmentation system.

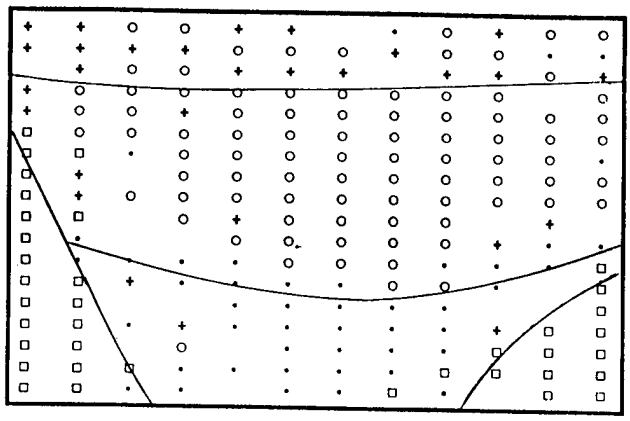

Figure 3: A segmentation of the test image obtained using the knowledge-based run length statistics system. The four zones are labeled + (zone 1), o (zone 2), • (zone 3), and □ (zone 4).

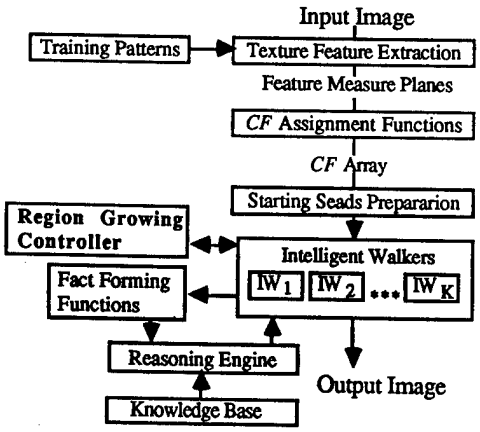

Figure 4: Block diagram of a knowledge-based region growing texture image segmentation system.

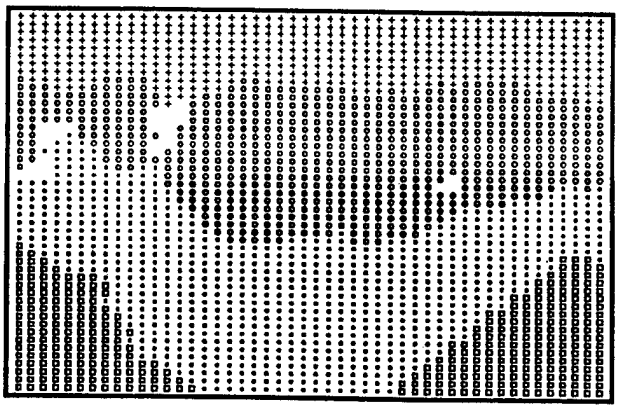

Figure 5: A segmentation of the test image obtained using the knowledge-based region growing system. The four zones are labeled + (zone 1), o (zone 2), • (zone 3), and □ (zone 4).

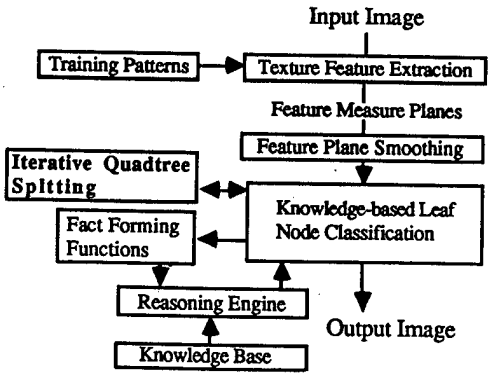

Figure 6: Block diagram of a knowledge-based iterative quadtree splitting texture image segmentation system.

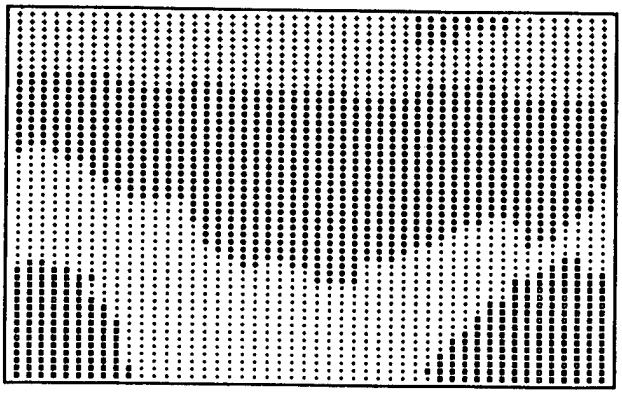

Figure 7: A segmentation of the test image obtained using the knowledge-based iterative quadtree splitting system. The four zones are labeled + (zone 1), o (zone 2), • (zone 3), and □ (zone 4).

Segmentation of Multispectral Remote-sensing Images based on Markov Random Fields

Iong-Wen Tsai and Din-Chang Tseng

Institute of Computer Science and Information Engineering
National Central University
Chung-li, Taiwan 320
Email: tsengdc@ip.csie.ncu.edu.tw

Abstract -- An unsupervised approach for texture segmentation of multispectral remote-sensing images based on Gaussian Markov random fields (GMRFs) is proposed. At first, we treat the false-color information of Spot satellite images as *RGB* attributes and then transform them to *HSI* attributes. Secondly, a scale-space filter is used to threshold the hue histogram to quantize the color set which represents the principal color components in the original image. Thirdly, the global GMRF parameters are estimated from the original image for global segmentation. Fourthly, we label each pixel of the image based on the quantized color set and the GMRF parameters to maximize a posterior color distribution probability to achieve the global segmentation. Fifthly, a criterion is used to judge whether every pixel in the global-segmented image is within a local textured region or not. Finally, the pixels in a local textured region are further estimated the local GMRF parameters and clustered based on the parameters. Seven Spot images were segmented to demonstrate the ability of the proposed approach. Moreover, the scale-space filter, the MRF-based global segmentation, and the pure local (texture) parameter classification are sequentially evaluated their performance.

1. INTRODUCTION

The purely intensity-based segmentation methods only use spectral information for image segmentation, then textured regions cannot be correctly segmented. To exactly segment multispectral remote-sensing images, spatial information should be considered to combine with spectral information. It means that neighborhood-based methods should be employed for textured multispectral-image segmentation.

The neighborhood-based approaches which use Markov random fields (MRFs) consider both spectral and spatial information [2, 6, 9, 10]. The utilization of both kinds of information can classify image region more exact than the intensity-based methods which only use spectral information. Many methods which supervise maximum a posterior probability (MAP) segmentation using MRFs are based on the methodology introduced by Geman and Geman [4]. The Hammersley-Clifford theorem [4, 5] established the equivalence between the conditional probabilities of the local characteristics in MRFs and the local energy potential in Gibbs distribution. The model parameters are assumed a priori known in supervised image segmentation; however, many researchers have addressed the difficult problem of unsupervised segmentation for which no priori knowledge of texture parameters is assumed. Most of the unsupervised segmentation methods assume an image model previously and estimate model parameters before clustering [3, 7].

In this paper, an unsupervised approach for texture segmentation of multispectral remote-sensing images based on MRFs is proposed. We assume that color of each pixel is under the influence of the colors of its neighboring pixels and an additive noise. The noise are assumed to form a Gaussian distribution. A Gaussian Markov random field (GMRF) is a special case of MRFs and we use a GMRF to model the multispectral remote-sensing images and then segment the images [1, 8].

2. SEGMENTATION

The proposed system is an unsupervised algorithm for segmenting the homogeneous textured regions in multispectral remote-sensing images without the prior information, such as the number of texture regions, texture parameters, and the color distribution. To achieve the goal, many processes are adopted here.

At first, we take the three spectra of a multispectral *SPOT* image as *RGB* components to compose the false-color image and transform *RGB* color space to *HSI* color space.

Secondly, we detect how many and what major types of colors compose the original image. There are several optimal approaches can achieve this goal; for example, k-means clustering, maximin clustering, and histogram thresholding. A number of clustering approaches need to know the number of clusters and spend much more time than the histogram-based approaches, so we adopt histogram thresholding method based on the scale-space filter to quantize the hue values. From this step, a few pixels at region contours may be mislabeled; however, we can know the major types of color which compose the image and call these quantized color values as *color set*.

0-7803-3836-7/97/$10.00 © 1997 IEEE

Thirdly, we use the least-squares method to estimate the global GMRF parameters to be included in a posterior color distribution for the global segmentation of the image.

Fourthly, we label each pixel of the image using *RGB* values based on the quantized *color set* and the GMRF parameters to maximize a posterior distribution probability (MAP) to reduce the cases of mislabeling at region contours. The global parameters used in this step are estimated from the statistical result of the whole image. The results of labeling provide more smooth region contours than the results of thresholding on *hue* histogram. In fact, the goal of this step is to separate the regions which is homogenous in color and it will provide more simplified texture distribution of the original image to benefit the local (texture) parameter estimation in the next step. The results of this step are called the *global-segmented* (*labeled*) *image*.

Fifthly, the pixels are classified into two classes based on their local random property. Pixels possessing higher randomness will be further processed with a local spatial information. We estimate local parameters for these pixels. In fact, the result of parameter classification for each pixel sometimes offers coarse boundaries around some regions which we don't think they are textured regions but regions homogeneous in color. This is the critical problem in local parameter classification. The parameter estimation occupies a large proportion of the whole computation time; therefore, we reserve partial results of the global-segmented image based on global parameters and estimate local parameters of remainder pixels for classification. A criterion is proposed to decide whether a pixel should be estimated local parameters or not. For the pixels should be estimated local parameters, we use a fixed-size window which centered at each one of them and estimate the local parameters from the statistical results of the range of the fixed-size window. The parameters we mention here represent the relationship between the central pixel and their neighboring pixels. However, to produce a better parameter vector to represent texture property of each pixel, the color mean and Gaussian noise variance of the window range are considered simultaneously.

Finally, we develop a criterion to classify the estimated local parameters of the higher-random pixels. The criterion takes the maximum of all component distances to represent the distance between two parameter vectors and classify these parameter vectors by the distances between each vector and each cluster center. Since the texture property of a pixel is represented by the local parameter vector, the homogeneous textured region can be separated after parameter classification [7].

3. EXPERIMENTS

Seven *SPOT* remote-sensing images were segmented by the proposed approach to demonstrate that the proposed approach is suitable for remote-sensing image segmentation. Moreover, the histogram thresholding based on the scale-space filter, the MRF-based global segmentation, and the pure local (texture) parameter classification are sequentially evaluated their performance.

One experimental result is shown here. An original 256×256 *SPOT* satellite image of SDS02 is shown in Fig.1(a), The result of histogram thresholding based on the scale-space filter, the MRF-based global segmentation result based on the previous thresholded result, the local texture segmentation result based on the previous two processed result, and the complete result without pixel classification are shown in Fig.1(b)~(e), respectively.

4. CONCLUSION

From the experimental results, we can draw several conclusions as follows:

(1) The proposed global segmentation can reduce the mislabeling problem in ssf-based histogram thresholding and simplify texture distribution for more effective local parameters estimation and classification.

(2) The MRF-based global segmentation is an unsupervised segmentation and can provide a better texture segmentation result than the local texture classification. Meanwhile, the proposed system spends less computation time to finish work for it selects partial specific pixels of the image for local parameters estimation and classification.

(3) The Manjuanth-Chellappa local segmentation [7] were partially implemented and applied to classify the estimated texture vectors; however, due to the special property of remote-sensing images, our proposed approach made much better results than the pure local texture segmentation.

ACKNOWLEDGMENTS

This research was partial supported by the National Science Council under grant of NSC 85-2213-E-008-014.

REFERENCES

[1] A. Baraldi and F. Parmiggiani, "A Nagao-Matsuyama approach to high-resolution satellite image classification," *IEEE Trans. on Geoscience and Remote Sensing*, Vol.32, No.4, pp.749-758, 1994.

[2] C. A. Bouman and M. Shapiro, "A multiscale random field model for Bayesian image segmentation," *IEEE Trans. on Image Processing*, Vol.3, No.2, pp.162-176, 1994.

[3] F. S. Cohen and Z. Fan, "Maximum likelihood unsupervised textured image segmentation," *Computer Vision, Graphics, and Image Processing: Graphical Models and Image Processing*, Vol.54, No.3, pp.239-251, 1992.

[4] S. Geman and D. Geman, "Stochastic relaxation, Gibbs distribution, and the Bayesian restoration of images," *IEEE Trans. Pattern Analysis and Machine Intelligence,* Vol.6, No.6, pp.721-741, 1984.

[5] D. Geman, S. Geman, C. Graffigne, and P. Dong, "Boundary detection by constrained optimization," *IEEE Trans. Pattern Analysis and Machine Intelligence,* Vol.12, No.5, pp.609-628, 1990.

[6] J. Liu and Y. H. Yang, "Multiresolution color image segmentation," *IEEE Trans. on Pattern Analysis and Machine Intelligence*, Vol.16, No.7, pp.689-700, 1994.

[7] B. S. Manjunath and R. Chellappa, "Unsupervised texture segmentation using Markov random field models," *IEEE Trans. on Pattern Analysis and Machine Intelligence*, Vol.13, No.5, pp.478-482, 1991.

[8] P. Masson and W. Pieczynski, "SEM algorithm and unsupervised statistical segmentation of satellite images," *IEEE Trans. on Geoscience and Remote Sensing*, Vol.31, No.3, pp.618-633, 1993.

[9] D. K. Panjwani and G. Healey, "Markov random field models for unsupervised segmentation of textured color images," *IEEE Trans. on Pattern Analysis and Machine Intelligence*, Vol.17, No.10, pp.939-954, 1995.

[10] T. Yamazaki and D. Gingras, "Image classification using spectral and spatial information based on MRF models," *IEEE Trans. on Image Processing*, Vol.4, No.9, pp.1333-1338, 1995.

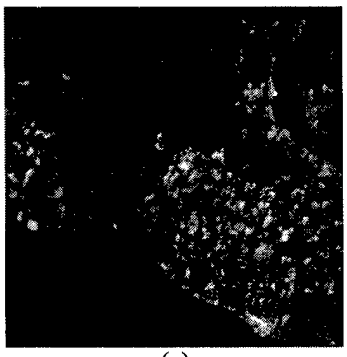

(a)

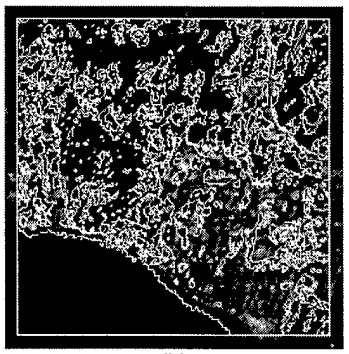

(b)

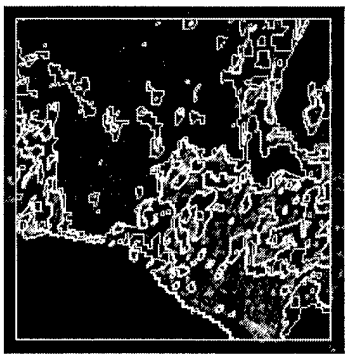

(c)

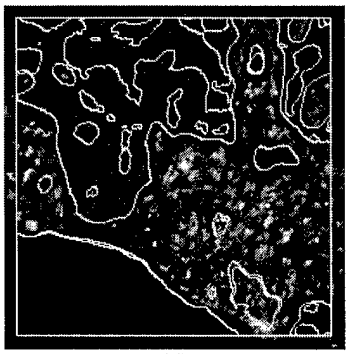

(d)

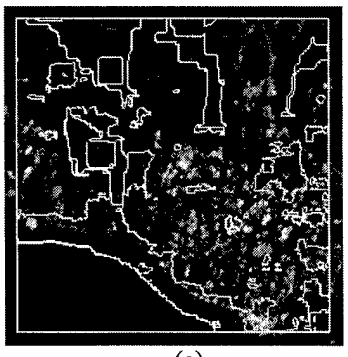

(e)

Fig. 1. Segment results of image SDS02. (a) The original image; (b) the ssf-based thresholded result; (c) the result after global segmentation; (d) the result after local segmentation; and (e) the local-segmented result without pixel classification.

IGARSS'97

1997 International Geoscience and Remote Sensing Symposium

03-08 August 1997

Singapore International Convention & Exhibition Centre

Technical Program

Interactive Area 15: Land Cover Applications

Land Cover Change: A Method For Assessing The Reliability Of Land Cover Changes Measured From Remotely-Sensed Data.

Richard J Aspinall
Macaulay Land Use Research Institute,
Craigiebuckler, Aberdeen, AB15 8QH
Tel: (0)1224 318611 FAX: (0)1224 318611 E-mail: r.aspinall@mluri.sari.ac.uk
and
Michael J Hill
CSIRO Centre for Mediterranean Agricultural Research
Private Bag, PO, Wembley, Western Australia, 6014
Tel: (09) 387 0316 FAX: (09) 387 8991 e-mail: m.hill@ccmar.csiro.au

Abstract -- A method for assessing the reliability of land cover changes measured using data from different dates is presented and tested using a study area in the Cairngorm mountains, Scotland. Two sources of uncertainty are recognised in the change detection process: a) slivers resulting from misalignment of boundaries of land cover polygons and b) false positive changes associated with mis-classification error in production of the land cover maps.

INTRODUCTION

Land cover maps produced using remotely sensed data are a significant source of information for monitoring the stock and change in land use across large areas. However, land cover maps contain a number of inherent uncertainties associated with the data sources, methods of interpretation, and representation of land cover variability as discrete, non-overlapping and internally homogenous map polygons [1]. These uncertainties include mis-identification of classes, positional inaccuracy in boundary location and omission of internal polygon heterogeneity [2] but are seldom described. Using a series of two or more land cover maps to measure change over time means that uncertainties associated with maps for each date will influence the ability to interpret change with known reliability. This paper presents a method for assessing the reliability of land cover changes measured from remotely-sensed data in the presence of uncertainty in the data.

STUDY AREA AND DATA

The study area is ~1000 km^2 of the central Cairngorm mountains in Scotland. The land cover of this area is described in the 1988 Land Cover of Scotland, LCS88, a digital dataset that contains detailed baseline information describing the land cover of Scotland at a scale of 1:25,000. The dataset is derived from 1:24,000 scale air photos by manual interpretation and has been field validated to assess the accuracy of interpretation; description of uncertainty is an integral part of the dataset and has been described in detail [2]. Land cover in the 1960s has also been described through interpretation of historic photographs compared with the 1988 dataset. The historic photographs were also of 1:24,000 scale and were interpreted using LCS88 methods with the 1988 photographs and land cover maps as a guide. The same individual interpreted the photos from the different dates. Where differences in land cover were apparent on the photos from the two dates the differences were recorded on 1:25,000 scale maps. The differences in the 1960s were then digitised into a digital copy of the LCS88 data; this method minimises the re-digitising of unchanged classes and boundaries between the two dates. Mapping used the basic 126 land cover classes of the LCS88. For both maps, and for the confusion matrix, the basic classes were reclassified to 34 categories for analysis here.

The descriptions of uncertainty in class identification generated from the field validation of the 1988 data [2] are coupled with both the 1988 and 1960s land cover data. This assumes that the uncertainties in class identification for the 1960s data are identical to those described for 1988; use of the same interpreter for both dates allows this assumption although, ideally, each date would have its own uncertainty analysis.

METHOD AND ANALYSIS

Conceptually, change in land cover between two dates is easily assessed using map overlay in GIS; differences between the two maps are change. In practice, this method does not account for two main sources of uncertainty. The first is uncertainty that results from mis-alignment of the polygon boundaries in the different representations. Sliver polygons in GIS overlay are typically identified by their size, shape, location or combination of these. The second source of uncertainty is associated with class identification; a false positive change may be recorded when no change has taken place because a polygon on one (or both) of the two maps is mis-classified. (Similarly, mis-classification may also lead to no change being identified when change has

0-7803-3836-7/97/$10.00 © 1997 IEEE

taken place; these false-negatives cannot be identified).

The method for assessing reliability of change identifies both slivers and false-positives. Slivers can be identified by their size and shape using standard criteria (eg length more than three times width) or by definition (eg they are smaller than the minimum mapping unit for the land cover map). False positives are found by analysis of the confusion matrices that describe uncertainty in class identification [2] combined with the changes that are recorded in the overlay of datasets. The confusion matrices are analysed to determine the probability that the classes on the two maps, whatever they are labelled, are the same class. This process is shown in Table 1. The confusion matrix is used to estimate upper and lower limits of the area of classes that can be expected due to mis-identification and confusion between classes (Table 1). This method incorporates the area of each class.

RESULTS AND DISCUSSION

Fig.1 shows the four different aspects of land cover change for the Cairngorm study area: all differences between the 1964 and 1988 land cover maps, slivers, changes that are not reliably detected, and the reliably detected changes.

The total area of difference between the two maps is 136.36 km^2, or 15.22% of the map area. Slivers are defined as changes smaller than 2 ha, the minimum mapping unit for woodlands. The slivers total 14.75 km^2, or 10.82% of all the differences between the 1960s and 1988 map. However, the method of data capture used, in which 1988 data was edited to incorporate 1960s differences only, should minimise slivers since unchanged boundaries are retrieved directly from the 1988 dataset. That there are still so many slivers with this method is partly due to their size definition, but also because the GIS used - ARC/INFO - adjusts the polygon geometry, and hence boundary location, when the maps sheets are edge-matched and this adjustment is different for the two dates even though many of the polygon boundaries are identical.

The method used to digitise the 1960s data is not typical of GIS data capture since land cover maps will more usually be collected independently of one another. In one 20 km x 10 km map sheet in the north of the study area all boundaries were redigitised for the 1960s dataset rather than being copied from the 1988 dataset. In this sheet about 20% of all change is slivers. This sheet will be more typical of the process by which land cover change is mapped and suggests that slivers may be a significant source of error when recording land cover change.

Differences between the 1960s and 1988 but that are unreliable due to confusion in interpretation between classes occupy 20.74 km^2, or 15.22% of all differences.

Table 1. Process for detecting reliable changes

1. Confusion Matrix: Map and Field Validation

Map\Field Validation:	Class 1	Class 2
Class 1	150	50
Class 2	40	210

2. Row Normalise Matrix

	Class 1	Class 2
Class 1	0.75	0.25
Class 2	0.16	0.84

3. Calculate upper and lower range (95% confidence interval) for row normalised values

	Class 1	Class 2
Class 1	0.69 -- 0.80	0.20 -- 0.31
Class 2	0.12 -- 0.21	0.79 -- 0.88

4. Calculate expected maximum and minimum areas (km^2) for classes at time (t+1) given area at time (t)

	Area time t	Class 1 (t+1)	Class 2 (t+1)
Class 1	100.0	69.0 -- 80.0	20.0 -- 31.1
Class 2	200.0	24.0 -- 42.0	158.0 --176.0

A total of 11.54 km^2, or 8.46% of all differences are both slivers and attributable to unreliable interpretation. These results show that using map overlay 15.22% of the map area has changed land cover between the 1960s and 1988 although the reliably detected change is only 12.9%.

The effects of uncertainty due to class identification are quantified using this methodology which is based on coupling the field validation data to digital land cover maps in the form of confusion matrices. The approach is based, therefore, on collection of field validation data using an appropriate sampling strategy. The methodology separates uncertainties due to digital processing (slivers) from those associated with mis-interpretation or mis-classification and shows that these uncertainties can form a considerable proportion of changes detected by comparing land cover maps.

Use of datasets such as LCS88 to assess land cover change will increase in future as they provide baselines for comparison with land cover maps from more recent sources. The uncertainties inherent in data capture present, however, a number of significant problems for assessing the extent of land cover changes. Class confusion during interpretation in the field validation, limit the confidence that can be attached to changes recorded in land cover data from different dates.

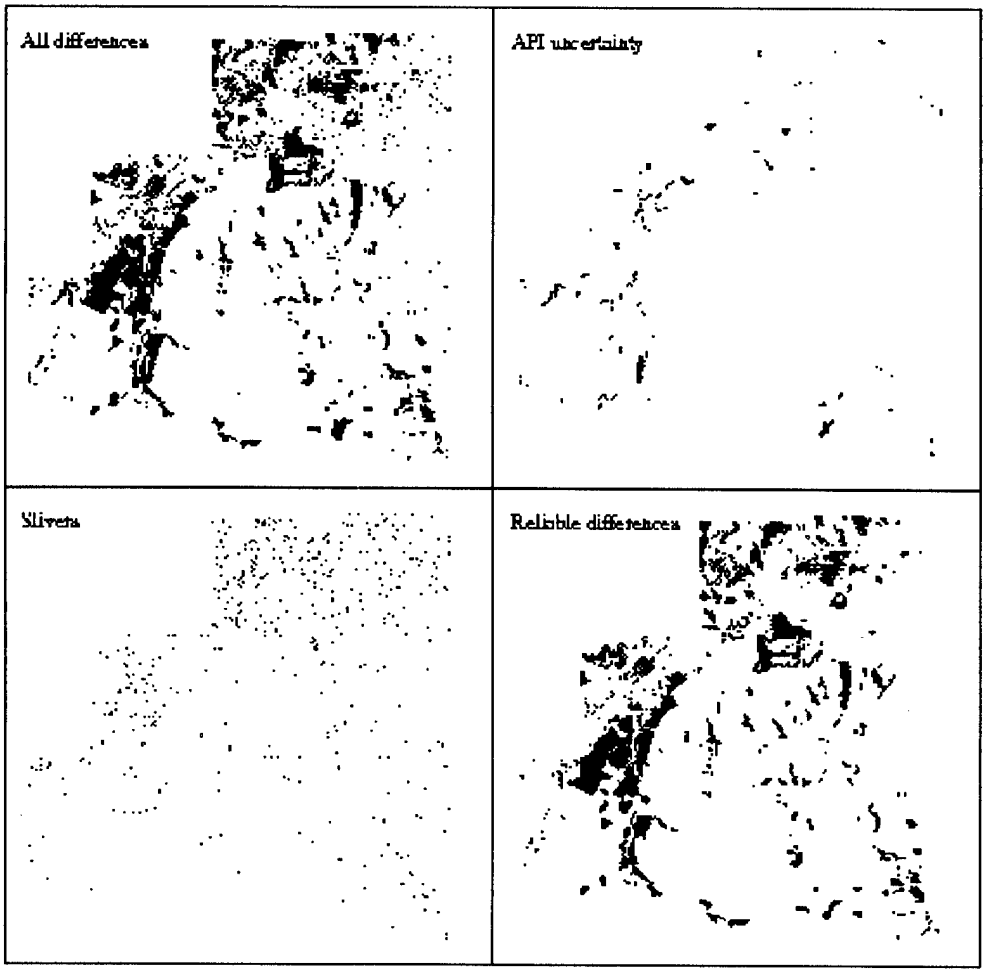

Figure. 1. Land cover change in the Cairngorm area, Scotland, UK between the 1960s and 1988. All differences, slivers, unreliable differences due to uncertainty in aerial photo interpretation (API), and reliable differences are shown

ACKNOWLEDGEMENTS

This work was funded by the Scottish Office Agriculture, Environment and Fisheries Department and carried out while MJH was visiting researcher at the Macaulay Land Use Research Institute. CSIRO Division of Animal Production is partially funded by Australian wool growers through the International Wool Secretariat.

REFERENCES

[1] Goodchild, M. F., Guoqing, S. and Shiren, Y. (1992) Development and test of an error model for categorical data. International Journal of Geographical Information Systems, **6**, 87-103.

[2] Aspinall, R. J. and Pearson, D. M. (1995) Describing and managing uncertainty of categorical maps in GIS. In: Fisher, P. F. (Ed) Innovations in GIS 2. Taylor and Francis, London.

Title: Remote Sensing of the Effects of Irrigation Activities on Vegetation Health in Ephemeral Wetlands of Semi-Arid Australia

Simon N. Benger
Department of Geography, School of Resource Management and Environmental Studies
Australian National University, Canberra ACT 2602, AUSTRALIA
ph. +61 6 249 3704 fax. +61 6 249 3770 Email: simon@dart.anu.edu.au

Abstract -- The ephemeral wetlands of semi-arid Australia provide important habitats for many species and play a significant role in the hydrological and biological regimes of these environments. As most inland wetlands owe their existence to unregulated cycles of flooding and drying, many wetlands are now being forced into decline through flow regulation associated with irrigation for large, highly productive agricultural enterprises. Time series of JERS-1 optical and radar imagery and Landsat TM imagery were used to determine the potential for employing various vegetation species as indicators of wetland decline in the Macquarie Marshes of central western New South Wales. River red gum, Water couch, Cumbungi and Common reed species could be detected at sufficient spatial and spectral resolution to be mappable from satellite imagery, and health gradients were detectable in certain species. The development of these techniques offers good potential to facilitate monitoring of wetland health and assist in management decisions regarding flood control within inland wetlands.

INTRODUCTION

Australia's inland wetlands are an extremely important natural resource. These systems are often highly productive, provide habitats for a large number of organisms, and are an essential ecosystem component in arid and semi-arid environments with limited water resources. Many of these wetlands are now being impacted in an uncontrolled fashion while the information available on their functioning and processes is inadequate for management purposes. The rivers which feed and comprise many inland wetlands are often essential sources of irrigation water for many large and highly productive agricultural systems. In recent decades millions of ML of irrigation water have been diverted from regular river flows each year, impacting significantly on river, riparian and wetland ecosystems.

As most inland wetlands owe their existence to an unregulated cycle of flooding and drying based on seasonal and episodic rainfall events, interference with these cycles through flow regulation is forcing many wetlands into decline. This decline usually manifests itself in the early stages through a deterioration in the health of wetland vegetation. Remote sensing has been widely used for the monitoring of vegetation health from space, on both regional and global scales. Strong reflectance in the NIR region is characteristic of healthy leaf tissue, while photosynthetically active vegetation reflects less radiation in the visible range [1]. Using simple combinations of reflectance from vegetation in the red and near infrared (NIR) wavebands, numerous indices have been developed which have been shown to correlate well with various vegetation parameters. Various researchers have established a strong correlation between these vegetation indices and Leaf Area Index (LAI), biomass, percent green cover, productivity and photosynthetic activity [2,3].

Typically, the size and inaccessibility of many inland wetlands has meant that declines in wetland health are only partially visible and difficult to quantify. The application of remote sensing techniques offers the possibility of examining wetland health on a scale that would be impossible using ground-based observation. The techniques outlined in this paper offer significant potential for the development of an effective monitoring and assessment tool for inland wetlands.

METHODS

Study Area

The Macquarie Marshes, which are located in central western New South Wales, Australia, are the focus of this study. The Marshes are comprised of a large permanent core of wetlands surrounded by thousands of hectares of ephemeral wetland subject (under normal conditions) to periodic inundation. This seasonal and episodic flooding cycle and its relationship to local variations in elevation are the primary determinant of vegetation distribution and abundance within the wetland system. The Macquarie Marshes Nature Reserve is currently listed as a significant wetland under the Ramsar Convention and is protected under Australia's migratory bird agreements.

The expansion of the cotton industry and concurrent increase in pumping of water for irrigation has meant that since the early 1990's, the Macquarie Marshes now receive as little as 30% of their original flow [4]. The most damaging effects of this flow regulation have been observed in the more ephemeral areas of the wetlands but are also thought to be impacting significantly on the core areas.

Data

JERS-1 optical and L-band SAR data and Landsat TM data were acquired over the study area. The better spatial resolution of the JERS-1 data (18m pixel size compared to 30m pixel size on the Landsat data) contrasted with the better spectral information available from the Landsat data

0-7803-3836-7/97/$10.00 © 1997 IEEE

(7 bands as opposed to JERS-1 3 band data). The imagery examined was from 1994 and 1995 and therefore represented the vegetation in the Marshes after a prolonged period of general decline. Hydrographs of flows into the Marshes show that there has not been any significant flooding since 1990.

Four general fieldsites were chosen based on local knowledge of areas within the Marshes where significant problems in vegetation health were known to exist and where likely indicator species were present in homogeneous stands at a scale suitable for analysis using remote sensing. Within three of these fieldsites subplots were selected and mapped for respective species. The fourth fieldsite covered a much larger area and was used for verification purposes.

The subplots were surveyed using a Nikon DTM-720 surveying instrument in conjunction with a Magellan GPS to produce a series of spot heights across the fieldsites. These spot heights were transferred into Arc/Info and used to generate surface models for the subplots. The results of this surface modelling demonstrated the expected relationship between elevation and species distribution within the ephemeral portions of the Marshes, and confirmed that transitions in health of indicator species are a function of local elevation. The surveying data also facilitated precise georeferencing of vegetation boundaries and relative distances across and between vegetation stands.

Analysis

Several dominant species within the wetlands were examined to determine their usefulness as indicators of wetland decline. In many systems such an approach would be unsuitable due to the inherent complexities of natural vegetation and mixes of plant species over a relatively small spatial scale [5]. However, in inland wetlands such as the Macquarie Marshes, the vegetation is often characterised by its occurrence in discrete, homogenous stands, usually defined by elevation (and hence relationship to flooding) and local hydrology. This inherent characteristic of Australian inland wetland vegetation has been successfully exploited in other studies [6].

The vegetation species examined as part of this study included River red gum *Eucalyptus camaldulensus*, Black box *Eucalyptus largiflorens*, Poplar box *Eucalyptus populnea*, Coolibah *Eucalyptus coolabah*, River cooba *Acacia stenophylla*, Cumbungi reed *Typha orientalis*, Common reed *Phragmites australis*, and Water couch *Paspaulum paspalodes*. Fieldwork investigations showed that all of these species showed signs of stress in many parts of the Marshes. The larger tree species were likely to be the best indicators of long term decline, whereas the smaller reed and grass species tend to respond quickly to short term changes in the hydrologic regime. The type of response is very important in determining the suitability of a species for use as an remotely sensed indicator of declines in wetland health. Following fieldwork and initial classifications, four species (River red gum, Cumbungi reed, Common reed and Water couch) were selected for more detailed analysis.

Each of these four species has a distinctive response to changes in the flooding regime. River red gums respond very slowly to changes in the flooding regime and individual trees can live for up to 400 years. The grass and reed species tend to the most obvious indicators of wetland decline because they degrade very quickly due to their shallow root systems which afford access to soil moisture only in the upper portions of the soil profile.

Image processing and classification of the remotely sensed data was carried out on a SUN Sparc 5 using ERMapper 5.2. GIS analysis was performed on the same machine using Arc/Info 7.2.

Classification

The maximum likelihood classifier (MLC) was chosen for use because of its superior accuracy for classification of natural resource data [7]. For each fieldsite a series of ISOCLASS unsupervised classifications, supervised classifications and combination unsupervised/supervised classification techniques were applied to selected band combinations to determine how well the indicator species could be classified in the imagery. The ease of classification of particular vegetation stands provided an indication of the degree to which these species might be mappable over larger areas. Normalised Radar Cross Section (NRCS) values were computed from JERS-1 SAR imagery across the fieldsites. Using the classification information derived from spectral and radar datasets over the fieldsites, classifications were undertaken over larger areas of the marshes to determine whether the indicator species were mappable on a regional scale.

Detection of Changes in Vegetation Health

Field observations revealed that transitions in physiological health of River red gum and Water couch were visibly apparent on the ground; a feature of the vegetation recorded in other studies. Having determined that the river red gum stands and the water couch pastures could be spatially defined from the satellite imagery, statistical analyses were undertaken to determine whether the transitions in health observed on the ground existed as discrete spectral entities. This involved examining the shift in spectral response along vectors parallel to the transition in vegetation health, and hence perpendicular to elevation contour lines. The commonly used vegetation indices of NDVI and OSAVI were used as relative measures of vegetation health. Derived values were averaged and plotted over distance to reveal patterns in spectral response.

RESULTS

Of the selected indicator species examined, it was found that Cumbungi and Common reed could be effectively classified in the JERS-1 OPS imagery over the fieldsites, but classifications over larger areas were less reliable as more spectral variance was introduced. Classifications of

the Cumbungi and Common reed produced using the Landsat TM imagery were not as successful, suggesting that the better spatial resolution of the JERS-1 data was an important factor affecting classification accuracy. The Water couch pastures were more amenable to classification than the reed species, due to broader areal extent, and could be effectively classified in both the JERS-1 and the Landsat TM imagery. The stands of River red gum were readily classifiable in both the JERS-1 data and the Landsat TM, although the spatially narrower bands of vegetation did not show up well in the latter. Classifications over larger areas were successful and showed a high degree of correlation with vegetation maps of the Marshes. Combined time series of TM data showing seasonal variation produced the most accurate classifications of indicator species. The SAR data was useful for discriminating between cover types, but could not effectively discriminate between indicator species. Combined SAR/TM classifications of River red gum were highly accurate.

Analysis of spectral response across the River red gum plots showed that in all of the plots there is a linear change in NDVI and OSAVI values perpendicular to the adjacent river channels and parallel to the observed transitional vectors. NDVI and OSAVI values decrease with distance along these vectors and with increases in elevation, and are most likely related to changes in Leaf Area Index (LAI) and photosynthetic activity associated with declines in tree health and reduced sub-canopy regeneration.

The analysis of the Water couch subplots showed an opposite response in vegetation index values to those observed for the River red gums. In all of the Water couch subplots there was a definite linear change in NDVI and OSAVI values, once again perpendicular to adjacent river channels and parallel to observed transitional vectors. However, in the case of the Water couch, these values increase with distance from the water channel and with increasing elevation. This is most likely due to herbaceous groundcover increasingly outcompeting Water couch as it becomes more degraded, and returning increasingly higher index values.

In both River red gum and Water couch indicator species there is a definite spectral gradient that exists within the separate spectral entities that define these species as landscape components.

CONCLUSIONS

The results of this study suggest that the indicator species examined can be effectively mapped from remotely sensed imagery. Cumbungi and Common reed species operate as good quick response indicators of changes in wetland health as they manifest a rapid deterioration in leaf area and percentage cover due to changes in the flooding regime. However, they may be difficult to accurately map on a regional scale without some prior knowledge of location.

The River red gum and Water couch species offer the best potential as indicators of declines in wetland health. They occur in a broader spatial context than the other indicator species examined in this study, making them more readily mappable on a regional scale, and they possess clearly defined spectral signatures facilitating accurate classification. Additionally, the existence of transition zones within homogenous stands, and their detectability in the spectral domain as distinct entities, mean that single date imagery could potentially be used to identify wetland systems in decline.

In all of the potential indicator species examined, the improved spatial resolution of the JERS-1 sensor afforded more accurate classification and detection of homogeneous stands within the landscape than Landsat TM. The spatial extent of particular landscape units is therefore critical in assessing their potential use as indicators. The wider range of spectral information available from the Landsat TM data did not necessarily afford more accurate detection of health transitions, probably because most information on vegetation functioning and health is only detectable in the red and NIR spectral domain [8]. In all test sites, classifications from remotely sensed imagery afforded more accurate vegetation mapping than that produced from aerial photography.

REFERENCES

[1] Hobbs, R.J. (1990) Remote sensing of spatial and temporal dynamics of vegetation, in Hobbs, R.J. and Mooney, H.A. (eds) **Remote Sensing of Biosphere Functioning**, Springer-Verlag, New York, pp.203-219

[2] Asrar, G., Fuchs, M., Kanemasu, E.T., and Hatfield, J.L. (1984) Estimating adsorbed photosynthetic radiation and leaf area index from spectral reflectance in wheat, **Agronomy J. 76**, pp.300-306.

[3] Huete, A.R and Jackson, R.D. (1987) Suitability of spectral indices for evaluating vegetation characteristics on arid rangelands, **Remote Sens. Environ. 23**, pp.213-232

[4] Brereton, G.J. (1993a) **The History of Investigations into the Macquarie Marshes**, Macquarie Marshes Management Strategy - Stage 1, Biophysical Investigations, NSW DLWC Report, 35p.

[5] Graetz, R.D. (1990) Remote sensing of terrestrial ecosystem structure: An ecologists pragmatic view, in Hobbs, R.J. and Mooney, H.A. (eds) **Remote Sensing of Biosphere Functioning**, Springer-Verlag, New York, 312p.

[6] Richards, J.A., Woodgate, P.W., and Skidmore, A.K. (1987) An explanation of enhanced radar backscattering from flooded forests, **Int. J. of Remote Sens. 8**, pp.1093-1100

[7] Bolstad, P.V. and Lillesand, T.M. (1991) Rapid maximum likelihood classification, **Photogram, Eng. Remote Sens. 57**, pp.67-74

[8] Chen, J.M. and Cihlar, C. (1996) Retrieving leaf area index of Boreal conifer forests using Landsat TM images, **Remote Sens. Environ. 55**, pp.153-162

Mapping Pastures in Eastern Australia with NOAA-AVHRR NDVI and Landsat TM Data

Michael J. Hill and Graham E. Donald
CSIRO Division of Animal Production
CCMAR, PMB PO, Wembley, WA, 6025, Australia
Ph: 61 9 3870316 Fax: 61 9 387 8991 Email: m.hill@ccmar.csiro.au

Abstract -- Monthly NOAA-AVHRR NDVI data, and single date Landsat TM data at 10 sites within the AVHRR area, were used to classify pastoral land cover for the High Rainfall Zone of SE Australia for 1993. NDVI profiles and Landsat TM pixel compositions for typical pasture types are presented for a summer rainfall area in Northern NSW and a seasonal Mediterranean climate in Western Victoria. Agreement between the classification and results of a survey of pasture types by professional agriculturalists is examined.

INTRODUCTION

Research agencies working with the grazing industry need independent information on the type and condition of pastures in the temperate High Rainfall Zone (HRZ) of eastern Australia to focus research on producer needs and provide a benchmark for assessment of research impacts. In a recent study, we provided this type of information by analysis of a sequence of monthly NDVI images derived from NOAA-AVHRR data to provide a pasture land cover classification using 1993 as the benchmark year [1]. These NDVI data were combined with single date, spring, Landsat TM imagery at 10 sites within the study area to provide a measure of the composition of the NDVI pixels in terms of a known pasture classification [2]. The results of this study were presented in relation to Local Government Area (LGA) polygons to facilitate integration with other statistics. In this paper, we examine the characteristics of major pasture classes for two pastoral areas with contrasting climates, the Severn LGA on the Northern Tablelands of NSW and the Dundas LGA in the Western District of Victoria. The two areas are prime pastoral regions of Australia with native pasture predominating in Severn and sown annual pasture predominating in Dundas. However, the areas have a minority component of sown perennial pasture in common. The classification is tested by comparing the characteristics and areas of assigned classes with the results of a national survey of pasture types [3] carried out at the same time,

METHODS

The original study covered temperate pasture areas in Tasmania, South Australia, Victoria, New South Wales and Queensland where annual rainfall exceeded 600 mm. For this paper, classified NDVI data were masked for the Severn and Dundas LGAs and used as a template to extract NDVI profiles and class compositions in terms of classified Landsat TM data for these two LGA areas. A detailed description of the methods used in deriving the classification is given in [1]. Briefly, the study area was split into northern and southern zones based on the temporal pattern of moisture indices, and masked to include only freehold/leasehold land. Pre-processed, monthly composited, NDVI data for 1993 from atmospherically corrected NOAA-AVHRR data were used. NDVI data from 11 monthly composite images were classified using the same polythetic divisive clustering procedure used for the 3-channel (2,3,4) Landsat TM images at 10 sites [4]. The TM classification results in six grassland classes which provide a qualitative measure of potential pasture growth rate - 1, very fast; 2 fast; 3, medium; 4, medium slow; 5, slow; and 6, very slow [2]. Additional classes identify sparse vegetation, woodland and forest. Tree cover is well measured by the classification [5]. The slower growth classes are predominantly associated with native pasture, while the faster growth classes are associated with improved pasture [6].

We defined three main types of NDVI profile associated with the vegetation of the HRZ: "annual herbage" with a distinct low autumn section, a distinct, high spring section and a large seasonal difference; "perennial herbage" with a moderate autumn section, high spring section and a moderate seasonal difference; and "forest" with a relatively uniform, high profile, a small spring flush and little seasonal difference. In addition, Australian native pasture tends to appear much less green than sown pasture due to lower fertility, frost sensitivity and general adaptation to arid conditions. This means that native grassland should have a general perennial profile but with a lower overall greenness. The basic profile types could all occur in varying proportions within a single NDVI pixel. As a result, profiles covered the extremes of patterns described and various intermediate combinations depending on the uniformity of land cover within an NDVI pixel.

The NDVI classification was aggregated to form the NDVI classes using the seasonal shape of the NDVI profiles, the geographical location of the classes, the association between classes and the composition of NDVI class pixels in terms of Landsat TM classes. The classified NDVI data were combined with LGA boundary data to allow the particular pasture state of each LGA to be estimated.

0-7803-3836-7/97/$10.00 © 1997 IEEE

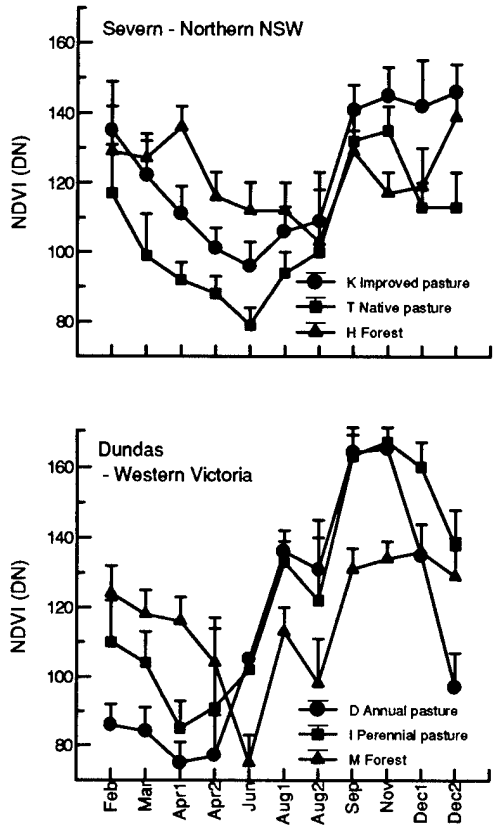

Figure 1. NDVI profiles for example classes of two major pasture types and forest for Severn LGA in Northern NSW and Dundas LGA in Western Victoria. Bars indicate standard errors.

RESULTS AND DISCUSSION

The classification procedure identified 21 and 22 classes in the northern and southern zones respectively [1]. These classes could be broadly grouped into five types: perennial pastures, annual pastures (southern zone only), mixed pasture and cropping, native pastures with woodland, and forest. Fig. 1 shows NDVI profiles for examples of classes ascribed to improved and native perennial pastures for the Severn LGA in Northern NSW, and sown annual and perennial pastures for the Dundas LGA in Western Victoria. A profile for forest is shown to provide a contrast in each case. The general difference in NDVI profiles between locations reflect summer rainfall, mild summers and cold frosty winters for Severn and hot, dry summers and moist wet winters for Dundas. The effect of these climatic patterns can be seen in the pattern of greenness in similar sown perennial pastures at each location. Improved perennial pasture would be expected to senesce and turn brown in late summer and autumn in Dundas and rapidly green up in late autumn when the first rains arrive reaching a peak in mid-spring. The same pasture would be expected to be heavily frosted and barely growing in winter in Severn, but to green-up in mid-spring, retaining their greenness over summer and gradually brown off in autumn and into winter.

Within the Severn location, the class ascribed to improved perennial pasture is generally greener, and extends the spring peak into early summer much more than the class ascribed to native pasture (Fig. 1); the classification provided several other "native" classes which are not shown. Within the Dundas location, both pasture types are sown exotics, but have different life cycles. The annual pasture becomes senescent by late spring and turns brown. The perennial pasture maintains greenness longer and does not decline as much in greenness over summer as the annual pasture.

The composition of pixels of NDVI classes displayed in Fig. 1 in terms of Landsat TM classes is shown in Table 1. For the Severn area, the Landsat image was acquired on November 5 at the peak of spring growth in this montane environment. The improved pasture class shows an equal composition of the Landsat TM pasture classes. The native pasture class has a lower composition of the very fast and fast Landsat TM growth classes (1 and 2).

The Landsat image for the Dundas area was acquired on December 19, after the annual pastures have begun to senesce and after the peak of spring growth. The annual pasture class contains none of the very fast and fast Landsat TM growth classes and is predominantly made up of the slower growth classes reflecting the senescent state of the pasture. The perennial pasture class is predominantly made up of the faster Landsat TM growth classes with almost none of the slower growth classes reflecting the capacity of perennial pasture to grow on into the summer.

The aggregated results of a survey of professional agriculturalists are shown in Table 2. The survey estimates the area of pastoral land occupied by particular pasture types for the Severn and Dundas LGAs. Pastoral activities form 99% of agricultural land use in these LGAs according to agricultural census statistics from the Australian Bureau of Statistics. Table 3. shows the estimated area of broad pasture types in these LGAs based on the NDVI classification. If the non-agricultural and other classes are discounted, it appears that the classification for Severn underestimates the area of sown perennial pasture. However, for Dundas, the estimates of improved annual and perennial pasture are about the same for the NDVI classification as for the survey.

The survey comparison points to the greater difficulty of using NDVI profiles in less seasonal climates, such as experienced in Severn, where greening waves are not so strongly associated with particular times of the year. Many native pastures in Severn have been fertilised or oversown with exotic legume species at some stage in the past 40 years. Therefore, a brief greening wave in early spring due

Table 1. Composition (%) of NDVI classes in Fig. 1 in terms of Landsat TM pasture classes. Columns do not sum to 100 as remaining TM classes are not shown.

Severn	*NDVI Class*		
TM Class	Improved K	Native T	Forest H
Grass 1 + 2	30.0	14.1	1.1
Grass 3 + 4	29.6	35.6	8.2
Grass 5 + 6	29.4	32.4	16.5
Forest/Wood	10.8	14.7	73.3

Dundas	*NDVI Class*		
TM Class	Annual D	Perennial I	Forest M
Grass 1 + 2	0	40.5	0
Grass 3 + 4	32.8	41.6	0.6
Grass 5 + 6	40.8	5.5	1.5
Forest/Wood	12.3	11.2	97.1

Table 2. Percentage of pastured area occupied by pasture type (based on a survey of professional agriculturalists).

Pasture Type	*Severn*	*Dundas*
Sown annual	0	67
Sown perennial	53	32
Native/naturalised	45	0
Other	2	1

Table 3. Percentage of total freehold/leasehold area occupied by pasture type based on classification using monthly NDVI and classified Landsat TM data for spring.

Pasture type	*Severn*	*Dundas*
Annual	0	64
Perennial	13	27
Native	41	0
Forest	46	3
Other	10	6

to the growth of annual legume species may occur in most of them. This greening coincides with the date of the classified Landsat TM data leading to the small difference in TM class composition between improved and native NDVI classes in Table 1. Significant tree cover in other native pasture classes contributed to uncertainty in the allocation of native pasture classes. In Dundas, by contrast, the differences in TM class composition and NDVI profiles appear to accurately reflect the notional differences in pasture type and growth pattern. The physiological responses of different pasture types together with the seasonality of the greening wave clarify interpretation.

CONCLUSIONS

The NDVI classes provide a broad picture of the mix of pasture and tree cover within a 1.2 km^2 area. based on a greenness profile and an estimate of their composition in terms of Landsat TM growth rate classes. The reliability of the classification depends on the geographical uniformity of pasture type or mix of pasture types, and may be better where pasture type and growth pattern are constrained by seasonal climate. The results provide a benchmark for pasture condition in 1993 for SE Australia. The classification may be used as a template for detecting significant change in NDVI profiles, or TM class composition, from future monitoring.

ACKNOWLEDGMENTS

This work was supported by the Australian Meat Research Corporation. CSIRO Division of Animal Production is partially funded by Australian woolgrowers through the International Wool Secretariat.

REFERENCES

[1] M. J. Hill, P. J. Vickery E P. Furnival and G. E. Donald, "Using NOAA-AVHRR NDVI and classified Landsat TM data to describe pastures in the temperate high rainfall zone (HRZ) of eastern Australia." unpublished.

[2] P. J. Vickery, and E. P. Furnival, "Development and commercial use of Landsat derived maps as an aid to more effective use of fertiliser," Proc. of the 6th Aust. Soc. Agron. Conf. pp. 392-395. 1992.

[3] C. J. Pearson,, R. Brown, W. J. Collins, K. A. Archer, M. S. Wood, C. Petersen, and B. Bootle, "An Australian temperate pastures database," Aust. J. Agric. Res. (in press).

[4] D. A. Hedges, and P. J. Vickery, "Use of a principal components strategy as the basis for an unsupervised classification routine to examine Landsat data from grassland vegetation," Proc. 4th Austral. Remote Sens. Conf., pp 178-188, 1987.

[5] M. J. Hill, G. E. Donald, P. J. Vickery, and E. P. Furnival, "Integration of satellite remote sensing, simple bioclimatic models and GIS for assessment of pasture suitability for a commercial grazing enterprise," Aust. J. Exp. Agric. 36: 309-21, 1996.

[6] P. J. Vickery, M. J. Hill, and G. E. Donald, "Landsat derived maps for pasture growth status: association of classification with botanical composition," unpublished.

Evaluating Quaternary climatic change in West Africa using the NOAA AVHRR 1KM Land Dataset

Janet Nichol
Nanyang Technological University, Singapore
469 Bukit Timah Rd, Singapore 259756
Fax: (65) 469 2427, Email: nicholj@nievax.nie.ac.sg

INTRODUCTION

Previous estimates of the extent and magnitude of climatic change in West Africa and other desert marginal areas, based on observations of fossil fixed dunes, have assumed a maximum shift in climatic zones during the quaternary period of 500-700kms, with rainfall totals some 600-700mm higher today than at the height of desert expansion. Such estimates have been able to utilise air photo and satellite images readily available in desert marginal areas with little cloud cover, but have not previously extended into more humid regions. The daily coverage of the NOAA AVHRR sensor gives a higher probability of cloud free images in humid regions, permitting a synoptic view across whole continents and climatic zones, with similar date and illumination conditions. The current availability, on a USGS website of the NOAA 1km Land Dataset has enabled observation of desert landforms well into the rainforest zone of Nigeria and Cameroon, approximating the 2000mm isohyet and a former desert margin at 1200kms south of the present desert. Although the desert landforms are now highly degraded by eluviation and weathering, the sands of the former dunes are highly fertile fine sandy clay loams, ideal for cereal and groundnut cultivation, though the former interdune areas, with heavier clay soils, often remain uncultivated. Surprisingly, traditional soil surveys in West Africa have been unaware of these highly contrasting soil differences over short distances, though inexplicable disparities have often been noted on soil survey sheets.

The study is therefore relevant not only in terms of estimating the magnitude of climatic change in tropical regions but also provide a different perspective for soil surveys and agricultural development in the tropics.

STUDY AREAS

1. Kano region

This is in the Sudan zone of Nigeria at 12°N (annual rainfall 800mm) (Figure 1). Land use is intensively cultivated rainfed farming with main crops, millet and guinea corn, interspersed with economic trees which mainly shed their leaves during the long dry season (October to May). At the time of imaging, mid-dry season, soil is bare and trees mainly leafless. Perennial shrubs occupy uncultivated areas of poor soils and at the mid-dry season time of imaging, would be in an senesced state. Soils are predominantly yellowish-red (5YR 5/5) ferruginous soils, low in organic matter and clay, thus having low consistency. A previous study (Nichol, 1991) used LANDSAT MSS data to identify fossil dune features across this region and extend the previous estimate as far south as the 1000mm isohyet. Field observations confirmed that landscape inversion had taken place, with the former interdunes comprising grey coloured gley soils with a higher clay content and now occupying more elevated landscape positions than the former dunes whose soils are red due to iron-oxide staining. These types are hereafter referred as Type A (former interdune) and Type B (former dune).

Figure 1

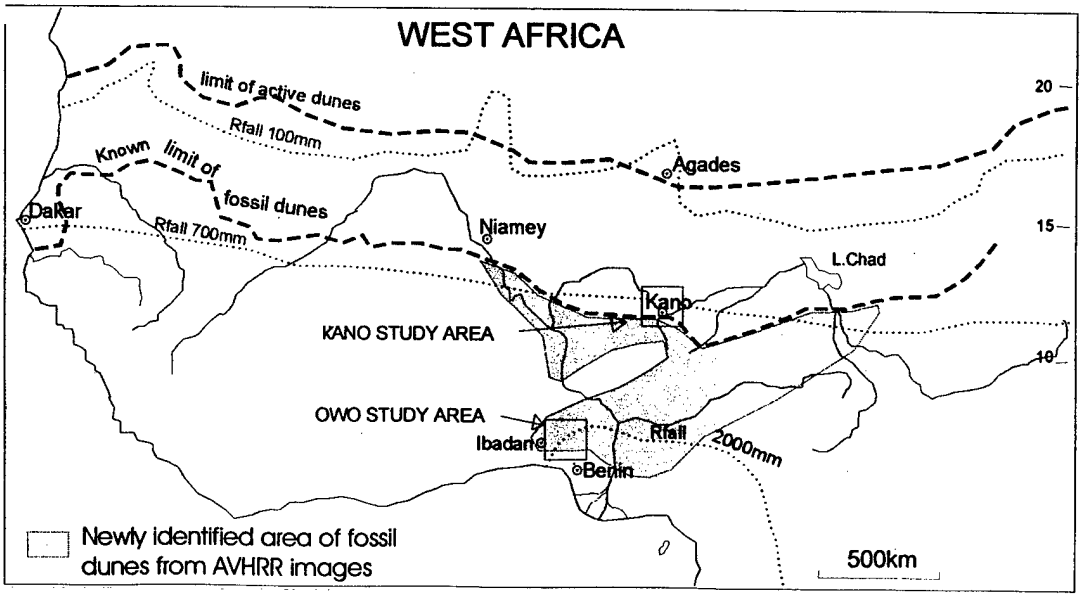

0-7803-3836-7/97/$10.00 © 1997 IEEE

2. Owo-Akure region

This study area lies within the Tropical Rain Forest climatic zone of Nigeria at 6°N (annual rainfall 2000mm) and adjoins the coastal mangrove belt near Benin City. Various stages of shifting agriculture presently occupy the greater part of this zone, except in forest reserves or areas of permanent agriculture such as oil palm, cocoa, cola or food cash crops. A short dry season extends between November and February when the greenness and vigour of the vegetation depends on adequate residual soil moisture locally.

METHODS

Image interpretation was carried out using an image composite from the NOAA AVHRR 1km Land Dataset. of 21st -30th January 1993, the mid-dry season. The image is an afternoon pass aquired on one cloud-free date during this period, with no pixel compositing, and since the visible wavebands for this dataset are atmospherically corrected, acccurate reflectance values can be derived. The image includes the whole of Nigeria. Visible wavebands were converted to reflectance, and thermal wavebands to surface temperature using Eidenschink, and Faundeen (1994).

IMAGE INTERPRETATION

Figure 2 shows spectral information for training areas in Red/NIR and thermal data space for interdune (Type A) and dune (Type B) features in each study area for the whole image. On an NDVI image, former inter-dune features in the rain forest zone (Owo study area) are identifiable by higher vegetation status (Figure 3) and are cooler (31°) than inter-dune areas (32°)(Figure 2). The interdune lineations are 1.5km apart and direction is ENE-WSW. Comparison with topographic maps of the area shows the dunefield to correspond to upland areas, the edges of which are being eroded by southward-flowing streams, leaving prominent laterite-capped plateaus upon which the inverted relief and drainage pattern corresponding to dune lineations is still evident.

In Kano study area in the semi-arid Sudan zone where soil and vegetation are completely senesced in mid-January, NDVI and surface temperatures between dune and inter-dune are similar (Figure 2). Since crops were harvested 2 months previously the greater portion of each pixel comprises bare soil.. An IHS-based decorrelation stretch of visible LANDSAT TM data (Figures 4 and 5) was found to enhance the inherent soil tonal differences between the darker red dune sands (due to iron oxide staining) and the light grey interdune depressions (due to gleying and weathering under anaerobic conditions). This is particularly due to decorrelation stretching of the Intensity component, since a low range of Intensity values typifies arid environments and may inhibit interpretability, even if Hue and Saturation values are distinct.

IMPLICATIONS

Fossil dune features in the humid rain forest zones of West Africa are significantly related to present land utilisation and land cover and can thus be easily identified over large areas using low resolution imagery such as AVHRR. **The dune lineations are not visible on the ground or on air photos in either study area.** Their discovery in extensive areas far south of the present desert, has implications for soil surveys and agricultural development in West Africa, though more extensive and detailed surveys in humid and sub-humid areas both within within West Africa and the tropics generally are required.

REFERENCES

[1] J.C. Eidenschink, and J.L Faundeen, "The 1KM AVHRR Global Land Data Set: first stages in implementation," Int. J. Remote Sensing, Vol. 15, No.17, pp.3443-3462, 1994.

[2] J.E Nichol, "The extent of desert dunes in northern Nigeria as shown by image enhancement," The Geographical Journal, UK, Vol. 157, No1, pp.13-24, 1991.

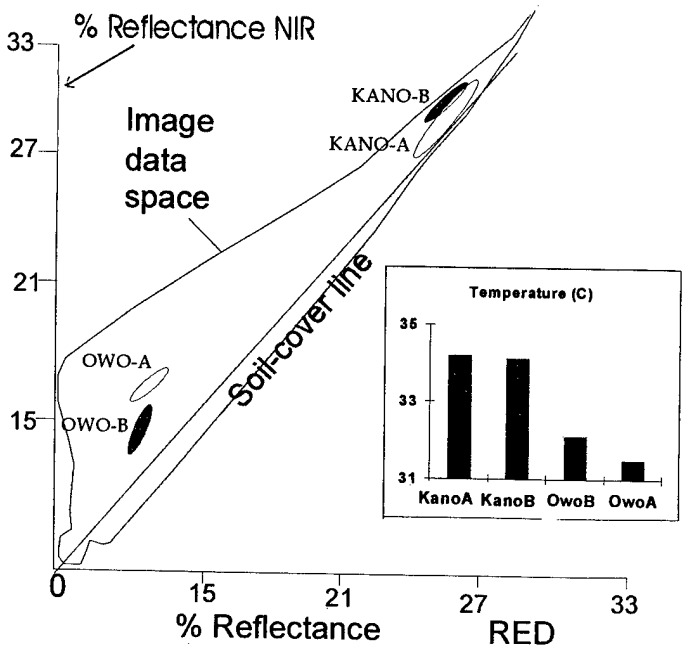

Figure 2. AVHRR spectral data

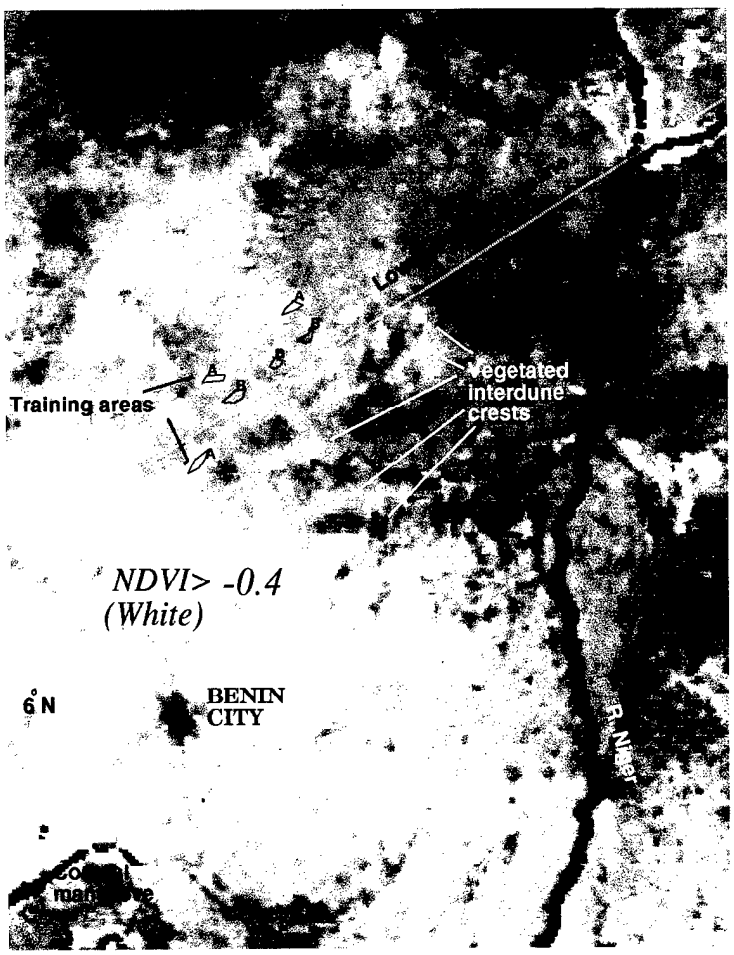

Figure 3. NDVI image: Owo-Akure Study Area, showing dune lineations downwind of Benue valley

NOAA AVHRR data

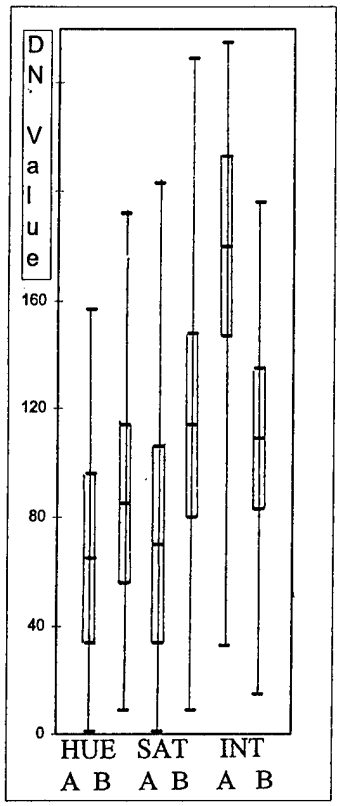

Figure 4. Coincident Spectral Plots LANDSAT TM Kano Study Area

Figure 5. Intensity image from LANDSAT TM, Kano Study Area

THE METHOD OF EARLY DROUGHT DETECTION WITH AVHRR/NOAA DATA

Lev Spivak, Alexei Terehov, Nadiya Muratova, Oleg Arkhipkin
Institute of Space Research, Ministry of Science and Academy of Sciences
Shevchenko 15, Almaty 480100, Kazakstan
Phone: 3272 492872, Fax: 3272 494355, E-mail: telonics@kaziki.alma-ata.su

Abstract. Special Vegetation Temporal Index (VTI) is introduced for estimation of Kazakstan spring temperature-moisture conditions and crop yield forecast. VTI values are defined for each polygons (16x16 km) from 8 to 22 weekly's NDVI AVHRR/NOAA data (PSQ format). The validation was carried out on 1991, 1992, 1995, 1996 years data. It shown the good correlation between VTI values and corresponding spring wheat crop.

INTRODUCTION

Kazakstan is a large grain producer. Cereal acreages occupy near 17,000,000 Ha. But a very large part of the Kazakstan arable land is situated in arid and semi-arid zones with low amount of precipitation (200-400 millimeters in year). Droughts are the most typical phenomenon of the climate and they cause considerable damage to Kazakstan economy. Grain production is changed in 2-3 times from good year to bad one (total grain 29,772,000 metric tons in good 1992 and 11,992,000 in bad 1991). Therefore the problem of early drought identification is very important for Kazakstan. Now different vegetation indexes based on remote sensing data are widely used for vegetation condition estimation of crop and pusture lands in many countries [1]. In recent years drought identification and monitoring method based on Vegetation Condition Index (VCI) was created by NOAA/NESDIS. This method is successfully used in regions with various economic and ecological conditions [2-3]. VCI-algorithms were incorporated in Kazakstan in 1995-1996 and they gave good results [4-5].

In this paper the improved method of early drought identification is presented.

CONCEPTION

Drought is very complex and not much studied natural phenomenon. Lack of reliable drought criterions prevent from its identification, especially at the very beginning, even if the appropriate weather observations are available. Kazakstan is characterized by diversity and changeability of spatial-temporal drought parameters. At the same time the general laws are in the scenarios of the drought evolution. Many years observations show that usually snowless winter and early warm spring lead to drought. But big quantity of winter and spring precipitations make favorable conditions for agriculture even in case of summer moisture deficit. This fact was taken as basis for technology of early identification of weather conditions and estimation of potentional affect for future yield.

CALCULATION METHOD

Calculation method based on the determination of shift of the active spring vegetation beginning relatively many years average conditions (standart). Special Vegetation Temporal Index (VTI) is introduced for integral estimation of spring temperature-moisture conditions and early drought identification. VTI values is defined on the basis of NDVI dynamics and they have values range from -5 to +5 weeks in Kazakhstan conditions. During this definition we analyze every polygon (16x16 km pixel) and fix its calendar time of reaching of NDVI "threhold" quantity and its shift value relatively its standart. After ordering of all shift values by calendar time it is formed the points set which characterize current temperature-moisture conditions of Kazakstan territory in analyzing year.

Interpretation of VTI values is simple. Early vegetation (VTI < 0) says about warm spring and accordingly about high probability of drought. Late vegetation (VTI > 0) indicates on cold spring and favourable conditions for vegetation growth. Note that climate conditions variations of different Kazakhstan regions are considerable. So for plain desserts the typical time of the vegetation beginning is during weeks 6 - 14, but for alpine grasslands during weeks 18- 24. There is possible to receive information about local Kazakstan's VTI values approximately from 7 to 22 weeks.

VALIDATION

For validation suggested technology of VTI-algorithm the 1991, 1992, 1995 and 1996 data were used. Intensive droughts took place above the Kazakstan territory in 1991, 1995. Vegetation conduct on temperature-moisture conditions in 1991 was the same as in 1995. Early and warm spring with insufficient quantity of precipitation created the conditions for intensive vegetation. On separate regions (16x16 km) the beginning of vegetation process occurred 3-4 weeks earlier than that of in normal

0-7803-3836-7/97/$10.00 © 1997 IEEE

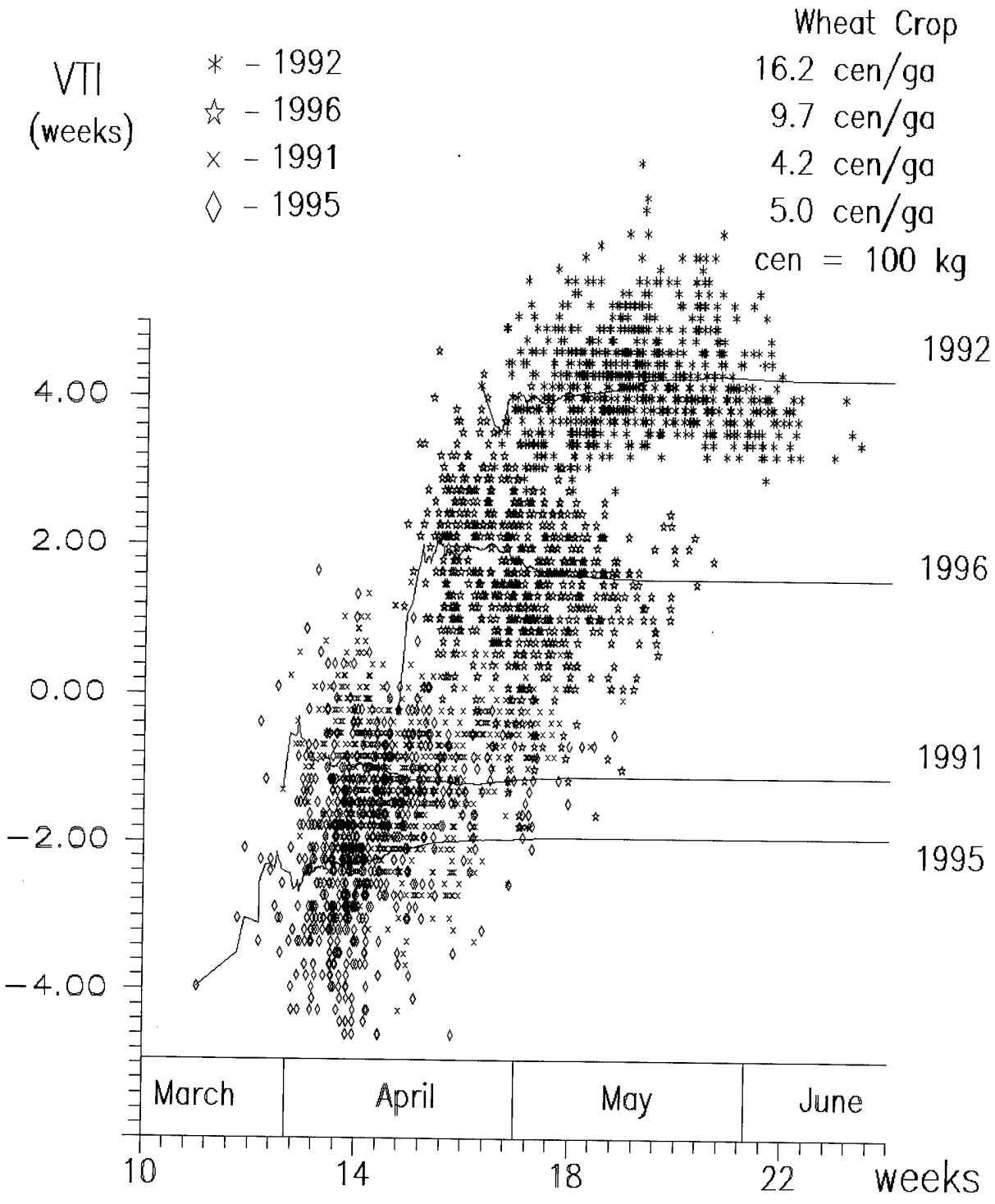

Fig.1 VTI distribution of Kustanai region

cases. The vegetation green biomass reached its maximum during weeks 16 - 18. Then quick degradation followed. The green biomass decreased and achieved minimum values.

Different situation was observed in 1992. Cold spring leaded to delay of vegetation beginning on 2-4 weeks than that of standart. Intensive development of vegetation began approximately from 23-th week and continued all vegetation period. As result the highest yield was obtained for later ten years.

The 1996 spring was late and cold that created the favourable conditions for high harvest's receiving. But due to the deficit of moisture in summer the yield was more less.

Fig.1 shows VTI-distribution for Kustanai region in 1991, 1992, 1995 and 1996. This region is one of main Kazakstan grain regions (in 1996 its cereal acreage occupied 2,800,000 Ha).

CONCLUSIONS

The results on technology validation on the 1991, 1992, 1995 and 1996 data showed that the VTI meanings in Kazakstan grain regions have good correlation with spring crops yield. So early vegetation is the necessary (but not sufficient) condition for drought. VTI-maps analysis allows to examine the intensity and scale of expected drought as well as to predict crop production before sowing. June quantity of precipitation affects on grain crop yield as well. This month is the most important one for crop forming in the main regions of the North Kazakstan.

During investigation it was noted that in early July 1991, 1995 drought zones correlates with anomalous of snow cover in January and February. On our mind drought zones arise in the sites with anomaly low non-typical cover for this territory and common unfavorable weather situation. This phenomenon requires additional checking up and in the case of confirmation of this fact it gives the possibility to predict the potential drought zones.

REFERENCES

[1] D.Lo Seen, E.Mougin, S.Rambal, A.Gaston, P.Hiernaux," A regional Sahelian Grassland Model tc be coupled with Multispectral Satellite Data. II: Toward the control off it's simulations by remotely sensed indices", Remote Sens. Environ. vol.52, pp. 194-206, 1995.

[2] F.N.Kogan, " Drought of the late 1980s in the Unated States as derived from NOAA polar-orbiting satellite data", Bul. of the Amer. Met. Soc.,76(5), 1995.

[3] F.N.Kogan, "Remote sensing of weather impacts on vegetation non-homogenous areas", Int. J. of Remote Sensing, vol.11, pp.1405-1419, 1990.

[4] A.A.Gitelson, F.N.Kogan, E.A.Zakarin, L.F.Spivak, L.V.Lebed, "Estimation of seasonal dynamics of arid zone pasture and crop productivity using NOAA/AVHRR data", FINAL REPORT, Submitted to the Office of the Science Advisor U.S. Agency for International Development, 1996.

[5] A.A.Gitelson, F.N.Kogan, E.A.Zakarin, L.F.Spivak, L.V.Lebed, "Validation of vegetation conditions derived from remote sensing data", International Geoscience and Remote Sensing Symposium, vol.1, pp. 209-211, IEEE, Lincoln, Nebraska, 1996.

Land Cover Classification of East Asia Using Fourier Spectra of Monthly NOAA AVHRR NDVI Data

Mikio Sugita
Yamanashi Institute of Environmental Sciences
5597-1 Kenmarubi, Kamiyoshida, Fujiyoshida, Yamanashi 403, Japan
Tel:+81-555-72-6187/Fax:+81-555-72-6205/Email:sugita@yies.pref.yamanashi.jp

Yoshifumi Yasuoka
National Institute for Environmental Studies
16-2 Onogawa 16-2, Tsukuba, Ibaraki 305, Japan
Tel:+81-298-50-2345/Fax:+81-298-50-2567/Email:yyasuoka@nies.go.jp

Abstract -- Land cover classification of East Asia is examined using Fourier power spectrum of multi-temporal NDVI data, which is sampled from 96 months extending from January 1982 to December 1989. Three components of spectrum (zero frequency component, 12 months period component and 6 months period component) have been used in the classification.

INTRODUCTION

In regarding the environmental problems at global scale, such as deforestation in tropic region, desertification, greenhouse gas emission, etc., the present land cover condition must be observed at the same global scale. Coarse spatial resolution, high temporal frequency satellite data from the NOAA AVHRR system are suitable for monitoring vegetation seasonal dynamics. Over years, the normalized difference vegetation index (NDVI), derived from Advanced Very High Resolution Radiometer (AVHRR) data, has been the common standard for monitoring vegetation condition on a global scale. Most land cover mapping applications at broad spatial scales have been based on multi-temporal AVHRR NDVI data. Many techniques have been applied to multi-temporal NDVI data to relate NDVI to land cover and to monitor vegetation phonology on global scales.

The Normalized Difference Vegetation Index (NDVI) derived from NOAA Advanced Very High Resolution Radiometer (AVHRR) has been widely used in monitoring land cover distribution and environmental change at global and continental scales. Several researchers have suggested and applied the use of measures such as maximum NDVI or length of growing season derived from a temporal profile of NDVI values, as an alternative to classifying land cover types using the monthly NDVI values directly[1,2]. In this study, the monthly NDVI data set derived from the NOAA AVHRR instrument is analyzed for the 1982-1989 period (8 years) over East Asia with a signal processing technique. Fourier power spectra of multi-temporal NDVI data is used to examine the land cover classification of East Asia. Three spectrum components (zero frequency, 12 month period component and 6 month period component) have been used to derive a land cover classification.

In this study, land cover classification was examined using the 8km resolution, 8 years of monthly AVHRR NDVI data

0-7803-3836-7/97/$10.00 © 1997 IEEE

set of East Asia, by using Fourier power density spectra of the data set as feature vectors for land cover classification.

MONTHLY AVHRR NDVI DATA

Data used in this study were monthly NDVI data sets produced from NOAA AVHRR daily level 1-b GAC data, with a spatial resolution of 8km [3]. Monthly NDVI data sets extending from January 1982 to December 1989 (8 years, i.e. 96 months) were used in the present study. Detailed information on the producing of the NDVI data set can be found in [3].

(2)

FOURIER SPECTRUM OF NDVI TIME SERIES DATA

Monthly NDVI time series data $V(t)$ at a certain satellite image coordinate of (x,y) is a function of time t. In this study, monthly NDVI data is not continuous signal, the time variance t is in discrete unit of month and has limited range from 1 to m. In this study, m=96If $V(t)$ is written in a form of discrete Fourier series such as

$$V(t) = \sum_{k=0}^{m-1} f(k) \exp\left(-i\frac{2\pi}{m}kt\right), \qquad (1)$$

k-th imaginary Fourier coefficient $f(k)$ is given by

$$f(k) = \sum_{t-1}^{m} V(t) \exp\left(-i\frac{2\pi}{m}kt\right),$$

where i is imaginary unit. This equation gives us a discrete Fourier transform of $V(t)$. The power density spectrum $P(k)$ of $V(t)$ is given by the Fourier transform of its autocorrelation function and is equal to the square of its Fourier transform $f(k)$:

$$P(k) = \frac{1}{m}|f(k)|^2 = \frac{1}{m}\left(\mathrm{Re}[f(k)]^2 + \mathrm{Im}[f(k)]^2\right) \qquad (3)$$

LAND COVER CLASSIFICATION

Fourier power density spectra is calculated for every point over NDVI data set covering East Asia. The original monthly NDVI data set includes missing data. These missing data were interpolated with the median value of 3 serial monthly NDVI value. The point in satellite image including 2 or more serial missing value was excluded from the analysis.

Fig.1 Fourier power spectral density images [left: log $P(0)$, right: log $P(8)$]

Fig. 1 shows the mapped image of logarithm of 0-th and 8-th Fourier power density spectra $P(0)$ and $P(8)$, respectively. In this figure, the black area corresponds to the area out of analysis because of missing values. $P(0)$ image and $P(8)$ image reflect the distribution of the average NDVI value and the amplitude of annual change in monthly NDVI data, respectively.

Next, Fourier power density spectra was examined. Fig. 2 shows typical Fourier power density spectra calculated for 7 different land cover in East Asia. With this figure, it is concluded that 0-th, 8-th and 16-th power spectrum $P(0)$, $P(8)$ and $P(16)$, corresponding to averaged value, 12 months period component and 6 months period component, respectively, are dominant spectra of all period components.

We took these three dominant spectra as feature vector of land cover, and classification using logarithm value of only 3 power density spectra, log *P(0)*, log *P(8)* and log *P(16)* were applied to monthly NDVI data set. After ISODATA unsupervised classification into 20 clusters, we selected and took clusters corresponding to 7 land cover categories (sea, desert, grassland, agriculture, forest1, forest2, and forest3) as training sample data, and then a maximum likelihood classification was applied to produce the final result. Fig. 3 shows the resultant land cover classification map

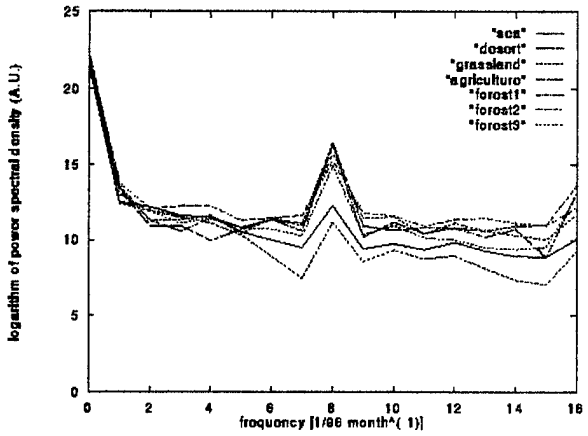

Fig.2. Fourier power spectra of 96 months Monthly NDVI data.

CONCLUSIONS

In this work, a study is made of the possibility of utilizing Fourier power density spectra of long term monthly AVHRR NDVI data. Land cover classification was demonstrated using the 8km resolution, 96 months monthly AVHRR NDVI data set of East Asia. It is concluded that the power density spectra corresponding to averaged value, 12 months period component and 6 months period component, respectively, are dominant spectra of all period components. Taking these three main spectra as a feature vectors of land cover, the monthly NDVI data set is classified into 7 categories (sea, desert, grassland, agriculture, forest1, forest2, and forest3). This study demonstrated the possibility to use spectral information as input in a land cover classification of Asia.

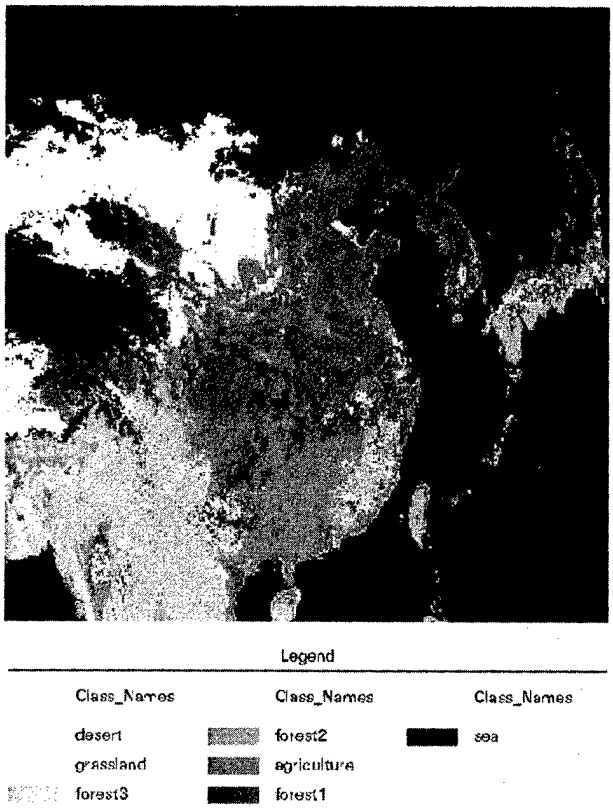

Fig.3. Classification result.

REFERENCES

[1] R.S. Defries and J.R.G. Townshend: NDVI-derived land cover classification at a global scale, Int. J. Remote Sens, Vol.15, No.17, pp.3675-3586, 1994.

[2] L. Andres, W.A. Salas, and D. Skole: Fourier analysis of multi-temporal AVHRR data applied to a land classification, Int. J. Remote Sens., Vol.15, No.5, pp.1115-1121, 1994.

[3] C.J. Tucker, W.W. Newcomb, and H.E. Dregne: AVHRR data sets for determination of desert spatial extent, Int. J. Remote Sens., Vol.15, No.17, pp.3547-3565, 1994.

Identifying Urban Features Using RADARSAT Images Taken at Multiple Incidence Angles

Dan Johan Weydahl
Norwegian Defence Research Establishment, PO Box 25, N–2007 Kjeller, Norway
Phone:+47 63 80 70 00 Fax:+47 63 80 72 12 E–mail:dan–johan.weydahl@ffi.no

Abstract— RADARSAT gives the opportunity to acquire SAR data over a wide range of incidence angles over the same geographical area. This gives additional backscatter information from built–up areas since different building types and objects will give backscatter variations depending on the incidence angle. In this work, a statistical difference is found between the SAR backscatter from residential houses, industry roofs and cylindrical storage tanks, which may be used to distinguish between areas of these classes.

INTRODUCTION

ERS–1 SAR (synthetic aperture radar) images have been used to study strong backscatter from urban areas in an earlier study [1] and [2]. However, because of the small incidence angle (23°) of ERS–1 SAR, the detection and classification of man–made objects over urban areas are limited. In addition, the narrow swath width of ERS–1 SAR will give a limited range of radar incidence angles onto the same object. In contrast to this, RADARSAT gives the opportunity to acquire high spatial resolution (9 m) SAR data over a wide range of incidence angles (37°–48°) over the same geographical test area.

In our case, the test area covers 3.2x4 km of the Lillestrøm city with its surroundings, and is located 25 km outside Oslo in Norway. This relatively flat region consists of agricultural fields, forest, rivers, industry and large store houses, many residential houses, a city area with shops and office buildings, bridges, roads, railways and a runway.

THE DATA SET

Four RADARSAT images were acquired during the autumn 1996, see table 1. These images are processed and delivered by Tromsø Satellite Station in Norway. These RADARSAT fine mode (F) images covers each an area of approximately 50x50 km, with a pixel size of 6.25 m. The 19 December image is acquired from the same repeat cycle (24 days) as the 25 November image. All the RADARSAT images used here are taken from the descending satellite orbit. RADARSAT is operating with an incidence angle difference of 2.3° between the image mode F1 and F2, and a difference of 5.7° between F2 and F5.

Table 1 The dates of the different RADARSAT image modes together with their operating incidence angles and their clockwise(+) or anticlockwise(–) rotation with respect to the 24 September reference image.

Date	Orbit	Image Mode	Incidence angle (degrees)	Image rotation (degrees)
24 Sep	4640	F2	40.78	0.0
11 Oct	4883	F1	38.47	+0.9
25 Nov	5526	F5	46.49	–2.0
19 Dec	5869	F5	46.50	–1.9

PRE–PROCESSING OF THE SAR DATA

It is made sure that the test area is selected from a *flat* portion of the Lillestrøm region in order to avoid doing geocoding with terrain corrections on the SAR images.

Before analysing the radar response from the man–made objects present in the SAR images, one has to calibrate the images. This was done by using three 1.8 m large corner reflectors that were deployed in the region. The reflectors were adjusted at the dates of acquisition according to the RADARSAT incidence angles. The signal to clutter (S/C) point target response from the corner reflectors was quite good (> 25 dB), and using the 24 September image as a reference, a relative calibration was done by scaling the F1 image with a factor of 0.698, while the 25 November and 19 December images had scaling factors of 1.18 and 1.411 respectively.

A small image rotation (see table 1) was estimated when referencing to the positions of the local corner reflectors. This rotation is present because the RADARSAT images were acquired from different satellite tracks.

The RADARSAT image from 24 September 1996 was used as a reference for co–registration. Subsamples of the other RADARSAT images were registered and resampled into the geometry of the reference image by first selecting 8–10

0-7803-3836-7/97/$10.00 © 1997 IEEE

common ground control points that were spread throughout the test area. After the relative calibration and co–registration had taken place, the point target extraction and analysis could be carried out.

ANALYSIS

Objects giving a strong SAR backscatter are investigated in particular in order to see wether these objects will give a SAR backscatter variation that is somehow correlated with changes in the radar incidence angle. Pixels giving bright backscatter in one or several of the four RADARSAT images were extracted under the following restrictions:

– pixels having backscatter values above a certain threshold is selected. The threshold is set after inspection of several bright pixel areas within the whole test region.

– there should be at least 4–6 connected pixels to make up one object area

All together 614 objects were in this way extracted and given object numbers. The mean SAR backscatter value were then calculated from each object using the four RADARSAT images. When comparing RADARSAT images that are taken at different dates, then backscatter variations from man–made objects can come from temporal variations, aspect angle changes, or radar incidence angle changes.

The slight aspect angle rotation is not easily compensated for. However, from table 1 it is seen that the aspect angle change between two RADARSAT image modes are much less than the corresponding incidence angle change. It is therefore likely that radar incidence angle changes add more to the total SAR backscatter change registered between the different RADARSAT images used here, than the aspect angle rotation.

Table 2 Number of objects for various classes. Objects are selected with the criteria that the mean object amplitude between the two F5 RADARSAT images are < 3 dB.

1) Residential house	39
2) Residential house, azimuth direction	59
3) Industry– or Store house roof	23
4) Industry– or Store house roof,azimuth direction	66
5) Railroad	7
6) Railroad, azimuth direction	8
7) Storage area next to industry house	17
8) Construction work	3
9) Cylindrical storage tanks and pipes	7
10) Car parking	3

In an attempt to rule out backscatter changes caused by temporal variations, only the objects with a mean backscatter change less than 3 dB for the two F5 RADARSAT image acquisitions, were selected. These objects were then mapped into an 1:10000 economic map, and their class decided based on this map as well as aerial photos, see table 2.

RESULTS

Fig. 1 to 4 show how the RADARSAT backscatter amplitude vary with incidence angle for the different object classes. The background classes in fig.1 show stable backscatter values, apart from the fields that vary due to seasonal changes. No class has a systematic change in backscatter as a function of RADARSAT incidence angle (e.g. stronger backscatter with increasing incidence angle). The strong SAR backscatter from man–made objects is 10–25 dB higher than background targets. Residential areas give generally a larger spread in backscatter changes over incidence angles than industrial buildings and metal objects. Cylindrical metal storage tanks and pipes give the smallest backscatter difference and standard deviation when comparing the different incidence angle modes, see also table 3.

CONCLUSIONS

If we want to decide wether an area of a certain extend is residential, industrial or holds simple metal objects, then this

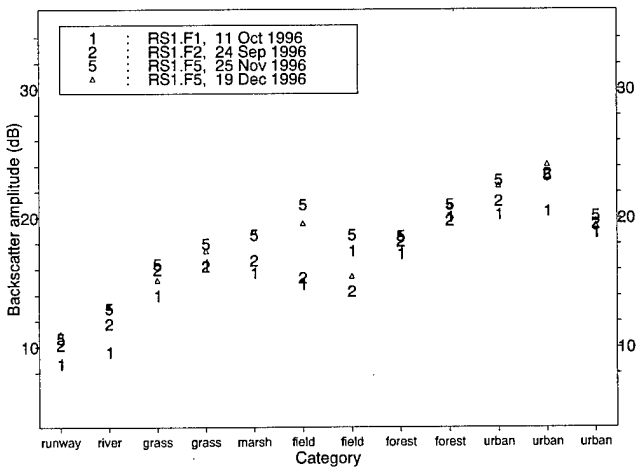

Figure 1 Examples of RADARSAT backscatter at various incidence angles for some background target categories found within the Lillestrøm test area. The urban areas are homogeneous housing estates with a relatively low SAR backscatter.

may be feasible if many bright SAR points found within the area can be evaluated over several incidence angles. It is still not possible to classify individual bright SAR objects based on three different incidence angles only. More RADARSAT images should therefore be used to verify these results, and it is recommended that closer attention is paid to material and construction type of the different man–made objects.

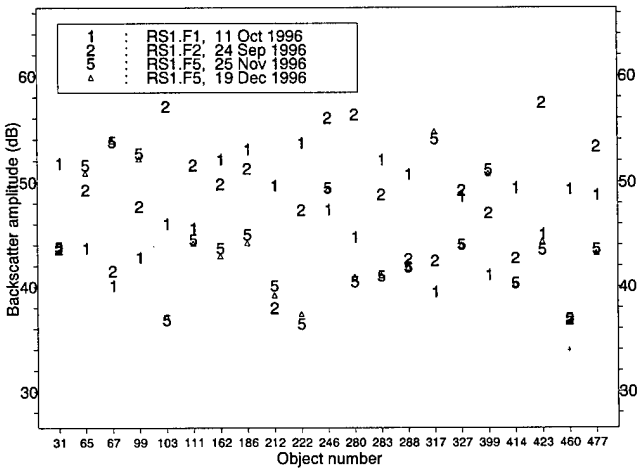

Figure 2 RADARSAT backscatter at various incidence angles for residential houses that are located more or less in the SAR azimuth direction. The plot shows objects where the backscatter difference between the two F5–acquisitions are less than 1 dB.

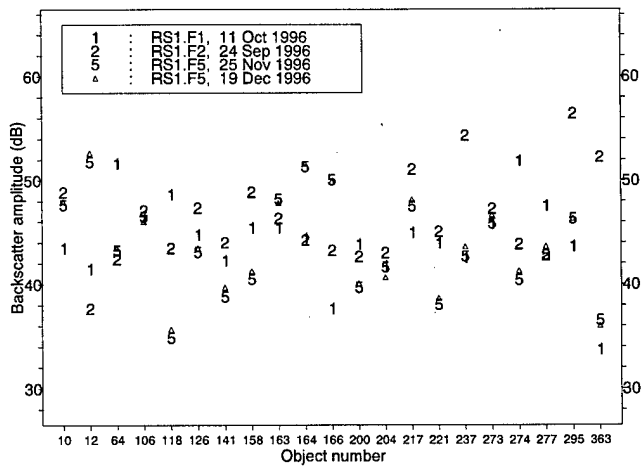

Figure 3 RADARSAT backscatter at various incidence angles for large industry/storage/office house roofs. The houses are located more or less in the SAR azimuth direction. The plot shows objects where the backscatter difference between the two F5–acquisitions are less than 1 dB.

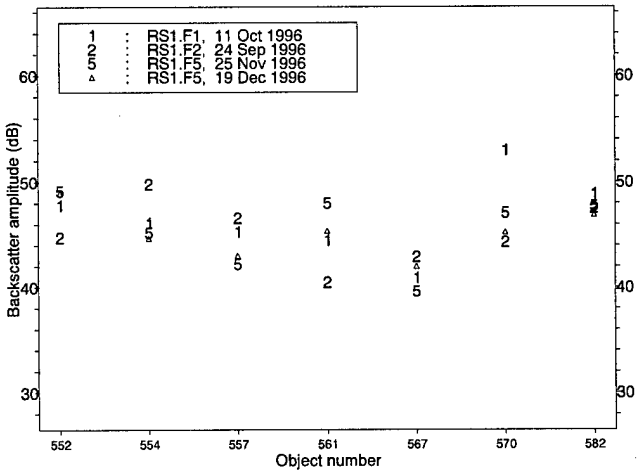

Figure 4 RADARSAT backscatter at various incidence angles for groups of cylindrical storage tanks that are found next to industry houses and chemical plants. The plot shows objects where the backscatter difference between the two F5–acquisitions are less than 3 dB.

Table 3 The mean and standard deviation of the absolute difference backscatter (in dB) found between the various RADARSAT modes. Refer class types to table 2.

Class type	Objects	Mean difference |F1–F2|		Mean difference |F2–F5|		Mean difference |F1–F5|	
		Mean	St.d.	Mean	St.d.	Mean	St.d.
1)	39	11.24	7.14	5.80	6.24	9.95	6.59
2)	59	5.71	4.29	7.00	4.97	7.25	4.27
3)	23	4.91	3.31	5.13	3.25	5.45	4.65
4)	66	4.63	4.51	5.02	3.85	5.64	4.65
7)	17	3.87	3.15	4.66	4.55	4.24	4.91
9)	7	3.44	2.36	3.87	2.05	2.45	1.70

REFERENCES

[1] X. Becquey and D.J. Weydahl, "SAR image processing applied to the radiometric modelling for urban areas: Backscatter variations in ERS–1 images", FFI/RAPPORT–95/03824, 21 August 1995, Kjeller, Norway.

[2] D.J. Weydahl, X. Becquey and T. Tollefsen, "Combining ERS–1 SAR with optical satellite data over urban areas", Proceedings of IGARSS, Vol.3, pp.2161–2163 Firenze, 10–14 juli 1995.

IGARSS'97

1997 International Geoscience and Remote Sensing Symposium

03-08 August 1997

Singapore International Convention & Exhibition Centre

Technical Program

Interactive Area 16: Optical Measurement of the Ocean

Resolution Enhancement in SAR Images

V. Guglielmi (*), F. Castanié (**) and P. Piau (***)
(*)(**) National Polytechnics Institute of Toulouse
(***) Alcatel Espace
(*)(**) ENSEEIHT-SIC, 2 rue Camichel, B.P. 7122, 31071 Toulouse Cedex 7, France
(***) 26 Av. J.F. Champollion, 31037 Toulouse, France
(*) Phone: (33) 0561588350, Fax: (33) 0561588237, email: guglielm@len7.enseeiht.fr
(**) Phone: (33) 0561588290, Fax: (33) 0561588237, email: castanie@len7.enseeiht.fr
(***) Phone: (33) 0561195180, Fax: (33) 0561195190

Abstract -- We present five algorithms which can improve classical resolution of Synthetic Aperture Radar (SAR) images, especially when the objects of interest are small bright targets against a weaker background. Through quantitative analysis of the resolution enhancement, we assess their different performances.

1) INTRODUCTION

As the SAR imaging operation consists of a convolution between the Earth's surface reflectivity and the radar Point Spread Function (PSF), the problem of SAR processing is to reconstruct the values of radar reflectivity from the collected data [1].

Instead of the conventional approach of pulse compression using matched filtering, we process the received signal through super-resolution techniques, to attempt to improve upon the matched filter well known resolution which is solely determined by the autocorrelation of the radar PSF.

Numerous super-resolution methods have been proposed for solving inverse problems [2]. The basic feature is the introduction of a compromise between fidelity to the data and fidelity to some prior information about the solution. To apply these techniques to SAR images, we adapt the theoretical methods to fit the particular demand in our specific application: special signal structures present in radar imaging scenario must be exploited, otherwise the methods are likely to fail [3].

So, section 2 introduces five different algorithms which can improve classical resolution. Next, in section 3, we describe the SAR simulation model built up in order to provide numerical evaluations of the performances. Then, section 4 displays quantitative analysis of the various results obtained. Conclusions are given in section 5.

2) SUPER-RESOLUTION ALGORITHMS

We present here some algorithms which can be applied to SAR processing in order to enhance resolution. Based on exploiting prior knowledge on the true image, they have been shown to yield better estimates than the matched filtering [3].

Constrained Iterative Restoration (CIR)

It allows for the incorporation of prior knowledge of the signal in terms of the specification of a constraint operator.

Gerchberg-Papoulis Generalized Inversion (GPGI)

This iterative algorithm leads to an adaptative spectral extrapolation of the solution beyond the finite band of the spectrum of the radar PSF. The a priori knowledge is introduced through an extrapolation subset defined at each iteration according to the available information.

Parametric Spectral Extrapolation (PSE)

The algorithm uses an autoregressive model which leads to a parametric spectral extrapolation of the solution. The model order is selected by incorporating prior information about the imaged scene.

Stochastic Regularization (SR)

In contrast to the previous techniques, prior information is expressed henceforward through stochastic models, set up from the speckle properties. Speckle refers to the scintillation which occurs because individual pixels contain unresolved scatterers whose returns add coherently with random phase. Speckle phenomenon is the primary reason that the signals coming up in SAR imaging operation may be considered as stochastic.

Maximum-Likelihood Estimation (MLE)

Because of the probabilistic nature of the scattering process, it can be shown that the scattered object field, namely the reflectivity, is only indirectly related to the properties of the object itself, whereas the scattering radar cross section is directly related. Therefore, the fifth algorithm represents a different approach to SAR processing: we address the inverse problem of recovering the underlying cross section, instead of the scattered field.

Hence, the problem can be considered as a maximum-likelihood one. To perform maximization of the likelihood function, we resort to some optimization techniques.

0-7803-3836-7/97/$10.00 © 1997 IEEE

3) SAR SIMULATION MODEL

To be able to compare the different performances in a more accurate way, we would rather apply the previous algorithms to simulated data instead of actual scenes. Furthermore, in so doing, range migration effects are avoided.

Thus, this section is devoted to the model assumed for SAR collected data. Let us note than the rightness of this approach has been verified on ERS-1 data [3].

Terrain simulation

To take into account the speckle effect, we formulate statistical characteristics for radar reflectivity: zero-mean gaussian stochastic model is set up for the scattered field. Its probability density function is defined by the covariance matrix, which is assumed to be diagonal and whose elements represent the scattering radar cross sections. This can produce a variety of scattered fields distributed according to the model, and we consider the particular realisation that occurred in our simulation.

Radar instrument simulation

We have restricted ourselves to the azimuth direction, but the range formulation of the SAR process is essentially identical. Then, as the radar PSF can be viewed as a continuous function which has been sampled in azimuth at a rate equal to the Pulse Repetition Frequency, the microwave imaging system is regarded as a one-dimensional discrete linear filter.

It is assumed that the radar transmitted waveform is a linear FM chirp, determined by the Doppler centroid frequency f_{DC} and the Doppler rate f_R.

Next, we incorporate the antenna pattern, being careful we do not neglect the portions of the beam that extend beyond the -3 dB edges. Clearly, the sampling theorem states that in so doing, we introduce some aliasing due to overlap of the sidelobe spectrum.

Additive noise simulation

Besides the speckle phenomenon, commonly thought of as multiplicative noise, we must consider also the unavoidable additive noise which comes to disrupt the data. This latter is assumed to have zero-mean gaussian probability distribution, and to be uncorrelated with the radar signal.

Numerical values

Regarding the different parameters of our SAR simulation model, we choose the values listed below. They correspond to an actual scenario of radar imaging, provided by the ERS-1 instrument.

Pulse Repetition Frequency: PRF = 1678.712 Hz
Doppler centroid frequency: f_{DC} = - 427.69 Hz
Doppler rate: f_R = - 2167.52 Hz/s
Velocity in the azimuth direction: V = 6630 m/s
Raw data spectrum band: $B_{-3\,dB}$ = 884 Hz
(spectrum band being defined by its -3 dB contour)

These experimental values yield a pixel length equal to 4 meters in the azimuth direction, whereas the half-power width of the radar autocorrelation function, which gives the theoretical value of the matched filtering spatial resolution, turns out to be 7.9 meters.

4) PERFORMANCES

This section displays numerical evaluations to assess the performances of the various algorithms outlined earlier.

Test data

We study the global impulse response of the SAR imaging mechanism. So, we consider for the terrain reflectivity a single point target embedded in a weak background.

We add gaussian noise so that the Signal-to-Noise Ratio for raw data ranges from -20 dB to +20 dB with 10 dB step. Notice that the SNR may be measured elsewhere: for example, after matched filtering, the corresponding SNR varies from +15 dB to +35 dB. Another relevant parameter here is the contrast ratio, also measured after matched filtering: it ranges from +15 dB to +26 dB.

Prior knowledge

Recall that super-resolution algorithms imply that some extra information about the imaged scene be included. We use the a priori information that the main component of the scene is clutter within which may be set a few significant targets. This prior knowledge, whilst being introduced fairly arbitrarily, may constitute a sensible assumption about the real world since the situation often occurs in radar imaging where the objects of interest are small bright targets.

Experimental results

Quality measurement of the different results obtained by the five super-resolution algorithms and the matched filter as well, is performed: we compute the Mean Square Error between the original terrain and the reconstruction, the correlation coefficient and the spatial resolution [3]. These measures, as a function of the additive noise level, are shown in figures 1, 2 and 3 respectively.

As expected, it can be seen that all the super-resolution algorithms provide better results than the matched filter, mainly due to the efficient use of the a priori information.

Among these five alternatives, the CIR appears the less efficient. But, as it allows to include a wide variety of prior informations in a simple way, it becomes very interesting when particular information on the true image is available.

Next comes the PSE, whose limitation lies in the introduction of prior knowledge restricted to the model order.

Finally, the GPGI, the SR and the MLE prove to be roughly comparable and to have the greatest restoration ability.

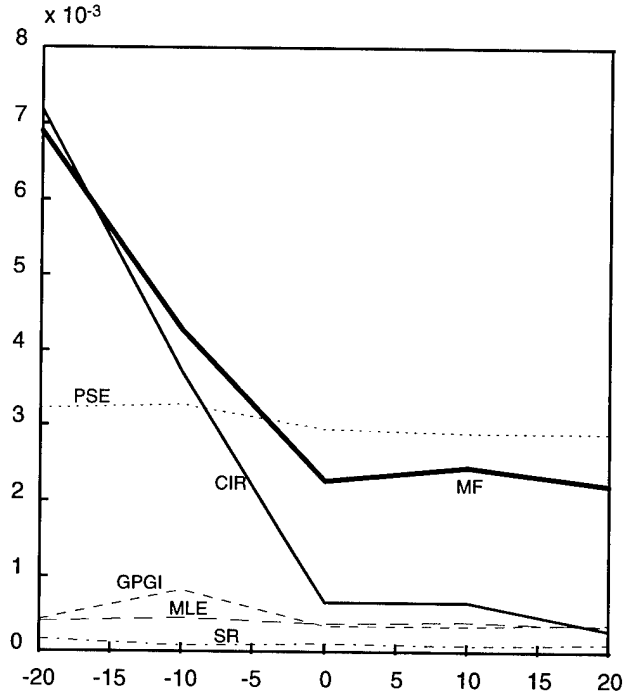

Fig.1 - MSE vs. SNR in dBs

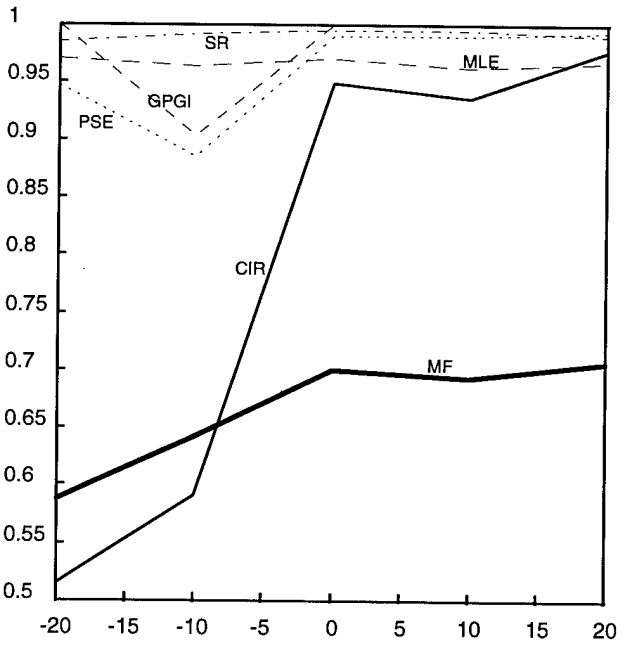

Fig.2 - Correlation vs. SNR in dBs

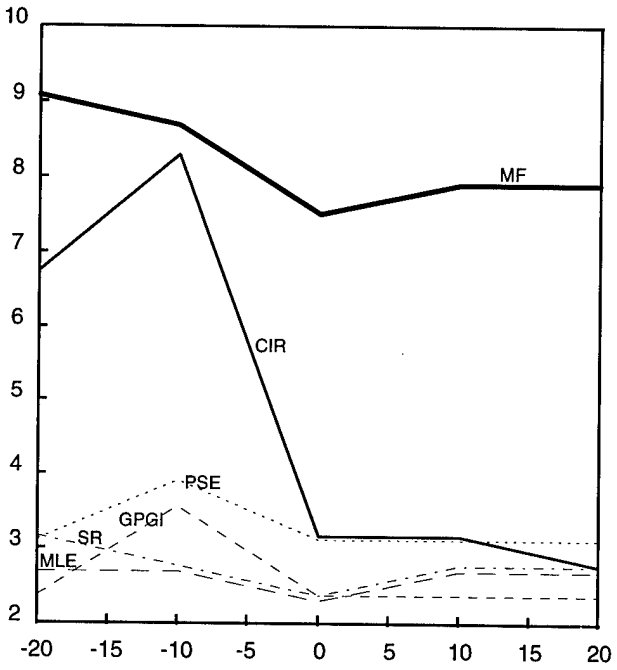

Fig.3 - Resolution vs. SNR in dBs

5) CONCLUSIONS

Instead of classical matched filtering, we propose five super-resolution algorithms to process the SAR received signal. In the presence of corraborating a priori information, they offer significant performances improvements in comparison to conventional method. To illustrate their ability, the a priori knowledge which has been used is the reasonable statement that objects of interest likely to be encountered in the real word are small brights targets against a weaker background. Then, we have stressed the fact that matched filter resolution can be overcome. Hence, it has been pointed out that these five techniques could really constitute an alternative approach to SAR processing, in order to produce very high quality imagery.

REFERENCES

[1] V. Guglielmi, F. Castanié & P. Piau, "Application of super-resolution methods to SAR data", IGARSS'95, pp. 2289-2292.

[2] V. Guglielmi, F. Castanié & P. Piau, "Overview of Regularization Methods Applied to the Inverse Problem of Synthetic Aperture Radar Processing", unpublished.

[3] V. Guglielmi, "Contribution à l'étude des méthodes super-résolvantes appliquées au radar à synthèse d'ouverture", Ph.D thesis, October 1996, National Polytechnics Institute of Toulouse.

Diffuse Reflectance of the Optically Deep Sea Under Combined Illumination of Its Surface

Vladimir I. Haltrin
Naval Research Laboratory, Ocean Sciences Branch, Code 7331, Stennis Space Center, MS 39529-5004, USA
Phone: 601-688-4528, fax: 601-688-5379, e-mail: <haltrin@nrlssc.navy.mil>

Abstract — The processing of remotely measured color imagery involves knowledge of the diffuse reflectance of the oceanic water. This paper presents two approaches to this problem. The first one is analytical and consists of an approximate solution to the radiative transfer equation. As a result it gives an equation for diffuse reflectance of the sea as a function of inherent optical properties, the sun elevation angle and the ratio of the direct illumination by sun to the diffuse illumination by sky. The second approach is a numerical Monte Carlo simulation. The results of this simulation are processed to produce regressions that connect diffuse reflectance of the seawater for different hydrooptical situations to the sun elevation angle.

INTRODUCTION

In papers by Haltrin [1], Gordon [2], Morel and Gentili [3] it was shown that the dependence of the diffuse reflection on the sun zenith angle is important and should be incorporated into remote sensing algorithms.

Two approaches to this problem are considered. The first approach is an analytical one and consists of approximate solution to the radiative transfer equation. As a result it gives Eqn. (20) for diffuse reflectance of the sea as a function of the inherent optical properties, sun elevation angle and the ratio of the direct illumination by the sun to the diffuse illumination by the sky. The second approach is a numerical Monte Carlo simulation. It is based on the modified by the author [4] approach by Kirk [5]. The results of this simulation are processed to produce a number of regressions that connect the diffuse reflectance of the seawater for different hydrooptical situations with the sun elevation angle. The results of both methods show that the corrections to the diffuse reflection of seawater due to the conditions of illumination can reach 40% at certain angular elevations and inherent optical properties of seawater.

THEORETICAL APPROACH

Let us consider a homogeneous sea illuminated by the skylight and the light of the sun elevated at h_s degrees. According to the Snellius law, the direct sunlight enters the sea at the angle $\cos^{-1}\mu_s$ from the vertical axis $0z$, directed from the sea surface to the sea bottom, where

$$\mu_s = \sqrt{1-\cos^2 h_s / n_w^2}, \tag{1}$$

here n_w is a refraction coefficient of seawater.

Let us start with the system of two flow equations for the downward E_d and upward E_u irradiances proposed in Ref. [1] and incorporated later into the elastic part of Ref. [6]:

$$\begin{aligned}&\left[\frac{d}{dz}+(2-\bar{\mu})(a+b_B)\right]E_d(z)-(2+\bar{\mu})b_B E_u(z)=f(z),\\ &-(2-\bar{\mu})b_B E_d(z)+\left[-\frac{d}{dz}+(2+\bar{\mu})(a+b_B)\right]E_u(z)=f(z).\end{aligned} \tag{2}$$

Here z is the depth coordinate. $\bar{\mu}$ is the average cosine over the irradiance angular distribution in the sea depth:

$$\bar{\mu}=\sqrt{\frac{1-x}{1+2x+\sqrt{x(4+5x)}}},\quad x=\frac{b_B}{a+b_B}\equiv\frac{B\omega_0}{1-\omega_0+B\omega_0}, \tag{3}$$

$b_B = bB$ is the backscattering coefficient, b is the scattering coefficient, $B=0.5\int_{\pi/2}^{\pi}p(\vartheta)\sin\vartheta\,d\vartheta$ is the probability of backscattering, $p(\vartheta)$ is the scattering phase function, ϑ is the scattering angle, x is the Gordon parameter, $\omega_0 = b/c$ is the single scattering albedo, $c=a+b$ is the attenuation coefficient, a is the absorption coefficient. The source functions in the right parts of Eqns. (2) are equal to:

$$f(z)=b_B E_S \exp(-\alpha z/\mu_s),\quad \alpha=a+2b_B, \tag{4}$$

where $\mu_s E_S$ is the sun irradiance just below the sea surface. In Eqns. (2) the direct sunlight is taken into account in the form of the source functions $f(z)$.

SOLUTIONS FOR IRRADIANCES

Solutions of Eqns. (2) with $f=0$ for the case of purely diffuse illumination of the sea surface are given in Refs. [1]. Let us find the solutions of these equations for the case of combined illumination, *i. e.* for the case when $f\neq 0$. Let us consider the irradiance of the skylight penetrated into the sea E_0 by the following boundary condition:

$$E_d(0)=E_0. \tag{5}$$

In addition let us accept that just below the sea surface the directed irradiance of the sun q times stronger than the irradiance of the sky, *i. e.*, $E_S = qE_0$. Let us also define the following quantities: let $E_u^D(z)$ be the portion of the diffuse light that is originated from the scattering of the skylight penetrated into the ocean, and let $E_u^S(z)$ be the portion of the diffuse light that is originated from the scattering of the sunlight penetrated into the sea.

Let us introduce the following definitions:

$$R_\infty = E_u^D(0)/E_d(0) \tag{6}$$

is the diffuse reflectance of the infinitely optically deep ocean illuminated by diffuse light; let

$$R_S = E_u^S(0)/(\mu_s E_S) \tag{7}$$

0-7803-3836-7/97/$10.00 © 1997 IEEE

be the diffuse reflectance of the infinitely optically deep ocean illuminated by directed light of the sun; let

$$R_C = E_u(0)/[E_d(0)+\mu_s E_S], \quad (8)$$

be the diffuse reflectance of the infinitely optically deep ocean illuminated by the combined light of sun and sky. Then the diffuse reflectance of the sea illuminated by the natural light is:

$$R_C = S_H R_\infty, \quad S_H = \frac{1+\mu_s q R_S/R_\infty}{1+\mu_s q}. \quad (9)$$

Let us look for a solution of the system of Eqns. (2) in the form of the sum of general and partial solutions:

$$E_d(z) = A_d e^{-\alpha_\infty z} + C_d e^{-\alpha z/\mu_s}, \quad E_u(z) = A_u e^{-\alpha_\infty z} + C_u e^{-\alpha z/\mu_s}, \quad (10)$$

here $-\alpha_\infty = -a/\overline{\mu}$ is a negative eigenvalue of Eqns (2). Inserting Eqns. (10) into Eqns. (2) and applying boundary condition (5) we have following equations for irradiances:

$$E_d(z) = E_d^D(z)+E_d^S(z), \quad E_u(z) = E_u^D(z)+E_u^S(z), \quad (11)$$

$$E_d^D(z) = E_0 e^{-\alpha_\infty z}, \quad E_u^D(z) = R_\infty E_0 e^{-\alpha_\infty z}, \quad (12)$$

$$E_d^S(z) = \mu_s q E_0 \frac{R_0(R_p+R_S)}{1-R_0 R_\infty}\left(e^{-\alpha z/\mu_s} - e^{-\alpha_\infty z}\right) \quad (13)$$

$$E_u^S(z) = \mu_s q E_0\left[R_S e^{-\alpha_\infty z} + \frac{R_S+R_p R_0 R_\infty}{1-R_0 R_\infty}\left(e^{-\alpha z/\mu_s} - e^{-\alpha_\infty z}\right)\right]$$

here (14)

$$R_\infty = \left(\frac{1-\overline{\mu}}{1-\overline{\mu}}\right)^2, \quad R_0 = \frac{2+\overline{\mu}}{2-\overline{\mu}} R_\infty, \quad (15)$$

$$R_S = \frac{\overline{\mu}\, s(1+R_\infty)}{\mu_s[1+2\overline{\mu}^2(1+s)]+\overline{\mu}(1+2s)}, \quad (16)$$

$$R_p = \frac{\overline{\mu}\, s(1+R_0^{-1})}{\mu_s - \overline{\mu}(1+2s)}, \quad s = \frac{b_B}{a} \equiv \frac{B\omega_0}{1-\omega_0}. \quad (17)$$

DIFFUSE REFLECTANCE COEFFICIENTS

After some algebra we have the following equations for the diffuse reflection coefficients of the sea illuminated by the different kinds of light: 1) the diffuse reflection coefficient of the sea illuminated by the light of the sky:

$$R_\infty = \left(\frac{1-\overline{\mu}}{1-\overline{\mu}}\right)^2, \quad \overline{\mu} = \sqrt{\frac{1-x}{1+2x+\sqrt{x(4+5x)}}}, \quad (18)$$

where $x = b_B/(a+b_B) \equiv B\omega_0/(1-\omega_0+B\omega_0)$;

2) the diffuse reflection coefficient of the sea illuminated by the direct sunlight:

$$R_S = \frac{(1-\overline{\mu})^2}{1+\mu_s\overline{\mu}(4-\overline{\mu}^2)}, \quad \mu_s = \sqrt{1-\cos^2 h_s/n_w^2}; \quad (19)$$

and 3) the diffuse reflection coefficient of the sea illuminated by the combined light of the sky and the sun:

$$R_C = \frac{R_\infty + \mu_s q R_S}{1+\mu_s q}. \quad (20)$$

The diffuse reflection coefficient R_C depends on the inherent optical properties of the water b_B and a, the sun elevation angle h_s, and the parameter q that determines the ratio of the direct sunlight to the light of the sky. Correct evaluation of this parameter should involve solution of the radiative transfer problem in atmosphere [7] and estimation of the transmission through the air-sea interface. More simple approach was proposed by Jerlov [8]. According to Ref. [8], in the case of the clear sky the ratio q depends only on the sun elevation angle h_s. Our approximation of the data published in Ref. [8] gives the following formula:

$$q = 0.25(1+0.3h_s), \quad (21)$$

here h_s is measured in degrees. Taking into account Eqns. (18)-(21), we have the following expression for the ratio of the diffuse reflectances $S_H = R_C/R_\infty$:

$$S_H = 1 - \frac{1-(1+\overline{\mu})^2\Big/\left[1+\overline{\mu}(4-\overline{\mu}^2)\sqrt{1-\cos^2 h_s/n_w^2}\right]}{1+4\Big/(1+0.3h_s)\sqrt{1-\cos^2 h_s/n_w^2}}. \quad (22)$$

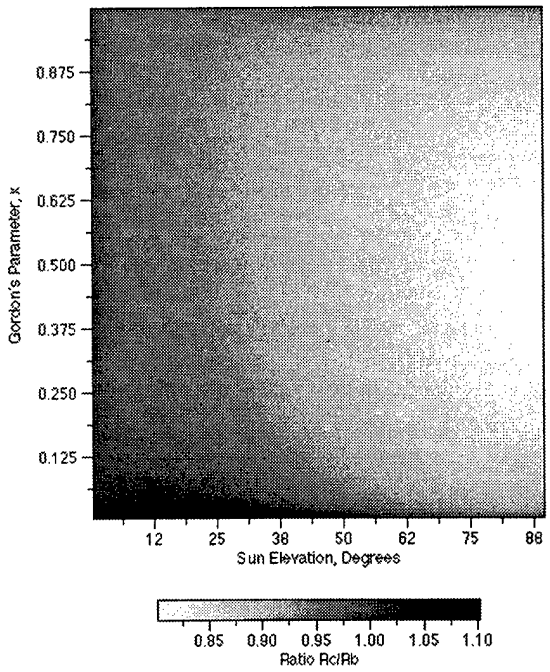

Fig. 1. Two-dimensional density plot of the ratio S_H as a function of the Gordon parameter x and the Sun elevation angle.

Figure 1 shows a two-dimensional density plot of the ratio S_H as a function of the Gordon parameter x and the sun elevation angle h_s. The difference between maximum and minimum values of this ratio lies in the range of 40%.

MONTE CARLO APPROACH

This approach is explained in detail in Ref. [4]. The main result of this approach related to the influence of sun elevation is the following regression equation:

$$r_\mu = R_S(90°)/R_S(\mu_s) = -c_0 + c_1\mu_s - c_2\mu_s^2, \quad (23)$$

that relates the ratio of diffuse reflectance coefficients to the cosine of the sun penetration angle μ_s. The coefficients of these regressions are given in Table 1. The difference between the theoretical diffuse reflectance (20) and the numerically simulated values do not exceed 20%.

Table 1. Coefficients c_0, c_1, and c_2 for each of the fifteen Petzold phase functions [9, 10].

#	x	c_0	c_1	c_2	r^2
01	0.03444	0.288392	1.58743	0.29775	0.999
02	0.01408	0.565779	3.23327	1.66143	0.995
03	0.01322	0.576934	3.18952	1.60944	0.997
04	0.01936	0.967853	3.86569	1.89692	0.999
05	0.01566	1.024818	4.03269	2.00333	0.999
06	0.08194	0.852371	3.32589	1.46969	0.999
07	0.09064	0.810208	3.24149	1.42623	0.999
08	0.14786	0.477916	2.38229	0.90046	0.999
09	0.01139	-0.02428	2.01621	1.03560	0.987
10	0.06660	0.847081	3.28663	1.43518	0.999
11	0.01265	1.108715	4.21634	2.10450	0.998
12	0.08947	0.762611	3.03790	1.26988	0.999
13	0.03550	1.057443	3.92840	1.86609	0.999
14	0.02131	0.718718	3.41994	1.69663	0.999
15	0.01355	0.040812	2.19756	1.14971	0.990

CONCLUSIONS

This paper presents two approaches to the problem of angular dependence of the sea diffuse reflection coefficient. One of the approaches is analytical and it consists of the approximate solution to the radiative transfer equation. The result of this approach is Eqn. (20) for diffuse reflectance of the sea as a function of inherent optical properties, the sun elevation angle and the ratio of direct illumination by the sun to the diffuse illumination by the sky. The second approach is a numerical Monte Carlo simulation. The results of this simulation are regressions given by Eqn. (23) that connect ratios of the diffuse reflectances of the seawater at 90° and arbitrary degrees with the sun elevation angle.

The results of both methods show that the corrections to the diffuse reflection of seawater due to the illumination conditions can reach 40%. This effect is significant and should be taken into account in processing optical remote sensing data.

ACKNOWLEDGMENT

The author thanks continuing support at the Naval Research Laboratory through the Littoral Optical Environment (LOE 6640-07) and Optical Oceanography (OO 73-5051-07) programs. This article represents NRL contribution NRL/PP/7331–97–0011.

REFERENCES

[1] V. I. Haltrin, (*a. k. a.* В. И. Халтурин, "The Self-Consistent Two-Stream Approximation in Radiative Transfer Theory for the Media with Anisotropic Scattering," *Izv., Atmos. Ocean Physics*, Vol. 21, p. 452-457, 1985.

[2] H. Gordon, "Dependence of the Diffuse Reflectance of Natural Waters on the Sun Angle," *Limn. Oceanogr.*, 34(8), p. 1484-1489, 1989.

[3] A. Morel and B. Gentili, "Diffuse reflectance of oceanic waters: its dependence on Sun angle as influenced by the molecular scattering contribution," *Appl. Optics*, Vol. 30, No. 30, pp. 4427-4438, 1991.

[4] V. I. Haltrin, "Monte Carlo Modeling of Light Field Parameters in Ocean with Petzold Laws of Scattering," in *Proceedings of the Fourth International Conference Remote Sensing for Marine and Coastal Environments: Technology and Applications*, Vol. I, Publ. by Envir. Res. Inst. of Michigan (ERIM), Ann Arbor, MI, pp. 502-508, 1997.

[5] J. T. O. Kirk, Monte-Carlo *Procedure for Simulating the Penetration of Light into Natural Waters.* - Division of Plant Industry Techn. Paper #. 36, CSIRO, Australia, pp. 16, 1981.

[6] V. I. Haltrin and G. W. Kattawar "Self-consistent solutions to the equation of transfer with elastic and inelastic scattering in oceanic optics: I. Model," *Appl. Optics*, Vol. 32, No. 27, pp. 5356-5367, 1993.

[7] V. I. Haltrin, "A Real-Time Algorithm for Atmospheric Corrections of Airborne Remote Optical Measurements above the Ocean," in *Proceedings of the Second International Airborne Remote Sensing Conference and Exhibition, Vol. III*, San Francisco, CA, Publ. by ERIM, pp. 63-72, 1996.

[8] N. G. Jerlov, *Marine Optics*, Elsevier, Amsterdam-Oxford - New York, pp. 247, 1976.

[9] T. J. Petzold, *Volume Scattering Functions for Selected Ocean Waters*, SIO Ref. 72-78, Scripps Institute of Oceanography, Visibility Laboratory, San Diego, CA, 1972, 79 p.

[10] V. I. Haltrin, "Theoretical and empirical phase functions for Monte Carlo calculations of light scattering in seawater," in *Proceedings of the Fourth International Conference Remote Sensing for Marine and Coastal Environments: Technology and Applications*, Vol. I, Publ. by Envir. Res. Inst. of Michigan (ERIM), Ann Arbor, MI, pp. 509-518, 1997.

Light Scattering Coefficient of Seawater for Arbitrary Concentrations of Hydrosols

Vladimir I. Haltrin
Naval Research Laboratory, Ocean Sciences Branch, Code 7331, Stennis Space Center, MS 39529-5004, USA
Phone: 601-688-4528, fax: 601-688-5379, e-mail: <haltrin@nrlssc.navy.mil>

Abstract — The scattering coefficient of seawater as a function of concentration of hydrosol particles is calculated. The approach used is based on the Maxwell's equations in a stochastically scattering seawater. The water is modeled as thermally fluctuated medium filled with the hydrosol particles. It is found that the scattering coefficient quadratically depends on concentration when the concentration of scatterers is very small. The scattering coefficient is linear to concentration of scatterers at values typical to the open ocean. At the values of concentrations typical to coastal waters the dependence on concentration weakens and reaches the saturation at very high values.

INTRODUCTION

In a majority of publications available today the light scattering coefficient by seawater is considered as linearly dependent on concentrations of hydrosols. The experiments by Prieur and Sathyendranath [1] show that at certain concentrations of chlorophyll C_C, typical to coastal waters, the dependence of seawater absorption coefficient on C_C is nonlinear. Clark and Backer [2] showed that the scattering coefficient of seawater is non-linearly dependent on chlorophyll concentration that is strongly correlated to the concentration of scattering matter of biologic origin.

In this paper an attempt is made to develop an approach to calculate the scattering coefficient of seawater as a function of concentration of hydrosol particles C_p. The approach is based on the solutions of the Maxwell's equations in a stochastically scattering medium (seawater). The seawater is modeled as thermally fluctuated medium filled with the hydrosol scatterers.

The final result of this paper is Eqn. (22) for the seawater scattering coefficient. The scattering coefficient b is linear with concentration of scattering particles at values typical to the open ocean. The coefficient quadratically depends on concentration when the concentration is very small (typical for the Sargasso Sea waters). At the concentrations close to the values that are typical to coastal waters, the dependence on concentrations weakens and reaches saturation at very high values. The results of this paper can explain some experimental data obtained in turbid coastal waters. They also can give a reasonable explanation to the phenomenon that some very clean ocean waters seem to be more transparent than the distilled water.

APPROACH

The radiative transfer theory, predominantly used in ocean optics, cannot explain nonlinear dependence of inherent optical properties on concentration of scatterers. In order to investigate this problem we should start from the Maxwell's equations in stochastically scattering medium. The mathematical formalism of scattering in stochastic medium is identical to the formalism of quantum statistical mechanics [3]. The photons themselves are always quantum particles. For these reasons we have chosen to use the quantum-mechanical statistical approach formulated in Ref. [4].

In this paper the scattering coefficient on hydrosol particles is calculated through the dielectric permittivity of the hydrosol component of the water. The dielectric permittivity (DP) is a constituent part of the Fourier transform of the Green's function of the Maxwell's equations in seawater. By definition, the Green's function is a solution of these equations when a source function is assumed as an infinitely short and localized at one point light pulse [5]. The approach adopted here is based on the theory proposed by the author in Refs. [6, 7] but abandoned at the time due to the lack of interest in coastal hydrooptics.

Hydrosol particles in this model are perceived as small potential holes in a Brownian motion. They are characterized by the size distribution function: $\varphi(a)$ ($\int_0^\infty \varphi(a)\,da = 1$). Such a model allows one to derive the following interaction Hamiltonian between photons and thermal density fluctuations [6]:

$$\hat{H}_{\text{int}}(t) = -\frac{g}{c^2}\int d^3r \frac{\partial \hat{A}_\alpha(\mathbf{r},t)}{\partial t}\hat{\psi}(\mathbf{r},t)\frac{\partial \hat{A}_\alpha(\mathbf{r},t)}{\partial t}, \quad \alpha = 1,2,3, \quad (1)$$

here $\hat{A}_\alpha$ is a photon field operator which corresponds to a vector potential of light wave, $\mathbf{r}$ is a coordinate, t is time, index α denotes vector's component, c is the speed of light,

$$g = C_V\,\delta\varepsilon_H\sqrt{\frac{k_B T}{\bar{a}^3\rho u^2}} \sim \gamma\, C_V, \quad \gamma \approx 10^3 \div 10^5, \quad (2)$$

C_V is the volume concentration of hydrosol, $\delta\varepsilon_H$ is the difference between average DP of the hydrosol and DP of pure water, k_B is the Boltzmann's constant, ρ is the water density, and u is the average velocity of a Brownian movement in water. Repeating indices everywhere in this article imply summation. The operator of thermal density fluctuations $\hat{\psi}$ is determined by the following equation [6]:

$$\hat{\psi}(\mathbf{r},t) = \frac{1}{4\pi}\sqrt{\bar{a}^3/(k_B T)}\int \Delta(\mathbf{r}-\mathbf{r}')\Phi(\mathbf{r}',t)\,d\mathbf{r}',$$
$$\Delta(\mathbf{r}) = \int_r^\infty \varphi(a)\,da \Big/ [4\pi\int_0^\infty r^2 dr \int_r^\infty \varphi(a)\,da], \quad (3)$$

here $\bar{a} = \int_0^\infty \varphi(a)\,a\,da$ is a mean radius of hydrosol particles, T is the absolute temperature.

THE GREEN'S FUNCTION

Let us write a Green's function of photons propagating in a nonscattering medium with the dielectric permittivity ε_0. It can be represented as a sum of the transverse and longitidinal

U.S. Government work not protected by
U.S. copyright.

components [6]. In the energetic-momentum representation the Green's function has the following form:

$$D^{(0)}_{\alpha\beta}(\omega,\mathbf{k}) = D^{tr}_0(\omega,\mathbf{k})(\delta_{\alpha\beta} - n_\alpha n_\beta) + D^{l}_0(\omega,\mathbf{k})\, n_\alpha n_\beta, \quad (4)$$

where

$$D^{tr}_0(\omega,\mathbf{k}) = \frac{4\pi}{\varepsilon_0\,\omega^2/c^2 - k^2},\ D^{l}_0(\omega,\mathbf{k}) = \frac{4\pi c^2}{\varepsilon_0\,\omega^2}, \quad (5)$$

n_α is the component of the unity vector in the direction of $\mathbf{k}$, $\delta_{\alpha\beta}$ is the Kroneker's symbol or the unity tensor.

The Green's function of photon field. that includes multiple scattering due to the interaction with thermal fluctuations described by the Hamiltonian (1). can be written as:

$$D_{\alpha\beta}(\omega,\mathbf{k}) = D^{tr}(\omega,\mathbf{k})(\delta_{\alpha\beta} - n_\alpha n_\beta) + D^{l}(\omega,\mathbf{k})\, n_\alpha n_\beta. \quad (6)$$

$$D^{tr}(\omega,\mathbf{k}) = \frac{4\pi}{\varepsilon^{tr}\,\omega^2/c^2 - k^2},\ D^{l}(\omega,\mathbf{k}) = \frac{4\pi c^2}{\varepsilon^{l}\,\omega^2}, \quad (7)$$

here ε^{tr} and ε^{l} are, correspondingly, the transverse and the longitidinal components of the following dielectric permittivity tensor:

$$\varepsilon_{\alpha\beta}(\omega,\mathbf{k}) = \varepsilon^{tr}(\omega,\mathbf{k})(\delta_{\alpha\beta} - n_\alpha n_\beta) + \varepsilon^{l}(\omega,\mathbf{k})\, n_\alpha n_\beta. \quad (8)$$

It is clear from Eqns (6)-(8) that the problem of finding the dielectric permittivity is equivalent to the problem of finding the Green's function.

Let us calculate the multiple scattering Green's function and the corresponding dielectric permittivity. As a starting zero approximation let us take the Green's function (4) which corresponds to the clear water. The DP of the clear water depends only on the circular frequency ω:

$$\varepsilon^0_{\alpha\beta}(\omega) = \varepsilon_0(\omega)\delta_{\alpha\beta} \equiv \varepsilon_0(\omega)(\delta_{\alpha\beta} - n_\alpha n_\beta) + \varepsilon_0(\omega) n_\alpha n_\beta. \quad (9)$$

It means that Eqn. (9) takes into account only temporal dispersion that is determined by the processes of absorption and emission of photons by the water molecules.

The transverse and longitidinal components of the seawater DP that take into account processes of multiple scattering on the hydrosol particles can be expressed as:

$$\begin{aligned} \varepsilon^{tr}(\omega,\mathbf{k}) &= \varepsilon_0(\omega) + \delta\varepsilon^{tr}(\omega,\mathbf{k}), \\ \varepsilon^{l}(\omega,\mathbf{k}) &= \varepsilon_0(\omega) + \delta\varepsilon^{l}(\omega,\mathbf{k}), \\ \varepsilon_0(\omega) &= \varepsilon'_0(\omega) + i\varepsilon''_0(\omega). \end{aligned} \quad (10)$$

here ε'_0 and ε''_0 are the real and the imaginary parts of the dielectric permittivity of pure water.

In order to calculate $\delta\varepsilon^{tr}$ and $\delta\varepsilon^{l}$ let us carry out the standard procedure [4, 6] to calculate corrections to the Green's function starting from the Hamiltonian given by Eqn. (1).

The Green's function of the photons in turbid water is expressed through the following Dyson's equation:

$$\begin{aligned} D_{\alpha\beta}(\omega_n,\mathbf{k}) &= D^{(0)}_{\alpha\beta}(\omega_n,\mathbf{k}) + D^{(0)}_{\alpha\gamma}(\omega_n,\mathbf{k})\pi_{\gamma\mu}(\omega_n,\mathbf{k})D_{\mu\beta}(\omega_n,\mathbf{k}), \\ \pi_{\alpha\beta}(\omega_n,\mathbf{k}) &= -gh\int d^3\mathbf{q}\,\Delta^2(\mathbf{q})\,D_{\alpha\gamma}(\omega_n,\mathbf{k}-\mathbf{q})\Gamma_{\gamma\beta}(\omega_n,\mathbf{k}-\mathbf{q},\mathbf{k}), \\ h &= \bar{a}^3\omega_n^4/(2\pi)^5, \end{aligned} \quad (11)$$

where $\pi_{\alpha\beta}$ is the polarization operator, and $\Gamma_{\gamma\beta}$ is the total apex part that corresponds to the sum of all orders of light scattering. The polarization operator is linked with the dielectric permittivity tensor by the equation:

$$\delta\varepsilon_{\alpha\beta}(\omega_n,\mathbf{k}) = \left(4\pi/\omega_n^2\right)\pi_{\alpha\beta}(\omega_n,\mathbf{k}). \quad (12)$$

By resolving the Dyson's equation (11) in respect to $\Gamma_{\alpha\beta}$, we have the following integral equation for the components of the apex part:

$$\Gamma_{\alpha\beta}(\mathbf{k}-\mathbf{p},\mathbf{k}) = g\,\delta_{\alpha\beta} + h\int d^3\mathbf{q}\,\Delta^2(\mathbf{q})\Gamma_{\alpha\mu}(\mathbf{k}-\mathbf{p},\mathbf{k}-\mathbf{p}-\mathbf{q})\times \quad (13)$$

$$D_{\mu\eta}(\mathbf{k}-\mathbf{p}-\mathbf{q})\Gamma_{\eta\nu}(\mathbf{k}-\mathbf{p}-\mathbf{q},\mathbf{k}-\mathbf{q})D_{\nu\kappa}(\mathbf{k}-\mathbf{q})\Gamma_{\kappa\beta}(\mathbf{k}-\mathbf{q},\mathbf{k}).$$

In solving Eqn. (13) let us restrict ourselves to the scattering on hydrosols with the large average size of particles, $2\bar{a} >> \lambda$. In this case $p < q < 1/\bar{a} << k$. By representing the apex part as the sum of transverse and longitudinal parts similar to Eqn. (8), integrating over $\mathbf{q}$, and analytically expanding to the real frequency axis, we obtain the following equations for the components of the apex part:

$$\Gamma^{tr} = g + \frac{\bar{a}^2\omega^4}{2\pi^2k^2c^4}\left(\Gamma^{tr}\right)^3,\ \Gamma^{l} = g + \frac{2}{3\pi^2(\varepsilon^{l})^2}\left(\Gamma^{l}\right)^3. \quad (14)$$

THE DIELECTRIC PERMITTIVITY

Let us derive equations that link corrections to the dielectric permittivity with the apex part. Using Eqns. (9)-(12), integrating over $\mathbf{q}$, and analytically transferring to the real frequency axis, we have the following equations:

$$\varepsilon^{tr} = \varepsilon_0 + ig\frac{\bar{a}\,\omega|\omega|}{16\pi k c^2}\Gamma^{tr},\ \varepsilon^{l} = \varepsilon_0 - \frac{g}{6\pi^2\varepsilon^{l}}\Gamma^{l}. \quad (15)$$

In order to have a complete system of equations let us add the dispersion relation taken from the Maxwell's equations:

$$k^2 = \varepsilon^{tr}\omega^2/c^2. \quad (16)$$

Now we have the complete system of five equations (14)-(16) for the five complex parameters: k, Γ^{tr}, Γ^{l}, ε^{tr}, and ε^{l}. In the general case of arbitrary values of g (which correspond to the arbitrary concentrations) this system of equations has no analytical solutions. For the value of the parameter

$$g < 4\sqrt{2}\,\varepsilon'_0/3,\ C_V < 2\cdot10^{-3}\ \left(\text{or } C_p < 2\ g/m^3\right), \quad (16)$$

we have the approximate solution for the longitudinal component of the dielectric permittivity tensor: (17)

$$\varepsilon^{l} = \varepsilon'_0\left\{1 - \frac{q_C}{3}\sin\left[\frac{1}{3}\sin^{-1}(3q_C)\right]\right\},\ q_C = \frac{C_V\delta\varepsilon_H}{\pi\varepsilon'_0}\sqrt{\frac{k_B T}{2\bar{a}^3\rho u^2}}.$$

Here $C_p \equiv \rho C_V$ is the concentration of hydrosol particles in conventional units (g/m^3).

According to Eqn. (17) ε^{l} is determined only by the water properties. As it is seen from the Eqns. (14)-(16) this is also true for any water turbidity. For the calculation of the transversal part of the dielectric permittivity let us consider only the case of a weak attenuation of light. Let us write the expression for the absolute value of the photon wave vector:

$$k = k_0 + i(a+b)/2, \quad (18)$$

here k_0 is the real part of the wave vector, a is the absorption coefficient, and b is the scattering coefficient. The condition of weak attenuation $a + b << k_0$ is equivalent to the following conditions:

$$\left|\delta\varepsilon''\right| << \varepsilon'_0,\ \text{or}\ C_V < 2\cdot10^{-3}\ \left(C_p < 2\ g/m^3\right). \quad (19)$$

In this case the solution of Eqns. (14)-(16) for the transversal part of the dielectric permittivity is:

$$\delta\varepsilon^{tr} = i\frac{16\pi}{\sqrt{3}}\varepsilon_0' q_C \operatorname{sign}\omega \begin{cases} 4\sin\left[(1/3)\sin^{-1}\zeta\right], \zeta < 1, \\ \psi_\varepsilon + 1/\psi_\varepsilon, \quad \zeta \geq 1, \end{cases} \quad (20)$$

where

$$\zeta = \frac{3C_V\delta\varepsilon_H}{4\pi}\sqrt{\frac{6k_BT}{\bar{a}\rho u^2}}\left(\frac{\omega^2}{k_0c^2}\right), \psi_\varepsilon = \sqrt[3]{f-\sqrt{f^2-1}}. \quad (21)$$

SCATTERING COEFFICIENT

The light scattering coefficient b is calculated by the substitution of Eqn. (20) into Eqns. (16) and (18). It has the following form:

$$b = \frac{\pi C_V\delta\varepsilon_H}{8\varepsilon_0'\lambda} \begin{cases} 4\sin\left(\frac{1}{3}\sin^{-1}\xi\right), \xi < 1, \\ \psi_b + 1/\psi_b, \quad \xi \geq 1, \end{cases} \quad (22)$$

where

$$\xi = \frac{3C_V\delta\varepsilon_H}{2\varepsilon_0'\lambda}\sqrt{\frac{6k_BT}{\bar{a}\rho u^2}}, \quad \psi_b = \sqrt[3]{\xi-\sqrt{\xi^2-1}}, \quad (23)$$

here λ is the wavelength of light in vacuum.

If $\xi << 1$ Eqns. (22)-(23) can be further simplified:

$$b = \frac{\pi^2 C_V^2\,\delta\varepsilon_H^2\,k_BT}{4\varepsilon_0'^2\rho\bar{a}^2u^2\lambda^2}, \quad C_V < 10^{-5}\left(\text{or } C_p < 10^{-2}\ g/m^3\right). \quad (24)$$

Equation (23) coincides with the formula for the scattering coefficient derived in Ref. [6] for the case of $\lambda << 2\bar{a}$.

In the general case of the arbitrary values of the parameter g (or arbitrary concentrations C_V or C_p) the system of Eqns. (14)-(16) has no solutions in analytic form. However it is easy to solve that system numerically. Figure 1 shows the dependence of the scattering coefficient of seawater as a function of the hydrosol particles concentration. The absolute values of b are not shown because they depend on the average radius of scattering particles $\bar{a}$ and the average density of the particles ρ that vary from a region to a region. The idea of displaying this picture is to show the dependence of the scattering coefficient b on concentration. At very small concentrations of particles ($C_p < 0.03\,mg/m^3$) the dependence $b(C_p)$ is quadratic. At the concentrations typical to the open ocean the dependence is linear. At higher concentrations ($5 < C_p < 50\,mg/m^3$) the dependence shown in Fig. 1 reminds the exprerimental one proposed in Ref. [1]. At even larger concentrations ($C_p > 50\ mg/m^3$) it reaches saturation.

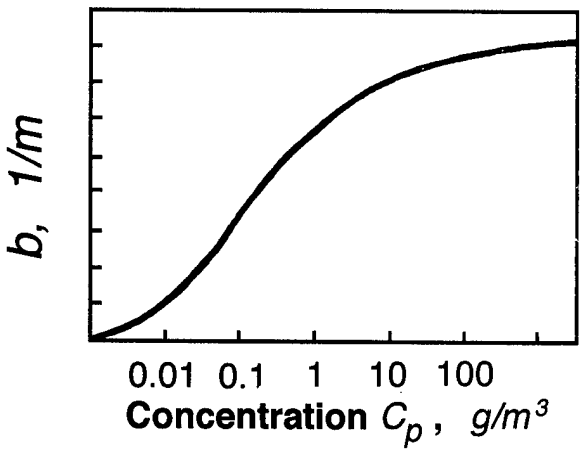

Figure 1. The scattering coefficient of seawater filled with the hydrosol particles as a function of the hydrosol particles concentration.

CONCLUSION

It is shown that the approach based on the Maxwell's theory in a stochastically scattering medium can be productively used in ocean optics. From the solutions of the Dyson's equation the dielectric permittivity tensor of seawater with the scattering particles is found. From the equations for the dielectric permittivity a nonlinear dependence of the scattering coefficient of water is derived. It is shown that the scattering coefficient of seawater quadratically depends on the concentration when the concentration of scattering particles is very small. It is linear to the concentration of scatterers at values typical to the open ocean. At the concentrations typical to the coastal waters the concentrational dependence weakens and reaches saturation at values higher than $100\,g/m^3$.

ACKNOWLEDGMENT

The author thanks continuing support at the Naval Research Laboratory through the Littoral Optical Environment (LOE 6640-07) program. This article represents NRL contribution NRL/PP/7331–97–0012.

REFERENCES

[1] L. Prieur, and S. Sathyendranath, "An Optical Classification of Coastal and oceanic waters based on the specific spectral absorption curves of phytoplankton pigments, dissolved organic matter, and other particulate materials," *Limnol. Oceanogr.*, 26(4), pp. 671-689, 1981.

[2] D. K. Clark, E. T. Backer, and. A. E. Strong, "Upwelled spectral radiance distribution in relation to particular matter in water," *Boundary-Layer Meteorol.*, 18 (3), pp. 287-298, 1980.

[3] U. Frish, "Wave propagation in random media," in *Probabilistic Methods in Applied Mathematics*, Vol. 1, Ed. by A. T. Bharucha-Reid, Academic Press, New York - London, pp. 75-198, 1968.

[4] A. A. Abrikosov, L. P. Gor'kov, I. E. Dzialoshinski, *Methods of Quantum Field Theory in Statistical Physics*, Dover, New York, pp. 352, 1963.

[5] P. M. Morse and Feshbach, H. *Methods of Theoretical Physics*, Part 1, p.122, McGraw-Hill, New York, 1953.

[6] V. I. Haltrin (*a.k.a.* В. И. Халтурин), "On the Dielectric Permittivity of Sea Water," *Marine Hydrophys. Research*, No. 3(78), pp. 121-144, 1977.

[7] V. I. Haltrin (*a.k.a.* V. I. Khalturin), "Scattering of Coherent Light in Seawater," *Marine Hydrophysical Research*, No. 1(88), pp. 128-137, 1980.

[8] V. S. Vladimirov, *Equations of Mathematical Physics*, Dekker, New York, 1971, p. 418.

Multi-wavelength Laser Scattering At The Air-Sea Interface

C. S. Lin
Remote Sensing Division
Naval Research Laboratory
Washington, D. C. 20375
Tel. (202)767-3639, Fax (202)767-7885, E-mail:cslin@ccf.nrl.navy.mil

Abstract

This paper describes a shore-based multi-wavelength lidar for air-sea interface studies. The lidar systems used lasers operated in near IR and visible wavelengths to collect waveform and imaging spectrograph data at both sides of the air-sea interface. This paper describes the lidars, the waveform sampling system and the imaging spectrograph system. This paper also describes the measurement results.

1. Introduction

Lidars using IR transmitters have been used to profile the water surface in various remote sensing applications. In most of the surface profiling applications, IR lasers such as the diode laser operated at 904 nm and the Nd:YAG laser operated near 1064 nm have been routinely used since these laser energies do not penetrate the water column. However, other applications such as the laser bathymetry and the laser induced water column fluorescence applications, require lasers operated at visible wavelengths. Using combination of different laser wavelengths, a lidar system can be used to obtain multi-parameter information of the air-sea interface, including the aerosol profile, sea state, water-column temperature profile, DOM (dissolved organic materials) and algae distributions.

This paper describes a lidar system equipped with an IR laser for the ocean surface profiling application and a tunable-visible laser for both ocean surface and water column profiling applications. For the sea surface profiling application, a waveform sampling system recorded laser waveforms reflected from the water surfaces. These waveforms included time of flight and amplitude information. For the water column applications, a range-gated ICCD array imaging spectrograph system was used to collect the laser induced inelastic scattering of the water column. This paper describes the lidar and the measurement data collected at Chesapeake Bay.

2. Lidar and Data Acquisition System

2.1 The lidar

The Visible wavelength laser was a tunable dye laser pumped by an excimer laser operated at 351 nm wavelength. The resulting laser pulses had a temporal pulse-width of approximately 13 ns. The wavelength tuning rang of the laser was between 480 and 530 nm for the experiments described in this paper. For the waveform data, a telescope coupled with a photomultiplier was used to collect the water surface reflected laser energies. The dye laser beam divergence was less than one mr. A wide band DC amplifier was placed between the photomultiplier output and the waveform sampling system to match the output signals with the dynamic range of the data acquisition system. The second laser was a 904 nm diode-laser with a temporal pulse-width of 10 ns. An avalanche photodiode detector was used to detect the laser energies reflected from the water surface. The diode-laser beam divergence was approximately 1.5 mr.

2.2 Waveform sampling system

A 350 MHz bandwidth video waveform-sampler with a 12 bits analog-to-digital converter digitized the laser-pulse waveforms reflected from the ocean surface. During the experiments, the laser-pulse waveforms were sampled at 500 MHz rate resulting in the lidar range resolution of 30 cm. The excimer laser triggers were used to trigger the IR laser and the waveform sampling system. This arrangement synchronized all the lasers with the waveform sampling system. An I/O processor integrated with a 586 computer controlled the waveform sampler and stored the collected waveforms in a mass storage tapes.

For the data shown in this paper, ocean-surface reflected laser waveforms were collected at approximately 32 Hz, 1024 data samples per waveform were collected for each trigger. At a 500 MHz waveform digitization rate, this corresponded to a total waveform sampling window of 2048 ns. This sampling window allowed the collection of laser scattering data for 2 us after each laser pulse was emitted.

0-7803-3836-7/97/$10.00 © 1997 IEEE

2.3 Imaging spectrograph system

The imaging spectrograph system used an imaging spectrometer coupled to a gateable intensified ICCD array camera. The imagine spectrometer was operated with 4 nm spectral resolution for the data described in this paper. However, the pixel format of the ICCD array is 1024 by 256 and can collect spectral data at a narrower resolution. The spectrograph system was equipped with a detector controller and a gate pulse generator. The spectrograph system can be operated with a 5 ns minimum gate-width, the typical gate width for our experiment was approximately 10 ns.

3. Lidar experiments

The lidar was installed in a trailer located on a cliff at Chesapeake Beach, Md. The elevation of the trailer was approximately 33 m from the water surface. The laser beam was directed toward the water surface with depression angles between 14 and 17 degrees. The average flight time of laser pulses was approximately 720 ns round-trip between the laser and the water surface. This corresponds to a 216 m round-trip distance travelled by a laser pulse. for the IR laser pulse, the round- distance travelled was 251 m. For the visible laser, the laser spot size at the water surface was 1.1 m along the direction of laser beam propagation. For the diode laser, the spot size was 0.11 m . Waveform data were collected for both the visible and IR lasers. Spectrograph data were collected only with the tunable-visible laser.

4. Lidar experiment data

Figure 1 shows an example of the visible laser waveform data. A two dimensional plot of the laser waveforms was displayed with the laser pulse flight-time plotted against the sequential laser pulse number. The laser-pulse flight-time sampling window shown in this figure is 2048 ns. 512 waveforms are plotted in this figure. At 16 Hz lidar triggering rate, this corresponded to 32 seconds of measurement time. The laser-pulse flight direction was from the bottom of the figure traveling toward the top while the laser pulse number is plotted form left to right in this figure. The data in figure 1 showed two distinct groups of parallel laser waveforms. The first group of waveforms were those of the emitted laser energies detected by the photomultiplier when exiting the laser. The second group of laser waveforms were those of the laser energies reflected from the water surface. The grey-scale showed the amplitude variations of both the emitted and the reflected laser pulses. The undulations of the water surface due to the wave motions were clearly shown in this figure. These data also showed the detection of the breaking waves.

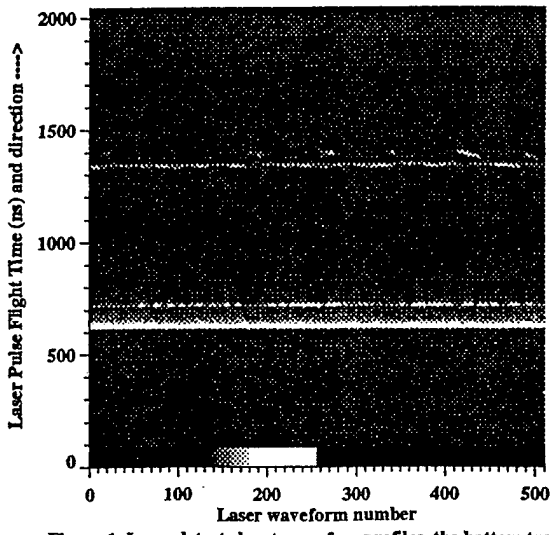

Figure 1. Laser detected water surface profiles, the bottom trace is the reference laser signal and the top trace is laser energies backscattered from the water surface

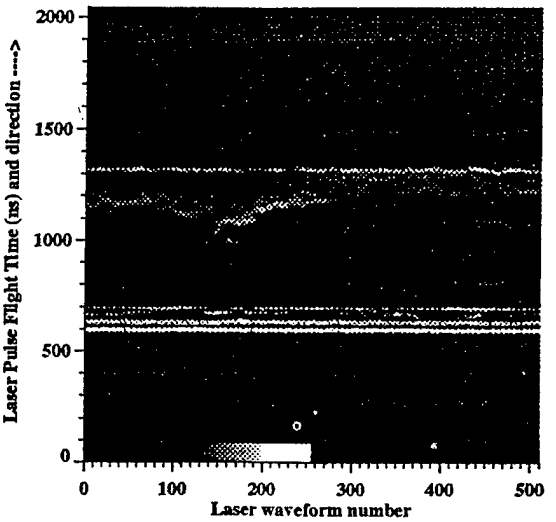

Figure 2. Laser detected aerosol and water surface profiles, the bottom trace is the reference laser signal and the top trace is laser energies backscattered from the water surface

In addition to detecting water waves, figure 2 shows the detection of aerosol in the atmosphere by the laser energies. Again, the range information show the spatial distribution of the aerosol and the amplitude information show the variations in the intensities of aerosol backscattered laser energies. Figure 3 shows the IR laser pulse waveforms reflected from the same water surface. These data were collected at the same time as the data shown in figure 1. Detailed comparisons between figure 1 and

figure 3 data show that the IR laser pulses only detected the water surface and the breaking waves above the water surface. The differences between the IR laser data and tunable visible laser data are most likely due to the difference in attenuation coefficients between two laser wavelengths at the air-sea interface. For a visible laser, the penetrating laser energies allow detections of water waves behind the initial backscattering surface. Meanwhile, IR laser energies were attenuated at the first scattering layer.

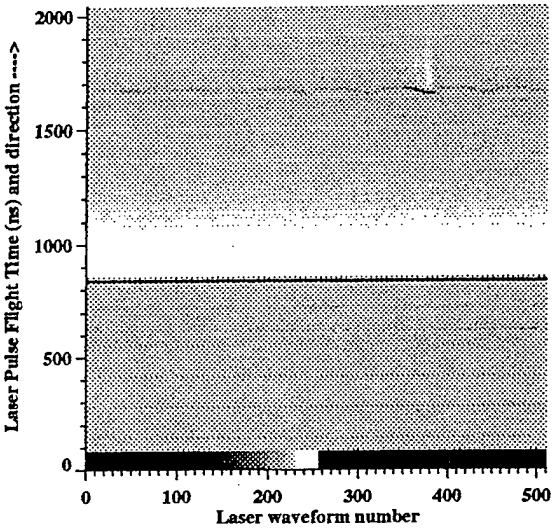

Figure 3. Laser detected water surface profiles, the bottom trace is the reference laser signal and the top trace is laser energies backscattered from the water surface

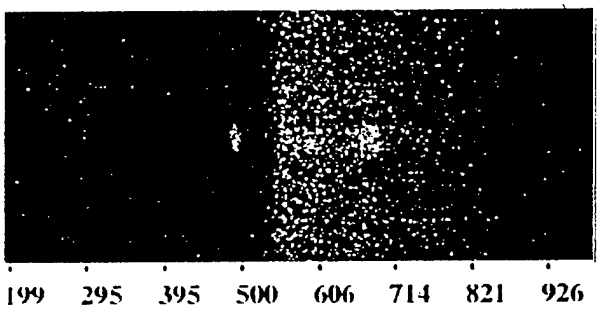

Figure 4. Image spectra induced by a tunable laser

Figure 4 shows a panel of spectrograph data. This figure shows the laser induced scattering signals in the water column using 500 nm laser energies. The x-dimension of the data corresponds to spectral dimension of the imaging spectrograph while the y-dimension is the spatial dimension. For this data set, the spatial dimension is approximately 18 m on the water surface. The spatial data show the laser spot in the water was located in the center of the y-dimension. The corresponding laser induced signals were also located in the center of the y-dimension. In the spectral dimension, The main Raman signals near 600 nm and the phytoplankton peak near 685 nm are clearly shown. Figure 5 is the line spectral plot which corresponds to the center(spatial) of the imaging spectrograph data shown in figure 4. For this spectral plot, the excitation laser line, and the corresponding laser induced Raman and the phytoplankton fluorescence can be identified.

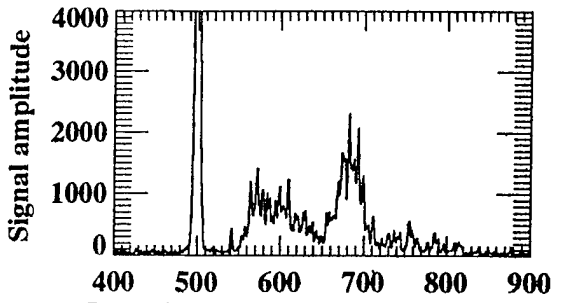

Figure 5. Line spectral plot of figure 4.

6. Conclusion

This paper describes a multi-wavelength lidar system and the measurement data collected at the air-sea interface. The measurement data show the simultaneous profiling of various geophysical parameters in the atmosphere and in the water column. Specifically, the lidar system detected the Raman signals, which can be used to derive the water column temperature. The lidar system also detected the water column fluorescence which can be used to derive the algae and DOM distribution. The detection of the near surface aerosols profiles and the breaking can be used to study the aerosol generation at the air-sea interface.

The multi-wavelength and multi-parameter lidars described in this paper can be used as a stand-alone remote sensor to study the physics and chemistry of both sides of air-sea interface. This lidar system also can be used as a ground-truth instrument for passive optical sensor operated in the air-sea interface environment especially in a complex littoral environment such as Chesapeake Bay.

Acknowledgment

Jeff James provided helps in the installation and the operation of the lidar system. This work is supported by ONR funds.

Line noise extraction of thermal infrared camera image in observing sea skin temperature

Sumio Tamba, Ryuzo Yokoyama
Department of Computer Science, Faculty of Engineering, Iwate University
4-3-5 Ueda, Morioka, Iwate, 020 JAPAN
Tel: +81-196-21-6478, Fax: +81-196-21-1170
E-mail: tanba@cis.iwate-u.ac.jp

Abstract: A thermal infrared camera provides relevant data to observe fine structure of sea skin temperature distribution. The image is exposed to various noises. We have developed two algorithms to correct a strip-type noise caused by the scanning mechanism and an inverse shading-type noise caused by spatial inhomogeneity of detecting sensitivity. The first algorithm is based on two dimensional Fourier transform, and the second one was based on a spatial weighting function. By applying to images of MUBEX[1], we could confirm the effectiveness of the algorithms.

INTRODUCTION

In MUBEX campaign, a thermal infrared camera (TIC, TH3102m of NEC San-ei) has been expensively used to observe the behaviors of sea skin surface temperature . Having a Hg-Cd-Te detector with spectral band of 8-13 micron meter, TIC was originally developed for industrial use with the temperature range of -30 - +300 deg.C. According to our purpose, it is modified for the temperature range into -20 - +80 deg.C. Table 1 shows its catalog specification.

Figure 1 An example of an original TIC image.

Table 1 Specifications of the TIC

temperature range	-20 ~ +80 deg.C
temperature resolution	0.075 deg.C
wave length	8 ~ 13 micro m
IFOV	1.5 mrad
FOV	(H) 30deg.x (V) 28.5deg.
scanning mode	Image mode Line mode
flame time	0.8 sec/flame
image size	255pixel x 207line

At the observation campaign, TIC was fixed on a stage at 5 m above the sea surface and its sight is 2.5 m square with a 1 cm pixel resolution. TIC has two modes of scanning mirror derive, i.e., "image scan mode" and "line scan mode." At the image scan, both a horizontal drive and a vertical drive are active to generate an image, but in the line scan only the horizontal drive is active. In the later case, one frame of image is formed by just collecting 207 lines detected by the horizontal scanning.

DOMINANT NOISE OF TIC

(1) Strip noise

Fig. 1 shows an example of an original TIC image of sea surface temperature by the line scanning mode. At the first glance, existence of a strip noise is evident. This is caused by vibration of a cooling pump for the detector keeping at -70 deg.C. At each stroke of the pump, the detector output by is superposed by piezo-electricity noise, of which amount is about 0.1 deg.C.

(2) Skewed sensitivity noise

Fig. 2 shows skewed sensitivities of temperature detection when TIC looked a sphere object coated by a black body paint of homogeneous temperature. The center of frame shows the lowest temperature. The further from the center, the higher temperature appeared. The kind of disturbance is caused by electromagnetic induction to the electronic circuit.

0-7803-3836-7/97/$10.00 © 1997 IEEE

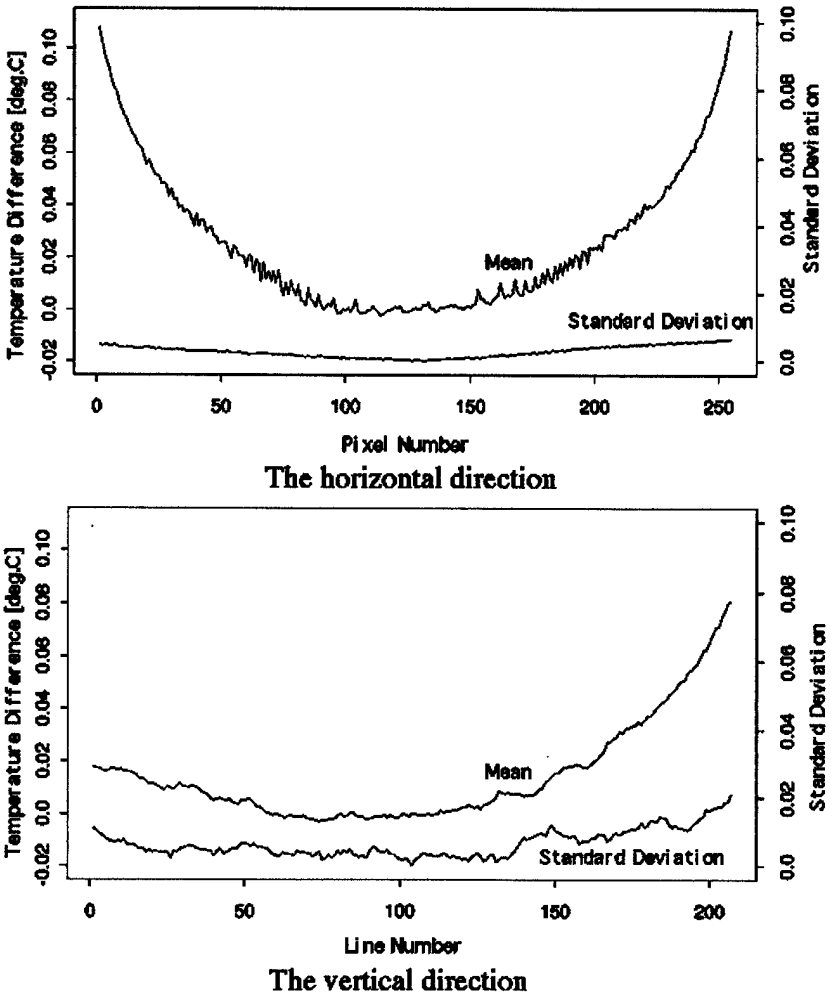

Figure 2 Skewed sensitivity noise of the horizontal and vertical direction.

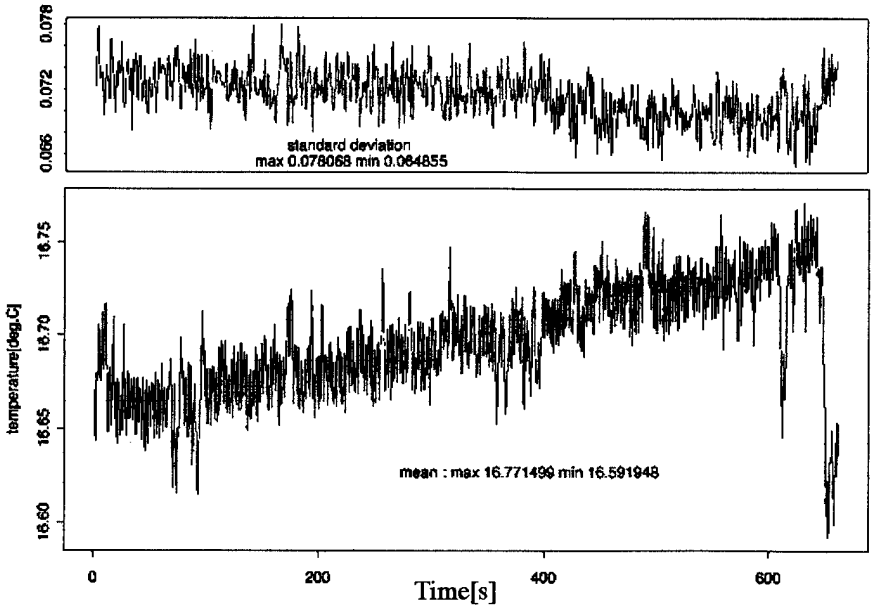

Figure 3 Quantization noise of black body temperature.

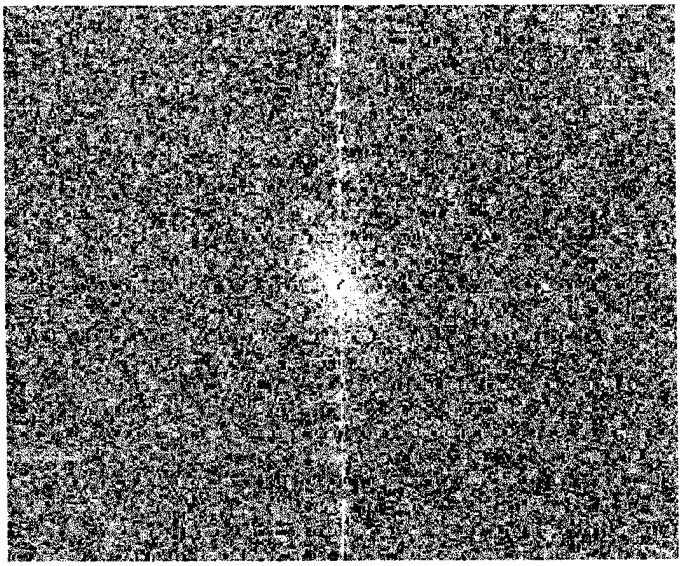

Figure 4 The results of Fourier Transform of Fig. 1.

Figure 5 The noise reduced image of Fig. 1.

(3) Quantization noise of black body temperature

The quantization step of the reference black body temperature of TIC is 0.1 deg.C. At each step change of the reference, the detected temperature is fluctuated. We call this fluctuation as quantization noise of black body temperature. Fig. 3 shows a typical quantization noise of reference blackbody temperature. The lower figure shows the mean value of each TIC image, and the upper figure shows the standard deviation of each TIC image.

REDUCTION OF NOISE ON TIC IMAGE

(1). Reduction of stripe noise

The stripe type noise appears only on horizontal direction with synchronized with the cooling pump action. Fig. 4 is the results of Fourier Transform of Fig. 1. It should be unrealistic for regular sea surface temperature distribution to have a directional spectral patterns.Those bright spots on the vertical axis are caused by the stripe noise .

For the noise reduction, we used to chop the sticks of bright spots. More precisely, we replace the spectrum of the vertical axis by the mean spectrum of its two sub-vertical axes. Fig. 5 is the inverse transform of the replaced image against Fig. 4. The strip noise is reduced considerably.

(2). Reduction of noise of sensitivity distortion

The pattern of spatial sensitivity distortion was found to be consistent for all images. We have calculated a two-dimensional function to approximate the sensitivity distortion. For the correction,amount of reduced temperature are calculated for each pixel based, and it is added to its original temperature.

By applying the two algorithms of noise reduction in the above, we could get the final accuracy of each TIC image as the absolute accuracy of 0.031 deg.C, and the relative accuracy of 0.071 deg.C.

CONCLUSION

By the noise reduction algorithms, accuracy of TIC was improved remarkably. TIC data , however, are affected by emissivity effect and sea skin effect, and further improvement might be expected in future.

ACKNOWLEDGMENTS

The MUBEX is supported by the grants from National Space Development Agency of Japan. We want to show sincere appreciation.

REFERENCES

[1] Tamba S., S. Oikawa, R. Yokoyama, I. Ridley, I. Parkes and D. Llewellyn-Jones, "The relationship between SST measured from ATSR to the spatial and temporal behavior of the ocean skin as observed with an in situ Thermal Infrared Camera", the proceedings of the 3rd ERS Symposium in Florence, Italy on March 1997.

Spatial and temporal behaviors of sea skin temperature observed by thermal infrared camera

Sumio Tamba, Shinnya Oikawa, Ryuzo Yokoyama
Department of Computer Science, Faculty of Engineering, Iwate University
4-3-5 Ueda, Morioka, Iwate, 020 JAPAN
Tel: +81-196-21-6478, Fax: +81-196-21-1170
E-mail: tanba@cis.iwate-u.ac.jp

Ian Redley, Isabelle Parkes, David Llewellyn-Jones
Earth Observation Science, Department of Physics and Astronomy, Leicester University
University road, Leicester, LE1 7RH, U.K.

Abstract: In MUBEX observation campaign, sea skin temperature was extensively observed by a thermal infrared camera. The total number of the image collected in the MUBEX campaign was about 50,000 frames, which provided various aspects of sea skin temperature behaviorism. The distribution pattern of sea skin temperature changes depending upon sun shine, cloud and wind. This paper describes the results of early stage of TIC image analyses concerned with sea skin temperature observation.

INTRODUCTION

The investigation of sea skin surface temperature is one of the main purposes of MUBEX campaign[1]. During MUBEX a thermal infrared camera (TIC) was installed on the mounting stage 5 m above the sea surface at the bow of a vessel. Its catalog identification is "TH3102m of NEC San-ei" and Table 1 shows its specification. One frame of TIC image has 207 rows and 255 columns. From the height of 5 m, it covers 2.5 m square of sea surface with a pixel resolution of about 1 cm.

Table 1 Specifications of TIC

temperature range	-20 ~ +80 deg.C
temperature resolution	0.075 deg.C
wave length	8 ~ 13 micro m
IFOV	1.5 mrad
FOV	(H)30deg. x (V)28.5deg.
scanning time for one frame	0.8 sec/frame
pixels in one frame	255(H) x 207(V)

DATA COLLECTION OF MUBEX/96 CAMPAIGN

MUBEX observation campaign in 1996 was held from July 15th to August 12th. Table 2 shows the list of TIC operation during the campaign. At the data collection, a research vessel was used to run along a transect one mile away and across the No. 6 buoy of Mutsu Bay Buoy System with the speed of one knot. The original TIC images are exposed to various kind of noises, but we have developed algorithms for data calibration and correction to guarantee the standard error to be less than

Table 2 TIC operation list in MUBEX/96 Campaign.

	operation time		# of collected	target
date	start	end	images	satellite
96/07/20	11:17:51	12:00:35	620	
	12:03:50	12:17:08	799	
	12:18:26	13:30:29	1045	NOAA-14
	13:30:33	15:24:46	1656	
96/07/21	12:22:20	14:03:31	1467	NOAA-14
96/07/22	12:31:12	13:57:45	1255	NOAA-14
	13:59:21	14:08:45	565	
	14:09:21	14:15:42	93	
96/07/24	18:03:13	18:31:51	416	NOAA-12
	20:29:29	22:35:10	1822	ERS-2
96/07/26	20:50:56	22:41:42	1606	ERS-1
96/07/27	1:19:28	2:22:33	915	NOAA-14
96/07/29	7:44:25	8:23:25	566	
	10:06:35	10:56:00	717	ERS-1
	11:35:32	11:52:17	1006	
	12:15:02	12:31:41	1000	
	20:25:25	22:29:51	1804	ERS-1
	23:47:42	23:58:01	620	
96/07/31	11:15:35	13:32:01	1978	NOAA-14
	13:37:52	14:07:52	1801	

	operation time		# of collected	target
date	start	end	images	satellite
96/08/01	9:22:05	11:00:47	1431	ERS-1
	11:58:25	13:01:14	911	NOAA-14
	17:32:04	18:49:51	1128	NOAA-12
96/08/02	8:38:31	8:55:10	1000	
	9:40:45	11:30:04	1585	ERS-2
	11:45:25	13:00:14	1085	NOAA-14
96/08/04	5:58:04	8:01:53	1795	NOAA-12
96/08/05	9:22:25	11:46:27	2088	ERS-2
	17:18:06	18:54:03	1261	NOAA-12
	20:36:04	22:00:08	1219	ERS-1
96/08/06	16:44:06	18:30:23	1541	NOAA-12
	20:34:52	22:00:39	1244	ERS-2
96/08/07	8:58:53	9:28:52	1800	
	9:38:05	11:00:09	1190	ERS-1
96/08/09	10:55:35	14:00:57	2687	NOAA-14
	20:35:45	21:46:13	1022	ERS-2
96/08/10	11:49:25	13:00:00	4236	NOAA-14

0-7803-3836-7/97/$10.00 © 1997 IEEE

0.07 deg.C[2].

Depending upon weather and sea state conditions, the pattern of temperature distribution changes delicately. Fig. 1 shows typical patterns of those.

Image A: This has a homogeneous spatial temperature distribution. The image was collected in the evening under cloud sky condition.

Image B: By existing patches of high and low temperature, this image has a large standard deviation of temperature. This was collected under clear sky and very calm condition at night.

Image C: The frame is divided into two distinct regions of low and high temperatures. The temperature difference of those is about 1.2 deg.C. This was collected in the evening under clear sky condition and the wind speed of 3 m/sec. M-SSO observed the vertical temperature difference between -0 cm and -50 cm about 1.2 deg.C. at the moment. The low temperature was caused by up-welling of the deeper water due to mixing by ship propeller.

Image D: This was collected under fear sky with cloud patches under the wind of 3 m/sec in the morning. The average of SST is about 21.1 deg.C, but the temperature at black spots

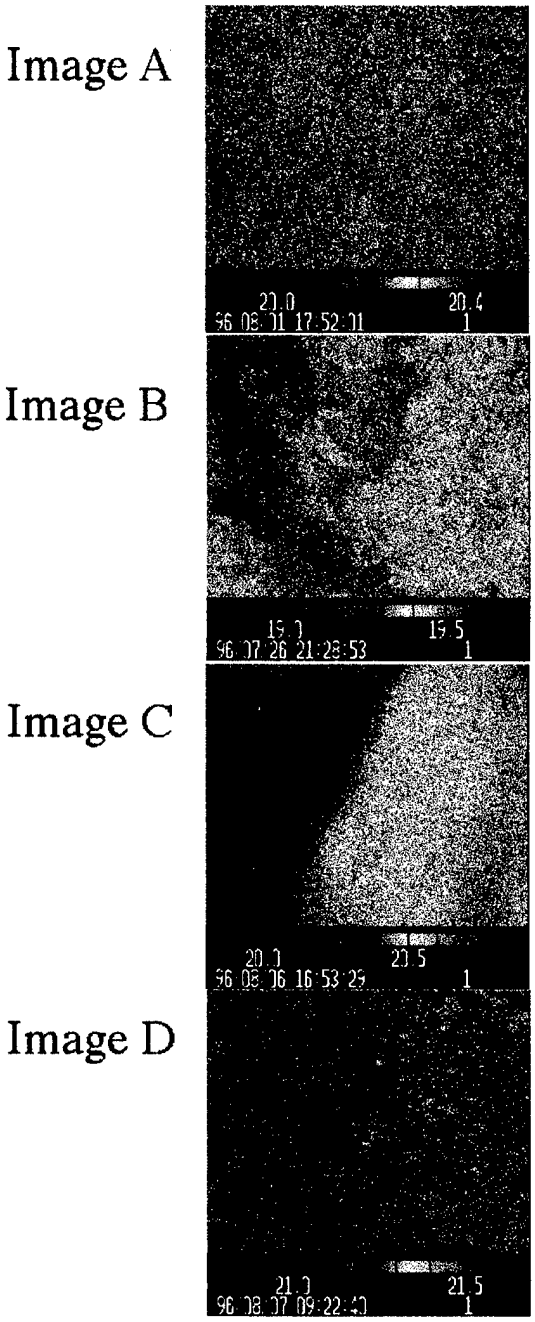

Image A

Date: 1996/8/1
Time: 17:52:01
Mean Temp.: 20.137 [deg.C]
S.D.: 0.088 [deg.C]
Max. Temp.: 20.39 [deg.C]
Min. Temp.: 19.89 [deg.C]
Sky: cloudy
Wind Speed: 3 [m/s]

Image B

Date: 1996/7/26
Time: 21:28:53
Mean Temp.: 19.255 [deg.C]
S.D.: 0.132 [deg.C]
Max. Temp.: 19.62 [deg.C]
Min. Temp.: 18.86 [deg.C]
Sky: clear
Wind Speed: 0 [m/s]

Image C

Date: 1996/8/6
Time: 16:53:29
Mean Temp.: 20.346 [deg.C]
S.D.: 0.241 [deg.C]
Max. Temp.: 20.94 [deg.C]
Min. Temp.: 19.77 [deg.C]
Sky: clear
Wind Speed: 3 [m/s]

Image D

Date: 1996/8/7
Time: 9:22:40
Mean Temp.: 21.115 [deg.C]
S.D.: 0.095 [deg.C]
Max. Temp.: 21.35 [deg.C]
Min. Temp.: 20.83 [deg.C]
Sky: patchy
Wind Speed: 3 [m/s]

Figure 1 Examples of TIC images under various weather conditions.

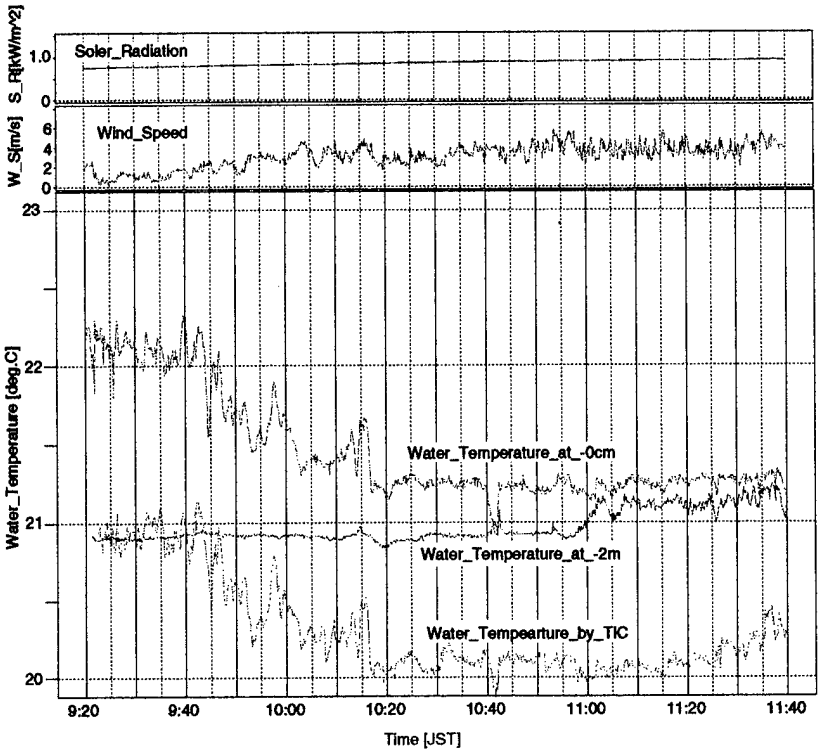

Figure 2 The combined data observed by the devices on the vessel from 09:20 to 11:40 (JST) on August 5th.

is higher than 30 deg.C. Those high temperature spots are caused by sun-glint. Usually, we have assumed the emissivity of sea surface to be 1.0, but this image suggests that the assumption is not necessarily correct.

Fig. 2 shows the combined graphs of data observed from 09:20 to 11:40 (JST: Japanese standard time) on August 5th. Solar radiation and wind speed were measured by M-Sta, water temperatures at -0 cm and -2 m were measured by M-SSO. TIC temperature means the average of each TIC image. The water temperature difference between -0 cm and -2 m was 1 deg.C at 9:20, but it gradually decreases as wind speed gradually increased from morning to noon. After 11:00, the temperature at -2 m increased a little and the temperature difference almost disappeared. The data relevantly show the process breaking the stratified temperature layers by wind. Another interesting aspect is the difference between water temperature at -0 cm and the water temperature by TIC. Although both temperatures changed temporally, their difference was kept almost constant as 1.0 deg.C. This suggests to estimate the amount of skin effect, but in order to get more definite answer, we need more data under various weather conditions.

CONCLUSION

Through MUBEX, we have established an observation system for validation of satellite SST and investigation of water temperature near sea surface. TIC data relevantly provides various aspects of spatial and temporal behaviors of sea skin temperature. MUBEX/97 will be held in the summer and we will get new data set. Because we have spent so much time to develop systems for data processing and correction algorithm, we are still in an early stage of data analysis. The MUBEX data will be expected to provide relevant aspects of air-sea interaction of heat exchange at sea surface.

ACKNOWLEDGMENTS

The MUBEX is supported by the grants from National Space Development Agency of Japan, Japanese Scientific Promotion Society, The Royal Society ,U.K., National Environmental Research Council, U.K. and DAIWA Anglo-Japanese Foundation. We want to show sincere appreciation to those organizations.

REFERENCES

[1] Tamba S., S. Oikawa, R. Yokoyama, I. Ridley, I. Parkes and D. Llewellyn-Jones, "The relationship between SST measured from ATSR to the spatial and temporal behavior of the ocean skin as observed with an in situ Thermal Infrared Camera", the proceedings of the 3rd ERS Symposium in Florence, Italy on March 1997.

[2] Tamba S., R. Yokoyama, "Line noise extraction of thermal infrared camera image in observing sea skin temperature," the proceedings of the IGARSS'97 Symposium, Singapore, August 1997.

MUBEX: Japan and U.K. Collaboration for Mutsu Bay sea surface temperature validation experiment

Ryuzo Yokoyama, Sumio Tamba, Takashi Souma
Department of Computer Science, Faculty of Engineering, Iwate University
4-3-5 Ueda, Morioka, Iwate, 020 JAPAN
Tel: +81-196-21-6478, Fax: +81-196-21-1170
E-mail: yokoyama@cis.iwate-u.ac.jp

David Llewellyn-Jones, Isabelle Parkes,
Earth Observation Science, Department of Physics and Astronomy, Leicester University
University road, Leicester, LE1 7RH, U.K.

Abstract: MUBEX (MUtsu Bay sea surface temperature validation EXperiment) is a Japan-UK joint research project for accuracy validation of sea surface temperature observed by satellite and investigating into the physical behavior of heat exchange at the ocean surface. The project started in 1995 with the term of three years. In this paper, we will describe the outline of MUBEX and introduce some data obtained.

INTRODUCTION

Mutsu Bay is located in the northern end of Honshu island of Japan as shown in Fig. 1. Composed of four moored buoys, Mutsu Bay Automatic Marine Monitoring Buoy System (MBAMMBS) has been measuring SST at 1m depth every hour. Five stations of Automatic Meteorological Data Acquisition System are distributed around the bay, and a radio sonde station at Misawa is located 30 km south-east of the bay. The data by those observation systems have been conveniently used for validation for SST estimated by satellite data.

Yokoyama, et al. proved that sea surface effect must be another major error factor in the SST estimation than atmospheric effect[1-4], and suggested the significance of investigation of air-sea interaction near sea surface.

OUTLINE OF MUBEX CAMPAIGN

MUBEX was organized by Prof. Yokoyama and Prof. Llewellyn-Jones. We have had two observation campaign in Mutsu Bay in the summer of 1995 and 1996 as follows [5].

MUBEX/95: from July 25th to August 28th,
MUBEX/96: from July 20th to August 19th.

For the campaign, we prepared devices to observed factors concerned with the air-sea interaction as much as possible. Those devices are classified into two categories, i.e., stationary observation devices and simultaneous observation devices.

SSO (Sea Surface Observer) and a sun-photo meter belong to the first group.

1) SSO: This is a newly developed device, of which measurement items and accuracy are shown in Table 1, and the data are stored in a logger. During the campaign, SSO had been set on No. 4 and No. 6 buoys of MBAMMBS, and operated with the measurements interval of 10 minutes. Fig. 2 shows the scheme of SSO setting on the buoy.
2) Sun-photometer: In order to observe aerosol density, a sun-

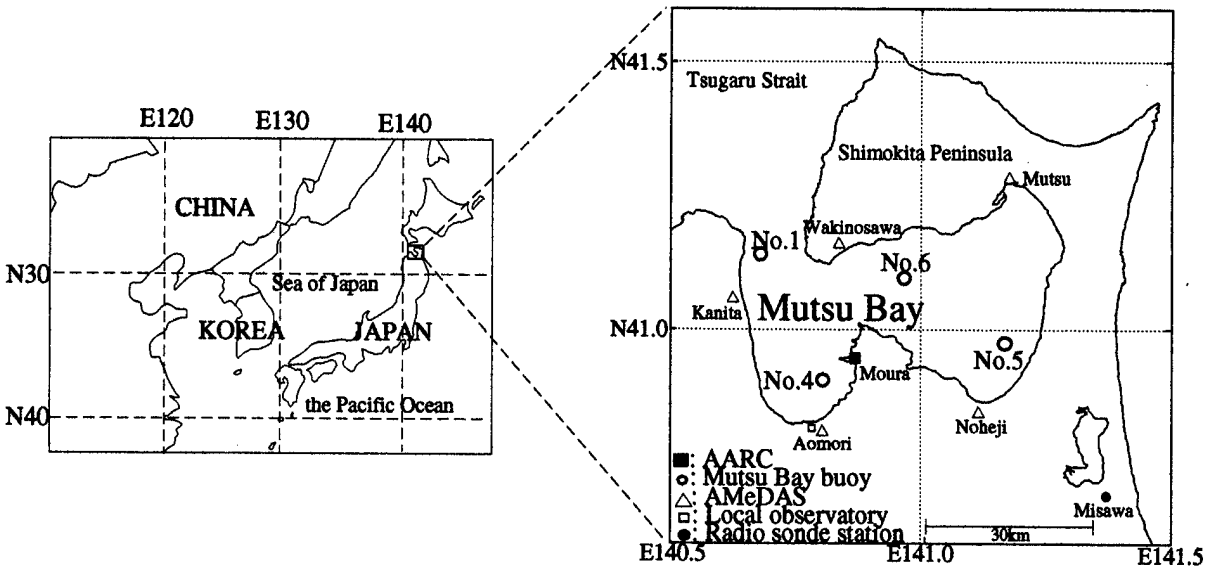

Figure 1 Geographical location of Mutsu Bay and various kinds of meteorological obsrvation positions.

0-7803-3836-7/97/$10.00 © 1997 IEEE

Table 1 Measurement Specifications of SSO and MSSO.

	Measurement Item	Measurement position	Nominal Accuracy
SSO	Water Temp.	0m, -0.3m, -1m, -2m	0.035[deg.C]
	Air Temp.	2m	0.31[deg.C]
	Humidity	2m	0.135[%]
	Wind Speed	3m	0.0275[m/s]
	Wind Direction	3m	0.27[deg.]
	Solar Radiation	3m	0.00125[mW/m/m]
MSSO	Air Temp.	0.3m	0.1[deg.C]
	Water Temp.	0m, -0.3m, -1m, -2m	0.1[deg.C]
	Solar Radiation	3m	0.00125[mW/m/m]

photometer was set on the roof of Aomori Aqua-culture Research Center, which is located at Moura (see Fig. 1). The measurement interval was set as 20 seconds for the whole term of the campaign.

Equipped on a special vessel as Fig. 3, devices of the second group are to observe the sea surface in detail. On a stage above 5 m sea surface at the bow, thermal radiometers and video cameras were fixed as follows.

3) Thermal infrared camera (TIC of NEC San-ei, TH3102m) to observe the sea skin temperature distribution,
4) Scanning Infrared Sea surface Temperature Radiometer (SISTeR developed by Rutherford Appleton Lab.) to observe thermal radiation from sea surface and sky,
5) Video camera to observe sea state,
6) Video camera to observe sky state,
7) Handy infrared thermometer (TASCO) to observe sea surface temperature, and
8) Handy infrared thermometer (TASCO) to observe sky temperature.

The following devices were fixed at various parts on the vessel.

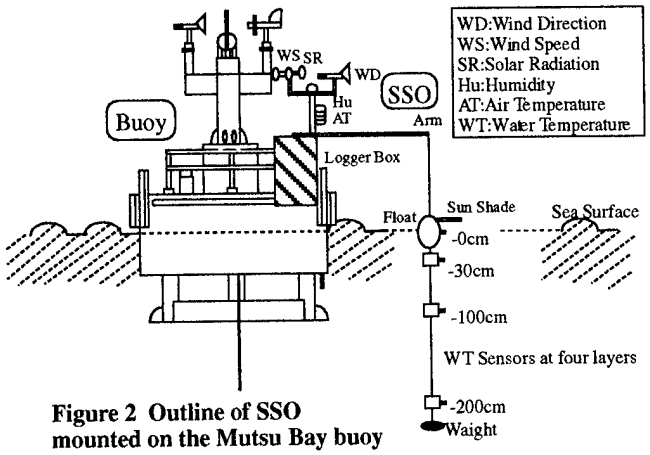

Figure 2 Outline of SSO mounted on the Mutsu Bay buoy

9) Moving-type SSO (M-SSO) to observe the vertical water temperature profile near the sea surface.
10) CTD to observe bulk temperature and conductivity of sea surface water.
11) Radiometer to observe solar radiation.
12) Meteorological Station.
13) Geographical positioning system (GPS) to record the vessel trace.
14) Video camera to record the azimuth of the vessel.

Under fine weather, the vessel was used to be operated from one hour before and to one hour after satellite overpass around No. 6 buoy, but the vessel was also operated under various weather conditions. The satellite sensors of object were ATSR/ERS-1 and ERS-2, AVHRR/NOAA-12 and NOAA-14, but OCTS/ADEOS is expected to be added in the MUBEX/97.

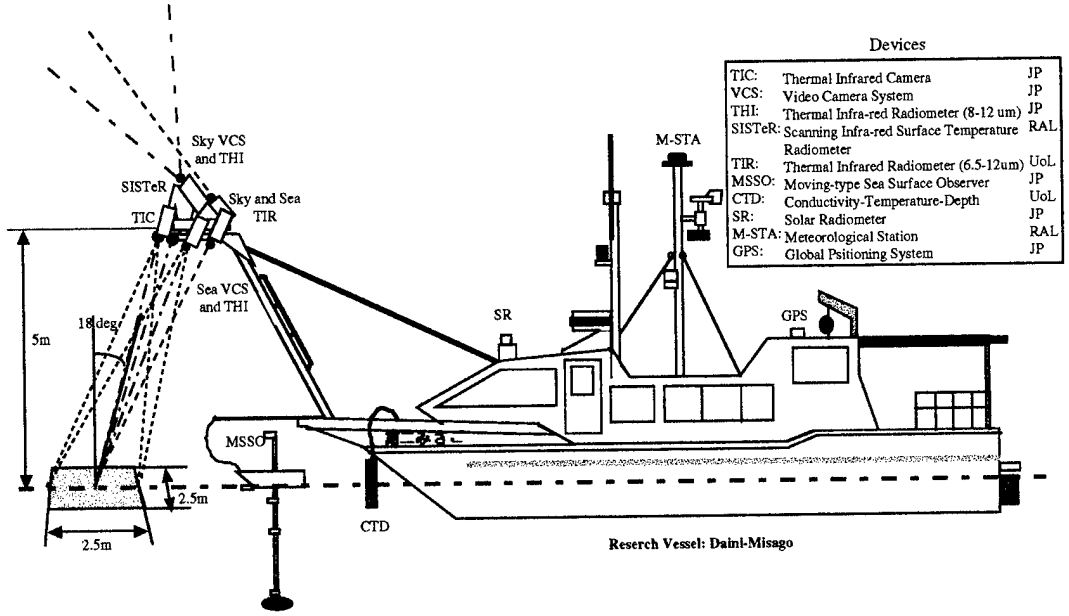

Figure 3 The schematic view of the instrumentation on the research vessel of MUBEX/96

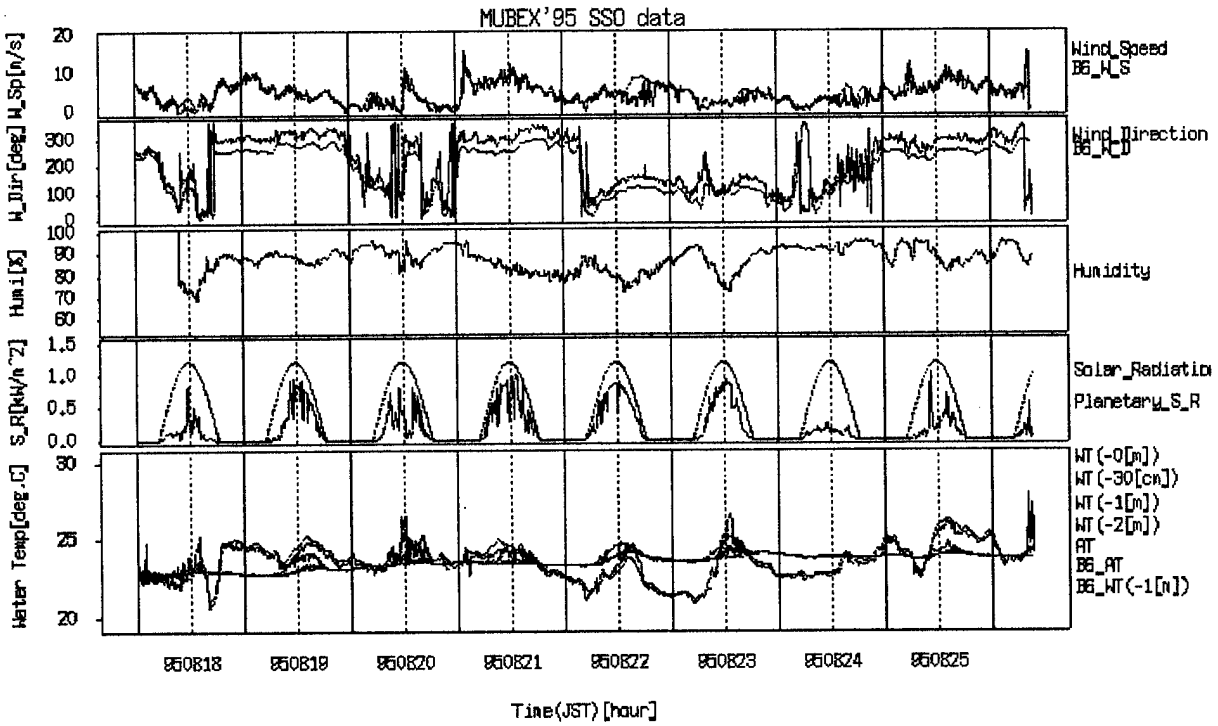

Figure 4 Example data by SSO on Mutsu Bay No. 6 buoy during 8/18 to 8/26/1995.

MUBEX DATA

In MUBEX/95, the total operation time of the vessel was about 50 hours. During the campaign, the total volume of digital data collected was about 3 GB, which include 30,000 frames of TIC images. There occurred various troubles in the devices, and we had to improve them thereafter. Also, we had intensively conducted in development of algorithms for data processing and noise extraction, inter-calibration between devices, etc. In MUBEX/96, the device improvement were almost successful, and the total volume of the collected digital data increased to 5 GB. Fig. 4 shows an example of the data by SSO during 8/18 to 8/26/1995. The large divergence of the water temperatures was observed on August 23 when it was very fine and calm during daytime.

CONCLUSION

We have been finding relevant behaviors of sea surface temperature through MUBEX data, but we are expecting the final observation campaign in the summer of 1997 with improved devices. In the final stage of the project, it is expected that the those results will contribute for better understanding of the physical process of heat exchange between air and sea, and improve the accuracy of SST observed by satellites.

ACKNOWLEDGMENTS

The MUBEX is supported by the grants from National Space Development Agency of Japan, Japanese Scientific Promotion Society, The Royal Society ,U.K., National Environmental Research Council, U.K. and DAIWA Anglo-Japanese Foundation. We want to show sincere appreciation to those organizations.

REFERENCES

[1] Yokoyama, R., and Tanba, S., "Estimation of sea surface temperature via AVHRR of NOAA-9 Comparison with fixed buoy data," Int. J. Remote Sens., vol. 12, pp. 2513-2528, 1991.

[2] Yokoyama, R., Tanba, S., and Souma, T., "Air-sea interacting effects to the sea surface temperature observation by NOAA/AVHRR," Int. J. Remote Sens., vol. 14, 2631-2646, 1993.

[3] Yokoyama, R., Tanba, S., and Souma, T., "Sea surface effects on the sea surface temperature estimation by remote sensing," Int. J. Remote Sens., vol. 16, 227-238, 1995.

[4] Yokoyama, R., Konda, M., "Sea surface effects on the sea surface temperature estimation by remote sensing - Part 2," Int. J. Remote Sens., vol. 17, 1293-1302, 1996.

[5] Tamba S., S. Oikawa, R. Yokoyama, I. Ridley, I. Parkes and D. Llewellyn-Jones, "The relationship between SST measured from ATSR to the spatial and temporal behavior of the ocean skin as observed with an in situ Thermal Infrared Camera", the proceedings of the 3rd ERS Symposium in Florence, Italy on March 1997.

IGARSS'97

1997 International Geoscience and Remote Sensing Symposium

03-08 August 1997

Singapore International Convention & Exhibition Centre

Technical Program

Interactive Area 17: Remote Sensing Data Processing Techniques

SIMULATION OF SPLIT-WINDOW ALGORITHM PERFORMANCE

Sune R.J. Axelsson
National Defence Research Establishment and Saab Dynamics AB
P.O. Box 1165, S-581 11 LINKÖPING
Fax:+46-13-186215, Email: sunax@weald.air.saab.se

Bengt Lundén
Department of Physical Geography
Stockholm University, S-106 91 STOCKHOLM
Fax:+46-8-164818

Abstract--Various methods for correction of the atmospheric influence in the thermal IR-windows 3-5μ and 10-13μ have been proposed. One such method is the split-window technique for correction of AVHRR data. From earlier work, there are significant variations in the suggested coefficients of this algorithm. Over land surfaces, variations in emissivity have also to be compensated for. In this paper, the optimum choice of coefficients is investigated against a set of standard atmospheres using a prediction model including the emissivity effects of a land surface. It is obvious from the results that instead of using fixed standard coefficients estimated over a wide spread of atmospheric conditions, the optimum coefficients should be computed based on the best guess of the present atmospheric path parameters and on estimated emissivity values of the individual pixels.

1. INTRODUCTION

The atmospheric transmittance in the thermal IR-windows 3-5μ and 10-13μ is mainly controlled by the water vapour content. Various methods for correction of the atmospheric influence have been proposed. One such method is the split-window technique for correction of thermal AVHRR data [2]-[7]. Most applications and verifications have been made against a sea-surface. Over land surfaces, the varying emissivity in the two bands has a dominating effect on the error of the estimated surface temperature and has to be compensated for [4], [7].

From earlier work, there are significant variations in the suggested coefficients of the linear split-window algorithm. In this paper, the optimum choice of coefficients was tested against a set of standard atmospheres and the optimum coefficients were evaluated, including the emissivity effects of a land surface.

It is obvious from the results that instead of using fixed standard coefficients estimated over a wide range of atmospheric conditions, the optimum coefficients should be computed based on the best guess of the atmospheric path parameters of the scene, using available information from near-by weather stations or satellite profiling observations as input.

2. SIMULATION MODEL

The thermal spectral radiance from the surface measured through a non-scattering atmosphere at wavelength λ can be described as follows

$$B(\lambda,T_d) = \tau_s B(\lambda,T_{IR}) + \int_{p_s}^{p_0} B[\lambda,T(p)](d\tau/dp)dp \qquad (1)$$

where T_{IR} represents the measured IR-temperature at surface level, B(λ,T) is the Planck function of the blackbody spectral radiance and p,T are the local atmospheric pressure and temperature along the path of observation.

The transmission function τ, which at slanting observations also depends on the nadir angle φ, denotes the transmittance between the satellite (pressure p_0) and the altitude corresponding to pressure p. The transmittance between satellite and surface (p_s) is represented by $\tau_s=\tau(p_s,\phi)$.

The IR-temperature measured at surface level (T_{IR}) differs from the real surface temperature (T_s) due to the reduced emissivity compared with a black-body radiator. A second term includes the reflected component of the down-welling radiation from the atmosphere having the equivalent black-body temperature T_{ad}. Hence,

$$B(\lambda,T_{IR}) = \varepsilon B(\lambda,T_s) + (1-\varepsilon) B(\lambda,T_{ad}) \qquad (2)$$

Usually $T_s>T_{ad}$, which means that T_{IR} gives an underestimation of the surface temperature ($T_{IR}<T_s$).

For Lambert reflecting surfaces

$$B(\lambda,T_{ad}) = (1/\pi) \int_0^{2\pi} \int_0^{\pi/2} B[\lambda,T,\theta,\varphi]\sin(\theta)\cos(\theta)d\theta d\varphi \qquad (3)$$

where $B[\lambda,T,\theta,\varphi]$ is the downwelling spectral sky radiance at zenith angle θ and azimuth angle φ and computed from

0-7803-3836-7/97/$10.00 © 1997 IEEE

$$B[\lambda,T,\theta,\varphi] = \int_{p_0}^{p_s} B[\lambda,T(p)][d\,\tau_d(p,\theta,\varphi]/dp]dp \quad (4)$$

and $\tau_d = \tau_s/\tau$ represents the path transmission between the surface and pressure level p.

In the computer program, N_0 horizontal layers (n=1,.., N_0) are defined, starting from satellite level. For each layer, pressure (p_n), specific humidity (q_n), and air temperature (Ta_n) are defined from an input data file. In the simulation model, rotation symmetry along the zenith axis is assumed i.e. no dependence on the azimuth angle φ and the computations are performed for K different wavelengths (k=1, ..,K).

The downward transmission from layer 1 to the underside of the n:th layer ($\tau d_{n,k}$) is described as a product of three transmission factors

$$\tau d_{n,k} = \tau lin_{n,k}\, \tau con_{n,k}\, \tau rest_{n,k} \quad (5)$$

where τlin takes into account the H_2O line absorption, τcon the H_2O continuum absorption and τrest the absorption from other gases. From Kneizy et al [1]

$$\tau rest_{n,k} = \exp[-\sum_{m=1}^{n} \Delta\alpha rest_{m,k}] \quad (6)$$

where

$$\Delta\alpha rest_{m,k} = 33\cdot 10^{-8} \Delta p_m (p_m/p_{sa})^{3/4} (T_{sa}/Ta_m)^{3/8} \quad (7)$$

and index *sa* refers to standard atmospheric conditions.

The line attenuation $\tau lin_{n,k}$ is computed from the Lowtran5 subroutinge C10TA, which contains the ^{10}logarithm of the line attenuation coefficients of water vapour versus wavelength ($Clin_k$). The weighted averages of air pressure and air temperature from layer 1 to n are estimated using the individual watermasses of the layers as weighting coefficients. From $p_{av}(n)$, $Ta_{av}(n)$ and the total watermass M(n), contained within layers 1 to n, a modified watermass is computed taking into account deviations from standard pressure and temperature

$$M_{mod}(n) = M(n)\{[p_{av}(n)/101300][273/Ta_{av}(n)]\}^{0.9} \quad (8)$$

From $X_{n,k}=\log[M_{mod}(n)]+Clin_k$ and table interpolation, the transmission $\tau lin_{n,k}$ is finally found. See [1].

The continuum transmission factor is computed from

$$\tau con_{n,k} = \exp[-\sum_{m=1}^{n} \Delta\alpha con_{m,k}] \quad (9)$$

where

$$\Delta\alpha con_{m,k} = k_{m,k} q_m \Delta p_m / g \quad (10)$$

with $\Delta p_m = p_m - p_{m-1}$ and

$$k_{m,k} = k_2(\lambda_k, Ta_m)[\gamma(p_m - e_m) + e_m] \quad (11)$$

where e_m is the water vapour pressure (Pa), γ=0.002 and

$$k_2(\lambda,T) = [4.18+5578\exp(-78.7/\lambda)]\exp[1800(1/T-1/296)] \quad (12)$$

The transmission from the top of the atmosphere to the surface in (1) is then $\tau d_{N0,k}$ and the transmission from the surface to the underside of layer n is derived from

$$\tau u_{n,k} = \tau d_{N0,k}/\tau d_{n,k} \quad (13)$$

The path radiance at a nadir angle ϕ representing the second term of (1) is estimated from

$$Bup_k = \sum_{n=1}^{N_0} B(\lambda_k, TA_n)[\,(\tau d_{n-1,k})^z - (\tau d_{n,k})^z] \quad (14)$$

where $z=1/\cos(\phi)$.

The down-welling radiance from the atmosphere in (2)-(4) is computed in the following way

$$Bdown_k = 2\sum_m \sum_n B(\lambda_k, TA_n)\,[(\tau d_{n-1,k})^{z(m)} - (\tau d_{n,k})^{z(m)}]\,\sin(\theta_m)\cos(\theta_m)\Delta\theta \quad (15)$$

where n=1 to N, m=1 to M, $\Delta\theta = \pi/(2M)$, $\theta_m = m\pi/(2M)$ and $z(m)=1/\cos(\theta_m)$.

From these basic relationships, the detected spectral radiance $Bdet_k$ of (1) is computed. The mean spectral radiance within the wavelength window is then obtained using the combined transmission coefficients (H_k) of the detector and filter (k=1,..,K)

$$B_{det} = \sum H_k Bdet_k / \sum H_k \quad (16)$$

By inversion of the relationship $B_d(T) = \sum H_k B(\lambda_k,T)/\sum H_k$, the equivalent blackbody temperature T_{det} is then estimated.

A more approximate method estimates the blackbody temperature from $T_k = B^{-1}(\lambda_k, Bdet_k)$ where $B^{-1}(x)$ is the inverse Planck function followed by

$$T_{det} = \sum H_k T_k / \sum H_k \quad (17)$$

Filter coefficients for AVHRR channel 4 and 5 and TM band 6 have been defined using a wavelength inverse step of 20 cm^{-1}.

3. INVERSION MODEL

At the temperature correction of thermal IR-data from satellites, there are several possible ways. One main method is to estimate the temperature correction computed from available atmospheric profiling data over the scene.

By using the above simulation model, the detected black-body temperature at TM band 6 and AVHRR channel 4 and 5 have been computed versus surface temperature in 5 degrees steps between 270 and 320 K (j=0,1,..,10) for surface emissivity varying in 0.02 steps (p=0, 1,...,5) between ε=0.9 to 1.0. For each band a table of the temperature error versus surface temperature and emissivity is formed

$$\Delta T_{j,p} = Tsurf_j - Tdet_{j,p} \quad (18)$$

From the inverted table, the correction ΔT is obtained using the emissivity and detected IR-temperature as input. Hence, the estimated surface temperature becomes

$$T_s = T_d + \Delta T(T_d,\varepsilon) \quad (19)$$

Tables have been computed for the standard atmospheres: tropical, subartic winter and summer, midlatitude winter and summer. A similar procedure has also been applied to correction of TM band 6 scenes using radiosonde data profiles as input [5].

For AVHRR, which contains two adjacent IR channels, the split window algorithm can be applied. In that case, the surface temperature is estimated from a linear relationship between the temperatures detected in channel 4 and 5.

$$T = a_0 + a_1T4 + a_2T5 \quad (20)$$

Figure 1 shows (18) for the standard atmosphere subartic summer for AVHRR 4 and 5 when ε=0.96 and ε=1.0. It is obvious that emissivity variations over land areas should be corrected for, if possible.

Figure 2 shows the predicted temperature difference T4-T5 of the AVHRR channel 4 and 5 for emissivity variations from 0.92 to 1.0.

The optimum selection of the coefficients of (20) has been studied by many investigators, in particular for sea surfaces, where the emissivity effects can be neglected.

For instance, Dechamps and Pulpin [2] apply: a_0=-2.2, a_1=3.6 and a_2=-2.6; Li and McDonnell [6]: a_0=-0.45, a_1=3.68 and a_2=-2.68; Price [3]: a_0=0, a_1=4.33 and a_2=-3.33.

Becker and Li [7] discuss the influence of emissivity (ε) on the split-window coefficients and give the following coefficients: a_0=1.274 and a_1=(P+M)/2, a_2=(P-M)/2, where P=1+0.156(1-ε)/ε and M=6.26+3.98(1-ε)/ε when $\varepsilon_4=\varepsilon_5=\varepsilon$.

In our study, the optimum choice of the split-window algorithm was investigated over a wide range of atmospheric conditions. The detected IR-temperatures of AVHRR channel 4 and 5 were first predicted versus surface temperature in 5 degrees steps for surface emissivities varying independently in the two channels in 0.02 steps between ε = 0.9-1.0. The selected standard atmospheres were tropical and midlatitude summer (both T_{surf}=280-320K), midlatitude winter (T_{surf}=270-290K), and subartic summer (T_{surf}=280-310K).

The linear regression coefficients of the split-window algorithm were then computed for each atmosphere and combination of ε-values in the two bands. Split-window coefficients were also estimated from combined data from all the four standard atmospheres. For this case, Figure 3 shows the error between the surface temperature and the predicted one for $\varepsilon_4=\varepsilon_5$=1 giving an rms errror of 0.64 K.

Significantly lower errors are obtained for coefficients adapted to one specific atmosphere, if the emissivity effects can be neglected. The simulation results also show that the error does not significantly increase, if we in (20) apply $a_2=1-a_1$ instead of using a true three-parameter algorithm.

Our simulations verify that the surface temperature estimation error is very sensitive to emissivity differences between channel 4 and 5. See also Becker and Li [7]. If for instance, the coefficients of (20) are selected from $\varepsilon_4=\varepsilon_5$=0.96, the rms-error will be 0.7 K when this assumption is true. If the true values are ε_4=0.96 and ε_5=0.94, however, the rms error is increased to 1.7 K.

Conversely, if ε_4=0.94 and ε_5=0.96, the rms error is increased further to 2.9 K. If the true emissivities are moved in the same direction $\varepsilon_4=\varepsilon_5$=0.94, the rms error 1.3 K will be obtained. Estimation of the local pixel emissivities is thus much important in optimizing the performance of the split-window algorithm for land surface temperature predictions.

Figure 4 shows the relationship between the needed correction of the IR-temperature from TM band 6 and the measured temperature difference between AVHRR channel 4 and 5, computed for ε=0.96. This relationship might be used as a first-order correction of TM-data using the AVHRR temperature difference T4-T5 as input.

4. CONCLUSIONS

In this paper, the optimum choice of split-window coefficients for AVHRR data in channel 4 and 5 was estimated against a set of standard atmospheres, including the two-channel emissivity effects of a land surface.

It is obvious from the results that instead of using fixed standard coefficients estimated over a wide spread of atmospheric conditions, the optimum coefficients of the split-window algorithm should be computed based on the available information about the atmospheric path parameters from the scene and the two-channel emissivity factors of the individual pixels. The use of available information from near-by weather stations, satellite sensors and GIS-data will thus significantly improve the accuracy compared with split-window algorithms using fixed coefficients.

REFERENCES

[1] F. X. Kneizys el al, Atmospheric transmittance/ radiance computer code Lowtran 5, Air Force Geophysics Laboratory, Massachusetts, Report No. AFGL-TR-80-0067.

[2] P.Y. Deschamps and T. Phulpin, Atmospheric correction of infrared measurements of sea surface temperature using channels 3.7, 11 and 12 μm, 1980, Bound. Layer Meteorol. 18:131-143.

[3] J.C. Price, Estimating surface temperatures from satellite thermal infrared data - a simple formulation for the atmospheric effect. Remote Sensing of Environment, 1983, 13:353-361.

[4] S.R.J. Axelsson, Estimation of land surface temperature from multiple channel AVHRR data. Proc. 19th Int. Symp. Rem. Sens. Env., Ann Arbor, Michigan, October 21-25, 1985, 511-522.

[5] S. R.J. Axelsson and B. Lundén, Atmospheric correction of thermal infrared data from Landsat-5 for surface temperature estimation, Proc. 4th Int. Colloq. Spectral Signatures of Objects in Remote Sensing, Aussois, France, 18-22 January, 1988, ESA SP-287, pp. 197-200.

[6] Z. R. Li and M. J. McDonnell, Atmospheric correction of thermal infrared images, Int. J. Remote Sensing, 1988, 8:107-121.

[7] F. Becker and Z-L Li, Towards a local split window method over land sufaces. Int. J. Remote Sensing, 1990,11:369-393.

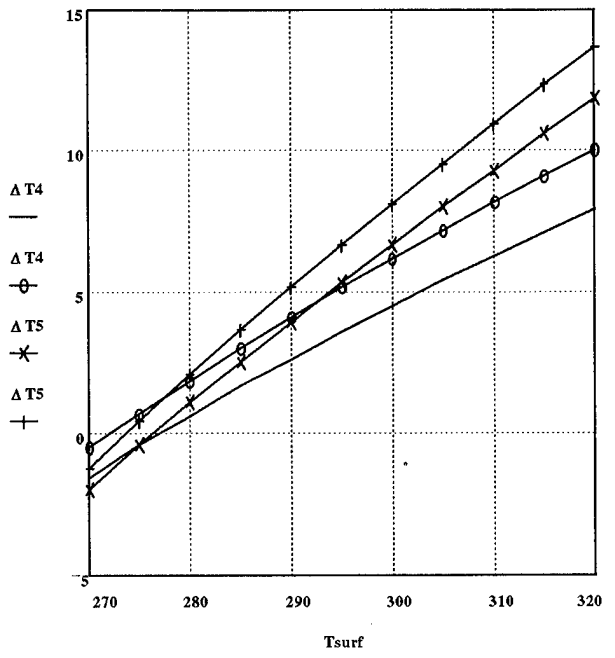

Figure 1: Predicted temperature error ΔT = Tsurf - Tdet of AVHRR channel 4 and 5 for subartic summer and ε=0.96 (0,+) and ε=1.0 (-- and x).

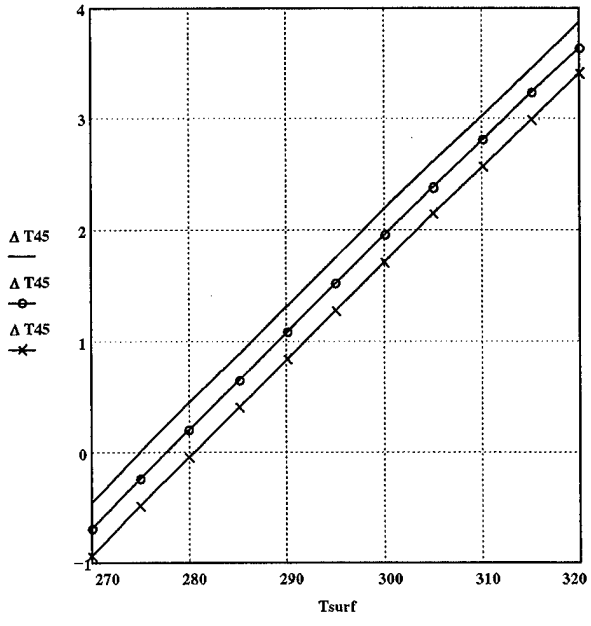

Figure 2: Temperature difference T4-T5 measured by AVHRR channel 4 and 5 for varying surface temperature and emissivity ε4=ε5=1.0 (---), 0.96 (-0-) and 0.92 (-x-)

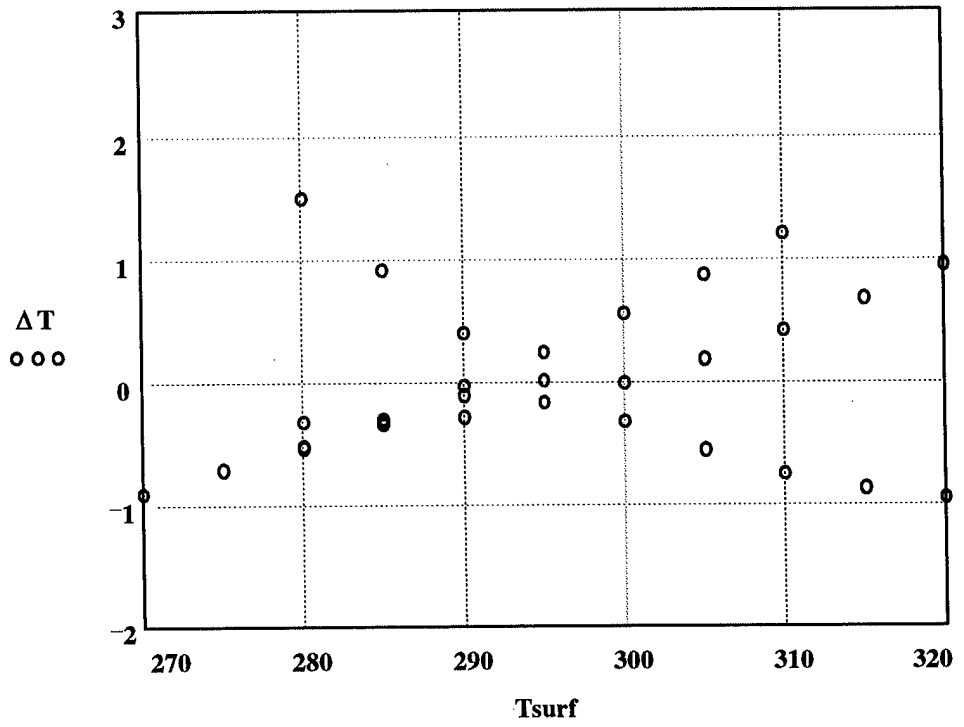

Figure 3: The error between the surface temperature and the predicted one for ε=1.

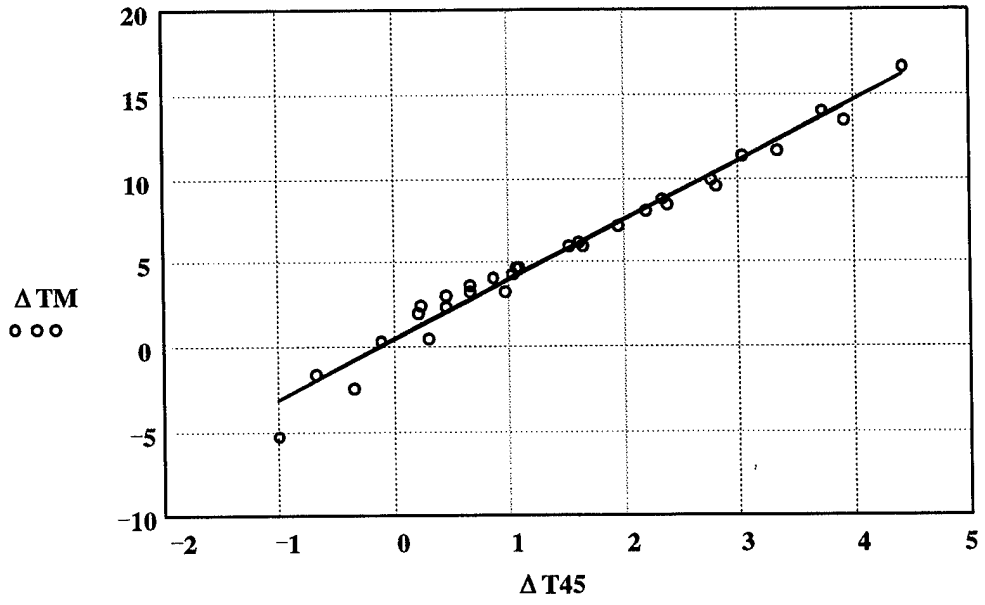

Figure 4: The relationship between the needed correction of IR-temperatures from TM band 6 and the measured temperature difference between AVHRR channel 4 and 5 computed for ε=0.96.

Analysis of Single and Multi-Channel SAR Data Using Fuzzy Logic

Ursula Benz
German Aerospace Research Establishment - Institute for Radio Frequency Technology
P.O. Box 116 / 82230 Wessling / Germany
tel.: 49 8153 28 2312 / fax.: 49 8153 28 1449 / e-mail: Ursula.Benz@dlr.de

INTRODUCTION

Synthetic aperture radar (SAR) delivers important information for remote sensing. High resolution images are obtained independent of weather conditions and daylight. The user community of SAR data increases steadily and is no more restricted to scientists. However, two main problems reduce the acceptance of SAR sensors: The huge data rate difficults real-time distribution and the interpretation of SAR images requires special SAR knowledge of the user. While scientific applications will still need the whole amount of data, many users will only consider SAR data for their tasks, if they can access pre-classified data easily and in (near) real-time. Therefore, an application dependent SAR classification has to be applied on the data to extract the required information. Classification will not only simplify data interpretation but it will also lead to a significant data compression.

This paper proposes a fuzzy system to build such an adaptive remote sensing classification module. Fuzzy Logic allows simple algorithms, gives the system a high tolerance to parameter variations and adaptivity can easily be implemented. Chapter 2 describes the system to classify one SAR channel. It allows a user to define interactively the data classes of interest and thus realizes a flexible analysis of SAR data. The system adapts itself to the various user requirements. In many cases one data source does not deliver enough information to perform the required classification. Data fusion of several sensors or various sensor channels has to be taken into account. Chapter 3 presents a new approach to fuse the classification results of three SAR polarization channels. The algorithm uses the FLVQ's output of each channel and consists mainly of a fuzzy rule base. This rule base is adaptive to the data sets and to the user requirements.

INTERACTIVE DATA ANALYSIS USING FUZZY LOGIC

The proposed fuzzy system (see fig. 1) consists of two parts, the supervised learning Fuzzy Comparison of Distributions (FCOD) and the unsupervised learning Fuzzy Learning Vector Quantizer (FLVQ). The FCOD forms the main part and was developed at DLR [1]. It is a blockwise classification method which compares the block's measured distribution to the typical distributions of selected data classes. The higher the similarity of measured and trained distribution, the higher is the possibility for the data block to belong the according object class. During training the user decides which object classes he wants to have classified and presents the system labelled training data for each class. The system divides the data into blocks and learns for each object class the SAR data block's typical intensity distribution. The user does not need to know any theoretic scattering models of the selected classes or their typical distributions.

The input of the FCOD is the measured distribution of a data block. Then the FCOD performs a non-parametric comparison of this distribution to the distributions learned during training. Thus, the FCOD delivers much more information about each data block than statistic parametric estimation does. For example, a parametric classification would not allow a discrimination between normal water and flooded region. The fuzzy system achieves in our experiment (compare fig. 2) an average classification accuracy of 60 %. The FCOD's output is a fuzzy variable containing the block's membership degrees to the classes defined by the user. In opposite to common classification systems, fuzzy systems do not force an exclusive membership of a data block to one class, but allow partial memberhips to more than one object class. Thus, the FCOD's fuzzy output variable does not only lead to SAR classification but also includes the degree of the unavoidable uncertainty of classification. This makes the results more meaningful.

Fig. 2 shows the classification result of an E-SAR data set taken during a flood monitoring mission in January 1995. Five

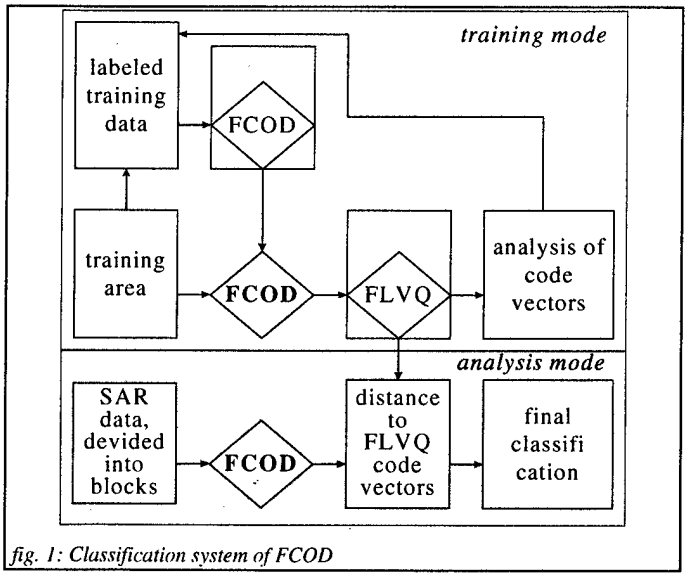

fig. 1: Classification system of FCOD

0-7803-3836-7/97/$10.00 © 1997 IEEE

classes should be distinguished: Forest, urban, shore, water and flooded region. Fig. 2a shows the SAR data set itself, fig. 2c and fig. 2e show the data block's membership degrees - evaluated by FCOD - to the object classes: "normal water" and "flooded region".

The FCOD's classification accuracy depends significantly on the chosen training data sets. If too few or not typical data sets are presented to the system the classification fails of course. The FLVQ [2], an unsupervised learning vector quantization, is applied on the FCOD's output to reduce this general disadvantage of supervised learning systems.

To train the FLVQ, first the FCOD is applied on the whole training area (see fig. 1). The FCOD's output vectors form the FLVQ's input vector space. The FLVQ finds unsupervised typical clusters and representative vectors μ in the input vector field. These vectors μ deliver information about the learning process. Their analysis is used to improve iteratively the classification system of FCOD and FLVQ. In opposite to the Learning Vector Quantization [3], the FLVQ is independent of the initial code book and the sequence of the training samples. Here, for SAR classification, the number of clusters is the number of user defined classes plus one. The additional object class gathers all unknown subjects (fig 2f) and reduces misclassification significantly. In most cases the FLVQ leads to higher dynamic in classification than the FCOD in its stand alone version does (compare fig. 2c and 2d).

Final classification is performed by mapping the SAR data block to the class with the highest membership degree. Fig. 2d shows the flood monitoring data set's final classification by FCOD and FLVQ.

If analysis of the FLVQ's code vectors tells that the system cannot distinguish between desired object classes the reason may be too few or bad training samples. In this case, iterative FCOD and FLVQ training will lead to improvements. However, if the reason is the disability to distinguish the selected object classes with the chosen sensor data at all only data fusion of several sensors will deliver sufficient classification.

DATA FUSION USING ADAPTIVE FUZZY OPERATIONS

Data fusion is an important research topic of the remote sensing community. There is no doubt about the necessity to use the synergy of various sensors and sensor channels. One presupposition for valid classification is the exact coregistration of the considered data sets. This is given for polarimetric SAR data. The full polarimetric mode of SAR delivers three different coregistered data sets (HH, VV, VH+HV).

Here, we don't aim at an optimum polarimetric classification, but we want to prove the ability to fuse sensor channels which are classified by FCOD and FLVQ. Therefore, we only use intensity data of the polarimetric SAR channels and apply the classification system described in the previous chapter on each channel separately. Thus any polarimetric phase information is neglected and the expected classification accuracy is of course less than it would be if special polarimetric classification systems are applied [5].

In our approach, the fusion of classification bases on a detailed analysis of the FLVQ's code vectors. Table 1 shows the code vectors for our polarimetric data set (see fig. 4a). It is taken by DLR's ESAR [4] and shows the runway of Oberpfaffenhofen with surrounding forest, low vegetation and urban areas. Four object classes, low vegetation, forest, road and urban, should be distinguished by the FCOD. Therefore, 5 clusters are to be found by the FLVQ and respectively 5 code

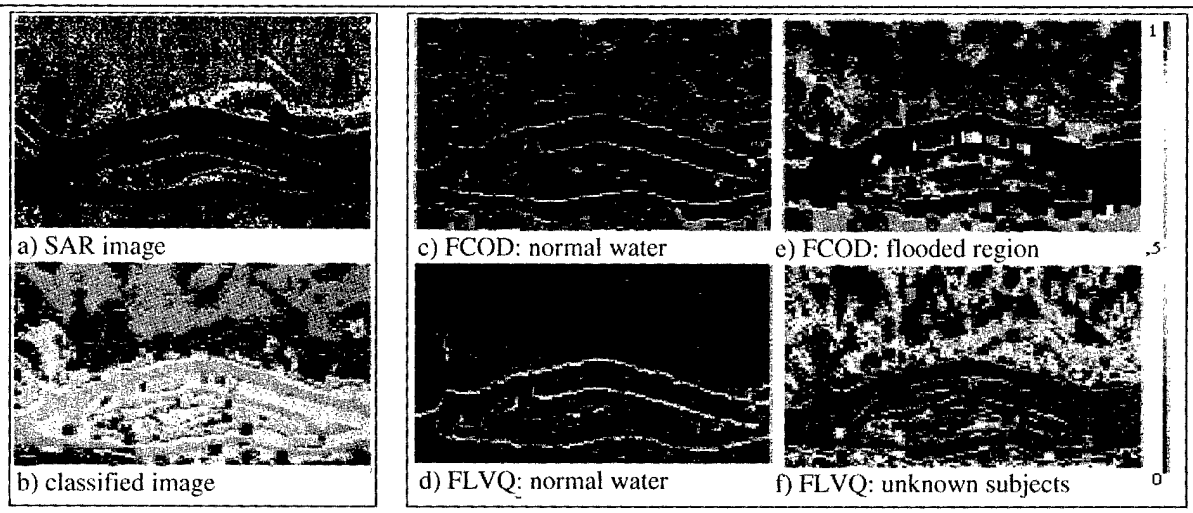

fig. 2: Classification by FCOD and FLVQ, trained to distinguish between water, shore, flooded region, forest and urban.
a) SAR image taken by the German E-SAR [4] during a mission for flood monitoring, the image shows a floods insular within two river arms
b) classification by FCOD and FLVQ, green: forest, red: urban, brown: shore, dark blue: normal water, light blue: flooded area ;
c) - f) false colour presentation of memberships: dark means no membership, red membership eq. to one, green is indifferent (see left bar) membership to: c) normal water after FCOD d) flooded region after FCOD, e) normal water after FLVQ f) class unknown after FLVQ

	low veg	forest	road	urban	automatic class mapping
μ_1(HH) =	(0.0,	**0.8**,	0.0,	**0.9**)	forest or urban
μ_2(HH) =	(0.0,	0.0,	**0.9**,	0.0)	road
μ_3(HH) =	(**1.0**,	0.0,	**1.0**,	0.0)	low veg or road
μ_4(HH) =	(0.1,	0.2,	0.2,	0.2)	
μ_5(HH) =	(0.2,	0.1,	0.2,	0.2)	
μ_1(VV) =	(0.0,	0.1,	0.0,	**0.9**)	urban
μ_2(VV) =	(0.0,	**0.9**,	0.0,	**1.0**)	forest or urban
μ_3(VV) =	(0.2,	0.0,	**1.0**,	0.0)	road
μ_4(VV) =	(**0.9**,	0.0,	0.2,	0.0)	low veg
μ_5(VV) =	(0.2,	0.2,	0.2,	0.2)	
μ_1(VH) =	(0.0,	0.0,	0.0,	**0.9**)	urban
μ_2(VH) =	(0.0,	**0.7**,	0.0,	**0.9**)	forest or urban
μ_3(VH) =	(0.1,	0.0,	**0.9**,	0.0)	road
μ_4(VH) =	(**1.0**,	0.0,	**1.0**,	0.0)	low veg or road
μ_5(VH) =	(0.1,	0.1,	0.2,	0.0)	

Tab. 1: FLVQ code vectors μ for polarizations HH, VV and VH and their automatic mapping to user defined) object classes (first row)

vectors μ for each polarisation channel are learned. The mapping of a code vector to an user defined object class is very straightforward. The first component gives the membership to class 1, the nth component to class n respectively. The cluster represented by the code vector μ consists of the union of those object classes n, where the code vector's components are approximately one. If only the nth component is close to one and all others are approximately zero, the represented class is exactly the user defined object class. If several components of a code vector are less than 0.5 and larger than zero, the according cluster contains a lot of unknown subjects. The possibility map to this cluster will not be used for data fusion. If this is the case for all code vectors of one sensor channel, this channel will not be used for data fusion and will be switched off for the considered application. The code vector analysis can be automatically performed (last column in table 1) and defines the fuzzy rule base of the data fusion system (see fig 3). The fuzzy operators in this rule base allow to handle the fuzzy output of the FLVQ, but they can also evaluate data fusion,

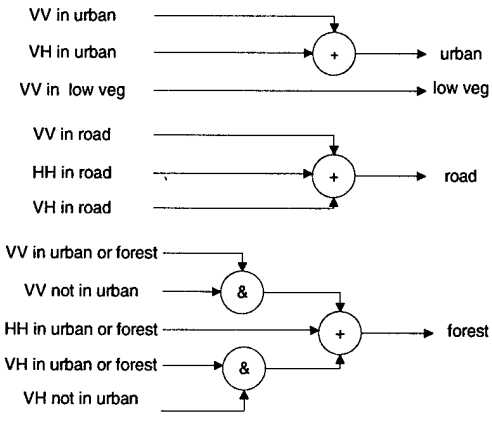

fig. 3: application dependent classification rule base, explanation of terminology: X in j means: classification of channel X maps the data block to object class j, the conjunctions are fuzzy oper ations to handle the multi-valued memberhip degrees.

if only bi-valued memberships ("member" and "no member") are fed into the system from a common classification system. Further, the rule base is not restricted to polarimetric SAR data classification. The data source is of no importance to the system design. However, our first classification results of polarimetric data are very promising (see fig.4).

CONCLUSION

Our simulations proved that fuzzy systems lead to highly adaptive classification systems of single and multi-channel SAR data. A flexible system was presented to classify polarimetric data. The results are transferable to other sensor data as long as coregistration is given.

The proposed fuzzy systems possesses only a small complexity. A lot of computations can be performed in parallel. This allows simple hardware realization. A (near) real-time SAR classification - adaptive to various remote sensing applications- is possible. Increased classification results will be achieved, if the FCOD not only learns typical intensity distributions but also typical (polarimetric) parameters. In operational mode measured distributions and parameters will be compared to the learned values. The system design itself remains unchanged. Of course, not only the classification accuracy, but also the computational complexity is increased. A careful tradeoff has to be performed.

REFERENCES

[1] U. Benz, "Possible improvements of Synthetic Aperture Radar (SAR) using Fuzzy Logic," SPIE vol. 2761, pp. 210-221, April 1996

[2] J. Bezdek, "Soft Learning Vector Quantization," SPIE vol. 2493, pp. 164-177, April 1995

[3] Y. Linde, A. Buzo, R. Gray,"An Algorithm for Vector Quantizer Design," IEEE Tr. on Com., pp. 84-94,1980

[4] R. Horn, A. Moreira, "Measurements and Results of the E- SAR System of DLR-The Archimedes IIa Experiment", Environment and Quality of Life, Lux,1990

[5] D. Evans, T. Farr, J. van Zyl, H. Zebker, "Radar Polarimetry: Analysis Tools and Applications," IEEE/GRSS, vol. 26, no. 6, pp. 774-789, Nov. 1988

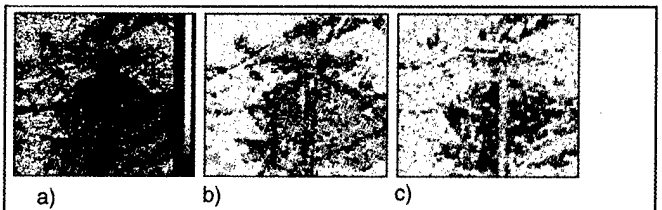

fig. 4:a) SAR image of the runway in Oberpfaffenhofen, data set was taken by E-SAR in L-band, b) red indicates membership to object class: roads and runway, c) green membership to object class: low veget ation.

PROCESSING AND VALIDATION OF THE ERS-1 RADAR ALTIMETER DATA AT THE ITALIAN PAF

C.Celani, A.Bartoloni
NUOVA TELESPAZIO S.p.a.-via Tiburtina 965 - 00156 Rome - Italy
E-mail : cristina_celani@telespazio.it, antonio_bartoloni@telespazio.it
Tel +39-6-40791 Telefax +39-6-40793843
F.Nirchio
ASI - Centro di Geodesia Spaziale - Contrada Terlecchia - 75100 Matera - ITALY
E-mail : nirchio@asimt0.mt.asi.it
Tel +39-835-3771 Telefax +39-835-339005 Telex 43812535

Abstract - As a result of the activity developed at the Italian PAF in order to process the ERS Radar Altimeter data, the off-line product ERS-1/2.ALT-MPR has been defined. In this paper we describe the validation activity that has been carried out at I-PAF in order to check the scientific quality of the product over different case studies.

1. INTRODUCTION

The problem of processing the ERS Radar Altimeter (R.A.) data over the Mediterranean Sea has been approached by the authors for the realization of the Italian Processing and Archiving Facility (I-PAF). This facility is a part of the ERS ground segment and was realized by Nuova Telespazio under contract of the Italian Space Agency (ASI).

The result of this activity is the generation of the I-PAF product ERS-1/2.ALT.MPR, which contains the following quantities relative to the Mediterranean Sea and with a time coverage of one month:

- 20 Hz and 1 Hz satellite range data;
- 20 Hz and 1 Hz satellite range geophysical corrections;
- 20 Hz and 1 Hz satellite orbital height data over a reference ellipsoid;
- 1 Hz Significant Wave Height (SWH);
- 1 Hz sigma-naught and wind speed at nadir;
- 1 Hz sea specular points elevation probability density function.

One of the main problems for the Radar Altimeter data processing over closed seas, like the Mediterranean Sea, is the frequent occurrence of areas where the sea is almost flat. As a consequence the algorithm used to exploit the Radar Altimeter data needs special care in the satellite-sea surface distance (i.e. satellite range) computation and in the SWH extraction. Moreover the weakness of the oceanographic signal to be detected in such a condition implies a full exploitation of the spatial resolution of the Radar Altimeter measurement (20 Hz data).

In previous works [2], [3] we described a method for the reconstruction of these geophysical quantities. The method (see also [1]) exploits heavily the properties in the Fourier domain of the convolution Brown model, which is the mathematical representation of the altimetric echo waveform stored in the telemetry (see [4]): the reconstruction procedure consists in the inversion of the Brown model using the Fast Fourier Transform (FFT) algorithm and its properties.

In order to asses the quality of the ERS-1.ALT.MPR product we chose the Mediterranean January 1993 data set, i.e. the Radar Altimeter telemetry relative to January 1993 over the Mediterranean Sea was processed and analyzed. The aim of this activity was

- to extract and compare the 1 Hz wind speed and the Significant Wave Height (SWH) stored in the MPR with the corresponding analyzed data delivered by ECMWF (European Centre for Medium-range Weather Forecasts); the validation data set was built by a spatial and temporal collocation process between the ECMWF data and the ERS-1 Radar Altimeter wind speed and SWH measurements;
- to extract and compare the MPR quantities with the corresponding ones stored in the F-PAF (French PAF) altimetric product ERS-1.ALT.OPR (version 3.0).

2. ECMWF DATA COMPARISON

Concerning the ECMWF and MPR wind speed data comparison, table 1 shows the results we found after that data were collocated.

Table 1. MPR-ECMWF 1 Hz Wind Speed Data Comparison

# OF MATCHED WIND SPEED DATA	11343
MPR WIND SPEED MEAN VALUE [m/sec]	5.03
ECMWF WIND SPEED MEAN VALUE [m/sec]	5.52
WIND SPEED MEAN DIFFERENCE (ECMWF-MPR) [m/sec]	0.49
RMS DIFFERENCE [m/sec]	1.90
BIAS [m/sec]	1.88
TILT	0.72

From the table we can deduce that the linear relation (in the least squares sense) between the two wind speed data sets is such that the ECMWF wind speed data are overestimated in correspondence of small values of the corresponding MPR data (i.e. for wind speed values less than 6.7 m/sec) and are underestimated for large wind speed values. The same trend in

0-7803-3836-7/97/$10.00 © 1997 IEEE

the behaviour of low values of the wind speed was found also in [5]. Also the rms difference (1.90 m/sec) and the mean difference ECMWF-MPR (0.49 m/sec) between the matched data is reasonable: very good results were found also in [5].

Table 2 show the results obtained from ECWMF SWH data derived from WAM (WAve Model) and MPR SWH data comparison after the collocation procedure. From the table we can deduce that the linear relation (in the least squares sense) between the two wind speed data sets is such that the ECMWF wind speed data are overestimated in correspondence of small values of the corresponding MPR data (i.e. for wind speed values less than 6.7 m/sec) and are underestimated for large wind speed values. The same trend in the behaviour of low values of the wind speed was found also in [5]. Also the rms difference (1.90 m/sec) and the mean difference ECMWF-MPR (0.49 m/sec) between the matched data is reasonable: very good results were found also in [5].

Table 2. MPR-ECMWF 1 Hz SWH Data Comparison

# OF MATCHED SWH DATA	6623
MPR SWH MEAN VALUE [m]	1.54
ECMWF SWH MEAN VALUE [m]	0.97
SWH MEAN DIFFERENCE (ECMWF-MPR) [m]	-0.56
RMS DIFFERENCE [m]	0.40
BIAS [m]	-0.37
TILT	0.88

From the table we can notice that the linear relation (in the least squares sense) between ECMWF SWH data and MPR data is such that the ECMWF SWH data are lower than the corresponding MPR SWH data. The same trend was found also in [5]. Also the mean difference ECMWF-MPR (-0.56 m) and the rms difference (0.40 m) shown in table 2 are very similar to the ones described in [5]: this is an indirect confirmation of the effectiveness of the SWH retracking algorithm implemented at I-PAF.

3. OPR (VERSION 3.0) DATA COMPARISON

Many quantities contained in the MPR product were compared with the corresponding ones stored in the OPR. In the following paragraphs we show the most meaningful results obtained from MPR-OPR data comparison.

3.1 1 Hz SSH Data and Geophysical Corrections

Table 3 summarizes the results relative to the comparison between the MPR and OPR 1 Hz SSH data uncorrected from geophysical effects. We can notice that the agreement between the SSH data is good: in particular the high values of the significance of the mean difference implies that no bias between the OPR and MPR SSH data is present.

About the satellite range geophysical corrections, table 4 shows the results that we obtained.

Table 3 : OPR-MPR 1 Hz Uncorrected SSH Data Comparison

# OF MATCHED 1 Hz SSH	11935
SSH MEAN DIFFERENCE (OPR-MPR) [cm]	1.48
SSH MEAN DIFFER. SIGNIFICANCE	0.93
RMS DIFFERENCE [cm]	9.65

Concerning the sea tide correction, at the moment the I-PAF processor computes it using preliminary tidal constituents (O_1, K_1, M_2 and S_2) evaluated on a gridded geographical map. In the very near future these maps will be updated with the tidal constituents delivered by the Proudman Oceanographic Laboratory (see [6]) where a very precise Mediterranean sea tide model over a finely gridded geographical map was developed.

Table 4 : OPR-MPR 1 Hz Geophysical Corrections Comparison

DRY TROPOSPHERIC CORRECTION MEAN DIFFERENCE [cm]	-0.50
WET TROPOSPHERIC CORRECTION (BY METEO) MEAN DIFFERENCE [cm]	-1.13
IONOSOPHERIC CORRECTION MEAN DIFFERENCE [cm]	0.30
BODY TIDE CORRECTION MEAN DIFFERENCE [cm]	-0.01

From table 4 we can notice in general that in OPR-MPR satellite range geophysical corrections comparison there are not remarkable differences.

The 1 Hz SSH data were investigated together with their corrections also by the crossover analysis. We applied this technique on the SSH data corrected from the all the geophysical effects available. The analysis was performed on 108 crossover points. Table 5 shows the results relative either to MPR or to OPR SSH crossover differences. From the table we can notice that there are not remarkable differences in OPR and MPR rms crossover difference.

Table 5 : Crossover Analysis Results

MPR SSH crossover differences		OPR SSH crossover differences	
MEAN [cm]	RMS [cm]	MEAN [cm]	RMS [cm]
-9.39	18.92	-11.07	19.61

3.2. 1 Hz Wind Speed Data

Table 6 summarizes the statistical parameters that were found in OPR-MPR wind speed data comparison. From the table and from the scatterplot shown in fig.1 we can not observe remarkable differences: this means that the F-PAF and I-PAF altimetric processors retrack the sigma-naught data with small differences and therefore the resulting wind speed data (obtained using the same model) are very similar.

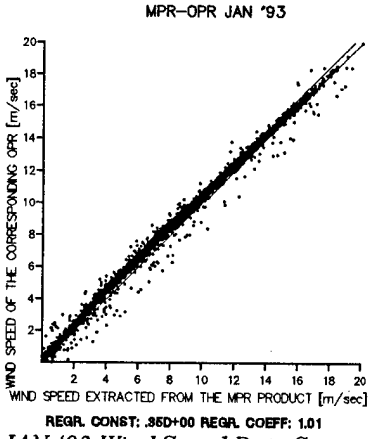

Fig.1. JAN '93 Wind Speed Data Scatterplot (OPR vs MPR)

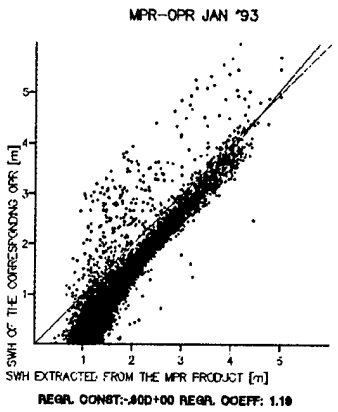

Fig.2. JAN '93 SWH Data Scatterplot (OPR vs MPR)

Table 6 : OPR-MPR 1 Hz Wind Speed Data Comparison

# OF MATCHED WIND SPEED DATA	11965
MPR WIND SPEED MEAN VALUE [m/sec]	5.39
OPR WIND SPEED MEAN VALUE [m/sec]	5.79
WIND SPEED MEAN DIFFERENCE (OPR-MPR) [m/sec]	0.39
RMS DIFFERENCE [m/sec]	0.25
BIAS [m/sec]	0.35
TILT	1.01

3.3. 1 Hz SWH Data

Concerning the 1 Hz SWH comparison, we observed the presence in the OPR product of many outlaiers (i.e. SWH data whose values are greater than 5 meters until to 18 meters): this phenomenon is probably related to problematic performances of the F-PAF retracking algorithm (the so-called slope saturation).

Table 7 : OPR-MPR 1 Hz SWH Data Comparison

# OF MATCHED SWH	9687
MPR SWH MEAN VALUE [m]	1.81
OPR SWH MEAN VALUE [m]	1.27
SWH MEAN DIFFERENCE (OPR-MPR) [m]	-0.55
RMS DIFFERENCE [m]	0.36
BIAS [m]	-0.90
TILT	1.19

After that the OPR SWH outlaiers were discarded, the statistical parameters that we found are shown in table 7 and in fig.2. We can notice that the OPR and MPR data have a good agreement in correspondence of SWH values larger than 1.5 meters, while there are large differences in correspondence of small SWH values. The origin of these differences have to be further investigated.

4. CONCLUSIONS

After the analysis of the geophysical quantities stored in the ERS Mediterranean altimetric product MPR and after the comparison of these parameters with external data (ECMWF data, OPR data), we found that the MPR data quality assessment performed good results: the agreement between the MPR data and the collocated external data is reasonable and the results we found are similar to the ones described by different authors in the comparison of altimetric data with meteorological data or data derived from mathematical models.

REFERENCES

[1] D.E.Barrick, B.J.Lipa, "Analysis and interpretation of altimeter sea echo". *Advances in Geophysics*, **27**, pp.60-99, 1985.

[2] A.Bartoloni, C.Celani, "A new algorithm for the reconstruction of the time delay from sea echo data of a Radar Altimeter". In *Proceedings of IGARSS '93 Symposium*, Tokyo, Japan, pp. 1570-1573, 18-21 August 1993.

[3] A.Bartoloni, C.Celani, F.Nirchio, "ERS-1 altimeter data processing over the Mediterranean Sea: algorithmical tailoring and validation at I-PAF". In *Proceedings of IGARSS '93 Symposium*, Tokyo, Japan, 1753-1755, 18-21 August 1993.

[4] G.S.Brown, "The average impulse response of a rough surface and its applications". *IEEE Trans. Antennas Propag*, **AP-25**, pp.67-74, 1977.

[5] A.Guillame, B.Hansen, "Real time validation of the ERS-1 altimeter fast delivery product". In *ERS-1 workshop at "Department d'Oceanographie spatiale" IFREMER*, BREST, France, pp 46-47, 15-17 September 1992.

[6] M.N.Tsimplis, R.Proctor, R.A.Flather, "A two-dimensional tidal model for the Mediterranean Sea". *Journal of Geophysical Research*, **100**, No.C8, pp.16223-12239, August 1995.

A VISUAL TOOL FOR CAPTURING THE KNOWLEDGE OF EXPERT IMAGE INTERPRETERS: A PICTURE IS WORTH MORE THAN A THOUSAND WORDS

P. Crowther, J. Hartnett and R. N. Williams
Artificial Intelligence and Spatial Systems Research Group
Department of Computing
University of Tasmania
PO Box 1214
LAUNCESTON
Tasmania 7250, Australia
Telephone: 61 3 63 243404
Fax: 61 3 63 243368
P.Crowther@ utas.edu.au

Abstract -- This paper describes a system, KAGES (Knowledge Acquisition for Geographic Expert Systems), being developed to use visual means to extract the expertise of image interpreters. The system presents an image either as a single band or as various combinations of bands and allows an expert to use a mouse to point at or draw around features of interest. It then allows the user to interact with the system to confirm or adjust the identifying characteristics that the system suggests define the feature. These characteristics are not confined to pixel characteristics, and their relationship between image bands but, also includes spatial analysis capabilities.

This paper also discusses some of the problems associated with the visual representation of the elicited knowledge and the verification of that knowledge. In order to verify a spatial rule, the human image interpreter needs to see it. For expert systems the usual way to view a rule is as an if - then - else triplet. This may be an unfamiliar construct to a user who works with visual cues, and may result in problems with verification.

INTRODUCTION

It is well recognised that one of the problems with the use of remote sensing data is that of building computer systems to assist human experts in the task of extracting information from the images produced by satellites and other systems. The aim is for fully automatic interpretation and analysis of images but to date most success has been with systems that pre-process images for presentation to a human expert. The Artificial Intelligence and Spatial Systems Research Group has had some success in building such systems for the interpretation of satellite images of sea ice by using expert systems linked to a GIS and provided with a graphical user interface [1]. The difficulties of gaining the knowledge required for this system led us to the conclusion that traditional text and oral based methods of gaining this knowledge were not well suited to the task. Likewise systems based on clustering have limitations where knowledge and expertise is to be captured. The result has been the development of the KAGES toolkit using IDL [2].

SPATIAL KNOWLEDGE

One of the biggest problems faced when developing expert systems is the capture of expert knowledge. This problem, which is not restricted to spatial systems is often referred to as the knowledge acquisition bottleneck [3]. Experts will apply their expertise without thinking explicitly how and why they are taking particular action, and hence often have problems verbalising their procedures. Spatial systems have the added problem that what the expert image interpreter uses to classify an image is essentially visual knowledge.

This visual knowledge has been divided into a number of types [4]. Type 1 knowledge is knowledge of individual features or scene primitives which are usually identified by groups of similar pixels. These can be point, line or areal in nature. Knowledge of the spatial relationships between scene primitives is Type 2 knowledge. Type 3 knowledge is grouping of scene primitives. Type 4 is an interpretation of an entire scene and Type 5 is knowledge related to resolving inconsistencies.

PICTURES VERSUS WORDS

The primary aim of the KAGES toolkit is to provide procedures to convert what an expert sees and shows on an image into rules. To do this such a system has to be built using the first three visual knowledge types as a base. This is a progressive exercise as one needs to identify scene primitives before one can identify the relationships between these scene primitives. One also needs more than one scene primitive before using the Type 3 tool.

As an alternative tool, an interview manager based on repertory grids is provided as part of the KAGES tool kit [5]. The function of this tool is to give an alternative method of acquiring knowledge and to be used for comparison with the graphical tools. The expert image interpreter is therefore

0-7803-3836-7/97/$10.00 © 1997 IEEE

given the option to describe a feature in words, if that is more appropriate.

TYPE 1 TOOL

This is a per pixel tool (Fig 1) designed to acquire knowledge about line, point and area features. The expert image interpreter points to a typical example of a feature and is stepped through a threshold setting and naming routine.

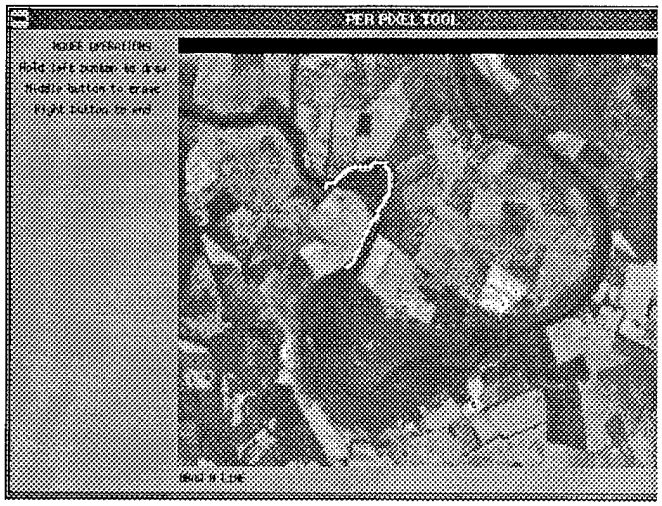

Figure 1: The pixel based Type 1 line tracing tool being used to trace part of the South Esk River in Northern Tasmania on a Landsat image

Line features have been found to be the most complex to deal with [6]. There are 'real' lines such as roads and conceptual lines such as administrative boundaries. Two types of tool are provided. The first is a line following tool which uses adjacent pixel values within thresholds. The second is a line tracing tool which allows a user to draw lines on the image.

The areal feature identifier allows an image interpreter to point at an object, then adjust the pixel thresholds of that object until the object is defined.

The knowledge about an object which is stored in the form of rules, depends on the type of object being investigated. All objects have a name, an optional generic type, the band they were identified on and the identification of the image. Lines and areal objects also have knowledge about thresholds, orientation and extent associated with them.

TYPE 2 TOOL

This spatial tool requires a user to select two objects identified by the Type 1 tool (Fig 2). All possible relationships between the two objects are then determined. This includes proximity, overlap and orientation [7]. Relationships between all classifications of objects (point, line and areal) can be determined.

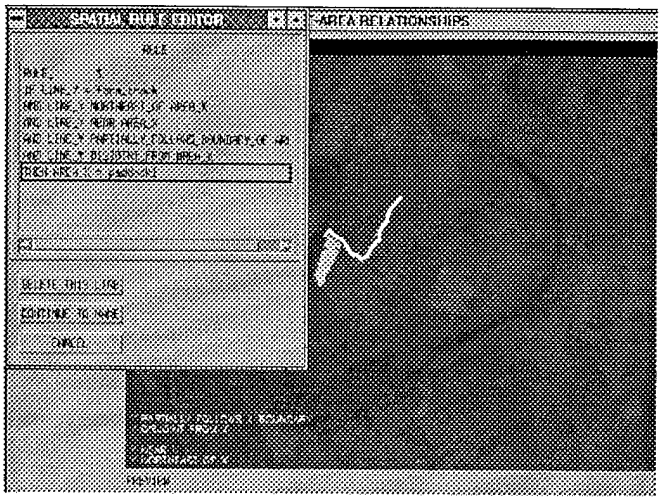

Figure 2: The spatial Type 2 tool being used to determine the relationships between a line object (a road) and an areal object (field). The relationships are shown on the image and as a rule in the rule editor window

The results are displayed as a rule defining the relationships between two objects. The user can edit this rule as some of the results can be spurious due to random associations.

TYPE 3 TOOL

The object grouping tool (Fig 3) allows a user to delimit an area on the image and capture information about scene primitives which are both fully and partially

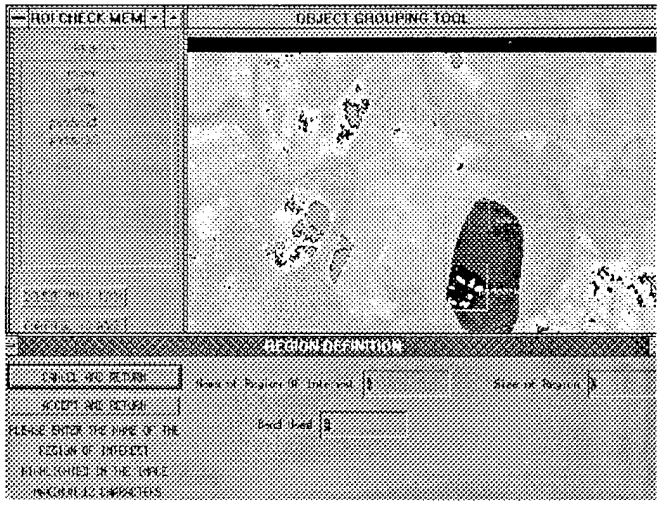

Figure 3 The type 3 tool defining an area and determining its component scene primitives. The naming window and rule editor window are shown open.

contained within it. Objects are often grouped and classified together. This classification may have little to do with the pixel thresholds or even the spatial distribution of objects. Rather it is a human based classification. These type of features are normally classified by a user drawing a line around them. This boundary then determines what is and what is not part of the classification.

VERIFICATION TOOL

One potential problem with a visual tool is verification of the rules it produces. An expert may select a 'typical' scene primitive and set thresholds for that feature so the system selects it perfectly. The system also needs to be able to select other occurrences of that feature type elsewhere in the image and also in other images. To do this, it is possible to select an apply rule option. Once the rule is selected, it is applied to the whole image (Fig 4). The user then has the ability to modify the rule either manually or by using the visual tools if the result is unsatisfactory.

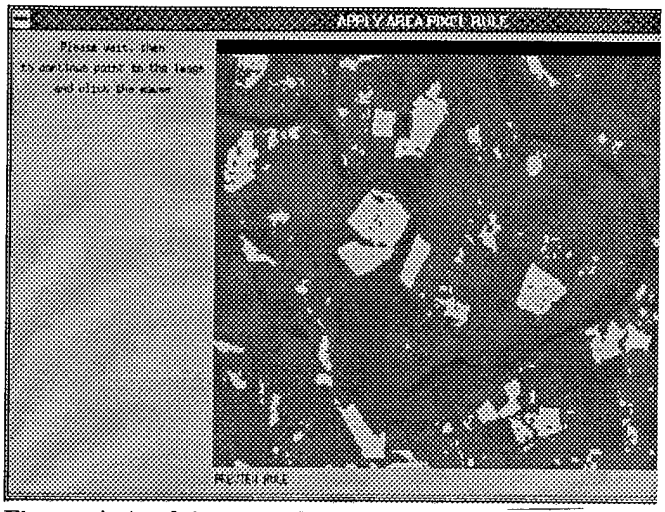

Figure 4 Applying a rule to the whole image allows testing at the image level. The rule can also be applied to other images. In this case the rule for the area object in Figure 2 has been applied. The light areas are those identified by the rule

RESULTS

The system has been used on two sets of images. The first being used are AVHRR NOAA images of Vincennes Bay in Antarctica for a sea ice identification project. The second involves Landsat TM images of agricultural land in Northern Tasmania for a project involving crop identification. The results are presented as rules to the image interpreter who can then modify them by removing spurious or irrelevant clauses. The rules generated in the sea ice domain give similar results to those entered manually, but were created significantly more quickly.

Because of the scarcity of experts who interpret images, a controlled comparison with traditional techniques has not been possible. Rather user acceptance and preference of the visual system has been taken as a measure of its success in terms of human factors.

CONCLUSION

It is quicker and more accurate to generate rules based on the graphical tools than by traditional knowledge acquisition methods such as interviewing or protocol analysis. Once an image interpreter has selected an object and adjusted thresholds, the system gives an immediate response. By building tools which elicit knowledge based on the spatial knowledge types, a structured approach to creating spatial knowledge bases is being developed.

REFERENCES

[1] Hartnett, J. Williams, R. Crowther, P. and Hill, K. (1996),'Providing a Graphical User Interface for Customised GIS Applications', in *Geographical Information, From Research to Applications through Cooperation*, Rumor, M., McMillan, R. and Ottens, H. F. L. (eds), IOS Press, Vol 1.

[2] Research Systems, Inc. (1994), *Interactive Data Language Version 3.6.*

[3] Gaines, B.R. (1988) : An overview of Knowledge Acquisition and Transfer. In: *Knowledge-based Systems Vol. 1.*, Gaines, B.R. and Boose, J.H.(eds)., Academic Press, pp. 3-21

[4] McKeown, D.M., Harvey, W.A. and Wixson, L.E. (1989), 'Automating Knowledge Acquisition for Aerial Image Interpretation', *Computer Vision & Graphics*, Vol. 46, pp. 37-81.

[5] Crowther, P. and Hartnett, J. (1996), 'Using Repertory Grids for Knowledge Acquisition for Spatial Expert Systems', *Proceedings of the 4th Australian and New Zealand Conference on Intelligent Information Systems.* Adelaide.

[6] Crowther, P. and Hartnett, J. (1997), 'The Problem with Lines - Spatial Reasoning with One Dimensional Objects in a Two Dimensional Representation of Three Dimensional Space', *Proceedings of the 8th Joint European Conference and Exhibition on Geographic Information Systems.* Vienna.

[7] Egenhofer, M. J. (1991), 'Reasoning About Binary Topological Relations', in *Advances in Spatial Databases, 2nd Symposium SSD '91*, Gunther, O and Schek, H.J. (eds), Springer Verlag, pp. 143-159.

Congestion Data Acquisition Using High Resolution Satellite Imagery and Frequency Analysis Techniques

Kyong-Ho Kim[1], Jong-Hun Lee[1] and Bong Gyou Lee[2]
[1]Image Processing Dept. Systems Engineering Research Institute (SERI)
P.O. Box 1, Yusung, Taejon, 305-600, South Korea
Phone: +82-42-869-1460 Fax: +82-42-869-1479 E-mail: khkim@seri.re.kr, jong@seri.re.kr
[2]311 W. Sibley Hall, Dept. of CRP
Cornell University, Ithaca, NY 14853
Phone: +1-607- 272-9432 Fax: +1-607- 272-5900 E-mail: bgl3@cornell.edu

Abstract -- The purpose of this study is to examine a method of traffic congestion data collection using scanned high resolution panchromatic imagery acquired from satellite. The existing traffic monitoring systems including manual and automatic vehicle recording technologies have several limitations in terms of accuracy and spatial coverage ranges. In this paper, traffic information is achieved by frequency analysis techniques from the bridge and/or road images segmented. Especially, the study simulated digital images by *fast Fourier transform* (FFT) and applied the technique to different two cases in terms of un-clustered vehicles and clustered vehicles.

INTRODUCTION

The objective of this study is to examine a methodology of traffic congestion data acquisition using high resolution satellite imagery. The current traffic monitoring systems including manual and automatic vehicle recording technologies have several limitations in terms of accuracy and spatial coverage ranges.

In the case of manual data acquisition, there may be accuracy problems due to human errors. One of severe weakness of manual acquisition method would be coverage ranges, in other words, to cover large areas, much manpower should be needed.

In the case of automatic acquisition, there may be measurement errors due to sensitivity of detectors and change of axles in traffic flow. In order to obtain traffic information from large areas, one must install data collecting equipment in the areas of interests.

Using satellite imagery and GIS to obtain traffic information has many strengths over current manual acquisition or automatic acquisition systems. Traffic data can be collected easily and widely using remote sensing imagery and geographic vector data properly[1][2][3].

TRAFFIC DATA ACQUISITION USING REMOTELY SENSED IMAGERY

Extracting quick and consistent traffic information from satellite imagery is necessary to analyze traffic congestion.

Segmentation of satellite imagery was suggested as one method to obtain traffic information. Cho(1995) developed a vehicle identifying method through imagery segmentation[4]. In this case, after extracting vehicle candidate by edge detection and binary system, vehicle was identified by applying decision rule. However, some difficulty is expected using binary system due to noise effects from road surface and reflection on edge of the vehicle (see, Fig. 1 and 2). In other words, using the segmentation based method is not desirable because it is sensitive to noises in imagery and it costs high due to pre- and post- processes.

Therefore, in this paper, the global feature based method by applying Fourier transform is developed. Fig. 3 shows the procedure of this method. From the satellite imagery, we perform the geometric correction using ground control point(GCP) to adjust the geometry of a digital image for scaling, skewing, and other spatial distortions. In order to find out the position of a bridge on the satellite image, we integrate horizontal control points in GCP and geographic vector data in the existing GIS. With this information, the bridge areas can be segmented out by some image processing steps[5]. The initial step of the image processing is to binarize the bridge area with local thresholding technique. Due to the homogeneity of the image of water, it is easy to fragment the bridge area from the binarized image. The segmented bridge image part can be analyzed by the image rotation algorithm to conduct the following analysis. Using attribute and vector data in the GIS, additional information such as the width of road lane in the image can be obtained.

Figure 1. Road image.

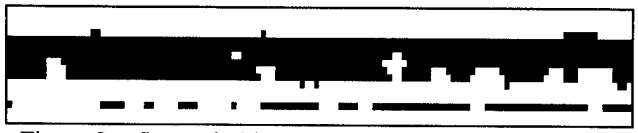

Figure 2. Image in binary system.

0-7803-3836-7/97/$10.00 © 1997 IEEE

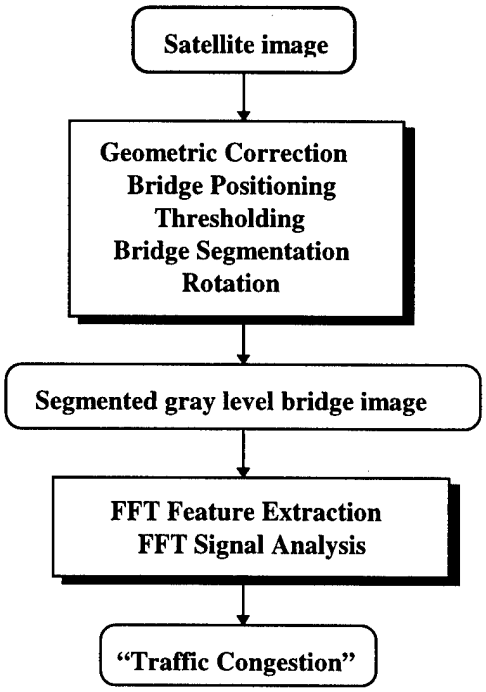

Figure 3. Procedure of global feature based method.

A line of one-pixel-width along the road lane on which vehicles are placed is extracted. Each pixel value of this line is examined by the FFT[6]. Finally, to estimate traffic congestion properly the frequency analysis method is employed.

SIGNAL ANALYSIS OF SIMULATED TRAFFIC IMAGE USING FFT

After carrying out and analyzing results of Fourier transform on a few test images of simulated road traffic, it is necessary to find out the rules to predict congestion of real satellite images. Since the resolution of satellite images used in this study is known, the width and length of roads and/or bridge can be predicted. Hence the location of the roads can be determined and the size of traffic can be obtained by carrying out Fourier transform.

Case 1: Un-clustered Vehicles

In the case of regular spacing among seven cars in roads and/or bridges, the frequency of signal is as follows. Here, the 0-frequency element, while containing no special information, has an extremely large magnitude; hence, to use analysis of frequency, the relevant frequency is set to 0.

The estimated number of vehicles is seven, since the most predominant frequency in this case is seven. Similarly, one can estimate in other cases, such as ten and fifteen vehicles by finding the predominant frequencies as in Fig. 4.

Figure 4(a). Simulated image that 10 vehicles are distributed evenly.

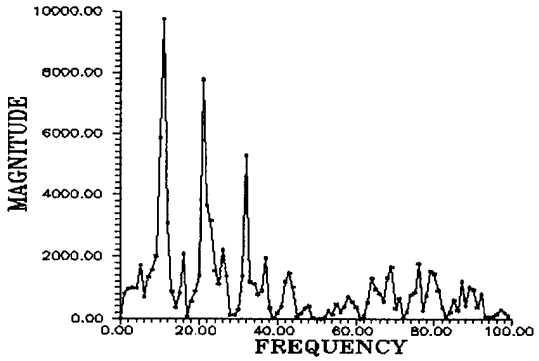

Figure 4(b). Frequency signal of Fig. 4(a). Predominant frequency is 10 (magnitude is 9750).

Case 2: Clustered Vehicles

In order to estimate real traffic flow rates, traffic congestion in urban bridges and/or intersections should be measured. Traffic congestion in urban areas, for example, occurs when there are accidents at intersections and bridges. Fig. 5 presents the case of clustered vehicles. In this case, there are two predominant frequencies, 1 and 26. Frequency 1 represents clustering, so we will call it "*clustering frequency*". Frequency 26 is the most prevalent frequency element and reflects the traffic congestion, so we will call it "*congestion frequency*". Here, the sum of the vehicle's length is given by the ratio between the total length of imagery and its clustering frequency.

Figure 5 (a). Simulated image of clustered vehicles.

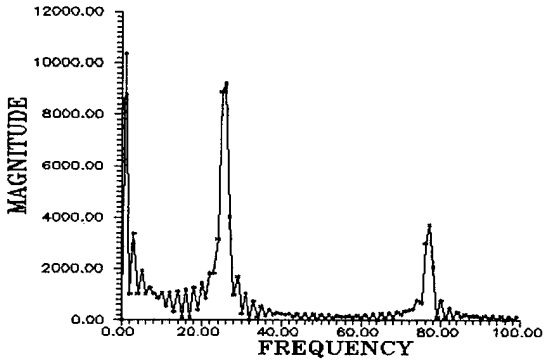

Figure 5 (b). Frequency signal of Fig. 5(a).

$$L_{vehicle} = \frac{L_{image}}{2f_{cluster}} f_{cluster} = \frac{L_{image}}{2} \quad (1)$$

This is a case that the groups of clustered uniform number of vehicles are arranged with the distance of cluster length between each other. The sum of each cluster becomes the half of the total length of imagery. This has no relation to the number of clusters. It is a very complex case that the number of vehicles in each cluster is various and the distances between clusters are different.

The distance between head-to-head of vehicles, *d* becomes:

$$d = \frac{L_{image}}{f_{congestion}} \quad (2)$$

Therefore, the number of vehicles is given by the ratio length of area that the vehicle is on, against the distance between head-to-head of vehicle,

$$N_{vehicle} = \frac{\frac{L_{image}}{2}}{\frac{L_{image}}{f_{congestion}}} = \frac{f_{congestion}}{2} \quad (3)$$

And the number of vehicles per cluster is,

$$N_{vehicle\ -\ per\ -\ cluster} = \frac{N_{vehicle}}{f_{cluster}} = \frac{f_{congestion}}{2f_{cluster}} \quad (4)$$

By using (3), one can obtain the number of vehicles from the above imagery,

$$N_{vehicle} = \frac{26}{2} = 13(\text{vehicles})$$

In this case, one can know that the number of vehicles per cluster is 13 by using (4), because the clustering frequency is 1.

There is a couple of reasons for not having an actual number of 12 vehicles. First, the length of vehicle segment, $L_{vehicle}$, is not accurate due to the difference between clustering frequency and actual clustering grade, that is *clustering frequency error*. The second reason is the error coming from the weak dominant grade of selected frequency as the congestion frequency, that is *congestion frequency error*. As one can see on the above example, the magnitude of frequency 25(magnitude is 8866) and frequency 26 (magnitude is 9201) has only about 3.6%. The third is the variation of vehicle size and the distance between vehicles that can cause the error on the number of vehicles.

RESULTS

A satellite imagery with a resolution of 2 meter was simulated. The segmented road and bridge imagery have a width of 256 pixels and an approximate length of 30 pixels. The frequency of vehicles has been achieved by FFT from the road lanes. Since the accuracy of the imagery is not clear enough to count the number of vehicles, simulated results cannot be compared with real cases.

If we assume that the average vehicle length is 4m and there is no variation on the length, the most prominent and highest congestion frequency will occur when the vehicles are spaced by 4m distance. So, the maximum number of vehicles that can be caught in 256-pixel length image is 64 when the satellite image resolution is 2m. As the spacing between the vehicles goes narrower, the prominency of congestion frequency becomes weaker and this will make the frequency analysis more difficult. By this reason, it can be reasonable to confine the frequency range being studied to 100 for analytical easiness.

Fig. 6(a) shows the bridge on satellite imagery. The dark portions present shadows of the vehicles and the bright display vehicles. The gray color represents the road surface that has a relatively homogenous color. According to Fig. 6 (b) which shows frequency signal, congestion frequency is 15, that is, there are 15 vehicles on the bridge. Vehicles are distributed evenly, since there is no clustering frequency.

Figure 6(a). Road segment extracted from satellite image.

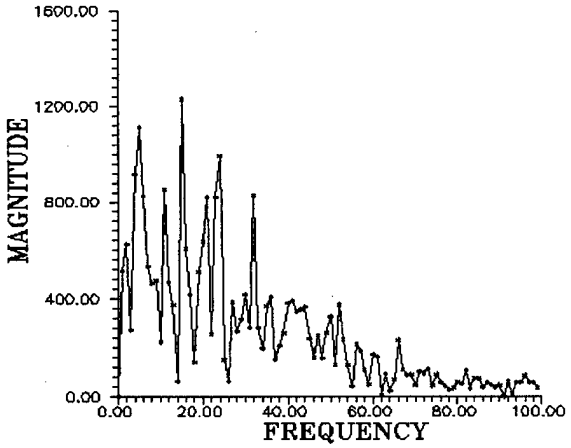

Figure 6(b). Frequency signal of Fig. 6(a). $f_{congestion}$ is 15 (magnitude is 1228). So, $N_{vehicle}$ is 15 (vehicles)

Fig. 7(a) shows the case of clustered vehicles on the bridge. According to Fig. 7(b), congestion frequency is 8 and clustering frequency is 1, that is, there are 8 vehicles in one specific area.

CONCLUSIONS

This paper examined a proposed technique that estimates traffic flow rates in urban bridges and/or roads by high resolution satellite imagery. The advantage of this technique is that it is less sensitive to noise effect on imagery than the existing segmentation method, so high cost pre- and post-processes can be eliminated. Applying digitized images from satellites and/or airplanes enables one to cover large areas at once. Furthermore, the development of communication systems will allow instant transmission of the data on measurement of traffic flow.

Figure 7(a). Road segment extracted from satellite image

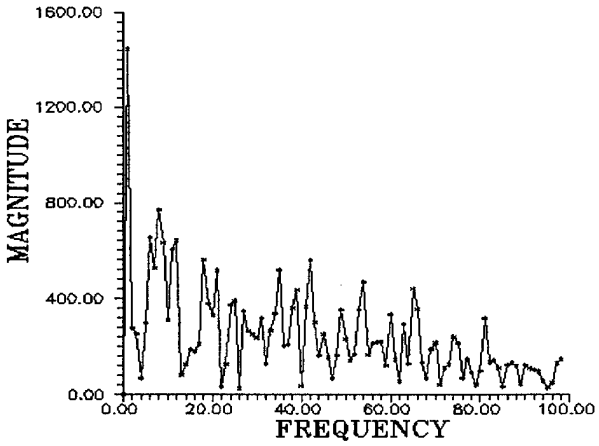

Figure 7(b). Frequency signal of Fig. 7(a). $f_{cluster}$ is 1 (magnitude is 1444). $f_{congestion}$ is 8 (magnitude is 770). So, $N_{vehicle}$ is 4(8/2) (vehicles)

Although the resolution of satellite images in this paper does not permit one to count each car, one can still measure the traffic flow rate. The simulated digital imagery resulted from the method of frequency transformation. The bridge position on the imagery was able to be extracted using vector data in GIS. Traffic congestion was analyzed on two cases. In one case, the vehicles are distributed evenly on the bridge or road, and in another case, the vehicles are gathered in group with a uniform distance to each group. For more accurate and reliable traffic information, the analysis for different sizes of vehicles and difference in distance between vehicles will be required.

REFERENCES

[1] Budge, Amelia M. and Stanley A. Morain. "Access Remote Sensing for GIS," *GIS World*, Vol. 8, No. 2, pp. 45-49. 1995.

[2] Henderson III., Frederick B. "Remote Sensing for GIS," *GIS World*, Vol. 8, No. 2, pp. 42-44. 1995.

[3] Lengyel, Patrick and John Fairs. "Remote Sensing and GIS Technology Applied to Hydrocarbon Exploration," *Earth Observation Magazine*, Vol. 4, No. 10, pp. 25-28. 1995.

[4] Cho, Woosug. "Automatic Traffic Data Collection Using Simulated Satellite Imagery," *Journal of the Korean Society of Remote Sensing*, Vol. 11, No. 3, pp. 101-116. 1995.

[5] Lillesand, Thomas and Ralph Kiefer. *Remote Sensing and Image Interpretation*, John Wiley & Sons., Inc., New York. 1994.

[6] Gonzalez, Rafael C. and Richard E. Woods. *Digital Image Processing*, Addison-Wesley Publishing Co., New York. 1992.

A Framework for SAR Image Classification : Comparison of Co-occurrence and a Gabor based method

Vidya Manian and Ramón Vásquez
Department of Electrical and Computer Engineering
University of Puerto Rico at Mayaguez, PR 00681-5000
Tel: (787) 832-4040 x 3094, Fax: (787) 831-7564,
email: manian@exodo.upr.clu.edu, reve@rmece13.upr.clu.edu

Abstract -- A framework for SAR image classification is presented. The grey level co-occurrence method is used for classifying real SAR images. The Gabor transform of the SAR images are computed and the coefficients are used for classifications. The results of using these two methods are discussed.

INTRODUCTION

A general framework for classifying images consists of the following modules. 1) a pre-processing module which removes noise from the image and enhances the image for further processing, 2) the algorithm implementation module, 3) the feature extraction and selection module, and 4) the classifier module. The outline of the framework is shown in Fig. 1.

CO-OCCURRENCE METHOD

The spatial Grey Level Co-occurrence (GLC) method has been used widely for classifying ordinary and remotely sensed images. This computes the second order gray level statistics which generates a matrix of relative frequencies P_{ij}, with which two neighboring resolution cells separated by distance d occur on the image, one with gray level i and the other with gray level j. Several statistical features such as entropy, homogeneity, correlation, and contrast are computed from the co-occurrence matrix [1]. The GLC features have been used for classifying photographic textures from the Brodatz album [2]. The features have also been investigated for classifying scaled and rotated textures [3].

GABOR BASED METHOD

Gabor transform localizes the signal in both time and frequency domains and it has been used widely in image processing, to segment textured images by constructing adaptive Gabor filters. It has also been used in remote sensing applications to characterize oceans in SAR images[4]. This transform expands a signal into a disrete set of Gaussian elementary functions which are localized in time and frequency.

Partially sponsored by NASA NCCW-0088, NSF CDA 9417659 and the Dept. of Electrical and Computer Engineering, University of Puerto Rico at Mayaguez.

It is a difficult process to determine which frequencies and orientations best describe a region in a remotely sensed image. The Gaussian elementary functions are also not orthogonal to each other, and the computation of the coefficients is a complex process. Hence, in this paper an optimization method was used to compute the Gabor coefficients. Details of this algorithm can be found in [5]. The expansion coefficients are obtained as a solution to a minimization problem, where the difference between the original signal and the signal that is to be reconstructed from the coefficients is minimized.

The original image is first windowed using overlapping windows. Each of the widow is further processed with nonoverlapping widows to select horizontal and vertical frequencies to obtain the Gabor coefficients. The Gabor functions generated using a complex sinusoidal grating modulated by a 2-D Gaussian with an aspect ratio of 1.0 and standard deviation of 0.8. The expansion coefficient image is complex and is of the same size as the original image. Then features are computed from this coefficient image by widowing and the center pixel of each window is assigned a vector of features. Statistical features such as mean, variance, entropy, residual, energy and angular second moment are computed from the coefficients. Some of the feature equations are listed below:

Mean: $$m_{ij} = \frac{1}{N^2}\sum_{i=1}^{M}\sum_{j=1}^{N} x_{ij} \qquad (1)$$

where x_{ij} are the coefficient values for $1 \le m \le M,\ 1 \le n \le N$.

Variance:

$$s_{ij} = \left[\frac{1}{N^2}\sum_{i}\sum_{j}(x_{ij} - m_{ij})^2 x_{ij}\right] \qquad (2)$$

Energy: $$e_{ij} = \frac{1}{N^2}\sum_{i}\sum_{j}|x_{ij}| \qquad (3)$$

Entropy: $$ent_{ij} = -\sum_{i}\sum_{j} x_{ij}\log\left(x_{ij}\right) \qquad (4)$$

The features were then used by the minimum distance classifier and the maximum likelihood classifiers to classify the SAR images.

0-7803-3836-7/97/$10.00 © 1997 IEEE

RESULTS

For the experiments a SIR-C/X-SAR image of Manaus, Brazil shown in Fig. 2 was used. This image contains flooded forest, unflooded fields, unflooded forest, open water flooded shrubs and floating grasses. The classification result using co-occurrence features is shown in Fig. 3. The experimentation were done with sets of 3, 2 and 1 features with different combinations of parameters. The parameters used were angles of 0, 45, 90 and 135 degrees, and distances of 1, 2 and 3 with window sizes of 3x3, 5x5 and 7x7. The windows are moved with a pixel increment of 1 and a line increment of 1. The full gray level range of the image was used, as quantization might lead to loss of information. The original image was also used as a feature for the GLC method. The best feature was entropy followed by correlation, kurtosis, skewness and energy. The set of features that performed next to the above is homogeneity and variance. Inertia did not perform well. The best window size was 5x5 with interpixel distance of 1. Using larger windows increases the computational effort and does not give better classifications. The most suitable angle for computing the GLC matrices was 90°. The difficulties in distinguishing the features arose between different types of forests and, between open water and flooded regions.

The Gabor coefficients were computed with nonoverlapping windows of size 16x16 and 32x32. Window size of 16x16 gave better results. The coefficient image for using window size of 16x16 is shown in Fig. 4. Once the coefficient image was obtained, different window sizes of 3x3, 5x5 and 7x7 were used to compute the features for the center pixel of each of the windows. The best window size was 3x3 as higher window sizes tended to give smoother features with lesser class discrimination. More than 3 features were not necessary for the classifications. The best features were mean, variance and entropy. The contrast feature on Gabor coefficients did not give good results. Adding one or two features to the mean and variance feature did not change the classification much. But, more than four features degraded the classification. The classified image using this method is shown in Fig. 5. It was also seen that having fewer number of classes was essential for Gabor based classification. This is because the Gabor functions were fixed for all types of image regions. This helped in speeding up the algorithm and giving optimal Gabor coefficients. But, it was not suitable to characterize all regions. The same method could be adopted by tuning the Gabor functions, to the various region types. This however requires a lot more computational and experimental effort and needs parallel implementations [6].

The minimum distance classifier was used with GLC and Gabor features for comparisons. Also, the maximum likelihood classifier was used with the Gabor method. It gave better results than the minimum distance classifier for the Gabor method. The other image used in the experiments, is also a SIR-C/X-SAR image of Raco, Michigan. The GLC features did not give good results with this image. The regions contained in this image are frozen lakes, non-forested areas and agricultural fields. The different biomass areas were not distinguishable by the GLC method as the gray levels in these regions were all the range of 175-195. As the GLC method depends on gray tone variations, the features could not characterize the regions distinctly. Also, the use of the original image as a feature biased the classification results of this image.

CONCLUSIONS

A framework was proposed for SAR image classification. Classifications of real SAR images were done using GLC features and Gabor features. Best GLC features were identified. The GLC features performed better than the Gabor features for the Brazil image (Fig. 2). Gabor features using a four class definition has given good results. This may be further extended by using tuned Gabor functions. Since, GLC method depends highly on gray tones, some regions are not identifiable by the features.

ACKNOWLEDGMENT

The authors thank the LARSIP (Laboratory for Applied Remote Sensing and Image Processing) group for their cooperation in completing the paper.

REFERENCES

[1] R. M. Haralick, K. Shanmugam and I. Distein, "Textural features for image classification," IEEE. Trans. on systems, man and cybernetics, Vol. SMC-3, pp. 610-621, Nov. 1973.

[2] V. Manian and R. Vasquez, "A computational framework for analyzing texture image classification," Proceedings of 1995 IEEE international conference on SMC, Vol. 1, Vancouver, Canada, Oct. 1995.

[3] V. Manian and R. Vasquez, "Feature analysis for scaled and rotated texture segmentation," Proceedings of 21st international conference on computers and industrial engineering, San Juan, Puerto Rico, March 1997.

[4] J.G. Teti, Jr. And H. N. Kritikos, "SAR ocean image decomposition using the Gabor expansion," IEEE. trans. geoscience and remote sensing, Vol. 30, No. 1, pp. 192-196, January 1992.

[5]V. Manian and R. Vasquez, "On scaled and rotated texture segmentation using a class of basis functions," Proceedings of SPIE's symposium on AeroSense'96, Conf. 3078, Orlando, FL, April 1997.

[6] V. Manian and R. Vasquez, "Efficient algorithms for discrete Gabor transforms using multicomputer networks," Proceedings of SPIE's symposium on AeroSense'95, Conf. 2755, Orlando, FL, April 1996.

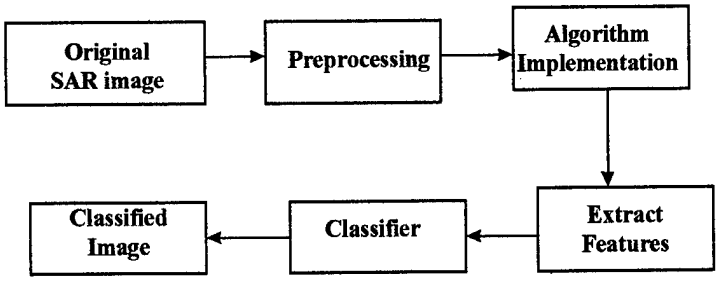

Fig. 1 SAR Image Classification Framework

Fig. 2 Original SAR image of Manaus, Brazil

Fig. 3 Classification using co-occurrence features

Fig. 4 Gabor coefficient image

Fig. 5 Classification using Gabor features

Fuzzy Supervised Classification of JERS-1 SAR Data for Soil Salinity Studies

G. I. Metternicht
Curtin University of Technology, School of Surveying and Land Information,
GPO Box U 1987, Perth 6001, Western Australia
TE: + 618 9266 3935 - Fax: +618 9266 2703 - Email:Metternicht@cage.curtin.edu.au

Abstract -- Remote sensing of surface features has been intensively used to identify and map salt-affected areas. Salt-tolerant vegetation is among the indicators used to separate saline-alkaline areas from non-affected ones. However, the vegetation cause spectral confusion and erroneous labelling between salinity and alkalinity classes when working with optical sensors such as Landsat TM or Spot. Thus, this paper evaluates the capabilities of the L-band of the Japanese JERS-1 SAR radar satellite to resolve spectral confusions caused by topsoil textures and vegetation, thus improving the detection and mapping of areas degraded by salinity processes.

A fuzzy overlay model is used to classify the JERS-1 radar satellite image. The study shows that fuzzy classification of JERS-1 SAR data provides overall reliable detection of areas degraded by salinity-alkalinity processes.

INTRODUCTION

Land salinization is a major form of environmental degradation in agricultural areas. Information on the extent and severity of soil salinity is needed for effective planning and soil reclamation measures. Remote sensing of surface features has been intensively used to identify and map salt-affected areas. Salt-tolerant plants are among the indicators used to separate saline-alkaline areas from non-affected ones. However, they cause spectral confusion an erroneous labelling between salinity and alkalinity classes.

Therefore, this paper evaluates the capabilities of the L-band of the Japanese JERS-1 SAR data to resolve spectral confusion commonly caused by topsoil textures and vegetation when working with optical sensors, as mentioned by [1]. Implementing a supervised fuzzy classification of the JERS-1 data set assesses improvements in the detection and mapping of areas degraded by salinity processes.

DATA SET

The data set consisted of 95 geo-referenced composite topsoil samples of 5 cm depth, collected from a surface area of about 9,000 ha concurrently with the acquisition of a JERS-1 SAR scene. Soil saturation extracts were prepared to determine ion types and contents, electrical conductivity and soil reaction (pH). These and other ancillary data such as ground cover type and percentage, soil particle size distribution and organic matter content were stored in a database.

A gamma MAP filter [8], with variable window size was applied to the JERS-1 scene in order to reduce the speckle and improve feature discrimination [1]

METHOD

Fuzzy modelling of the saline and alkaline classes

The first step in the fully fuzzy supervised classification is class determination, by using the ranges established by [2] for saline, saline-alkaline and alkaline areas. The following rules define the four information categories considered:

(a) *'Non-affected soils'* if EC <= 4 dS/m and pH < 8.5;
(b) *'Alkaline areas'* if EC <=4 dS/m and pH >= 8.5;
(c) *'Saline areas'* if EC > 4 dS/m and pH < 8.5; and
(d) *'Saline-alkaline areas'* if EC > 4dS/m and pH >=8.5.

Accordingly, four fuzzy sets, namely *'non-alkaline'*, *'alkaline'*, *'saline'* and *'non-saline'* are necessary to characterise these categories.

A bell-shaped model [3] was used to build up the functions. The membership function is written as:

$$\mu A(x)=[(1-v)^{\lambda-1}(x-a)^{\lambda}]/[(1-v)^{\lambda-1}(x-a)^{\lambda}+v^{\lambda-1}(b-x)^{\lambda}]\ x\in[a,b] \quad (1)$$

$$\mu A(x)=[(1-v)^{\lambda-1}(c-x)^{\lambda}]/[(1-v)^{\lambda-1}(c-x)^{\lambda}+v^{\lambda-1}(x-b)^{\lambda}]\ x\in[b,c] \quad (2)$$

where equations (1) and (2) represent the monotonically increasing and decreasing parts. Dombi's membership function is optimal because there are two parameters, λ and v, allowing to modify the inflection and sharpness of the membership curves respectively (figure 1). In this study inflection was set equal to 3 and sharpness to 0.7

Figure 2 illustrates the fuzzy membership function obtained for the soil reaction (pH). A pH value of 7 has a membership degree of 1 in the fuzzy set 'non-alkaline', while a pH equal to 10 has a certainty factor of zero in that same set but of 1 in the fuzzy set 'alkaline'. The membership grades of the soil samples to the four different fuzzy sets were computed As a result, a soil sample can be alkaline to a degree of 0.7, saline to a degree of 0.2, while also having a possibility of being saline-alkaline (0.2) or non-affected (0.9).

Membership grades

Subsequently, the backscattering values of the soil samples pertaining to the four sets were extracted from the geo-referenced JERS-1 SAR scene using a neighbourhood-based operator. These bakscattering values were allocated to one of the four categories, according to their degree of membership to the sets.

The median value of each class was adopted as standard point, with a membership degree of 1 to the set under consideration. Other fuzzy classification models take the mean value of a cluster as the standard point (4,5,6]. However, the median is preferable to the mean as the latter is very sensitive to extreme scores or measurements. Histogram tails were taken as the typical points, thus having a membership grade of zero.

0-7803-3836-7/97/$10.00 © 1997 IEEE

Per-layer fuzzy classification of the JERS-1 scene

This approach also requires the user to define the type of membership function (eg. linear, sigmoidal) to be applied for fuzzy modelling of the layers representing the s 'non-alkaline', 'alkaline', non-saline' and 'saline' classes. A sigmoidal function of the form:

$\mu = cos2\alpha$ (3) was selected.

Where, in the case of a monotonically increasing function,

$\alpha = (x-a)/(b-a)*pi/2$ for $x < b$ (4)

being x the backscattering value the of pixel analysed, a the typical point and b the standard point of the function [7].

The fuzzy overlay model

After generating four different class outputs a fuzzy overlay model was implemented in a Geographic Information System (figure 3). Such a model is useful for natural resource applications [9]. Individual layers are created for each of the categories under consideration, and processed using fuzzy minimum and maximum operators [10]. Layers can be combined through user defined rules of the type *if-then* statements, as follows:

1. IF 'non-alkaline' AND 'non-saline', THEN 'non-affected areas;
2. IF 'alkaline' AND 'non-saline', THEN 'alkaline areas';
3. IF 'non-alkaline' AND 'saline', THEN 'saline areas';
4. IF 'alkaline' AND 'saline', THEN 'saline-alkaline areas'.

The membership grade of a pixel *(x)* to the new categories (eg. non-affected areas) is computed using a minimum operator:

$$\mu_{non\text{-}affected}(x) = \text{MIN}\,[\mu_{'non\text{-}alkaline'}(x), \mu_{'non\text{-}saline'}(x)] \quad (5)$$

In other words, the membership grade of a pixel *(x)* in the fuzzy set 'non-affected areas' is the smallest of its membership grades in the sets 'non-alkaline' and 'non saline'. Membership grades to the other sets are computed in the same way, using the minimum operator [10, 11, and 12].

Accordingly, each pixel has attached to it a group of membership grades to indicate the extent to which the pixel belongs to the four different classes. Pixels with mixed classes or in transitional conditions can now be described. For example, if a ground cell contains two classes such as 'saline areas' and 'saline-alkaline areas', it has two membership grades indicating the extent to which the pixel is associated with the two classes. The closer the value of $f_{'non\text{-}affected'}(x)$, which represents the membership grade of *(x)* to the *'non-affected'* set, is to one, the more the pixel belongs to that class.

The union of the classes provides the final map. A pixel will take the label of the group where it has the highest certainty factor. This is implemented by using a maximum operator:

$$\mu_{'final\ map'}(x) = \text{MAX}\,[\mu_{'non\text{-}affected'}, \mu_{'alkaline'}, \mu_{'saline'}, \mu_{'saline\text{-}alkaline'}] \quad (6)$$

The membership grade of a pixel (x) in the output map is either its membership grade in 'alkaline' or 'saline' or 'saline-alkaline' or 'non-affected', whichever has the largest value.

The amount of layers may be a drawback in the modelling. For instance, the combination of four salinity-alkalinity classes an one satellite band generates a 4-layer output. But if the number of bands increases to 6, 24-output layers will be created.

DATA INTERPRETATION

A confusion matrix was computed to evaluate the final classification (table 1). Soil sites belong to the saline class were identified on its entirety. The poorest performance corresponds to the proper identification of alkaline and saline-alkaline areas. They were spread all over the information categories, especially that of the non-affected areas. The reason of the failure may be related to the roughness of the soil surface, heavily affecting the radar backscattering.

During the field campaign, it was observed that farmers cultivate land parcels with pH values up to 9, belonging thus to alkaline areas. The statistical analysis between radar signal and pH showed a negative correlation, that is, when the pH increases the backscattering decreases because the surface is smoother. The latter occurs when the land becomes unsuitable for cultivation.

Soil roughness also explains the good discrimination of saline areas. Saline topsoils are generally smoother than non-saline ones, thus presenting lower backscattering values as less energy returns to the radar antenna. As a consequence, darker colours are present in the image.

CONCLUSION

Fuzzy classification of JERS-1 SAR data, using a fuzzy overlay model provided an overall reliable detection of areas degraded by salinity-alkalinity processes. Radar backscattering was mostly affected by the roughness of the surface, produced by land cultivation. This was identified as the main factor causing erroneous allocation of alkaline and saline-alkaline soils to non-affected areas.

REFERENCES:

[1] G. Metternicht 'Detecting and monitoring land degradation features and processes in the Cochabamba valleys, Bolivia. A synergistic approach'. PhD dissertation, Gent Univ., Belgium, 399 pages, 1996.

[2] United States Salinity Laboratory Staff, 'Diagnosis and improvement of saline and alkali soils. Agriculture Handbook No.60. US Dept. of Agriculture. Ed. L.Richards, 1954.

[3] J. Dombi, 'Membership function as an evaluation'. Fuzzy sets and systems. vol. 35:1-21, 1990.

[4] G. Foody, 'Fuzzy modelling of vegetation from remotely sensed imagery. Ecological modelling, 1994.

[5] F. Wang, 'Fuzzy supervised classification of remote sensing'. IEEE Transactions on geoscience and rem. sens., vol.28(2):194-201, 1990.
[6] J. Key, J. Maslanik and R. Barry, 'Cloud classification from satellite data using a fuzzy set algorithm: a polar example. Int.J.Rem.Sens. vol.10(12):1823-1842, 1989.
[7] IDRISI for windows, 'User's manual v.1'. Clark Univ. USA, 1995.
[8] A. Lopez, R. Touzi and E. Nezry, 'Adaptive speckle filters and scene heterogeneity'. IEEE Trans. on Geoscience and Rem. Sens., vol.28,No.6, 1990.
[9] B Jiang, 'Fuzzy overlay and visualisation in GIS. PhD thesis, Utrecht Univ. The Netherlands, 165 pages, 1996.
[10] L. Zadeh, 'Fuzzy sets'. Information and control, vol. 8, pp.338-353, 1965.
[11]C. Negoita, 'Expert systems and fuzzy systems'. Ed. The Benjamin/Cummings Publishing, Inc. 1985.
[12] G.Klir and T. Folger, 'Fuzzy sets, Uncertainty and Information. Ed.: Prentice-Hall Int., Inc. 1988.

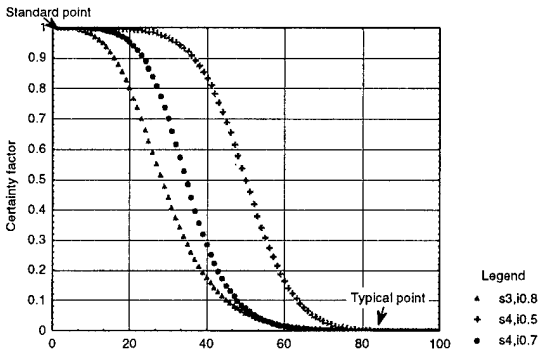

Figure 1: An S-shaped membership function: sharpness (s) and inflection (i) variations.

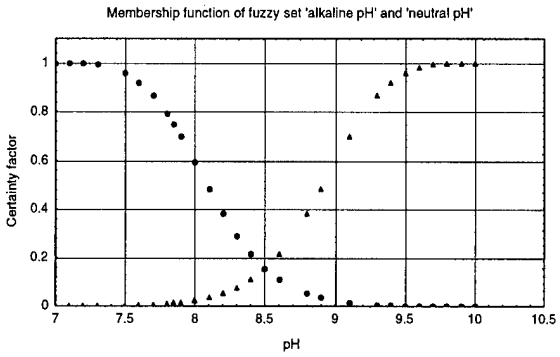

Figure 2: A fuzzy membership function for pH

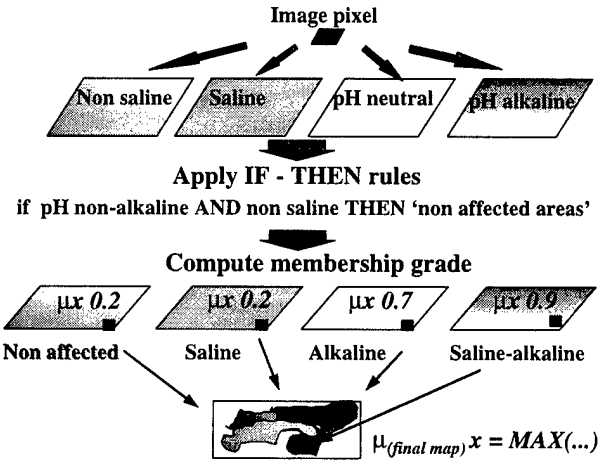

Figure 3: The fuzzy overlay model

Table 1: Confusion matrix of the fuzzy supervised classification

CLASSIFIED DATA	REFERENCE DATA					
	Non-affected	Alkaline	Saline	Saline-alkaline	TOTAL	ACC.%
Non-affected	180	40		50	270	67
Alkaline		10		10	20	50
Saline		10	220	20	250	88
Saline-alkaline	10	10		220	240	92
TOTAL	190	70	220	300	780	
REL.%	95	14	100	73		

Overall accuracy: 80.7; average reliability: 70; average accuracy: 74

Quality Assurance of Global Vegetation Index Compositing Algorithms Using AVHRR Data

Wim J.D. van Leeuwen, Trevor W. Laing, Alfredo R. Huete
University of Arizona, Department of Soil, Water and Environmental Science,
1200 E South Campus Drive Room 429, Tucson, AZ 85721, USA.
Tel.:(1) 520 621 8514; fax:(1) 520 621 5401; leeuw@ag.arizona.edu.

Abstract -- In this study the quality control aspects of the vegetation index produced by the MODIS (MODerate resolution Imaging Spectroradiometer) algorithm were evaluated and compared with the results of the currently used maximum value composite (MVC), which chooses the highest NDVI (normalized difference vegetation index) over a certain time interval. The composite scenarios were evaluated with respect to: 1) quality flags related to data integrity, cloud cover and composite method, 2) temporal evolution of the VI for different continents and vegetation cover types, and 3) accuracy of the standardization of reflectance values to standard view angles (nadir). On a continental scale the composited NDVI results from the MODIS algorithm were 1 to 24% lower than the off-nadir NDVI results based on the MVC criteria. A simple BRDF (Bidirectional Reflectance Distribution Function) model was adequate to produce nadir equivalent reflectance values from which the NDVI could be computed. The temporal evolution of the NDVI derived with the MODIS algorithm was similar to or smoother than the NDVI derived from the MVC algorithm. The composite method applied in the MODIS algorithm, was dependent on the global position and season, e.g. the BRDF interpolation was most frequently applied in arid and semi-arid regions and during the dry season over tropical rain forests. Examples of a global NDVI and quality flags were displayed using a pseudo color bit mapping scheme.

INTRODUCTION

A vegetation index composite scenario was developed for the MODIS sensor in the MODIS (Moderate resolution imaging spectroradiometer) framework to minimize effects of cloud cover, atmosphere, bidirectional reflectance factors (BRF) and spatial distortions, while maintaining the finest spatial resolution [1].

MODIS Compositing Objectives

- Provide accurate and cloud-free vegetation index (VI) imagery over set temporal intervals.
- Maximize global and temporal land coverage at the finest spatial and temporal resolutions possible.
- Standardize variable sensor view and sun angles.
- Ensure the quality and consistency of the composited data.
- Depict and reconstruct phenological variations.

MODIS Angular Considerations

- Sensor view angles vary +/- 55° cross track.
- Solar zenith angles may vary up to 20° across an image.
- Solar zenith angles vary with latitude and day of year.
- The NDVI tends to increase with both larger view and larger solar zenith angles.
- The pixel size is increasing with view angle (whiskbroom).

Current AVHRR Maximum Value Composite (MVC) Approach and MODIS Considerations

The MVC selects maximum NDVI values on a per pixel basis over set compositing periods and is designed to minimize atmospheric effects, including residual clouds. However, the MVC becomes inconsistent and unpredictable over anisotropic vegetated canopies. Pixel selection is biased toward large view angles in the forward scatter (shaded) view direction and large solar zenith angles. The MVC becomes even less appropriate with atmospherically-corrected data sets.

Therefore, the MODIS compositing criteria need to be weighted more toward angular considerations. This is done by incorporating a BRDF compositing approach, which has the goal to standardize the VI to nadir view and constant solar angles. The purpose of the nadir view approach is to achieve the finest spatial resolution and detail. It also has the most accurate atmospheric correction. Furthermore, validation of VI - bio-physical relationships will generally be coupled to nadir view in the field and nadir Landsat-7 observations. Finally, VI - saturation problems decrease for nadir view angle observations.

MODIS VI COMPOSITING ALGORITHM

Daily, global 8 km Pathfinder AVHRR (Advanced very high resolution radiometer) data were processed to prototype the MODIS and MVC vegetation index algorithms for the MODIS era. The version 1 (V1) MODIS algorithm selects the reflectance data for a 16-day period, based on data integrity and cloud flags, and applies a BRDF (bidirectional reflectance distribution function) model to the individual band data (if more than 4 data points are of good quality) to standardize the reflectances to nadir view angles. The accuracy of the BRDF algorithm was evaluated through temporal NDVI profiles. Nadir interpolated values were rejected when the resulting NDVI was higher than the MVC based NDVI. Since not all pixels had more than 4 cloud-free data points during a 16-day period, a back-up algorithm was used which selected the highest NDVI for two, cloud-free, view angles closest to nadir. If all data during a 16-day period was affected by clouds, based on the cloud flags, the MVC criterion was applied. The empirical Walthall BRDF model is [2]:

$$\rho(\theta_v,\phi_s,\phi_v)=a\theta_v^2+b\theta_v\cos(\phi_v-\phi_s)+c \qquad (1)$$

0-7803-3836-7/97/$10.00 © 1997 IEEE

where the reflectance ρ is a function of the view zenith angle (θ_v), and sun (ϕ_s) and view (ϕ_v) azimuth angles. a, b and c are coefficients obtained using a least squares curve fitting procedure, "c" is equal to the reflectance at nadir. The BRDF model was inverted, after which nadir-equivalent reflectance and NDVI values were derived using forward modeling. Back-up algorithms were: 1) the constraint view angle MVC (CV-MVC; MVC based on two cloud-free observations with the view angles closest to nadir) and 2) the MVC algorithm (MVC; MVC will choose the maximum NDVI value based on all observations without considering the quality).

The current quality control (QC) flags for a global NDVI composite using a BRDF approach include 8 flags/bits related to: data integrity (1); land/water mask (2); the composite approach applied (3-5) (BRDF, CV-MVC, MVC); and the cloud mask (6-8) (cloudy, mixed cloudy/clear, shadow).

RESULTS AND DISCUSSION

Figs. 1 and 2 are prototypes of the global MODIS NDVI and QC product. Notice that the BRDF correction is limited to the semi-arid/arid regions. An increased number of BRDF corrections might be obtained using longer time steps and spatially aggregated observations, while taking into account the land cover type. Fig. 3 shows seasonal profiles of the current version 1 (V1) MODIS-NDVI and the MVC-NDVI for each

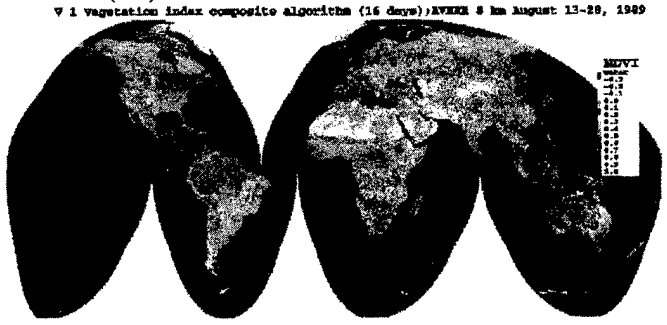

Fig. 1, Global NDVI image (pseudo color) using the MODIS VI composite algorithm (BRDF/ CV-MVC/ MVC approach).

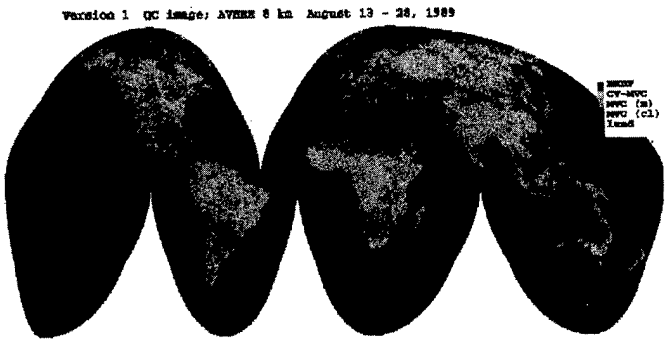

Fig. 2, Color coded quality control flags for a Global NDVI composite using a BRDF approach (MODIS V1); red=BRDF composite method applied; green=CV-MVC; blue =MVC; (m) mixed cloud/clear; (cl)=cloudy pixels; gray=land; black=water.

continent. Fig. 4 indicates the relative difference (ranging between 1 and 24 %) between the MVC derived NDVI and the MODIS derived NDVI for each continent and all 16-day composite periods during the 1989 AVHRR observations. An example of the quality of the NDVI product is illustrated in Fig. 5, where the fractions of pixels for which the NDVI was derived from either BRDF, CV-MVC or MVC part of the MODIS algorithm were given as function of time/season. In Fig. 6, the temporal profiles of the MODIS-NDVI and MVC-NDVI are compared. NDVI estimates from the MVC approach are always higher or equal to the MODIS approach. The peak of the growing season is also different for the examples in Fig. 6. The view angle distribution for the MVC algorithm is more biased towards the forward scatter direction than for the MODIS algorithm (Fig. 7). Notice the strong peak at nadir view angles due to the BRDF standardization of the reflectance factors to nadir. Future research will address more effective ways of standardizing reflectance observations with BRDF models to increase the spatial representation on a global scale.

CONCLUDING REMARKS

- A simple BRDF model and few observations (≥ 5) per pixel were needed the standardize the NDVI to nadir view angles (VIs behave anisotropic).
- The Walthall BRDF model was successfully used in global AVHRR/NDVI composite scenarios.
- Backup composite algorithms were needed for the pixels with limited number of observations (BRDF model can not be inverted with limited observations).
- On a continental scale, the composited MVC-based off-nadir NDVI results were 1 to 24 % overestimated compared to the NDVI results from the MODIS algorithm.
- A BRDF approach is more representative of vegetation changes over a 16-day period than the MVC approach.
- A BRDF scenario automatically extrapolates to finer spatial resolutions.
- The MODIS- BRDF approach had few spatial discontinuities (AVHRR, 8 km).

ACKNOWLEDGMENTS

The authors would like to thank the DAAC at GSFC for providing the AVHRR data. This research was supported by MODIS contract NAS5-31364 (A.R. Huete).

REFERENCES

[1] Huete, A.R., Justice, C.O., van Leeuwen, W.J.D., 1996. "MODIS vegetation Index, Algorithm Theoretical Basis Document," http://eospso.gsfc.nasa.gov/atbd/modistables. html.

[2] Walthall, C.L., Norman, J.M., Welles, J.M., Campbell, G., and Blad, B.L., 1985. "Simple equation to approximate the bi-directional reflectance from vegetative canopies and bare soil surfaces," Applied Optics, 24(3), pp. 383-387.

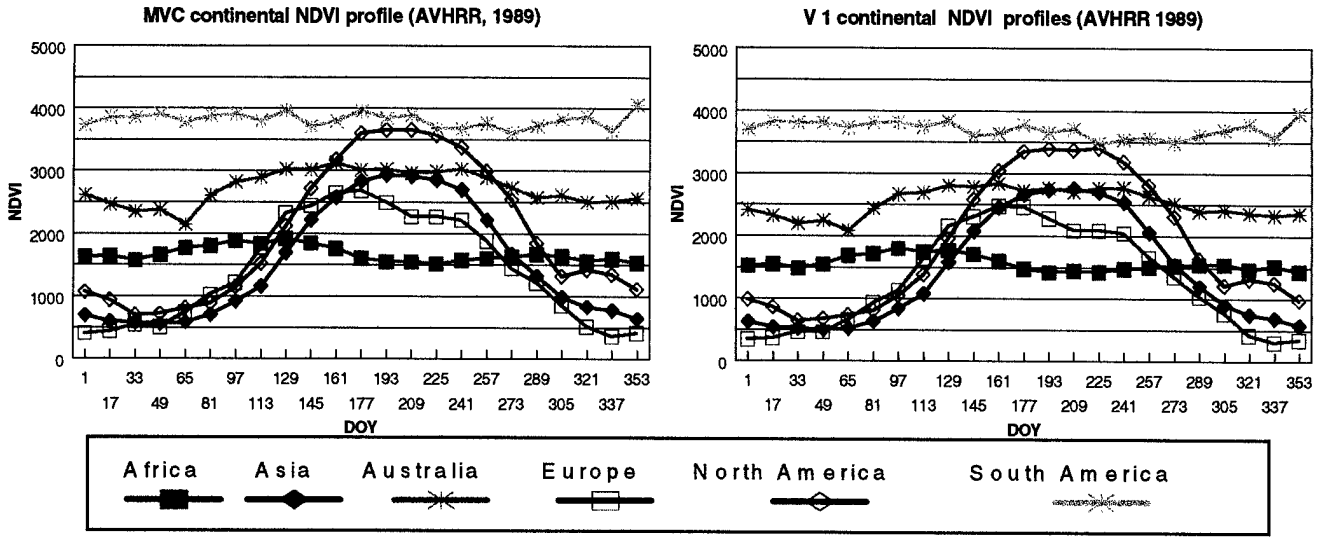

Fig. 3, Continental NDVI profiles for the current (V1) MODIS composite algorithm and MVC algorithm; AVHRR (8km).

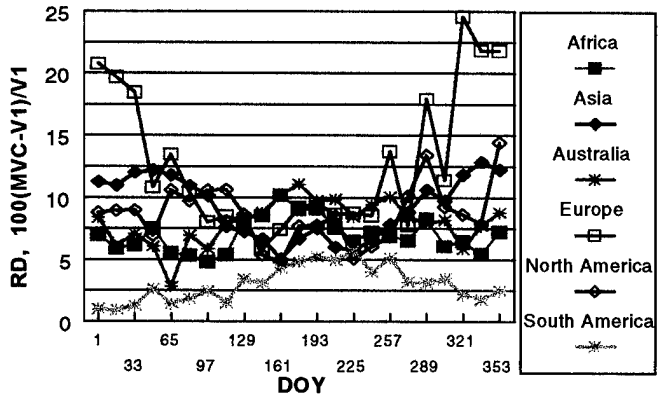

Fig. 4, Percent relative difference between MVC and V1 MODIS derived NDVI for 16-day composite periods (1989).

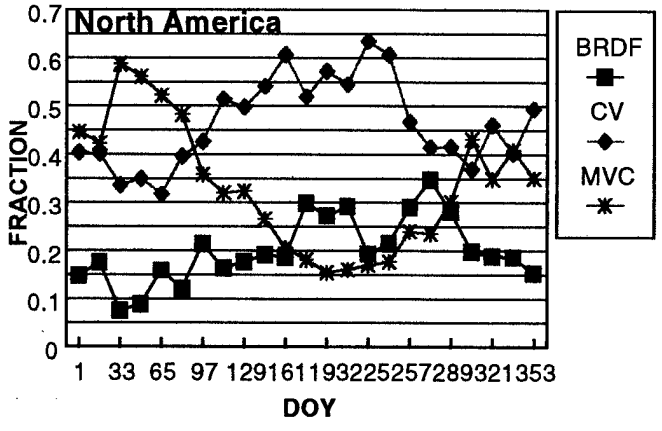

Fig. 5, Temporal profile of the fractions of pixels (North American continent) where the BRDF, CV-MVC or MVC was used as part of the MODIS composite algorithm.

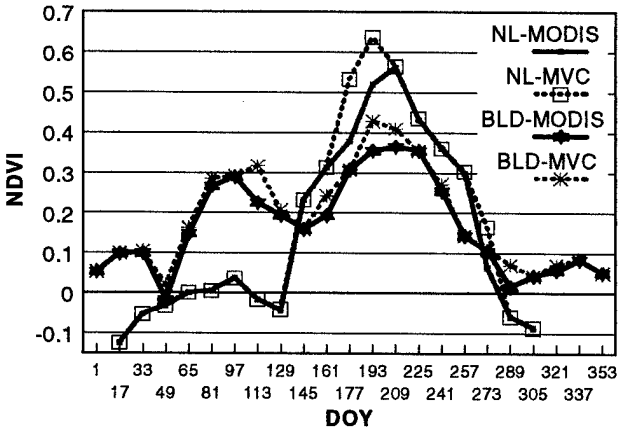

Fig. 6, Temporal profile of NDVI for needleleaf (NL; Lat. 63.2°N, Long. 92.7°E) and broadleaf deciduous (BLD; Lat. 32.0°N, Long. 115.5°E) forest for the MODIS V1 and the MVC composite approaches.

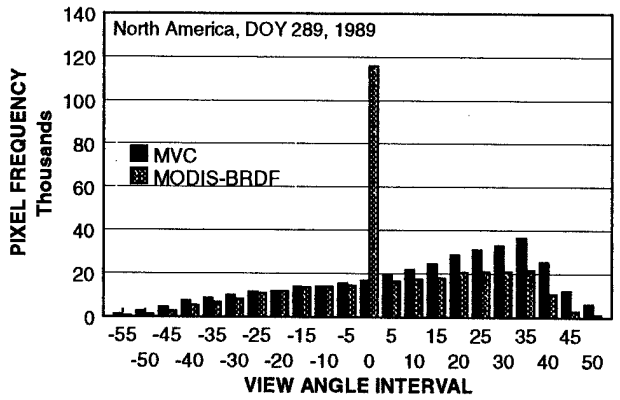

Fig. 7, View angle distribution for North America for a 16-day composite period for the MODIS V1 and MVC algorithms.

IGARSS'97

1997 International Geoscience and Remote Sensing Symposium

03-08 August 1997

Singapore International Convention & Exhibition Centre

Technical Program

Interactive Area 18: Remote Sensing of the Ocean

Investigations of possibilities of using SAR data for monitoring of Volga estuary and Kalmykija shore of Caspian Sea.

N. A. Armand[1], A. S. Shmalenyuk[1], Yu. F. Knizhnikov [2], V. I. Kravtsova [2], E. N. Baldina[2]

1-Institute of Radioengineering and Electronics, RAS, Mokhovaja st., 11, Moscow, GSP-3, 103907, Russia,
Phone: (095) 526-92-68, Fax: (095) 203-84-14,
EMail: shmal@ire.rssi.su

2- Moscow State University, Leninski gory, 119899, Moscow, Russia
Phone: (7)-095-939-34-20

Abstract - In work the possibility of using of radar data for the analysis of a region state are considered. SAR data of SIR-C, taken during joint Russian-American experiment in April, October 1994 are analyzed. Data are received from JPL NASA. The consideration are carried out for region of Astrakhan reserve and Kalmykija shore of Caspian Sea for which exist of the long-term monitoring data. Possibilities of application SAR data for an estimation of a state, types of vegetation, estimation of a condition of flooded zones are analyzed. Comparison with data of optical scanners and data of field inspections are carried out.

INTRODUCTION

The investigation of Volga estuary region and shore of Caspian Sea is one of the important problems of ecological monitoring. It is connected on the one hand with unique conditions of the region, on the other hand with typical conditions of a zone, as flooded zones . The problem of research of these regions has risen recently on the first plan in connection with fluctuations of a Caspian Sea level. The ground monitoring in zones of such type are complicated and for separate places the remote sensing tecniques is only one.

In this paper the area of the Astrakhanskiy Biosphere Reserve and site of Kalmykia shore of Caspian Sea are considered.

In 1993, the Dutch organization for scientific research (NWO) funded a project to establish a GIS to assist in the management of the Astrakhansky Biosphere Reserve in Russia. The project has been carried out by Faculty of Geography of Moscow State University, and staff from Astrakhanskiy Biosphere Reserve, ITC and Wageningen Agricultural University. The participants decided that the project should also include research on both ecologic and geochemical parts of the ecosystems. Data on different natural components of Russia's nature reserves, as well as biophysical and environmental factors, mainly floristic and faunistic, have been collected for many years [1-3].

The investigations of considered regions have been carried out also in frame Russian-American experiment in April and October 1994 during SIR-C missions.

The results of investigations presented in this paper are based on these two project.

Investigations of this region are planned also in frame International project PRIRODA in 1997-1999 years[4-6]. One of the goals of this paper is the assessment of possibilities of using PRIRODA SAR data for monitoring of Volga estuary.

DESCRIPTION OF AREAS

Akstrakhanskiy Biosphere Reserve , established in 1919, is the oldest nature reserve in Russia and includes number of the natural delta landscapes. It is situated in the lower Volga delta, along the nothern shore of the Caspian Sea . The vegetations shows a marked zonation which is related to the elevation of the terrain relative to flood waters. The various ecosystems of the area form the habitats for wildlife, including both migrating and resident bird species and fish.

The Astrakhanskiy Bioshere Reserve is threatened by the combined action of two processes. First, the level of the Caspian Sea fluctuates. From the 1930s to the 1970s, the sea level declined. Since then, the Caspian Sea level has risen more than 2 m. Second, the construction of hydroelectric dams has altered the discharge of water into the delta. Together, these two factors effect the frequency of the floods to which the vegetation in the reserve is subjected.

Site of Kalmykija shore Caspian sea covers a site of northwest coast of the Caspiane sea from a beginning Volga-Caspian channel on north up to a Ilmen gulf Gorshkovskiy Zaton in the south , near to city Caspian(Lagan). The sea area is shallow. Sandbank of shallow zone and artificial islands formed in result of clearings of the sea channel are engaged the reed growth. Coasts of drain type are fringed with wind drain strip (width up to 10 km) engaged reed grodth with mode of variable flooding. The land represents low-lying half-deserted plain with Baer's mounds which is characteristic for territories from west to east of Volga delta, alternating

0-7803-3836-7/97/$10.00 © 1997 IEEE

with lowering, engaged ilmen lake, bogs, saline land. The basic areas of a land are engaged half-deserted white wormwood and cereal white wormwood pasture.

MATERIALS AND METHODS.

For the analysis of SIR-C data the next additional materials are used: the vegetation map and map of dynamics of a coastal zone, which derived from earlier data of airspace remote sensing and field inspections. There were used also photographic image, derived with the chamber KT-1000 at the Russian satellites "Kosmos" in 1982, 1991, 1993 in scale 1:200 000 with the resolution 10-12 m. These scale and resolution are comparable with the resolution SIR-C images.

The SIR-C data of two (April and October) missions were analyzed. During April mission the radar measurements have been carried out with all polarization and crosspolarization channel. At the October there were used only HH, HV channel.

For purpose of research of possibilities of using SAR data for vegetation monitoring the synthesis of the SAR image in pceudo-colours with selected channel were used. For facilitation of the analysis the SAR images were georeference to contours of the vegetation map.

RESULTS

The result of analyze have shown, that it is possible to distinguish four basic groups of objects:

- open water surfaces of various types;
- the reed growth in drainage zones and around ilmen lakes;
- moistened sites of a land with saline grassland vegetation;
- dry sites of a land with half-deserted vegetation and agricultural grounds on them.

Open water surfaces. There were recognized of open water surfaces of next types: shallow sea surface, wind induced sea water reservoirs, surface of water reservoir detained by dams, lagoons, internal reservoirs. Some detained wind induced water surface are recognize owing to contours of flooded reed growth.

Reed growth. Detail analyze of radar signal have shown that various type of reed growth can be differed. Comparison of radar signal levels and vegetation parameters allowed to make conclusion that at least 5 gradation of density of reed growth can be determined from radar data. However for an exact estimation of opportunities of a method special field inspections are required.

Flooded sites of a land with saline grassland and grassland vegetation on coast along a drainage zone, former lagoon, on slopes of ilmen lowering, overmoistening of which is caused by rise of a level of subsoil waters, accompanying rise of a sea level, are allocated on radar images as strips bordered around a coast and valleys. Sites of poor lowering of land between Baer's mounds are allocated at the images too, these sites are flooded sites of land caused by rise of subsoil waters, engaged grassland and saline grassland vegetation, which at the moment of survey in April not yet was rather developed. They differ by increased levels of crosspolarization signals in L and C bands.

Channels, flooded zones with weak projective covering by vegetation are well allocated. Some narrow channels with size lesser then radar resolution is not showed up on the SAR images but they can be allocated on distribution of coastal vegetation, which is well allocated on radar image at L band. On signals of these channels it is possible to differentiate rather raised sites of a land, engaged half-deserted vegetation with white sagebrush and cereal white sagebrush associations.

The cultivated agricultural grounds - artifical irrigation fields and meadows are allocated on SAR images on a drawing of the objects: rectangular shape (by use of system of irrigation channels) or round shape (at bore irrigation). Meadow with irrigation are allocated at the images due to a network of narrow rectangulars, formed irrigation channels.

Coastal woods. The borders of coastal woods are allocated on a background of motley grassland. However the levels of signals of coastal woods are close to levels of signals from continuous reed growth.

As a whole of a general contour of vegetation are well identified on signals L band. Crosspolarization channels allow to specify borders of separate types of vegetation, details of which are lacked in the previous airspace data. These changes are connected to development of vegetation of a site.

Comparison of two mission's radar data. Comparison spring and autumn images allows to detect numerous changes, connected mainly to seasonal development of vegetation and different supplying territory with water.

On a site of sea area appreciably the spreading of spotty parterred growths - increasing of their area and projection covering.

The vegetation of reed drainage zone are more varied. Rarefied reed-mace growth are more precisely allocated at the images. The density of growth can serve an indicator attribute for allocation of the old form of a coastal line and relief.

On autumn images the contours of former agricultural grounds in drainage zones, partially overgrown with reed are precisely allocated. Sites of reed growths and grassland vegetation are differed at the image.

Changes connected with reduction of supplying land with water in the autumn are well allocated.

The surface of half-deserted areas of a land in October images has more varied vegetation, than in April one, this is connected with development of vegetation in poor ilmen lowering between Baer's mounds. In April grassland and saline grassland vegetation, which grows at these sites, have been at early vegetative stages. At the autumn images these

sites of a land are better allocated on a background of vegetation Baer's mounds.

On October images the lines of dams, channels, roads, borders of agricultural fields are more precisely identified. Rectangular - mesh structure of the populated area image is more revealed , the borders of which can be specified.

CONCLUSION

The results of analysis of SAR data have shown the opportunities of monitoring condition of environment in a coastal zone of Caspian sea, being in a perilous ecological situation. The radar data can be used for identification of vegetation type, seaside meadows and half-deserted pasture, detection of flooded sites and overmoistening of territory, which caused by rise of subsoil waters, which connected with fluctuations of Caspian seas level. Derived results will be used in future experiments on these regions by means of PRIRODA module [6].

AKNOWLEDGMENTS

The authors would like to thank NASA/JPL for data acquisition and processing.

Authors also knowledge Dr. Zakaharov A. I. and Dr. Sinilo V.P. for their help in preparation data for processing.

REFERENCES

[1] M. Y. Lychagin, E. A. Baldina, A. K. Gorbunov et al, "The Astrahanskiy Biosphere Reserve GIS; Part 1: Present status and perspectives," ITC Journal, 1995-3, pp. 189-192.

[2] E. A. Baldina, Yu. F. Knizhnikov, I. A. Labutina, "The Astrahanskiy Biosphere Reserve GIS; Part 2: Aerospace and cartographic maintenance," ITC Journal, 1995-3, pp. 193-196.

[3] I. A. Labutina, A. F. Zhivogliad, et al, "The Astrahanskiy Biosphere Reserve GIS; Part 3: Vegetation map," ITC Journal, 1995-3, pp. 197-201.

[4] "Complex of Remote Sensing of the Earth PRIRODA. Scientific program, " Version 2, Moscow, 1993.

[5] "Complex of Remote Sensing of the Earth PRIRODA. Scientific program. Proposals of Bulgaria, Germany, Italy, Poland, Romania, USA, Czechoslovakia, France, Switzerland," Moscow, 1993.

[6] "International Project PRIRODA. Instruments," Reference handbook, Moscow, 1993.

LABORATORY INVESTIGATIONS OF NONLINEAR SURFACE WAVE TRANSFORMATION IN A FIELD OF TWO-DIMENSIONALLY INHOMOGENEOUS CURRENTS[1]

Bakhanov,V.V., S.D.Bogatyrev, V.I.Kazakov, O.N.Kemarskaya.
Institute of Applied Physics, Russian Academy of Science
46 Uljanov Str. Nizhny Novgorod 603600 RUSSIA
T: 7.8312.384356 F: 7.8312.365976 Email: bakh@hydro.appl.sci-nnov.ru

ABSTRACT

The variability of various-amplitude surface waves in a field of inhomogeneous currents was investigated in the laboratory tank of the Institute of Applied Physics, Russian Academy of Sciences. Inhomogeneous currents were produced by streamlining of submerged spheres of diameters 0.15 m and 0.3 m moving with velocity 0.4 m/s. The spheres were submerged at depths of 0.3 m, 0.45 m, 0.6 m and 0.9 m. Surface waves of frequencies 1.7 Hz and 2 Hz and amplitudes 2 mm, 6 mm and 10 mm were generated by a wavemaker at the end of the tank from which a sphere started its motion and were absorbed by a wave absorber at the other end of the tank. The surface deviation was recorded by acoustic sensors at distances 8 m from the wavemaker. On the assumption of smooth variation of the surface wave amplitude the spatial two-dimensional distribution of the surface wave amplitude was reconstructed.

Experiments have demonstrated that the variability of 2 Hz surface waves whose group velocity is close to the velocity of sphere motion is more essential than that of surface waves of the frequency 1.7 Hz. Arrangement of regions of the surface wave amplitude increase and decrease greatly depends on the surface wave frequency and is practically independent of the sphere sizes and the depth of its submersion. At a large depth of the small sphere motion cases are recorded when surface wave anomalies caused by an inhomogeneous current are absent for small amplitudes of surface waves but occur at an increased amplitude of surface waves generated by a wavemaker.

Comparison of experimental data to the results of theoretical calculations have shown that they agree well as far as the arrangement of regions of the surface wave amplitude increase and decrease are concerned. At the same time the variation values of the surface wave amplitude in theoretical calculations is, as a rule, smaller than that recorded in the experiment.

INTRODUCTION

The interest to investigation of surface wave transformation in a field of two-dimensionally inhomogeneous flows is due to the development of remote sensing methods for subsurface processes. It is no easy matter to carry out field experiments on this problem, for example, to perform detailed recording of surface wave transformation in a field of inhomogeneous streamlining of a submarine rise. Thus, laboratory experiments seem to be of high priority at the present stage of research. A laboratory experiment [1] was devoted to the influence of a flow inhomogeneous only along its direction on the characteristics of a counterrunning surface wave flow. This report deals with laboratory investigation results of the surface wave amplitude variability in a field of two-dimensionally inhomogeneous sphere streamlining and with comparison of the experimental data to the results of related theoretical calculations made using the model described in [2].

EXPERIMENTAL METHOD

Experiments were carried out in a large thermostratified tank. Now in the tank the region of length 10 m and width 2 m can be used for surface wave experiments. Quasi-monochromatic surface waves of the frequency f were generated by wavemaker placed at one end of the tank and were absorbed by wave absorber at the other end of the tank. Sphere of a radius r was fixed at the end of a narrow streamlined knife and was submerged at a depth h (a distance from unperturbed water surface to sphere centre). The knife was attached to a trolley moving it along the tank with the velocity V=0.4 m/s. A rod with acoustic sensors of water surface deviation was placed across the tank. The acoustic sensors developed in IAP RAS are based on the ultrasound location phase method of measuring reflecting surface movements in continuous regime of ultrasound wave radiation. The rod was located at a distance R from the point where the trolley gained the velocity V (R is slightly less than the distance from the rod to the wavemaker). The instant of knife intersection of the sensor plane was recorded by a special contact marker. In the experiments we used 2 water surface deviation sensors placed at different distances from the tank axis. Data of the sensors and the contact marker of sensor plane intersection by a sphere were recorded by IBM PC computer.

[1] The work was suppoted by Russian Fund of Fundamental Investigation (code No 96-05-65128) and NOAA/DOD Advanced Sensor Application Program.

0-7803-3836-7/97/$10.00 © 1997 IEEE

The aim of the experiments was to determine the spatial structure of surface wave amplitude anomalies in the vicinity of the sphere. This problem was solved in the following way:

- on the assumption that during the time of passing of essential surface wave anomalies caused by sphere motion, by acoustic sensors (~ 5 s) the characteristics of the anomalies vary slightly, the recorded time variations of the surface wave amplitude were converted to the dependence of the surface wave amplitude on the coordinate directed along the tank axis (the x axis).
- after sphere motion ceased the acoustic sensors shifted by 0.1 m and new realization was recorded. Therefore, using the contact marker data we could combine the data of several experimental realizations and obtain spatial distribution of surface wave characteristics in the plane x, y (y is the coordinate across the tank).

An image provided by telecamera during experiments was recorded in IBM PC. Black grid was in the field of view of telecamera, the arrangement of which in the image could be used to calculate surface wave slopes. Processing of data yielded by telecamera is at the initial stage now, and thus only data of the acoustic sensors are analyzed in the present paper.

EXPERIMENTAL RESULTS AND THEIR COMPARISON WITH OF THEORETICAL RESULTS

First experiments were performed without a knife and with a moving knife without a sphere. First type experiments have demonstrated that there is inhomogeneity of the surface wave amplitude across the tank. Comparison of the experiments of the first and second types has shown that a knife without a sphere does not change the surface wave field.

Received experimentally spatial distributions of the surface wave amplitude for r = 0.15 m, h = 0.6 m, R = 7 m, surface wave amplitude A = 10 mm are shown in fig. 1a (f = 2 Hz) and in fig. 2a (f = 1.7 Hz). The horizontal axis in these figures corresponds to the x axis, and the vertical to the y axis. Surface deviations were measured only on one side of the tank axis, the second half of the figure is obtained by reflection with respect to the tank axis. The axes are graduated in cm, the position of the sphere centre corresponds to the point x = 700, y = 0. Data on the y axis are given only up to y = 70 cm, reading of more remote sensors from the tank axis are strongly perturbed by walls. The value of relative variation of the surface wave amplitude A is given in the figures. In each experimental realization the surface wave amplitude was normalized over its average value. Variation of A is shown in accordance with the scale presented to the left of the spatial distribution. Note that in fig. 1 and fig. 2 the boundaries of scales are different.

As is seen from figs. 1, 2 spatial structures of surface wave amplitude anomalies essentially depend on the surface wave frequency f. Thus, in fig. 2 (the group velocity of surface waves is more than V) the region of A decrease is shifted forward with respect to the sphere, while in fig. 1 (the group velocity of surface waves is equal V) the region of A decrease is practically above the sphere. The value of A variability at f = 2 Hz is more, than at f = 1.7 Hz. This difference grows with increase of value of unperturbed surface wave amplitude.

Analogous structures of surface wave amplitude anomalies are also given by theoretical calculation results. In the reference system related to the sphere, we deal with a physical situation adequate to that considered in [2]. Results of appropriate theoretical calculations are given in figs. 1b, 2b. Arrangement of regions and value of A increase and decrease, basically, correspond to the experimental data.

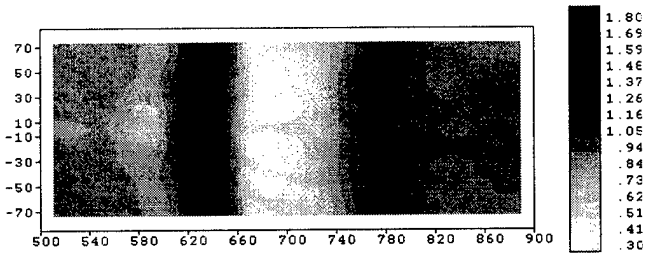

Fig. 1a.

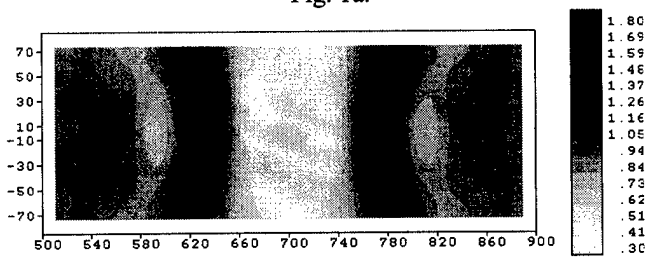

Fig. 1b.

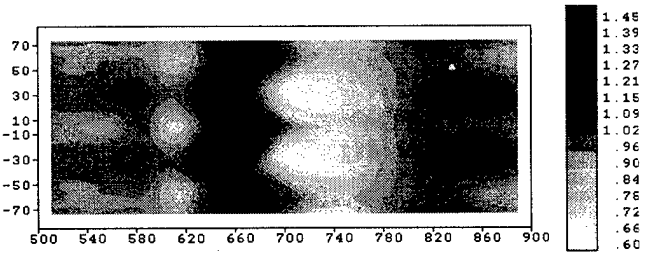

Fig. 2a.

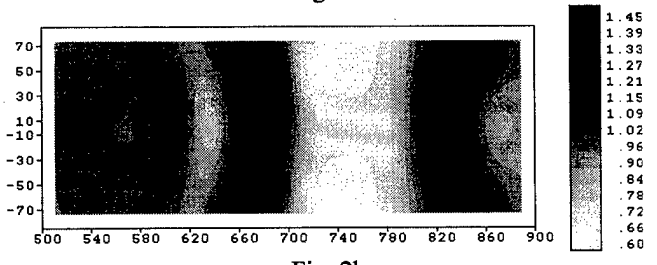

Fig. 2b.

Comparison of A spatial distributions at $R = 4$ m and $R = 7$ m enables one to draw some conclusions on the character of surface anomaly development with increase of R. The sizes of the spatial region above the sphere increase. Thus, the distance between the characteristic regions of surface anomaly structures for $R = 7$ m are, on average, by 0.3 m larger than for $R = 4$ m. The value of A variability for $R = 7$ m, on average, twice is more, than for $R = 4$ m, and this difference grows with increase of value of unperturbed surface wave amplitude. Analogous results are also yielded by theoretical calculations.

With increase of h in 1.5 time the value A of variability decreases on the average in 2 times, and the dependence of A variability value on h weakens at increase of value of unperturbed surface wave amplitude.

The most interesting result is dependence of A variability on value of unperturbed surface wave amplitude. So for a situation, similar to the fig. 1a, but at unperturbed surface wave amplitude 6 mm, the value of A varies in limits 0.5 - 1.5. With increase of value of unperturbed surface wave amplitude group speed of surface waves grows and, accordingly, the areas of increase and reduction of A are displaced in a direction of a sphere movement. At $r = 0.075$ m and $h = 0.6$ m for unperturbed surface wave amplitude 2 mm the appropriate structures of surface wave anomalies in a vicinity of sphere are not observed, and for unperturbed surface wave amplitude 10 mm they occur and the A varies in limits 0.75 - 1.15.

CONCLUSION

The performed experiments have shown the dependence of the surface wave anomaly structure in the field of inhomogeneous streamlining of a submerged sphere on the surface wave frequency. In this case such structures slightly vary with time and variation of sphere depth. For larger time and decreased depth of sphere submersion the value of surface wave amplitude variation increases. The value of surface waves amplitude variability grows at increase of unperturbed surface waves amplitude. The results of theoretical calculations of surface wave transformation in the sphere streamlining field agree with the experimental data concerning arrangement of regions of the surface wave amplitude increase and decrease.. The dependences of the value of surface wave amplitude variation on sphere motion time and its depth of submersion in theoretical calculations are analogous to those obtained in experiments.

Further it is planned to process experimental data on transformation of surface wave slopes in the sphere streamlining field recorded by a telecamera.

REFERENCES

[1] S.I. Badulin, K.V. Pokazeev, and A.D. Rozenberg, "Laboratory investigation of regular gravity-capillary wave transformation in inhomogeneous flows," Izv.AN SSSR. FAO, v.19, No.10, pp.1035-1041, 1983.

[2] V.V. Bakhanov, O.N. Kemarskaya, V.I. Pozdnyakova, I.A. Okomel'kova, and I.A. Shereshevskii, "Evolution of surface waves of finite amplitude in field of inhomogeneous current," 1996 International Geoscience and Remote Sensing Sympozium Proceedings, v.I, pp.609-611,1996.

Global Optimization Algorithms for Field-Wise Scatterometer Wind Estimation

Charles G. Brown and David G. Long
Brigham Young University, MERS Laboratory
459 CB, Provo, UT 84602
801-378-4884, FAX: 801-378-6586 browncg@salt.ee.byu.edu

Abstract—Field-wise scatterometer wind estimation determines the vector wind at many resolution elements simultaneously by estimating the parameters of a wind field model. According to simulations, it results in more accurate estimates than traditional point-wise estimation, which estimates the vector wind one resolution element at a time. Further, field-wise estimation produces fewer ambiguities than point-wise estimation.

Field-wise estimation necessitates locating the local minima of a high-dimensional, non-linear objective function. Conventional optimization techniques can be employed if initial search points within the capture regions of the local minima can be found. We develop and evaluate two novel approaches for determining initial search points for field-wise estimation. The accuracy of each algorithm is evaluated using simulated NASA Scatterometer (NSCAT) data.

INTRODUCTION

Field-wise scatterometer wind estimation involves indentifying the local minima of the high-dimensional and non-linear field-wise objective function. The local minima correspond to the optimized model-based estimates of the true wind field, and the goal of field-wise estimation is to locate the local minimum closest to the true wind.

Conventional optimization techniques may be used for field-wise estimation if initial values close to the true wind can be found. Previous approaches have used point-wise retrieved wind fields as initial values for gradient-search algorithms. When the retrieved field has few ambiguity removal errors, local optimization using its model fit as the initial value converges to the closest local minimum to the true wind. However, if the retrieved field has excessive errors, then it might yield a minimum far from the true wind. Consequently, we investigate global optimization algorithms that do not rely on pre-processing by point-wise ambiguity removal schemes in their search for initial values.

We develop algorithms to locate all of the local minima of the field-wise objective function, or at least a subset of the local minima that contains the closest to the true wind. Due to the computational expense of evaluating the objective function, traditional global optimization schemes prove intractable. In this paper we present two problem-specific algorithms that seek to identify initial values close to the true wind. First, a brief definition of field-wise wind estimation is provided, and descriptions of the pseudo-objective function and cluster-based algorithms follow. The performance of the two algorithms is evaluated using simulated NSCAT data.

FIELD-WISE WIND ESTIMATION

Field-wise wind estimation is the process of estimating wind field model parameters, denoted by the column vector $\hat{\mathbf{X}}$, from scatterometer backscatter measurements. The model-based wind field is the matrix product $\hat{\mathbf{W}} = F\hat{\mathbf{X}}$, where $\hat{\mathbf{W}}$ is a column vector containing the rectangular components of the wind vector cells. The matrix F is the wind field model, and the model fit to the wind field $\mathbf{W}$ is $\hat{\mathbf{X}} = F^{\dagger}\mathbf{W}$, where $F^{\dagger}$ is the pseudo-inverse of F [3].

Estimates of the model parameters are all the local minima of the field-wise objective function

$$J(\hat{\mathbf{W}} = F\hat{\mathbf{X}}) = -\sum_{n=1}^{N^2}\sum_{k=1}^{L_n} \ln p(z_n(k) \mid \hat{\mathbf{X}})$$

with

$$p(z_n(k) \mid \hat{\mathbf{X}}) = \frac{1}{\sqrt{2\pi}} \frac{1}{\sqrt{Var\left[z_n(k)\right]}} \cdot \exp\left\{-\frac{1}{2}\left[z_n(k) - \sigma_n^0(k)\right]^2 / Var\left[z_n(k)\right]\right\},$$

and

$$\sigma_n^0(k) = \mathcal{M}\left\{(u_n, v_n), k\right\}.$$

N is the number of cells on each side of the square region, and n is the wind vector cell index [3]. L_n is the number of measurements in cell n. The k^{th} measurement in cell n is denoted $z_n(k)$, and $p(z_n(k) \mid \hat{\mathbf{X}})$ is the likelihood of observing $z_n(k)$ given that $\hat{\mathbf{W}} = F\hat{\mathbf{X}}$ is the parameter vector of the model fit to the true wind. $\mathcal{M}$ represents the geophysical model function that relates (u_n, v_n), the vector wind in cell n, to the true value of $\sigma_n^0(k)$, which is the noiseless measurement that would be observed for the vector wind (u_n, v_n). Note that J may be expressed either as a function of $\hat{\mathbf{W}}$ or $\hat{\mathbf{X}}$.

In the following sections, we present two algorithms for globally optimizing the field-wise objective function. They are designed to locate a subset of the local minima of $J(\hat{\mathbf{X}})$ that contains the minimum closest to the true wind.

0-7803-3836-7/97/$10.00 © 1997 IEEE

PSEUDO-OBJECTIVE FUNCTION ALGORITHM

The pseudo-objective function (POF) algorithm locates the local minima of a simplified objective function, called the pseudo-objective function, and the local minima of the POF are then used as initial values in local optimizations of the full objective function J.

The model used in the POF describes the wind direction field by the polynomial model $p(c_1, c_2, c_3) = c_1 + c_2 x + c_3 y$, where x and y are the rectangular coordinates of the wind vector cell, and the origin of the coordinate system is such that c_1 is the mean direction of the wind field. The POF value of the model parameter set (c_1, c_2, c_3) is found by combining the direction field described by $p(c_1, c_2, c_3)$ with point-wise speed estimates, which are taken from the true simulated wind in this paper. Then, the resulting vector wind field is converted into the rectangular form $\hat{\mathbf{W}}$, and $J(\hat{\mathbf{W}})$ is the POF value of the parameter set (c_1, c_2, c_3).

The POF algorithm searches the reduced parameter space (c_1, c_2, c_3) for all local minima. The wind fields $\hat{\mathbf{W}}$ corresponding to local minima are constructed according to the POF model, and their wind field model parameter vectors $\hat{\mathbf{X}}$ are calculated from $\hat{\mathbf{X}} = F^{\dagger}\hat{\mathbf{W}}$, with F defined by the KL model [1]. The model vectors $\hat{\mathbf{X}}$ then are used as initial values in local optimizations of the full objective function J with a higher-order model. For simplicity the 6 parameter KL model is used in this paper.

CLUSTER-BASED ALGORITHM

The cluster-based (CB) algorithm (refer to Fig. 1) identifies initial values for local optimization by examining combinations of point-wise ambiguities. Before the CB algorithm is executed on a region, spurious ambiguities are removed according to [4] with a threshold of $\alpha = 10^{-4}$.

Examination of all possible ambiguity combinations for a given region is computationally intractable, even after removing improbable ambiguities, so the CB algorithm limits the search to typical wind fields. For each region a random set of 20 000 typical wind fields, represented by 6 parameter KL model parameter vectors, is generated. The model parameter vector for each typical wind field is drawn from a multi-variate normal population. Parameter means are assumed to be zero and variances are dictated by the eigenvalues of the autocorrelation matrix used to generate the KL model [1], [2].

In the next stage of the algorithm, the typical wind fields are used to select combinations of point-wise ambiguities. For each typical wind field, each of its vectors is compared with the point-wise ambiguity set in the same wind vector cell, and the closest ambiguity is selected. The field of point-wise ambiguities closest to the vectors of a typical wind field is its closest ambiguity field. The direction rms error between the 20 000 typical wind fields and their closest ambiguity fields is used to rank the typical winds in ascending order of error, and the model parameter vectors $\hat{\mathbf{X}}$ corresponding to the 500 highest ranked typical winds are clustered.

Finally, each cluster center is optimized to minimize direction rms error between the cluster center and its closest ambiguity field (the closest ambiguity field changes as the cluster center parameters are optimized). Note that this optimization step reduces direction rms error only. A more accurate speed field can be obtained by taking speeds from the closest point-wise ambiguities. The optimized cluster centers are the CB estimates of the wind field.

TEST RESULTS

The POF and CB algorithms were tested on simulated NSCAT data generated from wind fields obtained from the European Center for Medium-Range Weather Forecasting (ECMWF). From the simulated wind set, 80 NSCAT half-revolutions were simulated, and ambiguous point-wise estimates were made for each of the half-revolutions [3].

In order to evaluate the performance of the POF and CW algorithms, we define the skill of a field-wise estimation algorithm as its ability to model the direction of each individual vector of the true wind. For each region, the POF and CB algorithms produce a set of estimates of the true wind field. The estimate closest to the true wind, in a direction rms sense, is compared with the true wind. If a vector in the closest to true field is more than 20° off the corresponding vector in the true field, then it is counted as a single error, otherwise it is a success. The error and success rates are calculated by summing the numbers of single errors and successes per region and dividing by the total number of vectors in all of the regions combined.

The POF algorithm was run on 13 simulated NSCAT half-revolutions. Each half-revolution was divided into square regions, 12 NSCAT 50 km wind vector cells to a side. The regions overlapped by 50%. Regions missing data were rejected. The total number of regions in the test set was 566. The POF algorithm generated a set of estimates for each region, and the closest to the true wind was selected. The success and error rates for the closest to true estimates are recorded in Table 1. One possible source of error in the POF algorithm is the 6 parameter KL model used in the final optimization stage. Table 2 displays the mean direction rms error, relative to the true wind, of the 6 parameter KL model fit and the closest to true estimate. Since the KL model error is close to that of the closest estimate, the POF algorithm introduces only a little more average error than the model fit.

The CB algorithm was tested on 19 simulated NSCAT revolutions. The revolutions were divided into regions in the same manner as for the POF test. Regions missing data were rejected. The total number of regions in the test set was 911. For each region the CB algorithm generated a set of wind field estimates, and out of this set the closest

Skill Statistics

Algorithm	Success Rate	Error Rate
POF	88%	12%
CB	93%	7%

Table 1: *The skill of the pseudo-objective function (POF) and cluster-based (CB) algorithms is evaluated by comparing the closest to true estimate with the true wind. The success rate represents the probability that any given vector of the closest estimate will be within* 20° *of its corresponding vector in the true wind field.*

Mean Direction RMS Error Statistics

Algorithm	Mean DRMS Error of Closest Estimate	Mean DRMS Error of KL Model Fit
POF	15.5°	9.9°
CB	13.1°	10.5°

Table 2: *This table compares the mean direction rms (DRMS) error of the pseudo-objective function (POF) and cluster-based (CB) algorithms to that of the 6 parameter KL model fit to the true wind. The closest to true estimate of the POF and CB algorithms introduces only a little more average error than the 6 parameter KL model fit alone.*

estimate to the true wind was selected. The success and error rates for the closest to true estimates are recorded in Table 1. Since the CB algorithm also uses the 6 parameter KL model, one possible reason for inaccuracy in the estimates is modeling error due to the simplistic wind field model. Table 2 displays the mean direction rms error, relative to the true wind, of the 6 parameter KL model fit and the closest to true estimate. The average error for the closest estimate is not much different than that of the KL model fit, so the closest estimate of the CB performs almost as well, on average, as the KL model fit to the true wind.

CONCLUSION

The POF and CB algorithms locate a set of local minima of the field-wise objective function without relying on pre-processing by point-wise ambiguity removal algorithms. Both algorithms identify local minima that are close to the true wind a high percentage of the time, and some of the errors in the closest to true estimates can be attributed to modeling error in the 6 parameter KL model. Subsequent local optimizations using higher-order models

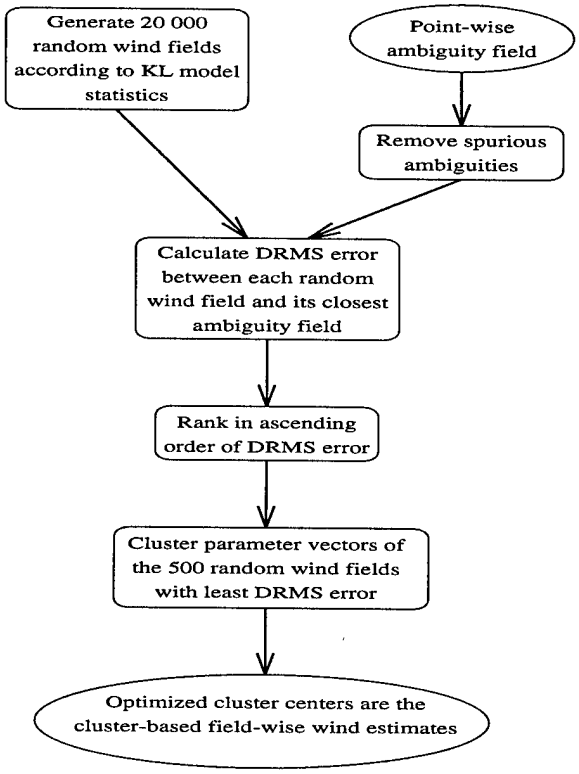

Figure 1: Cluster-Based Algorithm

can be expected to make the estimates more accurate. Further improvements in accuracy might be obtained by using POF and CB estimates as initial values for median filter processing.

References

[1] C. G. Brown *et al.*, "Wind Field Models and Model Order Selection for Wind Estimation," IGARSS, August 1997.

[2] A. E. Gonzalez and D. G. Long, "A Quality Assurance Algorithm for NASA Scatterometer Ambiguity Removal," IGARSS, August 1997.

[3] D. G. Long and J. M. Mendel, "Model-Based Estimation of Wind Fields Over the Ocean From Wind Scatterometer Measurements, Part II: Model Parameter Estimation," IEEE Trans. Geosci. Remote Sensing, vol. 28, no. 3, pp. 361-373, May 1990.

[4] T. E. Oliphant and D. G. Long, "Development of a Statistical Methods for Eliminating Improbable Wind Aliases in Scatterometer Wind Retrieval," IGARSS, pp. 1715-1717, May 1996.

Ocean Wave Spectrum Reconstruction from ERS-1 Satellite Scatterometer Data

Yijun He and Jinping Zhao

Ocean Remote Sensing Laboratory/Institute of Oceanology/Chinese Academy of Sciences
7 Nan Hai Road, Qingdao 266071/ P. R. China
Phone: 86-532-2879062 ext. 5804
Fax: 86-532-2870882
email: jpzhao@ms.qdio.ac.cn

Abstract--Satellite scatterometer has been used to measure ocean surface wind speed. Now, We suggest that the directional ocean wave spectrum can also be measured by satellite scatterometer for the first time. We define the optimal fit wave spectrum as the spectrum which minimize the cost function including observation and calculation normalized radar cross-section. The two-scale model of ocean wave is used in calculating the NRCS σ^0. The solution of the general nonlinear problem was obtained by an iterative technique. The tentative results are shown.

I Introduction

Sea state can be completely characterized statistically by the two dimensional directional wave spectrum describing the distribution of wave energy with respect to the wave propagation wave number. In the past, ocean waves have been studied using in-situ point probes capable of making non-directional, time-series measurements of wave properties. Directional wave spectrum can now be obtained using SAR[1]. However, the SAR cannot work all the time due to the power energy limited.

A spaceborne scatterometer can be used to measure σ^0, the wind speeds on the ocean surface can be reconstructed using them. There have been very good results of wind speeds for the ERS and Seasat satellites. Because the σ^0 depends on the ocean wave spectrum greatly we suggest that ocean wave spectrum is reconstructed by satellite scatterometer data. Next section the theories of microwave backscatter from the ocean surface are reviewed. A parametric directional ocean wave spectrum is also shown in section II. The next is the reconstruction of ocean wave spectrum and results analysis.

II Ocean Surface microwave scatter model

This section gives the theoretical model calculating normalized radar cross-section (NRCS) of ocean surface for reconstructing ocean wave spectrum.

The first attempts to develop theoretical model to calculate the NRCS from ocean wave in the 1950's, when investigators applied physical optics or Kirchhoff approximation to the ocean surface. However, these models could not explain the weaker returns for horizontal polarization compared to vertical[2]. It was not until 1968 the Wright[3] and Bass[4] independently derived a theoretical model known as the composite surface model (two-scale theory). The total NRCS is the summation of the cross section of each facet, which each facet was assumed to be independent of the next, weighted by the slope probability of the long waves $P(\xi_{x'},\xi_{y'})$ [5]. It's given by

$$\sigma^0 = \int_{-\infty}^{+\infty}\int_{-\infty}^{+\infty} \sigma_{pp}^{(1)}(\theta_{il},\phi_0)(1+\xi_x tg\theta_i)p(\xi_{x'},\xi_{y'})d\xi_x d\xi_y \quad (1)$$

where (x',y',z) and (x,y,z) are the ocean surface coordinate system and main coordinate system, respectively. ϕ_0 is an angle between x and x' (shown Fig. 1). $\xi_{x'}$, $\xi_{y'}$, ξ_x, ξ_y are the space derivative of ocean wave height to ocean surface coordinate system and main coordinate system, respectively. Then,

$$\begin{cases} \xi_{x'} = \xi_x \cos\phi_0 + \xi_y \sin\phi_0 \\ \xi_{y'} = \xi_y \cos\phi_0 - \xi_x \sin\phi_0 \end{cases}$$

θ_{il}, θ_I are local incidence angle, incidence angle, respectively, and

$$\cos\theta_{il} = \frac{\cos\theta_i}{(1+\xi_x^2+\xi_y^2)^{1/2}}(1+\xi_x tg\theta_i) \quad (2)$$

$\sigma_{pp}^{(1)}(\theta_{il}, \phi)$ is the NRCS of a slightly rough surface. The subscripts pp represent the transmit and receive polarizations. The two-scale model seems to describe well the microwave backscatter at intermediate incidence angles from the ocean surface.

Considering the anisotropy of wind wave, assume the directional wave spectrum [6]

0-7803-3836-7/97/$10.00 © 1997 IEEE

$$W(k,\phi) = \frac{1}{2\pi k} S(k,\phi) = \frac{1}{(2\pi)^2 k} S(k)[1 + a_1(1 - e^{-bk^2})\cos 2\phi) \quad (3)$$

where $b \approx 1.5 cm^2$

$$a_1 = \frac{2(1-R)}{(1-B)(1+R)}$$

$$B = \frac{1}{S_t^2} \int_0^\infty k^2 S(k) e^{-bk^2} dk$$

$$R = \frac{S_{ct}^2}{S_{ut}^2}$$

$$S_t^2 = S_{ut}^2 + S_{ct}^2$$

$$S_{ut}^2 = \int_0^\infty \int_0^{2\pi} (k\cos\phi)^2 S(k,\phi) dk d\phi$$

$$S_{ct}^2 = \int_0^\infty \int_0^{2\pi} (k\sin\phi)^2 S(k,\phi) dk d\phi$$

The slope probability of the long wave $p(\xi_{x'}, \xi_{y'})$ was given by Cox and Munk[7]. The ocean wave spectrum in our research is assumed to be,

$$S(k) = \begin{cases} \frac{a}{k^3} \exp(-\frac{0.74 g^2}{k^2 u^4}) & k < 0.04 \\ 0.875(2\pi)^{(p-1)} \frac{g + 3gk^2/13.177}{(gk + gk^3/13.177)^{(p+1)/2}} & k > 0.04 \end{cases} \quad (4)$$

where u is wind speed (cm/s)

$a = 4.05 \times 10^{-3}$

$g = 980 cm/s^2$

III Reconstruction of directional ocean wave spectrum and tentative results

The definition of the method for the reconstruction of the sea spectrum can be approached by following the standard procedure for solving the inversion problem. The optimal reconstruction of the directional ocean wave spectrum is obtained by minimizing the cost functional,

$$J = \sum_{i=1}^{3} (\sigma_{io}^0 - \sigma_{is}^o)^2 \quad (5)$$

where σ_{io}^0, σ_{is}^0 are the observed and the simulated NRCS in the ith direction, respectively. σ_{is}^0 is a nonlinear function of ocean wave spectrum $W(k,\phi)$, which is the function of a_1, ϕ and p (see (3) and (4)). The parameters which minimizes the functional J are obtained by using a complex method of optimization[8]. Samples of numerical results are shown to demonstrate the effectiveness of the technique proposed.

The directional ocean wave spectrum reconstruction from satellite scatterometer data is shown in Fig. 2. Table 1 shows the comparison of wave height, wave length and wave direction between buoy data and simulation data. The NRCS of observation and simulation is shown in table 2. Our results are mainly agreement with in-situ data. We only test one result because we have not enough in-situ data in synchronism with satellite scatterometer data.

Although we have done a few work, it is only begin. There are a large number of problems to be solved in reconstruction methods and validation in order to realize completely the directional ocean wave spectrum reconstruction from satellite scatterometer data.

Acknowledgments

The authors would like to thank ESA French PAF for providing ERS-1 scatterometer data.

References

[1] K. Hasselmann and S. Hasselmann, "On the nonlinear mapping of an ocean wave spectrum into a synthetic aperture radar image spectrum and its inversion", J. Geophys. Res., Vol. 96, pp10713-10729, 1991.

[2] R. K. Moore, "Radar Determination of Winds at Sea", Pro. IEEE, Vol. 67, No. 11, 1979

[3] J. W. Wright, "A New model for Sea Clutter", IEEE Trans. Antennas Propagat., Vol. AP-16, pp. 217-223, 1968.

[4] F. G. Bass, I. M. Fuks, A. I. Kalmykov, I. E. Ostrovsky, and A. D. Rosenberg, "Very High Frequency Radiowave Scattering by a Disturbed Sea Surface Part 1: Scattering from a Slightly Disturbed Boundary", IEEE Trans. Antennas Propagat., Vol. AP-16, pp. 554, 1968.

[5] S. T. Wu and A. K. Fung, "A Noncoherent Model for Microwave Emission and Backscattering from the Sea Surface", J. Geophys. Res., Vol. 77, No. 3, pp. 5917-5929, 1972.

[6] H. L. Chan and A. K. Fung, "A Theory of Sea Scatter at Large Incident Angles", , J. Geophys. Res., Vol. 82, No. 2, pp. 3439-3444, 1977.

[7] C. Cox and W. Munk, "Measurement of the Roughness of the Sea Surface from Photographs of the Sun Glitter, J. Opt. Soc. Amer., Vol. 44, No. 11, pp.839-850, 1954.

[8] M. J. Box, "A New Method of Constrained Optimization and a Comparison with Other Methods", Computer Journal, 8, 1965.

Table 1 The comparison of wave height, wave length and wave direction between simulation and in-situ data

	Time	Place	Wind speed	Wind direction	Wave height ($h_{1/10}$)	Wave length	Wave direction
Buoy data	12:00	24.52N 118.56E	7.0(m/s)	NNE	0.5(m)	25(m)	NNE
Numerical simulation data	14:44	24.03N 118.76E	7.39(m/s)	209°	0.42(m)	30.6(m)	225°

Table 2 The comparison of NRCS between observation and numerical simulation

Incidence angle (degree)	54.3	43.0	54.3
Observation NRCS(dB)	-18.90	-18.40	-24.80
Numerical simulation NRCS(dB)	-18.96	-18.43	-24.77

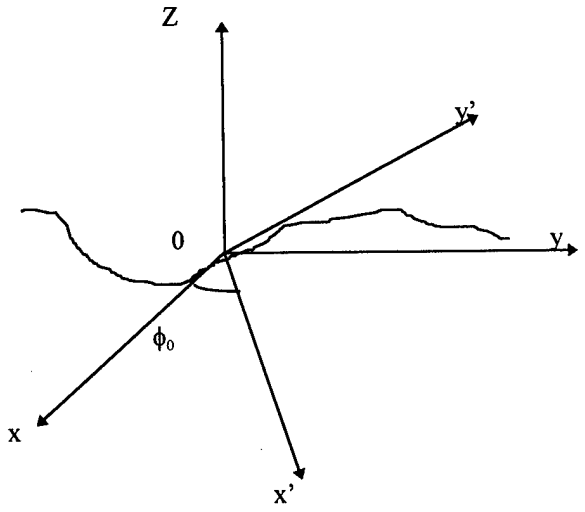

Fig. 1 The coordinate system

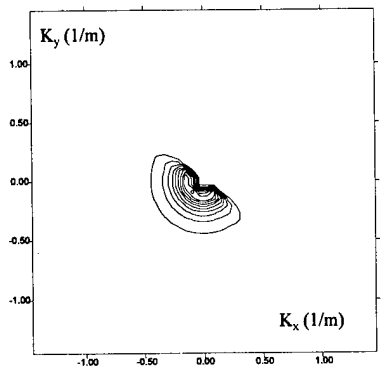

Fig. 2 The direction ocean wave spectrum reconstruction from ERS-1 scatterometer data on 11 Nov., 1993.

Validation of Models and Algorithms for Microwave Radiometric Investigations of Tropical Cyclones

Petrenko B.Z, Nerushev A.F* Milekhin L.I*, Zagorin G.K

Institute of Radioengineering and Electronics
141120, 1, Vvedensky sq., Fryasino, Moscow reg., Russia; E-mail: petrenko@ire.rssi.ru

***NPO "Typhoon",**
249020, 82, Lenin av., Obninsk, Kaluga reg., Russia; E-mail: typhoon@storm.iasnet.com

Abstract - The applicability of standard passive microwave data interpreting techniques to observing tropical cyclones is studied basing on the SSM/I observations of tropical cyclones in July - September 1994. It is shown that spatial distributions of wind speed retrieved from the SSM/I data provide a good description of tropical cyclones structure at distances of 200-300 km from the cyclone center including some quantitative parameters. The existing rain rate retrieval algorithms from the SSM/I data are classified according to results of their application to tropical cyclones observations.

INTRODUCTION

Microwave radiometric observations of tropical cyclones (TC) are important for studies of energy exchange in the ocean - atmosphere system and for forecast of dangerous atmospheric events as well. The microwave thermal emission of the ocean-atmosphere system depends on such parameters as wind speed over sea surface, atmospheric cloud liquid water and water vapor contents and rain rate. Variations of these parameters govern the energy exchange between the ocean and the atmosphere and they are of the great importance for understanding of tropical cyclones evolution.

A large amount of TC microwave observations were made from the "Nimbus-7" and DMSP satellites [1,2]. Combined TC observations in microwave, IR and visible spectral regions are scheduled within the framework of the PRIRODA mission [3]. The future TRMM mission is aimed to measuring rainfall in the tropical zone [4].

However, the potential of the meteorological interpretation of data of TC microwave radiometric sounding is limited due to the lack of geophysical parameters retrieval algorithms developed especially for abnormal meteorological conditions inherent in TC. For this reason, it is worthwhile to study to what extent routine algorithms can be used for TC investigations. The goal of this article is to assess the performance of wind speed and rain rate retrieval algorithms. Our analysis is based on processing data of TC soundings with the radiometer SSM/I from the DMSP F10 satellite in July - September 1994 over the North West Pacific and, where possible, on comparisons with the available meteorological information. The analysis was performed for three typhoons: Tim (7.07-11.07.94.), Walt (14.07-26.07.94.) and Kinna (5.09-12.09. 94г.).

WIND SPEED FIELD VALIDATION

The most of existing algorithms and models for near surface wind speed retrieval are valid within the range of V values V < 20 m/s [5]. Since in the central part of well-developed TC values of V can be of 60 m/s and more, these algorithms can be used for V retrieval at the TC outlying area only. To retrieve V absolute values (not wind direction) from the DMSP F10 SSM/I data [6] we used a well-detailed model [7] which uses SSM/I channels 37 (V and H), 22V and 19(V and H). The inversion of this model was performed with the method [8]. Wind speed estimates were compared with the data of regular storm warnings received from the Japan Meteorological Center (Tokyo).

One of important parameters of the wind speed field is a mean distance from the TC center R_{30} at which V is of 30 knots (15.42 m/s). Table 1 presents values of this parameter estimated SSM/I data (R_S) and those obtained from storm messages (R_M) for 5 observations of TC Walt and Kinna. The Maximum wind speed values V_m taken from [9] are also presented in this table. For all cases $R_S > R_M$, with the mean difference $R_S - R_H = 38$ km being closed to the SSM/I footprint size at the frequency 37 GHz which is the most critical for V retrieval.

In the most cases retrieved V distributions are asymmetric relative to the TC centers. This is a real feature of the TC wind speed fields caused by the TC motion as a whole with a speed V_W. According to [9], for the TC Walt V_W was 4-6 m/s, for TC Tim - V_W=5-7 m/s, and for TC Kinna V_W=2-3 m/s. Assuming quasy-symmetry of the wind speed field of the motionless TC, in the most cases the observed asymmetry TC corresponds to the directions of the TC motion and to V_W values. Fig. 1 demonstrates this effect for TC Walt (North-East moving direction) and Tim (North-West movement direction).

Fig. 2 shows an image of TC Walt where the typhoon "eye" is seen as the area at the TC center where V = 14 m/s.

0-7803-3836-7/97/$10.00 © 1997 IEEE

Taking into account the maximum wind speed value V_M.=40 m/s of TC Walt for this time.[9] a real size of the TC "eye" was estimated as D = 30 km.

So, we concluded that the application of standard microwave radiometric models and algorithms to TC observations enables one to determine following important wind speed field parameters:

- A size of a storm zone defined as a distance from the TC center at which V=30 knots;
- An asymmetry of the wind speed field caused by the TC motion as a whole;
- A size of a TC "eye", taking into account the maximum TC wind speed.

ANALYSIS OF RAIN RATE RETRIEVAL ALGORITHMS

Up to now, more than 20 algorithms have been proposed for rain rate (RR) retrieval over the ocean from the SSM/I data [10,11], and algorithms [12,13] were developed for TC especially. The goal of our study was to analyze a possible scatter of RR estimates made with different algorithms over TC area. We found that it is convenient to divide the whole TC area into two sub-areas where different algorithms are effective. The criterion to discriminate these areas is the value of brightness temperature measured in the 85H SSM/I channel with a threshold T85H=244 K. This threshold is close to one introduced in [14] to discriminate stratiform (T85H>245K) and cumulus (T85H<245K) types of cloud cover. Accordingly, below we shall distinguish S-algorithms applicable in the S-area where T85H>245K and C-algorithms applicable in the C-area where T85H<245K. We note that according to our estimates, more then 90% of precipitations in TC occur in the C-area.

S - algorithms underestimate RR values over the C - area and give RR rate values of 1 - 3 mm/h over the S-area. RR estimates made with the most of C-algorithms are correlated over the C-area with a correlation coefficient of 0.9 and more. However, C-algorithms often yield essentially negative RR values over the S-area. Fig. 3 represents RR estimates made over TC Walt with one of the algorithms of S-group ("K", as classified in [11]) and with the Adler algorithm [10] which belongs to the C-group. Since the Adler algorithm was undergone to a comprehensive validation [10], we considered it as a reference algorithm for the C-area of TC.

We found that RR estimates made with some of C - algorithms are essentially lower then those made with the Adler algorithm and assumed that this discrepancy was caused by neglecting the effect of partial antenna beam filling with precipitations. We corrected these algorithms with the procedure proposed in [15].

$$RR_1=RR_0/(0.5964-0.0198/RR_0), \quad (1)$$

where RR_0 is the initial RR estimate and RR_1 is corrected RR value. This procedure allowed us to reduce essentially the scatter of RR estimates in the C-area. The best coincidence with the Adler algorithm with the RMS deviation of 1.9 mm/h over the C-area was achieved for the Liu-Curry algorithm [13]:

$$RR_0=.0001163*(T19V-T85V+90)^{2.276} \quad (2)$$

Fig. 4 demonstrates results of correction of the Liu Curry algorithm.

Our conclusion is that the Liu-Curry algorithm [13], when adjusted for partial antenna beam filling with precipitations (1), appears the most adequate for rain rate retrieval over the whole TC area, both in C- and S-zones. Over C-zone it provides RR estimates close to the well-validated Adler algorithm and over S-zone RR estimates made with the Liu-Curry algorithm are close to those made with other S-algorithms ("K", for example).

ACKNOWLEDGEMENT

The authors' thanks to Mr. Frank Wentz (Remote Sensing Systems Inc.) who provided us with the data of the F10 and F11 SSM/I radiometers.

REFERENCES

[1] Kidder S.Q., W.M.Gray, T.H.Haar. estimating tropical cyclone central pressure and outer winds from satellite microwave data. Monthly Weather Review, v. 106, pp.1558 - 1464, October, 1978.

[2] Rodgers E.B., S.W.Chang, H.F.Pierce. A satellite and numerical study of precipitation characteristics in Western North Atlantic tropical cyclones. Journal of Applied Meteorology, v. 33, pp. 129-139, Febryary, 1994.

[3] International remote Sensing Project PRIRODA. Science Plan. Armand N.A., ed. IRE RAS, Moscow,1995.

[4] Han D. Tropical Rainfall Measuring Mission science data and information system. Proceedings of IGARSS'93, v. 2, pp.421-422.

[5] Sasaki Y., Asanuma I., Muneyama K. et al. The dependence of sea-surface microwave emission on wind speed, frequency, incidence angle and polarization over the frequency range from 1 to 40 GHz. IEEE Trans. Geosci. and Remote Sensing, 19.. ,vol. GE-25, N 2, pp. 138- 146.

[6] Hollinger J.P., Peirce J.L., Poe G.A. SSM/I Instrument Evaluation. IEEE Trans. Geosci. and Remote Sensing,1990, v. 28, N 5, pp. 781-790.

[7] Wentz F.J. Measurement of oceanic wind vector using satellite microwave radiometers. IEEE Trans. Geosci. and Remote Sens., 1992, vol. 30, N 5, pp. 960-972.

[8] Petrenko B.Z. External calibration of satellite passive microwave measurements and retrieval of geophysical parameters. Proceedings of IGARSS'91, v. 4, pp. 2385-2387.

[9] Annual Tropical Cyclone Report. NAVPACMETOCCEN WEST/JTWC. USA. 1994.

[10] T.Wilheit et.al. Algorithms for the Retrieval of Rainfall From Passive Microwave Measurements.Remote Sensing Reviews 1994, v.11, pp.116-194.

[11] G.L.Liberti Review of the SSM/I-based algorithms submitted for the GPCP-AIP/2. Microwave Radiometry and Remote Sensing of the Environment. ed. D. Solimini. Utrecht, the Netherlands, 1995, pp.297-306.

Typhoon	V_m, m/s	R_S, km	R_M, km	$R_P - R_H$, km
Walt	33.4	444	451	7
Walt	38.5	482	529	47
Walt	46.26	500	537	37
Walt	51,4	556	618	62
Kinna	20.5	279	314	35
Mean				38

Table 1: Maximum wind speed V, observed (R_S) and obtained from storm messages (R_M) values of R_{30} for some observations of TC Walt and Kinna.

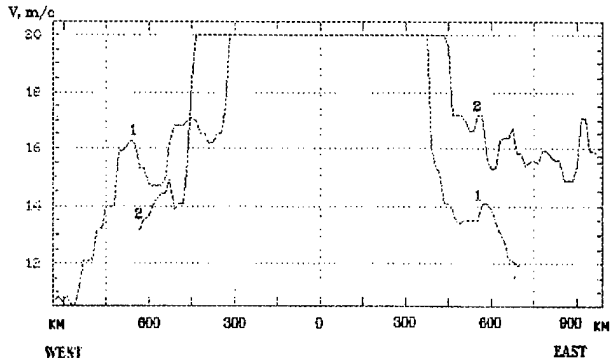

Fig. 1. West-East wind speed field cross-sections for TC Walt (1) and Tim (2).

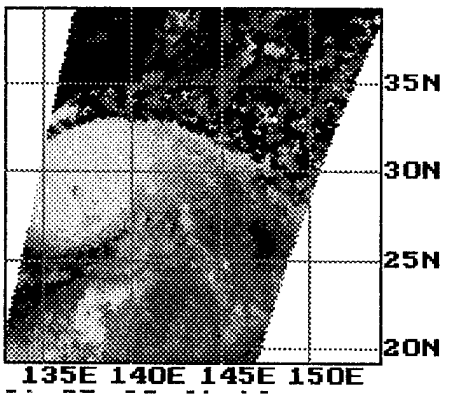

Fig.2. The image of the wind speed field of TC Walt.

[12] W.S.Olson Physical Retrieval of Rainfall Rates Over the Ocean by Multispectral Microwave Radiometry: Application to Tropical Cyclones Journ. of Geophys. Research v.94, ND2,pp. 2267-2280, 1989.

[13] G.Liu, J.A.Curry Retrieval of Precipitation From Satellite Microwave Measurement Using Both Emission and Scattering. Journ.Geophys.Res. v.97, ND9, pp. 9959-9974, 1992.

[14] G.Dalu et.al. Rainfall Estimation over the Ocean from 37 GHz Radiometric Measurements. IL Nuovo Cimento, Maggio-Giugno,1994, pp.349-358.

[15] L.S.Chiu et.al. Rain estimation from satellites: effect of finite fields of view. Journ of Geophysical Research v.95,ND3, pp.2177-2185,1990.

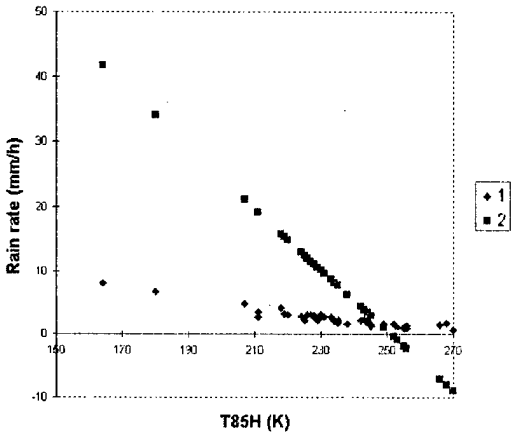

Fig.3. RR estimates by the algorithms K (1) and Adler (2) versus T85 H for TC Walt.

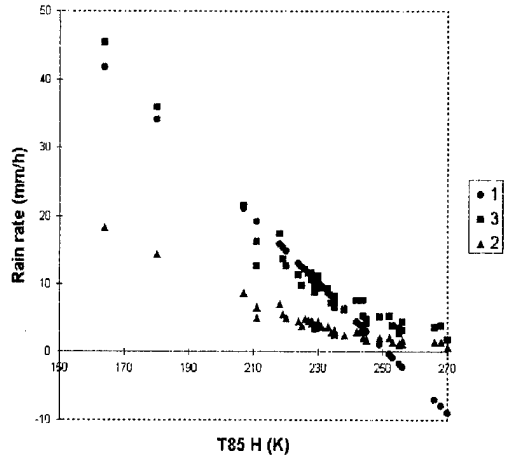

Fig.4. RR estimates by algorithms of Adler (1), Liu-Curry (2) and corrected Liu-Curry (3) versus T85H for TC Walt.

THE SURFACE ACTIVE SEA FILMS: PROPERTIES AND DYNAMICS

Tatjana Talipova
Institute of Applied Physics, 46 Uljanov Str., 603600, Nizhny Novgorod, Russia.
Fax: +(8312) 365976, Email: tata@appl.sci-nnov.ru

Abstract

The surface-active substance (SAS) films plays important role for an interpretation of remote sensing of the ocean surface. The review of the results of the theoretical and experimental (as laboratory well as nature) study is presented. The physical properties of thin (monomolecular and composite) organic films on the water surface have been studied with accent on the main mechanical characteristics: film pressure and film elasticity (Young modules). These values are responsible on the variations of the dispersive properties of gravity-capillary waves, in particular, the growth of decrement of these waves with the film presence, and the appearance the second type of waves on the water surface covered by thin film - the Marangoni waves. Usually marine films are composed from some organic molecules and their specific properties as hysteresis, connection between the film elasticity and the concentration of the organic matter in the subsurface microlayer and the wind velocity have been observed. The mathematical model of the surface film hysteresis is proposed. The exact dispersion relations for linear waves on a fluid surface covered by a film has been obtained and calculated numerically in the wide range of the viscosity and elasticity. The nonlinear theory of the surfactant film effects on short wind ripple within the kinetic equation for the wind wave spectrum is proposed and the results of corresponding field and laboratory tests are reported. The theory of the surface manifestation of internal waves due to surfactant films based on a nonlinear model of the interaction between short wind waves and the current field induced by internal waves, taking into account real properties of the surfactants, is developed.

Elasticity properties of SAS films

One of the principal characteristics of SAS films is the isotherm - the dependence of the film pressure F, arising during compression of the film on the area A occupied by it. The elasticity module $P = -A\ dF/dA$, which determines the damping coefficient γ of surface waves in the presence of film (Yermakov et al, 1980) may be obtained from the isotherm. Most of sea film show the isotherm $F(A)$ with the sharp increasing of P from practically 0 to the significant values when the film concentration becomes over some characteristic value. It is observed experimentally for the coastal zone of the Black Sea: the film elasticity is decreased mainly with increasing of wind speed V from 0 to 6 m/s as $P = -6.23\ lnV + 14.4$. This result is presented on Fig. 1. Also the experimental fact is - after the wind speed influence on the sea surface is excluded the film elasticity P grows to the value about 32 dyn/cm.

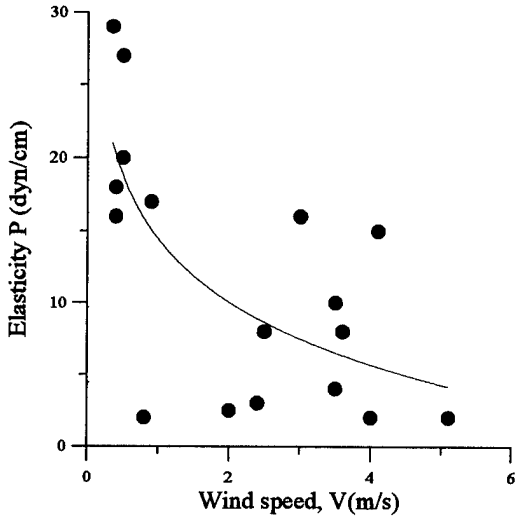

Fig.1 The experimental points for film elasticity P on wind speed V.

The experimental dependence of film elasticity on the under surface layer concentration of organic matter is following

$$P(dyn/cm) = (0.3 \pm 0.05)C(\mu\mu g/dm^3) - (0.33 \pm 3)(dyn/cm) \quad (1)$$

(Demin et al, 1985). The hysteresis phenomena is observed experimentally for SAS films. The film pressure F is depended on dimensionless film deformation e and film elasticity P with time t is following

$$F(t) = Pe - P\int_{-\infty}^{t} G(t-\xi)e(\xi)d\xi \quad (2)$$

when

$$G(t) = \frac{1}{\tau}\left(1 - \frac{P_e}{P}\right)\exp(-t/\tau). \quad (3)$$

τ is the typical time of film relaxation and P_e is the elasticity module after infinity. The loss of energy W for periodical process of film area variation is described by the experimental dependence on elasticity P and deformation e

$$W = e^2(0.11 \pm 0.01)P(dyn/cm) + (0.15 \pm 0.18) \quad (4)$$

(Ermakov S.A., Talipova T.G., 1985). The statistical analysis for film isotherms in the Atlantic regions gives the nonlinear connection between film pressure and their elasticity in the

0-7803-3836-7/97/$10.00 © 1997 IEEE

form $P = \alpha(F)F$, where $\alpha(F)$ has the following experimental expression: $\alpha(F) = -1.74\ ln(F/62.2)$, Fig. 2. (Panchenko et al., 1990).

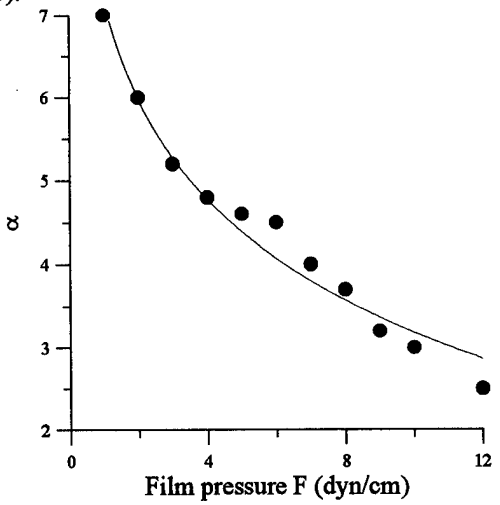

Fig. 2. The experimental dependence α on film pressure F

The SAS film influence on the wind ripple

It is known that the nature of wind waves on the sea surface id determined in large part by the extent to which the surface is covered with SAS. Field experiments performed with artificial slicks have shown that the intensity of the wind waves decreases markedly in the region covered by SAS film (Ermakov et al. 1986). The theory and experiment of wind ripple damping by SAS film is presented by (Yermakov, Pelinovsky, Talipova, 1980, 1982 ; Ermakov, Panchenko, Talipova, 1985, Ermakov et al, 1986). Considering the variability of short wind wave spectra in slicks, the degree of the variability is characterized by a value of the relation of spectral intensity for given wave number k into the slick E_s to the non slick region spectral intensity E_0: $K = lg\ (E_s/E_0)$. This value is characterized the hydrophysical contrast between slick and non slick area and is very important for remote sensing. From the developed theory it is following that for slow breeze

$$K(k,P,V) = \frac{\gamma(k,P_0) - \beta(k,V_0)}{\gamma(k,P_s) - \beta(k,V_s)}, \qquad (5)$$

where γ is the decrement and β is the increment of ripple. For moderate wind we have

$$K(k,P,V) = \frac{\beta(k,V_s) - \gamma(k,P_s)}{\beta(k,V_0) - \gamma(k,P_0)} \qquad (6)$$

The ripple decrement in SAS film present is described by

$$\gamma(k,P) = 2\nu k^2 \frac{\frac{2\nu k^2}{\omega_0} - \sqrt{\frac{2\nu k^2}{\omega_0}\frac{Pk^3}{\rho\omega_0^2}} - \left(\frac{Pk^3}{\rho\omega_0^2}\right)^2 / 2\sqrt{\frac{2\nu k^2}{\omega_0}}}{\frac{2\nu k^2}{\omega_0} - 2\sqrt{\frac{2\nu k^2}{\omega_0}\frac{Pk^3}{\rho\omega_0^2}} + 2\left(\frac{Pk^3}{\rho\omega_0^2}\right)^2} \qquad (7)$$

The results of sea experiments with the artificial slicks for film elasticity gives a good agreement with developed theory.

The theory of the sea surface slick formation

The theory of sea surface slick formation is based on the equation (7) for ripple decrement, formulas (5)-(6) for hydrophysical contrast between slick and non slick area and the equation for SAS concentration balance Γ:

$$\frac{\partial\Gamma}{\partial t} + div\Gamma u = Q \qquad (8)$$

where u is the surface particles velocity and Q is the source of SAS matter. The theory of variation of film concentration in the field of internal and surface waves and currents is developed by (Kozlov, Pelinovsky, Talipova, 1987 a,b; Kozlov, Talipova 1991). The surface diffusion and film relaxation processes (as hysteresis and dependence on wind speed) is taken into account. It is shown that the relaxation processes can limit the growth of film concentration in the zones of current convergence only for long relaxation time and can not for short relaxation time but the horizontal diffusion can limit it always. As example for Langmuir circulation:

$$\frac{\Gamma}{\Gamma_0} = 1 - \frac{\cos kx}{\frac{kD}{u_0} + \frac{1}{u_0 k\tau}}\left(e^{-(Dk^2 + \frac{1}{\tau})t} - 1\right) \qquad (9)$$

For the internal waves there is not the convergence zones on the surface, because the speed of internal wave propagation c is more than the particle velocity on the surface u. For sinusoidal internal wave without relaxation and diffusion of SAS the film concentration variations are periodical for every fixed phase of internal wave:

$$\frac{\Gamma}{\Gamma_0} = (1-\varepsilon^2)[1 - \varepsilon^2(1 - \cos(\sqrt{1-\varepsilon^2}\,\omega t))\sin kx + \\ + \varepsilon\sqrt{1-\varepsilon^2}\cos kz \sin(\sqrt{1-\varepsilon^2}\,\omega t) - \\ - \varepsilon^2\cos(\sqrt{1-\varepsilon^2}\,\omega t)]^{-1} \qquad (10)$$

ε is amplitude of internal wave U_0 divided by wave speed c_0. For internal soliton

$$\frac{\Gamma}{\Gamma_0} = \frac{1}{1 - \varepsilon\sec h^2 kz} \qquad (11)$$

Due to relaxation and horizontal diffusion of SAS the film concentration in the field of sinusoidal internal wave of small amplitude is

$$\frac{\Gamma}{\Gamma_0} = 1 + \varepsilon \frac{\sin(kx - \omega t - \theta)}{\sqrt{1 + \omega_r^{2/\omega^2}}}, \theta = arctg \frac{\omega_r}{\omega} \qquad (12)$$

where $\omega_r = 1/\tau + Dk^2$. So, internal waves and currents change the film concentration and due to change the film elasticity also. Film elasticity changes sharply from zero to sufficient values. Correspondingly the ripple damping coefficient changes sharply from $2\nu k^2$ for clear water surface to values 5-10 times more and the hydrodynamic contrast K becomes sufficient too. For example the growths of film elasticity and corresponding to wave damping coefficient for one of sea-surface film sample are given on the Figures 3 and 4 (Yermakov, Pelinovsky, Talipova, 1980).

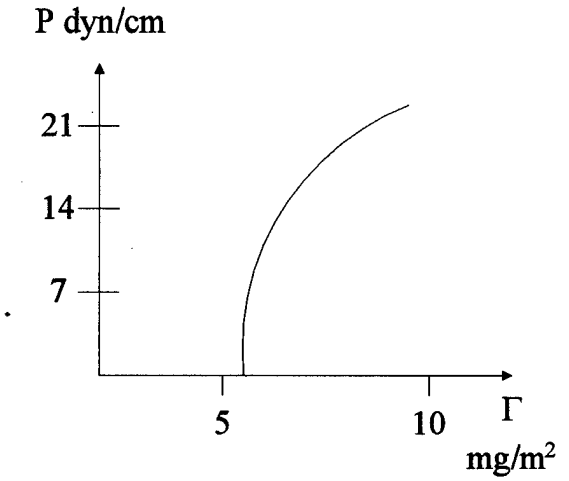

Fig. 3. The sharp increasing of the film elasticity with the film concentration.

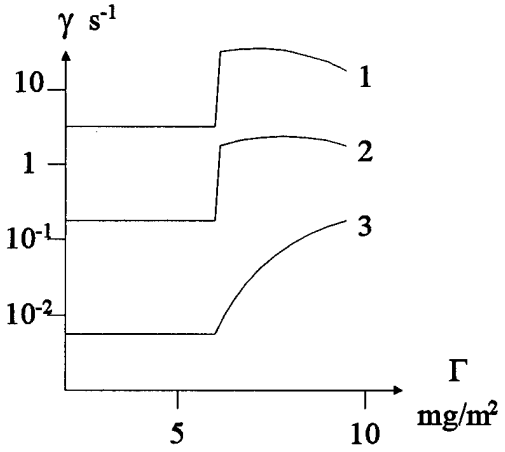

Fig. 4. The corresponding variation of wind ripple decrement with the film concentration. 1- wavelength $\lambda = 0.5$ cm; 2 - $\lambda = 2$ cm; 3 - $\lambda = 10$ cm.

For this example, the hydrodynamic contrast K for very slow wind and wavelength is equal 2 cm is varied from 0 to 10 dB when film concentration is varied under the internal wave action from 6 to 6.2 mg/m^2.

Acknowledgement

The participation in IGARSS'97 for TT is supported by the ISF. This work is supported by a grants RFBR 96-05-64108 and Program of the Technical Universities,.

References

Ermakov S.A., Pelinovsky E.N., Talipova T.G. Influence of Internal Waves on Short Wind Ripple by Means of Surface - Active Films. - in Issue: The Influence of Internal Waves on Sea Surface. (Ed. Pelinovsky E.) Gorky: Institute of Applied Phys., 1982, pp. 31 - 51.

Ermakov S.A., Talipova T.G. Elastic Hysteresis of Sea Surface - Active Films. - Doklady AN SSSR, 1985, v. 281, No. 4, pp. 941 - 944.

Ermakov S.A., Panchenko A.R., Salashin S.G., Talipova T.G., Titov V.I., Zujkova A.M., Surface film effect on short wind waves. - Dynamics of Atmospheres and Oceans., 1986, v. 10, pp. 31 - 50.

Kozlov S.I., Pelinovsky E.N., Talipova T.G. Dynamics of Surface - Active Films in a Non - Uniform Current Field. - Sov. Meteorology and Hydrology 1987 a, No. 1, pp. 84 - 93.

Kozlov S.I., Pelinovsky E.N., Talipova T.G. Dynamics of Surface - Active Films at the Sea Surface During Internal Waves Passing. - Sov. J. Phys. Oceanogr., 1987b, 4, 3 - 8.

Kozlov S.I., Talipova T.G. Transformation of Slicks on Sea Surface under the Influence of Wind Waves Spectrum Variations. Izvestiya, Atmospheric and Oceanic Physics, 1991, v. 27, No. 8, pp. 862 - 866.

Panchenko A.R., Pelinovsky E.N., Talipova T.G. The Probability Distribution of Film Elasticity in Slicks. - Preprint, Institute of Applied Physics, 1990, N. 274, 22 p.

Pelinovsky E.N., Talipova T.G. Surface - Active Films on Sea Surface. Novosibirsk: Heat Transfer Institute Press. 1990, N. 219, 41p.

Yermakov S.A., Pelinovsky E.N., Talipova T.G. On the Surface - Active Film Influence on Wind Wave Spectrum Variation under Internal Wave Action. - Izvestiya, Atmospheric and Oceanic Physics, 1980, v. 16, No. 10, pp. 1068 - 1078.

Yermakov S.A., Panchenko A.R., Talipova T.G. High - Frequency Wind Wave Damping by Artificial Surface - Active Films. Izvestiya, Atmospheric and Oceanic Physics, 1985, v. 21, No. 1, pp. 76-82.

Pelinovsky E., Talipova T. Scaling effects at internal wave modelling in a basin covered by surface - active films. Izvestija, Atmospheric and Oceanic Physics}, 1995, v. 31, N. 5, 701 - 704

IGARSS'97

1997 International Geoscience and Remote Sensing Symposium

03-08 August 1997

Singapore International Convention & Exhibition Centre

Technical Program

Interactive Area 19: Remote Sensing Techniques and Instrumentation

L-band 300-watt Solid State Pulse Power Amplifiers for SAR

Yunkai Deng
Institute of Electronic Academia Science, P.O.BOX 2702, Beijing 100080, CHINA
Tel:62613849 / Fac:62567363 / Email:wang.dong@bj.col.con

Abstract—To meet the special requirement of SAR, a solid state power amplifier, with an integral heat-sink requiring forced air cooling, has been developed. The amplifier delivers 300 watts of pulsed power output into 1.5:1 load VSWR with 36 dB minimum gain at 28 volt, and provides about eight percent bandwidth(1 dB) while maintaining an efficiency of approximately thirty percent. High reliability, simplicity and model repeatability are featured in this amplifier design. It has an integrated and compact structure. This paper describes the designed and development of the amplifier and presents some of important performance, includes some tested data.

INSTRUCTION

Advantages for completely solid state power amplifier such as high reliability and graceful degradation, easy to achieve the very wide operational bandwidths, can be replaced while the radar continues to operate, be ideally suited for phase array system, low weight and volume and high efficiency has been clearly demonstrated by some very high power radar systems. But many performances need still to be improved further for amplifier suitable to be applied to a satellite-borne SAR or airborne SAR. It has found that an integrate technology approach to the modular amplifier design will offer significant performance improvements, The performances that can be improved by integrated approach are:

- Higher power output per module and module reliability.
- Amplifier efficiency and bandwidth.
- Reduced module cost and improved manufacturability.
- Ease of combining large number of amplifier modules.
- Increases in power output per cubic centimeter of module volume.

The following sections will address some of these important performance as they apply to the design of L-band 300 watts pulse power amplifier for SAR and will give some development details and the performance curves of peak output power.

SYSTEM CONSIDERATIONS

System aspects

Assume that the beam of phase array antenna of SAR is scanned electrically only in elevation plane. The alternative uses distributed solid state transmitters and distributed receivers in modules close to each antenna line array in azimuth(Fig.1). A central exciter generates a pulse RF signal at low power level. In order to increase T/R modules drive power level or reduce T/R transmit gain, The low power level is amplified by a higher power amplifier and distributed uniformly by a feed network to the modules. The same feed network is summing up the amplified received signals from the modules and transmits them to a central receiver. A summary of the requiring performance of the higher power amplifier is shown in table 1.

Amplifier architecture

Fig.2 is a modular structure of 300 watts amplifier architecture. Approximate power level distribution when the amplifier is supplying 300 watts to output are given on the block diagram. A low level driver modules delivers power to driver which then drive two single stage transistor amplifier via a 2-way divider. The single stage amplifier are then combined through 2-way combiner and that output is put through an isolator for VSWR protection of the amplifier. The divider-/combiner and the single stage amplifier are composed a standard sub-module. A monitor module and a calibration are also included in the amplifier architecture.

AMPLIFIER DESIGN AND ANALYSIS

Matching network optimization

The impedance matching network of each single state circuit were to be constructed using microstrip circuit on aluminum substrates incorporating impedance transformation

Table 1. Performances of 300 watts pulse power amplifier

Power output:	300 watts min.
Operation frequency:	L band
Efficiency:	24% min.
Pulse width :	34 microsecond
Duty circle:	5.4% ~ 6.5%
Operation voltage:	28 volt
Rise/fall time:	0.5/0.2 microsecond
Droop:	0.6 dB max.

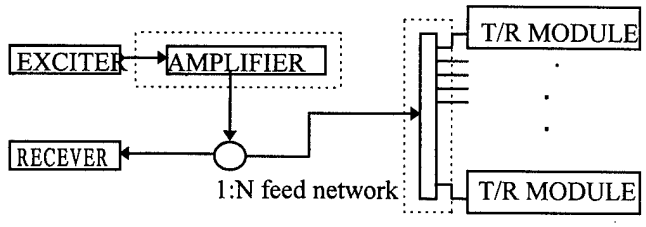

Fig.1 System block diagram

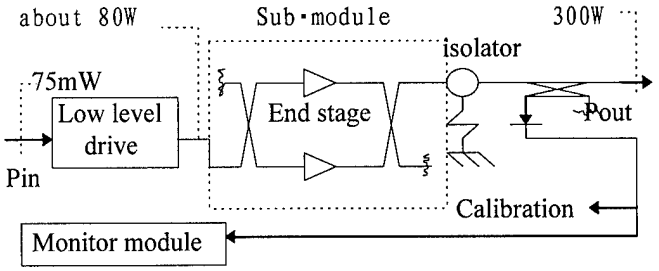

Fig.2 A modular structure of 300 watts amplifier

sections. This matching technique required an accurate model for step discontinuities in microstrip. this model was required for circuit generation with the use of a computer-aided design procedure. The computer-aided design of the matching networks was accomplished by an optimization procedure that minimized the function[1]

$$\sum_{i=1}^{n}(R_{mi}-R_{ci})^2+(X_{mi}-X_{ci})^2 \qquad (1)$$

for minimizing the absolute error, Where R_{mi} and X_{mi} are the measured resistance and reactance respectively, R_{ci} and X_{ci} are the calculated impedance at different frequency. The function selected for any particular case is determined by the relative values of the real and imaginary parts of the set of measured impedance and the desired type of match.

The computer-aided design was based on a set of transistor impedances that yielded maximum power gain. Good correlation was obtained between the final calculated and measured values for both gains and input VSWR. Some error can also be expected because of the tolerance in the fabrication, junction model and measurement accuracy. Factor such as efficiency, junction temperature, saturation, response flatness and load variation effects were not considered and may lead to other set of impedances. Matching circuits for these sets could be designed by identical procedure in experiments.

Sub-module design

The Sub-module uses two separate transistors that are thermally independent. These two transistors are interconnected in a parallel configuration (Fig.2), It has advantages of smaller size and reduced complexity. This block is optimized for use a wide-band power amplifier with 50ohm interface impedance level. As a result the sub-module becomes an easy to use building block throughout the amplifier.

This sub·module has been combined using hybrid power combine and divide networks. The combine and divide network are 3 dB hybrid couplers, Then the signal phase becomes important consideration. Because both magnitude and phase of signals are underlying factors that affect the coupler performance. To combine two signal, the signal must be of equal magnitude and 90° out of phase. Any magnitude or phase deviation will result in a power loss. This leads to additional considerations for the design of the matching networks. The matching circuits for the transistors must be of identical electrical length when the signal phase and gain of transistors are identical. However, if the transistor s are not identical, then the matching circuits must cancel the difference, and if the difference is observed throughout the transistor impedance measurements, then the computer-aided design for each stage will result in proper identical matching.

Low level driver

The block diagram for this driver is shown in Fig.3. There are four stages that make up the driver plus two 2.0 dB attenuator. The first attenautor at the input of the driver is for reducing the drive to the first stage for overdrive protection and input VSWR improvement. The second at the output of the second stage provides VSWR isolation and overdrive protection between the output of the second stage and the input of the third stage. this driver delivers about 80 watts output power to drive the sub·module.

Thermal design

A good thermal analysis and the implementation of good thermal construction techniques are very important in power amplifier fabrication. The sub-module configuration in our designing use two active areas that are physically separate to better distribute the heat, resulting in lower active area temperatures and improved reliability.

A heat sink surface under sub·module was used. The heat sink thermal resistance(R_S) requirement for the amplifier transistor can be calculated using the DC current values from the test data, the power levels and the thermal data of devices in following equations[2].

$$R_s=\frac{(T_J-T_A)}{P_D}-R_{JS}-R_{CS} \qquad (2)$$

Where T_J is the maximum permitted junction temperature, T_A is the ambient temperature, P_D is the device dissipation power, R_{JC} and R_{CS} are the junction-to-case thermal resistance and the case-to-heat sink thermal resistance.

According to the calculated R_S, we can to calculate the dimension of the heat sink. It is fact that reducing the R_S can result in a increase in heat sink thermal resistance, thus causing a smaller dimension of heat sink requirement. So the mounting surface of the transistors should be flat and clean.

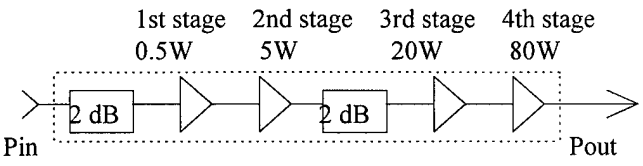

Fig.3 Block diagram of low level driver

Important parameter

Some parameters are important when designing the amplifier of SAR, Such as drop during pulse, gain as a function of temperature and phase variation during pulse. Phase measurements during the pulse indicate that after the first 5 microsecond the phase variation is less then 2° for the rest of pulse.

Testing data indicate that a loss in power of about 0.56dB is obtained if the ambient temperature is change from−10 to 50°C. this result must to be modified throughout some method of temperature compensation when the amplifier using in satellite−borne SAR system. We are considering and developing this technology to meet the application requirement.

Temperature rise within the pulse will lead to changes in DC parameters of the transistor die and causes drop in output power during the pulse[3]. The total pulse drop of the amplifier is determined mainly in the output stage and may be reduced as a result of RF impedance changes with temperature affecting the output matches.

PERFORMANCE DATA

Fig.4 shows the insertion loss of the 90°hybrid power divide and combine networks in the sub−module. The amplitude balance between the direct and coupled is typically less than 0.2 dB over the bandwidth. The physical size is 80(length) × 28 (width) × 1(high) (unit: millimeter) for the combiner including one isolation termination. The isolation termination is mounted to the bottom of the amplifier flat for better heatsinking. The phase difference of the hybrid network at its two ports is illustrated in Fig.5 and the phase deviation is less than 2°.

Fig.6 shows the final output power performance data of the amplifier. The pulse width used was 34 microsecond, and the duty factor was constant at 6%. The output power curves are shown for input supply power of 50, 75and 100 milliwatt. The operation of the amplifier is stable with a large dynamic response.

The curves in Fig.7 provide bandwidth performance of the amplifier. It shows the instantaneous 1 dB bandwidth of 8% at the band center(f_0). The efficiency curve is plotted in Fig 7.

The other parameters are listed in table 2. It can be seen that the amplifier meets or exceeds the design goal set down in Table 1.

Table 2. performance data of amplifier

Rise/Fall time:	0.36/0.2 microsecond
Pulse droop:	0.3 dB
Output VSWR:	1.2 (typically)
Device weight:	3.5 kilogram
Device total size:	210 × 210 × 48 (mm^3)

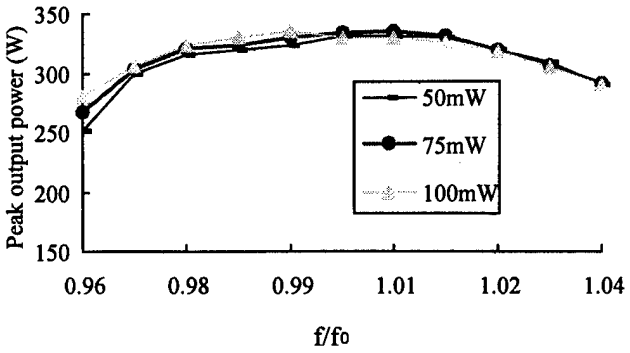

Fig.6 Otput power versus frequency
duty cycle = 6%, pulse width =34

REFERENCES

[1] R. E. Neidert and H. heddings, NRL Report 7745, 1978.

[2] J. Hatchett and T. Sallet, "13-watt microstrip amplifier for 220-225 MHz operation", Application Note AN-282A.

[3] R. E. Neidert and H. heddings, NRL Report 7682, 1974.

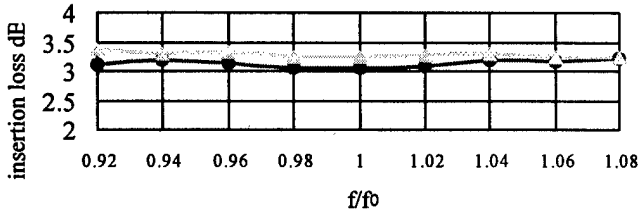

Fig.4 Magntitude performance of divider

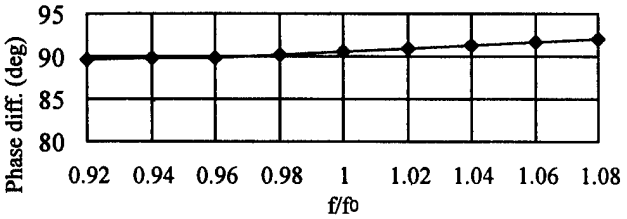

Fig.5 Phase deviation of divider at two port

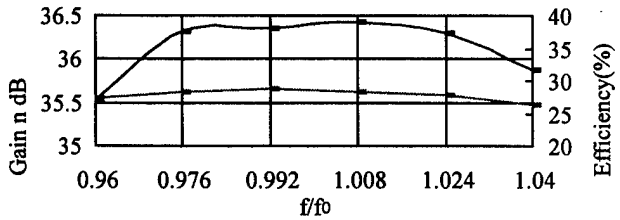

Fig.7 Bandwidth and efficiency performances

Development of a PC Based System for Real-Time, Local Reception of High Resolution Satellite Data for Environmental Monitoring

Ian .D. Downey, Jim B. Williams
Environmental Science Department, Natural Resources Institute, Central Avenue, Chatham maritime, Kent, ME4 4TB, UK
Tel: +44-1634-880088, Fax: +44-1634-880066/77, Email: ian.downey @ nri.org

John .R. Stephenson, Richard. Stephenson
Bradford University Remote Sensing (BURS) Limited, New York Industrial Estate, Summerbridge, Nr. Harrogate, North Yorkshire, HG3 4LL, UK
Tel: +44-1423-780193, fax: +44-1423-780331, Email: shirley @ burs.demon.co.uk

Wim Looyen
Natioanaal Lucht - en Ruimtevaart - Laboratorium (NLR), National Aerospace Laboratory NLR
Remote Sensing Department, PO Box 153, 8300 AD Emmeloord, The Netherlands
Tel: +31 527 248247, Fax: +31 527 248210, Email: looyen @ nlr.nl

ABSTRACT

A recent EU funded study on the constraints and opportunities of Earth Observation in developing countries has identified the lack of more direct access to satellite data as a major global restriction on resource management needs in these countries. The removal of this obstacle lies in direct readout satellite transmissions and the capabilities of low-cost, reception systems for data acquisition and processing. Direct, local reception of low resolution satellite data (e.g. NOAA) is a proven capability and its use in developing countries is growing. Improvements in the cost and performance of computing components, means that the potential for low cost, high resolution data capture can now begin to be realised. NRI, BURS and NLR are collaborating closely together in researching innovative approaches to progress such capabilities. UK government funded research is demonstrating that PC based systems can be designed to enable local, direct acquisition and processing of high resolution satellite data. These developments will enable the deployment of smaller reception antennae thereby reducing system costs, improving portability and enabling localised operation. They will also enable institutes and organisations in developing countries (and elsewhere) to access and utilise this technology for improved understanding and management of their natural resources. The technical approach and current results are presented.

INTRODUCTION

Direct, local reception of low resolution satellite data is a proven capability [1]. Increasingly, institutes and organisations in developing countries are able to access and utilise this technology for improved understanding and management of natural resources. Access to similar capabilities for high resolution data (optical, SAR) is required in regions where there are constraints of infrastructure (e.g. poor regional dissemination) and/or environment (e.g. continuous cloud cover) and thus where the need for such environmental information is likely to be acute.

Following research developments funded by the UK Government Overseas Development Administration (ODA), the British National Space Centre (BNSC) is funding a 2 year research project at NRI to develop a prototype low cost (PC based) local reception and processing system for ERS data. The thrust of the development work is to improve local access to high resolution data locally, in-country, so that the data can be used directly The project uses innovative design and the increasing availability of improved, high performance PC compliant technology. The project is running in parallel with ongoing ODA and EU projects in Indonesia to provide linkage with appropriate in-country institutional capabilities and end user requirements. Also in parallel, The Netherlands Remote Sensing Board (BCRS), the Netherlands Agency for Aerospace Programmes (NIVR) and NLR are funding the development of the processing system for ERS data and the demonstration of the system in Indonesia.. Demonstration of this capability in Southeast Asia will show that the technology is capable of operating in difficult, cloud affected tropical environments (where it is required) to provide useful environmental data routinely. There is evidence of strong demand for radar capabilities in the region from government and private sector interests.

0-7803-3836-7/97/$10.00 © 1997 IEEE

BACKGROUND

The great potential offered by ERS data (particularly SAR and ATSR) in the field of natural resource management has been demonstrated experimentally in recent years for a number of different applications [2, 3, 4] showing that the physical nature of the environment can be observed in most weathers, day and night. Operational and potential users of EO data are therefore starting to expect delivery of reliable information through utilising and adapting this technology. Not least of these are users in the developing countries, often cited as where the comparative advantage of SAR all weather and illumination capabilities will be of most direct benefit.

An EU funded project on the constraints and opportunities of EO in developing countries has recently been completed [5]. A principal finding of the study was that there is a major global restriction on access to satellite data for meeting vital resource management needs in developing countries. The comparative advantage of satellites is their large overview in real-time. However, in operation this real-time element is frequently lost. This is due to supply side factors which include: the tendency to centralise ground segment facilities (reception and archiving), the operational characteristics of data downlinks from EO missions, infrastructure or financial constraints on data delivery and the availability of suitable data processing equipment at the user end. Centralised facilities can be very difficult to sustain in practice. As requests from smaller users increase, the extra administration leads to delays and higher costs. Operators of high resolution EO satellites (NASA, ESA and SPOT) identify slow and disorganised data processing at existing ground segments in the developing world as a major obstacle to increased data dissemination and uptake.

Clearly, both in developing and industrialised countries, the lack of timely access to data is a major restriction on the wider use of satellite EO data. Consequently an alternative approach is needed for stimulating high resolution EO data markets, (such as has been done in enabling PC reception of Meteosat and NOAA) through the removal of the fundamental (data access) obstacle between the satellite and the users. This would provide a more effective, distributed ground segment, so that resource managers have better access to data from the next available satellite when disasters, unforeseen or exceptional events occur, and when information is needed now.

By analogy, only the NOAA series and geostationary Meteorological platforms have, to date, really achieved the same level of user accessibility as communications satellites (Comsats) whereby the satellite "sees" everything and everyone can access the satellite information. High resolution satellites see everything but widely available access is restricted. However, NASDA (Japan) and NASA (USA) have recently expanded plans to use direct broadcast and low-cost receiving stations for future upgraded satellite systems such as the Earth Observing System (EOS). This is a consequence of the new technology making local access to data much more practical and cost effective.

TECHNICAL APPROACH

Background

The design philosophy of the high resolution receiver system developed by BURS is to meet national or local needs for timely environmental data. In most countries, a large number of resource managers, planners and decision makers could make good use of satellite imagery (in small unit quantities) if it were to be available promptly, reliably and as inexpensively as possible. It is difficult to operate large receiving stations cost effectively and meet the needs of many small users. By targeting the majority of 'local' users who usually reside within an area of 'high satellite angle' adjacent to a reception site, the majority of customers' data needs can be satisfied efficiently.

High-angle satellite antennae need be only a fraction of the size and robustness required for horizon to horizon systems. Smaller, lighter dishes are very much easier to control with precision; the resulting antenna system being inexpensive, easy to transport, install and maintain. In addition, since user data needs from a specified target area are very much less than from full sky archive requirement, capture and processing can be easily satisfied by means of standard low cost computer systems. The basic system is not designed for complete, all weather, horizon to horizon reception, and would require modification or more than one station to provide this capability.

NLR have developed their QSAR data processing system. A standard PC operating under Windows 95 was selected as the processing platform because of the degree of local acceptance, local serviceability and local integration of these systems. QSAR is based on the range/Doppler algorithm and provides a reduced resolution image of the area covered, after which an area can be selected for full resolution processing.

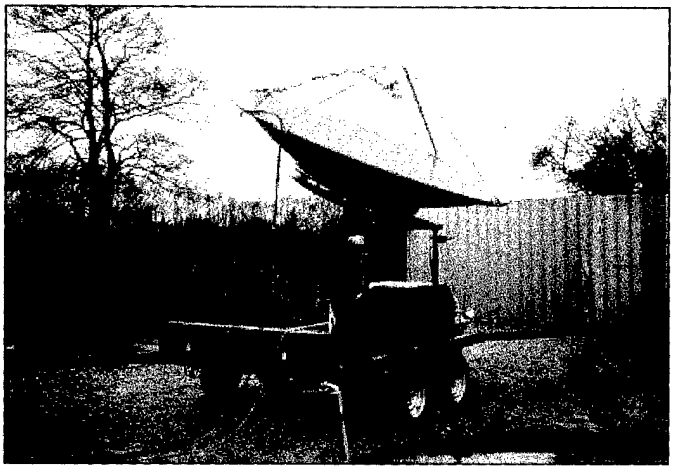

Figure 1. BURS Prototype High Resolution (ERS) receiver antenna showing: 2.7m dish, hydraulic control arms deployed and the combined 2.2Ghz tracking patch antenna and 8Ghz data receiver assembly mounted in position.

Overview of the Data Capture System

The requirement is for a system to handle capture for local areas when the satellite is within $\pm$ 45° of the overhead position. Many high resolution satellites include a beacon (e.g. ERS) or data (e.g. Landsat MSS) operating on a 2.2 Ghertz signal, the satellite tracking is done using this frequency. All the current high resolution satellites transmit data on the 8 Ghertz band and these data streams are collected separately so as not to mix the tracking function with data collection issues. The system is general purpose in that it can track and collect data from a number of satellites in low earth orbit which have beacons (or data) on 2.2Ghz and transmit sensor data on the 8Ghz band. Satellites which can be tracked include ERS, SPOT, JERS, ADEOS and LANDSAT. Data has been collected for the first three of these. ADEOS has not been observed in operation on over Europe but the satellite has been tracked. No attempt has been made to build a demodulator for the LANDSAT data stream to date.

Beacon signals are collected using four patch aerials around the focus of the dish. Differences between the pick up signals on each patch show where the satellite is with respect to the dish axis and are used to keep the antenna on-track. High resolution satellites are much more closely controlled in position than are lower resolution satellites as, with their small swath ranges, it is important to keep the scanning on target. The 8Ghz data low noise amplifier is mounted at the focus of the dish in the centre of the four patches. The centre frequency and bandwidth of the receiver can be selected automatically to match the transmitted frequency and various demodulators selected for the different satellites. The bit serial data is converted to 32 bit parallel before being input via a special I/O card and the PCI bus into the memory of the computer.

In operation the aerial is moved to a point at a specific location on the expected orbit and, as the satellite moves into the beam of the dish aerial, the signal is detected and locked. The aerial is then moved to keep the four patch signals in balance. Acquisition of the signal is normally within 2 or 3 seconds from first detection and the initial pointing accuracy needs only to be within a few degrees for the system "to pull in".
To make the operation as automatic as possible the system contains a number of micro-controllers built into the receiver electronics to control, optimise and monitor the performance. These micro-controllers communicate via RS232 links to a PC controlling the tracking and another PC controlling the data reception. One or two "large" PCs are used to collect and process the data. Because the system is so automatic it is possible to receive data from different satellites in quick succession - typically 5 minutes is needed to move the dish into a new position and set up all the electronics for a new capture.

The configuration of the prototype system currently under development includes a number of innovative features:

- **SMALL ANTENNA SIZE** - multiple satellite reception with 2.7m dish, 3.7m option
- **RELIABLE DATA CAPTURE** - unique patch precision lock-on and tracking of satellites
- **HYDRAULIC TILT DISH CONTROL** - cost effective, simple, allows overhead reception.
- **TRAILER BASED** mounting - for easy transport, installation and mobility.
- **SELF CHECKING ELECTRONICS** - for reliable capture and easy maintenance.
- **PC DATA CAPTURE AND PC PROCESSING** - for cost effective operation and expandability,
- **LOW COST** - due to small antenna size and utilisation of standard PC equipment

RESULTS

The satellite tracking capability is well developed and is almost routine now. The prototype system with a 2.7 metre dish antenna automatically searches for a variety of target satellites in the sky, locks on to the required beacon, and tracks the satellite smoothly across the sky to within about 5° of the horizon. Data signals from several of these satellites

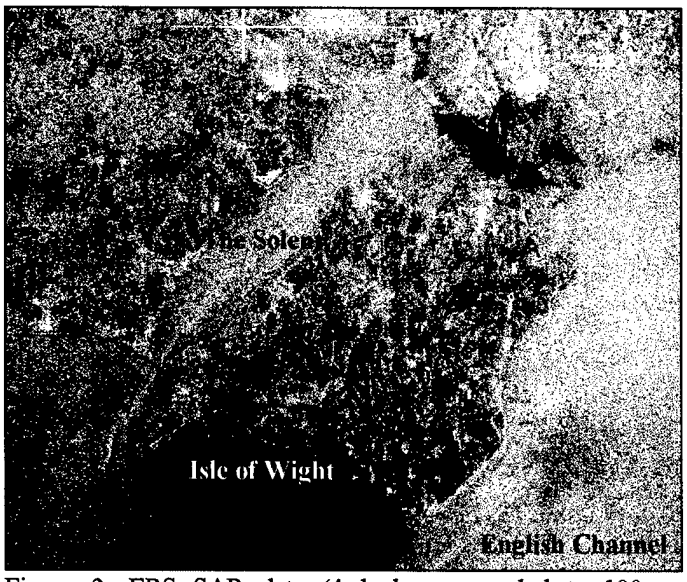

Figure 2: ERS SAR data (4 looks, resampled to 100 m resolution) of the Isle of Wight, UK acquired by the BURS prototype high resolution data capture system and processed by NLR.

can be demodulated and signal quality monitored electronically. The main data receiver design and construction is complete with the rf demodulator and simulator working well. The demodulator (for selected satellites) produces a clear analogue signal ready for conversion to digital data. Developments with computer memory and data storage in recent months have radically reduced the problems and costs of receiving, processing and storing the large quantities of data likely to be produced from 100 Megabit sec^{-1} data streams.

Operation and testing of the prototype in the UK, including digitisation and storage of data, has been successful and is ongoing. These data have been successfully reconstituted as ERS SAR image data using the PC SAR processor developed by NLR (fig. 2). The first production systems are planned for 1997.

CONCLUSIONS

There is a clear (environmental and commercial) need to stimulate high resolution data markets and product uptake in both developed and developing world. It is believed that lower data (capital and running) costs together with better temporal availability of data will be highly advantageous for applications development and market growth. So much so, that access to remote sensing data will become increasingly open to many potential users that would otherwise not be aware of, or inclined to utilise, EO products and information.

The development of a low cost, high resolution data reception capability will further enable data uptake as future missions move from the research to operational status as, for example, is planned for ENVISAT and RADARSAT. Because of improvements in the cost and performance in electronic/computing components, these capabilities are becoming more tangible realities and are actively under development by BURS and NRI, through BNSC funding, and collaboration with NLR, in preparation for the imminent expansion in satellite and sensor availability.

The prototype BURS High Resolution Receiver System (HIRRS) is designed to provide users with rapid access to EO satellite data at least cost. With very low capital and operational costs, it is optimally suited to regular reception of moderate amounts of data, to meet the real-time needs of customers and users within a radius of about 1000 km. Capability includes ERS, SPOT and potentially other (e.g. Indian, Japanese, LANDSAT, et al) satellites. The prototype results demonstrate that these capabilities can be realised. The potential benefits could be truly staggering.

REFERENCES

[1] J.B. Williams and L.J. Rosenberg. "Operational reception, processing and applications of satellite data in developing countries, theory and practice", Proceedings Remote Sensing Society Conference "Towards Operational Applications", pp: 76 - 81, September 1993, Chester, UK

[2] European Commission (EC) - Association of Southeast Asian Nations (ASEAN) (1993), "Developing ERS-1 Applications in the ASEAN Region", EC-ASEAN ERS-1 Project Newsletter, Issue 1.

[3] European Commission (EC) - Association of Southeast Asian Nations (ASEAN) (1994), "ERS-1 Data Availability and Processing", EC-ASEAN ERS-1 Project Newsletter, Issue 2.

[4] European Space Agency (ESA) (1995) "New Views of the Earth - Scientific Achievements of ERS-1", ESA SP-1176/I

[5] Earth Observation Sciences (EOS), Natural Resources Institute (NRI), Natioanaal Lucht - en Ruimtevaart - Laboratorium (NLR), and Instituto de Investagação Científica Tropical (IICT) (1996), "Analysis of the Constraints and Opportunities for Cost-Effective Implementation of Earth Observation Techniques in Developing Countries", Final Report, Ref. ETES-93-0042.

A Real Aperture Radar for Low Resolution Mapping at Low Costs

F. Impagnatiello, G. Angino, G. Leggeri
Alenia Aerospazio Space Division
Remote Sensing Engineering
Via Saccomuro 24, 00131 Rome ITALY
tel. +39-6-4151-1, fax +39-6-41512102
Email : f.impagnatiello@roma.alespazio.it

Abstract. This paper briefly describes the results obtained in the course of the trade-off analysis activity of low cost scatterometers based on real aperture measurement. This has been carried out at Alenia Aerospazio - Space Division in the frame of internal research activities and of the European Space Agency (ESA) "Modest Resolution Radar for Radar/Radiometer Applications" contract.

The idea of low resolution radar operating in scatter mode is not recent. Some years ago ESA proposed to analyse the synergism between scatterometers and radiometers in order the achieve a more complete mission for environmental application and sea temperature surveillance.

From this consideration ESA generated a ITT on "Modest Resolution Radars" suitable for a synergetic employment on a devoted mission with a radiometer very similar to MIMR (Multi Frequency Microwave Radiometer).

Alenia Aerospazio, together with the Canadian MPB Technology and British ESYS, have developed a research work in order to disclose new instrument concepts such to fit as much as possible the requirement imposed by World Scientific Community.

The paper describes some studied concepts presenting them in terms of measurement principle, theoretical performance and estimated cost/weight.

INTRODUCTION

In the course of the *Modest Resolution Radar* study, is aimed to define an active microwave instrument capable of high precision backscatter measurements over a very wide swath. more than 53 possible applications have been identified from ESYS. For each of them a parametric requirement analysis has been generated with a view to perform a reasonable trade of among concepts. The new concept that has been selected at the end of Phase I is well suited especially for Global Ocean Circulation (GOC) whose behaviour is fundamental in climate understanding and forecasting.

The importance of the high precision, that here shall to be understood as a high radiometric resolution together with a very good intrinsic instrument accuracy, is requested for a synergetic usage in connection with a microwave radiometer.

This kind of passive instruments is characterised by few tens of Celsius degree accuracy in radiance emission estimation so that similar accuracy/precision should also characterise the active counterpart.

The scientists are in the position to take remarkable advantages from the simultaneous availability of both emission and reflectivity data over large Earth surface areas and assert that only if the two measurements are comparable in terms of geometric and radiometric resolution the models built for their own purposes can work well.

The benefits of wide swath coverage (up to 1500 km is the present baseline) would allow short revisit times, with two full Earth coverage within a 48 hours period. This aspect is fundamental in medium and long term climate monitoring, especially at European latitudes.

At the end of the Phase 1 of MRR study a promising instrument concept has been selected. The Fan Rotating Beam Scatterometer seemed to guarantee both wide swath coverage and an acceptable radiometric precision in the measurements.

The analysis has been also carried out in connection with a tentative mission scenario. The assessment on orbit requirements is really relevant for the instrument definition and the related analysis. Other mission aspects, such as the number of the satellites and the communication profile, do not impact on instrument design.

FAN BEAM ROTATING SCATTEROMETER PRINCIPLE OF WORK

The selected concept from the end of first phase of the study was the ***Fan Rotating Beam (FRB) Scatterometer***. The selection was essentially due to the possibility of getting multiple measurements of backscatter coefficient at different incidence angles. The only alternative concept was identified in connection with the *Pencil Beam Rotating (PRB) Scatterometer* that, in a very similar operation way to MIMR, the Multi-Frequency Image Microwave Radiometer, performs a backscatter measurement at one-only incidence angle. For that, together with other major drawbacks, the *Fan Rotating Beam Scatterometer* concept was preferred.

The description of instrument principle of operation is quite easy. A rectangular antenna operates as radar TX/RX antenna and generates a microwave beam having a small horizontal aperture together with a wide elevation aperture.

The antenna is horizontally mounted on the spacecraft and pointed with an off-nadir angle such to illuminate a swath as in Figure 1.

The main assumptions on the horizontal and elevation beam apertures are that those values have to be compatible with a footprint ground sizes of about 10-20 km (cross) x 350-500 km (along). This is achieved if the horizontal aperture is in the order of 1° and the elevation beam angle ranges from about 20° to about 50° off-nadir, depending on platform orbiting altitude (typically from 600 to 1100 km).

0-7803-3836-7/97/$10.00 © 1997 IEEE

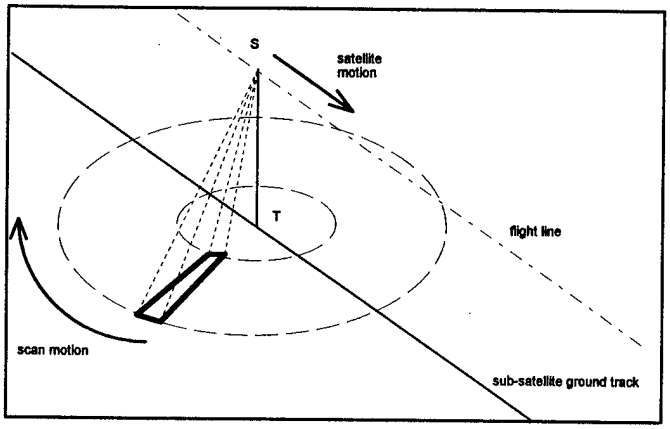

Figure 1: Circular Scanning acquisition principle.
Nadir axis geometry is analogue to MIMR

A regular and slow rotation of the antenna around the nadir axis causes the beam to be steered according a double conical surface.

Never mind if the antenna motion is obtained by a devoted mechanism or by a satellite rotation. The orbital spacecraft motion, combined with the regular fan beam rotation, generates an epicycloidal footprint pattern.

The radar technique applied at such geometry allows the acquisition of a large number of geometric cells at the same time.

In one radar echo measurement many individual contributions are acquired. The individual cell contribution can be distinguished using the radar slant resolution, associating one range bin to each cell. Both orbit geometry and geode model are required to this purpose.

In the following the geometric characteristic of the measurement area cell will be addressed as *resolution cell.*

The scheme accounted for is shown in Figure 3.1-2. Assume that a narrow cross-rotational beam is pointed with an off-nadir angle ϕ_{el} over the Earth surface. The beam apertures are θ_{el} and θ_{tr}, where

$$\theta_{el} >> \theta_{tr}$$

while the spacecraft velocity is v_A at an geodetic altitude h.

The main advantage with respect to the pencil beam concept is that the rotational speed can be dramatically reduced since the swath radial extension is much wider. In fact, with a view to a regular wide swath coverage, the instrument shall guarantee a proper overlap between consecutive scans in both forward and backward directions.

If Ω (rad/s) is the rotating rate of the microwave antenna, the satellite motion causes a relative the average walk between two passes can be estimated with

$$\Delta x = v_A \frac{2\pi}{\Omega}$$

where v_A is a parameter quite independent from the specific design (7-7.5 km/s). Therefore the overlap Δx, proportional to radial footprint size, is inversely related to the rotational speed Ω.

Given the long shaped beam, a large Δx can be accepted by the instrument without introducing gaps between adjacent scans, in the order of 120-200 km. By a really rough estimation the value of Ω can be reduced to few rounds per minutes (from 2 to 6) with respect to the PRB scatterometer concept.

A drawback effect is that the misalignment between the left and right side portions of acquired surface shall be taken into account due to the higher weight of spacecraft speed in relative velocity computation. For this reason the illumination period t for each resolution cell varies between two extreme values in correspondence to left and right side vs. line of flight

$$t_{\min} = \left| \frac{\theta_{tr}}{\Omega} - \frac{\theta_{tr} \cdot R}{v_A} \right|$$

$$t_{\max} = \left| \frac{\theta_{tr}}{\Omega} + \frac{\theta_{tr} \cdot R}{v_A} \right|$$

If in the beam limited swath acquisition it is convenient to introduce a overlap criteria among consecutive scans, here it is better to define the number of possible acquisition of the same cell while the cell remains under the antenna beam.

If N_θ is the minimum number of *incidence angle measurements* to be met during acquisition for each resolution cell then the minimum swath radial size on ground shall be

$$S_{rad} \geq \frac{v_A N_\theta \pi}{\Omega}$$

where both forward and backward sight have been accounted for. It ranges from 4 to 15 depending on the selected geometry.

N_θ has nothing to do with the effective number of radar looks used to improve the radiometric resolution.

It only represents the number of total measurements acquired at diverse incidence angles that, therefore, cannot be compared for further radiometric resolution improvement.

The transverse swath size S_{tr}, which is only related to the horizontal beam aperture and the local slant range, shall be determined on the basis of instrument operational mode.

Since the RAR operation has been supposed in the Phase I, no restrictions are applicable to the minimum S_{tr} value except for the round trip beam coupling.

The antenna shall be in the position to receive the scattered echo energy even when it moves away from the position it had when was transmitting (5-7 ms before).

The RTX mismatch M_{RTX} is thus defined as the coupling power between TX beam and RX beam due to the beam rotation during the round-trip time. It can be managed as an additional loss term in the radar equation.

SYSTEM DESIGN AND PERFORMANCE

The results from trade-off consist of a list of instrument engineering parameters which lead to an optimal configuration. Table 1 lists two possible options which differ for the operative altitudes (725 and 1075 km). These orbits corresponds to two available solutions for the exact 2-day Sun-synchronous polar orbit problem.

In both cases the full Earth coverage is guaranteed twice within a 48 hours period using one only satellite.

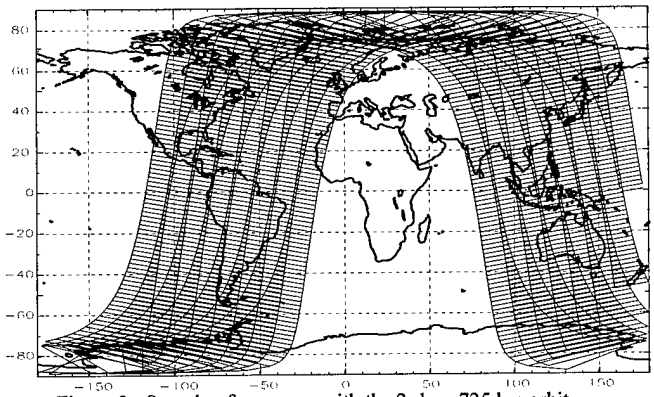

Figure 2 : Sample of coverage with the 2-days 725 km orbit (a subset of ascending or descending)

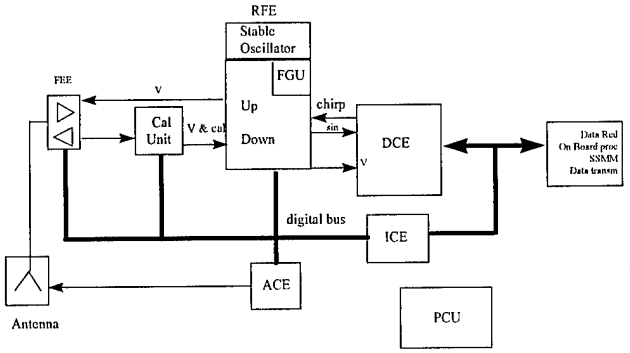

Figure 3 : MRR Preliminary Block Diagram

The preliminary Block Diagram of the instrument is shown. The echo signal is amplified and translated at a suitable video (1-2 MHz) centre, the DCE up-chirp is transmitted on ground using TWTA (or SSPA, if available). The echo data are collected and partially processed on board. For the radar, a calibration concept similar to the ERS-1 is not applicable in a simple way, because of the delay needed in new MRR FRB scatterometer.

satellite altitude		725 km	1075 km
cell size	km^2	15 x 15 km^2	18 x 18 km^2
radiometric res. @ σ^0=-23 dB	dB	< 0.35 (C) < 1.10 (Ku)	< 0.30 (C) < 0.96 (Ku)
reflector type		slotted waveguide array	slotted waveguide
reflector size	m^2	3.56 x 0.15 (C) 1.4 x 0.08 (Ku)	3.82 x 0.17 (C) 1.47 x 0.09 (Ku)
beam elevation aperture (-3dB)	deg	19.3	17.5
beam horizontal aperture (-3dB)	deg	0.79	0.75
off-nadir point.	deg	34.6	26.6
rotation period	s	18 sec	25 sec
M_{RTX}	dB	< 0.35	< 0.28
radar footprint	km	408.6 km	450.5 Km
total swath	km	1500 km	1600 Km
RF peak power	W	800 W (C) 800 W (Ku)	1200 W (C) 1200 W (Ku)
pulse length	μs	937	716
pulse BW	MHz	1.06	1.39
pulse duty	%	22.4	15.3
noise bandwidth	kHz	25.5	33.5
frequency looks	-	50	50
acquired echoes	-	13.7	16.0
SNR @mid swath	dB	8.5 (C) 0.2 (Ku)	7.6 (C) -0.7 (Ku)
SNR @far swath	dB	-0.5 (C) -8.8 (Ku)	-0.4 (C) -8.7 (Ku)
pulse cmp. Gain	dB	13 dB	13 dB
Rank	-	1	1
PRF	Hz	239 +/- 12	179 +/- 28 Hz
Ave. RF power	W	180	184

Table 1 : Reference System Design Parameters

The preliminary Block Diagram of the instrument is shown. The echo signal is amplified and translated at a suitable video (1-2 MHz) centre, the DCE up-chirp is transmitted on ground using TWTA (or SSPA, if available). The echo data are collected and partially processed on board. For the Radar signal in Table 1, a Calibration concept similar to the ERS-1 is not applicable in a simple way, because of the delay needed for MRR.

A more simple passive Calibrator as in RADARSAT seems applicable, having in mind the possibility to provide Calibration Data, during some PRI, twice for each Antenna turn. For the signal timing, this should mean the availability of an HPA switched off during these PRI.

The only drawback for this approach is the processing more complicated than in ERS-1, but the HW uses only passive components (switches and attenuators), so it is less complicated than the ERS-1. For the Bandwidth and the power needed, no particular difficulties in the implementation are expected. On the other hand an effort will be produced to develop the rotating antenna mechanical infrastructure and related controller.

The data rate can be properly reduced via on-board multi-looking processing.

REFERENCES

[1] Fawwaz T. Ulaby and others, "Millimeter Network Analyzer Based Scaterometer", IEEE Trans Geo & RS, vol. 26, no. 1, Jan 1988

[2] Michael W. Spencer, Wu-Yang Tsai, Gregory Neumann, "NASA Scatterometer (NSCAT) Pre-Launch Calibration Results and Post-Launch Calibration Plan", IEEE Trans. Geo & RS, vol. 33, 1995

[3] C. Wu, J. Graf, M. Freilich, D. Long, M. Spencer, W. Tsai, D. Lisman, C. Winn, "The SeaWinds Scatterometer Instrument", IEEE Trans. Geo & RS, vol. 32, 1994

[4] M. Freilich, D. Long, W. Spencer, "A scanning Scatterometer for ADEOS II - Science Overview", Proc. IGARSS '94

[5] Yoshio Yamaguchi, Masashi Mitsumoto, Masakazu Sengoku, Takeo Abe, "Synthetic Aperture FM-CW Radar Applied to the Detection of Objects Buried in Snowpack", IEEE Trans. Geo. & RS, vol. 32, no. 1, Jan 1994

[6] C.L. Rufenach, "Relationship between Radar Cross Section and Surface Wind in two oceanic regions: ERS-1 Scatterometer and Buoy Measurements", Proc. IGARSS '95, pp 1633-6

[7] C.C. Lin, P. Mancini, "A SAR Instrument for Global Monitoring of Land and Polar Ice", Proc. IGARSS '94

[8] R.D. Magagi, Y.H. Kerr, "Temporal and Spatial Variabilities of Surface roughness response over Hapex-Sahel area: Use of ERS-1 Windscatterometer", Proc. IGARSS '95

Effects of Faraday Rotation on Microwave Remote Sensing from Space at L-Band

D.M. Le Vine and M. Kao
Laboratory for Hydrospheric Processes/Code 975
NASA/Goddard Space Flight Center
Greenbelt, Maryland 20771
Phone: 301-286-8059; FAX: 301-286-0294; Email: dmlevine@meneg.gsfc.nasa.gov

Abstract -- The effect of Faraday rotation on the remote sensing of soil moisture from space is investigated using the International Reference Ionosphere (IRI) to obtain electron density profiles and the International Geomagnetic Reference Field (IGRF) to model the magnetic field. With a judicious choice of satellite orbit (6 am, sunsynchronous) the errors caused by ignoring Faraday rotation are less than 1 K at incidence angles less than 40 degrees.

INTRODUCTION

An L-band radiometer in space could provide global maps of surface soil moisture and contribute to the measurement of other important parameters of the earth surface [1]. Furthermore, advances in technology such as the development of aperture synthesis [2] and inflatable structures [3] have enhanced the prospect that a practical sensor can be deployed in space in the near future. Among the concerns associated with operating at this low frequency is rotation of the polarization vector due to the ionosphere (Faraday rotation). Faraday rotation can result in errors for conical scanners and cross-track imagers which view the surface a non-nadir incidence angles (i.e. where the emissivity at vertical and horizontal polarization differ).

At frequencies near L-band (1.4 GHz) the change in direction of the polarization vector of a linearly polarized wave propagating through the ionosphere can be written [4]:

$$\Delta\phi = (\pi/c\upsilon^2) \int \upsilon_p^2 \, \upsilon_B \cos(\theta_B) \, ds \qquad (1)$$

where $\Delta\phi$ is the change in direction (radians), ds is distance along the ray path, υ = frequency (Hz), υ_p = electron plasma frequency (Hz) $\approx 9\sqrt{N_e}$ where N_e is the electron density in #/m^3, υ_B = electron "cyclotron" frequency (Hz) = $qB/(2\pi M_e)$, and θ_B is the angle between the magnetic field, B, and the direction of propagation, θ. The effect of $\Delta\phi$ on a linearly polarized radiometer is to mix horizontally and vertically polarized emissions received from the surface. For example, in the case of a horizontally polarized receiver, the apparent brightness temperature, T_B, is:

$$T_B = [\epsilon_h \cos^2(\Delta\phi) + \epsilon_v \sin^2(\Delta\phi)] \, T_o \qquad (2)$$

and the error incurred by ignoring Faraday rotation is:

$$\Delta T_B = T_o \, [\epsilon_h - \epsilon_v] \sin^2(\Delta\phi) \qquad (3)$$

where T_o is the physical temperature of the surface and ϵ_h and ϵ_v are the emissivities of the surface for horizontal and vertical polarization, respectively.

EXAMPLES OF FARADAY ROTATION

Faraday rotation, $\Delta\phi$, has been computed using the International Reference Ionosphere [5] to generate electron density profiles and the International Geomagnetic Reference Field (IGRF) to model the earth's magnetic field. Figure 1 shows Faraday rotation as a function of local time for a hypothetical sensor at an altitude of 675 km and at 35° N. latitude and 75° W. longitude. Curves are shown for summer and winter of 1995 (solar minimum) and 1990 (solar maximum). Notice that $\Delta\phi$ is minimum near 6 am and that the evening (6 pm) is somewhat worse than the morning. A sun-synchronous orbit is advantageous for the measurement of soil moisture (to avoid diurnal effects), and the 6 am crossing clearly is a good choice as far as Faraday rotation is concerned. Figure 2 shows Faraday rotation as a function of longitude for latitude of 20 and 60 degrees. These examples are for 6 am, 675 km altitude and for the summer of 1990 and 1995. Summer 1990 (solar maximum is a worse case. The $\Delta\phi$ for 1995 (solar minimum) is much less. The angles, $\Delta\phi$, shown in this case (1995) are also representative of the values of Faraday rotation obtained in winter for both 1990 and 1995 at latitudes between 20-60 degrees. Faraday rotation also depends on orbit altitude and this is illustrated in Figure 3 for local time of 6 am. Note that the $\Delta\phi$ in Figures 1-3 are for a nadir directed ray path (θ = 0). The results can be corrected approximately for incidence angle, θ, using: $\Delta\phi(\theta) \approx \Delta\phi(0)/\cos(\theta)$.

U.S. Government work not protected by
U.S. copyright.

EFFECT ON BRIGHTNESS TEMPERATURE

The effect of Faraday rotation on observed brightness temperature, depends on the emissivities, $\epsilon_{h,v}$, of the surface as shown in (2) and (3). Assuming a flat, homogenous half-space and neglecting effects such as roughness and vegetation cover:

$$\epsilon_{h,v}(\theta) = 1 - |R_{h,v}(\theta)|^2 \qquad (4)$$

where $R_{h,v}(\theta)$ is the Fresnel reflection coefficient of the surface. For the ideal (i.e. flat) surface the Fresnel reflection coefficients are functions of the incidence angle, θ, and the relative dielectric constant of the soil, e_r, in the form:

$$R_v(\theta) = \frac{e_r\cos(\theta) - \sqrt{e_r - \sin^2(\theta)}}{e_r\cos(\theta) + \sqrt{e_r - \sin^2(\theta)}} \qquad (5)$$

$$R_h(\theta) = \frac{\cos(\theta) - \sqrt{e_r - \sin^2(\theta)}}{\cos(\theta) + \sqrt{e_r - \sin^2(\theta)}}$$

In the calculatins done here, the relative dielectric constant, e_r, has been expressed as a function of volumetric moisture, W, in the form:

$$e_{real} = 3.1 + 17.36W + 63.12W^2$$
$$e_{imag} = 0.031 + 4.65W + 20.42W^2 \qquad (4)$$

which were obtained from Wang [6; Eqns 7-8] assuming a frequency of 1.4 GHz, a soil porosity of 0.5, a relative dielectric constant of rocks of 5, and letting the parameter $\beta = 6.5$ and $f_m = 5$. This is a reasonable representation for clay soils.

Figure 4 shows the error in brightness temperature incurred by ignoring Faraday rotation for a moderately wet soil (W = 0.4) as a function of incidence angle. Figure 5 shows how this error depends on soil wetness. Notice that the error is somewhat larger for wet soil. This occurs even though brightness temperature decreases with increased water content because the error depends on the difference between the emissivity at horizontal and vertical polarization. Figures 4-5 have been plotted as a function of $\Delta\phi$ along a nadir path to facilitate comparison with Figures 1-3, but $\Delta\phi$ along the appropriate (i.e. slant) path was used to calculate ΔT_B.

CONCLUSION

Assuming a sensor in a sunsynchronous orbit with a 6 am crossing time, Figures 1-3 indicate Faraday rotation on the order of 6 degrees or less is to be expected at nadir (except possibly near the poles). Figure 4-5 indicate that not correcting for this change in polarization will result in errors of less than 1 K in observations over a flat soil surface, even at incidence angles as large as 40 degrees. Such an error is comparable to requirements for accuracy of sensors to monitor soil moisture [1].

REFERENCES

[1]. Le Vine, D.M., T.T. Wilheit, R.E. Murphy and C.T. Swift, "A Multifrequency Microwave Radiometer of the Future", IEEE Trans. Geosci. Remote Sensing, Vol; 27 (#2), pp 193-199, 1989.

[2]. Le Vine, D.M., A.J. Griffis, C.T. Swift and T.J. Jackson, "ESTAR: A Synthetic Aperture Microwave Radiometer for Remote Sensing Applications", Proc. IEEE, Vol 82 (#12), pp 1787-1801, Dec., 1994.

[3]. Njoku, E, J. Sercel, W. Wilson and Y. Rahmat-Samii, "Soil Moisture Path-Finder, A Low Cost Passive Spaceborne System Using Inflatable Structures", Presented at Meeting on Microwave Radiometry & Remote Sensing, Boston, MA, November, 1996.

[4]. Thompson, A.R., J.M. Moran, G.W. Swenson, Interferometry and Synthesis in Radio Astronomy, J. Wiley & Sons, pp 442-445, 1986.

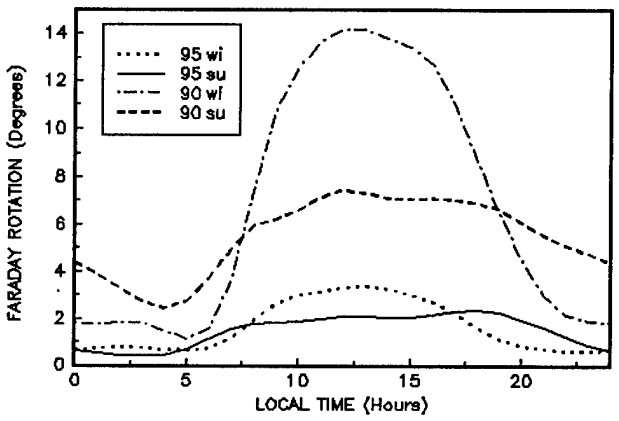

Fig.1: Faraday rotation (degrees) as a function of local time. Location: 35° N. Latitude & 75° W. Longitude; Altitude = 675 km; 1990 is a solar maximum and 1995 is a solar minimum. Su = summer and wi = winter.

[5]. Bilitza, D., K. Rawer, L. Bossy and T. Gulyaeva, "International Reference Ionosphere -- Past, Present and Future", Adv. Space Res., Vol 13 (#3), pp 3-23, 1993.

[6]. Wang, J.R., "The Dielectric Properties of Soil Water Mixtures at Microwave Frequencies", Radio Sci, Vol 15, pp 970-985, 1980.

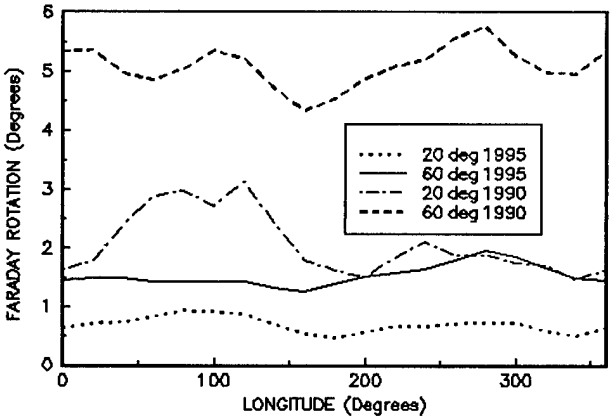

Fig.2: Faradaay rotation (degrees) as a function of longitude. Latitude = 20 and 60 degrees; Local time = 6 am; Altitude = 675 km. 1990 = solar maximum and 1995 = solar minimum. The curves are for summer.

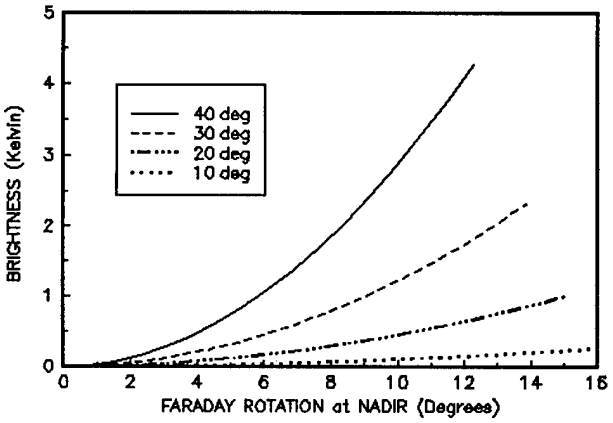

Fig.4: Error caused by Faraday rotation for several different incidence angles. The abscissa is Faraday rotation angle along the nadir path. W = 0.4; Surface Temperature = 293 K; Horizontal polarization.

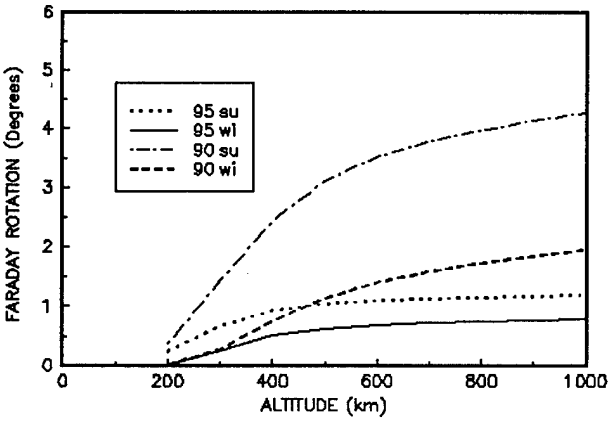

Fig.3: Faraday rotation (at nadir) as a function of altitude. Location: 35° N. Latitude & 75° W. Longitude; Local time = 6 am; 1990 is a solar maximum and 1995 is a solar minimum. Su = summer and wi = winter.

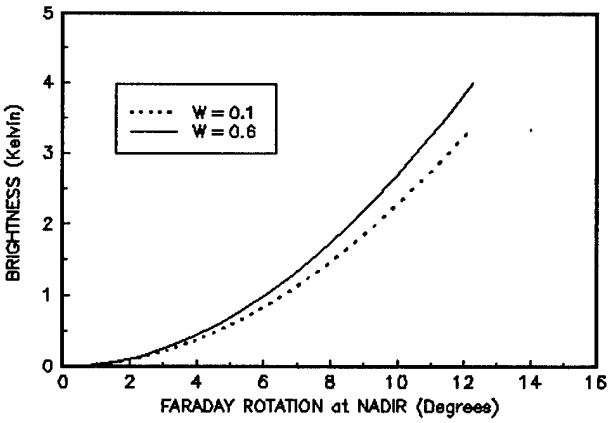

Fig.5: Dependence of brightness temperature error caused by ignoring Faraday rotation on soil water content. The abscissa is the Faraday rotation at nadir. Examples are for volumetric water content W = 0.1 and 0.6 and for an incidence angle of 40 degrees. Horizontal polarization.

Using JPEG Data Compression for Remote Moving Window Display

Ping S. Leung, Michael Adair, Joseph H. Lam

Canada Centre for Remote Sensing (CCRS), Natural Resources Canada (NRCan)
588 Booth Street, Ottawa, Ontario, Canada K1A 0Y7
Tel: (613) 995-7266, Fax: (613) 947-1408
Email: ping.leung@ccrs.nrcan.gc.ca

Abstract -- CCRS operates two remote sensing data satellite receiving ground stations (one in Prince Albert, Saskatchewan and the other in Cantley, Quebec), capable of receiving RADARSAT data, which are geographically distant from the RADARSAT mission control and data processing centres. In order to provide sensor data quickly and downlink quality assessment to the mission control centre and for other time-critical monitoring applications (quality assurance, ice monitoring, etc.), CCRS has developed two FastScan systems with industry. Each Fastscan is capable of processing the RADARSAT downlinked data into imagery and generates a moving window display (MWD) in real-time. The MWD imagery is also JPEG compressed into digital browse imagery which is suitable for electronic transmission to a remote site immediately following downlink reception. At the remote site, these JPEG files will then be re-assembled back and displayed on a MWD station as a complete swath, simulating a near real-time reduced resolution MWD. This paper describes the hardware and software development of the remote MWD station and its data communication link to the two satellite ground stations.

INTRODUCTION

On November 4, 1995, Canada launched its first remote sensing satellite, RADARSAT, equipped with an advanced Synthetic Aperture Radar (SAR) sensor [1]. The Canadian Space Agency (CSA), located at Saint-Hubert, Quebec, is responsible for the satellite mission control while CCRS of the Department of Natural Resources Canada (NRCan), is responsible for the reception of the RADARSAT downlinked data via the Prince Albert Satellite Station (PASS) and the Gatineau Satellite Station (GSS). CCRS has recently developed with industry and taken delivery of two FastScan systems [2], one at each ground station. FastScan is capable of processing real-time (RT) data downlinked from RADARSAT and produce reduced resolution (1Kx1K) imagery in real-time on a Moving Window Display (MWD) as well as JPEG [3] compressed digital browse (512x512) imagery and catalogue update files. FastScan can also generate CEOS level 0 raw products. As the two satellite ground stations are geographically distant from the mission control and other processing centres, there is a requirement to provide satellite feedback to these centres quickly for sensor and downlink data quality assurance and for other time-critical monitoring applications, such as ocean ice movement, forests fire, floods and environmental disaster monitoring, etc. CCRS has started the development of a Remote Moving Window Display Station (ReMWinDS) which can accept JPEG images electronically from the FastScan following a RADARSAT downlink reception, re-assemble and display them locally as a complete swath to effect a (near) real-time MWD. ReMWinDS can be installed at the mission control centre or other processing centres to allow users to verify the correct imaging of target areas, to assess data quality and even to fulfill quick turn-around reconnaissance applications. The initial ReMWinDS has been implemented on a low cost PC-based system equipped with software to receive digital browse imagery and catalogue files from the FastScans, and to combine and display the browse images on a scrolling display at CCRS, Ottawa. The system operates in near real-time fashion whereby the time required for imagery transmission to the ReMWinDS is the main delay overhead.

SYSTEM OVERVIEW

Figure 1 shows the ReMWinDS system overview. The two FastScans are used to process RADARSAT real-time (RT) and playback (PB) downlink data at GSS and PASS. When the satellite is within the reception coverage circle of the two stations, the antenna reception facility converts the satellite downlinked signal into digital baseband serial data stream and routes the data to FastScan for processing. In addition to performing the real-time MWD processing, FastScan also generates the corresponding JPEG image files and catalogue update file. These files are then transmitted to the Global Change Network (GCNet) [4] via the CCRS communication network immediately following each downlink reception. GCNet, a multi-satellite data catalogue and query system located at CCRS, Ottawa, Ontario, stores and maintains all the digital browse imagery and catalogue information generated by the two ground stations. Additional functions will be added to GCNet to enable it to generate the associated HyperText Markup Language (HTML) files from the catalogue update files received from the FastScans and to

0-7803-3836-7/97/$10.00 © 1997
Canadian Crown Copyright

transmit these files with the JPEG imagery to the designated remote MWD site(s). The first ReMWinDS, to be installed at CSA headquarters in Saint-Hubert, Quebec, will be a PC-based system equipped with a communication link to GCNet.

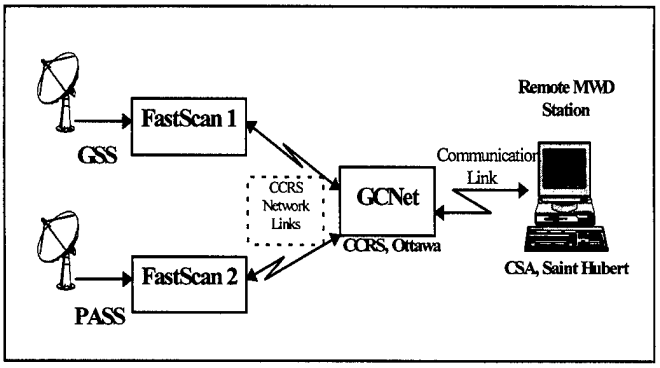

Figure 1 Remote MWD System Overview

SYSTEM DESCRIPTION --- HARDWARE

FastScan, implemented with commercial off-the-shelf hardware, includes three main subsystems: the Radar Data Interface (RDI); the Signal Processing Computer (SPC) and the System Control Computer (SCC). The RDI's main tasks are to detect the satellite downlink data frame synchronization pattern and to decode and extract the data fields from the RADARSAT downlink bit stream. The SPC, which consists of two i860-based Mercury MCV6 boards, is responsible for all functions of the SAR signal processing [5]. The SCC consists of a fast, real-time, system control computer (FSCC) and a slow system control computer (SSCC). The FSCC is a Motorola 68040-based single board computer which takes care of the tasks of input data and distribution, image data buffering, and display. The SSCC is a Sun SPARC station 20 server which performs most of the general purpose functions, such as the user interface, data analysis and report generation.

GCNet is a Sun SPARC based workstation which offers services that assist users in locating remote sensing data and products for Canada. It provides the user interface, network links to other data centres, CCRS image inventory and bulletin board services. For details, please refer to the CCRS GCNet web site: http://www.ccrs.nrcan.gc.ca/gcnet.

ReMWinDS is the Remote MWD Station that can be implemented on any PC-based system running Windows NT and Netscape browser software. The CCRS ReMWinDS prototype was implemented on a Pentium-based computer platform equipped with 32 MB memory, 2GB hard drive, an Exabyte tape drive and a super VGA colour monitor. The system also has TCP/IP networking capability to communicate with the GCNet.

SYSTEM DESCRIPTION --- SOFTWARE

The software for control and display of the ReMWinDS is implemented using the JavaScript capabilities of the Netscape (v3.01) browser. When the MWD is started, four separate frame areas are created: a title and navigation frame, an index frame and two frames for display of the swath imagery and metadata. An example of these frames is shown in Figure 2.

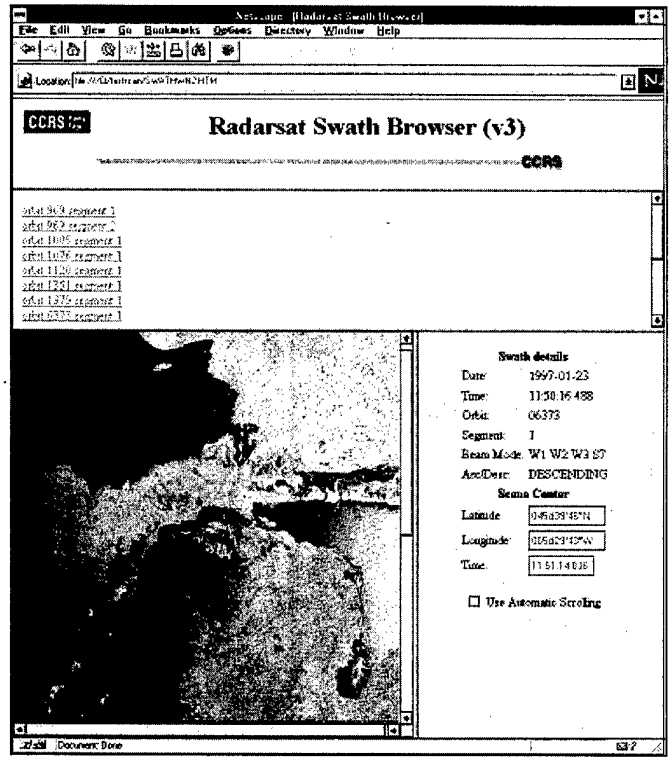

Figure 2 - Imagery and metadata frames

The catalogue update files and JPEG compressed imagery files generated by the FastScan system will be automatically copied from the receiving stations (GSS and PASS) to CCRS in Ottawa over a TCP/IP network implemented on the communication links described below. Automation will be achieved by using a client /server implementation running as background processes at each end to minimize operator involvement. A similar process will be used to transfer the necessary files from CCRS, Ottawa to CSA, Saint-Hubert.

The catalogue update files generated by FastScan are parsed as they are received to generate swath objects in JavaScript. Each swath object captures all information relevant to the swath including imaging date, time, orbit number, beam mode, etc. Each swath object is in turn composed of one or more scene objects which represent each individual framed

scene of the swath. File parsing is carried out using Perl scripts to generate an HTML file for each swath object, which may then be loaded into the imagery frame.

The swath objects available on disk are listed in the index frame for selection by the user. Once a swath is selected, the associated scene objects and their JPEG files are loaded from disk into the imagery frame in the proper order. This frame is then scrolled at a rate which is determined from the beam-mode of the sensor. The user may also stop the automatic scrolling function and scroll through the imagery manually using the scroll bars.

The metadata frame displays the imaging date and time, orbit number, beam mode, etc. The scene center latitude and longitude are updated in real time as the imagery is automatically scrolled through the imagery frame. This feature is not available using manual scrolling.

COMMUNICATION LINKS

The FastScan systems at GSS and PASS communicate with GCNet at CCRS, Ottawa via the CCRS network links. The network between GSS and CCRS is a 56 kbps dedicated communication line, and between PASS and Ottawa is a 56 kbps frame relay data line. There is currently a 12 kbps frame relay link between CCRS, Ottawa and CSA, Saint-Hubert that is proposed to be upgraded to 56 kbps. Table 1 illustrates the estimated data transmission time based on the data volume of a 10-minute downlink pass, for the various satellite beam modes, using a nominal average 4:1 JPEG compression ratio and JPEG quality factor of 75, and a 56 kbps link.

Beam mode	*Standard*	*Wide*	*Fine*	*SCN Narrow*	*SCN Wide*
JPEG data	2.5 MB	1.7 MB	5.0 MB	0.8 MB	0.5 MB
Trans-mission time	6.0 min.	4.0 min.	12.0 min.	1.9 min.	1.2 min.

Table 1. JPEG browse imagery data volume and transmission time estimation for a 10-minute pass

SUMMARY AND FURTHER WORK

The ReMWinDS software was prototyped and successfully demonstrated on a PC-based system running Windows NT and Netscape browser. Numerous passes of JPEG imagery and catalogue update files have been collected and used to generate indexes of the swath objects for further testing. After a user selects a swath object, the current ReMWinDS processes the JPEG imagery and the associated HTML files to form a continuous swath which can be displayed on a MWD scrolling at real-time rate. Information about the satellite pass are also displayed on the MWD as annotations to inform users about the satellite orbit number, sensor imaging time, geographical locations of the swath, etc.

CCRS and CSA are now planning to complete development of the ReMWinDS and install a unit at CSA, Saint-Hubert. This ReMWinDS will use a Pentium-based PC. Additional features and functionalities already identified include a World Map to allow a user to locate the satellite orbital and imaging positions and a higher resolution JPEG image display (e.g. from the current 512x512 to 1024x1024). Also, the ReMWinDS technology can easily be expanded to accommodate other sensors, such as LANDSAT, SPOT, NOAA AVHRR, ERS, etc. Copies of the ReMWinDS can also be easily installed at other locations to satisfy different user application requirements.

ACKNOWLEDGMENTS

The authors wish to acknowledge the important contributions to this paper by N. Davis, T. Feehan, M. Lalonde, R. Boudreau and R. Shergold, and to thank CSA, RADAR SAT International (RSI) and CCRS for providing the RADARSAT digital browse imagery for this presentation.

REFERENCES

[1] Anthony P. Luscombe, "Radar Imaging from Space: Making the most of the opportunities", Canadian symposium on Remote Sensing, June 1993, pp. 349-352.

[2] Joseph H. Lam, Marc A. D'Iorio, Alan A. Thompson and Michael J.Manore, "The RADARSAT FastScan Processor System and Applications ", Canadian Journal of Remote Sensing, 1995, pp. 527-530.

[3] Gregory K. Wallace, "Overview of the JPEG Still Picture Compression Algorithm," Electronic Imaging East '90, October 1990, pp. 66-71.

[4] T. A. Fisher, J. Cihlar and R. Boudreau. "Global Change Network (GCNet)", Canadian symposium on Remote Sensing, May 1991, pp. 153-157.

[5] John C. Curlander and Robert N. McDonough, 1991. Synthetic Aperture Radar and Signal Processing, New York, John Wiley & Sons, Inc.

The Universal Multychannel Technique for Enhancing Images Obtained from Different Sensors

B.Z. Petrenko
RAS Institute of Radioengineering and Electronics
141120, 1 Vvedenskogo sq., Fryasino, Moscow reg., Russia.
Telephone: (095) 526-92-68, Fax: (095) 203-84-14, E-mail: petrenko@ire.rssi.ru

Abstract – The technique is described which embodies a robust approach to enhancing spatial resolution of aerospace images basing on images made with another sensor with a better spatial resolution. The technique does not require an exact knowledge of the sensor angular functions replacing it with the analysis of a local signals spatial structure The extent of correction of a low resolution image depends on its correlation with high resolution images. The universality of the technique is demonstrated by its applications to data of microwave and optical sensors.

INTRODUCTION

The typical problem of imaging remote sensed data is to provide as good spatial resolution of images as possible. This problem arises when processing data of very different sensors types - from microwave radiometers whose footprint sizes on the Earth's surface are of several tens km to optical sensors having footprint sizes of tens meters. Two ways are known for attaining the spatial resolution of the image better then a sensor footprint size: (1) using a spatial redundancy of signal samples [1,2] and (2) invoking a priori information on contrast objects boundaries locations from images obtained with other sensors having a better spatial resolution [3-5]. The common feature of the most of proposed approaches [1-4] is that they require angular functions of sensors to be known exactly. By a sensor angular function we mean a point spread function for optical sensors or an antenna pattern for microwave sensors. In contrast, the robust two-channel technique [5] do not require the exact knowledge of sensor angular functions replacing it with the analysis of spatial structure and correlation of sensor signals. For this reason the robust technique is less sensitive to angular function variations and, besides, it can be applied with small modifications to very different types of sensors. This article considers in more details the two-channel and multychannel robust techniques and demonstrates its applications to imaging data of optical and microwave sensors.

PRINCIPLES OF THE ROBUST TECHNIQUE

We assume that a certain scene is observed by a low resolution sensor (L-sensor) and by N high resolution sensors (H-sensors). The L-sensor has the angular function $\phi_L(\mathbf{r}-\mathbf{q})$ and the effective footprint size on the Earth's surface ρ_L; each of H-sensors have the angular function $\phi_H(\mathbf{r}-\mathbf{q})$ with the effective footprint size $\rho_H<\rho_L$. Output signals of sensors are:

$$U_L(\mathbf{r})=\int \phi_L(\mathbf{r}-\mathbf{q})\, I_L(\mathbf{q})ds,$$

$$U_{Hi}(\mathbf{r})=\int \phi_H(\mathbf{r}-\mathbf{q})\, I_{Hi}(\mathbf{q})ds, \qquad i=1,2,\ldots,N,$$

where $\mathbf{r}$ is a coordinate of a footprint center, $I_L(\mathbf{q})$ and $I_{Hi}(\mathbf{q})$ are distributions of measured radiation intensities over the scene, ds is a scene element observed at the direction $\mathbf{q}$. Our goal is to estimate for each pixel of the image a signal $U_{LH}(\mathbf{r})$:

$$U_{LH}(\mathbf{r})=\int \phi_H(\mathbf{r}-\mathbf{q})\, I_L(\mathbf{q})ds$$

We assume the interpolated value of a low-resolution signal $U_L(\mathbf{r})$ as the first guess of $U_{LR}(\mathbf{r})$:

$$U_{LH}(\mathbf{r})= U_{LH}(\mathbf{r})+ \varepsilon(\mathbf{r}), \qquad (1)$$

where the error $\varepsilon(\mathbf{r})$ is caused by inequality of angular functions $\phi_L(\mathbf{r}-\mathbf{q})$ and $\phi_H(\mathbf{r}-\mathbf{q})$. The interpolation can be performed with one of single channel techniques [5].

If a correlation takes place between radiation intensities measured with LR- and HR-sensors, an alternate estimate of $U_{LH}(\mathbf{r})$ can be made as a linear combination of HR-sensors signals:

$$U_{LH}(\mathbf{r})=U_{LH}^*(\mathbf{r}) + \mu(\mathbf{r}),$$

$$U_{LH}^*(\mathbf{r}) = a + \sum_{i=1}^{N} b_i U_{hi}(\mathbf{r}), \qquad (2)$$

Assuming that the spatial correlation of signals does not change in the range of scales from ρ_H to ρ_L, coefficients a, $b_1,\ldots,b_N$ are determined by regression of the LR-sensor signal with HR-sensor signals averaged with the spatial scale ρ_L. over a local area around the pixel $\mathbf{r}$. The error $\mu(\mathbf{r})$ in (2) is caused by incomplete correlation between LR and HR sensors, i.e. by independent information which exists in the data of the LR-sensor. Since errors of estimates (1) and (2) are caused by different factors, they can be considered as independent, and the final estimate of $U_{LH}(\mathbf{r})$ can be constructed as a least square combination of (1) and (2):

$$U_{LH}^{**}(\mathbf{r})= U_L(\mathbf{r})\,\alpha + U_{LH}^*(\mathbf{r})(1-\alpha), \qquad (3)$$

0-7803-3836-7/97/$10.00 © 1997 IEEE

where $\alpha=D_\varepsilon/(D_\mu+D_\varepsilon)$, D and D* are dispersions of $\varepsilon(\mathbf{r})$ and $\mu(\mathbf{r})$ correspondingly. The value of D_μ can be found as a dispersion of the regression (2) and D_ε we estimate as a dispersion of U_{LH}* estimates taken within the field of view of LR-sensor with a center at the pixel **r**. The contribution of estimates (1) and (2) into (3) depends on signals local structure at the neighborhood of the pixel **r**. In locally homogeneous areas the correlation between LR and HR-sensors is low, and $|b_i|\approx 0$, i=1,...,N. In these areas D_μ is determined by a dispersion of the LR signal, $D_\varepsilon \rightarrow 0$ and $U_{LH}^{**}(\mathbf{r}) \cong U_L(\mathbf{r})$. In boundary zones between contrast objects, $D_\varepsilon >> D_\mu$, and $U_{LH}^{**}(\mathbf{p}) \cong U_L^{*}(\mathbf{p})$. The proposed method of combining low resolution and regression estimates makes the robust technique adaptive, allowing a strong correction in the neighborhood of contrast objects boundaries and weak correction in locally homogeneous areas. This prevents introducing artifacts into the image corrected. One can see that a certain information on sensors angular functions is only used when estimating dispersion D_ε over the field of view of the LR-sensor. Evidently, the variations of angular functions only slightly affect the final signal estimate (3).

A separate problem of implementation this technique arises when a number of strongly correlated HR-channels are used to correct the LR image. In this case it is necessary to take special measures to obtain stable estimates of regression coefficients in (2). The routine methods of regression analysis [4] can be used for this purpose.

ENHANCING IMAGES OF TROPICAL CYCLONE IN THE 19 GHZ SSM/I CHANNEL

The example of robust synthesis of the Earth surface image from the SSM/I microwave radiometer data was given in [3]. The average footprint sizes of this radiometer on the Earth's surface are 13 km in the 85 GHz channels and 56 km in the 19 GHz channels. Here we show that this technique can be applied for enhancing microwave images not only of the Earth surface objects but of large cloudy systems too. Fig. 1 (a-c) shows images of the tropical cyclone Tim (9 July 1994) synthesized from measurements of the F10 SSM/I in 85 H and 19H channels. Fig. 1 (a,b) demonstrates images made with a single-channel robust technique [3] This technique, when applied to data of the 19H channel, allows to use the spatial redundancy of signal samples for to obtain spatial resolution better then a footprint size. Furthermore, a high negative correlation between 19H and 85H signals existing in the tropical cyclone area (correlation coefficient is -0.7 - -0.9) enables one to effectively apply the two-channel robust technique described above. Fig. 1c shows that the two-channel correction allows to resolve on the 19H image a number of small details of the cloudy system including the "eye" of the tropical cyclone.

ENHANCING OPTICAL IMAGES MADE WITH THE MSU-E AND MSU-SK INSTRUMENTS

The optical scanners MSU-E and MSU-SK operate on Russian "Resource" and "Meteor" satellites and on the "Priroda" module [5]. Footprint sizes on the Earth surface for the "Resource" satellite are of 28×28 m for the MSU-E instrument and of 175 × 243 m for the MSU-SK instrument. The MSU-E scans the Earth's surface linearly and the MSU-SK scans conically. To avoid the necessity of accounting for the differences in the scanning geometry of both sensors a relatively small fragments of images were taken for testing the two-channel technique. Fig. 2 (a,b) shows the images of the same 4200m * 5600 m area near the Pripyat river, made with the MSU-SK and MSU-E instruments in May 1992 and in July 1995 correspondingly. These images are synthesized with a single-channel robust algorithm [3]. Fig. 3,c shows the MSU-SK image enhanced with the use of MSU-E data. One can see that the two-channel algorithm allows to enhance spatial resolution in those parts of image where a high correlation between MSU-SK and MSU-E data takes place, particularly in the neighborhood of the river. On the other hand, signals at the relatively homogeneous areas of the image remain unchangeable.

CONCLUSIONS

The technique is described which embodies a multychannel robust approach to enhancing spatial resolution of aerospace images using matched images made with other sensors with better spatial resolution. The analysis of a local spatial structure and correlation of signals on which the robust technique is based, imparts to this technique adaptive properties and allows to avoid the requirement of the exact knowledge of the sensors angular functions. For the same reason, the robust technique can be applied with small modifications to very different types and combinations of sensors. The extent of correction of the low resolution image depends on correlation between signals of low resolution and high resolution sensors. Results of enhancing microwave and optical images visually confirm the effectiveness and universality of the multychannel robust technique. The firther work on this technique will involve quantitative studying of its performance.

AKNOWLEDGMENTS

The author thanks Mr. F. Wentz (Remote Sensing Systems Inc.) for delivering SSM/I data and A.A.Semenov (IRE RAS) for preparation of the data of MSU-SK and MSU-E instruments.

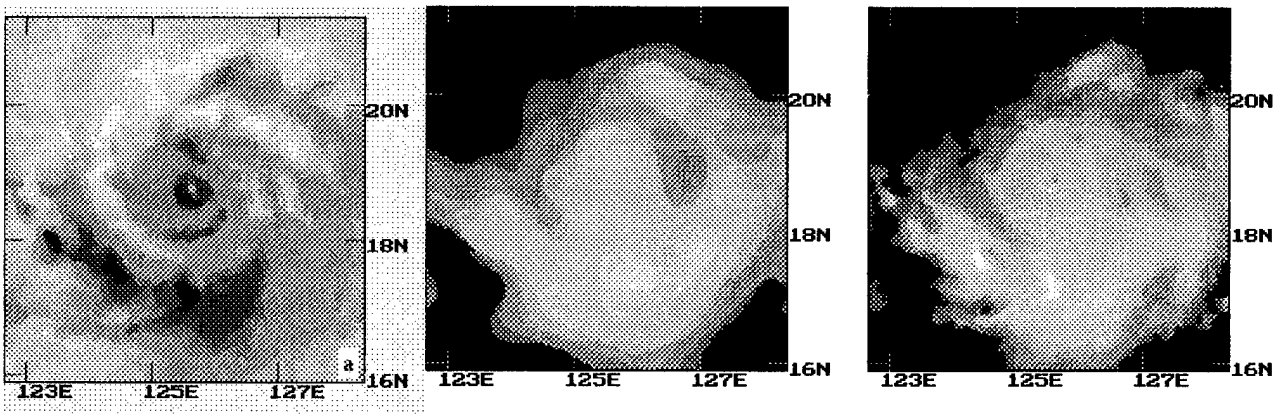

a) b) c)

Fig. 1. Microwave radiometric images of the tropical cyclone Tim in the DMSP F10 SSM/I channels. a- 85H channel, b- 19H channel, c - 19H channel image enhanced with the use of the 85H image.

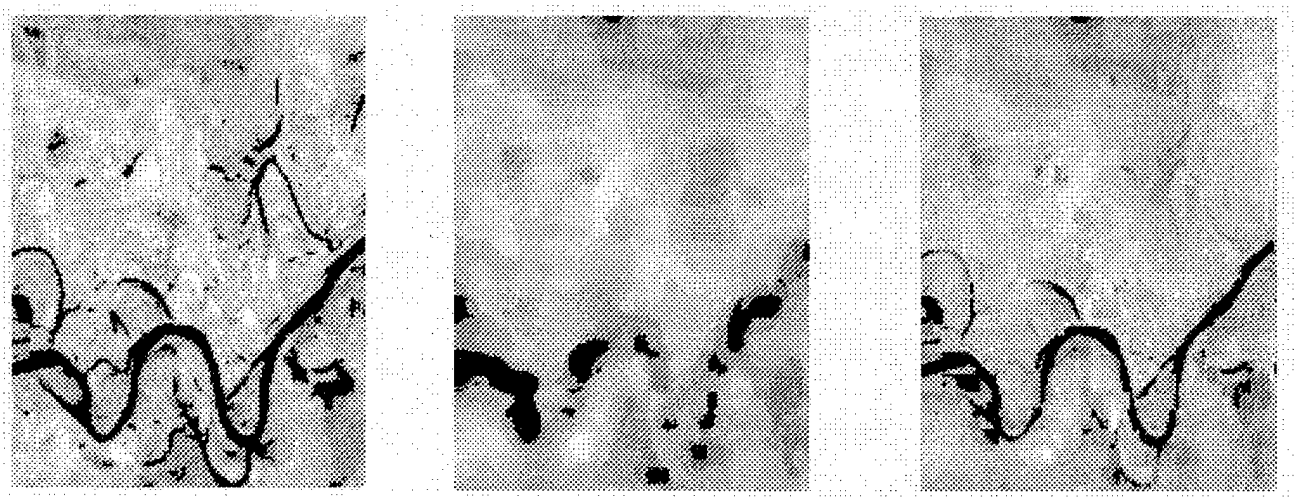

a) b) c)

Рис. 2. The images of the Pripyat river region made with MSU-E (a) and MSU-SK (b) instruments and (c) MSU-SK image enhanced with the use of MSU-E image.

REFERENCES

[1] M.R.Farrar, E.A.Smith. Spatial resolution enhancement of terrestrial features using deconvolved SSM/I microwave brightness temperatures. IEEE Trans. on Geosci. Rem. Sens., 1992, v. GE-30, pp.349-355.

[2] Sethmann R., Burns B.A., Heygster G.C., Spatial resolution improvement of SSM/I data with image restoration technique. IEEE Trans. Geosci. Rem. Sensing, 1994, v. GE-32, No. 6, p. 1144.

[3] Nishii R., et al. Spatial resolution enhancement of low resolution thermal infrared image based on other high resolution band images. Proc. IGARSS'95, v. 1, pp.667-669, Firenze, Italy, 10-14 July, 1995.

[4] Zhukov B., M. Berger, F. Lanzl. H. Kaufmann. A new technique for merging multispectral and panchromatic images revealing sub-pixel spectral variation. Proc. IGARSS'95, v. 3, pp.2154-2156, Firenze, Italy, 10-14 July, 1995.

[5] Petrenko B.Z.. Robust restoration of microwave brightness contrasts from the DMSP SSM/I data. Proc. IGARSS'96, v. 1, pp.481-483, Lincoln, Nebraska, 27-31 May 1996.

[6] Seber J.A.F. Linear regression analysis. J.Whiley&sons, 1980.

[7] Hollinger J.P., Peirce J.L., Poe G.A. SSM/I Instrument Evaluation. IEEE Trans. Geosci. and Remote Sensing,1990, v. 28, N 5, p. 781-790.

[8] Armand N.A., ed. International Project PRIRODA. Instruments. Reference handbook. IRE RAS, Moscow, 1993.

YSAR: A Compact, Low-Cost Synthetic Aperture Radar

Douglas G. Thompson, David V. Arnold, David G. Long,
Gayle F. Miner, Thomas W. Karlinsey, Adam E. Robertson
Brigham Young University
459 CB, Provo, UT 84602
voice: 801-378-4884, FAX: 801-378-6586, e-mail: thompsod@salt.ee.byu.edu

Abstract: The Brigham Young University Synthetic Aperture Radar (YSAR) is a compact, inexpensive SAR system which can be flown on a small aircraft. The system has exhibited a resolution of approximately 0.8 m by 0.8 m in test flights in calm conditions. YSAR was used to collect data over archeological sites in Israel. Using a relatively low frequency (2.1GHz), we hope to be able to identify walls or other archeological features to assist in excavation. A large data set of radar and photographic data were collected over sites at Tel Safi, Qumran, Tel Micnah, and the Zippori National Forest in Israel. We show sample images from the archeological data. We are currently working on improved autofocus algorithms for this data and are developing a small, low-cost interferometric SAR system (YINSAR) for operation from a small aircraft.

INTRODUCTION

A Synthetic Aperture Radar (SAR) is an imaging radar which uses signal processing to improve the resolution beyond the limitation of the physical antenna aperture. Typical SAR systems are complex and expensive. The BYU SAR (YSAR) is a relatively inexpensive, lightweight system. The system is designed to be flown in a four or six passenger aircraft at altitudes up to 2000 feet. The system cost and complexity are kept low by using commercially available parts for most of the components, as described in [1]. Initial system tests in calm weather estimated the effective resolution to be about 0.8m by 0.8m.

The system was used to take data over several archaeological sites in Israel to help map the areas for excavation. These areas include Zippori National Forest, Tel Safi, Tel Micnah, and Qumran. These data have slightly worse resolution than the initial tests because of uncorrected aircraft motion. We are currently working on applying autofocus methods to this data.

This paper describes the YSAR system and presents results obtained from the Israel flights. The first section shows the block diagram and briefly describes the system. The next section shows some results from the Israel data. The third section describes current and future work.

SYSTEM DESCRIPTION

The YSAR system is composed of an RF subsystem, a chirp generation subsystem, a digital subsystem, and an antenna subsystem. A block diagram of the system is shown in Fig. 1. The entire system weighs approximately 360 lbs, with over half that coming from a battery-power supply.

The RF subsystem mixes the 100 MHz bandwidth chirp up to 2.1 GHz for transmission and mixes the RF radar return from the antenna to an offset baseband which is sampled by the digital subsystem. The chirp is transmitted and received with double-sideband modulation. Though non-optimum, this avoids the cost associated with single-sideband chirp generation and increases the effective bandwidth of the chirp. The baseband chirp and timing signals are generated by a commercial arbitrary waveform generator, synchronized to the RF local oscillator. The antennas used are custom microstrip patch arrays.

ISRAEL RESULTS

The YSAR system was taken to Israel to collect data over archaeological sites in September 1996. Data was collected using the radar and 35mm cameras in six flights over four sites, from 12 September to 17 September. The sites were in Zippori National Forest, Tel Safi, Tel Micnah, and Qumran. Sample images from two of these sites are shown and described below. Each of the images shown in this section has been averaged to 64 looks in order to show an entire strip on the page. The flight direction is top to bottom, with the radar looking to the left. Each strip is approximately 600m by 3.5km, with pixels about 2.5m by 2.5m. The resolution of the one-look images is

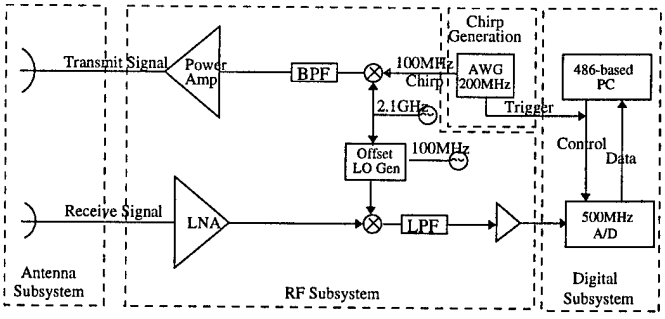

Figure 1: YSAR Block Diagram

0-7803-3836-7/97/$10.00 © 1997 IEEE

comparable to that obtained in the test flights.

The Zippori National Forest contains a large planted forest, a fortress built by the Crusaders, and ruins believed to be the site of a large center of learning after the fall of Jerusalem in CE 70. The site sits on a large hill and contains many partially excavated ruins. Some of the ruins are largely covered with trees and brush. The biggest challenges to imaging this area are the rocky ground and the hilly topography. A sample image of the area is shown in Fig. 2. The photo-mosaic in Fig. 3 correspond to the area indicated by the box in Fig. 2, which is below the hill of the main site. The main archaeological site is just above the upper right corner of the portion covered by these photographs.

Another image from the Zippori site is shown in Fig. 4. This image covers much of the main site of interest. A set of corner reflectors arranged in a cross can be seen in a field near the start (top of the page) of the image, indicated by the arrow. The 2-foot trihedral corner reflectors are spaced 10m apart. Many rock fences, excavations, buildings, roads, and trees can be seen throughout the image. Analysis of these images is continuing, both for better focusing and for archaeological interpretation.

Tel Safi is believed to be the site of the ancient Philistine city of Gath, home of Goliath as mentioned in the Bible. There is also evidence of other, more recent settlements on the site. The site sits on a small hill (tel) in a large, mostly flat plain. Figure 5 shows an image from Tel Safi. The tel spans the middle portion of the image. Many features can be seen in this portion which were not evident from the ground. A set of 2-foot corner reflectors in an 'L' configuration is indicated by the arrow. Variations in field types can also be seen, and a large wadi is evident near the start of the image.

CURRENT AND FUTURE WORK

We are currently working on and planning several projects to improve the imaging capabilities of the YSAR system. Some of these are described in the following.

Motion compensation is a significant problem in all SAR systems, and more so in the small, low-flying aircraft used for YSAR. The initial system tests were conducted in good weather conditions and at optimum times of the day. We were not able to choose our flight times as well for the flights in Israel, so these images are more corrupted by motion of the aircraft. We are currently adding more motion measurement to the system and working on improved methods of autofocusing. Future YSAR flights will include measurements from a kinematic GPS system which gives both attitude and position. There will also be a set of accelerometers set up to measure linear and rotational motion and to interpolate between the GPS measurements. The accelerometers are based on recent advances in MEMS technology and thus provide good performance while preserving the low cost of the YSAR system.

Autofocus for YSAR is made more complicated than in traditional systems by several factors. Most of the autofocus algorithms currently in the literature are for spotlight SAR, while YSAR is a stripmap system. YSAR covers a much wider range of incidence angles (nadir to 60° in many cases). We are working on modifying autofocus algorithms to apply them to our system.

We are also in the final stages of building a 10 GHz interferometric SAR (YINSAR) which will be operational this summer. We plan to operate both systems together to obtain 10 GHz and 2 GHz images of the same areas.

References

[1] Douglas G. Thompson, David V. Arnold, David G. Long, Gayle F. Miner, and Thomas W. Karlinsey. Ysar: A compact, low-cost synthetic aperture radar. In Proceedings, IGARSS '96, pages 1892–1894, Lincoln, Nebraska, May 1996.

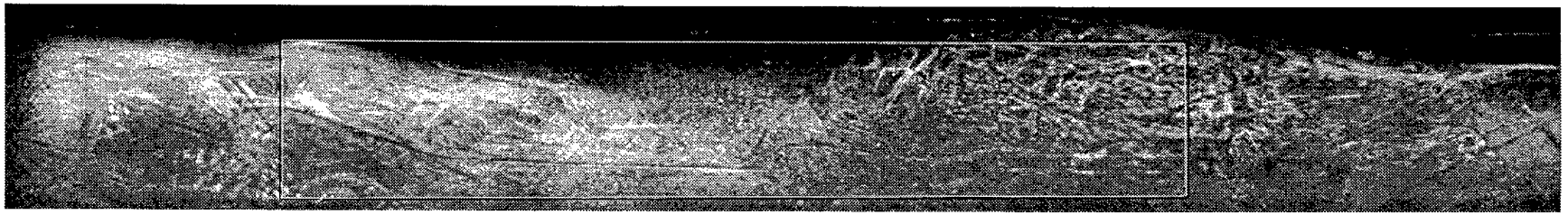

Figure 2. A sample image from the Zippori site. The portion of the image indicated by the box corresponds to the photo-mosaic in Fig. 3

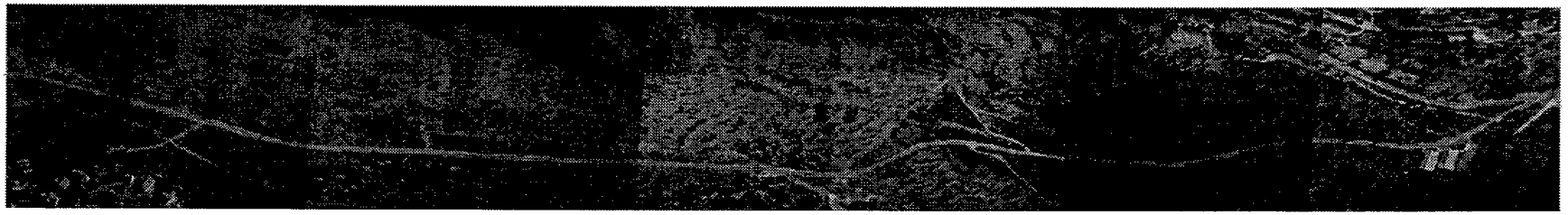

Figure 3. A photo-mosaic of the Zippori site corresponding to the boxed portion of Fig. 1.

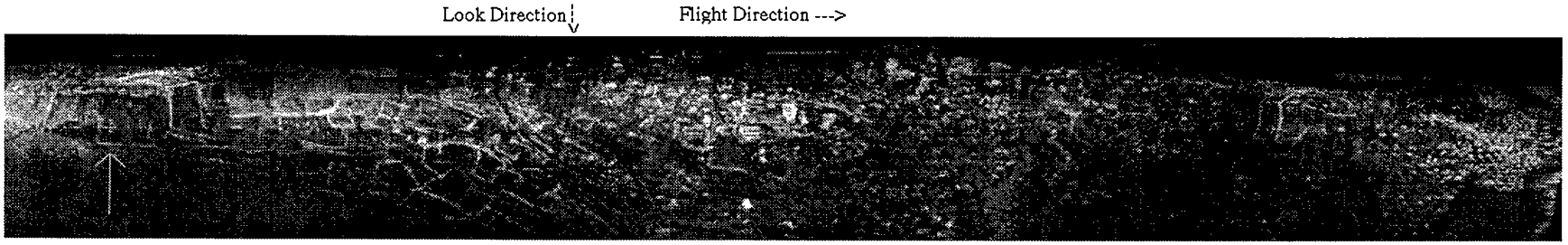

Figure 4. An image showing the main Zippori site. A cross of corner reflectors is indicated in a field near the left edge.

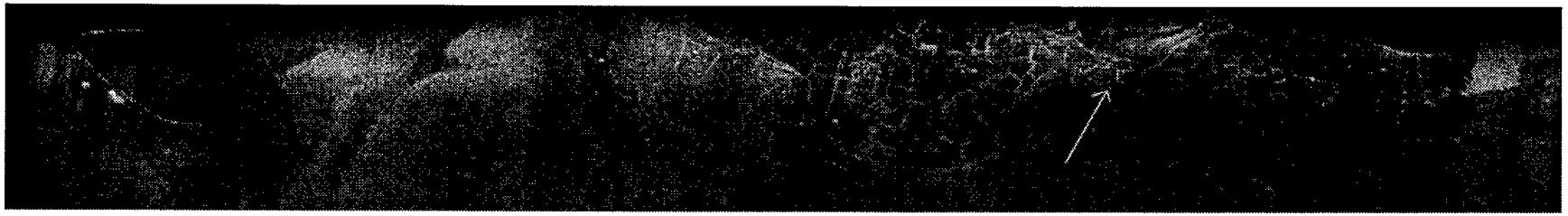

Figure 5. An image from the Tel Safi site. An 'L' of corner reflectors is indicated.

The China Airborne Radar Altimeter Control System

Xu Ke Li Maotang Zhou Ning Xue YongLin Liu YueSheng
MIRIT, Center for Space Science and Applied Research
P.O. Box 8701, Beijing 100080, P.R. China, Tel.:+86 10 62559944-3419, Fax:+86 10 62576921

Abstract -- A airborne radar altimeter (ARA) was developed in our country in 1995. The airborne radar altimeter control system (ARACS) is discussed in this paper. The ARACS consists of industrial control computer (ICC), controller and data sampling system (DSS). Besides controlling and managing the ARA, the ICC has charge of the ARA calibrating, acquiring, tracking and data processing. The controller has the functions of controlling the microwave switches, generating chirp controlling signals and other controlling signals. The DSS has the functions of sampling and holding data. The ARA software consists of the Initialization, Noise, Bias, Calibration, Acquisition and Track program elements. After being developed the ARA was tested in QingDao and had gotten a satisfactory success.

Keywords: Airborne altimeter, Data sampling, Computer control

1 INTRODUCTION

During recent 20 years, the space borne radar altimeter has begun to find wide applicability in studying the oceanology and earth geodesy. The primary goal of the ocean radar altimeter is to measure the distance from the sea surface to the airborne platform (or satellite platform), the ocean significant waveheight and the backscatter cross-section[1].

The China airborne ocean radar altimeter has successfully been developed at Center for Space Science & Applied Research (CSSAR), Academia Sinica, and finished fight test in a helicopter platform on April 19, 1995. The radar altimeter is an active microwave instrument. It operates in the pulse-width limited mode and uses the full deramp system of pulse compression[2].

2 THE RADAR ALTIMETER CONTROL SYSTEM

The airborne radar altimeter control system (ARACS) consists of industrial control computer (ICC), controller and data sampling system (DSS). Besides controlling and managing the airborne radar altimeter, the ICC has charge of calibrating, acquiring, tracking and data processing of the airborne radar altimeter. The controller has the function of controlling the microwave switches, generating chirp controlling signals and other controlling signals. The sampling system has the functions of sampling and holding data. In this paper, we only discuss the basic theory of the controller and the sampling system.

The Basic Theory of the Controller

The controller consists of shaping circuit, switch control circuit, clock circuit, pulse producing circuit, chirp controlling circuit, interruption producing circuit, delay time circuit and data loading circuit. Fig.1 represents the controller circuit diagram.

The working theory of the controller is discussed as follows: After controller is initialized, the shaping circuit shapes the PRF cycle square signal that comes from the ICC and converts the PRF cycle square signal into the electrical level signal. The electrical level signal has two functions: one is to control the switch control circuit working status. When the electrical level signal is of high level, the switch control circuit sets the microwave switches to transmitting status. When it is of low level, the switch control circuit sets the microwave switches to receiving status.

The second function of the electrical level signal is to control the pulse producing circuit to produce a pulse signal. The pulse signal is sent to interruption producing circuit that can produce a transmitting power sampling pulse and the pulse signal is also sent to the chirp controlling circuit that can produce a transmitting pulse to control the transmitter work. After the controller is initialized or the return signal is relieved, the data loading circuit sends the height value or initial value into the delay time circuit under the control of the shaping circuit. In the meantime, the clock splitting circuit controls the delay time circuit to delay the time. When the delay time is over, the delay time circuit sends a pulse signal to the interruption producing circuit and chirp controlling circuit.

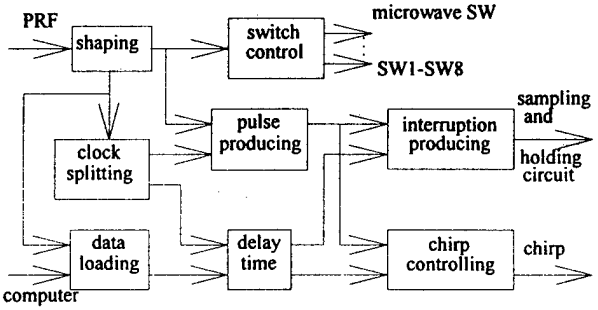

Fig. 1 Controller Circuit Diagram

0-7803-3836-7/97/$10.00 © 1997 IEEE

The interruption producing circuit gives a signal sampling pulse to the sampling and holding circuit. The chirp controlling circuit can produce a repeat transmitting pulse to trigger the linearity modulated frequency signal generator to produce the linearity modulated frequency signal that is used as a full deramp signal.

The Basic Theory of the Sampling System

The sampling system consists of control circuit, peak-value holder and conversion circuit. when the positive pulse signals that come from the controller are sent to the control circuit, the peak-value holder releases the holding voltage of the controller to zero. When the positive pulse signal is over, the peak-value holder begins to be charged. When the voltage in the peak-value holder is lower than that in the ramp filter, the peak-value holder is charged. On the contrary, when the voltage in the peak-value holder is higher than that in the ramp filter, the voltage of the peak-value holder is not changed. When the A/D conversion signal from industrial control computer is received, the conversion circuit begins to sample the voltage signal in the peak-value holder. There are 16 voltage signals that come from 12 ramp filters, early filter, late filter, power measuring circuit and accelerator, respectively, so that conversion circuit samples and converts the 16 voltage signals into relative data automatically, and uses the handled data to control and regulate the AGC value, chirp production time and so on, as well as to calculate the altitude, sea wave height and sea reflectivity.

3 THE SOFTWARE DESIGN OF THE RADAR ALTIMETER

The software of the digital signal processing unit has a key role in the radar altimeter system. The software provides the Noise, Bias, Calibration, Acquisition, and Track submodes[3]. when the system is operating under computer control ,sub-modes are controlled or sequenced automatically by software.

In the Noise submode, the software commands zero db of AGC and the filter output signals consist of the receiver noise. The purpose of the Noise is to obtain average noise levels both for extraction from the signal plus noise levels in track and, also, for gain correction of the filters in the event the filters are not accurately manually aligned.

The Bias submode is intended to provide the filter biases, by commanding maximum AGC, all signals and noise are suppressed. The residual outputs are receiver filter biases.

The Calibration submode is designed to monitor the time delays within the system. It utilizes a test target. The signal amplitudes of the Ramp filters are processed to determine the position of the test target and thereby the time delay within the system.

Acquisition and Track submodes consist of radiating through antenna and receiving the sea return signals which are then processed by the computer. The tracker utilizes Early gate and Late gate to determine track error with respect to the selected track point, and the output of the α-β filter is the prediction of the tracker estimate while the input is the tracker error. Fig.2 illustrates the tracker block diagram.

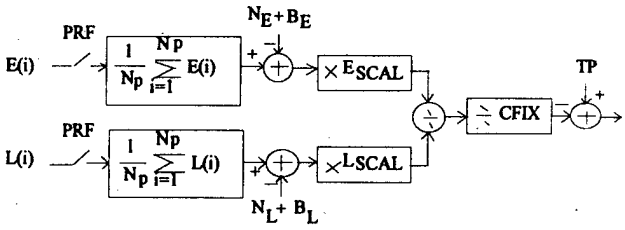

fig2. Tracker Block Diagram

Equation (1) expresses the transmission function of the α-β filter.

$$H(z)=[(\alpha+\beta)-\alpha Z^{-1}]/[(1+\alpha+\beta)-(2+\alpha)Z^{-1}+Z^{-2}] \quad (1)$$

The software flowchart is illustrated in fig.3.

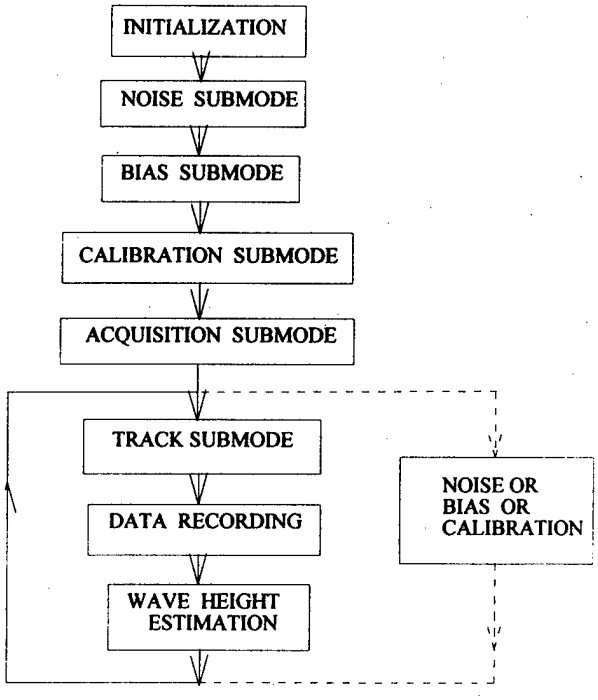

fig.3 Software Flowchart

4 EXPERIMENT RESULT

After designed, The Airborne Radar Altimeter is tested in a helicopter platform on April 19, 1995. The achieved performance figures are summarized in Table 1 .

Table 1. Key Technical Objective and Demonstrated Performance

Parameter	Objective	Achieved
Altitude Resolution	50cm	15cm
Wave Height	25%	15%
Acquisition Time	<5 seconds	<4 seconds
Drift Rate	<50cm/HR	<10cm/HR
S/N	10dB	25dB

In the flight experiment, when the aircraft flights at the same height and the interval time between radiating and receiving is being increased, the sea return signals will "move" from the higher ramp filters down to the lower ones. Fig.4 illustrates this course, the horizontal axis represents ramp filters and the vertical axis represents the normalized intensity of the sea return signal, the interval time is increased form (a) to (d).

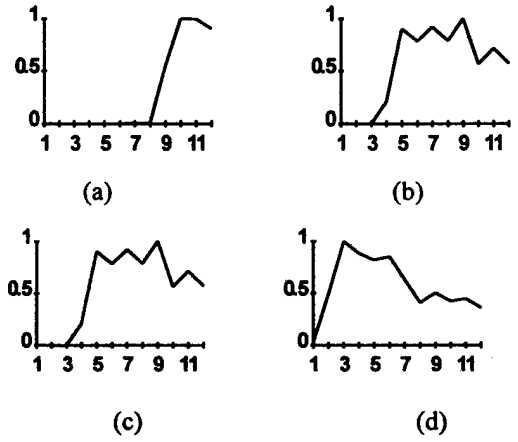

fig 4. Acquisition Process

Since the clock splitting unit has the ability to distinguish 1 ns, the sea return signal curve can be smoothed by a great deal of recording data, and the wave height resolution can be proved to be improved to 15cm with error less than 10%. The processed sea return signal curve is indicated in Fig.5, the horizontal axis represents time and the vertical axis represents the normalized intensity of the return signal.

fig 5. Processed Sea Return Signal

5 REFERENCES

[1] G.S.Brown, "The Average Impulse Response of a Rough surface and its Application, "IEEE Trans. on Antenna and Propagation, Vol. AP 25, No.1, pp.67-74, January 1977.

[2] H.G.Liu, J.S.Jiang, M.T.Li, and K.Xu, "The China Airborne Ocean Radar Altimeter-ZHG-1," the second International Airborne Remote Sensing Conference and Exhibition, San Francisco, California, 24-27 June 1996.

[3] D.B.Chelton, E.J.Walsh, and J.L.MacArthur, "Pulse Compression and Sea Level Tracking in Satellite Altimetry, " J.Atmospheric and Oceanic Technol., Vol.6, No.3, pp.407-438, June 1989.

Computer Simulation of Spaceborne Multimode Microwave Sensors

Zhang Yunhua Jiang Jingshan
Center for Space Science and Applied Research,Chinese Academy of Sciences
P.O.Box 8701, Beijing 100080, P.R.China
Tel: 86-10-62559944 exit 3479 Fax: 86-10-62576921
Email: calibra@sun20.cssar.ac.cn

Abstract -- In this paper, we give a brief introduction about our works on the development of computer software for simulation of the Spaceborne Multimode Microwave Sensors which will be launched in the future in China as scheduled. We have selected Borland C++ 3.1 for Windows based on Pentium PC as the developing platform, so plenty of colors can be guaranteed and friendly interface can be easily realized. We have used some techniques of VISC (Vusalization in Scientific Computing)[1] for demo and graph presentation. This software is being improved and not completed yet. We believe that it will be very useful not only in the design of spaceborne microwave sensors but also for enriching the measurement data library after it has been completed.

INTRODUCTION

We know that the development of spaceborne microwave sensors usually needs very large investment, so the guarantee of these successes is very importment. As the rapid development of computer technologies,the computer simulation are becoming more and more important means to guarrantee the preasumed income for the investment. The space-borne multimode microwave sensors are being developed in our institute now and it will be completed at the end of this century. At the same time computer simulation software is also being developed. Using this software we can simulate the inner working processes(may be changeable under different space environments) and external working processes of radar altimeter (13.9GHz), scatterometer (13.9GHz) and radiometers (6.6GHz, 13.9GHz, 19.35GHz, 22.38GHz, 37GHz) (for monitoring the sea and measuring various parameters of the sea such as significant wave height, wind field and temperature of sea surface) and furtherly we can predict and evaluate the working results of these sensors. This software is being improved and not completed yet. We believe that it will be very useful not only in the design of spaceborne microwave sensors but also for enriching the measurement data library after it has been completed. In this paper we give a introduction about the primary results and the whole work scheme.

THE DEVELOPMENT OF COMPUTER SOFTWARE

1. The Software Platform

The selection of software platform is the first step in the development of computer simulation. We select the Borland C++3.1 for windows as the software platform in consideration of the very large amount of library funtions, the rich kinds of colors and the easy implement to other computers. It is very important in software development with the guarantee of kindly interface between people and computer. The plenty of functions which can be called directly make it possible to complete complex process by concise programes. The all 256 colors make the simulated figures more visual. Another advantage of this platform is that multitask can be easily handled by several windows process simutaneously.

2. The Main functions of This Software

The main functions of this software includes: (1) the demo of the whole system, including the structure and the working process of system. (2) the information inquring of this system,including the working principle and the technical criteriors of altimeter, scatterometer and radiometer mode. (3) the simulation of inner working process of this system, including each single mode and transfering from one mode to another mode.

0-7803-3836-7/97/$10.00 © 1997 IEEE

(4) the simulation of external measurement process, including the trajactory simulation, the footprint simulation of antenna and the simulation of radiation and scattering characteristics of atmosphere and typical earth surface,such as the ocean surface. (5) the prediction and evaluation of the system performance, including the simulation of spacecraft trajactory, the space environment and the variation of the microwave components. All these functions are schemed by fig.1(at the end of this paper)

3. The Main Used Methods

3.1 Mathematical Methods

Two main mathematical methods are used, they are 'Monte Carlo method' and 'Maximum likelihood estimation method'.

Monte Carlo method is used to simulate the performances of every single mode and the key devices after establishing various objective functions.

The Maximum Likelihood estimation method is used in the working process simulation of altimeter and scatterometer.

3.2 Physical Methods

In order to simulate the working process of radiometer, the calculation of the radiation brightness temperature of atmosphere is needed. In practice, the atmosphere usually contains the cloud and rain so the scattering effection should be considered. One method named as "Running-after-iteration"method[2-3] is applied which can be used to calculate the brightness temperature of atmosphere containing multilayer scattering media such as cloud and rain more quickly.

Two-scale method[4] is used to calculate the backscattering coefficient σ^0 of sea surface.

4. Some Illustration About This System

The software is developed based on Pentium/133 PC, the speed cannot meet the requirement when multi-tasks are handled and multi-windows are opened. So this software will be implemented to workstation in the future.

Up to now the whole software frame has been established and some key programes have been completed, but some computer models for the subsystems are being underdeveloped.

TYPICAL FEATURES OF THIS HARDWARE SYSTEM

The technical criteriors and applied criteriors are similar with that of ERS-1. The most typical feature of these multimode sensors is the antenna system of the scatterometer mode. We know that all of the launched scatterometers have the fan-beam antenna system, however our scatterometer has the scanning pencil-beam antenna, so the coresponding footprint, cells and Doppler signal are different from that of fan-beam antenna. The pencil beam antenna makes the scatterometer more compact and yielding greater ocean coverage. Another feature of these sensors is that a group of common RF components for three modes are used, such as LNA, mixer, etc., so high function density can be achieved with small volume and lighter weight.

Acknowledgments. The author gratefully acknowledges the support of K.C. Wong Education Foundation, Hong Kong.

REFERENCES

[1] Zhang Yunhua, "Simulation Techniques for the Spaceborne Multimode Microwave Sensors", technical report of CSSAR, 1996,No. IR105.

[2] Zou Yingyin, Zhang Yunhua, Chen Kangsheng, "A New Method for Solving the RTE of Multi-layer Medium Containing Scattering Layers". Proceedings of Second Topical on Combined-Microwave Earth and Atmosphere Sensing (CO-MEAS'95), pp.49-51, Atlanta, U.S.A., April,1995.

[3] Zhang Yunhua, "The Simulation of Spaceborne Radiometer", Space Electronical Techniques (in Chinese), pp.26-28,No.4,1996.

[4] F.T.Ulaby, R.K.Moore, and A.K. Fung, "Microwave Remote Sensing - Active and Passive". Reading,MA: Addison-Wesley,1981.

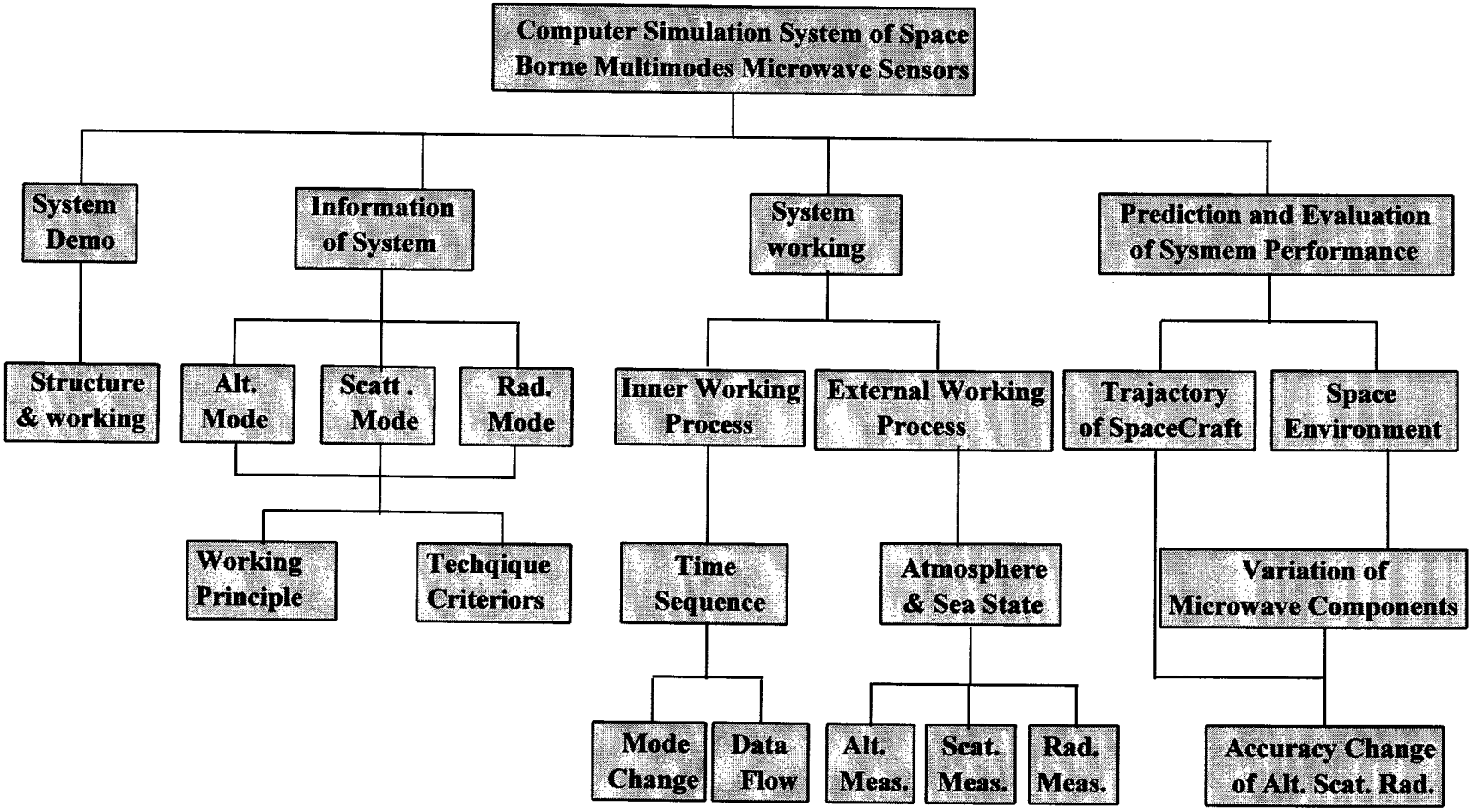

Fig.1 Diagram Chart of the Computer Simulation System

IGARSS'97

1997 International Geoscience and Remote Sensing Symposium

03-08 August 1997

Singapore International Convention & Exhibition Centre

Technical Program

Interactive Area 20: Snow and Glaciers

Improved Elevation Change Measurement of the Greenland Ice Sheet from Satellite Radar Altimetry

Curt H. Davis and Cesar Perez
Electrical & Computer Engineering
University of Missouri - Columbia/Kansas City
5605 Troost Ave
Kansas City, MO 64110 USA
T: 816/235-1276 F: 816/235-1260 Email: curt@polar.cuep.umkc.edu

ABSTRACT: Elevation change measurements from satellite altimetry for the southern Greenland ice sheet (south of 72 °N) are re-examined after incorporating technical advancements that significantly improve measurement accuracy. A spatial average of 33,610 crossover points between the Seasat and Geosat altimeters yields a 5.4 ± 0.4 cm/yr growth rate from 1978 to 1988. This is over four times smaller than previously reported results. Large spatial variations in elevation change from -7 to +20 cm/yr are observed over the ice sheet for the first time. Interannual variations in elevation change of 5-10 cm/yr are also observed. Given the large spatial and interannual variations in elevation change, the 5.4 ± 0.4 cm/yr growth rate is too small to determine whether or not the Greenland ice sheet is undergoing a long-term change due to a warmer polar climate.

INTRODUCTION

Understanding the current state of the polar ice sheets is critical for determining their contribution to sea level rise and predicting their future response to climate change. Current sea-level estimates attribute a globally coherent rise of 1.8 ± 0.7 mm/yr due to ongoing glacier and ice-sheet melting [1]. It is uncertain, however, what the individual contributions of the Greenland and Antarctic ice sheets are to sea level rise at this time. The Greenland ice sheet is of particular interest in climate change studies for two reasons. First, it is significantly warmer than the Antarctic ice sheet, where temperatures remain well below freezing over the vast majority of its surface. Second, the potential for polar amplification of a global warming trend in the northern hemisphere is very probable [2]. Thus, the Greenland ice sheet is likely to undergo more dramatic change in response to a global warming trend. Because of these important issues, NASA recently began a focused initiative whose primary goal is the measurement and understanding of the mass balance of the Greenland ice sheet [3]. Mass balance refers to the rate at which the volume of the ice sheet is changing.

Time series of ice-sheet surface elevations from satellite radar altimeters can be used to study the mass balance of the ice sheets. Zwally *et al.* [4] estimated that the southern portion of the Greenland ice sheet (south of 72 °N) grew at an average rate of 23 cm/yr from 1978-1986 by analyzing elevation data from the Seasat and Geosat satellite altimeters. Zwally [5] suggested an increase in precipitation rates caused by a warmer polar climate as a possible cause of the volume growth. These studies have generated considerable discussion among scientists about the magnitude of the growth measurement and its possible cause [6-10]. Technical arguments regarding orbit errors, inter/intra-satellite biases, and retracking algorithms have left considerable uncertainty as to the accuracy of the original results.

It is important to point out that when the Greenland growth results were first published, altimetric studies of ice-sheet change were in their infancy. Substantial progress has been made in recent years on important technical issues through the efforts of many investigators crossing various disciplines. Ice-sheet satellite altimetry has now evolved to a sufficient state of maturity that a new examination of these first results is now in order. In this paper, we re-examine the elevation change of the Greenland ice sheet using Seasat and Geosat altimeter data after incorporating several technical advancements.

METHODS AND APPROACH

In the original study by Zwally *et al.* [4], the Geosat x Seasat comparison used orbit solutions that were derived from different gravity models. This was a major factor in the incorporation of a 40 ± 40 cm systematic correction (plus uncertainty) in their analysis. Since then, several consistent sets of orbit solutions have been developed for both Seasat and Geosat datasets. In addition to eliminating the 40 ± 40 cm correction, the new orbit solutions have significantly reduced the RMS radial orbit error, which in turn have significantly improved error estimates for elevation-change rates. Table 1 provides a summary of altimeter crossover variability over the ocean for various generations of orbit solutions.

The Joint Gravity Model-3 (JGM-3) orbit solutions are used in our study and are currently available for Seasat, Geosat-Geodetic Mission (GM), and the Geosat-Exact Repeat

0-7803-3836-7/97/$10.00 © 1997 IEEE

Mission (ERM) satellite datasets. The JGM-3 solutions offer an average reduction in radial orbit error anywhere from 15-60 cm (Table 1) when compared to previous solutions. It should also be noted that in addition to improving elevation-change error budgets, the new solutions can remove systematic orbit errors present in earlier orbit solutions that could lead to erroneous elevation-change results. This is an important point that is not widely understood.

Table 1. Typical SD of Ocean Crossover Differences for Various Altimeter Orbit Solutions

Gravity Model	Seasat SD (cm)	Geosat SD (cm)	Avg. Error Increase Relative to JGM-3 (cm)
GEM-T2	70	60	59 / 59
JGM-2	40	25	15 / 22
JGM-3	37	12	-- / --

All ice-sheet altimeter data must be post-processed to produce accurate surface elevation measurements. This post-processing is called "retracking" and is required because the leading edge of the ice-sheet return pulse deviates from the on-board tracking gate, causing an error in the telemetered range measurement. Retracking altimetry data is achieved by computing the departure of the waveform's leading edge from the altimeter tracking gate and correcting the satellite range measurement (and surface elevation) accordingly. By comparing the repeatability of surface elevations produced from different ice-sheet retracking algorithms, Davis [8] demonstrated that the retracking algorithm [11] used in the Zwally *et al.* [4] study, hereafter referred to as the NASA algorithm, introduced significantly larger errors in the elevation data than three other retracking algorithms. In addition, the NASA algorithm was shown to produce ice-sheet growth rate estimates that were 30-55% larger than the other three algorithms, which all produced nearly identical results. Several refinements of the NASA algorithm have been done since the original study. However, a recent analysis has shown that the current NASA algorithm (NASA-V4) is still a significant source of error in the ice-sheet datasets [12]. Table 2 provides a summary of the performance of various ice-sheet retracking algorithms computed using Greenland crossover datasets.

The crossover datasets use the JGM-3 orbit solutions and were obtained where the time difference between the satellite crossing tracks was less than 30 days. In addition, a 3 SD edit with SD convergent to 2% was used on the crossover residuals to eliminate data outliers [4]. The results in the table show that the threshold algorithm offers a reduction in average error of 18-35 cm relative to the other retracking algorithms. These improvements are comparable to that obtained by using the latest JGM-3 orbit solutions. The threshold algorithm was developed specifically for measurement and detection of ice-sheet elevation change [12], and elevations produced from this retracking algorithm are used in this study.

Table 2. Typical SD of Ice-Sheet Crossover Differences for Various Retracking Algorithms

Algorithm	Geosat - GM SD (cm)	Geosat-ERM SD (cm)	Avg. Error Increase Relative to Threshold (cm)
NASA-V4	41	46	29 / 35
ESA	34	36	18 / 20
Threshold	29	30	-- / --

Previous ice-sheet elevation studies have relied upon a local or regional approach for analyzing altimeter orbit errors and deriving various orbit error corrections. Typically, a reference ocean surface in the vicinity of the ice sheet (e.g. the North Atlantic for Greenland) is created and altimeter orbits over this reference surface are analyzed to derive the orbit error corrections. While suitable for removing orbit error in some applications, this approach cannot fully exploit the fundamental nature of the orbit error. First, the predominant radial orbit error is a long-wavelength signal, i.e. its spatial variation is over large distances. Second, these orbit errors are concentrated at the circular frequency of the orbital period (1/rev frequency). A global analysis of ocean altimeter data is required to capitalize on these inherent characteristics.

While a significant amount of effort is required to assemble and analyze a global altimeter database, this type of analysis offers several unique advantages that cannot be achieved using a regional analysis of orbit error. First, a global analysis will unveil correlations and long-period (seasonal and interannual) time-dependent variations in the 1/rev orbit errors. These time-dependent orbit error variations were not considered by Zwally *et al.* in the Geosat x Geosat portion of their study. Second, robust optimal estimation filters can be designed specifically to separate orbit errors at the 1/rev frequency from true geophysical signals in the data. Finally, systematic biases that may be present in inter-satellite comparisons (e.g. Geosat x Seasat) can be characterized separately from the orbital errors. Thus, this study adopts a global treatment of the altimeter data to characterize and reduce the predominant long-wavelength orbit errors. This is the first ice-sheet elevation study to incorporate such an analysis of orbit error.

ORBIT ERROR ANALYSIS

The global ocean altimeter datasets used in the orbit error analysis were provided by the NASA Ocean Altimeter Pathfinder program. A consistent reference frame (ITRF) and geoid model (JGM-3) were used to calculate the orbits for both the Seasat and Geosat satellites. In addition, a consistent set of atmospheric and geophysical corrections were used whenever possible. The radial orbit errors were identified by passing the global ocean data through a stochastic filter designed for estimating high-precision Global Positioning System (GPS) orbits. The 1/rev orbit errors were parameterized by sine and cosine functions with frequencies of one orbital period and time-varying amplitudes. The time-varying amplitudes were treated as stochastic processes and determined by the estimation software. In order to identify long-term trends in the orbit error, the sea-height residuals were formed by differencing the complete global data with a long-term mean of the sea-height measurements. The effective removal of orbit error was observed by tuning various filter parameters such as the steady-state standard deviation and the decorrelation time constant for the stochastic process. By properly tuning the filter, an adequate trade-off between removing the 1/rev orbit error and preserving the true underlying geophysical signals was obtained.

A collinear orbit error analysis was performed using the initial three years of the Geosat-ERM global ocean database. A global reference sea-height surface was formed by averaging the first two years (43 cycles) of the ERM dataset. Only the first two years of the ERM mission were used for the reference surface since the orbit solutions were degraded by solar activity starting with repeat cycle 44. The 1/rev orbit errors were then removed by the stochastic estimation software by two distinct filtering schemes. The first scheme treated the sinusoidal coefficients as a colored noise process with correlation between neighboring orbit revolutions, and the second scheme assumed a white noise process with all coefficients completely decorrelated. Table 3 provides a comparison of the two filtering schemes on the global ERM data. The first two-years of the ERM data were treated separately from the third year because of the significant difference in orbit-error magnitudes.

Table 3. RMS of ERM Global Sea-Height Residuals from Collinear Orbit Analysis

ERM Dataset	Uncorrected RMS (cm)	Colored Noise Filter RMS (cm)	White Noise Filter RMS (cm)
First 2 years	12.2	10.8	8.9
Third Year	52.4	22.2	9.5

Both orbit correction methods demonstrate a reduction of the overall residual RMS, with substantial improvement during the third year of the ERM data. It should be noted that further analysis of the white noise correction scheme showed that it removed much of the true geophysical ocean signal along with the 1/rev orbit errors (e.g. El Nino). Thus, while the white noise scheme exhibits the lowest RMS values, it is not used to correct the orbits for our ice-sheet study. The white-noise orbit error corrections contain true oceanic signals that would be erroneously introduced into the ice-sheet elevations. It should be noted that this is an important concern when only a regional orbit-error strategy is used, as it is difficult to separate true ocean signals from 1/rev orbit errors in this type of approach. The white-noise scheme does demonstrate the noise floor of the altimeter dataset in an RMS sense after removal of orbit error and most of the geophysical signal. Further analysis of the global ocean signals showed that the colored-noise scheme preserved much of the true ocean energy while eliminating significant orbit error.

Based upon these results, orbit-error corrections derived from the colored noise scheme were generated for the first 2 years of the Geosat-ERM data. Orbit-error corrections for the Seasat data could not be produced as the Ocean Pathfinder data was not available for this mission at the time of this study.

ICE SHEET ELEVATION CHANGE

The Seasat (6 July - 10 Oct 1978) and Geosat-ERM (9 Nov 1986 - 11 Nov 1988) Greenland datasets were provided by the NASA Ice Sheet Altimeter Pathfinder program. Both satellites provided coverage up to a maximum latitude of 72 °N. The ice-sheet surface elevations were produced using the same reference frame, geoid model, and atmospheric corrections as the ocean altimeter datasets. Only the first two years (43 cycles) of the ERM data were utilized as solar activity seriously degraded the performance of the satellite beyond this time. Orbit adjustments from the method described in the previous section were applied to the Geosat-ERM data. Elevation differences were computed by crossing the ERM and Seasat datasets.

Preliminary results from the ERM x Seasat elevation change study are shown in Table 4. The first two datasets (87 x S, 88 x S) used the same 3-month time period for the ERM and Seasat data to avoid seasonal biases. The last dataset (ERM x S) used the first two-years of the ERM data with all the Seasat data to provide a larger number of crossovers (N) and a better spatial distribution. Note that the inclusion of a full two years of ERM data will also tend to average out seasonal variations. The regular dH/dt analysis is simply the average change in elevation (dH) divided by the average time interval (dt) using all the crossovers. The spatial dH/dt analysis grids the data into 50 x 50 km cells and

computes a spatial average using the mean dH and dt in each cell. This is done because the regular dH/dt analysis will be biased towards the northern interior of the ice sheet due to the non-uniform distribution of the satellite tracks [5]. Error bounds are computed using 95% confidence intervals. The results for all the datasets and both types of dH/dt analysis are consistent, with growth rates from 4-7 cm/yr. These growth rates are approximately four to five times smaller than the original results given by Zwally *et al.* [4].

Analysis of the spatial distribution of the crossover data indicates that there are large geographic variations in the dH/dt values (Fig. 1). The dH/dt values for the northern interior of the ice sheet are quite small (2-4 cm/yr) and are consistent with mass balance estimates reported for this region. Modest thinning of 3-7 cm/yr is indicated for the lower elevations of the eastern and western flanks of the ice sheet between 70-72° N. The thinning along the western flank is supported by observations showing a retreat of the western margin of the sheet around the Jakoshabvn glacier. The growth rates west of the ice divide between 65-69 °N vary from 10-15 cm/yr. These agree well with growth rates derived from a comparison of airborne laser altimeter and geoceiver ground survey data spanning the period from 1980 to 1993/94 [13]. In addition, modest thinning is indicated by the few grid cells east of the ice divide between 63-67 °N, which is also consistent with the laser altimeter results [13]. However, confidence of thinning in this area east of the ice divide is low due to the poor spatial coverage. The large spatial variation in the growth rates (-7 to +20 cm/yr) contradicts earlier results where large growth rates (>20 cm/yr) were reported for all elevation and latitude bands [5].

The spatially averaged result for the growth of the southern Greenland ice sheet (south of 72 °N) from 1978 to 1987-88 is 5.4 ± 0.4 cm/yr. We note that over 95 percent of the data used in this study occurs at elevations greater than 2000 m. Thus, no conclusion can be made as to the behavior of the lower elevations nearer the ice-sheet margin. While this modest growth rate is statistically significant at the 95% level, natural fluctuations in snow-accumulation rates can cause decadal changes in surface elevation [10]. Our own analysis of interannual variations in ice-sheet surface elevation from the ERM dataset indicates natural fluctuations of 5-10 cm/yr. Given these large variations, the 5.4 ± 0.4 cm/yr growth rate is too small to determine whether or not the Greenland ice sheet is undergoing a long-term change due to a warmer polar climate. Unambiguous detection of long-term trends requires that satellite altimeter measurements be continued to extend the existing time series of ice-sheet surface elevations.

The results presented here are preliminary because we have not been able to conduct an analysis of the Seasat orbit error. However, the new JGM-3 orbit solutions are so accurate that we expect that the orbit-error corrections will be small, as they were for the Geosat-ERM data. Thus, we do not expect the magnitude of the elevation-change measurements to change dramatically. Thus, we feel that the central conclusions of this study are correct. Specifically, the average change in elevation from 1978-88 is many times smaller than the previously reported 23 cm/yr growth rate, and that the revised growth rate is too small to determine whether or not the Greenland ice sheet is experiencing climate-induced change.

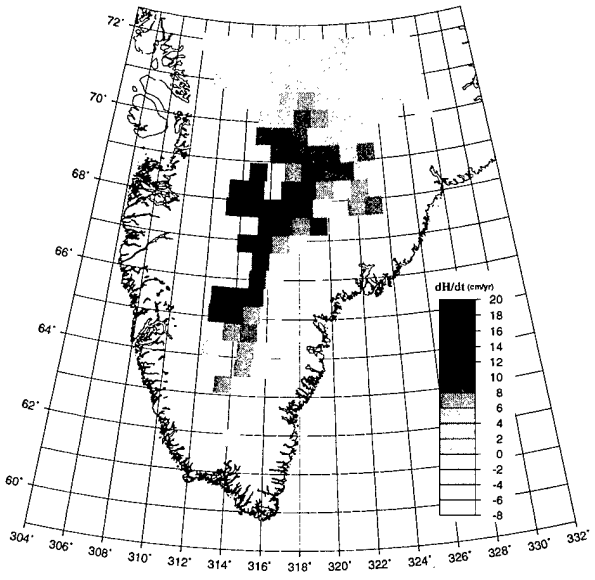

Figure 1. Spatial distribution of elevation change from 1978-1988 showing large variations in dH/dt values. A spatial average yields a mean growth rate of 5.4 ± 0.4 cm/yr.

Table 4. ERM x Seasat Elevation Change Analysis - Regular dH/dt Analysis

Dataset	dH (cm)	dt (yr)	N	dH/dt (cm/yr)
87 x S	49 ± 3	9	4,540	5.4 ± 0.3
88 x S	49 ± 4	10	2,910	4.9 ± 0.4
ERM x S	38 ± 2	9.25	34,725	4.1 ± 0.2

Table 5. ERM x Seasat Elevation Change Analysis - Spatial dH/dt Analysis

Dataset	dH (cm)	dt (yr)	N	dH/dt (cm/yr)
87 x S	61 ± 5	9.00	3,815	6.8 ± 0.6
88 x S	35 ± 6	10.00	1,994	3.5 ± 0.6
ERM x S	50 ± 4	9.25	33,610	5.4 ± 0.4

ACKNOWLEDGMENTS

We are grateful to R. Thomas for his continued support of this work. We thank the NASA Pathfinder Program for the ocean and ice sheet altimeter datasets; in particular we acknowledge the help of H.J. Zwally, C. Koblinsky, A. Brenner, J. DiMarzio, and B. Beckley for their assistance in obtaining these data. This research was supported by funds from NASA's Office of Mission to Planet Earth under grants NAGW-5010 and NAGW-5243.

REFERENCES AND NOTES

[1] Peltier, W.R. and A.M. Tushingham (1989), "Global sea level rise and the greenhouse effect: might they be connected?" *Science*, Vol. 244, pp. 806-810.

[2] Barron, E. (1995), "Forum on global change modeling," *USGCRP Report 95-02*, Washington, DC.

[3] Abdalati, W. (1996), *Program for Arctic Regional Climate Assessment (PARCA) - Greenland Science and Planning Meeting*, CIRES, University of Colorado, Boulder, CO, 17-18 Sept 1996.

[4] Zwally, H.J., A.C. Brenner, J.A. Major, R.A. Bindschadler, and J.G. Marsh (1989), "Growth of Greenland ice sheet: measurement," *Science*, Vol. 246, pp. 1587-1589.

[5] Zwally, H.J. (1989), "Growth of Greenland ice sheet: interpretation," *Science*, Vol. 246, pp. 1589-1591.

[6] Douglas, B.C., R.E. Cheney, L. Miller, R.W. Agreen (1990), "Greenland ice sheet: is it growing or shrinking?," *Science*, Vol. 248, pg. 288.

[7] Zwally, H.J., A.C. Brenner, J.A. Major, R.A. Bindschadler, and J.G. Marsh (1990), "Response - Greenland ice sheet: is it growing or shrinking?," *Science*, Vol. 248, pp. 288-289.

[8] Davis, C.H. (1995), "Growth of the Greenland ice sheet: a performance assessment of altimeter retracking algorithms," *IEEE Transactions on Geoscience & Remote Sensing*, Vol. 33, No. 5, pp. 1108-1116.

[9] Schneider, S.H. (1992), "Will sea levels rise or fall?" *Nature*, Vol. 356, No. 5, pp. 11-12.

[10] Van der Veen, C.J. (1993), "Interpretation of short-term ice-sheet elevation changes inferred from satellite altimetry," *Climatic Change*, Vol. 23, pp. 383-405.

[11] Martin, T.V., H.J. Zwally, A.C. Brenner, and R.A. Bindschadler (1983), "Analysis and retracking of continental ice sheet radar altimeter waveforms," *J. Geophys. Res.*, Vol. 88, pp. 1608-1616.

[12] Davis, C.H. (1997), "A robust threshold retracking algorithm for measuring ice-sheet surface elevation change from satellite radar altimeters," *IEEE Transactions on Geoscience & Remote Sensing*, in press.

[13] Krabill, W., R. Thomas, K. Jezek, K. Kuivinen, and S. Manizade (1995), "Greenland ice sheet thickness changes measured by laser altimetry," *Geophys. Res. Lett.*, Vol 22, No. 17, pp. 2341-2344.

Multi-Year Ice Concentration From RADARSAT

Florence Fetterer[1], Cheryl Bertoia[2], Jing Ping Ye[1]
[1]National Snow and Ice Data Center
CIRES Campus Box 449, University of Colorado
303-492-4421/303-492-2468(FAX)/fetterer@kryos.colorado.edu

[2]National Ice Center
4251 Suitland Road, FOB4
Washington, D. C., 20395-5180
301-457-5314 x302/ 301-457-5300(FAX)/cbertoia@icecen.fb4.noaa.gov

Abstract

The U.S. National Ice Center requires a robust mulityear ice classification algorithm that can handle variability in backscatter across uncalibrated 500 km Radarsat scenes. ERS-1 images are used to test a dynamic threshold algorithm. The best results were obtained with a window size of 32, delta of 0.8, Fisher partition criterion and closing.

INTRODUCTION

The U. S. National Ice Center (NIC) depends on Radarsat SAR imagery for its Arctic-wide weekly ice analysis. NIC will receive up to 3 GB of Radarsat imagery per week; far too much to be handled by manual analysis alone. We are developing an algorithm that will automatically map and contour multiyear (MY) ice in Radarsat imagery. MY ice is the thickest ice type and presents a danger to navigation.

Experience with ERS-1 imagery for ice mapping showed that the large difference between class means for MY and first-year (FY) ice in winter allowed for robust classification of MY ice with a maximum likelihood (ML) algorithm [1, 2]. This method used a class backscatter lookup table which depended on calibrated imagery. For Radarsat ScanSAR imagery, however, we do not want algorithm performance to hinge on having calibrated imagery. A dynamic (i.e. local or adaptive) threshold method is a more appropriate choice. In addition, a dynamic threshold (DT) algorithm should handle the variability in backscatter across a 500 km Radarsat scene. Here a DT algorithm is tested using ERS-1 imagery (Radarsat data were not available when work began).

THE ERS-1 TEST SET

In [2] and [3] we compared the results of supervised ML classification using manually selected training sets to unsupervised ML classification [1] with a set of 86 images. We found that unsupervised ML performed well (6% RMS error) in the Beaufort Sea and Central Arctic, but not as well in the East Siberian Sea (16% RMS) where the backscatter distribution of MY ice is wide and skewed, and MY floes are often small and indistinct. Regional differences in ice type backscatter and scene composition can affect DT algorithm performance as well. Therefore, we selected 17 images from the previously analyzed data set representing five different ice regimes. These are Central Arctic (with greater than 90% MY and some leads), Beaufort (mixed FY and MY), East Siberian (indistinct floes in a matrix of younger ice), Small MY floes (surrounded by vast areas of FY ice, generally near the MY pack edge), and Other (this includes two images that straddle the MY pack/fast ice boundary). Fig. 1 shows subimages typical of three of these regimes. Each image is 100 km square with 100 m pixel spacing. The algorithm is run on calibrated intensity images. Here FY refers to everything other than MY: younger types cannot be reliably distinguished and are less important operationally.

THE DYNAMIC THRESHOLD ALGORITHM

The algorithm described in [4] is used as a starting point. The algorithm assumes three classes are present, and that the class having the highest backscatter is MY ice. (The division between the two lower FY classes is ignored. Generally only two classes are detectable in any image based on backscatter alone. However, assuming two classes results in gross overestimation of MY for all but Central Arctic cases).

Fig. 1. These regimes pose different problems for a DT classifier. In the Beaufort Sea (left), dark areas within MY floes are misclassified. In areas of small MY floes (center), error is caused by the relative infrequency of the MY class. In the E. Siberian Sea (right), small floe size and indistinct MY backscatter causes error. Images Copyright ESA (1992).

This is NASA ADRO project number 103. This work is sponsored by the Chief of Naval Operations under program element 603207N, CDR Tim Sheridan, program manager.

0-7803-3836-7/97/$10.00 © 1997 IEEE

A window is passed over the image, and the backscatter histogram within each window is tested for bimodality. A bimodal distribution indicates two classes in the window, and the saddle point is chosen as the local threshold. The position of the threshold in the image is retained. Finally, the distribution of all the accumulated local thresholds is split using a minimum variance criterion. The location of this split point is critical to determining how much MY ice the algorithm finds.

The thresholds above the split point are used to separate MY from FY2, while those below separate FY2 from FY1. Each pixel's value in the image must be compared with two local thresholds. Local thresholds for each pixel are obtained by interpolating to the pixel location from the thresholds that result from the windowing operation.

Fig. 2 shows the global image histogram and the distribution of thresholds for a Beaufort Sea image. In general, only Beaufort Sea global image histograms are bimodal, reflecting relatively large amounts of FY ice and distinct separation in backscatter between MY and FY ice. Threshold histograms, which in an idealized case are bimodal when three distinct classes are present, were bimodal for the Central Arctic and Beaufort, and unimodal for other regimes (with exceptions).

RESULTS

Fig. 3 (left) compares supervised ML classification with DT results using standard DT algorithm parameters. The DT algorithm underestimates MY in the Central Arctic and also errs significantly for the two small MY floe cases and one East Siberian case. Algorithm parameters were varied to test their effect on results.

Window Size

There is an interdependency between window size, feature size, and image size, since window size and image size together determine the number of thresholds potentially contributing to the threshold distribution, and the feature size relative to the window size will play a part in how many local regions are found to have bimodal histograms. Window sizes of 16, 32, 64 and 128 pixels square were used. Smaller

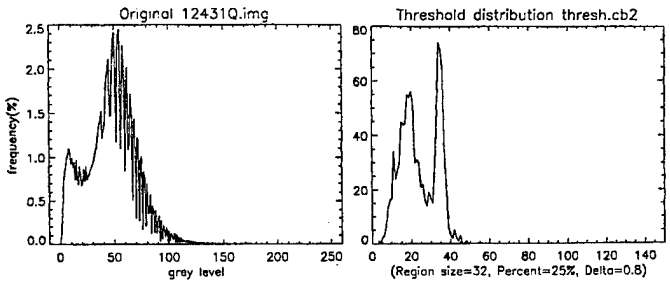

Fig. 2. Histogram of image gray level (left) and distribution of thresholds (right) for a Beaufort Sea image.

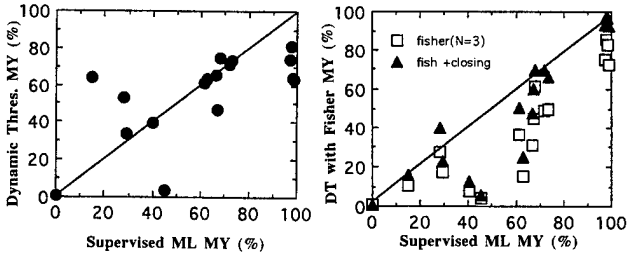

Fig 3. DT with the minimim varience criterion (left) and Fisher criterion with and without closing (right) versus supervised ML classification.

windows can give better definition of small features, but at the expense of "noise" within larger features, and of greater computing time. However, larger windows result in noisy threshold distributions because there are too few bimodal regions contributing. Results using 16 and 32 for window sizes were compared for all 17 images. In only two cases did results vary by more than a few percent. Because small features are not routinely depicted on NIC products, 32 was chosen as the best window size for the 100 km images.

Bimodality Tests

Local histograms that pass the initial test for bimodality are then subjected to another test that incorporates a peak-to-valley, or delta, ratio. A higher delta parameter indicates a less stringent criterion. Fig. 4 shows the number of window regions passing the initial test, and the number selected with the delta parameter, for all regimes with standard parameters of window size 32 and delta equal to 0.8. When the number of regions passing initially is low, changing delta can have a radical effect. Raising delta to 0.9 improved results from 40% error to less than 10% error for one of the small MY floe images by allowing more regions to contribute to the threshold distribution. At the same time it worsened results for two other images that had a large

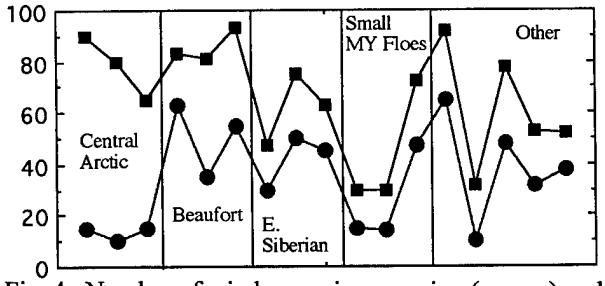

Fig. 4. Number of window regions passing (square) and selected (circle) for thresholds, in percentage of the total number of window regions. In the Central Arctic, most windows cover MY floes with wide backscatter distributions that pass the initial variance test for bimodality. The delta test recognizes that they are not bimodal. In areas of low MY concentration and small floes, there are few feature boundaries, thus the low number of passing regions.

number passing initially. The effect is similar to changing window size in that a greater number of regions contributing to the threshold distribution can improve results if there are few candidate bimodal regions. Delta equal to 0.8 was chosen as the standard.

Criterion Function

An undesirable trait of the algorithm is that a slight change in parameters that leads to a slight change in the threshold distribution can radically change the amount of MY ice the algorithm finds. This is because a criterion function is used to split a distribution that may not have two distinct clusters, so that a slight change in distribution may lead to a radically different split point. The standard minimum variance criterion splits the threshold distribution by seeking to minimize $(\sigma_l^2 + \sigma_r^2)$, where σ_l^2 and σ_r^2 are variances for the left and right sides of candidate partitions. The Fisher criterion seeks the partition that minimizes $(\sigma_l^2 + \sigma_r^2)$ while maximizing $(\mu_l - \mu_r)^2$, the squared difference of the left and right means. The Fisher criterion seeks well-separated peaks, but when these are not present the effect is to drive the split point away from the center of the distribution. The result is a slight improvement for cases with very little of either FY or MY ice but an underestimation of MY for other cases. However, using the mathematical morphology closing operation on MY ice pixels with a structuring element of 3 by 3 pixels was found to improve results considerably (Fig 3 (right)).

Manually analyzed images allow a pixel by pixel comparison and are the preferred standard by which to judge this algorithm. However, we used supervised ML classification because manual analysis is too time-consuming for a large image set. One problem, though, is that if equal amounts of FY and MY are misclassified, the net error will be zero and the erroneous mapping will not be obvious. To test our assumptions about algorithm performance we compared algorithm results with manual classification by NIC analysts for six images. Confusion matrices for three cases are below. These comparisons confirmed that the Fisher criterion with closing gave results most similar to manual analysis.

Table 1. Classification accuracy (percent) for three images classified using the Fisher criterion function and closing compared with manual analysis.

	Algorithm					
	Small MY Floes		Beaufort		Central Arctic	
Manual	MY	FY	MY	FY	MY	FY
MY	20	3	62	4	90	3
FY	10	68	7	27	4	4
Overall	82		89		81	

Table 2. Classification accuracy (percent) for three images classified using the minimum variance criterion function compared with manual analysis.

	Algorithm					
	Small MY Floes		Beaufort		Central Arctic	
Manual	MY	FY	MY	FY	MY	FY
MY	22	11	65	8	73	2
FY	7	59	4	23	21	5
Overall	80		84		75	

CONCLUSION

We have adapted an algorithm designed to perform well for images with three locally well-separated classes to imagery with at best two well-separated classes. In spite of the somewhat arbitrary nature of the division of thresholds for FY1/FY2 and FY2/MY separation, the algorithm gives results that are only slightly worse than maximum likelihood classification. The advantage is that the DT algorithm is fast, simple, and can run on uncalibrated imagery. The algorithm gave the best overall results with a window size of 32 100 m pixels, delta of 0.8, Fisher partition criterion, and closing. Preliminary results with Radarsat show no differences from results with ERS-1, when the algorithm is run on 100 km subimages. Subdividing may give better results than applying the algorithm to the entire 500 km scene.

REFERENCES

[1] R. Kwok, E. Rignot, B. Holt, and R. Onstott, "Identification of sea ice types in spaceborne synthetic aperture radar data," Journal of Geophysical Research, vol. 97, pp. 2391-2402, 1992.

[2] F. M. Fetterer, D. Gineris, and R. Kwok, "Sea ice type maps from Alaska Synthetic Aperture Radar Facility imagery: An assessment," Journal of Geophysical Research, vol. 99, pp. 22,443-22,458, 1994.

[3] D. J. Gineris and F. M. Fetterer, "An examination of the radar backscatter of sea ice in the East Siberian and Chukchi Seas," Proceedings, IGARSS '94, pp. 499-502, Pasadena, CA, 1994.

[4] D. Haverkamp, L. K. Soh, and C. Tsatsoulis, "A comprehensive, automated approach to determining sea ice thickness from SAR data.," IEEE Transactions on Geoscience and Remote Sensing, vol. 33, pp. 46-57, 1995.

ACKNOWLEDGMENTS

We thank LeenKiat Soh and Costas Tsatsoulis of the University of Kansas for generously providing the initial dynamic threshold algorithm code, and Jim Conner of the Alaska SAR Facility for Radarsat test images.

Vector Radiative Transfer for Scattering Signature from Multi-Layer Snow/Vegetation at SSM/I Channels

Ya-Qiu Jin
Wave Scattering and Remote Sensing Center
and Department of Electronic Engineering
Fudan University, Shanghai, China 200433

Abstract: Vector radiative transfer (VRT) at the DMSP SSM/I channels (from 19 to 85 GHz) for multi-layer of discrete scatterers as a model of snowpack/vegetation canopy is developed. Using the physical optics approximation, the scattering, extinction coefficients and phase function of VRT equation for vegetation canopy are derived. The dense medium VRT is applied to the snow-layer. Numerical results of two coupled VRT equations simulate scattering and emission signature from snowpack/vegetation canopy at SSM/I channels. Numerical results are applied to simulation and analysis of the SSM/I observations over China's northeast forest and Tibet Naqu pasture areas.

INTRODUCTION

Areal extent and properties of snow/ vegetation cover are of great importance for climate research, global and regional water cycle, as well as agriculture management. Space-born microwave radiometers are primary tools for global surface cover monitoring because of the potential of microwaves to observe the earth surfaces through clouds and to provide information on the internal properties of snow/vegetation covers. One of the latest and most advanced passive microwave sensors is the DMSP SSM/I (Special Sensor Microwave Imager) operated at seven channels (19,37,85GHz with dual polarization and 22 GHz with vertical polarization only). The 85 GHz channel is employed due to strong scattering sensitivity. As frequency such as 85 GHz is high, scattering becomes much stronger and it leads to lower thermal emission and brightness temperature from the underlying media. Scattering produces a positive difference between low and high frequency channels. The scattering index is usually defined as $SI \equiv T_{B22v} - T_{B85v} > 0$ as a rule to identify snowpack and rainfall. When the thick forest canopy covers the underlying land, polarization and emission signature are governed by the canopy cover. However, it has been observed that snowpack signature can pass through the forest canopy. The positive scattering index can be identified from the snowpack in winter season. It has been measured during defoliated period in winter that the opacity of forest canopy is very weakly dependent on frequency, and the much larger variability is due to the heterogeneity of the forest. Most of works on opacity, transmittivity and scattering of vegetation canopy are largely limited in low frequency and would overestimate attenuation if simply applied at high frequency. Theoretical scattering models of non-spherical particles as available now only concern with the back-scat-tering in the first-order Born approxi-mation and seem not tractable yet to take account of multiple scattering and emission.

In this paper, we develop a multi-layer model for snowpack/vegetation canopy to take into account scattering signature and spectral characteristics of thermal emission at SSM/I channels. Vegetation canopy is modeled by a layer of non-spherical particles, and the physical optics approximation [1] is applied to derive the scattering, extinction and phase matrix of the VRT (vector radia-tive transfer) of the forest canopy. Snowpack is modeled as a layer of dense Rayleigh spherical particles, and the dense medium VRT is applied to the snowpack layer [2,3]. Solving two coupled VRT equations by discrete ordinate and eigenanalysis method [3,4], numerical results can simulate multiple scattering and thermal emission from snowpack/ vegetation canopy and present the spectral characteristics at the SSM/I channels. Numerical results are applied to simulation and analysis of the SSM/I measurements over China's northeast forest and Tibet Naqu pasture areas.

VRT WITH PHYSICAL OPTICS APPROXIMATION

As an electromagnetic wave is incident on a disk-like particle, the scattered field is obtained by solving the unknown internal field of the particle. Using the physical optics approximation at high frequency limit [1], the internal field is assumed the same as would exist in a dielectric slab of the same thickness and orientation. Then the scattering amplitude function $f_{pq}, (p,q = v,h)$ can be obtained. At high frequency limit, scattering will be concentrated in a very small angular region in the forward direction. For our purpose of high frequency approximation, we assume that scattering occurs in the specular direction.

For a non-spherical particle such as a disk with an arbitrary orientation defined by the Euler angles, the local coordinates can be transformed into the principal coordinates by orientation of the Euler angles [2,3]. The scattering amplitude functions $f_{pq}, (p,q = v,h)$ for a non-spherical particle with arbitrary orientation, and its ensemble averages such as the scattering, absorption, extinction coefficients $\kappa_s, \kappa_a, \kappa_e$ and phase functions $< f_{pq} f_{st}^* >$, $p,q,s,t = v,h$ of the VRT equation of random particles can be derived. We have derived the

0-7803-3836-7/97/$10.00 © 1997 IEEE

scattering, absorption and extinction coefficients and the phase matrix in discrete ordinates for Gaussian quadrature method [5].

TWO COUPLED VRT EQUATIONS

Snowpack is a typical dense scatterer medium since the fractional volume of ice grains is always appreciable as f > 0.1. Independent scattering assumption in conventional VRT equation becomes invalid and scattering coherence from dense scatterers should be taken into account. This was called the DMRT (dense medium radiative transfer). It has been proved that DMRT equation has the same form as conventional VRT, but the effective propagation constant K should be used to take account of scattering coherence. The extinction and scattering coefficients can be calculated from K. We adopt DMRT to calculate K, extin-ction and scattering coefficients in our VRT approach for snowpack at SSM/I channels.

A multi-layer model is developed for snowpack/ vegetation canopy. The top layer-f is for forest canopy, the next layer-1 is for snowpack, and the under-lying medium-2 is soil land. The physical optics approximation is employed for VRT of the layer-f, and DMRT is used for the layer-1. These two coupled VRT equations and four boundary conditions are solved by using the discrete ordinate and eigenanalysis method [3,4].

The p-(v,h) polarized brightness temperture observed by the satellite born SSM/I is obtained by the VRT equation of atmosphere free of rain as

$$T_{Bp}^{SSM/I} = e_{sp}T_s e^{-\tau_a} + (1-e^{-\tau_a})(1+r_{sp}e^{-\tau_a})T_a$$

where the first term $e_{sp}T_s$ on RHS is obtained from two coupled VRT solution of the multi-layer model (f,1,2) at the SSM/I observation angle. Here $e_{sp}, p = v, h$ is the p-polarized emissivity of underlying media (f,1,2) and r_{sp} is the surface reflectivity as $r_{sp} = 1 - e_{sp}$, T_s, T_a, τ_a are the surface physical temperature, atmospheric effective temperature, and atmospheric opacity, respectively.

NUMERICAL RESULTS AND DISCUSSIONS

Fig.1 gives the temporal variation of vertically polarized brightness tempe-rature in China northeast forest during the year 1995 observed by SSM/I DS-F10 (descending flight F10, LST 10am at 50.83°N, 123.17°E°).

We simulate the emission of snow/forest and compare with the SSM/I data of Fig.1 during the days of February (snow/forest) and July (forest only). Numerical results of brightness tempe-rature vs frequency are given by the solid lines in Fig.2. It can be seen that snowpack signature can pass through the forest canopy.

Fig.3 gives temporal variation of vertically polarized brightness tempe-rature in Tibet Naqu pasture during the year 1995 by SSM/I AS-F13 (ascending flight F13, LST 6pm at 31.5°N, 92.7°E).

After snowfall, the grass field was covered by a snow layer. It significantly cools the brightness temperature due to scattering by ice particles. During summer time, the

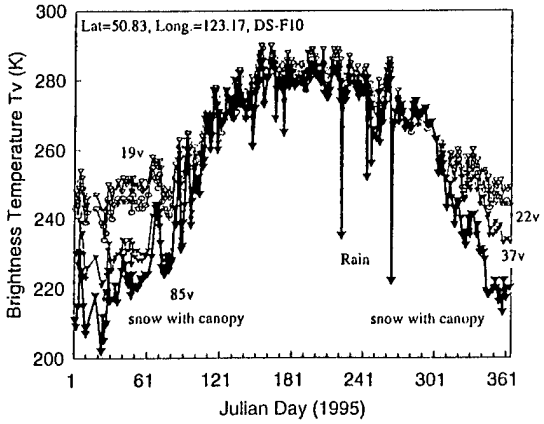

Fig.1 SSM/I data of China northeast forest in 1995.

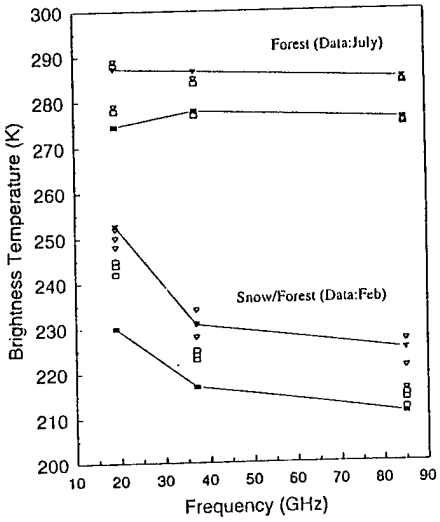

Fig.2 VRT simulation and comparison with data.

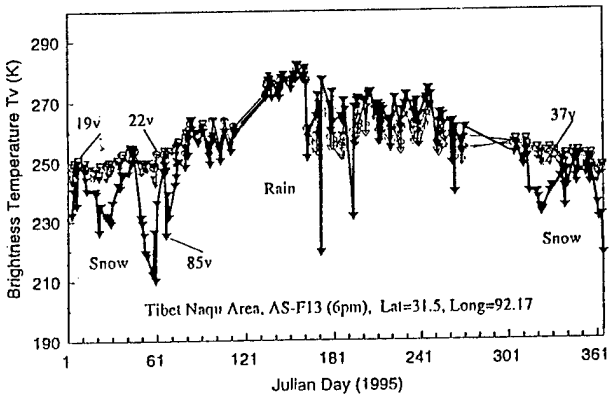

Fig.3 SSM/I data of China Tibet Naqu in 1995.

diurnal difference of physical temperature in Tibet area is usually very large due to high elevation of Tibet Plateau. There was precipitation happened in Day 172 (June 21) detected by SSM/I AS-F13. It is a single event and was not detected by other SSM/I flights DS-F10, F13 or AS-F10. That is why there is large polarization difference during June-July, since several precipi- tation in that period caused surface much wetter and enhanced polarization diffe-rence, especially at low frequency e.g., 19 GHz.

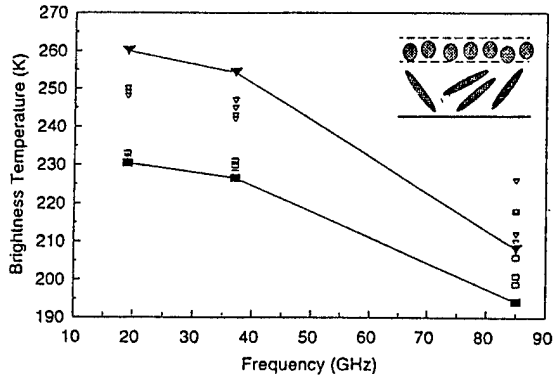

Fig.4 VRT simulation for snow/pasture.

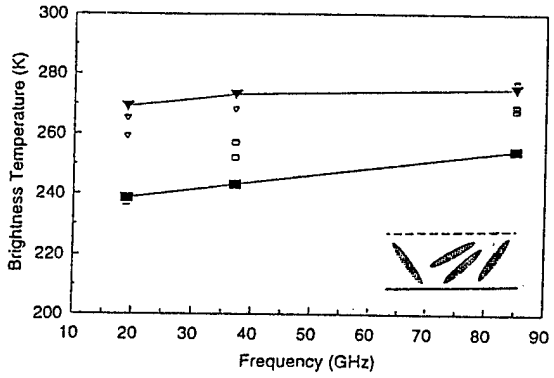

Fig.5 VRT simulation for pasture.

In the case of pasture covered by snow, we alternatively model the snow cover as the layer-f and grass medium as the layer-1.. Numerical simulations for the pasture/snow and pasture only are shown in Figs. 4,5. Validation with ground-based measurements will be our next program.

CONCLUSIONS

We developed a multi-layer model of the vector radiative transfer for snowpack/vegetation canopy at SSM/I channels. By using the physical optics approximation, the scattering, extinction coefficients and phase function of VRT equation for the layer of non-spherical particles as forest canopy are derived. The dense medium

VRT is applied to the snow-layer. Scattering coherence of dense scatterers is taken into account. By using discrete ordinate and eigenanalysis method to solve these two-coupled VRT equation with multiple scattering, numerical results are obtained. It illustrates the scattering and emission signatures from snowpack and vegetation canopy in space-born SSM/I remote sensing. Numerical results are applied to simulation and analysis of the observations by the SSM/I over China's northeast forest and Tibet Naqu pasture areas.

ACKNOWLEDGMENTS

This work was supported by the CNSF (China National Science Foundation), the Shanghai Research Center for Applied Physics. The SSM/I data analysis was performed while the author held the USA National Research Council Senior Research Associateship at NOAA/NESDIS.

REFERENCES

1. LeVine D.M., R. Meneghini, R.H. Lang, and S.S. Seker, "Scattering from arbitrarily oriented dielectric disks in the physical optics regime" , J. Opt. Soc. Am., Vol.73, No.10, pp 1255-1262,1983.

2. Tsang L., J.A. Kong and R. Shin, "*Microwave Remote Sensing Theory*", Wiley Inter., New York, 1985.

3. Jin Y.Q., "*Electromagnetic Scattering Modelling for Quantitative Remote Sensing*", World Scientific, Singapore, 1994.

4. Jin Y.Q., "Size of snow grains in scattering and emission models", in "*Passive Microwave Remote Sensing of Land-Atmosphere Intera-ctions*" ed. by B.J. Choudhury et al., VST, Netherlands, pp 273-283,1995.

5. Jin Y.Q, "Radiative transfer for snowpack -vegetation canopy at SSM/I channels and satellite data analysis", Rem. Sens. Environ., 1997 in press.

Deriving Glaciers Variation Integrated Remote Sensing and GIS in the Tibetan Plateau

Zhen Li and Qunzhu Zeng
Lanzhou Institute of Glaciology and Geocryology
Academia Sinica, Lanzhou, 730000, China
Tel (86/931) 8847953, Fax (86/931) 8885241 zengqz@ns.lzb.ac.cn

Abstract -- Glaciers on the Tibetan plateau play an important role in the Earth's climate system. Because of high altitude and difficulties in access, regular, systematic surveys of glacier variation are almost impossible in some regions of the Tibetan plateau. As a result, remote sensing techniques are at present the primary, in many cases the only way to measure the state of glaciers. In combination with GIS, it provides an efficient tool to analyze the current state and changes in glaciers. We used a technique of integrated remote sensing and GIS to map and measure on the changes in glaciers using a 21-year series of Landsat images (from 1973 to 1994) and topographic maps on a study site on the Tibetan plateau. The details of glacier fluctuation, such as area of glaciers and the changes in the magnitude of recession or advance of a glacier terminus on different dates, are described based on the results of image analysis, including coregistration, classification, vector analysis, and area calculation. Within the study area, during the 21 years, it was determined that the northern glaciers advanced and the southern glaciers retreated, the average rate of change was 50 to 105 m a^{-1}. The results show that Landsat data provide an important source of information for studies of glacier variation.

INTRODUCTION

Glaciers are sensitive indicators of climate change and play important interactive roles in regional climates through the effect of changes in surface albedo. Understanding details of glacier change, such as glacier velocity, fluctuation of glacier termini and calving fluxes, would greatly enhance efforts to model accurately the response of glaciers to climatic change. Regular measurements glacier variation are carried out by ground surveys or aerial photographic surveys, but ground surveys are nearly impossible to carry out in some areas of the Tibetan plateau, and aerial photographic surveys are irregular. Satellite imagery has provided an invaluable source of data for mapping and glaciological interpretation. Landsat data has been used to study glaciers by Williams and others [1][2], Hall and others [3], and Dwyer [4].The use of remote sensing to monitor glacier area to measure changes in area or position of a terminus or glacier margin (e.g. ice cap) can be an index in the prediction of local or regional climatic change, especially in areas where regular measurement can not be carried out. Landsat imagery provides a means for monitoring glacier variation during the past two decades.

Glaciers on the Tibetan plateau were of considerable to many scientists, because it is considered to be a specially sensitive area to measure global climatic change [5]. Therefore, it is very important to measure accurately glacier area and glacier fluctuations, but regular surveys are very difficult to accomplish, because of high attitude, difficult to access because of lack of ground-transportation network, climatic conditions, and other logistical impediments. In this paper, we selected the Moromaha ice field ($36^0$03'N, $91^0$00'E), located in the middle part of the Kunlun Shan in the Tibetan plateau, as the primary study area. Elevations in the study area range from 3300 to 5445 m, and the upper part of Moromaha is covered by ice field and associated outlet glaciers and cirque/valley glaciers. There are 46 glaciers in the study area; the glacier area is 419.91 km^2. Remotely-sensed data used included Landsat RBV camera images , Landsat MSS images, and Landsat TM images during the period from July 1973 to December 1994. The size of the study area is 36 km long by 26 km wide. This study is based on a time sequence at visible and near-infrared Landsat imagery that demonstrates the usefulness of the integrated remote sensing and GIS technique for glacier studies and for analysis of analyze the movement of glaciers in the study area.

DATA SOURCES AND IMAGE REGISTRATION

The Landsat image data sets used include the following, Landsat RBV images acquired on 16 July 1973; Landsat MSS images acquired on 30 November 1976 and on 8 August 1979, and Landsat TM images acquired on 29 November 1987 (fig. 1) and on 18 December 1994. The digital elevation model (DEM) was digitized from a 1:50,000 scale topographic map that had been compiled in 1976 from 1971 aerial photographs using stereophotogrammetric methods. The primary analysis was based on 1976, 1987, and 1994 images, because a three-band false-color composite Landsat MSS image (30 November 1976) and digitally enhanced 1987 and 1994 Landsat TM images in various multiband combinations were available. There are only single-band images in other years. All images were digitized to permit analysis with other digital images. Digitization was carried out with over-sampling to avoid loss of spatial resolution.

To establish coregistration of all images, control points

0-7803-3836-7/97/$10.00 © 1997 IEEE

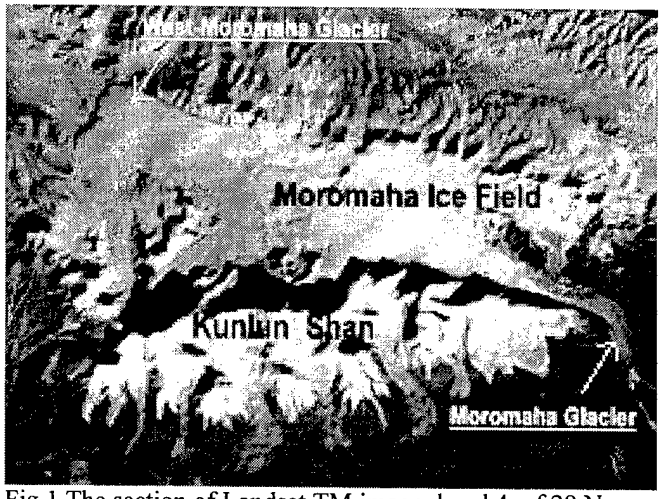

Fig.1 The section of Landsat TM image, band 4, of 29 Nov. 1987, showing study area for glaciers in the Kunlun Shan, Tibetan plateau, China.

from the topographic map were used as a reference for the images from different years that could be identified on each image. Approximately 15 to 20 ground-control points were selected from topographic map. An independent set of points was selected and used to assess the accuracy of the coregistration. The root-mean-square error (rms) of verification points is a better estimator of registration accuracy than the rms of the control points used for developing the rectification model [4]. The maximum verification error from coregistration of all images was 53m in the X and 67m in the Y direction. The total residual rms of verification points in each coregistration image compared with the 1994 TM image is shown in table 1. The coregistration accuracy compared with 1994 image is better in the 1976 and 1987 images, compared with other images, because of high quality of these images. Therefore all coregistered images are in the same coordinate system; this makes it easy to compare each image with other images to transform the image annotations into a geographic information system (GIS).

TOPOGRAPHIC CORRECTION AND CLASSIFICATION

The Moromaha ice field is located in an alpine region; the Landsat images acquired on different dates will be influenced by mountainous terrain because of different local solar azimuth and elevation. Changes in reflectivity and shadows cast by the terrain will reduce the accuracy of the classification. Therefore it is necessary to correct the effect of terrain. Digital elevation models (DEM) were widely used for geoscience analyses [6]. Using a DEM of the study area, we normalized the images to accurately discriminate the area covered by glaciers and analyze glacier fluctuation. A equations was employed to normalize the images:

$$E = E_s / (\cos\theta_i) \quad (1)$$

Table 1 The residual root-mean-square error (rms) of verification points in each coregistered image compared with the 1994 TM image.

Time	1973			1976			1979			1987		
Direction	X	Y	Total	X	Y	Total	X	Y	Total	X	Y	Total
rms (m)	53	46	70	40	32	51	47	67	82	17	23	29

Where, E_s is the original image grid; E is the normalized image grid; θ_i is the local solar illumination angle that can be computed from the DEM, the azimuth of solar illumination, and solar illumination angle on a horizontal surface. Spectral discrimination of features can be significantly improved by using topographic normalization. The digital enhancement of the images also helped to better define the boundary between the glacier and surrounding terrain.

Two basic surface types were classified on all Landsat images: glacier ice, and all other land cover (mainly rock and some vegetation). Multiband Landsat images were classified using a supervised-classification method, and images with a single-spectral band were classified with the unsupervised-classification method. The results showed that the supervised-classification method with multiband images is significantly better than the unsupervised-classification method. A factor that contributes to the difficulty in delineating the precise boundary of a glacier terminus or margin on Landsat images during certain times includes the terrain being covered by snow. Though the margin may be delineated because of morphologic differences, discrimination of glacier, snow, and rock on images cannot be done spectrally because of similarity in the radiative characteristics. Under such circumstances, in order to improve the classification accuracy, we interacted with the computer monitor to digitize the glacier margin in areas of the satellite image that were obviously incorrectly classified. By overriding the supervised-classification method, we were able to delineate the glacier terminus, based on the different texture and other features. Therefore, glacier margin digitized by interaction was used to correct errors in the map produced by the supervised-classification method.

VARIATION ANALYSIS OF GLACIERS

Geographic information system (GIS), a strong geoscience tool, can be used to analyze various geographic phenomena. All image annotations were transformed to the topographic map coordinate system; an additional transformation converted the data from grid to vector. The data was transferred to a GIS to construct polygons for calculation of glacier and analysis of changes in area, position of glacier margins/termini, and average glacier velocities.

The change in glacier margins can be obviously seen in the overlay map using the different time polygons. The map demonstrates that the northern part of the glacier (Moromaha ice field) was slightly advancing, especially the West-

Table 2. Changes in the area extent of all glaciers in the Kunlun Shan.

	1973	1976	1979	1987	1994
Area(km^2)	417.57	429.51	453.19	423.26	424.36
Area Change		+11.94	+23.68	-29.93	+1.10
Change(1976-87, 1987-94)			-5.69		+1.10

Moromaha Glacier (outlet glacier), while the southern part of the glacier was retreating, especially the Moromaha Glacier (outlet glacier) during the period 1976 to 1994. The area extent and variations in different years for all the outlet glaciers and cirque/valley glaciers during the period 1973-76; 1976-79; 1979-87 and 1987-94, based on analysis of the polygons from analyzed images, are summarized in table 2.

Two different general trends are revealed from analysis of the Moromaha ice field and cirque/valley glaciers in the Kunlun Shan. Glaciers on the northern margin of the Moromaha ice field on the northern side of Kunlun Shan, have been advancing from 1973 to 1994; cirque/valley glaciers on the southern part of Kunlun Shan have been retreating during the same period. However the change in total area is relatively small. The area calculation on the 1979 Landsat MSS image (8 August 1979) was higher than others. On several images, including the 1979 one, both glacier and snow were classified the same. Therefore the 1976, 1987, and 1994 images were mainly used in this study; the 1973 and 1979 images just were used only as a reference because of too much snow cover on the images.

The distance change in terminus positions greatly exceeded the coregistration-verification errors, so the data can be used to analyze glacier movement. Two outlet glaciers, Moromaha Glacier and West-Moromaha Glacier, were selected for glacier advance (or retreat) velocity analysis. To compare the area or terminus change and to calculate the average velocity of glacier advance (or retreat), the method drawing profile line in different main direction on the glacial tongue and averaging these values was employed. The results showed in table 3.

CONCLUSIONS

This paper reports on the results of determining fluctuations in glaciers in a study area in Kunlun Shan, Tibetan plateau, with a time series of Landsat images from 1973 to 1994. It also shows the capability of studying glaciers through an integration of remotely sensed data with a geographic information system. The total area of change in glaciers in the study area was quite small during the two decades. The two northern outlet glaciers on the northern side of Kunlun Shan advanced with an average velocity of 58 m a^{-1} during the period 1976 to 1987;105 m a^{-1} during the period 1987 to 1994. The southern cirque/valley glaciers on the southern side of Kunlun Shan retreated with an average velocity 83 m a^{-1} during the period 1976 to 1987;

Table 3. The cumulative fluctuation and average velocity of the two main outlet glacier terminus positions (unit: m)

	Moromaha Glacier				West-Moromaha Glacier			
Change	Line1	Line2	Line3	V(ma^{-1})	Line4	Line5	Line6	V
1976-87	-1371*	-984	-398	-83	+754*	+568	+580	+58
1987-94	-191	-538	-313	-50	+670	+686	+844	+105

*Negative number means retreat; positive number means advance

and 50 m a^{-1} during the period 1987 to 1994. These results showed that sequential Landsat images can be used to map glacier-covered areas and to monitor fluctuations of glaciers.

The use of Landsat data provides information about glaciological features; this is specially evident when a time series of images is available for analysis. The accuracy of classification of glacier area is improved when the scientist overrides the supervised classification method under some circumstances (e.g. considerable snow cover). Other problems included the lack of field observations to verify the results, the use of a DEM to correct for different solar elevation angle and azimuth, and difficulty in acquiring cloud free Landsat images. The increasing availability of remotely-sensed from Earth-orbiting satellite data, especially synthetic aperture radar (SAR) data will provide some advantages over Landsat images, in that image acquisitions is not constrained by cloud cover or solar-illumination conditions. Satellite SAR will provide opportunities for monitoring glacier fluctuations on a systematic, repetitive basis, and SAR interferometry will be used in future studies for obtaining accurate information on glacier velocity.

REFERENCES

[1] Williams, R. S., and Jr., "Satellite remote sensing of Vatnajökull, Iceland," Ann. Glaciol., vol.9, p.127-135,1987.

[2] Williams, R. S., Jr., Hall, D. K., and Benson, C. S., "Analysis of glacier facies using satellite techniques,"J. Glaciol., vol.125, p.120-128, 1991.

[3] Hall, D. K., Chang, A. T. C., Foster, J. L., Benson, C. S., and Kovalick, W. M., "Comparison of in situ and Landsat derived reflectance of Alaskan glaciers,"Remote Sens. Environ., vol.28, p.23-31, 1989.

[4] Dwyer, J. L., "Mapping tide-water glacier dynamics in East Greenland using Landsat data,"J. Glaciol., vol. 139, p.584-595, 1995.

[5] Thompson, L. G., Mosley-Thompson, E., Bolzan, J. F., "Holocene-late Pleistocene climatic ice core records from Qinghai-Tibetan plateau,"Science, vol. 246, p.474-477,1989.

[6] Rentsch, H., Welsch, W., Heipke, C., and Miller, M. M., "Digital terrain models as a tool for glacier studies,"J. Glaciol., vol.124, p.273-278, 1990.

On the accuracy of snow cover segmentation in optical sattelite images

D. Luca[1], K Seidel[1], M. Datcu[2]

[1] Swiss Federal Institute of Technology ETH Zurich, Institute for Communication Technology, Gloriastr. 35 CH-8092 Zurich
Tel. + 41 1 632 5284, Fax. + 41 1 632 1251 {dluca, seidel}@vision.ee.ethz.ch

[2] German Aerospace Research Establishment DLR, German Remote Sensing Data Center DFD, Oberpfaffenhofen, D-82234 Weßling
Phone + 49 8153 28 1388, Fax + 49 8153 28 1448, Emai: Mihai.Datcu@dlr.de

Abstract: In our paper we make a comparison of the state of the art algorithms for snow areas segmentation in optical satellite images. The comparison address the accuracy of the "forward model" used and the informational theoretical aspects characterising the detection/segmentation algorithms. We also, comparatively, introduce and a new approach: the segmentation of the snow cover as ill-posed inverse problem and its solution in the frame of the Bayesian inference.

INTRODUCTION

The radiometry of remote sensing images in rough mountainous areas is severly affected by topographic artifacts. Shadow areas, diffuse and indirect secondary lighting due to slopes covered by highly reflective snow as well as perturbant atmospheric effects cause ambiguities that appear in the interpretation of these images. Three approaches have mainly been used for the topographic correction of images in rough terrain areas.

The first one uses multispectral image analysis based on the observation that in several infrared bands the images have weak dependency on the land cover and strong dependency on the topography. Image correction is then performed using band ratios or some statistical transformations based mainly on regression techniques [2, 7]. This method is rather simple to implement but it contains some heuristic assumptions and has often a poor numeric performance.

The second approach uses a radiative transfer code to obtain a deterministic description of the correction of topographic effects [3, 8, 9, 12, 13]. While this approach avoids empirical techniques, it is more difficult to implement and encounters problems in the correct description of radiances and other lighting parameters of the scene.

The approach we suggest is the third one and represents a model based Bayesian solution [5, 6]. Our algorithm uses computer graphics techniques (ray-tracing and radiosity) to synthesize an image of the observed scene starting from the Digital Elevation Model (DEM), the position of the sun and the characteristics of the imaging sensor. But unlike other approaches, critical parameters related to the description of scene radiances are not postulated or deduced in advance but estimated on-line in an optimization loop. This loop performs a search in the parameter space to find the set of parameters that minimizes the error between the synthesized and the observed remote sensing image. In this way we avoid problems related to the off-line estimation of radiance values; we make only basic assumptions on reflectances and lighting and let the algorithm extract from the measured data the appropriate values.

THE PROPOSED METHOD: A BAYESIAN APPROACH

The method of *Bayesian inference* consists in interpreting probabilities as incomplete information rather than randomness and gives an alternative understanding of the information hidden in the measured data [11]. If we denote θ the set of parameters describing a scene then the a priori information available on θ will be $p(\theta)$. The image formation process represents the generation of the observed data D conditioned by the set of parameters θ. The information available on the image formation process can thus be written as $p(D|\theta)$. The goal is the inversion of $p(D|\theta)$ in $p(\theta|D)$ to extract a guess of the parameters θ which describ the scene.

$$p(\theta|D) = \frac{p(D|\theta)p(\theta)}{p(D)}$$

In our case, D represents the observed data and $p(D)$ is the sensitivity of our observations to the geometric structure of the scene, i.e. to the DEM. $p(D)$ is called *the evidence*. θ represents the set of parameters that describes the reflectance function of snow and $p(\theta)$ is called *the prior*. The term, $p(\theta|D)$, represents our incertitude on the image formation process and is called *the likelihood*. The optimal reflectance parameters are selected by maximising $p(\theta|D)$ (*the posterior*). This reformulates the topographic correction problem in the general frame of ill-posed inverse problems.

For high complexity scenes or for scenes in mountainous areas the application of classical image analysis methods is a weak approach. Significant radiometric uncertainties remain unsolved and as a consequence the signature analysis, structural

0-7803-3836-7/97/$10.00 © 1997 IEEE

interpretation and classification are affected by errors. Alternatively, in this paper the scene understanding approach is proposed. Scene understanding is the attempt to extract knowledge about the physical characterization, the structure and geometry of the three-dimensional scene from the two-dimensional image. The major task of the scene understanding process is thus to find the scene which best explains the observed data [4]. The solutions to this challenge are usually model based in the general frame of the Bayesian inference.

DESCRIPTION OF THE PROPOSED MODEL

The image synthesis is based on the knowledge of the DEM, on the position and physical properties of the light source and on the scattering process for different cover types. To derive an accurate model a multiresolution approach is used that includes three scales [5]:

- •At macro-scale the scene is described by the DEM and the position of the light source. These parameters are input to a computer graphics program that combines ray-tracing and radiosity techniques [1] and can render with accuracy both specular and diffuse reflections. The simulation is performed at a resolution higher than the sensor's spatial resolution.
- •At meso-scale a spatial integration is performed that models the image formation process of the sensor. The resolution of the simulated image is reduced to match the observed data. Due to the nonlinear description of the light scattering process, the result of the operation does not equal the reflection value obtained without integration.
- •At micro-scale the facets of the DEM surface are characterized by reflectance functions. We model the reflectance function as a superposition of Lambertian and specular behaviour. In order to catch the interreflections between slopes we suppose that each facette may be illuminated by several light sources.

SCENE PARAMETER ESTIMATION

As described before the model contains some parameters that have to be set like e.g. the percentage of specular reflection and of Lambertian reflection, the level of the ambient light, etc. In our approach, these parameters are not preset, but are determined on-line in an optimization loop with the gradient method. The mean square error between the synthetic and the observed image is used as an objective function of the minimization. In this way we avoid the common difficulties that appear in estimating the radiances for each image pixel and let the algorithm adapt the parameters to the available measurements. The block diagram of the model is shown in Fig. 1. We have been testing our method on a Landsat-5 TM image from April 26th 1992 of the Davos region in Switzerland. The data is an Earthnet standard product, i.e. system corrected for both radiometry and geometry. It was resampled to both 25 meters and 10 meters using nearest neighbour interpolation to fit the available DEMs.

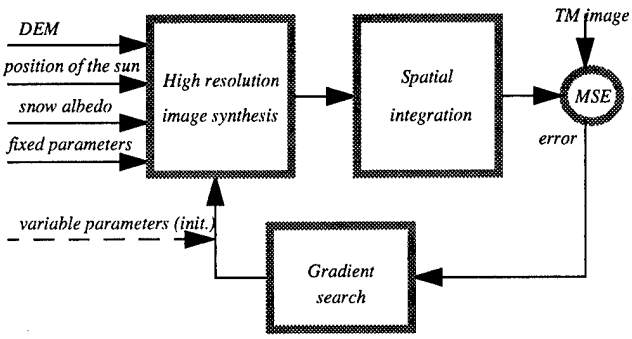

Fig. 1: The block diagram of the parameter estimation

The 10 meter data is used for the high resolution image synthesis, the 25 meter data for the computation of the error.Fig. 2a shows the geocorrected image, from which a small rectangular area which contains several shadows and interreflections was selected as test data (Fig.2b). For the computer graphics simulation we used the RADIANCE 2.5 public domain software from the Lawrence Berkeley Laboratory, Berkeley, California. This software combines ray-tracing and radiosity techniques.

For comparison we performed simulations of the same area with the model we proposed, the "cosine of incidence" model and the Minnaert model [10] and compared the results. The mean square error of the "cosine of incidence" model is 1569, the Minnaert model achieves lower errors in the range 650-1500 depending on the value of the Minnaert constant. Both these mean square errors are substantially higher than that of 233 achieved with our algorithm. Especially shadow areas show a high level of error, the models do not manage to render accurately the pixel intensity in these zones. The results are summarised in figures 3-5 and Table I.

CONCLUSIONS

This paper describes a new model for the correction of topographic effects in satellite images of snow covered rough terrain. The topography influence alleviation is obtained as a parameter estimation process and can be interpreted in the frame of Bayesian inference. The model simulates a syntethic image using computer graphic techniques that rely on a multiresolution approach. Its parameters are estimated in an optimization loop which minimizes the mean square error between the synthetic and the real image.

REFERENCES

[1] Ashdown, I. (1994). *Radiosity – A Programmer's Perspective*. John Wiley & Sons, Inc.

[2] Colby, J. D. (1991). Topographic normalization in rugged

terrain. *Photogrametric Engineering & Remote Sensing*, 57(5):531–537.

[3] Conese, C., Gilabert, M. A., Maselli, F., and Bottai, L. (1993). Topographic normalization of TM scenes through the use of an atmospheric correction method and digital terrain models. *Photogrammetric Engineering and Remote Sensing*, 59:1745–1753.

[4] Datcu, M. (1996). Scene understanding from SAR images. In Stein, T. I., editor, *Remote Sensing for a Sustainable Future, IGARSS'96*, volume 1, pages 310–314.

[5] Datcu, M. and Holecz, F. (1993). Generation of synthetic images for radiometric topographic correction of optical imagery. Proc. SPIE Vol. 1938, pages 260–271.

[6] Datcu, M., Luca, D. Seidel, K. (1997), A New Image Formation Model for the Segmentation of the Snow Cover in Mountainous Areas. *In: EARSeL Workshop on Remote Sensing of Land Ice and Snow.* Freiburg, Germany, April 1997.

[7] Dozier, J. (1989). Spectral signature of alpine snow cover from the Landsat Thematic Mapper. *Remote Sensing Environment*, 28:9–22.

[8] Goel, N. S., Rozehnal, I., and Thompson, R. L. (1991). A computer graphics based model for scattering from objects of arbitrary shapes in the optical region. *Remote Sensing Environment*, 36:73–104.

[9] Hill, J., Mehl, W., and Radeloff, V. (1995). Improved forrest mapping by combining corrections of atmospheric and topographic effects in Landsat TM imagery. In Askne, J., editor, *Sensors and Environmental Applications of Remote Sensing, 14th EARSeL Symposium 1994 in Göteborg, Sweden*, pages 253–258. A. A. Balkema Rotterdam/Brookfield.

[10] Itten, K. I., Kellenberger, T., Leu, R., Sandmeier, S., Bitter, P., and Seidel, K. (1992). Correction of the impact of topography and atmosphere on Landsat-TM forest mapping of alpine regions. Remote Sensing Series 18, University of Zürich.

[11] MacKay, D. J. C. (1991). Bayesian Interpolation. In Smith, C. R., Erickson, G. J., and Neudorfer, P. O., editors, *Maximum Entropy and Bayesian Methods*, pages 39–66. Kluwer Academic Publishers.

[12] Oren, M. and Nayar, S. K. (1995). Generalization of the lambertian model and implications for machine vision. *International Journal of Computer Vision*, 14:227–251.

[13] Richter, R. (1997). Correction of atmospheric and topographic effects for high spatial resolution satellite imagery. *International Journal of Remote Sensing*, 18(5):1099–1111.

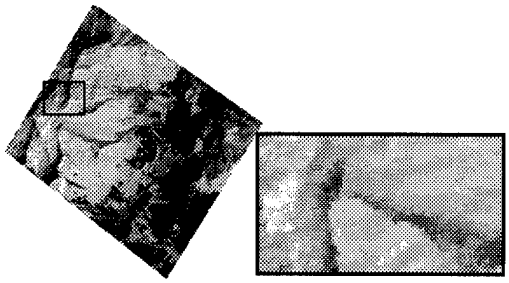

Fig. 2: a) Geocorreced Landsat-TM image from April 26th of the Davos region, Switzerland. b) Test area (zoom of the selected area in a)).

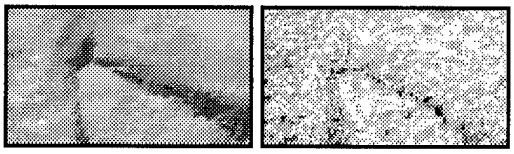

Fig. 3: a) Simulated image performed on a high resolution DEM and the resolution was subsequently reduced to account for the image formation process of the sensor. b) Error image between the simulated and the original TM images. The error image is inverted, white represents zero error.

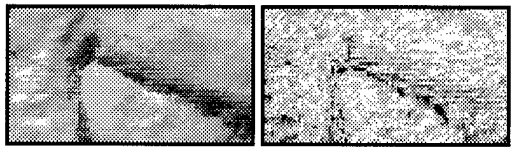

Fig. 4: a) Simulated image after minimization of error. The simulation was performed on a low resolution DEM. b) Error image between the simulated and the original TM images. The error image is inverted, white represents zero error.

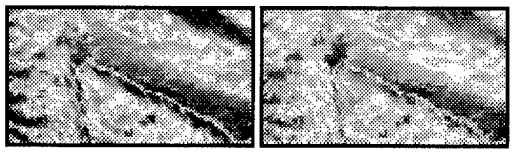

Fig.5: a) Error image between an image simulated with the "cosine of incidence" model and the original TM image. b) Error image between an image simulated with the Minnaert model (k=0.5) and the original TM image. The error images are inverted, white represents zero error.

Table 1: Overview of results

Model:	Bayes High Res.	Bayes Low Res.	Cos of incidence	Minnaert $k = 0.8$	Minnaert $k = 0.5$	Minnaert $k = 0.2$
MSE	233	334	1569	1241	855	655

Sea Ice Concentration and Floe Size Distribution in the Antarctic Using Video Image Processing

Ken-ichiro MURAMOTO[†], Tatsuo ENDOH[‡], Mamoru KUBO[§] and Kohki MATSUURA[†]

[†]Faculty of Engineering, Kanazawa University, 2-40-20, Kodatsuno, Kanazawa 920, Japan
E-mail : muramoto@t.kanazawa-u.ac.jp

[‡]Institute of Low Temperature Science, Hokkaido University, Kita-19, Nishi-8, Kita-ku, Sapporo 060

[§]Toyama National College of Technology, 13, Hongo, Toyama 939, Japan

Abstract – A technique is described for measuring sea ice characteristics over a wide area of ice covered water. The sea ice was photographed by video camera from the ship. Continuous video images are obtained using geometric transformation and template matching. Both size of the ice and concentration along the ship's route can be obtained continuously.

INTRODUCTION

Measurement of the seasonal cycle and interannual variations of Antarctic sea ice is important for investigations of global climate and weather as well as for ship navigation [1]-[3]. While satellite data give a great amount of information about ice conditions [3]-[5], there still remains a need for in situ validations [4],[6]. Resolution of ground truth reference data is much higher than NOAA satellite data. In order to compare the ground truth data with satellite data, analyzing area of ground truth data have to be expanded by patching the ground based data continuously; and both need to be analyzed quantitatively.

In this paper, a technique for measuring sea ice characteristics over a wide area using video images taken from a ship is proposed. Preliminary experiments to test the system have been carried out using video images photographed in ice-covered water in the Southern Ocean.

SYSTEM CONFIGURATION

The sea ice was photographed by a video camera mounted on board the icebreaker SHIRASE. The camera was located at the upper steering house pointing at an angle of 10-degrees downward from the horizon. The image was divided into 256 × 256 pixels using an image digitizer. At each pixel location, the image brightness was quantified into 256 gray levels.

METHOD OF IMAGE ANALYSIS

In order to measure the sea ice characteristics over a wide area using video images, first, geometric transformation is performed to obtain an orthographic projection. Next, these transformed images are combined by template matching. Using these wide field images, sea ice characteristics are analyzed.

Perspective Transformation

Fig.1 shows the spatial relation between the sea surface and perspective projection in the image plane. The xy plane is the camera image coordinate system, and (u,v) is the world coordinate system. Equations of perspective transformation are given by

$$u = (a_1x + a_2y + a_3)/(a_7x + a_8y + 1)$$
$$v = (a_4x + a_5y + a_6)/(a_7x + a_8y + 1)$$

where the coefficients of perspective transformation are determined by known position such as hatch cover points (a-d) and sea surface positions (e-h) calculated from camera height and angle of depres sion of the camera [7]. By this transformation, a

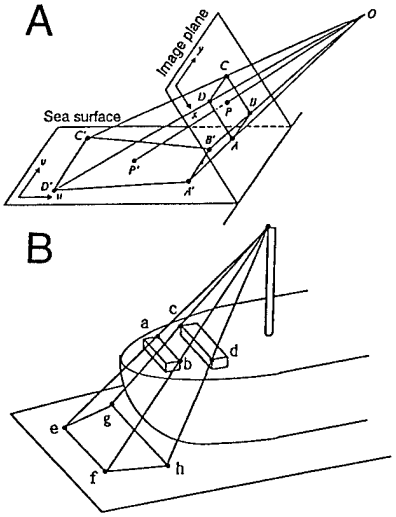

Fig. 1. A: Spatial relation between the sea surface and its perspective projection in the image plane. B: Using known points (a-h), initial coordinates A-D are transformed to A'-D'.

0-7803-3836-7/97/$10.00 © 1997 IEEE

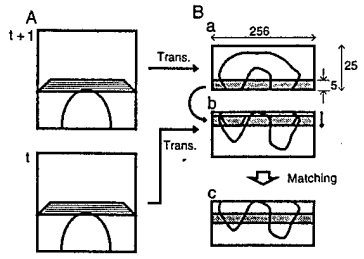

Fig. 2. Schema of template matching. A: Oblique projections at times t and (t+1). B: Orthographic projection transformed from the trapezoidal region shown in A by oblique projection. a: Template pattern. b: Search picture. c: Result of matching at offset location.

square region of sea with a side of 180 m is analyzed, and each sea ice image is transformed to an orthographic projection. In the geometric operation, the output pixels are mapped into the input image to establish their gray levels. If an output pixel falls between four input pixels, interpolation is necessary to determine the gray level of the output pixel. In this process, bilinear interpolation is used [8].

Template Matching

In order to measure the sea ice concentration and shape over a wide area, the orthographic projection images are joined by template matching [9]. A template is chosen from the bottom of the transformed image where the pixel accuracy is highest and used to match a video image at time t with the next scene at time (t+1). This method is illustrated in Fig.2. A subimage of size 5×256 pixels within the orthographic projection image at time t is taken as the template shown in Fig.2Ba. It is desired to determine the vertical location of the template within the image at time (t+1) of size 25×256 pixels shown in Fig.2Bb. In this way, the continuous image shown in Fig.2Bc was obtained.

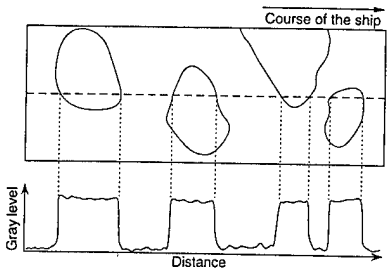

Fig. 3. Method of calculation of floe size distribution.

Characteristics of Sea Ice

Sea ice concentration is calculated from the ratio of ice to water for each row of matched images. Floe size distribution can be calculated along a line, such as the center line of the wide field image shown in Fig.3. Although the floe size obtained by this method is only one-dimensional, it will be enough to compare with satellite data.

RESULTS

The sea ice image from the ship was recorded between Fremantle, Australia and Syowa Station in 1988.

Continuous analysis was performed at predetermined time intervals using images photographed during navigation. Figs.4A and 5A show examples of sea ice images recorded on December 26 and 27, 1988. These areas were transformed continuously by orthographic projection and patched continuously. Figs.4B and 5B show the continuous images. These transformed images are rotated 90° against the photographed image for convenience of display. Marks of a-a', b-b', c-c' and d-d' show the positions on the images correspondingly. Fig.6 shows normalized gray level graph extracted along the center line of images of Figs.4B and 5B. Large gray level is supposed to be ice and small to be sea water. Area of ice and water will be separated by thresholding op-

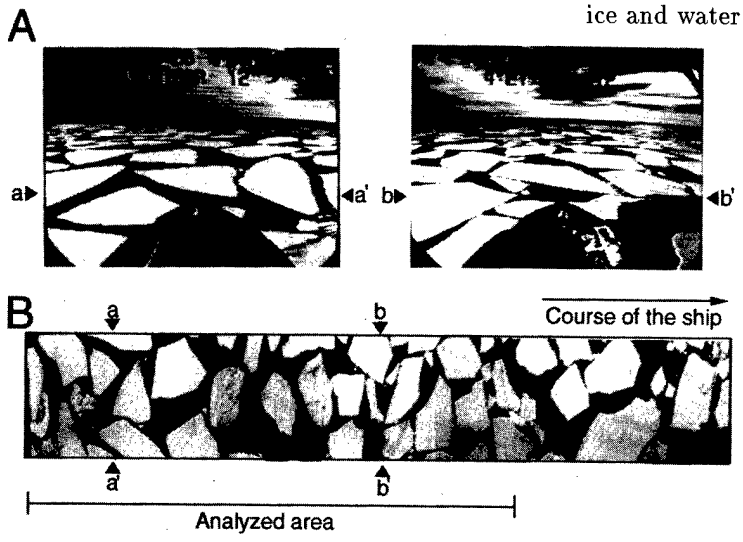

Fig. 4. A : The trapezoid regions on ice-covered water photographed from a ship were transformed continuously by orthographic projection. B : Transformed images are rotated 90° against the photographed image for convenience of display. Marks of a-a' and b-b' show the positions in the images correspondingly.

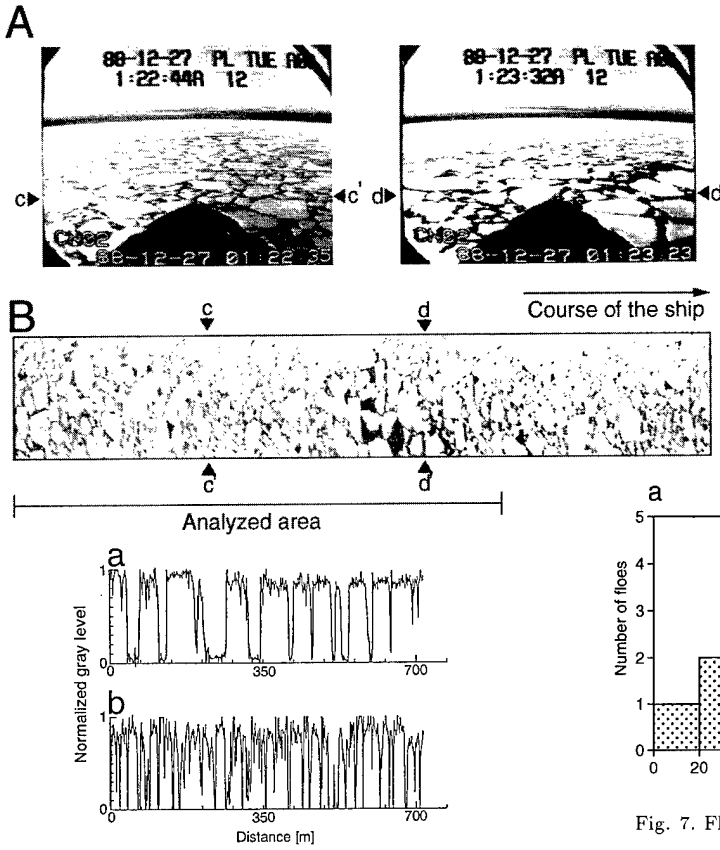

Fig. 6. Normalized gray level graph for analyzed areas of Figs. 4B and 5B. The brightest pixel was set to 1 and darkest pixel was set to 0.

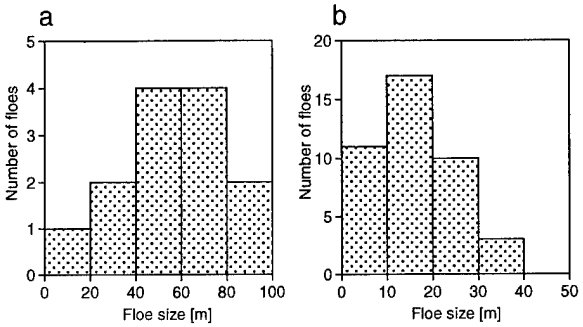

Fig. 7. Floe size distributions calculated from Fig. 6.

Fig. 5. Small floe size area, the others are the same as Fig.4.

eration. Fig.7 shows the floe size distributions calculated for the binary value by thresholding operation to the normalized gray level graphs of Fig.6. We can say that ratio of summation of length of all floes to analyzed area shows the ice concentration. Ice concentration calculated by this approach was 74.6% for Fig.7a and 69.2% for 7b.

CONCLUSION

A system for analyzing wide field image data recorded during ship navigation has been proposed. The difference of the resolution between satellite and surface based data is very large. Therefore, many images recorded from the ground have to be patched together to compare them. Since it is now possible to obtain wide field quantitative data along ship route, we can analyze satellite information in detail.

ACKNOWLEDGMENTS

This work was supported partly by the Japanese Ministry of Education, Science, Sports and Culture Grants- in-Aid for Scientific Research (08650482).

REFERENCES

[1] I. Allison, "The East Antarctic sea ice zone : Ice characteristics and drift," Geo Journal, vol.18, pp.103-115, 1989.

[2] A.L. Gordon and H.W. Taylor, "Seasonal change of Antarctic sea ice cover," Science, vol.187, pp.346-347, 1975.

[3] A.P. Sturman and M.R. Anderson, "A comparison of Antarctic sea ice data sets and inferred trends in ice area," J. Climate and Appl. Meteorol., vol.24, pp.275-280, 1985.

[4] J.C. Comiso and H.J. Zwally, "Antarctic sea-ice concentrations inferred from Nimbus 5 ESMR and Landsat imagery," J. Geophys. Res., vol.87, pp.5836-5844, 1982.

[5] H.J. Zwally, J.C. Comiso, C.L. Parkinson, W.J. Campbell, F.D. Carsey and P. Gloersen, "Antarctic sea-ice, 1973-1976: satellite passive-microwave observations," NASA SP-459, Washington, 1983.

[6] T.H. Jacka, I. Allison, R. Thwaites and J.C. Wilson, "Characteristics of the seasonal sea ice of East Antarctica and comparisons with satellite observations," Ann. Glaciol., vol.9, pp.85-91, 1987.

[7] R.A. Schowengerdt, "Techniques for image processing and classification in remote sensing," Academic Press p.249, 1983.

[8] K. Muramoto, K. Matsuura and T. Endoh, "Measuring of sea ice concentration and floe-size distribution by image processing," Ann. Glaciol., vol.18, pp.33-38, 1993.

[9] E.L. Hall, "Computer image processing and recognition," Academic Press p.584, 1979.

Compatibility of Sea Ice Edges Detected in ERS-SAR Images and SSM/I Data

R. Schmidt, T. Hunewinkel
Institute of Environmental Physics, University of Bremen
P.O. Box 330440, D-28334 Bremen, Germany
phone: +49 421 218 2584, fax: +49 421 218 4555, E-mail: rschmidt@diana.physik.uni-bremen.de

Abstract – The determination of an ice covered ocean surface from ERS-SAR images is not directly possible if the values of the normalized radar cross section are similar for open water and sea ice. SAR imagery of ocean surface waves can be used to detect the ice coverage in such cases. Sea ice changes directly the wave dynamics and has an impact on the nonlinear imaging of ocean waves by SAR. The energy distribution of the SAR image spectrum of a wave system propagating in sea ice deviates characteristicaly from the energy distribution of the same wave system propagating in open water. In this study parameters have been derived from the second moments of SAR image spectra, which are suitable to describe this effect quantitatively. These parameters are used to define an ice edge. Results of this analysis are compared with ice concentration isolines derived from SSM/I data using the NASA Team algorithm, and with a high resolving ice edge detection algorithm based on the 85 GHz channels of the SSM/I. Ice edges detected in ERS-SAR images agree well with the 30% ice concentration isolines of the NASA Team algorithm. The ice edge detection algorithm for the SSM/I data is in good agreement with the SAR ice edge.

INTRODUCTION

Imaging of the marginal ice zone (MIZ) by active space borne microwave sensors like the ERS-SAR (European Remote Sensing satellite-Synthetic Aperture Radar) is an important tool for the remote sensing of the sea ice coverage in the polar oceans. Independent from daylight and weather conditions it allows the study of sea ice and the transition zone between ice covered and open water surface. Several methods for the classification of different ice types in ERS-SAR images have been developed and are well established (e.g.[1]). Giving sufficient results for the discrimination between multiyear and first-year sea ice within a closed ice pack, all methods are affected by the ocurrance of open water which is a severe problem in the MIZ. Ice types are distinguishable in SAR images by their radar backscattering properties described by the normalized radar cross section (NRCS). But the NRCS for sea ice and open water is often similar depending on ice type and wind conditions above the water surface. The discrimination between sea ice and open water which is necessary for the detection of the ice edge becomes difficult. Thus in many ERS-SAR images taken in the MIZ a unique separation of sea ice from open water is not possible. A different approach for the detection of the ice edge in ERS SAR images is the analysis of the imaging of ocean surface waves propagating into the MIZ. For the operational mapping and monitoring the ice coverage passive microwave systems like SSM/I (Special Sensor Microwave /Imager) are commonly used. But ice concentration calculations for the MIZ from passive microwave data exhibits an error up to 20% depending on weather and seasonal conditions and ice type [2]. The analysis of ERS-SAR images allows to improve and validate algorithms developed for the detection of the ice edge and the calculation of ice concentrations from passive microwave data. Information about the MIZ coming from ERS-SAR take the place of in situ measurements which are almost lacking in this regions due to weather and ice conditions, high costs, and restricted potentialities of ship expeditions.

USE OF SAR IMAGE SPECTRA

Sea ice changes directly the dynamics of a wave system, and its imaging by SAR is modified in a characteristic way. These effects are visible in SAR image spectra and have been described by many authors (e.g. [3,4]). In this paper will use the analysis of SAR image spectra for the detection of the ice edge. The impact of sea ice on ocean wave imaging can serve as an unique indicator for the presence of an ice coverage.

Fig. 1 shows an ERS-1 SAR PRI intensity image taken in the Bellingshausen Sea. In the upper left part of the image an area covered by sea ice is visible but even if the transition zone between open water and sea ice can be identified by human eye the automatic detection of the ice edge using the NRCS is

This work was supported by ESA under contract AO2.D146-3 and by the German Bundesministerium für Bildung, Wissenschaft, Forschung und Technologie (BMBF) under contract 03PL018A.

0-7803-3836-7/97/$10.00 © 1997 IEEE

difficult. In this ERS-1 image an unimodal ocean surface wave field propagating into the ice covered region is imaged but not visible in this reproduction.

In our study we calculate SAR image spectra for the ERS-SAR image in Fig. 1 in boxes of 256 x 256 pixels (i.e. 1600 m $\times$ 1600 m) with an overlap of 128 pixels (i.e. 800 m) in both directions. For a SAR image spectrum $F(\vec{k})$, where $\vec{k}$ is the wavenumber vector, the spectral moments

$$M_{mn} = \int d^2\vec{k}\, F(\vec{k})\, k_x^m\, k_y^n \;\; ; \;\; m,n = 0,1,2 \qquad (1)$$

are calculated, where k_x is the wave number component in azimuth direction and k_y the wave number component in range direction. The moment M_{00} represents the total energy of the spectrum. The moments $M_{01} = M_{10}$ vanish due to the point symmetry of the spectrum. The moments M_{20}, M_{11}, and M_{02} describe the deviation of the spectral energy distribution from rotational symmetry to the second order and form a symmetric 2 $\times$ 2 tensor, which can be represented by its eigenvalues M_+ and M_- and its angle of principal axis ϕ_M by applying a principal axis transform. From these variables we derived three spectral parameters:

1. Directionality:

$$D = 1 - \frac{M_-}{M_+} \qquad (2)$$

The directionality describes how strong the spectral energy is concentrated in one spectral maximum.

2. Angle of principal axis:

$$\phi_M \qquad (3)$$

The angle of principal axis describes the orientation of the spectral energy distribution in wave number space.

3.Normalized difference of the spectral energy extension between azimuth and range, short normalized extension difference, **NED**:

$$NED = \frac{M_{20} - M_{02}}{M_{20} + M_{02}} \qquad (4)$$

The NED measures how strong the spectral energy is concentrated in a small band in the range direction in wavenumber space.

USE OF SSM/I DATA

Ice concentration isolines are calculated from SSM/I data using the NASA Team algorithm [5]. The NASA Team algorithm uses the 19 GHz vertical polarized and the 37 GHz vertical and horizontal polarized channels of the SSM/I. Due to the coarse resolution of these SSM/I channels the isolines exhibit the ice concentration with a spatial accuracy in the order of 25 km. Because the ice edge derived from ERS-SAR images by the method described above owns a accuracy in the order of the size of the boxes these ice concentration isolines are of limited use for a comparision. A high resolving ice edge detection (IED) algorithm was developed using the 85 GHz channels of the SSM/I [6] producing ice edges with a spatial accuracy in the order of 5–6 km which becomes comparable to ice edge derived from ERS-SAR images.

RESULTS

The results of the calculation of spectral parameters for the image in Fig. 1 are presented exemplarily for the directionalty in Fig. 2. In Fig. 2 the open water surface is characterized by high values for the directionality from 0.75 to 1.0. This is consistent with the appearance of a single spectral maximum in the SAR image spectrum indicating that a unimodal wave system is imaged. In the upper left part of the image where sea ice is present, an area of high directionality is separated from the area of open water by a band of directionalities lower than 0.75. This can be explained by the diffuse structure of the transition zone between ice and open water. In the adjacent bright area the wavesystem has changed its wavelength and propagation direction and only one spectral maximum appears in the SAR image spectrum. This leads to values for the directionality higher than 0.75. In the upper left corner of the image the wave system disappears due to the dissipation of wave energy by damping. Consistent with this interpretation are the values for the angle of principal axis and the NED which are not presented here. The dark band of in Fig. 2 is in good agreement with the 30% ice concentration isoline presented in Fig. 2 calculated using the NASA Team algorithm but its upper border shows a better agreement with the ice edge derived from from SSM/I data using the IED which corresponds to the border of the consolidated icepack. If the outer border of influence of the the sea ice on the imaging of ocean waves by ERS-SAR is considerd as the ice edge it is underestimated by the ice edge calculated by the IED.

CONCLUSIONS

The imaging of ocean surface waves by ERS-SAR allows the detection of the ice edge in the marginal ice zone. The analysis of SAR image spectra reveals the existence of an ice covered water surface. Parameters have been derived describing the essential properties of SAR image spectra. Changes of the wave imaging at the transition from open water to sea ice are clearly detectable by these spectral parameters. The ice edge in ERS-SAR images is defined as an the outer border of influence of sea ice on the imaging of ocean surface waves measurable by the spectral parameters. This ice edge is in good agreement

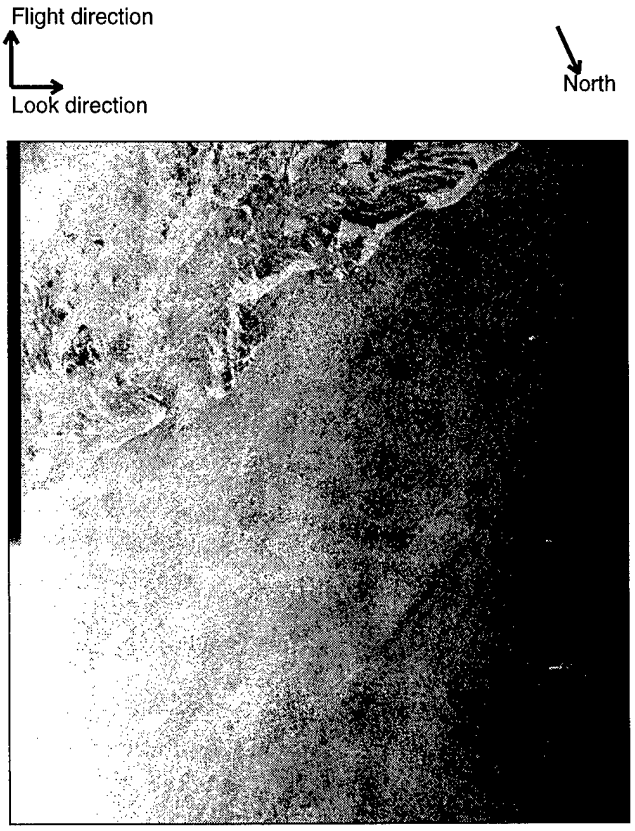

Figure 1: ERS-1 SAR PRI image (orbit 22270, frame 4869) taken at October 18, 1995, 12:59 UTC, center coordinates: 61.49° S, 59.39° W, the flight direction is 205° to N.

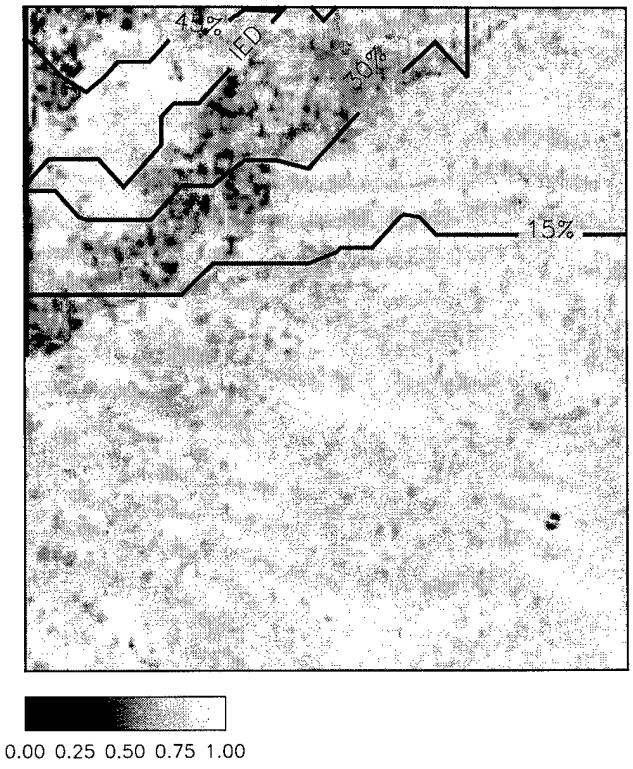

Figure 2: Image presenting the values for the directionality calculated from the image in Figure 1. The ice concentration isoline and the IED ice edge are calculted from SSM/I data taken at October 18, 1995, 2:13 UTC.

with the 30% ice concentration isoline caculated from SSM/I data using the NASA Team algorithm. The ice edge calculated by a high resolving algorithm for SSM/I data underestimates the ice edge derived from ERS-SAR.

REFERENCES

[1] F.M. Fetterer, D. Gineris, and R. Kwok, " Sea ice type maps from Alaska Synthetic Aperture Radar Facility imagery: An assessment", 1994, J. Geophys. Res., 99, pp. 22443-22458

[2] G. Heygster, B. Burns, T. Hunewinkel, K. Künzi, L. Meyer-Lerbs, H. Schottmüller, C. Thomas, P. Lemke, T. Viehoff, J. Turner, S. Harangozo, T. Lachlan-Cope, L. Toudal Pedersen, "PELICON: Project for Estimation of Long-term Variability of Ice Concentration", final report to EC contract E V5C-CT93-0268 (DG 12 DTEE), Bremen, 1996

[3] A.K. Liu, C.Y. Peng, and T.J. Weingartner, "Ocean-ice interaction in the marginal ice zone using synthetic aperture radar imagery", 1994, J. Geophys. Res., 99, pp. 22391-22400

[4] R.A. Shuchman, C.L. Rufenach, and O.M. Johannessen, "Extraction of marginal ice zone thickness using gravity wave imagery", 1994, J. Geophys. Res., 99, pp. 901-918

[5] D.J. Cavaleri, P.J. Gloersen, and W.J. Campbell, "Determination of sea ice parameters with the Nimbus-7 SMMR", 1984, J. Geophys. Res., 89, pp. 5355-5369

[6] T. Hunewinkel, T. Markus, and G. Heygster, "Improved determination of the sea ice edge with SSM/I data for small-scale analyses,1997, submitted to IEEE Trans. Geosci. Remote Sensing

IGARSS'97

1997 International Geoscience and Remote Sensing Symposium

03-08 August 1997

Singapore International Convention & Exhibition Centre

Technical Program

Interactive Area 21: Lidars

Accurate Height Information from Airborne Laser-Altimetry

Mathias J.P.M. Lemmens
Delft University of Technology Faculty of Geodetic Engineering
Thijsseweg 11, 2629 JA Delft, The Netherlands
tel. 031-15-278-1042; fax. 031-15-278-2745; email: m.j.p.m.lemmens@geo.tudelft.nl

Abstract High single point precision and high point density can be obtained by airborne laser-altimetry, using GPS positioning and INS attitude determination. In this paper we analyse the main error sources, including (1) internal laser sensor errors, (2) GPS and INS errors, (3) atmospheric effects, (4) terrain roughness, reflectivity and slope, (5) presence, height and type of vegetation, and (6) integration and synchronization of laser, GPS and INS. Our analysis reveals that when laser-altimeters are well-calibrated accuracies at decimetre level can be achieved. However, the accuracy is very sensitive to terrain type, terrain coverage and used filters to remove from the DEM undesired objects such as buildings and trees. In particular pointing accuracy, which depends on the pointing jitter of the scanning mirror and INS attitude determination, is a main error source, especially over high relief terrain. Another major problem is the automatic removal of undesired objects, such as houses.

Introduction

Airborne laser-altimetry is a new method for capturing the topography of the earth surface in the form of Digital Elevation Models (DEMs). Accurate DEMs are essential for a multitude of remote sensing purposes, such as geometric and radiometric rectification of images, additional information source for multispectral classification, and modelling and simulation in GIS, where several information (remote sensing) layers are combined, e.g. for hydrological modelling. In the Netherlands Laser DEMs are used for a variety of remote sensing applications, including: determination of beach and dune erosion, delineation of ecozones, mapping of flood plains of rivers, mapping of coastal zones, and hydrological modelling.

Airborne laser-altimetry has proven to be superior to other 3D capturing methods, such as photogrammetry, tachymetry and terrestrial GPS, concerning the mixture of criteria: accuracy, point density, time-efficiency and costs. Especially in forest areas and coastal zones it has several benefits compared to conventional methods:

- By recording the last part of the reflected pulse the bare surface of the earth is measured; the first part of the reflected pulse is related to tree-heights.
- Beaches and dunes in coastal zones have often low texture causing problems for photogrammetric DEM generation.

Other beneficial properties are:

- data capture rates of 100 km^2/h are possible;
- high automatization degree of the entire process;
- since it is an active system no shadows are generated;
- costs per point are low.

The quality of a DEM depends on:

- amount of outliers and undesired terrain objects;
- accuracy of the individual points;
- interpolation method to compute heights at wanted locations from the measured heights;
- point density (the sampling distance should sufficiently well correspond to the terrain relief fluctuations).

This paper aims at analyzing the error-sources that affect the precision of the individual points. The removal of outliers and undesired objects are briefly discussed as well. The paper is organized as follows. First a description of the laser system is given. Then the error budget is analyzed. Next methods for accuracy improvement are considered. Then an extensive discussion on several unsolved problems is presented. The paper finishes with concluding remarks.

System Description

Airborne laser-altimeters are multisensor systems consisting of a reflectorless laser range system and a positioning system.

Laser Range System

The task of the laser range system is to measure the distance from the aircraft to the earth surface. The two main parts are a sensor and a rotating or nutating mirror (Figure 1).

A laserdiode in the *sensor* generates pulses with frequencies varying from 100 to 7000 Hz and a length of 1 to 10 Ns (30 - 300 cm). Owing to the high intensity and the small beam divergence, laser pulses (1) can bridge long distances, (2) enable reflectorless measuring, and (3) have a small footprint (radius typically 10 to 50 cm). Usually the wavelength lies in the near infrared, typically values are 1.047 μm, 1.064 μm and 1.54 μm. These wavelengths do not penetrate material. In forest areas the laser pulse reflects on leaves. Depending on the density of the vegetation cover and the size of the footprint a part of the pulse will not meet any foliage and will reach the ground. By recording the last part of the reflected pulse the distance to the ground is obtained. In summertime penetration rates of about 25 % to 30 % for both foliage and pine forest are reported [2]. In wintertime these figures are higher for foliage forest.

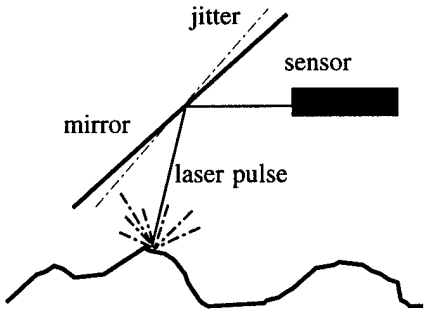

Figure 1: *Principal parts of a laser system. Instability of the mirror introduces pointing jitter. Terrain properties determine the amount of signal returning to the sensor.*

The ranging accuracy depends among others on the signal-to-noise ratio (SNR) of the laser sensor. SNR depends on: (1) pulse intensity, (2) atmospheric transmittance (largely determined by

0-7803-3836-7/97/$10.00 © 1997 IEEE

moisture), (3) size of the footprint, (4) reflection characteristics of the terrain, (5) size of the detector aperture, and (6) sensitivity of the detector.

The scanning mirror enables recording of the terrain perpendicular to the flying direction. The swath width may reach values up to the flying height, which usually varies between 300 and 1000 meter. There is a trade-off between swath width and point density; the broader the strip the coarser the point density.

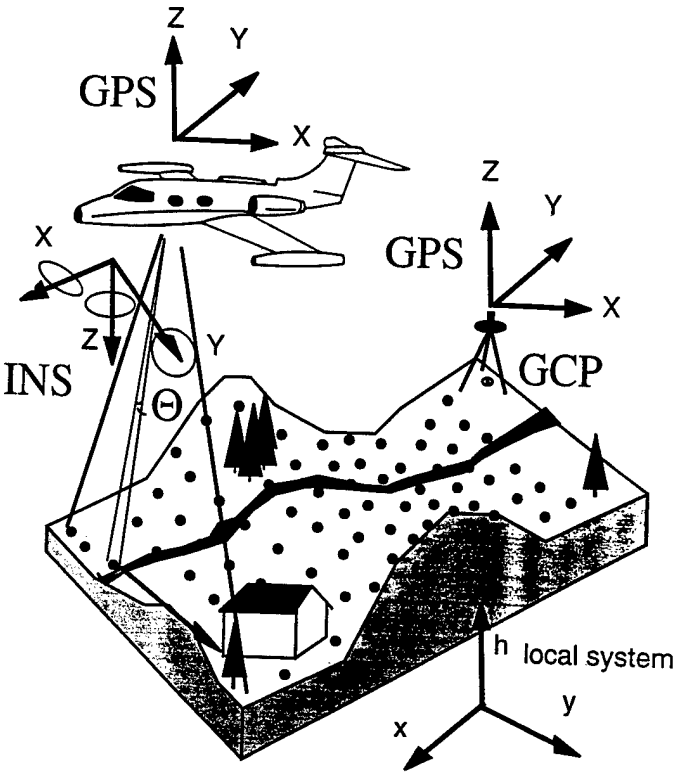

Figure 2: *Sketch of an airborne laser survey. GCP: ground control point. Θ: laser beam divergence, which defines the footprint size. GPS coordinates are in the WGS84 system.*

Positioning System

The task of the positioning system is to determine position and attitude of the laser sensor during measurement. This is necessary for geo-referencing purposes, i.e. to determine the coordinates of the measured points in a local or national system. Operational systems use Differential GPS (DGPS) for position determination and inertial navigation systems (INS) for determination of the roll, pitch and yaw. GPS provides WGS84 coordinates. One GPS receiver is installed in the aircraft. One or more GPS receivers are located at known ground positions (GCP).

Integration and Synchronization

To assign to each single laser distance position and attitude the position and attitude of the sensors in the aircraft have to be measured (Figure 2). Furthermore, the sensors have to be synchronized. The sampling rate of GPS is low (1 - 10 Hz) compared to that of the laser sensor and the INS system. For interpolation purposes a model of the flight path is necessary. Transformation from the WGS84 coordinate system to a local (height) system requires the use of the geoid.

Error Budget

To obtain accurate height data from laser-altimeters it is important to have insight into the error budget. For that purpose we examined possible error sources, developed mathematical expressions for each of them, and evaluated the error ranges using a realistic range of parameter-values [3]. We will not annoy the reader with derivations and computational details. Table 1 presents the final results for several terrain types. In the sequel we discuss these results.

- Detector bias is due to the difference between electronical and mechanical sensor origin. Detector gain is caused by fluctuations in the pulse travelling time due to atmospheric effects. The main random effects are introduced by pulse detection inaccuracy and pointing jitter. The accuracy of the pulse detection depends on (1) SNR, (2) the variance of the pulse length and (3) the variance of the sampling frequency ($\sigma^2_{\Delta t}$) [1]. Since $\sigma^2_{\Delta t}$ is related to the sampling interval (Δt) as $\sigma^2_{\Delta t} = \Delta t/12$ the sampling frequency has to be at least one Ghz to obtain pulse detection accuracy at the decimetre level. The accuracy of the determination of the horizontal position depends for a large part on the pointing accuracy of the scanning mirror. Instability of the mirror causes a random effect called pointing jitter. Since the influence of pointing jitter depends on the tangent of the terrain slope, in areas where relief is high pointing jitter may result in large inaccuracies (Figure 1).
- Errors due to misalignment and time-dependent gyro-drift of the INS system, cause pointing inaccuracies as well, resulting in relatively large positional errors.
- The main GPS inaccuracies concern (1) orbit errors, (2) ionospheric and (3) tropospheric delays, (4) phase ambiguities and (5) multi-path. The influence of orbit errors depends on the length of the base line, i.e. the distance between aircraft and ground receiver. The error increases linearly with base line length. Ionospheric delays can introduce errors at the level of several decimetres when using one-frequency receivers. By using two-frequency receivers the effect is largely eliminated. Tropospheric inaccuracies are mainly due to the difference in path length between groundstation and aircraft. Phase ambiguities and multi-path errors are difficult to model.
- Atmospheric influences on the laser pulse are related to propagation delays, diffraction, absorption and scattering. The propagation delay depends on the flying height. For a flying height of 1000 m, the delay results in a height error of approximately 2 cm, while for 2000 m this error is approximately 7 cm. Diffraction causes beam curvature which is small for near-infrared signals. Absorption and scattering are mainly affected by the amount of moisture in the atmosphere. Moisture causes attenuation of the signal resulting in a poor SNR, influencing the geometric accuracy negatively.
- Terrain slope causes a part of the footprint to hit the ground earlier than other parts. The influence depends, besides slope, on the footprint size and the SNR. The error is at most several centimetres.
- The reflectivity of the terrain influences the SNR and consequently the point precision. A low SNR combined with a high terrain roughness may cause inaccuracies at the decimetre level.
- Depending on the accuracy of the determination of the mutual position and attitude of the laser sensor, GPS and INS, the integration error may reach up to one decimetre. To minimize this influence the integration measurements should be carried out carefully.
- When the laser, GPS and INS use the same clock, synchronization errors are minimal. If not, asynchronism of the clocks cause

Error Estimation for Six Terrain Types						
Error source	**Terrain Type**					
	F1	F2	F3	H1	H2	H3
Systematic Errors						
detector bias and gain	*	*	*	*	*	*
laser pulse delay	*	*	*	*	*	*
INS misalignment	**	**	**	****	****	****
INS gyro drift	*	*	*	***	***	***
GPS base-line error[1)]	*	*	*	*	*	*
GPS ionospheric delays[2)]	***	***	***	***	***	***
GPS tropospheric delays	**	**	**	**	**	**
beam curvature	0	0	0	0	0	0
terrain slope	0	0	0	*	*	*
vegetation[3)]	0	0	****	0	0	****
positional integration	**	**	**	**	**	**
synchronization	0	0	0	0	0	0
Overall (cm)	5 - 20	5 - 20	20 - 200	5 - 20	5 - 20	20 - 200
Random Errors						
pulse detection[4)]	***	***	***	***	***	***
pointing jitter	0	0	0	****	****	****
INS	not investigated					
GPS	*	*	*	*	*	*
absorption & scattering	depends on moisture					
terrain roughness	0	*	**	0	*	**
reflectivity	**	**	**	**	**	**
Overall (cm)	10 - 20	10 - 50	10 - 50	20 - 200	20 - 200	20 - 200

Table 1: *Systematic and random errors for six terrain types as defined in table 2. The random errors are expressed as root mean square (RMS) errors. The * 's indicate a range. 0 neglectable effect. *: several centimetres; **: several centimeters - one decimetre; ***: one to several decimetres; ****: > several decimetres.* [1)] *For base lines up to 20 km.* [2)] *Only for one-frequency receivers, two-frequency receivers eliminate largely tropospheric effects.* [3)] *Depends on foliage transmittance and applied postprocessing filters.* [4)] *Depends on sampling frequency.*

positioning errors in the order of the velocity of the aircraft times the synchronization error.

• Although some errors can be quite large, the final accuracy may be better than one may expect from the above figures, owing to:

- Some systematic errors may partly eliminate each other. For example the DGPS errors may, depending on the sign of the error, compensate for detector bias or sensor integration errors.
- When one determines the total effect of random errors, not the RMS's have to be added but the mean square errors, resulting in the squared RMS.

Definition of Terrain Types			
	paved	barren	grass & scrubs
flat	F1	F2	F3
hilly	H1	H2	H3

Table 2: *Definition of Terrain types used in Table 1. Examples: F1: roads and parking places, F2: beaches, H2 and H3: dunes.*

Improving Accuracy

To obtain high precision results the laser survey has to be carefully planned. Three sources of information are available to improve the precision of the raw data: (1) a priori calibration, (2) redundant laser data, and (3) external information.

A Priori Calibration

A priori calibration of the individual sensors includes:

- Determination of bias (k_0) and gain (k_1) of the laser sensor: $L = k_0 + k_1 \cdot L'$, with L' measured distance and L actual distance.
- INS alignment prior to flight.
- Positional integration of the sensors, i.e. mutual position and attitude determination of the sensors in the aircraft.
- Synchronization of the sensors.

Redundant Laser Data

Redundant laser data can be obtained by choosing an overlapping flight configuration. Across and side overlap help to eliminate horizontal and vertical time-dependent shifts due to systematic INS and GPS errors. A good time model of the shifts is required.

External Information

External information consists of height and horizontal control points.

Height control points help to eliminate errors introduced by:

- Tropospheric effects on DGPS position;
- Ionospheric effects on DGPS position when using one-frequency receivers (two-frequency receivers are highly preferred since they largely eliminate ionospheric delays);
- height errors introduced by INS gyro drift;
- off-set of the laser sensor;
- positional integration errors;
- atmospheric delay of the laser pulse.

Horizontal control points, e.g. corners of buildings, help to eliminate horizontal shifts introduced mainly by INS gyrodrift. A problem is to trace them in the laser range data, since the laser range data do not contain thematic information. When the sampling rate is high, e.g. one point per m^2, the recognition may become easier by using control objects like houses.

Discussion

Airborne laser-altimetry is able to generate accurate DEMs with high point density while a high degree of automatization can be achieved. However, several problems remain:

• The technique is non-discriminating: all objects hit by laser pulses are recorded. Often one needs a DEM that refers to the bare ground, inducing the need for removal of unwanted objects, such as buildings, trees, hedges, and cars. Manual removal is too time-consuming; a computational solution is needed. However, filtering techniques alone can not solve the entire problem, since shape and size of the objects to be removed are filter tuning parameters. Shape and size of wanted objects may correspond with those of the unwanted ones, introducing errors of omission. For example filters tuned for removing buildings may also remove the tops of dunes with heavy slopes. Also errors of commission are likely to occur owing to the variety of shapes and sizes of unwanted objects. Additional information is needed. Several types can be distinguished, including: (1) digital topographic data bases containing the location and the ground contours of the undesired objects, like houses. (2) generic information about terrain types such as rural, urban, wetland and coastal zone, enabling area-depending fine-tuning of the filters, and (3) older, coarser DEMs. At the other hand, laser DEMs provide height information of 3D objects stored in 2D format in topographical data bases, such as houses.

• Lasers are well known in land surveying for their ability to measure distances with high accuracy using reflectors. The precision is usually expressed as a bias (α) and a gain (β): $\sigma = \alpha + \beta$ppm Since laser-altimetry is necessarily a reflectorless technique, terrain aspects affect precision, including terrain type, slope and roughness reflectivity and vegetation coverage. The above observation has two consequences: (1) a uniform accuracy description of DEM points measured during one laser survey is not possible, and (2) checking with ground truth requires a careful selection of reference points. In particular flat and paved terrain is suited, such as road crossings and parkings. Accordingly, an appropriate precision description requires the assignment of a series of parameters, including: signal strength, flying height, vegetation cover, terrain type and slope, pulse angle under which the terrain is recorded, and type of filtering used to remove undesired objects.

• INS provides both attitude and position information, although usually for laser-altimetry only the attitude information is used. Due to gyrodrift and alignment errors INS forms the weakest part of the multisensor system since it is characterized by a good short term but a poor long term stability. GPS, at the contrary, has a good long term stability, but a poor short term stability. To obtain an optimal positioning/attitude performance, INS data and GPS measurements can be integrated, using a Kalman filter [5]. The main principle is that at the short term (a few seconds) INS is used to check the GPS-positions, which may be contaminated by phase ambiguities. When the GPS-positions are found okay, the INS-positions are updated with the GPS-positions.

• Surveys over wetlands, where parts of the area are covered by (shallow) water, may introduce serious problems with respect to (1) low return values over water, (2) non-penetrating properties of near-infrared wavelengths (i.e. depths can not be measured), (3) separation of water and land (i.e. additional information is needed), and (4) obtaining depth values for areas covered by water.

• Since integration of remote sensing and GIS data bases needs to be done along the positional component, the accuracy of data fusion depends largely on how well identical coordinates in different data bases refer to the same terrain point. Further research is necessary to arrive at insight into data fusion error budgets.

Concluding Remarks

Airborne laser-altimetry is a valuable remote sensing data gathering technique that can provide high precision DEMs. It is fast and efficient, especially suited for forest areas and coastal zones. Although already half a dozen commercial systems are available its potential is still in vivid development and under current research. When the strength of the reflected pulse is recorded, thematic information may be derived from the near-infrared band. Possibly this band may be fused with other remote sensing imaging data for (multispectral) classification purposes. Further research is necessary on: (1) integration of laser DEMs and topographical data bases for removal of undesired objects, and, alternatively, for assigning heights to topographical objects, (2) relations among point density, terrain relief and application requirements with respect to DEM quality, (3) full integration of GPS and INS for improvement of position and attitude determination, and (4) the capabilities of laser-altimetry for wetland surveys.

Acknowledgments

Financial support by the Survey Department of Rijkswaterstaat Delft The Netherlands is gratefully acknowledged. Research contributions of dr. Hans van der Marel and ir. Ewald Fortuin on the subjects of GPS and INS, respectively, are acknowledged.

References

[1] Gardner, C.S., Ranging performance of satellite laser altimeters, *IEEE Trans. on Geoscience and Remote Sensing*, vol. 30, no. 5, 1992, pp. 1061-1072.

[2] Kilian, J., Haala, N., Englich, M., Capture and evaluation of airborne laser scanner data, *International Archives of Photogrammetry and Remote Sensing*, vol. 31/B3, 1996, pp. 383-388.

[3] Lemmens, M.J.P.M., Fortuin, E.H.W., Error-analysis of airborne laser-altimetry (in Dutch), Survey Department of Rijkswaterstaat, Delft, February 1997, 70 p.

[4] Lindenberger, J., Laser-Profilmessungen zur topographischen Geländeaufnahme, *Deutsche Geodätische Kommission*, 1993, Reihe C, Heft nr. 400.

[5] Skaloud, J., Cramer, M., Schwarz, K.P., Exterior orientation by direct measurement of camera position and attitude, *International Archives of Photogrammetry and Remote Sensing*, vol. 31/B3, 1996, pp. 125-129.

A New Airborne Remote Sensing System Integrating Scanning Altimeter with Infrared Scanner

Liu Zhen Li Shukai

Institute of Remote Sensing Applications, Chinese Academy of Sciences
PBX 9718, Beijing 100101, PRC. Tel:+86-10-6491-9232 Email:sfdirsa@public3.bta.net.cn

ABSRTACT--With the development of Global Position System and Inertial Navigation System(INS), the precise position and attitude parameters of airborne platform can be obtained. The new systems, such as INSAR and Scanning Laser Ranger, are excellent equipment for acquiring the relative height of earth objects. At the same time optical remote sensing sensor make rapid progress. It is time to integrate these system into a new one, which can provide high accurate DEM and remote sensing image synchronically.

INTRODUCTION

The system, which integrates differential GPS receiver, INS, SLR and IS, is loaded on a specially developed platform. The optical axis of IS and that of SLR are coupled in the same virtual optical axis, so every SLR point fit in a pixel of inferred image accurately. The integrated INS and GPS system can provide high accurate position and attitude parameters of the platform. DEM is generated form INS, GPS and SLR data. Because SLR point fit in a pixel of inferred image accurately, every DEM data have a corresponding image pixel. These points have the same function as the GCPs. It is easy to correct the error of images. On the other hand, generating DEM need some information of earth surface, which can be drawn from images. It is useful to generate more accurate DEM and correct some error in DEM generated. The result of test in North China proves that good quality DEM, geocoding images, ortho-images and 3D perspective images can be obtained in 2 hours after flying.

Obviously, the system can save much more money and job than the old method can. It has the advantage than INSAR in that the data processing need not super computer such as Cray, Sun workstation is enough. Although INSAR has more high accuracy of relative height, to generate interfergram from INSAR data is a time consuming job and the accuracy of DEM is unsatisfied without GCP.

PRINCIPLE OF THE SYSTEM

G, P is one point in space and ground respectively. If the coordinates $G(Xg,Yg,Zg)$ are given, and the vector $\overrightarrow{GP}$ from G to P are given, then the coordinates of P can be obtained. The parameters of optical center are drawn from GPS data, INS provide three angle of the vector: sidespin α, angle of pitch ω and angle of yaw κ。 SLR records the length of the vector: the range S is G to P.

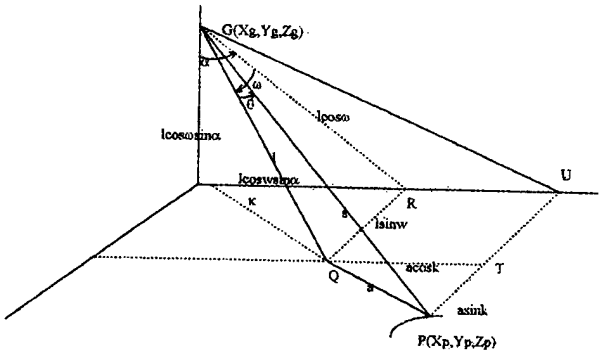

Figure 1 Principle of the System

$$\begin{cases} Xp = Xg + (S\cos\theta - \dfrac{S\sin\theta}{\sqrt{1-b^2}})\cos\omega\sin\alpha + \dfrac{S\sin\theta}{\sqrt{1-b^2}}\cos\kappa \\ Yp = Yg + (S\cos\theta - \dfrac{S\sin\theta}{\sqrt{1-b^2}}b)\sin\omega + \dfrac{S\sin\theta}{\sqrt{1-b^2}}\sin\kappa \\ Zp = Zg(S\cos\theta - \dfrac{S\sin\theta}{\sqrt{1-b^2}}b)\cos\omega\cos\alpha \end{cases} \quad (1)^{[1]}$$

Where θ is the angle between scanning line and vertical line.

STRUCTURE OF SYSTEM

The system includes two subsystem: System of Data Acquisition(SDA), System of Data Processing(SDP).

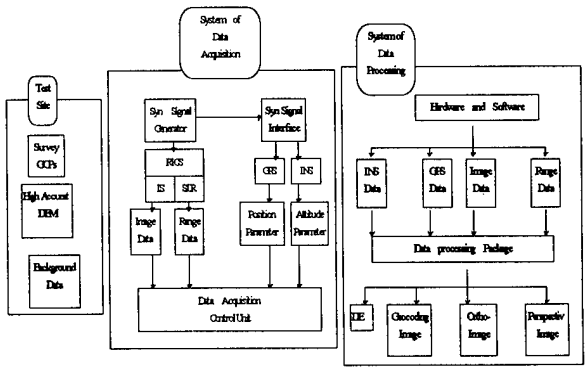

Figure 2 Structure of System

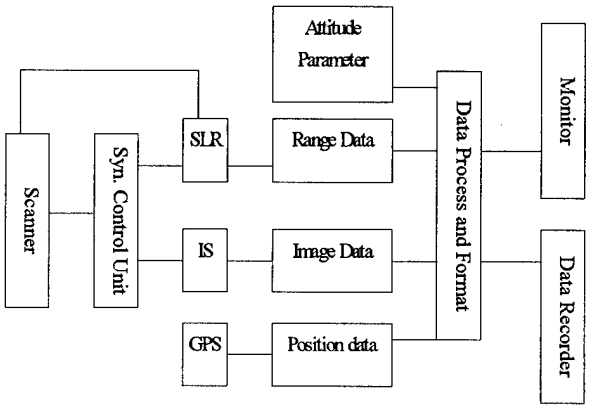

Figure 3 System of Data Acquisition

SDA is composed of differential GPS receiver, INS, IS, SLR and a set of recorder and power system. A special platform was developed, on which sensors of SLR, IS, and INS were loaded. The deformation of the platform is limited in $15''$, so SLR, IS, and INS have the same parameters of position and attitude. The function of SDA is to receive, gather and record the data of GPS, INS, SLR, IS.

The function of SDP is to input the data from SDA and to output different degree digital products, such as DEM, geocoding-image, ortho-image, 3D perspective image. The network , which is composed of Sun 20 workstation and 5 PCs, is the SDP software platform. A special soft package was developed.

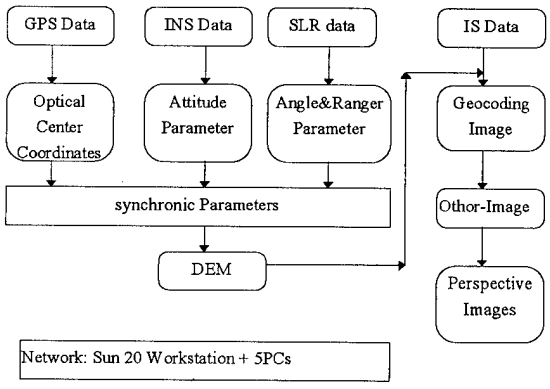

Figure 4 System of Data Processing

TEST AND RESULT

Test Site: Datangshan test site locate at Changping County, Beijing, north edge of North China plain, 116°18'45"–116°22'30"E , 40°10'40"–40°12'30"N. It cover 25 km. There is a hill which is 120 meter high in test site.

Flight:

- Type: Y — 5 , Made in China
- Max Load : 1240 kg
- Min safe speed: 140 — 160 km/h
- Windows : Top ϕ 560mm, Bottom ϕ 720mm
- Power : 60A , 28V
- Passenger Compartment: 4.1X1.6X1.8m

System Parameters :

- Flying Altitude : 600 m
- Max Visual angle : 45°
- Frequency of IS : 10/20/40 (lines/second)
- Image Band : $8-12.5\,um$
- Instant Field View : 3mrad
- Divergent Angle of SLR : 2.6
- Frequency of SLR : 1000Hz
- Model of SLR : Line

- Datangshan Farm Image (Picture 6)
- Datangshan Farm Perspective Image (Picture 7)

CONCLUSION AND DISCUSSION

The spatial quality of Datangshan hill image(Picture 1) and farm image(Picture 6) is very poor, it is impossible to correct the image by use of GCPs since at least over hundred GCPs need. Picture4 is the DEM of test site by use of the new system. Picture2,6 are geocoding images after correction. Picture3,7 are perspective images The time from receiving data to generation of all picture is in 2 hours. The result is satisfied.

Eleven control point were used in evaluating the spatial accuracy of the system.

$$u(X,Y,H) = (6.479,9.605,2.897)$$
$$\sigma(X,Y,H) = (8.825,10.695,6.002)$$

It is conclude that there is obvious system error in flying direction, which is caused by the unsatisfied accuracy of the INS. The error of the system is bigger that aero-cameral, which is cause by the propagation and accumulation of error of sub-systems. There are a lot of research to be conducted:

- Improve the accuracy of INS, GPS .
- Analysis how the error propagate and accumulate.
- Develop new algorithm for the data process to meet the real-time requirement.

RFERENCES

[1] Li Shukai, Xue Yongqi, Liu Zhen. "Report on Three Dimensional Information Gathering and Processing System – Test and Evaluation of Accuracy". Beijing, Feb.,1997.

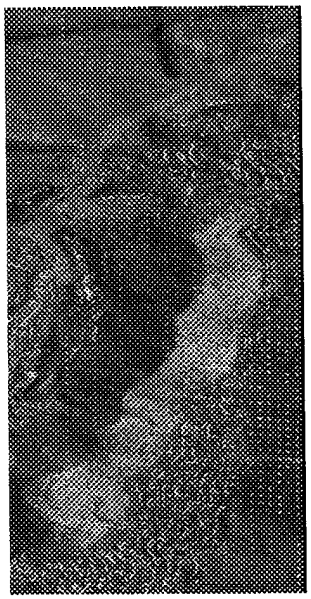

Picture 1 Datangshan Hill Image

Picture 2 Datangshan Hill Geocoding Image

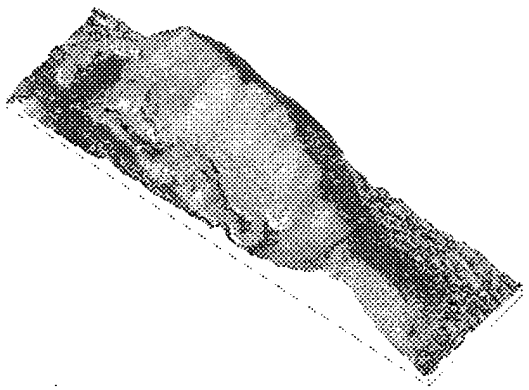

Picture 3 Datangshan Hill Perspective Image

Picture 4 Datangshan Hill DEM

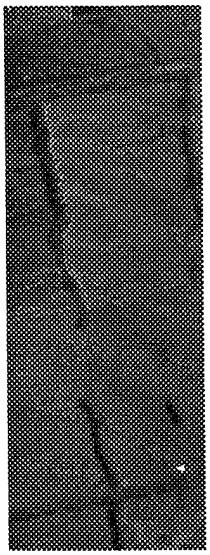

Pic. 5 Datangshan Farm Image

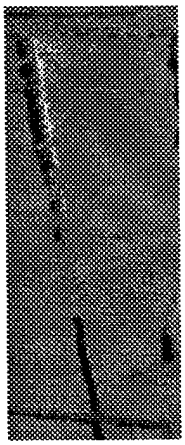

Picture 6 Datangshan Farm Geocoding Image

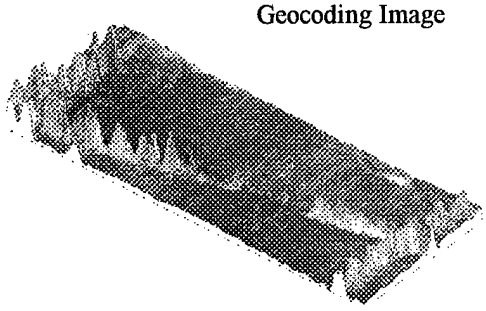

Picture 7 Datangshan Farm Perspective Image

IGARSS'97

1997 International Geoscience and Remote Sensing Symposium

03-08 August 1997

Singapore International Convention & Exhibition Centre

Technical Program

Interactive Area 22: SAR Interferometry

LOCAL , GLOBAL AND UNCONVENTIONAL PHASE UNWRAPPING TECHNIQUES

A. Collaro[2], G. Fornaro[1], G. Franceschetti [1,2], R. Lanari[1], E. Sansosti[1], M. Tesauro[2]

[1] Consiglio Nazionale delle Ricerche, *Istituto di Ricerca per l'Elettromagnetismo e i Componenti Elettronici (I.R.E.C.E.)*, Via Diocleziano 328, 80124 Napoli, Italy.
☎ +(39)-81-5704945 fax +(39)-81-5705734 email: {fornaro, lanari, sansosti}@irece1.irece.na.cnr.it

[2] Università di Napoli, Federico II, *Dipartimento di Ingegneria Elettronica*, Via Claudio 21, 80125 Napoli, Italy.
☎ +(39)-81-7681111 fax +(39)-81-5934438 email: {francesc, manlio, collaro}@irece1.irece.na.cnr.it

Abstract-- We present a comparison among phase unwrapping techniques based on local, global and a new procedure similar to a genetic algorithms.

INTRODUCTION

In SAR interferometry (IFSAR) the topography is related to the absolute phase of the interferogram, whereas the phase of each pixel of the interferogram is known module 2π.

One-dimensional (1-D) Phase Unwrapping (PhU) consists of evaluating the difference between the wrapped-values at adjacent sites of the discrete pixel. If the absolute value of this difference is greater than π, one adds or subtracts an integer multiple of 2π to make it less than π. The result is unique due to the 1-D nature of the problem and the result is always less than π.

Two-dimensional (2-D) PhU is the result of PhU for each row and for each column of the phase interferogram to yield to phase gradient fields φ_x, φ_y defined as:

$$\begin{aligned} \varphi_x &= \Delta_x \varphi + 2\pi k_x \\ \varphi_y &= \Delta_y \varphi + 2\pi k_y \\ \mathbf{s} &= \varphi_x \mathbf{i}_x + \varphi_y \mathbf{i}_y \end{aligned} \quad , \qquad (1)$$

wherein φ is the observed wrapped phase field, Δ_x, Δ_y are the backward-difference operators in the x and y directions, k_x, k_y are integers chosen so that $-\pi \le \varphi_x, \varphi_y \le \pi$ and $\mathbf{s}$ is the estimated gradient. The unwrapped phase can be obtained, in principle, by simple line integration of $\mathbf{s}$ [1] (see Fig. 1A):

$$\hat{\varphi}(\mathbf{r}) = \hat{\varphi}_0 + \int_0^r dc\, \mathbf{s}\cdot\hat{\mathbf{c}} \quad , \quad \hat{\varphi}_0 = \hat{\varphi}(0) \quad . \qquad (2)$$

where the integers k_x, k_y are independently chosen. A check for the success of phase unwrapping (missing in the 1-D case) is that the equality

$$\Delta_x \varphi_y = \Delta_y \varphi_x \qquad (3)$$

is met. This may not be the case everywhere (inconsistency areas) namely,
(1) undersampling (layover regions),
(2) noise (low coherence regions).
making the 2-D unwrapped field depending on the chosen integration path.

PHASE UNWRAPPING TECHNIQUES CLASSIFICATION

Several methods have been proposed to handle the inconsistency problem.

A first procedure is local. It introduces cuts on the image around those regions where the difference fields are inconsistent. Then the difference fields is integrated over the consistent regions [1]. Branch cut, that interconnect residua of opposite polarity where eq (3) falls, may be set in different ways but only one is correct. This procedure requires the detection of the correct branch cuts and ancillary informations are needed. The success of local integration PhU depends on the detection and interconnection of all residua. This operation may fail and a global error may affect the whole image. The algorithms for setting branch cuts may exclude from local integration large slices of the image where the coherence is low (very recurring problem in IFSAR).

A second procedure is global. It attempts to minimize the distance between the phase gradient estimate, $\mathbf{s}$, and the true gradient $\nabla\varphi$, thus minimizing the functional [3]

$$\left\| \mathbf{s} - \nabla\hat{\varphi} \right\|^2 = \sum_{x,y} \left[\Delta_x \hat{\varphi} - \varphi_x\right]^2 + \left[\Delta_y \hat{\varphi} - \varphi_y\right]^2 = \min \qquad (4)$$

0-7803-3836-7/97/$10.00 © 1997 IEEE

An elegant solution [2] to this problem is provided by the integral equation:

$$\varphi(\mathbf{r}') = -\iint_S dS\mathbf{s}(\mathbf{r})\cdot\nabla g(\mathbf{r}'-\mathbf{r}) + \\ + \oint_C dc\varphi(\mathbf{r}_C)\frac{\partial g(\mathbf{r}'-\mathbf{r}_C)}{\partial n}, \quad \mathbf{r}'\in S, \tag{5}$$

where S is the image area and C its 2-D boundary. In eq. (5) $g(r)$ is the unbounded Green's function. It can be shown that eq. (5) is equivalent to average all paths from the phase point to the boundary (see Fig. 1B). Accordingly, the presence of inconsistent areas introduce errors that spread over all the image although decaying with the distance from these area. A way to reduce this error is to blank these areas, introducing blank-out weights in eq. (4). This, however requires pre-processing of the image as well as in the local procedures. It is noted that noise areas generate a bias on the retrieved phase [4] that can be eliminated by an iterative algorithm [5].

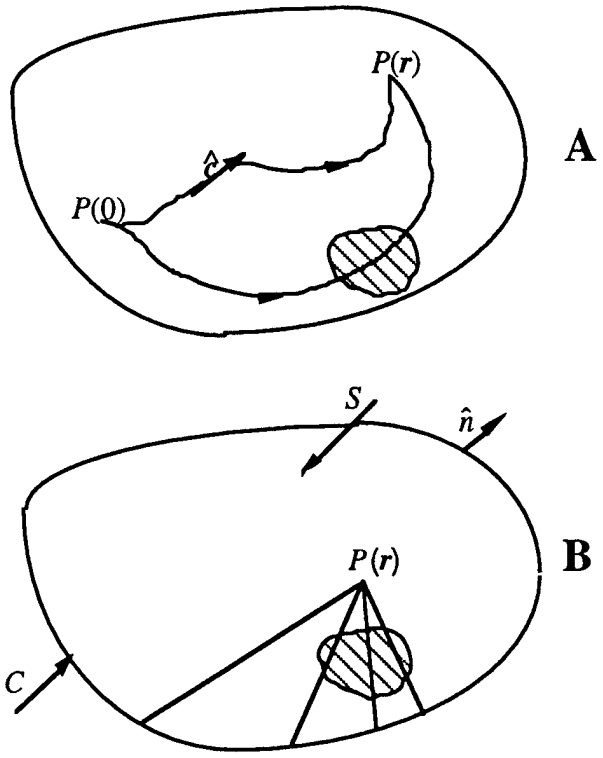

Fig. 1 Local (A) and Global (B) integration method in a domain with a inconsistent region.

A third procedure is still local but the integration paths is selected by defining a cost function for path propagation. These algorithms do not require any branch cut detection and their success depend on path selection. Many rules can be used to select appropriately path propagation. The simplest one being to choose, among all feasible paths, the ones that correspond to the most frequently retrieved values. Its rationale resides on the observation that the occurrence of inconsistent regions in the image is not too likely, it is expected that most paths will be *good* paths. Accordingly, the frequency of these paths generally tends to spread over different values of the phase and, for each phase value, the probability of occurrence is expected to be lower compared to that of *good* paths. It must be noted that, in spite of the above, selection may proceed to wrong value of the phase in some isolated cases.

COMPARISON

In order to test the performance of the illustrated algorithms, we consider a simulated phase pattern of 256 × 256 pixels representing a pyramid with a ledge on one side (see Fig.2). Note the presence of an undersampled region.

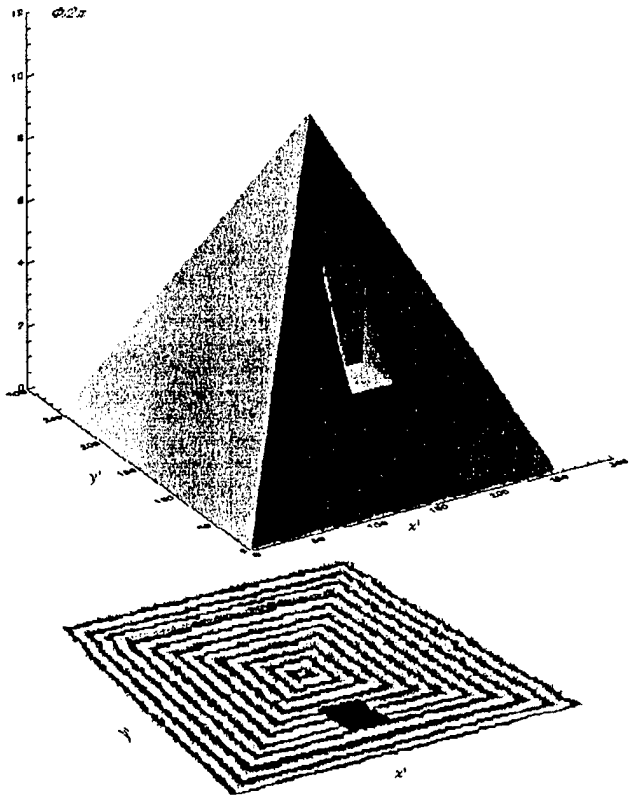

Fig.2 Three-D representation of the test pyramidal phase pattern normalized to 2π with a ledge.

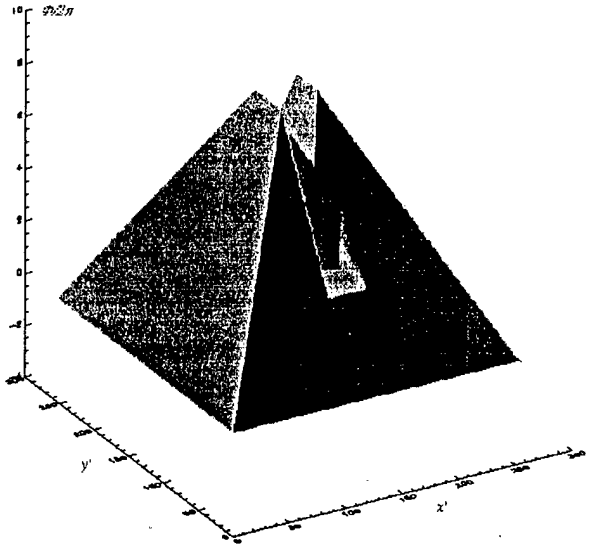

Fig.3 Reconstructed pyramidal phase pattern retrieved from Fig.2 data, by using local algorithm without branch cut.

The reconstructed phase pattern via local integration without any detection of residua is shown in Fig.3. A global error, due to undetected undersampling region, affects the whole reconstruction.

The same pyramid has been reconstructed by a global algorithm [5] and is presented in Fig. 4. The presence of the undersampled phase values causes a reconstruction error mostly confined to the region around the ledge.

The reconstructed phase pattern via the genetic search is shown in Fig.5. The presence of the undersampled phase values clearly affects the reconstruction. However, the results is very different from any local [1] or global [2,3] integration method as the error remains strictly confined to the undersampled area. The genetic algorithm does not allow propagation of the error out of the inconsistent region. This is achieved with no need of fences and/or blanking weights [1,3].

REFERENCES

[1] R. M. Goldenstein, H. A. Zebker, and C. L. Werner, "Satellite Radar Interferometry: Two-dimensional Phase Unwrapping," *Radio Sci.* **23**, pp. 713-720, (1988).

[2] G. Fornaro, G. Franceschetti, and R. Lanari, "Interferometric SAR Phase Unwrapping using Green's Formulation," *IEEE Trans. Geosci. Remote Sens.* **34**, pp. 720-727, (1996).

[3] D. C. Ghiglia and L. A. Romero, "Robust Two-dimensional Weighted and Unweighted Phase Unwrapping that uses Fast Transform and Iterative Methods," *J. Opt. Soc. Am. A* **11**, pp. 107-117, (1994).

[4] R. Bamler, G. W. Davinson, N. Adam, "On the nature of Noise in 2-D phase Unwrapping ", EUROPTO 96, Taormina, Italy, 216-225, 1996.

[5] G. Fornaro, G. Franceschetti, R. Lanari, D. Rossi and M. Tesauro ,"Finite Element Method for Interferometric SAR Phase Unwrapping " EUROPTO 96, Taormina, Italy, 238-249, 1996.

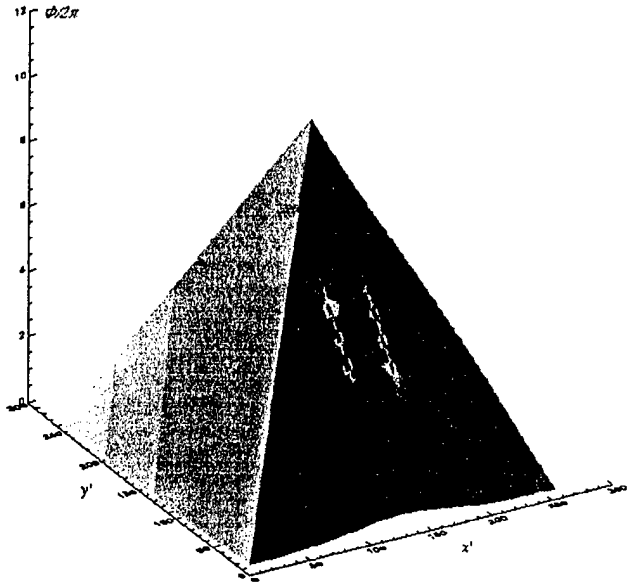

Fig.4 Reconstructed pyramidal phase patternretrieved from Fig.2 data, by using a global method.

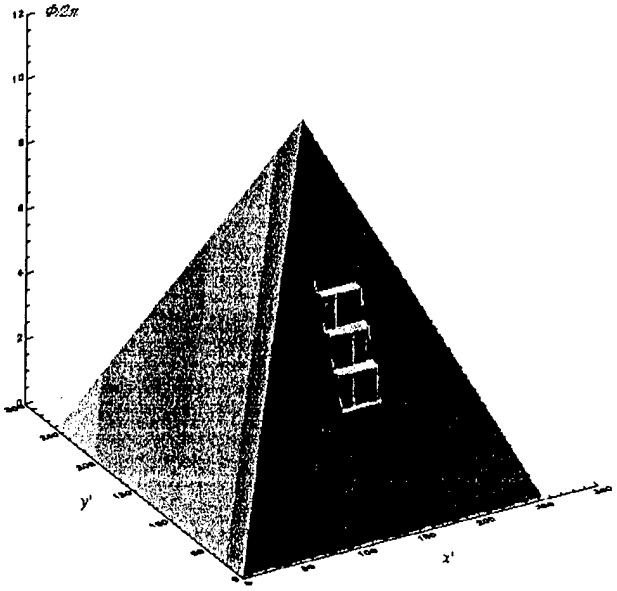

Fig.5 Reconstructed pyramidal phase pattern retrieved from Fig.2 data, by using genetic algorithm.

Motion compensation effects in wavelength- resolution VHF SAR interferometry

P.O. Frölind, L.M.H. Ulander,
Defence Research Establishment (FOA)
P.O. Box 1165, S-581 11 Linköping, Sweden
Phone: (+46)-13-318457 Fax: (+46)-13-318100, email: perfro@lin.foa.se

Abstract-- An investigation of target azimuth displacement due to motion compensation of ultra-wide beam VHF SAR data has been performed. The displacement is caused by a height deviation between the target and the assumed reference height. An approximativ expression is derived for a line which the motion compensation inflicts on the range trajectory of the target. The azimuth displacement is illustrated for different flight tracks versus range.

INTRODUCTION

Across track synthetic aperture radar (SAR) interferometry is a technique used for topographic mapping. It is based on using two complex SAR images of a stable scene which have been acquired with all geometric parameters fixed except the incidence angle. In the VHF implementation [1], two images corresponding to parallel flight tracks separated by a baseline of the order of a kilometre, and an aperture length of the order of several kilometres are acquired. After registration and resampling of the images, the corresponding image resolution cells are made to match the same ground area and thus the ground height level can be measured.

In this paper we investigate in detail the ultra wide band SAR system, CARABAS, operating in the band 20-90 MHz and at an altitude of 1500 m [2]. The topography varies in height by about 100 m over a 3 by 3 km large area. It was concluded that the interferogram coherence was degraded by geometrical displacement of known target pairs in the two images. Many different explanations were investigated, which could cause this effect. The motion compensation was the number one suspect combined with the accompanied azimuth compression algorithm. We will in this paper focus on the cause for the geometric displacement. The ideal tracks of the two repeat passes were chosen parallel. At a closer look the actual tracks deviated in average about 3-8 degrees from being parallel over an aperture length.

INTERFEROMETRIC PROCESSING

In the repeat pass interferometry the objective is to image the same target area with different incident angles, and flight passes are normally assumed to be parallel. The images made so far have been processed using the Fourier Hankel inversion method [3] which precedes with motion compensation of the data to a chosen ideal straight line [1].

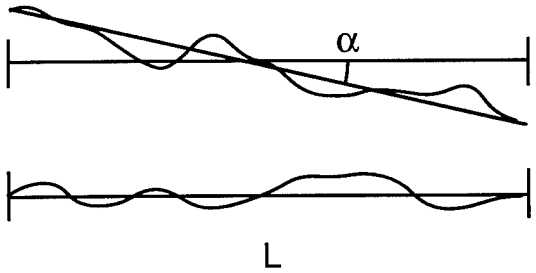

Figure 1. Two repeat-pass trajectories, where the two tracks form a constant angle α from each other on average over the aperture L. L has a typical length of about 4 km.

The actual flight track, however, deviates due to wind and other practical difficulties of completing a planned heading (see Fig 1). The chosen ideal track may therefor be displaced of the order +-150 meter from the actual track. When performing the motion compensation to the chosen ideal track, resampling errors due to the lack of known target height are introduced. Simulations have shown that for a simple configuration with a straight line starting at +150 meter off and ending -150 meter off an ideal track 4 kilometres long, a target at in the centre of scene a will typically be displaced in azimuth 2-8 meter from heights error 100-300m. Locally over an aperture length the average deviation could be even more severe.

NO MOTION COMPENSATION CASE

First we discuss a simple case with similar azimuth displacement by matching to none parallel images. If the paths has been flown on straight lines but differing by an angle α in the x-y plane the motion compensation is not necessary. If we process the data without making any corrections the target will focus at its near range. The next step would be to perform a slant- to ground- range resampling and rotate the image in order to match the image pair. The azimuth error induced by the rotation for a target at a different height compared to the reference height is easily derived.

Fig. 2 shows that resampling slant- to ground- range for a reference level that is lower than the actual target will produce a target position closer to the flight track. When performing the rotation of the ground co-ordinates the target therefore deviates not only in range but also in azimuth as shown in Fig. 3

0-7803-3836-7/97/$10.00 © 1997 IEEE

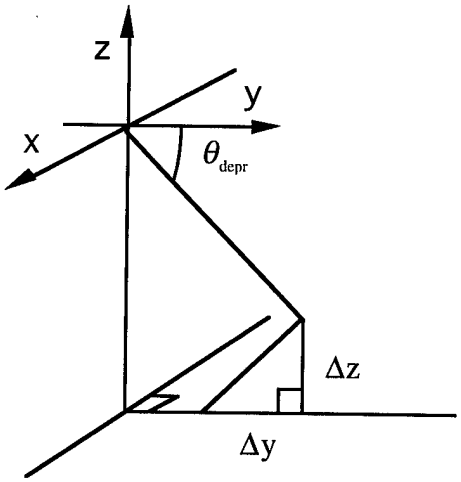

Fig. 2. Illustration of the projection error from a target at height Δz above the assumed reference level.

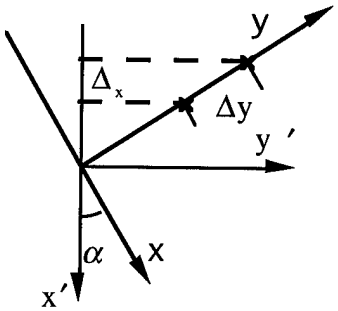

Fig.3. Illustrates the effect of rotation of targets displaced in ground range Δy to a resulting azimuth error Δ_x in a new coordinate system $x' - y'$ deviating with an angle α from the original x - y co-ordinates.

After rotation of the image, we end up with a expression for the azimuth displacement Δ_x

$$\Delta y \approx \Delta z \cdot \tan\theta_{depr}$$
$$\Delta_x = \Delta y \cdot \sin\alpha \qquad (1)$$

MOTION COMPENSATION IMPLEMENTATION

The motion compensation recalculates the slant range radar data along the aperture to a target from a flight track deviating from an ideal straight track in three dimensions, assuming that the target is situated at a references height. Because the ideal straight track is of our choice, we may choose the two interferometric images to be parallel. The geometry is illustrated in Fig.4

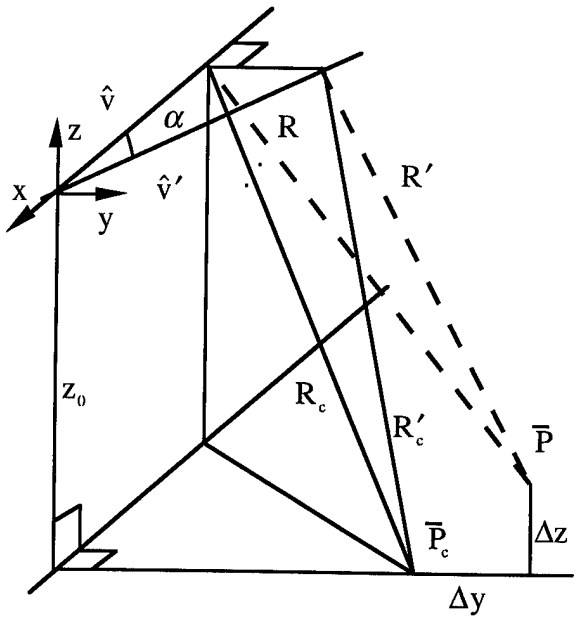

Fig 4. Illustration of the motion compensation geometry for resolution cell $\bar{P}_c$, which corresponds to the correct azimuth position. The reference height is z_0 and actual target $\bar{P}$ is positioned at a height Δz above the reference level. R is the measured slant range to the target, R_c is the range to the calculated target position. R′ is the ideal slant range, and R_c' is the calculated ideal slant range. α is angle between the unit vectors $\hat{v}$ pointing in the actual flight track and $\hat{v}'$ pointing in the ideal track direction.

The aim goal is now to determine the resampling range error of the resulting hyperbola to azimuth compress that will give rise to a new straight line differing from the selected ideal path angle both in z and y axis where this particular target will project itself along the x-axis. From the Fig. 4. follows

$$\begin{aligned} R &= R_c \\ R' &= \sqrt{x^2 + (y_0 + \Delta y + x\tan\alpha)^2 + (z_0 - \Delta z)^2} \\ R_c' &= \sqrt{x^2 + (y_0 + x\tan\alpha)^2 + z_0^2} \\ \Delta_R &= (R' - R) - (R_c' - R_c) = R' - R_c' \end{aligned} \qquad (2)$$

An approximate derivation of the range error is given by

$$\Delta_R \approx \frac{2y_0\Delta y + \Delta y^2 + 2\Delta y x\tan\alpha - 2z_0\Delta z + \Delta z^2}{2R_c} \qquad (3)$$

We solve Δy according to

$$R = R_c \Rightarrow$$
$$\Delta y^2 + 2y_0\Delta y + \Delta z^2 - 2z_0\Delta z = 0 \qquad (4)$$
$$\Delta y \approx -\frac{\Delta z^2 - 2z_0\Delta z}{2y_0}$$

We insert this in the formula above and ignore terms of second order, which results in

$$\Delta_R \approx \frac{z_0 x \tan\alpha}{y_0 R_c} \cdot \Delta z \qquad (5)$$

The expression indicates that when Δz is zero then Δ_R is also zero, for other heights the transformation will not be performed correctly. The Δ_R for a certain height error is linearly growing along the flight track and is pointing in the $\overline{P}$ direction. The final straight line which the target will be resampled to is therefore $\overline{v}'' = x \cdot \hat{v}' + \Delta_R \cdot \overline{P}/|\overline{P}|$, which has its near range coordinate displaced Δ_x from the chosen ideal track derived by

$$\hat{v}'' - \hat{v}' \approx \left[0, \frac{\Delta_R}{x}\cos\theta_{depr}, \frac{\Delta_R}{x}\sin\theta_{depr}\right]/|\overline{v}''|$$
$$\overline{P} = [0, y_0 + \Delta y, z_0 - \Delta z] \qquad (6)$$
$$\Delta_x = (\hat{v}'' - \hat{v}') \cdot \overline{P} \approx \tan\alpha \cdot \tan\theta_{depr} \cdot \Delta z$$

Thus (1) and (6) are identical for small angles α. Note that the calculation only holds for small angles from broadside. We thus calculate the final track keeping the depression angle fixed, which results in a focus point although that target is defocused by the second- and higher- order terms. A plot of Δ_x for two different track deviation versus range is shown in Fig.5.

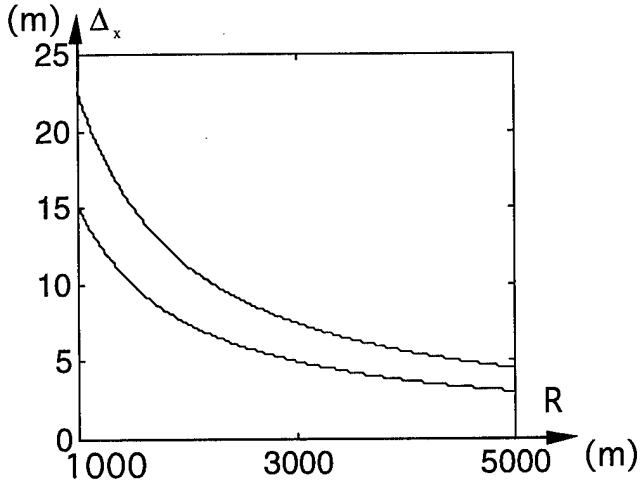

Fig. 5 A plot of the calculated azimuth displacement versus range for typical figures with z=1500, Δz=100, α=5 respectively 8 degrees

CONCLUSION

During motion compensation the minimum deviation from the actual flight track should be chosen as ideal track in order to minimise the height error effects. This also has the advantage of minimising the reduction in overall quality due to approximate motion compensation. We thus end up with an images pair which needs to be rotated in azimuth to get two images resolution cells to match. Future work will focus on displacement tolerance for the final interferometry image versus its resolution and track curvature. It could also be of interest to process the height data in an iterative way, and insert the first output of the interferometry results in the motion compensation algorithm in order to improve the image quality and geometry.

REFERENCES

[1] L.M.H. Ulander and P.O. Frölind, Ultra-Wideband and Low-Frequency SAR interferometry IGARSS'96, Lincoln Nebraska USA, 27-31 May 1996, pp. 668-670, 1996

[2] A. Gustavsson et al., The Airborne VHF SAR System CARABAS, Proc. IGARSS'93, Tokyo, 18-21 August 1993, pp. 558-562, 1993

[3] H. Hellsten and L.E. Andersson, An Inverse Method for the Processing of Synthetic Aperture radar Data, Inverse problems, vol. 3, pp. 111-124, 1987

The Exact Solution of the Imaging Equations for Crosstrack Interferometers

Wolfgang Goblirsch
An der Leite 15, 97762 Hammelburg, Germany
fax: +49 9732 2144, email: gobi@geo.unizh.ch

ABSTRACT

The focus of this paper is on deriving the exact solution of the two sets of Interferometric Range-Doppler Equations for airborne and spaceborne crosstrack interferometers. Due to the generality of the presented problem the obtained solution process is also valid for Stereo-SAR applications. Selecting a special moving coordinate system the equations simplify sufficiently to result in a very efficient algorithm which offers several advantages over existing phase-to-height transformations: The influence of relevant parameter errors on DTM deformation can be studied, nonstandard imaging geometries are properly described, part of the solution is given in an analytic form which considerably increases processing speed and precision, the DTM is obtained with its natural earth curvature thus no additional ellipsoidal model is required. It is shown that phase calibration with ground control coordinates in the presence of parameter errors invariably leads to a tilted DTM and that the DTM deformation cannot be traced back to particular errors which means their separation is not possible.

1. INTRODUCTION

In DTM generation from interferometric SAR data special care has to be taken to preserve geometric fidelity. Especially high resolution DTM's from airborne interferometers are susceptible to deformation from errors in the modeling of the actual imaging geometry. With carefully calibrated hardware the majority of DEM deformations originate from motion compensation errors induced by varying terrain and unstable SAR platforms. Since all present-day software motion compensation methods leave residual motion errors it is advisable to use as little motion compensation as possible. This usually leads to nonstandard imaging geometries such as crossed inclined tracks and squint which can be handled by the algorithm briefly sketched in [1]. Here a more general and detailed description of the algorithm is being presented. From the obtained formulation one is then able to draw already some important conclusions before resorting to more careful error analysis.

2. THE INTERFEROMETRIC RANGE-DOPPLER EQUATIONS

In order to make this paper more self-contained the original formulation of the Interferometric Range-Doppler Equations (IRDE) as presented in [1] is simply stated once more. The interested reader should check [1] for further details. The Range-Doppler Equations are:

$$\left|\vec{p}(t_p)-\vec{x}(t_p)\right| = r_p \qquad (1)$$

$$\left(\dot{\vec{x}}(t_p)-\dot{\vec{p}}(t_p)\right)\cdot\left(\vec{p}(t_p)-\vec{x}(t_p)\right) = r_p\left|\dot{\vec{x}}(t_p)-\dot{\vec{p}}(t_p)\right|\sin\alpha \qquad (2)$$

$$\left|\vec{q}(t_q)-\vec{x}(t_q)\right| = r_q \qquad (3)$$

$$\left(\dot{\vec{x}}(t_q)-\dot{\vec{q}}(t_q)\right)\cdot\left(\vec{q}(t_q)-\vec{x}(t_q)\right) = r_q\left|\dot{\vec{x}}(t_q)-\dot{\vec{q}}(t_q)\right|\sin\beta \qquad (4)$$

where: $\vec{x}$ = *(x , y , z) , position of the imaged groundpoint*

$\dot{\vec{p}}(t_p)$ = *velocity of antenna p*

$\dot{\vec{q}}(t_q)$ = *velocity of antenna q*

$\dot{\vec{x}}$ = *velocity of the groundpoint*

α = *processed squint angle track p*

β = *processed squint angle track q*

The ranges r_p and r_q are connected via the calibrated unwrapped phase difference $\Delta\phi$ and the wavelength λ by the phase relation:

$$\Delta r = r_q - r_p = \frac{\Delta\phi\lambda}{4\pi} \qquad (5)$$

For single-pass Interferometry the two antenna tracks occur simultaneously and we denote the time difference t_q - t_p by Δt. The interferometric baseline vector $\vec{B} = (B_x, B_y, B_z)$ is then:

$$\vec{B} = \vec{q}(t+\Delta t) - \vec{p}(t) \qquad (6)$$

where we replace t_p by t and r_p by r. (The antenna tracks are given as polynomial spline fits).

Equations *(1)* - *(6)* are formulated for an arbitrary coordinate system, which is usually earth-fixed. However the IRDE can be reformulated in a much simpler manner by selecting the following moving coordinate system which originates in $\vec{p}(t) = (p_1(t), p_2(t), p_3(t))$ denoting the master track.

The unit vector in the new *xs*-direction is given by:

$$\vec{e}_{xs} = \frac{\dot{\vec{p}}}{\left|\dot{\vec{p}}\right|} \qquad (7)$$

In order to define the *zs*-direction we introduce the following unit vector:

$$\vec{e}_c = \frac{(-\dot{p}_1, -\dot{p}_2, 0)}{\sqrt{\dot{p}_1^{\,2} + \dot{p}_2^{\,2}}} \qquad (8)$$

and the two angles $\vartheta \in [0, 2\pi)$ and $\zeta \in (-\pi/2, \pi/2)$ which are given by:

$$\cos\vartheta = \frac{\dot{p}_1}{\sqrt{\dot{p}_1^{\,2} + \dot{p}_2^{\,2}}} \qquad (9)$$

$$\sin\zeta = \frac{\dot{p}_3}{\sqrt{\dot{p}_1^{\,2} + \dot{p}_2^{\,2} + \dot{p}_3^{\,2}}} \qquad (10)$$

Then the unit vector in *zs*-direction is given by:

$$\vec{e}_{zs} = \vec{e}_c \sin\zeta + \vec{e}_z \cos\zeta \qquad (11)$$

Finally the *ys*-direction completes the right-handed orthonormal system:

$$\vec{e}_{ys} = \vec{e}_{zs} \times \vec{e}_{xs} \qquad (12)$$

In Figure 1 the rotations necessary for the coordinate change are indicated:

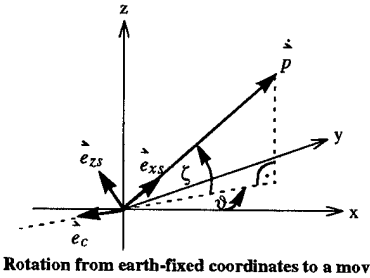

Figure 1: Rotation from earth-fixed coordinates to a moving system

In the system $[\vec{e}_{xs}, \vec{e}_{ys}, \vec{e}_{zs}]$ equation *(2)* is simply:

$$x_s = r\sin\alpha \qquad (13)$$

which in turn is inserted into *(1)* to result in:

0-7803-3836-7/97/$10.00 © 1997 IEEE

$$y_s^2 + z_s^2 = (r\sin\alpha)^2 \qquad (14)$$

or:

$$y_s = signb\sqrt{(r\sin\alpha)^2 - z_s^2} \qquad (15)$$

where signb is 1 when the antennae point to the left of the flight track and -1 for right pointing antennae.

Equation *(4)* now takes on the form:

$$(r\sin\alpha - B_{xs})^2 + (y_s - B_{ys})^2 + (z_s - B_{zs})^2 = (r + \Delta r)^2 \qquad (16)$$

where (B_{xs}, B_{ys}, B_{zs}) denote the baseline components in the moving system.

Finally setting $v = \left|\frac{\dot{s}}{\dot{p}}\right|$ for the speed of the master antenna we transform *(4)* to the moving system:

$$(\dot{B}_{xs} + v)(r\sin\alpha - B_{xs}) + \dot{B}_{ys}(y_s - B_{ys}) + \dot{B}_{zs}(z_s - B_{zs}) = D$$

$$D = (r + \Delta r)\sqrt{(\dot{B}_{xs} + v)^2 + \dot{B}_{ys}^2 + \dot{B}_{zs}^2}\sin\beta \qquad (17)$$

where the groundpixel coordinates (x_s, y_s, z_s) transform to the original system as follows:

$$\begin{bmatrix} x \\ y \\ z \end{bmatrix} = \begin{bmatrix} \cos\vartheta & -\sin\vartheta & 0 \\ \sin\vartheta & \cos\vartheta & 0 \\ 0 & 0 & 1 \end{bmatrix} \begin{bmatrix} \cos\zeta & 0 & -\sin\zeta \\ 0 & 1 & 0 \\ \sin\zeta & 0 & \cos\zeta \end{bmatrix} \begin{bmatrix} x_s \\ y_s \\ z_s \end{bmatrix} + \begin{bmatrix} p_1 \\ p_2 \\ p_3 \end{bmatrix} \qquad (18)$$

3. SOLUTION METHOD FOR THE INTERFEROMETRIC RANGE-DOPPLER EQUATIONS

Inserting *(15)* into *(16)* one solves for z_s:

$$z_s = \frac{1}{2(B_{ys}^2 + B_{zs}^2)}[EB_{zs} + FB_{ys}] \qquad (19)$$

where:

$$E = B^2 - (2r + \Delta r)\Delta r - 2rB_{xs}\sin\alpha$$

$$F = \sqrt{(2r\cos\alpha)^2(B_{ys}^2 + B_{zs}^2) - E^2}$$

Starting with an initial imaging time offset Δt one can now set up an iteration scheme by inserting the baseline components, obtained with the help of *(6)*, into *(19)* to calculate z_s. The crosstrack coordinate y_s of the groundpixel is then obtained with *(15)*. Equation *(17)* is used to test the precision of the solution $(y_s, z_s, \Delta t)$ and increase or decrease Δt accordingly. The initial offset Δt is obtained from image correlation for correlation coefficients above a certain threshold. For lower correlation values Δt is obtained by nearest neighbor interpolation. Figure 2 outlines the IRDE solving algorithm.

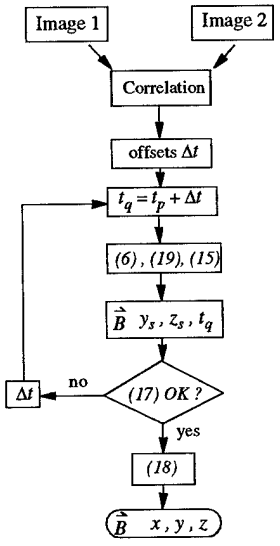

Figure 2: Flowchart for solving the IRDE

On the condition that the third time derivative of the antenna tracks are continuous one can show that the algorithm is converging to a solution. Tests show that an optimized version of the algorithm runs faster than any other accurate phase-to-height conversion method presently known. In addition the presented algorithm also has the following advantages:

- It uses no approximations
- It also allows the 3D-mapping of irregular shaped celestial bodies since no ellipsoid model is necessary
- It can handle highly nonlinear flight tracks and arbitrary squint
- It can be used for UWB-SAR-Interferometry and Stereo-SAR.

4. SOLUTIONS FOR SPECIAL CASES

In the case of a linear master track ϑ and ζ are constant. If the master track is also horizontal then $\zeta = 0$. Then we may select the x-direction of the original earth-fixed system in direction of the velocity direction of the master track thus $\vartheta = 0$ and the transformation *(18)* is only a translation in the x-z plane.

Further simplifications result when the slave track is also linear. Then one can show that the solution can be found by inspecting the real roots of a 4th order polynomial [2]. An analytical expression can be derived when the antenna tracks are parallel. Then *(17)* is:

$$B_x = r(\sin\alpha - \sin\beta) - \Delta r\sin\alpha \qquad (20)$$

Usually both parallel tracks are processed to the same squint which means, that the alongtrack baseline component is simply $-\Delta r\sin\alpha$. In this case the solution is merely a function of the alongtrack and crosstrack baseline components:

$$z = p_3 + G\frac{B_z}{2} - \sqrt{\frac{(2r\cos\alpha)^2}{B_y^2 + B_z^2} - G^2}\frac{B_y}{2} \qquad (21)$$

where:

$$G = 1 - \frac{(2r + \Delta r)\Delta r(\cos\alpha)^2}{B_y^2 + B_z^2}$$

and the crosstrack and alongtrack coordinates are now:

$$y = signb\sqrt{(r\sin\alpha)^2 - (p_3 - z)^2} \qquad (22)$$

$$x = r\sin\alpha + \bar{v}t \qquad (23)$$

where $\bar{v}$ denotes the normalized alongtrack speed.

Equations *(21)* - *(23)* can still be used for orbital parallel track segments in spaceborne Interferometry as comparisons with the general iterative method show. Simulations have also shown that for small values of the angle of track convergence γ these equations can still be used as long as one adds $(vt)\tan\gamma$ to B_y. Thus for single-pass airborne Interferometry with a vertical antenna configuration these equations are applicable as long as $|\gamma| < 0.01^0$ for an azimuth pixel spacing of about 1 m.

5. ESTIMATION OF ERRORS

Since we derived analytical expressions for the cases considered we are also able to give first estimates of the error influences of all relevant parameters in phase-to-height transformation on the resulting DTM. We first note that since the alongtrack coordinate x does not depend on z or the other important modeling parameters, errors in x only have notational character not leading to a real alongtrack deformation of the DTM. Errors in x leading to DTM deformation are rather caused by motion compensation and processing errors. Thus for example v might not really be constant leading to contraction or expansion type errors in alongtrack direction. Also by inspecting *(22)* we realize that any constant input parameter error would lead to an hyperbolic-type contraction or expansion in crosstrack direction warped by the elevation profile which is confirmed by simulation [2].

Turning now to elevation errors we inspect *(21)* more closely. First we have to take note how phase calibration was achieved. Usually this is done with the help of a phase calibration patch (pcp) and *(16)* which is used to calculate Δr_c for the center coordinates of the pcp and a given imaging geometry configuration [3]. An error in the imaging ge-

ometry will then translate into a constant error in Δr for the whole scene overlaying the effect the imaging geometry errors themselves would have on z without this geometry induced constant error of Δr.

Since there are ways of phase calibration which get by without the knowledge of the imaging geometry we first assume that phase calibration was performed without an error and there is no error in the unwrapped phases themselves. Let's assume further that we have a nominal vertical antennae configuration for which the crosstrack baseline component is much smaller than the vertical component. First we will consider only errors in z due to a wrong sensor altitude p_3. Equation *(22)* shows right away that the error in z is: $dz = dp_3$. Constant ranging errors dr are known to occur in SAR sometimes due to unknown internal delay times. Based on our assumptions we obtain from *(22)*:

$$dz \approx -\left(\Delta r\cos\alpha + \sqrt{1-\left(\frac{\Delta r\cos\alpha}{B_z}\right)^2}B_y\right)\frac{dr}{B_z} \qquad (24)$$

With *(16)* one obtains for a vertical antennae configuration approximately:

$$dz \approx -\frac{p_3 + \frac{B_z}{2} - z}{r\cos\alpha}dr \qquad (25)$$

which shows that the terrain sensitive elevation errors are inversely proportional to slant range and directly proportional to the ranging error in this case. Next we consider errors in z due to dB_y and dB_z:

$$dz \approx \frac{1}{B_z^2}(\Delta r\cos\alpha\, dB_z - \sqrt{B_z^2-(\Delta r\cos\alpha)^2}\,dB_y)r + K \qquad (26)$$

where:

$$K = \left(1-\left(\frac{\Delta r\cos\alpha}{B_z}\right)^2\right)\frac{dB_z}{2}$$

With *(16)* one obtains:

$$dz \approx -B_z dB_y r + M^2\left(\frac{B_z dB_z}{2r} - \frac{dB_z}{2r^2}\right) + \left(\frac{1}{2}+\frac{M}{B_z}\right)dB_z \qquad (27)$$

where:

$$M = \frac{p_3 + \frac{B_z}{2} - z}{\cos\alpha}$$

Thus baseline errors cause mainly a linear increase of the elevation error in slant range direction which is often compensated by constant slope correction. While the worst error is thus eliminated there remain terrain sensitive elevation distortions which are on the order of $\Delta z dB_z$ where Δz denotes the maximum terrain variation. The uncertainty in B_z for interferometric crosstrack systems is usually less than a couple of cm under normal flying conditions therefore the terrain sensitive errors escape detection for moderate terrain variation.

So far sensor altitude errors can be separated from ranging and baseline errors with the help of at least two ground control points (gcp's). Distinguishing between ranging and baseline errors is more difficult and hinges upon the availability of several gcp's with sufficient slant range separation. Thus with phase calibration independent from the imaging geometry model one may at least in principle separate the considered parameter errors.

When a pcp centered at slant range r_c and elevation z_c is used for phase calibration the distinct characteristics of the considered errors disappear. For the sensor altitude error one obtains for $\alpha = 0$:

$$dz \approx \frac{dp_3}{r_c}r + \left(\frac{p_3 + \frac{B_z}{2} - z}{r_c r}B_z - 1\right)dp_3 + \frac{B_z}{2r_c}(dp_3)^2 \qquad (28)$$

inserting typical values into *(28)* shows that one can simplify further:

$$dz \approx \left(\frac{r}{r_c} - 1\right)dp_3 \qquad (29)$$

Now the DTM is tilted and the fixed point is close to the center of the pcp. (Considering *(22)* one realizes that the center of the pcp is no fixed point only in the case of sensor altitude errors and ranging errors.) Terrain dependent DSM deformation, however, is still practically nonexistent.

For the ranging error influence on z based on pcp-phase-calibration we obtain:

$$dz \approx (Ndr)r + \left(N - \frac{1}{B_z}\right)\frac{\left(p_3 - z + \frac{B_z}{2}\right)B_z dr}{r} + \left(1 - N\frac{B_z^2}{2}\right)N(dr)^2 \qquad (30)$$

where:

$$N = \frac{2(p_3 - z_c) + B_z}{2r_c^2} \qquad (31)$$

Inserting typical values into *(31)* we find that the magnitude of N is on the order of 10^{-4} and one neglects the last term in *(30)* for $dr < 10^2$ m. Removing a constant slope leaves an hyperbolic error in range direction which is slightly warped by the elevation profile. Differentiating between pure sensor elevation errors and pure ranging errors on the basis of a few gcp's, however, hardly is possible.

Finally, let us investigate an error in z due to dB_z when pcp-phase-calibration is used. For this we obtain approximately:

$$dz \approx \frac{(p_3 + B_z - z_c)dB_z}{B_z r_c}r - \frac{p_3 + B_z - z}{B_z}dB_z \qquad (32)$$

Removing the constant slope results in terrain dependent elevation errors of the magnitude $(\Delta z/B_z)dB_z$. (In [2] it is shown that one obtains a similar result by combining dB_z and dB_y.) Again we note the similarity to the sensor elevation error and ranging error influence. In practical application of a well calibrated crosstrack interferometer it is therefore possible to cancel typical errors due to dB, dp_3, and dr by a small rotation of the baseline vector. This approach was used in [3]. For the same reason it is impossible to distinguish between the types of errors as long as the magnitude of the errors remains in the range of well calibrated interferometric systems. We further point out that baseline errors leave the pcp-center as fixed point.

Another important class of geometric input errors into the IRDE are errors in the horizontal and vertical angles of track-convergence. These are best investigated by running simulations with the algorithm derived in section 3. In [2] it is shown that for single-pass crosstrack interferometers the encountered angles are very small yet their influence leads to considerable hyperbolic elevation errors in azimuth direction. Fortunately these errors show hardly any terrain dependency and can be compensated by the adjusted parallel tracks approach indicated at the end of section 3.

6. CONCLUSION

The new IRDE solving algorithm gets by without any approximations and is the best possible method to solve the Interferometric Range-Doppler Equations for any given geometric configuration. As it turns out the algorithm is simple enough to efficiently transform the unwrapped interferometric phase to the DTM. Due to its formulation in terms of simple geometric parameters, adjustments are easily made to account for unknown input parameter errors. The algorithm can also be used as a realistic simulation instrument in order to study particular error influences for any given configuration and terrain variation.

The IRDE algorithm is the method of choice for UWB-SAR-Interferometry. Due to the repeat-pass nature of this evolving technique nonstandard imaging geometries with large converging angles, curved tracks, and large squint is normal. Up to now no other phase-to-height algorithm is able to precisely execute this transformation under these conditions.

REFERENCES

[1] W. Goblirsch, P. Pasquali, "New Algorithms for the Calculation of Digital Surface Models from the Unwrapped Interferometric Phase", IGARSS' 96 , vol. 1, pp. 656-658

[2] W. Goblirsch: "Optimization of Geometric Parameters for Interferometric Surface Model Generation", thesis, Zürich, 1997

[3] W. Goblirsch et al: "Accuracy of Interferometric Elevation Models Generated from DOSAR Airborne Data", IGARSS'95 vol. 1, pp. 770 - 774

Baseline Estimation Using Ground Points for Interferometric SAR

Hiroshi Kimura* and Masahiro Todo**
*Gifu University
1-1 Yanagido Gifu-shi, 501-11 Japan
Phone +81-58-293-2725 / Facsimile +81-58-230-1109 / E-mail hkimura@cc.gifu-u.ac.jp

**Kokusai Kogyo Co., Ltd.
2 Rokuban-cho Chiyoda-ku Tokyo, 102 Japan
Phone +81-33-262-6221 / Facsimile +81-33-262-6150 / E-mail mtodo@ichi.kkc.co.jp

Abstract -- Baseline estimation is important to generate accurate DEM with SAR interferometry. We often meet problems in calculated baselines from satellite position data. We propose a method to estimate baseline using ground points (GPs) with heights and their interferometric phases. GPs are selected in an amplitude master intensity image, and then interferometric phase of each GP is measured and used to tune baseline. Analysis is done to compare baseline estimation accuracy with the method using tiepoints with heights on both master and slave intensity images. It shows that the proposed method extremely improves accuracy. The example of three JERS-1 SAR datasets demonstrates accuracy of this method.

INTRODUCTION

Synthetic Aperture Radar (SAR) interferometry is a promising tool for mapping topography [1], detecting small surface displacement caused by earthquake [2], volcanic activity, and ice movement [3]. Problem on a repeat-pass SAR interferometry, such as JERS-1 SAR, is uncertainty of baseline separation and platform altitude. Even if a good quality interferogram is obtained, accurate knowledge of baseline separation and platform altitude is requiring for conversion of interferogram phase to absolute pixel height or displacement. To measure pixel height in meter order and pixel displacement in centimeter order, baseline separation should be determined in centimeter order [4]. Generally, orbit information attached to signal data is not accurate enough to derive them for practical use. Interferometric fringes appearing in flat areas or coastlines are sometimes used to estimate baseline, because there should be no fringe after the removal of orbital fringes (flattening). However, it is usually difficult to find such areas in most image.

Previously, we propose a method to estimate baseline and platform altitude from only three sets of interferograms with three observations [5]. Theoretically three baselines are determined without any other information by this method. However, Least-square solution tends to reach the local minimum, it is hard to meet always true solutions. In this paper, we modify this method. Our new method allows to estimate baseline, platform altitude and their time variation using several GPs. There is no need to know anything except their heights about them. In photogrammetry, several ground reference points are used. In this sense, our approach is practical and valid.

ALGORITHM OF BASELINE ESTIMATION

Fig. 1 shows interferometric SAR geometry in the plane consisting of SAR and a range line at a certain time. In case of repeat-pass interferometric SAR, interferometric phase measurement of target T_i can be written as

$$\phi_i + 2n_1\pi = 4\pi(R_{si} - R_{mi})/\lambda \quad (1)$$

$$\phi_i = \phi_1 + 2n_i\pi \quad (2)$$

where ϕ_i is the unwrapped phase from base T_1, n_1 is unknown integer number and ϕ_1+n_1 is absolute interferometric phase of base T_1 ($0 \le \phi_1 < 2\pi$), R_{si} and R_{mi} are slant range distance to target T_i of slave image and master image respectively, and λ is radar wavelength.

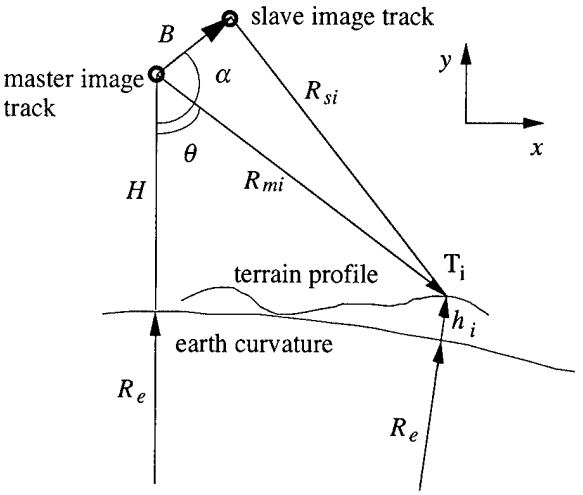

Fig. 1 Geometry of interferometric SAR.

0-7803-3836-7/97/$10.00 © 1997 IEEE

From Fig. 1, R_{si} can be expressed as

$$R_{si}^2 = R_{mi}^2 + B^2 - 2(R_{mix}B_x + R_{miy}B_y) \quad (3)$$

where B is baseline separation, B_x, B_y and R_{mix}, R_{miy} are x and y components of B and R_{mi} respectively. R_{mix} and R_{miy} are given as

$$R_{mix} = R_{mi}\cos\theta_i \quad . \quad (4)$$

$$R_{miy} = -R_{mi}\sin\theta_i \quad (5)$$

$$\cos\theta_i = \frac{R_{mi}^2 + H^2 - h_i^2 + 2R_e(H - h_i)}{2R_{mi}(R_e + H)} \quad (6)$$

where θ_i is off-nadir angle to target T_i, H is radar altitude, h_i is terrain height above the earth ellipsoid , and R_e is the radius of the earth ellipsoid curvature. Unknown parameters B_x, B_y H and n_1 can be resolved from (1) to (6), if 4 and more sets of (ϕ_i, R_{mi}, h_i) of GP on the range line are given. However, it is supposed to be hard to find several GPs with heights on one range line.

Parameters B_x, B_y H and n_1 are usually not constant over the scene, but their change rates can be expected small and linear.

$$B_x(t) = B_{x0} + B_{x1}t \quad (7)$$

$$B_y(t) = B_{y0} + B_{y1}(t) \quad (8)$$

$$H(t) = H_0 + H_1(t) \quad (9)$$

where t is azimuth pixel coordinate. Unknown parameters B_{x0}, B_{x1}, B_{y0}, B_{y1}, H_0, H_1 and n_1 can be resolved, if 7 and more sets of (ϕ_i, R_{mi}, t_i, h_i) of GP over the scene are given. We can expect that finding several ground points with heights over the scene is relatively easy.

ERROR ANALYSIS

Our method uses unwrapped interferometric phase in (1) and (2). Therefore, difference of slant range distance R_{mi} and R_{si} is given with high accuracy in less than wavelength order . On the other hand, R_{mi} and R_{si} are usually given separately. So baseline can be estimated from only (3) to (6) using tiepoints with heights on both master and slave intensity images. Here we express the angle which B and R_{mi} in Fig. 1 makes as α, (3) is modified and approximated to

$$B^2 - 2BR_{mi}\cos\alpha = 2(R_{si} - R_{mi})R_{mi} \quad (10)$$

This yields

$$\sigma_B = R_m\sigma_{dR}/(B - R_m\cos\alpha) \quad (11)$$

where σ_B and σ_{dR} are the variation of baseline separation and slant range difference dR=R_{si}–R_{mi} respectively. Equation (11) means σ_B is proportional to σ_{dR}. With our method, accuracy of dR is expected to be $\lambda/20$, while it is supposed to be the tenth of slant range pixel spacing with the method using tiepoints on intensity images. Variation of baseline separation due to dR measurement can be extremely reduced with our method, i.e., 75 times smaller in JERS-1 SAR case.

Variation of baseline separation due to height error of GP is approximately estimated from (3) to (6)

$$\sigma_B = -B\sigma_h\tan\alpha/R_m\sin\theta \quad (12)$$

Equation (12) gives requirement for height accuracy of GP, which depends on baseline separation and the angle α.

EXAMPLE

The proposed method was applied to three JERS-1 SAR data sets. Fortunately we have three interferograms from these data. Table I shows the initial estimate from the platform position data. From (12), presumed requirements for height accuracy of GP are about 160 m, 10 m and 5 m respectively for pair-A, B and C, when assuming σ_B being less than 0.1 m at the scene center. Twelve GPs are selected over the image and their slant range and azimuth coordinates are measured on the master image. Their heights are obtained from a geographical maps with accuracy less than 100 m. GPs are not necessarily point objects, so some extended flat areas are chosen because they are easy to identify.

Least-square estimation was performed using more than the minimum number of GPs, taking account of phase variation due to noise. Initial values of B_{x0}, B_{y0} and H_0 are given as ones in Table I, and those of B_{x1} and B_{y1} are 0, Altitude change rate H_1 is fixed as one in Table I, because we can expect that the relative value is much more accurate than the absolute value. Initial n_1 is roughly given by

$$n_{1\,\mathrm{int}} = 2(R_{s1} - R_{m1})/\lambda \quad (13)$$

Exact value should be in the range of

$$n_{1\,\mathrm{int}} - \rho/\lambda < n_1 < n_{1\,\mathrm{int}} + \rho/\lambda \quad (14)$$

where ρ is slant range pixel spacing.

Table II shows the final estimates and RMS phase error for used GPs by the proposed method. RMS phase errors show good convergence.

Table I Initial estimate from the platform position data

	pair-A(1&2)	pair-B(1&3)	pair-C(2&3)
B_{x0} (m)	34.283	-383.393	-417.622
B_{x1} (m/pixel)	-0.0004580	-0.0010167	0.0005607
B_{y0} (m)	83.827	407.130	323.313
B_{y1} (m/pixel)	-0.0000246	-0.0002872	0.0002626
H_0 (m)	574479.0	574479.0	574563.2
H_1 (m/pixel)	-0.0070729	-0.0070729	-0.0070982

Each estimate was carried out separately, but three baselines makes a triangle. Therefore, there is the relation

$$x(C) = x(B) - x(A) + \varepsilon \qquad (15)$$

where x is parameter B_{x0}, B_{y0}, B_{x1} or B_{y1} of interferometric pair A, B or C, and ε is error. Presumed errors of the final estimate of baseline C are −0.045 m for B_{x0}, −0.019 m for B_{y0}, 0.000013 m/pixel for B_{x1} and 0.000010 m/pixel for B_{y1}. These are less than 0.01% of the baseline distance and less than 4% of change rate. This means the final estimates are very good. Fig. 2 shows part of flattened interferogram from pair-A processed with the parameters in Table I (Fig. 2(a)) and the estimated ones in Table II by the proposed method (Fig. 2(b)). In Fig. 2(b), fringes are parallel to coastline, while those aren't in Fig. 2(a). This indicates that the estimate by our method is much better than that from platform position data.

CONCLUSION

This paper has given a method of baseline estimation of interferometric SAR using ground points (GPs) with heights. There in no need to know exact geographical positions of them. Unwrapped interferometric phase is also used, and this extremely improves estimation accuracy. Several GPs are sufficient to estimate baseline, its change rate and platform altitude over the scene. Requirement for height accuracy of GP was also assessed. The example of three baselines from three JERS-1 observations demonstrated that the proposed method gave good estimate, and each estimate is well consistent with others.

ACKNOWLEDGMENT

We would like to thank National Space Development Agency of Japan (NASDA) for providing us with JERS-1 SAR data.

Table II Final estimates and RMS phase error for used GPs by the proposed method

	pair-A(1&2)	pair-B(1&3)	pair-C(2&3)
B_{x0} (m)	66.144	-419.582	-485.771
B_{x1} (m/pixel)	-0.0005911	-0.0009603	-0.0003563
B_{y0} (m)	101.548	406.795	305.228
B_{y1} (m/pixel)	0.0000435	-0.0003005	-0.0003347
H_0 (m)	574480.6	574479.0	574563.2
H_1 (m/pixel)	-0.0070729	-0.0070729	-0.0070982
RMS phase error (deg)	1.4	18.8	19.5

REFERENCES

[1] Zebker, H.A., C. L. Werner, P. Rosen, and S. Hensley, "Accuracy of topographic maps derived from ERS-1 interferometric radars," IEEE Trans. on Geoscience and Remote Sensing, vol. 32, no. 4, pp. 823-836, 1994.

[2] Massonnet, D., M. Rossi, C. Carmona, F. Adragna, G. Peltzer, K. Feigl, and T. Rabaute, "The displacement field of the Landers earthquake mapped by radar interferometry," Nature, vol. 364, pp. 138-142, 1993.

[3] Goldstein R. M., H. Englehardt, B. Kamb and R. M. Frolich, "Satellite radar interferometry for monitoring ice sheet motion: Application to an Antarctic Ice Stream," Science, vol. 262, no. 1, pp. 525-1,530, 1993.

[4] Kimura, H., F. Nishio and T. Furukawa, "Analysis of error due to baseline uncertainty of SAR interferometry," Proceedings of the 20th International Symposium on Space Technology and Science, pp. 1247-1249, 1996.

[5] Kimura, H., "A method to estimate baseline and platform altitude for SAR interferometry," Proceedings of 1995 International Geoscience and Remote Sensing Symposium, pp. 199-201, 1995.

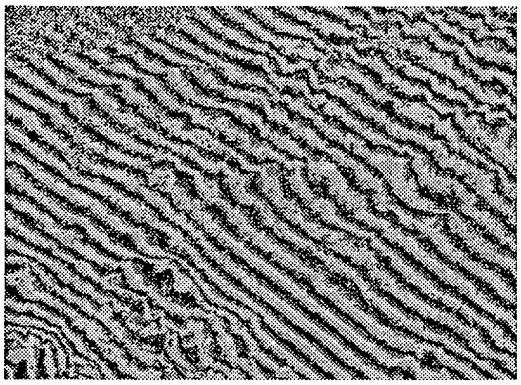

(a) With the initial estimate from platform position data

(b) With the estimate by the proposed method

Fig. 2 Part of flattened interferogram from pair-A.

Phase Noise Filter for Interferometric SAR

I. Lim, T.S. Yeo, C.S. Ng, Y.H. Lu, C.B. Zhang
National University of Singapore, Dept. of Elect. Engr.
Radar and Signal Processing Laboratory
10, Kent Ridge Crescent, Singapore 119260
Tel: (65)7728035, Fax: (65)7791103
Email: elelimwk@nus.sg

Abstract -- Interferometric phase data acquired using a pair of synthetic aperture radar (SAR) sensors, need to be phase unwrapped before useful information can be extracted. This proves to be difficult because measurements tend to be corrupted by additive random phase noise. A common way to reduce random phase noise before phase unwrapping, is to make use of a coherent averaging or mean filter. Unfortunately, noise reduction is achieved at the expense of a loss in spatial resolution. We propose adopting the technique of using local statistics, to adaptively suppress the noise in the wrapped interferometric image. This technique has been applied to multiplicative SAR speckle noise filtering and shown to have good feature retention capabilities. However, because the local statistics (LS) filter is essentially designed for non-directional (non-circular) data, modifications have to be made before it can be applied in the wrapped-phase domain. For this purpose, an angular complement compensation technique is devised and circular variances are used. In instances when the local statistics of the signal can no longer be assumed stationary i.e. dense fringes with spacing in the order of the window size, the non-stationary phase signal is first removed using a two-dimensional multiple-signal classification (MUSIC) algorithm. The result is a noise-filtered wrapped interferogram with retained spatial resolution, independent of the density of the fringes. Quantitative evaluation using synthetic fringe patterns and computed residues, reveals that the noise reduction capabilities of the proposed LS filter is comparable to the mean filter.

I. INTRODUCTION

Across-track interferometry using a pair of correlated SAR images, has been shown to be a viable means of deriving high-resolution digital-elevation model (DEM) or topographical map of the imaged scene. However, the process has not acquired sufficient robustness to automatically generate DEMs. Random phase noise due to decorrelation between the images and effects such as layover and shadowing, disturb the quality of the interferometric image, making direct unwrapping impossible. Besides, there are also deterministic low-frequency phase noise that cause geometric distortion in the final DEM. Deterministic noises are due to processing with inaccurate geometrical parameters, uncompensated motion errors and phase aliasing in the presence of steep relief.

For this paper, we shall confine our scope to the suppression of phase noise immediately after interferogram generation as an aid to phase unwrapping. Only unbiased random phase noises i.e. those due to thermal noise, geometric and temporal decorrelation, are considered. Deterministic phase noises cannot be estimated at this stage and they bear no consequence on phase unwrapping. Besides, they can only be removed using ground-control points. As for biased random phase noises i.e. those due to thick vegetation in the scene and defocusing during SAR processing, their correction require additional removal of the introduced bias, which is beyond our scope. Layover and shadowing will also be ignored although it is vital that affected regions be masked out prior to phase unwrapping. To do this, classification has to be carried out using the merger of phase, correlation and intensity data.

II. STATISTICS OF INTERFEROMETRIC PHASE

We now recall some salient characteristics of interferometric data to facilitate discussion.

Modelling the real and imaginary parts of a complex SAR image $\boldsymbol{S}$ as consisting of independent, zero mean and identically distributed Gaussian random variables, we may express $\boldsymbol{S}$ as

$$S = |S|\exp[j\Psi] = X\zeta\exp[j(\Phi+\varphi)] \qquad (1)$$

where $|\boldsymbol{S}| = X\zeta$ is the amplitude across the image. X is the deterministic signal component while ζ is a spatially random noise that obeys a unit-mean Rayleigh distribution. Ψ is the observed phase consisting of a deterministic Φ that is a function of slant range and a spatially random phase noise φ, that is uniformly distributed between $-\pi$ and π.

The interferogram, formed by the Hermitian product of complex images $\boldsymbol{S}_1$ and $\boldsymbol{S}_2$, then consists of an argument that provides a measure of the deterministic wrapped phase difference $(\Phi_1-\Phi_2)|_{\text{mod}2\pi}$ or ϕ_S,

$$\begin{aligned}\phi &= \arg\{S_1 S_2^*\} = \left[(\Phi_1+\varphi_1)-(\Phi_2+\varphi_2)\right]_{\text{mod}\,2\pi} \\ &= \left[(\Phi_1-\Phi_2)+(\varphi_1-\varphi_2)\right]_{\text{mod}\,2\pi} = \phi_S+\eta\end{aligned} \qquad (2)$$

The probability density function (PDF) of ϕ can be obtained from the joint PDF of $\boldsymbol{S}_1$ and $\boldsymbol{S}_2$ [1] as being

$$\text{PDF}(\phi) = \frac{1-|\alpha|^2}{2\pi}\frac{1}{1-\beta^2}\left\{1+\frac{\beta\arccos(-\beta)}{\sqrt{1-\beta^2}}\right\} \qquad (3)$$

where $\beta = |\alpha|\cos(\phi-\phi_0)$ and α is the correlation between $\boldsymbol{S}_1$ and $\boldsymbol{S}_2$. Here, ϕ_0 is the mode of the distribution; determined largely by system parameters to equal ϕ_S (assumed constant locally) and any phase bias that may be introduced. PDF(ϕ) is symmetrical about ϕ_0. The noise variance is independent of ϕ_0 but remains a function of α [2]:

$$\begin{aligned}\text{var}(\phi) = \text{var}(\eta) = \frac{\pi^2}{6}\left[2-\frac{3}{\pi^2}\sum_{m=1}^{\infty}\frac{|\alpha|^{2m}}{m^2}\right] \\ -\pi\arcsin(|\alpha|)+\arcsin^2(|\alpha|)\end{aligned} \qquad (4)$$

These phase statistics can be extended to the multi-look process in which

$$\phi_{(N)} = \arg\left\{\sum_{n=1}^{N} S_1(n)S_2^*(n)\right\} \qquad (5)$$

0-7803-3836-7/97/$10.00 © 1997 IEEE

We note that $\phi_{(N)}$ is an unbiased estimate of ϕ_0. A first-order approximation of the variance of the resulting PDF($\phi_{(N)}$), valid only when $|\alpha|^2 \rightarrow 1$, is given by [3] to be

$$\mathrm{var}\left(\phi_{(N)}\right) \approx \frac{1-|\alpha|^2}{2(N-1)} \qquad (6)$$

These statistical properties show that interferometric phase noise η is additive and zero-mean (assuming no phase bias), with a variance that can be reduced by increasing the number of looks N or the correlation α between the SAR images.

III. APPROACHES TO PHASE NOISE SUPPRESSION

There are generally two approaches to reducing random phase noise. In the first approach, α is modelled as a function of the input image signals and an unknown transfer function contributing to the phase aberration. An adaptive algorithm is then designed to compensate for the transfer function by maximising α, either during or after the SAR processing stage. Generally, these techniques require accurate knowledge of the scene which is rarely available. As such, initial estimation is based on the rough interferogram, and subsequently improved upon by iteration. The more popular second approach involves the coherent averaging of several independent looks (pixels) in the interferogram as discussed earlier. While this approach is simple and the SNR of the phase field is increased, there is a drop in spatial resolution, which also decreases the theoretical slope limit before phase aliasing sets in.

IV. THE LOCAL STATISTICS FILTER

Using an additive noise model and minimising the mean square error, the following LS estimation algorithm [4] (an extension of the mean filter) is obtained:

$$\hat{\phi}_S = E[\phi] + \left(1 - \frac{\mathrm{var}(\eta)}{\mathrm{var}(\phi)}\right) \cdot \left(\phi - E[\phi]\right) \qquad (7)$$

$E[\phi]$ is estimated by $\phi_{(N)}$ as expressed in (5), using a sliding window of N pixels over the entire complex interferogram.

To obtain var(η), an intermediate image

$$S_3 = |S_3| \exp(j\psi_3) = |S_2| \exp(j\psi_2) \cdot \exp\left(j\phi_{(L)}\right) \qquad (8)$$

is first generated, where $\phi_{(L)}$ is the mean with L looks ($L \ll N$). The maximum-likelihood correlation estimate [5] is then computed using

$$\tilde{\alpha} = \frac{\sum_{n=1}^{N} \sqrt{I_{1,n} I_{3,n}} \cos\left(\psi_{1,n} - \psi_{3,n} - \tilde{\eta}_{(N)}\right)}{\frac{1}{2}\sum_{n=1}^{N}\left(I_{1,n} + I_{3,n}\right)} \qquad (9)$$

where

$$I_{1,n} = |S_1 S_1^*|_n \; ; \; I_{3,n} = I_{2,n} = |S_2 S_2^*|_n \qquad (10)$$

$$\psi_{1,n} = \arg\left(S_1|_n\right) ; \; \psi_{3,n} = \arg\left(S_3|_n\right) = \psi_{2,n} + \phi_{(L)} \qquad (11)$$

$$\begin{aligned} \tilde{\eta}_{(N)} &= \arg\left\{\sum_{n=1}^{N} S_1(n) \cdot S_3^*(n)\right\} \\ &= \arg\left\{\sum_{n=1}^{N}\left[|S_1||S_2| \exp(\tilde{\eta})\right](n)\right\} \end{aligned} \qquad (12)$$

This effectively eliminates the effect of ϕ_S and $\tilde{\alpha}$ becomes an estimate of the decorrelation due to noise field

$$\exp(j\tilde{\eta}) = \exp(j\phi) \cdot \exp\left(-j\phi_{(L)}\right) \approx \exp(j\eta) \qquad (13)$$

Noise variance var(η) can then be evaluated from (4) with $\tilde{\eta}$ as the observed noise phase since $\mathrm{var}(\eta) \approx \mathrm{var}(\tilde{\eta})$.

V. COMPENSATION FOR WRAPPING EFFECT

In order to ensure that the estimated variance of ϕ is independent of the location of ϕ_0 in the wrapped domain, a complex version of the corrected-two-pass algorithm [6] is devised and used. We term this as the circular variance:

$$\mathrm{var}_c(\phi) = \frac{1}{N-1}\left\{\begin{aligned} &\sum_{n=1}^{N}\left[\arg\left\{\exp\left(j\phi_n - j\phi_{(N)}\right)\right\}\right]^2 \\ &-\frac{1}{N}\left[\sum_{n=1}^{N}\arg\left\{\exp\left(j\phi_n - j\phi_{(N)}\right)\right\}\right]^2 \end{aligned}\right\} \qquad (14)$$

This has been verified to be an unbiased estimate that tends towards $\pi^2/3$ as $\alpha \rightarrow 0$ and $N \rightarrow \infty$.

To account for the wrapping effect, compensation is carried out using the (ϕ - $E[\phi]$) term. Assume a PDF(ϕ) such that the mode ϕ_0 is located near one of the transitional ends of the principal phase period ($\phi_0 \approx -\pi$ or π). When the ϕ in question is almost equal to ϕ_0, the resulting $\hat{\phi}_S$ from the LS algorithm will be correctly bounded between E[ϕ] and the original ϕ (typically within $\pm 2\sqrt{\mathrm{var}_c(\phi)}$ of ϕ_0). However when ϕ deviates greatly from ϕ_0 such that it is "wrapped" (relative to ϕ_0), |ϕ - E[ϕ]| is made to be erroneously greater than π. As such, $\hat{\phi}_S$ will fall outside $\pm 2\sqrt{\mathrm{var}_c(\phi)}$ of ϕ_0. To remove this error, the estimated (ϕ - $E[\phi]$) is substituted by its angular complement (ϕ - $E[\phi]$)' when its absolute value exceeds π.

$$\left(\phi - E[\phi]\right)' = -\arg\left\{\exp\left[-j\left(\phi - E[\phi]\right)\right]\right\} \qquad (15)$$

VI. FILTER ENHANCEMENTS

To deal with the problem of noisy edge boundaries produced by the LS filter, refinement is carried out using edge directed windows [7]. The center pixel is first classified as belonging to one of eight pre-determined edge types. Having done that, estimation of $E[\phi]$ and var(ϕ) is carried out using a subset of the original N window pixels. With this refined LS filter, better edge retention is expected since E[ϕ] and var(ϕ) near edges are estimated with greater accuracy.

A further enhancement is carried out for cases when the signal phase ϕ_S is not locally constant i.e. when the local phase statistics is non-stationary. This occurs when the terrain gradient is very steep i.e. near the threshold before phase aliasing sets in. In such cases, the narrow signal fringes will be lost after spatial filtering (both the multilook and LS filter). In [8], a two-dimensional MUSIC algorithm is proposed to estimate and remove the high-frequency signal phase before mean filtering is carried out. Although this algorithm is sensitive to monochromatic high-frequency phase signals, it remains insensitive to step phase jumps e.g. edges, which consist of multiple-frequency components. For our work, we have

replaced the mean filter with the refined LS filter. With that, edge retention is expected even in regions where fringe density is high.

VII. EXPERIMENTAL RESULTS

To compare filter performances, a synthetic fringe pattern is used. The noise-free interferometric phase signal consists of fringes of increasing frequencies, superimposed by a center strip of zero radian and two stepped phase strips at 0.8π radian. SAR images are generated using two correlated random fields. Multiplying the second image by the conjugate of the fringe pattern, we obtain the two complex images needed for processing. For the results here, α equals 0.85. The noisy interferometric phase that results is shown in Fig 1.

A total of five phase-noise filters are evaluated using the synthetic fringe pattern. They are the multi-look filter (N=5×5), the LS and refined LS filters (N=7×7; L=3×3), the original MUSIC with multi-look and the improved one with refined LS filtering.

Visual inspection of the filtered outputs reveals that while the mean filter is effective in removing noise (when the fringe density is low), it does so at the expense of spatial resolution, resulting in smeared edges (Fig 2). In comparison, the LS filters (Fig 3 & 4) are able to retain edge information despite the use of larger windows. As expected, the refined LS filter is better able to suppress noise at edges. However, because of the inherent assumption of stationarity that the three filters make, high density fringes are lost. These fringes are recovered when the MUSIC algorithm is used (Fig 5 & 6).

Using the method of residues on a similar set of regular low-density fringe pattern (not shown here), occurrences of singular points of phase increments are located and counted. The results are tabulated in Table 1.

The results show that a slight compromise in error reduction has been made in both the LS and refined LS filters, in exchange for edge (spatial resolution) retention.

Table 1. Effect of filters on residues.

Phase Noise Filters	R (%)	ΔR (%)
1-Look Original	$R_0 = 5.348$	-
3×3 Mean	0.124	97.687
5×5 Mean	0.076	98.578
7×7 LS	0.310	94.203
7×7 Refined LS	0.284	94.679

R = No. of residual pixels ÷ Total pixels; ΔR = Error Reduction = $(R_0-R)/R_0$

VIII. CONCLUSIONS

The classical LS speckle filter has been adapted for phase noise suppression in the wrapped-phase domain. Results show that edge retention is superior to the multilook filter. Spatial resolution is retained. Using refined statistics, noise near edges are suppressed. In cases when fringe density is high, the LS filter can be used together with the MUSIC algorithm. In view of the application of airborne SAR interferometry in extracting information of man-made features, the LS filter will help in reducing random phase noise to allow for phase unwrapping, without degrading spatial resolution which is of paramount importance in this case.

REFERENCES

[1] D Just & R Balmer, "Phase Statistics of Interferograms with Applications to Synthetic Aperture Radar", *Applied Optics*, Vol.33 No.20 July 1994, pp 4361-4368

[2] O Loffeld & R Kramer, "Phase Unwrapping for SAR Interferometry", *Proc. Int. Geosci. Remote Sensing Symp. (IGARSS'94)*, 1994, pp 2282-2284

[3] RJA Tough et. al., "Estimators and Distributions in Single and Multi-look Polarimetric and Interferometric Data", *Proc. Int. Geosci. Remote Sensing Symp. (IGARSS'94)*, 1994, pp 2176-2178

[4] JS Lee, "Digital Image Enhancement and Noise Filtering by Use of Local Statistics", *IEEE Trans. Pattern Anlys. Machine Intelligence*, Vol.PAMI-2 No.2 March 1980, pp 165-168

[5] MS Seymour & IG Cumming, "Maximum Likelihood Estimation for SAR Interferometry", *Proc. Int. Geosci. Remote Sensing Symp. (IGARSS'94)*, 1994, pp 2272-2274

[6] WH Press et. al., "Statistical Description of Data", *Numerical Recipes in C - The Art of Scientific Computing*, 2nd ed., Cambridge Univ. Press, 1992, Ch.15, pp 613

[7] JS Lee, "Refined Filtering of Image Noise Using Local Statistics", *Computer Graphics and Image Processing*, Vol.15, 1981, pp 380-389

[8] E Trouvé et. al., "Fringe Detection in Noisy Complex Interferograms", *Applied Optics*, Vol.35 No.20 July 1996, pp 3799-3806

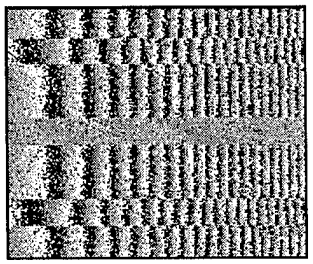

Fig 1: Noisy wrapped synthetic interferometric phase image with $\alpha = 0.85$.

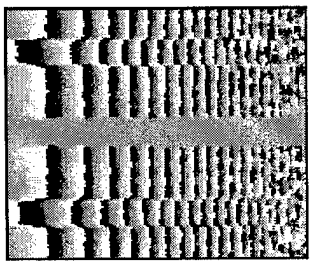

Fig 2: Interferometric phase after 5×5 mean filtering, with a loss in spatial resolution.

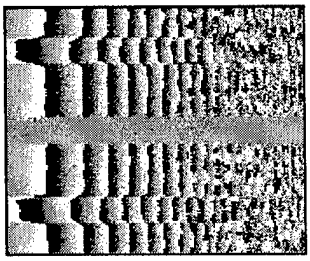

Fig 3: Interferometric phase after 7×7 LS filtering with features retained.

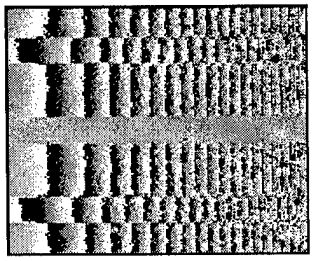

Fig 4: Edge noises are better suppressed after refined 7×7 LS filtering.

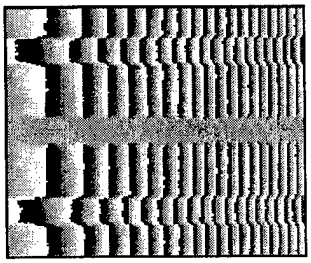

Fig 5: MUSIC with 5×5 mean filtering retains high-density fringes but loses spatial resolution.

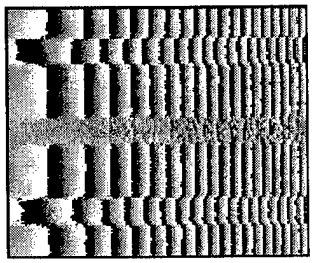

Fig 6: MUSIC with 7×7 refined LS filtering retains high density fringes and spatial resolution.

NOTE: Each revolution of the grey scale (black to white) represents one cycle of phase ($-\pi$ to π)

CALIBRATION AND CLASSIFICATION OF SIR-C POLARIMETRIC AND INTERFEROMETRIC SAR DATA IN AREAS WITH SLOPE VARIATIONS

Paolo Pasquali[1], Francesco Holecz[1], David Small[1], and Thierry Michel[2]

1 Remote Sensing Laboratories, University of Zurich, Winterthurerstrasse 190, CH - 8057 Zurich
Fax: +41 1 362 52 27, E-mail: paolo@geo.unizh.ch

2 Jet Propulsion Laboratory, 4800 Oak Grove Drive, M/S 300-243, CA 91109 Pasadena
Fax: +1 818 393 6943, E-mail: trm@sibyl.jpl.nasa.gov

ABSTRACT

The goal of this paper is to present the capabilities and the limitations of SIR-C SAR magnitude data (dual frequency, dual polarization) and dual frequency interferometric SAR data for land cover classification purposes in areas with slope variations. The work consists of three parts. In a first step SIR-C SAR magnitude HH-, HV-polarized data acquired during the SRL-2 mission (DT 110.00) over an area with terrain ranging from hilly to mountainous (around 1800 sq. km) in Central Switzerland is geometrically and radiometrically calibrated, considering scattering area variations and radiometric errors due to topographic effects on the antenna gain pattern. After this step the backscattering coefficient is classified using a supervised method taking a-priori information into account (thematic and topographic information). In a second step, repeat-pass SIR-C InSAR VV-polarized data (DT 142.12 and 158.12) acquired 24 hours later over the same site is interferometrically processed. In order to correct the interferometric phase for slope variations and therefore to improve the coherence estimation the InSAR data is terrain geocoded. Only after these calibration steps can the backscattering coefficient and coherence data be qualitatively and quantitatively analysed.

Keywords: Interferometric Synthetic Aperture Radar (InSAR), geometric and radiometric calibration, backscattering coefficient, coherence, antenna gain pattern (AGP).

1. INTRODUCTION

For a qualitative and quantitative analysis of SAR/InSAR data, the backscattering coefficient and coherence need to be properly normalized to correct for biases introduced by topography, baseline, and processing. For a test site in an area surrounding Lucerne, Switzerland, we present examples showing why such normalization is necessary, followed by presentation and interpretation of the SAR/InSAR data.

2. TEST SITE AND DATA

The SAR data (DT110.00) used in this study were acquired during the second Shuttle Radar Laboratory (SRL-2) mission on October 7th 1994, over a hilly (450 m) to mountainous (2800 m) area of Central Switzerland, located at 47.00°N, 8.60°E. The SAR image (C- and L-band HH-, HV-polarization), collected with an incidence angle of 54.6°, covers an area of around 1800 sqkm. The repeat-pass InSAR C- and L-band VV-polarized data (DT142.12 and DT158.12) were acquired 48 hours after the DT110.00 (October 9th and 10th, respectively) over the same test site. The DEM used is a high quality model (DHM25) derived from digitized map sheets, arranged in the Swiss national (Oblique Mercator) map projection at an original horizontal grid spacing of 25m, while the heights are quantized to integer decimetres.

3. SAR DATA CALIBRATION AND CLASSIFICATION

From the radar equation for distributed targets it is known that the received power is modulated with the 2-way-antenna gain $G(\theta_l)^2$ and with the reciprocal value of $\sin\theta_i$, where θ_i is the local incidence angle. For each pixel these quantities are therefore dependent on the radar look angle θ_l the depression angle of the antenna, the sensor position and attitude, the position of the backscatter element, as well as on the processed pixel spacing in range and azimuth. Since SAR processing does not include topographic information, these two radiometric corrections are omitted during the processing procedure, and therefore require consideration in a post-processing step. Figure 1 shows terrain geocoded and calibrated L-HH data and the corresponding local incidence angle map. It should be pointed out that the achieved geometric accuracy amounts to fless than half pixel, while the radiometric calibration distortions due to the topographic effects are up to 6.1 dB, 1.2 dB (AGP L-HH, -HV), and 1.5 dB (AGP C-HH, -HV) in magnitude (Holecz et al., 1996).

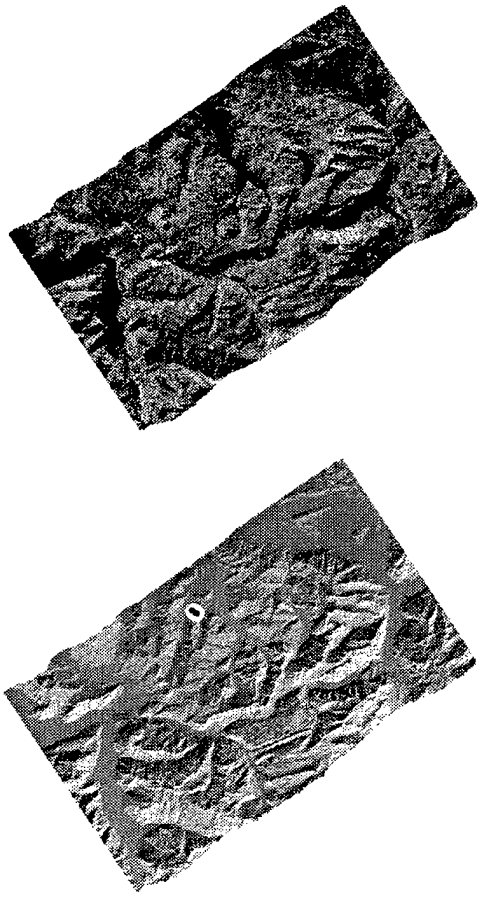

Figure 1: Terrain geocoded and calibrated L-HH data (top) and corresponding local incidence angle map (bottom).

The ability to acquire multi-frequency polarimetric SAR data implies multidimensional data. Potentially, this improves the capability to obtain more information about backscatter signatures of various terrain types and land cover. However, the task of extracting the large amount of information present in these images is still a challenging problem. Furthermore, in the remote sensing case, a-priori knowledge about the land cover is generally hard to come by, hindering the use of supervised methods. On the other hand, unsupervised techniques such as the cluster analysis offer the opportunity to explore the data in an objective way. Roughly speaking, the goal of clustering is to partition a given data set into subgroups in such a way that the data in each group is as homogeneous as possible. Figure 2 illustrates the classification results based on the supervised method including a-priori topographic information. The a-priori topographic information was included during the classification step by means of three simple conditions, i.e. 1) urban areas are not on sloped areas, 2) agricultural fields are not located above a given altitude, 3) pasture does not occour in flat areas. Omitting this topographic knowledge, significant classification errors occur for urban area vs rocks, agricultural fields vs pastures and pastures vs agricultural fields, due to similar radar return characteristics at both frequencies and polarizations. This is especially evident in the mountainous area where rocks could be confused with urban areas. In the surrounding surfaces, unvegetated soil (in this case bare soil at about 2500 m) would be mis-classified as agricultural fields. One should remember the acquisition date, namely October 7th. In this period of the year several agricultural fields are bare soil, and therefore not discriminable by radar from unvegetated soil at any frequency and polarization. The same ambiguity is seen between pasture and agricultural fields.

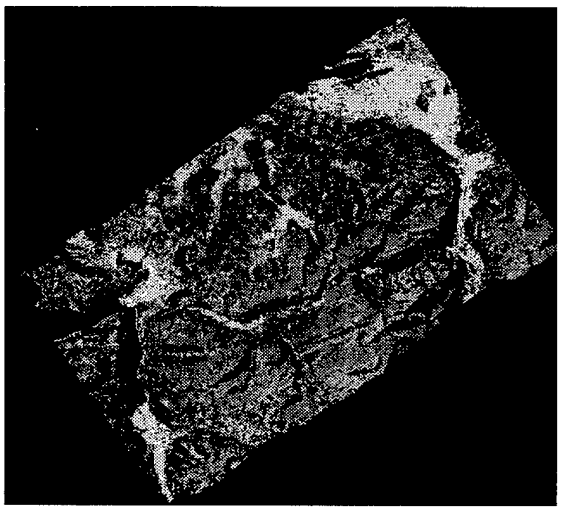

Figure 2: Supervised classification with topographic information. From black to white: shadow/layover, water, forest, pasture, unvegetated, agricultural fields, urban areas.

4. COHERENCE ESTIMATION

Coherence is defined as the magnitude of the correlation coefficient of the complex interferometric data; it is directly related to the phase noise that is present in a SAR interferogram. This information provides an estimate of the achievable elevation accuracy during DEM generation, and allows to investigate temporal changes of an observed area in repeat-pass interferometry.

The estimation is carried out on a window basis; the maximum likelihood estimator has been derived for this step. The statistical confidence of the estimated coherence is a function of the number of independent samples (degrees of freedom n) and the true coherence value. The estimator is biased for all values of coherence, especially for areas with low coherence; estimates in these areas show a high variance.

Other sources of coherence mis-estimation are introduced by 'baseline decorrelation', processing effects and topographic modulation of the interferometric phase. Therefore, to perform a correct estimation, a careful design of the processing has to be carried out, i.e. including spectral shift filtering. In the SIR-C C-band case an adequate filtering is also necessary in the azimuth direction, due to the large changes in the Doppler centroid and platform heading between succeeding acquisitions.

Consideration of the local slope improves the estimation of the coherence, and minimizes the bias introduced by the topography. Figure 3 shows coherence histograms. The interferograms were flattened with (a) an ellipsoid model, (b) InSAR derived slopes and (c) with DHM25.

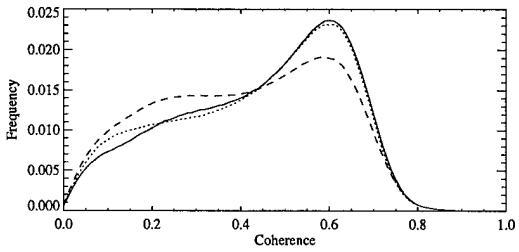

Figure 3: Histogram of coherence after flattening with DEM (solid line), InSAR derived local slopes (dotted line) and with ellipsoid model.

The use of pre-existing DEMs (when available) can allow accurate modelling of the topography. With this information, an accurate coherence estimation is possible also in low coherence areas, where the InSAR derived slopes are poor. InSAR-derived slopes, on the other hand, provide better bias removal in areas where an independent DEM is no longer current, or where the DEM heights differ from the interferometric measurement (ground vs. tree height) (Small et al., 1995). An existing DEM can also be used to drive the spectral shift filtering to adapt to the varying topography.

The knowledge of the effective number of degrees of freedom n involved in the estimation is necessary for a quantitative interpretation of the coherence values. This value is equal to the number of independent samples contained in the moving window used for the estimation. The system resolution and the sampling of the single look complex data in general do not correspond, a spectral weighting is present in the data, and defocussing effects can influence the images: the number of degrees of freedom therefore differs from the estimation window size in pixels. In general it is not easy to obtain an analytical value for n: in the present work it has been estimated in an area with known homogeneous coherence (e.g. large water areas, where it is assumed to be zero). When an adaptive spectral shift filtering is performed incorporating knowledge of the local topography, the coherence estimation window size must also be varied to keep the value of n constant over the whole image.

Figure 4 left shows the L-band interferogram flattened with ellipsoid model, while on the right side the DEM flattened interferogram is presented, with the topographic influences removed from the interferometric phase.

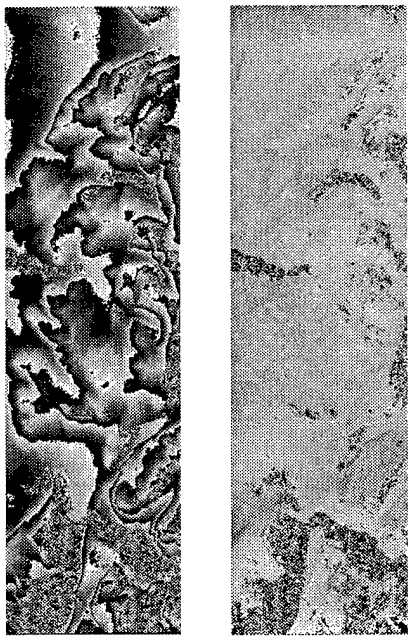

Figure 4: L-band interferograms: ellipsoid model (left) and DEM flattening (right) in slant range geometry.

Figure 5 illustrates coherence maps derived from L- and C-band data. Comparing the interferometric correlation maps, we note that the L-band coherence is higher and more homogeneous than at C-band, in particular over forested areas, where motions in the leaves and branches or volume scattering effects cause C-band returns to decorrelate faster than at L-band, where mainly surface scattering effects are present. A first interpretation of the coherence can be obtained noticing that differences in frequency imply variable penetration depths in the scatterers, and diversified scattering mechanisms result in different information contents.

Agricultural fields and pasture show lower interferometric correlation. This decorrelation can occur as a result of changes of moisture conditions and/or of surface roughness. The highest interferometric correlation is observed over urban areas, and in the rocky mountainous areas. Therefore the temporal variability is not significant due to the high stability of the scatterers.

In Figure 6 two close ups of the same area of the L- and C-band coherence maps are presented. The results clearly show how in this case the generally lower value of the coherence increases the estimator variance. One is not able to distinguish agricultural areas from forested areas already characterized by low correlation values. The same areas can be more correctly identified in the L-band image, where a generally higher value of the coherence provides a lower estimator variance.

5. CONCLUSIONS

It has been clearly shown that an analysis of backscatter coefficients and coherence can be carried out only after an appropriate correction of the effects due to topographic variations within the imaged areas.

Furthermore it has been shown that polarimetric magnitude and interferometric coherence data have a high and complementary information content, usefull for classification purposes as well as for phisical parameter estimation.

6. ACKNOWLEDGMENTS

Thanks are due to the Swiss Federal Office of Topography for the DHM25.

7. REFERENCES

Holecz F., T. Michel, and M. Keller, 'Calibration and classification of SIR-C SAR data in moderate slope areas', Proceedings of. IGARSS'96, Lincoln, 1996.

Small D., F. Holecz, and D. Nuesch, 'Combination of Ascending/Descending ERS-1 InSAR Data for Calibration and Validation, Proceedings of IGARSS'95, Firenze, 1995.

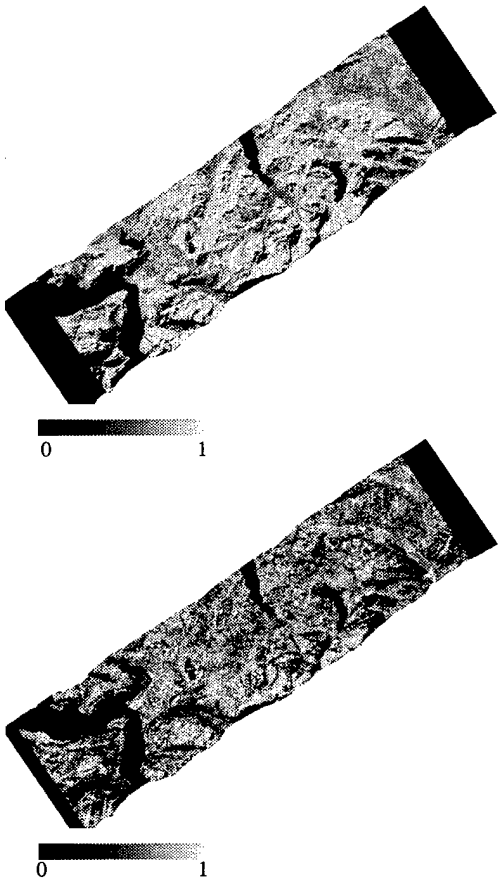

Figure 5: Geocoded interferometric coherence maps: L-band (top) and C-band (bottom). The same scale, ranging from 0 (black) to 1 (white) has been used.

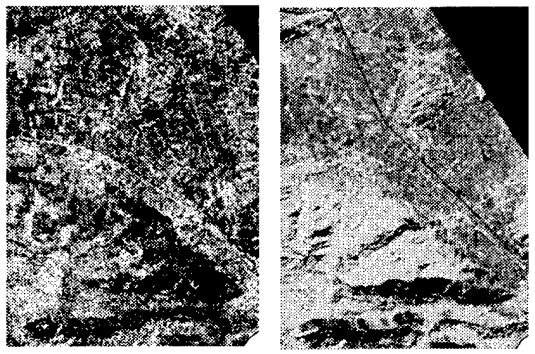

Figure 6: Interferometric coherence map close ups: C-band (left) and L-band (right).

On the Motion Compensation and Geocoding of Airborne Interferometric SAR Data

E. Sansosti[(1)], R. Scheiber[(2)], G. Fornaro[(1)], M. Tesauro[(3)], R. Lanari[(1)], A. Moreira[(2)]

[(1)] Istituto di Ricerca per l'Elettromagnetismo e i Componenti Elettronici (I.R.E.C.E.)
National Research Council (CNR)
via Diocleziano, 328 I-80124 Napoli Italy
Tel.: +39-81-5707999 Fax.: +39-81-5705734 email: fornaro@irece1.irece.na.cnr.it

[(2)] Institut fuer Hochfrequenztechnik
German Aerospace Research Establishment (DLR)
P.O.Box 1116, D-82234 Wessling, Germany
Tel.: +49-81-53282360 Fax.: +49-81-53281449 email: alberto.moreira@dlr.de

[(3)]Dipartimento di Ingegneria Elettronica
University of Naples "Federico II",
via Claudio, 21 I-80125 Napoli, Italy

Abstract-- The paper is concerned about the application of motion compensation algorithms in interferometric SAR data processing.
An analysis of the effects of the error induced by the flat earth assumption in motion compensating the data is included. Possible solutions to this problem via adjustments during and after the SAR processing and the geocoding are also discussed.

1. MOTION COMPENSATION IN SAR PROCESSING

Motion Compensation (MoCo) of airborne Synthetic Aperture Radar (SAR) raw data is a crucial step in the SAR processing chain. Uncompensated motion errors produce defocusing and geometric errors in the final images. For interferometric and polarimatric applications additional requirements are put on the quality of the motion compensation approach in order to ensure the relative phase mapping of the different channels. This section first explains the generation of the MoCo phase and line of sight (LOS) displacement vectors and then deals with the precise and efficient implementation of these functions into the extended chirp scaling algorithm (ECS) [1].

1.1. Generation of the motion compensation functions.

For airborne systems, the measurement of the motion errors is generally performed by using an inertial measurement unit. In most cases it is fixed to the aircraft body and is sensitive to accelerations and attitude (roll, pitch and yaw) variations. The update rate is usually around 50 Hz. Since for motion compensation the displacements from an ideal track are used, the accelerations must be integrated up in two steps. This can only be performed regardless of two integration constants. Additionally, the accelerometers may be biased. To remove these offsets additional information must be used, e.g. kinematically processed GPS measurements [2]. The advantage is that the track of the aircraft (GPS antenna) is now known within some centimeters accuracy within a global reference system.
The next step is to precisely evaluate and update the position of the SAR antenna in a local coordinate system: this can be carried out via three matrix Euler rotations [3]:

$$\mathbf{l} = C_{nb} \cdot \mathbf{l}_0 \qquad (1)$$

where $\mathbf{l}_0$ is the lever-arm from the GPS antenna to the SAR antenna in an aircraft body fixed coordinate system; C_{nb} is the rotation matrix which depends on the time variant aircraft attitude; $\mathbf{l}$ is the resulting SAR antenna position in the local coordinate system.
Next, the computation of the MoCo phase and the LOS displacements must be performed. These are both range dependent and must be accounted for very precisely during the raw data processing (see next subsection). The phase correction is:

$$\Delta\phi = -4 \cdot \pi / \lambda \cdot (|\mathbf{r}'| - |\mathbf{r}|) \qquad (2)$$

where $\mathbf{r}$ and $\mathbf{r}'$ are the range vectors with respect to the actual and the rectified trajectory, respectively.
In order to perform this correction the terrain must be assumed flat at some reference level without any a priori height terrain profile knowledge: this causes height errors for regions of different topography (see next section). The effects of roll angle variation are compensated by this approach for all areas at the referenced topographic height.

0-7803-3836-7/97/$10.00 © 1997 IEEE

1.2. The implementation of the motion compensation in the processing algorithm

The extended chirp scaling algorithm (ECS) [1] allows motion compensation in two steps. First the LOS displacements and the phase errors are corrected for a reference range. After range compression and range cell migration correction a very precise one-dimensional range dependent residual MoCo phase correction is applied before the azimuth compression step. This strategy avoids range dependent spectral shifts due to the range varying motion compensation phase [4]. Thus even for high squint and large motion errors consistent interferometric pairs can be processed without segmentation of the reference tracks.

2. ERRORS INDUCED BY MOCO IN IFSAR PROCESSING

This section is aimed to a discussion about the errors induced by the flat earth assumption in the MoCo applied to a SAR interferometric pair.
It is clear that the phase correction presented in the previous section with reference to the SAR processing of a single raw data set must be extended to the two antennas of an interferometric SAR system.

Because of the difference in the two lever-arms and aircraft attitude instabilities, in general the phase corrections are different for the two antennas. As explained in the previous section, the phase corrections can be computed without any a priori knowledge of the terrain profile, only by assuming a reference flat earth. Let us refer to Fig.1 where the geometry relevant to the problem is depicted. The points A and B represent the actual antenna positions, while A' and B' are relative to the reference parallel and straight trajectories [5].

The right correction, in terms of slant range displacement, is in shifting the first antenna from the position A to A':

$$\Delta_A = r'_A - r_A \quad , \tag{3}$$

while the applied correction is :

$$\Delta_{A0} = r'_{A0} - r_{A0} \quad . \tag{4}$$

Similarly, for the second antenna we have:

$$\Delta_B = r'_B - r_B \quad , \quad \Delta_{B0} = r'_{B0} - r_{B0} \quad , \tag{5}$$

It is evident that the slant range errors induced on the two antennas by the flat earth assumption are:

$$e_A = \Delta_A - \Delta_{A0} \quad , \quad e_B = \Delta_B - \Delta_{B0} \quad , \tag{6}$$

which results on a differential slant range error of:

$$e = e_B - e_A = (r'_B - r_B) - (r'_{B0} - r_{B0}) - (r'_A - r_A) + (r'_{A0} - r_{A0}) \quad . \tag{7}$$

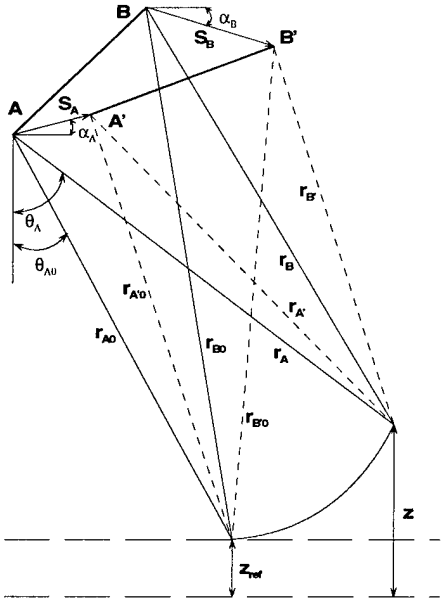

Fig.1: Geometry for the MoCo corrections.

For fixed antenna displacements and terrain profile this error can be evaluated numerically. However, a first order approximation can be evaluated via the following formula [6]:

$$e = \left[-\frac{s_A \cos(\vartheta_A - \alpha_A)}{r'_A \sin(\vartheta_A)} + \frac{s_B \cos(\vartheta_B - \alpha_B)}{r'_B \sin(\vartheta_B)} \right] \Delta z \quad , \tag{8}$$

where Δz is the height displacement between the target and the reference flat Earth used in MoCo. A discussion about eq.8 is now in order. It is clear that if the vector displacements $\mathbf{s}_A$ and $\mathbf{s}_B$ are aligned and of equal modulus (i.e., $s_A = s_B$ and $\alpha_A = \alpha_B$) the two errors cancel each other. On the other hand, they sum if $\alpha_A - \alpha_B = 180°$; this is for baseline length changes and tilt angle variation due to the aircraft roll angle.
From this differential slant range error we can easily calculate the error induced on the height of imaged points. This can be done either via numerical calculation or using again a first order approximation. In the latter case the error can be written as:

$$\delta z = -\frac{r'_B \sin(\vartheta'_A)}{B' \cos(\vartheta'_A - \alpha_B)} e \tag{9}$$

A plot of this height errors is shown in Figs.2 and 3, where a terrain height variation of 1000m (with respect to the reference

height) is considered and we use the geometrical parameters of the E-SAR system [7].
In Fig.2 only a horizontal displacement of 40m is considered; the continuous line refers to the exact calculation, while the dot-dashed one to the first order approximation. It is shown that in a region of 1000 m of height variation the proposed double-track approach motion compensation introduces errors less than 5 meters.

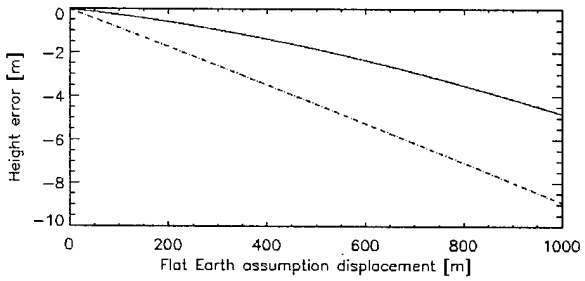

Fig.2: Error induced by 40m of horizontal displacement (height error versus Δz)

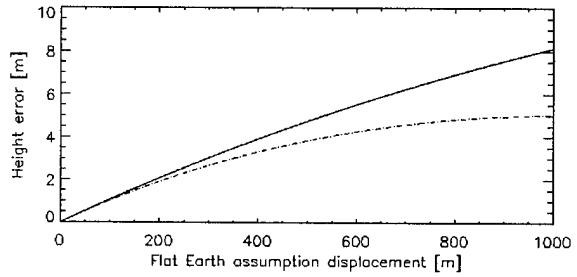

Fig.3: Error induced by 1° of roll angle (height error versus Δz)

The error shown in fig.3 refers to a roll angle of one degree and no additional displacement.
It is clear that, especially for the horizontal displacement, the approximate evaluation can be used only to evaluate the magnitude order of the error introduced in the MoCo procedure: further expansion terms should be considered. On the other hand, eq.8 gives a very clear idea of the error mechanism involved in the MoCo corrections.
The error analysis carried out in this section is in complete agreement with the experimental results of [7] where the errors of the reconstructed SAR DEM with respect to a reference photogrammetric one (5m height accuracy) were assessed to be on the order of 8m.

CONCLUSIONS AND FUTURE DEVELOPMENTS

The phase errors introduced by the flat earth assumption in the MoCo step may be viewed as an error in rectifying the two trajectories. This error degrades the resulting DEM reconstruction after the geocoding operation and the accuracy requirements may not be fulfilled. One possible solution to this problem could be to bring back to the actual trajectories the focused data by applying the corrections discussed in the two previous sections in the opposite sense. This means that the rectification is used only to proper focus the raw data while the interferometric phase is again sensible to the actual positions of the antennas.

However, this solution can be easily performed in absence of any squint angle. As a matter of fact, in presence of squint angle there are two different ways in processing the raw data depending on the output geometry which can be with respect to the zero Doppler or fixed by the squint angle present during the data acquisition. In the first case the corrections after the focusing have to be related to the output geometry.

In the other case azimuth registration problems may arise; this is due to the fact that the output geometry for the two interferometric antennas is different if the same Doppler Centroid is used. This misregistration can introduce strong phase errors because of the presence of a rapidly varying azimuth phase function due to the presence of squint angle.
Both this solutions are still under investigation; tests on simulated data have been already performed giving promising results.

REFERENCES

[1] A.Moreira, Y.Huang, ' Airborne SAR Processing of Highly Squinted Data Using a Chirp Scaling Approach with Integrated Motion Compensation', IEEE Trans. on Geosci. Remote Sens., vol. 32, pp. 1029-1040, September 1994.

[2] S.Buckreuß, 'Motion Compensation for Airborne SAR based on Inertial Data, RDM and GPS', *Proc.* of IGARSS Symposium, Firenze, 1994.

[3] C.R.Vaughn, et al, 'Georeferencing of airborne laser altimeter measurements', Int. J. Remote Sensing, vol.17, no.11, pp. 2185-2200,1996

[4] S.N.Madsen, H.A.Zebker, J.Martin, 'Topographic Mapping Using Radar Interferometry: Processing Techniques', IEEE Trans. on Geosc. Rem Sens., vol.31, no.1, pp. 246-256, 1993

[5] D.R.Stevens, I.G.Cumming, A.L.Gray, 'Options for Airborne Interferometric SAR Motion Compensation', IEEE Trans. on Geosc. Rem. Sens., vol.33, no.2, pp. 409-419, 1995

[6] E.Rodriguez, J.M.Martin, 'Theory and design of interferometric synthetic aperture radars', IEE Proc.-F, vol.139, pp 147-159, April 1992.

[7] M.Coltelli, et al., 'Results of the Mt. Etna Interferometric E-SAR campaign', Proc. of IGARSS Symposium, Singapore, 1997.

Baseline Estimation In Interferometric SAR

Kuldip Singh, Nicolas Stussi, Kwoh Leong Keong and Lim Hock
Center for Remote Imaging Sensing and Processing
National University of Singapore, Singapore 119260
Tel : (65) 771 5070 Fax: (65) 775 7717 Email : crsksingh@nus.sg

Abstract : In this paper we propose a new method of determining the baseline in SAR Interferometry. In particular, we show how the baseline parameters can be retrieved from a Fourier analysis of the interferometric fringes.

1. INTRODUCTION

An accurate estimation of the baseline in spaceborne interferometric SAR [1] has been shown to be an important factor in absolute surface height determination [2]. While baselines can be estimated from orbit ephemerides, the uncertainties associated with some of these parameters may introduce errors that may be unacceptable for many INSAR applications. For instance in differential inteferometry work where measurements of earth displacements of the order of a few centimeters are required [3], a high level of accuracy in the baseline is often needed.

In this contribution we examine the issue of baseline computation. In this regard we provide a theoretical framework in which the baseline can be determined from a given interferogram. The method proposed here is suitable for applications such as differential interferometry where knowledge of the ground terrain (DEM) is assumed to be known.

2. FOURIER ANALYSIS ON PHASE

Consider two radar systems S_1 and S_2 , separated by a baseline vector $\boldsymbol{b}$ illuminating the same ground area as illustrated in Fig.1.

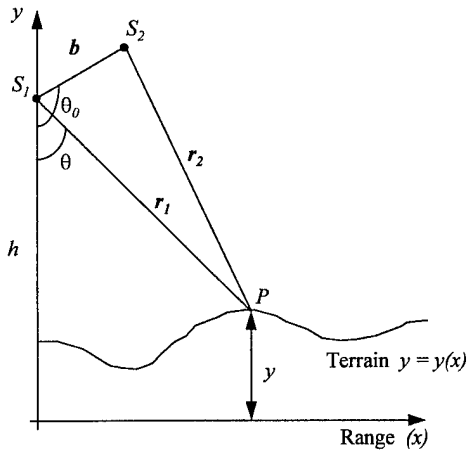

Fig.1: Typical geometry of a cross-track interferometric SAR

For a typical ground point P with elevation height y the interferometric phase difference associated with a signal transmitted by both S_1 and S_2 is

$$\begin{aligned}\phi &= \phi_1 - \phi_2 \\ &= \frac{4\pi}{\lambda}(r_1 - r_2)\end{aligned} \tag{1}$$

which simplifies to:

$$\phi = \frac{4\pi b}{\lambda}\cdot\cos(\theta_0 - \theta) \tag{2}$$

in the case of spaceborne systems with $b = |\boldsymbol{b}| << r_1$. (Angles θ and θ_0 in equation (2) are angles defined in Fig.1). It should be noted that the phase difference ϕ appearing in equation (1) or (2) is the absolute unwrapped phase which cannot be measured directly. In practice, what one does measure is the wrapped phase:

$$\phi_{wrapped} = \phi - 2\pi n \tag{3}$$

where n is sum integer. Here the value of n has to determined independently; a process known as phase unwrapping.

In the following we analyse the phase function in thefourier domain. To this end, we begin by considering a flat terrain characterized by the equation

$$r\cdot\cos\theta = h \tag{4}$$

where h represents the height of the satellite. It is advantages to recast eqn (2) in slant range coordinate r since complex images are always acquired in this projection. On substituiting (4) into (2) one obtains

$$\phi(r) = \frac{4\pi b}{\lambda}\left\{\cos\theta_o\frac{h}{r} + \sin\theta_o\frac{\sqrt{r^2 - h^2}}{r}\right\} \tag{5}$$

Here, without loss of generality, we need only to consider values of θ_o between 0 and π. Now the above phase, as mentioned earlier, is the unwrapped phase . It is instructive, at this stage to consider the function

$$\psi(r) = e^{i\phi(r)} \tag{6}$$

0-7803-3836-7/97/$10.00 © 1997 IEEE

which does not distinguish between the wrapped and the unwrapped phases. Here one can construct ψ from the measured wrapped phase without losing its validity as being defined for the unwrapped phase. Moreover, its Fourier transform

$$\psi(k) = \int_{r_{min}}^{r_{max}} e^{i(\phi(r)-kr)} dr \qquad (7)$$

can also be evaluated analytically using the stationary phase approximation. The limits r_{min} and r_{max} correspond to the range values of the boundary pixels chosen from the interferogram. For instance in the case of the interferogram below, if we limit ourselves to a subset defined by the boundary (within the figure), this values correspond to range values of the left-most and the right-most pixels of the rectangle.

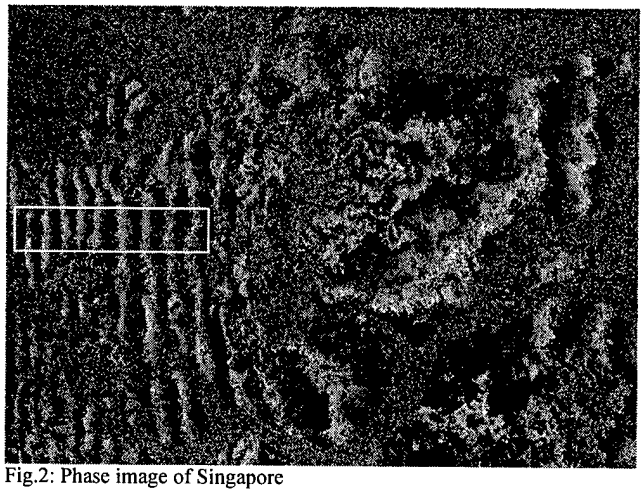

Fig.2: Phase image of Singapore

Before proceeding further, it is instructive to consider the power spectrum of this function for the interferogram of Fig.2.

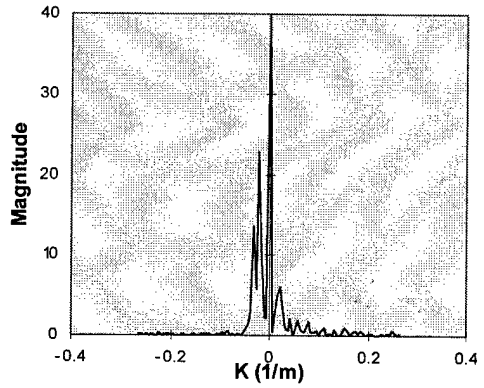

Fig.3 Power spectrum corresponding to $\Psi(k)$ evaluated for the phase image of Fig.2. Here the fourier tansform has been taken for the region enclosed in the rectangle.

Now for the integral (7), with ϕ given by (5), the non vanishing contribution comes from values of k given by

$$k = \frac{d\phi}{dr} = \frac{4\pi b}{\lambda} \cdot \frac{h}{r^2} \cdot \left\{ \sin\theta_0 \frac{h}{\sqrt{r^2 - h^2}} - \cos\theta_0 \right\} \qquad (8)$$

Here it is important to note that the spectrum of $\Psi(k)$ is bandlimited. This follows from the limits inherent in r. More importantly, the above function displays a monotonic dependence on r which is also single-valued. This effectively means that one can expect a spectrum that is characterized by a single band $k \in [k_1, k_2]$ where k_1 and k_2 are k values evaluated at the boundaries of r. These features are exemplified by the following simulated results:

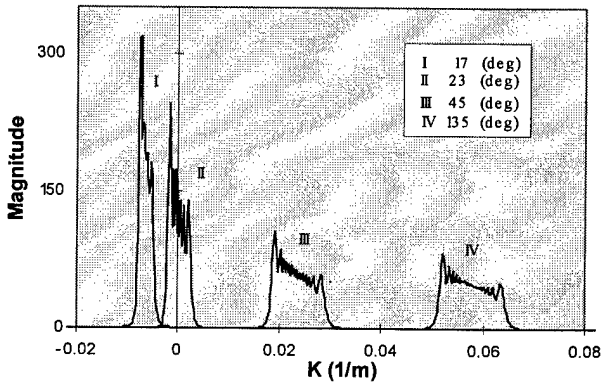

Fig. 4 Power spectrum of $\Psi(k)$ obtained for various angles θ_o with the baseline fixed at 100m.

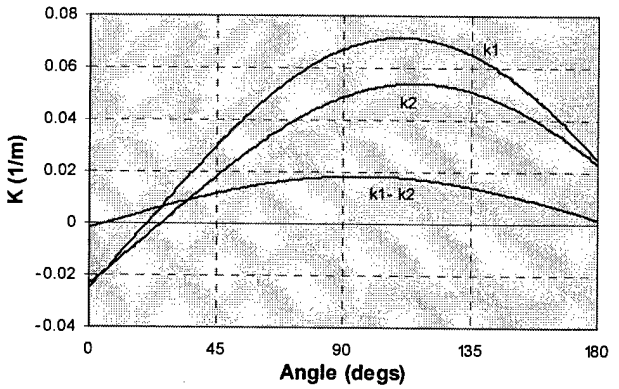

Fig.5: Values of k_1 and k_2 corresponding to k values evaluated at r_{min} and r_{max} respectively, plotted against θ_o.

A closer analysis of k_1 and k_2 further ellucidates the following characteristics:

$0 \le \theta < \theta_{min}$	$\theta_{min} \le \theta \le \theta_{max}$	$\theta_{max} < \theta \le \pi$
$k_1 < 0$	$k_1 > 0$	$k_1 > 0$
$k_2 < 0$	$k_2 < 0$	$k_2 > 0$

Here $\theta_{min} = \cos^{-1}(h/r_{min})$ and $\theta_{max} = \cos^{-1}(h/r_{max})$.

The analysis so far is valid only for a terrain which is flat. In most realistic situations, however this is often not the case. In the following we generalize the equations above, so that its applicability can be extended to a terrain which is not flat.

To the end, we begin by replacing (5) by:

$$\phi(k)=\frac{4\pi b}{\lambda}\cdot\left\{\cos\theta_0\frac{h-y(x)}{\sqrt{x^2+(h-y(x))^2}}+\sin\theta_0\frac{x}{\sqrt{x^2+(h-y(x))^2}}\right\} \quad (9)$$

where y a function of x, is assumed to be known. In the present case, it is convenient to recast the integral (7) back to the ground range coordinates:

$$\Psi(k)=\int_{r_{\min}}^{r_{\max}}e^{i(\phi(r)-kr)}dr=\int_{x_{\min}}^{x_{\max}}e^{i\left[\phi(x)-k\sqrt{x^2+(h-y)^2}\right]}\cdot\left|\frac{dr}{dx}\right|\cdot dx \quad (10)$$

where $x_{\min}$ and $x_{\max}$ are related to $r_{\min}$ and $r_{\max}$ respectively through the equation $r=\sqrt{x^2+(h-y)^2}$.

Here, if the Jacobian does not vary rapidly within the limits of the integration, one can apply the method of stationary phase to evaluate the spectral function. Indeed by setting:

$$\frac{d}{dx}\left[\phi(x)-k\sqrt{x^2+(h-y)^2}\right]=0 \quad (11)$$

one obtains:

$$k=\frac{\frac{d\phi}{dx}\cdot\sqrt{x^2+(h-y)^2}}{x-(h-y)\frac{dy}{dx}} \quad (12)$$

which can be further reduced to:

$$k=\frac{4\pi b}{\lambda}\left\{\frac{(h-y)\sin\theta_0-x\cdot\cos\theta_0}{x^2+(h-y)^2}\right\}\cdot\left\{\frac{h-y+x\cdot\frac{dy}{dx}}{x-(h-y)\cdot\frac{dy}{dx}}\right\} \quad (13)$$

Again, this equation is to be taken within the limits of x imposed in (10). It is interesting to note that when y=0 the above equation reduces to (8). Now, for the present case, the above function, depending on y, may not be monotonic or even single valued for the specified range of x values.
If this happens to be the case, equation (13) can be used in determining a subset over which these conditions are satisfied.These boundary values can then be fed into (13) to yield the corresponding k values.

3. BASELINE DETERMINATION

From measured values of k_1 and k_2 , the baseline parameters (b,θ_0) can be evaluated as follows. By denoting

$$\begin{cases}f(r)=\frac{4\pi h}{\lambda r^2}\\ g(r)=\frac{h}{\sqrt{r^2-h^2}}\end{cases} \quad (14.a, b)$$

$$\begin{cases}b_x=b\cdot\sin\theta_0\\ b_y=b\cdot\cos\theta_0\end{cases} \quad (15.a, b)$$

in equation (11) or (13), one obtains two equations:

$$\begin{pmatrix}f(r_{\min})\cdot g(r_{\min}) & f(r_{\min})\\ f(r_{\max})\cdot g(r_{\max}) & f(r_{\max})\end{pmatrix}\cdot\begin{pmatrix}b_x\\ b_y\end{pmatrix}=\begin{pmatrix}k_1\\ k_2\end{pmatrix} \quad (16)$$

which can be solved for b_x and b_y. The baseline parameters (b, θ_0) are then recovered via:

$$b=\sqrt{b_x^2+b_y^2} \quad (17.a)$$

$$\theta_0=\tan^{-1}\left(\frac{b_x}{b_y}\right) \quad (17.b)$$

To summarize briefly, we have shown how the baseline can be determined from an interferogram. Traditionally, the baseline parameters usually serve as inputs in DEM generation. Here, we do the converse. In other word, from knowledge on the ground terrain, we show that the baseline (both the normal and perpendicular components) can be obtained from a detailed analysis of the interferometric fringes. This is particulary useful in differential interferometric work where the DEM is assumed known, and an accurate value of the baseline is required.

REFERENCES

[1] L.C. Graham, "Synthetic interferometer radar for topographic mapping", in *Proc. Inst. Electron. Eng.*, Vol 62, p. 763, 1974.

[2] C. Reigber et al., "Impact of Precise Orbit on SAR Interferometry", FRINGE 96 ESA Workshop, 30 Sept.-02 Oct. 1996, Zurich, Switzerland.

[3] H.A. Zebker et al., "On the derivation of coseismic displacement fields using differential radar interferometry: The Landers earthquake", Journal of Geophysical Research, Vol.99, No. B10, Pages 19617-19634, October 10, 1994

Removal of Residual Errors From SAR-Derived Digital Elevation Models For Improved Topographic Mapping of Low-Relief Areas

K. Clint Slatton[1], Melba M. Crawford[1], James C. Gibeaut[2], and Roberto Gutierrez[2]
(1): Center for Space Research, University of Texas at Austin
3925 W. Braker Ln., Suite 200, Austin, TX 78759-5321
(2): Bureau of Economic Geology, University of Texas at Austin
E-mail: slatton@csr.utexas.edu; Ph: (512) 471-5509; Fax: (512) 471-3570

Abstract -- Interferometric synthetic aperture radar data can be used to precisely map topography, but low-relief areas are problematic because errors in the data can be large compared to the topographic variations. The NASA/JPL TOPSAR system acquired data over a low-relief test site on the Texas coast in 1996. Due to unusually high turbulence during the acquisition and the mild topography, residual height errors were visible in the Digital Elevation Model (DEM). The characteristics of the error signal are described and a method is outlined for removing the residual error and mosaicking the affected TOPSAR frames.

INTRODUCTION

Land surfaces with mild topography, such as river floodplains and coastal zones, are typically very prone to flooding due to precipitation and storm-surge events. Topography-based flood models have been developed that predict the extent and severity of flooding in such areas under a variety of circumstances, and Digital Elevation Models (DEMs) are needed as inputs to these topography-based models [1]. Because errors in the DEMs propagate directly into the predictions of flood extent, it is important to maximize the accuracy and precision of the DEMs that are used in these models.

Standardized and georeferenced DEMs are produced by the United States Geological Survey (USGS) and are widely available for most of the United States. These DEMs are often sufficiently precise for areas with significant topography because any height errors will typically be small relative to the actual surface height variations. The specification for the Level 1 USGS DEM is ≤15 m vertical root mean square (rms) error. Figure 1 shows a Level 1 DEM for the test site. The horizontal data spacing is 30 m and the vertical data spacing is 1 ft [2]. However, greater precision is needed when mapping low-relief areas because these errors in the DEMs may be of similar magnitude to the surface height variations, and so have a great effect on the accuracy of flood models that use the DEMs. DEMs used for flood modeling must also have fine horizontal resolution so that small hydrologically-important features, such as stream beds, are accurately mapped. Improved resolution can potentially be achieved by generating DEMs using radar data.

In June 1996, the NASA/JPL AIRSAR system collected interferometric synthetic aperture radar (INSAR) data over low-relief regions on the coast of Texas, USA. To collect INSAR data, the AIRSAR system operates in its topographic (TOPSAR) mode. Figure 2 shows two mosaicked TOPSAR frames over Mission Bay, Texas. The ground-range-projected TOPSAR DEMs have data spacings of 10 m horizontally and 0.1 m vertically. The TOPSAR data are within sensor specifications in terms of rms height error [3]. However, small systematic height errors are still visible in the original DEMs because the area has such low relief. This paper describes some of the errors observed in the data and outlines the procedures used to minimize those errors and mosaic the DEMs.

INSAR BACKGROUND

DEMs, like those produced by the USGS, have traditionally been derived from stereo processing of aerial photography or optical spaceborne data. In recent years, DEMs have also been derived from SAR data using interferometric processing. The data for INSAR DEMs may be acquired day or night and in most weather conditions, but the primary advantage of INSAR methods is that the elevation of each pixel is determined independently. In stereo-optical DEMs, individual pixels are binned into discrete elevations to create noise-free closed-contour topographic maps. The primary disadvantages of INSAR DEMs are their sensitivity to sensor motion and their noise characteristics.

DEMs can be generated from INSAR data by combining two complex (phase and magnitude) SAR images acquired from similar vantage points [4]. Once the two images are co-registered, a differential phase can be calculated for each pixel. Using a known position of at least one pixel and unwrapping the modulo 2π phase, a map of absolute phase differences is generated. Geometric relationships can then be used to create a height map (DEM) relative to the radar position. The height map can be referenced to a geocentric coordinate system by collecting Global Positioning System (GPS) data onboard the sensor platform.

Most of the work to date in generating INSAR DEMs has focused on data collected from spaceborne systems using multiple observations (repeat-pass). In particular, the European Remote Sensing satellites (ERS-1 and -2) have been used extensively for this purpose [5]. However, any

This work was supported by the Texas Regional Change Program through the Texas Space Grant Consortium and the Johnson Space Center, a National Aeronautics and Space Administration grant under the Topography and Surface Change Program (Grant NAG5-2954), and the Texas Advanced Technology Program.

0-7803-3836-7/97/$10.00 © 1997 IEEE

changes that occur in surface or atmospheric conditions in the imaged area between observations will introduce errors into the subsequent DEM. The shortest time interval between observations suitable for INSAR processing is about one day for the tandem ERS system [6]. Significant changes in the backscattering properties of the surface or refractive properties of the atmosphere due to precipitation or humidity changes can occur on this time scale, thus reducing the number of suitable image pairs [7].

INSAR systems with more than one antenna, such as TOPSAR, can make dual observations simultaneously so that decorrelation of the scene through time is not a factor. This is especially important for vegetated, humid regions, such as the Texas coast, which can decorrelate rapidly. TOPSAR data are also available at higher spatial resolution than currently-available spaceborne data, (e.g. 25 m for ERS-1). This improves the mapping of small-scale features. The primary disadvantage of single-pass airborne systems is that the platform motion is perturbed more frequently and in a less deterministic manner than spaceborne platforms. Standard processing of TOPSAR data does include motion compensation, but if the motion is severe or high-frequency, residual errors on the order of ± 1.5 m may be observed in the DEMs. If the actual topographic variations are on the order of ≤10 times this magnitude, the error signal may be visible in the DEMs.

TEST SITE

TOPSAR flightlines were acquired along coastal stream beds in the San Antonio-Nueces watershed on the Texas coast. This watershed is located on a low-lying coastal plain. Flightlines were oriented approximately normal to the shoreline to observe the topography along the streams that carry most of the water runoff to the bays. The topographic variation in the 20 km nearest to the shore is only about 13 m. The TOPSAR data analyzed for this paper are from a flightline over Mission Bay. Hurricane models implemented for similar areas along the Texas coast predict storm surge penetrations of up to 15 km inland for a category 1 hurricane (74-95 mph winds), with flooding distributions that are highly dependent upon small topographic variations such as stream beds [1].

CHARACTERIZING THE DATA

1st order errors in the TOPSAR DEMs are manifest as planar tilting in range. This tilting is the result of uncompensated path delays in the radar system. When mapped into heights, those time delays can produce linear slopes in the DEMs. The DEMs can also exhibit higher order errors due to aircraft motion. Errors due to aircraft motion were observed in one of the TOPSAR frames over the Mission Bay test site.

Two adjacent 10 km x 10 km TOPSAR frames were acquired from a single flightline. A periodic signal superimposed on the topography was apparent in one of the frames. This "ripple" was primarily a function of azimuth, but also exhibited a weak inverse dependence on range. The approximate peak-to-peak amplitude was 3 m, and there were 8 complete periods in the frame. A printout of the aircraft motion file was obtained and the ripple signal appeared to be exactly correlated with the roll motion of the aircraft, which exhibited an 8 Hz frequency and peak-to-peak amplitude of 1°. Neither yaw nor pitch motion exhibited any significant correlation with the ripple signal.

TOPSAR DEMs have demonstrated relative rms height errors of 1-2 m in relatively flat areas [3]. The DEMs acquired over this test site exhibited rms error levels well within those reported levels. The residual errors due to aircraft motion were visible because nearby storms produced excessive turbulence during the acquisition and the total topographic variation in the test site is only about 10 times the magnitude of the residual signal.

ERROR REMOVAL AND EVALUATION

To produce a mosaicked DEM strip from individual TOPSAR frames, the relative errors must be corrected. After an internally consistent DEM strip is produced, it can be georeferenced using GPS data collected on the ground. The following procedures were followed.

1.0 Correct relative errors
- 1.1 filter out the motion signal
- 1.2 image-to-image registration
  - 1.2.1 1st order correction of elevations
  - 1.2.2 standard 2-dimensional registration
- 1.3 smooth noise over low-backscatter targets

2.0 Georeference the DEM strip
- 2.1 image-to-GPS registration
  - 2.1.1 1st order correction of elevations
  - 2.1.2 standard 2-dimensional registration

It is necessary to correct the relative errors before georeferencing so that overlapping portions of adjacent DEMs will only differ to a 1st order. A stop-band Infinite Impulse Response (IIR) filter was used to remove the ripple signal. The filter removed the 8 Hz ripple while preserving small-scale topographic features.

Elevations of features in the overlap between the two DEMs were used to add the best planar correction (in a least squares sense) to the slave DEM to obtain agreement with the master DEM's elevations to a 1st order. Those same control points were then used to do a 2-dimensional image-to-image registration to mosaic the two DEMs. JPL is currently developing the capability to output continuous strips of TOPSAR data, which will eliminate the need for mosaicking frames on a single flightline. Some open water areas in the far range of the DEMs exhibited very low signal to noise ratios (SNR), which were manifest as regions with very high-frequency, large-magnitude noise. These areas were assigned a constant elevation equal to elevation of the surrounding bank.

Georeferencing the DEMs was accomplished via 3-dimensional registration to GPS tie points after the DEMs were made internally consistent and mosaicked. The DEMs are georeferenced during the operational processing at JPL by giving the latitude/longitude of the scene center, but more accurate *in situ* georeferencing is needed for the DEMs in low-relief areas.

Static GPS points were collected for georeferencing, but more static GPS points will be collected to validate these results. Kinematic GPS transects have also been collected along several roads in the imagery, but the solutions have not yet been analyzed. Figure 3 shows transects extracted from the co-registered TOPSAR and USGS DEMs. The transects show that the superior resolution of TOPSAR allows it to capture topographic variations that are not resolved in the USGS DEM. The TOPSAR data also exhibit greater variability due to noise and non-surface features such as trees.

CONCLUSIONS

The higher-order errors observed in these data do not appear to be significant in most TOPSAR DEMs. The errors were visible in these data because of the extreme low-relief of the region and the proximity of storms during the acquisition.

Future work will include improvements to the filtering of the motion signals and validation of the results with more GPS surveys. However, these preliminary results do indicate that systematic errors can be minimized and precise DEMs can be generated for low-relief areas using TOPSAR data.

REFERENCES

[1] Texas A&M University, College of Architecture, Storm Atlas: Brazoria, Galveston, and Harris Counties, Texas A&M University, pg. 3-1, September 1993.

[2] United States Geologic Survey (USGS), Digital Elevation Models: Data Users Guide 5, USGS, pg. 14, 1993.

[3] Madsen, S. N., J. M. Martin, and H. A. Zebker, "Analysis and Evaluation of the NASA/JPL TOPSAR Across-Track Interferometric SAR System", *IEEE Trans. Geosci. Remote Sensing*, vol. 33, no. 2, pg. 383-391, March, 1995.

[4] Zebker, H. A. and R. M. Goldstein, "Topographic Mapping from Interferometric Synthetic Aperture Radar Observations", *Journal of Geophysical Research*, vol. 91, no. B5, pg. 4993-4999, April 10, 1986.

[5] Massonnet, D. and K. L. Feigl, "Discrimination of Geophysical Phenomena In Satellite Radar Interferograms", *Geophysical Research Letters*, vol. 22, no. 12, pg. 1537-1540, June 15, 1995.

[6] Schwäbisch, M., M. Matschke, W. Knöpfle, and A. Roth, "Quality Assessment of INSAR-Derived DEMs Generated With ERS Tandem Data", *Proceedings of IGARSS'96*, pg. 802-804, 1996.

[7] Kenyi, L. W. and Hannes Raggam, "Atmospheric Induced Errors In Interferometric DEM Generation", *Proceedings of IGARSS'96*, pg. 353-355, 1996.

FIGURES

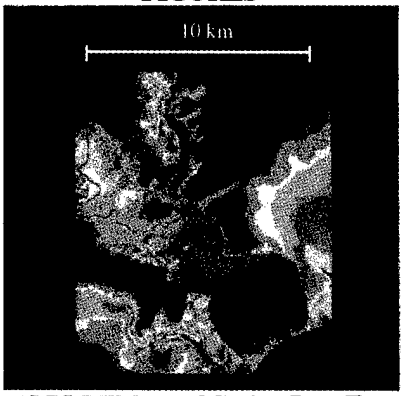

Fig. 1: USGS DEM over Mission Bay, Texas, USA

Fig. 2: TOPSAR DEM over Mission Bay, Texas, USA

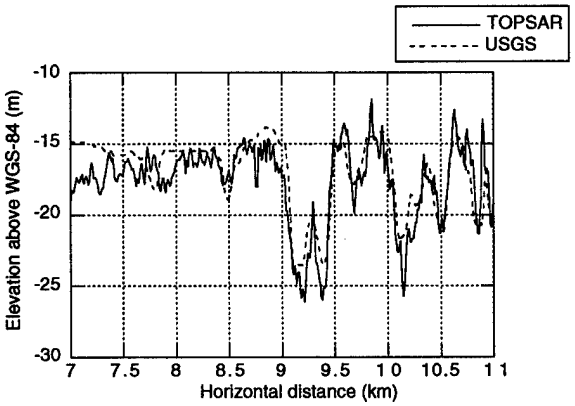

Fig. 3: Transects extracted from co-registered DEMs

Digital Elevation Models from SIR-C Interferometric and Shuttle Laser Altimeter (SLA) data

G. Sun[1] and K. J. Ranson[2]

[1] Univ. of Maryland, Department of Geography, College Park, MD 20742 USA. Tel: (301)286-2485, Fax: (301)286-0239, E-mail: guoqing@aspen.gsfc.nasa.gov

[2] NASA's GSFC, Biospheric Sciences Branch, Code 923, Greenbelt, MD 20771 USA. Tel: (301)286-4041, Fax: (301)286-1757, E-mail: jon.ranson@gsfc.nasa.gov

ABSTRACT

Because of the uncertainties of orbit parameters and baseline, the accuracy of the DEM derived from SIR-C/XSAR interferometric data is limited. In this paper, we describe the use of SLA (Shuttle Laser Altimeter) data as tie-points to construct a DEM from SIR-C interferometry data. The methods and results using preliminary SLA are reported and discussed.

INTRODUCTION

In April and October 1994, the Space radar Laboratory (SRL) aboard shuttle Endeavor measured the surface radar backscatter intensity and phase at similar orbits, and especially during the October flight (SRL-2) collected 1-day repeat interferometric data. These repeat SIR-C/XSAR interferometric data have been used for topographic mapping [1-2]. Successful implementation of interferometric topographic mapping requires that both the uncertainty in the baseline components and the phase noise be minimized [3]. Baseline estimation is a key step in estimation of topography from near-repeat pass radar interferometric data. For SIR-C data, 10 meters accuracy in height requires 5 mm accuracy in baseline [6]. This is not possible without using calibration data.

Two methods have been used to improve the baseline estimation: using tie-points [3,4] or existing DEM data [5]. Both methods require careful registration of elevation data to a radar reference image. If the height measurement of the tie-points is accurate, and more than 5 points per 50 km^2 are used, the error in the baseline components has been reported to be in the centimeter level [6].

In this paper, we describe the use of SLA data as tie-points to construct a DEM from SIR-C interferometry data. The methods and results using preliminary SLA data are reported and discussed.

DATA DESCRIPTION

SIR-C Interferometry Data:

Two L-band SIR-C interferometric Single-Look Complex images over Pu'u O'o, Hawaii were used. The images were acquired at 22:54 GMT, Oct. 7, 1994 and 22:31 GMT, Oct. 8, 1994, respectively, with incidence angle of 61.2° and ground tracing angle of 146.0°, right-looking. Figure 1 shows the SIR-C image coverage and SLA path.

SLA data:

The SLA-01 (Shuttle Laser Altimeter-01) was flown from January 11 to 20, 1996 on Mission STS-72 [7]. The pulse rate of SLA-01 is 0.1 seconds, corresponding to a horizontal sampling distance of about 740 m and a 100 m footprint. Precise orbits have been computed from Tracking and data Relay Satellite System (TDRSS) Doppler observations [8]. A new technique utilizing TOPEX/Poseidon's (T/P) precise orbit knowledge plus the TDRSS-T/P Doppler tracking was used to significantly reduce the TDRS orbit errors. The SLA observations of the ocean surface have been compared to the Ohio State Mean Sea Surface 95 plus the effect of tides computed using the Ray Ocean Altimeter Pathfinder tide model. The ocean height comparisons show the SLA SDP v2 (Standard Data Product Version 2) to be at the level of 2-3 meter RMS in height, and horizontal positioning is estimated to be less than 200 meters. This data is available at Web site http://denali.gsfc.nasa.gov/research/laser/sla. Future Enhanced

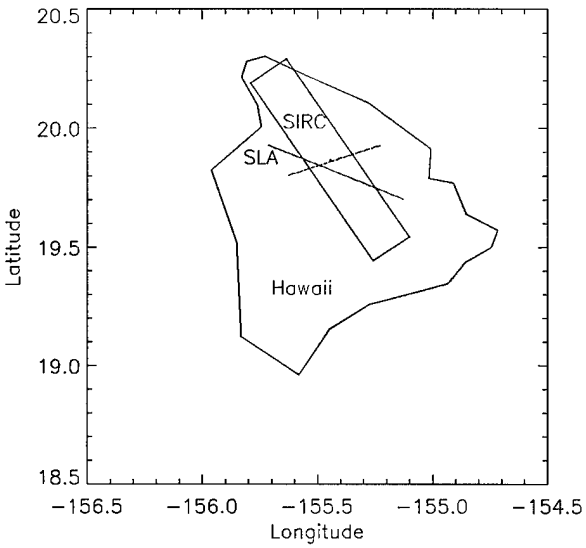

Figure 1. Coverage of SIRC images and SLA path.

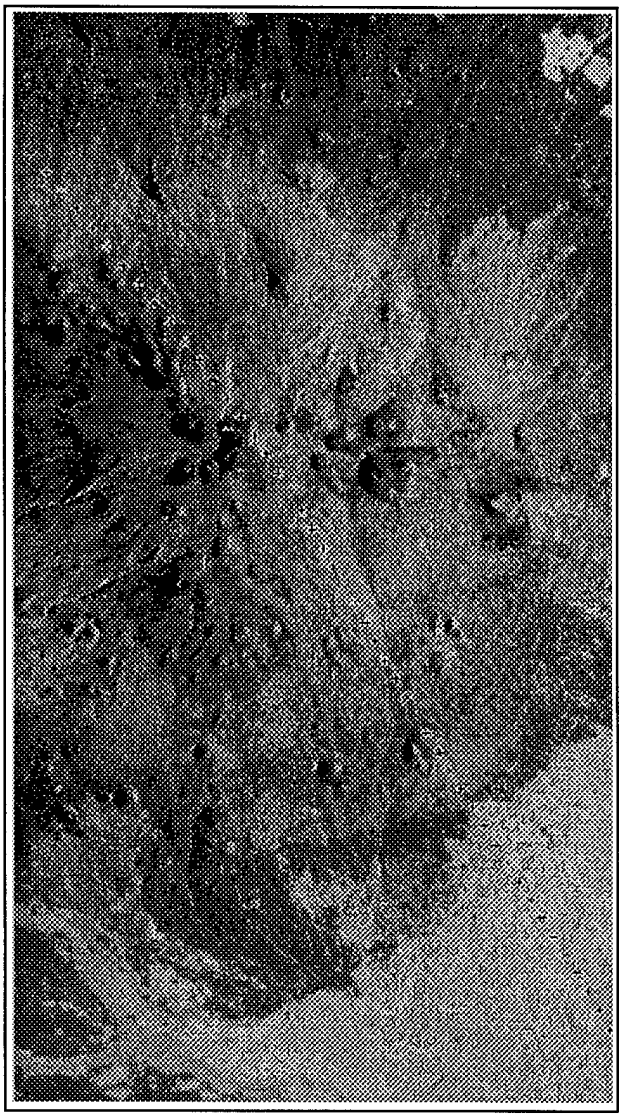

Figure 2. A part of L-band VV-pol SIR-C image with SLA data points registered (+).

Data Product (EDP) will become available with RMS height of 1 m and less than 100 m horizontal positioning error. Because there is only one descending SLA path in the SIR-C data used in this study, another ascending path was assumed and the elevation of these points were read from USGS 1:250000 DEM model. Figure 1 shows the SIR-C image coverage and SLA path (solid), and an assumed ascending SLA path (dotted).

METHODS

Registration of SLA data points to radar reference image:

The latitude, longitude and height of a tie-point were used to map it onto SIR-C slant-range image using SIR-C imaging parameters. Figure 2 shows part of the SIR-C image with SLA data points (+).

Baseline estimation:

The slant range difference between two orbits from a pixel can be expressed as:

$$\Delta r = r_2 - r = \sqrt{r^2 - 2rB\sin(\theta - \alpha) + B^2} - r \quad (1)$$

where r and r_2 are the slant ranges in the reference and repeat orbits, respectively. B is the baseline, Θ is the radar look angle and α is the angle of the baseline with respect to horizontal. This range difference Δr is related to the pixel offset between the two interferometry images. If there are no tie-points, i.e. no height information for any points, Δr can be directly calculated from the positions of a pixel on two radar images by assuming a spherical Earth. Since the two SIR-C orbits may be not parallel, a matrix of points in the reference image with high correlation and lower phase noise were used to estimate the baseline in an iterative least-square fit process.

Conversion of phase difference to height

A DEM was first generated from the baselines estimated above. A profile of the terrain heights at the SLA data points were extracted and plotted in Figure 3 as "Interferometry 1", which shows that this DEM is tilted.

Using SLA data to improve baseline estimation:

The SLA data were used to correct this tilt by a two dimensional linear least square fit. The calibrated DEM then was used for refining the baseline estimation as follows. The interferometric topography accuracy is also dependent on the uncertainty of interferometer phase, and the phase noise can be reduced by maximizing the correlation [3]. The pixels with correlation greater than 0.85 were selected to form a new set of points. The pixel offsets at these points were estimated from amplitude cross-correlation with image oversampling of 2. The height of these points were extracted from the calibrated interferometric DEM. The baselines were then estimated using the same iteration fit of Equation 1, with the slant range r as a

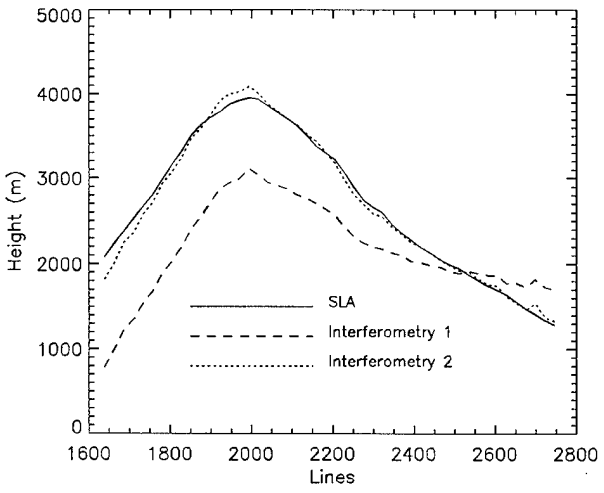

Figure 3. Comparisons of height estimation from SIR-C interferometry data with SLA data. The 'Interferometry 2" is the result using refined baseline.

function of local height. The refined baselines were then used to convert the unwrapped interferogram into a new topographic map. The height profile extracted from this map along SLA path were also plotted in Figure 3 (Interferometry 2), which shows the improvement of the height estimation. Figure 4 is this topographic map, which is not fully spatially interpolated and smoothed. The small bright spots are where phases were not unwrapped because of low correlation/high phase noises, so no height data were estimated.

SUMMARY

The elevation data from Shuttle Laser Altimeter were used to improve the baseline estimation in SIR-C interferometric processing. The improvement depends on the accuracy of the SLA data, as well as image processing procedure, especially the data registration. The SLA data used in this study are not the best products from SLA-01 mission. When the Enhanced Data Product is available, an iterative analysis will be conducted to evaluate the improvement in SIR-C interferometric height mapping by using SLA data as tie-points.

ACKNOWLEDGMENTS

Many thanks to Drs. Howard Zebker, Eric Fielding, and Wei Xu for providing software and advice on interferometric data processing.

REFERENCES

[1] P. A. Rosen, S. Hensley, H. A. Zebker, F. H. Webb, and E. J. Fielding, Surface deformation and coherence measurements of Kilauea Volcano, Hawaii, from SIR-C radar interferometry, Journal of Geophysical Research, Vol. 101, No. E10, pp. 23,109-23,125, Oct. 1996.

[2] R. Lanari, G. Fornaro, D. Riccio, M. Migliaccio, K. P. Papathanassiou, J. R. Moreira, M. Schwabisch, L. Dutra, G. Puglisi, G. Franceschetti, and M. Coltelli, Generation of digital elevation models by using SIR-C/X-SAR multifrequency two-pass interferometry: the Etna case study, IEEE Transaction on Geoscience and Remote Sensing, Vol. 34, No. 5, pp.1097-1113, Sept. 1996.

[3] H. A. Zebker, C. L. Werner, P. Rosen, and S. Hensley, Accuracy of topographic maps derived from ERS-1 radar interferometry, IEEE Transactions on Geoscience and Remote Sensing, Vol. 32, No. 4, pp.823-836, July 1994.

[4] D. Small, C. Werner, and D. Neusch, Baseline modeling for ERS-1 SAR interferometry, IGARSS'93, pp. 1204-1206, Tokyo, Aug. 1993.

[5] M. Seymour and I. Cumming, InSAR' terrain height estimation using low-quality sparse DEMs, 3rd ERS Symposium, Florence, March 1997.

[6] H. A. Zebker, "Interferometric SAR processing tutorial", 1996.

[7] J. B. Garvin, J. B. Blair, J. L. Bufton, and D. J. Harding, The Shuttle Laser Altimeter (SLA-01) Experiment, EOS Transactions of the American Geophysical Union, Vol. 77, No. 7, pp. S239, April 1996.

[8] D. D. Rowlands, S. B. Luthcke, J. A. Marshall, C. M. Cox, R. G. Williamson, and S. C. Rowton, Space shuttle precision orbit determination in support of SLA-01 Using TDRSS and GPS tracking data, Journal of Astronautical Sciences, Vol. 45, No. 1, January-March 1997.

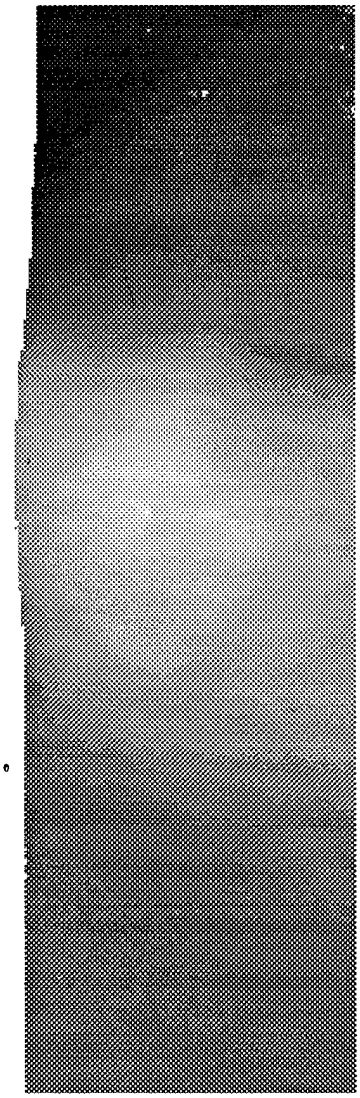

Figure 4. Height map generated from SIR-C interferometry data.

IGARSS'97

1997 International Geoscience and Remote Sensing Symposium

03-08 August 1997

Singapore International Convention & Exhibition Centre

Technical Program

Interactive Area 23: SAR Techniques

A High Precision Workstation–Based Chirp Scaling SAR Processor

Helko Breit, Birgit Schättler, Ulrich Steinbrecher

German Aerospace Research Establishment (DLR)
German Remote Sensing Data Center (DFD)
Oberpfaffenhofen, D–82234 Wessling, Germany
phone: +49–8153–28–1396, fax: +49–8153–28–1420, e–mail: Helko.Breit@dlr.de

Abstract —In order to meet the challenges of new spaceborne multi–mode SAR sensors and missions, a multi–sensor chirp scaling SAR processor is currently under development at the German Remote Sensing Data Center DFD. High precision data processing is ensured by floating point data representation, frequent processing parameter update as well as the underlying phase preserving chirp scaling algorithm enhanced to deal with arbitrary Doppler centroid variations over range. The availability of high performance general purpose computers enables the use of standard programming languages and hardware, even if a high throughput is required for operational applications. Multithreading software techniques lead to scalable processing systems running efficiently on different platforms ranging from single CPU workstations to multiprocessor systems.

This paper describes the algorithms, the design and the implementation concept of this highly flexible SAR processor. Detailed image quality and throughput results based on simulated as well as real SAR data are presented.

INTRODUCTION

Since 1980, operational SAR data processing has been performed at the German Remote Sensing Data Center DFD for a series of space–borne SAR sensors (SEASAT, ERS–1/2, J–ERS and X–SAR). All processors installed, including the in–house developed X–SAR precision processor, are range–Doppler implementations using specialized hardware (e.g. an array processor). Their usage is restricted to routine operational production work for which they are more or less tailored.

In the mean time, the on–going SAR and InSAR algorithm developments as well as the off–line calibration, validation and product quality support work, revealed the growing demand in a flexible, configurable and extendable SAR processor running completely on a general purpose computer.

The most prominent requirements put onto this new processor development were:

- enable multi–sensor SAR processing, at least for ERS, X–SAR and Radarsat,
- ensure a phase–preserving processing using the chirp scaling algorithm CSA [1],
- facilitate further processor expansions, especially for ScanSAR,
- serve as a basis for future operational SAR processor.

In its experimental instantiation, the processor will be used for the processing of single–beam as well as ScanSAR Radarsat data within the working frame of an on–going NASA ADRO proposal [2]. The first and very important operational use will be the processing of interferometric data from the X–SAR sensor to be flown as part of the Shuttle Radar Topography Mission SRTM scheduled for 1999 [3].

PROCESSOR SYSTEM LAYOUT

The major requirements cited above called for a very modular system design. Therefore, the processor system is built up of several independent SAR components (being program executables), which are meant to perform specific SAR processing steps. These components are passive in that sense, that they don't communicate with each other (no mutual activation).

The processor setup and control (e.g. in terms of component activation) is done by a supervisor module. The parameter exchange between the components is done via an ASCII parameter pool, the signal data itself are transported using plain binary data files. Each SAR component has a command line interface and gets its control parameter (file names etc.) from an individual process control file. It returns its status (failure, success etc.) in a status file.

As a consequence of this modular concept, new modules can be plugged into the processor by just taking care of the appropriate binary data and ASCII parameter interfaces. There is no restriction on the programming language used. Individual components may even run on different hardware platforms. The ASCII parameter representation enables a direct processing parameter monitoring.

The modularity of the system is furthermore supported by an object–oriented software development approach. Ada has been chosen as programming language. A comprehensive SAR software library has been coded, which provides the basic functionalities required for SAR processing (e.g. time system handling, orbit calculations, range and azimuth processing, block merging and deskewing).

All components are classified into sensor–dependent and sensor–independent ones. The sensor–dependent functionalities

0-7803-3836-7/97/$10.00 © 1997 IEEE

are restricted to as few components as possible, i.e. to those components which are in charge of raw data input, telemetry analysis, orbit and external parameter handling as well as final product annotation parameter handling. Fig.1 gives a simplified view of the functional processor decomposition (data and control flow):

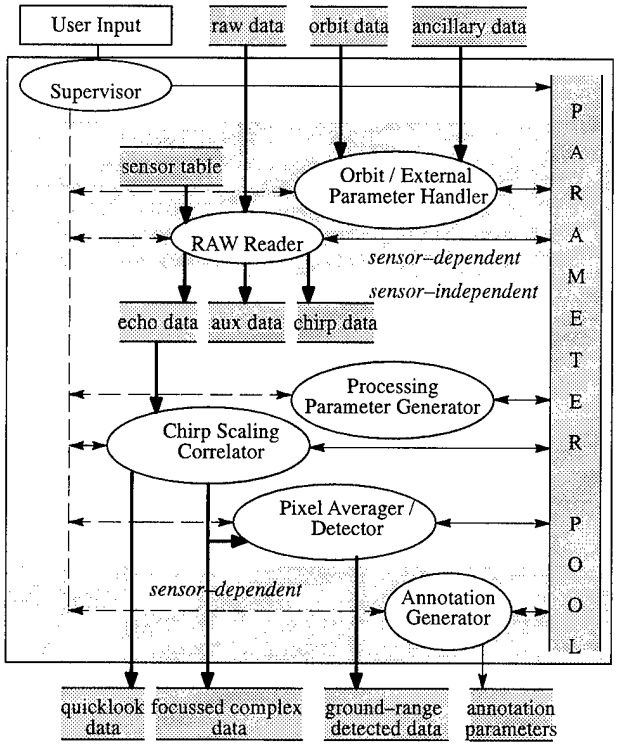

Figure 1: Simplified system diagram

For each sensor, a *RAW Reader* component takes care of the decomposition of the unprocessed data into echo, auxiliary and replica data. It splits ScanSAR echo data into separate beams. Processing relevant telemetry parameters are evaluated. The *Orbit Handler* transforms a given orbit into a scene–related earth–centered state vector description. The *Processing Parameter Generator* provides processing parameters like the azimuth frequency rate. The *Pixel Averager / Detector* generates ground–range projected resampled data sets. The *Annotation Parameter Generator* finally provides the product annotation parameters. The sensor–independent generic single beam *Chirp Scaling Correlator* is the heart of the processor system. It correlates the unprocessed echo data into complex focussed data sets. A detailed description follows.

CHIRP SCALING ALGORITHM

The implementation of the chirp scaling algorithm is based on [4] and [5]. The following explanation summarizes the principles of this algorithm.

In the first step the SAR raw data is Fourier transformed into the range–Doppler domain. Thus, the range pulse frequency rate K becomes dependent on the azimuth frequency f. This allows for secondary range compression (SRC) during range compression (RC) depending on f, which is a great advantage compared to the Range–Doppler algorithm. Prior to RC each range line is multiplied by the chirp scaling phase function. This function is a quadratic function of range time τ depending on azimuth frequency f. This operation removes the range dependency of the range cell migration (RCM). The following multiplication of the data with the range compression filter in the frequency domain implicitly performs the RCM correction (RCMC) and SRC. This way an explicit interpolation step as in the range–Doppler algorithm is avoided. After a back transformation into the range–Doppler domain the range compressed data is multiplied by the azimuth compression filter which contains an additional phase term taking into account the phase perturbation caused by the chirp scaling multiplier.

CORRELATOR FUNCTIONAL DESCRIPTION

The chirp scaling correlator is designed to generate focussed images of arbitrary scene length. Therefore, consecutive overlapping azimuth blocks are focussed, merged and deskewed. The block length in azimuth direction can be up to 16K. Range dependent parameters are updated at pixel level, azimuth dependent parameters at block level. All filtering operations preserve the original raw data sampling grid, thus, successive SAR images may be combined without resampling. Fig. 2 gives a schematic overview of the correlator.

In the *initiation* phase the scene length and the range swath of the final image are determined. One azimuth block is kept in memory for all signal processing steps.

Raw data correction comprises missing lines correction, A/D converter corrections, data window and gain setting changes. All correction values may be updated at a range line by range line level.

Since CSA requires a quadratic phase function an optional *range precompression* step allows for the incorporation of a variety of range pulse functions. After range focussing the data has to be smeared out again by an ideal range chirp. The new range chirp may be much shorter then the original range pulse, thus, the quality of a successive Doppler centroid estimation is improved.

Range processing is performed in the range–Doppler domain. They data are left in their baseband representation during processing. Since CSA depends on the unwrapped azimuth frequency f, each range line has to be decomposed into segments of constant f. After RC, SRC and RCMC the segments have to be rearranged into one range line.

Azimuth compression is followed by a *block merging* step. Incomplete zero Doppler deskewed range lines of the previous azimuth block are kept in a so–called block merging buffer

(BMB) and are merged with the current azimuth block data. *Deskewing* of the current azimuth block is done on the fly during the write to disk operation.

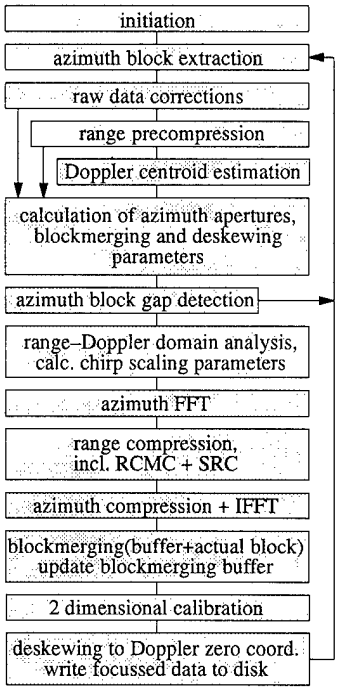

Figure 2: Chirp scaling correlator, schematic overview

IMAGE QUALITY MEASUREMENTS

The focussing quality has been demonstrated on simulated X–band point targets tainted by a high Doppler centroid variation over range (120 Hz/μs) and azimuth (300 Hz/s). The range and azimuth resolution of the measured point targets are at their theoretical limits. Fig 3. shows the interpolated azimuth cut of a focussed point target affected by a Doppler centroid of –22.5 kHz. The range and azimuth PSLR are also as expected (az. –19.3 dB, rng. –13,1 dB).

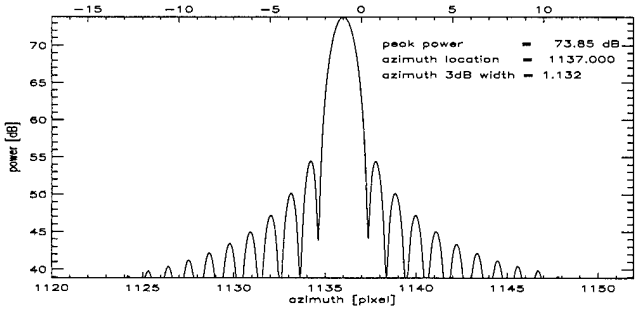

Figure 3: Interpolated point target, azimuth direction

Furthermore. an ERS–1 Flevoland scene (acquired on August 03, 1995) has been processed. A point target analysis has been performed on the three ESA transponders. The azimuth resolution has been measured to be 5.4 m, the range resolution about 10 m, values being common for operational ERS SAR processors. All other parameters are also according to expectation.

Four 100 km by 100 km ERS tandem scenes have been phase preservingly processed to interferometric pairs. These pairs have been successfully processed with the new DFD InSAR processor GENESIS [6]. Interferometric offset tests ([7], [8]) with simulated noise and ERS–1 data showed the processor introduced phase noise to be in the order of 0.5 deg .. 2.0 deg for single look data

PARALLELISATION AND THROUGHPUT

All processing steps which access the data in memory (except deskewing and block merging) have been individually parallelised. This has been achieved by embedding independent operations into Ada task objects which are automatically mapped to threads by the operating system. At about 88% of the overall execution time the processor code is running on all available CPUs. The operational processor hardware environment consist of a SUN ET4000 equipped with 8 167Mhz UltraSparc CPUs. The processing time for 100km by 100km ERS1 scene is less then 20 minutes. The same code runs without limitations on a single CPU workstation.

REFERENCES

[1] R. K. Raney, H. Runge, R. Bamler, I. G. Cumming, F. H. Wong, "Precision SAR processing using chirp scaling", IEEE Transactions on Geoscience and Remote Sensing, vol. 32, pp. 786 – 799, 1994.

[2] R. Bamler, "Multiscale Topography Reconstruction from Radarsat Multi–Mode Interferometric Data", Radarsat ADRO proposal, approved by NASA, Project ID no 25

[3] Shuttle Radar Topography Mission, Presentation, JPL, Aug. 15, 1995

[4] G. W. Davidson, "Specification for Chirp Scaling Single Beam Correlator", Technical Note, DLR, 1995

[5] G. W. Davidson, "Image Formation From Squint Mode Synthetic Aperture Radar Data", Ph.D.Thesis, Univ.of British Colombia, 1994

[6] M. Eineder, N. Adam, "A Flexible System for the Generation of Interferometric SAR Products", to be presented at IGARSS'97, Singapore

[7] R. Bamler, B. Schättler, "Phase–Preservation in SAR Processing: Definition, Requirements and Tests", Technical Note, DLR, May 1995

[8] B. Rosich Tell, H. Laur, "Phase Preservation in SAR processing: The Interferometric Offset Test", Proc. IGARSS'96, pp. 477–480, 1996

Automated Acquisition of Ground Control Using SAR Layover and Shadows

M. Gelautz [1], E. Mitteregger [1], and F. Leberl [2]

[1] Institute for Computer Vision and Graphics, Technical University Graz,
Münzgrabenstraße 11, A-8010 Graz, Austria
Tel.: ++43/316/873-5031, Fax: ++43/316/873-5050, Email: gelautz@icg.tu-graz.ac.at
[2] Currently on leave and with the Austrian Research Center Seibersdorf,
A-2444 Seibersdorf, Austria

Abstract – We present an algorithm which uses SAR layover and shadows for the automated acquisition of ground control. The control points are then utilized to refine the SAR sensor parameters. Tests are carried out on ERS-1 and X-SAR images of the Austrian Alps. The accuracy of the layover/shadow matching algorithm is assessed by comparison with the results obtained by conventional cross-correlation of real-simulated gray value images.

1. INTRODUCTION

The acquisition of ground control points (GCPs) between a map and SAR image is an important prerequisite for the geocoding of SAR images, since sensor flight path and other SAR processing parameters are normally only approximately known. However, the manual determination of GCPs constitutes a tedious and time-consuming task, especially in mountainous regions, where terrain induced distortions are strongest. In order to overcome the dissimilarities between the map and image geometry, the use of simulation and subsequent determination of match points between the real and simulated image has been suggested by several authors (e.g., [3], [6], [5], and [2]).

The algorithm we propose is specially suited to SAR imagery of high-relief terrain where layover and shadows occur frequently and are distributed all across the image. It differs from most other simulation based approaches in that it does not require the simulation of the complete gray value image, but only the determination of the location of layover and/or shadows. Thus the problems which are normally associated with the proper modeling of SAR backscatter and the suppression of real-simulated radiometric differences in the matching procedure (see [2]) are avoided.

Previous research on the use of layover and shadows as features for matching was carried out by [7] and [8]. Contrary to our study, the aim of [8] was not to develop a fully automated system, but to provide support to a human operator in an interactive procedure. The algorithm developed by [7] relies on vectorizing shadow boundaries and searching them for points of high curvature. Examples of established correspondences are shown, but no quantitative analysis of the matching accuracy is presented. Layover was not considered in that work.

In the following, we review the principles of our layover/shadow (L/S) matching algorithm and present some results obtained from tests on ERS-1 and X-SAR images of a rugged terrain in the Austrian Alps.

2. TEST SITE

Our study area is the Oetztal, a high alpine X-SAR/SIR-C "super-test-site". The area exhibits strong topographic relief, with elevations ranging from 1750 m to more than 3750 m. The available DEM has a grid width of 25 m, and a height accuracy of better than 20 m. It covers an area of approximately 26 km x 16 km.

The layover version of our algorithm was tested on an ERS-1 subscene (23 deg look angle, descending orbit). The matching of shadow features is demonstrated in its application to an X-SAR image acquired during an ascending orbit, at a look angle of 50 deg. Both images have a pixel size of 12.5 m x 12.5 m.

3. ALGORITHM

A software has been implemented which first searches a simulated layover and shadow map for suitable features for matching (chips). The presumed L/S regions in the corresponding real image are extracted by thresholding, with the threshold value being derived from the percentage of L/S pixels in the simulated map. A binary overlap technique is applied to compute for each selected chip the location of maximum overlap in the binarized real image. The match points are then employed to refine the SAR imaging model. We perform the parameter refinement by using an already existing optimization modul which is part of the RSG software package [4].

After sensor parameter refinement, the simulation is carried out once more with the now improved imaging model, and the algorithm is applied again to collect a new set of real-simulated match points. This second iteration step allows to verify the success of the previous refinement procedure. If necessary, a further stepwise refinement of the imaging model may be achieved iteratively, with each iteration loop containing the three steps *matching*, *refinement*, and *simulation*, until some predefined accuracy requirement is fulfilled.

4. EXPERIMENTS AND RESULTS

We tested our matching algorithm in its application to ERS-1 layover and X-SAR shadows. For both test scenes, the initial simulation parameters were those extracted from the SAR leader files; no previous manual adjustment of the sensor parameters was carried out.

Figs.1 and 2 show the real ERS-1 image before and after thresholding, respectively. The corresponding simulated

0-7803-3836-7/97/$10.00 © 1997 IEEE

gray value image is given in Fig.3. The synthetic ERS-1 and X-SAR images are used later to derive correlation based reference matches, in order to compare the results obtained by two different algorithms. The ERS-1 layover map produced by simulation can be seen from Fig.4: Layover areas are displayed in white, and the location of several automatically selected matching chips is marked. In our tests, a smaller chip extension in the range than in azimuth direction appeared to be more suitable than a square template, since it reflects the typical elongated shape of layover. Furthermore, in the spaceborne test data we have investigated until now, the scaling error due to imprecise sensor parameters was found to be clearly bigger in the range than in azimuth direction. Since the binary overlap - like any correlation technique - is based on the assumption of only negligible scaling errors, a too large chip extension in the range direction might therefore produce less accurate correlation results.

A detailed view of the overlap result obtained from one of these chips is presented in Fig.5. Note that there is a well-pronounced peak in the correlation surface shown in (d), which indicates the validity of the match.

A set of 27 (ERS-1) and 25 (X-SAR) match points, distributed all across the area covered by the DEM, was input to the RSG refinement modul. For both images, the main deviation between the assumed and actual image geometry was found to be a shift in both range and azimuth direction. Furthermore, a range scaling error of about 0.3 % was detected for ERS-1.

The simulations were then run again with the refined imaging model and a new set of match points was collected, in order to determine the remaining geometric distortions. Table 1 gives the differences between the absolute location of the real and simulated L/S match points in range (r) and azimuth (a) direction in terms of the mean value and standard deviation σ. For comparison, the correlation based matching algorithm CORR developed by [1] was applied to the corresponding real-simulated pairs of gray value images. A mean value and rms error of better than 0.5 pixels and 1.5 pixels, respectively, computed from the new L/S match points demonstrate that the refinement procedure has successfully eliminated the detected distortions. For ERS-1, comparable figures were obtained by algorithm CORR, which confirms our results. The X-SAR results produced by the two algorithms differ slightly more: A difference in $\overline{r}$ of 2.5 pixels, with no notable increase in the corresponding rms values, indicates a systematic shift between the two sets of match points.

Further tests based on threshold variations were carried out to investigate this effect. Generally, the shadow match points were found to be more sensitive to threshold deviations than their layover counterparts. This lack of robustness, together with a slightly asymetric distribution of shadow gray values - in our example, shadow pixels at the near range tended to be darker than at the far range - may be a possible explaination for the observed offset.

Table 1 Matching results after parameter refinement.

Data	Algorithm	$\overline{r}$ pixel	σ_r pixel	$\overline{a}$ pixel	σ_a pixel
ERS-1	L/S (layover)	0.2	1.3	0.0	1.0
ERS-1	CORR	0.2	2.2	0.9	1.3
X-SAR	L/S (shadows)	0.0	1.2	0.4	1.3
X-SAR	CORR	-2.5	1.6	-0.6	1.4

5. SUMMARY AND DISCUSSION

We have demonstrated that SAR layover and shadows, in conjunction with a binary overlapping technique, can be employed successfully for the automated acquisition of ground control and the subsequent imaging model refinement. After parameter refinement, deviations between the real and simulated ERS-1 image geometry could be described by a mean and rms error of less than 12 m and 28 m, respectively. This result was confirmed by comparison with match points delivered by conventional cross-correlation of image gray values.

The matching algorithm is straightforward, and hence easy to implement and fast. Furthermore, it has proven to be robust to SAR speckle; no previous filtering of the images was required. Regarding robustness to scaling errors, tests on resized images have shown that even at a range scaling error of 25 % corresponding features could still be identified. Further research would be needed to study the influence of inaccurate or low-resolution DEMs on the performance of the matching algorithm. The effects introduced by deviations between the actual and assumed initial sensor parameters are expected to be less critical due to the robustness of the algorithm and the possibility of a successive refinement in several iteration steps.

6. ACKNOWLEDGMENTS

The authors wish to thank Scott Hensley from NASA/JPL for providing his matching software. The ERS-1 and X-SAR data were made available by Dr. H. Rott from the University of Innsbruck. We gratefully acknowledge his cooperation. This study was funded by the Austrian Academy of Sciences and the Austrian Ministry of Science.

7. REFERENCES

[1] R. Frankot, S. Hensley, and S. Shafer. Noise resistant estimation techniques for SAR image registration and stereo matching. In *Proc. IGARSS'94, Pasadena, CA*, pages 1151–1153, 1994.

[2] B. Guindon. Performance evaluation of real-simulated image matching techniques in the acquisition of ground control for ERS-1 image geocoding. *ISPRS Journal of Photogrammetry and Remote Sensing*, 50(1):2–11, 1995.

[3] B. Guindon and H. Maruyama. Automated matching of real and simulated SAR imagery as a tool for ground control point acquisition. *Can. J. Remote Sensing*, 12(2):149–158, 1986.

[4] Institute for Digital Image Processing, JOANNEUM RESEARCH, Graz. *Remote Sensing Software Package Graz, Software User Manual*, 3.0 edition, 1993.

[5] H. Kimura and T. Iijima. Automated matching of real and simulated SAR imagery for geometric correction. In *Proc. IGARSS'90*, pages 309–312, 1990.

[6] R. Kwok, J. Curlander, and S. Pang. An automated system for mosaicking spaceborne SAR imagery. *Int. J. Remote Sensing*, 11(2):202–223, 1990.

[7] F. Leberl. *Radargrammetric image processing*, chapter 10. Artech House, Norwood, MA, 1990.

[8] M. Plößnig, W. Kropatsch, and D. Strobl. Sherlock supports the geocoding of SAR images. In A. Pinz, editor, *Wissensbasierte Mustererkennung*, pages 112–119. Oldenburg, Vienna, 1989.

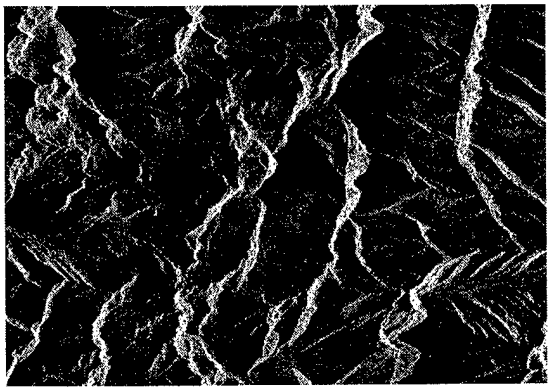

Fig.1 A 2412 x 1679 pixels subsection of an ERS–1 scene acquired of the Oetztal, Austria. The image was illuminated from the right.

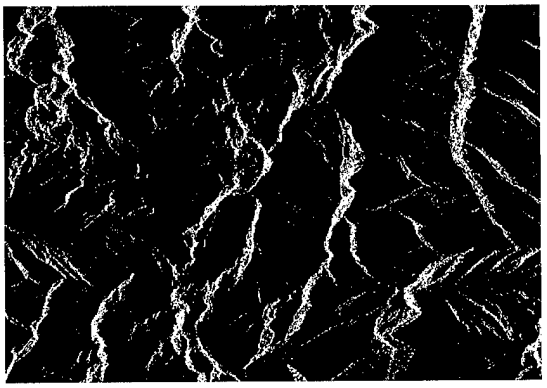

Fig.2 Layover candidates extracted from Fig.1 by thresholding.

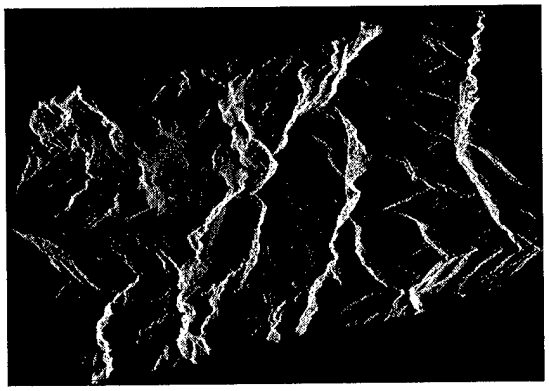

Fig.3 Simulated ERS–1 image corresponding to the actual image from Fig.1. The simulation was produced by assuming a cosine reflectance model.

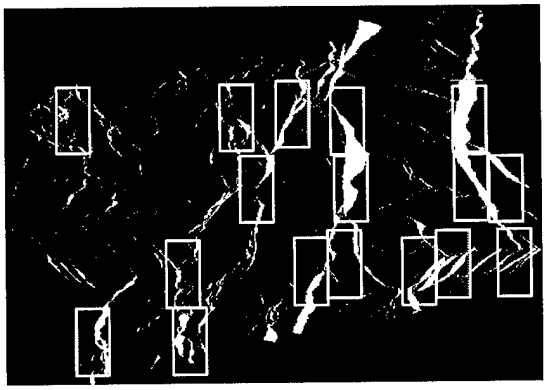

Fig.4 The simulated layover map with examples of automatically selected matching templates. Chip size is 150 x 300 pixels.

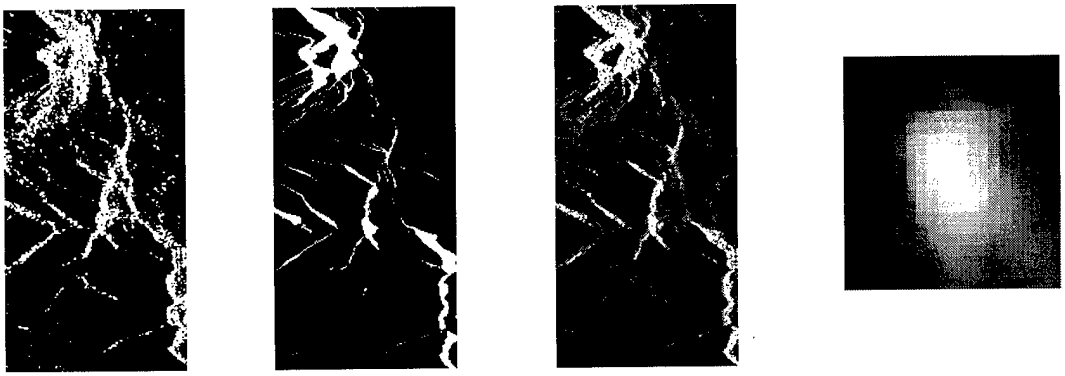

(a) (b) (c) (d)

Fig.5 A detailed view of a real (a) and corresponding simulated (b) chip at the position of maximum overlap (c). White pixels in (c) denote layover in both the real and simulated mask, gray pixels in only one of them. Subfigure (d) shows the gray value encoded correlation surface (21 x 21 pixels).

An accelerated chirp scaling algorithm for synthetic aperture imaging

D. W. Hawkins
California Institute of Technology—Owens Valley Radio Observatory,
Big Pine, CA 93513, e-mail: dwh@ovro.caltech.edu.

P. T. Gough
Department of Electrical and Electronic Engineering, University of Canterbury,
Christchurch, New Zealand, e-mail: gough@elec.canterbury.ac.nz.

Abstract— **The accelerated chirp scaling (ACS) algorithm is based on the chirp scaling (CS) algorithm, with the difference that the ACS algorithm processes pulse compressed data. To remove the range variant nature of the system impulse response, the ACS algorithm operates by chirp scaling the linear frequency modulated (LFM) signal that already exists in the range-Doppler domain of the pulse compressed data. This LFM signal is commonly compensated for in the CS algorithm and the range-Doppler algorithm by secondary range compression (SRC). Chirp scaling of the uncompensated SRC signal allows the ACS algorithm to operate on pulse compressed data, removing the overhead associated with the processing of data that still contains the LFM transmitted pulse (as is necessary in the CS algorithm).**

In cases where chirp scaling of the uncompensated SRC chirp does not yield adequate results, a range chirp with a chirp length on the order of the maximum differential range migration across the scene can be inserted into the data, and this new chirp can be scaled during processing.

Keywords— **synthetic aperture radar, synthetic aperture sonar, chirp scaling.**

I. Introduction

The chirp scaling (CS) algorithm was developed independently in 1992 by researchers at the Canada Center for Remote Sensing (CCRS) and German Aerospace (DLR) [1–3]. The algorithm has obtained considerable attention in the SAR community due to is use of only fast Fourier transforms (FFTs) and multiplies. The more commonly used range-Doppler and wavenumber algorithms require an interpolation step that tends to dominate the overall processing time [4–7]. The removal of this interpolation step in the chirp scaling algorithm has resulted in a dramatic increase in the achievable processing speed.

This paper shows that by exploiting the uncompensated SRC chirp, or by inserting a small range chirp, it is possible to substantially reduce the raw data set used in the CS algorithm, leading to a significant reduction in the image processing time.

II. The chirp scaling algorithm

The key element of the CS algorithm is the use of chirp scaling to replace the interpolator used in the range-Doppler algorithm. The CS algorithm operates in the following manner: given the prerequisite that the range impulse response of an unprocessed target in the range-Doppler domain consists of a linear frequency modulated (LFM) or *chirped* phase function (such as would be expected from the echo of a LFM transmitted pulse), then the phase center of this LFM pulse can be shifted by altering the FM rate of the target's echo. (The alteration of the target's FM rate is the *chirp scaling* operation.) By altering the FM rate of all target echoes with respect to a target's range and its along-track Doppler wavenumber, the range variant nature of the system impulse response is removed. Thus, there are two basic assumptions in the chirp scaling algorithm; the first is that the transmitted signal is a LFM pulse and the second is that the algorithm processes the raw echo data, i.e., pulse compression of the transmitted LFM signal is not performed in the receiver during data collection.

Some of the processing gain that the CS algorithm obtains by removing the interpolator needed by the range-Doppler or wavenumber algorithm is lost due to the fact that the CS algorithm must operate on data containing the LFM transmitted chirp. The presence of this range chirp means that it is necessary to apply the required phase multiplies and FFTs to a large data set (the increase in the processed matrix size occurs in the range dimension and is given by the number of samples in the transmitted LFM chirp). Both the range-Doppler algorithm and the wavenumber algorithm process pulse compressed data, so even though they require interpolators, those interpolators are operating on a smaller data set than the CS algorithm (actually, the wavenumber algorithm can process either pulse compressed or chirped data). In many radar systems (especially tomographic spotlight systems), and almost all sonar systems, the chirp lengths employed in the transmitted LFM pulse are comparable to, or *larger*, than the actual scene size being imaged! These extra samples are discarded once the final image is produced, so they represent a significant processing overhead.

III. The accelerated chirp scaling algorithm

The ACS algorithm is based on the following reasoning. In the CS algorithm, the range chirps that are due to echoes of the transmitted LFM pulse are scaled so that the phase centers of all the target echoes follow the same locus in range-Doppler space. This operation removes the range variance of the target impulse responses (in the range-Doppler algorithm, the interpolator performs

0-7803-3836-7/97/$10.00 © 1997 IEEE

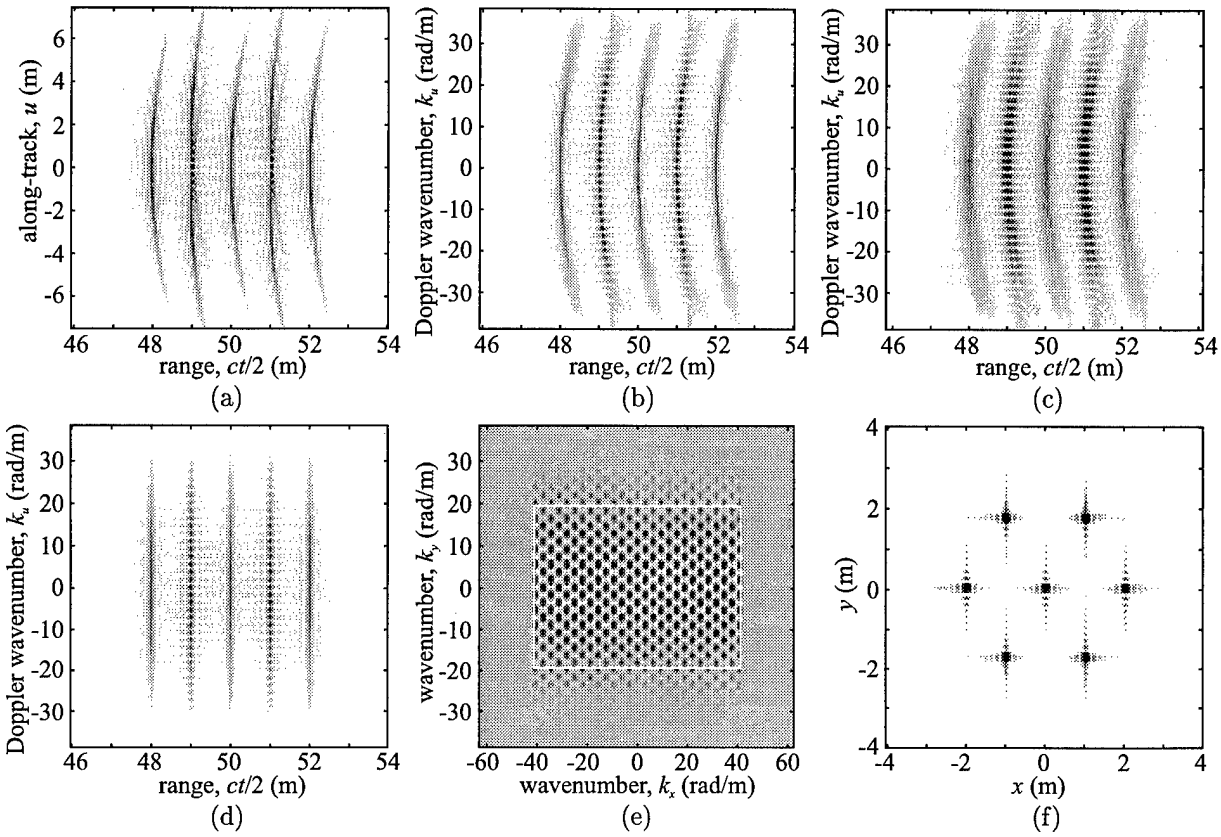

Fig. 1. Broadside stripmap mode synthetic aperture image processing via the accelerated chirp scaling algorithm. See the text for the system parameters and more details.

an analogous operation). If the range of the reference locus is chosen to be the scene center, then the maximum distance that the chirp scaling operation has to move the phase center of the target echo chirp is given by the maximum *differential* range migration across the imaged scene, where the maximum differential range migration is the difference in curvature between a target at the scene center (the reference range) and a target at the far range of an image. This observation then implies that the range chirp only needs to be large enough to support a shift of its phase center over a distance equivalent to the maximum differential range migration, which is often on the order of tens of pixels, not the thousands of pixels typically covered by an uncompressed LFM echo[1].

This observation implies that a more efficient application of the chirp scaling algorithm would be to begin with *pulse compressed data* and then reinsert a LFM chirp in the range dimension with a chirp length of say twice the expected differential range migration of the targets in the scene. However, due to the appearance of the uncompensated SRC LFM signal in the range-Doppler domain of the pulse compressed data, the required LFM chirp already exists! (For details of SRC see [2, 4, 7, 8]). The *accelerated chirp scaling algorithm* operates by exploiting this inherent LFM signal. The ACS algorithm begins by along-track Fourier transforming the pulse compressed data into the range-Doppler domain, then the phase centers of the target responses away from the reference range are shifted (chirp scaled) so that they have loci identical to the reference range, the processing then follows the chirp scaling algorithm (minus the no longer necessary pulse compression phase multiply)[2].

IV. A STRIP-MAP MODE PROCESSING EXAMPLE

Fig. 1 shows a number of the processing domains for target echoes received by a broadside stripmap synthetic aperture sonar (SAS) system with the following characteristics; standoff range $X_0 = 50$m, swath width $X_s = 8$m, aperture length $D = 0.3$m, along-track extent 15m, carrier frequency $f_0 = 30$kHz, transmitted chirp bandwidth $B_c = 10$kHz. The baseband signal of the receiver was

[1]Once the chirp scaling operation has been performed, the remaining range migration of the targets, which is now identical for all targets, is removed by the bulk range migration correction step of the chirp scaling algorithm

[2]There is a slight variation in the order of some of the phase multiplies depending on whether the processor is for stripmap or spotlight data

sampled at $f_s = 1.5B_c = 15$kHz, while along-track samples were taken at $D/4$. In Fig. 1, range time t has its origin at the collecting aperture, the along-track dimension travelled by the sonar is u, x, the range ordinate of the final image, has its origin at a distance X_0 from the temporal origin and y and u are defined from the same origin. The wavenumber ordinates are the Fourier transform ordinates of the spatial quantities, with subscripts indicating the spatial parameter.

The raw data in Fig. 1(a) shows the distinctive *pulse compressed* loci of the 7 (identically) reflecting targets. Fig. 1(b) is the along-track Fourier transform of the data in Fig. 1(a) , i.e., it is the range-Doppler data. The broadening of the target response (seen more clearly at the extreme wavenumbers) in Fig. 1(b) is due to the LFM component that is typically compensated for by SRC. Fig. 1(c) also shows the range-Doppler domain of the target data, where this time a small range chirp has been added. The application of a Doppler wavenumber-dependent chirp scaling to Fig. 1(b), followed by compression of the now scaled SRC LFM signal, bulk range migration correction and phase residual removal yields the impulse invariant range-Doppler signal in Fig. 1(d). A range Fourier transform of this data gives the 2-D wavenumber data in Fig. 1(e), from this data a rectangular region of data is extracted, the effect of the antenna pattern is deconvolved, and a 2-D inverse FFT is performed to yield the image estimate in Fig. 1(f). It is important to note that this image estimate was produced using a *chirp scaling*-based algorithm on *pulse compressed* data, so there was no chirp in the original raw (t, u)-domain data!

If the system parameters used by a particular synthetic aperture system are such that the chirp scaling of the SRC LFM signal does not yield adequate results, then it is possible to insert the appropriate range chirp into the pulse compressed data. Fig. 1(c) shows the range-Doppler data for the targets in Fig. 1(a), but this time a LFM pulse with a chirp length given by the maximum *differential* range migration in the scene has been inserted into the data (via a multiplication in the range-frequency domain)(in the rest of this paper, the inserted range chirp is referred to as the differential range chirp, to distinguish it from the uncompensated SRC range chirp). Processing of the data in Fig. 1(c) yields figures identical to those in Figs. 1(d), (e), and (f). It is important to note that Fig. 1(c) still contains the SRC chirp. It could have been removed when the differential range chirp was inserted, but it was left in to emphasise the following point: the chirp rate of the differential range chirp *must* be less than zero (a down chirp) so that it *reinforces* the SRC chirp. If an up-chirp is used, it partially compresses the SRC chirp and the resulting range chirp length is reduced. If SRC is compensated prior to the introduction of the differential range chirp, then the chirp direction is arbitrary[3].

V. A comment on spotlight mode processing

Due to page limitations of this publication, it is not possible to include a spotlight processing example. The ACS algorithm works equally well for spotlight systems. Spotlight systems employing large squint angles produce an SRC chirp in the range-Doppler domain that is often much longer in the range dimension than is required for the chirp scaling operation. In high-squint spotlight systems then, it is more appropriate to compensate for SRC and then insert the differential range chirp for use in the chirp scaling operation. The processing of squinted spotlight systems (and stripmap systems) is described in more detail in [9].

VI. Conclusion

This paper has shown that the chirp scaling algorithm in its original formulation is sub-optimal and that by beginning the processing with pulse compressed data, a more efficient *accelerated chirp scaling* processor can be used. The realisation that the range-Doppler data of pulse compressed data often already contains the required range chirp (in the form of the uncompensated SRC chirp) or that the required differential range chirp can be easily inserted into the data is seen as a significant observation.

References

[1] R. K. Raney, I. G. Cumming, and F. H. Wong, "Synthetic aperture radar processor to handle large squint with high phase and geometric accuracy," United States Patent 5,179,383, Jan. 1993.

[2] R. K. Raney, H. Runge, R. Bamler, I. G. Cumming, and F. H. Wong, "Precision SAR processing using chirp scaling," *IEEE Transactions on Geoscience and Remote Sensing*, vol. 32, no. 4, pp. 786–799, July 1994.

[3] A. Moreira, "Method of image generation by means of two-dimensional data processing in connection with radar with synthetic aperture," Canadian Patent Application 2,155,502, 1995.

[4] J. C. Curlander and R. N. McDonough, *Synthetic Aperture Radar: systems and signal processing*, John Wiley & Sons, Inc., 1991.

[5] M. Soumekh, *Fourier Array Imaging*, Prentice Hall, Englewood Cliffs, NJ, 1994.

[6] W. G. Carrara, R. S. Goodman, and R. M. Majewski, *Spotlight synthetic aperture radar: signal processing algorithms*, Artech House, 1995.

[7] D. W. Hawkins, *Synthetic aperture imaging algorithms: with application to wide bandwidth sonar*, Electrical and Electronic Engineering, University of Canterbury, Christchurch, New Zealand, Oct. 1996.

[8] A. Moreira, "Airborne SAR processing of highly squinted data using a chirp scaling approach with integrated motion compensation," *IEEE Transactions on Geoscience and Remote Sensing*, vol. 32, no. 5, pp. 1029–1040, Sept. 1994.

[9] D. W. Hawkins and P. T. Gough, "Synthetic aperture imaging using accelerated chirp scaling," *in preparation for IEEE Transactions on Geoscience and Remote Sensing (unpublished)*, 1997.

[3] When it is necessary to insert the differential range chirp, pixels at the range extremities of the final image estimate will be corrupted by wrap-around errors, so they should be discarded. Zero padding in the range dimension, prior to the insertion of the differential range chirp, can avoid these errors

Analysis of Code Error Effect in Space borne SAR Imaging Processing

Zaihan Jiang
Center for Communications and Signal Processing Research, Dept of ECE ,New Jersey Institute of Technology,University Heights, Newark, NJ 07102, USA
Jianjun Song
Institute of Electronics, Academia Sinica, Beijing, 100080, P.R.China

Abstract

We analyze the formulation of code error in Space borne Synthetic Aperture Radar(SBSAR) and the modes of code error first. Then we infer the effete of code error in SBSAR point-target imaging processing. By simulation, we validate our interference and get some important statistical curves. These are the relationship of code error ratio with width of main lobe, code error ratio with integrated side lobe ratio(ISLR), code error ratio with peak, with peak of side lobe. By these curves we analyze code error effect in SBSAR imaging processing and get the allowable code error ratio in SBSAR.

Key Words: Code Error Ratio point target Space borne Synthetic Aperture Radar Statistical Curve

1. Introduction

Because of the existence of noise and disturbance and quality of record, there will be some error codes in the process of SBSAR imaging processing. Code Error will affect the Imaging Processing of SBSAR to some degree. In some case, the effect is obvious(1).

2. The formulation of Code Error and Modes of Code Error

Code Error is occur in the process of formulating, transferring, processing of SAR response. There are 3 factors: a.Noise and Disturbances in the accepting channel b. Impairment of record media, unsteady of magnetic tape station's velocity c.The code error of digital circuits.

We can classify code error as 3 modes. Those are: a. Lost Code. The sequence of code will be disorderly; b. Error Code. c. Add Code. The effect is as similar as Lost code.

3. Analysis of Code Error Effect in SBSAR Imaging Processing(2)

4. Result of Simulation

1) When response is correct we could get simulated image of point-target as illustrated in Figure 4.1.
2) Error Code(Code Error Ratio=24%), as illustrated in Figure 4.2.
3) Lost Code(Code Error Ratio=.48%), as illustrated in Figure 4.3.

5. Analysis of Statistical Curves

With the result of a lot of simulation, we get following curves as illustrated in Figure 5.1,5.2 5.3, 5.4.

6. Conclusions

There exist code error in the process of transferring , recording, processing of response of SBSAR. We could classify code error as Error Code, Lost Code, Add Code. It will affect the imaging processing of SBSAR to some degree. In some cases, the effect may be obvious. Our requirement of code error ratio is lower than 0.05%. To suppress code error ratio, one way is to choose high quality tape and magnetic tape station. The other way is to choose proper ways of channel coding(3).

Acknowledgment

The authors wish to thank the colleagues of the Department of Remote Sensing and Information Processing, Institute of Electronics, Academia Sinica and Associate Professor Yanfei Wang for helpful discussions related to the work.

Reference:
(1) Chengbo Zhang, "Synthetic Aperture Radar, Theory, System Analysis and Application", Science Inc.,1989
(2) Zaihan Jiang "The Analysis of Code Error Effect in Synthetic Aperture Radar Imaging Processing and the Implementation of its Simulation Software", 1996, Master Thesis of Institute of Electronics, Academia Sinica
(3) E.Gorog: "Some New Classes of Cyclic Code Used for Burst Error Correction", IBM J.Res. Dec, 7, 1965

Figures

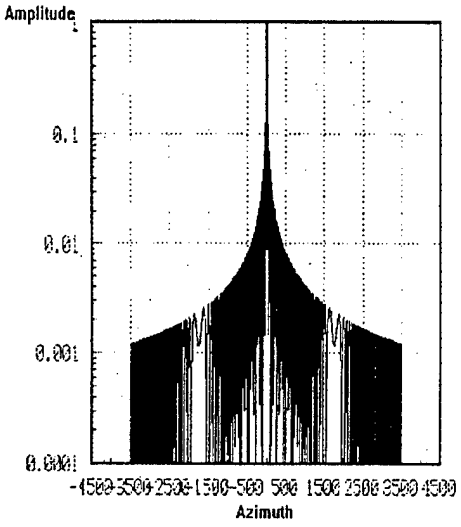

Figure 4.1

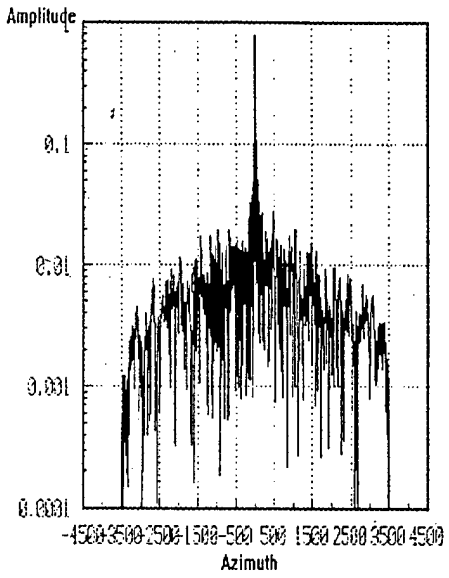

Figure 4.2

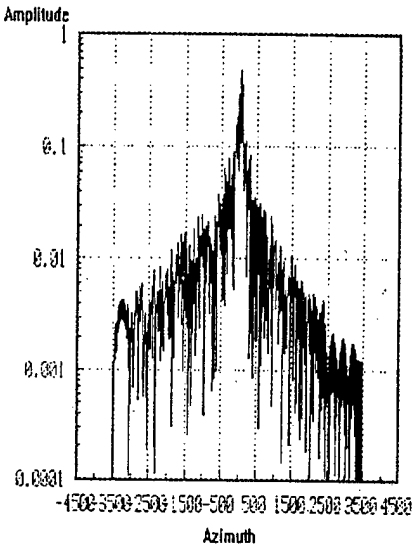

Figure 4.3

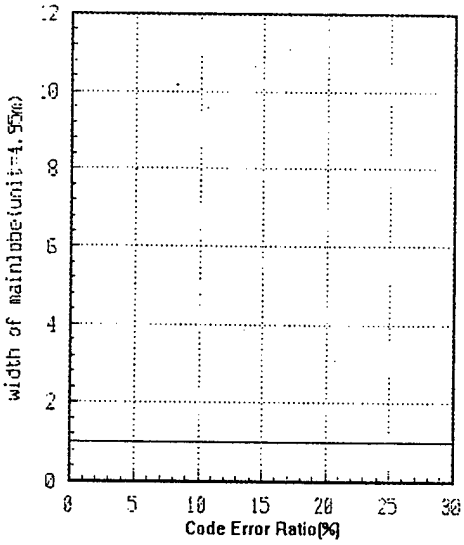

(a)Error Code

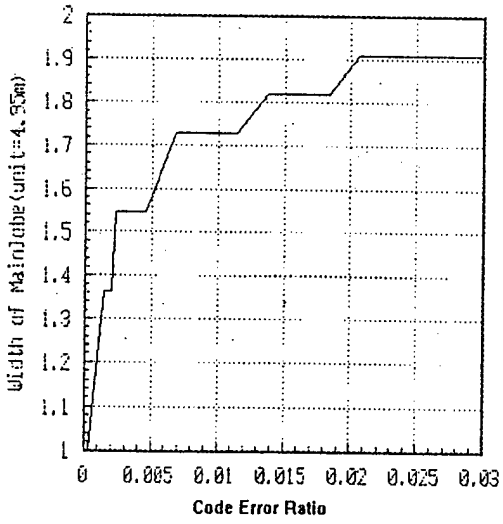

(b)Lost Code

Figure5.1 Curve of Code Error Ratio with Mainlobe width

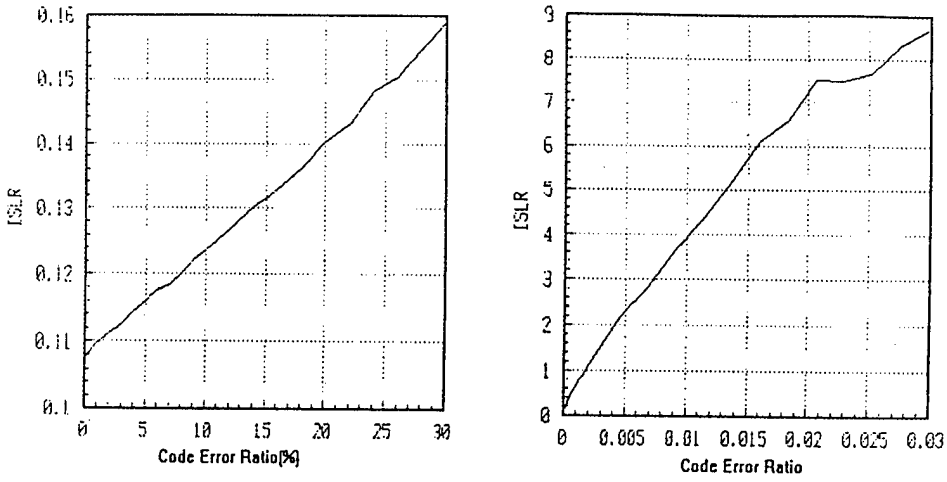

(a)Error Code (b)Lost Code

Figure 5.2 Curve of Code Error Ratio with ISLR

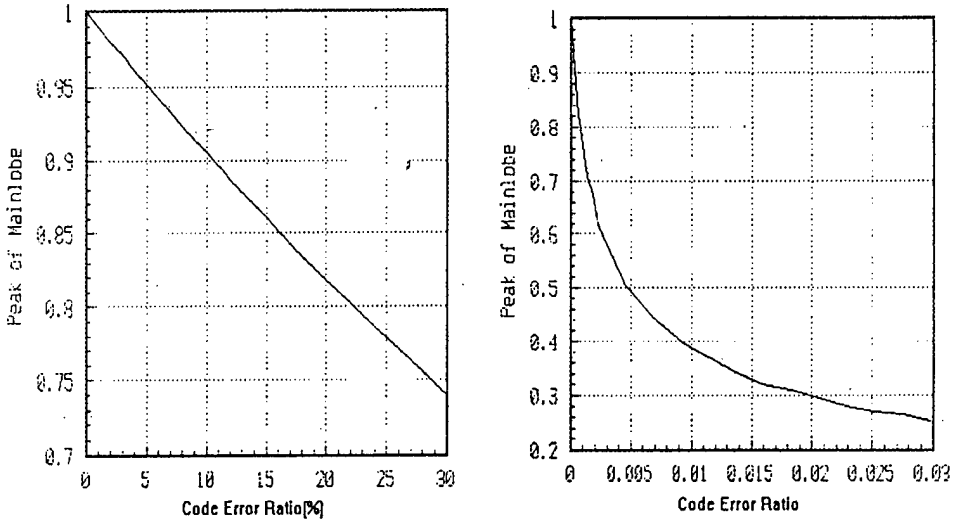

(a) Error Code (b)Lost Code

Figure 5.3 Curve of Code Error Ratio with Peak

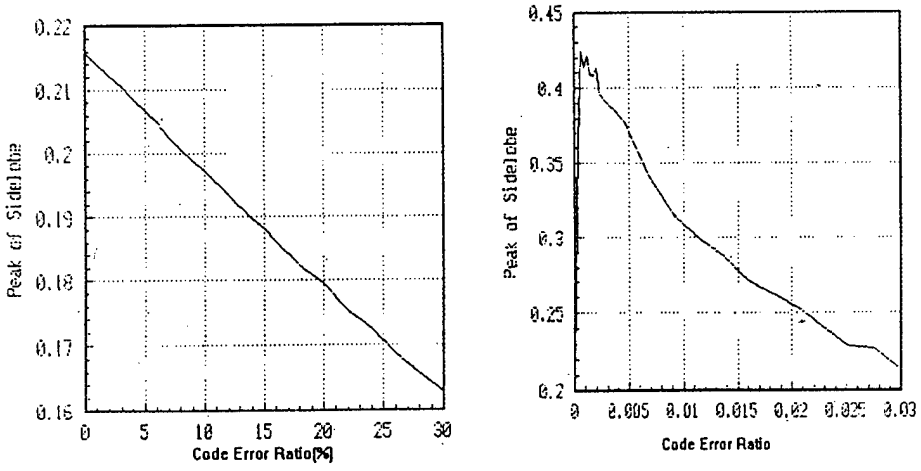

(a) Error Code (b)Lost Code

Figure 5.4 Curve of Code Error Ratio with Peak of Sidelobe

High Quality Spotlight SAR Processing Algorithm Designed for LightSAR Mission

Michael. Y. Jin

Jet Propulsion Laboratory , California Institute of Technology
Ms 300/243, 4800 Oak Grove Dr., Pasadena, California 91109, USA
Tel: (818) 354-3778/Fax: (818) 393-0202/Email: michael_jin@radar-email.jpl.nasa.gov

Abstract -- A high quality spotlight SAR processing algorithm is presented. In this algorithm, subband images of the radar illuminated spot are processed using well known strip mode processing algorithms. A full resolution image is then formed by (1) merging the spectra of subband images into a full band spectrum, and (2) taking an Inverse FFT. Advantages of this algorithm include (1) higher image quality, (2) higher processing throughput rate, and (3) lower S/W development cost. The image quality achieved by this algorithm is better than that previously achieved by the backprojection algorithm. The fine image quality is demonstrated by the SIR-C spotlight SAR images.

INTRODUCTION

LightSAR is a new program aimed at validating key advances in synthetic aperture radar (SAR) technology, that will reduce the cost and enhance the performance of this and future U.S. SAR missions. To boost commercial interest in LightSAR program, the LightSAR is designed to be capable of many imaging modes including a high resolution spotlight SAR mode. Developing a spotlight processing algorithm for the LightSAR platform and meeting its requirement is one of the high priority task in the present project phase.

The concept of Spotlight SAR has been previously related to computed tomography [1]. The similarity between a spotlight SAR and an X-ray computed tomography (CT) system includes: (1) both are problems of reducing image sample values from measurements of signal strength from line integrals, (2) imaging areas are spatially bounded. The difference between these two systems includes: (1) the radar is operated with a coherent signal with a carrier frequency usually higher than its bandwidth, where the X-ray CT system is operated with non coherent signal and its equivalent bandwidth is determined by the width of X-ray beam contained in each detector, (2) in spotlight SAR, the line integral is defined along the segment of a circle, where in the X-ray CT system, the line integral is defined along a straight line.

Despite their difference, tomography processing algorithms such as convolution backprojection [2] and Inverse Fourier transform on polar spectrum [1] have been applied to spotlight SAR processing. Previous reports [2] showed that the image quality achieved by backprojection is generally better than the Inverse Fourier method. This is because that the polar spectrum is formed based on the approximation that the iso-range lines running through the radar spot approach straight lines. But, this approximation is not needed in the backprojection algorithm. In the LightSAR system, the curvature of the iso-range lines is on the order of ten slant range resolution cells. Therefore, it is obvious that Inverse Fourier method will not meet the image performance requirement of the LightSAR mission. Furthermore, the convolution backprojection algorithm is also not considered for its lower throughput rate. Instead, a new spotlight processing algorithm based on synthesis of subband image spectra, to be described below, is found to be a good candidate for processing LightSAR spotlight mode SAR data.

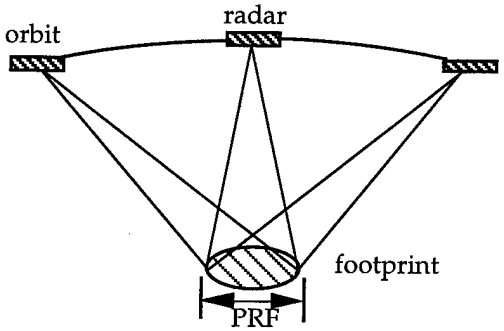

Figure 1. Spotlight Mode SAR Geometry

ALGORITHM

To generate a full resolution image from a conventional strip mode SAR data, the azimuth compression process may be realized in many ways. One simple approach is to perform a fast Fourier correlation type processing with a full length aperture. Typical example of this fast Fourier correlation include well known range-Doppler algorithm [4], wave domain algorithm [5], and the chirp scaling algorithm [6]. One may also perform fast Fourier correlation with sub apertures to generate several images with lower

0-7803-3836-7/97/$10.00 © 1997 IEEE

resolution. These images are then superposed to form a full resolution image provided that the azimuth sampling rate exceeds the Nyquist rate of the full resolution image. Or, one may merge the spectra of these subband images to form the full band spectrum and then take an inverse Fourier transform. Another approach is to divide the SAR data into a number of bursts, process each burst data into low resolution phase-preserved images, and superpose these images. It is interesting to point out that the backprojection algorithm may be viewed as an extreme case, i.e. one line per burst, of the burst processing approach.

In spotlight SAR data, the signal bandwidth is much greater than the pulse repetition rate (PRF). Consequently, full aperture processing by fast Fourier correlation is not possible because the PRF is less than the Nyquist rate of the full resolution image. Previously reported algorithms, other than the inverse Fourier from polar spectrum method, have proposed the backprojection algorithm [2] and the burst processing approache [3]. However, the subband processing approach was not explored at all. For an airborne SAR platform, the burst processing approach may be more adaptable to a system where motion compensation is required. But, in a spaceborne SAR, orbital trajectory is more stable and high frequency motion effect does not exist, the subband processing approach is, therefore, a very good candidate.

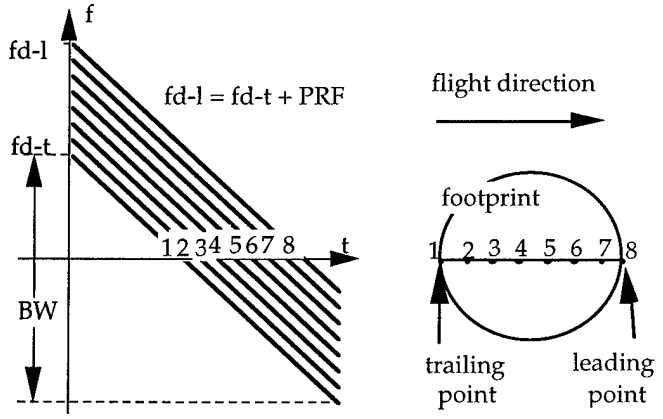

Figure 2. Targets Frequency Profiles

FORMULATION

In spotlight mode SAR operation, the radar pointing is constantly steered to keep the radar footprint illuminating a fixed spot on the ground during a time period several times longer than the conventional SAR aperture interval. This geometry is shown in Fig. 1. To simplify the illustration for the processing algorithm, it is assumed that the slant range history of each target within the radar footprint can be modeled by a polynomial limited to a second order. Therefore, the Doppler frequency profile associated with a point-like target within the radar footprint can be modeled as a ramp function with a negative slope. Since the along-track size of the processed spotlight image is limited to that equivalent to a Doppler range of PRF, the Doppler profile depicted in Fig. 2 may well characterize those targets within the final image and at a constant range to the radar.

Frequency Interval in Subband Image

To apply a fast Fourier correlation to the spotlight data, the SAR data is divided into several segments first. Each segment data shall lead to a subband image of the illuminated ground spot. Let B_s be the bandwidth of each subband image satisfying $B_s \le PRF$, $[0, T]$ be the time interval of the spotlight data. Denote f_{d-l} and f_{d-t} as the Doppler frequencies, at time origin, associated with the leading and trailing points, respectively, of the radar footprint. Let f_r be the Doppler frequency change rate. The first segment of the data should lead to an image covering the frequency interval of $[f_{d-l} - B_s, f_{d-l}]$. The i-th data segment should lead to an image covering $[f_{d-l} - i \cdot B_s, f_{d-l} - (i-1) \cdot B_s]$. Let the frequency bandwidth of each target be given by BW, the total number of segment N is given by the least integer satisfying $N \cdot B_s \ge BW + PRF$.

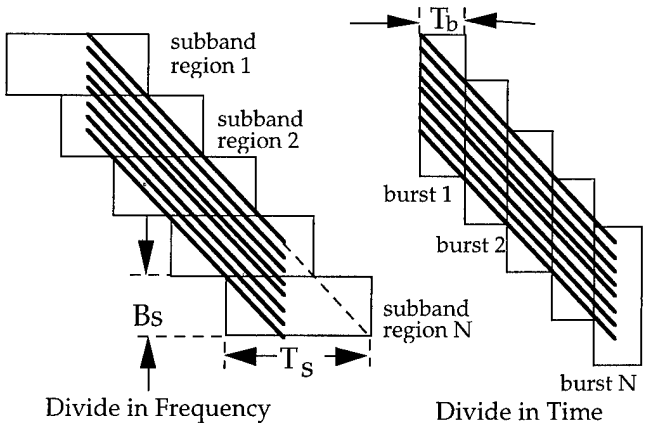

Figure 3. Subband and Burst Division

Time Interval in Subband Image

In fast Fourier correlation, the number of valid image samples is equal to the number of reference samples subtracted from the number of input samples. In a subband image processing, the number of valid image samples is given by the product of PRF and the equivalent time interval of the ground spot, PRF / f_r. The number of reference samples is $PRF \cdot B_s / f_r$. Hence, the first data segment contain the time interval

of $[B_s/|f_r|-(B_s+PRF)/|f_r|,\ B_s/|f_r|]$. The i-th data segment should contain the time interval of $[i\cdot B_s/|f_r|-(B_s+PRF)/|f_r|,\ i\cdot B_s/|f_r|]$. The time and frequency intervals of these segments are shown in Fig. 3. The time intervals of burst processing approach is also given for comparison.

Spectra Merging

To merge the spectra from subband images into the full spectrum, one need to determine the sampling frequency of the final image. It should be no less than $T\cdot f_r$. To take the advantage of FFT, the sampling frequency must be the product of an integer power of two and PRF. Denote this sampling frequency by f_s. Let a spectral component corresponding to a Doppler frequency of f_d. Its frequency value in the spectrum of the corresponding subband image is

$$f_{d-sub} = Mod[f_d + 100\cdot PRF,\ PRF]$$

Its frequency value in the spectrum of the full resolution image is given by

$$f_{d-full} = Mod[f_d + 100\cdot f_s,\ f_s]$$

SPOTLIGHT SAR DATA PROCESSING

The processing diagram of the proposed algorithm is given in Fig. 4. The radiometric compensation process is to remove the antenna pattern modulation and to eliminate the substandard image pixels near the edges of PRF boundary. This algorithm has been implemented in FORTRAN with both the range-Doppler and chirp scaling algorithms for subband processing.

This algorithm has been tested using both simulated spotlight point-target data and the spotlight data taken during the SIR-C mission. Analysis performed over the processed point-target data indicates that its Phase accuracy, 3-dB resolution width, peak-sidelobe ratio, and integrated-sidelobe ratio meet the LightSAR requirement. Fig. 5 is a SIR-C spotlight SAR image, in full resolution and in multi-look lower resolution, of Sydney, Australia. By examining the point-targets performance in this and other images, we conclude that the expected 1.25 meter resolution is met.

DISCUSSION

A squinted spotlight data may require a constantly changing PRF to let the echo fall between the transmitted pulses. To use the proposed algorithm for processing this kind data, resampling the raw data for a constant PRF is necessary. Depending on the bandwidth of the spotlight data, a 3rd and 4th order polynomial may be required for modeling the phase history accurately. Similar to a strip mode SAR processing system, an automated spotlight SAR processor will also require preprocessing steps such as Doppler analysis and autofocus.

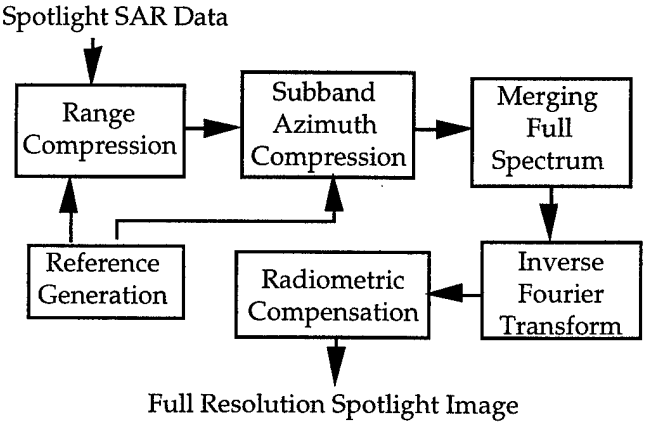

Figure 4. Spotlight SAR Data Processing Diagram

ACKNOWLEDGMENTS

This work was carried out at the Jet Propulsion Laboratory, California Institute of Technology. The author would like to thank my colleague Dr. Y. Shen and S. Shaffer for valuable discussions about the SIR-C phase steering mechanism, Dr. K. Leung and B. Swift for providing the SIR-C spotlight SAR data, Dr. M. Chen for data ingest and initial processing test, and E. Chu for setting up the workstation system.

REFERENCES

[1] D. Munson, J. O'Brien, and W. Jenkins, "A Tomographic formulation of spotlight-mode synthetic aperture radar", Proceedings of the IEEE, Vol. 71, No. 8, August, 1983.

[2] M. Desa and W. Jenkins, "Convolution backprojection image reconstruction for spotlight mode synthetic aperture radar", IEEE Trans. on Image Processing, Vol. 1, No. 4, October 1992.

[3] Fujisaka et. al., "Spotlight Mapping Radar System", US Patent # 4989008, 1991.

[4] C. Wu, K. Liu, and M. Jin, "Modeling and a Correlation Algorithm for Spaceborne SAR Signals", IEEE Transactions on Aerospace and Electronics Systems, Vol. AES-18, No.5, Sept., 1982.

[5] C. Cafforio, C. Prati, and F. Rocca, "SAR data focusing using seismic migration techniques", IEEE Trans. on Aerospace and Electronic Systems, vol. 27, no. 2, pp. 194-207, March, 1991.

[6] R. K. Raney, H. Runge, R. Bamler, I. G. Cumming, and F. H. Wong, "Precision SAR Processing Using Chirp Scaling," IEEE GE-32, pp.786-799, 1994.

Site: Sydney, Australia
Image Size: 1.3 km along-track, 10 km cross-track
Look Angle: 42 degree

Range Resolution: 10 meter
Frequency: C band, Polarization: VV

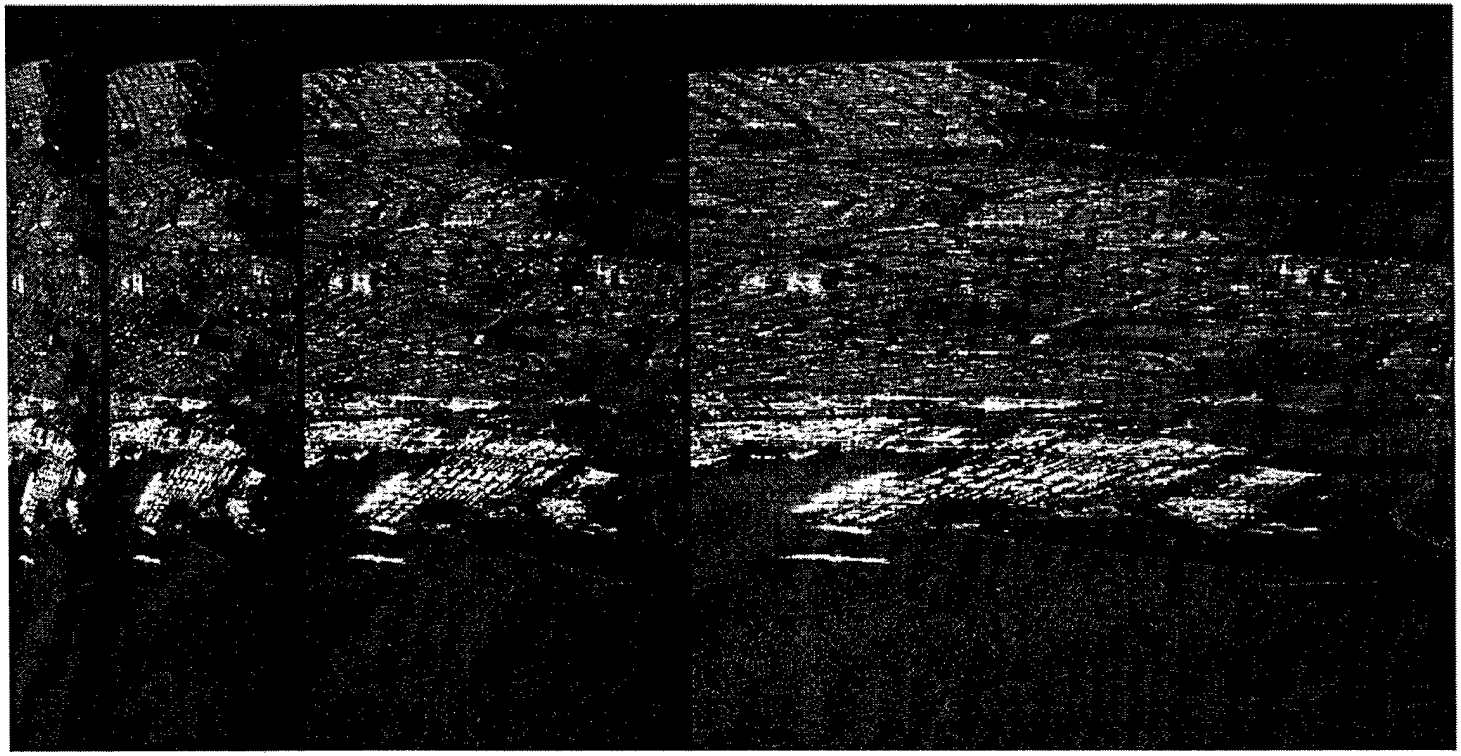

Azimuth Resolution	10	5	2.5	1.25 (meter)
Looks	8	4	2	1

Figure 5. SIR-C Spotlight-Mode SAR Image

INTERPRETATION OF BRIGHTNESS TEMPERATURE RETRIEVED BY SUPERSYNTHESIS RADIOMETER

Koji Komiyama, Yoshihiko Kato and Katsumi Furuya

Electrotechnical Laboratory, AIST, MITI

1-1-4, Umezono, Tsukuba, Ibaraki, Japan 305

Tel.+81-298-58-5637, Fax. +81-298-58-5640, komiyama@etl.go.jp

ABSTRACT-- The supersynthesis radiometer is a kind of synthetic aperture interferometric radiometer. The principle is an interferometric synthesis on the basis of the phase change of the complex correlation(visibility function) between two signals received by two antennas aligned along the vehicle track. The brightness temperature retrieved by the synthesis is the result of the integration of many data measured through different observation angle to the ground. The temperature is numerically evaluated in the case of a flat ground model using the Fresnel reflection coefficients. The off-nadir angle of the interferometer baseline, propagation attenuation of the microwave emission, the angular variation of the emissivity and polarization are taken into consideration for the calculation of the retrieved brightness temperature with three complex dielectric constants of different emissivities.

INTRODUCTION

The spatial resolution of a conventional microwave imaging radiometer with an aperture antenna for the earth remote sensing is restricted by the physical antenna beam, that is, the dimension of the antenna. There are shown the comparison of three techniques for along-track imaging of the microwave radiometers in Fig.1. Fig. 1(A) is single aperture which must be physically large enough to make a fine resolution on the ground. Fig.1(B) is a synthesizing radiometer by multiple interferometers which needs some small antennas aligned along the track for having different inter-spaces to make many interferometers with different baselines in length. Fig. 1(C) shows the supersynthesis technique which is the subject of the paper.

The supersynthesis technique is popular in radio astronomy to make a high spatial resolution by moving an interferometer baseline utilizing the earth rotation. The technique can also be applied to an imaging microwave radiometer for the earth surface as the supersynthesis radiometer(SSR)[1][2][3]. The principle is an interferometric synthesis using the phase change of the complex correlation (visibility function) between two signals received by two antennas aligned along the vehicle track. The phase history is attributed to the variable incidence angle of the ground microwave emission to the baseline of the interferometer along with the relative position change of a satellite over the ground. Small antennas along the track are required to receive ground microwave emission through broad beams with large change of the incidence-angle to the interferometer baseline. The small antennas are consequently adequate to use on a small satellite.

Though the supersynthesis radiometer basically need only an interferometer as a hardware to synthesize a fine resolution along the satellite track, it is a subject that many sequential samples of the visibility function with various observation conditions are integrated for the synthesis. For example, a fraction of the visibility function used for the synthesis is weakened due to the propagation through long distance by oblique observation. The microwave emissivity of the ground is also variable depending on the terrain condition, observation angle and polarization.

In the paper, the principle of the supersynthesis technique is explained by a simple model without variation of ground microwave emissivity and propagation attenuation. Then the interpretation of the retrieved brightness temperature is discussed considering the ground emissivity and propagation attenuation.

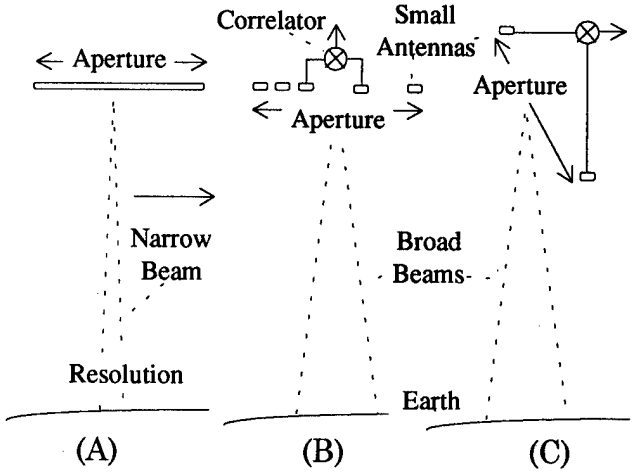

Fig.1 Techniques for the passive microwave imaging
(A)Narrow beam by single aperture antenna
(B)Synthesis by multiple interferometers
(C)Supersynthesis technique

SUPERSYNTHESIS TECHNIQUE

The behavior of the SSR is shown in Fig.2. Since the supersynthesis technique is based on the relative movement of an interferometer to the target ground, it can be applied only to the along track synthesis in the case, for example,

0-7803-3836-7/97/$10.00 © 1997 IEEE

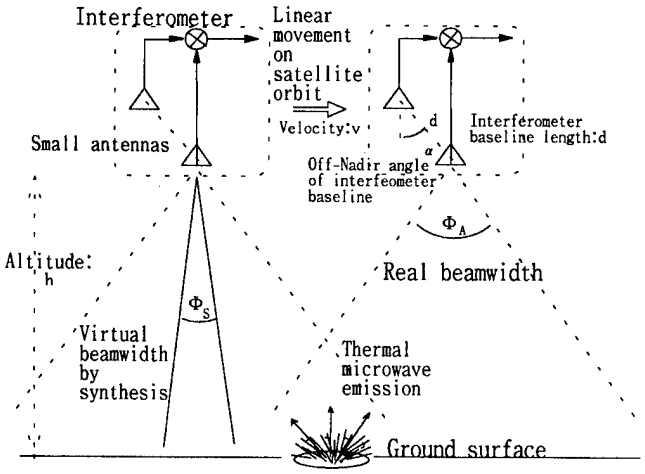

Fig.2 Behavior of an interferometer of supersynthesis radiometer

using a LEO satellite whose orbit is almost locally linear. Hereafter, we consider only one-dimensional synthesis restricted in a vertical plane including the satellite orbit for simplicity of the explanation of the along-track synthesis. Though the ground patch corresponding to the resolution by synthesis has a finite area, a point source target is adopted to illustrate the performance of the radiometer and the process of image retrieval. The phase of the correlation output, that is, a visibility function is expressed by,

$$\phi(t) = \frac{2d\pi(hCos\alpha - vtCos\alpha)}{\lambda\sqrt{h^2 + v^2t^2}} \qquad (1)$$

The frequency of the visibility function is calculated as a time differential function of the $\phi(t)$. Some examples of the frequency histories are shown in Fig.3 calculated by a model of the altitude h, velocity v and the baseline length d of 700Km, 7Km/s and 50 wavelength, respectively.

Matched filtering technique is used for the supersynthesis. Since the frequency variation near the target locating at the origin is monotonous and nearly linear, a matched filtering technique is possibly adopted. It is an analogy to the imaging process of a synthetic aperture radar(SAR) which uses the technique for both the range and azimuth compression. The visibility function of the supersynthesis radiometer is similar to the azimuth history of the SAR.

The spatial resolution depends fundamentally on the bandwidth of the visibility function used for the matched filtering. The central part between two zero-derivative

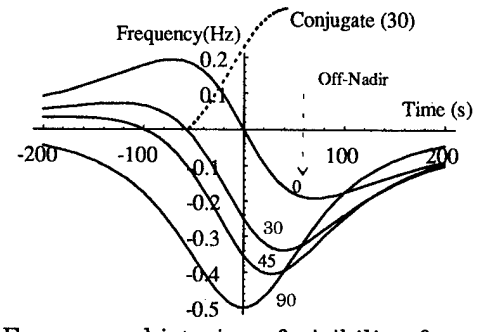

Fig. 3 Frequency histories of visibility function of a point target which locates at the origin in the time axis

points can be the maximum available portion for the matched filtering. As the frequency history is not exactly linear, a specific taper window is practically used in addition to a triangular taper for sidelobe reduction. Taper window is one of the influence factors to the retrieved temperature.

An alternative technique[4] is possible for the synthesis using almost twice the bandwidth using the conjugate signal as shown in Fig. 3 for the case of 30 degree off-nadir angle, but the ordinary matched filtering is adopted to evaluate the retrieved brightness temperature.

EFFECTS OF THE MICROWAVE EMISSIVITY OF THE GROUND AND PROPAGATION ATTENUATION

There are important factors such as the ground emissivity ε_r and the attenuation L_a and emissive brightness temperature T_{UP} of the atmosphere in the passive microwave observation of the earth terrain. The noise temperature T_{AP} observed by an aperture antenna is expressed by

$$T_{AP} = L_a\{\varepsilon_r T_G + (1-\varepsilon_r)T_{DN}\} + T_{UP} \qquad (2)$$

where T_G and T_{DN} are the physical ground and sky brightness temperatures, respectively. In long wave-length microwave radiometry the sky temperature and the attenuation and brightness temperature of the atmosphere are small enough to be neglected and so the ground brightness temperature is observed as the product $T_G\varepsilon_r$ of the ground physical temperature and the emissivity.

The brightness temperature is retrieved by the integration of a long sequence of signal data with broad angular variation in the supersynthesis technique. The angular variation and propagation attenuation must be considered for the interpretation of the retrieved brightness temperature. The angular characteristics of the terrain microwave emissivity are various on the condition of the surface roughness, plant coverage, and soil constituents. An increase in roughness and the existence of plants generally reduce the angular variation [5] . Since unique model is not available to the various terrain conditions, a simple specular model of microwave emission is adopted to evaluate the behavior of the supersynthesis radiometer. Fig.4(A) shows emissivities by three different complex permitivities. Large variations are shown especially in large angle region. As the resultant resolution of the synthesized brightness map is constant by supersynthesis technique independently of the temporary observation angle, the emission energy flux from the corresponding ground patch is reduced by propagation through long distance in the case of oblique observation. Fig. 4(B) shows the angular variation of the effective emission flux (field strength) from a ground patch with finite area. In the larger observation angles the more reduced the emission energy is. The emission signal seriously decreases over 30 degree of the observation angle.

An example of the visibility function calculated with baseline off-nadir angle of 30 degree from the specular ground model with propagation extinction is shown in Fig. 5. The brightness temperature is calculated by in-phase integration of such visibility functions as that in Fig.5

without taper window. Fig.6 shows the angular variation of the calculated normalized brightness temperature corresponding to the variation of the interferometer baseline off-nadir angle. Real ground emissivity is also depicted for comparison. The angular characteristic of the retrieved temperature by supersynthesis is similar to the angular variation of the ground emissivity itself in spite that the angular variation of the effective signal flux from the patch ground is different from these two lines.

Only an example has been shown by calculation using a simple model of specular emission, but the real terrain is too various to evaluate using a model. So further investigation is necessary to exactly interpret the brightness temperature retrieved by the supersynthesis radiometer.

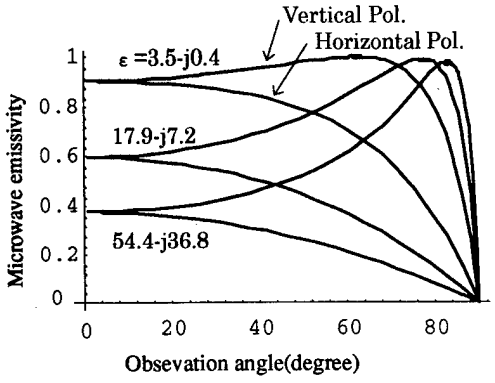

(A)Real emissivity of specular surface

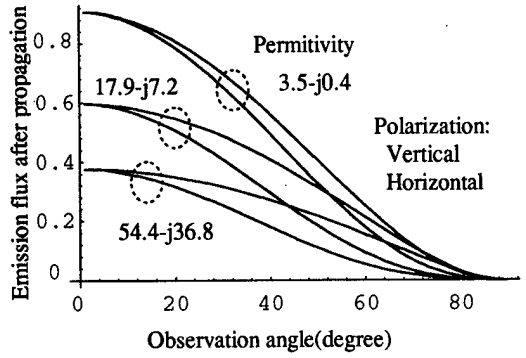

(B)Effective signal flux with propagation attenuation

Fig.4 Comparison of real emissivity and effective signal flux with propagation attenuation through slant path

CONCLUSIONS

The ground brightness temperature retrieved by the supersynthesis technique is evaluated by numerical calculation using a specular microwave emission model including propagation attenuation from the surface to the antennas. The angular variation of the temperature respecting the interferometer baseline off-nadir angle of the supersynthesis radiometer is similar to the microwave ground emissivity. But the real terrain is too various to evaluate using a model, further investigation of the ground emissivity is necessary to exactly interpret the brightness temperature retrieved by the supersynthesis radiometer and to properly determine the system parameters for the design of a practical radiometer system.

REFERENCES

[1]K. Komiyama, "Supersynthesis radiometer for passive remote sensing," Int. GRS Sy. (IGARSS'92) 1992.

[2]K. Komiyama, Y. Kato, and T. Iwasaki, "Indoor experiment of two-dimensional supersynthesis radiometer," Int. GRS Sy. (IGARSS'94) 1994.

[3]K.Komiyama, Y.Kato, "Two-dimensional supersynthesis radiometer for field experiment," Int.GRS Sy.(IGARSS'95) 1995

[4]K.Komiyama, Y.Kato, " Characteristics of the baseline off-nadir angle of supersynthesis radiometer ", Int.GRS Sy.(IGARSS'96) 1996

[5]F.T. Ulaby, R.K. Moore and A.K. Fung, "MICROWAVE REMOTE SENSING, ACTIVE AND PASSIVE," Vol. III, Artech House 1986.

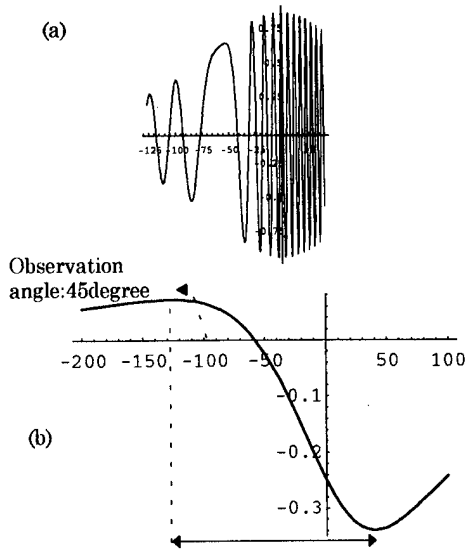

Fig.5 Visibility function of supersynthesis radiometer of a specular ground emission model and propagation attenuation, (a)visibility function and (b)frequency history.

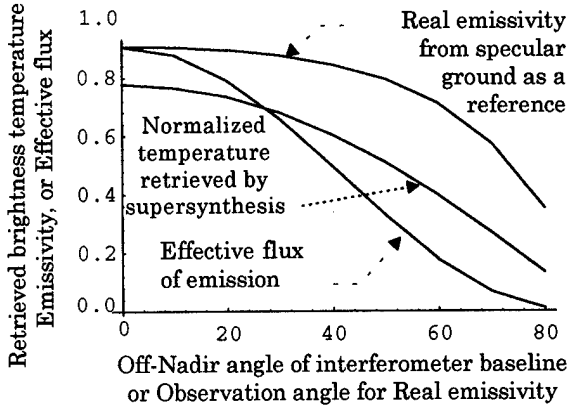

Fig.6 Angular variation of normalized brightness temperature retrieved by supersynthesis with the off-nadir angle variation of the interferometer baseline.

Non-Iterative Spotlight SAR Autofocusing Using A Modified Phase-Gradient Approach

Chan Hian Lim, Yeo Tat Soon
National University of Singapore
Department of Electrical Engineering
Radar and Signal Processing Laboratory
10 Kent Ridge Cresent, Singapore 0511
Email : chianlim@singnet.com.sg

Abstract -- Phase-Gradient autofocus (PGA) technique is robust over a wide range of imagery and phase error functions but the convergence usually requires 4-6 iterations. In this paper, we propose to speed up the estimation convergence by selectively increasing the pool of quality synchronisation sources and not to be limited by the range pixels of the SAR map. This is highly probable since each range bin contains more than 1 prominent scatterers across the integration aperture. It is also highly probable that the least brightest selected scatterer in a range gate may turn out to be of higher energy as compared to the maximum brightest scatterer of another gate. With appropriate target filtering to final select the quality scatterers out of the large pool and higher-order phase error measurement tool, the new algorithm achieves near convergence quality without iteration. We named this solution the Quality PGA algorithm (QPGA).

Introduction

In recent years, the Phase-Gradient (PGA) technique in [1],[2] for Spotlight mode SAR imagery has become a favourable autofocusing tool for correcting both low and high order phase errors suffered mainly from undesired platform motions. Uncompensated phase errors give rise to target positioning errors as well as bluring of target impulse responses. Advanced autofocusing algorithms are therefore required, especially with increasing demand for higher resolution, to remove the azimuth phase distortions by using the SAR data themselves to derive the motion parameters needed to focus those same set of data. Traditionally, most SAR autofocus solution uses the Map-Drift technique. According to [3], PGA generally produces much better image quality than the Map-Drift method. Although both techniques have similar computational requirements per iteration, the PGA typically requires five or more iterations versus only two or three for Map-Drift. Thus the choice of autofocus solution is very much a trade-off between SAR processing speed and image quality demand in target analysis applications.

Is PGA Necessarily Iterative?

In PGA, the choice of target isolation size (in terms of number of pixels) greatly influence the required number of iteration cycles for a quality estimation. The isolation size must be large enough to capture the image blur function while yet small enough so as not to increase the noise bandwidth and neighboring clutter interferences. Thus PGA has to start its first iteration with a sufficiently large target isolation size to try to capture the entire but a noisy error function. After the phase compensation with the present estimate, the next iteration will work on a smaller target isolation size since the blurring function is expected to be smaller. The smaller target isolation size will then give a better estimate of the residual phase error function since the noise bandwidth is decrease. PGA will then iterate with decremental target window sizes until the estimated error function satisfies a certain threshold condition.

Hence in conventional Phase-Gradient solution, iterations are necessary! However, iterations are time-consuming as they involve repeating forward and reverse azimuth Fourier Transformations of the SAR map, data circular shiftings, phase estimation and compensation procedures. Now the question is ***are there anything that we can modify to the exiting PGA algorithm such that the near convergence focusing quality can be achieved without any iterations?*** The observations that the author made are that if we can (a) increase significantly the total synchronisation scattering sources by 3-4 times right at the beginning of the estimation stage and (b) to ensure that those selected scatterers must be optimal in terms of sufficient Signal-to-Noise energy and negligible impulse response interferences from neighboring target and clutter scatterers, there is a high probability that a near or complete converging phase error function can be measured just on the first iteration. In the next section, a proposal on some modifications to the existing PGA that satisfy the latter-mentioned two criteria, will be discussed. The author called this modified Phase-Gradient approach the Quality Phase Gradient Autofocus (QPGA) algorithm.

QPGA Concept and Implementation

PGA usually limits its target search to the number of range pixels in the SAR map. As each range bin contains many scatterers distributed across the integration aperture, it is highly probable to gather more than 1 prominent scatterers. It is also highly probable that the least brightest

0-7803-3836-7/97/$10.00 © 1997 IEEE

selected scatterer in a range gate may turn out to be of higher intensity as compared to the maximum brightest scatterer of another gate. A "growing" process is proposed by extracting the phase histories of the next few brightest scatterers within that same range gate to increase the pool of quality synchronisation sources. ***This allows the use of a sufficiently large blurring kernel (window size) for each selected prominent targets such that the error function can be near completely captured on the first iteration while the increase noise bandwidth will be suppressed by the increased statistical averaging from the extra synchronisation scatterers***. For example, if N is the total SAR map range pixels and M 'potential candidates' based on next M brightest intensities in each single range gates are selected, a total of N×M "ideal" prominent scatterers are gathered. From empirical experiments with real SAR images, M value of 3 to 6 is appropriate and larger values of M will result in a diminishing returns on the quality of synchronisation scatterers. The window size to be used in such a non-iterative solution (QPGA) is derived from the in-depth knowledge of the characteristics of the radar electronics, antenna in-flight dynamics and motion compensation reliability.

However, as the selection criteria is based purely on the relative image intensities within that range gate, measure has to be taken to avoid selecting multiple targets that are (a) interfered by clutter and neighboring target signatures or (b) points that are featureless across the synthetic aperture of that range gate. Using such synchronisation scatterers can degrade the phase error estimation quality. A ***target filtering process*** is especially important in this proposed solution since the algorithm works on a large blur kernel size and the pool of potential synchronisation sources is now much larger than conventional PGA. The criteria for an image domain scatterer to be filtered as "quality" are (a) the mainlobe energy has to be much higher as compared to the noise floor, and (b) there is negligible distortion/interference to both the mainlobe and sidelobes.

A technique to select quality scatterers is to look at the contrast measure of the scatterer's range-compressed phase history [4]. This is a measure of the dominant scatterer intensity variance normalized by the mean power. Complex doppler histories of potential scatterers with low contrast values (typically<0.1) are indications of good synchronisation quality and will be selected for use in the phase error estimation process. Alternatively, to speed up the QPGA algorithm, the contrast measurement can also be made using the scatterer's image impulse response. To enhance near convergence focusing quality in QPGA, this single iteration method uses noise-robust, higher order difference equation to perform the differentiation operation in the phase estimation process. This is important since differentiation is highly less accurate than performing an integration operation, especially when the phase function has larger absolute gradients.

Results

Fig.1 is an image defocused by a phase error function that is dominantly quadratic and has some sinusoidal variations. Prominent features of this image like the array of reflectors at the top left corner, major road intersections and tree shadows are blurred, and the image contrast is degraded. The Mean Square Error (MSE) between the injected and estimated phase errors is used for performance measure. Fig.2 and Fig.3 demonstrate the quality differences between PGA and QPGA, both after 1 iteration procedure. Image features corrected using QPGA, with synchronisation sources gathered from the four next prominent scatterers per range gate, are more focused and the contrast is improved. Fig.4 shows the phase error estimation plots. It is observed that for PGA to achieve the same convergence as QPGA, it requires about 4 iterations for that defocused image. Comparing in terms of computational speed (Pentium 200 platform), the QPGA is 3 times faster for the same focusing quality. QPGA also delivers significant performance impact when focusing a clutter-dominant map. An important application is the focusing of SAR image containing isolated vehicles in a vegetation-dominant area.

Conclusions

The QPGA technique has demonstrated the feasibility of enhancing SAR image focus with a faster convergence in error estimation as compared to the conventional PGA solution. The fact that near convergence image quality has been achieved at the first iteration suggests the possibility of a non-iterative Spotlight SAR autofocusing algorithm.

References

[1] D.E. Wahl, P.H. Eichel, D.C. Ghiglia, C.V. Jakowatz, "Phase Gradient Autofocus-A Robust Tool for High Resolution SAR Phase Correction", IEEE Trans. AES, Vol. 30, No. 3, pp. 827-834, July 1994.

[2] C.V. Jakowatz, D.E. Wahl, "Eigenvector Method for Maximum-Likelihood Estimation of Phase Errors in Synthetic-Aperture-Radar Imagery", J. Opt. Soc. Am:A, Vol. 10, No. 12, December 1993.

[3] T.C. Calloway, G. Donohoe, "Subaperture Autofocus for Synthetic Aperture Radar", IEEE Trans. AES, Vol. 30, No. 2, pp. 617-621, April 1994.

[4] E. Yadin, "SAR Autofocusing Viewed as Adaptive Beamforming on Prominent Scatterers", IEE Radar 94 Conf., Brighton UK, pp. 138-143.

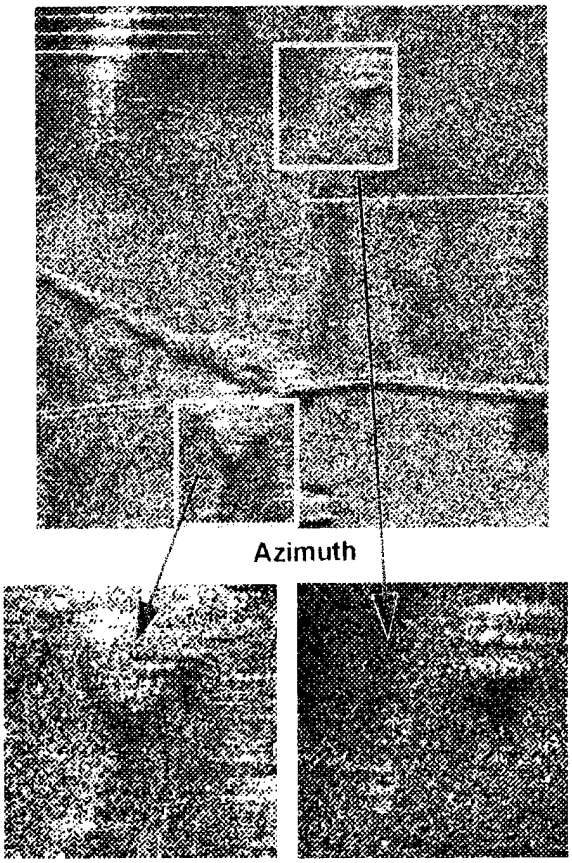

Fig 1 : A defocused Spotlight SAR image

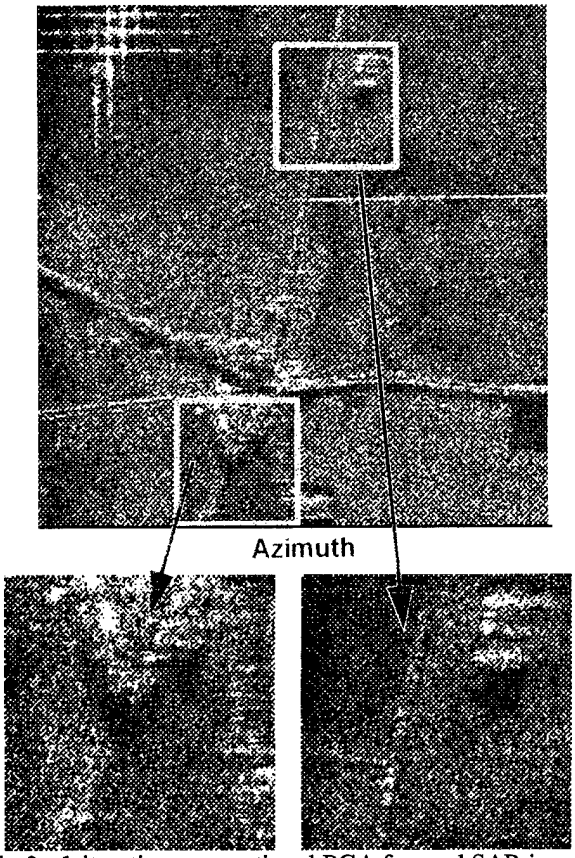

Fig 2 : 1-iteration conventional PGA focused SAR image

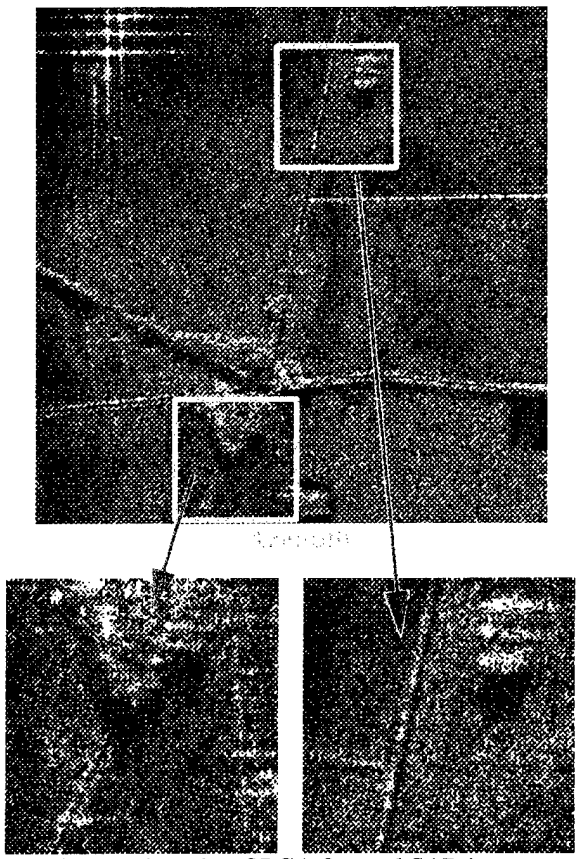

Fig 3 : 1-iteration QPGA focused SAR image

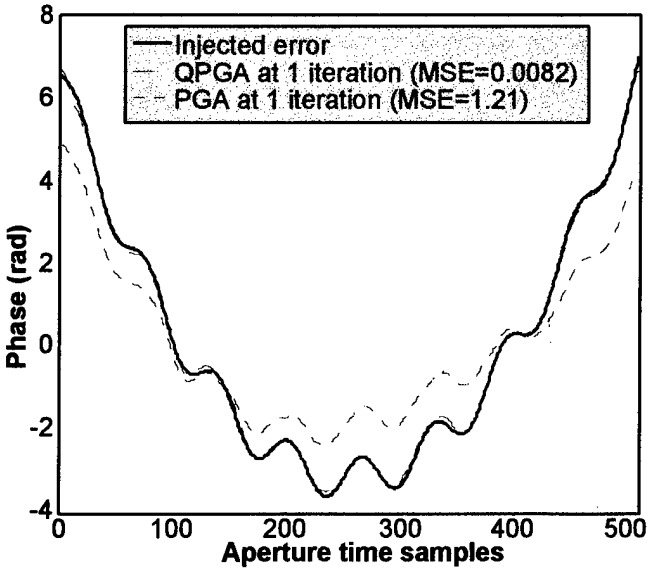

Fig 4 : Phase error estimation with various Phase-Gradient schemes

Real Time Synthetic Aperture Radar (SAR) Preprocessor Design Via Three-Dimensional Modular Filtering Architecture

Chan Hian Lim, Yeo Tat Soon
National University of Singapore
Department of Electrical Engineering
Radar and Signal Processing Laboratory
10 Kent Ridge Cresent, Singapore 0511
Email : chianlim@singnet.com.sg

Abstract – Synthetic Aperture Radar (SAR) systems are increasingly demanding for real real-time performance. As part of an effort to develop a real-time Range-Doppler digital SAR processor to produce image maps of that scanned area immediately as raw data are collected, this paper describes the conceptual architecture design for a high-speed front-end video pre-filtering. The evolved architecture consists of richly interconnected planes of novelly-adapted Modified Transverse FIR parallel tapped delay elements. Both the range and azimuth prefilterings are performed simultaneously in a continuous input-output flow without the need to worry about corner turning caused by azimuth preprocessing on data samples that are collected in the range direction.

Introduction

Synthetic Aperture Radar (SAR) is one of the most important airborne active sensor system that provides all-weather high-resolution imaging for military surveillance, and for remote sensing in geology, agriculture, oceanography etc. A fundamental characteristic of SAR sensor is that a small antenna is used to synthesize an effective antenna aperture that is much longer, based on the motion of the radar to collect data at different points on the flight-path and sophisticated signal processing as the prerequisites.

The video data comes from the RF front end in bursts coinciding with the received microwave pulses from the scene. The preprocessing consists of a range high-pass filter for DC bias cancellation and an azimuth presummer (see Fig.1). The filtering stages are commonly implemented by the use of *finite impulse response* (FIR) structures since they can be designed to have exactly linear phase response and no image artifacts like blurring and geometric distortion will be introduced. As timely surveillance is important for successful military maneuvers, building an on-board real-time video filter which could meet the throughput requirements of SAR processing is important. With the advent of VLSI technology, a recent solution on the use of a class of FIR filter called the Modified Transverse FIR structure, has been proposed as the basic architecture for implementing real-time SAR correlators [1] and it forms the motivation for the proposed SAR preprocessor design.

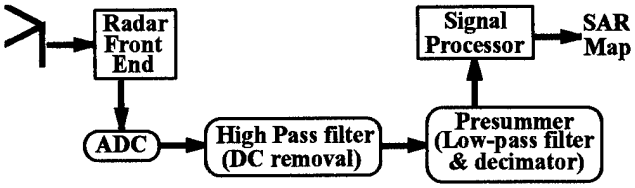

Fig 1 : SAR high-pass filter and presummer configuration

Range Prefiltering

An artifact of the ADC (analog-to-digital conversion) stage is the presence of DC component in the digitized SAR raw data. The presence is due to the component tolerances and temperature drift of the hardware. This DC residual will cause signal saturation in some of the range bins, meaning a voltage spike in the zero frequency bin, since the Fourier transform integrates this DC value over the image. Simple removal of the frequency bins surrounding the DC value is not acceptable since critical scene data may be contained in these bins. High-pass FIR digital filtering is the preferred real-time solution [2] for the elimination of the DC bias in the sampled video data (range lines) before azimuth presumming starts.

For real-time application, the range prefiltering can be performed using high-density programmable gate array consisting of fast multipliers, adders and logic gates. The filtering speed can be significantly improved by exploiting parallelism in the FIR processing flow in a modified transverse structure as shown in Fig.2. The filter coefficients are computed with a designed cut-off frequency that is slightly above zero and the values are pre-stored in discrete memory cells. Data samples collected on every pulse repetition interval (PRI) are fed in sequence into the high-pass filter as they arrived at the outputs of the ADCs. The same set of coefficients is used for filtering in every PRI and each output has a computation latency of only 1 complex multiply and 1 complex add.

Azimuth Presumming

Azimuth presumming [3] is a digital technique for reducing the data rates in the SAR processor. This is possible when the maximum doppler bandwidth is greater than needed for the desired resolution, which is frequently

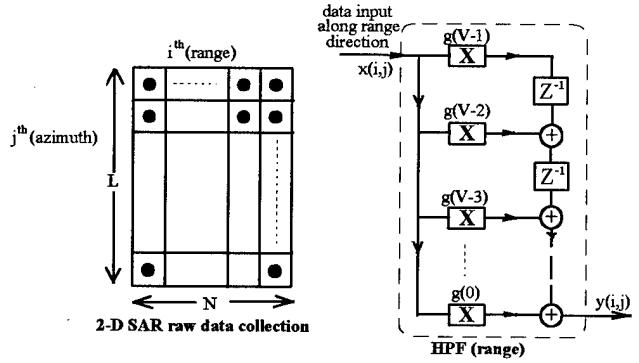

Fig 2 : High-pass filter design for DC bias removal

the case. In SAR processing, azimuth presumming is normally carried out before the range compression stage since it will effectively reduce the number of azimuth data bins. The presummer is commonly implemented using a low-pass FIR filter, followed by a decimator. Due to the low-pass nature of the presumming operation, the signal-to-noise ratio at the output of the presummer is also enhanced.

After the high-pass filtering operation for DC bias cancellation, each range vector is then accumulated in the presummer (vector accumulation in the azimuth direction). For real-time solution, the proposed presumming architecture uses the same modular filtering design as the DC bias cancellation circuitry as shown in Fig.2. However, the SAR presummer needs some novel modifications to take into account that the raw data are collected in the range direction instead of the azimuth direction, by utilising delay elements of length N cells each (size of a range line). This modification will allow continuous data flow and simultaneous pre-filtering operations (see Fig.3). A demultiplexing and timing circuitries are used for implementing the presum decimator.

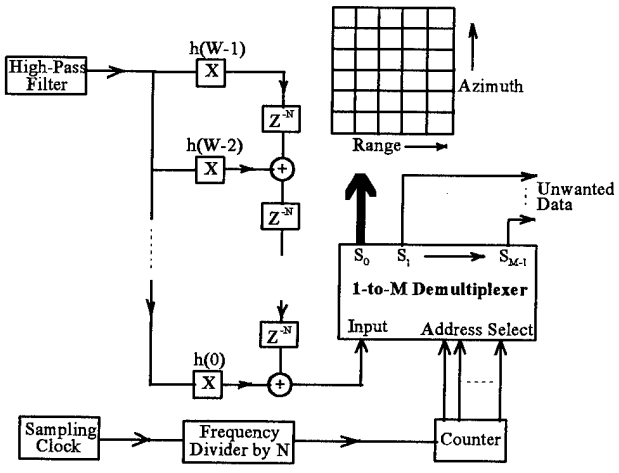

W : FIR filter length
M : Presumming factor
N : Total number of range bins in one range line

Fig 3 : Real-time implementation of Presummer circuitry

The computation latency for just the azimuth presummer is 1 complex multiply, 1 complex add and the signal propagation delay through the demultiplexer. The filter coefficients are computed with a low-pass cut-off frequency response determined by the minimum Doppler bandwidth.

3-Dimensional SAR Video Filtering Architecture

An integrated video filter design for DC bias cancellation and presumming operation is shown in Fig.4. The structure shows high modularity and regularity. The combined compute latency time for a raw data sample to undergo the two-stage filterings is 2 complex multiplies, 2 complex adds and the propagation delay through the demultiplexer. As multiply operation takes much longer time to compute as compared to adding and the demultiplexer signal delay is also negligible, effort is made to improve the video filter speed via novel architectural modifications. The input SAR raw data is a two-dimensional array, X(i,j). Be it range or azimuth, each filtering stages is 1-dimensional convolution with pre-determined coefficients. The final output of the range/azimuth preprocessing can be written as

$$Z(i,j) = \sum_{k=0}^{L-1} \sum_{l=0}^{N-1} X(l,k) \times \{g(i-l).h(j-k)\} \quad (1)$$

where L : the number of azimuth pulses (very large),
N : number of range gates per range line,
g(i) : range filtering coefficients of length V, and
h(j) : azimuth filtering coefficients of length W.

Equation (1) shows that the two sequence filtering operations can be formulated as the convolution between the incoming raw data and a 2-dimensional filter coefficient set (product of two separable 1-D coefficient sets). Thus for simultaneous range/azimuth filtering operations, the convolution operation is now two-dimensional. Moreover, to account for the fact that the raw data are collected in the range direction instead of the azimuth direction, the final evolved architecture for the SAR preprocessor consists of richly interconnected planes of novelly-adapted Modified Transverse FIR parallel tapped delay elements (see Fig.5). The preprocessor architecture is 3-dimensional and each raw data sample is simultaneously range and azimuth pre-processed in 1 complex multiply and 2 complex adds. The novel design offers rapid continuous input-output data flow without the need to worry about corner turning caused by azimuth preprocessing on data samples that are collected in the range direction.

This modular structure translates easily into an ASIC implementation using high-density programmable gate array consisting of fast multipliers, adders and logic gates. The typical lengths for the 2-D filter coefficients, V and W, are 16 or 32. The coefficients are pre-computed and pre-stored

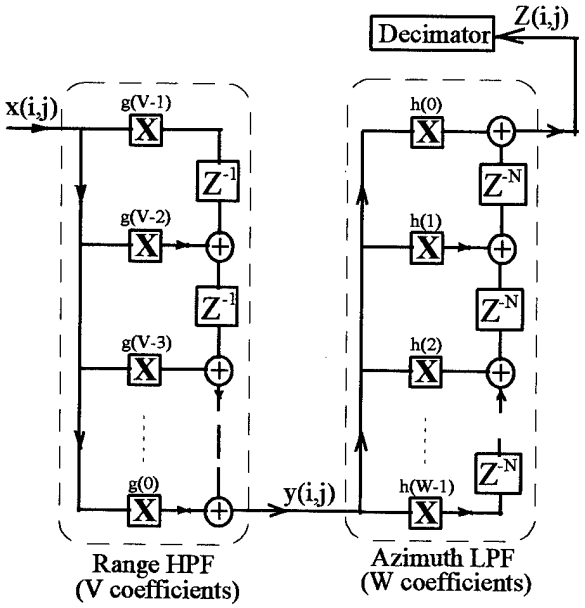

Fig 4 : Cascading of range filter and azimuth presummer

in some memories. Instead of using discrete fast multipliers, the multiplication time between an input sample and the coefficient can be reduced further by using EPROMs as a look-up table. The computation time is only the memory access time which with GaAs technology, is just about 3 ns or less. EPROMs are preferred so that in future when the filter coefficients have to be altered, it can be changed easily. The programmability gives high flexibility to the preprocessor for use in different imaging modes. The real-time SAR prefiltering process is achieved as a result of the high modular data flow in the 3-D processing architecture as well as VLSI advances. However, such a speed enhancement is at the expense of significant increase in hardware complexity.

Conclusions

Real-time SAR image formation is highly important for military surveillance, especially for effective timely actions to counteract any assessed threats. As part of an effort to develop a real-time Range-Doppler digital SAR processor, a conceptual high-speed architecture design for the front-end video pre-filtering is proposed. The DC bias cancellation and azimuth presummer operations are embedded into a single 3-dimensional richly interconnected planes of novelly-adapted Modified Transverse FIR parallel tapped delay elements. The novel design offers rapid continuous input-output data flow without to worry about corner turning caused by azimuth preprocessing on data samples that are collected in the range direction. The compute

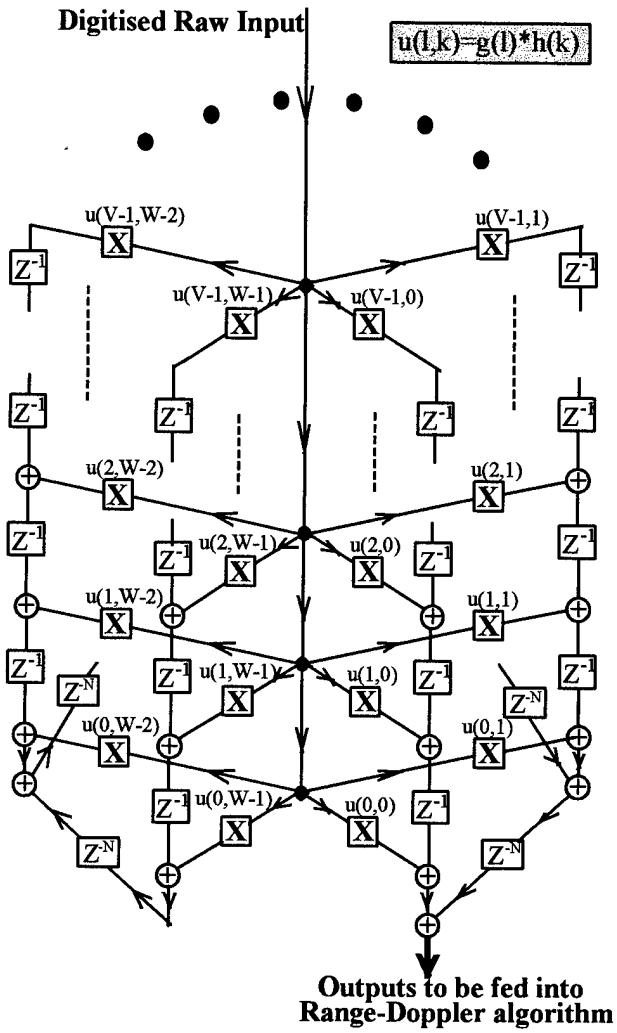

Fig 5 : 3-D geometrical filter for SAR preprocessor

latency has been enhanced to just 1 complex multiply and 2 complex adds. This design is best suited for ASIC implementation.

References

[1] A. B. Premkumar, "Real-Time Synthetic Aperture Radar Imaging : A Model and Design Using VLSI Correlators", University of Michigan, Phd thesis, 1991.

[2] B. L. Remund, C. Jimmy, "A Digital ASIC Implementation Of A Video Filter For Synthetic Aperture Radar", GaAs IC Symposium, pp. 345-348, 1991.

[3] Walter W. Goj, *Synthetic-Aperture Radar and Electronic Warfare*, Artech House, pp. 11-16.

High Resolution SAR Processing Using Stepped-Frequencies

Richard T. Lord and **Michael R. Inggs**
Radar Remote Sensing Group, Dept of Electrical Engineering, University of Cape Town
Private Bag, Rondebosch 7700, South Africa
Tel: +27 21 650 3756 Fax: +27 21 650 3465
Email: rlord@eleceng.uct.ac.za

Abstract—This paper demonstrates a method to produce high resolution SAR images using stepped-frequencies. An advantage of the stepped-frequency approach is the reduction of the instantaneous bandwidth and sampling rate requirements of the radar system, as well as the possibility of skipping frequencies that might be corrupted due to external interfering frequency sources. The technique described in this paper involves the construction of a wide-bandwidth chirp pulse produced from a burst of narrow-bandwidth chirp pulses transmitted at stepped-frequency intervals. A description of this technique is given and simulation results are shown.

INTRODUCTION

The use of stepped-frequency waveforms to obtain high range resolution is well documented [6]. Synthetic range profile (SRP) processing is a very effective method to obtain high downrange profiles of targets such as aircraft [5]. However this method has the unfortunate drawback that target energy spills over into consecutive coarse range bins due to the matched filter operation, causing "ghost images" in the resulting range profile [4]. This is the main reason why it is not regarded as a suitable method to process SAR images. In the following section another method is described which does not cause any "ghost images". This is demonstrated in Fig. 1, which shows a processed SAR image consisting of point targets in the shape of an "R", having been obtained using eight frequency steps.

This paper focuses mainly on the production of high range resolution. To obtain high resolution images, motion compensation and range curvature would also have to be addressed.

WAVEFORM MODELLING

The essence of the method described below is the construction of a fictitious wide-bandwidth chirp signal (with centre frequency f_c, bandwidth B, chirp rate γ and pulse length T_p) from a group or *burst* of n narrow-bandwidth chirp signals (with bandwidth B_n and pulse length T_{pn}). It is important that the narrow-bandwidth chirp pulses have the same chirp rate γ as the fictitious wide-bandwidth chirp signal. Therefore the narrow bandwidth B_n is obtained by reducing the pulse length T_p by a factor of n, where n is the number of pulses used to synthesize the total radar bandwidth B. The centre frequency of the narrow-bandwidth pulses, which are stepped in frequency to cover the whole synthesized bandwidth, is given by

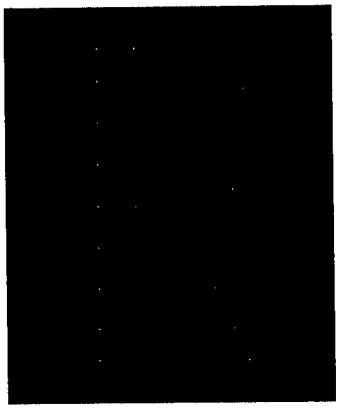

Figure 1: Synthetic SAR image processed using stepped-frequency waveforms

$$f_c(k) = f_c + \left(k + \frac{1}{2} - \frac{n}{2}\right) B_n \qquad (1)$$

where $k = 0 \ldots (n-1)$. The phase of the transmitted pulses belonging to one burst can be described by

$$s_x(t,k) = \text{rect}\left(\frac{t}{T_{pn}}\right) \exp\left[j2\pi f_c(k)\, t\right] \cdot \exp\left[j\pi\gamma t^2\right] \qquad (2)$$

The signal phase received by the SAR system from a single scatterer at a distance r_t is therefore given by

$$\begin{aligned} s_r(t,k) \;=\; & \text{rect}\left(\frac{t - \frac{2r_t}{c}}{T_{pn}}\right) \exp\left[j2\pi f_c(k)\left(t - \frac{2r_t}{c}\right)\right] \\ & \cdot \exp\left[j\pi\gamma\left(t - \frac{2r_t}{c}\right)^2\right] \end{aligned} \qquad (3)$$

The appropriate reference function for demodulating and

0-7803-3836-7/97/$10.00 © 1997 IEEE

motion compensating the received signal is

$$s_{ref}(t,k) = \exp\left[j2\pi f_c(k)\left(t - \frac{2r_s}{c}\right)\right] \quad (4)$$

where r_s is the distance from the radar to scene centre. The presence of the constant r_s in this reference function introduces a phase term in the demodulated signal which varies from pulse to pulse and therefore has to be cancelled. This cancellation is achieved by including a similar term involving r_s in the frequency-shift operation given by (6).

The signal that results from mixing the received signal of (3) and the complex conjugate of the reference function of (4) is

$$\begin{aligned} s(t,k) &= \text{rect}\left(\frac{t - \frac{2r_t}{c}}{T_{pn}}\right)\exp\left[j4\pi f_c(k)\left(\frac{r_s - r_t}{c}\right)\right] \\ &\quad \cdot \exp\left[j\pi\gamma\left(t - \frac{2r_t}{c}\right)^2\right] \end{aligned} \quad (5)$$

Fig. 2 gives an overview of the signal processing steps involved to reconstruct the wide-bandwidth chirp pulse from (5). In the figure, two narrow-bandwidth pulses at baseband are shown. These two pulses have to be upsampled and shifted in frequency, and a constant phase term has to be added to each of them, before they can be combined to yield the wide-bandwidth signal. These operations are described in the following subsections.

Upsampling

The narrow-bandwidth pulses are naturally sampled at a lower rate than the corresponding wide-bandwidth pulse. Before recombining the narrow-bandwidth pulses to obtain the wide-bandwidth pulse, they have to be upsampled, usually by a factor of n, where n is the number of pulses used to synthesize the wide bandwidth. This has been accomplished using a straightforward digital FIR filter. The upsampling operation, which is effectively an interpolation, is the only step in the procedure which introduces a certain amount of error in the reconstructed chirp pulse. However it has been found that this effect is negligible and hardly affects the final image resolution.

Frequency-Shift

Since all n narrow-bandwidth pulses described by (5) are at baseband, they need to be shifted in frequency before being combined. A frequency shift in the frequency domain corresponds to a multiplication with a phase ramp in the time domain. Therefore the received signal has to be multiplied by

$$\phi_1(t,k) = \exp\left[j2\pi\left[\left(k + \frac{1}{2} - \frac{n}{2}\right)B_n\right]\left(t - \frac{2r_s}{c}\right)\right] \quad (6)$$

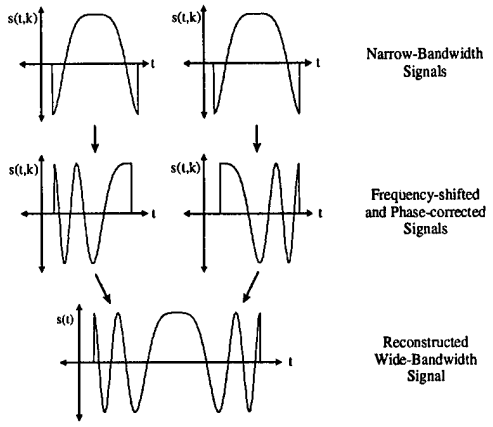

Figure 2: Construction of wide-bandwidth chirp pulse

Phase Correction

In order for the phase of the wide-bandwidth pulse to be continuous at the narrow-bandwidth pulse boundaries, it is required that the following phase-correcting term $\phi_2(k)$ be added to each pulse:

$$\phi_2(k) = \exp\left[\pi\gamma T_p^2\left(\frac{1}{4} - \frac{k+\frac{1}{2}}{n} + \frac{k^2+k+\frac{1}{4}}{n^2}\right)\right] \quad (7)$$

Note that the frequency-shift and phase-correcting terms can be applied simultaneously. In fact the phase-correcting terms can be applied before upsampling the signals, resulting in a faster implementation of the whole procedure.

Time-Shift

Before adding the individual pulses together, they have to be shifted in the time domain. The necessary time-shift is given by

$$\Delta t(k) = \left(k - \frac{n}{2} + \frac{1}{2}\right)T_{pn} \quad (8)$$

In order for the individual chirp pulses to align next to each other without discontinuity, care has to be taken to ensure that the time-shift is an integer number of discrete sample spacings. This can be achieved by either adjusting the pulse length T_{pn} or the A/D sample rate f_{ad}.

The raw image is now ready to be processed by a conventional SAR processor such as the Chirp Scaling algorithm, which also applies accurate range curvature correction.

SIMULATION RESULTS

Fig. 3 shows a surface plot of two point targets separated in range by a distance of 3 m. The radar parameters that were used to create the raw data are given in Table 1.

Every individual transmitted chirp pulse has a bandwidth of 15 MHz giving a slant-range resolution of 10 m. However the total synthesized bandwidth is 120 MHz, thereby making a slant-range resolution of 1.25 m possible. The Chirp Scaling algorithm, which was used to process the data, made use of the Taylor weighting function to reduce sidelobes, thereby broadening the mainlobe and reducing the range and azimuth resolution by a factor of 1.34. Nevertheless the two point targets shown in Fig. 3 are clearly distinguishable. It is important to note that there are no "ghost images" in the processed image. Furthermore, it was possible to reduce the minimum A/D sample rate from 120 MHz to 15 MHz (in the simulation 17.5 MHz was used), thereby alleviating the instantaneous sample rate requirements of the radar.

A disadvantage of stepped-frequency systems is the increase in PRF. If the increase in PRF becomes intolerable, one might have to resort to methods such as multiple PRF ranging [2 pg. 116].

INTERPOLATING MISSING FREQUENCIES

Recent advances in analogue-to-digital technology have made it increasingly more feasible to achieve high instantaneous bandwidths, thereby reducing the need to resort to stepped-frequency waveforms to obtain high range resolution. However the capability to omit frequencies in a transmit-burst that are corrupted due to external interference remains an important advantage, especially for high-resolution VHF systems that operate in a frequency band contaminated with broadcast FM and mobile radio. It is desirable to interpolate the missing data in order to obtain the highest possible range resolution. Suitable interpolation techniques are currently under investigation.

CONCLUSIONS

The method proposed in this paper to recombine a number of narrow-bandwidth chirp pulses to construct a wide-bandwidth chirp pulse has been shown to be feasible with the aid of simulated SAR data. It does not suffer from the "ghost image" effect as the SRP method, and it is fairly straightforward to implement. Further work will still have to be carried out to determine the optimal method to interpolate missing frequencies. The effect of radar imperfections, such as transmit pulses with finite rise and fall times and phase and amplitude errors due to dispersive effects, also have to be investigated.

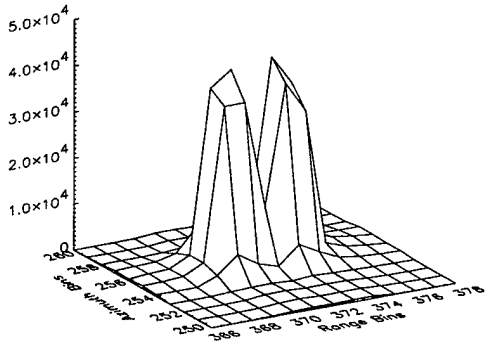

Figure 3: Surface plot of two point targets

Table 1: Radar Parameters

start centre frequency	f_0	347.5 MHz
frequency step size	Δf	15 MHz
number of steps	n	8
total radar bandwidth	B	120 MHz
slant-range resolution	$\rho_r = \frac{c}{2B}$	1.25 m
pulse length	T_{pn}	571.43 ns
chirp bandwidth	B_n	15 MHz
A/D (complex) sample rate	f_{ad}	17.5 MHz
PRF	f_{prf}	1.6 kHz

ACKNOWLEDGMENTS

The authors wish to thank Rolf Lengenfelder for his help with the production of the synthetic data.

REFERENCES

[1] A. Gustavsson, P.O. Frölind, H. Hellsten, T. Jonsson, B. Larsson, and G. Stenström, "The Airborne VHF SAR System CARABAS," Proc. IEEE Geoscience Remote Sensing Symp., IGARSS'93, Tokyo, Japan, vol. 2, pp. 558–562, August 1993.

[2] S.A. Hovanessian, Radar System Design and Analysis, Norwood, MA 02062: Artech House, 1984.

[3] Y. Huang, Z. Ma and S. Mao, "Stepped-frequency SAR System Design and Signal Processing," Proc. European Conference on Synthetic Aperture Radar, EUSAR'96, Königswinter, Germany, pp. 565–568, March 1996.

[4] R.T. Lord and M.R. Inggs, "High Resolution VHF SAR Processing Using Synthetic Range Profiling," Proc. IEEE Geoscience Remote Sensing Symp., IGARSS'96, Lincoln, Nebraska, vol. 1, pp. 454–456, June 1996.

[5] A.D. Robinson and M.R. Inggs, "Correlation Filters Applied to Synthetic Range Profiles of Aircraft Targets," IEEE Proc. of the South African Communications and Signal Processing Symp., COMSIG'94, October 1994.

[6] D.R. Wehner, High-Resolution Radar, Second Edition, Norwood, MA 02062: Artech House, 1995.

RADARSAT Attitude Estimates based on Doppler Centroid of Satellite Imagery

Said R. Marandi
Canadian Space Agency
6767 route de l'Aeroport, Saint-Hubert, Quebec J3Y 8Y9 Canada
(514) 926-4691; FAX: (514) 926-4695; Said.Marandi@space.gc.ca

Abstract – An algorithm is developed for computation of the expected Doppler shift in the returned SAR signal. The Doppler shift is a function of the attitude of the satellite, range time and the position of the satellite in the orbit. The least squares error between the results of the algorithm and the measured Doppler centroid of an image yields the yaw and pitch of the satellite corresponding to the time of the image.

Sixteen images, taken after a series of corrections to the Attitude Control System tables, are analyzed. The resulting yaw and pitch values were $-0.15° \pm 0.05°$ and $-0.06° \pm 0.12°$. The insensitivity of the calculated yaw and pitch values to small variations in the assumed roll of the satellite is demonstrated.

INTRODUCTION

In the following paragraphs, the motive behind this work is given. The principle of Doppler shift in SAR imagery is explained. The essential terminology needed for the description of this phenomenon is introduced. An outline of how the attitude of RADARSAT[1] is extracted from the Doppler shift measurements of the imagery completes the introduction.

During the commissioning of RADARSAT, a number of hand-overs between the primary and the secondary sensors were performed. The observed discrepancy between the respective attitude measurements highlighted the need for an independent truth source. The SAR imagery provides a potential truth source for attitude determination.

The site imaged by the SAR antenna has a relative velocity with respect to the satellite. The component of this relative velocity along the vector connecting the satellite to the imaged site results in a Doppler shift in the returned signal. The Doppler shift is positive, namely the returned signal has a higher frequency than the transmitted signal, when the satellite is moving towards the imaged site. The Doppler shift is negative when the satellite is receding from the imaged site.

Range time is the period between the transmission of a SAR pulse and the return of some portion of the signal. Associated with each image at a given range time is a function expressing the intensity of the returned signal versus frequency. This function is called the Doppler spectrum. Association of the frequency at maximum intensity in the Doppler spectrum with the range time is another function called measured Doppler centroid. Canadian Data Processing Facility, on the ground, estimates the measured Doppler centroid.

In the next section, an algorithm is formulated which calculates the expected Doppler centroid, henceforth referred to as the model Doppler centroid. The Doppler centroid depends on attitude of the satellite and the location of the satellite in orbit. The location of the satellite in orbit is parameterized by the argument of latitude—the angle between the earth-satellite line and the line of nodes. Denote argument of latitude by λ. Recall that the line of nodes is formed by the intersection of the orbital plane with the equatorial plane. Argument of latitude varies between 0 and 360°. The ascending and descending nodes are respectively denoted by 0° and 180°.

In general, if the attitude of satellite is nominal, the model Doppler centroid will be different from the measured Doppler centroid. This difference may be minimized by adjusting the yaw and pitch parameters of the algorithm. The yaw and pitch corresponding to the minimum error between the measured and calculated Doppler centroid represent the attitude of the satellite when the image was taken.

The described method determines yaw and pitch of the satellite provided the roll of the satellite is known. Fortunately, the yaw and pitch are fairly insensitive to variations in roll. For that reason, one may safely set the roll to zero and compute the yaw and pitch. The obtained result would be correct to within a few percent even if the roll deviates from zero by as large as one degree.

FORMULATION

Coordinate Frames

In the following paragraphs, the coordinate frames necessary in the computation of the Doppler shift are introduced. Three coordinate frames are of interest: the inertial system, the flight frame and the control frame. All the coordinate frames are right handed and vectors along the axes are of unit length.

Define the inertial frame $Ox_iy_iz_i$ with O located at the center of mass of the earth, $\hat{x}_i$ going through the vernal

[1]RADARSAT is a Canadian-led cooperative program with the U.S. to launch and operate a remote sensing satellite with a synthetic aperture radar. The launch was on November 4, 1995.

0-7803-3836-7/97/$10.00 © 1997 IEEE

equinox of the day, $\hat{z}_i$ along the spin axis of the earth and $\hat{y}_i$ completing the triad.

The flight frame $Sx_fy_fz_f$ has its origin at the center of mass of the satellite $\vec{S}$, $\hat{z}_f$ along the geodetic nadir and $\hat{y}_f$ in the direction of $\hat{z}_f \times \vec{v_S}$. Here $\vec{v_S}$ is the velocity vector of the satellite with respect to an inertial system. $\hat{x}_f$ completes the triad $Sx_fy_fz_f$. Note that $\hat{x}_f$ is not necessarily along the velocity vector. This will have an impact on the Doppler shift of the imagery.

Define the control frame $Sx_cy_cz_c$ to be a coordinate system obtained from the flight frame by a sequence of yaw ψ, roll ϕ and pitch θ rotations. The transformation from control to the flight frame is denoted T_{fc}. The control frame is rigidly attached to the satellite.

Doppler Shift

In the following paragraphs, the geometry of the Doppler shift calculations is outlined.

We start with the mathematical description of the beam shape. At a given range in the far-field of the SAR antenna the locus of the maximum beam intensity describes a curve. In the control frame, the beam shape is defined as a cone (non-circular) generated by this curve with apex at the center of the mass of the satellite. This cone is very close to the y_cz_c plane. However, the deviation is significant for our calculations.

The transformation from flight to inertial is

$$T_{if} = (\hat{x}_f, \hat{y}_f, \hat{z}_f), \tag{1}$$

where the right hand side is the matrix comprised of unit column vectors $\hat{x}_f$, $\hat{y}_f$ and $\hat{z}_f$. The unit vectors $\hat{x}_f$, $\hat{y}_f$ and $\hat{z}_f$ are expressed in the inertial frame. Then the transformation from control to inertial frame becomes

$$T_{ic} = T_{if}T_{fc}. \tag{2}$$

Given an arbitrary point $\vec{x} = (x_1, x_2, x_3)$ expressed in the inertial frame

$$\vec{y} = T_{ci}(\vec{x} - \vec{S}) \tag{3}$$

is the corresponding point expressed in the control frame $Sx_cy_cz_c$. Here T_{ci} is the transpose of T_{ic}. Define the elevation Θ and azimuth ϕ of the point $\vec{y}$ as follows, Fig. 1:

$$\Theta = \frac{180}{\pi} \arccos \frac{y_3}{|y|}, \tag{4}$$

$$\phi = \frac{180}{\pi} \arctan(y_2, -y_1), \tag{5}$$

where the arc tangent function has two arguments, $\cos\phi$ and $\sin\phi$, and yields a value between $-\pi$ and π.

Define an auxiliary elevation as $\vartheta = \Theta - 29.8$. The beam shape is given as a function relating a given auxiliary elevation with the azimuth at which the beam intensity at a given range in the far field is maximum:

$$\begin{aligned}\phi(\vartheta) = {} & 0.0000605\vartheta^3 - 0.001803\vartheta^2 \\ & -0.000185\vartheta + 0.0594361.\end{aligned} \tag{6}$$

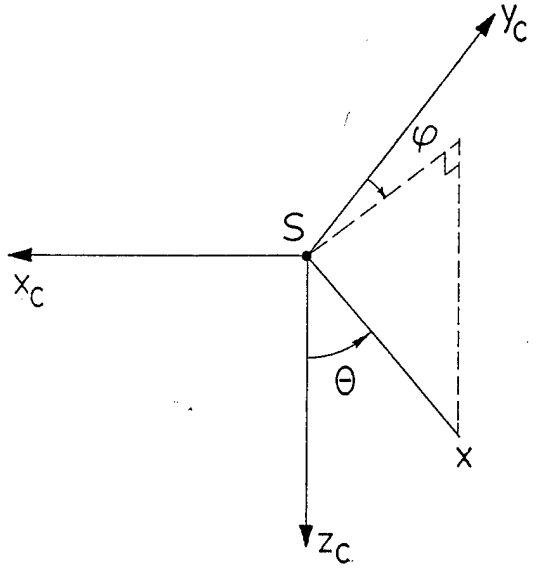

Figure 1: The elevation Θ and azimuth ϕ of a point $\vec{x}$ in the control frame.

This function was found as a third degree polynomial fit to the preflight calibration data for fine and standard beams of RADARSAT; see Fig. 2. The introduction of the auxiliary elevation was only necessary to relate the elevation and azimuth to the preflight calibration data; otherwise, it is superfluous to our presentation.

In the control frame, the set of points $\vec{y} \in \Re^3$ on the cone of maximum beam intensity satisfies the following equation:

$$C(\vec{y}) \equiv \frac{\pi}{180}\phi(\Theta(\vec{y}) - 29.8) + \arctan(y_2, y_1) = 0. \tag{7}$$

In the inertial frame the equation of the cone becomes

$$C(T_{ci}(\vec{x} - \vec{S})) = 0, \tag{8}$$

where the vector $\vec{x} = (x_1, x_2, x_3)$, expressed in the inertial frame, is an arbitrary point of the beam shape cone.

We proceed with the computation of intersection of the cone with the earth spheroid and the reach sphere (a sphere centered at $\vec{S}$ with radius equal to the distance electromagnetic radiation travels in half the range time $c\frac{t_r}{2}$); see Fig. 3(i). Here, c is the speed of light and t_r is the range time. The equation of the earth spheroid and reach sphere are respectively

$$\begin{aligned}\frac{x_1^2}{r_e^2} + \frac{x_2^2}{r_e^2} + \frac{x_3^2}{r_p^2} &= 1, \\ (\vec{x} - \vec{S}).(\vec{x} - \vec{S}) &= (c\tfrac{t_r}{2})^2.\end{aligned} \tag{9}$$

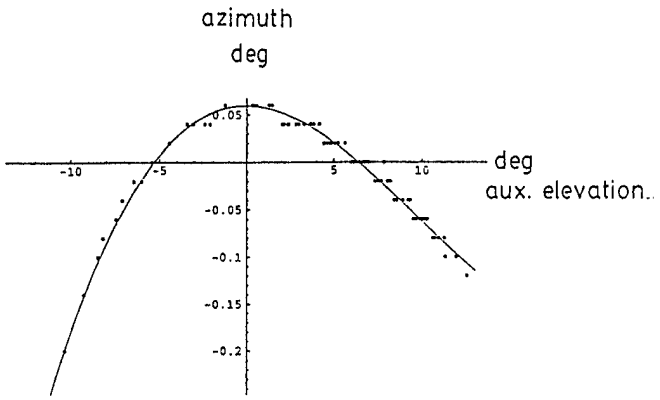

Figure 2: The beam shape of the RADARSAT SAR presented as azimuth ϕ versus the auxiliary elevation ϑ.

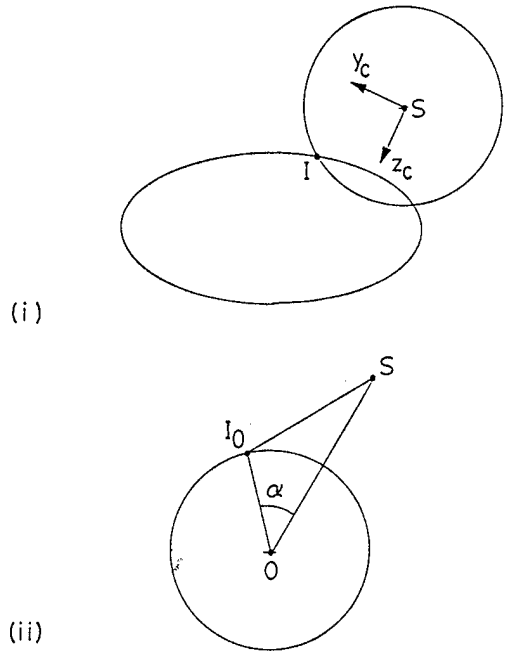

Figure 3: (i) The intersection of earth spheroid and reach sphere in the plane $y_c z_c$; (ii) Approximate location of the image site I_0 on the earth sphere with respect to the local vertical $\vec{OS}$.

The system of equations (8) and (9) is solved numerically by Newton's method with $\vec{x} = \vec{I_0}$ as the initial point of the iterative solution. The initial point $\vec{I_0}$ is obtained by rotating by α the sub-satellite point about an axis through O parallel to x_c, where

$$\alpha = \arccos\left(\frac{r_e^2 + |\vec{S}|^2 - (0.53ct_r)^2}{2|\vec{S}|r_e}\right); \qquad (10)$$

see Fig. 3(ii). The factor 0.53, which nominally should be 0.5, is chosen so that the numerical solution converges quickly. Denote the solution to the system of equations (8) and (9) as I standing for site imaged at range time of t_r located roughly on the intersection of $y_c z_c$ plane with the earth spheroid.

Denote the vector connecting the satellite to the image site as $\vec{SI} = \vec{I} - \vec{S}$. Then the component of the velocity of the image site with respect to that of satellite along $\vec{SI}$ becomes

$$\Delta v = (\vec{v_I} - \vec{v_S}).\frac{\vec{SI}}{|\vec{SI}|}, \qquad (11)$$

where v_I and v_S are respectively the inertial velocity of the image site and the satellite. The Doppler shift in the carrier frequency of the SAR antenna chirp can be written as

$$D(\psi, \phi, \theta, t, t_r) = -\frac{2\Delta v}{c}\nu, \qquad (12)$$

where $\nu = 5.3 \times 10^9$ Hz is the carrier frequency and parameters ψ, ϕ, θ, t and t_r denote the explicit dependence of the Doppler shift on yaw, roll and pitch of RADARSAT, time of the Doppler centroid and range time, respectively. The negative sign on the right hand side of the equation ensures that the Doppler shift is negative when the image site is receding and positive when the image site is approaching the satellite. The negative Doppler shift corresponds to the drop in the returning carrier frequency.

RADARSAT ATTITUDE

In this section, we outline the method of extracting yaw and pitch of the RADARSAT attitude from a comparison of the measured and the model Doppler centroid.

Table 1 lists sixteen images used for extraction of the measured Doppler centroid. The images are numbered, for identification, from one through sixteen in column one of the table. The second column contains the time of the measured Doppler centroid, formatted as follows: day of the year 1996, hour, minute and seconds. This time is estimated from the time of the first line of the image, the size of the image (1024 lines for all the chosen images) and the Pulse Repetition Frequency (PRF) of SAR at the time the image was taken; see column four. The third column contains the argument of latitude of the satellite which is derived from UTC time of the Doppler centroid via our elliptic orbital model. The fifth column contains

Table 1: SAR images used in calculation of the RADARSAT yaw and pitch in 1996

ID	time (UTC)	λ (°)	PRF (Hz)	beam
1	132-11:48:16.640	139.02	1304.71	S1
2	132-11:48:30.163	139.83	1304.71	S1
3	132-11:49:58.572	145.10	1291.65	S7
4	132-11:58:53.951	177.00	1293.20	S7
5	132-11:59:31.444	179.24	1296.94	F1
6	132-13:25:01.569	124.67	1354.16	S3
7	132-13:25:15.095	125.48	1354.16	S3
8	132-13:25:28.641	126.29	1354.16	S3
9	132-21:29:33.742	55.73	1341.51	S6
10	132-21:29:47.266	56.54	1341.51	S6
11	132-21:30:00.813	57.35	1341.51	S6
12	132-22:52:15.074	351.11	1359.29	S3
14	132-22:52:28.622	351.92	1359.29	S3
15	132-22:52:42.145	352.73	1359.29	S3
16	133-00:50:09.789	52.46	1274.08	S5
17	133-00:50:23.312	53.26	1274.08	S5

Table 2: The measured Doppler centroid

ID	d_0	$d_1 \times 10^{-6}$	$d_2 \times 10^{-8}$	d_3
1	4477.46	-4.193344	-8.719134	0.0055640
2	4510.43	4.366015	-11.64422	0.0055640
3	9633.55	2.175070	-2.021626	0.0070685
4	10884.82	2.461983	-1.155815	0.0070537
5	8975.58	3.030690	19.95111	0.0064507
6	4737.34	2.386300	-2.902745	0.0060279
7	4830.39	2.503874	-4.598744	0.0060279
8	4924.07	2.339740	1.249440	0.0060279
9	-5988.23	-0.817681	3.597004	0.0068165
10	-5840.76	-0.867324	5.516540	0.0068165
11	-5750.75	-0.720688	3.958633	0.0068165
12	-7109.37	-5.171375	26.28610	0.0059963
13	-7137.00	-5.259694	28.15499	0.0059963
14	-7171.34	-5.181704	26.52449	0.0059963
15	-5939.19	-1.726997	8.188181	0.0063932
16	-5786.28	-2.204031	18.44423	0.0063932

the beam used to image. All beams are selected from two classes: standard 1-7 and fine 1-5. The term high resolution is also used for the fine beams.

Table 2 contains the data for the measured Doppler centroid given as a quadratic function. The columns two, three and four contain the coefficients of the quadratic function $d_2 t_{r0}^2 + d_1 t_{r0} + d_0$. t_{r0} is defined in terms of t_r as follows:

$$t_{r0} = t_r - d_3. \tag{13}$$

d_3 is given in the fifth column. The measured Doppler centroid for each image is defined as the following quadratic function of t_r:

$$D_m(t_r) = d_2(t_r - d_3)^2 + d_1(t_r - d_3) + d_0. \tag{14}$$

Each image is obtained using a particular beam. Denote the minimum and maximum range times corresponding to a generic beam as t_m and t_M. Hence, the measured Doppler centroid is only of significance in the interval $[t_m, t_M]$. Define a root-mean-squared error function of yaw and pitch as follows:

$$E(\psi, \theta) = \sqrt{\frac{\sum_{j=1}^{n} (D(\psi, 0, \theta, t, t_j) - D_m(t_j))^2}{n}}, \tag{15}$$

where $t_1, \ldots, t_j, \ldots, t_n$ is a regular partitioning of the range time interval $[t_m, t_M]$. In practice, n was arbitrarily chosen anywhere from 6 to 10. E is an estimate of the rms error between the measured and model Doppler centroid. If the modeling was perfect in details and the measured Doppler centroid was exact, we would expect $E(\psi, \theta)$ to be zero when the yaw and pitch corresponding to that of satellite at the time of the image were used. Therefore, to find the yaw (ψ) and pitch (θ) of the satellite, we minimize E with respect to ψ and θ: the minimum point (ψ_0, θ_0) of function E is the desired attitude.

The yaw and pitch of the satellite at the argument of latitude corresponding to each image is calculated using the above procedure. The results are in Table 3. If we assume that the yaw and pitch of the satellite do not vary with the argument of latitude, then uncertainties on the attitude can be estimated. Choosing the reciprocal of the minimum rms error in the model and actual Doppler centroid as weights, one arrives at the following weighted mean and standard deviation for yaw and pitch: yaw $-0.15° \pm 0.05°$; pitch $-0.06° \pm 0.12°$. These values correspond to the attitude of RADARSAT after the corrections of Attitude Control System tables on May 11, 1996.

We have implicitly assumed the roll is zero. One may show that only the first column $\hat{x}_c$ out of three columns of T_{fc} is determined by our method. As a result, we may solve for only two out of three attitude parameters. We have chosen to specify the roll and calculate the yaw and pitch based on the assumed value of roll. In other words, given a measured Doppler centroid D_m, we are always confronted with, in absence of any other information, a one parameter family of solutions for yaw and pitch:

$$\begin{pmatrix} \psi(\phi) \\ \theta(\phi) \end{pmatrix}; \qquad \phi \in [-\frac{\pi}{2}, \frac{\pi}{2}]. \tag{16}$$

This one parameter family is plotted for image 16 in Fig. 4. Fortunately, the yaw and pitch are fairly insensitive to small variations in roll. As a result, one may safely set roll to zero in order to estimate yaw and pitch, as we have done. This justifies the choice of roll as an

Table 3: RADARSAT yaw, pitch and rms error in the Doppler shift deduced from SAR imagery

ID	yaw (°)	pitch (°)	rms error (Hz)
1	-0.11	-0.13	7.79
2	-0.11	-0.13	6.44
3	-0.27	-0.26	4.73
4	-0.18	-0.27	7.38
5	-0.08	-0.18	3.90
6	-0.16	-0.13	0.22
7	-0.14	-0.11	0.93
8	-0.09	-0.12	0.93
9	-0.15	0.02	0.30
10	-0.18	0.00	2.21
11	-0.23	-0.05	0.64
12	-0.07	0.06	1.65
13	-0.07	0.06	3.26
14	-0.07	0.06	1.85
15	-0.09	0.06	1.13
16	-0.13	0.03	13.2

assumed parameter.

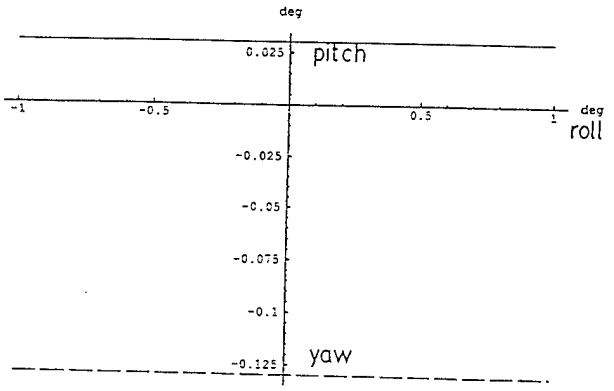

Figure 4: The family of yaw (dashed) and pitch versus roll for which the error function of the image 16 is minimized.

Error Sources

In the following paragraphs, possible sources of error in the attitude calculations are discussed.

The deviation of the maximum intensity surface of a beam from the cone $C(y) = 0$ is conjectured to be the dominant and systematic contributor to the error in the estimated attitudes.

Our results depend crucially upon the assumption that the cone $C(y) = 0$ determines the measured Doppler centroid. The truth of this assumption depends on the reflective properties of the imaged area, the topography of the imaged area and, most importantly, on the shape of the beam [1] and [2]. Shape of the beam refers to the distribution of the intensity level of the electromagnetic energy in the beam as a function of the elevation and azimuth.

CONCLUSION

The calibration of the attitude determination subsystem is critical to the success of a remote sensing mission and requires an independent truth source. One such truth source is the measured Doppler centroid.

Yaw and pitch of RADARSAT can be extracted from Doppler centroid measurements. For best results the imaged area should be of uniform reflective properties and of constant elevation.

The accuracy of the yaw and pitch estimates depends critically upon the beam shape of the SAR antenna. For improved attitude estimates an accurate far-field beam shape derived from exhaustive near-field measurements is compulsory.

For RADARSAT, roll can not reliably be estimated. Fortunately, yaw and pitch estimates are independent of roll. If significant departure from a plane is introduced into the beam shape of the SAR antenna, roll can also be estimated from measured Doppler centroid.

REFERENCES

[1] Robert O. Harger, *Synthetic Aperture Radar Systems: Theory and Design*, Academic Press, New York, 1970, chapter III.

[2] John C. Curlander and Robert N. McDonough, *Synthetic Aperture Radar*, John Wiley & Sons, Inc., New York, 1991, chapter 4.

A Research of Moving Targets Detection and Imaging by SAR

Runhong Pan, Gang Li, Xixing Zhu
Institute of Electronics, Academia Sinica, Beijing China,100080
Tel. 62565121 Fax. 62567363 E-mail. lrma@ieo.ie.ac.cn

Abstract--The motivation for this work has come from the problem of providing high resolution images of moving targets by Synthetic Aperture Radars (SAR). The paper investigates the application of joint time-frequent distribution (TFD) for detection and estimation of target motion parameters. Three kinds of TFD--Short Time Fourier Transform, Wavelet Transform and Wigner-Ville Distributions (WVD) are discussed. The WVD is chosen because it presents some important feature concerning detection and estimation issues. Furthermore, Hough Transform is employed to suppress the disturbing crossterms resulted from the bilinear character of WVD. The fast algorithm and the performance of the proposed approach are also involved in the paper. The simulation results have shown the effectiveness of the two algorithms.

Keywords: SAR, Moving Targets Imaging, Wigner-Ville Distributions , Hough Transform

INTRODUCTION

A conventional Synthetic Aperture Radar (SAR) achieves high range resolution through chirp pulse compression, and high azimuthal resolution by cross-correlating a theoretical stationary target's phase response with the collected data. If there exist moving targets on the ground, their images often appear ill-positioned and smeared. A solution to this problem is to analyze the actual Doppler frequency characteristics of the range compressed data.

In recent years, the representation of a signal in both the time and frequency domain has been of interest in time-varying nonstationary signals processing areas. It is known that the frequency part of SAR signal varies continuously with time. So a joint time-frequency analysis is a useful tool to estimate the actual Doppler frequency behavior by extracting the curve of instantaneous frequency (IF). Because the major difference between stationary objects and moving objects are that they have different central frequency and chirp rate. After the two key parameters are estimated, they may be subsequently used to adjust the processing to focus on the moving object.

Various different time-frequency distributions (TFD) have been proposed, each with its own merit and drawbacks. In the paper, three kinds of TFD--Short Time Fourier Transform (STFT), Wavelet Transform (WT) and Wigner-Ville Distributions (WVD) are discussed. The WVD has received a great deal of attention as a convenient tool for the analysis of monocomponent signals. However, as was pointed out by many authors, it is not effective for extended targets, because the inherent bilinear structure of distributions causes undesirable interfering cross terms. In our research, Hough Transform (HT) is employed to suppress the disturbing crossterms.

This paper is arranged as follows: the problem of SAR moving target imaging is introduced in part II, and the application of time-frequency analysis in this question is presented in part III. Then Hough Transform (HT) is presented to suppress the disturbing influence of spectral crossterms. Simulations and conclusions are shown in the end part.

SAR MOVING TARGETS IMAGING

The signal scattered by a stationary object can be expressed as[1]

$$Ss(x) = a(x)\exp\{-jkx^2 / R_0\} \quad x \in v_a t \qquad (1)$$

where T is the aperture time, $k=2\pi/\lambda$, λ is the wavelength of the carrier, a(x) is antenna function in azimuthal direction. Va is the velocity of the radar platform. Ro is the distance between the object and radar platform.

If the object is moving, and (Vr, ar) are the radial velocity and acceleration of the object. (Vc, ac) are the velocity and acceleration of the object along azimuth direction, then the scattered signal can be expressed as

$$S_m(x) = a[(1-\varepsilon_c')x]\exp(-2jk\varepsilon_r' x) \cdot \exp\{-jkx^2[(1-\varepsilon_c')^2 - \varepsilon_r'']\} \qquad (2)$$

where

$$\varepsilon_r' = v_r / v_a \quad \varepsilon_c' = v_c / v_a \quad \varepsilon_r'' = a_r R_0 / v_a^2 \qquad (3)$$

From(1) and (2), we can see that the major difference between stationary objects and moving objects are that they have different central frequency and chirp rate. In traditional

0-7803-3836-7/97/$10.00 © 1997 IEEE

SAR, the matched filtering method is used to get the focused images of objects. If used a reference function corresponding to stationary objects to match the moving targets, the maximum output of matched filtering is shifted from its original position, and the image of moving target is unfocused.

TIME-FREQUENCY REPRESENTATION

There are three basic methods to represent the time-frequency distribution (TFD) of a signal -- STFT, WT and WVD.

STFT: For a signal f(t), the definition of STFT is

$$F(t,f) = \int f(\tau) w[(\tau - t)f] \exp(-j2\pi f\tau) d\tau \quad (4)$$

where w(t) is window function. Since the STFT is based on a Fourier Transform (FT) applied to a time windowed version of the signal, with the window central instant varying with time, the frequency resolution is inversely proportional to the window duration. The narrower the window, the better is the time resolution, but the worse is the frequency resolution and vice versa.

Wavelet Transform: What the difference from STFT is, for WT, the width of window is variable. So its time and frequency resolution are not constant. When frequency is lower, WT uses wide window. Although time resolution is low, higher frequency resolution is gotten. When frequency is high, WT use narrow window. Although frequency resolution is low, higher time resolution is gotten.

Both STFT and WT, time resolution and frequency resolution are not able to get finer simultaneous. Hasenburg presented their resolution:

$$\Delta t \times \Delta f \geq (4\pi)^{-1} \quad (5)$$

where Δt and Δf is time resolution and frequency resolution respectively.

In SAR imaging processing, we demand very precision information of IF. That is both time resolution and frequency resolution should be finer simultaneous. So STFT and WT could not satisfy at this condition. Ideally, a distribution is desired, which provides a measure of the time-varying spectral component with a high resolution in time-frequency dimensions.

*WVD:*The continuos WVD is defined as[2]:

$$WVD(t,f) = \int_{-\infty}^{\infty} f(t+\tau/2) f^*(t-\tau/2) \exp(-j2\pi\tau f) d\tau \quad (6)$$

While analyzing a linear frequency modulated signal, which corresponds typically to the radar return of a moving target, the WVD offers the best time-frequency resolution in form of delta impulses along the IF of the signal.

Fast Algorithm: For a practical SAR system, the sweep rate is very small, only if the length of data was increased, the estimation accuracy of sweep rata could be improved. However it will cost the computation time and memories.

There presented a kind of extended WVD, which is defined as:

$$Ewvd(t,f) = \int_{-\infty}^{\infty} f(t + l \times \frac{\tau}{2}) f^*(t - l \times \frac{\tau}{2}) e^{-j2\pi\tau f} d\tau \quad (7)$$

where l is an integer bigger than 1.
It can be derived that

$$Ewvd(t,f) = \frac{1}{l} wvd(t, \frac{f}{l}) \quad (8)$$

the sweep rata is extended l times. when l is selected more than 1, the estimation accuracy will improved a lot.

In our experiment, l is 64, length of data is 64. The computational requirements is 64*64 complex multiplications plus 64 64-point FFT, while for WVD, the computational requirements is 64*4096 complex multiplications plus 64 4096-point FFT.

HOUGH TRANSFORM

The WVD contains the complete information but is sometimes difficult to interpret. In the case of multicomponent chirp signals, e.g. extended targets in the SAR signal, there appear artefacts or crossterms between different spectral and temporal parts of the signal due to the bilinear character of the TFD.

Because in the case of chirp signals, the WVD produces a distribution of the energy concentrated along straight lines. The problem of detecting chirp signal may be then interpreted as the problem of detecting lines in the t-f plane. The Hough Transform has been employed in the detection of curves in the images. If a F(.), defined in t-f plane assumes high positive values along a line, then in Hough domain, there exhibits a peak in a certain point. So if we apply the HT to the WVD of a chirp, we obtain a peak in the Hough domain, located in a position that depends on the chirp mean frequency and sweep rate.

Since the cross-terms produced by the WVD have an amplitude modulation, the integration, explicit in the Hough Transform, reduces them, while the useful contributions, being always positive, are correctly integrated. As the same

reason, HT produces an improvement of the signal to noise ratio in the presence of noise[3].

SIMULATIONS AND CONCLUSIONS

For a practical system, the parameters of radar are as follows:

λ=0.03m, V_a=150m/s, PRF=900Hz, R_0=20Km.

Fig.1 is the contours of two moving targets' WVD. Fig.2 is 3-dimension graphics of Fig.1. Because of the SNR is too low (0db), the peaks are difficult to be distinguished. Fig.3 is Hough Transform of the WVD shown in Fig.2. Table 1 is part of experiment results. Where k and c is the theoretical value of Doppler rate and centroid frequency respectively, $\underline{k}$ and $\underline{c}$ are estimation values and $|\varepsilon_k|$ and $|\varepsilon_c|$ denote error. The data in Table 1 showed that the average error of this approach is relative small.

Certainty there are several methods to restrain influences from cross parts, but they all trade-off the resolution of time and/or frequency, and the calculations are usually computationally expensive. We think combined WVD and HT is the best one. The performance of the proposed approach applied to practical data is under research.

REFERENCE

[1]A.Freeman and A.Currie, "SAR Image of Moving Targets", GEC Journal of Research, Vol.5, No2,PP.106-115, 1987.

[2]L.Cohen, "Time-Frequency Distributions - A Review", Proc. IEEE,Vol.77,PP.941-981,1989

[3]Tao Wang "SAR Imaging of Moving targets", Maser dissertation institute of Electronics, Academia Sinca, china 1994.

[4]S.Barbarassa, A. Farina, " Detection and Imaging of Moving Objects with SAR, Part 2", TEEE Proc-F, Vol.39,No.1,PP89-97,1992.

[5]H.I.Choi and W.J.williams, "Improved Time-Frequency Representation of Multicompoent Signals Using Exponential Kernels", IEEE Trans on ASSP.,Vol.37,No.6 PP.861-871, 1989.

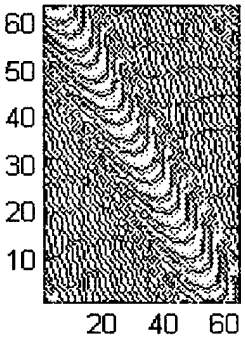

Fig. 1 Contour of 2 targets' WVD.

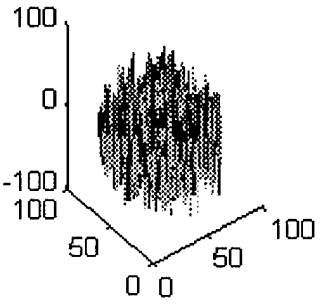

Fig. 2. WVD of two targets

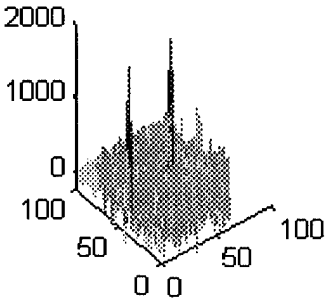

Fig.3 HT of signals in Fig.2

Table 1 Three groups (labeled a b c) experiment results of two targets (SNR=-20dB)

	v_r(m/s)	v_a(m/s)	position	$\underline{k}$	k	$\lvert\varepsilon_k\rvert$	$\underline{c}$	c	$\lvert\varepsilon_c\rvert$
a(1)	3	0	0	0.75321	0.75840	0.00148	28.5891	28.4760	0.1131
a(2)	5	10	50	0.66655	0.66064	0.00591	48.7913	47.6700	1.1213
b(1)	5	0	0	0.76658	0.76432	0.00226	47.5774	47.4411	0.1363
b(2)	5.5	0	50	0.76644	0.76432	0.00212	52.0637	52.0637	0.0461
c(1)	6	-20	-30	0.97302	0.97414	0.00112	56.0038	56.0038	0.3149
c(2)	3.5	10	50	0.66678	0.66099	0.00579	34.8912	34.8192	1.5296

TREE STRUCTURED FILTER BANKS FOR SPECKLE REDUCTION OF SAR IMAGES

Johannes R. Sveinsson and Jon Atli Benediktsson

Engineering Research Institute, University of Iceland,
Hjardarhagi 2-6, Reykjavik, IS-107, Iceland
E-mail: sveinsso@verk.hi.is, benedikt@verk.hi.is

ABSTRACT

Speckle reduction and enhancement of synthetic aperture radar (SAR) images with simple tree structured filter banks are proposed. The filter banks, which are based only on IIR allpass filters, are computationally efficient and can be easily adapted to different sampling rates of the SAR image data. The proposed structure is useful for speckle reduction through its subband-images and the speckle reduction is obtained by thresholding the subband-image coefficients of the digitized SAR images. The thresholding is a nonlinear function which can be adapted for each of selected subband-images. Three thresholding methods, soft thresholding, hard thresholding and thresholding based on sigmiod function, are studied.

The proposed tree structured filter bank methods show great promise for speckle removal and hence provide good detection performance for SAR based recognition.

1. INTRODUCTION

The role of SAR in gathering information from the Earth's surface is important since SAR has the ability to operate under all weather conditions. However, processing of SAR images has a major problem, i.e., the images contain speckle, a chaotic phomenon that results from coherent energy. The speckle noise can typically be modeled as multiplicative i.i.d. Gaussian noise [1][2]. Logarithmic transformation of a SAR image converts the multiplicative noise model to an additive noise model. When information details in the SAR image are important, speckle causes degradation and obscures the scene content of the image. Hence, speckle reduction is a necessary procedure before automatic and efficient class discrimination can be performed.

Shi and Fung [3] have compared several speckle filters, e.g., the Lee, Kuan, Enhanced Lee, Frost, Enhanced Frost, and Gamma MAP filters, all of which are based on the local variance statistic. They showed that these filters had some trade-off between speckle reduction and preservation of useful information in the image, but the research in this area is still open.

Multirate filter banks are the fundamental building blocks for multi-resolution decomposition of images. Filter banks have been used to implement the discrete wavelet transform (DWT) and DWT has been used for both noise reduction and compression of SAR images [4][5].

The proposed method is used for noise reduction of SAR image data. A logarithmic transformation of SAR image data is used to get an estimate of the signals from multiplicative noise models. The speckle reduction and image enhancement are then obtained by thresholding the subband-coefficients of the estimated signals (images). The thresholding of the subband-coefficients is done with one of the three thresholding methods; soft thresholding, hard thresholding or thresholding based on a sigmiod function. Results and comparison of the thresholding methods are given.

2. DENOISING OF SAR IMAGES

2.1. Multirated Filter Banks

The analysis part of our tree structured filter bank is shown in Figure 1 and each stage of the structure is shown in Figure 2. The rows of the image being processed are first low-pass (L) and high-pass (H) filtered and down-sampled by 2. Next each column of the row filtered images is again low-pass and high-pass filtered and down-sampled by 2. The output of each stage is then four subband images labeled LL, LH, HL, and HH, respectively. Only the LL-subband image goes through the same process of filtering and down-sampling to form the next stage of the tree structure. Every time a down-sampling is performed, the signal length is reduced by 2. The building elements for the analysis part of the tree structured filter bank are two-channel all-pass based IIR quadrature mirror filters (QMF) [6] and are shown in its polyphase form using the butterfly computation of DFT (or 2-point DFT) in Figure 3. The synthesis counterpart is shown in Figure 4. The same all-pass filters $A_0(z)$ and $A_1(z)$ are used in the analysis and synthesis part of the two-channel filter bank. The transfer function of an N-th order all-pass filter is

$$\begin{aligned} A_i(z) &= \frac{a_N + \ldots + a_1 z^{-(N-1)} + a_0 z^{-N}}{a_0 + \ldots + a_{N-1} z^{-(N-1)} + a_N z^{-N}} \\ &= z^{-N} \frac{D(z^{-1})}{D(z)} \qquad i = 0, 1 \end{aligned} \tag{1}$$

and the low-pass and high-pass filters of the two-channel all-pass IIR QMF bank are given by

$$\begin{aligned} H_{LP}(z) &= \tfrac{1}{2}[A_0(z^2) + z^{-1} A_1(z^2)] \\ H_{HP}(z) &= \tfrac{1}{2}[A_0(z^2) - z^{-1} A_1(z^2)]. \end{aligned} \tag{2}$$

This work was supported in part by the Research Fund of the University of Iceland and the Icelandic Research Council.

0-7803-3836-7/97/$10.00 © 1997 IEEE

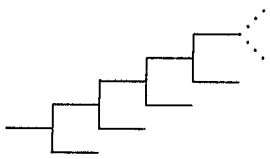

Figure 1: The implementation of tree filter bank transformation

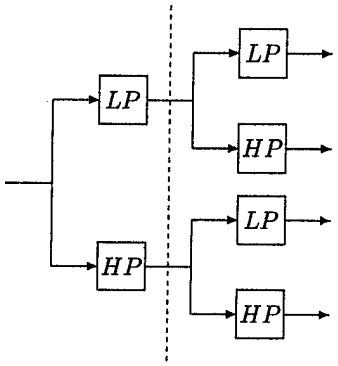

Figure 2: One stage in subband image decomposition

In this application, one of the all-pass filters, $A_0(z)$, is chosen to be a pure delay and hence the filters $H_{LP}(z)$ and $H_{HP}(z)$ have approximately linear phase in their passbands.

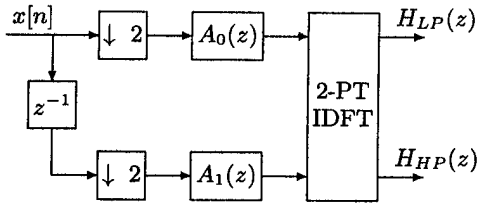

Figure 3: Analysis building block

2.2. Thresholding the Subband-Coefficients

For a digitized SAR image, we define $z(j,k)$ as the gray level (or the observed image intensity) of the (j,k)-th pixel of the image. For clarity, we will omit the pixel indices in the rest of this paper. Hence, the pixel level of an SAR image can be written as

$$z = xe \tag{3}$$

where x is the desired texture information and e is the multiplicative noise. Arsenault and April [7] showed that for a logarithmically transformed SAR image, the speckle is

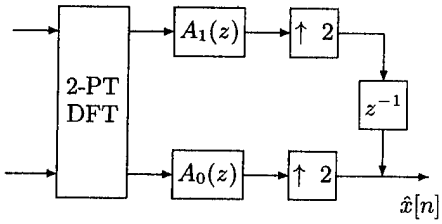

Figure 4: Synthesis building block

approximately Gaussian additive noise, i.e.,

$$\tilde{z} = \tilde{x} + \tilde{e} \tag{4}$$

where $\tilde{z} = \ln(|z|)$. In what follows $\tilde{y}$ will represent a logarithmically transformed gray level (or intensity), y.

All speckle reduction methods are applied within the tree structured filter bank multiresolution representation, i.e., if z represents the original image and $\mathcal{FBT}$ is the multilevel decomposition of the tree structured filter bank, then a multiresolution representation is given by the equation

$$\tilde{y} = \mathcal{FBT}\{\tilde{z}\}. \tag{5}$$

The noise level (variance), σ, in the multiresolution representation is not known in advance, and has to be estimated from the image data. In this paper, an estimate of σ is taken to be the standard deviation of the HH (high/high) subband-image of the first level of the filter bank decomposition [8]. Also, no filtering or thresholding is carried out on the LL (low/low) subband-image at the final level of the filter bank decomposition.

Below we present a general formula for processing the subband-images to accomplish speckle reduction of SAR images. Let f be a non-linear function designed to reduce speckle for selected subband-images. Then, an enhanced subband-image $\hat{y}$ may be given by

$$\hat{y} = f(y). \tag{6}$$

The thresholding of the subband-coefficients is carried out with one of the three thresholding methods; soft thresholding [8], hard thresholding [8], or thresholding based on sigmiod function [5]:

1. **Soft thresholding**: Choose a threshold $t = \gamma\sigma$ (where γ is a constant to be chosen) and apply the functional

$$f(\tilde{y}) = \begin{cases} \tilde{y} - t & \text{for } \tilde{y} > t \\ 0 & \text{for } |\tilde{y}| \le t \\ \tilde{y} + t & \text{for } \tilde{y} < -t \end{cases} \tag{7}$$

to obtain the enhanced subband filter bank coefficients, $\hat{\tilde{y}}$.

2. **Hard thresholding**: Choose a threshold $t = \gamma\sigma$ (where γ is a constant to be chosen) and apply the functional

$$f(\tilde{y}) = \begin{cases} \tilde{y} - t & \text{for } \tilde{y} > t \\ \tilde{y} + t & \text{for } \tilde{y} < -t \end{cases} \tag{8}$$

to obtain the enhanced subband filter bank coefficients, $\hat{\tilde{y}}$.

3. **Adaptive sigmoid thresholding**: For an input image, $\tilde{y}$, with maximum absolute amplitude, $\tilde{y}\max$, the image range $[-\tilde{y}\max, \tilde{y}\max]$ is mapped onto the interval $[-1, 1]$ with the function $f(\tilde{y})$ given by

$$f(\tilde{y}) = a\,\tilde{y}\max\left[\text{sigmoid}\left(c\left(\frac{\tilde{y}}{\tilde{y}\max} - b\right)\right) - \text{sigmoid}\left(-c\left(\frac{\tilde{y}}{\tilde{y}\max} - b\right)\right)\right] \quad (9)$$

where

$$a = \frac{1}{\text{sigmoid}\,(c(1-b)) - \text{sigmoid}\,(-c(1-b))} \quad (10)$$

and $\text{sigmoid}(\tilde{y})$ is defined by

$$\text{sigmoid}(\tilde{y}) = \frac{1}{1+\exp(-\tilde{y})}. \quad (11)$$

Because of the normalization, the transformation parameters, a, b, and c can be set independently of the dynamic range of the input image. Now choose the parameters $c = \gamma_1\sigma$ and $b = \gamma_2\sigma/\tilde{y}\max$ (γ_1 and γ_2 are constants to be chosen) where $\tilde{y}\max$ is the maximum absolute amplitude value of subband-images for the filter bank multiresolution representation. Apply the non-linear function $f(\tilde{y})$ in (6).

Finally, the speckle reduced image is obtained from the synthesis part of the filter bank decomposition of the enhanced subband-image $\hat{y}$.

3. EXPERIMENTAL RESULTS

The three denoising methods described in the previous section where applied in experiments to a single look 256 × 256, 256-gray-scale SAR image. Several parameters need to be chosen for the denoising methods. First, it is necessary to design the allpass filters. Here one of the all-pass filters $A_0(z)$ was chosen to be a pure delay, i.e., $A_0(z) = z^{-1}$ and the other all-pass filter was chosen as the first order ($N = 1$) filter $A_1(z) = \dfrac{0.375 + z^{-1}}{1 + 0.375z^{-1}}$. Also, the number of stages in the filter bank decomposition needs to be chosen. For the soft and hard thresholding methods, a four stages filter bank decomposition was used, but for the adaptive sigmoid thresholding method a five stage filter bank decomposition was applied. The thresholding coefficients for the denoising methods were chosen as: (i) $t = 1.2\sigma$ for the soft thresholding method; (ii) $t = 2.2\sigma$ for the hard thresholding method (iii) $\gamma_1 = 4$, $\gamma_2 = 1.6$ for the sigmoid thresholding method. The speckle phenomena is clearly visible in the original image (Figure 5) but greatly removed in the denoised images in figures 6-8.

4. CONCLUSIONS

Methods for speckle reduction and enhancement of SAR images using IIR QMF filter bank decomposition have been proposed. The new methods significantly reduce the speckle while preserving at the same time the resolution of the original SAR images. Cleaner images should improve classification and recognition.

Acknowledgemets

The authors are very grateful to Mr. Omar Hilmarsson and Mr. Finnur Palsson both of University of Iceland for their invaluable assistance in preparing this paper.

5. REFERENCES

[1] J.S. Lee, "Digital image enhancement and noise filtering by use of local statistics," *IEEE Trans. Pattern Anal. Machine Intell.*, vol. PAMI-2, pp. 165-168, March 1980.

[2] A. Lopes, R. Touzi, and E. Nezary, "Adaptive speckle filters and scene heterogeneity," *IEEE Trans. Geosci. Remote Sensing*, vol. GE-28, pp. 992-1000, Nov. 1990.

[3] Z. Shi and K.B. Fung, "A comparison of digital speckle filters," in *Proc. IEEE IGARSS'94*, vol. IV, pp. 2129-2133, Aug. 1994.

[4] H. Guo, J.E. Odegard, M. Lang, R.A. Gopinath, I. Selesnick, and C.S. Burrus, "Wavelet based speckle reduction with application to SAR based ATD/R," in *Proc. IEEE Int. Conf. Image Processing*, vol. 1, pp. 75-79, Austin, TX, Nov. 1994.

[5] J.R. Sveinsson and J.A. Benediktsson, "Speckle Reduction and enhancement of SAR images in the wavelet domain," in *Proc. IEEE IGARSS'96,* vol. I, pp. 63-66, 1996.

[6] T.Q. Nguyen, T.I. Laakso, and R.D. Koilpillai, "Eigenfilter approach for the design of allpass filters approximating a given phase response," *IEEE Trans. on Signal Processing,* vol. 42, pp. 2257-2263, 1994.

[7] H.H. Arsenault and G. April, "Properties of speckle intergrated with a finite aperture and logarithmically transformed," *J. Opt. Sco. Am.*, vol. 66, pp. 1160-1163, Nov. 1976.

[8] D.L. Donoho, "De-noising by soft-thresholding," *IEEE Trans. Inform. Theory.*, vol. IT-41, pp. 613-627, May 1995.

Figure 5: Original SAR image.

Figure 6: Denoised SAR image with soft thresholding $t = 1.2\sigma$ for four stages.

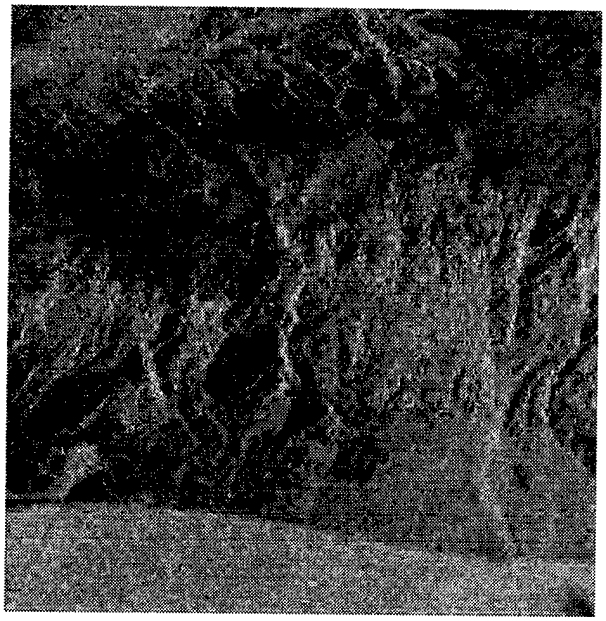

Figure 7: Denoised SAR image with hard thresholding $t = 2.2\sigma$ for four stages.

Figure 8: Denoised SAR image with adaptive sigmoid thresholding $\gamma_1 = 4$ og $\gamma_2 = 1.6$ for five stages.

Near Real-Time RADARSAT Data System for NOAA CoastWatch Applications

William Y. Tseng[1], William G. Pichel[1], Antony K. Liu[2], Pablo Clemente-Colón[1], George A. Leshkevich[3], Son V. Nghiem[4], Ronald Kwok[4], and Robert N. Stone[1]

[1]NOAA/National Environmental Satellite, Data, and Information Service, Washington D.C., 20233, USA
Tel: (301) 763-8142, Fax: (301) 899-9196, E-Mail: wtseng@nesdis.noaa.gov
[2]NASA/Goddard Space Flight Center, Oceans and Ice Branch, Greenbelt, MD 20770, USA
[3]NOAA/Great Lakes Environmental Research Laboratory, Ann Arbor, MI 48105, USA
[4]CIT/Jet Propulsion Laboratory, Center for Space Microelectronics Technology, Pasadena, CA 91109, USA

Abstract -- The National Oceanic and Atmospheric Administration (NOAA) in partnership with other U.S. Government agencies has augmented existing satellite reception and processing facilities at the Alaska SAR Facility (ASF) to provide near real-time access to synthetic aperture radar (SAR) data for U.S. Government operational applications. Access is available for RADARSAT SAR data acquired by the ASF in Fairbanks, Alaska, by the Canadian readout stations in Gatineau, Quebec and Prince Albert, Saskatchewan, and by the Norwegian station in Tromso. Qualified user access to these data is provided by the NOAA Satellite Active Archive (SAA). A major user of SAR data in NOAA is the CoastWatch program. This paper will provide an introduction of this near real-time RADARSAT data system and some preliminary results of the use of RADARSAT data for ocean applications.

INTRODUCTION

Current remote sensors aboard the U.S. civilian weather satellite system do not provide all the ocean measurements required by the U.S. operational and research communities. In order to remedy this situation in a cost effective manner, NOAA's National Environmental Satellite, Data, and Information Service (NESDIS) has been developing interagency and international agreements and data access systems to obtain data and products from Department of Defense (DoD) and foreign satellites. This activity is being coordinated and funded by the NOAA Satellite Ocean Remote Sensing (NSORS) project within NESDIS.

The NOAA CoastWatch program has the objective of making satellite data and in-situ data from NOAA environmental satellites and buoys available to Federal, state, and local marine scientists and coastal resource mangers for decision making. The NSORS project has the goal of providing not only NOAA satellite data, but also non-NOAA satellite data, such as RADARSAT SAR data, to qualified users in many participating Governmental agencies and research organizations. SAR instruments have very diversified applications, such as ice and coastal ocean monitoring, vessel surveillance, cartography and land use, as well as applications in geology, hydrology, agriculture, and forestry. SAR instruments are particularly useful for operational applications, since they operate through clouds and day or night.

NOAA, in partnership with the U.S. Navy through the U.S. National Ice Center (NIC), has been constructing a system which allows operational access to SAR imagery from the Canadian Space Agency RADARSAT satellite. Building on existing ground acquisition stations, NOAA and the Navy have co-funded processing, communications, data storage and display system enhancements in order to provide the U.S. Government with these data in near real-time. Initially, the major users of this system will be the NIC and NOAA CoastWatch; however, other Government agencies, such as the Department of Agriculture and U.S. Coast Guard, will also be assessing the operational utility of SAR imagery.

The goals of the NOAA/Navy operational RADARSAT data system efforts are to: (1) implement a near real-time processing, delivery, and access system for SAR imagery from RADARSAT for NIC, NOAA, and other U.S. Government operational agencies, (2) develop SAR workstation software for image display and product generation for use in an operational environment, (3) demonstrate and operationally implement practical applications of SAR imagery, and (4) experiment with the data fusion of SAR, ocean color, and thermal and visible imagery [1].

In order to apply SAR data to ocean research and applications, NOAA is cooperating with ocean and ice scientists of the National Aeronautics and Space Administration (NASA) Goddard Space Flight Center (GSFC), and the Jet Propulsion Laboratory (JPL). Cooperative projects include coastal ocean research, wavelet software development and applications to oceans, and exploration of algorithms for sea/lake ice cover mapping, classification, and monitoring. Examples of mesoscale feature mapping and tracking are demonstrated in this paper using a two-dimensional wavelet technique developed by

U.S. Government work not protected by U.S. copyright.

NASA. The development of the wavelet software [2] is still in the research phase, but the goal is to transfer the technique into an operational environment. An example of lake ice cover classification and mapping using RADARSAT SAR data will also be demonstrated.

SYSTEM DESCRIPTION

RADARSAT is equipped with an advanced SAR operating at a single microwave frequency, C-band (5.3 Ghz frequency or 5.6 cm wavelength). RADARSAT transmits its microwave energy in horizontal orientation and the energy that returns to its sensor is captured using the same polarization (HH polarization system). There are seven image sizes, termed beam modes, ranging from Fine (50x50 km coverage) to ScanSAR Wide (500x500 km coverage), with resolutions ranging from 10 m to 100 m, respectively.

The architecture and data flow of the operational near real-time RADARSAT data system is shown in Figure 1. Data will be acquired and processed into imagery principally at three acquisition stations: (1) Fairbanks, Alaska, (2) Gatineau, Quebec, and (3) Tromso, Norway. Some other data will probably be acquired at Prince Albert, Saskatchewan (processed in Gatineau) and at McMurdo in Antarctica (processed in Fairbanks). Data obtained via the on-board tape recorder, normally acquired by Gatineau, will be processed in Canada or sent via courier to Fairbanks for processing. SAR imagery then is forwarded electronically from the three processing centers to either the NOAA Satellite Active Archive or the NIC.

The primary acquisition station for U.S. users of near real-time SAR imagery is the ASF located at the University of Alaska Fairbanks (UAF), sponsored by NASA, with software and hardware systems built by JPL. Data are acquired by the ASF Receiving Ground Station (RGS), and processed by either the Alaska SAR Processor (ASP), which is a hardware SAR processor, or the ScanSAR Processor (SSP), which is a software SAR processor running on three 8-node IBM SP-2 computers. The full-system throughput at ASF is 58 minutes of Standard Mode and 51 minutes of ScanSAR data per day. The images formed from the processors are then sent to the Information Management System/Data Archive and Distribution System (IMS/DADS) which forms the normal user interface. Then the near real-time data are sent automatically to the Advanced Earth Observing Satellite (ADEOS) Data Stripper where data are transmitted over a dedicated T1 (1.544 megabits/sec) communication link to the NOAA/NESDIS/SAA first and then passed to the NIC automatically (both in Suitland, Maryland). Data from Gatineau and Tromso will arrive first at the NIC and then be passed on to the SAA. The registered users are notified by e-mail when imagery arrives, and is ready for downloading over the Internet. The data will be on-line in SAA for a week, then written to 8 mm tape for longer-term storage. In Phase II of the SAA SAR system, scheduled for implementation by the end of 1997, imagery will be stored on near-line robotic tape storage so that users can access them electronically for up to a year. Imagery will be maintained on tape for about three years by the NOAA National Climatic Data Center (NCDC).

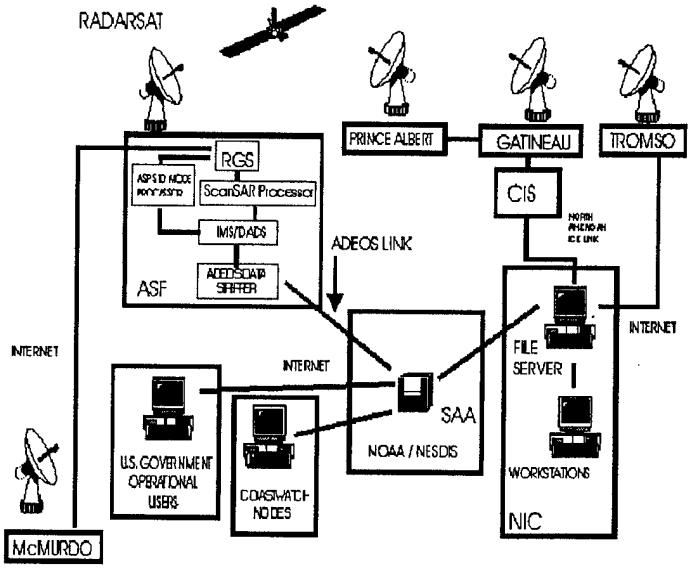

Figure 1. Architecture and Data Flow of the Operational Near Real-Time RADARSAT Data System

NOAA COASTWATCH APPLICATIONS

We have included here two RADARSAT images as examples. Figure 2, taken on February 26, 1997 along the east coast of Uruguay at the mouth of the Rio de la Plata, is a ScanSAR Narrow image with 25m pixel spacing. The Mexican hat wavelet transform was applied as an edge detector to separate high contrast boundaries. The possible location of an oil spill is characterized by darker areas circled by white lines in the upper part of the image. Similar patterns were also found in daytime AVHRR images in the form of higher skin sea surface temperature (the presence of oil spills needs to be confirmed by ground truth). In previous studies, under favorable oceanic and atmospheric conditions, the spilled oil was indicated by higher IR skin temperature than the surrounding water during daytime[3], and was revealed as darker areas in the SAR image due to a damping effect on the short surface waves [2]. This darker appearance is also found in low wind areas. Further studies of this oil spill case can be found in [5]. Figure 3, taken of western Lake Superior on March 16, 1996 is a ScanSAR Narrow image. Using the methodology of supervised, level slicing classification, the areas of open water, new lake ice, and snow ice have been identified [4].

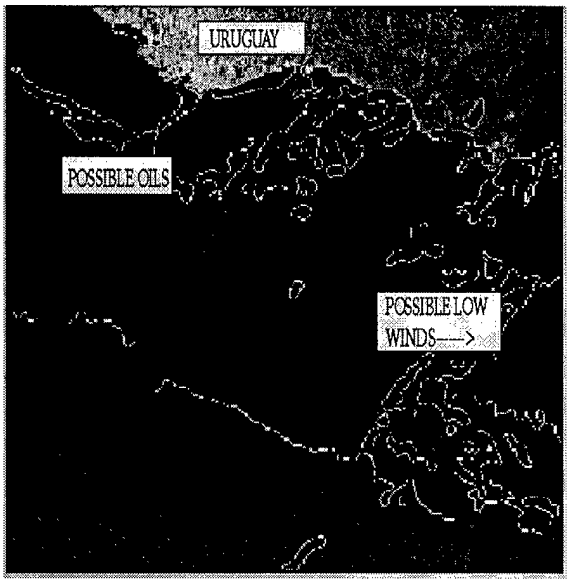

Figure 2. RADARSAT ScanSAR Narrow image, taken on February 26, 1997, showing oil spills along the coast of Uruguay at the mouth of the Rio de la Plata (Copyright CSA, 1997)

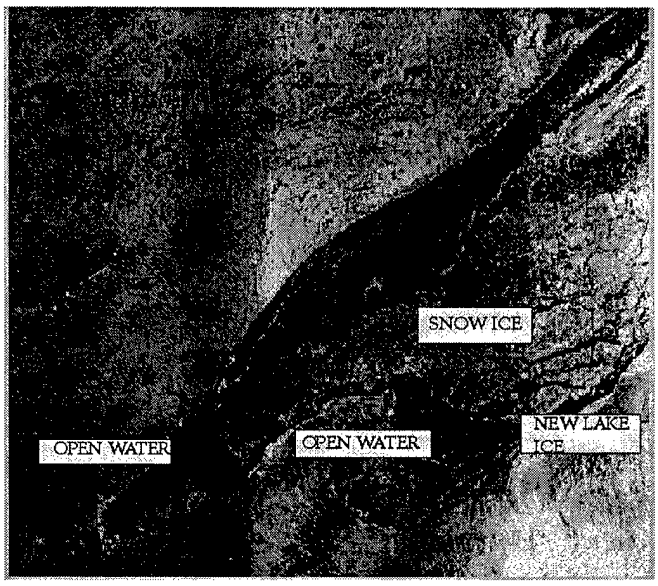

Figure 3. RADARSAT ScanSAR Narrow image, taken on March 16, 1996, showing open ice, new lake ice, and snow ice in Western Lake Superior (Copyright CSA, 1996)

Currently, within NOAA CoastWatch, the following applications of SAR data have been or will be assessed for operational utility and feasibility: (1) sea/lake ice applications, (2) fishery enforcement and applications, (3) ocean mesoscale feature detection, (4) wind and wave measurements, and (5) coastal hazards. Those CoastWatch sites participating in SAR studies are: the Anchorage Weather Service Forecast Office, the Great Lakes Environmental Research Laboratory, and the National Marine Fisheries Service Laboratories at Narragansett and at the Stennis Space Center.

ACKNOWLEDGMENT

The RADARSAT SAR system described above could not have been developed without the full partnership of the National Ice Center. Key NIC participants have been Ray Simmons, Cheryl Bertoia, Steve Rutherford, Mark Dunn, Frank Kniskern, Dave Howell, and John Dowdell. Special thinks to the Alaska SAR Facility staff including Carl Wales, Cindy Wilson, Greta Reynolds, Marc Forbes, and Dick Harding, and to Bruce Ramsay and John Falkingham at the Canadian Ice Service. Our thanks also to the large staff of Government and contract employees at NESDIS, NASA, NRL, and JPL who have and are still working toward the successful implementation and operation of this data system. We would like to thank the U.S. Coast Guard, Ninth District for providing ship and helicopter support. We also thank Dr. Sunny Wu of USRA for providing wavelet analysis in Figure 2. RADARSAT SAR images provided by the Canadian Space Agency are also acknowledged. This work was supported by the NOAA Coastal Ocean Program and NESDIS/NSORS Program.

REFERENCE

[1] W.G. Pichel, R.N. Stone, W. Tseng, P.Clemente-Colón, and D.S.Trush, "NOAA satellite ocean remote sensing near real-time system for providing synthetic aperture radar data for marine and coastal applications," *in Proc. Fourth International Conference on Remote Sensing for Marine and Coastal Environment*, 17-19, March 1997, Orlando, Florida, USA, Vol. I, pp. 331-340.

[2] A.K. Liu, C.Y. Peng, and S.Y.-S. Chang, "Wavelet analysis of satellite images for coastal watch," *IEEE Journal of Oceanic Engineering*, Vol. 22, NO. 1, 1997, pp. 9-17.

[3] W.Y. Tseng and L.S. Chiu, "AVHRR observations of Persian Gulf oil spills," in *Proc. IGARSS'94*, 1994, pp. 779-782.

[4] G.A. Leshkevich, S.V. Nghiem, and R. Kwok, "Satellite SAR remote sensing of Great Lakes ice cover using RADARSAT data," *in Proc. Fourth International Conference on Remote Sensing for Marine and Coastal Environment*, 17-19, March 1997, Orlando, Florida, USA, Vol. I, pp. 126-134.

[5] A.K. Liu, S.Y. Wu, and W.Y. Tseng, "Wavelet Analysis of Satellite Images for Coastal Monitoring," to be published in *Proc. IGARSS'97*, 1997.

IGARSS'97

1997 International Geoscience and Remote Sensing Symposium

03-08 August 1997

Singapore International Convention & Exhibition Centre

Technical Program

Interactive Area 24: Surface Temperatures

Land Surface Temperature Interpretation of Equatorial South America from AVHRR data

Gaiping Li, Perry J. Hardin. Department of Geography
676 SWKT, Brigham Young University, Provo, Utah 84602
Phone: 801-378-6062 Email: perry_hardin@byu.edu

I. INTRODUCTION

With human exploitation of resources on the earth and increasing population, pressures on land and resources are growing rapidly. As the life-supporting capacity of the earth decreases, people are becoming more aware of larger scale problems facing particular regions of the global environment. Within the last two decades, the scientific community has become increasingly concerned that the destruction of the world's rain forests may contribute to global warming and other environmental problems.

An important component of equatorial climate modeling is the measurement of forest transpiration rates. This in-turn is both highly correlated with, and functionally related to, forest canopy temperature.

An attractive and unique way to map and monitor land surface temperatures (LST) over a large area is by the use of satellite radiometers. However, these radiometers are not only influenced by surface parameters (i.e., emissivity and temperature), but also by the composition and thermal structure of the atmosphere. Therefore, the determination of LST from space requires the management of two thorny issues. The first problem is *atmospheric corruption.* It is common knowledge that the earth's atmospheric radiance contributes to the apparent brightness temperatures of the earth's surface itself. The second problem is the necessity to calculate a *radiometric inverse.* Momentarily ignoring atmospheric problems, this is the procedure which takes surface emissivity into account when calculating a surface temperature from an apparent temperature measured by the spaceborne radiometer.

This report summarizes preliminary research focused on the exploration and resolution of these two issues in order to retrieve land surface temperatures from the equatorial forests of Brazil. The precise study area is the tropical forest and woodland zone of South America between 10°N and 13°S.

II. SEA SURFACES VS. LAND SURFACES

Land Surface Temperature (LST) retrieval from AVHRR data has it roots primarily in Sea Surface Temperature (SST) retrieval efforts. The problem of LST retrieval is more complicated than its SST equivalent for several reasons. First, In contrast to the ocean surface, land surface emissivities are seldom unity. They are dependent on the surface physical properties, including material, surface roughness and moisture content. Furthermore, land surfaces are usually heterogeneous within a single radiometer pixel. The temperatures differ dramatically between day and night. Finally, the difference between the LST and the actual air temperatures above the surface may be quite different.

III. DATA AND METHODS

The image data used for this project was stacked second generation weekly composite Global Vegetation Index (GVI) arrays, produced from NOAA -11 Advanced Very High Resolution Radiometer (AVHRR) imagery. The channels used include

Channel 1: 0.58 to 0.68 μm
Channel 2: 0.725 to 1.10 μm
Channel 4: 10.30 to 11.30 μm
Channel 5: 11.50 to 12.50 μm

The image dates spanned July 1, 1990 to August 12, 1990. Area covered by each pixel was 19.5 x 19.5 km. The acquisition time was 14:30 local.

The data processing flow is depicted in Table 1. As shown there, the data from channels four and five were first converted to GEOS counts and then to absolute Channel 4 and 5 brightness temperatures (T_b) using formulae provided by Kidwell [2]: For T_b between 164K and 242K inclusive,

$$T_b = (\text{GEOS} - 419.05128) \div (-1.006412).$$

For T_b greater than 242K,

$$T_b = (\text{GEOS} - 661.88571) \div (-2.0057142).$$

It is important to remember that such conversions do not account for atmospheric problems or surface emissivity, but only create apparent brightness temperature images for Channel 4 (T_4) and Channel 5 (T_5).

In this research, the split window technique (SWT) described by Sobrino *et al.* [7] was used to convert T_4 and T_5 to LST (T). The interested reader is invited to review that reference for complete details on SWT. In their method, the atmospheric correction of T_4 and T_5 measurements depend on atmospheric conditions, surface emissivity, and viewing angle. The split window equation using NOAA-11

0-7803-3836-7/97/$10.00 © 1997 IEEE

Table 1. Data processing flow

AVHRR Channels 4 and 5		AVHRR Channels 1 and 2	
Input	**Output**	**Input**	**Output**
Channels 4, 5	GEOS counts	Channels 1,2	SAVI
GEOS counts	Brightness temperatures	SAVI	Green Cover
		Green Cover	Emissivity
Brightness temperatures and Emissivity	Estimated Land Surface Temperature (LST)		

AVHRR channels 4 and 5 is described by the following.

$$T = T_4 + A \times (T_4 - T_5) + (B_\alpha - B_\beta), \text{ where}$$
$$A = a_0 + a_1 \times (1 - \varepsilon_4) + a_2 \times (\varepsilon_4 - \varepsilon_5),$$
$$B_\alpha = ((1 - \varepsilon_4) \times B_4 \times T_4) \div \varepsilon_4, \text{ and}$$
$$B_\beta = ((1 - \varepsilon_5) \times B_5 \times T_5) \div \varepsilon_5.$$

In turn:

$$B_4 = b_{04} + b_{14} \times (\varepsilon_4 - \varepsilon_5) \text{ and}$$
$$B_5 = b_{05} + b_{15} \times (\varepsilon_4 - \varepsilon_5).$$

In the equations, ε_4 and ε_5 represent the emissivity of the land surface measured in AVHRR Channels 4 and 5 respectively. The coefficients a_0, a_1, a_2, b_{04}, b_{05}, b_{14}, and b_{15} are strongly dependent on the atmospheric profiles. Sobrino *et al.* [7] suggests 2.49, 4.33, 5.16, 0.075, -0.114, 0.027, and -0.089 respectively for tropical regions. The only remaining unknowns in the equations are ε_4 and ε_5.

As an intermediate step to calculate ε_4 and ε_5, AVHRR Channels 1 and 2 are first converted to Soil Adjusted Vegetation Index (SAVI) values. The formula for SAVI in this research was

$$SAVI = (\rho_2 - \rho_1) \times 1.5 \div (\rho_2 + \rho_1 + 1.5)$$

where ρ_1 and ρ_2 represent the reflectance in AVHRR Channels 1 and 2 respectively.

By the use of two relationships, SAVI provides an indirect method of estimating emissivity over heavily canopied surfaces. It has been demonstrated [6] that SAVI has a relationship with percentage green cover (GC) that can be approximated by interpolating between the entries shown in Table 2.

The second relationship allows emissivity to be estimated from GC. Two extremes bracket the anticipated emissivity values in the equatorial forest. The first extreme is where green cover is non-existent -- the bare soil case. According to Labed and Stoll [3] and Nerry *et al.* [4,5], the emissivity of a variety of soils between 8.0 μm and 13.5 μm was found to be 0.97 ± 0.01 with a very flat spectral response.

Table 2. Green cover and SAVI. From [6].

% Green cover	SAVI	% Green cover	SAVI
0	0.0597	75	0.6269
20	0.2239	90	0.6866
40	0.3881	98	0.7463
60	0.5224	≈ 100	> 0.7463

The second extreme is where green cover is 100% -- the full vegetation canopy case. Results from Label and Stoll [3,4] and Asrar [1] indicate that full equatorial vegetation canopy emissivity is approximately 0.998 ± 0.01. Between these two extremes, and assuming a linear relationship, a transfer equation can be created which estimates emissivity from green cover:

$$\varepsilon = GC \times 0.998 + (100 - GC) \times 0.970) - 100.$$

Given the flat response cited above, ε_4 can also be assumed equal to ε_5.

III. VERIFICATION

The result of the image processing described above was a single land surface temperature image of central South America for the month of July 1990 for 14:30 local time. In order to perform preliminary verification of the modeled temperatures, verification data were extracted from the ISMCS CD-ROM (produced by the National Climatic Data Center in cooperation with other agencies). The geographic position of 78 temperature collecting weather stations in the study area were plotted on the temperature image, and the calculated temperatures were then compared to the average recorded daily July maximum. The differences between the calculated model temperature and the weather station temperatures were then analyzed using a variety of statistical and graphical methods.

In using the available weather station data as verification information, an important caveat must be kept in mind. The weather station data do not record the actual 14:30 average air temperature for the pixel which encloses them. Instead, they represent an average maximum temperature for a small point within the pixel determined by several years of weather data acquisition.

IV. RESULTS AND CONCLUSIONS

The modeled temperature image created in the process above covers the study area shown in Figure 1. In general, although the temperature patterns are strongly correlated, the calculated LST values are slightly lower than the station data values. Without exception, the station data in the Amazon

basin matched the calculated data very well -- most modeled temperatures were within 2.9K of the station temperatures. Descriptive statistics for the differences between the modeled temperatures and the station temperatures are shown in Table 3.

For all the stations, the average difference between the modeled temperatures and the station temperatures was -1.94K with a standard deviation of 8.20K. Most of the temperatures calculated for the coastal stations are within 4.0K of the modeled temperatures. In contrast, data from some highland and mountain stations match the calculated LSTs poorly. Over 1/3 of these stations have temperature

Table 3. Descriptive statistics for differences between station temperatures and model temperatures. All values in K.

Station	n	Mean	Stdv.	Quartile 1	Quartile 3
Lowland (1)	21	-1.21	1.72	-2.21	-0.56
Highland (2)	20	-1.57	9.51	-5.66	1.39
Coastal (3)	18	-1.12	8.66	-3.55	2.82
Mountain (4)	18	-4.02	10.71	-5.91	1.45

deviations greater than ±6K from the modeled values. See Figure 2 for a graphical display of the deviations for all the stations used in the verification.

Clearly errors remain in the modeled temperature values. Some of the apparent error is due to the fact that long-term July average data is being compared to July 1990 data. In addition, the cause of the severe coastal and mountain temperature deviations can be traced to the heterogeneous nature of these areas. Not only does the terrain itself change quickly, but temperatures themselves change rapidly as well.

Figure 1. Geophysical regions of the study area.

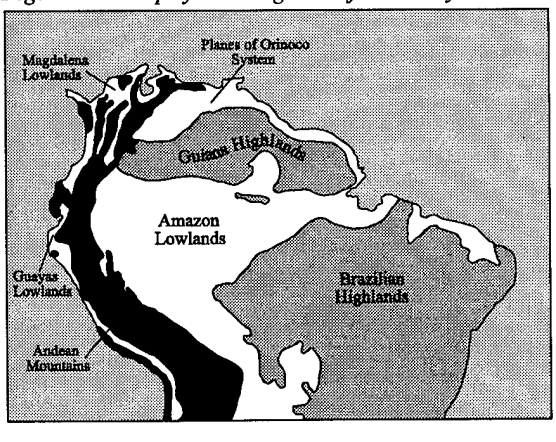

Continental summer temperatures increase with distance from the cooler ocean. Likewise, mountain summer temperatures decrease with increased elevation. None of this heterogeneity is adequately represented by the pixels which cover nearly 400 square kilometers. Water contamination of coastal pixels appears to be a problem in a few coastal station locations.

In addition to the problems with the verification data and satellite resolution, the satellite-based model used to calculate LST utilizes a variety of generalizations which introduce error. The first generalization is the use of the recommended tropical spectral absorption coefficients [7]. Albeit impossible to obtain, actual coefficients for the 14:30 July 1990 atmosphere would have been better. The second generalization is the use of a crude model for estimating emissivity from green cover and SAVI.

Figure 2. Differences between weather station data and LST calculations. Differences are in K.

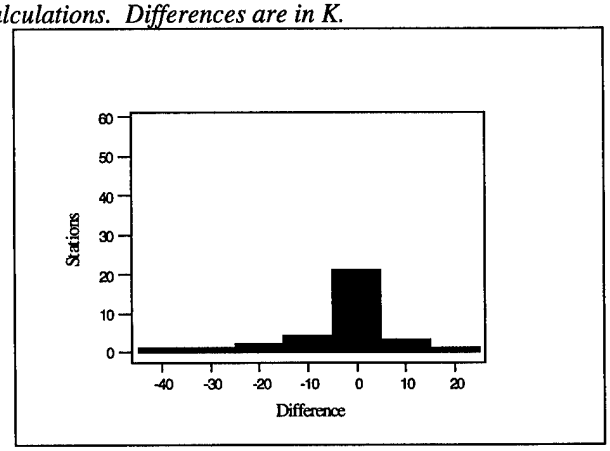

V. REFERENCES

[1] Asrar, G. 1990. *Theory and Applications of Optical Remote Sensing.* pp. 598 - 599.

[2] Kidwell, K.B. 1990. *Global Vegetation Index User's Guide.*

[3] Labed, J. and M.P. Stoll. 1991. Spatial variability of land surface emissivity in the thermal infrared band: spectral signatures and effective surface temperature. *Remote Sens. Environ.* 38:1-17.

[4] Nerry, F., Labed, J. and M.P. Stoll. 1990. Spectral properties of land surfaces in the thermal infrared: Laboratory measurements of absolute spectral emissivity signatures. *Water Resources Management,* 95 (B5):7027-7044.

[5] Nerry, F., Labed, J. and M.P. Stoll. 1990. Spectral properties of land surfaces in the thermal infrared: Field methods for spectrally averaged emissivity measurements. *Water Resources Management,* 95 (B5):7045-7054.

[6] Qi, J., Chehbouni, A., Huete, A.R., Kerr, Y.H. and S. Sorooshian. 1994. A modified soil adjusted vegetation index. *Remote Sensing of Environment.* 48:119-126.

[7] Sobrino, J.A., Coll, C. and V. Caselles. 1991. Atmospheric correction for land surface temperature using NOAA-11 AVHRR channels 4 and 5. *Remote Sensing of Environment.* 38:19-34.

IGARSS'97

1997 International Geoscience and Remote Sensing Symposium

03-08 August 1997

Singapore International Convention & Exhibition Centre

Technical Program

Interactive Area 25: Neural Network and Intelligent Systems

A Classification Of Multitemporal Landsat TM Data Using Principal Component Analysis & Artificial Neural Network

Hyo S. Chae
Water Resources Research Institute, KOWACO
462-1, Jonmin-dong, Yusung-ku, Taejon, 305-390, Korea
82-42-860-0374/82-42-860-0368/chaehs@kowaco.or.kr

Seong J. Kim
Water Resources Research Institute, KOWACO
462-1, Jonmin-dong, Yusung-ku, Taejon, 305-390, Korea
82-42-860-0320/82-42-860-0368/kimsj@kowaco.or.kr

Jeong A Ryu
Water Resources Research Institute, KOWACO
462-1, Jonmin-dong, Yusung-ku, Taejon, 305-390, Korea
82-42-860-0374/82-42-860-0368/chaehs@kowaco.or.kr

Abstract -- Multitemporal Landsat TM imagery were classified to extract land cover informations using principal component analysis (PCA) and backpropagation (BP) algorithm of artificial neural network. Data used are two Landsat TM data of in Jan. 1, 1991 (Data I) and May 9, 1994 (Data II). Twelve bands data were compressed to 4 bands data by the first and second PCA. Approximately 95 percent of the total variance of each Landsat TM data was included resulting from the first and second component analysis. Analyzed data through the PCA were classified by the BP training algorithm of artificial neural network. As a result of classification, it is concluded that this approach will become an attractive and effective method in extracting land cover or land use information using multitemporal Landsat TM data.

INTRODUCTION

Land cover or land use map contain many useful geographical informations in hydrology, agriculture, geology. These informations can be effectively extracted from remotely sensed data. Recently, there have been many studies in obtaining surface informations using artificial neural network techniques (Foody et al., 1996; Paola & Schowengerdt, 1995; Chen et al., 1995). In most studies, only one Landsat TM data have been used for classification. However, it is necessary to consider reflectance characteristics of surface objects varying with atmospheric conditions to enhance the accuracy. This can be easily solved using multitemporal remotely sensed data.

The PCA and BP algorithm were used to improve the accuracy of classification. Multitemporal Landsat TM data used consist of two Landsat TM data, and the PCA was applied in preprocessing stage. All training data set for 12 bands were not necessary in training stage for classification. Because of utilizing the PCA, only four traning data for the first and second principal component analysis were used for classification.

METHODS

Multitemporal Landsat TM Data

Data used in this study are two Landsat TM data acquired in Jan. 1, 1991 and May 9, 1994. Data size is 300 by 250 pixels and 12 bands data excluding thermal infrared (TIR) data were utilized.

Principal Component Analysis (PCA)

Extensive correlation between each bands is a problem frequently encountered in the analysis of multispectral data. This data often appear similar and include essentially the same information. The PCA is used to solve this problem or reduce data size, and simple linear combinations of the original data. It may be applied either as enhancement operation prior to visual interpretation or as a preprocessing stage prior to classification.

0-7803-3836-7/97/$10.00 © 1997 IEEE

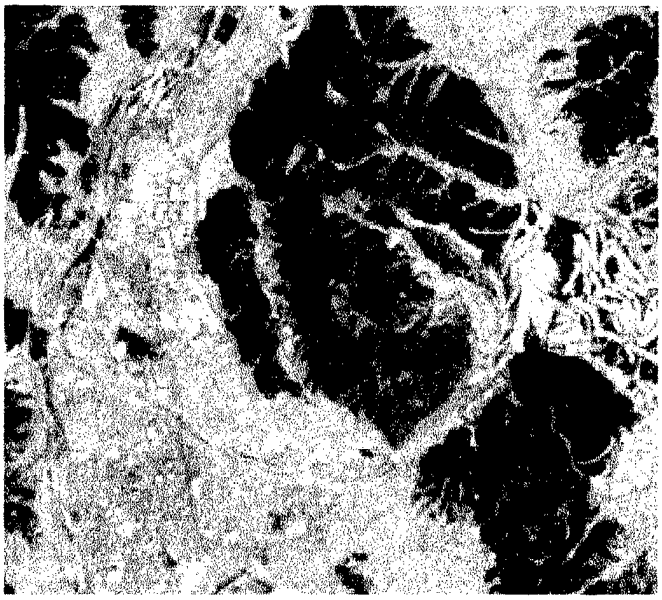

Fig. 1. Color composite image for Data I acquired in Jan. 1, 1991.

It transforms the highly correlated Landsat TM data into statistically independent orthogonal axes on which the original data are reprojected. The first and second principal component analysis are applied for each Landsat TM data, and 12 TM bands data were transformed into 4 bands data through the PCA.

Backpropagation (BP) Training Algorithm

The BP algorithm is an effective technique to adjust the interconnecting weight values to achieve minimal training error in multi-layer networks (Rumelhart et al., 1986). The aim of training in this algorithm is to minimize the error between the desired and actual outputs of the networks.

The input, I_k, from node j in hidden layer to node k in output layer is ΣWk_jO_j, where W_{kj} is a weight of node k in output layer and O_j is the output of output layer. Then, the output, O_k, is $f(I_k)$, where f is an activation function. The activation function is used sigmoid function in general. Some features of this function is important to network performance.

The BP training algorithm was performed with four bands data acquired through the PCA. Before classification, training data set has been selected for four class including urban/ residential area, vegetation, bare soil and water. The size of training data for each class is 100. The results were compared with the BP training algorithm without the PCA to evaluate the feasibility of this study.

Tabel 1. Principal component analysis : Data I

Component	Eigenvalues	Variance(%)	Total(%)
1	861.864	89.429	89.429
2	49.160	5.101	94.530
3	33.160	3.441	97.971
4	3.664	1.584	99.555
5	2.360	0.380	99.935
6	0.628	0.065	100.000

Eigenvector Matrix

TM	Principal Component					
Band	1	2	3	4	5	6
1	0.377	-0.511	-0.097	0.237	-0.707	-0.172
2	0.402	-0.338	-0.011	0.212	0.384	0.644
3	0.408	-0.276	0.062	0.048	0.561	-0.594
4	0.334	0.546	0.483	0.566	-0.108	0.045
5	0.396	0.254	0.209	-0.474	-0.078	-0.259
7	0.402	0.057	0.090	-0.581	-0.139	0.364

Tabel 2. Principal component analysis : Data II

Component	Eigenvalues	Variance(%)	Total(%)
1	2726.123	76.689	78.689
2	573.728	16.561	95.250
3	99.226	2.864	98.114
4	49.681	1.434	99.548
5	13.749	0.397	99.945
6	1.928	0.055	100.000

Eigenvector Matrix

TM	Principal Component					
Band	1	2	3	4	5	6
1	0.410	-0.207	-0.247	0.328	0.752	0.179
2	0.419	-0.105	-0.337	0.234	-0.309	-0.038
3	0.418	-0.160	-0.269	0.111	-0.547	0.023
4	0.079	0.911	-0.153	0.331	0.031	-0.148
5	0.396	0.298	0.075	-0.578	0.006	0.641
7	0.421	0.026	0.044	-0.503	0.181	-0.731

RESULTS

The PCA and BP training algorithm were applied to improve classification accuracy. The results of the PCA (Table 1 & 2) showed that the first principal component for Data I and Data II accounts for about 89.4 percent and 78.6 percent of the variance within entire TM data, respectively.

Approximately 95 percent of the total variance of each six TM bands (excluding TIR data) was explained by the first and second principal components. The first principal component identified the dominant trend within the data that explain the primary magnitude of the scene variance. Also the second component suppressed shadows and provided only moderate representation of vegetation.

Fig. 2 and Fig. 3 showed the result that only the BP training algorithm was applied for Data I and Data II. The data size was 300 by 250 pixels, and the size of training data is 100. Training data set has been selected for four class including urban/residential area, vegetation, bare soil and water in the same area of two Landsat TM data. Fig. 4 showed the result of applying the BP training algorithm after the PCA for two Landsat TM data.

As shown Fig. 2, urban/residential area was overclassified than the ground truth data. Vegetation and bare soil were misclassified to water and urban/ residential area, respectively.

In Fig. 3, the result of Data II was better than Data I. Water and road in the urban area were misclassified in Fig. 3. However, as shown in Fig. 4, the result was better than the others. Especially, road and water in the urban/ residential area were shown clearly.

Consequently, the results of classification using the BP training algorithm after the PCA have been enhanced than that of using merely the BP training algorithm.

Fig. 2. Classification using the BP algorithm for Data I.

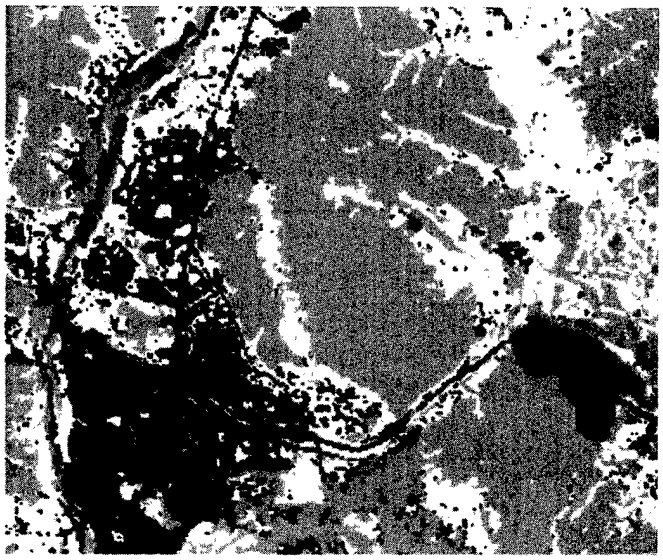

Fig. 3. Classification using the BP algorithm for Data II.

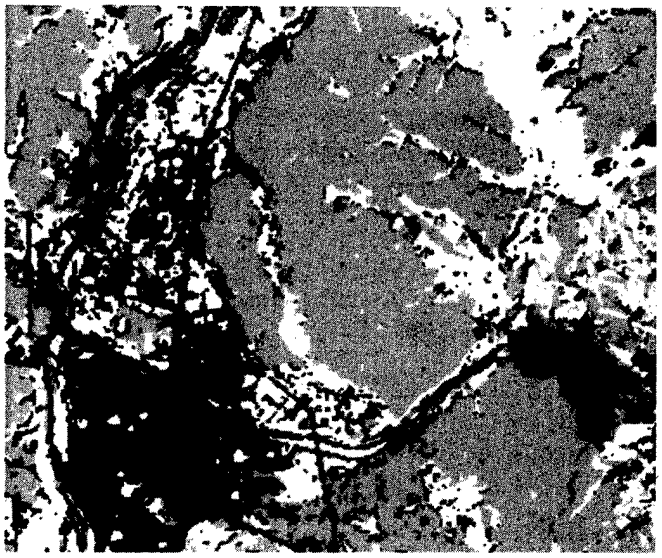

Fig. 4. Classification using the PCA and BP training algorithm.

Training time generally depends on the number of input node in the artificial neural network. Therefore, the number of input node was decreased in case of using the PCA, so that the consumed time in training stage was decreased. In the hyperspectral data, this approach is very useful and effective method for classification since the number of input node can be minimized.

CONCLUSIONS

The PCA and BP training algorithm of artificial neural

network were applied to enhance the accuracy and effectiveness of classification for mapping land cover map using multitemporal Landsat TM data. Two Landsat TM data were used to achieve this object, and two methods were compared. One is only applied with the BP training algorithm and the other with the PCA and artificial neural network. In the latter method, the BP algorithm was applied for 4 band data extracted through the first and second PCA. The result was compared with each other.

The results of classification using the BP algorithm after the PCA enhanced than that of merely the BP algorithm. Training time generally depends on the number of input node in the artificial neural network. Therefore, the number of input node was decreased in case of using the PCA, so that the consumed time in training stage was decreased. In the hyperspectral data, this approach was proved to be a useful and an effective method for classification since the number of input node could be minimized.

REFERECES

[1] C. Conese, G. Maracchi, and F. Maselli,"Improvement in maximum likelihood classifications performance on highly ruggied terrain using principal component analysis," Int. J. Remote Sensing, col.14, pp1371-1382, 1993.

[2] D. E. Rumelhart, G. E. Hinton, and R. J.Williams, "Learning internal representations by error propagation," In Parallel Distributed Processing: Explorations in the Microstructure of Cognition., vol. I . D. E. Rumelhart and J. L. McClelland, Eds. Cambridge MA:The MIT Press, 1986, pp.318-362

[3] G. M. Foody, "Approaches for the production and evaluation of fuzzy land cover classifications from remotely sensed data," Int. J. Remote Sensing, vol.17, pp.1317-1340, 1996.

[4] J. D. Paola and R. A. Schogengerdt, "A review and analysis of backpropagation neural networks for classification of remotely sensed multi-spectral imagery," Int. J. Remote Sensing, vol.16, pp.3033-3058, 1995.

[5] K. S. Chen, S. K. Yen, and D. W. Tsay, "Neural network classification of SPOT imagery through integration of intensity and fractal dimension," Int. J. Remote Sensing, vol. 18, pp. 763-783, 1997

[6] P. E. Roger, "Principal components transform with simple, automatic noise adjustment," Int. J. Remote Sensing, vol. 17, pp.2719-2727, 1996

[7] S. J. Walsh, J. W. Cooper, I. E. Von Essen, and K. R. Gallager, "Image enhancement of Landsat thematic mapper data and GIS data integration for evaluation of resource characteristics," Photo. Eng. & Remote Sensing, vol.56, pp.1135-1141, 1990.

Unsupervised Classification for Remotely Sensed Data using Fuzzy Set Theory

Dinesh.M.S, K.Chidananda Gowda and P.Nagabhushan.

Department of Computer Science & Engineering, S.J. College of Engineering,
Mysore - 5700 06, Karnataka, India. Fax (091) 821- 515770, ph. 512568,512292.

ABSTRACT

Fuzzy interpretations of data structures are a very natural and intuitively plausible way to formulate and solve various problems such as uncertainty, vagueness, decision making etc.

The concept of Fuzzy set theory without a priori assumption is used to devise a novel algorithm to carry out Fuzzy symbolic classification of remotely sensed data (IRS 1B Satellite). The proposed algorithm involves two stages. In the first stage, we will convert the data in to symbolic form, which involves data reduction followed by a new concept of finding the number of classes in the data based on the farthest neighbor index. In the second stage, fuzzy descriptions on symbolic objects of remotely sensed data is developed using membership function. Membership function is calculated using seed points determined from the farthest neighborhood concept instead of usual fuzzy means. Further classification is done, using fuzzy membership value.

The classification results of IRS 1B satellite data covering Hyderabad City is encouraging. Results signify that Fuzzy classification is more logic and more powerful than hard classification.

INTRODUCTION

In conventional data analysis, the objects are numerical vectors. The classification of such objects is achieved by minimizing intracluster dissimilarity and maximizing intercluster dissimilarity. A good survey of cluster analysis can be found in the literature [1],[2],[4],[5].

Remote sensing information is imprecise in nature. Many relevant concepts do not have precisely defined intension and extension. "Grassland" and "soil" are such concepts. In talking about landcover, a piece of land with sparse grass can be classified into either grassland or soil. There is not a well-specified criterion for distinguishing between the two cover-types. The impreciseness also results from natural variations or arises through original measurements, as well as data processing. Fuzzy set theory [16] provides useful concepts and tools to deal with imprecise information.

Symbolic objects are extensions of classical data types. In conventional data sets, the objects are "individualized", whereas in symbolic data sets, they are more "unified" by means of relationships. Based on the complexity, the symbolic objects can be of assertion, hoard or synthetic type. Some references to clustering of symbolic objects can be found in [3], [7], [8]. Remotely sensed satellite data is more complex at description and hence, are suitable for conversion to symbolic form.

This paper illustrates the use of fuzzy set theory by considering the problem of Remotely sensed data classification. An excellent review on fuzzy sets in pattern recognition can be found in[16]. Fuzzy interpretations of data structures are a very natural and intuitively plausible way to formulate and solve various problems such as uncertainty, vagueness, decision making etc.

The present algorithm involves two stages. In the first stage, the remotely sensed data is converted to symbolic form by incorporating data reduction, followed by finding the number of classes in the data, which involves a new farthest neighbor index concept. In the second stage, fuzzy classification for symbolic remotely sensed data is developed. Classification is perceived using membership function[14]. Membership function is calculated based on seed points obtained from the concept of farthest neighborhood.

I.DETERMINATION OF NUMBER OF CLASSES:

Remotely sensed data is converted to symbolic form involving data reduction using the method proposed by Gowda et. at [15]. After the data is converted to symbolic form, the size of the reduced data is represented by N composite symbolic objects.

0-7803-3836-7/97/$10.00 © 1997 IEEE

Steps involved in finding the number of classes present in the remotely sensed data are as follows :

1.Let {X1, X2, X3.. ..Xn} be a set of N symbolic objects on k dimensions. The distance matrix of size N x N is calculated using the distance measures proposed by [10].
2.The seed points belong to different classes are calculated using the farthest neighborhood concept [11]. Here distance between seedpoints represents discrimination between different classes.
3.Step 2 is repeated for 2 to N-1 seed points. The distance obtained at each step is stored in a queue against the number of seed points. The seed points represent individual classes are stored in memory for further computation.
4.The distances stored in queue are searched for minimum distance value. The corresponding number of seedpoints for minimum distance in a queue represents the number of classes presents in the data. Here number of seed points symbolize the number of classes C.

The above procedure is applied on symbolic remotely sensed data and the results such as, number of classes C and seed points are stored for further computation.

II. FUZZY CLASSIFICATION:

Classification of Remotely sensed data involves three steps such as formation of distance matrix, seed point selection and membership computation. The first two steps ie, formation of distance matrix and seed points evaluation is common as in the first stage. Hence, the results obtained in first stage is made use for membership computation.

Membership function is calculated as follows:

Membership for individual symbolic objects to particular class is computed as follows:

$$U_{ik} = \frac{1}{\sum_{j=1}^{c} \left(\frac{\|X_k - s_i\|^2}{\|X_k - s_j\|^2} \right)^{\frac{1}{m-1}}} \qquad (1)$$

$$\sum_{J=1}^{C} U_{IK} = 1$$

Uik $\Rightarrow$ [0, 1], $1 \le i \le c$, $1 \le k \le N$;

Where, C = number of classes present in the remotely sensed data, N = number of composite symbolic objects of remotely sensed data, Si = seed points representing different classes in the data.

From the membership value, membership matrix of C x N is formed. Since seed points are one of the symbolic objects itself, distance ||Xk - Si|| is easily selected from dissimilarity distance matrix of size N x N. M is the parameter used to control the degree of fuzziness of the class membership allocation. Here m value is selected according to the heuristic rule m >= N/N-2 [13] Depending on the membership value, individual symbolic objects are grouped to form different classes. Here symbolic object is assigned to a class that has highest membership.

ALGORITHM :

1.Let {X1, X2, X3.. ..Xn} be a set of N symbolic objects on k dimensions. The distance matrix of size N x N is calculated using the distance measures proposed by [10].
2.From the distance matrix, seed points are calculated using farthest neighbor concept. These seed points are further used to find the number of classes "C "present in the data as in stage I.
3.Membership for individual objects to particular class is computed using eqn 1. The membership value will be of C x N form. Where C is number of classes computed in step 2 and N is the number of symbolic objects.
4.From the membership value, individual symbolic objects are grouped to form different classes.
5.The samples involved during formation of symbolic objects will be assigned to the same class label as the symbolic objects belong to.

RESULTS

The proposed algorithm is applied on the Hyderabad image from IRS 1B satellite. In the first stage we obtained the number of classes as six. Further this result is made use in the second part where membership values are found using eqn 1. These membership values are used to classify the different classes present in the remotely sensed data. The classified map and area covered of the Hyderabad image is shown in fig 1. Results obtained are more logical when compared to conventional type and a pixel's partial membership enables more accurate statistical parameters.

DISCUSSION AND CONCLUSIONS

Most of the techniques used for fuzzy classification is of supervised or partially supervised. Where as, our method is totally of unsupervised type. Here the number of classes is found using farthest neighborhood concept. To find the efficacy of finding the number of classes concept, the concept is applied on several data sets whose classes are known. The results obtained confirms that the concept works satisfactorily. The results obtained with the multispectral images covers most of major classes of land cover.

In our methodology computation time is saved. Since, seed points are used for calculating membership value instead of usual fuzzy means. This requires fewer number of iterations and chances of local minima is avoided when compared to Bezdek membership function[14].

The results obtained cannot be validated because of non availability of ground truth information.

REFERENCE :

1.Bock, H.H. (1987). Classification and related methods of data Analysis. North-Holland, Amsterdam.

2.Diday, E., Ed. (1989). Data analysis, Learning symbolic and Numeric Knowledge, Nova Science, Antibes, France.

3.Diday.E. (1990). From numerical to symbolic clustering. Proc. Comp-stat, Dubrovnik, Yugoslavia, 9-15 sept.1990.

4.Diday. E. and Simon(1976). Clustering Analysis: Communication and Cybernetics, Vol.10. Springer, New York-92.

5.Duda, R.O. and P.E. Hart (1973). Pattern Classification and Scene Analysis. Wiley Interscience, New York.

6.P.J.Deer, P.W.Eklund and Norman. A Mahalanobis Distance Fuzzy Classifier. Proc.1996 Australian Newzeland Conf. on Intelligent /information Systems, 18-20, Nov 1996.

7.Gowda.K.C. and E.Diday(1991a). Symbolic clustering using new dissimilarity measure. Pattern Recognition 24 (6)", 567-678.

8. Gowda.K.C. and E.Diday(1991b). Unsupervised learning through symbolic clustering. Pattern Recognition Lett. 12, 259-264.

9.Gowda.K.C. and E.Diday(1992). Symbolic clustering using a new similarity measure. IEEE Trans. Syst. Man Cybernet. 22 (2), 368-378.

10.Gowda. K.C. and T.V.Ravi (1995). Agglomerative clustering of symbolic objects using the concepts of both similarity and dissimilarity. Pattern Recognition Lett. 16(1995) 647-652.

11.Gowda.K.C. A feature reduction and unsupervised classification algorithm for multispectral data. Pattern Recognition, vol. 17, No 6, pp 667-676, 1984

12.Gowda.K.C., P.Nagabhushan, H.N.SrikantaPrakash, et. Symbolic Clustering of Multispectral Data. 5th conference IFCS-96, March 1996, Kobe, Japan.

13.Ichino, M.(1998). General metrics for mixed features - The Cartesian space theory for pattern recognition. Proc. IEEE 1988 Conf. Syst. Man Cybernet.

14.James C. Bezdek (Aug 1974). Mathematical models for systematic and taxonomy. Proc. of 8th conf. on Numerical Taxonomy, San Francisco, 1975.

15.James C.Bezdek. Convergence theory for fuzzy c-means: counter examples and repairs. IEEE Trans. of sys. man. and cybernetics vol.17, No. 5, 1987.

16. James. C. Bezdek and Sankar. K.Pal. Fuzzy models for Pattern Recognition. A selected reprint volume. IEEE Press.

17.Wang F. Fuzzy Supervised Classification of Remote Sensing Images. IEEE Transactions on Geoscience and Remote Sensing, Vol. 28, N0 2, March 1990.

Classified FCC Image of IRS 1B of Hyderabad INDIA

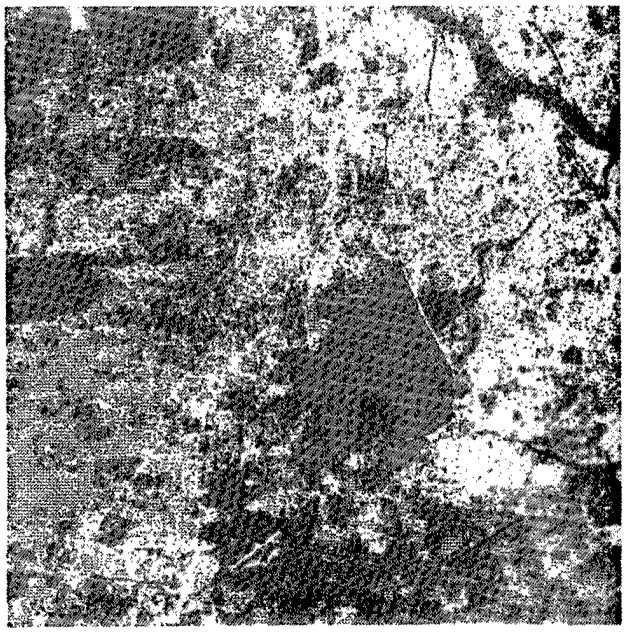

Fig.1.

Blue - water of area1972 sqkm, Green - concrete of area 15241.81sqkm, Purple-airstrip and road network of area 332 sqkm, Yellow - Aerodrome of area 375.355 sqkm, Red - vegetation of area 12049.69 sqkm, Lightpurple - Barenland of area 44756.434 sqk.

Development of an Intelligent Image Analysis System for the Detailed Analysis of Land Surface Information

Kyoung-Ok Kim, Young-Lyol Ha, In-Sook Jung, Jae-Yeon Lee, Kyung-Ho Choi and Jong-Hun Lee
GIS Lab. / Systems Engineering Research Institute (SERI)
P.O.Box. 1, Yusung, DAEJON, 305-600, KOREA
Tel: +82-42-869-1463 Fax: +82-42-869-1479
E-mail: kokim@seri.re.kr

Abstract– Several companies are preparing launching high resolution imaging satellites. Images from these satellites will have 1 to 3 meter ground resolution and will be very useful for analyzing current status of earth surface. An intelligent GIS and DB based image processing system, TIPS(Tactical Information Processing System) has been designed and implemented to support the detailed analysis of the land surface. This system is designed to provide a computer graphics environment in which the analyst can interactively operate the entire analyzing process such as digitizing, geometric correction by ground control points, interactive enhancement, various transforms, arithmetic operations, calculating vegetation indices, various classifications and estimations, etc. The TIPS is expected to be a valuable tool for investigating the various facts such as the change detection, land cover classification, capacity estimation of the industrial complex, urban information extraction, etc. using high resolution images.

INTRODUCTION

Recent development of earth imaging satellites by the commercial vendors have aroused big interest among the remote sensing experts in Korea. Korea is a small country and the land use pattern is so small that the ground resolution of existing Landsat (ground resolution 30 meters) and SPOT (ground resolution 10 meters) images are too coarse to extract useful information on the land surface. The analysis of the high resolution imagery requires more intelligent and complex image processing technique because the objects are captured in detail. For example, with high resolution images, the traditional pixel operation based classification would not work very well because the variation within one land use class could be big enough to be classified as a different class. The user needs a model based upon analysis techniques to extract detailed information on the buildings and terrain. Also the large image data size and its complex relationship with its auxiliary data requires very special data modeling and management techniques.

The development of an intelligent image processing technique has been one of the major research tasks among the advanced countries. Examples of these systems are IUE for computer vision and image processing, and the Khoros system that includes visual environment and utilities [2]. The TIPS (Tactical Image Processing System) also includes most of the image processing routines. Additionally efficient database management modules [3], GIS modules, model based analysis modules, terrain analysis modules and intelligent classification modules were developed and implemented.

DESIGN CONCEPT

TIPS has been designed as a high performance, interactive environment for image processing, GIS, object modeling and classification tool. Design emphasis was on user friendliness, good visualization and expansibility to ensure efficient use of the system and smooth expansion to a more advanced system in the future [4]. The consideration points in design process are as follows:

- ability to handle the satellite images, aerial photographs, digital maps, vector data, and documents
- ability to access and store the database during any image processing operation
- ability to transmit the parameters among the modules

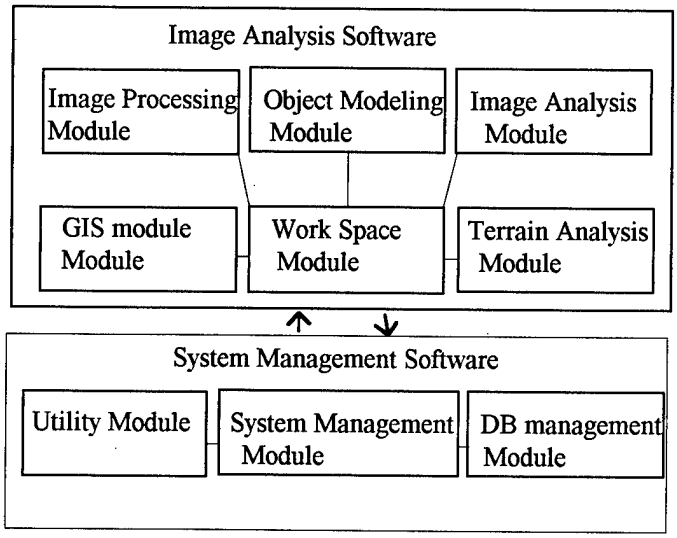

Figure 1. TIPS Software Configuration

0-7803-3836-7/97/$10.00 © 1997 IEEE

DATA MODELING & DATABASE DESIGN

A composite data modeling for the satellite image information system using the RDBMS plus file system that can efficiently handle the image and the auxiliary data was performed. This modeling method can provide semantic meanings to the image objects such as satellite images, aerial photographs, digitized maps, and relationships with alphanumeric information, entities such as map name, geographic coordinates, description of the objects, reports in document form, etc. The integrity rules over image objects and operations are included into the data model. Directly associating semantic meanings to the image entities and relationships helps the comprehensive and detailed analysis of image information.

TIPS SYSTEM IMPLEMENTATION

The specialized image analysis modules as well as general image processing modules have been implemented. The specialized functions of the system include semi-automatic settings of ground control points, intelligent recognition and classification using various features, Wavelet transforms and neural networks, very efficient database query scheme available during any image processing operation, handy report generation tool, etc. Using our system, we can present spatial 3D viewing simulation, flood inundation analysis, change detection, land use classification, estimation of city population, and estimation of industrial complex capacity. In this system ORACLE DBMS is adopted as database management system and various information such as image names, target object information, map names, airplane flight plot information, and GIS topology data have been registered in the database system. Various access methods to get images such as by geographic name, by clicking from map position, coordination of the area, or by selecting from the file selection box are available. As an integrated raster/vector analysis system, GIS based analysis modules, vector overlay, flight simulation, 3D simulation, and object modeling techniques are also implemented. In addition to the modules for image and digital signal processing, the system provides many other interactive utilities such as toolbox, an interactive image editor.

- System configuration

An Ultra workstation with Solaris2.5 equipped with a digitizer was used as platform for this system. Figure 1 shows the functional diagram of our system. The following are the specialized functions in our system.

- On-screen GCP correction

We used an semi automated geometric correction method that can correct the geometric distortion of satellite images by automatic GCP(Ground Control Point) selection. This method can predict the next corresponding points in the image to be corrected. This method is implemented on Ultra with the Micro-Grid IIII digitizer .

- Recognition and Classification with AI techniques

In our system target recognition that is invariant to translation, rotation, and scale transformation is achieved by a neural network based approach using geometrical moment and Zernike moment. This process has three stages: preprocessing, feature extraction and classification. For the preprocessing step, the morphological as well as spatial filtering were applied to suppress the noise. For the feature extraction Zernike moments are adopted. For the classification phase, the Multilayer perceptron (MLP), which is trained by a back-propagation learning algorithm, is used [5,6,7].

For classification, the remotely sensed data have often led to unsatisfactory results. The parametric procedures such as the Maximum Likelihood Classifier are statistically stable and robust. However they lack flexibility and the capability of making correct data estimates. On the other hand, non parametric classifiers are generally very sensitive to distribution of anomalies and critically dependent on training sample size. These problems can be overcome by providing prior probabilities derived from a non parametric strategies presented using a Kohonen neural network and multilayer neural network with a back-propagation algorithm [8,9,10,11,12].

The features from wavelet frames provide an attractive tool for the characterization of texture properties. Features from the wavelet frames were used in the error back-propagation algorithm for training, and classification[13,14].

- GIS Integration

The integrated Vector/Raster based geographic information system is implemented. The GIS system includes topology building function, buffering, overlaying raster to vector and overlaying vector to raster, unlimited zooming, and many useful functions like node, arc, polygon buffering, dangling node elimination, snap node , etc.

SYSTEM FUNCTIONALITY

The TIPS has over 250 modules that include the following:

1. Image processing

- Preprocessing

  o Geometric correction
  o Radiometric correction
  o Re-sampling
- Image Processing Routines
  - Enhancement software
  - Image Transformation
    o Standard algebra
    o Operation between two bands
    o FFT
    o inverse FFT
  - Spatial Filtering
  - Frequency Filtering
    o Low pass filter o High pass filter
    o Band reject filter o Band pass filer
  - Feature Extraction
  - Classification : K-means, Maximum Likelihood Classifier
    Neural Network Classifier
  - Image Compression and Matching Algorithm
  - Morphology

2. Image DBMS

Design of the database management system based on analysis of the prospective user's requirement and the DB function, and development of the database creation, retrieval, update program.

o. DB Input and Retrieval Program
o DB Update Program
o Various Analysis Modules

3. GIS and Terrain Analysis

Development of terrain analysis routines such as the analysis of a candidate sites for a relay station, the shortest path and supply road, 3D display, radar coverage, and intelligence preparation for the battlefield.

o. Shortest Path Analysis
o. Analysis of the Optimum Relay Station Sites
o. Supply Road Analysis
o. Radar Coverage Analysis
o IPB(Intelligence Preparation for the Battlefield)

4. User Interface

Basic research was undertaken on issues such as examination on current user interface technique based on a literature survey and research experience, studying the interface techniques between CRAY and SUN, and development of a menu system for the implemented image processing modules.

5. Utilities

Selection of standard file format for the image processing system, development of the file conversion and data conversion program and development of X-Y digitizer interface program.

o Image Display module
o 3D Image Display module
o Standard File Format Design and File I/O Routines
o Data Conversion Software
o Development of the Coordinate Conversion Software

CONCLUSION

This paper presented a general overview of TIPS with emphasis on its image processing, analysis tool. The TIPS system is built on top of the Oracle DBMS. The integration technique of remotely sensed images and GIS data such as precision registration, overlay, and on-line editing was implemented. The user interface is automatically generated by program with interpretation of the textual script. In the future, data flow visual programming should be integrated to be an efficient development tool for image processing system.

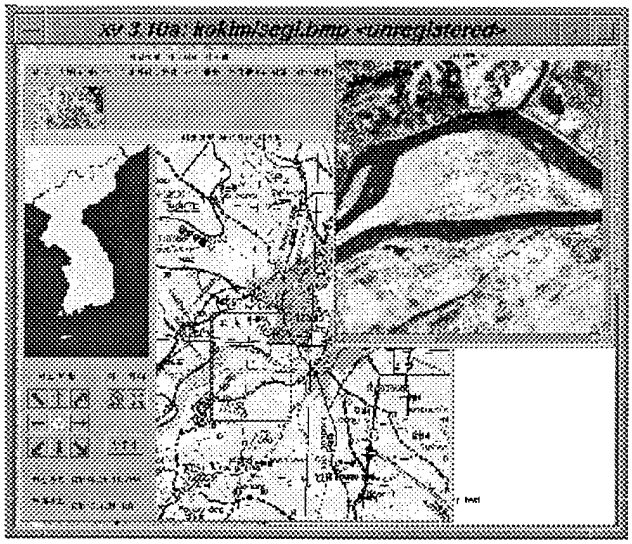

Figure 2. TIPS Main Menu

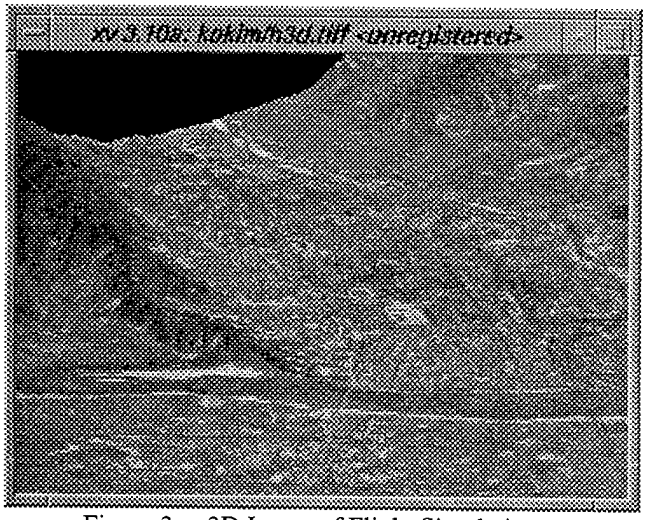

Figure 3. 3D Image of Flight Simulation

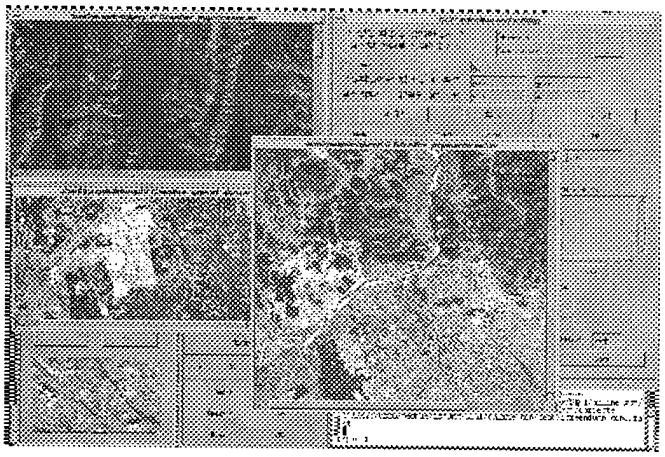

Figure 4. Geometric Correction of a Satellite Image.

REFERENCES

[1] Hunt, N., 1990, "IDF : A Graphical Data Flow Programming Language for Image Processing and Computer Vision", 1990 IEEE Int'l Conf. on Systems Man and Cybernetics, pp.352-360.

[2] Konstantinides K, "The Khoros Software Development Environment for Image and Signal Processing", IEEE Transactions on Image Processing . Vol.,3, NO. 3. pp. 243-252 May 1994.

[3] Henry, F.K. and Abraham, S., 1991, "Database System Concepts", McGraw-Hill, pp694.

[4] Hibbard, William L."A Next Generation MCIDAS Workstation." In Proc. Of Fourth International Conference on Interaction Information and Processing Systems for Meteorology Oceanography, and Hydrology, Feb. 1-5, 1988, Anaheim, Calif. U.S.A, pp. 57-61, 1988.

[5] Mather, P.M., 1987, "Computer Processing of Remotely-sensed Images".

[6] Bebis, George, N. and George, M., Papadourakis, 1992, "Object Recognition Using Invariant Object Boundary Representations and Neural Network Models", Pattern Recognition, Vol.25, No.1, pp.25-44.

[7] Khotanzad, A. and J. Lu, May 1990, "Classification of Invariant by Zernike Moments", IEEE Transactions on Patterns Analysis and Machine Intelligence, Vol.12, No.5.

[8] G. Pasquariello and P. Blonda, 1992, "Multitemporal Remote Sensing Data Classification Using Neural Network", Proceeding of ISPRS, Vol.29, pp.922-929, Washington D.C.

[9] Katarina Johnsson, January 1994, "Segment-Based Land-Use Classification from SPOT Satellite Data", Photogrammetric Engineering and Remote Sensing, Vol.60, No.1, pp.47-53.

[10] P. Blonda, V. la forgia, Pasquariello, Satalino, 1994, "Multispectral Classification by a Modular Neural Network Architecture", IGARSS '94, California Institute of Technology Pasadena, Vol.4, pp.1873-1876.

[11] Manoel F. Tenorio and Wei-Tshin Lee, March 1990, "Self-Organizing Network for Optimum Supervised Learning", IEEE Transaction on Neural Network, Vol.1, No.1, pp.100-110.

[12] Tomoji Yoshida and Sigeru Omatu, September 1994, "Neural Network Approach to Land Cover Mapping", IEEE Transaction on Geoscience and Remote Sensing, Vol.32, No.5, pp.1103-1109.

[13] M. Unser, "Texture Classification and Segmentation Using Wavelet Frames", IEEE Trans. On Image Processing, Vol. $, No. 11, pp. 1549-1560, Nov. 1995.

[14] S.G. Mallat, Multi-resolution Signal Decomposition: The Wavelet Representation", IEEE Trans. Patt. Analysis and Machine Intell., Vol. 11, No.7, pp.674-693, Jul. 1989.

[15] Kim, K. O., Y. K. Yang, et al., 1995. Invariant Image Recognition Using Neural Network, In Proc. of World Congress of Neural Net (WCNN) '95, Washington, D.C., August, 1995, pp. 244-248.

[16] Kim, K. O., Y. K. Yang, et al., 1995. Classification of Multispectral Image Using Neural Network, In Proc. of IEEE International Geoscience and Remote Sensing Symposium (IGARSS) '95, IEEE catalog #95CH35770, vol. 2. Firenze, Italy, Aug 1995, pp. 446-448.

[17] Kim, K. O., Y. K. Yang, Y. H. Park, T. K. Kim, Shape Discrimination by Descriptors and Moments Using Neural Network, International Archives of Photogrammetry and Remote Sensing, 1996, pp. 389-404.

[18] Kim, K. O., Y. K. Yang, Texture Classification Using Wavelet Frame and Neural Network, SERI Journal, Vol. 1, No. 1, Jan. 1997, pp. 63-82.

Study on the Characteristics of the Supervised Classification of Remotely Sensed Data Using Artificial Neural Networks

Kil N. Paek
Mining & Mineral Res. Eng., Chonbuk Nat'l Univ.
664-14, Duckjin-dong, Duckjin-ku, Chonju, 560-756, Korea
82-652-70-2358/82-652-70-2366/kilam@geophysics.chonbuk.ac.kr

Young S. Song
Mining & Mineral Res. Eng., Chonbuk Nat'l Univ.
664-14, Duckjin-dong, Duckjin-ku, Chonju, 560-756, Korea
82-652-70-2365/82-652-70-2366/geosys@moak.chonbuk.ac.kr

Hyo S. Chae
Water Resources Research Institute, KOWACO
462-1, Jonmin-dong, Yusung-ku, Taejon, 305-390, Korea
82-42-860-0374/82-42-860-0368/chaehs@kowaco.or.kr

Kwang E. Kim
Resources Exploration Division, KIGAM
30, Kajung-dong, Yusung-ku, Taejon, , Korea
82-42-868-3184/82-42-861-9721/kimke@rock25t.kigam.re.kr

Abstract -- The characteristics of classification of remotely sensed data using artificial neural networks were investigated. Training method of neural networks consists of generalized delta rule (GDR) and conjugate gradient (CG). The GDR is divided into two methods, data adaptive and block adaptive. The effects of the number and order of input data and learning rate were analyzed in the training. Data adaptive and block adaptive method showed similar trend of error convergence in the GDR. The CG especially with small data set had faster error convergence than the GDR. The CG having low error in the training didn't show a good accuracy in the testing stage because of the overtraining effect.

INTRODUCTION

Recently, artificial neural networks are widely used in pattern recognition. These methods are applied to classifying remotely sensed data, and many theories and characteristics are announced (Key et al., 1989; Heermann & Khazenie, 1992; Foody et al., 1995; Paola & Schowengerdt, 1995). The GDR generally gives a good result. However, it requires some trial and error for selecting the optimal learning rate and the size of hidden layer, and consumes much time for the training (Barnard & Cole, 1989). The CG can improve the speed of error convergence since it uses the optimal learning rate which is calculated in each iteration during the training stage (Luenberger et al., 1984).

There are few study for the characteristics of error convergence when the GDR and CG are applied to classify remotely sensed data. The characteristics of error convergence on the training of remotely sensed data were analyzed with experimental computer simulation in the present work.

THEORY

The GDR or backpropagation, presented in 1986 by Rumelhart et al., is one of the most commonly used in artificial neural network. It is an iterative, gradient descent training procedure. The goal of this algorithm is to minimize the error between the desired and actual outputs. The GDR consists of two methods, data adaptive

0-7803-3836-7/97/$10.00 © 1997 IEEE

and block adaptive. In data adaptive method, the error is described as (1).

$$E = \frac{1}{2}\sum_{k}(T_k - O_k)^2 \quad (1)$$

Here, T_k and O_k is the desired and actual output, respectively, and k is the number of output node.

System error may be expressed as (2) in block adaptive method.

$$E = \frac{1}{2}\sum_{m}\sum_{k}(T_k - O_k)^2 \quad (2)$$

In the above equation, m represents total data set.

The CG uses a optimal learning rate which is calculated in each iteration and it has proved to give a very useful result in handling objective function (Barnard & Cole 1989; Luenberger, 1984). Quadratic fit of the line search is widely used to get an optimal learning rate (Luenberger, 1984). Weighting factor is updated using conjugate direction vector ,d_k, as follows.

$$W_{k+1} = W_k + \eta \cdot d_k \quad (3)$$

RESULTS

The characteristics of error convergence on the training of remotely sensed data using artificial neural networks were analyzed. The analysis was divided into three aspects: (1) characteristics of error convergence according to the input data size and order, (2) the learning rate effects, and (3) training error and testing accuracy.

The number of training data set in each class was 10, 25, 50 and 100, and that of total training data set was 40, 100, 200 and 400, respectively. Input types of data set were pattern by pattern (type-α) and data by data (type-β). The data adaptive method were applied using two types, but it didn't need to discriminate the type-α and the type-β in block adaptive method and the CG. So the block adaptive and CG were applied only on the type-α. The convergent trends of training error were analogous with the data adaptive and block adaptive method, but the error oscillated as the number of training data increased in the block adaptive method. The error convergence of the CG was faster than that of the GDR using small training data set (Table 1).

The characteristics of error convergence varying with the learning rate were analyzed. The size of training data set was 400, and learning rate was 0.1, 0.2, 0.3, 0.5, 0.7 and 0.9. As shown in Table 2, the speed of error convergence of the data adaptive method increases with learning rate. However, as the more iteration was progressed, it is similar to that of low learning rate. In the case of the block adaptive method, the higher the learning rate was, the more frequently oscillation appeared.

The accuracy of classification was compared with each other after the training. To do this, test data set was selected which is similar to the training data. As shown in Table 3, the accuracy of the CG is higher than that of the GDR until 300 iteration, but it decreased after then.

CONCLUSIONS

The characteristics of supervised classification of remotely sensed data using artificial neural networks were investigated. The convergent trends of training error were independent on data type using data adaptive and block adaptive methods. The trend of error oscillated as the number of training data increased in block adaptive method.

Table 1. Result of the training data size

Method	Size	Iterations			
		500	1000	1500	2000
Data Adaptive/ Type-α	40	0.28656	0.19738	0.13124	0.08952
	100	0.16731	0.07895	0.05539	0.04203
	200	0.08645	0.04665	0.03373	0.02711
	400	0.09077	0.05620	0.04369	0.03756
Data Adaptive/ Type-β	40	0.28526	0.19662	0.12868	0.08734
	100	0.16379	0.07728	0.05271	0.04153
	200	0.07501	0.04155	0.03054	0.02476
	400	0.05051	0.03206	0.02520	0.02142
Block Adaptive/ Type-α	40	0.28688	0.19670	0.12852	0.08757
	100	0.16424	0.07841	0.05227	0.04111
	200	0.10920	0.04121	0.02807	0.02234
	400	0.10665	0.05913	0.02447	0.02217
CG Type-α	40	0.00952	0.00816	0.00721	0.00649
	100	0.00605	0.00490	0.00423	0.00377
	200	0.00535	0.00304	0.00269	0.00244
	400	0.00665	0.00346	0.00273	0.00221

Table 2. Result of learning rate

Method	Learning Rate	Iterations			
		500	1000	1500	2000
Data Adaptive Type-α	0.1	0.08645	0.04665	0.03373	0.02711
	0.2	0.06032	0.03395	0.02497	0.02068
	0.3	0.05317	0.03006	0.02287	0.01994
	0.5	0.04919	0.03050	0.02437	0.02148
	0.7	0.04560	0.02868	0.02360	0.02053
	0.9	0.0328	0.02660	0.02166	0.01962
Data Adaptive Type-β	0.1	0.07501	0.04155	0.03054	0.02476
	0.2	0.04365	0.02665	0.02032	0.01714
	0.3	0.03496	0.02219	0.01748	0.01479
	0.5	0.02935	0.01976	0.01598	0.13672
	0.7	0.02797	0.02018	0.01654	0.01397
	0.9	0.02764	0.02140	0.01614	0.01354
Block Adaptive Type-α	0.1	0.10920	0.04121	0.02807	0.02234
	0.2	0.09540	0.02288	0.01645	0.01360
	0.3	0.09647	0.01656	0.01202	0.00998
	0.5	0.10107	0.01039	0.00883	0.00788
	0.7	0.12885	0.10898	0.00706	0.00561
	0.9	0.14108	0.18378	0.13020	0.12994

Table 3. Results of overtraining effect

Method	Iterations					
	100	300	500	1500	1700	2000
Data Adaptiv	75.00	74.75	86.00	94.75	95.00	94.75
Block Adaptiv	70.50	71.75	78.75	97.75	96.50	96.75
CG	95.75	98.00	96.50	95.00	95.25	95.50

However, as the more iteration was progressed, it is similar to that of low learning rate. In the case of the block adaptive method, the higher the learning rate was, the more frequently oscillation appeared. The trend of errors was diverged on occasion. In the training stage, the neural networks had a overtraining effect which degraded the accuracy of the test data. So the development of the algorithm which can avoid the overtraining effect must need in the further study.

REFERENCES

[1] J. Key, J. A. Maslanik, A. J. Schweiger," Classification of merged AVHRR and SMMR arctic data with neural networks, " Photo. Eng. & Remote Sensing, vol. 55, pp.1331-1338. 1989.

[2] P. D. Heermann, and N. Khazenie, "Classification of multispectral remote sensing data using a back propagation neural network," IEEE Trans. on Geo. & Remote Sensing, vol.30, pp.81-88,1992.

[3] G. M. Foody, M. B. Mcculloch, and W. B. Yate, "The effect of training set size and composition of artificial neural network classification," Int. J. Remote Sensing, vol. 16, pp.1707-1723, 1995.

[4] J. D. Paola and R. A. Schogengerdt, "A review and analysis of backpropagation neural networks for classification of remotely sensed multi-spectral imagery", Int. J. Remote Sensing, vol. 16, pp. 3033-3058, 1995.

[5] E. Barnard, and R. A. Cole, "A Neural-Net training program based on conjugate gradient optimization," Technical Report No, CSE 89-014, Oregon Graduate Center Beaverton, OR 97006, 1989.

[6] D. E. Rumelhart, G. E. Hinton, and R. J. Williams, "Learning internal representations by error propagation. In Parallel Distributed Processing," Cambridge MA :The MIT Press, vol. 1, pp. 318-36. 1986.

[7] D. G., Luenberger, Linear and Nonlinear Programming, 2nd ed., Addison-Wesley, 1984.

IGARSS'97

1997 International Geoscience and Remote Sensing Symposium

03-08 August 1997

Singapore International Convention & Exhibition Centre

Technical Program

Interactive Area 26: Missions and Programs

THE ADVANCED REMOTE SENSING DATA FROM MOMS-2P ON PRIRODA

Johann BODECHTEL and Qingxia LEI
AGF, Institute for General and Applied Geology, University of Munich
Luisenstr. 37, 80333 Munich, Germany
Tel: 49 89 5203 222, Fax: 49 89 5203 393
email: joh.bod@iaag.geo.uni-muenchen.de

Abstract -- The German Modular Optoelectronic Multispectral Stereo Scanner MOMS-2P was launched May 1996 aboard the Russian space platform MIR-PRIRODA on a preoperational mission for about two years duration. Technical features of the Sensor are three-line along-track stereo imaging, high spatial and spectral resolution, optimized multispectral imaging and combination of stereo and multispectral imaging. Advantages of the sensor have been confirmed by the Second German Spacelab D2 Mission on the Space Shuttle flight STS-55 1993, during which useful data were acquired for a broad range of geoscientific objectives [2]. The advanced sensor can receive data covering the Earth surface from N51.6° to S51.6° with a repetition rate of 2 to 7 days during the present 2P mission. This paper gives an overview of the technical advantages of the sensor and demonstrate the first image results of the MOMS-2P mission.

TECHNICAL PROPERTIES OF THE MOMS-2P

The development of the Modular Optoelectronic Multispectral Stereo Scanner MOMS sensor started with MOMS-01 in 1979. Bodechtel and Zilger described the development history from the MOMS-01 to MOMS-02 [2]. Using the pushbroom principle with CCD detector arrays, the camera MOMS-02 is an up-to-date space sensor. Followed on the German Spacelab D2 mission, the photogrammetric and geoscientific goals of the MOMS-2P PRIRODA mission are further focused on the combination of topographic and spectral information derived from the simultaneously acquired multispectral (MS), multiresolution and stereoscopic (ST) data.

The capability to acquire inflight ST data forms the first one of the important advantages of the MOMS sensor. Fig.1 shows the MOMS-2P imaging geometry and its ground covering track. The swath width for the high resolution (HR) channel is between 36 and 50 km, depending on the recording mode, and for the other channels between 90 and 105 km, depending on a nominal orbit altitude between 390 and 420 km. Because of their 21.4° viewing angle, the two off-nadir stereo channels are separated from the image swath of other nadir channels by about 150 km. The camera system consists of five lenses, three for ST imaging and the other two for acquiring data of 4 nadir MS channels. The central lens forms the core of the system and achieves HR panchromatic (PAN) data. The system can receive ST data simultaneously within the same orbit, the forward- and backward-viewing channels covering the same ground area only with a few seconds difference. Significant is further combination of the nadir HR data (6 m) with lower resolution data of the tilted channels (18 m). The threefold, along-track ST imaging enables derivation of Didital Terrain Models (DTM) with high accuracy [1].

The optimized spectral bands make up the second one of the important advantages of the MOMS system. It inclodes 4 MS and 3 PAN bands. Defination of the 7 spectral bands is shown in Fig.2. Wavelength and width of the MS bands (1-4) were optimized for detection of the spectral response of vegetation and for discrimination of Fe-bearing rocks and soil surfaces [3]. Band 1 covers the blue absorption of vegetation and allows good penetration in water bodies. Additionally it includes the right wing of the charge transfer band for Fe-bearing rocks and soils. Band 2 is centred on the "green peak" of vegetation. This position allows to avoid the high correlation between the green and the red bands. Band 3, only 32 nm wide, lies exactly in the principal absorption of chlorophyll-a in the red wavelength region. This enables the acquisition of precise reflectance values at the "red edge", an important indicator for the detection of vegetation stress. Band 4 was placed on the infrared plateau of vegetation between two significant water absorption bands. This position guarantees exactly the maximum reflectance of vegetation. This band is also centred for the charge transfer absorption of iron. The HR band (5) and the 2 stereo PAN bands (6,7) were defined to get most contrast between albedo of vegetation and of non vegetated targets (rocks, soils and sealed areas). The short-wave end of the PAN bands was selected to avoid most of the noise and lowpass characteristics introduced by atmospheric scattering, but also allows some penetration of water bodies. The long wave edge was determined to enclose the steep raise of vegetation reflectance at the "red edge".

The third important advantage is the combination of multi-resolution, multispectral and stereo imaging in one system. This capability makes the MOMS data really valuable for three points: 1) the simutaneously acquired data in the same weather circumstance with the same orbit geometry are easier to be calibrated and registered

0-7803-3836-7/97/$10.00 © 1997 IEEE

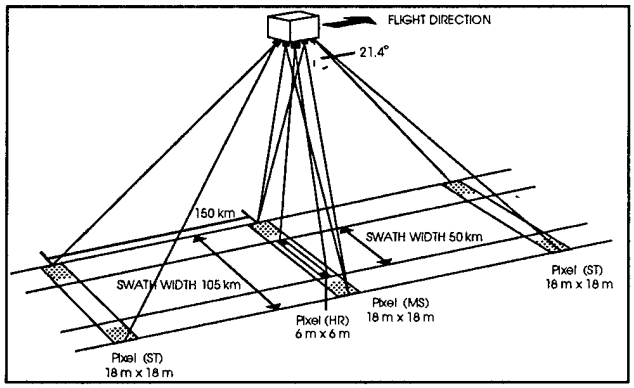

Fig.1: MOMS-2P imaging geometry

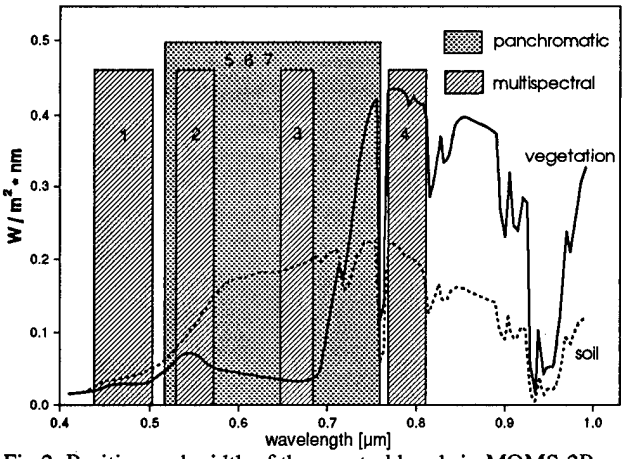

Fig.2: Position and width of the spectral bands in MOMS-2P

than the data from different sensors or orbits; 2) flexible combination of the spectral bands enables the data suitable to various thematic applications and 3) the data possess properties of both space and aircraft images and significantly improves the detectability of surface phenomena such as tectonic features and stratigraphic layers in a 3-dimensional space. A comparison of images taken in different viewing angles allows to investigate the directional effects of surface texture on the spectral response and to assess the transparency and depths of coastal waters.

THEMATIC APPLICATIONS

Based on data assessment and experience of the D2 mission, the MOMS-2P will acquire data in 4 operation modes (Tal.1). Each mode means a different combination of spectral bands. Therefore the special thematic applications and the requireded methods for image processing are closely related with the data take modes. Tal.2 lists some methods and the possible results according to the 4 modes. Mode A consists of the 3 PAN bands to acquire the full stereo data. Besides to derive DTM's, the HR data can be merged with the other MS data or the data from other space sensors (e.g. TM, SPOT). Mode B includes the 4 narrow MS bands which lead to an improved differentiation of spectral signatures of minerals, rocks, soils, vegetation and other man made features. Mode C is a combination of the HR band with 3 MS bands (2,3,4). The multiresolution data sets are easier to be merged to gain optimal result for thematic evaluation and to resolve spectral signatures for targets with small-scale surface pattern in the mix-pixel domain of the lower resolution MS pixels. Mode D comprises 2 MS bands (1,4) and the 2 off-nadir stereo bands. These simutaneously acquired data sets with topographic and spectral information enable an enhanced interpretation such as detection of the orientation of plane or linear texures, besides the derivation of DTM's and 3D color images. With the high spatial and spectral resolution and the inflight stereo features, the MOMS data sets can be applied for a variety of thematic objectives, such as environment monitoring, assessment of erosion risk and natural hazards, landuse, urban planning, coastal studies, geological survey and exploration, etc..

Tab.1: Highlights of MOMS-2P in 4 operation modes A-B-C-D

Highlights of MOMS-2P for Thematic Applications

A - Stereo in High Spatial Resolution
derivation of high quality digital terrain models (6 m)

B - 4 Multispectral Bands
enhanced detection of relevant surface parameters
- optimized position of bands
- narrow spectral bandwidths

C - High Spatial Resolution (6 m) & Multispectral Bands (18 m)
detection of smallscale textures of the earth surface (e.g. landuse, urban)

D - Stereo & Multispectral Bands
topographic information for an enhanced evaluation of remote sensing data

FIRST RESULTS OF MOMS-2P DATA

Fig. 3 shows a subscene of Daqing, the biggest oil field in the People's Republic of China. The data were acquired on November 1, 1996 in the mode B with the 4 MS bands. This subscene displays the first principal component of the 4 bands as a black-and-white (BW) image and a color

Tab.2: Possible image products of MOMS-2P data

Mode	Spectral Bands	Processing and Enhancement	Possible Image Products
A	5, 6, 7	Correction and registration Texture extraction Image merging	ST images (→DTM) HR black-and-white image Merged image of the HR data with other data set
B	1, 2, 3, 4	Color composite IHS Tranform (I+S Enhancement) Decorrelation	Real color image False color image Decorrelated image
C	2, 3, 4, 5	Colour composite IHS Transform (I+S Enhancement) Image merging	False color image HR black-and-white image Merged HR color image Merged image of the HR data with other data set
D	1, 4, 6, 7	Color composite IHS transform (Hue-modelling: ratio→H; NDVI→H)	ST images (→DTM) False color image 3D false color image

display of band 432 as RGB is given in the same paper on the CD-ROM. The spatial resolution of this image is about 17.1 meters. It is in this area that more than half output of oil in the whole China has been produced since the oil field went into operation 1959. The image demonstrates the capability of advanced remote sensing data from the MOMS-2P to detect small objects up to individual buildings, boring towers and fine surface features such as borders of cultivated fields. Due to opti-mization of the spectral bands, spectral information of dif-ferences in vegetation types and water contents on the field surface can be recognized through variation in grey values (in the BW image) and in color tunes (in the color image). Lakes with pollution caused by sewage of petro-chemical works in the area can be distinguished in their changed color tones from the normal water bodies in blue tone.

REFRENCES

[1] Ackermann F., Bodechtel J., Dorrer E., Ebner H., Kaufmann H.,Koch B.,Lanzl F., Seige P., Winkenbach H. & Zilger J., "MOMS-02/D2- Wissenschaftsplan", DLR, Oberpfaffenhofen, 1989, pp. 85-166.

[2] Bodechtel J. and Zilger J., "MOMS - History, Concepts, Goals," Proceedings of the MOMS Symposium, Koeln, July 1995, EARSeL-Special Publication, pp.12-25.

[3] Kaufmann H., Meissner D., Bodechtel J. & Behr F.J., "Design of Spectral and Panchromatic Bands for the German MOMS-02 Sensor", Photogr. Engineering and Rem. Sens., Vol.55, No.6, 1989, pp.875-881.

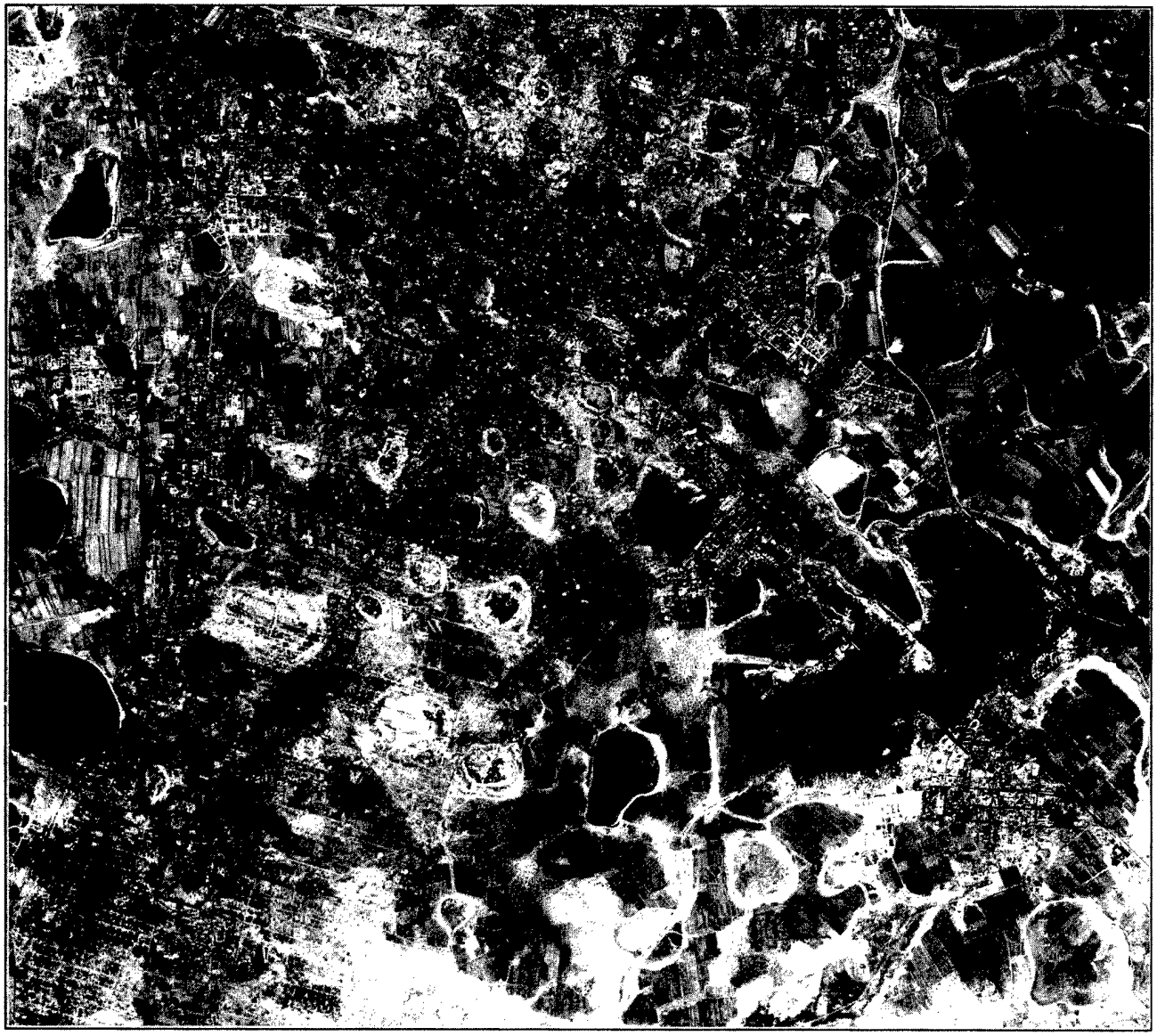

Fig.3: A subscene of MOMS-2P data showing the Daqing oil field, PR China.

Multi-Frequency and Multi-polarization SAR System Analysis with Simulation Software Developed at CSA

Yonghong Huang, Guy Séguin and Nizar Sultan
Canadian Space Agency, Space Technology, 6767, route de l' aéroport
Saint-Hubert, QC, Canada, J3Y 8Y9,
Tel: +1,514,926,4645, Fax: +1,514,926,4613
Email: Yonghong.huang@space.gc.ca, Guy.seguin@space.gc.ca, Nizar.sultan@space.gc.ca

Abstract – Multi-frequency and multi-polarization SAR simulator developed at CSA is aimed to study an advanced SAR system performance in the simulated SAR images. This simulator is designed either as a SAR system simulator which concentrates on Radar system and SAR processing techniques, or as a SAR image product simulator which focuses on target model and radar backscattering model, so as to understand SAR polarization characteristics completely. The paper presents the simulation approach of point target model and distribute target model for spaceborne SAR which is adopt in our simulator. The current results are given and the status of SAR simulator software is addressed in the paper.

INTRODUCTION

The specification of future multi-frequency and multi-polarization SAR instrument for Space borne Remote Sensing requires the prior knowledge of the impact of the backscatter characteristics on the SAR image. The backscatter characteristics are influenced by many SAR system parameters such as shown in table 1. SAR images obtained from existing sensors can be used to study the backscatter characteristics. However they can only provide information for the conditions under which they are obtained. A SAR data simulator represents a more flexible tool to analyse the backscatter characteristics even if the results depend on the model used to represent the scattering of the distributed targets.

SAR simulators are catalogued as SAR System End-to-end Simulator and SAR Product Simulator[1]. End-to-end simulation is used to simulate modeled system components (which include radar transmitter, antenna, receiver, etc), to generate SAR raw data based on accurate orbit model, and to form final SAR image through SAR data processor. Usually, a point target model is employed through the complete simulation chain since the System performance can be reflected from the impulse response function (IRF). SAR image simulator involves the generation of distributed target images considering terrain geometry, shadow, layover, roughness, statistical characteristics, polarization, etc. It can be achieved by convoluting reflectivity map with the SAR system IRF.

Several SAR simulators used for new missions planning and various SAR applications[2] have been developed in the past decades. Most of them are SAR product simulators, such as the Radar Image Simulator (RIS) by the Kansas University, the Updated RIS by the Technical University of Berlin, the SIMRISA/SIMROSA by the University of Graz and JPL. Some SAR system End-to-end Simulators are available, for example, SARSIM by Ferranti, System End-to-end simulator by DLR, etc. However, multi-frequency and multi-polarization SAR simulation algorithms have hardly been considered in these simulators. Publications on this topic are also limited..

In this paper, we describes an approach to generate simulated SAR raw data frequency and polarization characteristics for distributed target model based on an accurate satellite orbit model. This work results in a flexible tool to simulate SAR raw data under different conditions..

SAR SIMULATOR DIAGRAM

The study of frequency and polarization characteristics of a target model requires a System End-to-end simulation rather than a SAR image simulation.. The simulation parameters which have an influence on the final images and which will be investigated are summarized in table 1.

Table. 1 Parameters influencing the quality of SAR data

Orbit	• accuracy of orbit modeling • attitude variation • perturbation of the nominal orbit
Terrain	• surface roughness • dielectric properties • structure and geometric
Sensor	• frequency • polarization • antenna pattern • incident angle • azimuth angle • bandwidth • waveform distortion • timing control • signal to noise ratio • quantification
Processor	• resolution • range migration correction • motion compensation • weighting function • multi-look processing (speckle noise) • accuracy of calibration

0-7803-3836-7/97/$10.00 © 1997 IEEE

The simulator consists of four modular major parts that can be upgraded independently:

- **Satellite orbit model**: In the preliminary simulation the equatorial (inertial) coordinated system[4] is used. The earth is assumed to be a uniform sphere and the satellite displacement is on a strict elliptical orbit with the center of the earth at one of the foci of the ellipse. A more accurate satellite orbit software, developed at CSA, will be used for the orbit model in future simulation.
- **Terrain model:** Point target model, multiple targets model and distributed targets model are considered. For distributed targets, terrain roughness, height information, shadow and layover are being modeled.
- **SAR sensor model:** This model simulate the radar instrument behavior. The model generate the antenna pattern, the receiver gain, the pulse repetion frequency (PRF), the bandwidth and the transmitter characteristics.
- **SAR processor:** Custom software based on Range-Doppler algorithm is used to process simulated raw data. In the future a software package named EVSARP will be used.

Figure.1 shows the software logical diagram.

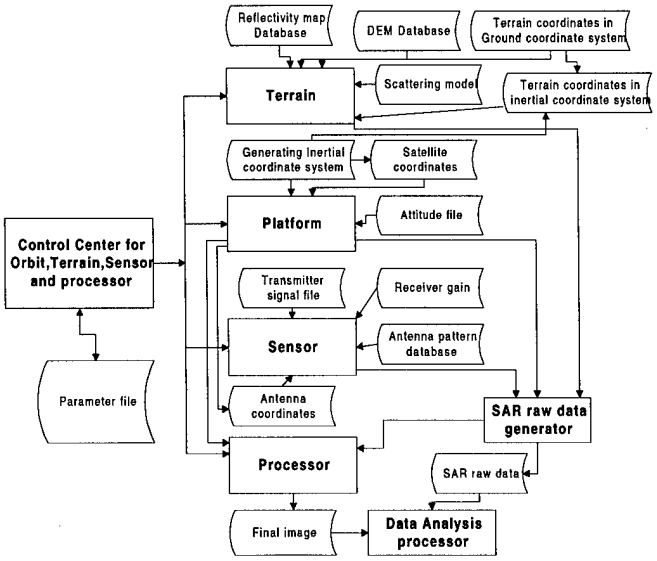

Fig.1 Diagram of SAR simulator

MATHEMATICAL MODEL

In the simulation, it is common to assume that surface terrain is segmented into many tiny scatters. The superposition of return signals from these scatters can generate SAR raw data for distributed target.

Let us assume, that the SAR sensor transmits a chirp signal at frequency f_0 with chirp rate k_r, which is expressed as,

$$s(t) = a(t)\exp[-j2\pi(f_0 t + k_r t^2 / 2.)] \quad (1)$$

where $a(t)$ is a rectangular function related with pulse duration. The radar received signal from any scatter on the ground is,

$$s_i'(t) = k_i(t) \cdot a(t - \frac{2R_i(t)}{c}) \cdot \exp[-j\varphi_i(t)] \quad (2)$$

Where

$$\varphi_i(t) = -2\pi \cdot f_0(t - \frac{2R_i(t)}{c}) - \pi \cdot k_r(t - \frac{2R_i(t)}{c})^2$$

and the range $R_i(t) = |\vec{R}_s - \vec{R}_t|$

which is calculated based on orbit model. $k_i(t)$ is given by the following radar equation.

$$k_i(t) = \sigma_i \cdot p_t \cdot G^2(\theta_a, \phi_a) \cdot \lambda^2 / (4\pi)^2 R_i^4(t) \quad (3)$$

where $G(\theta_a, \phi_a)$ is the antenna gain, σ_i is the backscattering cross section of the target and p_t is the radar power. If we consider radar polarization, σ_i is strongly influenced by polarization direction as follow:

$$\sigma_i^{pq} = \lim_{R_i(t)\to\infty} (4\pi \cdot R_i(t) \frac{|E_q^s|^2}{|E_p^i|^2}) = |S_{pq}|^2 \quad (4)$$

where p,q represent the polarization direction of the incident and scattered waves, respectively; S_{pq} is related to the terrain roughness, dielectric constant, sensor frequency, incident angle and azimuth angle. The sensor parameters which influence S_{pq} are of main interest for these simulations. There are two solutions to simulate polarization behavior in the SAR image. One approach is to use facet model[5]. This approach is believed to be efficient in simulating man-made targets. However, it is quite time consuming because the number of scatters in one resolution cell is extremely large due to the fact that each scatter is at the same scale as the wavelength. Another solution is the distributed target scattering models[6]. These models allow us to simulate terrain based on statistical distributions. Optical model and physical model are used in the simulation. Although none of those models can completely demonstrate the scattering characteristics, each of them is helpful to generate information about them..

The Radar raw data is formed as a summation of the return from the different scatters,

$$s'(t) = \sum_i s_i'(t) \quad (5)$$

SAR processing is implemented after raw data has been formed. Range-doppler algorithm is used in the processing. Doppler parameters can be extracted either from SAR raw

data or provided by satellite parameters. The comparison of the quality of the final images processed with different SAR instrument parameters allows an evaluation of the radar system performance..

SIMULATION EXAMPLES

The simulation is based on the existing spaceborne sensor parameters. Examples of point target and distributed targets are given in Fig.2 and Fig.3. Fig.2a shows the raw data (real part) map of a point target on a non-reflecting background. Fig.2b shows the final image plot of the single target with rectangular weighting in range and azimuth by Range-Doppler algorithm. Fig.3a shows the reflectivity map of an assumed terrain model. The raw data generated based on this map is shown in Fig.3b. Fig.3c shows final image of the distributed target without implementing speckle noise in it. The speckle image is shown in Fig.3d. These examples show that the simulation algorithm is efficient to generate SAR raw data as well as SAR image.

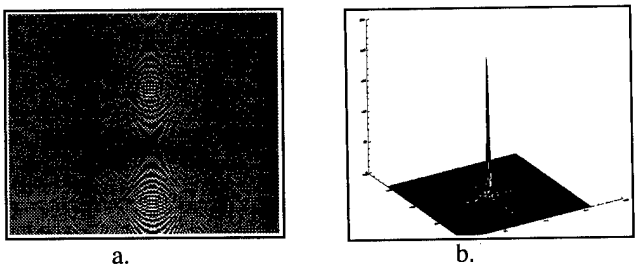

Fig.2a. Real part of raw data for a point target.
2b. processed map for a point target.

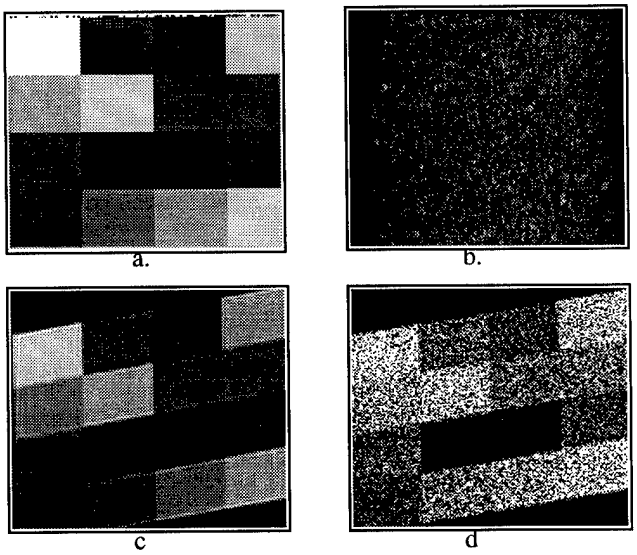

Fig.3a: Reflectivity map of distributed targets.
3b: SAR raw data of distributed targets.
3c: SAR image without speckle noise.
3d: SAR image with speckle noise.

CONCLUSIONS AND DISCUSSIONS

The preliminary results have demonstrated the capability to simulate SAR distributed target model with basic requirement. The simulation algorithm is a proper analysis tool for spaceborne SAR systems. However, this algorithm is very time consuming, and a lot of components are still in a development stages. Further works will focus on computation time reduction and image quality evaluation as a function of the system parameters.

ACKNOWLEDGMENTS

The first author would like to acknowledge NSERC to support this work at CSA.

REFERENCES

[1] T.K.Pike, " SARSIM: A Synthetic Aperture Radar System Simulation Model", DFVLR-Mitteilung, 85-11,1985.
[2] Claudio Camporeala and Gaspare Galati, " Digital Computer Simulation of Synthetic Aperture Systems and Images", European Transactions on Telecommunications and Related Technologies, Vol. 2, No. 3, pp.59-68, 1991.
[3] Ch. Gierull and M. Ruppel, " An End-to-end Synthetic Aperture Radar Simulator", EUSAR'96, Germany, pp.569-572, 1996.
[4] J.C. Curlender and R.N.Monough, " Synthetic Aperture Radar: Systems and Signal processing", Wiley
[5] Giorgio Franceschetti, Maurizio Migliaccio, Daniele Riccio, and Gilda Schirinzi, " SARAS: A Synthetic Aperture Radar(SAR) Raw Signal Simulator", IEEE Transac. On Geosci. And Remote Sensing, Vol.30, No.1, pp.110-123, 1992.
[6] F.T.Ulaby, R.K.Moore and A.K.Fung, " Microwave Remote Sensing", Vol.II, Artech House, 1982.
[7] F.T.Ulaby and Charles Elachi, " Radar Polarimetry for Geoscience Applications", Artech House, 1990.

Oceanological Results from the ALMAZ-1 Mission: an Overview

A.Yu. Ivanov* and K.Ts. Litovchenko**

*NPO Mashinostroenia, Center ALMAZ, Gagarina 33, Reutov, Moscow Region, 143952, Russia
tel.: 7-(095) 307 9194, fax: 7-(095) 302 2001, e-mail: NPO@mashstroy.msk.su

**Space Research Institute, Russian Academy of Sciences, Profsoyuznaya 84/32, Moscow, 117810, Russia
tel.: 7-(095) 333 4256, fax: 7-(095) 333 1056, e-mail: kostya.litovchenko@asp.iki.rssi.ru

Abstract -The potential of the S-band Synthetic Aperture Radar (SAR) aboard the Russian Satellite ALMAZ-1 in observing the ocean phenomena has been studied. The ALMAZ-1 SAR images acquired over the ocean show different ocean phenomena: surface waves, internal waves, oceanic fronts, upwellings, bottom topography, sea ice and oil slicks as well as atmospheric phenomena. This review paper presents the oceanological results from the ALMAZ-1 mission and evaluates the effectiveness of the ALMAZ-1 SAR for ocean studies. Examples of interpreted ALMAZ-1 SAR images are presented.

INTRODUCTION

The Russian Satellite ALMAZ-1 was operated 1991-1992. It carried a SAR capable of providing high resolution images of the ocean. The ALMAZ-1 SAR was operating at frequency of 3.1 GHz (S-band) using horizontal polarization (HH) for transmission and reception. The incidence angle of the ALMAZ-1 SAR could be varied between 20° and 60°. The backscatter signal received by the antenna was digitized aboard ALMAZ-1 and stored by onboard recorder, then the data were transmitted via a relay satellite to the ground station in Russia. This method permits to acquire SAR images of any region of the Earth. The ALMAZ-1 SAR had operational mode with swath width between 30 and 40 km. The duration of the SAR data takes was about usually 30 s due to storage capacity limitation of the onboard recorder. The detail specifications of the SAR aboard the ALMAZ-1 can be found in [1,2].

Although the ALMAZ-1 SAR wasn't primary oceanological tool it was valuable for oceanological applications. The results of Russian space campaigns and radar imagery are not well-known in the west. This review paper presents oceanological results from the ALMAZ-1 mission obtained by analysis interpretation of the ALMAZ-1 SAR imagery acquired over the ocean. The objective of this paper is also to provide an evaluation of the oceanological capability of the S-band SAR in preparation of future programs of ocean investigation from space.

SURFACE WAVES

In order to study the imaging of ocean waves by the SAR aboard the ALMAZ-1 satellite a special joint ALMAZ-1/ERS-1 experiment was carried out [1,2]. The SAR images were acquired quasi-simultaneously over same ocean sites in the North Atlantic. All quasi-simultaneous ALMAZ-1/ERS-1 coincidences were studied [3]. The ALMAZ-1 and ERS-1 satellites had quite different orbital altitudes: one had average orbital altitude of 350 km during the mission and another one with 785 km. This has important consequence on SAR imaging of ocean waves since the degree of non-linearity of the SAR imaging mechanism depends on R/V ratio [4]. For ALMAZ-1 this ratio is approximately 60 s while for ERS-1 it is 130 s.Because of absence of in situ data the analysis is restricted by comparison only between two satellite data. The image spectra were calculated over 6 collocated image pairs taken quasi-simultaneously. In general 16 wave systems were identified in these 6 experiments, 13 of them being presented in both ERS-1 and ALMAZ-1 spectra. The 13 wave systems covered almost all possible mutual directions of wave propagation and satellite flight. In general, the correspondence between ALMAZ-1 and ERS-1 estimates is quite satisfactory.

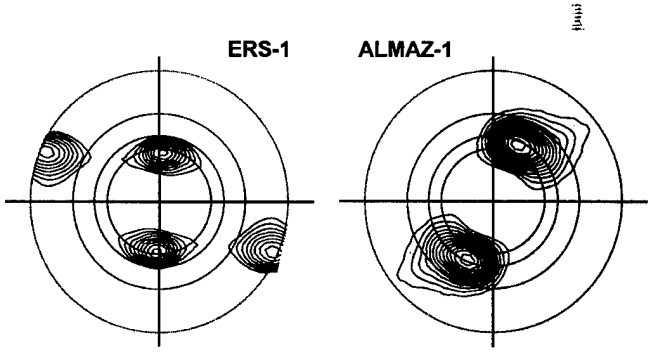

Fig.1 ERS-1 and ALMAZ-1 SAR image spectrum calculated from SAR images acquired on Jan. 7, 1992 at 14:21 (ERS-1) and 13:52 UTC (ALMAZ-1) off the Newfoundland; the circles correspond to constant moduli of wavenumber with wavelength 100, 150, 200, 250 m

The discrepancy can be explained by different parameters of two SARs. The ERS-1 and ALMAZ-1 SAR image spectra shown in Fig.1 give different wavelength and wave direction when waves were propagating close to the azimuth direction: 262 m and 4° (ERS-1), 208 m and 23°(ALMAZ-1). Both these SAR images were acquired when satellites were in a descending orbit and angle between the azimuth and wave propagation direction, was almost identical: 172°(ERS-1) and 177°(ALMAZ-1). The analysis, in which ALMAZ-1 SAR wavelengths and directions of dominant waves have been compared with those of the ERS-1 by means of scatter plots, has been also carried out. Comparisons of wavelengths and wave directions measured in SAR image spectra of ERS-1 and ALMAZ-1 are presented in [3]. ERS-1 SAR estimates of wavelength are biased with respect to the ALMAZ-1 ones, but there is no high bias for wave directions. The distributions may be explained by the fact that the velocity bunching mechanism is the strongest for azimuth traveling waves. Due to higher (appox. 2 times) R/V ratio the spectra of the ERS-1 are affected by a strong azimuth cut-off compared with those of the ALMAZ-1 and that the imaging of ocean waves by ALMAZ-1 SAR due to the lower orbital altitude is more linear than by ERS-1 but ALMAZ-1 SAR images are noisier. The comparison of the ALMAZ-1 and ERS-1 SAR image spectra shows a strong influence of R/V ratio and viewing geometry on the imaging of ocean waves. The obtained results establish that the ALMAZ-1 SAR could image the dominant waves and provide wave measurements as a finding of SAR image spectrum peaks. The analysis ALMAZ-1/ERS-1 pairs allows to conclude that an optimal SAR for mapping of ocean waves should have a low R/V ratio (35-60 s) as well as a high resolution and HH-polarization, but such a SAR will not be all-purpose applied.

OCEANIC FRONTS & UPWELLING

The capability of the ALMAZ-1 SAR to image dominant ocean waves can be illustrated by observations of spacial evolution of surface waves in the strong ocean currents. ALMAZ-1 SAR imagery of the Gulf Stream (GS) from five overpasses and subsatellite contact measurements have been collected in the end of August and the beginning of September, 1991 and examined to determine the capability of the ALMAZ-1 SAR to image

0-7803-3836-7/97/$10.00 © 1997 IEEE

dynamic boundaries of the oceanic currents. Sea surface temperature was measured from the RV "Akademik Vernadsky" and by AVHRR of NOAA satellite. A SAR image spectra variability in the situation when long surface waves propagated across the GS boundary and evolution of wave system crossing the GS imaged by the ALMAZ-1 SAR has been analyzed [5,6]. The SAR images covers an area across the GS and shows a presence of two component long wave system under west wind of 7-10 m/s. Surface waves incoming the GS had wave number component along current direction. SAR image spectra have been calculated from the full image and revealed different wave fields in the upwave and downwave GS current sides. The SAR image spectra exhibit two wave number peaks in the upwave GS current slope but only one wave system has been observed in the downwave part of the GS. The modification of wave field may be explained by reflection of surface waves on a shear current. By using contact measurements and wave/current interaction model, simulated spectra were calculated and compared with spectra derived from the SAR images. As input for the model the contact measurements and NOAA data have been used. Computational results also show that complicated wave field in the GS area may be produced by unimodal background waves due to reflection by strong current [5,6]. The studies have shown that the ALMAZ-1 SAR can be effectively used for observations of spacial evolution of the wave field and determination the boundaries of currents and fronts via observation of wave/current interaction.

Fig.2 ALMAZ-1 SAR image of July 5, 1991, 06:42 UTC, showing large slicks and manifestations of internal waves associated with upwelling near the coast of England

Although, an upwelling has been studied early using contact oceanographic techniques, its features remain to be investigated. A SAR imagery allows us to obtain additional information on this phenomenon. The SAR image in Fig.2 was taken over the North Atlantic to the southwest of England. The areas covered by slicks (dark areas) and identified on the image due to low backscatter occupy approximately 20% of the full image and they have been attributed to an upwelling [7]. The generation of ripples in upwelling region is lowered both by increased concentration of surface active substances and/or by stable atmospheric boundary layer over cold water. Under weak winds these two effects may play an important role in reducing a backscatter simultaneously. At present there are no accurate experimental evidences what effect is leading, and we can't discriminate between them. In literature the backscatter reduction of 2-5 dB in upwelling regions was presented. A dissipation of short waves also becomes higher than in the surrounding water partially because of subsurface turbulence associated with upwelling, increasing of the viscosity and surface tension with decrease of surface temperature. These factors may give a significant contribution to reduction backscatter at significant temperature contrasts. Evidently, an upwelling forming the large low backscatter areas and appearing due to this fact in a SAR imagery is sufficiently complex phenomenon and future studies have to be done.

INTERNAL WAVES

Internal waves (IW) in the ocean are very often detected by a SAR. Fig.2 also shows numerous manifestations of IW. They were generated by the upwelling and located over the continental shelf slope between 200 and 300 m isobathes. Although, the tidal IW are predominant among other types of internal waves which occur at the shelf edge or in condition with sharp depth changes and which are frequently visible in SAR imagery, another types are infrequent. Using the ALMAZ-1 SAR we have detected an existence of another types of IW generated in Lake Ladoga by atmospheric forcing [8] and by upwelling in the ocean [7].

COASTAL PROCESSES & UNDERWATER TOPOGRAPHY

The ALMAZ-1 SAR also had a potential for detection mapping of coastal and tidal processes as well as bottom topography [7]. The constant dynamic changes on the tidal flats caused by strong tidal currents. Due to high resolution the most coastal, estuarine and bottom features exposed during low tide can be observed in details. The characteristic network of tidal channels formed jointly under the influence of river flow and tides on the tidal flat near the mouth of Elbe River has been studied in [9]. In general, a comparison of the SAR image and existing bathimetric maps shows that mapping of bottom topography was not provided with such details and accuracy by other remote sensors. The mapping of the bottom topography in the sea with ALMAZ-1 SAR was also possible. The SAR images taken over the North Sea show surface manifestations of bottom sand banks on the sea bed including secondary features on the bank slopes, so-called sand waves [7]. According to a theory they were imaged due to interaction of underwater relief, short surface waves and tidal flow, but note that existing theories and models are not capable to explain all aspects of imaging mechanism. We can conclude from the studies that ALMAZ-1 SAR could really provide a high resolution mapping of tidal flats and bottom topography than previous satellite radars.

OIL SPILLS

The ALMAZ-1 SAR imagery made possible detailed identification, localization of oil spills and furnishing with information on the dimensions, structure and dynamics of the oil slick. To evaluate capability of the ALMAZ-1 SAR to detect oil spills in the sea, the ALMAZ-1 SAR images collected during the ALMAZ-1 mission [11] and the DOSE-91 [10] have been analyzed. The DOSE-91 experiment was performed in the Norwegian Sea, 100 km off the western coast of Norway around the Haltenbanken. Three artificial slicks have been produced by

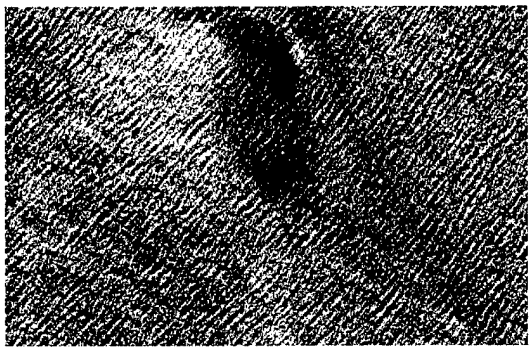

Fig.3 The oil spill released in the Norwegian Sea during the DOSE-91 on the ALMAZ-1 SAR image of July 27, 1991

Norwegian RV on August 21, 24 and 27, 1991 that also has collected data on sea and weather conditions. The ALMAZ-1 SAR image of the second oil spill (Fig.3) shows oil slick affected by long waves about 2 days. Wind speed of 12 m/s from the SW and long waves of 3.1 m waveheight and 12 s period was reported [10]. Oil spill detection with use of the ALMAZ-1 SAR is more suitable incidence angles of 30-40°. The spectral analysis of SAR image subscenes has shown an image spectrum variability both around the oil slick and within the slick. The area occupied by oil is found strongly depends on sea surface conditions. Oil slicks equal 0.1-0.3 km^3 were easily detected by visual inspection of the images at favorable wind conditions. The ALMAZ-1 SAR permitted to detect and identify oil spills under moderate and strong winds (up to 12 m/s) [11].

SEA ICE

ALMAZ-1 has also contributed to mapping sea ice cover. Operational sea ice mapping with use of ALMAZ-1 SAR was performed and validated in Antarctica in winter 1991 when Russian RV "Michail Somov" was blocked by heavy sea ice off the Molodezhnaya Antarctic Station [7]. From July 24 to Sept. 4, 1991 the area of RV drift was imaged by the ALMAZ-1 SAR. Collected imagery made possible to assess the SAR ability and to make single correct solution. A series of consequent SAR images allowed to estimate parameters of ice motion. This experiment has clearly demonstrated the capability of ALMAZ-1 SAR not only map and quantify sea ice types/parameters but also to detect ships in sea ice cover. The determination of common ice types (firstyear, multiyear, pancake, grease etc.) using ALMAZ-1 SAR imagery was also possible. Due to HH polarization the SAR can provide better discrimination between open water and ice, between ice types and better determination the location of ice edge including high sea conditions than VV-polarized SARs because of less sensitivity to wind stress. The sensitivity of the SAR to surface roughness of sea ice and high resolution permitted to detect the most of structure and texture ice features such as fractures, polynyas, leads, ice hummocks etc. Minimum size of 30-50 m of floes and leads which the ALMAZ-1 SAR was capable to detect, was established [7].

ATMOSPHERIC PHENOMENA

The ALMAZ-1 SAR images acquired over the ocean show not only ocean phenomena but also different atmospheric phenomena. The phenomena detected by the ALMAZ-1 SAR are atmospheric gravity waves, atmospheric boundary layer rolls and convective cells. Atmospheric gravity waves shown in Fig.4 were attributed to waves associated with a passage of atmospheric front. Some characteristics of this phenomena can be obtained from the SAR image but in the most cases one must additionally have contact measurements and meteorological data for analysis. In the most cases study of the ALMAZ-1 SAR image allows to derive only quantitative information. The SAR aboard ALMAZ-1 satellite was less sensitive to wind stress variation due to HH-polarization and S-band. The ALMAZ-1 SAR reveals a low capability of detection of atmospheric features on the sea surface: they could be imaged only in individual cases and under certain viewing geometry. Nevertheless, the ALMAZ-1 SAR imagery allowed to identify a small-scale phenomena at the ocean/atmosphere interface, such as Langmuir strips [12].

CONCLUSION

On the one hand the ALMAZ-1 results support an idea that SAR techniques is a valuable tool for observation and monitoring ocean dynamic features of different scale at high resolution. The ALMAZ-1 SAR images of the ocean phenomena give strong evidence that the SAR was a reliable instrument for imaging ocean surface and internal waves, fronts, upwellings, bottom topography, coastal processes, oil slicks and sea ice. But, on the other hand the recent spaceborne SARs are not measuring instruments in the sense that observed field of short waves intensity or radar cross section depends on a number of the phenomena on the ocean/atmosphere interface, and therefore interpretation of SAR images often becomes problematic.

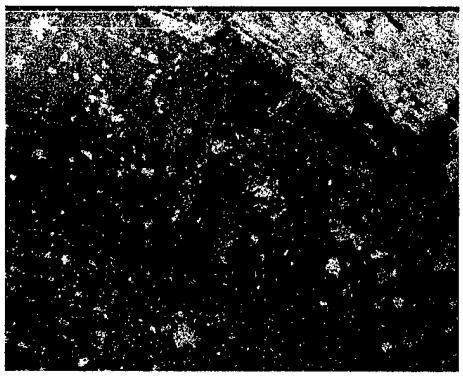

Fig.4 Atmospheric gravity waves in the Barents Sea off Isl. Vaigach on the ALMAZ-1 SAR image of July 27,1991, 21:26 UTC

The need of the operational measuring and monitoring ocean fields of ocean level, currents, waves and the phenomena associated with ocean/atmosphere interaction requires appropriate special spaceborne techniques. A spacial resolution of 0.1-0,5 km, swath width of 500-1000 km and revisit time from hours to days are required to understand mesoscale variability of the ocean fields.

REFERENCES

[1] Alpers W. et al. Comparison of ocean wave imaging by ERS-1 and ALMAZ-1 synthetic aperture radar. Proc. 2nd ERS-1 Symposium, Hamburg, Germany, 11-14 Oct. 1993, v.1, p.239-245

[2] Alpers W. et al. Ocean wave imaging by synthetic aperture radars (A comparative analysis of the ALMAZ-1 and ERS-1 satellite data). Earth Observation & Remote Sensing, 1995, v.12, N 6, p.903-918

[3] Litovchenko K.Ts. et al. Estimation of ocean waves parameters from image spectra obtained with satellite SARs in orbits of different altitude. Earth Observation & Remote Sensing, 1995, v.13, N 3, p.397-408

[4] Alpers W., D.B.Ross, C.L.Rufenach.On the detectability of ocean surface waves by real and synthetic aperture radar. J.Geophys.Res.,1981, v.86, N C6, p.6481-6498.

[5] Grodsky S.A. et al. Surface wave observation in the Gulf Stream using ALMAZ-1 SAR. Earth Observation & Remote Sensing, 1996, v.14, N 3

[6] Grodsky S.A., V.N.Kudryavtsev and A.Yu.Ivanov. Study the Gulf Stream zone using ALMAZ-1 SAR and contact ship measurements. Earth Observation & Remote Sensing 1996, N6

[7] Ivanov A.Yu, P.A.Shirokov, S.S.Semenov. ALMAZ-1 and radar oceanology. Proc. OI'96, Brighton, UK, March 6-9, 1996

[8]Dikinis A.V. et al. Interpretation of the ALMAZ-1 SAR imagery of internal waves using hydrometeorological and hydrographical data. Earth Observation & Remote Sensing 1996, v.14, N5

[9] Avenarius I.G., A.Yu.Ivanov, P.A.Shirokov, V.E.Shkarin. Morphostructural interpretation of the ALMAZ-1 SAR image of the Helgoland Bay shelf of the North Sea. Earth Observation & Remote Sensing, 1995, v.12, N 5, p.744-751

[10] Bern T.-I., T.Wahl, T.Anderssen,R.Olsen. Oil spills detection using satellite based SAR: Experience from a field experiment. Proc. 1st ERS-1 Symposium, 1992, v.2, p.829-834

[11] Ivanov A.Yu. Oil sea pollution on the KOSMOS-1870 and ALMAZ-1 SAR imagery. 1997 (to be printed in Earth Observation & Remote Sensing)

[12] Viter V.V. et al. ALMAZ-1 spacecraft - OCEAN-I Project: Preliminary results of high resolution radar observation of ocean processes. Currents, other phenomena sea surface, bottom forms. Earth Observation & Remote Sensing, 1995, v.12, N 1, p.70-82

A Summary of the Upper Atmosphere Research Satellite (UARS)

Mark R. Schoeberl
Anne R. Douglass
Charles H. Jackman
NASA Goddard Space Flight Center
Code 916
Greenbelt, MD 20771
301-286-5819/301-286-1662/schom@zephyr.gsfc.nasa.gov

Abstract -- The UARS satellite has been operating for six years and has gathered an unprecedented amount of data on the stratosphere. The most significant findings from UARS are associated with the mapping of the polar ozone depletions and the observations of the long term trends in chlorine gases in the stratosphere.

INTRODUCTION

In the early 1980's, following the success of the Nimbus 7, NASA proposed to develop and launch a more comprehensive satellite mission to understand the chemistry and physics of the stratosphere. Nimbus 7 instrumentation had focused on the stratospheric nitrogen species, and it was realized that critical chlorine species would need to be measured as well. At that time, before the discovery of the ozone hole, atmospheric chemical models were predicting that the first signals of CFC driven ozone loss would appear in the mid-stratosphere (30-40 km). This region is too high to be accessible by aircraft. High altitude balloons had made measurements in this region, but the high altitude balloons cannot provide a global - seasonal picture of the evolving chemistry of the mid-stratosphere since they can only be launched from the southern US during early late spring and early fall.

After studying a number of options, the Upper Atmosphere Research Satellite (UARS) was developed with intended launch in the late 1980's. The suite of instruments included measurements of all the important components of the chlorine and nitrogen radicals, source gases and long lived tracers. UARS was also designed to measure the solar UV flux with unprecedented precision and to estimate the energetic particle input from outer space. (Energetic particles can generate large quantities of nitrogen oxide which destroys ozone in the mesosphere and upper stratosphere.) Finally, UARS included two novel direct wind measurement instruments to improve our understanding of the stratospheric dynamics. Table 1 summarizes the UARS payload.

The launch of UARS was delayed by the Challenger accident; new NASA safety rules also required the redesign of the CLAES instrument which had used a solid hydrogen cryogen. UARS was finally launched on September 15, 1991 aboard the Shuttle Discovery. UARS is considered as the first of the Mission to Planet Earth series of NASA spacecraft, As of this writing, (mid 1997), UARS is still operating well beyond its original mission lifetime of 18 months. Of the original 10 instruments, 8 are still operational (see Table).

CHLORINE MEASUREMENTS

Within a few months after launch, the UARS MLS instrument was able to map ClO (chlorine monoxide - an ozone destroying radical) within the Arctic vortex showing the extent of ClO formation and its close association with polar stratospheric cloud formation [1]. Prior to this mapping, knowledge of the ClO build up in the Northern Hemisphere had come from the two polar aircraft missions. Not only was the UARS measurement an important confirmation of earlier aircraft results, but it also showed the extent of the zone of elevated ClO. Since these initial observations, UARS has continued to monitor both the Arctic and Antarctic late winter-spring ozone depletions. The UARS data have shown that northern hemisphere ozone depletion in January-March 1997 is the largest ever measured.

At the time of the launch of UARS, some scientists speculated that the ozone destroying chemicals within the polar vortex would leak to mid-latitudes. Other scientists argued from a hydrodynamical perspective that containment of the chemicals must occur. Scientists on the HALOE team were the first to notice very low concentrations of the long lived trace gas methane in the center of the spring Antarctic polar vortex [2]. Analysis showed that very low values of methane exist within the mid and upper stratosphere in late fall and these values descend to the lower stratosphere by late spring, a net descent of 12-15 km over six months. These measurements were confirmed by the UARS CLAES later by model calculations [3]. The unmixed descent of long lived trace gases requires a very isolated polar vortex system. Thus It was not until the launch of UARS and the mapping of long lived gases whose distributions reveal patterns of transport by the winds that chemical containment of the vortex could be demonstrated.

U.S. Government work not protected by
U.S. copyright.

Despite decades of measurements and observations, a few vocal critics of anthropogenic ozone loss theory have continued to argue ozone loss is natural. Some have argued that the heavy chlorofluorocarbons molecules will never rise into the stratosphere. Instead, the high levels of observed stratospheric chlorine are due to volcanic activity. UARS has made a number of measurements that refute these ideas. UARS CLAES has detected large amounts of both CFCl3 (F11) and CF2Cl2 (F12) in the stratosphere proving that these chemicals can easily get into the stratosphere [4]. Furthermore, as the chlorofluorocarbons are broken down in the stratosphere, they release chlorine and fluorine which form hydrogen fluoride (HF) and hydrogen chloride (HCl). HF is a long lived trace gas with no important natural stratospheric sources. UARS HALOE has detected HF and HCl in the stratosphere and found that both gases are increasing at the same rate as the CFCs are increasing in the troposphere with about a 5 year lag time [5]. This would not occur if chlorine came from intermittent volcanic sources.

The long lifetime of the UARS mission has led to some remarkable trace gas trend information. One of the more dramatic observations has been the vertical transport of water vapor upward in the tropical stratosphere. The amount of water vapor entering the stratosphere changes throughout the year as the tropical tropopause gets colder and warmer. These variations in water vapor ascend slowly into the stratosphere and appear coherent to about 30 km (from 16 km) [6]. The water vapor observations tell us that the tropical region must be relatively isolated from the rest of the stratosphere or these variations would be diluted.

REFERENCES

[1] J.W. Waters, "Microwave Limb Sounding," in Atmospheric Remote Sensing by Microwave Radiometry, edited by M. A. Janssen, John Wiley and Sons, New York, 1993.

[2] J.M. Russell, J.M., III, A.F. Tuck, L.L. Gordley, J.H. Park, S.R. Drayson, J.E. Harries, R.J. Cicerone, and P.J. Crutzen, "HALOE Antarctic observations in the spring of 1991," Geophys. Res. Lett., 20, 719-722, 1993.

[3] G.L. Manney, W.A. Lahoz, R.S. Harwood, R.W. Zurek, J.B. Kumer, J. Mergenthaler, A.E. Roche, A. O'Neill, R. Swinbank, and J.W. Waters, "Lagrangian transport calculations using UARS data, Part I: Passive tracers," J. Atmos. Sci., 3049-3068, 1995.

[4] R.W. Nightingale, A.E. Roche, J.B. Kumer, J.L. Mergenthaler, J.C. Gille, S.T. Massie, P.L. Bailey, D.P. Edwards, M.R. Gunson, G.C. Toon, B. Sen, and P.S. Connell, "Global CF2Cl2 measurements by UARSCLAES: Validation by correlative data and models," J. Geophys. Res., UARS special issue, 101, 9711-9736, 1996.

[5] J.M. Russell, III, M. Luo, R.J. Cicerone, and L.E. Deaver, "Satellite confirmation of the dominance of chlorofluorocarbons in the global stratospheric chlorine budget," Nature, 379, 526-529, 1996.

[6] P.W. Mote, K.H. Rosenlof, M.E. McIntyre, E.S. Carr, J.R. Holton, J.S. Kinnersley, H.C. Pumphrey, J.M. Russell III, J.W. Waters, and J.C. Gille, "An atmospheric tape recorder: The imprint of tropopause temperatures on stratospheric water vapor," J. Geophys. Res., 101, 3989-4006, 1996.

UARS Instrument	Measurement	Primary Objectives	Status
ACRIM - Active Cavity Radiometer Irradiance Monitor	Total solar irradiance	Trends in total solar irradiance	operational
CLAES - Cryogenic Limb Array Etalon Spectrometer	Ozone, chlorine nitrate, nitric acid, nitrous oxide, methane, water, aerosols, N2O5, NO, NO2, CFC11, CFC12, temperature	Observe ozone, nitrogen and chlorine reservoir species in the stratosphere	mission completed May 5, 1993
HALOE - Halogen Occultation Experiment	Ozone, water, methane, aerosols, HCl, HF, NO, NO2, temperature	Observes trends in stratospheric ozone, methane, water and the products of chlorofluorocarbon photolysis	operational
HRDI - High Resolution Doppler Imager	Mesospheric, stratospheric winds, aerosols	Observe stratospheric and mesospheric winds	operational
ISAMS - Improved Stratospheric and Mesospheric Sounder	Ozone, aerosols, CO, methane, nitric acid, nitrous oxide, NO, NO2, N2O5, temperature	Observe ozone, nitrogen radical and reservoir species	failed July 1992
MLS - Microwave Limb Sounder	Ozone, water, chlorine monoxide, nitirc acid, temperature	Observe ozone, water, and chlorine monoxide radical	water vapor radiometer failed April 23, 1993 otherwise operational
PEM - Particle Environment Monitor	Energetic particle flux, xray backscatter, magnetic field	Observe high energy particles that would influence atmospheric chemistry	operational
SOLSTICE - Solar Stellar Irradiance Comparison Experiment	Solar UV spectra	Provide long-term measurements of solar ultraviolet and far-ultraviolet radiation at the top of the Earth's atmosphere	operational
SUSIM - Solar Ultraviolet Spectral Irradiance Monitor	Solar UV spectra	Provide long-term measurements of solar ultraviolet and far-ultraviolet radiation at the top of the Earth's atmosphere	operational
WINDII - Wind Imaging Interferometer	Mesospheric and thermospheric winds	Observe winds in the mesosphere and thermosphere	operational

BEAWARE : budget effective all weather accurate radar for Earth observation

N. Vincent, E. Soulères, N. Suinot

ALCATEL ESPACE, 26 av J.F Champollion, 31037 Toulouse Cedex, FRANCE
Phone : 33 (0)5 61 19 52 25, Fax : 33 (0)5 61 19 61 63, E-Mail : FRDK8N58@IBMMAIL.COM

ABSTRACT

Today progress in technology and budget constraints have recently highlighted the large interest of a new type of mission definition which consists of one or several dedicated small-satellites, lighter than 700 kg for a moderate cost.
For a given mass and cost objective, the design of the SAR instrument to be embarked on a small satellite is the result of a compromise between the required imaging performances, the mission definition from user specifications and the available technology. This paper describes results of an internal system analysis where it has been identified several dedicated missions compatible with a large set of buses and launchers. The design of the SAR instrument incorporates standard hardware products and well established technology.

1. INTRODUCTION

During the last ten years, Earth Observation by SAR satellite has been developed greatly by the elaboration of multi-mission and large satellites based upon important funding. Indeed, the all weather and round the clock capability of spaceborne SAR technique has opened great possibilities for a large set of applications such as resource monitoring, natural hazards and civilian or military surveillance.

However, the budget constraints and the recent progress in space technology based upon developments during these large programs have leading to a different mission definition. It consists in one or several dedicated small-satellites, lighter than 700 kg typically and for a moderate cost.

In the overall context of Earth Observation, such a new approach presents at least the two following advantages. In complement with images delivered on the market by ERS or RADARSAT, it first guarantees the acquisition and the independence of the needed data. Besides, in case of small-satellites constellation, the information can be provided with very short time delay and whatever the required domain of interest.

The present paper presents the definition of the BEAWARE « budget effective all weather accurate radar for Earth observation » mission as well as typical guidelines of the radar design.

2. BEAWARE MISSION DEFINITION

The basic characteristic of a SAR satellite system is its all weather, round the clock capability, this means that all the images can be used and any application obscured by the dark or by clouds can be performed.

BEAWARE mission is designed for diverse range of field of applications. The following list, while not a complete of all possible applications, is at least representative of realistic opportunities which are foreseen for operational exploitation of BEAWARE.

2.1 Resource monitoring

Resource monitoring, using data from SAR satellite covers the inventory and monitoring of agriculture activity (crop measurement), the mapping of deforestation, ship routing, geology (oil exploration). For cartography purpose, topographic mapping with interferometric measurements can be performed.

2.2 Natural hazards

SAR data may be used in flooding monitoring, seismic area, volcanoes monitoring by interferometry, and in general to assist for the assessment of the damage to crops, population, industries due to volcanic eruptions, earthquakes, hurricanes, flooding.

2.3 Surveillance

This application addresses the enforcement of treaties, regulations, laws and surveillance of national security. For pollution surveillance, SAR data can be used to aid in the detection and tracking of oil spills and to assess the damages.

3. BEAWARE OPERATIONAL CAPABILITY

As any remote sensing system, SAR data are used to complete or to allow acquisition of new information or specific signatures in relation with other technics (weather sensors, data collecting of sensors on ground, other remote

0-7803-3836-7/97/$10.00 © 1997 IEEE

sensors like optic) in an overall system of information. The satellite orbit is defined to provide observation on local area extended in latitude with 24 hours mean revisit time. This capability in complementary with images from other system (RADARSAT, ERS1/2, ...) guarantees an independence of the information.

The control segment will be compatible with a simple and efficient operational concept; it is based on off the shelf hardware and software.

Regarding the image production and distribution, the data will be transmitted directly to ground for reception within the operational centre or field centre and will be processed in quasi-real time.

4. ORBIT CHARACTERISTICS

Regarding the mission specifications, the orbit must be determined in order to get over a given area of interest a maximum revisit time of a few days, a global coverage every orbit cycle and a 48-hour coverage better than 75% typically.

Depending on the application, sun-synchronous or inclined orbits may be selected with an altitude in the range 480 to 630 Km and a visibility domain of 350 to 500 km.

As an example, a 57-deg inclined orbit at an altitude of 630 km with a repeat cycle of 5 days and a visibility domain included between 14 and 50 degrees of incidence angle gives the performances summarised in Table 1 over an area of interest from 10 degree South to 60 degree North (Figure 1).

Table 1 : Mission performances

PARAMETER	PERFORMANCE
Mean revisit time	48 hours
Global coverage	in 110 hours (~ 5 days)
75 % of coverage	in 46 hours

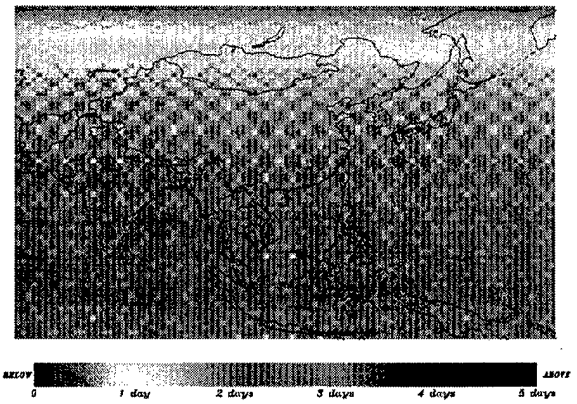

Figure 1 : Mean Revisit time performances

5. BEAWARE SAR DESIGN

5.1 Definition

The definition of the SAR instrument design is sufficiently flexible to take into account the mission requirements, the orbit characteristics as well as the environment constraints. The altitude range is set between 500 and 650 km as a good compromise between instrument constraints and atmospheric drag effects.

X-band, C-band or S-band are preselected bands to satisfy the different fields of application without requiring too large antenna sizes.

The satellite is typically in the range 500 kg and is compatible with a large set of variety launchers. The mission duration is 5 years.

By the mean of an instantaneous pointing agility of the antenna beam, a very extended range is accessible and it is possible to image in five days maximum any area included in a large domain in latitude.

▼ Strip Map mode :
- resolution : 4 m
- swath : 20 km

▼ Swath expending mode :
- resolution : 4 m
- image : 40 km * 40 km

▼ Spotbeam mode :
- resolution : 2.7 m
- image : 20 km * 20 km

▼ Scansar mode :
- resolution : 25 m (6 looks)
- swath : 100 km

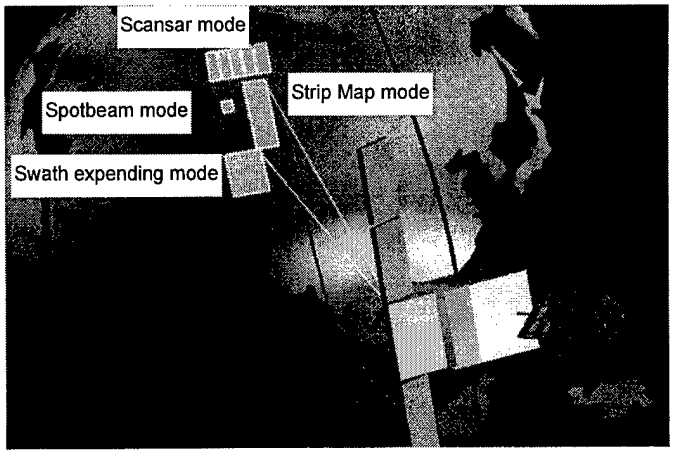

Figure 2 : BEAWARE operating modes

5.2 Operating modes

Four different modes can be operated by the design SAR instrument. Performances associated with a typical solution in X-band are given as an example in the figure 2.

In a strip-map mode (1), a 20 km swath width can be imaged with a resolution around 4 meters for situation and activity monitoring.

The opportunity to accommodate an active antenna offers a capability to make square image of twice the width (swath expending mode - 2) and an improvement of the resolution on a smaller size image (spot beam mode - 3).

For environmental purpose or wide area monitoring, a Scansar mode (4) gives large swath images with a typical spatial resolution around 20 meters.

5.3 SAR design

The design of SAR instrument incorporates whenever possible standard hardware products and well established technology.

Active antennas are implemented to guarantee a large pointing flexibility in elevation as well as azimuth directions.

As an example of design in X-band, Table 2 summarizes main system and instrument characteristics.

Table 2 : Typical values of system/instrument characteristics

PARAMETER	VALUE
Frequencies	9.65 GHz
Active antenna size	6.95 m length by 1.066 m height
Polarization	HH or VV
Noise equivalent Sigma-naught	-20 dB
Maximum peak power	< 3 kW
SSPA output peak power	3 W (MMIC)

The instrument block diagram is represented schematically in Figure 3. It consists in three main subsystems :

- the Digital subsystem for pulse generation, pulse compression and data formatting,
- the RF subsystem for up and down conversion,
- the antenna subsystem for high power amplification and transmission/reception of RF signals.

The active antenna is divided into 30 tiles with 32 Tx/Rx modules per tile. The active antenna and tile design are depicted in Figure 4 and 5.

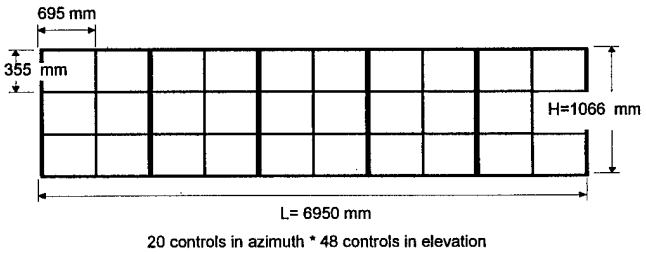

Figure 4 : Active antenna design

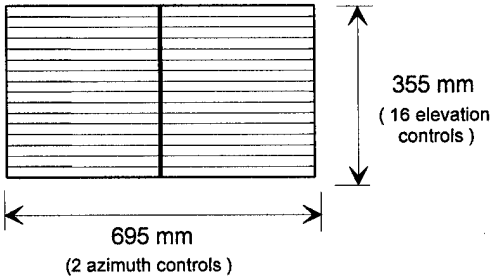

Figure 5 : Tile design

4. BUDGETS

The antenna is sized to be compatible with a large set of small launcher fairings : LMLLV2, Taurus, Soyouz...

The needed resources and mass budget are compatible with a large set of platforms such as PROTEUS. Indeed, depending greatly on the selected frequency, the satellite mass is in the range 600 to 800 kg and the power consumption about 1.5 to 2.5 kW in imaging mode about 5 to 10 minutes per day.

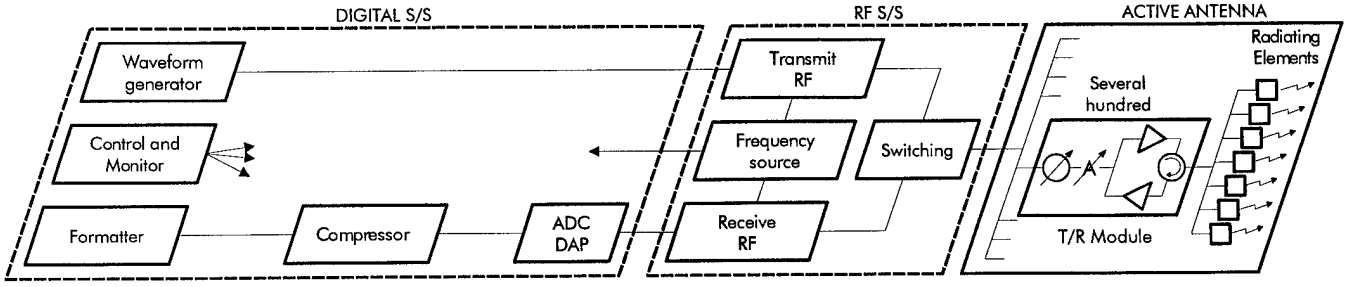

Figure 3 : Instrument block diagram

Design of MACSIM Cloud Radar for Earth Observation Radiation Mission

N. Vincent, N. Suinot

ALCATEL ESPACE, 26 av J.F Champollion, 31037 Toulouse Cedex, FRANCE
Phone : 33 (0)5 61 19 52 25, Fax : 33 (0)5 61 19 61 63, E-Mail : FRDK8N58@IBMMAIL.COM

C. C. Lin

ESA-ESTEC, 2200 AG Noordwijk, THE NETHERLANDS
Phone : (31) 71 56 5 58 13, Fax : (31) 71 56 5 46 96

ABSTRACT

Based upon results of a pre-phase A study, this paper presents the design of MACSIM Cloud Radar, which is one of the two active instruments of the Radiation Mission. This radar is a 95 or 79 GHz non-scanning instrument which collects echoes reflected by cloud particles. Its main measurement objectives are the altitudes of the cloud top and base with an accuracy of ± 250 m and the Ice/Liquid Water Content as a function of the altitude of the different cloud layers.
As a result of several trade-offs, a nadir looking radar transmitting unmodulated pulses of about 3 μs is designed with a primary design objective of improving the sensitivity.
In the last section, detection results for a set of typical clouds are summarised which demonstrates the feasibility of a light instrument in compliance with the user requirements.

1. INTRODUCTION

The ESA Radiation Mission is one of the four Earth Explorer Missions preselected for a Mission phase A study. The Radiation Mission is planned for a better understanding of climate variability and change through the radiative processes in the atmosphere.

The two main instruments of this mission are a cloud profiling radar called MACSIM (Millimeter-wave Active Cloud Structure Imaging Mission) associated with the ATLID backscatter lidar. These are to be complemented by a broadband radiometer, a GPS/GLONASS receiver and a passive imager.

Based upon a pre-phase A study funded by ESA and led by ALCATEL ESPACE with five other European companies as subcontractors, this paper presents the preliminary radar design as a result of several trade-offs at system and subsystem level. Despite the critical requirement on instrument sensitivity, a performance analysis demonstrates the feasibility of such an instrument for relatively low mass and power consumption budgets.

2. MISSION OBJECTIVES

The primary objectives of the Earth Radiation mission are to provide data essential for :

1. the quantification of key radiative processes which control the Earth's climate system;
2. the improvement and validation of the general circulation models used to predict the response of climate to anthropogenic perturbations of the Earth's radiation budget.

The Earth Radiation mission is intended to provide a picture as complete as possible of the three dimensional spatial and the temporal structure of radiative transfer at the top of the atmosphere, within the atmosphere, and at the Earth's surface. It is the main goal of this mission to quantify the impact of cloud and aerosol fields associated with a number of atmospheric processes on the radiation balance, globally as well as regionally.

The specific measurement requirements are shortwave and longwave radiation fluxes at the top of the atmosphere, cloud top and base heights, cloud type, cloud fractional coverage, cloud optical thickness, liquid or ice water content (LWC/IWC), effective particle size, aerosol layer top/base heights, aerosol optical thickness.

The presence of multiple layers must be explicitly considered, and the corresponding parameters must be retrieved for each individual layer.

The payload of the Earth Radiation mission comprises :

- a backscatter lidar to observe the characteristics of aerosol and thin cloud layers as well as cloud top heights;
- a cloud profiling radar (MACSIM) for the retrieval of the geometrical properties of thick clouds, LWC/IWC distribution within the clouds and light precipitations;
- a broadband scanning radiometer to measure shortwave and longwave fluxes at the top of the atmosphere;

0-7803-3836-7/97/$10.00 © 1997 IEEE

- a visible/infrared cloud imager to provide the link to standard measurements as made from operational platforms (i.e. cloud fractional coverage, aerosol optical thickness, layer tops, surface temperature and emissivity), and to provide the necessary information for interpolating the fields measured with the different instruments having different sampling properties;
- plus a GPS/GLONASS receiver to provide navigational data as well as atmospheric profiles of temperature and water vapour.

The considered orbit is circular, sun-synchronous, and assumed presently to be at an altitude range of 500 to 600 km with an Equator descending time of 14:00 hrs.

3. CLOUD RADAR DESIGN

3.1 Concept selection

Despite the selected W-band (79 or 95 GHz), one of the most critical point of a cloud radar instrument is the level of the signals backscattered by the cloud particles. In case of typical stratus, the cloud signal reflectivity is about -30 dBZ which is 75 dB below typical surface return at nadir.

A well-known method for improving the radar sensitivity consists in implementing on-board pulse compression.

Despite an optimisation of pulse and replica waveforms, such a concept is discarded as it cannot protect cloud echoes from ground contamination especially near the ground, an area of particular interest for radiation budget. In presence of an even small uncompensated Doppler shift, the time sidelobe level largely exceeds the requirement.

The MACSIM cloud radar must collect data along the subsatellite track but the radar can be tilted off-nadir in the along track plane. The main advantage is the decrease of the surface echo level and then a relaxed requirement on pulse response range sidelobes. However, in W-band, the variation of land reflectivity is not so large and the effective gain does not compensate for the increased level of range ambiguities and the resulting antenna criticality.

As a result of this study, the proposed concept is a nadir looking radar which unmodulated transmit pulses of a few microseconds length.

3.2 Design

As represented in Figure 1, the baseline architecture is composed of six main units : the digital electronic subsystem (DE s/s), the RF subsystem (RF s/s), the High Power Amplifier subsystem (HPA s/s), the Front-End subsystem, the antenna subsystem and the data storage subsystem.

Pulse generation is performed within the RF s/s at reception of a control signal transmitted by D.E. s/s. Up and down conversions are performed from a 8 MHz intermediate frequency to a RF frequency close to 79 or 95 GHz.

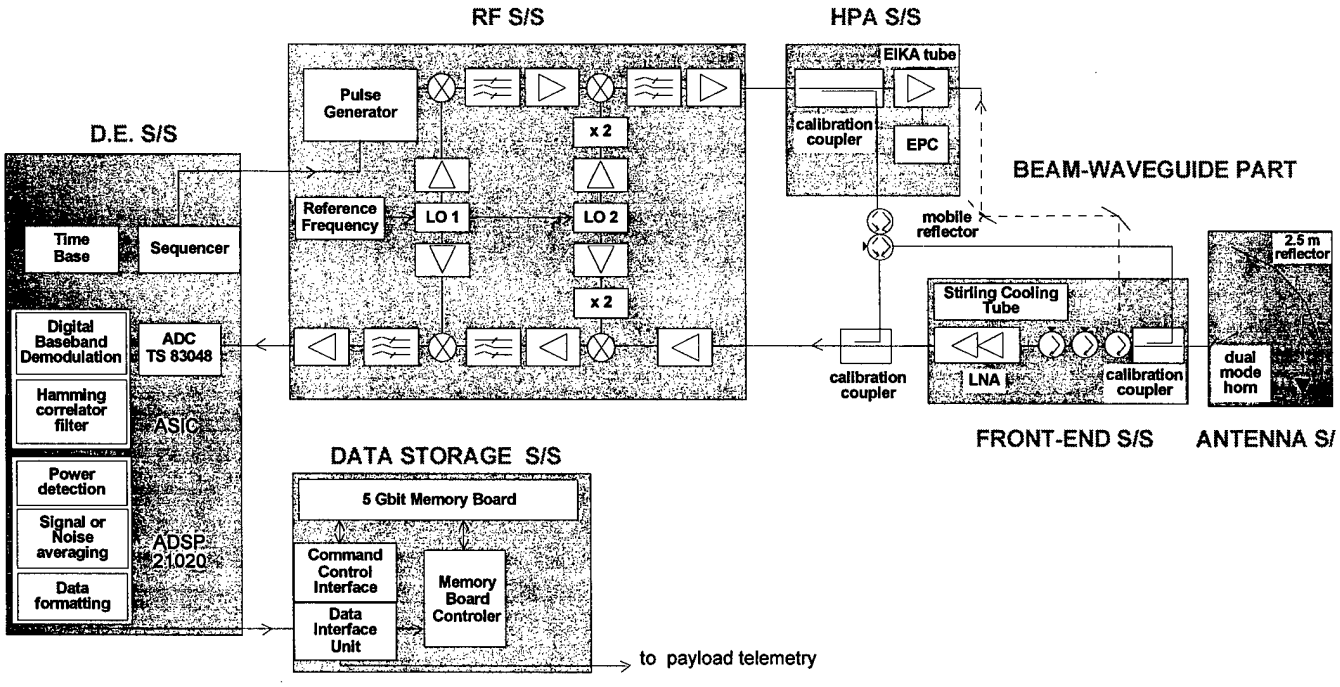

Figure 1 : Instrument block diagram

The MACSIM radar is a single frequency instrument but no selection is proposed among these both RF frequencies as it depends mainly on the CCIR regulations.

High power amplification is performed through an Extended Interaction Klystron Amplifier tube (EIKA) that achieves an output peak power of about 1.7 kW. Because of the low cathode lifetime, an one among four passive redundancy scheme is proposed for the tube and associated EPC devices.

In order to reduce the transmit losses, the high-level signal is distributed via a Beam-Waveguide device based upon sub-reflectors and horns. This innovative concept at millimeterwave frequencies offers a very large flexibility in terms of accommodation and redundancy. Rotating sub-reflectors directly replace redundancy switches at the HPA outputs. The proposed design is depicted in Figure 2.

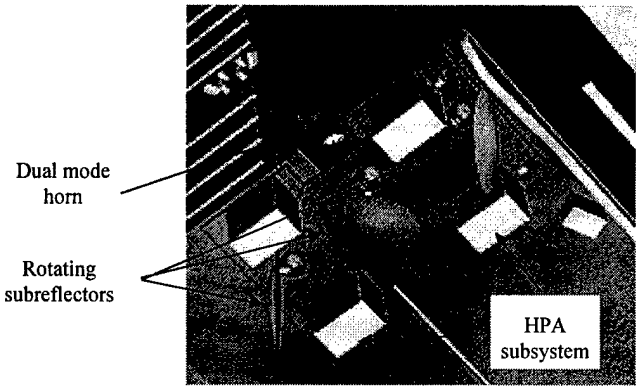

Fig. 2 : Beam-Waveguide distribution

The waveguide Front-End s/s is located as close as possible to the antenna port and includes cold redundant LNAs which are cooled down to 150 K by a Stirling Tube in order to improve the noise figure.

The antenna is a single offset 2.5 m reflector illuminated by a dual mode horn for improvement of antenna directivity. The reflector can be either accommodated on the satellite face perpendicular to the flight direction or on the upper satellite face, parallel to the flight direction.

The Digital Electronic s/s is mainly composed of an ADC and an ASIC for pulse correlation with low leading sidelobes and an ADSP for data processing.

The storage s/s with a capacity of 5 Gbit is designed for MACSIM instrument, but this subsystem is thought to be developed in order to store data of all Radiation Mission instruments.

Main system and instrument characteristics are summarised in Table 1.

Table 1 : Main system/instrument characteristics

PARAMETER	VALUE
RF Frequency	79 or 95 GHz
Footprint resolution	< 1 km
Vertical resolution	500 m
Observed altitude	600 m to 25 km
Detection of clouds dynamic range	-30 dBZ to +20 dBZ
Along-track sampling distance	1 km

4. PERFORMANCES AND CONCLUSION

A performance analysis applied to a set of typical cloud models shows that the most critical clouds for the designed instrument are the Fair Weather Cumulus because of their low reflectivity factor, thickness and altitude. Yet, other clouds such as Cirrus, Stratus and Cumulo-Nimbus are to be very well detected by MACSIM instrument.

Based on a performance model (30 km integration distance), performance budgets are described in Table 2.

Table 2 : Performance budgets

PARAMETER	VALUE
Absolute radiometric accuracy	< 1.7 dB
Radiometric stability	0.35 dB over 1 orbit 0.6 dB over mission
Localisation accuracy of the cloud base altitude	< ± 250 m
Mass budget (with margin of 20 %)	140 kg
Power consumption budget (with margin of 20 %)	250 W
Data rate	43 kbit/s
Reliability figure for the 4-year mission	82 % at 95 GHz 92 % at 79 GHz

In conclusion, this study has demonstrated the feasibility of a spaceborne millimeter-wave cloud radar which meets the performances needed for better understanding of the role played by clouds in the radiation budget.

5. ACKNOWLEDGMENTS

This work has been supported by the European Space Agency under contract no. 11752/95/NL/CN. We would like to express our thanks to all subcontractors involved in this study.

IGARSS'97

1997 International Geoscience and Remote Sensing Symposium

03-08 August 1997

Singapore International Convention & Exhibition Centre

Technical Program

Interactive Area 27: Inverse Techniques

ICE CONCENTRATION ESTIMATION BASED ON LOCAL INVERSION

Kohei Arai
Dept. of Information Science, Saga University, 1 Honjo, Saga 840 Japan
arai@is.saga-u.ac.jp

ABSTRACT

Methods for ice concentration estimation with passive microwave instrument data by means of inversion techniques as well as adaptive local inversion method are proposed. The experimental results with DMSP/SSM/I data show better accuracy through a comparison to the existing methods, NASA, Comiso algorithms.

INTRODUCTION

Passive microwave instrument data is widely used for ice concentration estimation. For instance, ESMR-5 algorithm used to compute first year sea ice concentration in the Antarctic is given by the following expression:

$$C=(Tb-135) / (e\ Ts-135) \times 100(\%) \quad (1)$$

where C represents the percent ice concentration within a field of view, Tb the observed brightness temperature, e the assumed sea ice emissivity taken to be 0.92(nadir viewing) for first year ice having an effective physical temperature of Ts. The 135 K brightness temperature represents a combined contribution from open sea water(120 K) and atmospheric emitters(15 K). The uncertainties in the assumed values are estimated to result in a 10 - 15% error in the computed ice concentrations[1]. The other algorithms for ice concentration estimation show almost same accuracies[2], [3]. All the factors of the above equation have not so small uncertainties so that ice concentration estimation accuracy is not good enough. The above equation would work for the foot-print(field of view) without any contamination. For example, brightness temperature of 22 GHz channel might be contaminated with water vapor in the atmosphere while that of 37 GHz channel might be contaminated with cloud liquid so that some corrections should be taken into account. Fig.1 shows a scatterogram of the open ocean, clouds and two types of sea ice, first year and multi-year ice on the 2D plane between 19GHz and 37GHz of vertical polarization. The distribution of clouds is overlapped with the other two categories so that it is not easy to discriminate. Furthermore it is difficult to discriminate between first and multi-year ice types. NASA and Comiso proposed weather and ocean filtering which allows to remove clouds as well as ocean from the microwave radiometer imagery data in advance with ice concentration estimation. It is not sufficient and require a time consumable process. In order to overcome such a situation, new methods will be proposed in this paper. First an ice concentration estimation method based on inversion is proposed followed by local inversion. Then ice concentration accuracy for the existing and the proposed methods will be assessed with DMSP/SSM/I data.

ICE CONCENTRATION ESTIMATION BASED ON INVERSION

There are a number of inversion problem solving methods. The most primitive methods involve Inverse Matrix Methods, in particular, well-known Generalized Inverse Matrices Methods such as Moor-Penrose, Least Square, as well as the Inverse Matrix Methods with Constraints or A Prior Knowledge.

Generalized Inverse Matrix

Let us assume a three dimensional feature space for an image classification. Mixels can be expressed with mixing ratio for each designated class. Let the vector in the feature

0-7803-3836-7/97/$10.00 © 1997 IEEE

space be V, mixing vector be M and the matrix which represent the spectral characteristics for the designated classes be S, then,

$$V=SM \quad (2)$$

The mixing ratio vector can be estimated with the following equation, if there exists inverse matrix of S.

$$M=S\text{-}1\ V \quad (3)$$

There does not always exist such an inverse matrix so that a certain regularization is necessary for such a matrix. If the elements of S are independent, then the inverse matrix for St S can be calculated. Then we can get the well known generalized inverse matrix of Moor-Penrose type, (St S)-1 St. In such case, M can be calculated with the following equation,

$$M=(St\ S)\text{-}1\ St\ V= S+\ V \quad (4)$$

This method is referred to as the Generalized Inversion Matrix Method, GIMM.

Least Square Methods

Another approach is the least square method with constraints such that |M-M '| be minimized,

$$M=S+V(1\text{-}ut\ S+V)(StS)\text{-}1u\ /\ ut(StS)\text{-}1u \quad (5)$$

where M' denotes an estimated mixing ratio vector and u denotes unitary matrix. If instead, we minimize |V - V'|, then,

$$M=S+V + (1\text{-}utS+V)u\ /\ |u|2. \quad (6)$$

These two least square methods are referred as the Least Square method minimizing estimation error of Mixing ratio, LSMR and the Least Square method minimizing estimation error of Observation vector, LSOV.

Maximum Likelihood Method

Further, Maximum Likelihood Method maximizing the likelihood function of the observation vector(Usually Multi-variate Normal Distribution) with the constraints is also applicable[4]. This method is referred to Maximum Likelihood Method, MLH.

Adaptive Least Square Method

The aforementioned least square methods can be used adaptively with the local property of the image of interest.

Local Inversion

Meanwhile this inversion process can be applied to the imagery data by region by region or even for pixel by pixel. The parameters for such this method can be adaptively changed for regional characteristics of the imagery data. Improvement on the estimation accuracy can be expected. This is referred to Local Inversion Method, LIM.

EXPERIMENTAL RESULTS

A comparative study on ice concentration estimation with SSM/I data was conducted between Comiso algorithm and the proposed methods. The results which are shown in Table 1 show that the proposed methods are slightly superior to the Comiso algorithm. Comiso algorithm is widely used for ice concentration(IC) estimation that is IC is estimated with the following equation,

$$IC = \sqrt{\frac{(Tb1-Tb1w)^2+(Tb2-Tb2w)^2}{(Tb1i-Tb1w)^2+(Tb2i-Tb2w)^2}} \quad (7)$$

where Tb1, Tb2 are brightness temperatures of the different bands, Tb1w, Tb2w are brightness temperature for open ocean, Tb1i, Tb2i are brightness temperature for sea ice.

CONCLUDING REMARKS

Approximately 9.5% of improvement in terms of ice concentration estimation accuracy was achieved for proposed method compared with the existing Comiso method.

REFERENCES

[1] P. Gloersen, H.J. Zwally, T.C. Chang, D.K. Hall, W.J. Campbell and R.O. Ramseier, Time-Dependence of sea ice concentration and multi-year ice fraction in the Arctic basin, Boundary-Layer Meteorology, 13, 339 - 359, 1978.

[2] H.J. Zwally and P. Gloersen, Passive microwave images of polar regions and research applications, Polar Record, 18, 116, 431 - 450, 1977.

[3] P. Gloersen, D. Cavalieri and W.J. Campbell, Derivation of sea ice concentration, age and surface temperature from multi-spectral Microwave Radiance obtained with the NIMBUS-7 Scanning Multi-Channel Microwave Radiometer, Oceanography from Space, Plenum Publishing Corp., 823 - 830, 1981.

[4] K. Arai, Inversion techniques for proportion estimation of MIXELs in high resolution satellite image analysis, Proceedings of the 29th COSPAR A8.M.2.01, 1993.

Table 1 RMS error for the proposed methods compared to the Comiso algorithm

RMS error (%) Comiso	GIMM	LSMR	LSOV	MLH	LIM
8.36	9.76	9.31	8.43	7.84	7.56

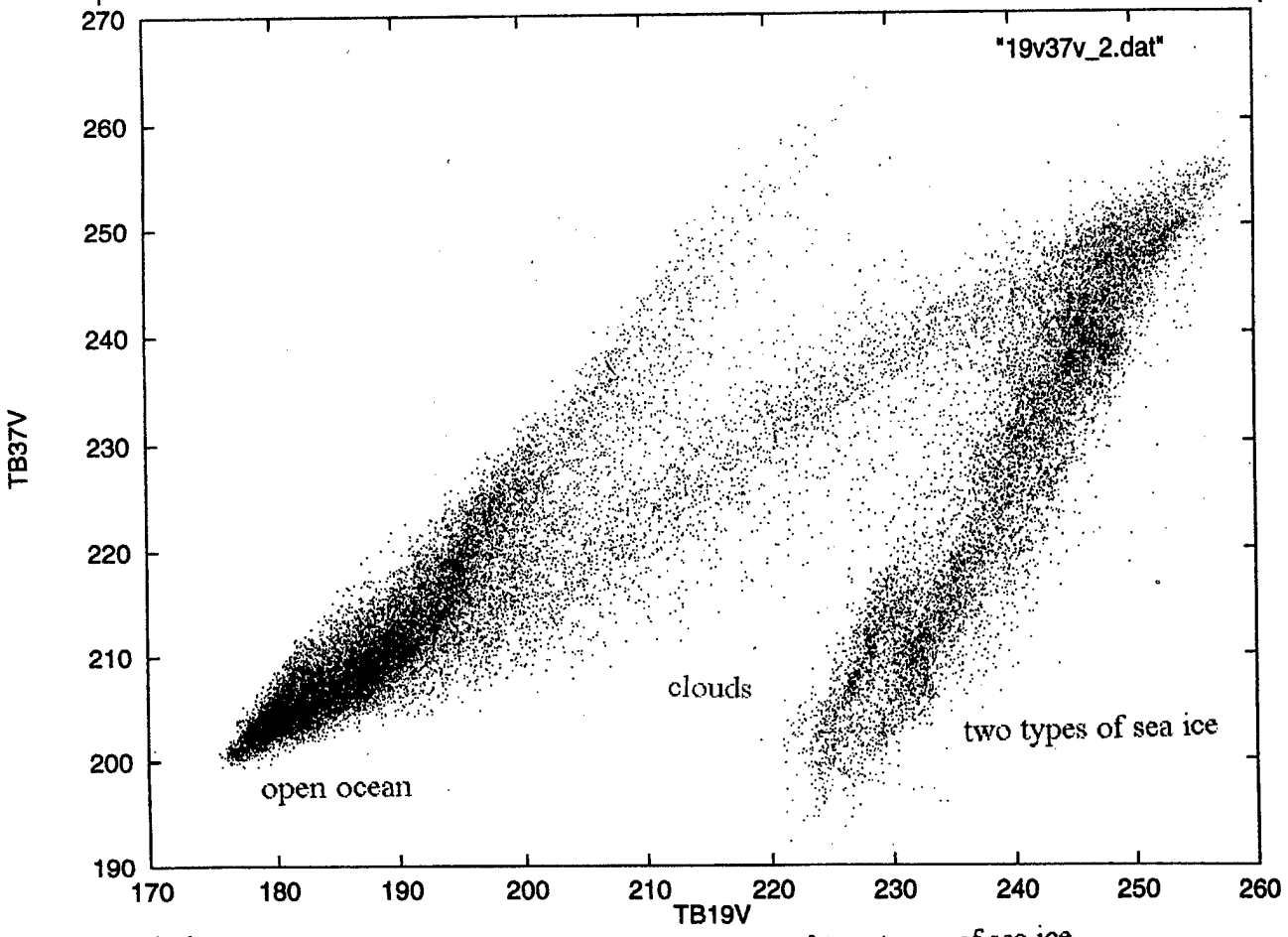

Fig.1 scatterogram of the open ocean, clouds and two types of sea ice

Retrieving of LAI and fAPAR with airborne POLDER data over various biomes

P. Bicheron, M. Leroy and O. Hautecoeur
Centre d'Etudes Spatiale de la BIOsphère (CESBIO)
18 av. E. Belin, 31055 TOULOUSE CEDEX, FRANCE.
Tel :33 5 61 55 85 06 / Fax :33 5 61 55 85 00
email : bicheron@cesbio.cnes.fr

ABSTRACT

The objectives of the paper is to study a method of retrieval of LAI and fAPAR parameters based on the inversion of a BRDF model against remote sensing data from forthcoming wide field of view optical satellite sensors such as POLDER/ADEOS, VGT/SPOT4, MODIS/EOS,MISR/EOS. The model used is that of Kuusk [1]. The evaluation of this approach is made with field data and airborne POLDER acquired during BOREAS 94 and HAPEX 92. The results show that the LAI is restituted with an accuracy higher than that obtained with a semi-empirical relationship LAI-vegetation index. The daily fAPAR is also very well restituted. It is concluded that the retrieval of biophysical parameters from inversion of a BRDF model is promising in the perspective of a quantitative characterization of the terrestrial biosphere.

INTRODUCTION

One of important challenges for these last years is to link up the spatial observation to biophysical surface parameters, such as the Leaf Area Index (LAI), the fraction of absorbed photosynthetically active radiation (fAPAR), or the vegetation density (veg). The veg and LAI quantities are used as input parameters of General Circulation Models (GCMs) [2] . The fAPAR is a key quantity driving at the estimation of the Net Primary Production (NPP). The knowledge of these parameters is necessary for the establishment of a real terrestrial biogeography.

AVHRR has been the only spatial sensor able to observe the photosynthetic activity with a sufficient temporal frequency at regional and global scales. Through these data, the first world wide LAI and fAPAR maps at a resolution of 100km x 100km have been produced using various semi-empirical relations following the biomes.

With the new generation of sensors characterized by a stronger spectral and directional richness, we may expect to improve the spatial and temporal resolution, and the accuracy of biophysical parameters. Among the new spaceborne sensors, appear in particular POLDER launched in August 1996 on board platform ADEOS, VEGETATION on SPOT-4 (March 98), MODIS and MISR on EOS (June 98). The abundance of measurements by pixel brought by these new instruments should allow to overtake the exclusive use of vegetation indices. We may conceive of using more complex and more precise models for the interpretation of the spatial measurement in term of biophysical parameters.

APPROACH

Model

Many radiative transfer models have been developed to describe the reflection of optical radiation from vegetation canopies. Our goal is to prepare BRDF inversion techniques to be applied on spaceborne POLDER data. Since satellite measurements by pixel contains all the same a limited information, it is strongly preferable to use a model weakly parametrized. Therefore, we have chosen the Kuusk's model, which realizes a synthesis between the model of Nilson and Kuusk (1989) [3], Jacquemoud and Baret (1990) [4], Price (1990) [5], and Verhoef [6]. It predicts the BRDF of the canopy as a function of wavelength, illumination and viewing angles, LAI, chlorophyll content Cab, leaf orientation, ratio of leaf size to canopy height, spectral and directional ground parameters, and structural and optical parameters of leaves. The solutions of the inversion are determined fixing some of the parameters to reasonable values, and to free values the others in the minimization of the merit function, chosen identically to Nilson and Kuusk.

Validation

To validate our approach, we have considered therefore the results of two campaigns using the airborne version of the POLDER instrument (BOREAS 94 and HAPEX 92). A clear description of the instrumental concept is given in Deschamps et al., 1994 [7].

For HAPEX 92, the dataset on which we are working consists of 5 flights over Millet Crop site and Shrub Fallow site at the following days : August 28, Sept. 3, 13, 17, and October 4. In the case of the BOREAS experiment, different flights have been done over the super sites, during the 2 intensive field campaigns. For the particular day of July 21, we have processed POLDER data on different subsites near Young Jack Pine and Old Black Spruce. Various ground measurements of LAI, daily fAPAR have been done by Chen and Cihlar (1995) [8], and Plummer (1995) [9]. The inversion

0-7803-3836-7/97/$10.00 © 1997 IEEE

has been realized choosing as free parameters LAI, leafsize, Cab, structural leaf parameter N, and first spectral ground parameter. We assumed a spherical angular distribution of the leaves. The ground directional parameters are generally those

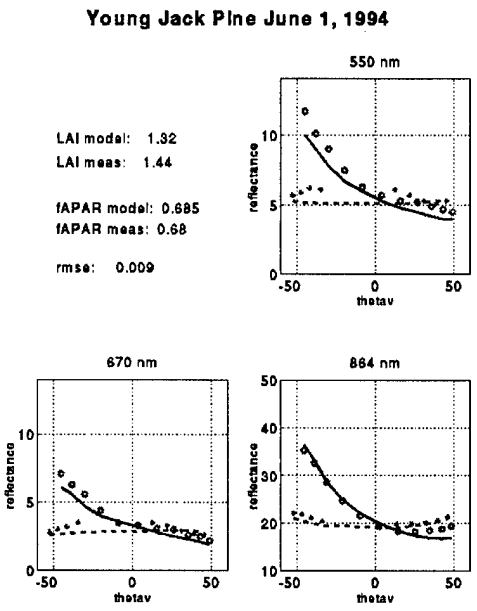

Fig. 1 POLDER data in the principal (o) and perpendicular (+) plane, compared to model's prediction for the same geometry at 550nm, 670nm, 864nm for YJP 06/01/94.

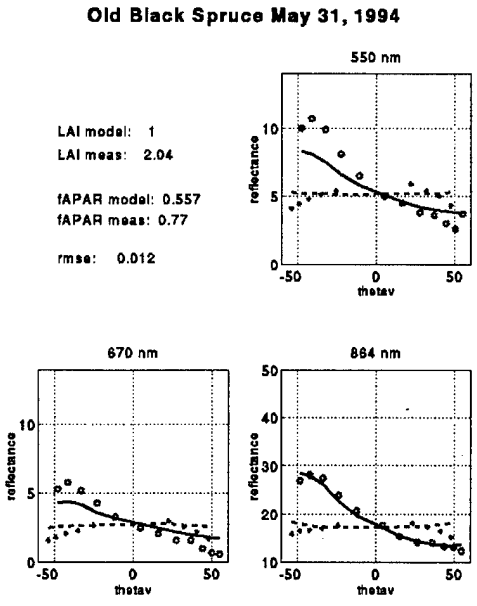

Fig. 3 : the same as Fig.1 for OBS 05/31/94.

of Kuusk, but we have let them free in the case of HAPEX for the August 28, and keep these values for the other days.

Results

The fig. 1 and 2 show 2 examples of comparison between the measured POLDER reflectances in the principal and perpendicular plane, and those retrieved by the model in the same configurations on sites of pine and spruce. The rmse considering all the reflectances at the 3 wavelength is on the order of 0.01. The agreement between the biophysical parameters measured and modelled are quite different in the 2 figures. For the Jack Pine site (fig. 1), the agreement is excellent, whereas for the Black Spruce site (fig. 2), it is mediocre, with factors LAI and fAPAR differing respectively from 2 and 1.4. The turbid model finds here its limitations in the situation of developed spruces, characterized by important vertical structures, and by a shadowing distribution very different from this existing in a homogeneous media.

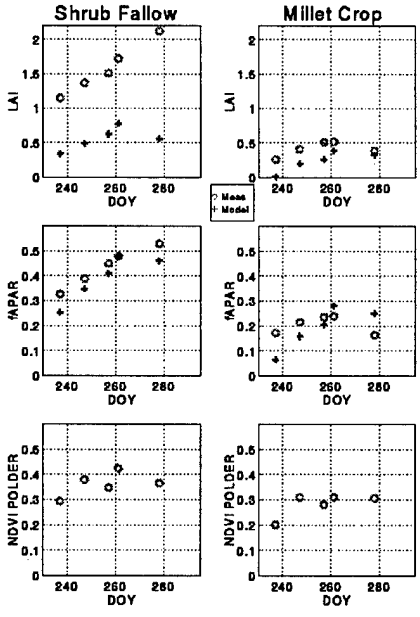

Fig. 3 : Comparison of LAI and daily fAPAR measured and modelised for Shrub Fallow and Millet Crop for different days. The vegetation index measured by POLDER (selecting the nearest direction of nadir) is also mentionned.

On the contrary of the boreal forest which is quite stable from May-June and July-August, the HAPEX area is characterized by an abrupt growth of the vegetation during the end of the summer. In this context, it is interesting to know if we are able to restitute the temporal evolution of the LAI and fAPAR. The fig. 3 shows that the observed tendancies are correct in the whole, but that the retrieved orders of magnitude (0.4 up to 0.8) are inferior to those

measured (on the order of 1.5 to 2). However, it is not impossible that the measurements are a little overestimated, when we considered the very small variation of the vegetation indice measured by POLDER during the same time.

The synthesis of the results comparing the biophysical parameters measured on the ground and derived from POLDER data are depicted in the fig. 4 for all the available data. The figure shows that the retrieval of the fAPAR is quite precise on the whole of the dynamic of this quantity (between 0 and 1), with an absolute standard deviation equal to 0.09. The assesment of the measured LAI is obtained with larger dispersion since the standart deviation, in absolute value of LAI, has a value of 0.8. These results suggest that we measure precisely the fAPAR and accurately enough the LAI. The results are also compared with methods having similar objectives, such as the FASIR index. The fig. 4 shows that the FASIR overestimates the LAI for boreal region, but that in the same time, it underestimates greatly the LAI in the sahelian region. The retrieval of the fAPAR by FASIR is more precise than this of the LAI, with however an accuracy less good than our method.

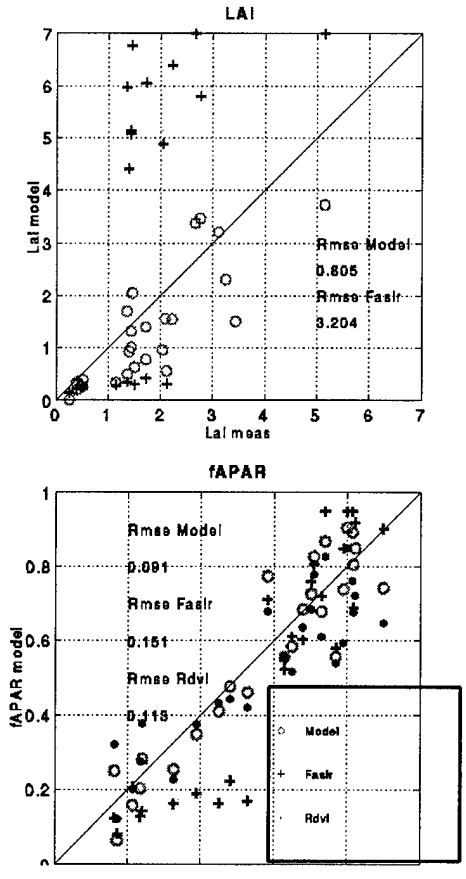

Fig.4 : Comparison of LAI and daily fAPAR measured and modelled on the whole HAPEX and BOREAS data.

CONCLUSIONS

The extraction of biophysical parameters through the fitting of BRDF models on spectral and directional data is a promising track for the biosphere's characterization. The realised trying on airborne data acquired on boreal forests and savannah sites have shown that the LAI is quite well estimated, with an accuracy greater than this of methods based on semi-empirical indice-LAI. The fAPAR is retrieved precisely with a better precision. The reconstituted reflectances are generally in a good agreement with the measured reflectances on the whole of the spectral and directional dynamic with a standart deviation of 0.01. The results demonstrate that is is interesting to continue to explore the inversion of BRDF models on spatial data, in particular those coming from sensors with wide field of view. This method will be also applied on airborne data acquired during the ReSeDa-Alpilles 96-97 campaign on agricultural parcels. An important work still remains to carry out examinating different sites than those described in this article, and doing experiences with spatial data. Finally, numerous theoritical problems such as scale changing, mathematical methods of the inversion, and the precision of the model used, arise.

REFERENCES

[1] Kuusk A., « A multispectral canopy reflectance model », *Remote sensing of Environnement*, 50, pp. 75-82, 1994.

[2] Sellers P. J., C.J. Tucker, G.J. Collatz, S.O. Los, C.O. Justice, D.A. Dazlich, et D. A. Randall « A global 1° by 1° NDVI data set for climate studies. Part 2 : The generation of gloabl fields of terrestrial biophysical parameters from the NDVI », *International Journal of Remote Sensing*, 15, pp. 3519-3545, 1994.

[3] Nilson T. Et A. Kuusk, « A reflectance model for the homogeneous plant canopy and its inversion », *Remote Sensing of Environment*, 27, pp. 157-167, 1989.

[4] Jacquemoud S. et F. Baret, « PROSPECT : a model of leaf optical properties spectra », *Remote Sensing of Environment*, 34, pp. 75-91, 1992.

[5] Price J.C., « On the information of soil reflectance spectra » , *Remote Sensing of Environment*, 58, pp. 187-200, 1990.

[6] Verhoef W., « Light scattering by leaf layers with application to canopy reflectance modeling : the SAIL model », *Remote Sensing of Environment*, 16, pp 125-141, 1984

[7] Deschamps P.Y., F.M. Bréon, M. Leroy, A. Podaire, A. Bricaud, J.C. Buriez, G. Sèze, « The POLDER scientifi mission : instrument characteristics and scientific objectives », *IEEE Transactions on Geosciences and Remote Sensing*, 32, pp. 598-615, 1994.

[8] Chen J.M. et J. Cihlar, « Retrieving LAI of boreal conifer forest using Landsat TM images », *Remote Sensing of Environment*, 55, pp153-162, 1996.

[9] Plummer S., Base de données BORIS, 1995.

Geometry-Based Deconvolution of Geophysical Data

Marwan A. Simaan
Department of Electrical Engineering, University of Pittsburgh
348 Benedum Hall, Pittsburgh, PA 15261
Tel: (412) 624-8002, Fax: (412) 624-8003, email: simaan@ee.pitt.edu

Abstract – A seismic trace can be modeled as a convolution of a source wavelet and the reflectivity sequence of the earth at a common depth point midway between the source and receiver. In a common depth point gather, the reflectivity sequence associated with each source-receiver pair is a compressed version of the zero-offset reflectivity sequence at that point. The process of normal moveout correction to align the traces to the zero-offset trace, stretches both the reflectivity sequences and wavelet simultaneously. While stretching the compressed reflectivity sequences is desirable, stretching the wavelet is not. If an inverse operator is applied to spike the wavelet prior to the normal moveout correction, the amount of stretch encountered by the wavelet will be reduced. If the wavelet has been perfectly spiked, the amount of stretch will be reduced to zero. This suggests that the zero-offset trace along with a non-zero offset trace could provide two nonlinear simultaneous equations that can be solved to determine the deconvolution filter. That is, a filter to spike the wavelet before Normal Moveout. Additional traces, however, will be needed to minimize the effect of noise and random errors.

In this paper we formulate this deconvolution problem and show that it can be solved using a constrained least square minimization technique. The solution process can be shown to reduce to an eigenvalue problem.

We will also discuss a generalization of this work to data where the stretch in the reflectivity sequences is introduced in the recorded data because of the geometry of the propagation medium relative to the array data acquisition system. This geometry-based deconvolution approach could be very effective in numerous remote sensing applications.

INTRODUCTION

In seismic data processing, it is well known that the process of Normal Moveout (NMO) correction causes stretch in the seismic traces [1-3]. This effect can be exploited to design a deconvolution filter to recover the signals' two main constituents; the earth reflectivity sequence and the source wavelet [4-5]. Spectral assumptions regarding these two entities are not required. The stretching of the wavelet caused by NMO correction on the seismic traces will lead to considerable dissimilarities among the corrected traces. The filter design process is based on the assumption that similarity among NMO corrected traces will be increased if the time duration of the source wavelet is shortened. Thus, if a filter is applied to the traces prior to NMO correction which shortens the length of the wavelet (i.e spike the wavelet), then their similarity after NMO will be increased. Mathematically, this can be achieved by constructing an error function whose minimum is a measure of similarity among a number of traces.

In this paper, we construct this function as the sum of the error norms between all pairs of traces. The minimum of such a function will correspond to traces whose similarity has been maximized. We will use this function to derive the coefficients of the deconvolution filter. A mathematical description of this process is given in the next section.

DECONVOLUTION FILTER

Consider a linear array of K geophones. The seismic trace recorded at the k^{th} geophone can be represented as:

$$y_k(t) = w(t) * h_k(t) + \eta_k(t) \quad , \quad k = 1,\ldots K \qquad (1)$$

where $w(t)$ is the source wavelet, $h_k(t)$ is the earth reflectivity sequence associated with k^{th} geophone and $\eta_k(t)$ is an additive zero-mean Gaussian noise and * denotes deconvolution. When NMO correction is applied to $y_k(t)$, distortion will result due to a redistribution of the spikes of the reflectivity sequence on the time axis. If the arrival times of the same reflection on the zero-offset and on the k^{th} offset trace respectively are t_0 and t_k, then we must have $h_k(t_k) = h_0(t_0)$. It is straightforward to show that t_k and t_0 are related by the well known Normal Moveout formula

$$t_k^2 = t_0^2 + \frac{d_k^2}{V^2} \qquad (2)$$

where d_k is the offset distance of the k^{th} trace, as illustrated in Figure 1, and V is the stacking velocity. The above expression can be written as

$$t_k = \alpha_k t_0 \qquad (3)$$

where α_k is the NMO stretch factor which varies from trace to trace. We note that equation (2) is derived from the geometry of the various source receiver paths. A different

0-7803-3836-7/97/$10.00 © 1997 IEEE

geometry (for example a non-horizontal reflectors) will clearly lead to different values of α_k in equation (3). Now at time t_k, equation (1) can be written as

$$y_k(t_k) = w(t_k) * h_k(t_k) + \eta_k(t_k) \tag{4}$$

or

$$y_k(\alpha_k t_0) = w(\alpha_k t_0) * h_0(t_0) + \eta_k(\alpha_k t_0) \tag{5}$$

If we let the NMO corrected trace be denoted by

$$Z_k(t_0) = y_k(\alpha_k t_0) \tag{6}$$

then

$$Z_k(t_0) = w(\alpha_k t_0) * h_0(t_0) + \eta_k(\alpha_k t_0) \tag{7}$$

Comparing equations (7) and (1), we see that the NMO correction (or more specifically, the geometry of the source receiver paths) has passed the nonlinear compression from the reflectivity sequence to the wavelet as a nonlinear stretching. This geometry-based stretching will be exploited to design the deconvolution filter.

Using matrix notation, and assuming that the data is in digital form, the filter design process can be summarized as follows:

$$\begin{aligned} X_k &= LG_k Y_k \overline{w} \\ &= Q_k \overline{w} \end{aligned} \tag{8}$$

where $\overline{w}$ is the filter vector (dim $W \times 1$), $\boldsymbol{Y}_k$ is the seismic data in matrix form (dim $N \times W$), $\boldsymbol{G}_k$ is the geometry matrix which performs the NMO correction (dim $N \times N$) and $\boldsymbol{L}$ is the error gate matrix (dim $M \times N$) which defines a window of data over which the error is computed. A measure of similarity among all $\boldsymbol{X}_k$'s may be chosen as the energy (norm) E of all error vectors $\varepsilon_{kp} = X_k - X_p$ for $k \neq p$. That is

$$E = \sum_{k=1}^{K} \sum_{p=1}^{K} \left\| \varepsilon_{kp} \right\|^2 \tag{9}$$

which after some algebraic manipulations, can be written as the quadratic form

$$E = \frac{1}{2} \overline{w}' A \overline{w} \tag{10}$$

where the W x W matrix A is expressed as

$$A = (K \sum_{k=1}^{K} Q_k' Q_k) - (\sum_{k=1}^{K} Q_k)' (\sum_{k=1}^{K} Q_k) \tag{11}$$

The minimization of E clearly must be accompanied with a constraint that precludes solutions which yield filters other those that spike the wavelet. For example, a filter that reduces the wavelet to a step function or a filter with all zero coefficients are also consistent with minimizing the value of E. Possible constraints that will preclude these types of solutions include: (a) An energy constraint on the filter of the form

$$\overline{w}' w = 1. \tag{12}$$

and, (b) fixing one sample of the filter, so that

$$\overline{w}_j = 1 \tag{13}$$

for some sample j of the vector $\overline{w}$.

In the case of constraint (12), the derivation of the filter is straightforward and it can be easily shown [6] that the minimum of (10) subject to (12) is attained when $\overline{w}$ is chosen to be the eigenvector which corresponds to the smallest eigenvalue of the matrix $\boldsymbol{A}$. In the case of constraint (13) the derivation of the filter is slightly more involved [6] and provides the opportunity for minimizing E also with respect to the location j. The minimizing vector $\overline{w}$ of (10) subject to (13) can be derived as

$$\overline{w} = \sum_{i=1}^{W} \left(\frac{\frac{e_{ji}}{\lambda_i}}{\sum_{k=1}^{W} \frac{e_{jk}^2}{\lambda_k}} \right) \overline{e}_i \tag{14}$$

where j refers to the sample of $\overline{w}$ set equal to 1 (ie $\overline{w}_j = 1$) and e_{ji} is the jth element of the ith eigenvector $\overline{e}_i$ of the matrix **A**. The corresponding minimum of E as function of j simplifies to

$$E_j = \frac{1}{\left(\sum_{k=1}^{W} \frac{e_{jk}^2}{\lambda_k} \right)} \tag{15}$$

and then it is possible to choose j such that E_j is minimized over all possible values of j.

GENERALIZATION

Many signal processing applications in remote sensing can be described using the convolutional model given in (1). If there exists a relationship as in equation (3) between an arrival time t_k on the k^{th} sensor of the array and the corresponding arrival time t_0 on a reference sensor (which may or may not be a part of the array), then it would be possible to carry out the same mathematical steps in equations (3) to (11) to arrive at the matrix A necessary to derive the deconvolution filter coefficients. The only difference will be in the entries of the geometry matrix G in equation (8). An example of such an application would be the two-reflector geometry illustrated in Figure (2).

CONCLUSION

In this paper we considered a hands-off (i.e. no knowledge of the wavelet is necessary) deconvolution method in which the deconvolution filter is derived from the outputs of an array of geophones and the non-linearities introduced by the source-receiver geometry in the NMO correction process. The procedure exploits the fact that NMO corrected traces are more similar the shorter the wavelet is made by applying the inverse filter. Two possible constraints on the filter coefficients to insure the derivation of a spiking filter are discussed.

REFERENCES

[1] Robinson, E.A. and Durrani T.S. *Geophysical Signal Processing*, Prentice Hall, Englewood Cliffs, NJ, 1986

[2] Simaan, M. (ed), *Advances in Geophysical Data Processing- Two Dimensional Transforms*, Vol 2., JAI Press Inc., Greenwich, CT, 1985.

[3] Dunkin, J.W. and Levin, F.K., "Effect of Normal Moveout on a Seismic Pulse, *Geophysics*, Vol. 49, 1984, pp. 2109-2116.

[4] Akgul, T, El-Jaroudi, A., and Simaan, M., "Multi-Scale Deconvolution of Sensor Array Signals," *Signal Processing*, Vol. 57, No. 1, 1997, pp. 35-42

[5] Akgul, T, El-Jaroudi, A., and Simaan, M., "Multi-Scale Deconvolution of Sensor Array Signals Via Sum-of-Cumulants," *IEEE Trans. On Signal Processing*, Vol. 45, No. 6, 1997.

[6] Luenberger , D.G., *Optimization by Vector Space Methods*, John Wiley & Sons, New York, NY, 1969.

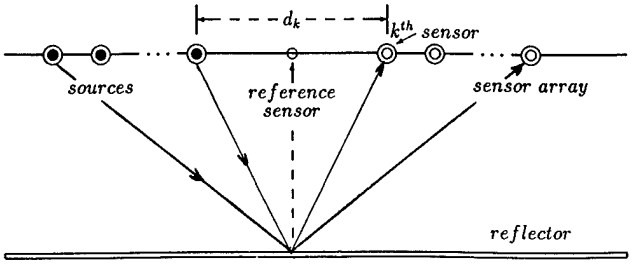

Figure 1. Common-depth point seismic acquisition geometry.

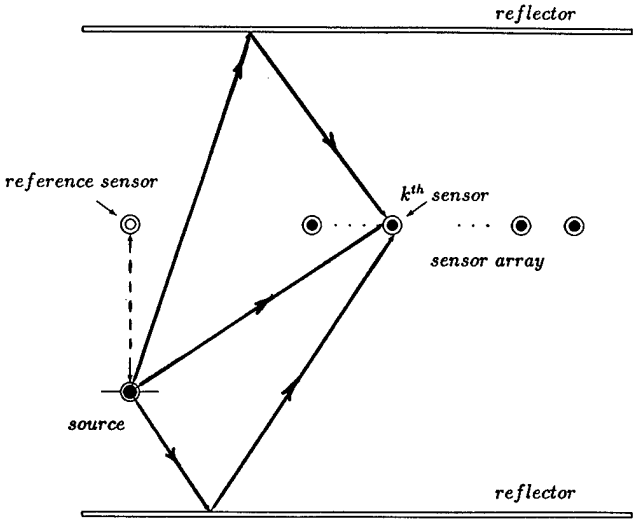

Figure 2. Two-reflector geometry

A Priori Information in Inverse Problems of Atmospheric Optics

Yu. M. Timofeyev*
Research Institute of Physics at St.Petersburg State University,
Ulyanovskaya 1, St.Petersburg-Petrodvorets, 198904, Russia,
tel.: +7-812-428-44-86, fax: +7-812-428-72-40, e-mail: tim@troll.niif.spb.su

Abstract – Classification of different *a priori* information used in inverse problems of atmospheric optics is performed and its influence on the accuracy of retrieving the atmospheric parameters is discussed.

When solving direct and inverse problems of atmospheric optics, one deals with the following parameters and characteristics (Table 1):

Algorithm of solving the direct problems of atmospheric optics may be represent by the following way:

$$X + A + G + S \Rightarrow J \qquad (1)$$

Classification of different inverse problems of atmospheric optics is given in Table 2 on the condition that a geometry of the medium is specified.

Table 1. Classification of parameters and characteristics

Parameter or characteristic	Examples	Notat.
Characteristics of radiation field	Stokes vector-parameter, radiance, etc.	J
Parameters of medium physical state	Temperature of the atmosphere and underlying surface; concentration of absorbing, scattering and radiating molecules and aerosol particles; wind velocity; soil moisture, etc.	X
Parameters of "radiation - medium" interaction	Einstein coefficients; absorption, scattering and emission coefficients; dispersion index, etc.	A
Boundary conditions	Solar radiation at upper boundary of atmosphere; radiance of underlying surface, etc.	G
Geometry of medium model	Plane atmosphere; spherical atmosphere	S

Table 2. Classification of inverse problems of atmospheric optics

Type	Preset values	Defined values	Remark
1	J, A, G	X	Retrieving the physical parameters of a medium
2	J, X, G	A	Retrieving the optical parameters of a medium
3	J, X, A	G	Retrieving the boundary conditions

1 type of the inverse problems involves different remote methods of deriving the physical parameters of the atmosphere and underlying surface.

2 type of the inverse problems is directed on determination of specified optical characteristics of the atmosphere. This model is traditional approach in practice of laboratory studies of optical characteristics of atmospheric gases.

3 type of the problems is formulated relative to boundary conditions. An example of the inverse problem of such kind is a task of defining the solar constant from ground-based or balloon measurements of direct solar radiation.

Remote methods of sounding the atmospheric and surface parameters represent a totality of a measurement device, various an *a priori* information and an algorithm of processing the measurement data (Fig.1). In physics-mathematical approach, a radiative transfer model is the basis for the remote methods. In this case, *a priori* information includes the following components:

- instrument characteristics (spectral and angular slit functions, the value and statistical structure of measurement errors, etc.);
- radiation transfer model, for example, radiative transfer equation in one or other form;
- quantitative characteristics of interaction between radiation and medium;
- measurement and medium geometry;
- boundary conditions.

*This work was supported in part by RFFI (Grant No. 97-05-65492)

0-7803-3836-7/97/$10.00 © 1997 IEEE

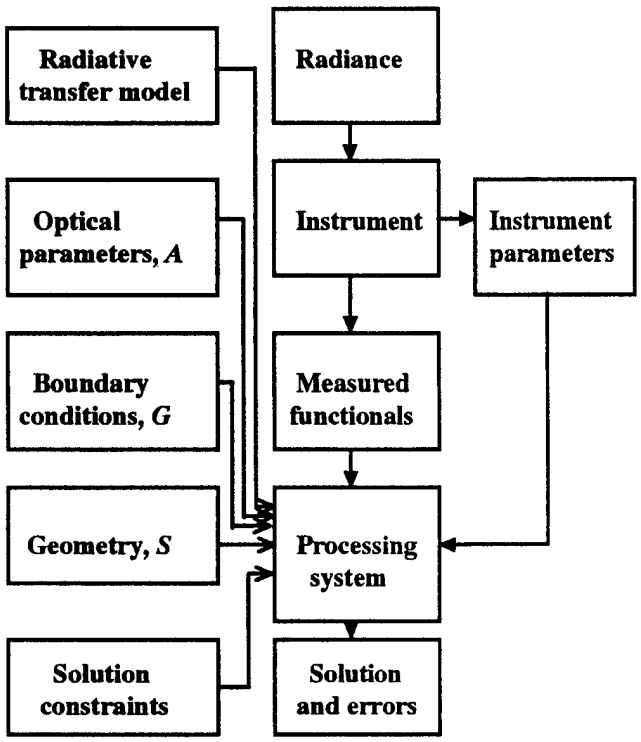

Fig. 1. Principal description of inverse method (1 type)

All the above components of inverse method define, to specific extent, the quality of remote sensing. The device characteristics do define, in great part, the information content of radiation measurements and hence an accuracy of remote sounding the atmosphere and underlying surface. But the quality of *a priori* information used influences the remote sensing accuracy not to a smaller degree. And the better is the measurement quality, the higher the requirements to the exactness of *a priori* information [1,2].

To analyze an influence of the *a priori* information on the accuracy of remote sensing, it is necessary to know the uncertainties of each specific its component represented in Fig.1. Then for obtaining the quantitative estimates of the *a priori* information impact, one can use the closed numerical experiments on solving the inverse problem with intoducing the various disturbances in the *a priori* information. The simplest approach to analyzing the *a priori* information influence is the calculations of the "effective" noise from the relations:

$$(A + \Delta A)\,\varphi = f + \varepsilon; \qquad A\varphi + \Delta A\,\varphi = f + \varepsilon \qquad (2)$$

Equations (2) describe the inverse problem in the operator form, f and ε are the measured radiation characteristics and measurement errors, respectively, A and ΔA are the exact operator of a direct problem and its disturbances and φ is sought function. Calculation of $\Delta A\varphi$ values and comparing those with the measurement errors give a possibility to estimate the degree of influencing one or other errors of the *a priori* information on the solution. More correct approach consists in the calculation of statistical characteristics of $\Delta A\varphi$ and calls for spatial, temporal, spectral and angular behavior of the ΔA operator disturbances. General consideration of this problem has been performed in [3,4].

Let us discuss the typical examples of the *a priori* information uncertainties and estimate their impact on the accuracy of atmospheric remote sensing.

Uncertainties in radiative transfer model. This model does not contain the noticeable errors only when using the transmittance method of atmospheric sounding. The LTE condition and the neglect of scattering effects are usual assumptions in the methods using atmospheric radiation measurements. The first of those, as shown in numerous works, may fail even in the stratosphere, for example, in the O_3 and NO absorption bands [5,6]. Neglecting the scattering effects may give the essential additional errors under conditions of high atmospheric turbidity in IR spectral range and of thick cloudiness and precipitation in microwave spectral range. Considerable uncertainties arise in UV and visible spectral ranges due to variety of the processes of transforming the solar radiation by molecular and aerosol scattering, multiple scattering and polarization, surface reflection and etc.

Uncertainties in spectroscopic parameters. The calculation of molecular absorption is an integral part of practically all remote sensing methods and demands the knowledge of numerous spectroscopic parameters: the spectral line positions, intensities, shapes and their pressure and temperature dependencies, line-mixing effect, etc. The well-known databases (HITRAN) give the values of spectral parameter uncertainties reaching to 20-40 % and more. Table 2 is clearly demonstrates the influence of these uncertainties on the accuracy of atmospheric remote sensing.

Table 2. Systematical errors of the CLAES remote sensing due to uncertainties of spectral parameters [7].

Parameter	Pressure, mb	Systematical error	Total system. error,
Temperature	0.46-100	1.2 -1.5 K	1.95 -2.5 K
$ClONO_2$	4.6 -100	20 -21.5 %	23 -100 %
HNO_3	3.0 -70	5.0 -8.5 %	8.1 -14.4 %
N_2O_5	1.5-3.16	9 %	14 -21 %
CH_4	0.46 -68	2.4 -8.6 %	11.0 -47 %
N_2O	1.0 -68	7.0 -9.5 %	2.1 -62.5 %
CF_2Cl_2	5.0 -90	10 -11 %	12.2 -22.3 %
O_3	0.46-100	4.5 -6.0 %	9.4 -18.3 %

As following from the above data, the uncertainties of spectroscopic parameters bring, in many cases, the major contribution in the total systematical error.

At present the remote sensing methods using not only radiative but physical models of atmospheric processes (radiative-physical inverse problems) has received wide recognition. For example, stationary equations describing the populations of exited molecular levels are widely attracted for interpreting the non-LTE radiation measurements of the upper atmosphere. There is a number of essential peculiarities of the non-LTE inverse problems: a) the number of parameters characterizing the atmospheric state is much more than in the LTE case (For example, in [8] 40 sought vertical profiles were determined for non-LTE atmosphere instead of 4 for similar task if the LTE conditions were provided); b) A new set of parameters (B) describing the processes of exciting and quenching the molecules have appeared. It is appropriate to formulate two new types (so-called radiative-kinetical) inverse problems of non-LTE atmosphere:

a) relative to the parameters of atmospheric physical state

$$J + A + G + B \Rightarrow X, \quad (3)$$

b) relative to the parameters B

$$J + A + G + X \Rightarrow B \quad (4)$$

The influence of amount and quality of *a priori* information on accuracy of retrieval under non-LTE conditions as great as it is in the above inverse problems.

Uncertainties in solution constraints. Necessity of such information is caused by the character of a Fredholm first-kind integral equation to which the majority of inverse problems are reduced [9]. Information on sought solution may be various - from severe constraints in the form of parametric solution to soft assumptions on solution smoothness and monotonicity. *A priori* information presents in inverse operator of the problem and impact on the estimate of solution. The smaller is the information content of the measurements, the greater is this influence. For example, the informativity of the MIPAS earth-limb radiation measurements (in 8-55 km altitude range) is high and methods of temperature retrieval, used various amount of the information (optimal estimation and global fit methods), lead to practically indentical results [10]. But the initial guess and *a priori* information on the estimate are very important in solving the small-informative problem of O_3 profile retrieval from the 9.6 μm outgoing nadir radiation measurements.

Summary. Remote sensing of the atmosphere and underlying surface is the combination of an instrument, various *a priori* information and an algorithm of data processing. To a considerable degree, an accuracy of remote sensing is defined by the amount and quality of the *a priori* information. To realize the potential capability of recent devices, it is necessary to assign the *a priori* information with high accuracy. At present, the uncertainties of its assignment bring the notable contribution in the total error of remote sensing. The new class of remote sensing methods - radiative-physical - involving the models of physical processes and as a result a great amount of additional *a priori* information. Effective application of these methods demands the relevant studies both the physical processes and the parameters defining those.

REFERENCES

[1] K.Ya. Kondratyev and Yu.M. Timofeyev, Meteorological Sounding of the Atmosphere from Space. Leningrad: Gidrometeoizdat, 1978, 280 pp. (in Russian).

[2] J.T. Houghton, F.W. Taylor, and C.D. Rodgers, Remote Sounding of Atmospheres. Cambridge: University Press, 1984,.426 pp.

[3] Yu.M. Timofeyev, and A.A. Yakovlev, "Influence of the uncertainties in atmospheric radiative model on the accuracy of thermal sounding from satellite", in Aviation and Space Meteorology, Leningrad: LGMI, No. 70, 1979, pp.10-26, (in Russian).

[4] V.P. Kozlov, "An stability of the solution of inverse problems of atmospheric optics relative to the kernal variations", in Aviation and Space Meteorology, Leningrad: LGMI, No. 70, 1979, pp.27-39, (in Russian).

[5] R.O. Manuilova, G.M. Shved, "The 4.8 and 9.6 μm O_3 band emission in the middle atmosphere", J. Terr. Phys., vol. 54, 1992, pp.1149-1168.

[6] J.A. Kaye, and J.B. Kumer, "Nonlocal thermodynamic equilibrium effects in stratospheric NO and implications for remote sensing, Appl. Opt., vol. 26, pp. 4747-4754, November 1987.

[7] Journ. Geoph. Res., vol. 101, 1996, pp. 9583-9602.

[8] Yu.M. Timofeyev, V.S. Kostsov, and H. Grassl, "Numerical investigations of the accuracy of the remote sensing of non-LTE atmosphere by space-borne spectral measurements of limb IR radiation: 15 μm CO_2 bands, 9.6 μm O_3 bands and 10 μm CO_2 laser bands", J.Q.S.R.T., vol. 53, 1995, pp. 613-632.

[9] A.N. Tikhonov, V.Ya. Arsenin, Methods of Solving the Ill-posed Problems, Moscow: Nauka, 1979, 285 pp., (in Russian).

[10] V.S. Kostsov, A.V. Polyakov, Yu.M. Timofeyev, Study for the Intercomparison between the Global Fit and the Optimal Estimation Methods in Case of the MIPAS Space Experiment, Final Report FZK Purch. Or. No. 315/20044710/IMK, 1997, unpublished.

IGARSS'97

1997 International Geoscience and Remote Sensing Symposium

03-08 August 1997

Singapore International Convention & Exhibition Centre

Technical Program

Interactive Area 28: Calibration

Some Issues on Calibration/Validation Algorithms of SSM/I Data

Ya-Qiu Jin
Wave Scattering and Remote Sensing Center
and Department of Electronic Engineering
Shanghai, China 200433

Abstract: Identification of atmospheric precipitation and earth surfaces and algorithms of the parameter retrieval have been extensively studied during the course of SSM/I Calibration/ Validation effort. However, we have found that some conventional algorithms are not proper in many applications. We have developed the vector radiative transfer modeling at SSM/I channels for earth surfaces such as snow/vegetation, rough sea surface, scattering media of sea ice, etc., and derived several new algorithms to invert some parameters from SSM/I dada. Our retrieval results are well compared with the ground truth measurements.

INTRODUCTION

Space-born microwave radiometers are primary tools for global surface monitoring because of the potential of microwave to observe the earth surfaces through clouds and to provide information of the internal properties of surface covers. One of the latest and most advanced passive microwave sensors is the DMSP SSM/I operated at seven channels (19, 37, 85 GHz with dual polarization and 22 GHz with vertical polarization only). Identification of atmospheric precipitation and earth surfaces and algorithms for the parameter retrieval have been extensively studied during the course of SSM/I Calibration/ Validation effort. However, we have found that some conventional algorithms are not proper in many applications. We have developed the vector radiative transfer modeling at SSM/I channels for earth surfaces such as snow/ vegetation, rough sea surface, scattering media of sea ice etc., and derived several new algorithms based on our modeling to invert geophysical and hydrological parameters from SSM/I dada. Our retrieval results are well compared with the ground truth measurements. In this paper, we introduce some approaches for retrievals of snow depth, atmospheric precipitation, sea surface wind speed, monitoring sea ice and floods.

RETRIEVAL OF SNOW DEPTH

Some algorithms for inverting snow depth (SD) and snow water equivalent (SWE) from satellite data have been empirically derived. For example, SD is inverted by the horizontal T_B gradient as

$$SD(cm) = 1.59(T_{B19h} - T_{B37h})$$

or SWE is estimated by the vertical T_B gradient

$$SWE = A_1 + A_2(T_{B19v} - T_{B37v}).$$

In fact, all coefficients in above approaches always show considerable regional variation due to different surface type, e.g. forest, pasture and crop canopy. We propose a mesh graph of two scattering indices

$SI_1 = T_{B22v} - T_{B85v}$ and $SI_2 = T_{B19v} - T_{B37v}$

which are calculated by the vector radiative transfer (VRT) modeling of snowpack/vegetation canopy for various snow depth, ice grain size etc. It takes into account regional snow morphology and land cover. When the SSM/I data is observed, its location in the mesh graph can indicate the estimation of SD. Our results compare well with the SSM/I data of the USA east coast January blizzard 1996. Fig. 1 shows a mesh graph derived by numerical VRT simulation of snow/vegetation canopy. Discrete points are the SSM/I data. Fig.2 shows a comparison of SD retrievals and ground truth data.

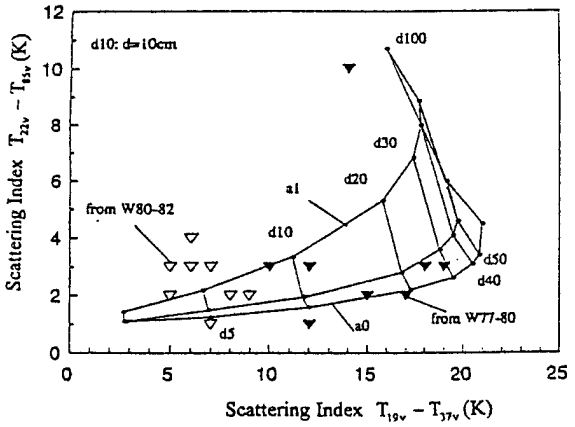

Fig.1 A mesh graph of two scattering indices.

RETRIEVAL OF PRECIPITATION

Precipitation is highly varied in time and space. Limited sampling by satellite observations might miss precipitation events. Also, the conventional algorithm of rain retrieval has not been well studied for light rain over land. As an example, rainfall lasted over half month of March 1996 in

0-7803-3836-7/97/$10.00 © 1997 IEEE

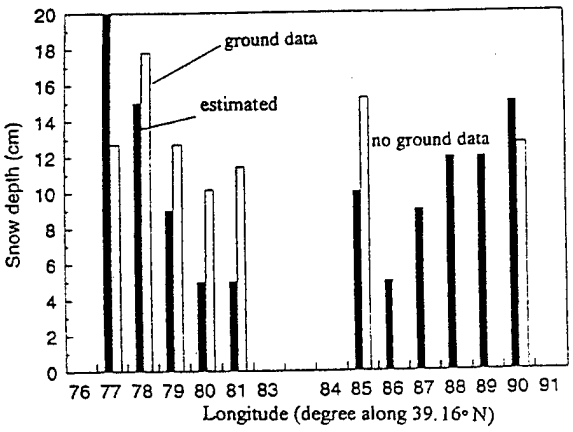

Fig.2 Retrieved results and ground-truth data.

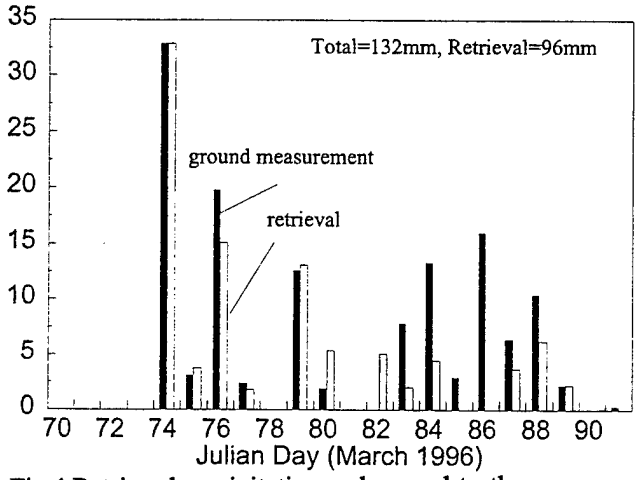

Fig.4 Retrieved precipitation and ground-truth.

Shanghai area was not detected by SSM/I data. We define a new index as

$$S_\upsilon = [R(t+\Delta t) - R] / \Delta t$$

where $R = T_{Bv} / T_{Bh}$ at $\upsilon = 19$ or 85 GHz

This index is the slope tangent of polarized TB (brightness temperature) ratio at the channels 19 or 85 GHz between observation time t+Δt and t. This locally-derived index can show the change of surface wetness after rains happening at previous time. Precipitation at time t might be inferred from variation of polarization ratio at time t+Δt. Fig.3 shows the SSM/I data of March 1996 in Shanghai area, which missed most of rains. Fig.4 shows retrieved precipitation and comparison with ground-truth data.

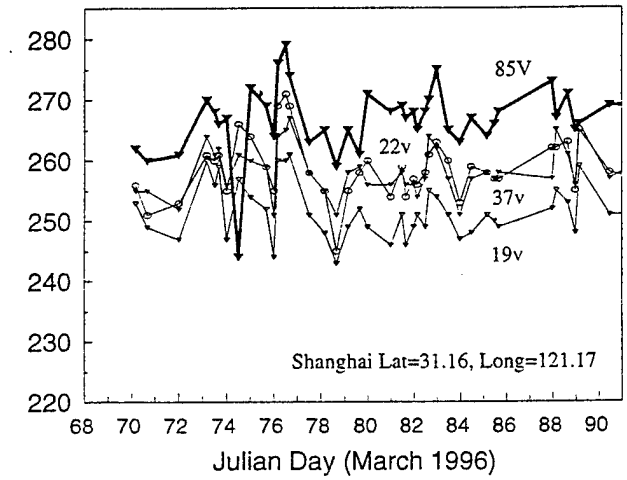

Fig.3 SSM/I Data of v-polarized TB.

RETRIEVAL OF SEA SURFACE WIND SPEED

A conventional formula to retrieve sea surface wind speed was derived from globally collected data by using statistical D-matrix method. It is a empirical combinations of 4-channels TB data. No physics can explicitly illustrate each term of this formula and no rule can guide how the coefficients can be re-calibrated if the sea status is changing.

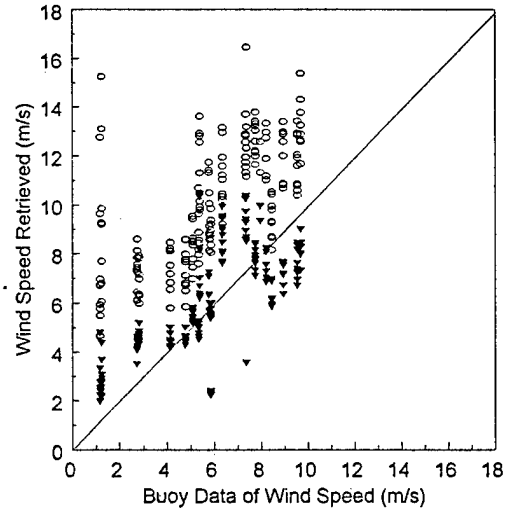

Fig.5 Retrieval of sea surface speeds.

We derived a new formula for retrieval of wind speed as

$$u = \frac{1}{K}[-\ln R_0 + \ln(\frac{T_0 - T_{Bv}}{T_0 - T_{Bh}} + \Delta_f]$$

where K, T_0, R_0, Δ_f take into account the atmospheric opacity, effective temperature, the ratio of v,h- polarized reflectivity of smooth sea surface and effect of white foams, respectively. We use the observation at 37GHz to retrieve the wind speed. Fig.5 shows the results by using our formula (black points) and conventional algorithm (circle points) and comparison with the buoys data.

MONITORING SEA ICE

A flow chart of brightness temperature index (TBI) was developed as a rule for monitoring sea ice. Another approach as available is the ocean scattering index (OSI)

derived by regression method. However, it was found that both TBI and OSI cannot well applied to monitoring sea ice of the Bohai Sea of north China. Fig. 6 shows temporal variation of OSI of the Bohai Sea. It is a mistake that all occurrences of OSI>70 were detected as sea ice. We developed the radiative transfer modeling for sea ice. The scattering and polarization indices,

$SI = T_{B22v} - T_{B85v}$, $PI = T_{B19v} - T_{B19h}$,

can be numerically simulated for physical variation of sea ice. Numerical simulations categorize the SI/PI graph. Sea ice can be detected by the location of the SI/PI observations. Fig.7 shows our SI/PI graph, which is well validated by the SSM/I and ground truth observations of the Bohai Sea.

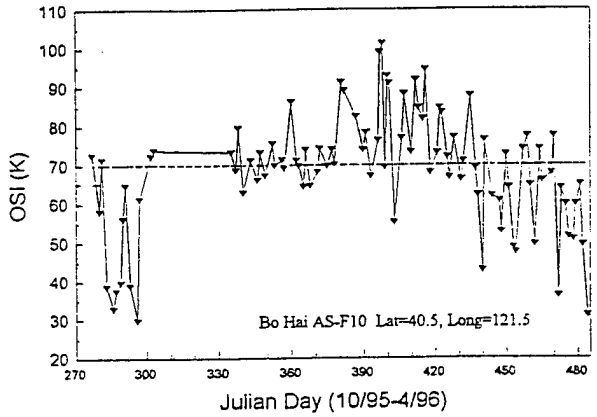

Fig.6 Temporal variation of OSI of the Bohai Sea.

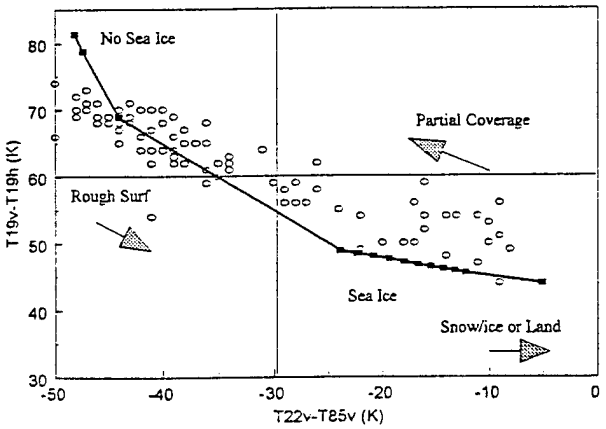

Fig.7 The SI/PI graph derived from VRT model.

MONITORING FLOODS

We propose a flooding index defined as $FI = T_{B37h} - T_{B85h}$ for monitoring floods during heavy rain time. Sustained water and floods show the surface emission from water bodies such that FI is significantly decreased and might become less than a certain negative value F_0. This negative value is a regional constant and can be determined in advance. As $FI < F_0$, flooding is detected. Fig.8 shows the flooding index FI, and other two scattering and polarization indices from January to July 1996 in China Wuhan area (30.5°N,114.5°E). The floods in July can be detected by the index FI.

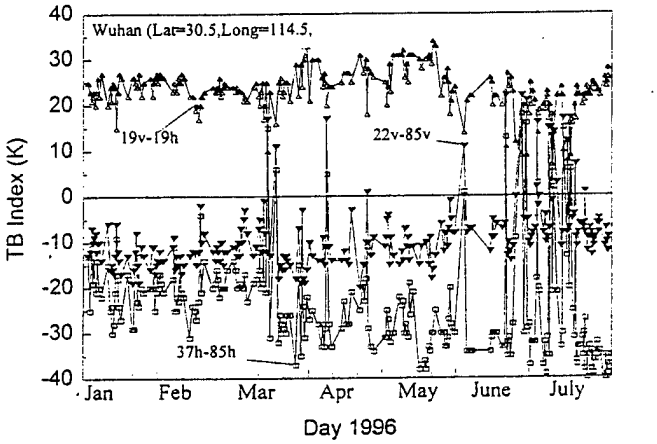

Fig.8 The flooding index FI, and other two scattering and polarization indices for flooding detection.

CONCLUSIONS

We have shown that some conventional algorithms of SSM/I data calibration/ validation are not proper in many applications. We have developed the VRT modeling at SSM/I channels for earth surfaces such as snow/vegetation, rough sea surface, scattering media of sea ice, etc., and derived several new algorithms to invert some parameters from SSM/I dada. Our retrieval results are well compared with the ground truth measurements.

ACKNOWLEDGMENT

This work was supported by the China National Science Foundation and the Shanghai Research Center for Applied Physics.

REFERENCES

[1].Hollinger J., DMSP SSM/I Calibration/Validation", Naval Research Laboratory, Washington D.C., Vol.2, 1992.

[2].Jin Y.Q., Remote Sensing of Environment, 1997 in press.

[3].Jin Y.Q., International Journal of Remote Sensing, 1997 in press.

[4].Jin Y.Q., Acta Oceanography, 1997 in press.

Calibration Experiments of the CRL/NASDA X/L-band Airborne Synthetic Aperture Radar

Makoto Satake*, Tatsuharu Kobayashi, Harunobu Masuko and Masanobu Shimada†
Communications Research Laboratory († National Space Development Agency of Japan)
Koganei, Tokyo 184, Japan
*** telephone: +81-423-27-6101, facsimile: +81-423-27-6110, e-mail: satake@crl.go.jp**

Abstract-- Communications Research Laboratory (CRL) and National Space Development Agency of Japan (NASDA) have jointly developed a new airborne synthetic aperture radar system operated at X-band and L-band. Both the X and L-band radar's have polarimetric capability and the X-band one has interferometric capability. The radar system is on board a Gulfstream-2 aircraft whose navigation altitude is 20000 to 40000 feet. Following to system performance test flights in August 1996, a series of calibration flights is ongoing. For calibration of the X-band SAR, we have developed an active radar calibrator (ARC) in CRL. The ARC is designed to return H and V radar signals simultaneously with two transmission antennas for polarimetric calibration. It will be employed, along with several corner reflectors, in calibration experiments planned in May and October 1997 at Tottori dune area in Japan. In this paper, we present plan of the experiments and procedure to calibrate the SAR system, focusing on the X-band SAR.

INTRODUCTION

It is becoming more important to monitor natural hazards such as floods, volcano eruption, earthquake, ocean pollution, not only for damage investigation but for warning. Airborne imaging radar has great potential to observe natural hazards, because it can make prompt and wide observation in day and night. As a joint project of Communications Research Laboratory (CRL) and National Space Development Agency of Japan (NASDA), we have recently developed a multifrequency (X/L-band) synthetic aperture radar (SAR) system that can observe earth surfaces in detail with high resolution (1.5m). Both the X and L-band radar's have polarimetric capability to transmit and to receive both horizontal and vertical (H/V) polarization components (amplitude and phase), while only the X-band has interferometric capability receiving surface echoes by two antennas with 2.3 meter cross-track separation. Prior to the data distribution among science users, calibration of the radar system is necessary to make the data quantitatively qualified.

After system performance test flights in August 1996, a series of calibration flights of the SAR system is ongoing. In November 1996, a calibration experiment was made with corner reflectors (CR's) and L-band active radar calibrators (ARC's) that NASDA had developed for JERS-1/SAR sited in a dry riverbed in Niigata, Japan. Meanwhile, we measured system losses of the radar's equipped on the airplane. For the X-band, an ARC and CR's have been developed by CRL those are to be employed in calibration experiments planned in May and October 1997 at Tottori Dune, Japan. We will make the SAR system calibrated with results of those measurements. In this paper, we present plans of the experiment at Tottori Dune, and address procedure of calibration of the SAR system, with emphasis on the X-band.

CRL/NASDA X/L-BAND AIRBORNE SAR

Features of the SAR system are summarized in Table 1 and its simplified block diagram is shown in Fig.1. Required calibration accuracy is 0.5 dB of power and 5 degrees of phase both for X and L-band. NASDA has main responsibility of developing and maintaining the L-band and CRL for the X-band, although they are operated together in principle.

CALIBRATION SITE

Calibration experiments, mainly for the X-band, are planned in spring and fall, 1997, in Tottori Dune, the largest dune area in Japan. We chose it because sand area is expected to show very low cross section ($\sigma 0 \approx -20$dB; at X-band, ~50 deg. incidence angle [1]). It is preferable as background to place reflectors over.

We use an ARC and 20 CR's (4 sizes by 5) for X-band, and two CR's for L-band. Planned arrangement of those reflectors is shown in Fig.2. That many CR's are used to obtain more reliable (statistically accurate) data for radiometric calibration. CR's of a size are scattered so that all the 4 sizes could be included even in a part of the array.

CALIBRATION TARGETS

Corner Reflector (CR)

We use triangle trihedral CR's of four different leg lengths (10, 15, 20, 30 cm) for the X-band. Table 2 shows their calculated $\sigma 0$, along with those of square trihedrals used for the L-band. Their $\sigma 0$ are about 10 to 30 dB higher than the background $\sigma 0$. Because of high resolution of the X-band SAR rather small size CR is of use, which eases the deployment of the reflectors. The 3-dB beam width of the triangle trihedrals is so broad as 40 degrees [2] that error of $\sigma 0$, if the alignment error is within 3 degrees, may be less than 0.05 dB assuming Gaussian beam.

Active Radar Calibrator (ARC)

An ARC has been developed for the X-band SAR calibration. Its simplified block diagram is shown in Fig. 3 and main parameters in Table 3. For polarimetric calibration, two antennas are used to transmit both horizontal (H) and vertical (V) polarized signals. For the reception, a

0-7803-3836-7/97/$10.00 © 1997 IEEE

single antenna is used to receive either H or V signal, switched by rotating the antenna 0 to 90 degrees.

CALIBRATION PROCEDURE

We can consider calibration of the SAR system divided into two parts: Radiometric calibration, regarding absolute amplitude, and polarimetric calibration, regarding relative amplitude and phase.

Radiometric Calibration

Radiometric calibration is to relate image data number (quantized received power, P) with normalized radar cross section $\sigma 0$, that is, to decide constant K and a noise component N in

$$\sigma 0 = K P + N. \quad (1)$$

For this purpose we use SAR data of corner reflectors and of internal noise measurement mode.

Polarimetric Calibration

We use a model of polarimetric measured matrix, M (amplitude and phase), expressed as a product of the target matrix (S) with transmitting and receiving system matrices (T, R), after van Zyl [3] :

$$M = [R^t]\,[S]\,[T], \text{ or}$$

$$\begin{pmatrix} Mhh & Mvh \\ Mhv & Mvv \end{pmatrix} = \begin{pmatrix} 1 & \partial 1 \\ \partial 2\, f1 & f1 \end{pmatrix} \begin{pmatrix} Shh & Svh \\ Shv & Svv \end{pmatrix} \begin{pmatrix} 1 & \partial 4 \\ \partial 3\, f2 & f2 \end{pmatrix} \quad (2)$$

where

$\partial 1$, $\partial 2$: HV, VH cross-talk of R,
$\partial 3$, $\partial 4$: HV, VH cross-talk of T,
$f1$, $f2$: Channel imbalance btwn H and V, of R, T.

The ARC is used to make polarimetric calibration (to resolve ∂'s and f's). To obtain the 6 unknowns in (2), we should operate the ARC by a pair of two modes following:
(A1) Receive H- Trans. H and V (Shh=Shv=1, Svh=Svv=0)
(A2) Receive V- Trans. H and V (Svh=Svv=1, Shh=Shv=0)
or
(B1) Receive H- Trans. V (Shv=1, Shh=Svh=Svv=0)
(B2) Receive V- Trans. H (Svh=1, Shh=Shv=Svv=0).
That means we need two repeat-pass SAR observations over the ARC.

We should notice that the ARC's scattering matrix is practically not ideal as above but deteriorated by some cross-talk and imbalance just like the SAR system in (2). However they could be precisely measured beforehand.

FUTURE WORK

Results of the calibration experiments should be examined to be presented in another paper.

REFERENCES

[1] F. T. Ulaby and M. C. Dobson, Handbook of radar scattering statistics for terrain, Artech House, 1988.
[2] G. T. Ruck, ed., Radar Cross Section Handbook, Plenum Press, New York, 1970.
[3] J. J. van Zyl, "Calibration of polarimetric radar images using only image parameters and trihedral corner reflector responses", IEEE Trans. GE-28, pp 337-348, 1990.

Table 1 Features of the CRL/NASDA Airborne SAR system.

Frequency	X-band (9.55GHz)	L-band (1.27GHz)
Antenna - Type - Length x Width - Incidence Angle	 Slotted Waveguide 1.0 m x 0.19 m (x3) 10 ~75 deg. Var.	 Microstrip 1.7 m x 0.7 m 20 ~ 60 deg. Fix
Transmission (H/V pol.) - Power (Peak) - Pulse Width - Bandwidth	 10 kW 10 µsec 100 MHz	 3.5 kW 10 µsec 50 MHz
Noise Equivalent NRCS (typ.)	≈ –30 dB (HH)	≈ –30 dB (HH)
Calibration Requirements **- Radiometric Accuracy** **- Phase Accuracy**	 **≤ 0.5 dB** **≤ 5 deg.**	 **≤ 0.5 dB** **≤ 5 deg.**
Slant Range Resolution Azimuth Resolution (4-Look)	1.5 / 3 m 1.5 / 3 m	3 m 3 m
Data Recording - Sampling Rate - Quantization (I and Q) - Data Rate [# of Recorders]	 123.45 MHz 8 bits 512 Mbps [2]	 61.7 MHz 8 bits 256 Mbps [1]
Interferometry - Base Line - Topographic Accuracy	 2.3 m (max) < 2 m (rms)	 N/A
Airplane - Model - Navigation Altitude [Speed]	 GULFSTREAM-II 6,000 ~ 12,000 m [200 ~ 250 m/s]	

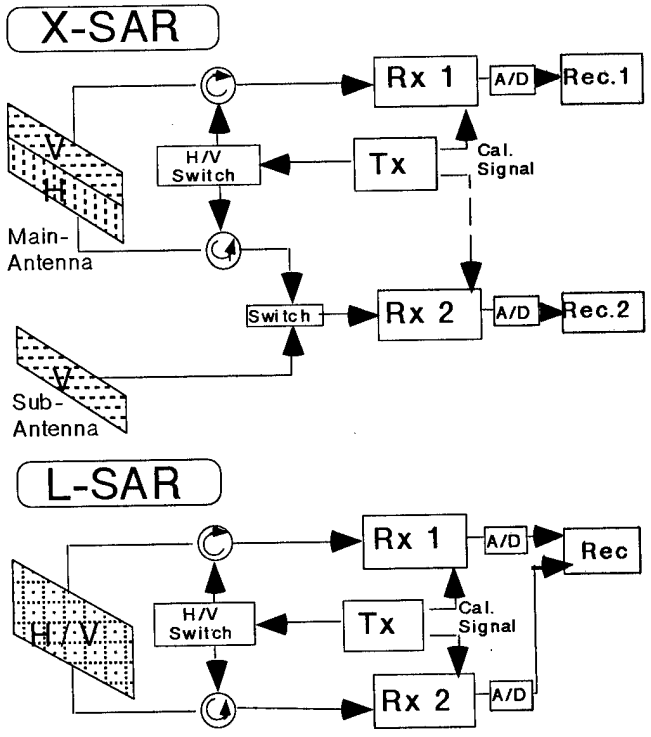

Fig.1 Block diagram of SAR system.

Table 2 Calculated cross sections of corner reflectors: triangle trihedral for X-band (assuming resolution of 1.5m by 1.5m) and square trihedral for L-band (3m by 3m). *Italic type* shows values might be out of the useful range.

Triangle Trihedral	X-band		*L-band*	
Size	σ [dBm2]	σ 0 [dB]	*σ [dBm2]*	*σ 0 [dB]*
0.10 m	-3.7	-7.2	*-21.2*	*-30.7*
0.15 m	3.3	-0.2	*-14.2*	*-23.7*
0.20 m	8.3	4.8	*-9.2*	*-18.7*
0.30 m	15.4	11.9	*-2.1*	*-11.6*
Square Trihedral	*X-band*		L-band	
Size	*σ [dBm2]*	*σ 0 [dB]*	σ [dBm2]	σ 0 [dB]
0.60 m	*36.8*	*33.3*	19.3	9.8
0.85 m	*42.8*	*39.3*	25.3	15.8

Table 3 Main Parameters of X-band ARC.

Frequency	9.4 ~ 9.7 GHz
Required σ0	-10 ~ +20 dB·
Antenna	Square Horn 1 for Rx and 2 for Tx
3-dB Beamwidth	≈ 30 degrees
Polarization - Reception - Transmission	 0° (H), 45° (H and V), or 90° (V) 0° (H) and/or 90° (V)

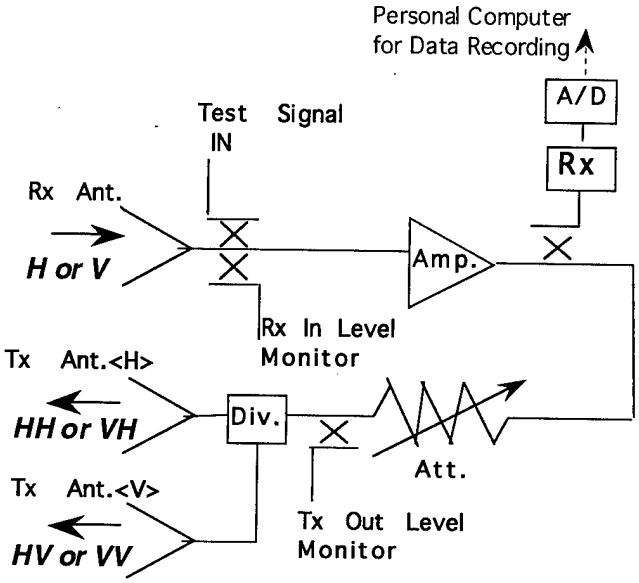

Fig. 3 Block diagram of ARC.

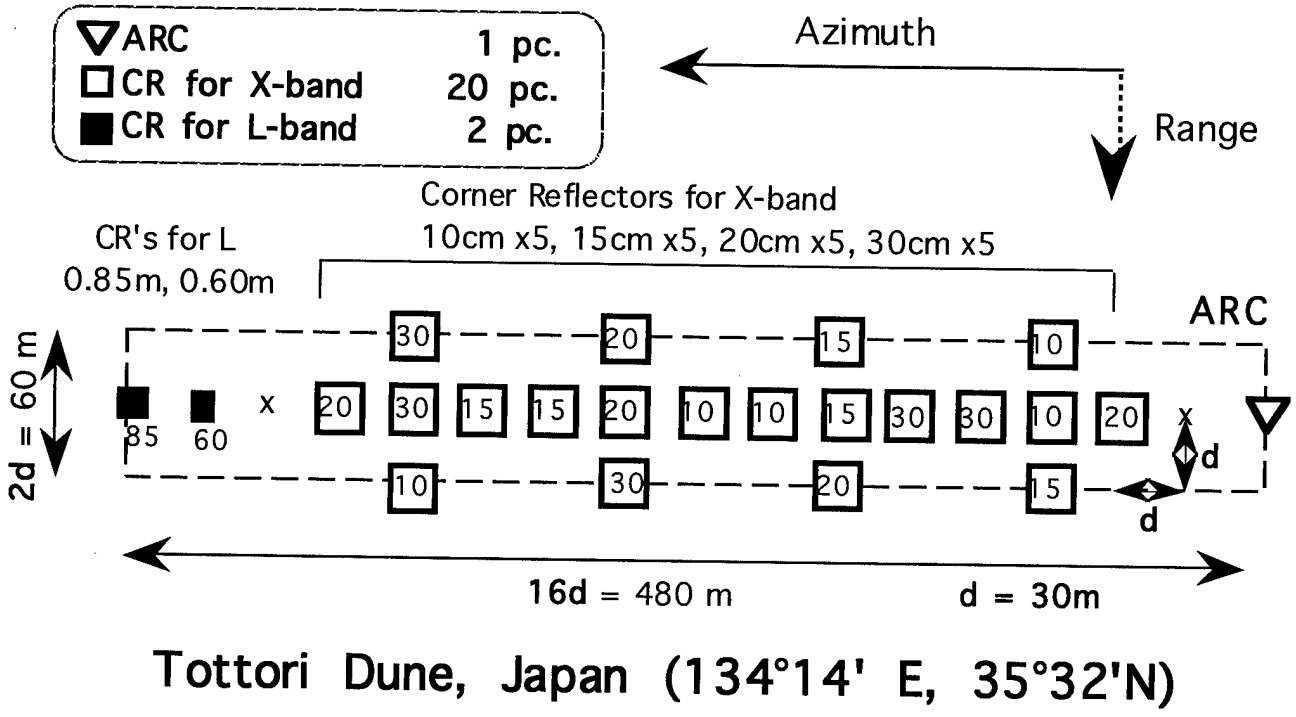

Fig. 2 Calibration target arrangement in Tottori Dune experiment.

IGARSS'97

1997 International Geoscience and Remote Sensing Symposium

03-08 August 1997

Singapore International Convention & Exhibition Centre

Technical Program

Interactive Area 29: Education and Information Systems

Meteorological Satellite Image Service via WWW

Ho-Geun Lee

GIS Lab./Systems Engineering Research Institute
P. O. Box 1, Yusung, Taejon 305-600, Korea
Tel: +82-42-869-1579, FAX:+ 82-42-869-1479
E-mail:leehg@seri.re.kr

Abstract -- This paper describes the database service of the GMS/WEFAX imagery based on the WWW. The WWW services basically display and animate the value-added images of the GMS/WEFAX. The GMS/WEFAX imagery types(Infra-Red, Visible, and Water Vapor) can be provided on a web browser. This is the integrated system that the receiving system, called WADIPS is directly connected with server Workstation and images transferred from WADIPS to server change into graphic formats that are for general service on WWW. In addition, multimedia functions can service in this system. The function of text service in Web browser is basic and the function of audio service is almost education for the system. Especially, image service formats in the system are GIF and MPEG. Binary WEFAX images received automatically from the WADIPS change into GIF and make the MPEG file by the encoder. Therefore, users can access the value-added images of the GMS/WEFAX in near-real time through the World Wide Web easily.

Introduction

Recently, it has been well recognized that the satellite remote sensing data is important for monitoring of environmental changes and protecting properties from the natural disasters [3]. However, there are several difficulties to use these data for the real applications : expensive cost to buy the receiving system, massive data, hard to process the images, to make the value-added data that specific techniques are necessary.

Nevertheless, the GMS (Geostationary Meteorological Satellite) /WEFAX (Weather Facsimile) among the meteorological are widely used for predict the weather or protect the natural disaster. It is also difficult to get the images from the GMS/WEFAX receiving system because of the expensive cost to buy the receiving system.

Due to the rapid increase in the demand and the buying difficulties of the meteorological satellite system, it is recognized that the computer network like the WWW(World Wide Web) will make an important contribution to promoting the application of satellite data. The WWW becomes very popular and many people can easily access the data on a remote site. WWW is used from Personal Computer to Workstation, and it has become also easy to build a multimedia environment, which is merged with text, sound, and visual images.

The service system for the meteorological satellite imagery is introduced in this paper, providing the updated imagery of the GMS/WEFAX in near-real time through the WWW. If clients have web browsers such as Netscape or NCSA navigator, client can be access the system. Also if clients are equipped with multimedia functions like MPEG(Motion Picture Experts Group) utility and audio tools, it is possible to make images animate and provide additional sound information.

The Meteorological Satellite Image Service System

The system is consisted of the automatic receiving and data processing part and the service part on the World Wide Web. The GMS/WEFAX image types(Infra-Red, Visible and Water Vapor Image) can be provided on a web browser [2], [6], [8]. The WWW services basically display and animate the value-added images of the GMS/WEFAX. The configuration of the system is shown in Fig. 1. The GMS/WEFAX images are received in the Receiving of the GMS/WEFAX images part

0-7803-3836-7/97/$10.00 © 1997 IEEE

and The images are processing to service in the Image Processing part, and The images are serviced in Internet Service part.

Automatic Data Receiving and Processing System of the GMS/WEFAX Images

The system, called WADIPS(WEFAX and APT Data Integrated Processing System), which was developed on IBM Personal Computer in 1992, was partly modified to automatically transfer the received images every hour to the meteorological satellite image server [1], [4], [5].

The WADIPS, which had been composed of antenna, IBM Personal Computer, image receiving software, and image transfer software to Workstation was partly modified and simplified to transfer the received images to the Image Information Server for network service(Fig. 2).

The WWW Service

WWW which has spread widely in these days is suitable for this system. NCSA or Netscape has provided a common environment to use the Internet. It has become very easy to built a multimedia environment, which is merged text, image, and sound.

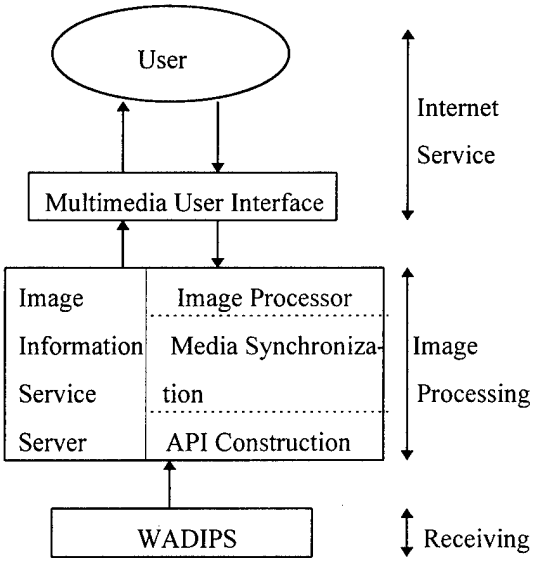

Fig. 1. Configuration of the Meteorological Satellite Image Service System.

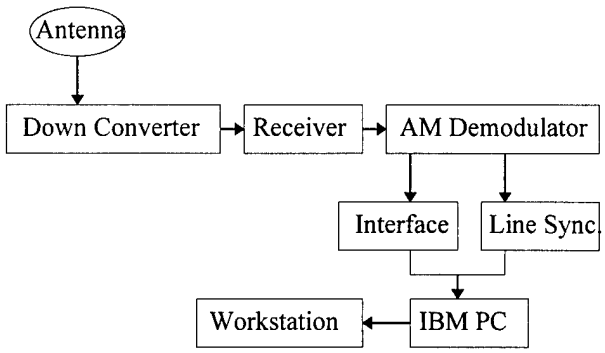

Fig. 2. Block Diagram of the WADIPS.

In the system , the method to search data based on quicklook image reduced from original images is useful. There are pages where users can search by browsing the past 1hour at once. Moreover, if it is equipped with multimedia functions, like a MPEG utility and audio tools, users can animate the images and hear a brief description of the system. An example of the quicklook images, which are the value-added one is shown Fig 3.

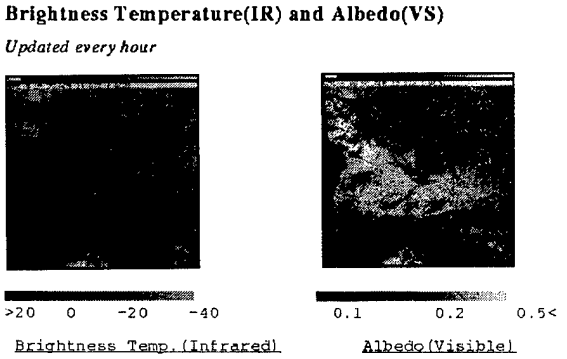

Fig. 3. An Example of the value-add images(Apr. , 1996)

Multimedia Service

As mentioned above, multimedia functions can service in this system. An example of text service in the web browser is Fig. 4. The audio service function is almost education that is for overview of the system and general of the satellite. Especially, image service formats in the system are

GIF(Graphics Interchange Format) and MPEG. The available images on the Web page are shown in Fig. 4. Original image is 2 bit binary data. Binary WEFAX Images received automatically from the WADIPS change into GIF every hour and make the MPEG file by the encoder.

The Berkley MPEG encoders are used for generation of the MPEG image [7]. However, parameter-file of the encoder must have been defined before the encoder was executed. A description of the parameter-file options is available in sequential encoding. In the following, the each parameter among the parameter file is describe.

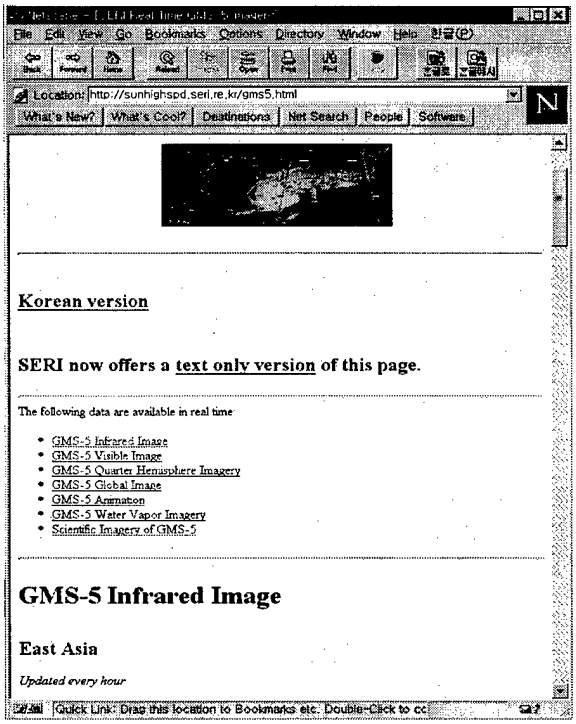

Fig. 4. Available Images on the Web Page.

- Q-Scale : The quantization scale values(Q-Scale) values can be set separately for I, P, and B frames. The minimal number 1 in all three cases is selected because of better quality.

- Search Techniques : Subsample is selected in P-frame and simple is selected in B-frame because of better compression, faster execution, and better quality.

- GOP : A Group of Pictures(GOP) is a roughly independently decodable sequence of frames. This MPEG video stream is made of 10 GOPs.

- Slice : A slice is an independently decodable unit in a frame. We just use one slice per frame.

- Search Window : We used half pixel motion vector because it results in both better quality and better compression. Number of range is set to 10 pixels.

- IPB Pattern : We can set the sequence of I, P, and B-frames. Because the pattern affects speed, quality, and compression, we selected the I-frame.

- Specifying Input Files : We selected the PPM and convert the input format into GIF which is one of base file types.

- Original or Decoded : We selected the original frame because the quality is not good enough.

If clients have web browsers such as Netscape or Mosaics, clients can be connect the browser of the server system in near-real time. Also If it is equipped with multimedia functions, MPEG utility and audio tools, it makes MPEG files animate and provides sound function to hear a description for the system. The user brings up our Web pages at: http://sunhighspd. seri.re.kr.

Conclusions

The meteorological satellite image(GMS/ WEFAX) service system, which is consisted of the automatic data receiving and processing part and the service part are developed. The system provides the updated GMS/WEFAX imagery in near-real time through the World Wide Web. The following images are available :

- GMS-5/WEFAX infra-red imagery
- GMS-5/WEFAX visible imagery
- GMS-5/WEFAX water vapor imagery

If it is equipped with multimedia functions like a MPEG utility and audio tools, it makes MPEG files animate the value-added images and provide sound function to hear a description for the system.

The more the number of WWW users will increase, the more such value-added images will be needed in near future.

References

[1] Gi Joon Yun, Kyoung Yoon Park and Myoung Seok Suh, "Development of the GMS/WEFAX Receiving and Image Processing System Using PC (I)", J. of the Korean Society of Remote Sensing, vol. 9. no. 1, 1993.

[2] Hee-Hoon Lee, Mi-Ja Lee, "The Observational Characteristics of the GMS-5 and GOES-8", Proceedings of Kor. Met. Soc. Spring Conference, 1995.

[3] M. Takagi, "Earth Environmental Remote Sensing and Image Processing", Computer Vision, 94-8, 1995.

[4] Ho-Geun Lee, Gi Joon Yoon, Myoung Seok Suh, and Kyoung Yoon Park, "Development of the Meteorological Satellite Image Service System", Proceeding of Korea Society of Remote Sensing pp. 190-193, 1996.

[5] Myoung Seok Suh, Kyoung Yoon Park, Gi Joon Yun, and Jong Hyun Park., "Development of the GMS/WEFAX Receiving and Image Processing System Using PC (II), J. of the Korean Society of Remote Sensing, vol. 9. no. 1, 1993.

[6] Murayama, "The GMS User's Guide", 1990.

[7] Plateau Research Group, "Berkeley MPEG-1 Video Encoder User's Guide", 1995.

[8] Seunghee Sohn, Miseon Lee, Chunsik Lee, Aesook Suh, "Estimation of Precipitation Water from GMS-5 Split Window Channels", Proceeding of Korea Society of Remote Sensing , pp. 171-176, 1996.

IGARSS'97

1997 International Geoscience and Remote Sensing Symposium

03-08 August 1997

Singapore International Convention & Exhibition Centre

Technical Program

Interactive Area 30: Wavelet Techniques in Remote Sensing

Wavelet Techniques applied to Lidar Temperature Profiles in the Middle Atmosphere to study Gravity Waves

Fabrice Chane-Ming, Franck Molinaro, Jean Leveau
Laboratoire de Physique de l'Atmosphère, Université de la Réunion
15 Av. René Cassin, BP 7151, 97715 SAINT DENIS CEDEX 9, FRANCE
Tel : (262) 93-82-39 Fax : (262) 93-81-66 e-mail : fchane@univ-reunion.fr

Abstract -- This paper puts forward wavelet based tools such as continuous wavelet transform, multiresolution and wavelet packet methods to study gravity wave motions and extract vertical characteristics (wavelength, phase speed) versus time and height in the middle atmosphere (30-60 km height) from vertical temperature perturbation profiles provided by a Rayleigh Lidar. Different dominant quasi-monochromatic structures with downward phase progres sion inferior to 1m/s are identified and extracted to be studied separately. Wave dissipation is observed in the stratopause with production of short waves less than 2 km at the boundary of the lower mesosphere. Longer waves have smaller phase speed than shorter waves.

1. INTRODUCTION

Since May 1994, a perform Rayleigh Lidar, with a Nd: Yag laser emitter, provides temperature measurements in the middle atmosphere at Réunion island (21°S, 55°E) located in the southern intertropical region. High time and spatial resolution of Lidar observational data enable to catch gravity wave patterns propagating vertically through the stratospheric and mesospheric regions.

Recent studies based on experimental data and theories put the stress on gravity wave energy contribution in the upper atmospheric circulation. Gravity waves are now recognized to be mainly generated by lower atmospheric forcings and transport energy upwards in the mesosphere [1]. The spectrum continously varies with height due to wave propagation processes as amplification, reflection, intermodulation, dissipation which may be responsible to the presence of observed dominant modes with increasing height. Lidar instrument appears to be useful to learn more about gravity wave characteristics and behavior in particular in the southern intertropical middle atmosphere where a lack of experimental data is noticed.

This paper is intended to present some wavelet technique capabilities (continuous wavelet transform, multiresolution analysis and wavelet packet decomposition) applied to Lidar temperature perturbation profiles associated to gravity wave structures to study time and spatial evolution of gravity wave parameters as vertical wavelength, phase speed and energy localisation in the middle atmosphere from 30 to 60 km height.

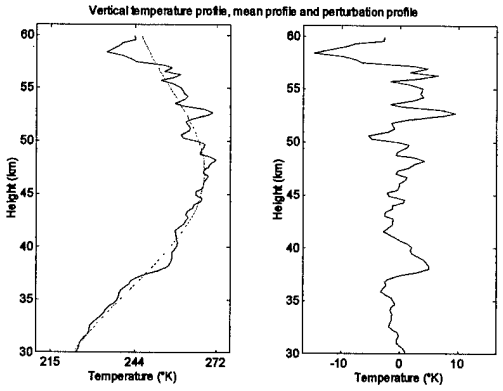

Figure 1: Averaged temperature profile, mean profile and 30-min integrated perturbation profile with 300-m spatial resolution on June 21 in 1994.

2. TEMPERATURE FLUCTUATION PROFILE

Fluctuations associated to gravity wave motions can be observed on vertical temperature profiles deduced from Lidar measurements and are extracted by substraction to the raw vertical temperature profile the mean vertical profile. The mean vertical temperature profile results from the application of a lowpass filter with a cutoff of 12 km vertical wavelength limiting the vertical wavelength space to our domain of interest. Vertical temperature profiles on which this study is based have 300-m vertical spatial resolution and are the result from 30-min time integration (Fig.1).

3. WAVELET TOOLS

3.1 Continuous Wavelet Transform

Originally, Continuous Wavelet Transform (CWT) was intuitively introduced by Gaupillaud, Grossmann and Morlet [2]. CWT coefficients are defined as projection terms of the studied signal on a set of functions deduced from a scale and shifted analysing or 'mother' wavelet :

0-7803-3836-7/97/$10.00 © 1997 IEEE

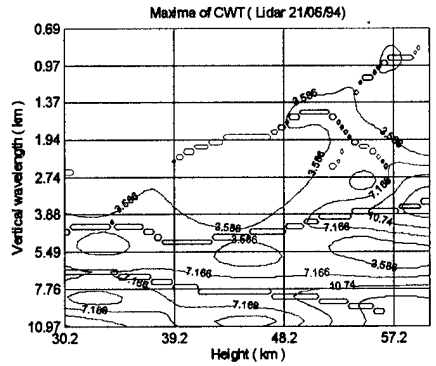

Figure 2: Contour lines of CWT modulus and extracted spectral lines show 3 dominant wavelike structures with 1.3-2, 3.5-5 and 7-11 km vertical wavelengths.

$$CWT(a,b) = \int f(t)\,\bar{g}_{ab}(t)\,dt = f(b) * \frac{1}{\sqrt{a}}\bar{g}\left(\frac{-b}{a}\right)$$

$$g_{ab}(t) = \frac{1}{\sqrt{a}}g\left(\frac{t-b}{a}\right)$$

with a, b : scale-time parameters
* : convolution product - : conjugaison
f : analysed signal g : 'mother' wavelet

Thus, CWT is well-suited to analyse scale features along the signal and provides time-scale diagrams or in our case altitude-wavelength diagrams [3]. In this study, Morlet wavelet, numerically admissible, is used. Essential information lies in CWT 'skeleton' or local maxima (Fig.2 and Fig.3).

3.2 Multiresolution and Wavelet Packet Analyses

Multiresolution analysis (MRA) is viewed as the application of a filter bank associated to orthonormal wavelet functions. It is constituted by a set of iterated filters spaced into octave bands over frequency space which allows perfect extraction of scale structures [2].

Thus, the original signal *s* is successively broken down into approximations *a* and details *d* at different scales or at each iteration i (Fig.4).

$s \cong d_1+d_2+d_3 \ldots +d_i+a_i$

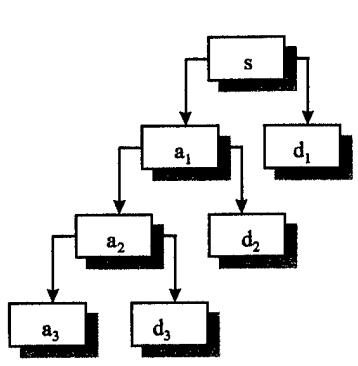

Figure 4: MRA decomposition tree.

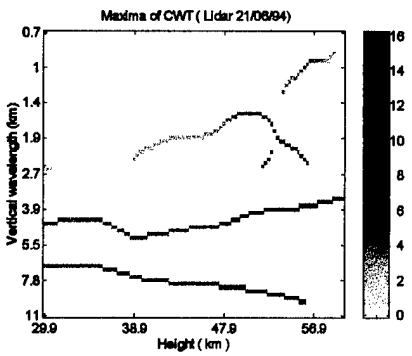

Figure 3 : CWT 'skeleton' intensities view 4-km vertical wavelength wave dissipation in the stratopause from where shorter wave of 2 km seems to be produced.

Wavelet Packet Decomposition (WPD) generalizes this decomposition and offers numerous possibilities to express the signal according to the 'WP decomposition tree' (Fig.5). Each aforementioned detail *d* is also successively broken down at each iteration i [2]. For example :

$s \cong a_1+aad_3+dad_3+dd_2 \cong aa_2+ada_3+dda_3+ad_2+add_3+ddd_3$

The smooth Daubechies' wavelet with eight vanishing moments is used in this work. For both methods, each extracted element corresponds to a vertical wavelength bandwidth which focuses on the dominant patterns.

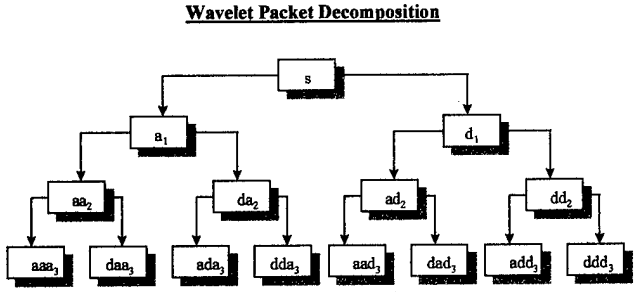

Figure 5: Wavelet packet decomposition tree.

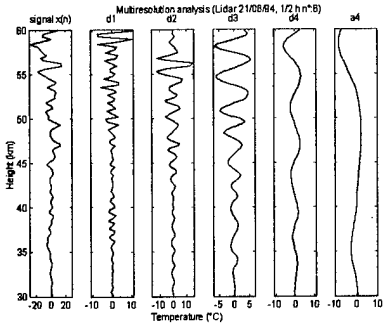

Figure 6: Perturbation temperature profile is broken down by MRA with vertical wavelength bandwidths (d_1 = 0.6-1.2 km, d_2 = 1.2-2.4 km, d_3 = 2.4-4.8 km, d_4 = 4.8-9.6 km, a_4 > 9.6 km). d_3 and d_4 reveal evident wavelike structures.

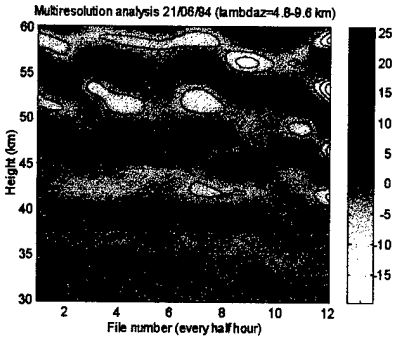

Figure 7: Night evolution of 4.8-9.6 km vertical wavelength waves (successive d_4) by MRA on June 21 in 1994.

4. RESULTS

CWT 'skeleton' for the night observation on June 21 in 1994 shows three evident dominant wavelike structures with night averaged vertical wavelengths of 1.3-2 km, 3.5-5 km and 7-11 km (Fig.2 and 3). Waves are viewed to be stable in the upper stratosphere. Dissipation of 4 km vertical wavelength wave occurs in the stratopause from where shorter wave of 2 km appears in the lower mesosphere. Location of mean structures and important events are here hightlighted. Such representations of successive 30-min temperature profiles for 6 hours' night observation give night evolution of wave patterns and their interactions [4].

The different observed scale structures previously identified are retrieved by MRA (Fig.6). Wavelike structures are depicted in details d_3 (2.4-4.8 km) and d_4 (4.8-9.6 km). Successive details d_4 for a complete night observation on June 21 show time and spatial evolution of 7 km vertical wavelength wave with -0.23 m/s downward phase progression visualized by extremum amplitude evolution (Fig.7). Night evolution representation is improved by WPD (Fig.8 and 9). Clear negative phase speed is observed for shorter waves from the stratopause.

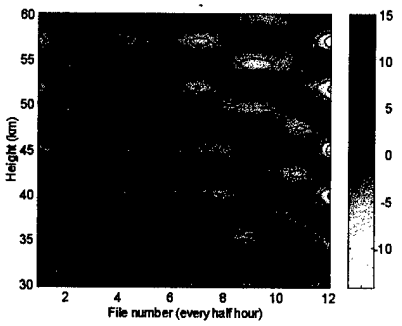

Figure 8: Night evolution of 4.8-7.2 km vertical wave length waves (successive $ddaaa_5$) by WPD on June 21.

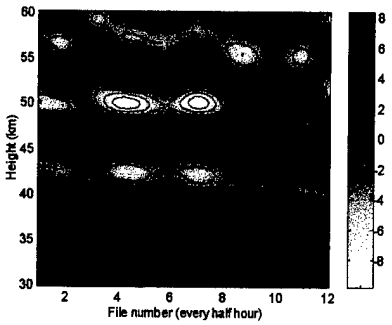

Figure 9: Night evolution of 7.2-9.8 km vertical wavelength waves (successive $adaaa_5$) by WPD on June 21.

No phase progression is noticed in the upper stratosphere. Wave reflection due to wave dissipation might explain this observation. On the contrary, longer waves reveal to have smaller phase speed from 30 to 60 km height. Results are consistent with gravity wave characteristics stating in recent studies by the use of lidar and radar systems in the northern hemisphere [4] [5].

5. CONCLUSION

Wavelet based methods presented in this work have enabled the study and the extraction of gravity wave characteristics from vertical temperature perturbation profiles provided by a Rayleigh lidar. Each method (CWT, MRA and WPD) have yielded additional information. 4.2-9.6 km averaged vertical wavelength waves versus height have been localized with downward phase progression inferior to 1m/s.

Radiosondes have been proved to be useful to catch gravity waves up to 30 km height. Studies are presently focused on such waves with these techniques to learn more about gravity wave sources in the lower atmosphere over Reunion island.

REFERENCES

[1] J.R Holton,''The dynamic meteorology of the stratosphe re and the mesosphere, ''Amer.Meteor.Soc., vol.15, 1975.

[2] M. Misiti, Y. Misiti, G. Oppenheim and J.P. Poggi, ''Wavelet toolbox user's guide,'' The MathWorks, 1996.

[3] F. Chane-Ming, F. Molinaro et J. Leveau,''Gravity wave activity in the southern intertropical middle atmosphere by wavelet analysis,'' The Proceedings of the 1st SPARC General Assembly Melbourne, 1996, in press.

[4] F. Chane-Ming, F. Molinaro et J. Leveau,''Gravity wave motions in the middle atmosphere over Reunion island (21°S, 55°E) studied by wavelet techniques,'' unpublished.

[5] C. S.Gardner, M. S. Miller, and C. H. Liu,''Rayleigh lidar observations of gravity wave activity in the upper stratosphere at Urbana, Illinois,'' J. Atmos. Sci., 46, pp. 1838-1854, 1989.

HIGH RESOLUSION IMAGE CLASSIFICATION WITH FEATURES FROM WAVELET FRAMES

Kyoung-Ok Kim, In-Sook Jung and Young-Kyu Yang
GIS Lab. / Systems Engineering Research Institute (SERI)
P.O.Box. 1, Yusung, DAEJON, 305-600, SOUTH KOREA
Tel: +82-42-869-1463 Fax: +82-42-869-1479
E-mail: kokim@seri.re.kr

Abstract – Scale and orientation are fundamental parameters of visual processing. The methods of multi-resolution feature extraction and enhancement of orientation features have been proposed for texture classification of a high resolution satellite image. A texture is characterized by a set of enhanced channel variances estimated at the output of the wavelet frame. Features from the wavelet frame are used as input to the error back-propagation algorithm for training, and classification. The results of the proposed method with MultiLayer Perceptron (MLP) classifier are compared with the results of the Maximum Likelihood Classifier (MLC).

The method is that texture segmentation divides the image into "homogeneous" regions where local texture properties are approximately invariant. The measurements remain reasonably constant in a region where the texture is considered to be homogeneous. The orientation of texture elements and their frequency contents seem to be important clues for discrimination. The proposed method is illustrated with the aid of examples on texture of high resolution satellite image of Seoul, Korea.

INTRODUCTION

The perception of textures depends upon local but not pointwise properties. There are many approaches to texture classification. Segmentation methods, are based on region growing, estimation theory, split-and-merge, Bayesian classification, relaxation, clustering, and neural networks [1], [8]. Commonly used texture features are: Fourier transform energy, local extrema, co-occurrence statistics [2], dominant local orientation and frequency [13], directional grey-level energy, directional filter masks including Gabor filters [7], [8], [9], finite prolate spheroidal sequences, as well as fractal dimension [3]. Features derived from the autoregressive moving average model, the Gaussian-Markov random field model, and the Gibbs random field model are also used [3].

Most conventional statistical methods are adequate for the analysis and segmentation of the class of microtextures. However, the neighborhood size over which texture can be analyzed is varied, and there is need for an internal spatial/frequency representation that is capable of preserving both local and global information [10]. Unser [10] used an over complete wavelet decomposition (the Discrete Wavelet Frame (DWF)) in which the output of the filter banks is not subsampled. He proved that an over complete wavelet analysis (DWF) is preferable to the standard subsample wavelet decomposition for feature extraction and concluded that the multi-resolution properties of the wavelet transform are beneficial for texture discrimination. In this paper, DWF and neural network are combined for texture classification and segmentation. DWF results in a texture description invariant with respect to translations of the input signal, which yield a better estimation of texture statistics. Neural network classifiers require no assumptions about the nature of distribution of the pattern data, and appear to perform as well as or better than other classification techniques [4], [6]. Because they have the capability to learn extremely complex patterns, and are also suitable for multichannel data fusion, multilayer neural network with a back-propagation algorithm can be very useful [11], [12]. This study combines the advantages of parametric and non-parametric strategies by using Kohonen neural network and multilayer neural network with a back-propagation algorithm. Also it experimentally evaluates different types of classification algorithms including Maximum Likelihood Classifier (MLC), and neural network approach of MultiLayer Perceptron (MLP).

ALGORITHMS

A texture segmentation divides the image into "homogeneous" regions where local texture properties are approximatively invariant [5]. The measurements remain approximately constant in a region where the texture is considered to be homogeneous. The orientation of texture elements and their frequency contents seem to be important clues for discrimination. For segmentation purposes it is necessary to localize texture measurements over neighborhoods of varying sizes.

Two different texture classification methods were applied to test the classification accuracy of each method. They are the wavelet frame with maximum likelihood method, and the wavelet frame with multilayer perceptron method.

There is a similarity between the wavelet transform and some of the biological information processing that occurs in the first stages of visual perception [5]. This paper shows the implementation of the suitable texture segmentation, and the

0-7803-3836-7/97/$10.00 © 1997 IEEE

modification of the wavelet based feature extraction method. The aim of the proposed method is to decompose the energy of an image in a multi-resolution frequency space and orientation space, because the spatial frequency and orientation are two fundamental dimensions in the visual analysis of images. These decomposed wavelet frame parameters are subsequently subjected to various feature extraction and dimension reduction algorithms to enhance and extract the features. The following shows the summary of the proposed algorithms.

Three channels of input data are derived from wavelet frame to be put into the Kohonen neural network. The proposed algorithm for this is as follows:

1) channel 1 image
- generate alowpass image of wavelet frame of depth 1 with cubic B-spline filtering

2) channel 2 image
- generate horizontal orientation images of wavelet frame of depths 1, 2, and 3.
- apply the Principal Component Analysis (PCA) to the 3 channels above
- apply the gradient filter algorithm to the first channel of the PCA result
- generate a lowpass image of the wavelet frame with cubic B-spline filtering to get the homogeneous locality of orientation image

3) channel 3 image
- generate vertical orientation images of wavelet frame of depths 1, 2, and 3.
- repeat the remainder of step 2)

The detailed process of proposed algorithm is as follows:

IMPLEMENTATION

1. Wavelet frame decomposition

The coefficient images of the Haar wavelet frames with multi-resolution for frequency decomposition were generated. The wavelet frame can be viewed as a special kind of spectral analyzer. The wavelet frame of lowpass information, horizontal (HL), and vertical (LH) components were obtained for depths 1, 2 and 3.

2. Feature extraction

These decomposed elements were then subjected to principal component analysis (PCA) for better feature extraction. Then the orientation parameter of these images was enhanced by applying a gradient algorithm to the PCA results, and the texture features are obtained by localized values computed over a sliding cubic B-spline window with appropriate size factors. We have chosen here to use a cubic B-spline window that provides a very close approximation of a Gaussian, yet offers the advantage of a fast algorithm whose complexity is independent of the parameter m (window size factor). To discriminate different textures, the local regions on which segmentation algorithms operate should extend over some significant area that is neither too small nor too large. When this area is too large, local feature difference may be lost; when it is too small, there may not be sufficient information to discriminate among similar textures. So we used window size of 8 x 8 in this experiment.

3. Neural network classification

The process of classification is comprised with two steps; the learning phase and the classification phase. The selected training areas are clustered by a Kohonen neural network in such a manner that the number of classified regions is much greater than the actually desired number of classes. Then the small regions with very few pixels, whose number is below a threshold value, are merged to the neighboring regions by giving consideration to the geometric and spatial factors. In this study the Kohonen network groups the image in 64 classes to get average feature values from each class. Then, the features of each class are computed and put into the neural network for training and classification. After selecting a training area, a three-layered neural network was used. The three-layered neural network has three neurons at the input layer and four neurons at the output layer. Both the MLC and MLP model were trained and applied to the test data and the results were evaluated with the classification accuracy. The MLC classifier is compared with the MLP, which is a standard error back-propagation (BP) neural network with a sigmoid function. After training the sample data using the BP algorithm, the same steps are applied to get the features of test data. Then the trained MLP is used to classify the test data.

EXPERIMENT RESULTS

The Haar wavelet frame method of depths 1,2 and 3 was applied to a satellite image of Seoul, Korea. The coefficient images of depth 1 for satellite image are shown in Figure 2 (b-d). The image (b-d) represent the horizontal, vertical, and diagonal components of wavelet frame, respectively. The wavelets from these elements were subsequently subjected to the transformation described in the proposed algorithm. The three channels resulting from wavelet transformation are clustered by the Kohonen neural network. The correct classification of ground truth data was made by an expert.

Figure 1 is a compilation of experimental data of experimental trials comparing the classification abilities of MLC and MLP methods used in a previous paper[14]. It is clear that the neural network (NN) is superior to the MLC method, particularly with noisy data. Figure 2 (a) and (e-f), respectively, show the input data and classification results for this experiment. As it is described in the feature extraction, prepared data consists of 3 channels ; channel 1 is a wavelet framed image of depth 1 with cubic B-spline filtering, channel 2 is a enhanced horizontal orientation image with cubic B-spline and channel 3 is a enhanced vertical orientation image with cubic B-spline. They are successful at preserving local uniformity. Image (f) represents classification result with MLC and (e) shows the classification result with the MLP neural network classifier. Tables 1 - 3 show the results of classification of a high resolution satellite image. The MLC method with raw data (Table1) was clearly the poorest performer of the three methods. When the MLC method was used on wavelet frame feature data (Table 2), a marked improvement was seen. However, the MLP method (Table 3) was clearly the most accurate classification method.

Also, enhanced features from PCA are very useful for the preprocessing of image before the data is submitted to the MLC for classification.

CONCLUSION

For segmentation purposes it is necessary to localize texture measurements over neighborhoods of varying sizes. The proposed method demonstrates that the multi-resolution properties of the wavelet transform are beneficial for texture discrimination. Quantitative comparison of conventional MLC (Maximum Likelihood Classifier) versus MLP classifier indicates that the conventional MLC was less capable of discriminating texture classes than the MLP classifier. In a BP neural network, there is no need to know the expression of the probability density and the prior probability for each category before the classification. Therefore, MLP is more flexible in handling texture data. Previous experimental trials have shown that the MLP method is particularly advatageous relative to MLC with noisy data But if the original texture is quite homogeneous, the result of MLC is as good as MLP. The proposed MLP with enhanced wavelet frame method proved to be a better approach than the conventional MLC.

REFERENCES

[1] M. F. Augusteijn, L. E. Clemens and K. A. Shaw, "Performance Evaluation of Texture Measures for Ground Cover Identification in Satellite Images by Means of a Neural Network classifier", IEEE Trans. Geoscience and Remote Sensing", Vol. 33, No. 3, pp. 616-626, May 1995.

[2] A. Baraldi and F. Parmiggiani, "An Investigation of the Textural Characteristics Associated with Grey Level Coocurrence Matrix Statistical Parameters", IEEE Trans. Geoscience and Remote Sensing, Vol. 33, No. 2, pp. 293-304, Mar. 1995.

[3] B. B. Chaudhuri and N. Sakar, "Texture Segmentation Using Fractal Dimension", IEEE Trans. Patt. Analysis and Machine Intell., Vol. 17, No. 1, pp. 72-77, Jan. 1995.

[4] K. O. Kim, et al., "Classification of Multispectral Image Using Neural Network", Proc. of IEEE International Geoscience and Remote Sensing Symposium (IGARSS) '95, vol. 2. Firenze, Italy, Aug. 1995, pp. 446-448.

[5] S. Mallat, "Wavelets for Vision", Proc. of the IEEE, Vol. 84, No. 4, pp. 604-614, Apr. 1996.

[6] G. Pasquariello and P. Blonda, "Multitemporal Remote Sensing Data Classification Using Neural Network", Proc. of ISPRS, Vol. 29, pp. 922-929, Washington D. C., 1992.

[7] H. W. Tang, V. Srinivasan and S. H. Ong, "Texture Segmentation via Nonlinear Interactions among Gabor Feature Pairs", Optical Engineering, Vol. 34, No. 1, pp. 125-134, Jan. 1995.

[8] M. F. Tenorio and W. T. Lee, "Self-Organizing Network for Optimum Supervised Learning", IEEE Trans. Neural Networks, Vol. 1, No. 1, pp. 100-110, Mar. 1990.

[9] A. Teuner, O. Pichler and B. J. Hosticka, "Unsupervised Texture Segmentation of Images Using Tuned Matched Gabor Filters", IEEE Trans. Image Processing, Vol. 4, No. 6, pp. 863-870, Jun. 1995.

[10] M. Unser, "Texture Classification and Segmentation Using Wavelet Frames", IEEE Trans. on Image Processing, Vol. 4, No. 11, pp. 1549-1560, Nov. 1995.

[11] Y. Wang and D. L. Civco, "Artificial Neural Networks in High Dimensional Spatial Data Classification: A Performance Evaluation", ACSM 55th Annual Convention and ASPRS 61st Annual Convention, pp. 662-671, Feb. 1995.

[12] J. Wu, H. Yan and A. N. Chalmers, "Color Image Segmentation Using Fuzzy Clustering and Supervised Learning", Journal of Electronic Imaging, Vol. 3, No. 4, pp. 397-403, Oct. 1994.

[13] Y. M. Zhu and Robert Goutte, "Analysis and Comparison of Space/spatial Frequency and Multiscale Methods for Texture Segmentation", Optical Engineering, Vol. 34, No. 1, pp. 269-282, Jan. 1995

[14] Kim, K. O., Y. K. Yang , "Texture Classification Using Wavelet Frame and Neural Network", SERI Journal, No. 1, Jan. 1997, pp. 63-82.

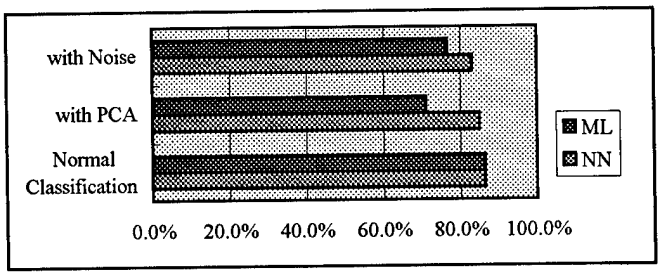

Figure. 1 Comparison of MLP(NN) and MLC with wavelet frame feature data.

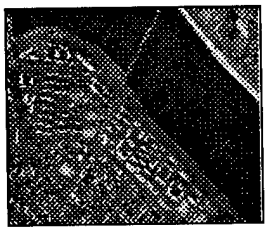

a) original image

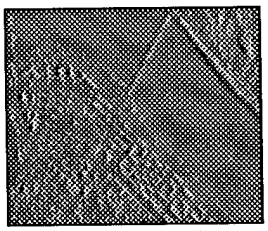

b) LH component image

c) HL component image

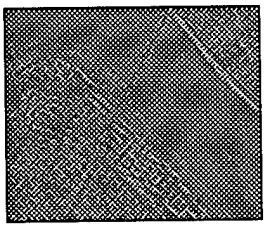

d) HH component image

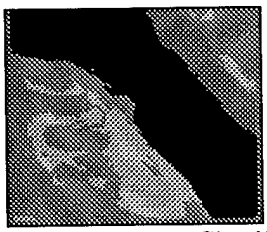

e) Result of MLP Classifier

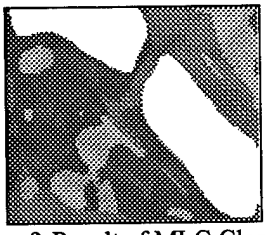

f) Result of MLC Classifier

Figure 2. Wavelet frame components and classification results of MLP and MLC Classifier.

Table 1. Result of Maximum Likelihood Classifier with raw data from a high resolusion saltellite image.

Class	1	2	3	4	Total	Percent
1	4831	478	25	36	5370	89.96
2	1334	565	1596	1331	4826	11.71
3	59	138	866	787	1850	46.81
4	241	96	1431	1639	3407	48.11
Total	6465	1277	3918	3793	15453	
Percent	74.73	44.24	22.10	43.21		51.13

Table 2. Result of Maximum Likelihood Classifier with wavelet frame feature of a high resolusion satellite image.

Class	1	2	3	4	Total	Percent
1	5138	18	272	0	5428	94.00
2	379	1133	763	294	2569	44.10
3	67	77	1674	533	2351	71.20
4	881	49	1209	2111	5105	58.10
Total	6465	1277	3918	3793	15453	
Percent	79.47	88.72	42.73	78.20		70.61

Table 3. Result of MLC classifier with wavelet frame feature of a high resolution satellite image .

Class	1	2	3	4	Total	Percent
1	4921	14	0	168	5093	96.623
2	61	975	23	0	1059	92.068
3	204	130	2599	1926	4859	53.488
4	0	28	374	1699	2101	80.866
Total	5187	1137	2996	3793	13113	
Percent	94.872	85.752	86.749	44.793		77.740

A Hierarchical Stereo Matching Algorithm Using Wavelet Representation Based on Edge and Area Information

Gi-Mun Um, Chul-Soo Ye, Kwae-Hi Lee
Dept. of Electronic Engineering, Sogang University
1 Shinsu-Dong Mapo-Gu, Seoul, Korea, 121-742
Tel.: +82-02-704-4088. Fax: +82-02-704-4088. Email : s293041@ccs.sognag.ac.kr

Abstract--In this paper, a hybrid approach that uses edge information is proposed. At the first step, edge pixels are matched using adaptive windows that vary their shapes according to the direction of edge. At the next step, pixels outside edges are matched using adaptive windows that are limited by edge contours. We also constructed a pyramid structure using a wavelet transform. The disparity information obtained by matching low resolution images is utilized for interpolating the disparities of high resolution pixels unmatched.

1. INTRODUCTION

Matching is one of the most important but difficult tasks for extracting 3D information from a couple of images. Many stereo matching algorithms have been suggested and they can be classified into largely two classes. One of them is a feature-based matching. Algorithms belong to this class use features such as edges and corners as matching primitives. This approach gives a sparse disparity map but a good localization of depth discontinuity. The other class is made with area based matching techniques, which can give dense disparity maps. But area based algorithm has problems of high noise sensitivity and the poor localization of depth discontinuity. Since the two algorithms have both advantages and disadvantages as stated above, recent researches are trying to integrate both algorithms [1][2]. Lotti proposed an adaptive window stereo matching algorithm using edge contour. His algorithm reduces lots of false matches but can generate many unmatched points. And this algorithm does not give disparity values for edge pixels. To tackle these problems we first modified matching score, and later proposed a new adaptive window matching algorithm for edge pixels. A pyramid structure using a wavelet transform is also proposed to interpolate pixels unmatched using the results of low resolution image matching.

2. PROPOSED STEREO MATCHING ALGORITHM

The block diagram of the proposed matching algorithm is shown in Fig.1. The process shown in the figure is repeated from the lowest resolution image to the original one. The proposed matching algorithm consists of three steps. In the first step, the pyramid structure is constructed using a wavelet transform. This structure has an advantage of less information loss compared with Gaussian or Laplacian pyramid. Edges are extracted from the left and right images. In the second step, we select the matching algorithm based on extracted edges. Using the selected matching algorithm we find a corresponding point in the right image for each left image point. In the third step, the two results of matching are merged and postprocesses are performed for removing mismatched points and for interpolation with unmatched points. We use the result of low resolution matching and 4 directional linear interpolation technique.

2.1 Edge Pixel Matching

In the edge pixel matching, we assume each edge pixel in the left image has a corresponding edge pixel in the right image. Firstly edges are extracted with Prewitt gradient masks and traced using Ramer's algorithm [3]. The direction of edge pixel is calculated in this step. Then we construct a matching window mask according to the direction of edge pixel. An example of window is shown in Fig.2. Using the window mask, normalized cross correlation (NCC) between two edge pixels is calculated and two edge pixels with the highest correlation is selected as an matched pair. Disparity refinement is also carried out using figural continuity constraint [4]. The figural continuity constraint reflects that disparity changes continuously along edge.

2.2 Non-Edge Pixel Matching

Usually an edge exists where intensity or depth discontinues. Although intensity discontinuity does not always agree with depth discontinuity, there is a high probability of the existence of depth discontinuity at the intensity discontinuity. If there is depth discontinuity in a window, the likeliness of false match is high. To remove false match, we use Lotti's 4 directional adaptive window size computation algorithm which constrains window size using edge contour. A pair of matching pixels is located at the 4 corner of rectangular window in the both image. Lotti's algorithm does not limit minimum or maximal window size but the size is limited by edges. Thus window size may be too small if there are many edges, or too big if there are few edges. This can bring false matches. To solve this problem, we limit minimum

0-7803-3836-7/97/$10.00 © 1997 IEEE

and maximum pixel numbers in a matching window. After computing 4 window sizes, Lotti computed matching score F(P,d) for considering correlation, noise, and texture conditions. Matching score F(P,d) is defined in (1). In (1) Nb_v is defined as the number of validated windows, and the validation of each window is checked by disparity limit validation v_{w_i} by (2). In (2), v_N is a noise validation Boolean variable, v_T is a texture validation Boolean variable, and v_C is correlation score validation Boolean variable. The detailed description of these variable is given in [1].

$$F(P,d) = \frac{Nb_V}{4} \sum_{i=1}^{4} (v_{w_i} C_{w_i}(P,d)) \quad (1)$$

$$v_{w_i} = v_{N_i} \cap v_{T_i} \cap v_{C_i} \quad (2)$$

$C_{w_i}(P,d)$ is a disparity limit score, which is defined as (3). In (3), Nb_{pt} is a pixel count in a given window, Nb_{max} is the maximum pixel number among four windows, $C(I_L,I_R)$ is NCC(Normalized Cross Correlation), and C_{ws} is a correlation threshold.

$$C_w(P,d) = \frac{Nb_{pt}}{Nb_{max}} \times (C(I_L,I_R) - C_{ws}) \quad (3)$$

As shown in (2), Lotti prefers two points which satisfies all the conditions as a correct matched pair. This can reduce many false matches but has a possibility of rejecting a correct matching pair. Furthermore, it can leave many points unmatched. To reduce these possibility, we modify disparity validation v_w to (4). In (4), we give nonzero value between 0 and 1 even if v_N or v_T is false.

$$v_w = (v_N + v_T) v_c \quad (4)$$

Using (4), we compute (1), and find two points which gives maximum F(P,d). The definition of validation is now modified to determining whether correlation score is larger than threshold or not. After these process, we remove falsely matched points using left-to-right and right-to-left uniqueness constraints. If some points still remain unmatched, the center window is applied. In this step, matching score is computed using (5).

$$F_5(P,d) = v_{w_5} C_{w_5}(P,d) \quad (5)$$

2.3 Construction of Final Disparity Map

After matching, two disparity maps are combined. To remove falsely matched points, we consider 4 neighboring pixels. All of 4 neighboring pixels are considered if there is no edge pixel to the directions. If center pixel does not satisfy (6), its disparity is removed. In (6), $\bar{d}$ is the average disparity of neighboring pixels and σ_d is the standard deviation. In computing these two variable, the disparity of center pixel d is excluded.

$$Prob[\bar{d} - 0.84\sigma_d < d < \bar{d} + 0.84\sigma_d] = 0.699 \quad (6)$$

2.4 Interpolation

We use two kinds of information to interpolate points left unmatched. First, the disparity map of low resolution images is used. If a doubled disparity from low resolution images satisfies (6), it is accepted. Otherwise, as a second information, 4 neighboring valid disparities are used. In this case, 4 neighboring pixels which are used for interpolation are the same to those used for disparity refinement. After finishing this step, we can obtain the final disparity map.

3. EXPERIMENTAL RESULTS

The matching algorithm proposed in this paper was applied to real stereo aerial images. We present one of the testing results in this paper. Fig.3 shows 512 ×512 left and right image of Pentagon. Fig.4(a) and (b) are the results of edge extraction. Fig.5(a) shows the disparity map of edge pixel matching with figural continuity constraint, and Fig. 5(b) is the disparity map of non-edge pixel matching. Fig.6(a) is a result of merging Fig.5(a) and (b), and Fig.6(b) is the disparity map by conventional area-based matching algorithm. Fig.5(a) shows better result than Fig.5(b) in terms of disparity continuity and false match reduction.

4. CONCLUSION

We have described a new stereo matching algorithm using edge information. According to edge image, different matching algorithm and windows are utilized. We modified adaptive window algorithm to reduce the number of unmatched points.

Experimental results show that the proposed algorithm can bring improved matching results compared with conventional area based algorithms. Future work will include the improvement of edge image and sub-pixel matching.

5. REFERENCE

[1] J. L. Lotti, and G. Giraudon , "Correlation algorithm with adaptive window for aerial image in stereo vision," Image and Signal Processing for Remote Sensing, Rome, Sept., pp. 26-30, 1994. EUROPTO, SPIE-The ISOE.

[2] S. D. Cochran and G. Medioni, "3D surface description from binocular stereo," IEEE Trans. Pattern Analysis and Machine Intelligence, vol. PAMI-11, no. 2, pp. 113-120, Feb. 1989.

[3] U. Ramer, "Extraction of line structures from photographs of curved objects, " Computer Graphics and Image Processing, vol. 4, no. 2, pp. 81-103, June 1975.

[4] R. Mohan, G. Medioni, and R. Nevatia, "Stereo Error Detection, Correction, and Evaluation," IEEE Trans. On Pattern Anal. Machine Intell., vol. PAMI-11, no. 2, pp. 113-120. Feb. 1989.

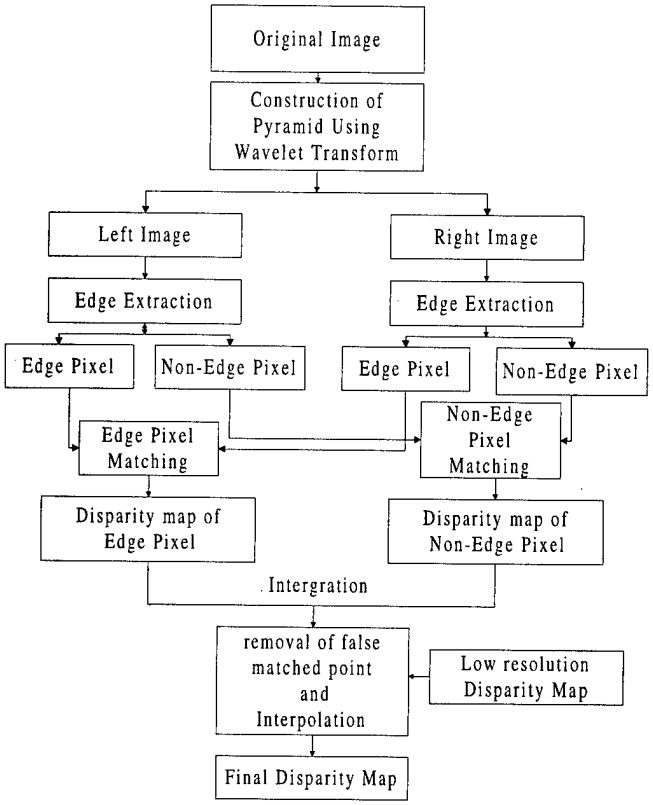

Fig. 1. Block diagram of proposed matching algorithm

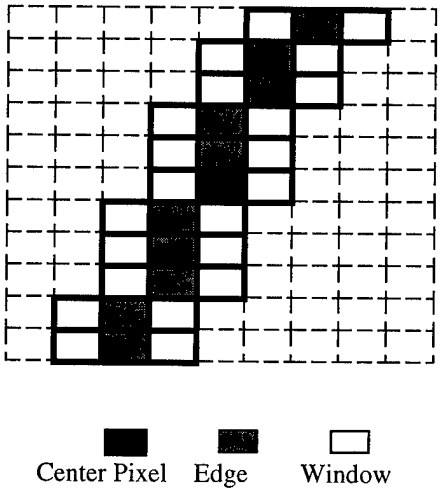

Fig.2. Edge Pixel Matching Window

(a) Left Image (b) Right Image

Fig. 3. Pentagon (512×512) stereo image pair.

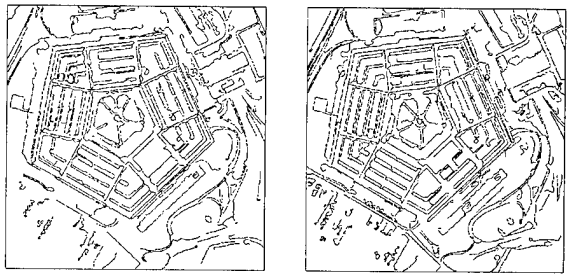

(a) Left Image (b) Right Image

Fig. 4. Edge image of Fig. 1.

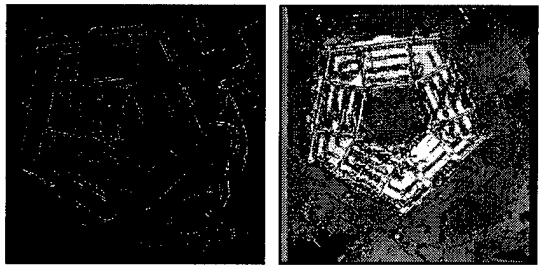

(a) Edge pixel matching (b) Non-Edge pixel matching

Fig. 5. Matching results of Fig. 1

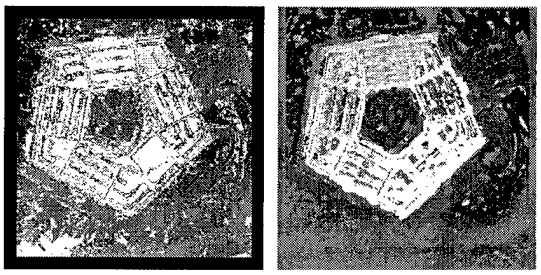

(a) Proposed algorithm (b) Conventional algorithm

Fig. 6. Final Disparity Map of Fig. 1

IGARSS'97

1997 International Geoscience and Remote Sensing Symposium

03-08 August 1997

Singapore International Convention & Exhibition Centre

Technical Program

Interactive Area 31: Classification

(No submissions for publication.)

IGARSS'97

1997 International Geoscience and Remote Sensing Symposium

03-08 August 1997

Singapore International Convention & Exhibition Centre

Technical Program

Interactive Area 32: Coastal Environment

Retrieval of Remote Radiance Reflection Coefficients of Coastal Waters from the Inherent Optical Properties

Vladimir I. Haltrin
Naval Research Laboratory, Ocean Sciences Branch, Code 7331, Stennis Space Center, MS 39529-5004, USA
Phone: 601-688-4528, fax: 601-688-5379, e-mail: <haltrin@nrlssc.navy.mil>

Abstract — Upwelling spectral radiances from the water surface and *in situ* inherent optical properties are measured concurrently at the same locations. Values of spectral radiance reflectance coefficients are derived from *in situ* data and compared with those obtained from spectral radiance data. An algorithm for estimating reflectance coefficients based on attenuation and absorption data is proposed and evaluated. This algorithm is based on the theoretically derived equations and the experimentally obtained regressions that connect scattering and backscattering coefficients. Overall comparison of derived and measured radiance coefficients shows that this algorithm is suitable for processing ground truth data for the purposes of calibration remote and *in situ* optical measurements.

INTRODUCTION

The results of the spectral measurements of radiance reflectance coefficient are compared with the results of the retrieval of these values from *in situ* measuments of inherent optical properties. These data are obtained simultaneously during the ground truth experiment near the West Florida coast in August 1994 (see Fig. 1). Upwelling spectral radiances from the water surface and *in situ* inherent optical properties are measured concurrently at the same locations. Values of spectral radiance reflectance coefficients are derived from *in situ* data and compared with those obtained from spectral radiance data. A model for estimating reflectance coefficients based on attenuation and absorption data is proposed and evaluated.

The measurement systems are: (a) spectral radiometer, with sensor bandwidth of 350-1000 nm and a one-degree acceptance angle (Analytical Spectral Devices, Inc. model FieldSpec™ VNIR); (b) nine-band beam absorption and attenuation meter (WETLabs, Inc. model A/C-9).

Data are collected at nine stations that range in depth from 2 meters to 23 meters. The spectral radiometer reflectance measurements are made at 30° from nadir and 180° azimuth from the sun. The examples of relative measurements are shown in Fig. 2. The vertical profiles of inherent optical properties are collected with the submersible A/C-9 beam transmissometer. The absorption and attenuation coefficients (see Figs. 3) are collected at nine stations transecting perpendicularly from the shoreline.

APPROACH

The experimental values of radiance reflection coefficient ρ_{mes} were calculated from three relative measurements of the sea N_{sea}, sky N_{sky}, and gray reference reflector N_{ref}:

$$\rho_{mes} = \left[A_{ref}\left(N_{sea} - R_F N_{sky}\right)\right] / \left(\pi N_{ref}\right), \qquad (1)$$

here A_{ref} is the reference albedo, and R_F is the Fresnel reflection coefficient of skylight [1]. Examples of measured radiance coefficients ρ_{mes} are shown in Fig. 4.

The radiance reflection coefficients ρ_{res} derived from the a and b profiles are calculated according to the equation:

$$\rho_{res} = T_d T_u R = R\left(1 - R_F\right)^2 / n_w^2, \quad R = R_1, \qquad (2)$$

here T_d and T_u are, respectively, downward and upward transmission coefficients of the sea surface, n_w is the water refractive index, and R is the diffuse reflectance of the water mass including effects of reflection from the bottom. The diffuse reflectance of a stratified n-layered shallow sea was computed using the following iteration formula:

$$R_n = \frac{R_n^\infty\left(1 - R_n^0 R_{n+1}\right) + \left(R_{n+1} - R_n^\infty\right)\exp\left[-\nu_n\left(z_{n+1} - z_n\right)\right]}{\left(1 - R_n^0 R_{n+1}\right) + R_n^0\left(R_{n+1} - R_n^\infty\right)\left[-\nu_n\left(z_{n+1} - z_n\right)\right]}, \qquad (3)$$

$$R_{n+1} = A_B, \quad z_{n+1} = z_B. \qquad (3a)$$

Here A_B is the bottom albedo and z_B is the sea depth. All other parameters are inherent optical properties of the n-th layer calculated through the absorption and scattering profiles (see Figs. 3) measured during the experiment.

$$\nu_n = 2 a_n \frac{2\left(x_n - R_n^\infty\right) - \overline{\mu}_n x_n}{\left(1 - x_n\right) R_n^\infty} \qquad (4)$$

$$R_n^\infty = \left(\frac{1 - \overline{\mu}_n}{1 + \overline{\mu}_n}\right)^2, \qquad R_n^0 = \frac{2 - \overline{\mu}_n}{2 - \overline{\mu}_n} R_n^\infty, \qquad (5)$$

$$\begin{aligned}\overline{\mu}_n = \eta_n (2.6178398 + \eta_n (-4.6024180 + \\ + \eta_n (9.0040600 + \eta_n (-14.59994 + \\ + \eta_n (14.83909 + \eta_n (-8.117954 + \\ + 1.8593222\,\eta_n))))))\end{aligned}, \quad \eta_n = \sqrt{1 - \omega_n^0}. \qquad (6)$$

$$\omega_n^0 = \frac{a_n}{a_n + b_n}, \quad x_n = \frac{\left(1 - \overline{\mu}_n^2\right)^2}{1 + \overline{\mu}_n^2\left(4 - \overline{\mu}_n^2\right)}, \quad b_n^B = \frac{x_n a_n}{1 - x_n} \qquad (7)$$

Equations (3)-(5), and (7) are based on the theory presented in Refs. [2]-[3]. The empirical Eqn. (6) is derived by the author from the experimental and *in situ* results published by Timofeyeva [4]. All values in Eqns. (4)-(7) with the subscript (n) are referred to the n-th layer. They are as follows: a_n is the absorption coefficient, x_n is the Gordon's parameter, b_n is the scattering coefficient, $\overline{\mu}_n$ is an average cosine, ω_n^0 is the single-scattering albedo, and b_n^B is the backscattering coefficient.

U.S. Government work not protected by
U.S. copyright.

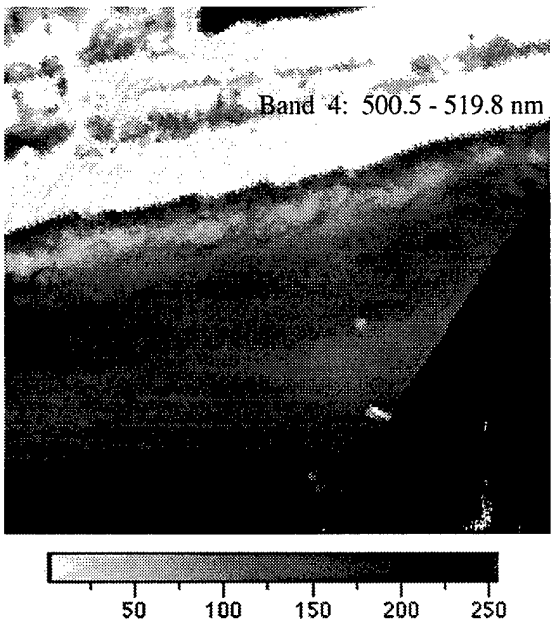

Fig. 1. The image of the investigation area obtained from an aircraft. The center of the optical channel is located near 510 nm. The white elongated spot near the right black border of the sea image is a research vessel.

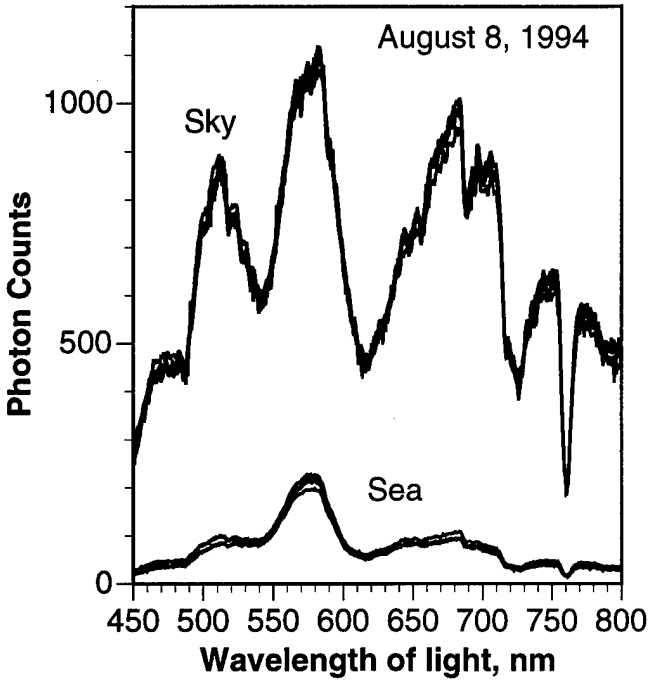

Fig. 2. Examples of the sea and the sky spectral radiances (in relative units) measured from the vessel in the area shown in Fig. 1.

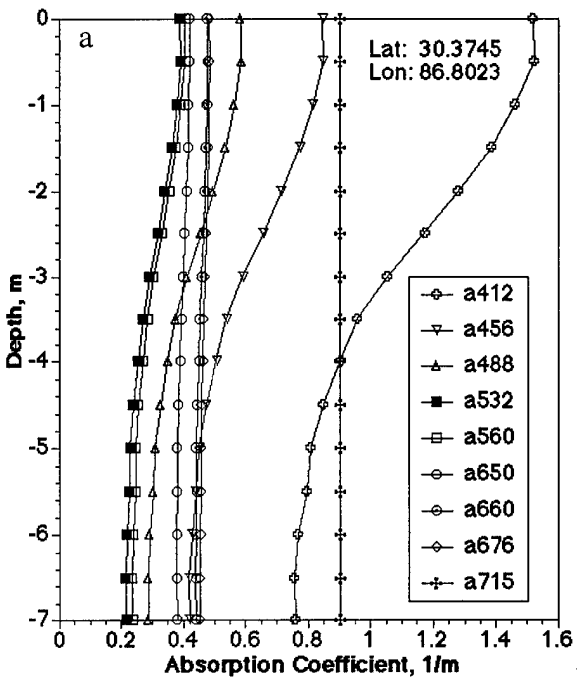

Fig. 3a. Experimental values of the absorption coefficient measured August 8, 1994, in the area shown in Fig. 1.

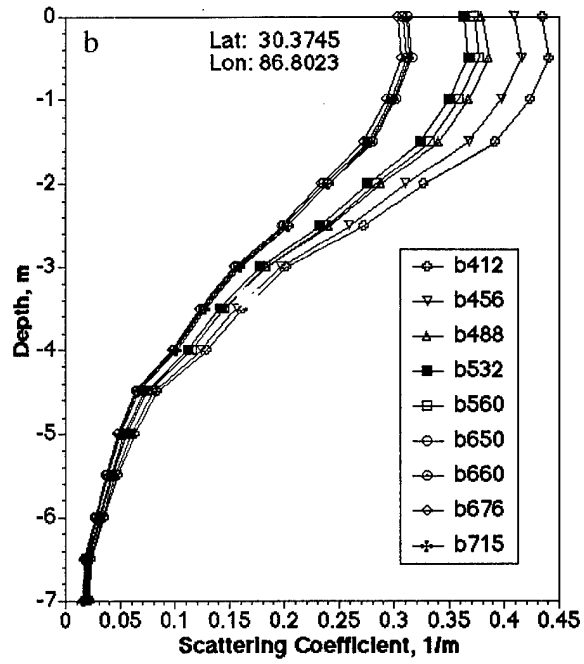

Fig. 3b. Experimental values of the scattering coefficient measured August 8, 1994, in the area shown in Fig. 1.

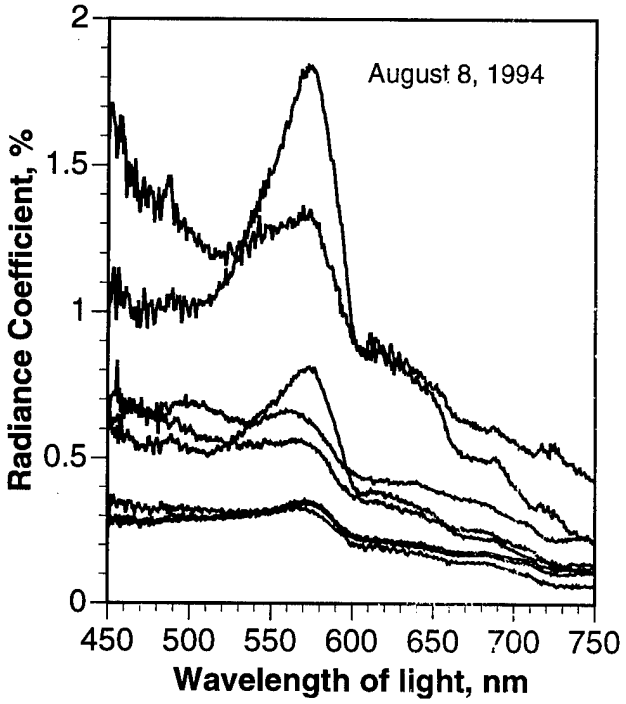

Fig. 4. Examples of the restored with Eqn. (1) radiance coefficients ρ_{exp} for different shallow water stations near the West Florida coast.

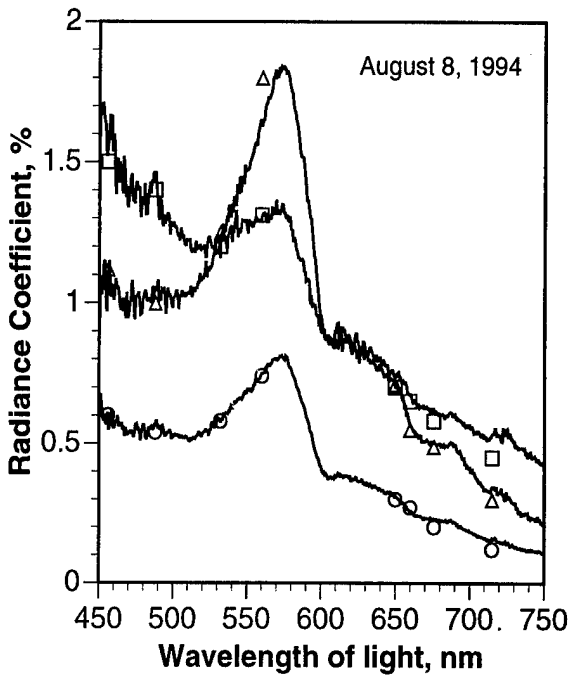

Fig. 5. Experimental (lines) and restored (symbols) values of radiance reflection coefficient for August 8, 1994, West Florida coastal waters.

Figure 5 shows the comparison of the measured and restored radiance reflection coefficients. The overall error of restoration of the spectral radiance reflection coefficients with the algorithm presented above does not exceed 20% for our experiment.

CONCLUSION

The results of the spectral measurements of the radiance reflectance coefficient measured remotely from a small ship are compared with the results of the retrieval of this values through the *in situ* measured profiles of absorption and scattering coefficients obtained simultaneously during the ground truth experiment near the West Florida coast.

The presented algorithm for retrieval of the radiance coefficient using observed depth profiles of absorption and scattering coefficients is stable. The derived values, in the worst cases, have error less then 20%. The overall comparison of the derived and measured radiance coefficients shows that this algorithm is suitable for the calibration remote data using *in situ* observations.

ACKNOWLEDGMENT

The author thanks continuing support at the Naval Research Laboratory through the Littoral Optical Environment (LOE 6640-07) and Optical Oceanography (OO 73-5051-07) programs. This article represents NRL contribution NRL/PP/7331–97–0010.

REFERENCES

[1] Jerlov, N. G., *Marine Optics*, Elsevier, Amsterdam-Oxford-New York, pp. 247, 1976.

[2] V. I. Haltrin (a. k. a. В. И. Халтурин), "The Self-Consistent Two-Stream Approximation in Radiative Transfer Theory for the Media with Anisotropic Scattering," *Izv., Atmos. Ocean Physics*, Vol. 21, pp. 452-457, 1985.

[3] V. I. Haltrin, "Algorithm for Computing Apparent Optical Properties of Shallow Waters under Arbitrary Surface Illumination," in: *Proceedings of the Third International Airborne Remote Sensing Conference and Exhibition*, 7-10 July 1997, Copenhagen, Denmark.

[4] V. A. Timofeyeva, "Optical characteristics of turbid media of the seawater type," *Izv. Atmos. Ocean Physics*, Vol. 7(12), pp. 1326-1329 (863-865), 1971.

[5] V. I. Haltrin, W. E. McBride III, and T. E. Bowers, "Predicting subsurface optical properties," in: *Ocean Technology at Stennis Space Center, Proceedings of the Gulf Coast Section Marine Technological Society, 23-24 April 1997*, Publ. by Naval Oceanographic Office, pp. 17-20, Stennis Space Center, MS, 1997.

Monitoring Coastal Water Systems: An Integrated Approach

Parthiphan s/o Krishnan
Department of Geography, National University of Singapore
10 Kent Ridge Crescent, Singapore 119260
Tel: +65 772 6809, Fax: +65 777 3091
Email: geopk@art1.nusstf.nus.sg

ABSTRACT

Remote sensing and geographical information systems (GIS) are important tools for monitoring coastal water systems. However, their limitations in complex, dynamic and mission critical situations demand alternative strategies. Integrating several computer-based systems offer one viable solution. The first phase of this research coupled a GIS with a simulation system. Using a shared database, a common user interface and a robust computer language to link the systems, spatial analyses enhanced by modelling were performed. The integrated MIKE21-ArcView2 GIS was tested in the southern coastal waters of Singapore. Ongoing research aims to extend the integrated system by encompassing remote sensing capabilities.

INTRODUCTION

The floundering of the oil tanker, the Sea Empress, off the coast of Wales in February 1996 highlights the damage we inflict on the environment. To mitigate the effects of such disasters requires a greater understanding of the environment, and a change in humanity's conducts. This two-pronged approach forms the basis for effective strategies to protect the environment.

While computer technology leads a visible and world wide revolution, remote sensing and GIS impact on the way we manage our lives. Computerised spatial analysis is a key methodology in environmental management programmes. Though remote sensing and GIS are *de facto* tools for environmental studies, in themselves they remain insufficient. Mission critical situations like oil spills highlight their weaknesses [1].

Innovative, yet effective, strategies are necessary for monitoring and managing the environment. A key aspect of such efforts is strong management to retain the environment's sustainability. This requires greater integration of scientific knowledge to improve our understanding of the environment. This can be achieved by employing a multidisciplinary approach using spatial modelling in an integrated system to provide quick responses to dynamic environmental issues [2].

THE COASTAL WATER SYSTEM

Today, more than 50% of the world's population live less than 60 km from the coast [3]. This results in competing and conflicting coastal water systems management issues. Such issues are exacerbated in small island states. In the case of Singapore, the original coastline has been and still is altered to cope with the increasing needs of urbanisation and industrialisation. This produces immediate and cumulative effects within the coastal water system that are not fully understood. For example, reclamation works along the west coast of the island posed a threat to the coral life. A three year effort at translocating viable corals was initiated in 1993. Yet, recent surveys of the relocated coral colonies reveal only a 35% survival rate. The other 65% of the corals were dead or dying due to waves and the sediment churned up by passing ferries [4].

This example highlights the need for a well integrated approach that utilises available data in an intelligent manner to solve coastal issues and resolve the inevitable conflicts. While remote sensing and GIS are used extensively for coastal research, experiences from past programmes indicate several limitations [5]. These include data issues such as availability, format, accuracy, precision and currency. However, issues of representation of reality, inability to handle multiscale and multidimensional spatio-temporal data, and the lack of algorithms to perform dynamic process modelling are the more serious limitations.

Simulations, on the other hand, use mathematical computer models to explain and understand the variations within systems. But they focus on system states and processes, while ignoring spatial interrelationships. They model behaviors without any indication of the features found within the system.

The obvious solution is to develop an integrated system to monitor and manage the coastal water system. The first phase of the my study linked the ArcView® Version 2 GIS with the MIKE21® simulation modelling system. The southern coastal water system of Singapore served as the test site for the integrated modelling system.

0-7803-3836-7/97/$10.00 © 1997 IEEE

The Integrated System - MIKE21-ArcView2 GIS

Two aims underpinned my research. The first sought to link a hydraulic simulation system with a GIS, using existing technology. A primary condition was tight coupling of the two systems. The second aim was developing an integrated system that ensured easy access to even novice users. This called for an easy to use, yet seamless, user interface between the two systems.

A well integrated system must posses a common user interface, a single spatial database, and a robust computer language to link the different systems together. The chosen systems for this research satisfied these conditions and the functional requirements of the integrated system.

The MIKE21® simulation modelling system was chosen for the study as it is a comprehensive numerical modelling system for simulating water level variations and flows in estuaries, bays and coastal waters [6]. Using only bathymetry and ancillary conditions like the resistance coefficient, wind fields and hydrographic boundary conditions, it simulates unsteady 2D free-surface flows in one layer (vertically homogeneous) fluids. The MIKE21 system is structured into a number of modules to simulate various coastal processes. This aided in the modular development of the integrated system.

ArcView® Version 2 served as the GIS for several reasons. These include its easy to use graphic user interface (GUI), interactive on-line help documentation, multi-platform support, interapplication communication (IAC) and data access [7]. While the ArcView GIS handles its themes as shapefiles, it can also work with ARC/INFO® coverages, remotely sensed images and scanned data. This was useful for the research as the data from the MIKE21 system were handled as both shapefiles and grid themes within the ArcView GIS. The object-oriented (OO) scripting language, Avenue™, was used to convert spatial data from the MIKE21 system into shapefiles.

Several design objectives guided the development of the MIKE21-ArcView2 GIS. Developed in a Windows environment, it has the capability to handle different types of input data such as scanned data and satellite imagery. Allowing users the flexibility to produce new and value-added information was a key objective. Coastal water system management issues can be clarified and enhanced by comparing past and present scenarios with simulations of the future.

The integrated system streamlines the process of conducting simulations. During simulation preparation, the GIS aids data query, retrieval and display. The input simulation model and parameters are generated from data retrieved from the GIS database, such as the bathymetry, tidal information, and boundary conditions. This model is calibrated and validated using reference data collected from the field and stored within the GIS database. In the simulation production stage, the GIS enhances results visualisation, as well as the integration of the simulation results with additional data to enable further analyses.

Integrating the simulation modelling system and the GIS necessitated an appropriate methodology for system analysis and design. The OO Method [8] was used in conjunction with the Avenue language to incorporate the functional aspects of the MIKE21-ArcView2 GIS during system analysis and design. As the Avenue language handles the data stored in the spatial database in terms of entities and objects, users only work with the spatial objects required for the simulation or other analyses without confronting elements like points, arcs, polygons or grids. Avenue scripts allow data exchanges between the simulation modelling system and the GIS without the need for complex data transformation procedures.

The OO method's flexibility in reusing programming codes also proved an advantage. For example, multi-input forms menus allow users to select from the list of bathymetric models (objects) for simulation, without the need for individual sets of codes for each operation.

However, the OO method alone was inadequate to develop the integrated system. The need for sequential procedures during simulation necessitated an algorithmic approach, even though systems analysis and design greatly benefited from the OO method. Hence a methodology using aspects of both the traditional structured approach and the OO method was used in developing the MIKE21-ArcView2 GIS.

Fig 1 illustrates the integrated system. The ArcView GIS was the common user interface for the coupled system. Avenue scripts enhanced the GUI abilities of the GIS, allowing users to input model parameter data to the dynamic simulation modelling system. Customised multi-input forms were created to allow users to select data available within the database for modelling and spatial analyses purposes.

Tight coupling of the component systems was achieved by using the GIS as the shared database for the integrated system. All data were stored as vector layers for easy display and analysis by the GIS. In addition, the base models for were also stored as grid layers for simulation purposes. The Avenue language afforded the manipulation of these layers in an OO manner, via the customised user interface.

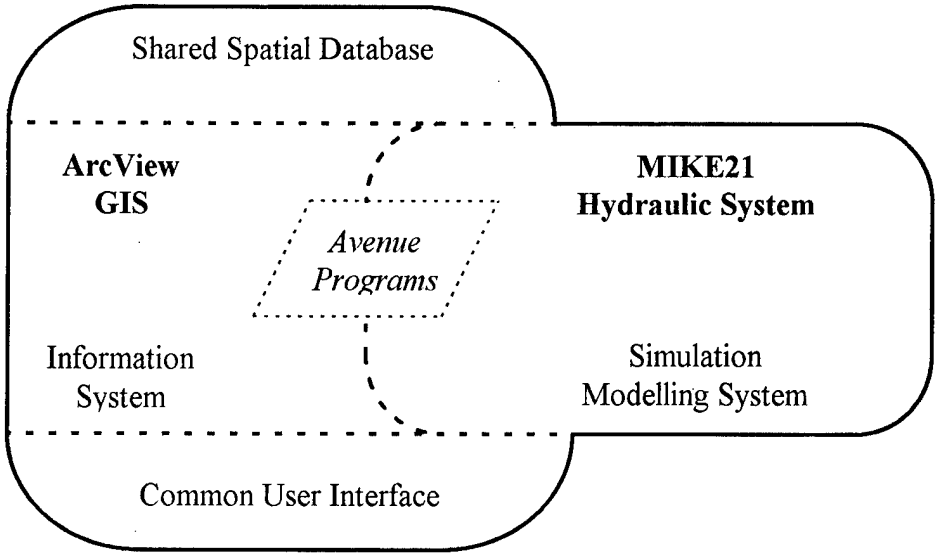

Fig. 1 The MIKE21-ArcView2 GIS

CONCLUSION

The present study highlights several issues associated with monitoring and managing the coastal water system. Firstly, the increasing urbanisation and industrialisation of the world's coasts will exacerbate the occurrence and severity of immediate and cumulative impacts at these locales.

Secondly, solving the coastal environmental problems require well formulated strategies that employ available data, science and technologies in intelligent and usable ways. This necessitates an integrated and multidisciplinary approach.

Linking available systems into a larger framework is one solution. The present study indicates that an integrated system using simulation and GIS technologies is possible. This requires three conditions to be met. They are; a common user interface, a single spatial database, and a robust programming language to couple the systems together.

ACKNOWLEDGMENTS

This research was conducted at the Hydro Informatics Centre of the Danish Hydraulic Institute. I thank Mr Ross Warren and Mr Henrik G. Muller for their invaluable assistance.

REFERENCES

[1] T.K. Hodges, Design and Development of an Expert System with a Map Based Interface for the Clean-up of Shoreline Oil Pollution, MSc Thesis, Dept. of Geog. University of Edinburgh, 1994.

[2] Parthiphan s/o Krishnan, "Linking GIS with a modelling system for coastal waters", Proc. GIS Asia Pacific '95, Singapore, 1995, 22 pgs.

[3] United Nations Conference on Environment and Development, Agenda 21: Programme of Action for Sustainable Development. NY: United Nations, 1992.

[4] D. Nathan "Coral rescue: only a third survived move to Sentosa site", The Straits Times. October 22 1996, pp. 27.

[5] D.J. Bartlett, GIS and the Coastal Zone: Past, Present and Future, AGI Publication 3/94. UK: Information and Education Committee Publication, 1994.

[6] Danish Hydraulic Institute, MIKE 21 - A Two-Dimensional Modelling System. Horsholm: DHI, 1993.

[7] Environmental Systems Research Institute, ArcView Functional Overview. Redlands: ESRI, 1995.

[8] G. Booch, Object-Oriented Analysis and Design with Applications. Redwood City: Benjamin/Cummings. 1994.

Near-Bottom Fluxes of Sediment Matter on a Shelf and Their Research by Remote Techniques

Felix R. Likht and Leonid M. Mitnik

Pacific Oceanological Institute, FEB RAS, 43 Baltiyskaya St., Vladivostok 690041, Russia
Tel: 7-4232-312-854/Fax: 7-4232-312-573/E-mail: mitnik%dan32@poi.marine.su

ABSTRACT

The fluxes of present-day fine sedimentary matter (usually known as black muds) were found among the relict sands of the broad shelves. They were named the Near-bottom Mud Fluxes (NMFs). The fluxes flow from a coast across shelf and further on continental slope and traced along the bottom deepenings which are connected with ancient river valleys submerged on the shelf. The valleys have different images in morphology of bottom relief. The NMFs have the great potential as natural profitable wastedisposal system from the urbanized coastal regions. The NMFs indicate the ancient rivers valleys and their potential mining placers and fresh water resources.

PROCESS OF SEDIMENTATION

Near-bottom flows of sediment matter directed from a coast towards continental slope and crossing a shelf make a sedimentation anomaly which disrupts zonality of near-continental sediment process. The zonality is expressed by sedimentation of terrigenous matter carried out from land within the floor areas. In accordance with morphostructure of a basin, there are two different types of zonality with the transition modifications between them. The first type is inherent in near-continental seas with wide and slightly inclined shelf which conjuncts morphologically well with a continental slope surrounding deep-sea basins. This type of zonality is depicted in section across shelf and slope of the Peter the Great Bay of the Japan Sea (Fig.1).

The main volume of material receiving from land is accumulated on a shoal down to a depth of 30 m. It is a shallow-water accumulation zone A(sw). It accumulates all creeping (drawing) and saltating (jumping) particles of terrigenous material. A major (70-90%) part of suspension is also settled down here. The highest accumulation rates of terrigenous material are typical for such zones. For example, they exceed 300 cm/100 year for the region shown in Fig.1.

The next accumulation zone is deep-water one A(dw). It locates within the lower part of continental slope and its foot. Accumulation rate of material here is more than two orders lower than in the A(sw) and is about 10-15 cm/1000 year. A greater part of shelf and the upper part of continental slope present the asedimentogene bottom field where the sediments are practically not accumulated except in a few cases. The above-mentioned flows of sediment matter are among these cases. They will be discussed below.

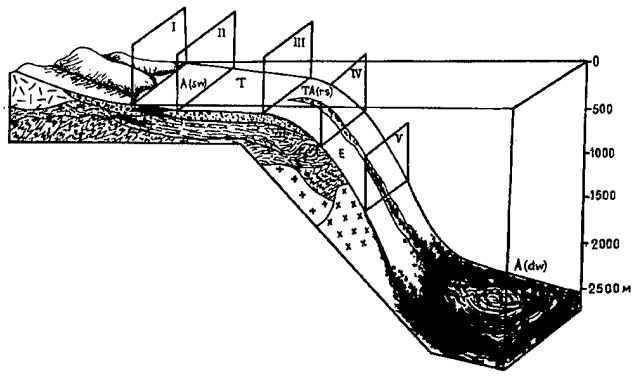

Fig. 1. Block-section across shelf and continental slope of the Peter the Great Bay.

In the asedimentogene field, three zones can be differentiated: transit zone T, transit-accumulative (for relict sediments) zone TA(rs) and erosion zone E. The zone T covers the almost whole outer shelf. Sediments which were formed in the past and known as relict occur here. They are not associated with present-day processes of supply and distribution of material. The zone TA(rs) is situated at joint of shelf with the upper part of continental slope. The most coarse-grained relict sediments are here. For example, 18-20 thousand years ago during the last phase of glacial period, when sea level was 110-150 m below than the present one, this zone was shallow-water reservoir. It corresponded to the present-day zones A(sw) and partly T.

In the erosion zone E, which is located in the upper part of continental slope, accumulation of sediments does not happen now as well as in the past. Ancient hard rocks are exposed on a bottom. Transformation of hydrophysical characteristics of water mass near the outer shelf boundary prevents here the deposition of suspension carried out from shelf [1]. Hydrophysical nonhomogenuity of water mass begins to take the properties of thermocline. Suspension of the water mass bypasses a shelf margin without sedimentation, flies by over the thermocline surface as if it is the jumping-off place and begins to settle downstream of the E zone boundary.

The second type of zonality is typical of the seas where shelf grades into continental slope. Coupled with the conditions which are favoring the deposition of suspension (sizable volume of supply, quiescent hydrodynamics) such a situation assists in mudding-up of that part of a bottom which is shown as asedimentogene in Fig.1. For example, the similar situation is typical for the practically entire bottom surface of

0-7803-3836-7/97/$10.00 © 1997 IEEE

the northern Tatar Strait in the Japan Sea, the Siam Bay of the South China Sea, for shelf and continental slope of the Northern Okhotsk Sea, etc.

Zonality of sedimentation shown in Fig.1 is characteristic of all basins with similar morphological type and independent of climate. The climatic features are expressed in processes of settling of material entering in basin. In high latitude provinces, predominance of the processes of physical weathering facilitates predominance of coarse material. In low latitude provinces, predominance of the processes of chemical weathering facilitates predominance of fine varieties of terrigenous material.

ANOMALIES OF SEDIMENTATION

Returning to the first type of zonality, it is necessary to emphasize that the possibilities of the material deposition are noted locally in the asedimentogene areas. In particular, when arising the quasiconcentric currents, the conditions for the deposition of suspension are produced. For example, the deposition of fine terrigenous material on the outer shelf of the Peter the Great Bay occurs just in the areas within almost circular branch of current.

The "shadows" on a bottom of suspension flows induced by river drift-over are the second source of the material deposition in an asedimentogene area. In particular, a band of alevritic and pelitic material stretched on the shelf from the Tumangan River's mouth southward along the Korean coast represents such a "shadow".

The similar entrances of river material superenrich near bottom waters. They make black the very diluted pelitic muds flowing downslope along a system of ancient river valleys flooded on the shelf. These muds were discriminated and described as the NMFs in [2]. They were found in Olga and Vostok bays and other regions of the Japan Sea, in the East China Sea, near mouth of the Mekong (the South China Sea) and in other places (Fig. 2 [3]).

Fig.2. Aerial image of the sea bottom showing submarine delta with distinctly pronounced NMFs.

Sometimes these valleys are retained in bottom relief. In such a case, they are "almost rivers" of liquid black mud among brown ancient sands. For example, such muds were found in submersible river valleys on the shelf of the East-Korean Bay (Fig.3).

DETECTION OF FLOODED VALLEYS

The special techniques were developed to reveal the flooded valleys on the shelf when only limited bathymetric data is available [4]. The first step involves calculation of depth marks for the centers of each cell of network using the measured values. The second step consists of an interpolation

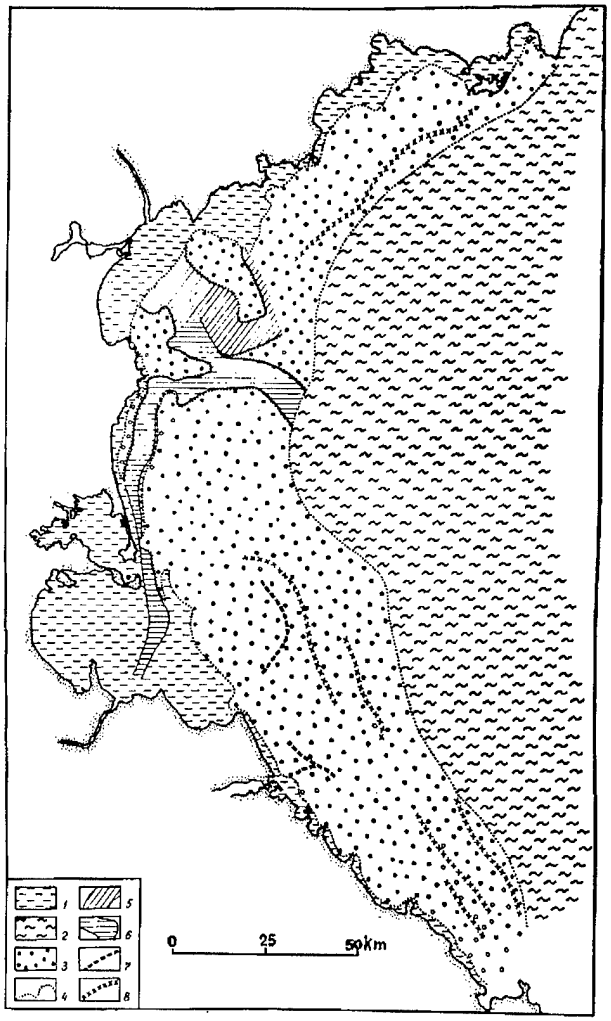

Fig. 3. NMF on the shelf of the East-Korean Bay: 1 - zone A(sw) near coastal line; 2 - mudding up of the outer shelf and slope due to drift-over of suspension of the Tumangan River; 3 - asedimentogene field; 4 -boundaries of sedimentation zones; 5-8 - forms of ancient relief flooded on shelf: 5 - more ancient river valleys with NMF; 6 -younger valleys with NMF, 7 - shallow valleys without NMF; 8 - ancient coastal lines.

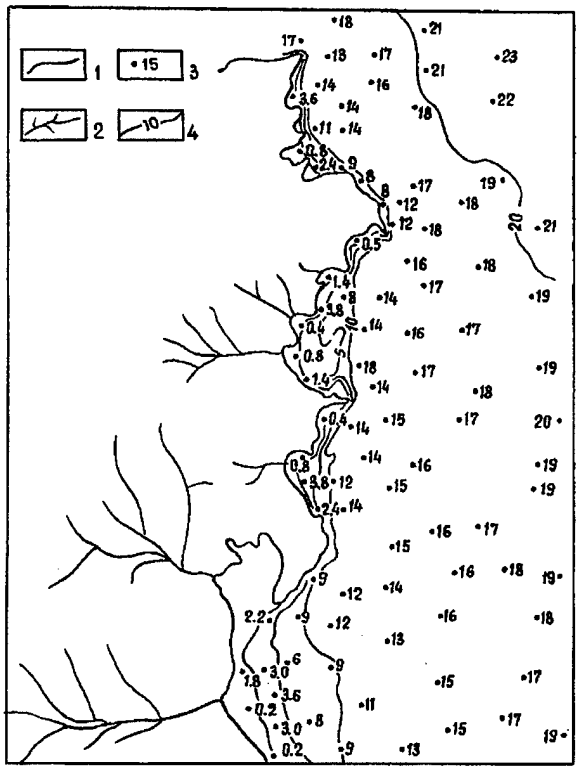

Fig. 4. Bathymetric data used for construction of flooded rivers on the Shantar Shelf of the Okhotsk Sea: 1 - coast line; 2 - hydrological network; 3 - depth marks; 4 - isobaths

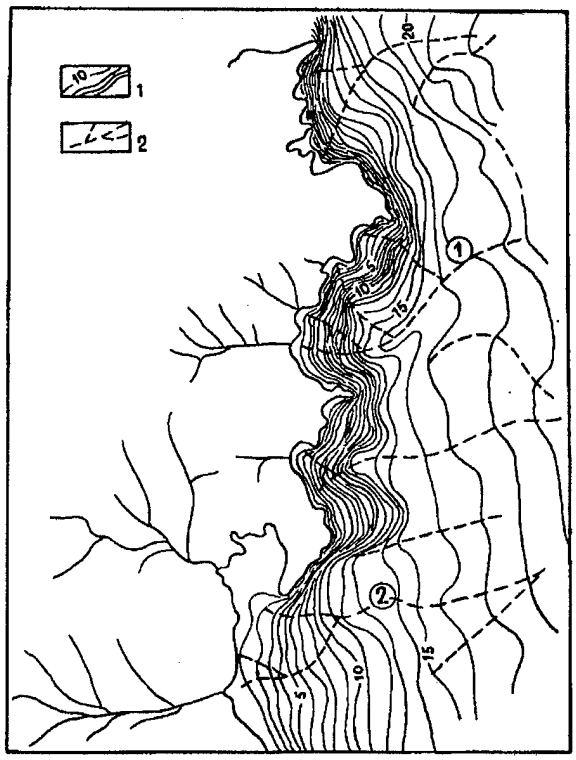

Fig.5. Reconstruction of flooded rivers on the basis of Fig.4: 1- calculated isobaths, 2- flooded rivers.

of the obtained depth marks and construction of the bathymetric map.

Sounding data for the Shantar Shelf of the Okhotsk Sea (Fig.4) allowed us to calculate isobaths, construct the map of bathymetry and mark the location of the flooded hydrological network (Fig.5). The NMFs were found in thalwegs of the flooded river valleys, marked by digits 1 and 2 (in circles).

CONCLUSION

The NMFs are still not clearly understood although they have great potential as natural profitable wastedisposal system from the urbanized coastal regions. Efficiency of such system increases if the NMFs enter in the upper part of canyons located on the shelf edge. It can be illustrated by the example of the NMFs emptying into canyons of continental slope of the Japan Sea. During one year, material arriving from coastal line transfers to the depths more than 2 km where its natural burial takes place. The position of the flooded river valleys indicated by the NMFs may be valuable for exploration of the alluvial placers and fresh water sources.

The dark NMFs stand out sharply against the light sands. The spectral visible data in conjunction with the SAR images can be used for detection of the NMFs in the shelf shallow waters and evaluation of the temporal changes. Analysis of the remote sensing data allows to choose the areas for comprehensive study from research vessel.

REFERENCES

[1] V.V. Navrotskiy, A.Yu. Lazaryuk, and A.A. Malyshev, "Features of structure of hydrophysical data and internal waves near shelf margins," Proc. of Academy of Sciences of the USSR, vol. 309, pp. 187-191, 1989 (in Russian).

[2] F.R.Likht, "Modern Near-Continental Sedimentogenesis and Reconstruction of Similar Environments in Geological Past of Asia," Vladivostok: Nauka, 1993, 237 pp. (in Russian).

[3] "Aerial Photography of the Sea Bottom: the Backbone of Thematic Mapping", VNIIKAM, Institute of Remote Sensing Methods for Geology, Leningrad: VNIIKAM, 1991.

[4] F.R. Likht and O.M. Gun, "The experiment of morphometric investigation of shelf within near-coastal shoal", in: "Geology and Geomorphology of Marginal Seas," Vladivostok, 1979, pp. 110-118 (in Russian).

IGARSS'97

1997 International Geoscience and Remote Sensing Symposium

03-08 August 1997

Singapore International Convention & Exhibition Centre

Technical Program

Interactive Area 33: General Applications

OZONE DISTRIBUTION IN THE STRATOSPHERE-TROPOSPHERE SYSTEM USING THE INTERDISCIPLINARY PHYSICS MODELLING

Florin Caldararu*, Stefan Patrascu**, Mira Caldararu*, Anca Paraschiv*, Dan Nicolaescu***
*ECOSEN Ltd., Geoecology Department, 38 Stefan Mihaileanu st., 1st floor, sect. 2, Bucharest 73101, Romania,
Tel. & fax: +40 1 3220495, E-mail: caldf@pcnet.pcnet.ro
**University of Bucharest, Faculty of Physics, Earth Sciences Department,
Magurele 20, PO Box MG 11, sect. 6, Bucharest, Romania
***Dept. of Electrical and Computer Engineering, NJIT, University Heights, Newark, NJ 07102, USA,
Tel: + 1 (201)-596-8464, Fax: +1 (201) 596-5680, E-mail: ndan@admin.njit.edu

Abstract - In the present paper a theoretical ozone distribution in the stratosphere-troposphere system is provided using the physical analogy between the stratosphere-troposphere system and the well-known illuminated semiconductor *p-n* junction The equations of 2-D model of the illuminated *p-n* junction were rewritten for the ozone and pollutant particles in the altitude-latitude co-ordinates. A comparison between the calculated curves and the recent experimental achievements is also given.

INTRODUCTION

The theoretical ozone distribution curves have been calculated starting from the chemical kinetics equations [1] or from general circulation model equations [2]. The relation between the ozone layer thickness and the parameters of the ozone concentration variation have not been provided yet. The statements of the sustainable development concept require the monitoring of the global changes of the environment [3], which cannot be performed without a theoretical model of the ozone distribution.

Using a simple phenomenological analogy between the illuminated semiconductor *p-n* junction, the authors have deduced, in a previous paper [4,5] the steady-state conditions of the ozone layer. In the present paper this analogy is developed in order to establish the correspondence between the parameters of the minority carrier distributions in the *p-n* junction and of the ozone and pollutant particle in the stratosphere-troposphere system.

Following this analyse, the equations developed by the authors [6] for the minority carrier distribution in the illuminated *p-n* semiconductor junction are rewritten for the ozone and the pollutant particle in the altitude-latitude co-ordinates.

INTERDISCIPLINARY PHYSICS MODELLING

The phenomenological comparison between the illuminated semiconductor *p-n* junction and the stratosphere-troposphere system given in [4] allows us to provide a detailed equivalence, stated in the Fig. 1.

(i) The physical structure

The semiconductor *p-n* junction is composed of two regions: a phosphorus doped semiconductor lattice where free electrons are produced (n-type semiconductor) and a boron doped semiconductor lattice where free holes are produced. Due to the large concentration difference of electrons and holes, these free charges diffuse from one region to the other. Near to the junction no free charges remain, giving rise to the space charge region, where an electric field arises. Due to it the diffusion of the holes and electrons stops. Thus, in a *p-n* junction, three different regions result: (1) the *p* quasineutral zone, where the minority carriers are the electrons, (2) the *n* quasineutral zone, where the minority carriers are the holes and (3) the space-charge region, where the electrons and holes are both absent.

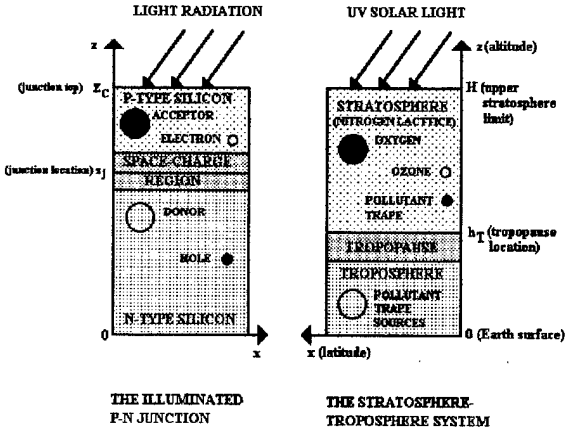

Fig. 1 - The physical analogy between the illuminated *p-n* junction and the stratosphere-troposphere system

The stratosphere-troposphere system is composed, mainly, by oxygen and nitrogen that can be assimilated to

0-7803-3836-7/97/$10.00 © 1997 IEEE

the silicon lattice. The system is composed, also, by three different regions: (1) the troposphere, (2) the stratosphere and (3) the tropopause that separates the two regions, where the thermal inversion starts. The ozone, which is produced in the stratosphere by the oxygen photodissociation, can be assimilated to a minority carrier. The pollutants-type particles are produced to the bottom boundary of the troposphere and arrive in the stratosphere due to upward diffusion through tropopause.

(ii) The generation-recombination processes

Due to the input radiation, the free carriers are photogenerated in the *p* quasineutral zone of the semiconductor *p-n* junction. The direct recombination processes are non-radiative, thermal energy being produced. The recombination processes are enhanced due to the "traps" which are metallic impurities or lattice defects.

In the stratosphere-troposphere system the ozone is produced by the oxygen photodissociation in the presence of the UV solar radiation. The recombination processes take place in the ozone system via photodissociation processes and in the chemical reactions: in the hydrogen system, in the nitrogen system and in the chlorine system a great thermal energy being produced. The water, the nitrogen oxides (NO_2 and N_2O) and the chlorine compounds are produced in the natural or in the antropogenethic ecosystems. Then, the pollutant type particles can be assimilated to the "traps" of the semiconductor *p-n* junction.

(iii) The transport phenomena

In the *p-n* junction the main transport phenomenon is diffusion of both *n* and *p* free carriers. In the stratosphere-troposphere system the main transport phenomenon is the ozone diffusion in the stratosphere. Due to turbulent motion that takes place in the troposphere, the pollutants type particles can be considered uniform in the stratosphere along the given altitude.

The above described comparison allows us to use the equations developed in [7] to calculate the ozone profile. The generation process is due to the photochemical absorption of the UV solar light by the molecular oxygen. The recombination processes are due to the ozone photochemical dissociation and to the chemical reactions with the "pollutant" types particles, considered as traps. The transport phenomena are represented only by the ozone molecular diffusion. The pollutants are considered uniform in the stratosphere due to strong turbulent motion in the troposphere and to the slow turbulent motion in the stratosphere.

THEORETICAL OZONE DISTRIBUTION

The equation for ozone distribution in the steady-state conditions is [6]

$$-D\nabla^2 c(z,x) = G(z,x) \qquad (1)$$

where c(z,x) is the ozone concentration and G(z,x) is the net generation rate [7]. The field term was neglected due to slow turbulent motion in the stratosphere.

$$G(z,x) = \frac{J_{ox}e^{-\alpha z}c_{ox}}{2} - \frac{k_{ox}J_{ox}e^{-\alpha z}c(z,x)}{2k_{oz}c_{ox}c_{nit}} - \frac{k_{ox}J_{oz}e^{-\alpha z}c^2(z,x)}{k_{oz}c_{ox}c_{nit}} - k_{HO}c_{HO}(x)c(z,x) - k_{NO}c_{NO}(x)c(z,x) - k_{Cl}c_{Cl}(x)c(z,x) \qquad (2)$$

The physical quantities from the above equation are [8]:

$D = 5.86*10^5$ cm^2 s^{-1} - ozone diffusion coefficient;
$J_{ox} = 6*10^{-3}$ s^{-1} - oxygen photodissociation coefficient;
$\alpha = 0.02$ km^{-1} - UV absorption coefficient of the oxygen;
$c_{ox} = 2*10^{17}$ cm^{-3} - steady-state oxygen concentration;
$k_{ox} = 9.56*10^{-16}$ cm^{-3} s^{-1} - constant rate {O_3,O} reaction;
$k_{oz} = 1.14*10^{-33}$ cm^{-6} s^{-1} - constant rate of the ozone creation;
$c_{nit} = 8.17*10^{17}$ cm^{-3} - steady-state nitrogen concentration;
$J_{oz} = 1.1*10^{-3}$ s^{-1} - ozone photodissociation coefficient;
$k_{OH} = 2.59*10^{-14}$ cm^{-3} s^{-1} - constant rate in {O_3,OH} reaction;
$c_{OH} = 1.5*10^6$ cm^{-3} - steady-state of the HO concentration;
$k_{NO} = 4.4*10^{-15}$ cm^{-3} s^{-1} - constant rate in {O_3,NO} reaction;
$c_{NO} = 10^9$ cm^{-3} - steady-state of the NO concentration;
$k_{Cl} = 9.08*10^{-12}$ cm^{-3} s^{-1} - constant rate in {O_3,Cl} reaction;
$c_{Cl} = 10^4$ cm^{-3} - steady-state of the Cl concentration.

Taking into account the steady-state value of the ozone concentration, calculated in [7], it results that the second and the third terms of the net ozone generation rate can be neglected being very small, and the net generation rate becomes:

$$G(z,x) = J_{ox}e^{-\alpha z}c_{ox}/2 - k_{HO}c_{HO}(x)c(z,x) - k_{NO}c_{NO}(x)c(z,x) - k_{Cl}c_{Cl}(x)c(z,x) = J_{ox}e^{-\alpha z}c_{ox}/2 - c(z,x)/\tau \qquad (3)$$

Following a procedure commonly used in the illuminated semiconductor p-n junction model, we have introduced τ as ozone life-time. The calculated value of the ozone life-time is 2.5 days, which seems to be a very reasonable value.

Let us consider now the one-dimensional problem in the altitude co-ordinate:

$$\frac{\partial^2 c(h)}{\partial h^2} = -\frac{J_{ox}c_{ox}}{2}e^{-\alpha(H-h)} + \frac{c}{\tau} \qquad (4)$$

with the boundary conditions

$$\int_0^H c(z)dz = c_0 H \qquad (5)$$

$$c(h_T) = 0 \qquad (6)$$

where H is the upper limit of the stratosphere and h_T is the tropopause location. c_0 is the global ozone concentration.

$$c(h) = \left(Lsh\frac{H}{L}\right)^{-1}\left[c_0 H - \frac{J_{ox}c_{ox}\tau}{\alpha(1-\alpha^2L^2)}\left(1-e^{-\alpha H}\right) - \frac{J_{ox}c_{ox}\tau L}{1-\alpha^2L^2}e^{-\alpha H}\left(ch\frac{H}{L}-1\right)\right]sh\frac{h-h_T}{L} - \frac{J_{ox}c_{ox}\tau}{1-\alpha^2L^2}e^{-\alpha H}ch\frac{h-h_T}{L} + \frac{J_{ox}c_{ox}\tau}{1-\alpha^2L^2}e^{-\alpha H}e^{-\alpha(h-h_T)} \qquad (7)$$

where $L^2 = D\tau$ is the ozone diffusion length. In Fig. 2 the theoretical calculations of the ozone vertical profile following the above equation is given together with a measured ozone profile [8].

The theoretical maximum location differs by the experimental one by 8 km, but recent measurements locate the maximum near to 30 km [9]. The differences that appear between the maximum concentration values are due to the fact that, in the theoretical model the steady-state value is used, while the measurements are done far to the steady-state conditions. The obtained value for ozone diffusion length is 165 km. That means that the attenuation of the ozone creation process depends only by the increase of the pollutants concentrations that leads to the decrease of lifetime τ.

As the parameters and one-dimensional equations of the two structures are so similar, the 2-D profile given in [6] can be used if pollutant concentrations are described by a function that depends on latitude.

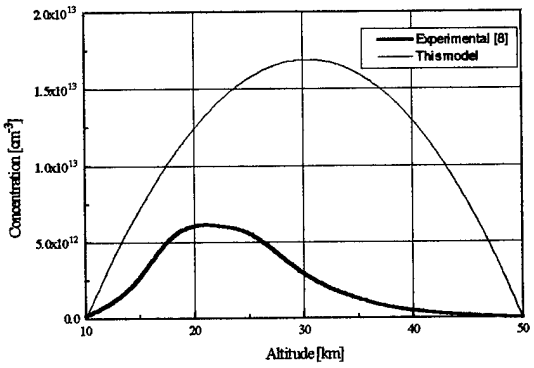

Fig. 2 - Ozone profile given by this model compared with the experimental data [8]

CONCLUSIONS

Using the physical analogy between the illuminated p-n junction and the stratosphere-troposphere system, an analytical expression for ozone concentration profile was deduced. This model should be very useful in order to establish a direct relation between the ozone layer thickness and the parameters of their evolution.

In the troposphere the measured ozone concentration is smaller by three magnitude orders due to pollutant "traps" from the troposphere.

Thus, the ozone vertical profile results:

REFERENCES

1. McEwan, M. J., Philips L. F., Chemistry of the Atmosphere, John Wiley & Sons, New York, 1975
2. James I.N., Introduction to the circulating atmospheres, Cambridge University Press, Cambridge, 1994
3. Rio Declaration on Environment and Development, Report of the United Nation Conference on Environment and Development, Rio de Janeiro, 3-14 June 1992, vol. I, Resolution Adopted by the Conference, U.N., New York
4. Caldararu F., Patrascu S., Caldararu M., Nicolaescu D., "Thermodynamically modelling of the ozone layer evolution", to be published in Rev. Roum. de Geophysique
5. Caldararu F., Nicolaescu D., Caldararu M., "Balance equations for UV solar spectrum using irreversible thermodynamics", presented at the Workshop organised by NATO Advanced Study Institute (ASI), 2-11 October 1995, Halkidiki, Greece
6. M. Caldararu, F.Craciunoiu, A.Paraschiv, D.Cristea, F.Caldararu, D.Dascalu, C.Klier, G.Mirea, A.Vasile, M.Nicolae, "Silicon Photodiode-Waveguide Coupling - Two-Dimensional Modelling, Software Simulation and Experiments", Solid State Electronics, Vol.39, No.11, 1996, pp.1649-1657
7. F. Caldararu, S. Patrascu, M. Caldararu, D. Nicolaescu, "Time Evolution of the Ozone Layer: Steady-State Conditions from Irreversible Thermodynamics Modelling", accepted at the Fourth SIAM Conference on Mathematical and Computational Aspects in the Geosciences, Albuquerque, New Mexico, USA, June 16-19, 1997
8. J. Levine, Editor, The Photochemistry of atmospheres, Earth, the Other Planets and the Comets, Academic Press, New York, 1985
9. F. Mencaraglia, A. Bonetti, P. Ciarpallini, M. Carlotti, F. Alboni, U. Cortesi and M. Ridolfi, "Stratospheric Composition from Balloon Based Measurements", Proceedings SPIE, Vol. 2311 "Atmospheric Sensing and Modelling", 1994, pp. 240-247

Spectral Identification of Coral Biological Vigour

Heather Holden and Ellsworth LeDrew
Waterloo Laboratory for Earth Observations
University of Waterloo, Waterloo, Ontario, Canada, N2L 3G1
519-888-4567 ext. 2689 (tel) 519-888-6768 (fax) hmholden@cousteau.uwaterloo.ca

Abstract --No quantitative means of remotely determining the biological vigour of a coral reef ecosystem exists. This renders consistent and replicable detection of coral health difficult. A quantitative index of submerged coral signatures would enable cost and time effective monitoring and management of coral reef resources, and would aid scientific studies of the extent and severity of coral bleaching. Principal components analysis is used to spectrally discriminate submerged bottom features, and broad band spectral albedos are used to estimate the SPOT and Landsat TM response.

INTRODUCTION

It is of immediate importance to increase our understanding of the mechanisms involved in coral bleaching as well as improve our ability to detect and monitor bleached coral via remote sensing techniques, as coral bleaching has recently been implicated as a harbinger of global climate change. Increased sea surface temperatures, a suggested consequence of global warming, is the main environmental cause of coral bleaching, or loss of essential photosynthetic algae from the coral polyp.

Our understanding of the global role of coral reefs is inadequate which suggests that a monitoring and mapping program is necessary, but has not yet been developed. Although less expensive than digital imagery, exclusive use of traditional surveying tools, such as topographic maps, nautical charts, existing aerial photographs and direct observations, may not be practical for monitoring large or remote coral reef ecosystems. Several researchers (Table 1) are attempting to develop an adequate coral reef mapping system based on remote sensing, but are impeded by issues such as effects of the intervening water column and spectral distinction of bottom types. There is great potential however, as demonstrated in other applications, for remote sensing to provide valuable information with respect to the geographic extent of coral reefs as well as biological vigour.

Table 1. Authors attempting to detect subsurface features, and the techniques used.

	TECHNIQUE
[1]	Supervised and unsupervised classification
[2]	Ratio processing algorithms, principal components analysis
[3]	BRIAN System; band ratios to separate depth and substrate type
[4]	Comparison with ground truth data and aerial photography, polar coordinate transformation, classification
[5]	Non-linear polar coordinate transformation, texture pseudo-channel, supervised classification
[6]	Eigenanalysis of in situ data to estimate bottom reflectance spectra for radiative transfer processes
[7]	Numerical transformation to decorrelate SPOT XS1 and 2
[8]	Laboratory study of remotely sensed laser induced fluorescence to monitor coral pigmentation
[9]	Eigenvector rotation of TM 1 and 2 to enhance bottom type variation and reduce the effect of water depth variation
[10]	Multivariate analysis of variance
[11]	Mathematical constraint to create residual representative of substrate reflectance
[12]	Integration with GIS
[13]	Supervised training classification
[14]	Optical correction of water column

Intuitively, healthy and bleached corals should have distinct spectral responses. A healthy coral possesses a photosynthetic pigment which provides the animal with its colour, but once that coral is placed under stress, it expels its pigment thus loosing its colour and becoming bleached. The hypothesis that bleached and healthy corals possess disparate spectral signatures is tested here. The spectral response of subsurface bottom features was measured with a hand held spectrometer while at depth on SCUBA, and compared using principal components analysis. Broad band albedos were calculated to represent the signal expected from Landsat TM and SPOT.

DATA COLLECTION AND METHODS

Spectral data were collected with a hand held spectrometer within a protected lagoon in Fiji under clear skies between 10:30 AM and 1:15 PM local time on 8 and 9 August 1996. The radiometer records reflectance at wavelengths from 341.5-1068.7nm with bandwidths of approximately 1.4nm. A submersible remote cosine receptor was used at the end of a 10m waterproof optical cable to enable measurement of substrate reflectance just above the target. The water column between the sensor and the target was thus assumed to be negligible, and no correction for attenuation was performed. Further, no calibration of the spectral data was necessary, as the values used in the analysis were reflectance values not radiance measures.

A hand-held sonar was used to record water depths that ranged between 2.7 and 2.8m which is a small range, so no correction was performed to account for differences in water attenuation between spectral measurements. A Global Positioning System provided geographic coordinates of 18°19.45'S, 178°06.48'E, and an underwater photographer identified and took a picture of each target measured for future reference. Twenty two spectra comprised the data set including healthy Acropora corals, dead coral debris, bleached Acropora corals and algae-covered dead corals.

0-7803-3836-7/97/$10.00 © 1997 IEEE

Principal components analysis (PCA) is a technique that transforms the original data set into a substantially smaller and easier to interpret set of uncorrelated variables that represents most of the information in the original data set [16]. Principal components (PCs) are derived from the original data such that the first PC accounts for the maximum proportion of the variance of the original data set, and subsequent orthogonal PCs account for the maximum proportion of the remaining variance, and so forth [15,16].

The purpose of this PCA is to (1) reduce the amount of data to representative spectra, and (2) attempt to relate the component spectra to coral health. An orthogonal transformation was applied to both data sets in this study which rotates the data to a new set of coordinate axes with component patterns that are more visually interpretable. A loading is calculated in PCA to describe how closely a particular spectra resembles or loads to the principal component.

RESULTS

The results of the principal components analysis revealed that the first two components explained nearly equal amounts of variance: 41.1% explained by PC1 and 40.9% explained by PC2. The spectra with the highest loading (0.922) to PC1 was measured over a healthy Acropora target, and the spectra with the highest loading (0.915) to PC2 was measured over a dead coral debris target. PC1 will therefore be called the healthy coral component, and PC2 will be called the dead coral component.

The PCA results are provided in Fig.1 where both the actual measured spectra and the computed component spectra are plotted. The measured spectra are in units of percent reflectance (left hand y-axis) and the computed component spectra are eigenvectors (right-hand y-axis).

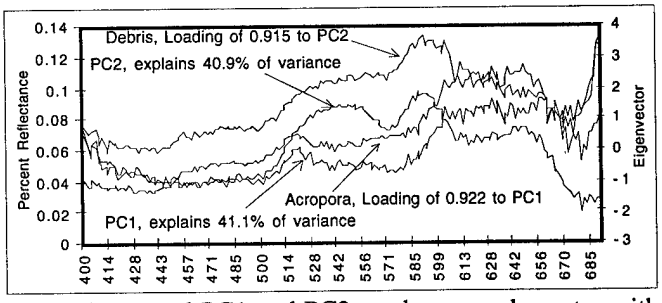

Fig.1. Computed PC1 and PC2, and measured spectra with the highest loadings to PC1 and PC2.

DISCUSSION

The separability of the healthy and dead coral spectra using principal components analysis suggests that it should be possible to remotely detect and delineate areas of submerged healthy and bleached coral. Although PC2, the dead coral component, is not an actual bleached coral measurement, the measured spectra of dead coral debris and bleached coral substrate are very similar with little variation. The average spectral reflectance of the nine bleached and dead coral samples was calculated and plotted in Fig.2 with an error range of one standard deviation also plotted. The greatest variability in reflectance among the bleached samples occurs at 600nm, but 0.19% is the maximum difference in reflectance among the nine samples. The discrepancy in spectral response may be due to the presence of macroalgae to varying degrees with respect to spatial coverage and density. No measurements were taken to quantify the macroalgae cover.

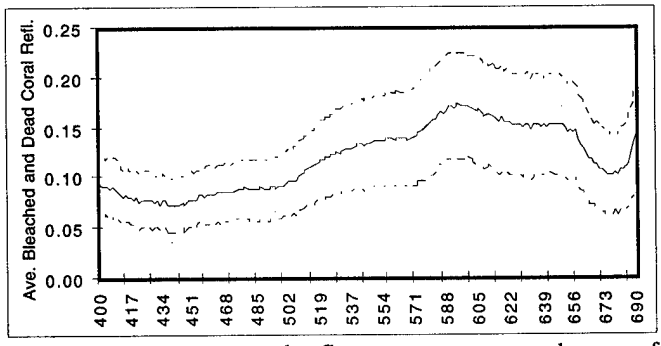

Fig.2. The average spectral reflectance response, and range of error within one standard deviation, of both dead and bleached coral.

The variability in spectral reflectance is even less for healthy Acropora targets than bleached and dead coral, as can be seen in Fig.3. The total number of healthy Acropora coral sampled was thirteen. The greatest variability in reflectance of healthy Acropora coral is 0.12% and occurs at 605nm. Further research is required involving a larger variety of sample targets, and a more controlled sampling procedure. A more controlled environment could be accomplished by using a tripod to maintain the cosine receptor at a consistent height above the target, and accounting for substrate reflectance contribution to the reflectance of a branching coral.

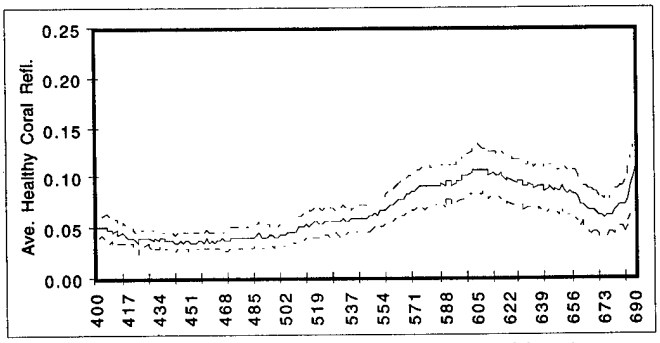

Fig.3. The average spectral reflectance of healthy Acropora coral targets with one standard deviation plotted on either side.

The plots of average spectral reflectance reveal that the major difference in response is in magnitude of reflectance

which is intuitive since a dead or bleached coral is white in colour. However, subtle reflectance peaks are present in the healthy coral spectra which are absent in the dead and bleached coral due to the presence of photosynthetic pigments in the living coral tissues. For example, there are small spectral peaks at approximately 485nm and 590nm present in the healthy coral spectra which are lacking in the bleached and dead spectra. Additionally, the principal components analysis detected subtle differences in spectral reflectance beyond the difference in magnitude. For example, a reflectance peak at approximately 520nm is present in the measured spectra with the highest loading to PC1 which is not present in the dead coral spectra as seen in Fig.1. Work is presently being done using derivative spectroscopy to further investigate these differences.

These subtle differences in pigment reflectance could be the basis of remote airborne detection using a high resolution spectroradiometer flown at low altitudes. The benefit of a spectroradiometer is that narrow reflectance peaks are detectable which would not be noticed with the use of broad bands. However, expected SPOT and Landsat TM broad band spectral albedos were calculated and plotted in Fig.4. Based on magnitude of reflectance alone, the signal captured by both satellite sensors from healthy coral and bleached coral appears to be discernible. By inspecting the photographs of the three bleached coral samples with the lowest reflectance, variable macroalgae cover can be seen which is less reflective than pure bleached coral. This variability may contribute to the confusion between partially bleached coral and dead or bleached coral which has been colonized by macroalgae.

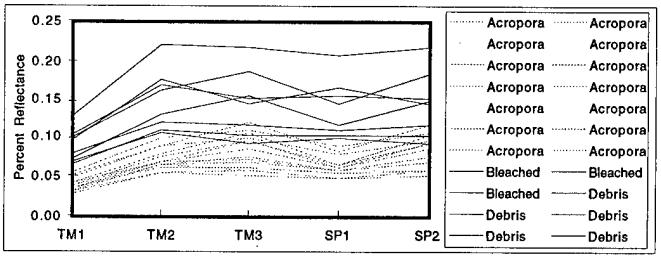

Fig.4. Broad band albedos calculated for SPOT XS 1 and 2, and Landsat TM bands 1-3. The solid black spectra correspond to bleached coral or dead coral debris, while the dotted gray spectra correspond to healthy Acropora corals.

Landsat TM bands 1 and 2 as well as SPOT XS1 provide good distinction based on magnitude of reflectance. The major problem to be overcome remains the confusion between healthy coral substrate, vegetation and deep water. Radiative transfer equations are presently being investigated for use in tropical coral reef environments to remove the confusing effects of the water column, so reflectance can be related solely to bottom type.

ACKNOWLEDGEMENTS

This research was supported by an NSERC grant to Ellsworth LeDrew. The authors are grateful to Drew Knight for technical support in the field.

REFERENCES

[1]R.Bina, K.Carpenter, W.Zacher, R.Jara, J.Lim. Coral Reef Mapping Using Landsat Data. Proc. 12th Int. Symp. Remote Sensing of Environment, Michigan. 2051-70, 1979.

[2]D.Lyzenga, Passive Remote Sensing Techniques for Mapping Water Depth and Bottom Features. Ap. Op. 17 (3), 379-383, 1978.

[3]D.Jupp, K.Mayo, D.Kuchler, D.Van Classen, R.Kenchington and P.Guerin. Remote Sensing for Planning and Managing the Great Barrier Reef of Australia. Photogrammetria. 40, 21-42, 1985.

[4]W.Bour, L.Loubersac and P.Rual. Thematic Mapping of Reefs by Processing of Simulated SPOT Satellite Data: Application to the Trochus niloticus Biotope, Marine Ecology, 34, 242-249, 1986.

[5]O.Vel, and W.Bour, The Structural and Thematic Mapping of Coral Reefs Using High Resolution SPOT Data, Geocarto Int. 2, 27-34, 1990.

[6]L.Estep, Eigenanalysis of Bottom Reflectance Spectra, Hydrographic Journal, 62, 1991.

[7]L.Loubersac, P.Burban, O.Lemaire, H.Varet and F.Chenon. Integrated Study of Aitutaki's Lagoon Using SPOT Satellite Data and *in situ* Measurements, Geocarto Int. 2, 31-7, 1991.

[8]J.Hardy, F.Hoge, J.Yungel, and R.Dodge. Remote Detection of Coral Bleaching Using Pulsed Laser Fluorescence Spectroscopy, Marine Ecology Prog. Series. 88, 247-255, 1992.

[9]M.Khan, Y.Fadlallah and K.Al-Hinai. Thematic Mapping of Subtidal Coastal Habitats in the Western Arabian Gulf using Landsat TM Data. Int J. Rem. Sen. 3 (4), 605-614, 1992.

[10]J. Luczkovich, T. Wagner, J. Michalek, and R. Stoffle. Discrimination of Coral Reefs, Seagrass and Sand Bottom Types from Space, Photo. Eng. and Rem. Sen. 59 (3), 385-9, 1993.

[11]P.Bierwirth, T.Lee, R.Burne, Shallow Sea Floor Reflectance and Water Depth Derived by Unmixing Multispectral Imagery. Photo. Eng. and Rem. Sen. 59 (3), 331-8, 1993.

[12]G.Borstad, R.Kerr, M.Zacharias. Monitoring Near Shore Water Quality and Mapping of Coastal Areas with a Small airborne system and GIS. Proc. 2nd Thematic Conference on Remote Sensing Marine and Coastal Environments, Louisiana. 2, 51-4, 1994.

[13]P.Mumby, M.Baker, P.Raines, J.Ridley, A.Phillips. The Potential of SPOT-pan imagery as a Tool for Mapping Coral Reefs. Proc. 2nd Thematic Conference on Remote Sensing Marine and Coastal Environments,Louisiana, 259-67, 1994.

[14]E.LeDrew, H.Holden, D.Peddle J.Morrow. Mapping Coral Ecosystem Stress in Fiji from SPOT imagery with *in situ* Optical Correction. Proc 26th Int Symp Remote Sensing of Environment, British Columbia, 581-584, 1996.

[15]G. Dunteman, Introduction to Multivariate Analysis. California: Sage Publishing, 1984.

[16]T. Fung, and E. LeDrew, Applications of Principal Components Analysis to Change Detection. Photo. Eng. and Rem. Sensing. Vol. 53 (12), 1649-1658, 1987.

A study of micro-scale disturbances associated with a shear layer in the lower atmosphere

Mini Praseedom Natarajan*[1] & Molly Issac**
**Department of Physics, All Saints College, Trivandrum, INDIA
*Block 701, #09-327, West Coast Road, SINGAPORE 120701.
Tel: 65 872 4167; Email:minipn@pacific.net.sg

Abstract – An investigation of the characteristics of the unstable modes around a shear region is carried out, using the Indian MST radar at Tirupati. The small-scale phenomena associated with the shear layer, existing in the lower atmosphere are brought out and presented in this paper.

INTRODUCTION

Remote sensing has become a widely used technique in the study of various atmospheric phenomena, in the recent years. Continuous observation of atmospheric wind motions have been carried out by means of laser radar [1], VHF [2] or UHF [3] radar, meteor radar [4], and partial reflection radar [5]. The MST (Mesosphere Stratosphere Troposphere) radar is an ultra-sensitive VHF or UHF radar, that make use of weak back-scattering arising from refractive index fluctuations in the neutral atmosphere, to measure the dynamical properties of the atmosphere, such as wind, waves, turbulence and atmospheric stability. The history of the MST radar dates back to 1974, when Woodman and Guillen first used the incoherent radar at Jicamarca to probe the lower atmosphere [6].

This paper deals with an investigation of the unstable modes around a shear layer. The study was carried out based on the wind velocity measurements made using the Indian MST radar, at Tirupati. The unstable regions were identified using the Richardson number criterion. The temporal evolution of Richardson number at three specified levels showed the existence of turbulence. Also, the critical levels were determined, and the propagation characteristics of some of the observed modes were brought out.

OBSERVATION

The horizontal and vertical wind velocity measurements in the troposphere were carried out using the National MST Radar Facility at Tirupati (13.47°N, 79.18°E), India. The MST radar at Tirupati is VHF phased array radar operating at 53MHz. The system was described earlier [7]. The observation scheme of the experiment and the method of evaluation of the wind velocity using the radar were described by the authors in their previous work [8]. The results presented in this paper are based on the horizontal wind velocity measurements made on March 18, 1992, using the MST radar at Tirupati.

DATA ANALYSIS

The vertical profile of the mean horizontal wind velocity measured for a height range from 3.75km to 9.00km, using the MST radar at Tirupati, during March 18, 1992, is depicted in fig.1. A casual perusal of the wind velocity profile showed a velocity maximum at 6.45km and a velocity minimum each at 5.10km and 7.65km. To check the stability at these layers, the Richardson number (Ri) was calculated at these layers, from 1543LT to 1650LT, at an interval of 90s. The Richardson number is given by the equation

$$Ri = N^2/[(dU/dz)^2 + (dV/dz)^2]$$

where N is the Vaisala-Brunt frequency and (dU/dz) and (dV/dz) represent the shear in the zonal and meridional winds, respectively [3].

The critical levels during the period of observation were searched for, by comparing the horizontal phase velocities and the mean horizontal wind velocities. At the critical level, the horizontal phase velocity of the wave equals the mean horizontal velocity. A critical level was observed at 5.85km for a wave of frequency $0.007875s^{-1}$ and vertical wavelength 1.05km. At the critical level, the background wind extracts energy from the wave motion. It is expected that this energy is used up to produce a region of high velocity somewhere above the critical level.

Now, a shear layer of thickness 900m was considered around 6.45km, where the wind shear was found to be a maximum. The lower boundary of the shear layer was set at 6.00km and the upper boundary at 6.90km. An investigation of the properties of the most probable unstable modes was carried out using the LE1976 model [9]. Two unstable modes were detected, which were designated as MI and MII. MI was the mode of frequency $0.006301s^{-1}$ and had a vertical wavelength of 0.875km. The mode MII had a frequency of

[1] Formerly at Department of Physics, University of Kerala, Kariavattom, Trivandrum, India 695 581.

0-7803-3836-7/97/$10.00 © 1997 IEEE

0.011029s^{-1} and a vertical wavelength of 1.05km. The possibilities of the detected modes to be propagating were studied using the critical wavelength, which is given by

$$\lambda_c = 2\pi (u - c) / N$$

where u is the mean horizontal velocity, c the horizontal phase velocity and N the Brunt-Vaisala frequency [10].

RESULTS AND DISCUSSION

A study of the wind velocity profile shows a minimum at 5.10km and 7.65km, and a maximum at 6.45km. Accordingly, a study of the Richardson number is carried out and these levels are found to be unstable. The temporal variation of Richardson number at these three levels is shown in fig.2. The variation of Richardson number with time shows that micro-scale activities existed in this region.

The region around 6.45km, is found to be unstable through out the period of observation. The Richardson number at this level is below 0.25, except at scan cycle 19, which represented 1620LT. During 1620LT, a jump in Richardson number is observed, but the value remained in the region where instability can be sustained. At 5.10km, though the instability persists for about 20 minutes, the level tends to be stable for very short periods. While carrying out the stability analysis at 7.65km, it is found that the level is fluctuating between stable and unstable conditions at short intervals, in the range of 3 to 7 minutes.

The Richardson number is an important criterion of dynamic stability for small-scale atmospheric motions. This parameter depends on the gradients of temperature and wind. The smaller the Richardson number, the less stable the flow with respect to shear instability. The most commonly accepted value for the onset of shear instability is Ri=0.25. Once turbulence is established within the shear layer, energetical considerations indicate that it should be sustained so long as Ri $\leq$1. Hence it is observed that at the 6.45km region, turbulence persisted for about one hour. The levels, 5.10km and 7.65km, oscillated between stable and unstable conditions for periods in the range of 3 to 7 minutes.

A critical level is observed at 5.85km, for a wave with a frequency of 0.007875s-1 and a vertical wavelength of 1.05km. At this level, the Richardson number is found to be very high. According to theory, when a wave encounters a critical level where the Richardson number is high, the wave is not transmitted further. The wave deposits its energy to the background wind and as a result, a velocity maximum is observed at a higher level. A study of the observed periodicities shows that the wave of frequency 0.007875s-1 and vertical wavelength 1.05km is not observed above the critical level, and due to the energy deposition, a velocity maximum is observed at 6.45km.

The properties of the two modes MI and MII are presented in table 1. It is found that MI is a propagating mode and radiates energy away from the shear layer. This is confirmed by determining the critical wavelength for the mode. The horizontal wavelength of the mode MI is found to be greater than its critical wavelength. The critical wavelength of the mode MII is greater than its horizontal wavelength. Hence, it is found that MII is trapped at the upper boundary. MI carries energy away from the shear layer and the lower value of growth rate confirms it. MII is an evanescent mode. The higher value of the growth rate shows that most of the energy carried by the wave is used for producing temporary growth of the disturbance around the shear layer.

Table 1 – The observed characteristics of MI and MII.

Characteristics	MI	MII
Frequency (s^{-1})	0.006301	0.11029
Vertical wavelength (km)	0.875	1.05
Phase velocity (ms^{-1})	2.465	2.541
Growth rate (s^{-1})	0.010103	0.01984
Critical wavelength (km)	2.029	1.986

CONCLUSION

An investigation of the properties of the unstable modes that existed around a shear region is carried out, based on the wind velocity measurements made using the Indian MST radar at Tirupati. The unstable modes that existed in between 3.75km and 9.00km are brought out. A study of the temporal evolution of the Richardson number shows the existence of turbulent structures, that has periodicities in the range of 3 to 7 minutes. The detection of a critical level explains the presence of the velocity peak at 6.45km. Also, two unstable modes are identified in the region of shear and their propagation characteristics are brought out.

The results presented in this work prove the capability of MST radar in studying the small-scale atmospheric phenomena in the lower atmosphere. The unstable regions in

the troposphere as well as the critical levels are brought out, thereby giving an idea of the wave propagation mechanism. The study of the unstable modes associated with the shear layer show that the mode with a smaller growth rate propagate energy away from the shear layer, while that with a greater growth rate tend to give up its energy as temporary disturbances. These results are based on the study carried out using the Indian MST radar. Thus the MST radar proves to be a powerful tool in the study of the dynamics of the lower atmosphere.

ACKNOWLEDGMENTS

The authors would like to thank Prof. S.R.P. Nayar, Dept. of Physics, and Dr. K Revathy, Dept of Computer Science, University of Kerala, for providing the necessary data for this work.

REFERENCES

[1] R.M. Huffaker, and R.M. Hardesty, "Remote sensing of atmospheric wind velocities using solid state and CO_2 coherent laser system," Proc. IEEE, vol.84, pp.181-204, 1996.

[2] B.B. Balsley, and D.A. Carter, "The spectrum of atmospheric velocity fluctuations at 8 and 86km," Geophys. Res. Lett., vol. 9, pp.465-468, 1982.

[3] S. Fukao, Y. Maekawa, T. Sato, and S. Kato, "Fine structure in atmospheric wind fluctuations observed by the Arecibo UHF Doppler radar," J. Geophys. Res., vol. 90, pp. 7547-7556, 1985.

[4] T. Aso, T. Tsuda, Y. Takashima, R. Ito, and S. Kato, "Observations of lower ionospheric wind dy the Kyoto meteor radar," J. Geophys. Res., vol.85, pp.177-184, 1980.

[5] A. H. Manson, C. E. Meek, and G. B. Gregory, "Gravity waves of short period (5–90 min) in the lower thermosphere at 52°N (Saskatoon, Canada):1978/79," J. Atmos. Terr. Phys., vol.43,pp. 35-43, 1981.

[6] R.F. Woohman, and A. Guillen, "Radar observations of wind and turbulence in the stratosphere and mesosphere," J. Atmos. Sci., vol.31, pp.493-505, 1974.

[7] P. B. Rao, A. R. Jain, G. Viswanathan, and S. K. Damle, "Indian MST radar in ST mode – an overview," Ind. J. Radio & Space Phys., vol. 23, pp. 1-5, 1994.

[8] K. Revathy, Mini Praseedom, and S. R. P. Nayar, "Short period fluctuations at low latitude tropospheric heights using MST radar," Ind. J. Radio & Space Phys., vol. 23, pp.12-20, 1994.

[9] D. P. Lalas, and F. Einaudi, "On characteristics of gravity waves generated by atmospheric shear layers," J. Atmas. Sci., vol. 33, pp. 59-69, 1976.

[10] J. C. King, S.D. Mobbs, M.S. Darby, and J.M Rees, "Observations of an internal gravity wave in the lower troposphere at Halley, Antarctica," Bound. Layer Meteorol., vol.39, pp. 1-13, 1987.

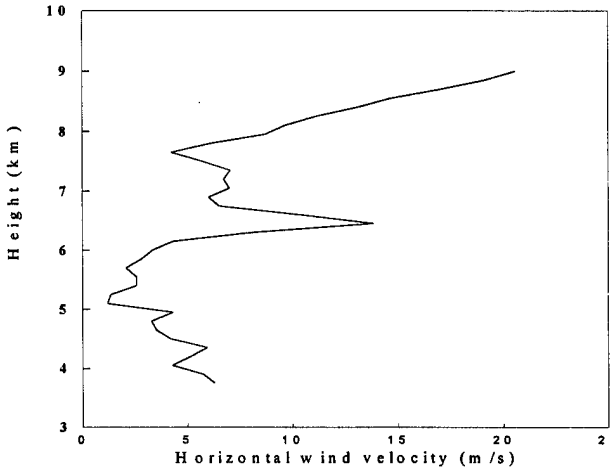

Figure 1. Vertical profile of the mean horizontal wind velocity

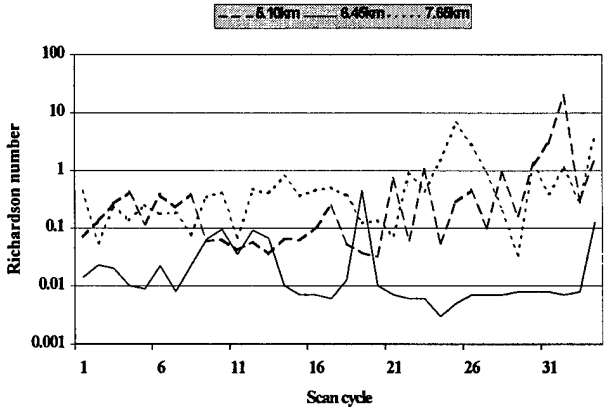

Figure 2. Temporal variation of Richardson number at (a) 5.10km, (b) 6.45km & (c) 7.65km

New Architectures for Remote Sensing Image Archives

K. Seidel[1], R. Mastropietro[2], M. Datcu[3]

[1] Swiss Federal Institute of Technology ETH Zurich, Institute for Communication Technology
Gloriastr. 35 CH-8092 Zurich
Phone + 41 1 632 5284, Fax + 41 1 632 1251, Email: seidel@vision.ee.ethz.ch

[2] Swiss Center for Scientific Computing CSCS
Via Cantonale, Galleria 2, CH-6928 Manno
Phone +41 91 610 8214, Fax +41 91 610 8383, Email: rmastro@cscs.ch

[3] German Aerospace Research Establishment DLR , German Remote Sensing Data Center DFD
Oberpfaffenhofen, D-82234 Weßling
Phone + 49 8153 28 1388, Fax + 49 8153 28 1448, Email: Mihai.Datcu@dlr.de

Abstract: Modern sensor systems have and are continuing to acquire data which serve as valuable information sources for scientists in multiple research and application disciplines. The intrinsic complexity of image data and their large volumes makes their archiving as "file systems" difficult and inefficient. We propose a unified treatment of the archivation of very diverse image products from the point of view of content-based picture query and retrieval systems.

INTRODUCTION

The intrinsic complexity of image data and their large volumes makes the archivation as "file systems" difficult and inefficient. Remote sensing was a privileged area, were queries can be specified by geographic area, time of acquisition or sensor type [7]. However, the latest developments in sensor technology, image interpretation, the enlargement of remote sensing application fields and the huge immensity of data acquired by the most recent generation of sensors make the "classical" archivation approaches unsatisfactory. Meanwhile, the developments in archivation facilities, computation power, and data communications changed the philosophy of both image users and owners [4].

NEW PERSPECTIVES

Image archives require both database systems and "vision capabilities", but a gap exists between these techniques. Classical databases, until recently, did not deal with multidimensional structures like pictures, and the vision systems were not designed to provide query and retrieval functions. Most existing image-databases have been created using some extensions of relational data models. Generally, the "content" of the images is described in a separate file and has a relational database representing the logical structures. The physical images are stored separately having, as a consequence, "rigid" manipulation systems. A better approach to deal with the image archivation problems is an integrated image analysis and/or pattern recognition sub-system in the retrieval system. The method is efficient for small archives and limited applications. The present trends in the field [3, 5, 8, 9] are mainly the inference of similarity measures for images, the integration of information representation and retrieval methods, and the synergy with cognitive systems.

The field of remote sensing, due to the very high image complexity and due to the huge volume of produced data, is one of the challenges of archivation technology. Only a few aspects of the query by image content have been approached and solved [1, 6].

Previous activities in remote sensing applications demonstrated that the main use of satellite data sets is for interdisciplinary, multitemporal or multisensor use. A frame of projects [11,12,13] was initiated with the goal to give solutions for several specific problems: presentation of comprehensive information about the data type leading the user to the right products for his application, easy access to thematic multisensor or multitemporal data, presentation of the information in an application suitable way, easy access to vaguely specified data, direct access to the original images, unified treatment of very diverse image products, easy and if possible fully automatic image database updating, substitution of archivation space with computation power for new products, elaboration of content-based picture retrieval systems.

The areas of investigation are: physical and logical representation of image data, image compression, stochastic and structural robust image feature selection, thematic image representation and understanding, pictorial abstract image representation, storage and access structures, definition of generic clusters and the associated algorithms for query processing, retrieval system specifications, interfaces and display of results, system architectures.

0-7803-3836-7/97/$10.00 © 1997 IEEE

QUERY & RETRIEVAL BY IMAGE CONTENT: PROBLEM FORMULATION

The problem formulation of the image content query and retrieval processes can be done from several perspectives and a short definition could not be sufficiently explanatory. For the goal of the present work we define it as *the process to find in an image archive the data which best suit to solve the user application.* It is an information retrieval problem and it is always a model based approach [10, 14]. We use the models as points of view over our data. Every model explains different features. A simple example is presented in Figure 1.

The query by image content is an inverse problem approached in a Bayesian way [2]. The I^{st} level of inference, model fitting, is implementd to extract thecharacteristic image features (Figure 1); the query by image content is the II^{nd} level of the Bayesian inference: the model selection. The query specification is analyzed and from a library of models the most likely ones to explain the query are selected (Figure 2). The prior evidence over the model space actually represents in an objective way the user interest in a certain application.

PROPOSED IMAGE ARCHIVATION SYSTEM

The methods for query by image-content we are implementing rely on:

1) A pyramidal representation of the image features as the basic strategy to discard, during the query, non-interesting images in a time efficient algorithm.

2) A hierarchical modelling approach used to link the semantic level of the query to image content (Figure 3). Three levels are defined:

a) modelling of the objective information content of the images; this is a pure signal processing approach;

b) conjecture modelling is the level which defines the adaptation to specific user applications, it transforms the evidence over the model space objectively;

c) the user application modelling explains the semantics of the query in the context of different applications.

The utilization of these strategies results in a scale dependent and user application dependent adaptive clustering of the archived images.

SUMMARY

We are developing image archives for remote sensing data, having as driving technology the methods of multidimensional signal modelling from an information theoretical perspective. The newly developed techniques are to be integrated in existing remote sensing image archivation systems with the aim to fill the gap between the logical and physical data representation.

REFERENCES

[1] S.A. Chien, H.B. Mortensen, 1996, "Automating Image Processing for Scientific Data Analysis of a Large Image Database", IEEE Tr. PAMI, Vol. 18, pp. 854-858.

[2] M. Datcu, 1996, "Scene Understanding from SAR Images", Proc. IGARSS '96, pp. 310-314.

[3] A. Dimai, M., Stricker, 1996, "Spectral Covariance and Fuzzy Regions for Image Indexing", BIWI Tech-Report, http://www.vision.ee.ethz.ch/cgi-bin/create_abshtml.pl?70.

[4] V.N. Gudivada, V.V. Raghavan, 1995, "Content-Based Image Retrieval Systems", IEEE Computer, Sept. 1995, pp. 18-22.

[5] A. Gupta, 1995, "Visual information retrieval technology, a Virage perspective", http://www.virage.com/wpaper/.

[6] G. Healy, A. Jain, 1996, "Retrieval Multispectral Satellite Images Using Physics-Based Invariant Representations", IEEE Tr. PAMI, Vol. 18, pp. 842-848.

[7] DLR-DFD, "ISIS - Intelligent Satellite Data Information System", http://isis.dlr.de/indexD.html.

[8] A. Pentland, R.W. Picard, S. Sclaroff, 1994, "Photobook: Tools for Content-Based Manipulation of Image Databases", Proc. SPIE, Vol. 185, pp. 34-47.

[9] R.W. Picard, T.P. Minka, M. Szummer, 1996, "Modeling user subjectivity in image libraries", Proc. IEEE Int. Conf. on Image Proc.

[10] H. Rehrauer, K Seidel, M. Datcu, 1997, "Multiscale Markov Random Fields for large image data-sets representation", in this Proc. IGARSS '97.

[11] K. Seidel, J.-P. Therre, 1994, "Remote Sensing Image Archive for National User Requirements", Proc. EEOS Workshop, ESA/JRC, http://www.vision.ee.ethz.ch/cgi-bin/create_abshtml.pl?37.

[12] K. Seidel, J.-P. Therre, 1995, "The Swiss National Remote Sensing Image Archive", Project description, http://www.vision.ee.ethz.ch/projects/Archive/RSIA_archive.html.

[13] K. Seidel, J.-P. Therre, M. Datcu, 1993/1994, "Advanced Query and Retrieval Techniques for Remote Sensing Image Databases", Project description, http://www.vision.ee.ethz.ch/projects/Archive/.

[14] M. Schroeder, K Seidel, M. Datcu, 1997, "Gibbs Random Field models for image content characterization", in this Proc. IGARSS '97.

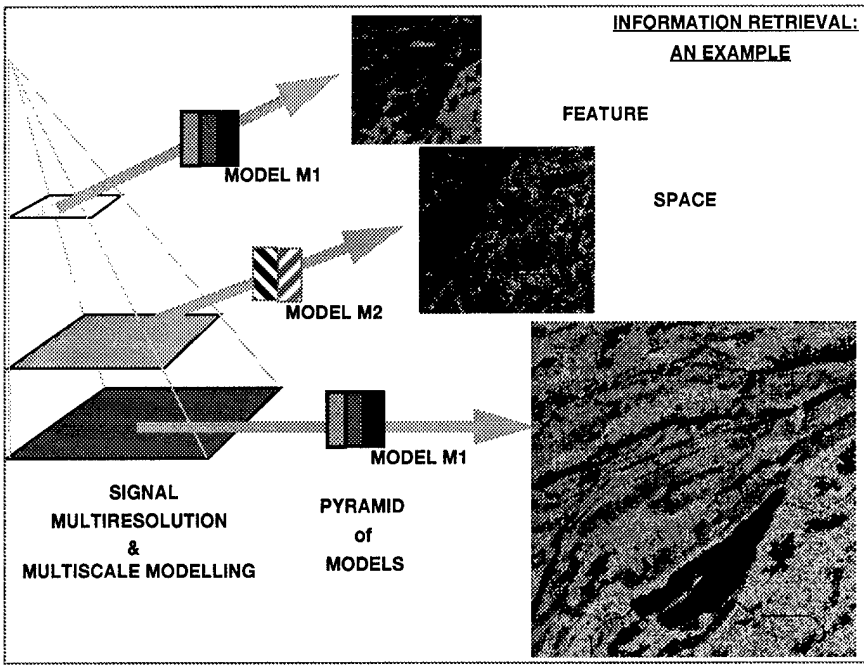

Figure 1: Information retrieval is always a model based approach. We use the models as points of view over our data. Every model explains different features. We exemplify how the utilization of two models (M1 [10] and M2 [14]) can explain the physically significant structures at multiple scales: pixel, pixel neighbourhood, and scene scale. The same scene is analyzed at several resolutions. M1, at coarse scale understands the image as being composed from large areas: agriculture, mountains, forest and lake. At intermediate scale, M2 recognizes the orientation of the agriculture parcels, and at the finer scale M1, again, explains this time, the pixel classes. The pyramidal representation of the image features is an important issue: it is the base for the strategy to discard during the query the non-interesting images in a time efficient algorithm.

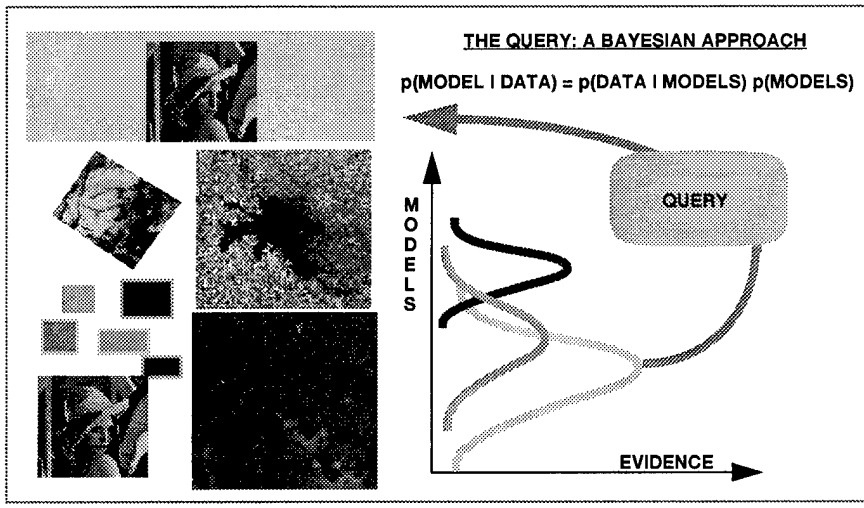

Figure 2: The query by image content is an inverse problem approached in a Bayesian way. The previous example (Fig.1) is the I^{st} level of inference: model fitting; the query by image content is the II^{nd} level of the Bayesian inference: model selection. The query specification is analyzed and from a library of models the most likely ones to explain the query are selected. With high probability, the reader will select from the small collection of images in the left column the one having the highest visual evidence: Lena. The prior evidence over the model space actually represents in an objective way the user interest in a certain application.

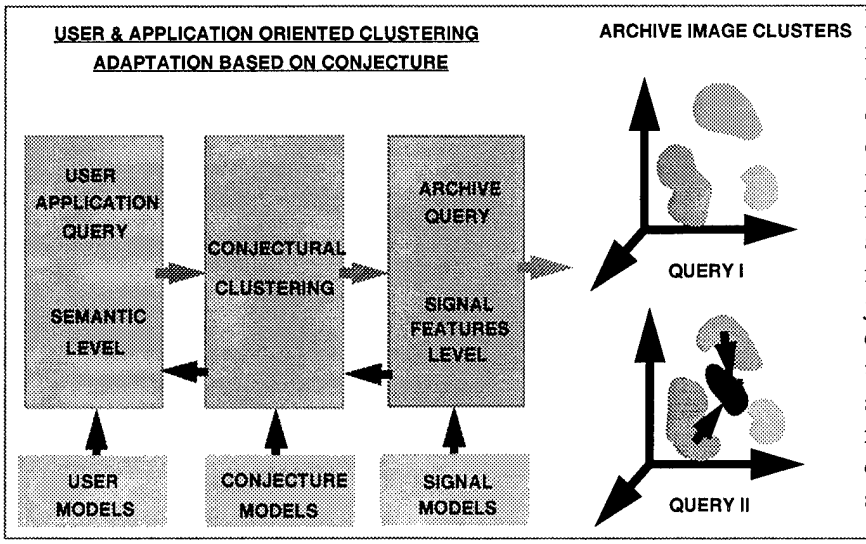

Figure 3: A hierarchical modelling approach is used to link the semantic level of the query to image content. Three levels are defined: a) objective modelling of the informational content of the images; this is a pure signal processing approach (Fig.1); b) conjecture modelling is the level which defines the adaptation to specific user applications, it makes the evidence over the model space objective (Fig. 2); c) the user application modelling explains the semantics of the query in the context of different applications: i.e. the same images could have very different meanings in an ecological or military application. The result of this strategies in the image space is a dynamic scale/application clustering.

Conference Author Index

A

Abdou, W. 1743
Abenant, E. 2015
Abou-El-Magd, A.M. 1458
Adair, M. 380
Adam, N. 1341
Adamovic, M. 1066, 1382
Adragna, F. 1533
Adrian, V. 1150
Afifi, M.S. 133
Ahmad, S. 1418
Ahmed, I. 1627
Aiazzi, B. 1054, 1990,
Ainsworth, T.L. 1371, 1407, 1716
Al-Ghamdi, A.G. 133
Alba, P.S. 1990
Aler, J. 1015
Alexandrov, V. 1681
Alparone, L. 1054, 1184, 1990, 2066
Alpers, W. 1162, 1518, 1521, 1527
Alumbaugh, D.L. 929, 933
Anbazhagan, S. 29
Andreadis, A. 1993
Andrianasolo, H.H. 1627
Andrick, B. 1947
Angino, G. 15, 374, 990
Antar, Y.M.M. 1594
Antonischki, G. 1805, 1820
Aoki, S. 1582
Arai, K. 553
Arkhipkin, O. 281
Armand, N.A. 347, 1953
Arnold, D.V. 386
Arthern, R.J. 1823
Askari, F. 1521
Askne, J. 793, 800
Asmus, V. 1681
Aspinall, R.J. 269
Atkinson, N.C. 1395, 2011
Auer, T. 1224
d'Auria, G. 2087, 2100
Awaka, J. 1633
Axelsson, S.R.J. 79, 317

B

Bachelier, E. 1606
Baerwald, W. 1022
Bai, Y. 1938
Bakar, S.B.A. 1069
Baker, J. 1796
Bakhanov, V.V. 350
Balababa, L. 1084
Baldina, E.N. 347
Baldini, L. 1454
Baldy, S. 6
Bali, S. 948
Bamler, R. 865, 1710
Bang, K. 237
Banik, B. 1066, 1382
Baquero, M. 1871
Barbieri, K. 1923
Barczi, J.F. 784, 787
Barducci, A. 888
Baraldi, A. 67
Barni, M. 1184
Baronti, S. 1054, 1990, 2066
Bartoloni, A. 325, 1908, 1853
Basili, P. 2087, 2100
Bauer, P. 1275
Beaudoin, A. 784, 787
Benediktsson, J.A. 501, 913, 1026, 1669
Benelli, G. 1993
Benger, S.N. 272
Bennett, J.C. 1211
Benz, U. 322, 2024
Berendes, T. 32
Bergen, K.M. 1072
Berthod, M. 1347
Bertoia, C. 402
Bessafi, M. 6
Betti, M. 1184
Betty, C.L. 1600
Beyth, M. 743
Bhatia, R.C. 1129
Bhogal, A.S. 670, 677
Bicheron, P. 165, 556
Bickel, D.L. 1545
Bittner, M. 1495
Blanchard, A.J. 643
Blindow, N. 227
Bobylev, L.P. 830, 1681
Bodechtel, J. 533, 743
Boechl, R. 1022
Boehnke, K. 1823. 1826
Boerner, W-M. 1401, 1591
Bogatyrev, S.D. 350
Boisvert, J. 1376
Bolen, S. 1114
Bonafoni, S. 2100
Bonn, F. 122, 189
Borderies, P. 1606
Borgeaud, M. 898, 1606
Borri, G. 1054
Bostater, Jr., C. R. 881
Botti, J.A. 692
Bradley, Q. 677
Bradshaw, B. 1766
Brandfaß, M. 2024
Braumann, H. 1935
Breit, H. 465
Brennan, K. 1624
Breton, E. 652
Brewster, A. 1766
Bricaud, A. 825
Bringi, V.N. 954, 1114, 1458
Brisco, B. 1376, 1430
Browell, E.V. 1969
Brown, C.G. 353, 1847
Bruegge, C. 1743
Brummer, B. 1162
Bruniquel, J. 1044, 1560, 1868
Brunzell, H. 1285
Bruzzone, L. 764, 1202
Buckley, J.R. 1015
Bullock, M.E. 1350
Burgess, D.W. 1075
Burnett, C.N. 84
Buscaglione, F. 18
Busu, I. 1398

C

Cabarrocas, D. 2069
Caetano, M. 240, 680
Calahan, R.F. 1444
Caldararu, F. 607
Caldararu, M. 607
Calhoun, J. 922
Calkoen, C. 1320
Calvet, J-C. 1090
Campagnolo, M.L. 680
Campbell, W. 819
Caraglio, Y. 784
Carla, R. 2066
Carswell, J.R. 1001
Casanova Roque, J.L. 87
Casarano, D. 719, 898, 1272
Casciati, F. 113
Casey, K. 2008
Castagnas, L. 784
Castanie, F. 293
Castel, T. 784, 787
Cavalieri, D.J. 1291
Ceballos Silva, A.P. 2041
Ceccato, P. 1569
Celani, C. 325
Cervino, M. 1908
Chae, H.S. 517, 528
Chan, H.L. 484, 487
Chan, P. 1255
Chan, T-K. 1138
Chandrasekar, V. 954, 1114, 1458
Chane-Ming, F. 581
Chang, A.T.C. 625
Chang, L.A. 1969
Chang, L.Y. 1424
Chang, P. 1009
Chanzy, A. 1090
Chapman, B. 104
Charlebois, D. 670
Chellappa, R. 171
Chen, A.J. 1424
Chen, C.F. 1424
Chen, C.H. 1190
Chen, C.T. 1199
Chen, F-C. 1474
Chen, J. 1862
Chen, J.M. 165
Chen, K-S. 806, 1199, 1208, 1365, 1368, 1424
Chen, P. 963, 1084, 2038
Chen, S. 938
Chenerie, I. 1606
Cheng, P. 839

Cherniakov, M. 1282
Chesters, D. 984
Chew, W.C. 938, 945, 1474
Chiu, T. 901
Choi, H-K. 136
Choi, K-H. 524
Choi, S.D. 1492
Chou, J. 32, 1760, 1911
Christopher, S.A. 32, 116, 1923
Chu, A. 1358
Chuah, H.T. 1069, 1421, 1427
Chuah, T. 996
Chubb, S.R. 1317, 1521, 1692
Chuideri, A. 1663
Cihlar, J. 165
Ciotti, P. 2087, 2100
Clark, B. 1947
Clemente-Colon, P. 505
Cloude, S.R. 1411, 1591, 1926, 1932
Cloutier, C. 1382
Colandrea, P. 1853
Coll, C. 1233
Collaro, A. 433
Coltelli, M. 1022
Comiso, J.C. 857, 1300
Conel, J.E. 1743
Connors, V.S. 116
Console, E. 646
Cook, M.S. 1814
Cooley, J.H. 1666
Cooley, T. 1654
Cooley, T.W. 1666
Cooper, A.L. 1317, 1692
Coppo, P. 904
Cornillon, P. 2008
Corsini, G. 1536
Costamagna, E. 655
Coster, W. 2024
Cottis, P.G. 1379
Cracknell, A.P. 1398
Crawford, M.M. 457, 667
Croci, R. 18
Crowther, P. 328, 1689
Cubero-Castan, E. 2060
Cuccoli, F. 1975
Cumming, I. 725, 731, 1704

D

Dai, X. 243, 1029, 1763
Daida, J.M. 1808, 1811
Daley, N. 670, 677
Dall, J. 1018
D'Amelio, C. 1853
Dams, R.V. 1350
Danduran, P. 1678
Daniels, D.J. 1278
Dano, E. 1168
Dargaud, G. 833
Darovskikh, A. 1675
da Silva, J.C. 1335
Datcu, M. 255, 258, 411, 616, 767, 2031
Davidson, G.W. 865
Davis, A. 1444
Davis, C.H. 397
Davis, H.B. 692
De Carolis, G. 719, 862
De Grandi, G. 1038, 1047, 1371, 1414, 1725, 1890
Dech, S.W. 1495, 1505
Deering, D. 165, 1787
Del Frate, F. 2097
Dell'Acqua, F. 1463
Dellepiane, S.G. 737, 907, 1174
Demarez, V. 1566
Deng, Y. 367
Derksen, C. 1672
Deroin, J-P. 1612
Desjardins, R. 207, 252
Desnos, Y-L. 722
Diani, M. 1536
Dias, J.M.B. 773
Dinardo, S.J. 1466
Dinesh, M.S. 521
Ding, K.H. 919
Dionisio, C. 987
Dmitriev, W.V. 1480
Dobson, M.C. 119, 1072, 1180, 1621, 1719
Doi, K. 1582
Donald, G.E. 275
Donato, T. 1521
Dong, Y. 891, 1057, 2054
Donlon, C.J. 2002
Donnelly, W.J. 1001
Douglass, A.R. 542
Downey, I.D. 370, 1569
Dozier, J. 628, 1451
Du, L.J. 1407
Ducrot, D. 1566
Dupont, S. 1347
Durden, S.L. 1466, 1639, 1642
Dymond, J.R. 1075

E

Early, D.S. 1838, 1844
Eck, T. 165
Ecklund, W.L. 1753
Edelstein, W.N. 1466
Edwin, J.M. 29
Efremenko, V.V. 1953
Eibert, T.F. 227
Eineder, M. 1341
El-Khattib, H.M. 197
El-Mowelhi, N.M. 197
El-Salam, A.A. 197
Emery, W.J. 1502, 1509, 2002
Emmett, C.F. 1557
Endoh, T. 414
Engdahl, M. 1081
England, A.W. 1096
Engman, E.T. 1093, 1269
d'Entremont, R. 1220
Erbe, E. 625
Erickson, J. 1654
Ermakov, S.A. 1335, 1530
Escalante, B. 38
Espedal, H.A. 1165, 1168
Esteban, H. 1871
Estevan de Quesada, R. 1361
Evans, D.L. 1734
Evans, R. 2008
Evtuchenko, A. 1126
Ewe, H.T. 1069, 1427

F

Facheris, L. 1975
Fairall, C.W. 2090
Fedor, L.S. 1001
Feng, Y. 216
Ferger, O. 21
Fermont, A. 95
Fernandez, D.M. 1808, 1811, 1814
Ferrazzoli, P. 1618
Fetterer, F. 402
Fischer, H. 1686
Fischer, K. 1808
Fishtahler, L.E. 1249
Fjortoft, R. 2060
Flasse, S.P. 1569
Fleig, A. 171
Fleury, D. 1678
Flood, B. 1214
Floury, N. 784, 787, 1560, 1868
Fornaro, G. 433, 451, 878
Forster, B. 891, 1057, 1576, 2054
Fortuny, J. 1871
Foster, J.L. 625
Franceschetti, G. 433, 878, 1701
Franchois, A. 925
Fraser, D. 1657
Frasier, S. 1539, 1972
Freeman, T. 104
Frei, M. 743
French, J. 1460
Frisch, A.S. 2090
Frison, P-L. 1832
Frolind, P-O. 436, 797, 1214
Fuchs, J. 714
Fujimura, S. 658, 975
Fujino, Y. 1941
Fujisaka, T. 966
Fujita, M. 1941
Fujiwara, S. 1585
Fukuda, S. 1187
Fullerton, K. 1660
Fung, A.K. 702, 1144, 1308, 1365, 1376, 1600
Fung, T. 836
Furseth, D.A. 1063
Furuya, K. 481
Fusina, R.A. 1317

G

Gabella, M. 3
Gader, P. 643
Gage, K.S. 1753
Gaillard, C. 122, 1787
Gaiser, P.W. 1009
Gaitley, B.J. 1743
Galati, G. 833, 1123
Galloway, J. 1012, 1460
Gamba, P. 113, 655, 1463
Garcia, F. 38
Garello, R. 1515, 1678, 2069
Garzelli, A. 1184, 1993
Gasiewski, A.J. 1001, 1006
Gastellu-Etchegorry, J.P. 1566, 1787
Gautam, N.C. 1775
Gelautz, M. 468
Georges, T.M. 1802
Ghinelli, B.M.G. 1211
Gibeaut, J.C. 457, 667
Giorgi, F. 113
Giorgini, F. 737
Giros, A. 652
Giuli, D. 1454, 1975
Goblirsch, W. 439
Goetz, A.F.H. 1385
Gogineni, S.P. 996, 1305
Goh, K.C. 813
Goldblat, V.Y. 1530
Gong, P. 895
Gonzales, A.E. 246
Gonzalez-Alonso, F. 87
Goodberlet, M. 1012
Goodenough, D.G. 84, 664, 670, 677
Goodison, B. 1672
Gorishnya, Y.V. 1105
Goto, S. 210
Gough, P.T. 471, 1588
Gowda, K.C. 521
Grandell, J. 622
Greidanus, H. 1078, 1320
Grim, R.J.A. 1078
Grinder-Pederson, J. 1018
Grischenko, V.D. 1681
Grunes, M.R. 1038, 1716
Guerreiro, L. 1618
Guglielmi, V. 293
Guillevic, P. 1787
Guneriussen, T. 631, 634
Guo, H. 746, 749
Guo, Y. 731, 845
Gurgel, K-W. 1805, 1820
Gustavsson, A. 797, 1214
Gutierrez, R. 457
Gutman, G. 1252
Guzzi, R. 1908
Gwyn, J. 128

H

Ha, Y-L. 524
Haboudane, D. 128, 189
Haddad, Z.S. 1639, 1642
Haefner, H. 640
Hagen, J.O. 634
Haimov, S. 1460
Hall, D.K. 619, 625
Hallikainen, M. 622, 637, 803, 1081, 1314, 1597, 1874
Haltrin, V.I. 296, 299, 595
Hamran, S-E. 634
Hamre, T. 1681
Han, Q. 1760, 1911
Han, Y. 2093
Hanada, T. 1486
Hanado, H. 1645
Hansen, P.E. 1808, 1811
Hansen, V. 227
Hanssen, R. 1710
Hara, Y. 966, 1392
Hardin, P.J. 511, 1557, 1563, 1835
Harlan, J.A. 1802
Hartnett, J. 328
Hatzopoulos, J.N. 1920
Hausknecht, P. 1022
Hautecoeur, O. 556, 1230
Hawkins, D.W. 471
Hawkins, R.K. 1066, 1382
Hay, G.J. 84, 664
He, Y. 356
Heer, C. 990, 993
Heidebrecht, K.B. 1385
Heikkonen. J. 1660
Hellmann, M. 1411
Hellsten, H. 797, 1214
Helmlinger, M.C. 1743
Heng, A. W-C. 734
Heng, W-C. 1518
Hennings, I. 1320
Hensley, S. 628, 1358
Hensley, W.H. 1545
Herland, E-A. 1344
Herries, G.M. 1032
Herzog, A. 951
Heygster, G. 58, 61, 1675
Hiernaux, P. 1832
Hill, M.J. 269, 275
Hilliard, L. 984
Hilmarsson, O. 1026
Hirosawa, H. 1187
Ho, A.T.S. 1996
Hock, L. 1512, 1850
Hodges, J. 1227
Hoeben, R. 1365, 1368
Hoekman, D.H. 1078, 1728, 1731
Holden, H. 610, 809, 885
Holecz, F. 448, 1929
Holloway, P.E. 1331
Homer, J. 1579, 2063
Honda, K. 1829
Hong, D. 237
Hong, S. 89, 92, 1793
Hook, S. 1233
Hope, A. 1766
Horie, H. 1645
Horn, R. 1022
Hornbostel, A. 1126
Horrell, J. 2015
Hoyano, A. 1239
Hsieh, C-Y. 702
Hsu, A. 1266, 1269
Hsu, M-K. 70, 806
Hu, B. 1220
Huadong, G. 50, 1978
Huang, C. 171
Huang, K-Y. 1196
Huang, S. 1999
Huang, X. 249
Huang, Y. 536
Huete, A.R. 98, 341, 1966
Hugh, Q. 128
Huimin, P. 1477
Hunewinkel, T. 417
Hunt, B.R. 1588
Hwang, L. 1996
Hwang, P.A. 1156, 1171
Hyman, A. 1227
Hyyppa, H. 1081
Hyyppa, J. 1081

I

Ignatov, A. 1252
Iguchi, T. 1111, 1117, 1633, 1636
Iino, A. 1239
Iisaka, J. 916
Im, E. 1642
Imanaka, M. 1899
Imhoff, M.L. 1624
Impagnatiello, F. 15, 374
Inanaga, A. 125, 969
Inggs, M. 490, 2015
Ingimundarson, J.I. 913
Inkinen, M. 1081
Iodice, A. 1701
Irion, Jr., H.G. 1132
Irisov, V.G. 2093
Irisov, V.I. 1001
Isaac, M. 613
Ishida, H. 9
Ishimaru, A. 1138
Ismail, S. 1969
Israelsson, H. 800, 1878
de Iulis, M. 1275
Ivanov, A.Y. 539
Iwamoto, M. 966

J

Jackman, C.H. 542
Jackson, T.J. 1093, 1099
Jacobs, G.A. 1156, 1171
Jaja, J. 174
Jansen, R.W. 1317
Jefferies, W.C. 1063
Jenkins, A.D. 1165

Jensen, R.R. 1557, 1563, 1835
Jensen, V. 1165, 1698
Jenstrom, D. 984
Jezek, K. 1305
Jha, R. 1382
Jia, X. 778
Jiang, J. 392, 1609, 1981
Jiang, X. 816
Jiang, Z. 474
Jianguo, N. 55
Jin, M.Y. 477
Jin, Y-Q. 405, 567, 2050
Johannessen, J.A. 1153, 1165, 1168
Johannessen, O.M. 1153, 1165, 1168, 1681, 1698
Johnsen, H. 631
Johnsen, K-P. 1675
Johnson, D.R. 688, 699
Johnson, P.E. 1847, 1856
Jonsson, T. 797, 1214
Jung, I-S. 524, 584
Jyo, Y. 1205

K

Kadygrov, E.N. 2093
Kahn, R. 698, 1743
Kalb, M. 688, 699
Kalluri, S.N.V. 171, 174
Kalma, J.D. 1263
Kam, S.P. 1084, 2038
Kamble, V.P. 1129
Kamiya, Y. 1392
Kanagaratnam, P. 1305
Kanellopoulos, I. 1660
Kanellopoulos, J.D. 1379
Kanevsky, M.B. 1530
Kao, M. 377
Karaev, V.Y. 1530
Karlinsky, T.W. 386
Kasilingam, D. 35, 1193, 1512, 1524, 1527, 1695, 1850, 1862
Kato, Y. 481
Kattenborn, G. 1087
Kattleman, R. 1451
Kaufmann, H. 743
Kawabata, K. 966
Kawai, Y. 2005
Kawamura, H. 1499, 1865, 2005, 2075
Kawanishi, T. 1630
Kawata, Y. 210, 1790, 1899, 1902, 2084
Kazakov, V.I. 350
Kellndorfer, J. 1180, 1719
Kelly, R. 1460
Kemarskaya, O.N. 350
Kemppinen, M. 1224
Kennedy, K.D. 957
Kennedy, W.D. 938
Kerr, Y. 1090
Khazenie, N. 685
Khoo, V. 35, 127, 151, 845, 848, 1512, 1695, 1850
Khorram, S. 243, 1029, 1763, 1769
Kijashko, S.V. 1335
Kim, J. 89
Kim, K-O. 24, 584
Kim, K.E. 528
Kim, K.H. 331
Kim, K.S. 200
Kim, M.S. 200, 850
Kim, S.J. 517
Kim, T. 1492
Kim, Y. 1358, 1404
Kimura, F. 1865
Kimura, H. 442
Kindel, B. 1385
Kitiyakara, A. 1639
Kiyasu, S. 975
Kjellgren, J. 1962
Klein, A.G. 619
Kliche, D.V. 32, 116
Kloster, K. 1681
Knapp, E. 1001
Knight, D. 809
Knizhnikov, Y.F. 347
Knulst, J.C. 1168
Kobayashi, T. 570, 1389
Koike, K. 1582
Kojima, M. 1630
Komiyama, K. 481
Kondo, N. 1392
Kong, J.A. 787
Koponen, S. 1314
Korsbakken, E. 1153, 1165
Koskinen, J. 44, 637
Kostina, V.L. 2047
Kozu, T. 1111, 1117, 1630, 1636
Kravtsova, V.I. 347
Kriebel, S.K.T. 1035
Krishnan, P. 598
Krovotyntsev, V.A. 1681
Kryvobok, O. 2044
Kubo, M. 414
Kudo, J-I. 1499
Kuga, Y. 1138, 1141
Kumagai, H. 1111, 1633
Kuo, K-S. 32, 1917
Kuroiwa, H. 1630
Kurvonen, L. 622, 1874
Kusaka, T. 210, 972, 1902, 2084
Kusanobu, S. 649
Kutuza, B.G. 1126
Kuze, H. 55
Kwarteng, A.Y. 119
Kwoh, L.K. 151, 213, 249, 454, 813, 1257, 1548
Kwok, R. 505

L

Ladd, D.N. 1648
Lahtinen, J. 1597
Laing, T.W. 341
Lakshmi, V. 1102
Lam, J.H. 380
Lanari, R. 433, 451, 878
Lang, R. 925
Larsson, B. 797, 1214
Lau, W.K.M. 1438
Laurore, L. 21
Lawrence, G. 1350
Lawrence, W.T. 1624
Le Caillec, J.M. 1515
Le Toan, T. 719, 784, 787, 898, 1272, 1560, 1606, 1868
Le Vine, D.M. 377
Leberl, F. 468
Leblanc, S.G. 165
Ledeboer, W.C. 1743
LeDrew, E. 610, 809, 885, 1672
Lee, B.G. 331
Lee, C.W. 92
Lee, H-G. 575, 850
Lee, J-H. 331, 524
Lee, J-Y. 524
Lee, J. 89, 1793
Lee, J.S. 1038, 1047, 1199, 1371, 1407, 1414, 1716
Lee, J.T. 92
Lee, K-H. 588
Lee, K. 200, 850
Lee, S. 661
Legarsky, J. 996
Leggeri, G. 374
Lei, Q. 533
Lemmems, M.J.P.M. 423
Leon, D. 1460
Leone, A. 3
LeQuere, P. 207, 252
Leroy, M. 165, 556, 1230, 1787
Leshkevich, G.A. 505
Lettvin, E. 1859
Leung, P.S. 380
Leusky, V. 2093
Leveau, J. 581
Leysen, M. 1047, 1725, 1890
Li, F. 1466, 1639
Li, G. 498, 511, 740
Li, L. 1009
Li, M. 249, 389
Li, S. 427, 683, 999, 1987
Li, X. 1220
Li, Z-J. 1144
Li, Z. 408
Liang, S. 174, 1781, 1959
Liao, J. 746
Liao, M. 204
Lichtenthaler, H.K. 1799
Liew, S.C. 734, 813, 848, 963, 1084, 1548, 1560, 1914, 2038
Lightstone, L. 154
Likht, F.R. 601
Lim, H. 213, 454, 734, 813, 1084, 1518, 1527, 1548, 2038
Lim, I. 445
Lim, O.K. 213

Lim, P. 722
Lim, T.K. 35, 1527, 1695
Lin, C.C. 548, 1150
Lin, C.S. 302
Lin, I-I. 35, 151, 845, 1512, 1527, 1695, 1850
Lin, Y-C. 151, 1887
Liou, Y-A. 1096
Litovchenko, K.T. 539
Liu, A.K. 505, 1441
Liu, H. 1749, 1966
Liu, J. 1120
Liu, Q.H. 942, 1147
Liu, W.T. 1435, 2082
Liu, Y.S. 389
Liu, Z. 427, 683, 999, 1987
Llewellyn-Jones, D. 308, 311
Lobanov, V. 806
Logar, A. 1947
Loh, K.F. 1418
Lolli, S. 904
Lombardini, F. 1536
Long, D.G. 246, 353, 386, 1557, 1563, 1835, 1838, 1841, 1844, 1847, 1856, 2063
Longstaff, I.D. 1282, 1579
Looyen, W. 370, 1078
Lopes, A. 758, 761, 1044, 2060
Lopez, J.M. 1361, 1871
Lopez, J.R. 38
Lord, R.T. 490
Lou, Y. 1358, 1404
Lu, D. 1120
Lu, Y.H. 445
Luca, D. 411
Luchinin, A.G. 1335
Lucht, W.W. 1220
Luckman, A. 1796
Lukowski, T.I. 1066, 1382
Lunden, B. 317
Luneberg, E. 1401, 1591
Luntama, J.P. 1314
Luo, R. 160
Luscombe, A.P. 154, 1063
Lyu, J-W. 1489
Lyzenga, D. 1168

M

Ma, K.K. 1996
Macelloni, G. 940, 1260
Madsen, S.N. 1018, 1358
Mahdi, S. 990
Mahmood, A. 1217
Mahmood, N.N. 1418
Mahootian, F. 695, 854
Makynen, M. 637, 803
Maldonado, L. 1404
Malingreau, J.P. 1725
Mancini, M. 1263, 1365, 1368
Mango, S.A. 1521
Manian, V. 335
Marandi, S.R. 493
Marazzi, A. 113, 655, 1463
Marcus, T. 1291
Marinelli, L. 21
Marshak, A. 1444
Marthon, P. 2060
Martin, T. 1878
Martin-Neira, M. 1470
Martonchik, J.V. 1743
Martuccelli, A. 737
Marzano, F.S. 2087, 2100
Massonnet, D. 652, 1338, 1533
Mastropietro, R. 616
Masuda, K. 9, 1893, 1896
Masuda, T. 1941
Masuko, H. 570, 1389
Mathieu-Marni, S. 171
Matsuura, K. 73, 414
Mattia, F. 719, 898, 1272
Mattikalli, N.M. 1093
Matwin, S. 670
Maupin, P. 207, 252
Mavrocordatos, C. 1470
Mayaux, P. 1725
Mazzetti, P. 1454
McIntosh, R.E. 1001, 1460, 1466, 1539, 1753, 1972
McNeill, S. 2057
Meagher, J. 2063
Mecocci, A. 113, 655
Meier, E. 1929
Meisner, R.E. 1495, 1505
Melentyev, V.V. 1681
Meloni, G.P. 67
Melville, W.K. 711
Mendez, R. 38, 128
Meneghini, R. 1636
Metternicht, G.I. 95, 338, 674
Miao, J. 58, 61
Miche, J.A. 1799
Michel, T. 448
Micosa, A.G. 125
Migliaccio, M. 1701, 1853
Milekhin, L.I. 359
Milekhin, O.E. 1681
Miller, T. 1404
Milne, A. 1057, 2054
Milne, A.K. 1433, 1573, 1624
Miner, G.F. 386
Minh, V.Q. 1084, 2038
Mirbagheri, M. 1576
Mishkin, V. 41
Mitchell, B.G. 825
Mitchell, G. 1060
Mitnik, L. 70, 601, 806
Mitnik, M.L. 70
Mitomi, Y. 2075
Mitteregger, E. 468
Mittermayer, J. 2021, 2028
Miura, T. 98
Mochi, M. 1908
Moctezuma, M. 38
Moghaddam, M. 1881, 1884
Molinaro, F. 581
Moller, D. 1539
Moran, M.S. 98
Moreira, A. 451, 2021, 2024, 2028
Moreira, J. 869, 1929
Morisette, J.T. 1769
Mott, H. 1401
Mouchot, M.C. 207, 252, 646, 1678
Mougin, E. 1832
Mourad, P.D. 1159
Moyssidis, M.A. 1379
Muchoney, D.M. 1227
Mukai, S. 9, 1896
Mukaida, A. 2075
Muller, G. 1162
Muller, H.J. 1603
Mura, F. 987
Murakami, M. 1585
Muralikrishna, I.V. 1772,
Murali Krishna, I.V. 1778
Muramoto, K. 73
Muratova, N. 281
Myers, R.J. 692

N

Nagabhushan, P. 521
Nahamura, H. 1585, 2075
Nakaoka, N. 649
Natarajan, M.P. 613
Nativi, S. 1454
Nault, J. 819
Navarro, A. 240
Navarro, P. 1569
Nazarenko, D.M. 1060
Nedlin, G.M. 1692
Nemoto, Y. 1392
Nerushev, A.F. 359
Nesti, G. 904, 1361, 1871
Neuenschwander, A.L. 667
Newman, G.A. 929, 933
Nezry, E. 758, 1044, 1051, 1087, 2035
Ng, C.S. 445
Ng, J. 848
Nghiem, S.V. 505
Nichol, J. 278, 813
Nicolaescu, D. 607
Niemann, K.O. 84, 664
Nirchio, F. 325
Nishii, R. 649, 658
Nitta, K. 1585
Nogami, Y. 1205
Nolf, S. 116
Nonin, P. 1347
Noon, D.A. 1282
Nualchawee, K. 1829
Nuesch, D. 1929
Nygaard, K. 1947

O

O'Leary, E. 1404
O'Neill, K. 1135, 1288
O'Neill, P. 1099, 1266, 1269
Oaku, H. 1389, 2075
Odegard, R. 634
Oelke, C. 1311, 1686
Oguma, H. 978
Oh, Y. 708
Ohkura, T. 125
Ohno, C. 1392
Iwamoto, M. 1392
Oikawa, K. 1630
Oikawa, S. 308
Okamoto, K. 1633, 1636
Okumura, T. 1899
Oleson, K.W. 1509
Omatu, S. 1205
Omura, M. 1582
Ong, J.T. 1757
Onstott, R.G. 177, 1294, 1808, 1811
Oricchio, M. 987
Oristaglio, M.L. 945
Oury, S. 1651
Ozawa, S. 1585

P

Padoin, M. 1454
Paduan, J.D. 1814
Paek, K.N. 528
Paget, R. 2063
Pairman, D. 2057
Paloscia, S. 1260
Pampaloni, P. 904, 1260
Pan, R. 498
Pantani, L. 1953
Papathanassiou, K.P. 1022, 1411, 1716, 1926, 1932
Paraschiv, A. 607
Pariman, D. 1075
Park, M.E. 92
Park, S.K. 136
Parkes, I. 308, 311
Parlange, M.B. 1099
Parmiggiani, F. 67, 862
Paronis, D.K. 1920
Pasquali, P. 448, 1929
Pasquariello, G. 719, 1272
Patrascu, S. 607
Pavan, G. 833, 1123
Pavlakis, P.J. 1332
Pazmany, A. 1460
Pelinovsky, E. 1331
Pellegrini, P.F. 981
Peloquin, S. 128, 189
Penaloza, M. 1947, 1950
Pendlebury, S.F. 1689
Peng, R. 1645
Perez, C. 397
Perona, G. 3
Peterson, D.L. 957
Petrenko, B.Z. 359, 383
Petrou, M. 737
Pettersson, L.H. 1681
Philpot, W. 1243
Phinn, S. 1766
Piau, P. 293
Piazza, E. 981
Picard, G. 787
Pichel, W.G. 505
Pichon, G. 1347
Pick, D.R. 1395
Piepmeier, J.R. 1001, 1006
Pierce, L. 1072, 1180, 1246, 1621, 2053
Pierdicca, N. 2087, 2100
Piesbergen, J. 640
Pilorz, S.H. 1743
Pineiro, Y. 925
Pinelli, G. 1536
Pinna Nossai, R. 2087
Pippi, I. 888, 1953
Podesta, G. 2008
Poiares Baptista, J.P.V. 1275
Pollard, B.D. 1972
Porter, D.L. 1539
Posa, F. 719, 898, 1272
Poujade, V. 21
Preston, M.I. 770
Pritt, M.D. 872, 875
Provvedi, F. 18
Puglisi, G. 1022
Pulliainen, J. 622, 637, 803, 1874

Q

Quegan, S. 770, 781, 1041
Quek, W. 963
Quigley, D. 711
Quinones, M.J. 1728

R

Ra, J-W. 136, 1489
Racette, P. 984, 1737, 1969
Raimadoya, M.A. 1569
Ramasamy, S.M. 29
Ramesh Babu, I. 1778
Randriambelo, T. 6
Rango, A. 625
Ranson, J. 1269
Ranson, K.J. 460, 1722
Rao, S.R. 1129
Rawls, W.J. 1099
Rayer, P.J. 1395
Reagan, J.A. 1749
Redley, I. 308
Regas, D. 714
Rehrauer, H. 255
Reigber, A. 869, 1022, 1716
Remond, A. 1612
Remund, Q.P. 1841
Renouard, L. 1347
Reulke, R. 1022
Ribbes, F. 1560
Ricard, M.R. 667
Riccio, D. 1701
Richards, S.L 1847
Riggs, G.A. 619
Rim, S. 89, 1793
Ritter, M. 711
Rivard, L.A. 128
Robertson, A.E. 386
Rodenas, J.A. 2069
Rodin, A. 41
Roenko, A.N. 2047
Romanov, A. 41
Romeiser, R. 1320, 1326
Romero, G. 1404
Rondal, J.D. 125
Rosen, P.A. 1585
Rouvier, S. 1606
Royer, A. 189
Rozanov, V.V. 1905
Rozenberg, A. 711
Rudolf, H. 1551
Ruisi, R. 904
Rundberg, W.B. 957
Russo, G. 833
Ruzek, M. 688, 699
Ryu, J.A. 517

S

Saatchi, S. 104, 1881
Sadowy, G.A. 1466
Saito, H. 73
Sakaida, F. 1499
Sakane, M. 972
Sakurada, Y. 55
Sakurai-Amano, T. 916
Samuel, P. 1698
Sandven, S. 1681
Sano, E.E. 98
Sano, I. 9, 1896
Sansosti, E. 433, 451, 878
Santalla del Rio, V. 1594
Santos, J. 240
Sarabandi, K. 901, 1887
Sasaki, M. 9
Sasano, Y. 2078
Satake, M. 570, 1389, 1941
Satalino, G. 1272
Sato, T. 1477, 1645
Satoh, C. 966
Sattchi, S. 1890
Sausa, R.C. 2103
Scarchilli, G. 1123
Schaaf, C.B. 1220
Schattler, B. 465
Scheele, M. 1022
Scheiber, R. 451, 1022, 1554, 2028
Schiavon, G. 1618, 2097

Schistad Solberg, A.H. 157
Schlick, T. 1805
Schlott, M. 1935
Schlueter, N. 61
Schmidt, R. 417
Schmitt, K. 1713
Schmugge, T. 1099, 1233, 1236
Schmullius, C.C. 1734
Schneider, T.L. 1466
Schnepf, N.G. 1808, 1811
Schoeberl, M.R. 542
Schou, J. 1041
Schroeder, M. 258
Schroth, A. 1126
Schuler, D. 1047, 1371, 1407, 1414
Schumann, R.L.G. 1829
Schwarz, G. 2031
Scott, J.C. 1335
Seguin, G. 536
Seidel, K. 255, 258, 411, 616
Sekelsky, S.M. 1753
Selige, T.M. 101, 1032, 1784
Serafini, C. 1908
Sergievskaya, I.A. 1335, 1530
Serpico, S.B. 764, 1202
Sery, F. 761, 1044
Shaari, A.T. 1069
Shah, A. 180
Shan, Y.Y. 1757
Shay, E.L. 692
Shay, L.K. 1817
Shchegol'kov, Y.B. 1335, 1530
Shepherd, J.D. 1075
Shi, J. 628, 1193, 1269, 1451
Shih, S.E. 919
Shikada, M. 210, 1899
Shimada, M. 570, 1389, 1585, 2075
Shimoda, H. 2072
Shin, J. 1793
Shmalenyuk, A.S. 347
Siddiqui, K.J. 1944
Sieber, A.J. 1361, 1551, 1871
Sigismondi, S. 1260
Silberstein, D. 1444
Silva, T.A.M. 773
da Silveira, M. 2015, 2018
Simaan, M.A. 261, 559
Simard, M. 1725, 1890
Simeonsson, J.B. 2103
Singh, K. 213, 454, 1548
Singhroy, V. 752
Siqueira, P. 104
Sisk, T.D. 1624
Sivaprakash, S. 848
Skiles, J.W. 957
Skotnicki, W. 1404
Slatton, K.C. 457
Slob, S. 192
Small, D. 448
Smirnov, V.G. 1681
Smith, G. 793
Smith, J. 1395
Smits, P.C. 737, 907, 1174
Snider, J.B. 2090
Soh, L-K. 1177
Solaiman, B. 207, 252
Solberg, R. 631
Solhaug, J. 1681
Sommer, S. 189
Song, H. 1938
Song, J. 474
Song, Y.S. 528
Souleres, E. 545
Souma, T. 311
Souyris, J.C. 719, 898, 1272, 1606, 1868
Spivak, L. 281
Srivastava, S.K. 1063, 1066, 1382
St-Onge, B. 207, 252
St.Germain, K. 1009, 1291
Stacy, N.J.S. 728
Standley, L. 1654
Staples, G.C. 1060
Stapleton, N. 1335, 1530
Steel, A. 1660
Steinbrecher, U. 465
Steinnocher, K. 910
Stenstrom, G. 797, 1214
Stephen, H. 1829
Stephens, G.L. 1466
Stephens, K. 180
Stephenson, J.R. 370
Stephenson, R. 370
Stephenson-Hawk, D. 180
Stevens, D. 722, 725
Stickley, G.F. 1282
Stock, L. 1300
Stockman, S. 685
Stone, R.N. 505
Stow, D. 1766
Strahler, A. 1220, 1227
Straka, M. 945
Stramski, D. 821, 825
Strapp, J.W. 1458
Strobl, P. 1022
Strozzi, T. 790
Sturm, J.M. 705
Stussi, N. 454, 813, 1548, 1560
Su, Z. 1365, 1368
Subhash, N. 1799
Sugimoto, N. 2078
Sugita, M. 284
Suinot, N. 545, 548, 1150, 1470
Sultan, N. 536
Sun, B. 24
Sun, G. 460, 1269, 1722
Sun, X. 168
Supit, I. 1051
Susini, S. 1993
Susskind, J. 1102
Suzuki, Y. 210
Sveinsson, J.R. 501, 913, 1026, 1669
Swift, C. 1001, 1012, 1297

T

Tadross, M. 862
Takagi, M. 916
Takamata, K. 2084
Takashima, T. 1893
Takemata, K. 1790
Takemura, K. 1477
Takeuchi, N. 55
Takeuchi, S. 107, 969, 1707
Talipova, T. 362, 1331
Tamba, S. 305, 308, 311
Tan, B.T.G. 734
Tan, F.Y. 963
Tanaka, D. 55
Tanaka, S. 658
Tanelli, S. 1975
Taniguchi, N. 1902
Tanner, A.b. 1466
Tarchi, D. 904, 1551
Tassan, S. 825
Tateiba, M. 184, 1486
Taylor, V. 1404
Teague, C.C. 1808, 1811
Teague, W.J. 1156, 1171
Teany, L.D. 1382
Teixeira, F.L. 945
Tennant, K. 1350
Teo, N.L. 848
Terehov, A. 281
Tesauro, M. 433, 451, 878, 1554
Testud, J. 1651
Thames, P.S. 1509
Thepaut, I. 1678
Thompson, D.G. 386
Thomson, K.P.B. 1890
Thurai, M. 1648
Ticehurst, C. 891, 1057, 2054
Tikhonov, V.V. 1108
Timchenko, A.I. 230, 1105
Timofeyev, Y.M. 562, 1905
Tishkovets, V.P. 230
Tjuatja, S. 1144, 1308, 1600
Tobita, M. 1585
Todo, M. 442
Toh, J. 845
Tomiyasu, K. 1615
Tommasini, M. 981
Torma, M. 44
Torre, A. 990
Torricella, F. 1908
Toutin, T. 839
Townshend, J.R.G. 171, 174, 1781
Trang, A.H. 1132
Tretter, W. 743
Treuhaft, R.N. 1881, 1884
Trichon, V. 1566
Triesky, M.E. 1969
Trinder, J.C. 1576
Troch, P.A. 1263, 1365, 1368
Trohkimovski, Y. 1323
Tsai, F. 1243

Tseng, D. 264, 1999
Tseng, R-S. 806
Tseng, W.Y. 505, 1441
Tseng, Y.C. 1208
Tulin, M.P. 714
Tungalagsaikhan, P. 1505
Tuong, T.P. 1084, 2038
Tuzlukov, V.P. 139
Tzeng, Y.C. 1096, 1199

U

Ulaby, F. 119, 1072, 1180, 1621, 1719
Ulander, L. 436, 797, 800, 1214, 1878
Um, G-M. 588
Umehara, T. 1389
Usai, S. 1542
Uttal, T. 2090

V

Vaccaro, R. 1174
Vali, G. 1460
van Leeuwen, W.J.D. 341, 1966
Van Zyl, J. 1358, 1404
Vandemark, D.C. 1001
Vanska, T. 803
Varfis, A. 1660
Vasilyev, A.V. 1905
Vasilyev, Y.F. 2047
Vasquez, R. 335
Vazouras, C.N. 1379
Velten, E. 993
Vernazza, G. 764
Vesecky, J. 1811, 1808, 1859
Vincent, N. 545, 548, 1470
Viswanathan, G. 1129
Vogelzang, J. 1320
Voigt, S. 1929
Volden, E. 157, 631
Volkov, A.M. 1681
Vuorela, A. 1344

W

Wadhams, P. 862
Wahl, T. 47
Walessa, M. 767, 2031
Walker, J.P. 1263
Wan, W. 1657
Wang, C. 746, 749
Wang, D.W. 1171
Wang, H. 142
Wang, J. 895, 1269, 1737, 1969
Wang, L. 1609
Wang, M. 116, 1923
Wang, T. 945
Wang, X. 749
Warner, R.A. 819
Waseda, T. 714
Wasrin, U.R. 1560
Watanabe, M. 125
Weger, R.C. 1917
Wegmuller, U. 790
Wehrman, M.J.G. 101
Weiss, J.M. 32, 160
Welch, R.M. 32, 116, 160, 1760, 1911, 1917, 1923, 1947, 1950
Welch, S. 714
Wensink, G.J. 1320
Wenzel, O. 1799
Wergin, W. 625
Werner, C. 790
West, J.C. 705
Westwater, E.R. 1001, 2093
Wever, T. 743
Wėydahl, D.J. 287
Wiesbeck, W. 1713
Wiesmann, A. 1675
Wigneron, J.P. 1090
Willgoose, G.R. 1263
Williams, J.B. 370
Williams, M.L. 755
Williams, R.N. 328, 1689
Wilson, C.L. 1648
Wilson, S.H.S. 1395, 2011
Wilson, W.J. 1466
Winebrenner, D.P. 1823
Winker, D.M. 1740
Wiscombe, W. 1444
Wismann, V. 1823, 1826
Wolfe, J. 1382
Wong, F. 722, 725, 731
Wood, E.F. 1266
Wu, J. 24, 1609
Wu, P. 1865
Wu, S-H. 1144
Wu, S.Y. 1441
Wu, T.D. 1365
Wynn, W.M. 1483

X

Xia, Y. 743
Xiao, W. 216
Xinqiao, L. 50
Xu, K. 389
Xu, W. 1704
Xue, Y.L. 389, 1987

Y

Yakam-Simen, F. 758, 1051
Yamagata, Y. 978Yamanouchi, T. 73
Yamazaki, A. 1899
Yamazaki, Y. 2084
Yang, K. 171
Yang, S-K. 1923
Yang, X. 219
Yang, Y.K. 584
Yanow, G. 951, 960
Yanquen, X. 55
Yasumoto, M. 9
Yasuoka, Y. 284
Ye, C-S. 588
Ye, J.P. 402
Yeo, T.S. 445, 484, 487
Yin, Z. 677
Ying, X. 145, 232
Yocky, D.A. 1545
Yoder, B.J. 1884
Yokoyama, R. 305, 308, 311
Yonezawa, C. 107, 1707
Yoshida, M. 125
Yoshikawa, M. 658, 1205
Yu, H. 145, 232
Yu, J.J. 781
Yun, C. 816
Yun, S. 50, 1430

Z

Zagolski, F. 122, 1051, 1566, 1787
Zagorin, G.K. 359
Zahn, R. 1935
Zamaraev, B.D. 2047
Zelli, C. 15, 18
Zeng, Q. 408
Zhang, C.B. 445
Zhang, G. 1141
Zhang, L. 1120
Zhang, Q. 222
Zhang, R. 35, 168, 222, 1695, 1956
Zhang, X. 1981
Zhang, Y. 392, 842
Zhang, Z. 174, 204, 845
Zhao, J. 356
Zhao, K. 58
Zhao, L. 963
Zhou, B. 1524
Zhou, N. 389
Zhou, P. 1144
Zhu, M. 740, 1938
Zhu, M.H.
Zhu, S. 1996
Zhu, X. 498, 740
Zhu, Z. 168
Zion, M. 1266
Ziskin, D.C. 1255
Zuikova, E.M. 1335, 1530
Zwally, H.J. 857